

X-RAY IMAGING

Fundamentals, Industrial Techniques, and Applications



Taylor & Francis

Taylor & Francis Group

<http://taylorandfrancis.com>

X-RAY IMAGING

Fundamentals, Industrial Techniques, and Applications

Harry E. Martz, Jr.

Lawrence Livermore National Laboratory, Livermore, CA, USA

Clint M. Logan

Pleasanton, CA, USA

Daniel J. Schneberk

Lawrence Livermore National Laboratory, Livermore, CA, USA

Peter J. Shull

The Pennsylvania State University, Altoona, USA



CRC Press

Taylor & Francis Group
Boca Raton London New York

CRC Press is an imprint of the
Taylor & Francis Group, an **informa** business

CRC Press
Taylor & Francis Group
6000 Broken Sound Parkway NW, Suite 300
Boca Raton, FL 33487-2742

© 2017 by Taylor & Francis Group, LLC
CRC Press is an imprint of Taylor & Francis Group, an Informa business

No claim to original U.S. Government works

Printed on acid-free paper
Version Date: 20151209

International Standard Book Number-13: 978-0-8493-9772-1 (Hardback)

This book contains information obtained from authentic and highly regarded sources. Reasonable efforts have been made to publish reliable data and information, but the author and publisher cannot assume responsibility for the validity of all materials or the consequences of their use. The authors and publishers have attempted to trace the copyright holders of all material reproduced in this publication and apologize to copyright holders if permission to publish in this form has not been obtained. If any copyright material has not been acknowledged please write and let us know so we may rectify in any future reprint.

Except as permitted under U.S. Copyright Law, no part of this book may be reprinted, reproduced, transmitted, or utilized in any form by any electronic, mechanical, or other means, now known or hereafter invented, including photocopying, microfilming, and recording, or in any information storage or retrieval system, without written permission from the publishers.

For permission to photocopy or use material electronically from this work, please access www.copyright.com (<http://www.copyright.com/>) or contact the Copyright Clearance Center, Inc. (CCC), 222 Rosewood Drive, Danvers, MA 01923, 978-750-8400. CCC is a not-for-profit organization that provides licenses and registration for a variety of users. For organizations that have been granted a photocopy license by the CCC, a separate system of payment has been arranged.

Trademark Notice: Product or corporate names may be trademarks or registered trademarks, and are used only for identification and explanation without intent to infringe.

Library of Congress Cataloging-in-Publication Data

Names: Martz, Harry E., 1957- author. | Logan, Clint M., 1941- | Schneberk, Daniel J., 1942- | Shull, Peter J., 1957-
Title: X-ray imaging : fundamentals, industrial techniques, and applications / authors, Harry E. Martz, Clint M. Logan, Daniel J. Schneberk, and Peter J. Shull Taylor & Francis.
Description: Boca Raton : Taylor & Francis, CRC Press, 2017. | Includes bibliographical references and index.
Identifiers: LCCN 2015047891 | ISBN 9780849397721
Subjects: LCSH: Radiography, Industrial.
Classification: LCC TA417.25 .M37 2017 | DDC 620.1/1272--dc23
LC record available at <http://lccn.loc.gov/2015047891>

Visit the Taylor & Francis Web site at
<http://www.taylorandfrancis.com>

and the CRC Press Web site at
<http://www.crcpress.com>

Contents

Preface.....	xiii
Acknowledgments.....	xv
Authors.....	xvii
Chapter 1 Introduction to Nondestructive Evaluation	1
1.1 A Brief History of NDE, NDT, and NDC.....	1
1.2 Application of NDE to Life Cycle Management.....	6
1.3 X-Ray and γ -Ray Imaging in Context	6
1.4 Other (Than X-Ray and γ -Ray or Energetic Particle) NDE Methods	9
1.4.1 Electromagnetic Radiation Methods	9
1.4.1.1 Optical Testing with Visible Photons	10
1.4.1.2 Thermal or Infrared Imaging	12
1.4.1.3 Gigahertz–Terahertz Waves (Microwaves and Millimeter Waves).....	14
1.4.2 NDE Methods Using Acoustic Energy	16
1.4.2.1 Ultrasonic Testing.....	16
1.4.2.2 Acoustic Emission	17
1.4.3 NDE Methods Using a Tracer	18
1.4.3.1 Dye Penetrant Testing.....	18
1.4.3.2 Magnetic Particle Inspection	18
1.4.3.3 Leak Testing	20
1.4.4 Other NDE Methods	20
1.4.4.1 Eddy Current NDE	20
1.5 Effectiveness and Statistics of NDE.....	21
1.5.1 Probability of Detection	21
1.5.2 Positive Predictive Value and Negative Predictive Value	21
1.5.3 Receiver Operating Characteristic Curve	23
1.6 When and How Much NDE	24
1.7 Industrial X-Ray Imaging Contrasted with Medical X-Ray Imaging.....	24
Chapter 2 X-Ray History	27
2.1 History Introduction	27
2.2 Laying the Foundation.....	27
2.3 Discovery of X-Rays.....	29
2.4 The Morning After	34
2.5 Discovery of Radioactivity	36
2.6 Radiation Therapy	38
2.7 Coolidge Tube.....	38
2.8 Computed Tomography	39
2.9 Industrial Computed Tomography.....	40
2.10 Radiation Accidents.....	41

Chapter 3	The Role of X-Ray and γ -Ray Imaging.....	43
3.1	Introduction	43
3.2	Where X-Ray and γ -Ray Imaging Excel	43
3.3	Where X-Ray and γ -Ray Imaging Fall Short	48
3.4	Practical and Operational Issues	53
3.5	Summary	53
Chapter 4	Physics of X-Ray and γ -Ray Sources	55
4.1	Introduction	55
4.2	Types of High-Energy Photons: X, γ , and Annihilation Radiation.....	55
4.2.1	Electrons and X-Ray Radiation Generation	57
4.2.1.1	Bremsstrahlung (Braking or Decelerating Electrons)	62
4.2.1.2	Characteristic X-Rays.....	64
4.2.1.3	Accelerating Charge	65
4.2.2	The Nucleus and γ -Ray and X-Ray Generation	66
4.2.3	Annihilation Radiation Generation.....	70
4.2.4	Units Used to Characterize and Describe High-Energy Photons	70
Chapter 5	High-Energy (X-Ray and γ -Ray) Photon Interactions with Matter.....	73
5.1	Introduction	73
5.2	Attenuation and Phase Contrast	73
5.2.1	Attenuation: Photoelectric Absorption, Scatter, and Pair Production	76
5.2.1.1	Absorption (Photoelectric Absorption).....	77
5.2.1.2	Scatter	81
5.2.1.3	Pair Production	85
5.2.1.4	Photonuclear	85
5.2.1.5	Photofission.....	85
5.3	Attenuation Measurement Units	86
5.3.1	Linear Attenuation Coefficient μ	86
5.3.2	Mass Attenuation Coefficient μ_m	88
5.3.3	Atomic Attenuation Coefficient μ_a	88
5.3.4	Molar Attenuation Coefficient μ_M	90
5.3.5	Relationship among the Various Attenuation Coefficients	90
5.3.6	Mixture Rule	90
5.3.7	Total Attenuation/X-Ray and γ -Ray Attenuation Phenomena	92
5.4	Reflection.....	96
5.5	X-Ray Phase Effects	99
5.5.1	Refraction	102
5.5.1.1	Snell's Law	104
5.5.1.2	Total External Reflection of X-Rays.....	105
5.5.2	Diffraction.....	106
5.5.3	X-Ray Phase-Contrast Radiography	108
Chapter 6	Radiation Transport Simulation	115
6.1	Introduction	115
6.2	Why Simulate Radiography	115

6.3	Types of Radiation Commonly Transported in Simulations	115
6.4	Methods of Simulation	116
6.4.1	Discrete Ordinates.....	116
6.4.2	Ray Tracing	117
6.4.2.1	XRSIM X-Ray Simulation.....	117
6.4.2.2	HADES, a Radiographic Simulation Code	119
6.4.2.3	Ray-Tracing Summary.....	122
6.4.3	Monte Carlo Method	122
6.4.3.1	Los Alamos National Laboratory Monte Carlo N-Particle (MCNP) Code	124
6.4.3.2	Lawrence Livermore National Laboratory TART, COG, Peregrine, and MERCURY Monte Carlo Codes....	125
6.5	Example Photon Transport Simulations	125
6.5.1	MCNP Used in Analysis of Albedo from Lead and Concrete.....	125
6.5.2	MCNP Applied to Collimator Design for a 9 MV Linac.....	126
6.5.3	MCNP to Determine Scatter Blur within a Flat-Panel Photodiode Array Detector	128
6.5.4	HADES Proton Radiographic Simulations to Study Hydrodynamics	130
6.5.5	COG Simulation Applied to Cargo Interrogation	132
Chapter 7	Radiation Dosimetry, Safety, and Shielding	135
7.1	Introduction	135
7.2	Metrics of Radiation Exposure, Absorbed Dose, Dose Equivalent, and Effective Dose.....	135
7.2.1	Radiation Exposure	136
7.2.2	Absorbed Dose	136
7.2.3	Linear Energy Transfer and Radiation Weighting Factor	136
7.2.4	Dose Equivalent	137
7.2.5	Effective Human-Equivalent Dose.....	137
7.3	Radiation Effects in Humans	138
7.3.1	Linear No-Threshold (LNT) Model	139
7.3.2	Human Risk from Low Effective Human-Equivalent Dose	140
7.4	Radiation Measurements for Monitoring Radiation Exposure and Absorbed Dose	140
7.4.1	Geiger–Müller Counter	140
7.4.2	Ionization Chamber Radiation Meter.....	143
7.4.3	Personal Dosimeter	145
7.5	Sources of Human Absorbed Dose	146
7.5.1	Natural Background Radiation.....	147
7.5.1.1	Radon.....	147
7.5.1.2	Terrestrial X and γ Radiation	148
7.5.1.3	Radioisotopes in Food and Beverages	148
7.5.1.4	Cosmic Radiation	149
7.5.2	Man-Made Radiation Absorbed Dose.....	149
7.5.2.1	Occupational Dose Limits	150
7.5.2.2	Marketing Radiation Dose.....	150
7.5.2.3	Mining Legacy.....	150

7.6	Basics of Radiation Protection	151
7.6.1	Internal Radiation Dose	152
7.6.2	External Radiation Dose	153
7.6.3	Shielding.....	153
7.6.3.1	Half-Value and Tenth-Value Layer Thickness	155
Chapter 8	Radiation Sources.....	157
8.1	Introduction	157
8.2	The Perfect Source	157
8.3	Source Attributes: Brightness, Brilliance, Irradiance, Photon Flux Density, Photon Energy Spectrum, and Source Size.....	160
8.4	Electrically Powered X-Ray Sources.....	161
8.4.1	X-Ray Tubes	161
8.4.1.1	Common Design Elements and Subsystems of X-Ray Tubes	161
8.4.1.2	X-Ray Tube Configurations and Tube-Like Sources	169
8.4.2	Electron Accelerator-Based Sources	175
8.4.2.1	Electrostatic Generator	175
8.4.2.2	Synchrotron X-Ray Source	175
8.4.2.3	Betatron	176
8.4.2.4	Linac	176
8.4.3	Pulsed Sources	177
8.4.3.1	Pulsed X-Ray Tube	178
8.4.3.2	Accelerators as Pulsed Sources	178
8.4.3.3	Plasma X-Ray Sources.....	179
8.4.4	Laser-Driven X-Ray Sources.....	179
8.4.4.1	K alpha (K_{α}) X-Ray Sources.....	179
8.4.4.2	Free-Electron Laser (FEL) X-Ray Source	179
8.4.4.3	Thomson/Inverse Compton Scattering X-Ray Source	179
8.5	Radioisotopic X-Ray and γ -Ray Sources.....	182
Chapter 9	Radiation Detectors	187
9.1	Introduction	187
9.2	The Perfect Detector.....	187
9.3	Fundamental Statistical Considerations	188
9.4	Detection Principles	190
9.5	Detector Types.....	191
9.5.1	Pulse Detection, Energy Discrimination, or Integrating Detection....	191
9.5.2	Point, Line, or Area Detection	191
9.6	Detector Technology.....	193
9.6.1	Film	193
9.6.2	Computed Radiography.....	193
9.6.3	Scintillators	194
9.6.3.1	Clear Crystals, Glass, or Ceramic Scintillators	194
9.6.3.2	Granular Composite Scintillators	195
9.6.3.3	Structured Scintillators.....	195
9.6.4	CCD-Based Area Detectors Employing a Scintillator.....	198
9.6.5	CMOS-Based Area Detectors Employing a Scintillator	200
9.6.6	Direct-Detection Flat Panels	201
9.6.7	Indirect-Detection Flat Panels.....	201

Chapter 10	Imaging System Components.....	203
10.1	Introduction	203
10.2	Sources of Detected Signal in X-Ray Imaging	204
10.2.1	Properties of Φ_p	211
10.2.2	Properties of Background or System Scatter, Φ_{Sbk}	212
10.2.3	Properties of Object Scatter, Φ_{Sobj}	213
10.2.4	X-Ray Scatter Corrections and the Subtleties of Radiographic Imaging	214
10.3	Shielding and Collimation.....	217
10.3.1	Collimators.....	218
10.4	Antiscatter Grids	222
10.5	Limiting Apertures.....	224
10.6	Staging for Object Positioning and Control.....	226
10.7	DR/CT Acquisition, Processing, Control, and Display	229
10.7.1	How Big Are the Data Sets?.....	230
10.7.2	On Screen and Interactive Tools of Value for CT	230
10.7.3	Computers for CT Data Acquisition.....	231
10.7.4	Computer Requirements for DR/CT Processing.....	232
10.7.5	Computers for CT Reconstruction	232
10.7.6	Displaying CT Data.....	234
Chapter 11	Imaging-System Configurations.....	237
11.1	Introduction	237
11.2	1-D X-Ray Gauging Systems.....	238
11.3	Radiography Systems	241
11.3.1	Radiography with a Linear-Detector Array	241
11.3.2	Radiography with an Area-Detector Array.....	246
11.4	3-D Computed Tomography	248
11.4.1	CT Scanning with 1-D Gauging Systems	250
11.4.2	CT Scanning with Linear-Detector Arrays.....	252
11.4.3	CT Scanning with Area-Detector Arrays	256
11.5	Summary	258
Chapter 12	Digital Radiography	261
12.1	Introduction	261
12.2	Physical Structure of Digital Radiographic Detectors	261
12.2.1	Single-Detector Systems	262
12.2.2	Linear-Detector Arrays	263
12.2.3	Area-Detector Arrays.....	264
12.3	Role of Image Calibration and Importance of the Φ_0 Measurement.....	267
12.4	DR/CT Acquisition and Use of the Φ_0 Image	270
12.5	Options in Data Processing of Digital Radiographic Image Data	271
12.6	Artifacts in Digital Radiographs	271
12.7	Phantoms/Test Objects and Image Quality Indicators (IQIs).....	276
12.8	Data Analysis and Interpretation.....	279
Chapter 13	Computed Tomography	285
13.1	Introduction	285
13.2	Foundational Ideas for CT Image Reconstruction	286

13.3	CT Data Acquisition and Processing.....	290
13.4	CT Data Processing and the Importance of Φ_0	294
13.5	CT Reconstruction Algorithms	296
13.5.1	Region of Interest and CT Field-of-View Extension Techniques	300
13.6	The Sinogram	301
13.7	Artifacts in CT Reconstructed Data.....	303
13.7.1	Centering Artifacts.....	307
13.7.2	Ring Artifacts.....	308
13.7.3	Bad-Pixel Artifacts.....	309
13.7.4	Angular Positioning Artifacts	312
13.7.5	X-Ray Magnification Artifacts.....	314
13.7.6	Midline Offset Artifacts.....	316
13.7.7	Incorrect Vertical Center Cone-Beam Artifacts	317
13.7.8	Cone-Beam Missing Data Artifacts	319
13.7.9	Beam-Hardening Artifacts.....	320
13.7.10	Scatter Artifacts for High-Aspect Ratio or High-Attenuating Objects.....	322
13.8	Test Phantoms and Test Objects for System Evaluation.....	324
13.9	Data Analysis and Interpretation.....	325
Chapter 14	Image Quality.....	329
14.1	Introduction	329
14.1.1	Components of Image Contrast.....	332
14.1.2	Components of Spatial Resolution	335
14.1.3	Components of Transmission Image Noise.....	339
14.1.4	X-Ray Transmission Imaging Artifacts	341
14.2	Photon Statistics	342
14.3	Measuring Components of Image Contrast.....	345
14.4	Modulation Transfer Function.....	348
14.5	Signal-to-Noise Ratio and Detective Quantum Efficiency.....	360
14.6	Probability of Detection and ROC Curves	365
Chapter 15	Special Techniques.....	369
15.1	Introduction	369
15.2	Contrast Agents	369
15.3	Dual Energy for Effective-Atomic Number	369
15.3.1	Physical Basis for Multiple-Energy Applications	370
15.3.1.1	Low-Energy Dual-Energy Techniques	370
15.3.1.2	High-Energy Dual-Energy Techniques	374
15.3.1.3	Summary of Dual-Energy Measurements	377
15.4	Active and Passive (Emission) CT.....	377
15.5	Tomosynthesis—Depth Information without CT.....	380
15.6	Automated Defect Recognition	384
15.7	X-Ray Forward and Backscatter.....	386
15.8	X-Ray Diffraction Topography.....	392
15.9	X-Ray Microscopy and X-Ray Optics	393
15.9.1	Pinhole Microscopes	395
15.9.2	Reflection Optics Microscopes.....	399

15.9.2.1 Kirkpatrick–Baez Reflection Optics Microscopes	400
15.9.2.2 Wölter Objective Reflection Optics Microscopes.....	401
15.9.3 Refractive Lens Microscopes	408
15.9.4 Diffraction Optics Microscopes.....	409
Chapter 16 Selected High-Energy Photon Applications.....	415
16.1 Introduction	415
16.2 1D Applications.....	415
16.3 2D Applications.....	417
16.3.1 X-Ray Digital Radiography of 40 mm Grenades.....	417
16.3.2 Automatic Transmission.....	418
16.3.3 Dual-MeV Radiography for High-Z Material Discrimination.....	419
16.3.4 Phase Contrast Radiography of a Deuterium–Tritium Solid-Layer Single-Shell Fusion Target	422
16.4 3D Applications.....	424
16.4.1 LoTRT Targets	424
16.4.2 Inspection of Joinery	425
16.4.2.1 Metal Weldment.....	426
16.4.2.2 Stardust Reentry Capsule Bond.....	427
16.4.3 Aviation Safety: DR and CT of Pitot Tubes	427
16.4.4 Characterization of LX-17 High Explosive	428
16.4.5 Automotive Applications.....	432
16.4.5.1 Metal Castings	434
16.4.5.2 Windshield Wiper Motor	440
16.4.5.3 Planetary Transmission Gear Assembly.....	440
16.4.5.4 Fuel Pump.....	441
16.4.6 Turbomolecular Vacuum Pump.....	441
16.4.7 NASA Space Hardware.....	442
16.4.7.1 NASA Advanced Ablator Materials	442
16.4.7.2 NASA Rocket Booster Nozzle.....	445
16.4.7.3 Diagnosis of Failure in Spare NASA Fuel Cell Pump	445
16.4.8 Exploring the Limits of MeV Imaging—9 MV and 15 MV Linacs	445
16.4.9 DS Laser ICF Targets	449
16.4.10 CT and Tomosynthesis of DoD Ordnance	452
16.4.10.1 CT of a WDU-17/B Conventional Warhead.....	453
16.4.10.2 CT and Tomosynthesis of a Multifunction Fuze	455
16.4.11 Tomosynthesis of an <i>Archaeopteryx</i> Fossil.....	457
16.4.12 DR and CT of Art and Objects of Cultural Significance	459
16.4.12.1 Concerns with Michelangelo Buonarroti’s Statue of David.....	462
16.4.13 CT of Structures Made by Additive Manufacturing	466
16.5 X-Ray Imaging to Defend the US Homeland.....	469
16.5.1 X-Ray DR and X-Ray Backscatter to Inspect Carry-On Luggage	472
16.5.2 X-Ray CT to Inspect Checked Luggage.....	474
16.5.3 X-Ray DR and Diffraction to Inspect Checked Luggage	478
16.5.4 Nonrotating Gantry Security CT Systems	480

16.5.4.1	SureScan Nonrotating Gantry CT System	481
16.5.4.2	Rapiscan Nonrotating Gantry CT System.....	482
16.5.4.3	XinRay Laboratory Prototype Nonrotating Gantry CT System.....	482
16.5.5	X-Ray Backscatter of Passengers	484
16.5.6	X-Ray Radiography and Backscatter for Cargo Nonintrusive Inspection	487
Chapter 17	Neutron and Proton Imaging.....	495
17.1	Imaging with Thermal Neutrons	495
17.2	Imaging with MeV Neutrons	504
17.3	Imaging with MeV Protons	504
Glossary	507	
List of Notations	523	
References	529	
Index.....	553	

Preface

A revolution is underway in industrial x-ray imaging. We focus on industrial nondestructive evaluation and characterization (NDE and NDC) and security screening as opposed to medical x-ray imaging. Digital detectors are pushing film out of the picture. We give our respects to film radiography, but our emphasis is on electronic detection. Distributed x-ray sources are slowly replacing single x-ray tube sources. Advanced algorithms are replacing older ones to provide fewer artifacts and noise-reduced x-ray images. New manufacturing methods such as additive manufacturing are pushing the need for quantitative, accurate, and precise x-ray imaging. Advances in industrial and security x-ray imaging are being driven by these new technologies and by applications requiring high throughput and fast access to imaging data, as discussed in the text. Recently in the United States, the Department of Homeland Security has been supporting rapid development and deployment of digital x-ray imaging systems. X-ray imaging systems research, development, implementation, demonstration, and evaluation are being supported by the US Department of Energy, industries, and academia.

This book is designed to fill the need for a comprehensive work on *modern* industrial and security x-ray and γ -ray imaging. In addition to the main focus on x-ray and γ -ray imaging, in the first chapter on history, we summarize some common NDE methods, and in the last chapter, we discuss neutron and proton imaging techniques. This book reviews the fundamental x-ray and γ -ray imaging science, use of simulations, dosimetry; addresses equipment and system configuration, image reconstruction and analysis, image quality, and special techniques; and is rich with applications. We present x-ray imaging inspection applications that range from 1-D gauging to 2-D and 3-D imaging. Applications range from cultural art objects through National Aeronautics and Space Administration (NASA) components, complex additive manufacturing parts to munitions, explosives, and special nuclear materials. The authors combined have a century of experience in the field. The authors' experience encompasses research, development, design, implementation, image processing, application, and education.

There is a high demand for x-ray imaging system designers, technologists to choose equipment, technologists to implement and apply x-ray imaging as well as analysts who are skilled in the x-ray imaging technologies and have knowledge on how to use them to solve problems. Problems include determining the state of art pieces; 3-D additive manufactured builds; characterizing the surety and safety of munitions; and screening luggage and cargo for contraband, explosives, and special nuclear materials. We intend that this text be useful to a broad range of practitioners of x-ray imaging. We present x-ray interactions with matter and carry the discussion through basic equations; 1-D, 2-D, and 3-D x-ray imaging methods; system configurations; and specific applications.

X-ray imaging can favorably impact all phases of a product life cycle, i.e., from cradle to grave. This includes evaluation of prototypes, especially during or after physical testing. X-ray imaging has opened the door to inspection during manufacturing, for process control, and/or product screening. Increasingly, in-service inspection is being used for making decisions such as repair or retirement for cause. The most visible example of this is pipelines transporting fuel or chemicals where the consequence of failure is high.

The first part of the book reviews principles usually presented in senior undergraduate and first-year graduate physics courses. The descriptions of equipment, techniques, and applications are unique in their scope and detail. We expect that practicing x-ray imaging scientists, engineers, and technicians will benefit from this material, but we also intend that it be useful to researchers and others who are extending the state of the art or applying these technologies in unconventional ways.



Taylor & Francis

Taylor & Francis Group

<http://taylorandfrancis.com>

Acknowledgments

We acknowledge the following:

- Dr. Spiros Dimolitsas, Georgetown University, for encouraging this undertaking at its birth.
Spiros was associate director at the Lawrence Livermore National Laboratory (LLNL) when we started writing this book.
- Jeff Bonivert, Kathy Seibert, Sabrina Fletcher, Pam Williams, Kitty Madison, and other LLNL artists, for their contribution in turning hand sketches into finished artwork and for keeping it all within the publisher's rules.
- Robert Green, Johns Hopkins University, and Richard Bossi, The Boeing Company, (both are now retired) for their review of the original preface and book outline.
- Yvonne Johnson, LLNL Library, for tracking down papers in journals that we didn't know existed.
- Bill Brown for his contributions to the Department of Defense (DoD) and high-energy density physics (HEDP) sections and for review of many portions of this book.
- Chuck Divin for his contributions to the CT for the section on additive manufacturing.
- Ryan Carney for providing images, text, and editorial comments on the *Archaeopteryx* section.
- Matthew Merzbacher for supplying Morpho Detection images and his editorial comments.
- Carl Bosch for supplying SureScan images and his editorial comments.
- Ed Franco for supplying Rapiscan images and his editorial comments, as well as Ed Morton for allowing us to use Rapiscan images.
- Brian Gonzales for providing XinRay images and his editorial comments.
- Cody Wilson for providing Passport Systems, Inc. images and his editorial comments.
- Steve Smith for providing Tek84 Engineering advanced image technology representations.
- Dan Empey, Gary Allen, Ethiraj Venkatapathy, Ajay Koshti, Jose Hernandez, Karen McNamara and Koorosh Araghi, for the use of images from inspections of National Aeronautics and Space Administration (NASA) objects and assemblies.
- Mike Pivovaroff for valuable comments on the x-ray optics sections; Steve Glenn for help in making sure that some of the equations and units were correct.
- Kyle Champlay and Steve Azevedo for reviewing the CT equations.
- Carl Crawford, Cuptwo, LLC, for his insightful review of the preface.
- Elizabeth Obregon and Amanda Lima at the Department of Homeland Security (DHS), Science and Technology (S&T), Explosives Division, and Mark Bernatowicz, DHS, Transportation Security Administration (TSA), for editorial comments and use of images and information as applied to explosives detection.
- Kevin Cronk, Namdoo Moon, and Joel Rynes, at DHS, Domestic Nuclear Detection Office (DNDO), for editorial comments and for allowing us to use images and data obtained by the Transformational and Applied Research Directorate.
- Ann Tyler and Jenessa Dozhier for helping us keep track of the permissions for some of the figures used. Also, we thank Jenessa for her help with logistics, printing copies for us to review, converting figure names as needed, and for coordinating the review and release of the book by LLNL. Diane Chinn helped in the review and release process.
- We thank our families, wives, and kids, for bearing with us as we worked on the book.



Taylor & Francis

Taylor & Francis Group

<http://taylorandfrancis.com>

Authors

Harry E. Martz, Jr. is the director of the Nondestructive Characterization Institute and a distinguished member of the technical staff at the Lawrence Livermore National Laboratory. He is also principal investigator for the Department of Homeland Security, Science and Technology, Explosives Division; the Domestic Nuclear Detection Office, Nuclear and Radiological Imaging Platform; and Passive and X-ray Imaging Scanning Projects. Harry joined the Laboratory in 1986 as a physicist to develop the area of x-ray imaging and proton energy loss computed tomography (CT) for the nondestructive inspection of materials, components, and assemblies. He received his MS and PhD in nuclear physics/inorganic chemistry from Florida State University and his BS in chemistry from Siena College.

Harry's interests include research, development, and application of nonintrusive characterization techniques to better understand material properties and inspection of components and assemblies and generation of finite element models from characterization data. He has applied CT to inspect 1-mm-sized laser targets, automobile and aircraft components, reactor fuel tubes, new production reactor target particles, high explosives, explosive shape charges, dinosaur eggs, and concrete and for nondestructive radioactive assays of waste drum contents. Recent research and development (R&D) efforts include CT imaging for conventional and homemade explosives detection in luggage and radiographic imaging of cargo to detect special nuclear materials and radiological dispersal devices. Dr. Martz has authored or coauthored over 300 papers and is coauthor of a chapter on radiology in *Non-destructive Evaluation: Theory, Techniques and Applications, Image Data Analysis in Non-destructive Testing Handbook*, third edition: volume 4, *Radiographic Testing*, and contributed a chapter entitled Industrial Computed Tomographic Imaging to the *Advanced Signal Processing Handbook: Theory and Implementation for Radar, Sonar and Medical Imaging Real-Time Systems*. He has also served on several National Academy of Sciences committees on aviation security and was the chair of the Committee on Airport Passenger Screening: Backscatter X-ray Machines. Harry is cochair of the Northeastern University Awareness and Localization of Explosives-Related Threats (ALERT) Advanced Development for Security Applications (ADSA) Workshops. Dr. Martz has presented a short course on CT imaging at the Center for Nondestructive Evaluation, Johns Hopkins University and a course on x-ray imaging for extension program of the University of California, Los Angeles (UCLA). Awards include the 2000 R&D 100 Waste Inspection Tomography for Nondestructive Assay (WIT-NDA), 1998 Director's Performance Award Active and Passive Computed Tomography, and Federal Laboratory Consortium for Technology Transfer 1990 Award of Merit. He is a member of the Physics Honor Society Sigma Pi Sigma.

Clinton M. Logan began his career at the Lawrence Livermore National Laboratory in 1963 after receiving his BSME degree from Montana State University. His first years were devoted to the design and testing of diagnostic systems for underground nuclear tests. This and subsequent positions in physics research led to a strong interest in the interaction of radiation with matter and a decade of materials research for the Magnetic Fusion Program. He received his MS in materials science from the University of California, Davis (UC Davis) in 1972. From 1977 to 1985, Clint was manager of Rotating Target Neutron Source (RTNS)-II, an accelerator-based neutron source devoted to research on fusion materials. In 1985, Clint returned to the Nuclear Weapons Program to serve as group leader of a group devoted to improving methods of material characterization for x-ray laser weapons. This group made significant advances in quantitative film radiography, x-ray gauging, ion beam characterization, computed tomography, noncontact measurements, and the integration of these technologies into a computer-assisted characterization system. In 1993, Clint won a US Department of Energy (DOE) grant to apply Lawrence Livermore National Laboratory (LLNL) resources to support Fischer Imaging Corporation in the design of their full-field digital mammography unit

for cancer screening. He ended his LLNL career in 2001 as leader of the nondestructive evaluation organization. Following his retirement from LLNL, he joined Bioptrics Inc. as VP of research, where he served until 2004. Clint holds five US patents in accelerator and x-ray technology. He is a registered professional engineer in California, a member emeritus of the American Association of Physicists in Medicine, and a fellow of the American Society of Mechanical Engineers.

Daniel J. Schneberk received undergraduate degrees (one of them in mathematics) from the University of Oregon and a master's in statistics from the University of California, Berkeley (UC Berkeley) in 1980. After a year at SRI International as an analyst and sampling statistician and a year at General Electric developing software for space applications, Dan was hired into the Laser Isotope Separation project at the Lawrence Livermore National Laboratory (LLNL). Dr. Lloyd Hackel mentored Dan and tutored him in physics and quantum mechanics. Together, they wrote a series of papers documenting a 3-D model of uranium vapor transport, the distribution of quantum states with height, and a system for real-time measurement of vapor-source output using diagnostic lasers. In 1988, Dan took an opportunity to join the nondestructive evaluation group at LLNL, collaborating with Harry Martz and initially working for Clint Logan on materials inspection and characterization issues in the x-Ray Laser Project. His work in NDE has continued to the present. Focus areas for Dan's work have been the scanning and characterization of explosives, high explosives, and detonators for weapons surveillance; digital radiography (DR)/computed tomography (CT) scanning of automotive parts; CT scanning of aerospace parts for the National Aeronautics and Space Administration (NASA); and CT scanning of nuclear weapons. Connected to the explosives work, Dan has served as a senior scientist with Harry Martz in projects focused on the analysis and certification of baggage scanners at airports. Dan participated in or was project leader for cooperative research and development projects with Caterpillar, Chrysler, GM, and Ford. Dan has participated in the design, development, and fielding of a number of digital radiographic and computed tomographic systems operating at LLNL and throughout the world. Most recently, the CoLOSSiS scanner is fielded and operating at Pantex for scanning nuclear weapons. CoLOSSiS is the highest-resolution CT scanner at 9 MeV. Dan is the lead author of Chapter 13, Image Analysis, in the third edition of the American Society for Nondestructive Testing (ASNT) handbook. He has received two LLNL Directors Performance Awards and awards from Ford and NASA. Dan is a member of Phi Beta Kappa.

Peter J. Shull is an associate professor of engineering at Penn State Altoona. Dr. Shull has worked in the field of NDE for over 20 years while at the Institute of Standards and Technology (NIST) in the Materials Reliability Division in Boulder, Colorado; at The Johns Hopkins University; and at The Pennsylvania State University. Dr. Shull's primary research focus is NDE applied to process control. He has authored numerous publications, including the popular textbook entitled *Nondestructive Evaluation: Theory, Technique, and Applications* (Marcel Dekker 2001), and is a member of the American Society of Nondestructive Testing, the American Society of Engineering Educators, and the Institute of Electrical and Electronic Engineers. He was invited to Argentina as a Fulbright Scholar (2006) in a multipronged effort to evaluate the viability of extending Argentina's nuclear power reactors beyond their life expectancy.

Peter received a BS degree (1982) in mechanical engineering from Bucknell University, Lewisburg, Pennsylvania, and an MS (1992) and a PhD (1996) degree from The Johns Hopkins University, Baltimore, Maryland. Dr. Shull is also an expert in engineering education.

1 Introduction to Nondestructive Evaluation

In this opening chapter of this book, we explore the background of nondestructive evaluation (NDE) and describe how the technology has matured into a full participatory partner in design and manufacturing and has gone beyond to waste disposal and life cycle management. We present a brief overview of the major NDE techniques and technologies, which will give the reader a sense of how x-ray imaging fits into the larger world of NDE. We introduce the language and methods of evaluating the performance of NDE systems and close the chapter with a discussion of the similarities among and differences between industrial x-ray imaging and medical x-ray imaging.

After completion of this chapter the student will have learned

- A brief history of *nondestructive evaluation* (NDE), *nondestructive testing* (NDT), *nondestructive characterization* (NDC), *nondestructive inspection* (NDI), *nonintrusive inspection* (NII), and so forth
- The role of NDE throughout a product life cycle
- Ionizing and nonionizing radiation
- The technology and major applications of
 - X-ray and γ -ray methods
 - Optical interferometric methods
 - Candling
 - Optical fluorescence
 - Thermal imaging
 - Gigahertz–terahertz waves (microwaves and millimeter waves)
 - Ultrasonic testing
 - Acoustic emission
 - Dye penetrant testing
 - Magnetic particle inspection
 - Leak testing using tracer gas
 - Eddy current testing
- Performance measures and metrics
- How medical and industrial imaging compare and contrast

1.1 A BRIEF HISTORY OF NDE, NDT, AND NDC

The inspection of materials and components, with the objective of locating and quantifying defects and degradation in material properties that would lead to failure, is essential to the safe utilization of engineering structures. Such inspections are thus an integral part of the science and technology needed to ensure product quality and reliability. A wide variety of noninvasive measurement techniques are employed, including ultrasonics, radiography, and electromagnetics (Shull 2002), which are familiar from other fields of noninvasive measurements such as medicine, geophysical prospecting, sonar, and radar. Depending on the manner of their utilization, inspection with such techniques is often referred to as NDT. NDT is what we refer to as traditional NDE in [Figure 1.1](#). NDT or traditional NDE had been used only as an end-product (final assembly) or

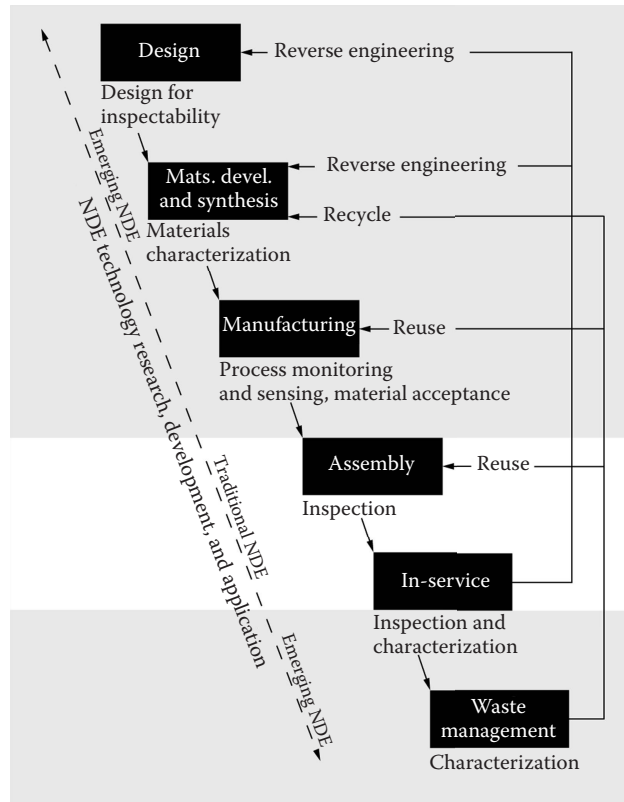


FIGURE 1.1 Nondestructive evaluation's traditional and expanding role in the life cycle of a product.

in-service inspection tool. More details on the terminology used in this field are contained in Panel 1.1.

PANEL 1.1 Testing, Evaluation, and Other Terms

Our scientific community utilizes several terms as identifiers of the technology and practice of nondestructive testing (NDT). There is no precise and widely agreed-upon distinction between these terms. We present here our sense of how the terms are used. We will attempt to follow these definitions in this book. NDT is the narrowest of these terms. It applies to a pass/fail test of a part or component. Historically, the term was applied when the situation was such that if a defect could be detected, then the part was rejected. Usually, only large defects could be detected, and part failure was likely in that event. When the NDT technology got better, it could detect small defects in every part. A decision was now necessary as to the life expectancy (or probability of failure over the service lifetime) of the part given the size distribution and location of defects. Now the word *testing* did not seem to convey the action, and NDE came into common usage. Recently, there has been greater effort at inspection of cargo and packages. For many of these situations, the technique has to be not only nondestructive but also nonintrusive. Thus, nonintrusive inspection (NII) has come into widespread use in this field.

Much of the recent frontier work in NDE was directed toward smaller objects and higher spatial resolution, but cargo inspection and waste characterization push the boundaries for large objects and lower spatial resolution. (See [Figure 1.2](#).)

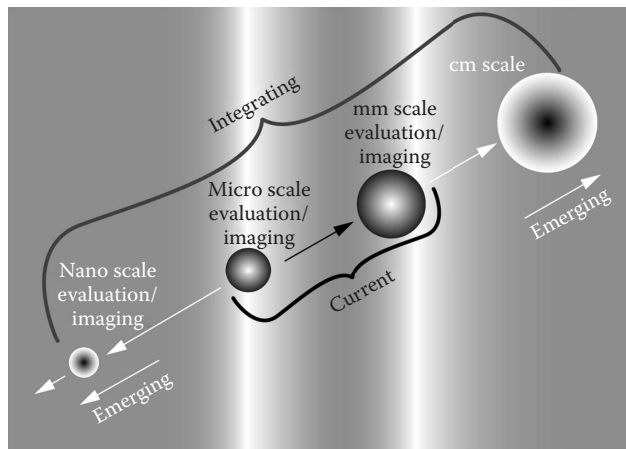


FIGURE 1.2 Just as with other fields, NDE needs to cover a very broad range of scale lengths. The main direction of change is toward smaller objects and finer spatial resolution. However, there are situations where larger objects and coarser spatial resolution is being developed, e.g., waste assay with resolution of about 6 cm.

NDE and quantitative nondestructive evaluation (QNDE) are similar terms indicating that more than defect characterization is taking place. For example, perhaps some continuous material variable is being measured, or a critical internal dimension is being evaluated.

NDT has been practiced for many decades. The technological advances that occurred during World War II and the subsequent defense effort spurred initial rapid developments in instrumentation. The primary purpose was the detection of macroscopic defects. As a part of safe-life design, it was intended that a structure should not develop macroscopic defects during its life, with the detection of such defects being a cause for removal of the component from service. This approach was generally satisfactory in the 1950s and 1960s, since the materials were most often utilized well below their ultimate yield strength and possessed a high resistance to crack propagation as well as a high fracture toughness (Buckley 1976). In response to the need to detect macroscopic defects, increasingly sophisticated techniques using ultrasonics, eddy currents, x-rays, dye penetrants, magnetic particles, and other forms of interrogating methods emerged.

The World Federation of NDE Centers claims that in the early 1970s, two events occurred that caused a major change (World Federation of NDE Centers 2015) in NDT:

The continued improvement of NDT technology, in particular its ability to detect small flaws, led to the unsatisfactory situation that more and more parts had to be rejected, even though the probability of failure had not changed. However, the discipline of fracture mechanics emerged, which enabled one to predict whether a crack of a given size would fail under a particular load if a material property, fracture toughness, were known. Other laws were developed to predict the rate of growth of cracks under cyclic loading (fatigue). This formed the basis for the new philosophy of ‘fail safe’ or ‘damage tolerant’ design. Components having known defects could continue in service as long as it could be established that those defects would not grow to a critical, failure-producing size.

Buckley corroborates this in his paper (Buckley 1976). This basic change in philosophy required the designer to assume the presence of an initial flaw in each critical manufactured structure and to design the structure such that the flaw would not grow to critical size during its intended service life. Thus, a new challenge was presented to the NDT community. Detection was not enough. One also needed to obtain quantitative information about flaw size to serve as an input to fracture mechanics-based predictions of life before service and remaining life in-service.

These concerns, which were felt particularly strongly in the defense, space, and nuclear power industries, led to the creation of a number of research programs directed toward high-value, high-consequence-of-failure components and assemblies around the world. About this time, the emergence of “quantitative” NDT became known as quantitative nondestructive evaluation (QNDE) or just NDE as a new discipline. The groups most active in the United States were the American Society for Nondestructive Testing (ASNT); Electric Power Research Institute (EPRI); American Welding Society; National Bureau of Standards (NBS, now named the National Institute for Standards and Technology [NIST]); Center for Nondestructive Evaluation (CNDE) at Iowa State University (growing out of a major research effort initiated at the Rockwell International Science Center); Center for Nondestructive Evaluation (CNDE) at Johns Hopkins University; and the NDE group at Lawrence Livermore National Laboratory (LLNL). Overseas were the Nondestructive Testing Centre Atomic Energy Establishment (England), Fraunhofer Institute for Nondestructive Testing (Germany), National Institute for Advanced Interdisciplinary Research (Japan), Russian Academy of Sciences, and similar organizations in a number of other countries. In the last few years, global security concerns have shifted NDE from weapons systems to NII of luggage and cargo. This is providing the next surge in technology development for NDE and NDC.

In the ensuing years, many important advances have been made. Quantitative theories have been developed to describe the interaction of the interrogating fields with flaws. Simulations incorporating these theories and results have been integrated with solid model descriptions of real-part geometries (we refer to this as *as-built* as opposed to *as-designed* modeling of the object) (Kokko et al. 2006) to simulate practical inspections (JCISE 2006). We illustrate in Figure 1.3 how, for example, as-built models are being used in the understanding of high-energy-density science (Brown and

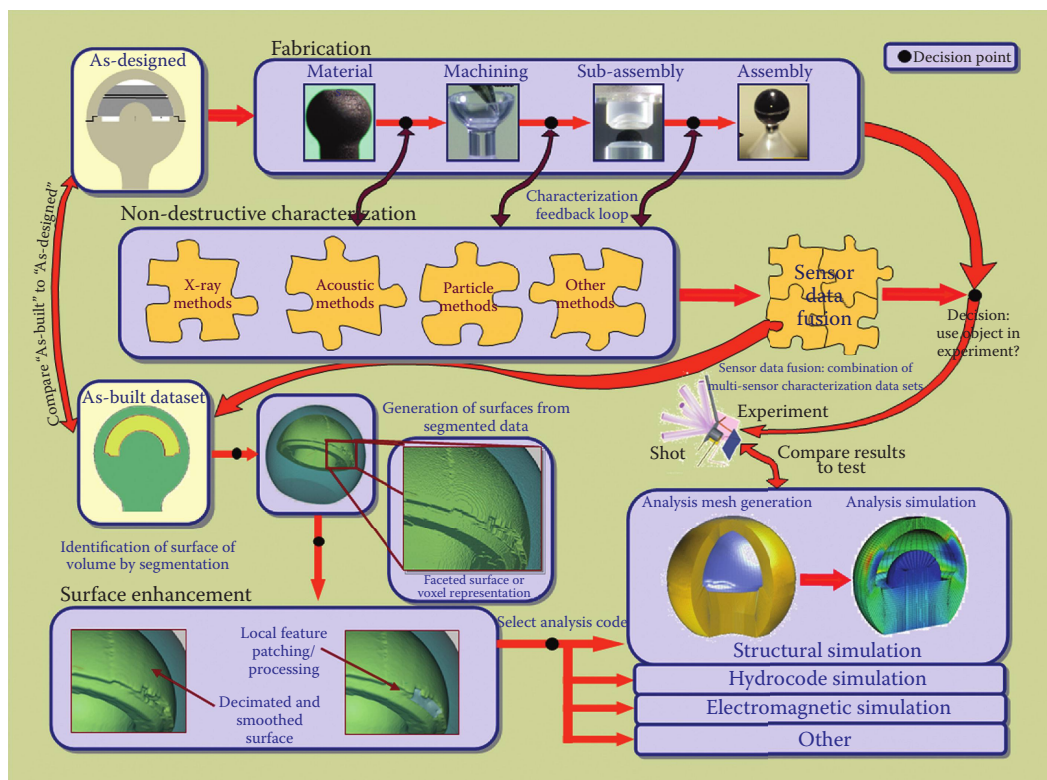


FIGURE 1.3 Example of the use of NDE for the life cycle of a high-energy-density science target of dimensions of about millimeter extent.

Martz 2006). These tools allow NDE to be considered, as a part of the design process, on equal footing with other failure-related science and engineering disciplines.

Quantitative descriptions of NDE performance, such as the probability of detection* (POD), have become an integral part of statistical risk assessment (Olin and Meeker 1996). A good summary of this is given by Buckley in a paper, “The Future Economic Role of NDE” (Buckley 1976). Measurement procedures initially developed for metals have been extended to engineered materials, such as composites, in which anisotropy and inhomogeneity become important issues (see Panel 1.2). The rapid advances in digitization and computing capabilities have changed the types of instruments and algorithms that can be used in processing the resulting data (Grampp et al. 1997; Laugier 2007). High-spatial resolution imaging systems and the fusion of information from multiple measurement modalities in characterizing a flaw have emerged (Gros 1997; Kokko et al. 2006). An increasing interest is found not only in detecting, characterizing, and sizing defects, but also in characterizing the materials in which they reside (Kouris et al. 1982; Martz et al. 1991b; Lewis et al. 1992; Martz 1998; Aufderheide et al. 2007). Goals can range from the determination of fundamental microstructural characteristics such as grain size, porosity, and texture (preferred grain orientation) (Krautkramer and Krautkramer 1990; Nicoletti and Anderson 1997; Karacan et al. 2001) to material properties related to such failure mechanisms as fatigue, creep, and fracture toughness (Seale and Madaras 1999; Shell et al. 2005; Dobmann 2006).

PANEL 1.2 In-Service NDE of Aerospace Structures

The selected method(s) and inspection requirements depend on the structural configuration and the life cycle stage of the inspected material. While in-service inspection of aerospace metallic structures required mostly the detection of fatigue cracks and corrosion, aerospace composite structures require the detection of delaminations and impact damage (Bar-Cohen 1999). Generally, cracks need to be detected above a critical size. From failure mechanics, we know that the severity of a material imperfection is generally a function of several parameters. For cracks, they include the length, width, opening, orientation and location (Perez 2006). In contrast to this relatively simple requirement, corrosion detection and characterization, and NDE of composite structures are more complex.

Generally, fatigue cracks are initiated at high-cycle stress areas, and therefore, it is relatively easy to determine when and where to expect them, and their geometry is relatively simple. NDE methods used to detect aerospace cracks include ultrasonics, thermography, and x-ray and neutron radiography (Shull 2002). On the other hand, the issue of corrosion damage to metals is much more complicated. Corrosion damage is not defined by a single discontinuity type, and it cannot be described by a simple geometrical configuration. Corrosion is the general term that describes the oxidative degradation of metals caused by a local galvanic cell. The corrosion process converts the metal into its oxide, or hydroxide forms, resulting in deterioration of its mechanical properties. Several NDE methods have been used to detect and characterize hidden corrosion, including x-ray and neutron radiography, ultrasonics, eddy current, and acoustic emission (Shull 2002). Since corrosion results from exposure to humid or corrosive environments, neutron radiography has been used to search for hydrogen in water or hydrogen in metal hydroxide (Fujishiro et al. 2004).

Composites are susceptible to the formation of many possible defects throughout their life cycle, mostly due to the multiple-step production process, their nonhomogeneity, and their brittle matrix. Composite defects include delaminations, cracking, fiber fracture, fiber pullout, matrix cracking, inclusions, voids, and impact damage. These defects can have a critical effect

* We discuss probability of detection and other performance measures in [Section 1.5](#), Effectiveness and Statistics of NDE and [Section 14.6](#), Probability of Detection and ROC Curves.

on the performance of the host structures. For example, the catastrophic failure of the space shuttle *Columbia* over Texas on February 1, 2003, was determined to be due to impact damage when a piece of foam fell off of the main propellant tank during launch and struck the leading edge of the shuttle's left wing, causing damage to thermal protection system panels (Columbia 2003). The findings have led to new developments of NDE methods to inspect shuttle composite structures for damage, especially impact damage. US-manned space flights did not resume for more than 2 years.

We are currently at another turning point in society's needs that dictate that a new set of institutional relationships be developed (World Federation of NDE Centers 2015). Some industries that played a major role in driving the emergence of NDE—defense and nuclear power—have been on the wane. Increases in global competition have dramatically changed the product development and business cycles. Finally, the aging of our civil infrastructure, from roads to buildings to aircraft, has presented a new set of measurement and monitoring challenges. Thus, NDE is being used throughout the entire life cycle of a product from cradle (initial concepts and design) to grave (the retirement and disposal of a product, even waste), as shown in [Figure 1.1](#).

1.2 APPLICATION OF NDE TO LIFE CYCLE MANAGEMENT

As stated, traditionally, NDE has been viewed only as an end-product inspection tool. The traditional view does not take advantage of the full economic benefit that NDE provides (Buckley 1976). NDE can ensure/improve safety, shorten the time between product conception and production, and help reduce waste, as shown in Figure 1.1 (Martz 1998). Examples include design for inspectability; synthesis of new material; material process development; raw material acceptance; process monitoring and control; finished product and in-service inspection; and retirement for cause, disposal, and reuse (Goebbel 1994; Martz 1998). Therefore, NDE is increasingly being used throughout the life cycle management of products (Cordell 1998).

Among the new applications of QNDE spawned by these changes is the increased emphasis on the use of QNDE to improve the productivity of manufacturing processes. Included are the characterization of materials during their development cycles, increasing both the amount of information about failure modes and the speed with which it can be obtained and thus reducing the development cycle time, and the development of in-line measurements for process monitoring and control (see [Figure 1.3](#)). Continued development of flaw detection and characterization techniques is also required for use at the end of manufacturing and during service. The use of advanced simulation tools (HADES, XRSIM, MCNP, and others covered in detail in Chapter 6, Radiation Transport Simulation) to design for inspectability and the integration of such tools into quantitative strategies for life management will be a key element in increasing the engineering applications of NDE throughout the life cycle. As the globalization of business continues, companies will increasingly seek to develop uniform practices for use throughout the world. In the area of QNDE, this will drive an increased emphasis on standards, enhanced educational offerings, and simulations that can be easily communicated electronically.

1.3 X-RAY AND γ -RAY IMAGING IN CONTEXT

Our emphasis in this book is the use of x-rays and γ -rays for NDE. These “rays” are referred to as *photons*. Each photon is a quantum of electromagnetic (EM) energy and can appear to have properties of waves and particles at the same time. The EM spectrum (see [Figure 1.4](#)) consists of photons over a wide energy range. Different energy regions of the EM spectrum are known by different names, such as microwaves, visible light, radio, and x-rays. X-rays and γ -rays are the most energetic of the photons in the EM spectrum. We describe x-rays and γ -rays along with their interaction with

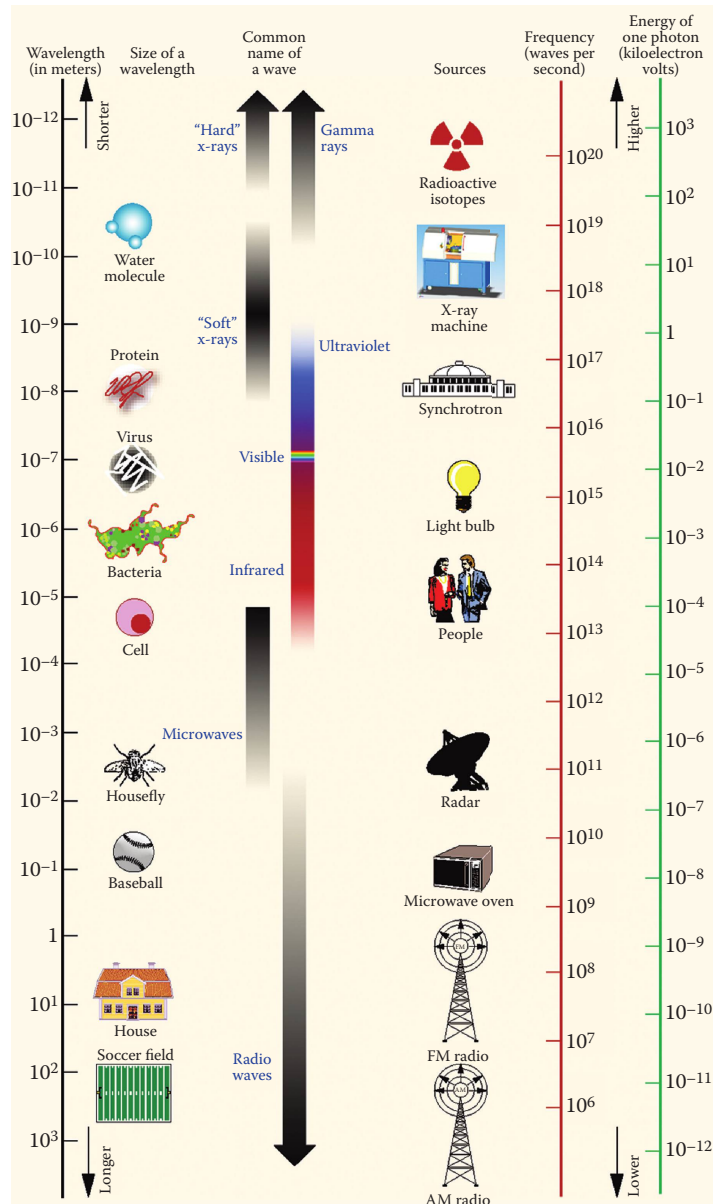


FIGURE 1.4 Electromagnetic spectrum showing the location of the various types of electromagnetic radiation as a function of wavelength, frequency, and energy. Representative sources of electromagnetic radiation in each region of the spectrum are also depicted.

matter in much more detail in Chapters 4 and 5. Here we introduce them and describe the properties that make them especially useful for NDE.

X-rays find such wide application in NDE because when they enter an object, some are absorbed, some are scattered, and some pass through unaltered. The most common form of x-ray imaging uses the transmitted x-rays (those that pass through) to derive information about the object. The information contained by the transmitted x-rays describes the entire volume of the object, even the inside. [Figure 1.5](#), which is an x-ray image of a poppy seed, demonstrates this. The use of x-rays for characterization of a high-energy-density double-shell target is described in [Panel 1.3](#).

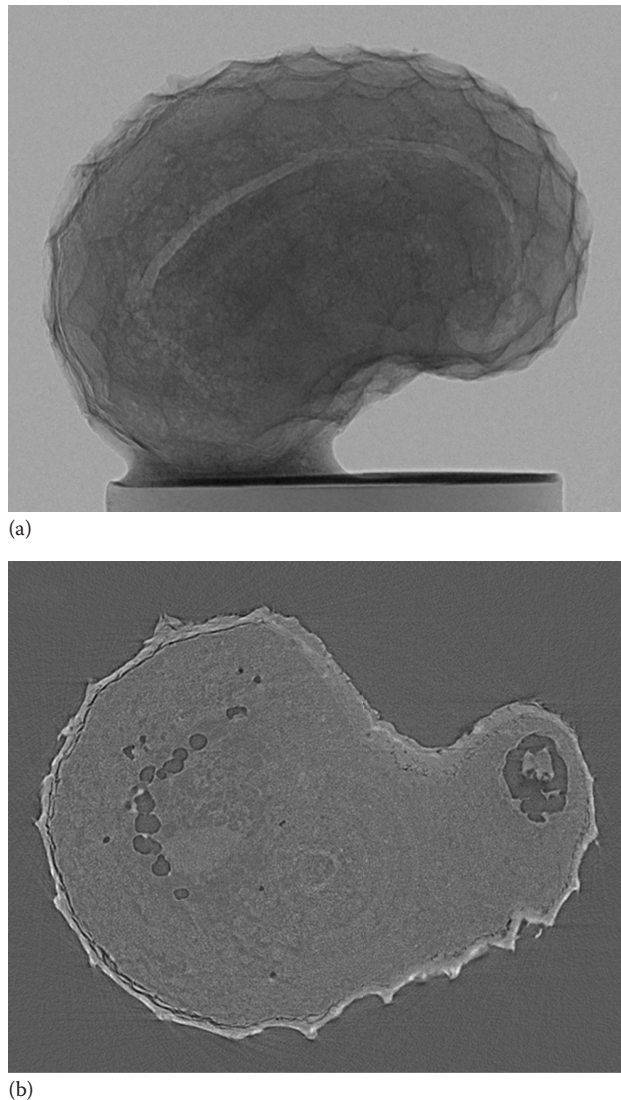


FIGURE 1.5 (a) Transmission x-ray digital radiograph of a poppy seed. The seed is glued to a stem. Note that the image reveals something about the inside of the seed but that three-dimensional information is collapsed into two dimensions. (b) Tomographic image of a cross section of the poppy seed shown in (a). Tomography produces (nondestructively) an image of a single plane through the object with all other planes eliminated.

The methods we address in detail (x-ray and γ -ray, neutron, and proton imaging) are part of the larger universe of NDE methods. Shull (2002) addresses a different NDE technology in each chapter of his book. Here we give just a brief introduction to the other main NDE methods to help the reader develop a context in which to compare x-ray and γ -ray imaging. We address proton and neutron imaging in Chapter 17.

PANEL 1.3 Double-Shell Target

For the 2004 LLNL Double-shell (DS) target campaign, computed tomography (CT) revealed concentricity within specifications, but two targets' wall thicknesses were not within

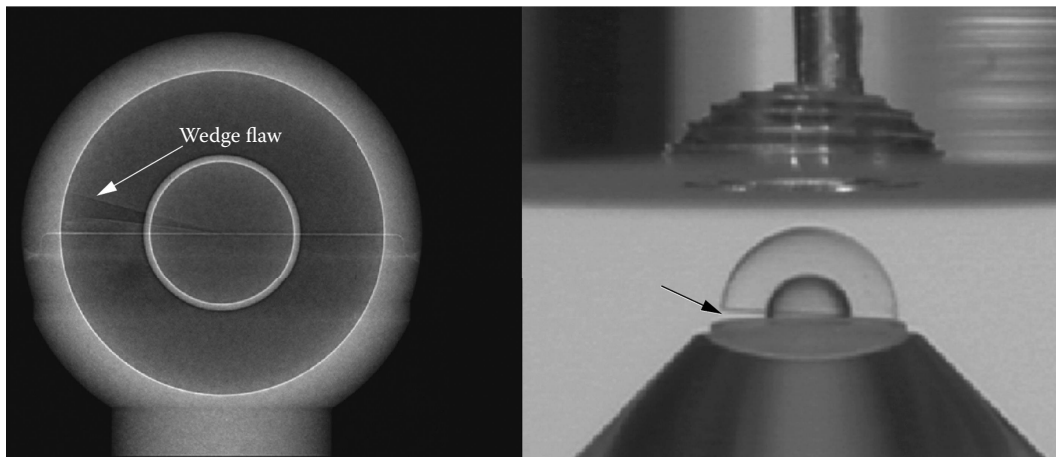


FIGURE 1.6 Representative x-ray DR from Xradia Micro-XCT system (left) reveals a wedge-shaped void. One can see why the wedge-shaped void may have occurred in the photo (right) of FY04 Double-shell (DS) target #7.

specifications (Brown and Martz 2006; Sain et al. 2006). In addition, digital radiography (DR) revealed step discontinuities and a wedge-shaped void in the aerogel (see Figure 1.6). Modeling results revealed that these wedge-shaped voids precluded meeting the performance specifications. Thus, the 2004 Double-shell (DS) target experiments were not executed. The x-ray data led to changes in the DS target manufacturing process and helped save the future of the DS program.

A new manufacturing process was developed to eliminate the wedge-shaped void and to better meet the other design specifications (Bono et al. 2007). X-ray data and extensive analysis revealed that the 2006 DS targets met the design specifications. Experiments confirmed the 2006 DS targets' performance. Additionally, our x-ray capability was used to help characterize Los Alamos National Laboratory (LANL) DS targets, and the success and documentation of our work has led to LANL, Sandia National Laboratories (SNL), and General Atomics purchasing Xradia Micro-XCT systems.

1.4 OTHER (THAN X-RAY AND γ -RAY OR ENERGETIC PARTICLE) NDE METHODS

There is no agreed-on or natural categorization of NDE methods. We have elected to make four categories for the methods that do not use x-rays and γ -rays, neutrons, or protons: (1) EM radiation methods, (2) acoustic methods, (3) tracer* methods, and (4) other.

1.4.1 ELECTROMAGNETIC RADIATION METHODS

EM radiation is a self-propagating wave in space with both electric and magnetic components. It is sometimes described as consisting of photons with varying energy that can be described as making up the *EM spectrum*. This EM spectrum is depicted in Figure 1.4. A photon can be defined by its energy, its wavelength, or its frequency. These are all interrelated, and the relationships are covered in detail in Chapter 4. Figure 1.4 presents all three metrics.

* A tracer is an identifiable substance, such as a dye, that is introduced into a mechanical system or object and followed to reveal information about the object or system.

The lowest-energy portion of the EM spectrum is classified as *radio waves*. Above this are *microwaves* and *radar*, and then *infrared (IR)*. The visible (to humans) spectrum makes up a very small fraction of the range of EM radiation. Next highest in energy after visible light is *ultraviolet* light. X-ray and γ -rays are the most energetic of the EM spectrum.

1.4.1.1 Optical Testing with Visible Photons

The easiest, most natural method of nondestructively inspecting an object is to look at it. When a person is considering purchase of an item such as an apple, he/she almost invariably visually inspects the item for insect damage and bruises. This method is simple, rapid, low cost, and intuitive. The major limitation is that it tests only the surface (except for transparent or translucent materials). A wide variety of optical aids can be employed to give visual access, illuminate, magnify, and record the scene.

The range and variety of optical testing is huge, and the boundary with the science of metrology is fuzzy (Allgaier and Ness 1993). Here we describe three examples of optical methods: candling, optical fluorescence, and exploiting interference fringes for flatness inspection.

1.4.1.1.1 Candling

The term *candling* is derived from the practice by farmers of inspecting chicken eggs under back illumination with a candle, as shown schematically in Figure 1.7. Electric light sources have replaced candles, but the principle is the same. A translucent material such as an egg or certain ceramics will reveal something about the internal structure when examined under bright light. Commercial ceramics are typically made by consolidation of powder. Some residual porosity remains. This causes translucency. Many types of internal flaws can be visualized in translucent materials using visible light. At LLNL, we have developed and patented (LLNL 2006) candling inspection for ceramic components that could not be characterized adequately with other methods. Our systems used transmitted, light but backscattered light is also used.



FIGURE 1.7 Translucent objects such as an egg reveal some internal defects when observed under illumination. The term *candling* is derived from the practice of using a candle as the light source to examine eggs. This technique is useful for examining translucent objects such as some industrial ceramics.

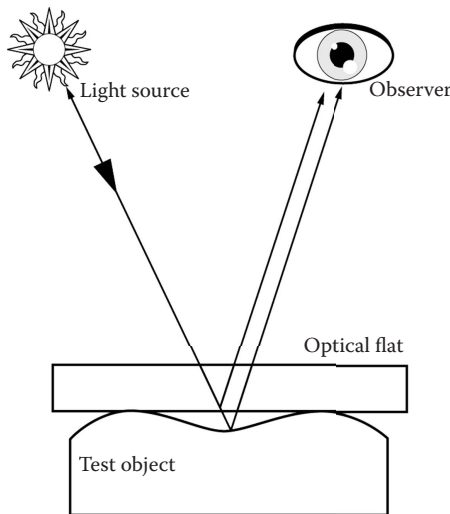


FIGURE 1.8 Schematic illustration of the use of interference fringes to access the flatness of a test object. Monochromatic light from a light source passes through an optical flat made of glass. The optical flat has a maximum deviation from planar of less than 25 nm. Waviness in the test object results in variation in the distance that the light must travel to the observer and creates constructive and destructive interference between the light reflected from the exit surface of the flat and the test object.

1.4.1.1.2 Optical Fluorescence

NDE methods are used extensively in food processing and packaging. The most common use is to guard against foreign material such as metal or glass. As in other areas, NDE is moving earlier in the life cycle of food production, to growth and harvest. For example, quantitative assessment of the sugar content of grapes has traditionally been done by destructive analysis of a small sample of berries manually selected from the growing crop. This destructive method limits the frequency and density of sampling. It is also subject to sampling error. Recently, German researchers have shown highly promising results in experiments to measure sugar concentration indirectly, via chlorophyll concentration. Chlorophyll fluorescence analysis has become a widely used technique in plant science. It is based on the principle that chlorophyll fluoresces when excited by light (Maxwell and Johnson 2000). Kolb et al. (2006) found that sugar type and concentration in two varieties of grapes are closely related to chlorophyll fluorescence. Their optical method is field portable, uses existing commercial instrumentation,* and provides a nondestructive analysis.

1.4.1.1.3 Optical Interferometric NDE Methods

There are many optical inspection methods that could be termed *interferometric*. That is, they are based on the interference of light with itself (Shull 2002, Chapter 10). The simplest interferometric method is used to assess the flatness of an object using fringes from a monochromatic light. The light source is usually a mercury arc lamp at 546 nm or He-Ne laser at 633 nm. There are many industrial objects whose flatness is a critical parameter. One method to determine flatness to high accuracy is to place a reference optical flat in contact with the surface to be inspected, as shown in Figure 1.8. Light reflected from the first surface of the optical flat is far from the inspection interface and does not (hopefully) interact with the desired light. Light from the second surface of the optical flat interferes with light reflected from the test object, producing fringes or bands of light and dark. These are called Newton rings or fringes and are shown in Figure 1.9. In general, if one places a flat part in contact with a flat reference surface, the two flat surfaces will not be exactly parallel,

* Such as Walz LS-C.



FIGURE 1.9 A photograph of the fringes formed by interference between a reference optical flat and a test object, as shown schematically in [Figure 1.8](#). In this case, the circular pattern indicates that the test surface is either concave or convex. This method cannot distinguish between concave and convex.

because of a varying thickness of the gas layer in the space between the flat surfaces. In this case, the fringes will be parallel. The fringes bend and swirl when a nonplanar surface is encountered. Departure from ideal flatness of less than one wavelength of the light being used (~500 nm) can be measured with this method.

Shearography is another optical interference technique that measures small surface deformations. When applied for NDE purposes, a component or assembly is stressed by some load, often pressure or vacuum. Defects are revealed by deformation anomalies (Hung and Ho 2005).

1.4.1.2 Thermal or Infrared Imaging

Starting in the 1980s, IR cameras became available that enabled imaging the surface temperature of an object or assembly. All objects emit IR radiation. Hot objects emit more IR photons, and they have higher energy than cool objects. IR wavelengths are just below the visible spectrum wavelengths (see [Figure 1.4](#)) at a wavelength of 1–100 μm . Objects whose temperature is from 200 to 1000 K emit strongly at IR wavelengths, and the quantity of radiation per unit surface area is a strong function of surface temperature.

Most commercial IR cameras are sensitive in some selected portion of the IR spectral region between 1 and 100 μm wavelength. They operate on the principle that the response of the detector is heavily dependent on the temperature of the surface emitting the radiation.

The development of IR imagers was strongly driven by the military *night vision* application. Industrially, these were applied as a process diagnostic or to evaluate thermal performance of insulation, electronic circuits, mechanical equipment, etc. These applications have become known as passive IR imaging or passive *thermography*. They are called passive because they rely on the emissions of the object under examination and use no external source of heat.

A much broader range of applications has sprung up in which active heating is employed (Shull 2002, Chapter 8). These applications are called active thermography and often rely on cameras that can acquire thermal images at video (or higher) rates. Broadly stated, these methods work because the flaws they detect disrupt the normal flow of heat by conduction in a material, or because the flaws can

be made to become sources of heat by external excitation. The most common implementation is to use optical excitation from an active source with temporal control (Wei and Lawn 1996) to introduce a thermal pulse at the surface of an object under examination. The heat source can be a lamp, a flashlamp, a laser, or even a hot air blower, depending on the temporal resolution required (Maldague 2001).

Less commonly, the heat for thermography is generated within the flaw by excitation with sound (Favro et al. 2000; Miller et al. 2003). The terms *vibrothermography* and *sonic IR* are sometimes applied to this method. Microwaves can also be used to generate heat at some types of flaws (Osiander et al. 1995).

A simple example helps to understand the principle involved in active IR imaging. Consider the schematic in Figure 1.10. The test object is steel with homogenous and isotropic thermal properties throughout except in the region of the flaw. Take the flaw to be a flat disk filled with oxides entrained during fabrication. Assume that the thermal diffusivity is lower in the flaw compared to the bulk material. If we subject the test object's top surface to a short pulse of energy from an IR laser, the surface temperature will rise uniformly. The surface temperature will decrease as the heat is conducted into the test object over time. But, the flaw reduces the heat flow away from the top surface so that at some time, the temperature at B will be higher than the temperature at A.

Some thermal imaging techniques employ periodic structure on the incident heat, though the mathematical description of the thermal transport involved has been the subject of professional disagreement.

Because it employs (special) optics, the field of view can range from microscopic to many meters. For a large field of view, the thermal source becomes unwieldy. Large data sets can be generated with thermal imaging since a test may generate several hundred images. The method has found frequent application in evaluating bonds, coatings, and lap joints (Maldague 2001).

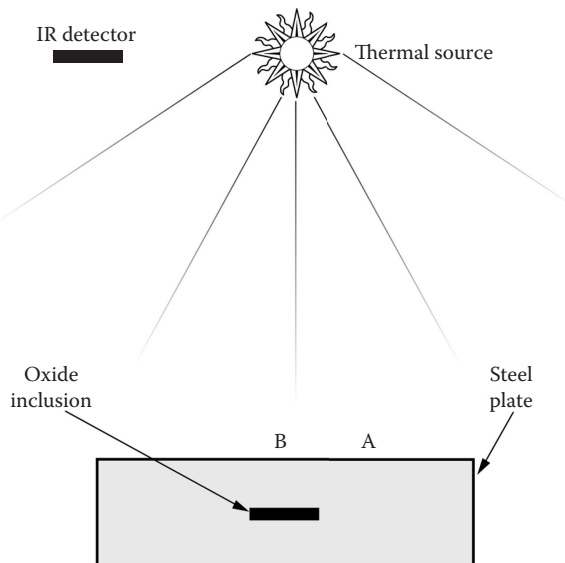


FIGURE 1.10 A schematic of how active thermography is done. In most active thermography, a thermal source is used, though other active heat generation schemes are possible. When a thermal source is used, it is temporally varied, usually pulsed. When the source in this illustration is pulsed, the surface of the steel plate is heated—initially uniformly. As heat is conducted down into the plate, it encounters a defect, an oxide inclusion. This defect is lower in thermal diffusivity than the surrounding steel, which causes the temperature at B to be higher than the temperature at A after some time has passed. A thermal area detector (e.g., IR camera) images variations in the surface temperature of the plate, and this is related to the thermal conductivity in depth.

1.4.1.3 Gigahertz–Terahertz Waves (Microwaves and Millimeter Waves)

There has been widespread misuse of the terms *microwaves* and *terahertz (THz)*. Microwaves are EM waves with wavelengths longer than those of THz wavelengths but are relatively short for radio waves. Microwaves have wavelengths approximately in the range of 30 cm (frequency = 1 GHz) to 1 mm (300 GHz) (see [Figure 1.4](#)). This range of wavelengths has led many to question the naming convention used for microwaves, as the name suggests a micrometer wavelength but they are more of the order of millimeter wavelength. However, the boundaries between far-IR light, THz radiation, microwaves, and ultra-high-frequency radio waves are fairly arbitrary and are used variously between different fields of study. Here we follow the NAS (2007) definition.

- Millimeter waves: the region from 30 to 300 GHz
- Submillimeter waves: the region from 300 to 1000 GHz
- THz: the region from 1000 to 10,000 GHz (1–10 THz)

Human utilization of millimeter waves has roots in radar and communication. By the 1960s, millimeter waves were being used in NDE applications. As is often the case with new methods, high-value components and systems such as aerospace hardware and military aircraft were among the first items where millimeter wave inspection was employed (Shull 2002, Chapter 9).

This method of NDE has seen rapid development in the past decade, especially for detection of weapons or explosives. Different descriptors are applied to similar technology. A few are millimeter wave, THz, submillimeter wave, and gigahertz (GHz). This type of system can be active (using a powered transmitter) or passive (detecting emitted millimeter waves).

Passive imaging detection techniques rely on collecting the radiation that is naturally occurring and using the contrast between apparently warmer and colder objects, which usually results from contrasts between different material emissivities. Active imaging systems illuminate (using a source/transmitter) space with a beam of GHz/THz power, either illuminating the entire space or as a focused beam that is scanned over the space (the area of the object of interest), the transmitted or reflected beam is recorded by detectors (receivers) specifically sensitive to the illuminating frequencies.

For example, in active millimeter wave imaging, GHz waves are sent into the object under test from a transmitter. The receiver may be on the same side of the object as (sometimes even collocated with) the transmitter (reflection mode), or it may be on the opposite side of the object from the transmitter (transmission mode). Millimeter waves have very limited penetration depth in electrical conductors, so they are generally not applicable to finding internal flaws in metals. They are useful for detecting surface cracks and sensing surface roughness of metals. Millimeter waves find wide application in NDE of coatings, plastics, wood, fiber composites, and ceramics. THz waves have been applied to NDE of the spray-on foam insulation used on the US Space Shuttle (Case et al. 2006). GHz and THz waves also form the basis for a class of instruments that determine moisture content in cereal grain and other agricultural products (Chua et al. 2004).

In 1993, Tom McEwan (1993) invented a unique type of radar at LLNL.* He built a single-shot transient digitizer that was then adapted into a remarkably small, low-power radar system. LLNL called this device a *micropower impulse radar* (MIR). Some of the applications for this technology are NDE in nature. An MIR sensor array is the heart of a bridge deck inspection system called HERMES (Davidson and Chase 1998). A monitor for cargo shipping containers is being developed. The technology and market status of these devices was reviewed in a 2004 publication (Azevedo 2004). These MIR sensors have been successfully commercialized for two applications. Magnetrol offers level sensors, and GE Security has motion detection products.

Passive and active GHz/THz imaging techniques are under research, development, and testing to detect metal guns concealed underneath newspapers, clothing, etc., by detecting the contrast between the warmer human body and the apparently cooler metal weapon (see [Figure 1.11](#)). Active

* Tom McEwan left LLNL in 1996 to found McEwan Technologies.



FIGURE 1.11 Representative passive 35 GHz images of a gun (top inset) and a knife (bottom left) concealed inside a newspaper. Note the high-contrast nature of the metallic weapons. The bottom is a mirror image of the one in http://www.vision4thefuture.org/s7_gallery/galleries/g_mmw/myalbum.html. (Bottom figure from Vijayalakshmi, P., Sumathi, M., *IOSR Journal of Computer Engineering (IOSR-JCE)*, 13, Issue 2, 25-32, 2013.)

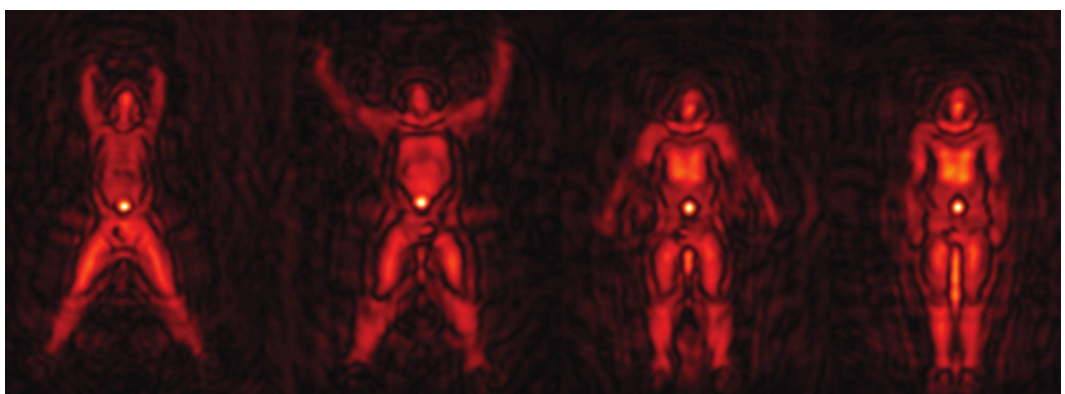


FIGURE 1.12 These images of a man were generated by reconstruction of data from an MIR array. Images can be presented in this human intuitive format at a rate of 4 frames per second.

GHz/THz techniques are of interest since they are nonionizing radiation that penetrates the human body to only about skin depth. Therefore, the potential health effects of this radiation are significantly lower than the competitive imaging technology using ionizing x-ray radiation.

Another more challenging application garnering interest from the military and law enforcement agencies is the ability to discern human activity through nonconductive walls. Recent developments in signal processing permit real-time visualization of GHz/THz images in a presentation that is intuitive to an untrained observer. The data of [Figure 1.12](#) were reconstructed and presented at a rate of 4 frames per second (Romero 2006). EM radiation of these frequencies can penetrate most common walls and even substantial concrete. The ability to determine the number and location of adversaries within a structure along with some information about their movement and activities might be useful in many situations.

1.4.2 NDE METHODS USING ACOUSTIC ENERGY

Acoustic energy, mainly sound above the frequency of human hearing (called ultrasound), is very widely employed in NDE. In most applications, ultrasound is generated and measured in a transducer. This type of active interrogation is called *ultrasonic testing*. When the ultrasound is generated by the process or object of interest, a transducer is used to listen, and the technique is called *acoustic emission*.

1.4.2.1 Ultrasonic Testing

Many NDE technologies have been spawned by military applications. In the case of ultrasonics, a civilian tragedy—the sinking of the Titanic ocean liner in 1912—provided the impetus for the first application. Ultrasonic methods were quickly developed to sense the presence of large icebergs at sea. This was quickly followed by systems designed to detect submarines.

Ultrasonic NDE utilizes sound waves that are above the range of human hearing. A frequency of 20 kHz is usually taken as defining the upper end of human hearing. Most NDE with ultrasound uses frequencies from 50 kHz to a few GHz (Krautkramer and Krautkramer 1990). Most industrial ultrasound NDE is performed by contact techniques. This simply means that some material other than air is used to couple the ultrasonic waves into the object being studied. Ultrasound is generated in a transducer, coupled into the test object, and then received by a transducer after transit through the test object. The receiving transducer may be either the sending transducer or a second transducer. When a second transducer is used, it may be used in transmission mode, where it measures the sound transmitted through an object, or it may be used in reflectance mode, where it measures sound reflected back in the direction of the source transducer. This latter configuration is most widely used and is often called the *pulse-echo* method. These configurations are shown schematically in [Figure 1.13](#).

Most people are probably somewhat familiar with medical ultrasound. The use of ultrasound to monitor and diagnose the fetus during pregnancy has become widespread in industrialized countries. An important attribute of ultrasound for medical applications is that it is inexpensive and safe compared to x-rays and magnetic resonance imaging.

One attribute of ultrasound that has a strong influence on the way it is used for NDE is that transmission across a solid/gas interface is low. This means that a liquid or gel *couplant* is usually used to get ultrasound from transducers into and out of the object. Often, industrial ultrasound inspection is done in a water tank—known as immersion ultrasound. For materials that are incompatible with water, other liquids (oils) can sometimes be used. Also, compliant solids such as rubber can serve as a couplant.

For some applications, such as in-service examination at elevated temperature, any common couplant is not acceptable. In the last decade, lasers have begun to be employed to both generate and detect ultrasound. This provides a noncontact means of performing ultrasonic NDE. For some applications, piezoelectric transducers using air coupling are sufficient. Another noncontact method, useful in metals, uses EM coupling to generate ultrasonic waves in the object to be examined. These transducers are known as electromagnetic acoustic transducers (EMATs) (Birks and Green 1991).

A consequence of low ultrasound propagation across solid/gas interfaces is that an air gap or large gas-filled defect effectively hides whatever is behind/beneath.

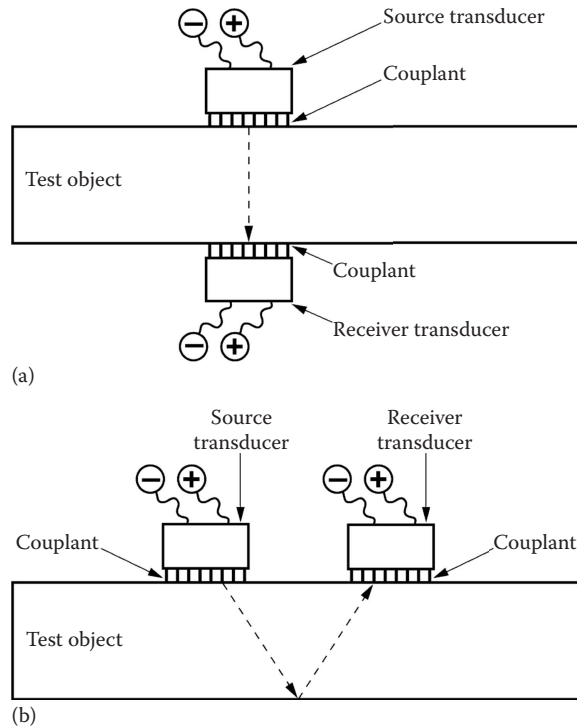


FIGURE 1.13 The essential features and components of an ultrasonic NDE system. A source transducer converts an electrical waveform to a mechanical displacement. The displacement is transferred through a couplant resulting in an acoustic wave in the test object. The receiving transducer converts the surface displacement back into an electrical waveform and may be on the opposite side of the test object as in (a), or it may be on the same side as in (b). The function of source and receiver transducer may also be combined into a single unit.

Ultrasonic techniques are most often used to detect internal flaws such as cracks or inclusions. The velocity of an acoustic wave depends on the elastic properties of the material and the mass density. This leads to applications of measuring thickness, material anisotropy, residual stress, and material microstructure such as grain size and orientation. If thickness and mass density can be determined, then Young's modulus can be measured. Ultrasound is the only mainstream NDE method applicable to thick objects with access to only one side.

1.4.2.2 Acoustic Emission

There exists a broad range of applications of ultrasound to diagnose a process and/or the state of a machine or component in which the sound energy is generated by the object or machine of interest. The method is simply to listen to what the object is saying. In addition to the more obvious situations, there is a broad range of less obvious situations. All of the following emit sound that is used to monitor/diagnose the process or machine:

- Crack propagation (Roberts and Talebzadeh 2003)
- Plastic deformation in crystals (James and Carpenter 1971)
- Machining (Li 2002)
- Leaks, especially gas leaks (Yoshida and Asano 2003)
- Rotating machinery (Mba and Rao 2006)
- Liquid cavitation in pumps (Alfayez et al. 2005)
- Impact damage (Madaras et al. 2005)

Before leaving the subject of acoustic emission, we must mention that there are many applications where sound within the range of human hearing is used to diagnose a process or machine. While these are not usually thought of as NDE, they have a close resemblance. Examples include the following:

- Pinging in an internal combustion engine
- Automotive water pump failure
- Air leak from a tire/tube
- Noise from a disk drive
- Crack of a baseball bat
- Faucet drip

1.4.3 NDE METHODS USING A TRACER

In this subsection, we describe three methods. The first two methods, dye penetrant and magnetic particle, are ultimately visual in that they rely on the inspector to see a marker or tracer material concentrated at a flaw. The third method uses a nonvisual tracer for leak detection.

1.4.3.1 Dye Penetrant Testing

Dye penetrant testing is used to accentuate surface-breaking cracks or other defects (Tracy and Moore 1999). The earliest penetrants were thinned oils. These were applied by immersion where possible. Then the surface was cleaned and coated with a white powder. As the penetrant leaked from the defect back to the surface, it stained the powder.

Contemporary penetrant testing includes these same basic steps. Modern materials are more effective, and dyes, either visible or fluorescing, are incorporated into the penetrant. For this method to be effective, the surface and the defects must be clean. Defects filled with oil or even water preclude entry of the penetrant. The inspector applies penetrant by spraying, brushing, or immersion. After a suitable dwell time, excess penetrant is removed, and *developer* applied. The developer serves to draw penetrant from flaws back to the surface and to cause it to spread, thereby enhancing visibility of the flaw. If the penetrant is of the fluorescing type, an ultraviolet light source is used for inspection. Finally, the inspected part is cleaned (ASTM E 1417 1999; Tracy and Moore 1999; Shull 2002, Chapter 2). [Figure 1.14](#) shows a graphic example of cracking revealed by fluorescing dye penetrant.

Dye penetrant testing is easy to use and highly flexible. It can be readily done in the field, and the equipment* is inexpensive. It can be used for inspecting any material so long as the surface condition is suitable. Dye penetrants can only detect surface-connected flaws in clean objects. They cannot be used reliably on porous, coated, or painted surfaces. Some machining and finishing operations can create false indications and hide serious flaws.

1.4.3.2 Magnetic Particle Inspection

Magnetic particle testing is a method that relies on magnetic flux leakage at the site of a crack or other surface defect (Schmidt et al. 1989). It can only be applied to ferromagnetic materials. A magnetic field is externally applied to the part to be inspected. Small magnetic particles are applied to the surface, and these are attracted to the flux leakage. The magnetic particles are often dyed or contain a fluorescent coating so that they can be made more visible (Betz 1967).

A magnetic field can be imposed on a test object in a variety of ways. Permanent magnets are sometimes used, especially where the local environment (underwater, in the presence of explosives) presents a danger if a spark or current leakage occurs. Electromagnets are more common. Magnetic particle equipment is often portable without regard to the type of magnet.

* Magnaflux is one company selling these products.

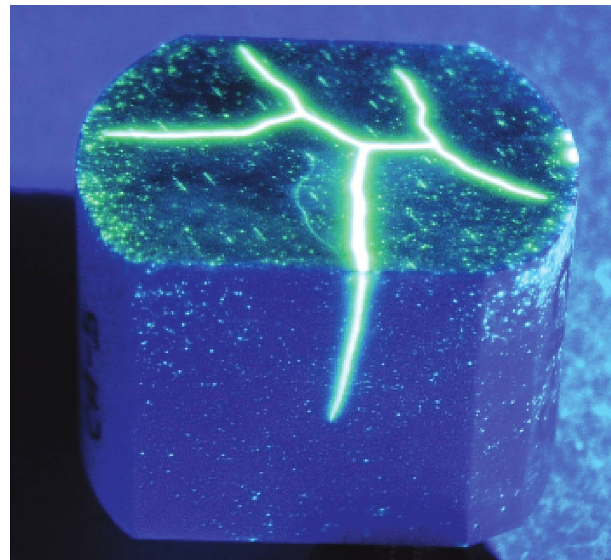


FIGURE 1.14 Digital photograph of a cracked alumina specimen that was treated with Magnaflux Zyglo ZL-37 fluorescent penetrant, Magnaflux SKC-HF cleaner/remover, and Magnaflux ZP-4B powder developer, and then illuminated with Magnaflux ZB-23A ultraviolet light.

This method is directional. The magnetic flux must cross a crack rather than run parallel to a crack for it to be revealed. This is shown schematically in Figure 1.15. In the orientation shown, flux leakage occurs at the crack. If the long axis of the crack were oriented parallel to the direction of the magnetic field lines, no leakage would take place, and the magnetic particles would not be attracted to the vicinity of the crack. The surface finish of the part is important when applying magnetic particle testing. Defects must be several times the surface roughness to be detected.

Magnetic particle inspection is used extensively. The equipment is simple, inexpensive, and reliable. The limitation of use only on ferromagnetic materials is less limiting than might be first imagined. Most manufactured objects are made of steel. Worldwide annual production of steel is 10^9 metric tons. This is 30,000 times the world's production of aluminum (USGS 2004).

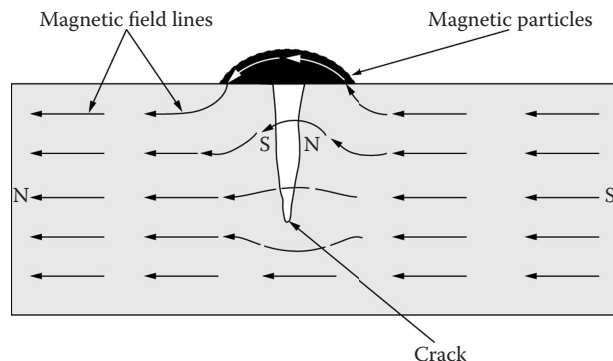


FIGURE 1.15 Schematic of a surface crack causing magnetic field lines to attract magnetic particles to the vicinity of the crack. This effect is exploited to help visualize surface flaws. Note that the technique requires that the magnetic field lines cross the crack, not run along with the crack. The material must be ferromagnetic.

1.4.3.3 Leak Testing

A large number of tanks, pipes, and packages are produced worldwide. Most of these are intended to contain gases, liquids, or food without leaking. Some type of leak test is frequently performed on such containers. In addition, these containers may be subjected to corrosion from contents and/or external environment and may require in-service or periodic testing.

One note of caution is in order. Leak testing frequently involves pressurization. This must be done with safety in mind. The rated pressure of a container must never be exceeded. This is especially true when gases are used. The stored energy in a gas-filled container can be an extreme hazard.

Perhaps the simplest leak test technique uses a dauber to apply soapy water to the low-pressure side of a (gas) leaking container. Most of us probably applied this method to bicycle inner tubes in our youth. Soapy water has been replaced with specially formulated liquids such as the Leak-Tec product series.* These liquids consist of mixtures of stable synthetic surfactants with low surface tension and low interfacial tension on metals. They wet the surface and spread evenly, forming cluster of bubbles, which collapse and reform at leaks. The moving bubbles are highly visible. These materials require little or no cleaning and do not interfere with painting as soap does. This method is very common on piping for refrigerants and natural gas (Jackson et al. 2000).

Another leak test technique employs a tracer gas or liquid. The tracer is chosen for compatibility with the container and availability of a detector. Helium is a popular tracer gas. Helium detectors based on mass spectrometry are expensive but commonly available. Another common tracer gas is sulfur hexafluoride (SF_6). It is an inert heavy gas for which sensitive detectors are inexpensive[†] and readily available.

One everyday tracer for leak detection is mercaptan, the odor we associate with natural gas. Mercaptan is intentionally added to natural gas so that the human nose can serve as a leak detector. Radioactive gases can provide superb leak detection sensitivity, but the issues associated with use and release of radioactive material limit the applicability of these materials.

1.4.4 OTHER NDE METHODS

One highly used NDE method does not fit our other categories. It does not use EM photons, acoustic waves, or tracers. That method is eddy current NDE.

1.4.4.1 Eddy Current NDE

Eddy (circulating) currents are induced in an electrically conductive material when it is exposed to a changing magnetic field. To exploit this principle for NDE, an alternating-current coil is used to produce changing magnetic fields in a test object. The changing magnetic field causes eddy currents to flow. This, in turn, produces magnetic fields. The interruption of eddy currents by a defect influences the magnetic field (Hagemaier 1990). Either the exciting coil or a separate sensing coil is used to observe the effect of a defect on induced eddy currents. This is shown schematically in [Figure 1.16](#).

Eddy current testing is a surface-sensitive NDE technique, although the penetration depth does vary with the frequency of the exciting coil. It can be frustrating to use because it just gives an indication that something is changing the eddy currents. It does not give much of a clue what the something is. For this reason, it is most often used when a specific defect type that can be detected by this method is expected and/or of concern. It is also coupled with modeling and simulation for improved understanding (Auld and Moulder 1999).

Eddy currents are influenced by the electrical conductivity of the object. This can be exploited to verify specific alloys and heat treatment. Eddy current response is very sensitive to spacing between the probe and the object under examination. This is a curse for most applications but can be used to determine coating thickness and uniformity. Also, on thin materials, the eddy current method can

* Leak-Tec is a product of Amtec.

[†] DILO makes SF_6 leak detectors.

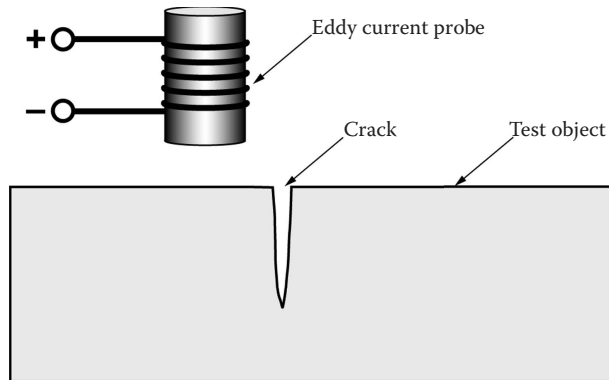


FIGURE 1.16 In the eddy current method of NDE, the material under test must be an electrical conductor. Alternating current in the probe induces alternating current in the test object, called eddy currents. These currents cause their own magnetic field that is sensed by the probe. A near-surface flaw influences eddy currents.

give indication of backside corrosion thinning. It is used on aircraft skins (Siegel and Gunatilake 1997) and on boiler tubing. This has also been used to inspect metal welds.

1.5 EFFECTIVENESS AND STATISTICS OF NDE

Many measures of performance for NDE methods and systems have been developed. We will define and discuss *POD*, *critical flaw*, *sensitivity*, *specificity*, *positive predictive value* (PPV), *negative predictive value* (NPV), *prevalence*, and *receiver operating characteristic* (ROC). More details are given in Section 14.6, Probability of Detection and ROC Curves.

1.5.1 PROBABILITY OF DETECTION

The United States Air Force (USAF) frequently uses a descriptor called *probability of detection* (*POD*) (USAF 1999). This descriptor is used in scattered applications throughout industrial NDE (Berens 1989; Olin and Meeker 1996; NTIAC 1997). POD is most often expressed as a function of flaw size. A hypothetical example is shown in Figure 1.17. Suppose the USAF wanted to detect the presence of porosity in Al welds of a certain configuration. They could choose to use pore volume as the relevant measure of flaw size. They could create a POD curve for a specific configuration of ultrasonic inspection by having test specimens with known pores. It turns out that larger pores are easier to detect. The POD curve developed would resemble the curve of Figure 1.17. Computational models can be used to reduce the number of test specimens required. This method is useful in qualifying a vendor or process, *but* it has two very substantial deficiencies:

1. POD tells you nothing about the rate of incorrect (false) “detections.”
2. The POD methodology may tell you very little about how the technique will perform on an actual product stream with unknown defects (Annis and Erland 1989; Matzkanin and Yolken 2001; Georgiou 2006).

1.5.2 POSITIVE PREDICTIVE VALUE AND NEGATIVE PREDICTIVE VALUE

We define a *critical flaw* as a flaw that is unacceptable. In NDE of critical flaws, *true positive* means correctly identifying an actual critical flaw, and *false negative* means not identifying an actual critical flaw. *Sensitivity* of an NDE method is the probability of detecting a critical flaw given that one exists. *Specificity* is the probability of an NDE method not indicating a critical flaw

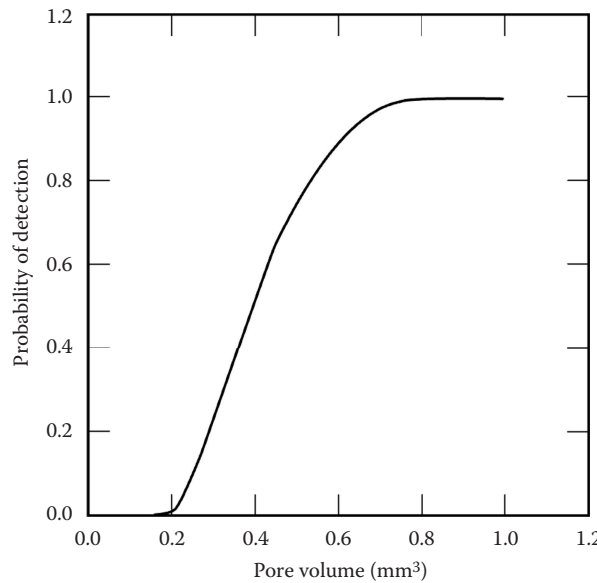


FIGURE 1.17 A hypothetical curve for probability of detection (POD).

when none exists. Some discussions refer to a false positive rate. In this case, NDE falsely identifies critical flaws that do not exist. The false positive rate is given by $(1 - \text{specificity})$. Specificity, sensitivity, and their variants depend on the NDE method, operator skill, the objects under evaluation and the flaw (Annis 2007). The numerical example in Panel 1.4 will prove helpful in understanding these terms, but first we need to understand two more very important metrics of NDE performance.

Often, the performance of an NDE method must be considered in the context of the flaws present in the product under inspection. Consider the following two questions: (1) Given that NDE has found a critical flaw, what is the probability that a critical flaw actually exists? (2) Given that NDE has declared a part to be free of critical flaws, what is the probability that the part is actually free of critical flaws? These two probabilities are called positive predictive value (PPV) and negative predictive value (NPV), respectively. These are not the same as sensitivity and specificity. PPV and NPV depend on sensitivity, specificity, and the *prevalence* of critical flaws in the parts under evaluation. This is a result that is worth repeating. *The sensitivity and the specificity depend on the NDE test. PPV and NPV depend on the NDE test and on the population of parts being tested.*

PANEL 1.4 Sensitivity, Specificity, PPV, and NPV: An Example

An imaginary example is helpful to illustrate these concepts. Suppose we have an NDE system for explosives detection in checked airline baggage. It has a sensitivity of 0.98, meaning it will detect 98% of the bags containing a threat amount (critical flaw) of explosives. This method has a specificity of 0.95, meaning that the method gives a false indication of explosives in 5% of the baggage inspected. An NDE method with this performance is a very high-performance system. It seldom gets better than this. But, consider what happens when it is applied to a baggage stream in which each bag has a very low probability of actually containing explosives, say 0.0001. After we have inspected a million bags, about 100 containing explosives will have passed through the system. Two will have slipped through and caused two hypothetical crashes

with a loss of 447 lives. Meanwhile, 50,000 bags were falsely accused of containing explosives. These were cleared manually at a hypothetical labor cost of US\$5 M and with 15,000 flight delays. The PPV of this system with this population of bags is 98 true positives divided by 50,098 total positives, or 0.00002. The NPV is 949,902 total negatives divided by 999,900 actual negatives, or 0.95. This explosives detection system may not be perceived as having high performance. There would likely be a lot of attention paid to 2 crashes and 50,000 bags (and owners) falsely accused.

In applications that might be thought of as “screening,” we often find a low probability of a critical flaw and limited tolerance for false positives. In medicine, this occurs in testing for disease with low prevalence. Application of x-ray imaging for detection of breast cancer (mammography) is an example. With mammography, false positives outnumber true positives by about 4:1. This is tolerable only because the cost (advanced breast cancer) of not screening is much higher than the cost (anxiety and additional medical procedures) of the false positives. In an industrial setting, when a manufacturing process and quality control are really good, then the prevalence of critical flaws is low, and the job of NDE is very difficult. This is exactly what the developer of explosives detection systems faces. The consequence of a false negative can be very high, while a high rate of false positives results in delays and inconvenience.

In the opposite extreme, when the prevalence of a critical flaw is high, say 50%, an NDE system with sensitivity of 0.98 and specificity of 0.95 might be seen as superb. After a million parts have been inspected, 490,000 bad parts will have been rejected (1,000,000 parts times 0.5 have critical flaws times 0.98 detection rate). Ten thousand bad parts slipped through (500,000 bad parts, but 490,000 were detected), and 25,000 good parts were falsely rejected (500,000 good parts times [1–0.95]). In the remaining population, the prevalence of critical flaws has been reduced from 50% to 2%. This system looks pretty good. The overwhelming majority of rejected parts were bad. And the chance of a critical flaw causing a problem has been reduced by a factor of 25 (0.50 initial prevalence divide by 0.02 prevalence after NDE).

With most NDE systems, it is possible to increase the sensitivity (by changing the decision criterion, for example), but this is invariably accompanied by a higher incidence of false positive indications. When the NDE method is x-ray imaging, the radiographer is usually part of the system. By this we mean that the radiographer observes the image and decides whether a critical flaw is present. With this system, if the radiographer is instructed to miss fewer actual flaws, the rate of false positives (rejected good parts) increases. In the limit, the radiographer can identify all the flawed parts by rejecting all parts. This is equally true of other NDE techniques and even automated (computerized) flaw detection. Changing limits/thresholds to increase sensitivity causes specificity to drop.

Sensitivity can be improved without a penalty in specificity if an improvement is made in the NDE method or if an additional independent measurement is added. This often involves combining NDE technologies, for example, performing both radiography and ultrasonic NDE.

1.5.3 RECEIVER OPERATING CHARACTERISTIC CURVE

The trade-off between sensitivity and specificity for an NDE system can be expressed as an ROC curve (Olin and Meeker 1996). Example ROC curves are shown in [Figure 1.18](#). The true positive fraction (sensitivity) is plotted versus the false positive fraction ($1 - \text{specificity}$). A system relying on random chance, such as a coin flip, will have an ROC curve that is a diagonal straight line, as depicted in Figure 1.18. A system that is a little bit better than random will bow upward, as the curve labeled “better” in Figure 1.18. A reasonable system will bow sharply up, as the curve labeled “best” in Figure 1.18. We see that with the system labeled “best,” we can operate so that we catch 80% of the critical flaws while rejecting 20% of the good parts.

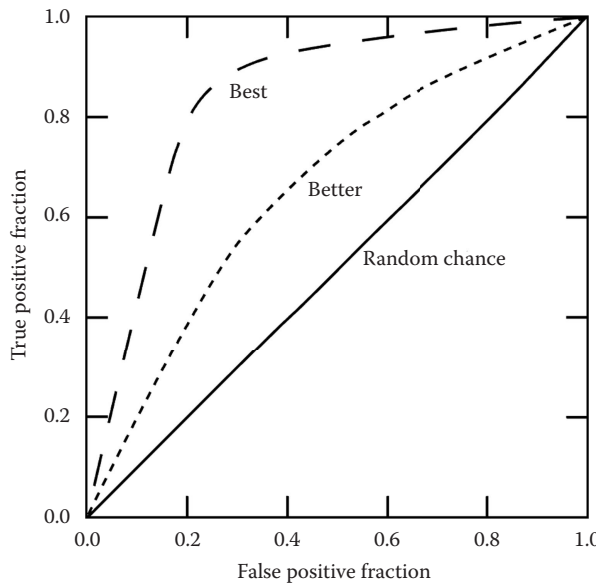


FIGURE 1.18 A receiver operating characteristic (ROC) curve expresses the true positive fraction as a function of the false negative fraction. The diagonal line represents a system that flips a coin to accept/reject. Useful NDE systems are bowed upward.

We can see from the preceding simple examples that the area under the ROC curve captures much of the essence of the situation. An area of 0.5 indicates that the NDE system is as good as a coin flip, while an area of 1.0 indicates a perfect system. It never misses a critical flaw, and it never rejects a good part.

The ROC curve is very widely applied in medicine, more often than in industrial applications. Zou (2006) has published an extensive bibliography of medical ROC literature. The ROC approach is now being increasingly applied in contraband (drugs, weapons, explosives, *special nuclear material*) detection.

1.6 WHEN AND HOW MUCH NDE

It is not always necessary or appropriate to perform NDE on 100% of the parts produced. In some instances, NDE is used as a component of process control. It may be sufficient to perform NDE on every tenth item and use that result to adjust the process. We have worked with manufacturing systems that produced very consistent parts (a weld, for example) over the short term but drifted out of compliance over several shifts of operation. NDE on the welds can be used to schedule maintenance before any defective parts are produced.

It can be more effective to perform NDE at the front end of a manufacturing process rather than on manufactured parts. We worked with an industrial application in which defective parts were being caused by defective feedstock, coiled sheet steel in this case. Inspecting the sheet steel as it entered the manufacturing line identified defective stock and diverted it to the scrap bin before any manufacturing effort was expended. It is also much simpler and easier to perform NDE on raw material in a simple flat geometry than on a deep-drawn part.

1.7 INDUSTRIAL X-RAY IMAGING CONTRASTED WITH MEDICAL X-RAY IMAGING

Even with the recent surge in funding for *homeland security*, the monetary value of the market for medical x-ray imaging equipment is many times that for industrial x-ray equipment. One result of

this is that much of the new x-ray technology being developed is aimed for medical and introduced into that market, and then subsequently adapted for industrial applications. Industrial applications without a medical analog have not generally been the beneficiaries of significant corporate research and development efforts.

Two examples help illustrate this situation. Electron accelerators, operating at several MeV electron energy, are widely used as x-ray sources for radiation therapy (as a treatment for cancer). This is the market for which they were developed. Some are sold for industrial radiography of thick sections and especially for high-density materials, but this market is insufficient to justify development and manufacturing of such machines. The medical market is about US\$2 B annually for these machines. The industrial market is about 5% of medical, even with the recent upturn in interest for cargo inspection (J. Clayton, pers. commun. 2005).

A second example is flat-panel imaging detectors (Varian 2014). Development of these panels probably required US\$500 M. Everything about them was focused on replacing film for medical radiography applications. Units with higher spatial resolution are possible and would be of great utility in industrial applications. These are not developed rapidly, because in medical applications, they would not be useful. The alert student should question why increased spatial resolution is not marketable to medicine. This leads to the next comparison between medical and industrial radiography—dose.

In medicine, radiation absorbed dose (defined and discussed in Chapter 7) to the patient is always of concern. It is a physical reality that maintaining good image fidelity with higher spatial resolution requires using more x-ray photons. This results in a higher radiation absorbed dose to the patient (Hasagawa 1991). Everything about the design of medical x-ray technology considers radiation absorbed dose. This is almost never a concern in industrial imaging. Using more x-rays may result in longer data acquisition times, but seldom does this endanger the specimen.

For decades, film was the only practical imaging detector for either medical or industrial radiography. The films for the two applications have almost nothing in common. In medicine, except for dental, film is designed to be sensitive to visible light emitted by a *scintillating screen*. The x-rays interact in the scintillating screen, producing visible light that in turn exposes the film. This two-stage process is necessary to achieve good dose efficiency. Medical film usually has light-sensitive coating on both sides of a structural base. The exceptions are (1) dental films, which resemble industrial films in that they are designed to be used without a scintillating screen, and (2) mammography films, which use a scintillating screen but are coated on only one side. In both cases, this design is to achieve good spatial resolution. Dental x-rays are a relatively high-dose procedure. Mammography delivers an acceptable dose because the relatively low energy of the x-rays used results in fairly high stopping efficiency in a single scintillating screen. Industrial film is most often used without scintillation screens. It is directly exposed by x-rays. When the highest spatial performance is needed, a single-emulsion film (coated only on one side) is used.

Film for medical usage is generally designed so that small changes in radiation create large changes in film darkness. This is needed as a consequence of combining the function of radiation detector with image display. Humans can only discriminate between about 100 different gray levels between black and white. Because of this, the image display has to present the important information with very high contrast. This means the medical film has a very small dynamic range. Industrial film, on the other hand, is usually designed to have a dynamic range five or more times that of medical film but lower contrast. Fortunately, most defects in industrial radiography have higher object contrast than medical applications. Also, the higher spatial resolution of industrial films allows digitization and digital manipulation.

We cover radiation detectors in depth in Chapter 9, Radiation Detectors, but there is not much about film since it is adequately covered by other references and it is diminishing in importance.

2 X-Ray History

2.1 HISTORY INTRODUCTION

In this chapter, we will introduce the student to the pivotal events and some of the interesting side roads in the history of industrial radiography. We begin with the *Crookes tube*, then describe Röntgen's discovery of x-rays in detail, and finally touch upon the other major historical developments that form the foundation for today's industrial radiography industry.

Upon completion of this chapter, you will have been introduced to the following:

- Crookes tube
- Cathode ray tube
- Röntgen's discovery of x-rays
- Röntgen's publication
- Events after the discovery
- Röntgen's Nobel Prize
- Injuries and inappropriate use of x-rays
- Coolidge's improved x-ray tube
- Pioneers in computed tomography (CT): Cormack and Hounsfield (with homage to Radon)
- The beginning of industrial CT
- Important enabling technologies for industrial CT

2.2 LAYING THE FOUNDATION

In 1875, Sir William Crookes invented what came to be known as the *Crookes tube*, the forerunner of cathode ray tubes (CRTs) used for computer and television imagery. The Crookes tube (sometimes referred to as a discharge tube*) is a partially evacuated device with two or more electrodes that penetrate the glass envelope (see [Figure 2.1](#)). The negative electrode is called the cathode, and the positive electrode is called the anode. A high voltage is applied across the electrodes, causing ionization of the low-pressure gas inside the tube. This in turn causes positive ions to bombard the cathode, liberating what was called, at that time, cathode rays. We now use the term *electrons*, denoted β^- , as synonymous with cathode rays.

The electrons produced at the cathode are accelerated by the imposed voltage in a direction generally perpendicular away from the surface of the cathode. These electrons traverse the tube. Some interact with the residual gas (gas that has not been evacuated) in the tube, but many strike the anode or the glass wall of the tube. We know now that these interactions produce x-rays.

Because of the fluorescence of the residual gas in a Crookes tube, the path of electrons is made visible, as shown in [Figure 2.2](#). The glass tube also would glow when struck by electrons. Scientists soon recognized that electrons could be deflected with a magnetic or electrostatic field. Some tubes had several anodes, as shown in the photograph in [Figure 2.3](#). Crookes tubes presented a striking appearance, and many were used for public demonstrations.

The scientists, technicians, and hobbyists using Crookes tubes were making what we now know as x-rays. But until 1895, no one recognized this fact or discovered their amazing properties.

* Two decades later, they were referred to as cold cathode tubes to differentiate them from the heated cathode x-ray tube invented by Coolidge.

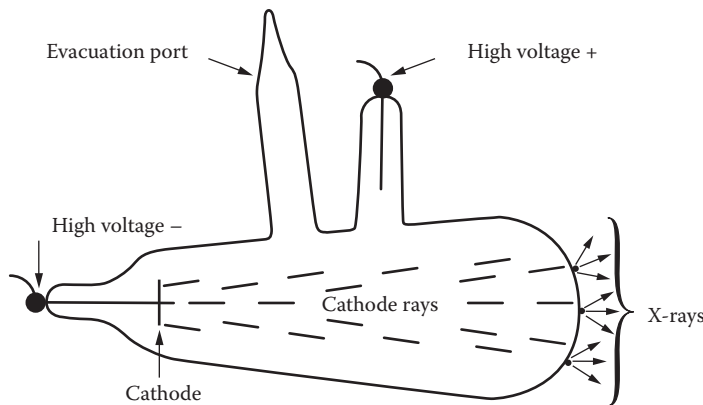


FIGURE 2.1 A schematic drawing of a Crookes tube. Crookes tubes are made of glass with metal electrodes. Cathode rays (electrons) are liberated from the cathode when it is bombarded with positive ions from the ionized gas inside the tube. The cathode rays are accelerated away from the cathode surface. Their direction tends to be normal to the cathode surface (along the potential gradient). X-rays are produced where the cathode rays hit the glass tube wall.



FIGURE 2.2 One type of Crookes tube photographed in operation. The path of the cathode rays can be seen clearly. This tube is contained in a collection at the American Museum of Radio and Electricity in Bellingham, Washington, USA. (From John Jenkins, Spark Museum, <http://www.sparkmuseum.com/GLASS.HTM>, 2015. With permission.)



FIGURE 2.3 A modern photograph of a Crookes tube. This tube is contained in a collection at the American Museum of Radio and Electricity in Bellingham, Washington, USA. (From John Jenkins, Spark Museum, <http://www.sparkmuseum.com/GLASS.HTM>, 2015. With permission.)

2.3 DISCOVERY OF X-RAYS

The interested student can find much written about the astounding news of the discovery of x-rays. Much of what is written is contradictory. This is in part because Röntgen never gave a descriptive account of what happened; he was, by nature, reserved, and he completed most of his work alone. A photograph of Röntgen is shown in [Figure 2.4](#).

At the time he discovered x-rays, Wilhelm Röntgen was 50 years old. He had been experimenting with cathode rays at the University of Würzburg for more than a year. Philipp E. von Lenard, another German physicist, had developed a type of Crookes tube with a thin aluminum window that Röntgen referred to as a Lenard tube in his subsequent publication. Lenard* established that cathode rays could penetrate the Al window and cause a fluorescent material on cardboard backing to glow at a distance of several centimeters from the tube (Kevles 1998). On November 8, 1895, Röntgen was experimenting with one of several tubes in his laboratory,

* For convenience, we follow Röntgen's lead in using *Lenard* rather than *von Lenard*.

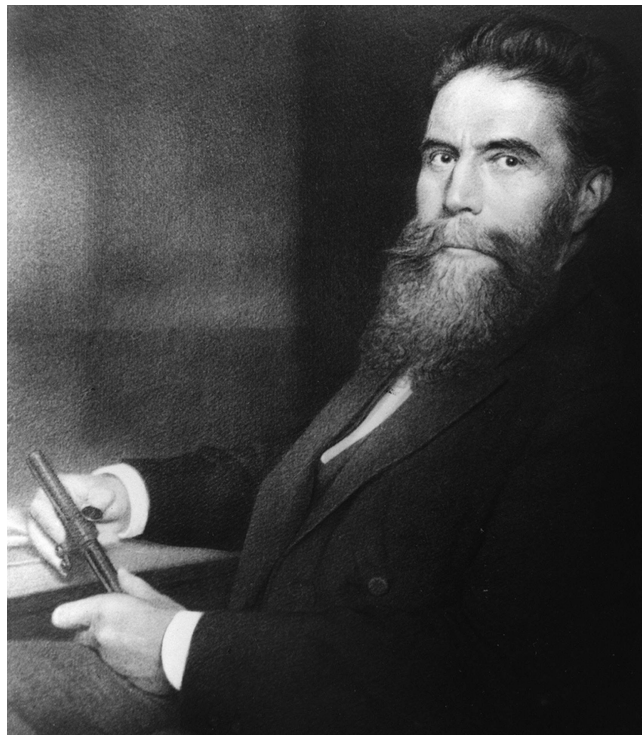


FIGURE 2.4 Wilhelm Conrad Röntgen. (From AIP Emilio Segre Visual Archives, W.F. Meggers Collection. With permission.)

perhaps even one made by Lenard.* He had covered the tube with black cardboard to block the light coming from within the tube. The lab was darkened. Röntgen noticed that a fluorescent screen was glowing about a meter distant from the tube. This must have been an amazing experience. The screen had the letter *A* written on it by a student with a finger dipped into the scintillating material when he or she had been preparing screens. He repeated the experiment numerous times and concluded that, indeed, something arising from the operation of the tube penetrated the glass vacuum container, the cardboard, through the air in the room and caused the letter *A* to glow (Farmelo 1995). (See also Panel 5.1 in Chapter 5, Section 5.2, Attenuation and Phase Contrast.)

Röntgen kept his discovery to himself, working alone late into the night for the next 7 weeks. His experience as a photographer may have helped prepare him to come up with possible explanations for the strange phenomenon he encountered. He soon discovered that photographic plates[†] respond to this new type of ray and that paper or cardboard packaging is transparent to them. He established that these x-rays, as he called them, are produced at the spot where cathode rays hit the glass tube or aluminum window/end plate. He verified this by magnetically deflecting the cathode rays (β^-) to a new location and noting that the location from which x-rays emanated always corresponded with the location where the cathode rays struck solid material. Röntgen conducted a remarkable set of experiments. Near the end of 1895, Röntgen told his wife, Bertha, about his work and recorded an image of her hand clearly revealing her bones and her wedding ring. Soon thereafter, Röntgen submitted a report to the *Proceedings of the Physico-Medical Society of Würzburg*. The report, “On a

* Röntgen had a Lenard-type tube that he had borrowed from Lenard. The literature is sharply divided over whether Röntgen used this tube when he discovered x-rays. This later became part of a general argument over the discovery of x-rays.

[†] Photographic plates are glass plates coated with light-sensitive material (grains of AgBr) on one side.

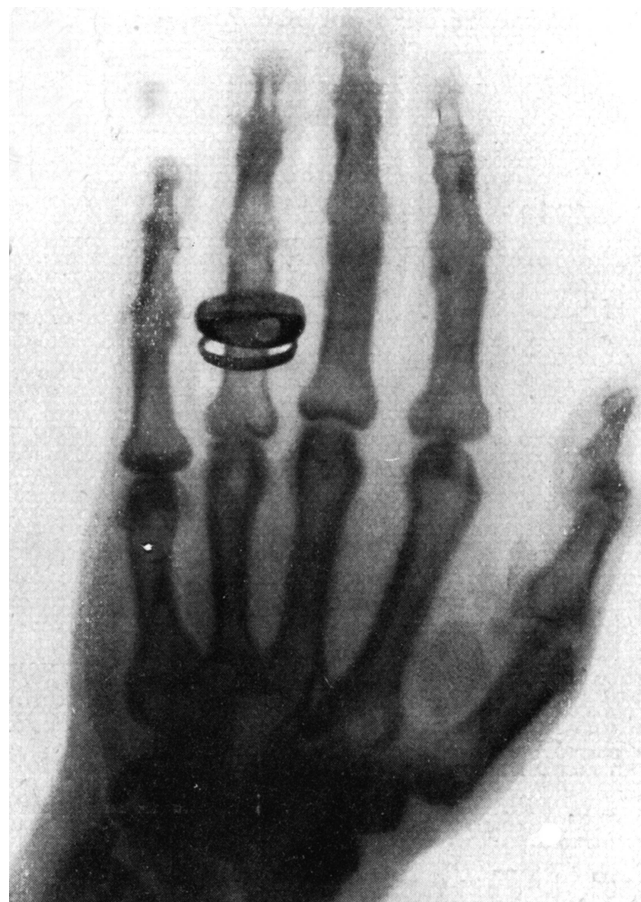


FIGURE 2.5 A radiograph of the hand of Rudolph Albert von Kölliker. This was made at the conclusion of a lecture and demonstration at the Würzburg Physical-Medical Society on January 23, 1896. (From AIP Emilio Segre Visual Archives. With permission.)

New Kind of Rays,” was published in 1896 with a date of December 28, 1895 (Röntgen 1895). Early in the year of 1896, he presented a lecture on his work that concluded with him producing an x-ray image of Rudolf Albert von Kölliker’s* hand (Harris 1995). This image is shown in Figure 2.5. By this time, Röntgen had demonstrated three major uses for x-rays that we continue today: medicine (various body parts), industrial inspection (his rifle complete with internal flaws), and baggage inspection (metal objects in a wooden box).

Röntgen’s publication (1895) is a remarkable piece of work. It presents the detailed study of a consummate experimentalist. The publication contains not a single equation and fewer than 3000 words. Any literate person could read it and understand that Röntgen had indeed discovered something amazing. Röntgen established that mass density is the property[†] “whose variation mainly affects their permeability.” But he also established that thickness and composition are strong influences. He published a table showing thicknesses of platinum, lead, zinc, and aluminum providing equal attenuation. He showed by their lack of response to magnetic fields that x-rays are quite different from cathode rays (electrons). Röntgen apparently felt strongly that x-rays were related to visible

* Rudolf Albert von Kölliker, a Swiss-born professor of physiology and of microscopic and comparative anatomy, was a colleague of Röntgen at the University of Würzburg.

[†] Quotations here are from Stanton’s English translation of Röntgen’s paper (Röntgen 1896).

light. Perhaps his strong interest in photography played a part in this. He tested his own eyes to see if they responded. They did not. He tried but failed to measure “caloric”* effects. He attempted to refract x-rays in a manner and with materials that refract visible light and reported no effect. He then tried prisms of aluminum and ebonite. He was thwarted using higher-Z materials by too much attenuation. He left the question of refraction open to additional experimentation. He made an x-ray pinhole image of his x-ray tube. Röntgen also performed a set of experiments to test for reflection and concluded that “regular reflection does not exist, but that bodies behave to the x-rays as turbid media to light” (Röntgen 1896).

Graham Farmelo[†] reports that a bank of batteries in the basement powered Röntgen’s cathode ray tube. He created pulses of about 35,000 volts (35 kV) by use of an induction coil operating at about 8 Hz (Farmelo 1995). We are struck in particular by the experiments Röntgen reports on his effort to observe reflection. Quoting from Stanton’s translation (Röntgen 1896),

I exposed a plate, protected by a black paper sheath, to the x-rays, so that the glass side lay next to the vacuum tube. The sensitive film was partly covered with star-shaped pieces of platinum, lead, zinc, and aluminium. On the developed negative the star-shaped impression showed dark under platinum, lead, and, more markedly, under zinc; the aluminium gave no image. It seems, therefore, that these three metals can reflect the x-rays; as, however, another explanation is possible, I repeated the experiment with this only difference, that a film of thin aluminium foil was interposed between the sensitive film and the metal stars. Such an aluminium plate is opaque to ultra-violet rays, but transparent to x-rays. In the result the images appeared as before, this pointing still to the existence of reflection at metal surfaces.

But Röntgen did not stop there. He continues,

If one considers this observation in connection with others, namely, on the transparency of powders, and on the state of the surface not being effective in altering the passage of the x-rays through a body, it leads to the probable conclusion that regular reflection does not exist, but that bodies behave to the x-rays as turbid media to light.

Since it took a second or third reading before we understood Röntgen’s reflection experiment, we offer a short elaboration. Röntgen prepared a glass plate with a coating (containing AgBr grains), known to be sensitive to x-rays, on one side of the glass. This coating, when chemically processed, turned dark after being exposed to x-rays. These plates along with the metal stars, and in one case an aluminum foil, were packaged into a lighttight black paper wrapper. The coated (sensitive) side was placed away from the x-ray source (see [Figure 2.6](#)) so that the x-rays passed through the packaging and the glass to reach the coating. In the first case, shown in [Figure 2.6a](#), the x-rays then encountered the metal stars. In the second case, [Figure 2.6b](#), they passed through a thin aluminum layer before encountering and interacting within the metal stars and scattering and reflecting back through the aluminum layer to the sensitive coating. The fact that the scattered rays penetrated the aluminum layer established that they were x-rays and could not be ultraviolet rays.

It seems surprising that x-rays had not been discovered before November 8, 1895. American Arthur Goodspeed had accidentally produced an x-ray image of some coins and brass weights 5 years before Röntgen’s work, but he and his colleague, William Jennings, could not explain the image and failed to pursue it (Walden 1991). Later, Goodspeed suggested that the term *radiography* be applied to the entire field of x-ray use, while in Europe, they are still sometimes called Röntgen rays, and the field is referred to as röntgenology. Crookes, inventor of the tubes that

* Heating.

[†] Graham Farmelo is Head of science communication at the Science Museum, London, and associate professor of physics at Northeastern University, United States. He wrote an anniversary article on the discovery of x-rays in *Scientific American* (Farmelo 1995).

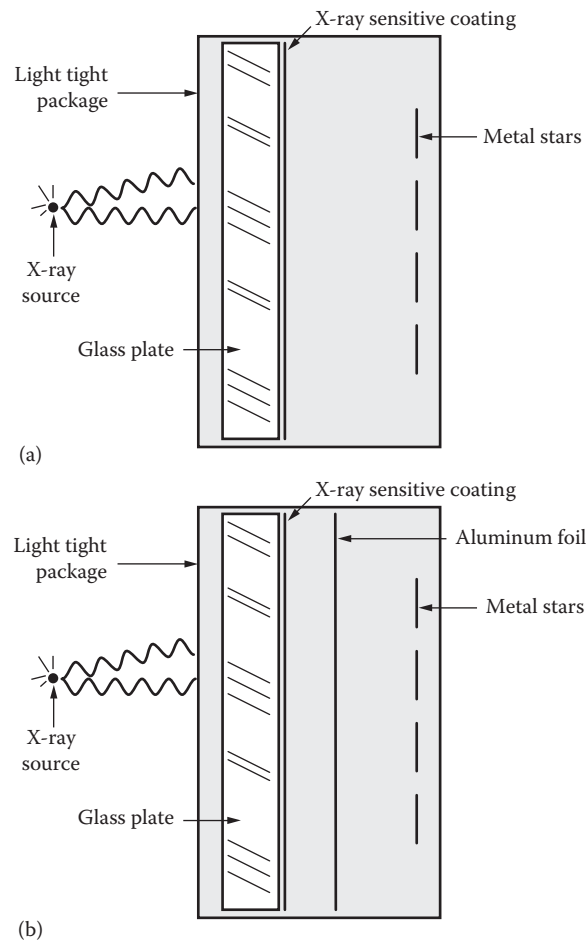


FIGURE 2.6 An expanded view of the geometry used by Röntgen for his experiments checking for x-ray reflection. (a) The configuration where Röntgen saw evidence of increased darkening of the sensitive coating in the areas of the metal stars. (The stars were physically close to the coating.) (b) After adding aluminum foil, he saw the same pattern and reasoned that it could not be caused by ultraviolet rays, because they would have been stopped by the aluminum foil.

produced the first x-rays, had repeatedly fogged photosensitive plates and complained of their quality to the manufacturer (Farmelo 1995). Probably, hundreds of experimentalists had observed evidence that they failed to pursue. Nearly as many later claimed to be the discoverer. Lenard in particular was ungracious and unprofessional. He loudly demanded credit for the discovery of x-rays and went about disparaging Röntgen's recognition, especially the 1901 Nobel Prize awarded to him. Indeed, when Lenard was awarded the Nobel Prize in 1905 for his work on cathode rays, he used the occasion for another attack on Röntgen, calling the discovery of x-rays a "lucky discovery" and in fact stating that their discovery was inevitable with the type of tube Lenard had developed (von Lenard 1906). It seems amazing, but this still happens today among some scientists and engineers.

In fact, Röntgen discovered x-rays where Lenard and others failed because he had the right training and experience, the best possible equipment, intense curiosity, and dedication to solving the riddle. He finished the job by writing a graphic and clear interpretation of his results. It seems to us more like good preparation and hard work than luck.

2.4 THE MORNING AFTER

Röntgen's discovery was easily duplicated in laboratories around the world. Within days of his scientific publication, x-rays made the front page of the *Viennese Chronicle*. This unleashed a torrent of newspaper articles. Many people had working Crookes tubes, and these were directed in this exciting new direction. In 1896, there were 49 books and more than 1000 technical papers published about x-rays. Edward Trevert (1896) published a handbook for the do-it-yourself x-ray experimenter. It contained drawings of 32 different configurations, Figure 2.7, being used for making x-rays.

Röntgen published a second paper on x-rays in 1896 and then a third paper in 1897. He never appeared in print on the topic again (Kevles 1997). Farmelo (1995) reports that Röntgen continued to work with x-rays but wrote nothing more about them. After his Nobel Prize in 1901, Röntgen was famous. He appears not to have worn this cloak well. The harping of Lenard in particular chafed him. He left instructions that after his death, all his notes concerning x-rays before 1900 be destroyed.

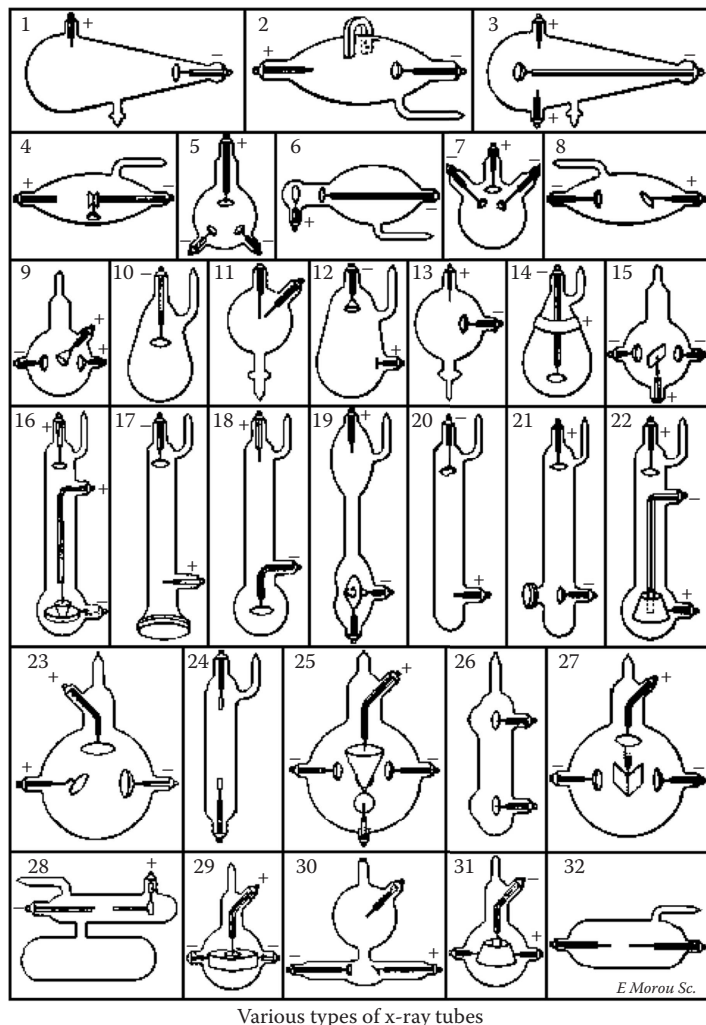


FIGURE 2.7 As word of Röntgen's discovery spread, various researchers modified the basic Crookes tube in efforts to enhance production of x-rays. Edward Trevert published this chart of configurations being used in 1896. (From Trevert, E., *Something about X-Rays for Everybody*, Bubier Publishing, 1896.)

The world instantly knew that x-rays were useful and entertaining but did not recognize that there could be dangers. Skin burns became obvious very soon. In fact, the radiation absorbed dose used to make clinical images routinely caused skin reddening and hair loss. This soon led to thriving businesses removing unwanted hair. Facial and underarm hair in women were the usual targets. This practice continued for 50 years (Lienhard 2005). The fact that x-rays could induce cancer with a long latent period was slow to dawn on the scientific community. Even the open sores that would not heal were dismissed as if they had arisen from some cause other than x-rays.

In the United States, Thomas Edison was widely known. He had invented the voice recorder and electric light bulb. Within 2 weeks of Röntgen's publication, Edison turned his considerable resources and talent to exploring x-rays. A careful set of experiments led to a new *scintillator*, calcium tungstate, which enabled the production of an x-ray instrument that made it possible to see internal organs in motion. Such a machine is referred to as a fluoroscope or real-time radiography. With a fluoroscope, a doctor could view a patient, but unfortunately, both patient and doctor were continuously irradiated. Edison arranged public demonstrations where people could view their own hand. After a few years, Edison decided that x-rays were the cause of his own sore eyes and skin rashes. At about the same time, Edison's assistant, Clarence Dally, began a painful descent toward x-ray-induced death. His suffering and death was widely reported (*New York Times* 2004). It became commonplace for technicians to have lost fingers to amputation (Goodman 2005). This happened because the usual practice was to use one's hand to test the x-ray system as Dally is doing while Edison views the image in Figure 2.8.

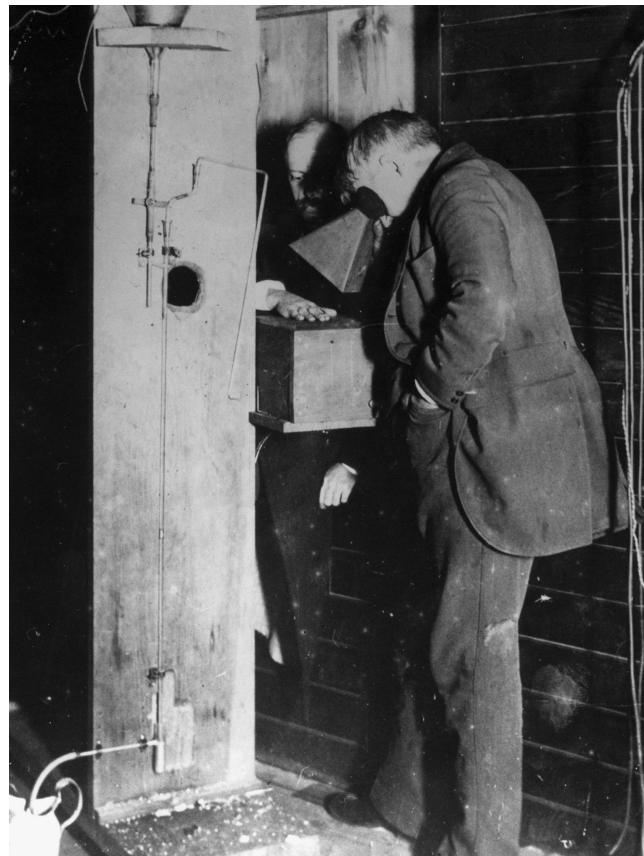


FIGURE 2.8 Edison looking through his fluoroscope at the hand of his assistant, Clarence Dally, in 1896. The x-ray tube is in the box near both men's navels. (Photo is courtesy of the US Department of Interior, National Park Service Edison National Historic Site.)

X-ray applications that now seem ill advised continued in widespread use for 50 years. We already mentioned the removal of unwanted hair. Shoe-fitting fluoroscopes (one is shown in Figure 2.9) were in use until 1960. One of the authors (Logan) would pop into the shoe store during the 1950s to view his toes wiggling within his shoes whenever the opportunity arose. These were high-dosage machines, delivering a dose to the feet about 1000 times that of a modern extremity x-ray. Fortunately, feet are among the most radiation-resistant portions of the body. Probably the greatest damage was done to the shoe salesman whose whole body was subjected to incessant scattered radiation while he or she was seated on a nearby stool. Other x-ray applications where the risk exceeded the benefit included the irradiation of female breasts with x-rays to relieve symptoms of mastitis. The Mayo Clinic reported in 1949 the treatment of 1000 patients for asthma. There were some cases of whole-body fluoroscopy of well babies as part of an annual checkup (Gofman 1999). Finally, one of the authors (Logan) has living relatives whose childhood facial acne was treated with x-rays without protecting the thyroid.

2.5 DISCOVERY OF RADIOACTIVITY

Just a few weeks after Röntgen's discovery of x-rays, Henri Becquerel was exploring whether there was a connection between natural phosphorescence and x-rays. He had a supply of uranium salts that emitted visible light following exposure to bright sunlight and discovered that these salts also exposed a photographic plate through a black paper wrapping in a manner similar to x-rays. Becquerel hypothesized that the substance absorbed energy from the sunlight and emitted both visible light and x-rays. His hypothesis was disproved when a period of overcast weather failed to provide conditions for "charging" his salts. The mineral had been left in contact with photographic plates. Becquerel developed his plates and discovered strong images even in the absence of sunlight.

Pierre and Marie Curie had only been married a short time when they took up the study of Becquerel's discovery. By 1898, they announced the discovery of radium and polonium. They had devised a method to extract uranium from ore and discovered to their surprise that the leftover ore had more radioactivity than the uranium. This led to the isolation of radium and polonium.

The Curies and Becquerel shared the Nobel Prize in Physics for 1903.

Just as x-rays had been used inappropriately, radioisotopes were also used in ways that turned out to be harmful. The most well-known example is that of women employed to paint luminous watch dials with luminous paint containing radioactive material. The principle radioactive material in the luminous paint was ^{226}Ra , though other radioactive decay products were also present in considerable amounts. A radium salt was mixed with zinc sulfide, a common scintillator, and linseed oil to make the luminous paint (Keane 1917). Energetic charged particles from ^{226}Ra decay excited the scintillator and produced a glowing numeral or hand on a watch or clock face. World War I created a large demand for luminous dials on instruments. After the war, these manufacturers turned their talents toward watches and clocks for personal use. The main harm befell not the wearer of the watch but the women employed to paint the watch faces. To get the fine tip needed for the best-quality work, they were taught to point their brushes by licking them, thus ingesting radium each time. Some of the radium was incorporated into their bone and eventually caused bone cancer in many instances. The first deaths occurred in the 1920s. The practice of "tipping" the brushes ended soon after, though use of this type of paint continued for another 35 years (Frame 2005). Lest we believe that we are too enlightened to participate in or allow such activities today, we point out that a business in Boulder, Montana, USA, collects admission from people to sit in an old mine and expose themselves to radon (Radon 2015). A Japanese company sells an elbow support containing thorium (Thorium 2015), claiming the decay products have soothing and germicidal properties. More current misuse of radiation is given in Chapter 7, Section 7.5.2.2, Marketing Radiation Dose.



FIGURE 2.9 This device was in wide use in shoe stores during the 1940s and 1950s. It was used to view the bones of the feet inside of shoes and was advertised as providing a perfect fit. Note that it has three viewing ports. One port is for the owner of the feet, one for the salesman, and one for the person who will pay for the shoes. (From Oak Ridge Associated Universities, <http://www.orau.org/ptp/collection/shoefittingfluor/shoe.htm>, 2015. With permission.)

2.6 RADIATION THERAPY

Our discussion of ill use of ionizing radiation is not complete without brief mention of one beneficial therapeutic use that has stood the test of time: radiation therapy for treatment of cancer. In the United States, 40% of the population will get cancer at some time during their lifetime (BEIR VII 2005). Half of these will be treated with radiation (American Cancer Society, 2015). It has been demonstrated that patients with some types of cancer live longer after radiation therapy than those who are not given radiation therapy.

2.7 COOLIDGE TUBE

Early x-ray tubes were unreliable and inconsistent. In 1913, William Coolidge made a large leap forward with the invention of what became known as the *Coolidge tube*. The Coolidge tube had three design characteristics that distinguished it from earlier x-ray tubes. It was thoroughly evacuated, to about 10-billionth of an atmosphere. Earlier tubes had internal gas pressure about 1000 times higher. It used tungsten for both the cathode and the anode. And, the cathode was heated. A photograph of a Coolidge tube is shown in Figure 2.10. Coolidge worked at General Electric (GE), where he had endeavored to develop tungsten filaments for electric light bulbs. GE had introduced the tungsten-filament light bulb in 1910. GE was able to employ some of the same manufacturing techniques and materials developed for making light bulbs to the production of x-ray tubes.

Because of the heated cathode, the Coolidge tube emitted electrons from a much smaller and more consistent location. The high vacuum allowed the electron beam to be transported consistently to the same location on the anode. Tungsten was much more refractory than earlier materials (often platinum), so it could tolerate a greater thermal load than earlier designs without melting and/or

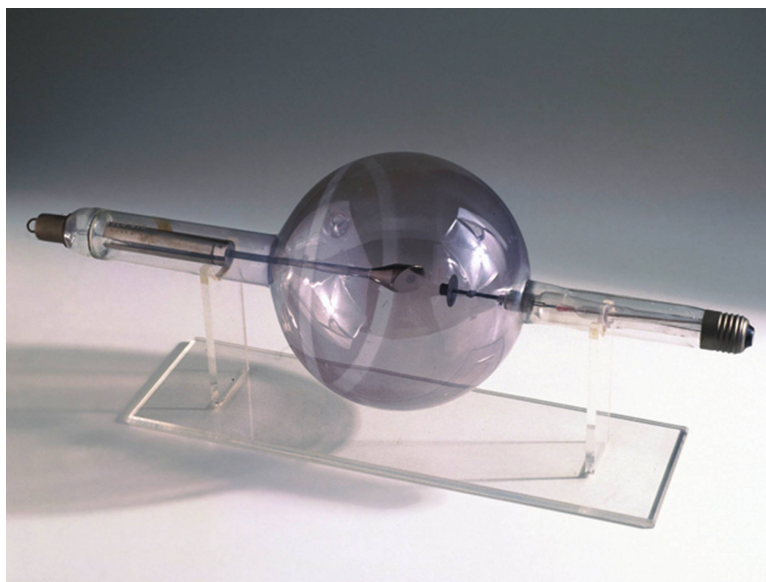


FIGURE 2.10 A photograph of a Coolidge tube that is slightly refined from his 1913 invention. This tube was probably made in the 1920s. The cathode entry is on the right. Electrons are emitted from the hot cathode tip and are accelerated into the anode near the center of the spherical region. The anode surface is planar and inclined at 45° to the electron beam axis. This tube would be used with the object to be irradiated positioned on a line that is 45° from the anode surface and 90° from the electron beam axis. Note that some pitting is evident on the anode where the cathode rays strike. (From Oak Ridge Associated Universities, <http://www.orau.org/ptp/collection/xraytubesc coolidge/coolidge.htm>, 2015. With permission.)

vaporizing onto the tube walls. This in turn permitted higher accelerating voltages. These features opened the door to more widespread industrial utilization of x-ray imaging.

Earlier x-ray tubes required rectified power, but the Coolidge tube could be driven by a simpler power source, even a transformer. This was because of the heated cathode; it would only conduct electricity (and make x-rays) when the cathode was at a negative potential. In effect, it could act as a diode.

2.8 COMPUTED TOMOGRAPHY

Another major event in the development of x-ray imaging took place in 1917, though it took another 50 years before its impact was felt or appreciated. Johann Radon published the mathematics of reconstructing a function from a set of projections (Radon 1917). The inverse process (decomposing a function into a set of projections) is now called the Radon transform. Radon was a mathematician and did not envision the application of his work to CT as Hounsfield and Cormack did in the 1970s; Hounsfield and Cormack received the Nobel Prize in Medicine for computer-assisted tomography. Indeed, even had Radon foreseen implementation of CT, it would have awaited the development of electronic x-ray detection and digital computers.

We will mention CT in almost every chapter of this book. It will be covered in detail in Chapter 13. For now, a simple description about the nature of CT will have to suffice. X-ray radiographs, such as those Röntgen made, collapse the three dimensions of an object onto a two-dimensional plane, usually called a projection. A projection reveals something about an object but leaves a great deal of ambiguity. If you take additional projections at different angles about the object, the ambiguity is lessened. What Radon showed was that if you take many radiographs (several thousand is not unusual), you could mathematically reconstruct* the full three dimensions of an object. Each point in a radiograph is a line integral[†] of the object function (for x-rays or γ -rays it can be the linear-attenuation coefficient). The line integral is sometimes referred to as the Radon transform of the object function.

Allan Cormack was more fortunate in the timing of his work in 1956, when he began thinking about the possibility of CT. Suitable digital detectors and computers were becoming available. Cormack, from the beginning, had medical CT in mind. Imaging the brain in particular had remained elusive because the soft tissue of interest is encased in high-opacity bone. Cormack's first data on a noncircular object used ^{60}Co gamma rays. Cormack published this work in 1963 and 1964 (Cormack 1963, 1964), but as he stated in his Nobel Prize speech (Cormack 1979), it generated little interest. He was rejected by medical colleagues at Massachusetts General Hospital, Boston, USA, when he tried to convince them that he could reconstruct the intensity of emission from radio-isotopes administered within the body. Today this is called single-photon emission CT (SPECT). Meanwhile, David Kuhl, at the University of Pennsylvania, Philadelphia, Pennsylvania, USA, made a CT scanner and published a CT image of a thorax (Kuhl 1966). He discussed this device with the Picker Corporation, but they saw no commercial value in it. Even Kuhl saw this imaging as an adjunct to SPECT, not as a breakthrough in imaging technology.

At about the same time, Godfrey Hounsfield pursued similar research at the Medical Systems Department of Central Research Laboratories EMI, London, England. The culture and environment at EMI were to develop a CT scanner in secrecy and launch it into the marketplace, where they could make a return on their investment. Hounsfield was set to build a CT machine capable of imaging a torso, but EMI redirected his effort toward completion of a brain scanner instead. In 1972, the first live patient brain was imaged in three dimensions with the EMI scanner. Hounsfield published information about the EMI scanner in 1973 (Hounsfield 1973), the first look inside the

* In x-ray CT, you reconstruct the x-ray attenuation coefficient of each volume element (voxel) of an object from a set of line integrals.

† Almost all CT image reconstruction codes assume line integrals are measured. A line integral is from a point source to a point detector and includes only absorption. Thus, it does not account for the fact that measurement systems have finite sources or detectors, a source spectrum if polyenergetic, or scatter or phase (due to refraction and diffraction) effects.

EMI development laboratory. Hounsfield traces much of the development in his 1979 Nobel Lecture (Hounsfield 1979). As soon as the first brain scan was a success, EMI introduced their brain CT scanner at the annual meeting of the Radiological Society of North America in 1973. Almost immediately after, they made a whole-body scanner. By 1980 there were 5000 CT scanners in service. EMI enjoyed a tremendous early advantage, and they had littered the landscape with patents, but they had no intention of becoming a medical instrument company. Their business was the making and marketing of recorded music. They concentrated their CT sales efforts in the United States, the only country with sufficient wealth and a competitive market in which CT could thrive. EMI soon fell victim to not servicing what they sold and sold the CT business to Picker. Today, their corporate website history contains no mention of the first CT scanner (EMI 2015).

In 1979, Cormack, a physicist, and Hounsfield, an electrical engineer, shared the Nobel Prize in Medicine for the invention of computer-assisted tomography.* This must have been sweet victory for Cormack, who was shunned by his physician colleagues when he proposed building the first SPECT machine. Cormack noted in his banquet speech that Alfred Nobel would be pleased that an engineer and a physicist were sharing an award in medicine. Cormack and Hounsfield seem to have shared the limelight graciously. Cormack gave the banquet speech on behalf of both of them. Cormack died in 1998 and Hounsfield in 2004.

When the first scanner from EMI was introduced, it presented data in *EMI numbers* (Bushberg et al. 1994). Later, other manufacturers invented other units until the field was cluttered with inconsistent units. By some miracle that does not seem to be recorded, the various manufacturers seem to have converged on a definition of *Hounsfield unit (HU)*, which has served the medical CT industry well. The scale is devised so that the attenuation of water is assigned a value of 0.0. Negative HU numbers are typical for fat, air, and lung tissues. Air is about -1000 HU, and bones may have HU numbers of +1000. The HU numbers are simply rescaled linear attenuation coefficients. While convenient for medical imaging, HU is never used in industrial CT, where the range of linear attenuation coefficients is many times larger than medical CT and x-ray energy ranges over decades as well.

2.9 INDUSTRIAL COMPUTED TOMOGRAPHY

As the 1970s had been the decade for implementation of CT in medical applications, the 1980s became the decade of rapid deployment of CT for industrial applications. In 1989, the American Society for Nondestructive Testing held their first topical meeting on industrial CT (ASNT 1989). The following year, 1990, there were 30 publications from just two national labs, Lawrence Livermore National Laboratory and Sandia California. See for example the work of Pontau et al. (1990), Kinney et al. (1990), Azevedo et al. (1990), Schneberk et al. (1990), and Martz et al. (1990, 1991a,b).

Several small companies emerged devoted to this new technology. Bio-Imaging Research (Harris et al. 1990), Advanced Research and Applications Corporation (Dusaussay et al. 1995), and Scientific Measurement Systems (Hopkins et al. 1982). They were all small businesses that were early contributors to the development of commercial industrial CT systems. None of these companies existed as independent companies in 2005. American Science and Engineering had been doing other x-ray work and entered the CT business in a big way in 1983 with a contract to build a scanner for 2-m-diameter Trident D-5 solid rocket motors (AS&E 2006). Others, including GE, developed scanners. GE's interest seemed to be mainly for their own use in manufacturing, especially turbine blades.

In the 1980s, several factors made the situation favorable for rapid progress with industrial CT. The first charge-coupled device (*CCD*) cameras were becoming available for scientific work. They had entered commercial television use in 1975. By using lenses and mirrors, CCDs could be used

* Computer-assisted tomography (CAT) was and still is more common in the medical field, while computed tomography is more common in the industrial field.

with area scintillators as a means to digitally capture and record x-ray images. The first commercial *microfocus x-ray source* (smaller than 100 μm) was offered by Feinfocus in 1982. This allowed the object to be placed closer to the x-ray source and a magnified image to be projected onto the image capture system. Funding was available for supporting CT work. The Cold War was in full swing. There were high-value weapon, aircraft, and rocket parts to inspect whose consequences of failure were high. These applications were not terribly cost sensitive, so a new and relatively expensive technique was feasible if it provided unique information.

Through the 1980s, computers were a bottleneck to the use of industrial CT. A CCD-based imaging system could acquire a data set that would reconstruct into a cube with 512 voxels in each direction. This was beyond the computing power and memory of most computers. Data that could be acquired in 1 day often took 2 months to reconstruct. In addition, there were just a few home-brewed ways to view and analyze data. By the middle 1990s, computers and software caught up and were no longer a significant barrier to the use of industrial CT.

The most recent major new component to enter the industrial CT toolbox is the *flat-panel imaging detector*. These detectors utilize manufacturing methods similar to that used to produce flat-panel computer displays. There are two basic types. Direct detectors collect charge produced in a semiconductor. Indirect detectors convert x-ray energy into visible light that is then sensed by a light-sensitive detector. The two types of indirect detectors in commercial use today are photodiode arrays and complementary metal-oxide semiconductors (CMOS) arrays. Some contain more than 30 million pixels. Radiation detectors for imaging are discussed in detail in Chapter 8.

2.10 RADIATION ACCIDENTS

Pioneers working with x-rays and other forms of ionizing radiation were frequently injured or even killed by radiation. We have mentioned Edison's associate, Dally. At first, the scientific and medical communities seemed unwilling to accept that such a useful new discovery could be causing harm. This reluctance would probably not have existed except for the fact that the effects of too much radiation were slow to become apparent. This long latency was not a common experience at that time. A radiation burn was quite different from a thermal burn in that there was no immediate pain, indeed no sensation at all in most cases.

By the 1940s, most of the world had established procedures and limits for working with ionizing radiation, and radiation injury became a rare occurrence (Ricks et al. 1999). In the United States, only 30 deaths have been attributed to radiation accidents from 1944 to 1999 (Ricks et al. 1999). None have occurred since. This is about 5% of the death rate from snakebites.

Of the radiation incidents/accidents reported worldwide since 2000, radioisotopes were the radiation source in all but one case. The most common isotope involved in accidents is $^{192}_{77}\text{Ir}$ (Turai and Veress 2001). This isotope is used in both medical procedures and industrial inspection. We describe briefly three accidents involving $^{192}_{77}\text{Ir}$ because the similarities convey a useful lesson. Radioactive sources are usually in a sealed capsule. The capsule is attached to a cable, and the assembly is housed within a guide tube. The source capsule can be pulled via the cable into a shielded container when not in use or pushed through the guide tube into position for use.

An accident was reported in 2002 that took place in Russia (Sevan'kaev et al. 2002). Three men were using an $^{192}_{77}\text{Ir}$ source to inspect welds in a gas pipeline. The source detached from the insertion cable. Correct technique calls for them to check that the source is within the shield using a portable radiation detector. They had a detector but had no batteries for it. They stored the source in their vehicle and slept in the same vehicle. They next morning, they experienced nausea and vomiting. They returned to base and went home to recover with the source still loose in the truck. Eight days later, they returned and went to the job site to begin work. One man saw and recognized the loose source. He picked it up with bare hands and inserted it into the shielded container. The men survived. The man who handled the source suffered disfiguring damage to the hand. These men had no personal dosimeters, so the radiation dose can only be estimated.

In 1992, a patient in Pennsylvania, USA, was killed by an $^{192}_{77}\text{Ir}$ source that was left in her body after brachytherapy* (US NRC 1993). The cable used for insertion broke near the source capsule, causing the source to remain in her body when the cable was reeled into the shielded container. A wall-mounted radiation alarm sounded several times when the source should have been retracted, but the staff chose to regard it as a false alarm. A portable radiation detector was available to perform the final check, but this was not used. The patient was returned to a nursing home and died of radiation exposure 5 days after the source was left inside her. The source was discovered and retrieved during autopsy.

In 2002, an $^{192}_{77}\text{Ir}$ source being used to inspect welds in a gas pipeline in Bolivia failed to retract into the shielded container but remained in the guide tube (IAEA 2004a). When preparing the equipment for movement to another job site, the radiographers were unable to disconnect the cable and guide tube from the shielded container. They did not recognize that this was an intentional mechanical interlock designed to warn the operator that the source was not correctly stowed. They also did not use their portable radiation detector. But, it gets worse. After consulting with their employer, they decided to ship the source assembly back to the company's office via long-haul passenger bus, their usual method of shipping. The radiographer packaged the source for shipment by cobbling a package together with cardboard and tape. It was shipped in the baggage compartment under the bus passenger seats. The worker who received the package used a radiation detector and discovered immediately that the source was exposed. Doses can only be estimated, since neither the workers nor the general public exposed on the bus ride wore dosimeters. No deaths or injuries were reported.

We hope the lessons to be learned from these three accidents are self-evident, but perhaps a brief summary is in order.

1. Mechanisms used to deploy and retrieve radioactive sources do fail.
2. Radiation detectors prevent serious accidents only when they work and are used and heeded.

One other type of accidental exposure occurs when sources are abandoned or inadequately controlled. In poor countries, these sources are seen as having value for their scrap metal content. Thieves usually have no concept of radiation or the risk that they are incurring. Stolen $^{60}_{27}\text{Co}$ was incorporated into consumer products in at least one case. In countries of the former Soviet Union, navigational buoys and lighthouses were equipped with radioactive thermal generators. These used decay heat from $^{90}_{38}\text{Sr}$ to produce electrical power. They have become the target of thieves. Three thefts were reported in 2001–2003 (Johnston 2014).

* Brachytherapy: radiotherapy in which the source of radiation is placed (as by implantation) in or close to the area being treated.

3 The Role of X-Ray and γ -Ray Imaging

3.1 INTRODUCTION

In this chapter, we will orient the student as to the applications where radiography and/or computed tomography (CT) using x-rays or γ -rays is especially appropriate and those situations where it is likely to be inappropriate or even yield misleading results. This discussion is given as an orientation without resort to mathematics or specialized knowledge. For this purpose, we limit our remarks to attenuation transmission imaging (radiography) and CT. We exclude from this discussion photon backscattering (see Section 15.7); techniques employing phase, i.e., refraction and diffraction (see Sections 15.9.3 and 15.9.4, respectively); and transmission imaging with other forms of ionizing radiation such as ions and neutrons (see Chapter 17).

Upon completion of this chapter, the student will be familiar with the following:

- Type of applications where radiography and CT can be used to advantage
- Specific examples of appropriate radiation applications
- Situations in which x-ray and γ -ray imaging should not be used

3.2 WHERE X-RAY AND γ -RAY IMAGING EXCEL

X-ray and γ -ray imaging methods are excellent tools for revealing internal features. An example is given in [Figure 3.1](#). These are x-ray radiographs of Mg tensile bars (Waters 2001; Waters et al. 1999b, 2000). One of these has an internal void. There is also a crack in the grip region of one specimen. As we discuss in the next section, x-ray and γ -ray radiography have severe limitations for crack identification. However, x-ray and γ -ray CT are excellent tools for finding and localizing cracks. Internal cracks in CT images of a steel bridge pin are shown in [Figure 3.2](#). This pin suffered shear damage in service. CT revealed a pattern of radial cracks in the zone near the most intense shear displacement (Waters et al. 1999a).

X-ray and γ -ray imaging enjoy an advantage over most other nondestructive evaluation (NDE) methods in that the information derived is inherently pictorial and interpretation is, to some extent, intuitive. Analyzing and interpreting the images requires skill and experience, but the casual user of radiation imaging services can easily recognize the item being imaged and can often recognize discontinuities without expert interpretation. For example, most persons who are familiar with wristwatches would recognize that [Figure 3.3](#) is an image of a wristwatch. In this case, the image was acquired using x-rays. [Figure 3.4](#) is a photograph of the same watch as was used for Figure 3.3. The orientation of these two figures is the same.

X-rays are very versatile and can be used to image objects that are complex and contain many materials ranging from high atomic number and density (e.g., lead or steel) to low atomic number and density (e.g., air or evacuated space). It is a very substantial advantage for x-ray and γ -ray imaging that air, gases, or vacuum spaces present no special difficulty for imaging. This is in contrast to the other main NDE method for seeing inside of objects, ultrasonics.* See the brief discussion on ultrasonics in Section 1.4.2.1. The watch in Figure 3.3 illustrates this point. We can examine internal

* Ultrasonic waves are not easily transmitted across the interface between a solid and a gas. They are not transmitted at all in a vacuum. For a good discussion of ultrasound and its application to nondestructive evaluation, we refer you to *Nondestructive Evaluation: Theory, Techniques and Applications*, Chapter 3, “Ultrasound” (Shull 2002).

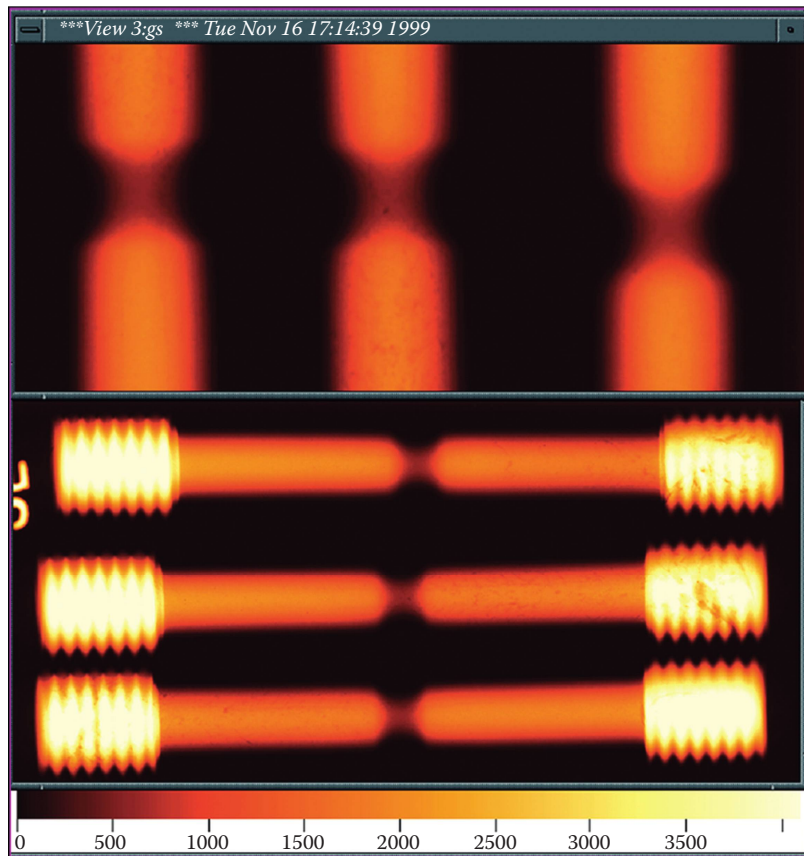


FIGURE 3.1 A transmission x-ray radiograph of three Mg tensile bars. These bars were machined with a necked area to concentrate deformation in the necked region. One bar has developed an internal void as a result of plastic deformation. Also, note a crack in the grip area of the right-hand end of the center bar in the bottom image.

parts even though the gears, springs, and other internal parts are immersed in air. The presence of multiple layers does not prevent us from obtaining a radiograph. If necessary, we could perform CT to separate the layers. This is in contrast to ultrasound, which, if applied to this watch, would have difficulty imaging the internal components that are immersed in air.

Extraction of dimensional information, even internal dimensions, is easily done with x-ray images, both with radiography and with CT. All that is needed is knowledge of the geometry with which the image was acquired. In a digital image, this quickly leads to knowing the distance from pixel* to pixel, the pixel pitch. This establishes the scale of the digital radiograph. Imaging an object of known size in the same geometry can readily check the scaling. A precisely engraved metal ruler is a favorite of radiographers. Precise solid spheres are also readily available and can be used to establish spatial scaling as well as to check for other measures of imaging performance. Other measures include source size (DIN EN 12543-5 1999), pixel distortion, and modulation transfer functions (MTFs).

An example of using CT to determine an internal dimension is shown in [Figure 3.5](#) (Schneberk et al. 2004). This object is a Au tube that is used as a test phantom. In this instance, the inside turned out to be a sort of fluted shape rather than the expected cylinder.

* Pixel: derived from picture element; the small discrete elements, that taken, together constitute a digital image.

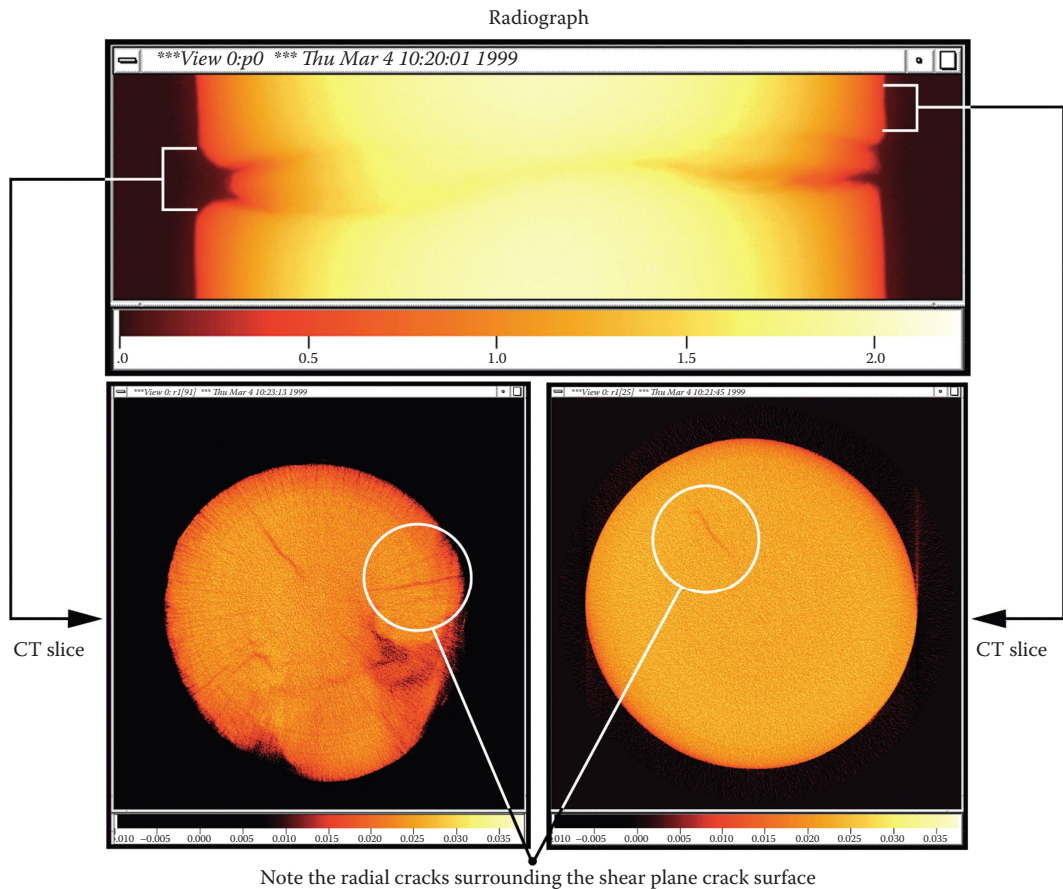


FIGURE 3.2 Digital radiograph and CT of a partially failed steel bridge pin. This pin is a 3 in. outer diameter (OD) and has undergone some shear deformation at the location where load is transferred between two bridge plates. CT reveals radial cracking, not only in the sheared region but extending away from the sheared region.

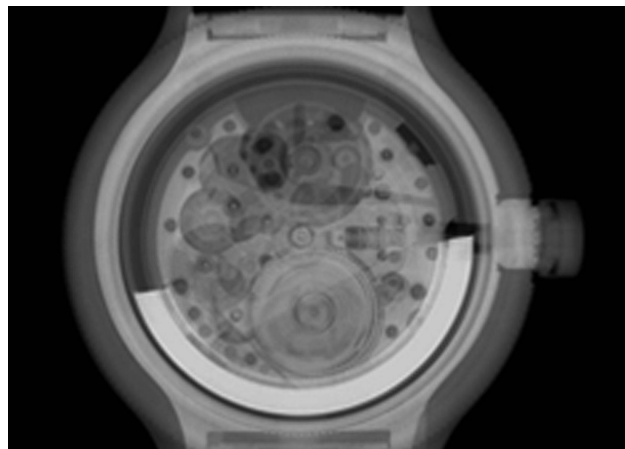


FIGURE 3.3 A transmission digital radiograph of a wristwatch. A spring (lower center) is the energy storage device for this watch. It is wound by the action of an eccentric weight (high-opacity arc extending from the 3 o'clock position to the 8 o'clock position) when the wearer moves.



FIGURE 3.4 Photograph of the face of the same watch used to produce the radiograph shown in [Figure 3.3](#).

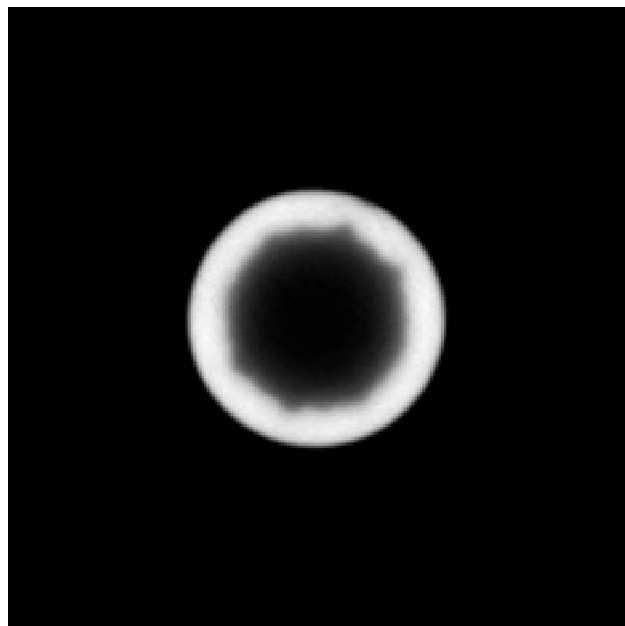


FIGURE 3.5 Computed tomography image of the cross section of a Au tube. The tube was intended for use as a phantom (or surrogate) for another object. We measured the outside diameter with a micrometer (0.270 ± 0.007 in.) and from the CT cross section (0.28 ± 0.02 in.). The inside diameter was expected to be circular. It is neither circular nor the expected dimension.

When dimensional information is to be extracted from radiographs or CT, care must be taken that the geometry is known and controlled. Film can present a special challenge in this regard since it often curls unless it is physically restrained in some manner. Also, film is not perfectly stable during chemical processing and storage. We did not find this fact appearing in the published literature, so for this book, we performed one test with Kodak MX125 film. After processing and drying, this film is larger by 0.2% than at the moment of irradiation. It remained stable over 1 year in a normal office environment.

X-ray imaging is now beginning to serve as a component of *as-built modeling* (Kokko et al. 2006). This approach is to use information derived from nondestructive characterization methods as the basis for generating an object model to study a physical process by simulation. Most computational analysis is based on idealized perfect geometry and does not include geometry or material deviation such as shape error, dents, voids, cracks, porosity, etc. Including these features, whether the result of manufacturing or use, can improve the results of the simulation process. The most advanced of these applications is finite-element modeling for structural analysis (Abdul-Aziz 2000). The as-built information can also serve as input for computing radiation transport, heat transfer (Katsuyama et al. 2002), and fluid flow (Katsuyama et al. 2003).

Closely related to as-built modeling is *reverse engineering*. This simply means deriving engineering information such as engineering drawings and specifications from the completed object. Sometimes, this is applied to a competitor's product, though no machine exists that can scan an automobile and produce production tooling, specifications, and drawings for the final product. A reverse engineering application that is part of current practice is to sculpt an object using methods as for art objects and then perform a CT scan to acquire dimensional information. It is also applied to parts with no existing documentation. Browne et al. (1998) present examples of making a replica of the US Liberty Bell and recovering the design of a control rod mechanism from an aging nuclear reactor. Crews et al. (1993) present an example of an aircraft control wheel that was shaped to achieve the desired ergonomic characteristics. The dimensionality of the wheel was then captured using CT.

One aspect of the versatility of x-ray imaging is that the photon energy can be varied to be appropriate for the object and attenuation properties of interest. Very small and/or low-density objects typically call for lower-energy x-rays than large dense objects. X-ray CT has been applied to objects ranging in size from 5×10^{-6} m (Haddad et al. 1994) to 2 m (Tonner and Stanley 1992).

Often, x-ray CT can be used to replace very labor-intensive, manual, destructive sectioning techniques. We demonstrated CT as an alternative to sectioning on a cylindrical core sample taken from a test section of asphalt roadway (Stergiopoulos 2001). We performed CT on the cylindrical core sample and then developed software to automatically assign one of five materials to each voxel based mainly on x-ray attenuation. This process is called *segmentation*. The five materials are (1) air outside the sample or connected to the outside of the sample, (2) internal void or air, (3) asphalt binder, (4) rock, and (5) inclusions. The material we call *inclusions* was not known in advance to be present within the core sample. X-ray CT shows the inclusions to be significantly more highly attenuating than any other material present. The breakdown of volume by material in this core sample is given in Table 3.1.

TABLE 3.1
Volume Fraction in Percent for the Different Materials within Asphalt Sample

Material	Percent by Volume
Aggregate (rock)	49
Asphalt (tar)	29
Void and crack	16
Inclusions	6

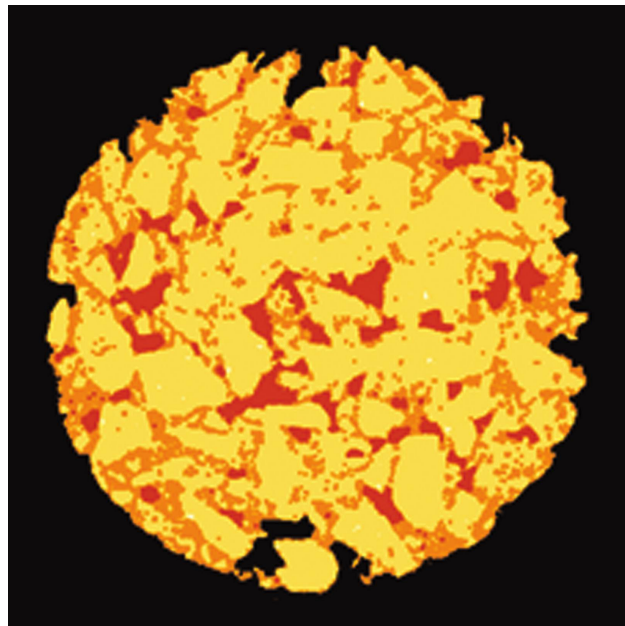


FIGURE 3.6 X-ray CT image of the cross section of a cylindrical core sample taken from a test section of asphalt roadway. The image has been analyzed and each pixel assigned a specific material from the known components of asphalt paving. The materials and the assigned color are as follows: (1) air outside the sample or connected to the outside of the sample—black; (2) internal void or air—orange; (3) asphalt binder—light orange; (4) rock—yellow; and (5) inclusions, maybe metal—white.

A cross-sectional view of one plane of an asphalt sample is shown in Figure 3.6. A different color has been assigned to each of the five named materials. These data were created for the entire 3-D cylindrical sample, permitting extensive analysis. Without CT, the only way to analyze this sample in this detail would have been to destructively section it and photograph a thousand sections. Even then, it is unlikely that manually sectioning would have discovered the inclusions since the destructive sectioning changes, sometimes can even destroy, the sample. CT offers the additional advantage that the sample can be observed as it is mechanically tested (Guvenilir et al. 1997), or at intervals (Waters 2001; Waters et al. 1999b, 2000) as deformation is applied.

The work of Katsuyama et al. (2002) presents a case where CT is being applied to replace manual sectioning of reactor fuel pins and as input to thermal simulation of the postirradiated configuration. In this instance, CT eliminates the need to remove individual fuel pins from an assembly and to perform manual sectioning on irradiated fast breeder reactor fuel pins. This is a considerable advantage as the irradiated assemblies are highly radioactive. The cylindrical pins develop voids along the axis with use. This affects the heat transfer within the pin. The location, shape, and size of the voids as revealed by CT are used as the object model (initial conditions) for heat transfer simulation studies.

Pyrotechnic devices such as munitions and explosive bolts typically have brass or steel cases filled with explosive. It is often desired to determine the amount and distribution of the explosive. This is often done with great success but must be applied with care so as to avoid situations where attenuation within the case is so large that sensitivity to the explosive becomes too small to be useful.

3.3 WHERE X-RAY AND γ -RAY IMAGING FALL SHORT

Transmission x-ray and γ -ray imaging require access to both sides of an object. This is not always possible.

Very large dense objects cannot be adequately penetrated with x-rays to form a quality image. An *areal density* of 250 g/cm² (product of thickness and density) is about the limit. For example, it is not practical to perform x-ray CT on a 2 m cube of marble (areal density, ~700 g/cm²) in order to devise a cutting plan.

Traditional x-ray and γ -ray CT require full access around the object and are difficult on objects with a high aspect ratio in the plane of interest. Platelike objects are one large class of such objects. Turbine blades are another difficult shape with high aspect ratio. The reasons for this are varied and will be discussed in Chapter 13, Computed Tomography.

Sometimes, x-ray and γ -ray methods have difficulty imaging low-density, low-Z components that are shielded by high-density, high-Z components.* The reason for this difficulty is rooted in their relative attenuation of x-rays. Low-density, low-Z materials tend to attenuate x-rays much less than high-density, high-Z materials. For example, imagine a steel storage cylinder containing compressed oxygen. The walls of the cylinder are 15 mm thick to contain the high pressure of the gas within the vessel. Radiography would be a poor method to attempt to determine the amount of gas remaining in the cylinder. The radiation attenuation taking place in the cylinder walls would far exceed (by several hundred times) that of the contained oxygen, so that sensitivity to the amount of oxygen would be very poor.

A more practical example is that of the watch shown in Figure 3.4. This watch is intended to be suitable for underwater use. In order to prevent water from penetrating into the watch around the stem, the stem is equipped with an elastomeric O-ring. It is quite difficult to determine if this O-ring is in the correct position and undamaged from a radiograph (Figure 3.3). This is because the radiographic image is almost entirely determined by attenuation in the steel watchcase and stem.[†]

Cracks and gaps are difficult to assess with x-ray radiography. The mere presence of a crack has no influence on a transmission radiograph unless there is a finite opening. Even when an opening exists, it must be oriented in a favorable direction to be detected in a radiograph. This is illustrated in Figure 3.7. It is impossible to image the crack in the configuration shown in Figure 3.7a with x-rays. The crack as shown in Figure 3.7b may be faintly imaged depending on the separation and other factors. There is a good chance of imaging the configuration in Figure 3.7c provided that a finite separation exists.

We observed a dramatic failure of x-ray radiography to image cracks during a study on NDE of ceramics. We prepared specimens (one is shown in Figure 3.8) of alumina (Al_2O_3) and beryllia (BeO) for this study. Some contained intentional flaws. One alumina specimen, meant to be perfect, appeared to be pristine in an x-ray radiograph, as shown in Figure 3.9. Figure 3.9 is an x-ray image that was recorded with film and subsequently digitized. When this specimen was examined with *dye penetrant*,[‡] a substantial, surface-breaking, branching crack was discovered, as shown in Figure 3.10. We believe these images should give pause to those enthusiasts using x-ray and γ -ray radiography to certify structures as free of cracks.[§]

Evaluating gaps in assemblies is a problem similar to crack detection in many respects (Georgiou et al. 2003). However, gaps are usually known or suspected to exist, and the question is often, *how big?* Our advice is, *do not answer this with x-ray radiography*. We illustrate our caution with the following study.

We produced film radiographs of known gaps between flat steel plates. The configuration is shown schematically in Figure 3.11. The steel plates were flat and smooth (root mean square surface roughness) to better than 0.1 μm . We carefully aligned the x-ray source to lie in the plane of the

* Some instances of poor attenuation contrast can be overcome by exploiting phase effects. These are covered in Section 5.5.

[†] Thermal (0.025 eV average energy) neutrons are useful for many of these applications. They are strongly attenuated by hydrogenous material. See Section 17.1.

[‡] A method of detecting surface cracks or pits in which dye is used to mark these areas. The dye is usually fluorescent under UV illumination. For more about this method see Chapter 2 of (Schull 2002).

[§] We emphasize again that finding cracks with X-radiography is folly while CT is a very powerful tool for this purpose.

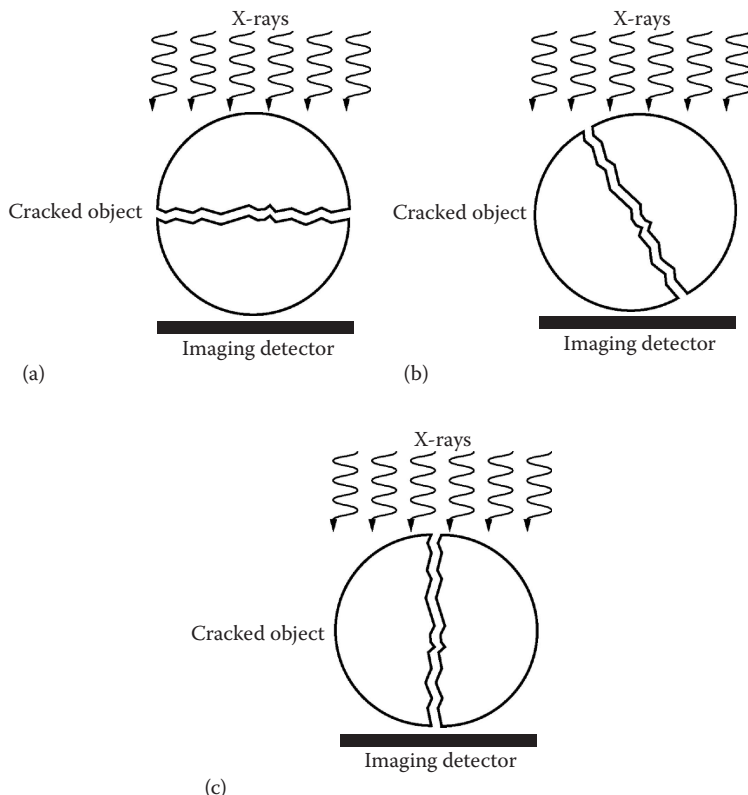


FIGURE 3.7 A schematic diagram illustrating the imaging of cracks in an object. (a) There is no chance of imaging the crack. (b) The alignment of the crack is such that it might be revealed in an x-ray image. (c) The crack will be evident in the x-ray image provided that the opening is sufficient.



FIGURE 3.8 Photo of a ceramic specimen made for a study of NDE methods. A US quarter dollar is included for scale.

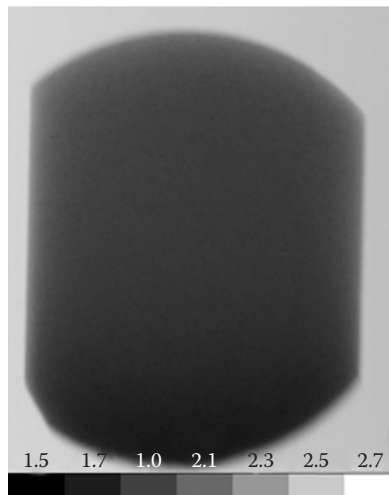


FIGURE 3.9 X-ray radiograph of the alumina specimen shown in Figure 3.8. This image was recorded on film and then digitized using a laser scanner. Scale at bottom of figure is in units of *film optical density*. No defects are revealed in either the film or the digitized radiograph.

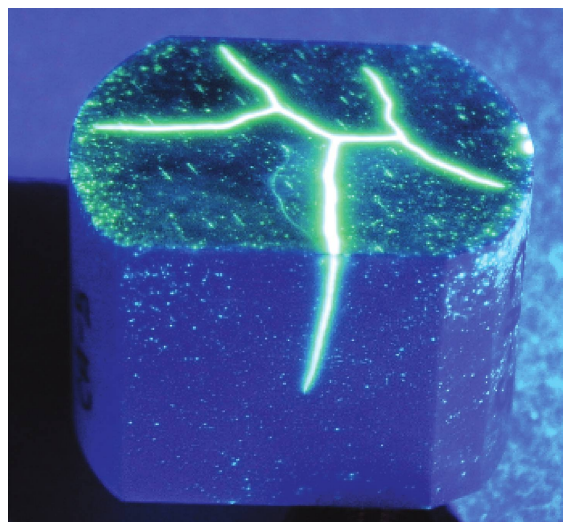


FIGURE 3.10 Digital photograph of the same alumina specimen shown in Figures 3.9 and 3.8. Prior to this image, the specimen was treated with Magnaflux Zyglo ZL-37 fluorescent penetrant, Magnaflux SKC-HF cleaner/remover, and Magnaflux ZP-4B powder developer. It was illuminated with a Magnaflux ZB-23A ultra-violet light for this photograph.

gap and used varying thicknesses (six different cases) of depleted uranium in front of the gap. This resulted in different attenuation cases. We also tested two different x-ray source sizes. Three different radiographers with 65 years of combined experience estimated the gap size from measurements made on an industrial x-ray film radiograph. We changed four variables:

- Attenuation (six different thicknesses)
- Gap size (eight values)
- Source size (two values)
- Observer (three radiographers)

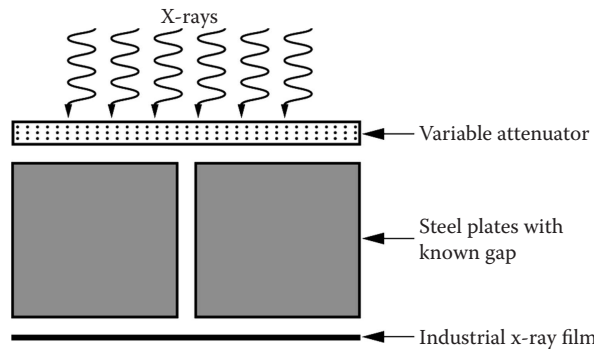


FIGURE 3.11 The geometry used for our study of gap radiographs recorded using x-ray film. We varied source size, attenuator, gap width, and the observer measuring the radiographs.

In total, we made 288 measurements. We found that the measured gap width did not depend on how much attenuation we used or what the source size was. Also, the measurements of the three radiographers were indistinguishable. We have 36 measurements of each gap width (3 radiographers, 2 spot sizes, 6 attenuators). The gap as interpreted versus actual gap width is presented in Figure 3.12. We summarize the results as follows:

- The gap with 0.0005 in. width always appeared smaller (36 of 36 interpretations) to our radiographers than the gap with 0.0000 in. (zero) width.
- Precision is poor and about the same (~ 0.002 in.) for all gaps measured.
- Our radiographers overestimated the gap width for gaps < 0.002 in. from 30% to $\infty\%$, the latter case being estimating a gap when none was present. Accuracy improved for wider gaps.

From these results, when evaluating planar gaps, it is important to emphasize that radiography should be used with caution. We suggest that you mock up the case to be studied and determine the limit of the gap accuracy and precision that you will be measuring.

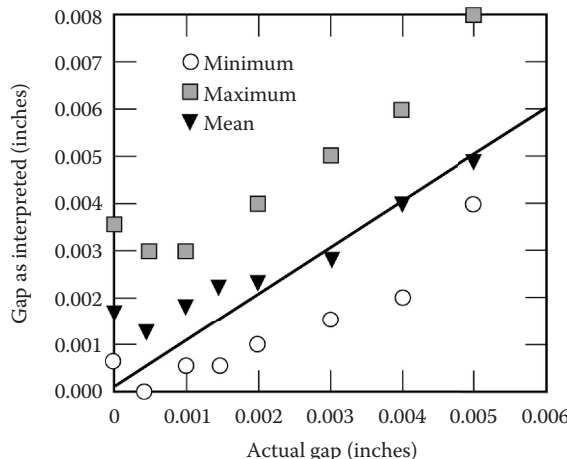


FIGURE 3.12 The gap width on x-ray film radiographs as interpreted by three experienced radiographers plotted versus the actual gap width. The gap was planar and generated by the separation of two steel plates (see Figure 3.11). Each triangle is the mean of 36 measurements (3 observers, 6 attenuators, and 2 source sizes). The solid line represents perfect interpretation accuracy. The squares and circles are the maximum and the minimum radiographer-interpreted gap, respectively, for each actual gap.

We later undertook a study in which the known gaps were between cylinders (a steel rod inside a steel pipe of inside radius 25 mm). We imaged with x-rays perpendicular to the cylinder axes. In this geometry, the results were much better. Every radiographer (four in this study) accurately interpreted the gap when it was zero width (no gap). We leave this situation at least partially as an open question. Clearly, planar gaps are troublesome to quantify with radiography. Even with nonplanar or unknown geometry, great caution is needed.

Before leaving the subject of gaps, we briefly address the use of CT for detection/measurement of gaps. Any possible issue of alignment of the object with the source and detector becomes irrelevant. The *detectability* of cracks and gaps is much higher with CT than with radiography (Waters et al. 1999a). We have seen cracks and gaps appear in a CT reconstruction made from radiographs in which no gaps or cracks could be seen. *Measurement* of small gaps with CT should be undertaken with utmost caution.* In most cases, the imaging system rather than the gap opening determines the apparent width of a gap.

3.4 PRACTICAL AND OPERATIONAL ISSUES

There are safety concerns that must be addressed to safely utilize x-ray imaging. The dangers associated with the method arise from high voltage used to generate x-rays, heavy shielding, and radiation. Because of these issues, radiation systems involve regulatory agencies and carry a compliance burden. They require highly trained and specialized staff. The method also involves higher capital cost than most competing NDE methods such as ultrasound, thermal imaging, and dye penetrant.

Radiography with radioisotopes (γ -ray imaging) presents a somewhat different set of safety issues. Radioisotopes are always “on.” We discuss the issue and appropriate controls in Chapter 7, Radiation Dosimetry, Safety, and Shielding.

Once equipment and staff for x-ray radiography and CT are established, they can become quite cost-effective. In part, this is because of high throughput. A CT configuration using an area detector can deliver data at about 10 Mbyte/s. Baggage scanners performing radiography have a data rate of >1 Mbyte/s.

3.5 SUMMARY

Radiation imaging is uniquely suited to seeing inside materials and assemblies. The data are inherently pictorial and have high customer acceptance. A drawback to the pictorial nature of x-ray images is that they can also be misinterpreted as well. Internal dimensions, configurations, assembly verification, etc. that are not otherwise easily accessed can be determined nondestructively from x-ray and γ -ray imaging. The method carries a cost, training, and safety burden.

* For example, phase effects can create the impression of gaps near surfaces where no gap exists. This is true for radiographs as well.

4 Physics of X-Ray and γ -Ray Sources

4.1 INTRODUCTION

In this chapter, you will be introduced to the physics of high-energy photon sources. In this text, high-energy photons mean electromagnetic radiation that is higher in energy than other more common electromagnetic radiation such as visible and ultraviolet photons (see [Figure 4.1](#)). Depending on their origin, these photons may be x-rays, gamma-rays (often denoted by the Greek letter gamma, γ), or annihilation radiation.

Upon completion of this chapter, you will be able to understand the following:

- Types and sources of high-energy photons
 - Generation of x-rays by electrons
 - Bremsstrahlung (braking or decelerating electrons)
 - Characteristic x-rays
 - Accelerating charge
 - Where γ -rays come from
 - Source of annihilation radiation
 - Units used to characterize and describe high-energy photons

4.2 TYPES OF HIGH-ENERGY PHOTONS: X , γ , AND ANNIHILATION RADIATION

Radiation of an unknown type and origin was discovered in the year 1895 by Wilhelm Röntgen. They were dubbed x-rays by their discoverer, while in his honor, some referred to them as Röntgen rays. They were soon found to be a form of electromagnetic radiation with extremely short wavelengths (very high energy). X, γ , and annihilation radiation are called ionizing because their interactions with matter can eject electrons* from an atom,[†] creating a positively charged ion. Here we provide the physics of how x-rays, γ -rays, and annihilation radiation are produced and how they differ in definition only. X-rays are a highly energetic form of electromagnetic radiation generated by accelerated or decelerated electrons or atomic energy (i.e., electronic) transitions. They have extremely short wavelengths (6.0×10^{-12} m to 1.5×10^{-8} m); most are smaller than the size of an atom ($\sim 10^{-10}$ m). γ -rays are an energetic form of electromagnetic radiation produced by nuclear energy (neutron or proton) transitions, typically by radioactive decay. Annihilation radiation is electromagnetic radiation produced

* An electron is a stable subatomic particle in the lepton family having a rest mass of 9.1066×10^{-28} g and a unit negative electric charge of approximately 1.602×10^{-19} C.

[†] The atom, in physics and chemistry, is a unit of matter, the smallest unit of an element, having all the characteristics of that element and consisting of a dense, central, positively charged nucleus surrounded by a system of electrons. The entire structure has an approximate diameter of 10^{-8} cm, and characteristically remains undivided in chemical reactions except for limited removal, transfer, or exchange of certain electrons. An element is a substance composed of atoms having an identical number of protons in each nucleus. Elements cannot be reduced to simpler substances by normal chemical means.

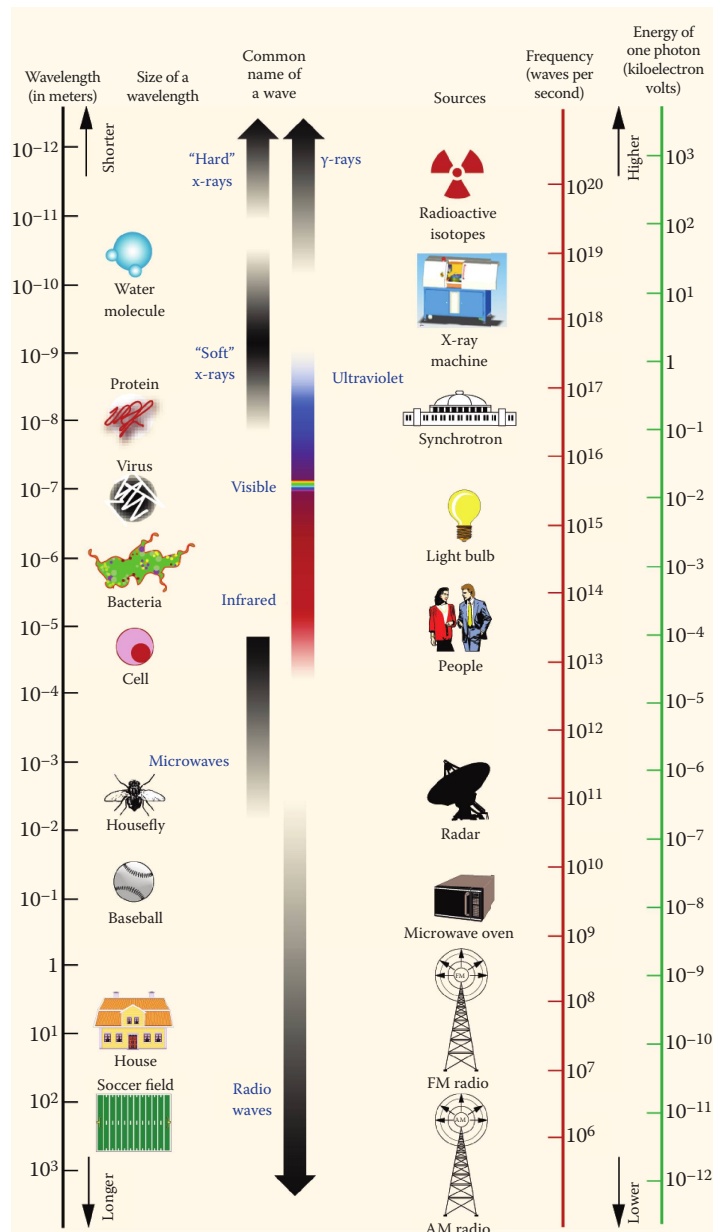


FIGURE 4.1 Electromagnetic spectrum showing the location of the various types of electromagnetic radiation as a function of wavelength, frequency, and energy. The visible light range is defined by the response of the human eye. Other boundaries are not distinct but only approximate classifications.

when a positron* (β^+) and electron (β^-) combine. The original positron and electron disappear and are replaced by two oppositely directed 0.511 MeV annihilation photons.

It is important to note that there is no physical difference between γ -rays, x-rays and annihilation radiation of the same energy—they are three names for the same electromagnetic radiation, just

* A positron (also called the positive electron or the antielectron) is an elementary particle; it is the antiparticle of the electron. It has the same mass and spin as an electron but has a positive charge (equal in magnitude to the charge of an electron). Sometimes, the abbreviation for a positron is e^+ and for an electron e^- . In this text, we will only use the abbreviations β^+ and β^- .

as sunlight, moonlight, and candlelight are three names for visible light. Annihilation radiation, γ -rays, and x-rays are distinguished by their origin. Because it is possible for some electron transitions to be of higher energy than some nuclear transitions, there is an overlap between what we call low-energy γ -rays and high-energy x-rays. Unfortunately, the error is often made that all γ -rays are higher in energy than x-rays, but this is not true; they only differ by definition. The production of ionizing radiation is well covered in the literature (Evans 1955; Bertin 1978; Halliday et al. 2001; Bossi et al. 2002). In the next few sections, we will summarize the production of x-ray, γ -ray, and annihilation radiation.

4.2.1 ELECTRONS AND X-RAY RADIATION GENERATION

Electromagnetic radiation comes in a broad range of wavelengths and frequencies (see [Figure 4.1](#)), although in vacuum, it all travels at the same speed ($c = 2.9979 \times 10^8$ m/s). Despite the fact that we distinguish different regions of the spectrum with names like radio waves, microwaves, infrared, visible, ultraviolet, x-rays, and so forth, there is only one entity, one essence of electromagnetic wave. Maxwell's equations are independent of wavelength and so suggest no fundamental differences in kind. Accordingly, it is reasonable to look for a common source mechanism for all electromagnetic radiation (Hecht 2002). What we find is that the various types of radiant energy seem to have a common origin in that they are all associated with nonuniformly moving charges. We are, of course, dealing with waves in the electromagnetic field, and charge is that which gives rise to the field, so this is not altogether surprising.

A stationary charge has a constant electric field and no magnetic field, and hence produces no radiation. A uniformly moving charge has both an electric and a magnetic field, but it does not radiate. If you traveled along with the charge, the current would thereupon vanish; hence, the magnetic field would vanish, and we would be back at the previous case, uniform motion being relative. That is reasonable, since it would make no sense at all if the charge stopped radiating just because you started moving along next to it. That leaves nonuniformly moving charges, which do radiate. The fundamental interactions between substantial matter and radiant energy are between photons and charges.

As discussed, by definition, x-rays are generated from the interaction of electrons as they are accelerated or decelerated or when electrons change energy levels in an atom. Here we discuss the atomic model since this will provide the current understanding of how x-rays are produced. The original interpretation of emission spectra using quantum theory was given by Bohr (1913a). In the Bohr model, the orbits are circular; in 1916, Sommerfeld suggested a modification of the Bohr theory to account for multiplicity of lines observed under high-energy-resolution spectroscopy. Sommerfeld's extension provided for elliptical orbits, with the atomic nucleus at a focus. In the Bohr–Sommerfeld atomic physics model, electrons surround the nucleus, orbiting in distinct elliptical shells or orbits related to their energy level (see [Figure 4.2](#)) (Lagowski 1973). Those close to the nucleus are lower energy and more tightly bound than those at distant orbits or shells. A Bohr–Sommerfeld atom is a solar system in miniature, with electrical (Coulomb) forces taking the place of gravitational forces. The positively charged central nucleus corresponds to the sun, while the electrons, moving around the nucleus under the electrical force of its attraction for them, correspond to the planets moving around the sun (but the orbits are not confined to a plane as is approximately true in the solar system) under the influence of its gravitational attraction.

The electrons are grouped in shells designated K, L, M, N, etc., in order of increasing distance from the nucleus (Bertin 1978). The electrons in each shell are classified further with respect to angular momentum and direction of spin. Each of these descriptions—shell, momentum, spin, etc.—is given by a quantum number, which may have only certain values, and no two electrons in an atom may have an identical set of quantum numbers (know as the Pauli exclusion principle). Unfortunately, several irreconcilable problems exist with the Bohr–Sommerfeld model for atomic

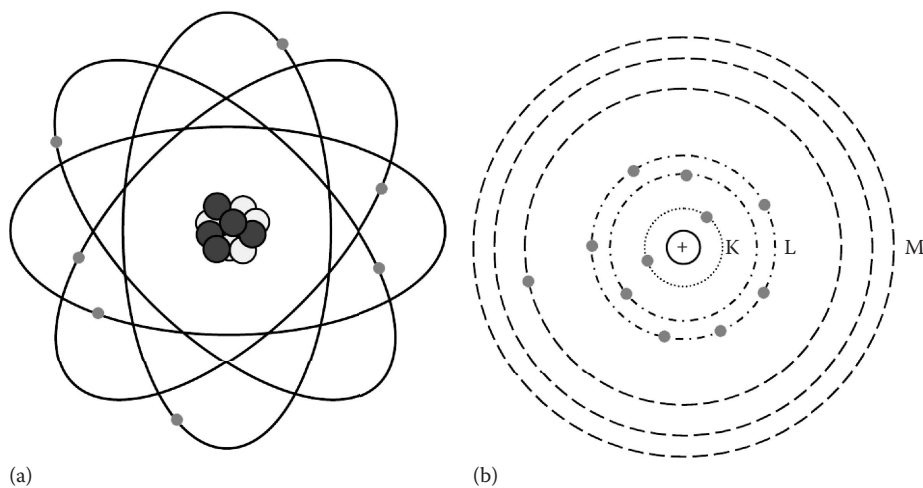


FIGURE 4.2 (a) In the Bohr–Sommerfeld atomic model, the neutrons and protons (symbolized by empty and black-filled circles) occupy a dense central region called the nucleus, and the electrons (gray-filled circles) orbit the nucleus. The image is not to scale since, in the realistic case, the radius of the nucleus is about 100,000 times smaller than the radius of the entire atom, and as far as we can tell, electrons are point particles without a physical extent. (b) A simplified representation of the Bohr–Sommerfeld atomic model is used throughout the text. In this representation, the nucleus is given by the inner circle with a plus sign, and the electrons (gray-filled circles) orbits are shown as circles of increasing radius from the nucleus. The energy of the electron orbit increases with increasing radius. Thus the K, L, and M orbitals (or shells) have electrons with increasing kinetic energy or decreasing binding energy, respectively.

structure. The basic difficulties of the Bohr–Sommerfeld atomic theory of the atom lay in treating the electron as a discrete particle traveling along a predictable path. It was de Broglie’s suggestion that electrons have a dual nature that provides an alternative to the Bohr–Sommerfeld atom (see Panel 4.1).

PANEL 4.1 De Broglie

The basic difficulties of the Bohr–Sommerfeld atomic theory of the atom lay in treating the electron as a discrete particle traveling along a predictable path. It was de Broglie’s suggestion that electrons have a dual nature that provides an alternative to the Bohr–Sommerfeld atom. The dual nature of light can be demonstrated by means of certain experiments: diffraction phenomena are best interpreted in terms of electromagnetic waves, while the photoelectric effect is more easily understood on a particulate basis. De Broglie suggested that certain properties of electrons can also be ascribed to a characteristic wave associated with electronic motion. The basic relationships between the wave nature of an electron and its particulate properties are given by

$$\lambda = \frac{h}{m_{\beta^-} c}, \quad (4.1)$$

where h is a fundamental constant of nature, called the Planck’s constant of action (6.6238×10^{-34} J s); λ is the wavelength (units, m) of the “electronic wave”; m_{β^-} is the rest mass (9.10×10^{-31} kg) of the electron; and c is the velocity of light (2.9979×10^8 m/s in a vacuum). De Broglie’s suggestion of electronic waves was verified when Davisson and Germer (1927)

discovered that electrons could be diffracted in the same manner as electromagnetic waves. For a given wavelength, there are only certain conditions for which the waves reinforce each other to form a standing wave; in all other cases, the same waves will interact destructively. Since the frequency of an electromagnetic wave is related to its energy,

$$E = h\nu, \quad (4.2)$$

where h is a fundamental constant of nature called the Planck's constant of action (6.6238×10^{-34} J s) and ν is the temporal frequency (s^{-1}) of the electron, there are only discrete energies associated with the electron. Just as the irradiance of an electromagnetic radiation is related to the number of photons per unit area per unit time, the amplitude of the electronic wave is associated with the number of electrons moving along a given path. The *irradiance** (average energy per unit area per unit time) or energy flux density is the square of the amplitude. The concept of waves associated with electrons lead to a description of the atom that is different from that suggested by Bohr–Sommerfeld. In the wave description, the exact positions of the electrons are not as important as they are in the Bohr–Sommerfeld theory. The emphasis is placed on describing the waves associated with the motion of an electron as it moves about the nucleus. The motion with which the waves reinforce each other to give a standing wave corresponds to a favorable electron energy. Thus, the establishment of standing waves is equivalent to the Bohr–Sommerfeld condition that electrons in atoms have discrete energies.

The mathematical description of the waves associated with electronic motion about a nucleus was first given by Erwin Schrödinger in a general form:

$$\frac{\partial^2\Psi}{\partial x^2} + \frac{\partial^2\Psi}{\partial y^2} + \frac{\partial^2\Psi}{\partial z^2} + \frac{8\pi^2m_{\beta^-}}{h^2}(E - E_{PE})\Psi = 0. \quad (4.3)$$

At any point in space, the 3-D wave associated with an electron possessing mass m_{β^-} , total energy E , and potential energy E_{PE} will have a certain amplitude Ψ that is a function of the Cartesian coordinates of that point. Solutions to the Schrödinger wave equation, called wave functions, are of the form $\Psi = f(x,y,z)$ and satisfy Equation 4.3. Mathematical details for the method of obtaining the solutions of a partial differential equation are not discussed in this text. For solutions to the Schrödinger wave equation, see, for example, the work of Hagelstein et al., *Introductory Applied Quantum and Statistical Mechanics* (2004), or Wouwer et al., *Adaptive Method of Lines* (2001). Only a brief outline of the mathematical solution will be presented, excerpted from Lagowski's (1973) *Modern Inorganic Chemistry* textbook.

First, the Schrödinger equation is transformed into polar coordinates so that $\Psi = f(\theta, \phi, r)$, and an expression for the potential energy of the electron is introduced. If the potential energy of the electron arises from electrostatic interactions, E_{PE} can be replaced by the quantity $-e^2/r$. Under these conditions, the Schrödinger equation takes the form

$$\begin{aligned} & \frac{1}{r^2} \frac{\partial}{\partial r} \left(r^2 \frac{\partial \Psi}{\partial r} \right) + \frac{1}{r^2 \sin^2 \theta} \frac{\partial^2 \Psi}{\partial \phi^2} \\ & + \frac{1}{r^2 \sin \theta} \frac{\partial}{\partial \theta} \left(\sin \theta \frac{\partial \Psi}{\partial \theta} \right) + \frac{8\pi^2m_{\beta^-}}{h^2} \left(E - \frac{e^2}{r} \right) \Psi = 0. \end{aligned} \quad (4.4)$$

* In the past, physicists and radiographers generally used the word *intensity* to mean the flow of energy per unit area per unit time. By international, if not universal, agreement, intensity is slowly being replaced in optics by the word *irradiance*. Here we suggest the same conversion for the field of radiography.

TABLE 4.1
Relationship among the Quantum Numbers n_q , l_q , and m_q

Quantum Number	Name	Allowed Values	Angular Momentum
n_q	Principal/primary	1, 2, 3, 4, ...	$\left(\frac{\hbar}{2\pi}\right)$
l_q	Secondary	0, 1, 2, 3, ..., $(n_q - 1)$	$(l_q - 1)^{1/2}$
m_q	Magnetic	$l_q, (l_q - 1), (l_q - 2), \dots, 0, -1, -2, \dots, (l_q - 1), l_q$	m_q
s_q^a	Electron spin ^a	+1/2, -1/2	s_q

Source: Lagowski, J.J., *Modern Inorganic Chemistry*, Marcel Dekker, Inc., New York, 1973.

^a Although the concept of spin is not explicitly found in the Schrödinger equation, Dirac has demonstrated that the relativistic form of quantum mechanics can yield the property of spin without a separate hypothesis.

A series of wave functions Ψ_i exist that are solutions to the Schrödinger equation when expressed in polar coordinates. For convenience, the solutions are given in terms of a radial part, $R(r)$, and angular parts, $\Theta(\theta)$ and $\Phi(\phi)$ ^{*}:

$$\Psi_i(r, \theta, \varphi) = R(r)\Theta(\theta)\Phi(\varphi) \quad (4.5)$$

The general form of the solutions represented by Equation 4.5 contains three quantum numbers, i.e., integers that may be assigned specific values. Since wave mechanical quantum numbers exhibit the same mathematical interrelationships as those developed in the Bohr-Sommerfeld theory, the same symbols are used. The quantum number[†] n_q appears in the $R(r)$ portion of the wave function. The secondary quantum number l_q appears in the $\Theta(\theta)$ part of the wave function and the magnetic quantum number m_q appears in the $\Phi(\phi)$ part. There are 14 solutions to the polar form of the Schrödinger equation for the hydrogen atom (Lagowski 1973). The wave functions can be identified by the values assigned to the quantum numbers n_q , l_q , and m_q . The relationships among these quantum numbers are summarized in Table 4.1. Generally, the wave functions are identified by giving the value of the principal and the secondary quantum numbers; the latter has been historically designated by a letter according to the following scheme (see Figure 4.3):

Value of l_q	0 1 2 3 4 5 6;
Letter designation	s p d f g h i.

The wave functions Ψ_i that are solutions to the polar wave equation (Equation 4.4) can, upon substitution into the latter, yield the corresponding values of the energy E_i of the stationary states. The energies that correspond to the solutions of the wave equation are identical to those determined from the Bohr theory for electrons occupying the corresponding Bohr orbits. The

* Please note that even though the same symbols as for irradiance and phase are used, these are not to be confused with the irradiance or phase symbols.

[†] In most texts, the quantum numbers n , l , and m do not have a subscript q ; we use this to distinguish these letters from other designations in the text.

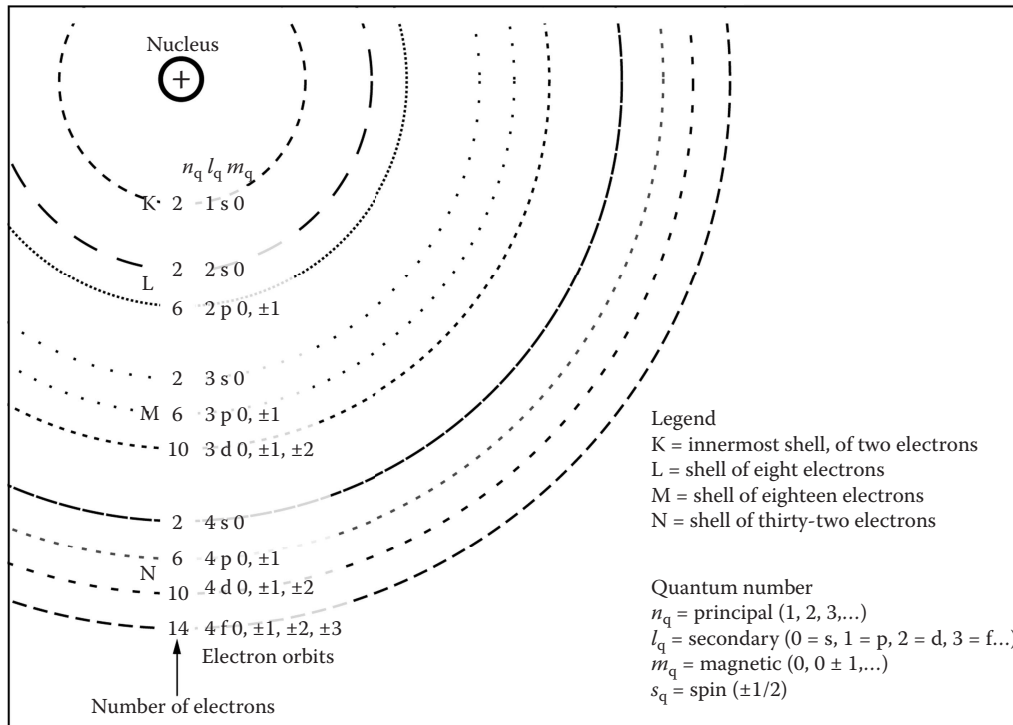


FIGURE 4.3 Relationship between the Siegbahn designation system of K, L, M, etc. and the wave equation quantum numbers for atomic structure.

wave functions are also related to the probability of finding an electron at a given point, the probability density function, P , being given by

$$P = \Psi(x, y, z)\Psi^*(x, y, z), \quad (4.6)$$

where Ψ^* is the complex conjugate of Ψ . Since Ψ can have imaginary or negative values, the product of Ψ and Ψ^* gives a probability consisting of real numbers. If Ψ is related to probability, it must have a certain mathematical characteristics:

- It must be single valued at each point in space.
- It must not go to infinity at any point.
- Its absolute value at all points must be such that Equation 4.7 must be obeyed:

$$\int_{-\infty}^{+\infty} \int_{-\infty}^{+\infty} \int_{-\infty}^{+\infty} \Psi(x, y, z)\Psi^*(x, y, z) dx dy dz = 1. \quad (4.7)$$

Since the angular dependence is the same for all values of r , the angular part of the wave function is sufficient to provide a representation of the electron probability in three dimensions. The angular dependence for the probability of finding an electron in space is proportional to $\Theta(\theta)^2\Phi(\phi)^2$, the square of the angular part of the wave function. The three-dimensional representation of these functions for $l = 0, 1$, and 2 appears in Figure 4.4 (Lagowski 1973). Note that the Schrödinger theory for the probability of finding an electron is a lot different than a circular

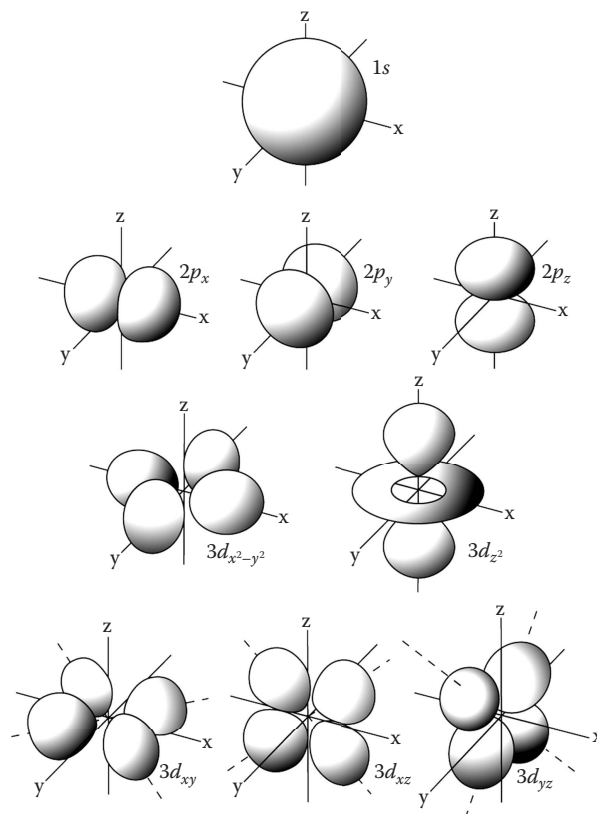


FIGURE 4.4 The electron probability function as calculated from the angular part of the wave function for $l_q = 0, 1$, and 2 . The figures are not drawn to scale. (Courtesy of Lagowski, J.J., *Modern Inorganic Chemistry*, Marcel Dekker, Inc., New York, 1973.)

or elliptical orbit as given by Bohr and the Bohr–Sommerfeld theories, respectively, as represented in [Figure 4.2](#).

4.2.1.1 Bremsstrahlung (Braking or Decelerating Electrons)

Here we describe how x-rays are generated by the deceleration (nonuniform movement) of electron charge, one of the most practical mechanisms for producing x-rays. The resulting broad-frequency bremsstrahlung (German for “braking radiation,” referring to the deceleration of electrons as the cause of the radiation) arises when a beam of energetic electrons is fired at a material target, such as a tungsten plate. Bremsstrahlung is generated when negatively charged electrons in motion are deflected by positively charged atomic nuclei. Representative bremsstrahlung spectra (Birch and Marshall 1979), also called general or white radiation, or polychromatic or polyenergetic spectra, are shown [Figure 4.5](#). The deflection of the electrons involves loss of kinetic energy* (velocity). This energy loss is promptly emitted as electromagnetic radiation (x-rays), called bremsstrahlung. Bremsstrahlung is the main source of x-rays produced by x-ray tubes. For details on x-ray tubes, see Section 8.4.1, X-ray Tubes.

* Kinetic energy = $1/2 (\text{mass})(\text{velocity})^2$. More details on this are given in the Section 4.2.4, Units Used to Characterize and Describe High-Energy Photons.

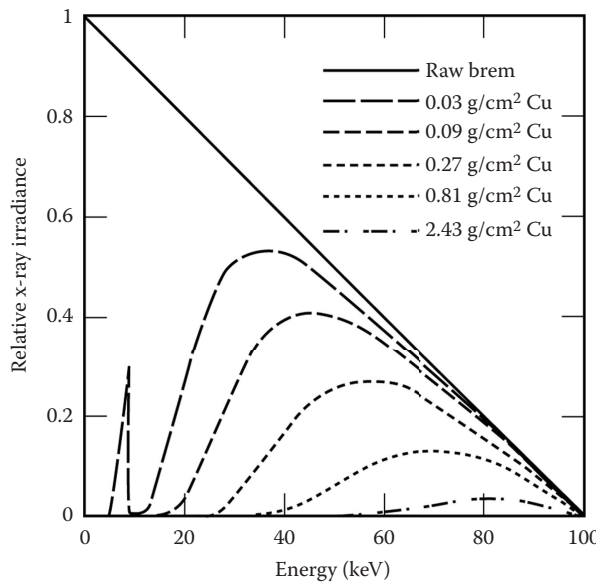


FIGURE 4.5 X-ray irradiance as a function of energy for a tungsten anode material using a voltage of 100 kV. The unfiltered spectrum does not include the attenuation in the anode, x-ray tube exit window, or flight path. Dotted curves show the effect of increasing areal densities of Cu filtration. Note that the lightest Cu filter shows the effect of the Cu K edge near 8 keV.

The amount of deflection, and hence the energy loss, is dependent upon the distance between the passing electron and the nucleus (Figure 4.6). The smaller the distance of the electron from the nucleus, the higher the energy loss, resulting in an x-ray of higher emitted photon energy. When electrons pass through material, they will generally lose their kinetic energy in steps. The likelihood of an event increases for lower energy loss. An event in which an incoming high-energy electron will lose all its kinetic energy to an emitted bremsstrahlung photon will therefore be very rare. The spectral distribution of the photon flux density (the number of photons passing per unit area per unit time) in the bremsstrahlung will therefore look like the downward convex curve in Figure 4.7. The irradiance (average energy per unit area per unit time) or energy flux density is the product of

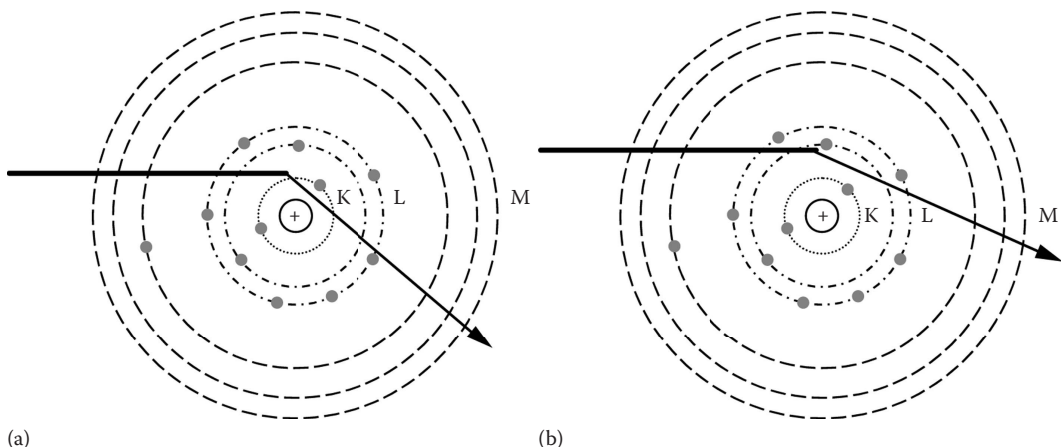


FIGURE 4.6 The distance between electron and nucleus is smaller in (a) than (b), resulting in a larger deflection of the electron and a higher energy of the emitted bremsstrahlung in (a).

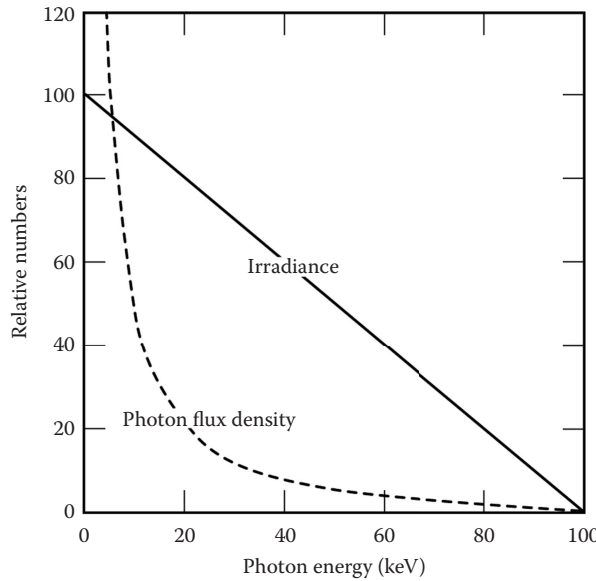


FIGURE 4.7 Bremsstrahlung spectral distribution of photon flux density and irradiance (energy flux density) for a source with no x-ray photon attenuation. Note that this is idealistic since all x-ray bremsstrahlung sources have x-ray attenuation in the anode.

the photon flux density at a certain energy and the energy. It will have the shape of a straight line (see Figure 4.7).

4.2.1.2 Characteristic X-Rays

When an orbiting electron is dislodged by incident radiation or a particle, the atom exists in an *excited state* (see Figure 4.8a). Shortly, the electrons will rearrange themselves to return the atom to the *ground state* or nonexcited state (see Figure 4.8b). During this transition, energy can be liberated in the form of an x-ray photon with energy equal to the difference between the excited state and the ground state. This x-ray is called a *characteristic x-ray* because its energy is characteristic of the atom/element undergoing the transition.

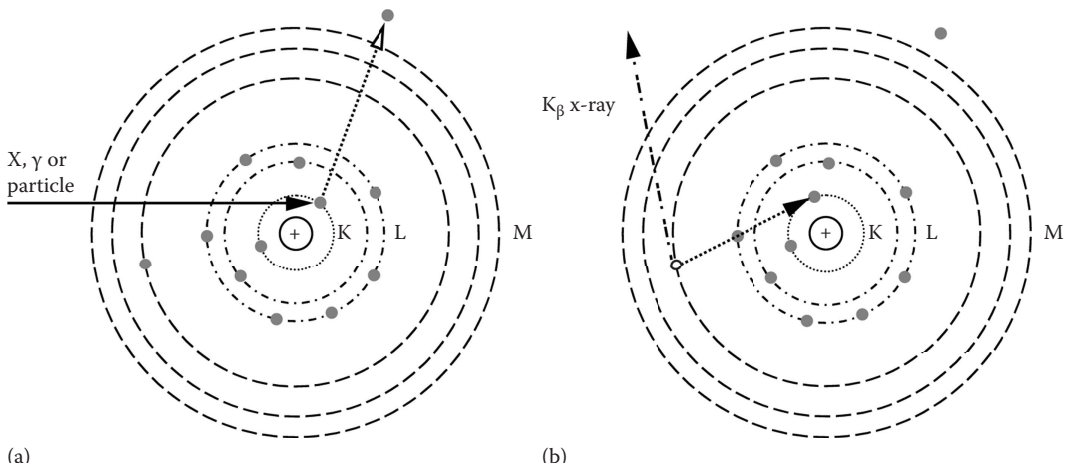


FIGURE 4.8 (a) An inner-shell electron is ejected from the atom. (b) It is then replaced by an outer shell electron, thus producing characteristic radiation.

From the principle of energy conservation, this electron has to come from one of the electron shells farther out from the nucleus, since these electrons are more loosely bound than the one that was ejected. Loosely bound (low-binding-energy*) electrons are more energetic than tightly bound (high-binding-energy) electrons. Following this process, the atom contains excess energy. This is due to the difference between binding energy of the “substituting” electron when it was bound in an outer shell and its new and higher binding energy. This excess energy can be emitted in two ways: either by pushing out one of the loosest bound electrons in the outermost shell or by emitting a photon (see Figure 4.8b). For heavy elements, photon emission is more common, while for lighter elements, electron emission dominates. The electrons emitted are called *Auger electrons*, and the photons emitted are called characteristic radiation. The name *characteristic* comes from the fact that the binding energies for electrons in an atom are unique for a specific element. Therefore, the difference in binding energy is also a unique characteristic for the element in question. Electron transitions cannot occur from any higher to any lower level. Only certain transitions are “permitted” by selection rules. For further discussions on selection rules, see the textbook *Principles and Practice of X-ray Spectroscopic Analysis* by Bertin (1978).

The characteristic radiation produced by electron transitions between shells is named according to the shell that captured the electron. This is given by the Siegbahn designation system; the symbol of an x-ray spectral line (e.g., Ni K _{α 1}, W K _{α 2}) consists of (1) the symbol of the chemical element; (2) the symbol of the shell (K, L, M, etc.), the electron was dislodged from or the shell with a missing electron; and (3) a lowercase Greek letter, usually with a numerical subscript (Bertin 1978).

Characteristic radiation resulting from an outer-shell (e.g., L or M) electron filling a vacant site in the K shell is thus named K-characteristic radiation; L-characteristic radiation occurs when a vacant site in the L shell is filled with an electron from a shell more distant to the nucleus. The letters K, L, etc., are given a Greek letter subscript (α , β), α referring to an adjacent shell transition (e.g., L to K, M to L) and β referring to a nonadjacent shell transition (e.g., M to K, N to K, N to L). A K _{α} radiation is therefore less energetic than a K _{β} radiation. Even between electrons within the same shell, there are energy differences; the resulting different characteristic radiation energies are designated by the subscript 1, 2, 3, etc. Several possibilities therefore exist for K-characteristic radiation, e.g., K _{α 1}, K _{α 2}, K _{β 1}, etc.

K-series x-rays are of utmost technological importance because they are of the highest energy and most penetrating. The highest-energy K-series x-ray is created when the vacancy is filled with a free (unbound) electron. The K-series x-rays increase in energy with increasing atomic number. The maximum for Fe is 7 keV, while that for W is 70 keV. Tables of characteristic energies are widely available and are easily found on the Internet, e.g., http://xdb.lbl.gov/Section1/Sec_1-2.html. Characteristic x-ray radiation is typically superimposed on the bremsstrahlung radiation, as shown in Figure 8.9 in Chapter 8.

4.2.1.3 Accelerating Charge

We know in general that free charges (those not bound within an atom) emit electromagnetic radiation when accelerated. That much is true for charges changing speed along a straight line within a linear accelerator, sailing around in a circle inside a cyclotron, or simply oscillating back and forth in a radio antenna—if a charge moves nonuniformly, it radiates. A free charged particle can spontaneously absorb or emit a photon, and an increasing number of important devices, ranging from the free-electron laser to the synchrotron radiation generator, utilize this mechanism on a practical level. For further discussions on these types of sources, see Section 8.4.

* The electron binding energy is the net energy required to remove an atomic electron to an infinitely remote position from its orbit.

4.2.2 THE NUCLEUS AND γ -RAY AND X-RAY GENERATION

γ -rays, by definition, are high-energy electromagnetic radiation that arise from the decay of a radioactive nucleus. Often people think that x-rays are lower in energy than γ -rays. This is not true. They only differ by definition, i.e., origin of the electromagnetic radiation. It is very important to point out that x-rays can be higher in energy or equal to γ -rays and visa versa.

The nucleus of a hydrogen atom (one proton) is stable without a neutron. If we add two neutrons to the stable hydrogen atom, it becomes the unstable radioactive isotope tritium. An isotope is any of two or more atoms of a chemical element with the same atomic number (number of protons) but different mass numbers, i.e., they differ in the number of neutrons. If a nucleus has too many or too few neutrons, it is energetically unstable and will decay to a more stable energy state. The decay process is accompanied by the emission of alpha particle (α), β , neutron, γ , or x radiation in some combination. Some common radioactive isotopes used in industrial imaging are given in Figure 4.9

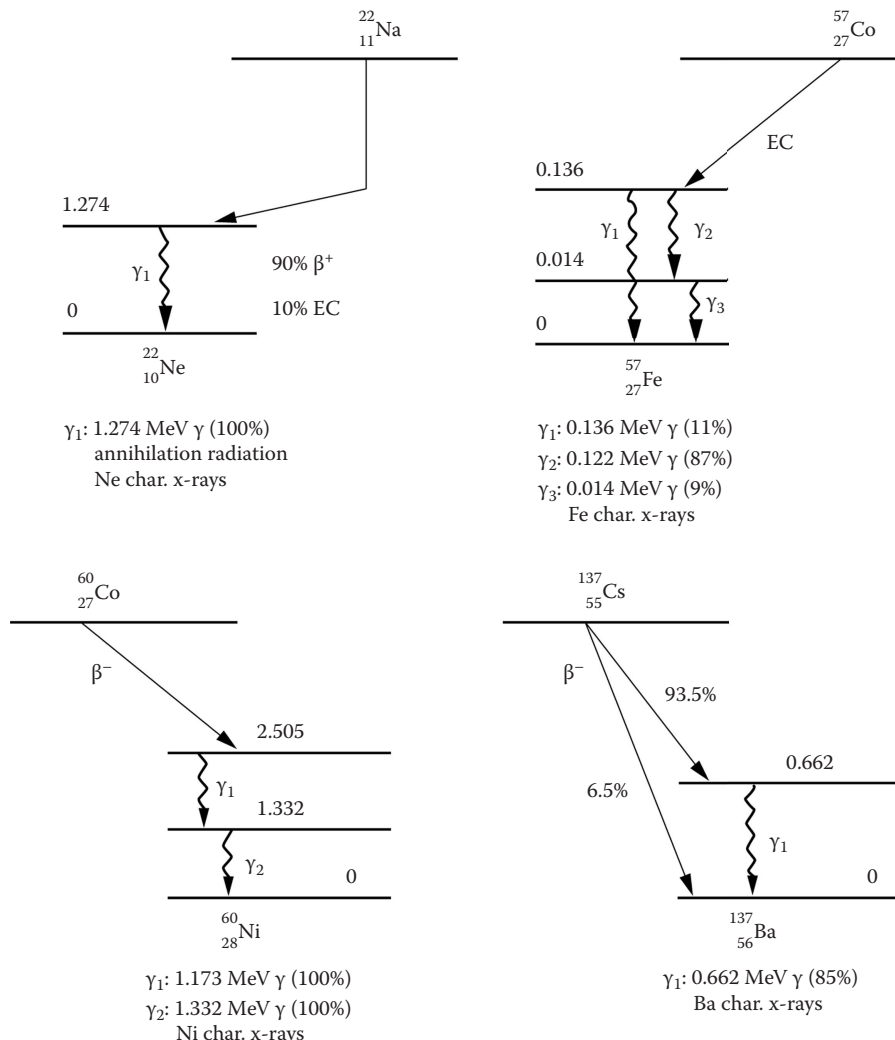


FIGURE 4.9 Decay schemes for some common γ radioactive sources. Only major transitions are shown. The energies and yields per disintegration of x-ray and γ -rays emitted in each decay are listed below each scheme. (Knoll, G.F.: *Radiation Detection and Measurement*, third edition. 2000. Copyright Wiley-VCH Verlag GmbH & Co. KGaA. Reproduced with permission.)

along with their decay mechanisms (Knoll 2000). A spectrum for ^{60}Co and ^{137}Cs is given in Figures 4.10 and 4.11, respectively (Heath 1974).

Since we have already defined x-rays as arising from orbiting electrons, an explanation is in order as to how *nuclear* decay can result in x-rays. There are two basic mechanisms. The nucleus can move toward stability by capturing an electron—*electron capture (EC)*. A proton within the nucleus is thereby converted to a neutron. This results in a transformation of the element to a new element with the same atomic mass number, A , as before, but a lower atomic number, Z . This new element is missing an electron from its inner shell. As we describe in the previous section, x-rays are then produced as the vacancy is filled. The second mechanism for nuclear decay to produce a missing electron and, consequently, x-rays is for α or β radiation from the nucleus to eject an orbiting electron as it moves through the material.

For a ^{22}Na atom, known as the radioactive parent, the radioactive decay is by either EC or the emission of a positron (see Figure 4.9). The branching ratio is 0.90 β^+ and 0.10 EC, given that the branching ratio is the number of decays of a particular type divided by the total number of decays. In either case, in essence, a proton is converted into a neutron, and the daughter atom becomes ^{22}Ne . The daughter atom is in a neutron-excited state, and the neutron transitions (decays) to the ground state via emission of a 1.274 MeV γ -ray. In addition to this γ -ray, the β^+ generates annihilation photons and Ne characteristic x-rays $K_{\alpha 1}$ and $K_{\alpha 2}$ both of 848.6 eV (Thompson et al. 2001). A representative ^{22}Na γ -ray/x-ray energy spectrum is shown in Figure 4.12. ^{57}Co decays by EC, as shown

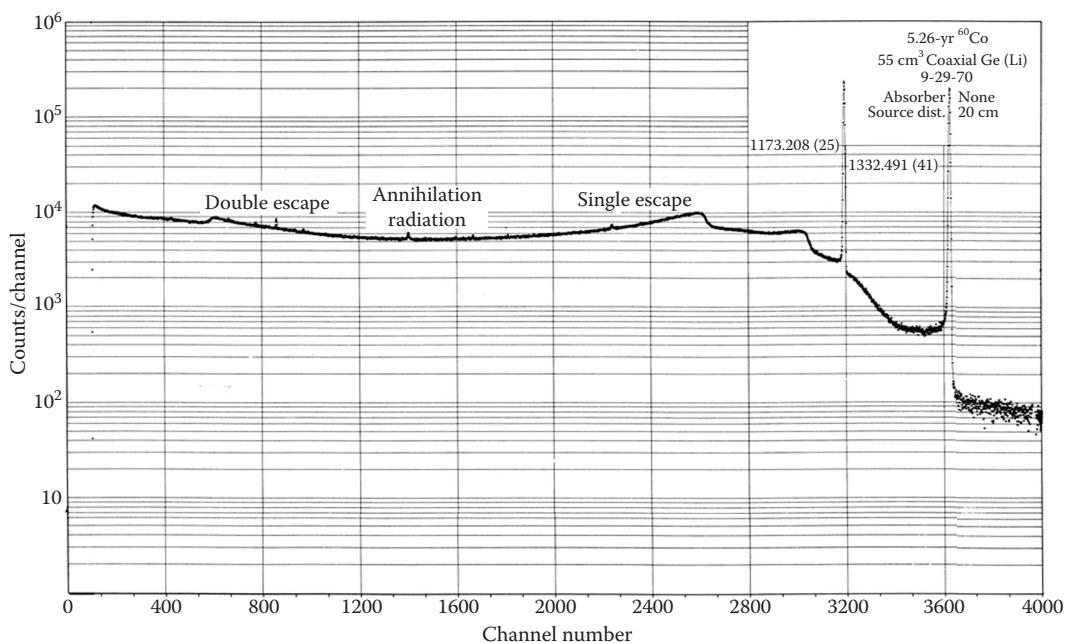


FIGURE 4.10 Representative ^{60}Co spectrum as measured with a lithium-drifted germanium detector, Ge(Li). In speaking, Ge(Li) is often pronounced “jelly.” This type of detector system records the charge produced in the semiconductor as a result of energy deposit by the radiation interacting in the detector. Increasing channel number corresponds with increasing energy deposit. The strong peaks are called *photopeaks* and result from deposit of all of the incident γ -ray energy from a photoelectric event within the detector. The other features of this spectrum result from the various interaction mechanisms that are covered in Chapter 5. ^{60}Co γ -rays are sufficiently energetic to cause pair production (Chapter 5). When one of the annihilation photons escapes the detector, a small peak, called a single-escape peak, is created 511 keV below the photopeak. When both annihilation photons escape, an analogous double-escape peak occurs. (From Heath, R.L., *Gamma-ray Spectrum Catalogue Ge (Li) and Si (Li) Spectrometry*, third edition, volume 2 of 2, Aerojet Nuclear Company, reproduced by National Technical Information Service, US Department of Commerce, Springfield, VA, 1974.)

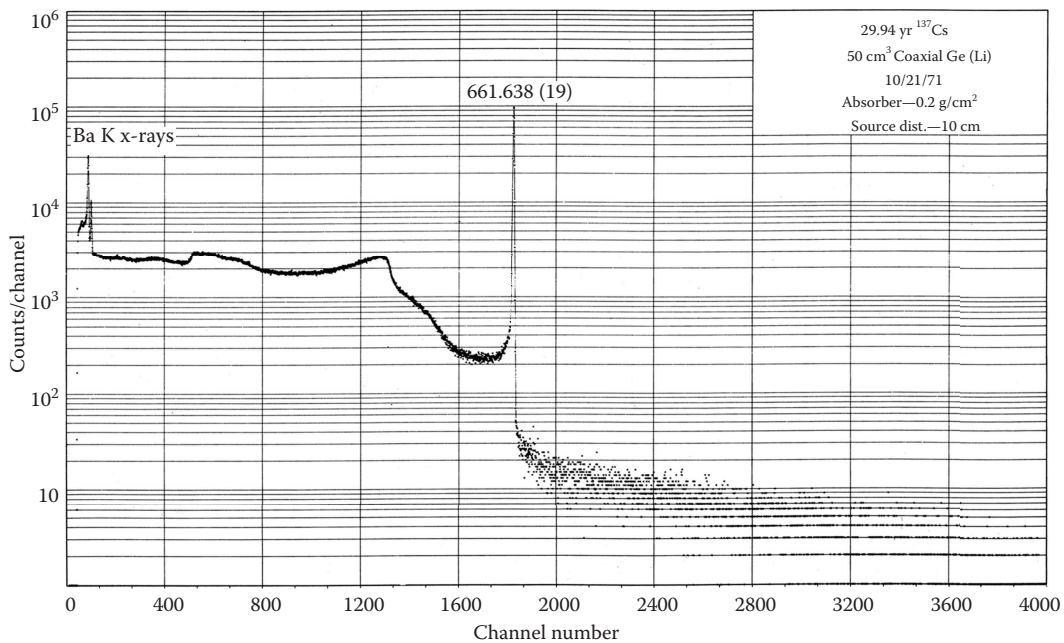


FIGURE 4.11 Representative measured pulse height spectrum for ^{137}Cs spectrum. (From Heath, R.L., *Gamma-ray Spectrum Catalogue Ge (Li) and Si (Li) Spectrometry*, third edition, volume 2 of 2, Aerojet Nuclear Company, reproduced by National Technical Information Service, US Department of Commerce, Springfield, VA, 1974.)

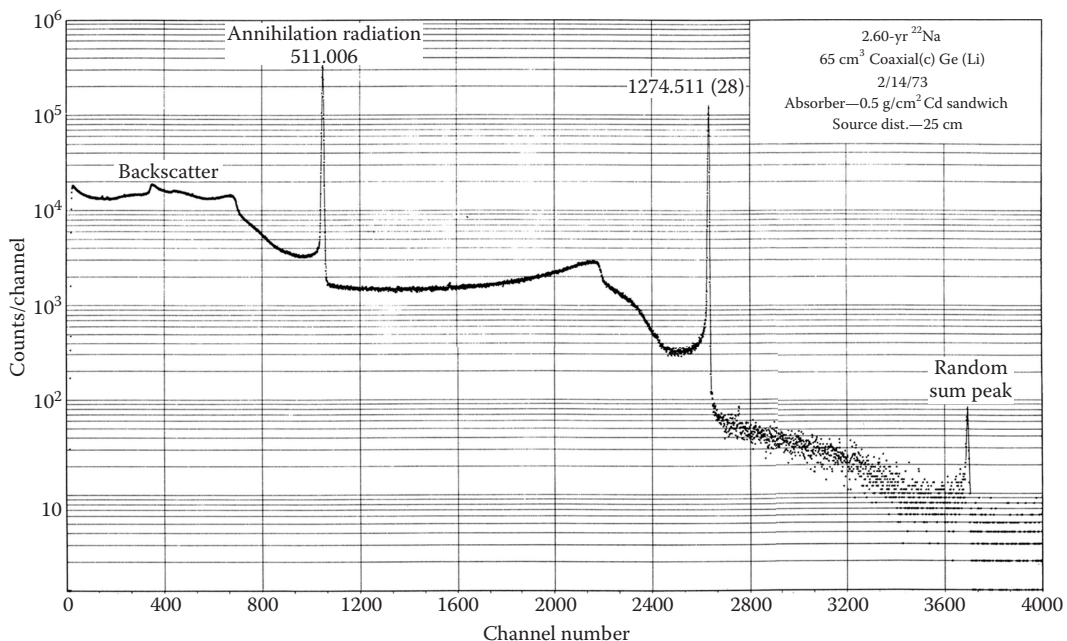


FIGURE 4.12 Representative measured pulse height spectrum for ^{22}Na spectrum. (From Heath, R.L., *Gamma-ray Spectrum Catalogue Ge (Li) and Si (Li) Spectrometry*, third edition, volume 2 of 2, Aerojet Nuclear Company, reproduced by National Technical Information Service, US Department of Commerce, Springfield, VA, 1974.)

in [Figure 4.9](#), and this decay generates γ -rays and x-rays. ^{60}Co and ^{137}Cs decay by β^- , as shown in [Figure 4.9](#). These radioactive isotopes emit an electron from the nucleus, and in so doing, a neutron is converted to a proton. ^{60}Co results in a proton in a 2.505 MeV excited energy level, which subsequently decays by emission of two γ -rays, 1.173 and 1.332 MeV, of equal intensity (see [Figure 4.10](#)). ^{137}Cs decays to the ground state and a 0.662 MeV excited state of Ba (see [Figure 4.9](#)). A representative ^{137}Cs γ -ray/x-ray energy spectrum is shown in [Figure 4.11](#).

Radioactive decay is a probabilistic phenomenon. The disintegration rate depends linearly on the number of radioactive atoms present. If one starts with a fixed quantity of radioactive nuclei, the number remaining continuously decreases, and the decay rate continually decreases. If the number of nuclei at time $t = 0$ is N_0 , then the number of nuclei, N_t , remaining at a later time, t , is given by

$$N_t = N_0 e^{-\lambda_r t}, \quad (4.8)$$

where λ_r is the *decay constant*.

The *half-life*, τ_{HL} , of a radioisotope is defined as the time required for the number of radioactive nuclei to be reduced by one-half. Therefore,

$$\tau_{HL} = \frac{\ln 2}{\lambda_r}. \quad (4.9)$$

The *activity*, Λ , of a radioisotope source is its rate of decay. From Equation 4.8,

$$\Lambda = \frac{dN_t}{dt} = -\lambda_r N_t. \quad (4.10)$$

The historical unit of activity is the Curie (Ci), defined as 3.7×10^{10} disintegrations per second. While Ci is still in widespread use, the SI unit of activity is the Becquerel (Bq), defined as 1.0 disintegration per second. Useful sources for radiography contain many MBq or even GBq. Another useful radioactive unit is specific activity (Ci/g):

Specific activity = activity per unit mass,

or

$$\Lambda_{sp}^j = \frac{\Lambda^j}{m_j}, \quad (4.11)$$

where m_j is the mass in grams and Λ^j is the radioactivity of radioisotope j . It is useful to note that specific activity does not include the mass of other isotopes, elements, or compounds in the radioactive source.

Two cautionary notes are in order before leaving the subject of radioactivity. A source does not always produce a given type of radiation on every disintegration. Therefore, the source strength of desired radiation might be only a fraction of the activity. In addition, absorption and scattering take place within the source itself, so that radiation escaping from the source may only be a fraction of the decay amount. Also, even for a pure γ decay at a single energy, scatter will produce some γ s at lower energy.

4.2.3 ANNIHILATION RADIATION GENERATION

Annihilation radiation is electromagnetic radiation produced when a positron (β^+) and electron (β^-) combine. When a parent nucleus undergoes β^+ decay, additional electromagnetic radiation is generated. The origin lies in the fate of the positrons emitted in the primary decay process. Because they generally travel only a few millimeters before losing their kinetic energy, the inherent encapsulation around the source is often sufficiently thick to stop the positrons. When their energy is low, near the end of their range, they combine with electrons. The original positron and electron disappear and are replaced by two oppositely directed 0.511 MeV electromagnetic photons called annihilation photons/radiation. This radiation is then superimposed on whatever γ radiation may be emitted in the subsequent decay of the radioactive daughter product. See, for example, the decay of ^{22}Na , as shown in Figures 4.9 and 4.12. Photons of both 0.511 and 1.274 MeV energy are emitted in addition to Ne characteristic x-rays of 848.6 eV.

4.2.4 UNITS USED TO CHARACTERIZE AND DESCRIBE HIGH-ENERGY PHOTONS

We begin by discussing individual photon measurement units. Electromagnetic radiation can be described by the energy, E , of the individual photons. The SI unit for energy is the joule (J), while the traditional unit for radiation energy is the electron volt (eV). One electron volt is the kinetic energy imparted to an electron when the electron is accelerated across a 1 V potential. The kinetic energy, E_K , of a particle is given by

$$E_K = \frac{1}{2}mv^2, \quad (4.12)$$

where m is the mass of the particle and v is the velocity of the particle. The traditional electromagnetic (kinetic) energy unit is electron volts ($1 \text{ eV} = 1.602 \times 10^{-19} \text{ J}$) and is most often used. Energy units other than electron volts, joules, or ergs ($1 \text{ J} = 1 \times 10^7 \text{ ergs}$) are not common, but photon energy can also be expressed in calories (cal), British thermal units (Btu), or even horsepower-hour or kilowatt-hour (kWh):

$$1 \text{ J} = 0.239 \text{ cal} = 9.48 \times 10^{-4} \text{ Btu} = 3.73 \times 10^{-7} \text{ horsepower-hour} = 2.78 \times 10^{-7} \text{ kWh}.$$

Photons can also be described by their wavelength, λ , in units of length (m) and/or by their frequency, ν , in units of inverse time (s^{-1} or Hz). Wavelength is the common descriptor in x-ray diffraction work. Wavelength and frequency are related by

$$c = \nu\lambda, \quad (4.13)$$

where c is the speed of light ($3.0 \times 10^8 \text{ m/s}$ in vacuum). As expected, the wavelength and frequency are inversely proportional.

The energy is related to the frequency by

$$E = h\nu, \quad (4.14)$$

where h is the Planck's constant,* whose value is $h = 6.626 \times 10^{-34} \text{ J s}$.

An example is given in Panel 4.2 of converting from frequency to energy to wavelength.

* Max Planck was German born in 1858. He discovered the relationship between energy and frequency in 1900 and was awarded the Nobel Prize for Physics in 1918. He died in 1947 (*Britannica* 2005).

PANEL 4.2 Example Problem

Here we present an example problem showing the relationship and range of unit values among these various and frequently used parameters that describe an individual photon.

A photon with a frequency of 1×10^{19} Hz has an energy of

$$E = (6.626 \times 10^{-34} \text{ J s})10^{19} \text{ s}^{-1} = 6.626 \times 10^{-15} \text{ J},$$

from Equation 4.14. Converting units to electron volts using the conversion factor $1 \text{ eV} = 1.602 \times 10^{-19} \text{ J}$ leads to

$$E = 4.1 \times 10^4 \text{ eV, or } E = 41 \text{ keV,}$$

and, from Equation 4.13, a wavelength of

$$\lambda = \frac{3 \times 10^8 \frac{\text{m}}{\text{s}}}{10^{19} \text{ s}^{-1}} = 3 \times 10^{-11} \text{ m} = 0.03 \text{ nm.}$$

The portion of the electromagnetic spectrum usually used for nondestructive evaluation (NDE) is 1 keV to 10 MeV (10^{-9} to 10^{-12} m wavelength). These are either γ -rays or x-rays* depending on whether they originate within the nucleus or the orbital electrons of an atom, respectively. Table 4.2 gives equivalent wavelength and frequency units for the range of NDE photon energies.

So far we have discussed parameters and their units as applied to describing or characterizing individual photons. We turn now to how an ensemble of photons is characterized. The quantity of photons passing across a planar surface can be expressed as the number of photons crossing a unit area of the surface per unit time. This is called *photon flux density* and has units of number of photons per unit area per unit time. The surface is usually considered to be normal to the direction of photon flow. The amount of photons passing a planar surface can also be expressed as energy flow rather than photon flow. The average energy passing across a unit area of the surface per unit time is called *irradiance*. Irradiance thus has the units of average energy per unit area per unit time. In the NDE literature, you will encounter the term *intensity* to describe a photon field. There is no uniformly accepted definition of this descriptor. Generally, it is synonymous with energy flux density. We prefer the term *irradiance* to describe energy flow per unit area per unit time, and this term is used throughout the text.

TABLE 4.2
Relationship among the Energy, Wavelength, and Frequency of a Photon as Given by Equations 4.13 and 4.14

Energy	Wavelength	Frequency
1 keV	$2.0 \times 10^{-9} \text{ m}$	$1.51 \times 10^{17} \text{ Hz}$
10 keV	$2.0 \times 10^{-10} \text{ m}$	$1.51 \times 10^{18} \text{ Hz}$
100 keV	$2.0 \times 10^{-11} \text{ m}$	$1.51 \times 10^{19} \text{ Hz}$
1 MeV	$2.0 \times 10^{-12} \text{ m}$	$1.51 \times 10^{20} \text{ Hz}$
10 MeV	$2.0 \times 10^{-13} \text{ m}$	$1.51 \times 10^{21} \text{ Hz}$

* The 511 keV annihilation photons are rarely used for industrial imaging.

When describing a spectrum of x-rays, the usual approach is to present a plot or table with values that are differential in energy. Normalization may be so that the integral over energy is the x-ray flux density at some stated location, or the spectrum may be normalized so that the integral over energy is unity. In the latter case, only the spectral shape is conveyed.

PROBLEMS

- 4.1 Describe why the type of x-ray transition depicted in [Figure 4.8b](#) is K_{β} .
- 4.2 Using the material in Section 4.2.4, Equation 4.1, and Chapter 7 of the book by Shull (2002), show that the wavelength in micrometers of the highest-energy bremsstrahlung x-ray in the spectrum from an x-ray tube with applied voltage of V in volts is given by
$$\lambda_{\min} = \frac{1.24}{V} \mu\text{m}.$$
- 4.3 Which spectrum has the higher average energy, a bremsstrahlung spectrum with a minimum wavelength of 2.0×10^{-10} m or a bremsstrahlung spectrum with a minimum wavelength of 1.0×10^{-10} m?
- 4.4 From the decay scheme in [Figure 4.9](#) for ^{57}Co , what energy γ -ray would be the strongest observed peak in the pulse height spectrum for ^{57}Co ?

5 High-Energy (X-Ray and γ -Ray) Photon Interactions with Matter

5.1 INTRODUCTION

In this chapter, you will become acquainted with the fundamental understanding needed to apply x-ray and gamma-ray (often denoted by the Greek letter gamma, γ) imaging to address industrial imaging requirements. We discuss the interaction of high-energy photons* with matter. In this text, high-energy photons mean electromagnetic radiation that is higher in energy than other more common electromagnetic radiation such as visible and ultraviolet photons (see [Figure 5.1](#)). The high-energy photons to which we refer are x-rays, γ -rays, and annihilation radiation. Sometimes, we may just refer to x-rays, but unless stated otherwise,[†] this term could also imply γ and annihilation radiation as well.

Upon completion of this chapter you will be able to understand the following:

- Interaction of high-energy photons with matter
 - Attenuation and phase effects
 - Processes contributing to attenuation
 - Photoelectric (or photoionization) absorption
 - Scatter
 - Pair production
 - Photonuclear
 - Photofission
 - Attenuation measurement units
 - Reflection
 - Processes contributing to x-ray phase effects
 - Refraction
 - Diffraction
 - X-ray phase-contrast radiography

5.2 ATTENUATION AND PHASE CONTRAST

The basic principles of x-ray image formation and interpretation in radiography have remained essentially unchanged since Röntgen first discovered x-rays over 100 years ago (see [Panel 5.1](#)). The conventional approach relies on x-ray *attenuation* as the sole source of contrast and draws

* The name *photon* is given to a small bundle or quantum of electromagnetic energy. It is used when describing the particle-like behavior of electromagnetic waves (including light waves).

[†] Recall from Chapter 4, Physics of X-Ray and γ -Ray Sources, that by definition, x-rays and γ -rays are high-energy electromagnetic radiation; they are distinguished only in definition. X-rays are generated by changes of electrons in an atom or by the acceleration or deceleration of charged particles such as electrons or protons and γ -rays are generated by nuclear transitions.

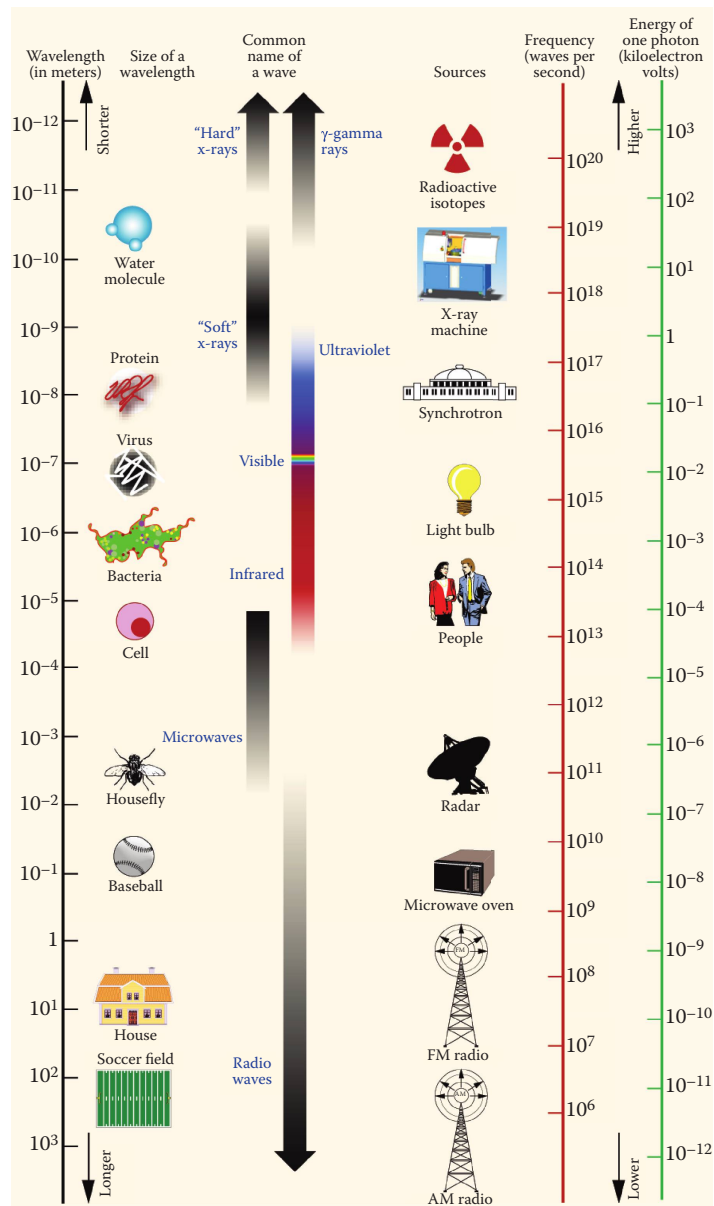


FIGURE 5.1 Electromagnetic spectrum showing the location of the various types of electromagnetic radiation as a function of wavelength, frequency, and energy. Representative sources of electromagnetic radiation in each region of the spectrum are also depicted.

exclusively on ray or geometrical optics (Smith 2000; Hecht 2002) to describe and interpret image formation. This approach ignores another, in some cases more useful, source of contrast due to x-ray *phase shifts*. Phase-sensitive techniques offer ways to augment or complement standard attenuation contrast. Phase techniques can be understood using wave optics rather than ray optics (Smith 2000; Hecht 2002).

PANEL 5.1 Röntgen

Within 2 months of Röntgen's discovery of x-rays, he published most of the important characteristics of x-rays (Röntgen 1895, 1896). Summarized in the following table, these characteristics remain valid more than a century later. For more on Röntgen's discovery of x-rays, see Chapter 2, X-Ray History.

Röntgen's Publication

The new kind of radiation can be produced by using several types of discharge tubes,^b which are available in many physics laboratories.

The source arises from the discharge apparatus and not from any other point in the conducting circuit.

All bodies are transparent to x-rays, though to different degrees. Paper is very transparent. Lead of a thickness of 1.5 mm is practically opaque.

Density is the most important attribute governing transparency, though transparency of glass, aluminum calcite, and quartz of nearly the same thickness and density are quite different. Increasing thickness reduces transparency. There is some characteristic of materials, other than density and thickness, that has an effect on transparency.

X-rays are unaffected by magnetic fields.

Background/Current Understanding

Cathode rays^a had recently been discovered, and many laboratories operated these tubes.

We now know that the x-rays arise from the interaction of electrons (cathode rays) with any material.

This is still true for the ~60 keV x-rays that were being generated in Röntgen's device. MeV x-rays penetrate 1.5 mm of Pb readily.

Röntgen did not quite make the leap that the atomic number was the important "other characteristic." One might today argue that the atomic number is *more important* than density, but given that the common forms of heavier elements are also typically more dense than light elements, Röntgen probably had insufficient observations to separate density from atomic number.

X-rays are still unaffected by magnetic fields.

^a Cathode rays are a stream of electrons emitted by the cathode in an electrical discharge tube.

^b A discharge tube is a closed insulating vessel containing a gas at low pressure through which an electric current flows when sufficient voltage is applied to its electrodes.

Many physicists automatically connect the notion of phase measurement with techniques involving interferometry. However, it has long been known that propagation of an optical field through free space can render the phase structure of an object visible in the measured intensity distribution (Zernike 1942). It should not be surprising that x-rays also contain phase information since x-rays are electromagnetic radiation similar to visible light (or radiation), but at shorter wavelengths (higher frequency/energy). Given that x-rays are electromagnetic waves, in addition to absorption, they can also be scattered (see [Figure 5.2](#)), reflected (see [Figure 5.3a](#)), refracted (see [Figure 5.3b](#)), and diffracted (see [Figure 5.4](#)). Sometimes, these wave properties of x-ray radiation cannot be ignored.

The effect of phase on the detected image can be thought of by analogy with normal visible light. For slowly varying structures, the object phase acts like a lens refracting the x-rays, redirecting the wave and forming contrast in a downstream image in much the same way that ripples on a swimming pool form bright and dark lines on the pool floor. For more sharply varying structures, such as the sharp phase gradients present at tangents to a sphere, the situation is analogous to the diffraction of laser light past a sharp barrier.

Attenuation contrast works well in distinguishing between materials with low and high x-ray attenuation, e.g., in humans, between soft and hard tissue, or in an object, between plastic and aluminum. In medicine and biology, attenuation contrast is often slight, e.g., between cancer and healthy tissue or between different types of healthy tissue in an ant head. Phase contrast, on the other hand, is substantial at material interfaces and can be used to highlight these interfaces, as shown in

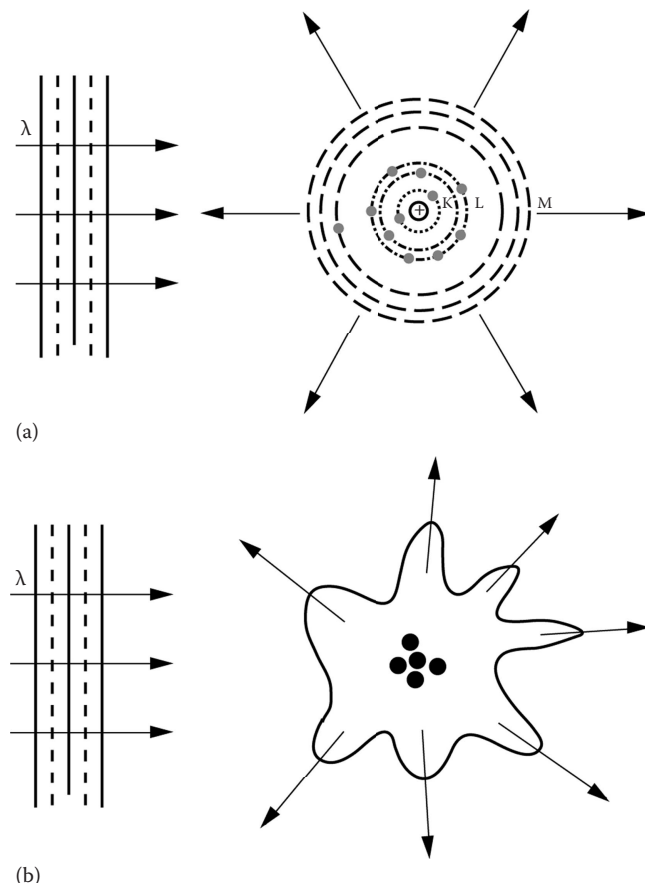


FIGURE 5.2 Just as with other electromagnetic radiation, x-rays, in addition to absorption, can be scattered (a) by a single atom or (b) by a grouping of atoms, molecules, or powder. λ is the wavelength of the incident photon and K, L and M are electron shells.

Figure 5.5. Thus, clinical and biological studies stand particularly well poised to benefit from the development of phase-sensitive techniques. There are industrial cases where phase-sensitive techniques provide the only useful contrast (see [Figure 5.6](#) and [Section 16.3.4, Phase-Contrast Radiography of a Deuterium–Tritium Solid-Layer Single-Shell Fusion Target](#)). However, x-ray phase effects are not commonly used in industrial nondestructive evaluation (NDE) imaging. Thus, the main part of this chapter emphasizes x-ray attenuation contrast effects. At the end of this chapter, we will briefly address x-ray phase effects (see [Section 5.5, X-Ray Phase Effects](#)).

5.2.1 ATTENUATION: PHOTOELECTRIC ABSORPTION, SCATTER, AND PAIR PRODUCTION

Earlier, we noted that x-rays or γ -rays can undergo attenuation or phase effects when they interact with matter. Here, we focus on attenuation interactions. When a parallel x-ray beam passes through matter, it becomes depleted or attenuated as photons are progressively removed from the beam. At energies below 1.02 MeV, this attenuation takes place by two competing processes: absorption* and scattering. To the first order, the distinction between absorption and scattering losses is clear. Absorption losses refer to an x-ray being completely removed from the primary beam by a dissipative

* In some texts, absorption and attenuation are interchanged; in this text, we use *attenuation* as the total loss (photoelectric absorption, scatter, and pair production) of photons as they interact with matter and *absorption* as only the photoelectric interaction with matter.

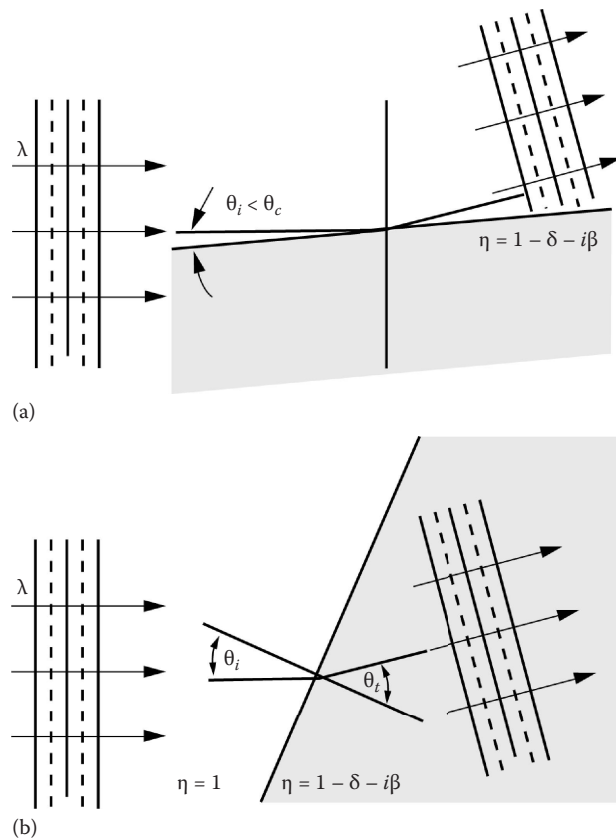


FIGURE 5.3 Just as with other electromagnetic radiation, x-rays, in addition to absorption, can be (a) reflected and (b) refracted. θ_i is the angle of incidence, θ_c is the critical angle, η is the index of refraction, δ is the phase shift, and β is the attenuation term of the refractive index.

process so that the energy is transferred locally to the material in the form of heat (see [Figure 5.7](#)). Scattering losses refer to the x-rays redirected away from the primary beam by (mainly incoherent or Compton) scattering events, as shown in [Figure 5.8](#). These photons move away from the site of the primary interaction. Scattering processes can involve local heat deposition (a recoil electron in a Compton event), but the distinguishing attribute of scattering is that a photon survives with a new direction. Coherent scatter is another attenuation mechanism but is very small and not discussed here.

When the incident or primary photon energy exceeds 1.02 MeV, another interaction, called pair production, becomes energetically possible. In this interaction, the x-ray or γ -ray disappears, and an electron–positron pair is produced (see [Figure 5.9](#)). The positron promptly annihilates producing two 511 keV annihilation photons that are collinear and departing the annihilation site in opposite directions (see Section 4.2.3, Annihilation Radiation Generation).

5.2.1.1 Absorption (Photoelectric Absorption)

Photoelectric absorption is dominant at low x-ray and γ -ray energies (see [Figure 5.10](#)). In photoelectric absorption, photons are absorbed and removed from the beam, as shown in Figure 5.7. It arises by the interaction of the photon with a tightly bound atomic electron. The energy of the incident photon is transferred to the electron, which is ejected from the atom. The energy of the incident photon, E_{p_0} , is given by

$$E_{p_0} = h\nu_0, \quad (5.1)$$

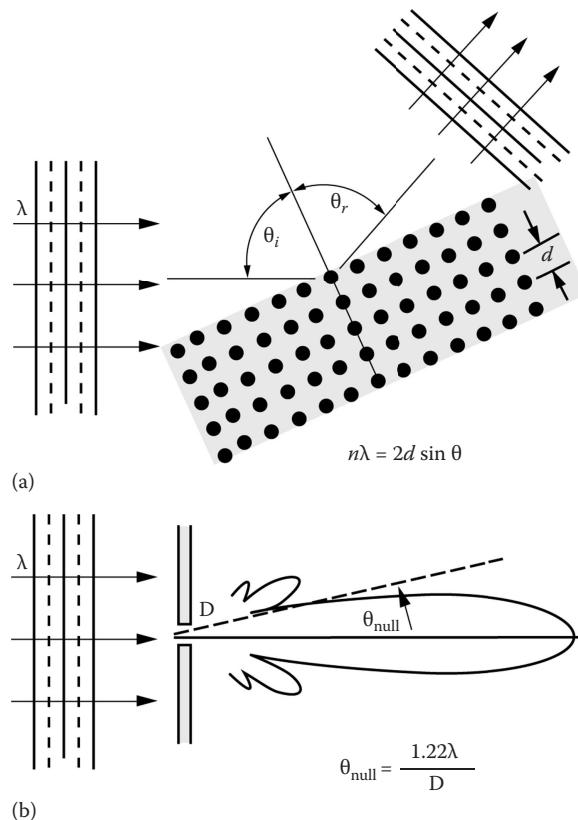


FIGURE 5.4 Just as with other electromagnetic radiation, x-rays, in addition to absorption, can be diffracted (a) by the atoms in a crystal lattice or (b) by an aperture. θ_r is the angle of reflection, d is the interplanar spacing of the crystal, and D is the diameter of the aperture.

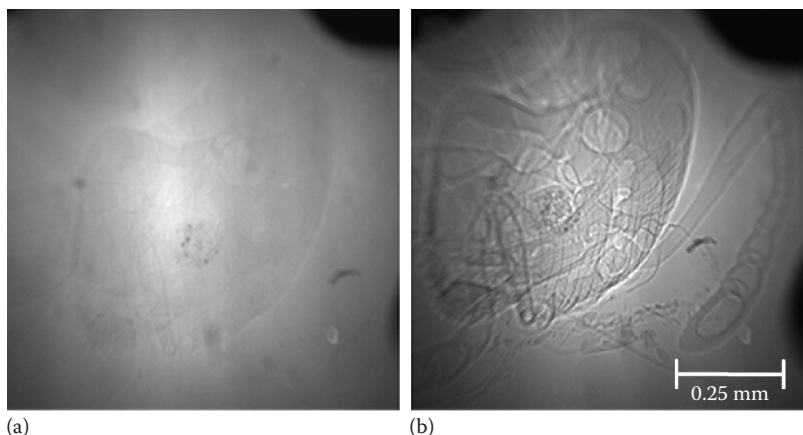


FIGURE 5.5 X-ray images (10 keV) of an ant head acquired at Argonne National Laboratory's Advanced Photon Source synchrotron facility. These results are useful in comparing (a) attenuation or amplitude/absorption and (b) phase-enhanced contrast effects. (From Lee, W. K., *Argonne National Laboratory, Argonne, Illinois*, managed and operated by the University of Chicago for the US Department of Energy under contract W-31-109-ENG-38.)

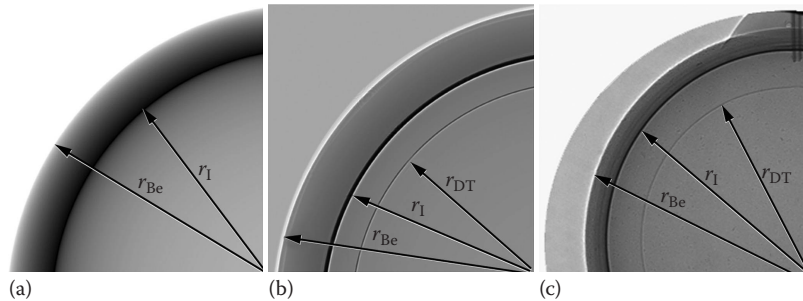


FIGURE 5.6 Images of (a) simulated attenuation contrast only and (b) attenuation plus phase contrast of one-quarter of a beryllium capsule with deuterium–tritium (D-T) ice and gas inside. The labels r_{Be} , r_{I} , and r_{DT} refer to the Be capsule outer and inner radii and the D-T ice and gas interface radius. The capsule is of 2 mm outer diameter with wall thickness 105 μm . Note that the inner D-T ice layer r_{DT} is not observed in the attenuation-only image (a) but is clearly resolved in the image of attenuation plus phase. (c) Experimentally measured results reveal that indeed, phase contrast can enable the imaging of the D-T ice layer.

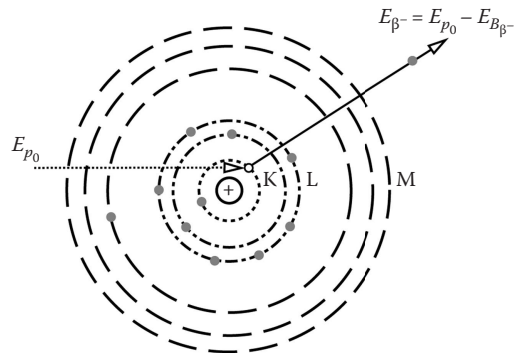


FIGURE 5.7 Schematic of photoelectric interaction between an incident photon and the orbital electron (given by a gray dot) of an atom. The interaction of the photon with the orbital electron can result in the ejection of an electron of kinetic energy $E_{\beta^-} = E_{p_0} - E_{B_{\beta^-}}$. As the electron slows down, it loses energy to the lattice in the form of heat or by generating new x-rays, called bremsstrahlung or braking radiation.

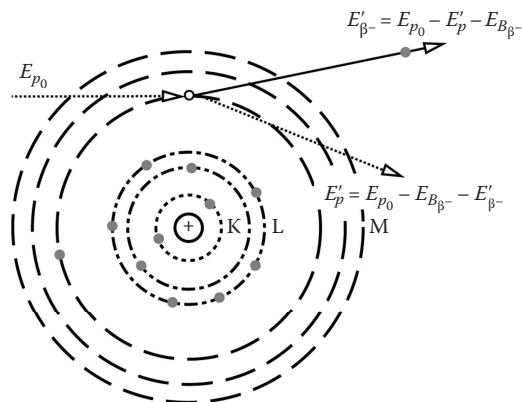


FIGURE 5.8 Schematic of Compton scattering of an incident photon in which the incident photon ejects an electron (or β^- particle) and a lower-energy scattered photon, E'_p , moves in a new direction.

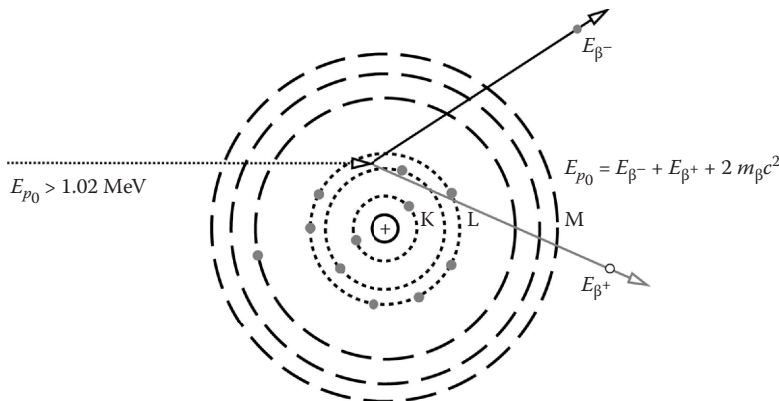


FIGURE 5.9 Schematic of pair production. Pair production is the generation of an electron, β^- (gray dot), and a positron, β^+ (open dot), which are created with kinetic energy E_{β^-} and E_{β^+} , respectively, from an incident photon whose energy, E_{p_0} , exceeds 1.02 MeV. The rest mass of the electron and positron are the same and are given by m_β , and c is the speed of light in a vacuum.

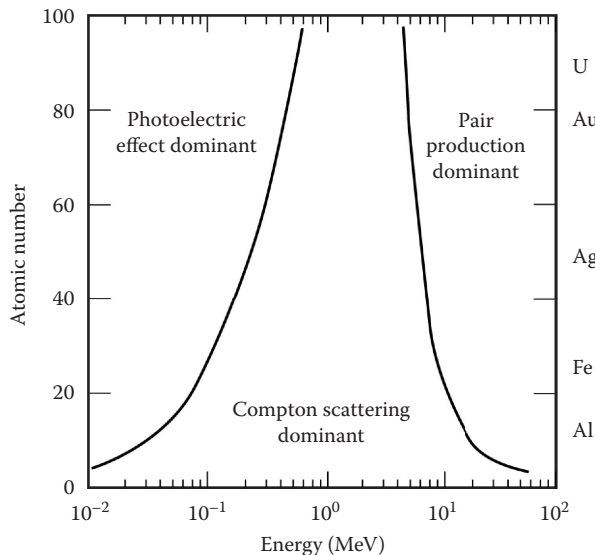


FIGURE 5.10 Photon attenuation between 10^{-2} MeV (10 keV) and 20 MeV is dominated by one of three processes: photoelectric, Compton scattering, or pair production. The plot identifies the regions in atomic number and photon energy space where each of the three processes dominates (contribute >50% of the photon interactions). (Adapted from Evans, R. D., *The Atomic Nucleus*, McGraw Hill, New York, 1955.)

where h is the Planck constant (6.626×10^{-27} erg s) and v_0 is the temporal frequency (s^{-1}) of the incident photon. The photon energy is transferred to the electron, sometimes referred to as a *photo-electron*, which is ejected from the atom with a kinetic energy E_{β^-} given by,

$$E_{\beta^-} = E_{p_0} - E_{B_{\beta^-}}, \quad (5.2)$$

where $E_{B_{\beta^-}}$ is the binding energy of the photoelectron in its original orbit or shell (see [Figure 5.7](#)). As the photoelectron is ejected, a vacancy is produced in the atomic orbital or electron shell, which is

then filled with an electron from a higher atomic orbit. This process typically results in the emission of an x-ray, which is itself absorbed in the material. This process is discussed in Section 4.2.1.2, Characteristic X-Rays.

The deepest available atomic level always has the largest photoelectric absorption. A K-shell* interaction is approximately four to five times more probable than an L-shell interaction if both interactions are energetically possible. Photoelectric absorption coefficient, μ^{pe} , is found to vary approximately with the atomic number (Z) of the interaction material, according to

$$\mu^{pe} \propto \sim Z^{4 \text{ or } 5}. \quad (5.3)$$

This approximation reveals why high- Z materials are *typically* used for shielding against x-rays and γ rays. Unfortunately, this very simple approximation is not always valid and can even be misleading. Therefore, for important problems, it is best to calculate the actual relationship as presented in [Section 5.3.7](#), Total Attenuation/X-Ray and γ -Ray Attenuation Phenomena.

5.2.1.1.1 Auger and Fluorescence

When an atom is ionized (has an electron vacancy in a normally complete electron shell), i.e., in an excited state, two competing processes can bring the atom back to equilibrium. The vacancy can be filled by an outer-shell electron accompanied by the emission of a characteristic x-ray (covered in Section 4.2.1.2, Characteristic X-Rays), or the excited energy of the atom may be transferred directly to an outer-shell electron, causing it to be ejected with a characteristic energy. This ejected electron is called an Auger† (pronounced “oh-jay”) electron, and this process is called the Auger effect.

The Auger effect is more prevalent in low-atomic-number elements and occurs more frequently when the photoelectron is ejected from the L shell than the K shell. Because of this, the typical Auger electron energy is a few kiloelectron volts, and most are stopped by self-absorption in the material of origin.

Because Auger electrons have energies that are characteristic of the element from which they originate, they form the basis of an elemental analysis method called Auger electron spectroscopy (Thompson et al. 1985). It is a surface-sensitive technique and is widely used in thin film and coating analysis.

The probability that an ionized atom will emit a characteristic x-ray is called the *fluorescent yield*. This is usually designated by shell. Thus, the K fluorescent yield is the number of x-rays of all lines in the K series that are emitted per K-shell vacancy. The K fluorescent yield is less than 0.1 for elements lighter than potassium and greater than 0.9 for elements heavier than Sm (Bertin 1978). Fluorescence forms the basis for an elemental analysis technique called x-ray fluorescence (XRF). We have explained that the probability of creating a K-shell vacancy (photoelectric effect) usually increases with atomic number. Since K fluorescence yield is also higher with atomic number, XRF is more applicable at higher atomic numbers. There is an annual conference‡ devoted to XRF and x-ray diffraction that has run for more than 50 years.

5.2.1.2 Scatter

In this section, we introduce the types of scatter and the vocabulary that is used to describe scattering processes. We explore *incoherent* or *Compton* scatter in detail. Scatter can involve a change in x-ray energy, phase, or both. Compton scatter is dominant at intermediate photon energies, as shown in [Figure 5.10](#). The scattered photon always has an energy equal to or less than the incident photon. Scatter with energy change is called *modified* (inelastic, Compton) scatter. Scatter with

* For the atomic number labeling, see Section 4.2.1.2, Characteristic X-Rays.

† Named after French physicist Pierre Auger, 1899–1993.

‡ The Denver X-Ray Conference (<http://www.dxcicdd.com>).

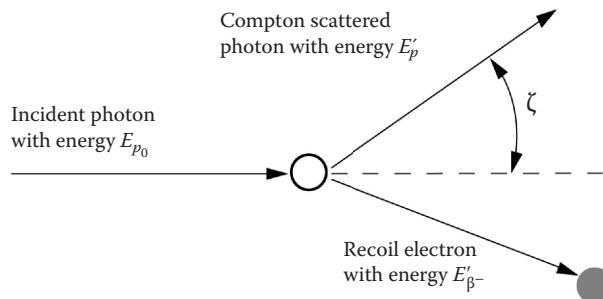


FIGURE 5.11 In a Compton scatter, the incident photon collides with an electron, usually loosely bound in an outer orbit. The electron (recoil electron) leaves the atom and deposits its energy, E'_{β^-} , locally as heat. The photon is deflected following the laws of conservation of energy and momentum with energy as given in Equation 5.4.

no energy change is called *unmodified* (elastic or Rayleigh) scatter. For *coherent* scatter, there is a phase relationship between the incident and scattered x-ray. *Incoherent* scatter occurs such that no phase relationship exists between incident and scattered x-ray. Any modified scatter has undergone a shift in wavelength (energy) and is then incoherent. This leads to the common practice of using the terms *modified* and *incoherent* interchangeably. However, not all incoherent scatter is necessarily modified (Bertin 1978). Diffraction of x-rays by crystals arises from unmodified coherent scatter and is discussed in [Section 5.5.2](#), Diffraction.

5.2.1.2.1 Incoherent (Compton) Scatter

The most important scatter process in industrial x-ray imaging is modified incoherent scatter. This is usually referred to as Compton scatter, after Arthur Compton* (Compton and Allison 1935). The mechanism is shown schematically in Figure 5.11. The incident x-ray collides with a loosely bound electron in an outer orbit. The (Compton) electron recoils from the impact, leaves the atom, and deposits its energy, E'_{β^-} , locally, mostly as heat. The photon is deflected following laws of conservation of energy and momentum. The energy of the scattered photon is given by

$$E'_p = \frac{E_{p_0}}{1 + \alpha_p(1 - \cos \zeta)}, \quad (5.4)$$

where E'_p is the scattered photon energy in keV and E_{p_0} is the incident photon energy in keV. The term α_p is the ratio of the incident photon energy to the rest mass energy of the electron (511 keV). The scattering angle is ζ . We see from Equation 5.4 that the energy of a Compton-scattered x-ray is least when the scattering angle is 180° , and as the scattering angle approaches 0° , the scattered x-ray energy approaches the incident x-ray energy.

This effect is shown graphically in [Figure 5.12](#) for incident photon energies of 50, 500, and 5000 keV. Figure 5.12 is a graphical representation of Equation 5.4. At 50 keV, even a backscattered (180° scatter) photon retains more than 80% of the incident energy. However, at 5 MeV, the scattered photon retains only 5% of the incident photon energy.

The scattered or recoil electron must always have some component of velocity in the direction of the incident x-ray in order to preserve momentum. Stated another way, the recoil electron always

* Arthur H. Compton was born in 1892. He received his PhD from Princeton in 1916. In 1918, he started a study of x-ray scattering. This led to his discovery, in 1922, of the increase of wavelength of x-rays due to scattering of the incident radiation by electrons and implies that the scattered photons or quanta have less energy than the photons or quanta of the original beam. This effect, known as the Compton effect, clearly illustrates the particle concept of electromagnetic radiation. Compton was awarded the Nobel Prize in Physics in 1927, "for his discovery of the effect named after him."

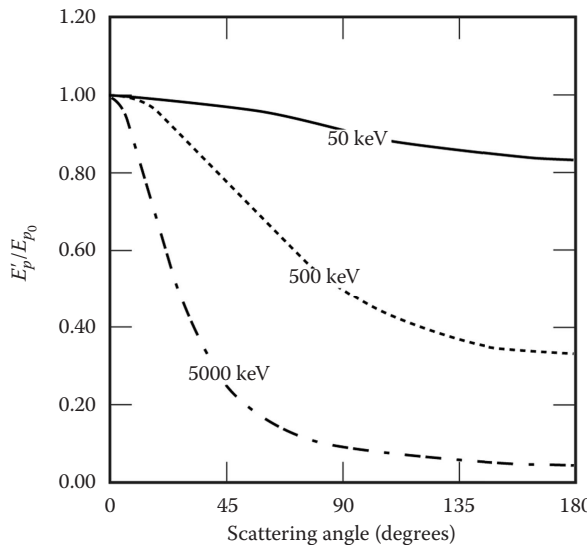


FIGURE 5.12 The ratio of the energy of the Compton-scattered x-ray to the energy of the incident x-ray as a function of the scattering angle for the scattered x-ray. This is shown for three different incident energies. As the energy of the incident x-ray increases, a more significant amount of its energy is lost to the recoil electron (see Equation 5.5).

moves in a direction $<90^\circ$ from the path of the incident x-ray. The recoil electron energy, E'_{β^-} , is given by

$$E'_{\beta^-} = E_{p_0} - E'_p - E_{B_{\beta^-}} \quad (5.5)$$

Electron binding energies, $E_{B_{\beta^-}}$, are given by Thompson et al. (2009). The scattered electron energy is highest when the x-ray photon scatters at 180° and the electron recoils at 0° . In a Compton event, the ratio of scatter to primary photon energy depends on the incident x-ray photon energy, given Equations 5.4 and 5.5.

One important practical effect of Equations 5.4 and 5.5 is that Compton electrons can be quite energetic for incident x-ray energies of hundreds of kiloelectron volts. For example, at 5 MeV, the scattered photon retains only $\sim 5\%$ of the incident photon energy; thus, the recoiling electron gets $\sim 95\%$ of the incident photon energy in a backscatter event. This is exploited in the use of electron-intensifying screens for imaging. These screens (addressed in Section 9.6.1, Detector Technology—Film) employ forward-scattered recoil electrons to expose a film or other detector.

Compton scatter events are not isotropic. To discuss the nature of the angular distribution of Compton-scattered photons, it is necessary to introduce the concept of differential cross section, since in physics, it is common to express angular distributions as a differential cross section, that is, differential in solid angle, Ω . The usual unit is barns per steradian (b/sr). A barn is 10^{-24} cm^2 . A cross section is a measure of the interaction probability given by unit area per atom, often given by b/atom, and is proportional to the mass attenuation coefficient, which is usually given in cm^2/g , since both units are area/quantity. For more on interaction probability and cross section, see Section 5.3.3, Atomic Attenuation Coefficient μ_a .

The interaction probability can equivalently be expressed as differential scattering mass attenuation coefficient, $d\mu_m/d\Omega$, with units of $\text{cm}^2/(\text{g sr})$. The angular distribution of Compton-scattered photons from any loosely bound electron can be expressed by an analytical formula, the

Klein–Nishina formula. The differential scattering mass attenuation coefficient, $d\mu_m/d\Omega$, can be approximated* as

$$\frac{d\mu_m}{d\Omega} = G \left(\frac{1}{1 + \alpha_p(1 - \cos \zeta)} \right)^2 \left(\frac{1 + \cos^2 \zeta}{2} \right) \left(1 + \frac{\alpha^2(1 - \cos \zeta)^2}{(1 + \cos^2 \zeta)[1 + \alpha(1 - \cos \zeta)]} \right), \quad (5.6)$$

where G is a constant, α_p is the ratio of the incident photon energy to the rest mass energy of the electron, and ζ is the photon scatter angle (see [Figure 5.11](#)). From Equation 5.4,

$$\frac{E'_p}{E_{p_0}} = \frac{1}{1 + \alpha_p(1 - \cos \zeta)}. \quad (5.7)$$

Substituting this into Equation 5.6 yields

$$\frac{d\mu_m}{d\Omega} = G' \left[\left(\frac{E'_p}{E_{p_0}} \right)^2 \left(\frac{E'_p}{E_{p_0}} + \frac{E_{p_0}}{E'_p} - \sin^2 \zeta \right) \right], \quad (5.8)$$

where G' is a constant, and substituting $d\Omega = 2\pi \sin \zeta d\zeta$ into this equation results in

$$\frac{d\mu_m}{d\Omega} = 2\pi G'' \left[\left(\frac{E'_p}{E_{p_0}} \right)^2 \left(\frac{E'_p}{E_{p_0}} + \frac{E_{p_0}}{E'_p} - \sin^2 \zeta \right) \right] \sin \zeta, \quad (5.9)$$

where G'' is a constant. Equation 5.9 is another Klein–Nishina formula, which is referred to later in Chapters 10 and 15.

The photon angular distribution in polar coordinates for Compton scattering at three incident photon energies is given in [Figure 5.13](#). We see from Figure 5.13 that Compton scattering becomes more forward peaked with increasing photon energy. This means that at the highest energies used for imaging, most Compton scattering events result in scattered x-rays that have been slightly deflected and have slightly reduced energy.

5.2.1.2.2 Coherent (Rayleigh) Scatter

There is a second type of scattering, coherent scattering. This is also called Rayleigh scattering, and it is an elastic process. In effect, the photon is given a new direction with no change in energy or phase. This is rarely an important attenuation mechanism compared to photoelectric absorption, Compton scattering, and/or pair production, but it is important to be aware that it can cause effects observed in x-ray imaging. The angular distribution of Rayleigh scattering is limited to small scattering angles. This means that the photon is likely to be intercepted by the detector. However, the coherent photon traverses a different path through the object from its incident path and typically causes a form of image blur. Coherent scatter also gives rise to diffraction. Coherently scattered photons (usually x-rays) interfere either destructively or constructively as they scatter from atoms in

* The Klein–Nishina formula assumes that the scatter takes place from a free electron. The form we use here additionally assumes that the number of electrons per unit mass of material is constant.

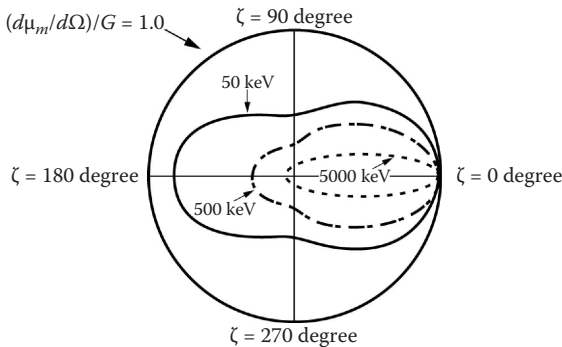


FIGURE 5.13 The angular distribution of Compton-scattered x-rays. This is just a polar plot of the Klein-Nishina formula in units of $\text{cm}^2/(\text{g sr})$ (Equation 5.6) for three incident x-ray energies.

a crystalline lattice (see [Figure 5.4](#)). The angles of peak interference depend on the wavelength of the x-rays and the lattice spacing of the crystal. Diffraction only rarely intrudes on a transmission image of ordinary materials. This is discussed more in [Section 5.5](#), X-Ray Phase Effects.

5.2.1.3 Pair Production

We noted earlier that when the photon energy exceeds 1.02 MeV, pair production becomes possible. When pair production occurs, the original photon disappears, and an electron–positron pair is born (see [Figure 5.9](#)). The electron–positron pair share the excess (above 1.02 MeV) kinetic energy of the incident photon. The electron deposits its energy as heat as it slows and stops in the material. The positron slows over a distance of a few mm and then finds an electron and annihilates. This creates two annihilation photons each with 511 keV and moving in opposite directions. Annihilation photons are emitted isotropically.

Pair production increases very roughly as the square of the atomic number of the interacting material. The importance of pair production increases strongly with increased photon energy above 1.02 MeV (see [Figure 5.10](#)). Applications where pair production dominates attenuation are not common but do exist. Inspection of uranium projectiles, for example, may require photons of several MeV to penetrate the object. In this energy range for uranium, pair production is the dominant attenuation mechanism.

From an imaging perspective, pair production causes the object under examination to “glow” with annihilation photons. The material with the highest Z will glow the brightest. This may create a low-frequency background or blurring in the x-ray image. The optical analog is a low-frequency background that is observed in a photographic image of a scene through an uneven (or patchy) fog. Pair production is used in Cargo screening as given in [Section 16.3.3](#).

5.2.1.4 Photonuclear

Photonuclear absorption, also called *photodisintegration* or *phototransmutation*, is a nuclear reaction in which the absorption of high-energy electromagnetic radiation (an x-ray or γ -ray photon) causes the absorbing nucleus to change to another species by ejecting a subatomic particle, such as a proton, neutron, or alpha particle. For example, ^{25}Mg , upon absorbing a photon of sufficient energy, emits a proton and becomes ^{24}Na . Photodisintegration differs from the nuclear reaction photofission, in which a nucleus, upon absorbing a photon, splits into two fragments of nearly equal mass. Photonuclear interaction of photons with matter is typically not a significant mode of attenuation for imaging. It can produce residual radioactivity.

5.2.1.5 Photofission

The height and shape of the fission barrier are dependent on the particular nucleus being considered. Fission can be induced by exciting the nucleus to an energy equal to or greater than that of the

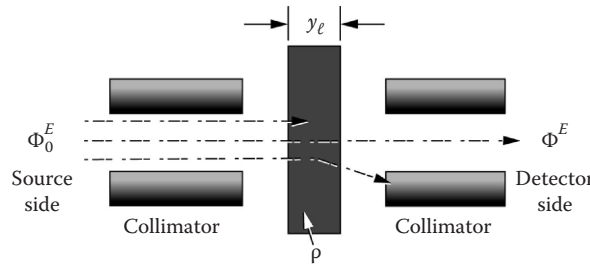


FIGURE 5.14 Arrangement for x-ray or γ -ray attenuation. The top, center, and bottom photons undergo photoelectric absorption, transmission, and scatter, respectively. (Adapted from Bertin, E. P., *Principles and Practice of X-Ray Spectroscopic Analysis*, second edition, Plenum Press, New York, 1978.)

barrier. This can be done by γ -ray excitation (photofission) or through excitation of the nucleus by the capture of a neutron, proton, or other particle (particle-induced fission).

5.3 ATTENUATION MEASUREMENT UNITS

Here we describe the measurement units used to describe the various attenuation processes commonly used in digital radiography and computed tomography.

5.3.1 LINEAR ATTENUATION COEFFICIENT μ

Let us assume that a perfectly parallel *monochromatic* (or *monoenergetic*, i.e., all photons are at a single energy value, E_{p_0}) x-ray beam of irradiance* Φ_0^E is directed on a thin single-material absorber having uniform thickness y_ℓ (cm) and mass density ρ (g/cm^3) (see Figure 5.14). The transmitted beam has irradiance Φ^E , which is always less than Φ_0^E , that is, the x-rays undergo attenuation passing through matter. The transmitted irradiance is given by

$$\frac{d\Phi^E}{\Phi^E} = -\mu(E, Z, \rho) dy_\ell, \quad (5.10)$$

where μ is the proportionality constant known as the linear attenuation coefficient and has the unit of reciprocal centimeters (cm^{-1}). The negative sign indicates that the irradiance always decreases on passing through matter. If the value of μ is independent of y_ℓ , integration of Equation 5.10 gives transmitted irradiance = (incident irradiance) exponential (minus linear attenuation times thickness) or

$$\Phi^E(E, Z, \rho, y_\ell) = \Phi_0^E(E) e^{-\mu(E, Z, \rho)y_\ell}, \quad (5.11)$$

where

$\Phi^E(E, Z, \rho, y_\ell)$ is the transmitted irradiance at monochromatic energy E through a thickness y_ℓ for a single material of atomic number Z with a mass density of ρ in energy per unit area per unit time;

$\Phi_0^E(E)$ is the incident irradiance in energy per unit area per unit time at monochromatic energy E ;

* In the past physicists and engineers generally used the word *intensity* to mean the flow of energy per unit area per unit time. In the optics field, this practice is changing. The word *intensity* is being replaced by the word *irradiance*. Here we suggest the same conversion for the field of radiography.

y_ℓ is the thickness along the direction of x-rays of the single-material uniform absorber in cm;
and
 $\mu(E, Z, \rho)$ is the linear attenuation coefficient in cm^{-1} at energy E for a single material with atomic number Z and mass density ρ .

Equation 5.11 can also be rewritten as

$$T(E, Z, \rho, y_\ell) = \frac{\Phi^E(E, Z, \rho, y_\ell)}{\Phi_0^E(E)} = e^{-\mu(E, Z, \rho)y_\ell}, \quad (5.12)$$

where $T(E, Z, \rho, y)$ is transmission.

Equation 5.11 is sometimes referred to as Beer's law.* In other words, $\Phi^E(E, Z, \rho, y_\ell)$ is the photon irradiance after traveling distance y_ℓ in the uniform absorber with linear attenuation coefficient μ . From Equation 5.11, *monoenergetic* x-rays are exponentially attenuated when passing through matter. Another useful quantity is the attenuation times path length (sometimes referred to as the radiographic attenuation), given by

$$\ln\left(\frac{\Phi_0^E(E)}{\Phi^E(E, Z, \rho, y_\ell)}\right) = \mu(E, Z, \rho)y_\ell. \quad (5.13)$$

For a single energy, $\Phi^E(E, Z, \rho, y_\ell)$ can be replaced by $\Phi^P(E, Z, \rho, y_\ell)$, i.e., the photon flux density (number of photons per unit area per unit time):

$$\Phi^P(E, Z, \rho, y_\ell) = \Phi_0^P(E)e^{-\mu(E, Z, \rho)y_\ell}. \quad (5.14)$$

Again, it is important to emphasize that Equations 5.10 through 5.14 are for the interaction of a single (monochromatic) photon energy, E , with a single uniform material.

For a polyenergetic source and single material, this expands to

$$\Phi^P[S(E), Z, \rho, y_\ell] = \int \Phi_0^P[S(E)]e^{-\mu[S(E), Z, \rho]y_\ell} dE, \quad (5.15)$$

where $S(E)$ is the x-ray or γ -ray source spectrum (photon flux density versus energy). $S(E)$ refers to a family of source functions, each specific source function depending upon the type of source and its operating parameters, for example, a tungsten-anode x-ray tube source at an operating voltage of 150 kV or a 100 mCi ^{109}Cd radioisotope (for more details on these sources, see Chapter 8, Radiation Sources). Each source has a particular source function that must accurately be represented by the function $S(E)$. Further expanding this to multiple (up to n) materials (1...n) results in

$$\Phi^P[S(E), \bar{Z}, \bar{\rho}, y_\ell] = \int \Phi_0^P[S(E)]e^{-\sum_i^n \mu_m^i[S(E), Z_i] \rho_i y_\ell^i} dE, \quad (5.16)$$

where $\mu_m^i[S(E), Z_i] = \mu_i[S(E), Z_i] \rho_i$ is the mass attenuation coefficient with mass density and atomic number for the i th material and \bar{Z} and $\bar{\rho}$ are the average or effective atomic number and

* In the literature, this is also referred to as Lambert's law or even Bouguer's law, sometimes even with their names in combination, e.g., Lambert–Beer's law.

average or effective mass density, respectively, across all n materials. The mass attenuation coefficient is given in [Section 5.3.2](#), Mass Attenuation Coefficient μ_m .

In the context of multiple energy and multiple materials, the transmission then becomes

$$T[S(E), \bar{Z}, \bar{\rho}, y_\ell] = \frac{\Phi^P[S(E), \bar{Z}, \bar{\rho}, y_\ell]}{\int \Phi_0^P[S(E)] dE} \approx \int e^{-\sum_i^n \mu_m^i [S(E), Z_i] \rho_i y_\ell^i} dE. \quad (5.17)$$

Sometimes this is simplified by replacing the integration over the energy spectrum on the right-hand side of Equation 5.17 by an effective energy given by \bar{E} . Replacing \bar{E} into the exponential yields

$$T[S(E), \bar{Z}, \bar{\rho}, y_\ell] = \frac{\Phi^P[S(E), \bar{Z}, \bar{\rho}, y_\ell]}{\int \Phi_0^P[S(E)] dE} \approx e^{-\sum_i^n \mu_m^i (\bar{E}, Z_i) \rho_i y_\ell^i}. \quad (5.18)$$

In this case, the attenuation times path length (or radiographic attenuation) is given by

$$\ln \left(\frac{\int \Phi_0^P[S(E)] dE}{\Phi^P[S(E), \bar{Z}, \bar{\rho}, y_\ell]} \right) \approx \sum_i^n \mu_m^i (\bar{E}, Z_i) \rho_i y_\ell^i. \quad (5.19)$$

5.3.2 MASS ATTENUATION COEFFICIENT μ_m

The mass attenuation coefficient is the linear attenuation coefficient divided by the mass density:

$$\mu_m(E, Z) = \frac{\mu(E, Z, \rho)}{\rho}. \quad (5.20)$$

The mass attenuation coefficient (the common unit is cm^2/g) is useful for calculating the mass of material required to attenuate a primary beam of x-rays by a prescribed amount, i.e., where y_m is the mass of the uniform absorber per unit area of beam (unit, g/cm^2), also called the areal density. The quantity y_m is simply the mass density times material thickness, i.e., ρy_ℓ . It has dimension of g/cm^2 , while (μ/ρ) has the dimension of cm^2/g .

5.3.3 ATOMIC ATTENUATION COEFFICIENT μ_a

The attenuating material may be described by a volume density of attenuating atoms, sometimes referred to as the atomic density, ρ_a (atoms/ cm^3). Each attenuating atom presents a *cross-sectional* area to the incident beam. Sometimes this cross-sectional area is given the symbol μ_a^* and called the atomic *cross section*; the most common unit is the barn, equal to $10^{-24} \text{ cm}^2/\text{atom}$. This is also referred to as the atomic attenuation coefficient and has the unit cm^2/atom (see [Panel 5.2](#)). A large

* Often, atomic cross section is given by σ , but since we use σ for standard deviation, we use μ_a .

atomic cross section corresponds to high attenuation of x-rays. A homogeneous, uniform material of thickness dy_ℓ will remove a fraction $\rho_a \mu_a dy_\ell$ of the incident photons from the beam:

$$\frac{d\Phi^E}{\Phi^E} = -\rho_a \mu_a dy_\ell. \quad (5.21)$$

The negative sign indicates that the irradiance always decreases on passing through matter. If μ_a is independent of y_ℓ , Equation 5.21 integrates to Equation 5.11 (Beer's law) if we make the substitution

$$\mu_a \rho_a = \mu. \quad (5.22)$$

Furthermore note that

$$\mu_a = \frac{\mu}{\rho_a} = \frac{\mu}{\rho} \frac{A}{N_A}, \quad (5.23)$$

where

- ρ is the mass density in g/cm³;
- A is the atomic weight in g/mol;
- N_A is Avogadro's number, 6.02×10^{23} atoms/mol;
- ρ_a is the number of atoms per cubic centimeter; and
- A/N_A is the number of grams per atom.

PANEL 5.2 Atomic Cross Section

One salient fact about the atomic attenuation coefficient, μ_a , bears emphasis, for it is often a very confusing parameter. The physics community commonly specifies the probability of a photon interaction with an atom in what is called a cross section. This term is synonymous with the atomic attenuation coefficient, μ_a . The common unit for cross section is the barn, numerically equal to 10^{-24} cm². During wartime research on the atomic bomb, American physicists who were bouncing neutrons off uranium nuclei described the uranium nucleus as "big as a barn." Physicists working on the project adopted the name *barn* for a unit equal to 10^{-24} cm², about the size of a uranium nucleus. Initially, they hoped the American slang name would obscure any reference to the study of nuclear structure; eventually, the word became a standard unit in particle physics. What is meant, but seldom stated, when specifying cross sections is that it is a property of the atom. When a physicist says that Au has a cross section of 2 b, what he/she means is that Au has a cross section of 2 b/atom. With this in mind, it is easy to see that cross section (per atom) and the various versions of attenuation coefficients are equivalent except for units. Except for the linear attenuation coefficient, they are all area/quantity. The quantity can be expressed in units of atoms, grams, or moles. By incorporating the mass density, attenuation can also be expressed as inverse length, also called the linear attenuation coefficient. Physically, this can be thought of as the inverse of the distance traveled in a substance (of a given composition and density) before the probability of an interaction equals 1/e.

5.3.4 MOLAR ATTENUATION COEFFICIENT μ_M

The molar attenuation coefficient (Bertin 1978) μ_M expresses attenuation as area per mole of material and is given by

$$\mu_M = \left(\frac{\mu}{\rho} \right) A. \quad (5.24)$$

The units of the molar attenuation coefficient are cm^2/mol .

5.3.5 RELATIONSHIP AMONG THE VARIOUS ATTENUATION COEFFICIENTS

The four attenuation coefficients are related as follows:

$$\mu = \mu_m \rho = \mu_a \rho_a = \mu_a \rho \left(\frac{N_A}{A} \right) = \mu_M \left(\frac{\rho}{A} \right), \quad (5.25)$$

where ρ is the mass density in g/cm^3 ; A is the atomic weight in g/mol ; N_A is Avogadro's number, 6.02×10^{23} atoms/mol; ρ_a is the atomic density in atoms/ cm^3 ; and N_A/A is the number of atoms per gram.

Of these four coefficients, mass attenuation coefficient, $\mu_m = \mu/\rho$, is by far the most useful. It is a mass property of each element independent—for practical purposes—of the state of chemical or physical aggregation. It is a function only of wavelength and atomic number, and the function of each is relatively simple. Values of μ_m or μ/ρ for different substances are directly comparable, and μ/ρ for a compound, solution, or mixture is readily calculated (see Section 5.3.6, Mixture Rule) from the values for the constituent elements. None of these advantages applies to the linear attenuation coefficient. This can be seen by a simple thought experiment described in Panel 5.3.

PANEL 5.3 Sproull: Mass vs. Linear Attenuation Coefficient

The power of mass attenuation coefficients is strikingly illustrated by a hypothetical experiment described by Sproull (1946): “A beam of X-rays passing from the ceiling to the floor of a chamber filled with hydrogen and oxygen may be [say] 10% absorbed, or 90% of it will reach the floor. If a spark explodes the hydrogen and oxygen, filling the chamber with steam, 90% of the X-rays will still reach the floor. Then if the chamber is chilled so that the steam condenses to a thin layer of water or ice on the floor, 90% of the X-rays will still reach the floor. This is not true for light or ultraviolet or infrared radiation, and it explains why the mass absorption [attenuation] coefficient of X-rays is commonly used, whereas the linear absorption [attenuation] coefficient is ordinarily used in optics.”

5.3.6 MIXTURE RULE

The chemical binding energies are so small compared to x-ray energies for industrial applications that chemical compounds may be treated as mixtures of elements. The mass attenuation coefficient for a mixture that consists of J components, each with mass attenuation coefficient $(\mu/\rho)_j$, $j = 1, 2, \dots, J$, is given by

$$\mu_m = \sum_{j=1}^J \mu_m^j W_j = \left(\frac{\mu}{\rho} \right) = \sum_{j=1}^J \left(\frac{\mu}{\rho} \right)_j W_j, \quad (5.26)$$

where μ_m^j is the mass attenuation coefficient and W_j is the fraction by weight of the j th element. The linear attenuation coefficient is obtained by multiplying both sides of Equation 5.26 by the mass density of the compound, solution, or mixture. A simple mixture problem solution is given in Panel 5.4.

PANEL 5.4 Mixture Problem

Leaded glass is used to shield optical cameras coupled to scintillators or people from x-rays or γ -rays. Thus, this is a good example to illustrate how to utilize the mixture rule. Ordinary glass is mostly SiO_2 and has a mass density of 2.5 g/cm^3 . Special glass is available for view windows in radiation environments that contains 50 wt% PbO and has a mass density of 3.5 g/cm^3 . The atomic weights of the elements of interest are

O	16 g/mol
Si	28 g/mol
Pb	207 g/mol

So SiO_2 is ($32/60$ g/mol), or 0.533 weight fraction oxygen, and ($28/60$ g/mol), or 0.467 weight fraction silicon. Similarly, leaded glass has a 0.170, 0.099, and 0.731 weight fraction of oxygen, silicon, and lead, respectively. A common requirement is to attenuate the tungsten K lines (near 60 keV) since tungsten is the most common x-ray tube anode material. Mass attenuation coefficients at 60 keV for the elements involved are

O	0.189 cm^2/g
Si	0.312 cm^2/g
Pb	4.86 cm^2/g

From Equation 5.26, the mass attenuation coefficients, μ_m , are given by

$$\begin{aligned}\mu_m &= \left(\frac{\mu}{\rho} \right) = [(0.189 \text{ cm}^2/\text{g})(0.533)] \\ &\quad + [(0.312 \text{ cm}^2/\text{g})(0.467)] = 0.246 \text{ cm}^2/\text{g}\end{aligned}$$

for ordinary glass and

$$\begin{aligned}\left(\frac{\mu}{\rho} \right) &= [(0.189 \text{ cm}^2/\text{g})(0.170)] + [(0.312 \text{ cm}^2/\text{g})(0.099)] \\ &\quad + [(4.86 \text{ cm}^2/\text{g})(0.731)] = 3.61 \text{ cm}^2/\text{g}\end{aligned}$$

for leaded glass.

According to Equation 5.17 or 5.18,

$$T[E, \bar{Z}, \bar{\rho}, y_\ell] = \frac{\Phi^P[E, \bar{Z}, \bar{\rho}, y_\ell]}{\Phi_0^P(E)} \approx e^{-\sum_i^n \mu_m^i(E, Z_i) \rho_i y_\ell^i} \approx e^{-\sum_i^n \frac{\mu_i(E, Z_i, \rho_i)}{\rho_i} y_m^i}.$$

We first need to determine the *areal* density, y_m . Recall that areal density is the product of linear thickness and mass density. If we have 2.54 cm of ordinary glass, the areal density is $(2.54 \text{ cm})(2.5 \text{ g/cm}^3) = 6.35 \text{ g/cm}^2$. So, for ordinary glass, transmission through 2.54 cm is $\Phi^P[E, \bar{Z}, \bar{\rho}, y_\ell]/\Phi_0^P(E) = 0.21$, while the same thickness of leaded glass provides a transmission of only $\Phi^P[E, \bar{Z}, \bar{\rho}, y_\ell]/\Phi_0^P(E) = 0.21 \times 10^{-14}$. This is a pretty strong argument for using leaded glass in this application to protect a camera or people.

5.3.7 TOTAL ATTENUATION/X-RAY AND γ -RAY ATTENUATION PHENOMENA

Now that we have defined the atomic attenuation coefficient (or atomic cross section) concept and its relationship to the linear attenuation coefficient (see Equation 5.25), we can describe the various interaction coefficients (cross sections) that are included in the overall attenuation of an x-ray or γ -ray beam as it passes through matter.

The linear or mass attenuation coefficients are measures of that portion of the incident collimated beam that does not appear in the emergent collimated beam, regardless of reason (see [Figure 5.14](#)). They are total attenuation coefficients and are (mainly) the result of three phenomena, each having its own linear and mass attenuation coefficients:

$$\mu = \mu^{pe} + \mu^s + \mu^{pp} \quad (5.27)$$

and

$$\mu_m = \left(\frac{\mu^{pe}}{\rho} \right) + \left(\frac{\mu^s}{\rho} \right) + \left(\frac{\mu^{pp}}{\rho} \right), \quad (5.28)$$

respectively. The superscripts *pe*, *s*, and *pp* represent the photoelectric absorption, scatter, and pair production portion of the coefficients, respectively. That is, the total attenuation coefficients are simply the sum of each of the attenuation coefficients from the three phenomena: photoelectric absorption, scatter, and pair production (see [Figure 5.15](#)).

Some authors suggest that attenuation can be estimated using simple rules. Panel 5.5, Rule of Thumb, shows that this is not advisable.

PANEL 5.5 Rule of Thumb

At some energies and over some range of atomic numbers, Z , the photoelectric mass attenuation coefficient increases strongly with Z . The student will find equations in the literature that give the impression that photoelectric attenuation coefficients can be calculated by formula, usually containing a Z^4 or Z^5 term. This impression is highly misleading. An example illustrates the problem. The United States National Institute of Standards and Technology (NIST) web-based XCOM program (available at <http://physics.nist.gov/PhysRefData/Xcom/Text/XCOM.html>) gives the photoelectric mass attenuation coefficient for Pb at 88 keV as $1.55 \text{ cm}^2/\text{g}$. Pb is $Z = 82$. At $Z = 80$, using the typical formula with Z^4 dependence and scaling from the value for Pb, we should expect the value for Hg to be $\sim 1.40 \text{ cm}^2/\text{g}$. XCOM says the photoelectric mass attenuation for Hg at 88 keV is $6.96 \text{ cm}^2/\text{g}$. This is a *huge* error for a term that is going to be used in the

exponent. In this instance, the reason the formula fails is that at 88 keV, the energy is insufficient to permit K-shell ejection in Pb but sufficient in Hg. Similar, though less dramatic, “rule” violations can be found by application over a wide range of Z even when energy is above all electron binding energies of the elements involved.

Also, it is seldom useful to know the photoelectric attenuation separate from other attenuation processes. Compton scatter is often more important in industrial NDE applications.

With the ready availability of computer files of attenuation coefficients, simple rules of thumb should not be used. High- Z materials usually have significantly higher photoelectric mass attenuation coefficients than low- Z materials, but the details matter. *Look it up!*

A certain minimum photon energy E_p is required to ionize an electron from an atom. The position of this so-called absorption edge is illustrated for Al, C, Fe, and Pb in Figures 5.16, 5.15, 5.17, and 5.18, respectively. These four elements are plotted together in Figure 5.19 for comparison purposes. Note that the K edge of carbon in Figure 5.15 is not shown, because it lies below the lowest energy plotted. As a very rough approximation for the K shell, E is proportional to Z^2 . Similar considerations apply to the L shell, except that there are several nondegenerate sublevels involved.

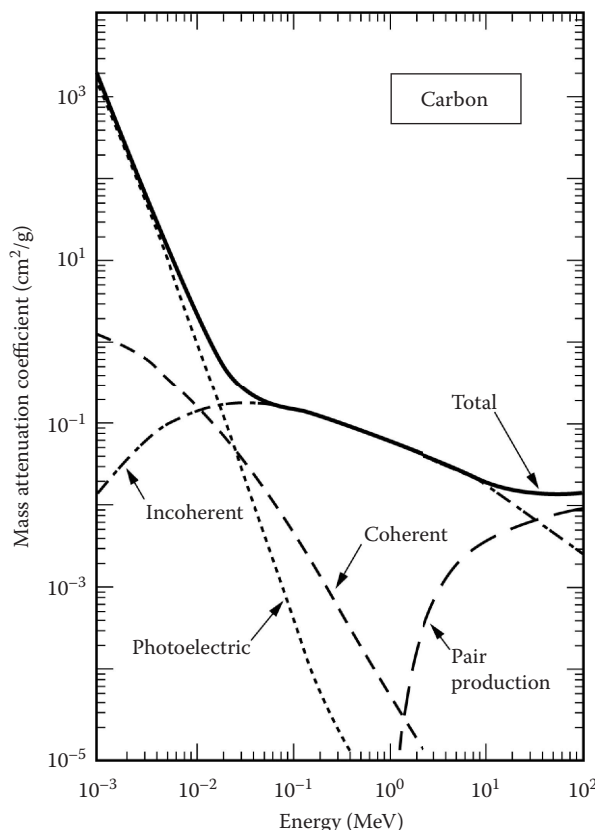


FIGURE 5.15 Mass attenuation coefficients of carbon. Shown are the separate mass attenuation coefficients for coherent and incoherent scattering, photoelectric absorption, and pair production. Also shown is the total mass attenuation coefficient. Note that coherent scatter never accounts for more than a few percent of the total. Also note that incoherent scatter is the major constituent of the total attenuation over a wide range of energies (10^{-1} to 10^1 MeV) for carbon.

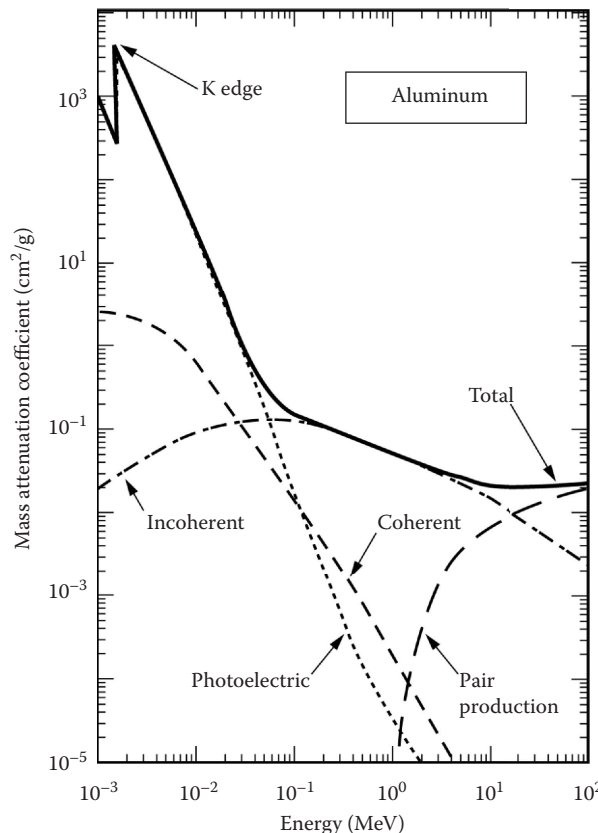


FIGURE 5.16 Mass attenuation coefficients of aluminum. Shown are the separate mass attenuation coefficients for coherent and incoherent scattering, photoelectric absorption, and pair production. Also shown is the total mass attenuation coefficient. Note that coherent scatter never accounts for more than a few percent of the total. Also note that incoherent scatter is the major constituent of the total over a modest energy range (10^{-1} to 5×10^0 MeV) for aluminum.

Photoelectric absorption predominates over scatter for the heavier elements (from Fe through U) at energies of less than 150 keV, as shown in Figure 5.10. At 50 keV, the photoelectric absorption effect dominates, and the mass attenuation coefficient strongly increases with atomic number from $Z = 3$ (Li) to $Z = 63$ (Eu), as shown in Figure 5.20.

In the scatter process, photons are not really absorbed but deflected from their collinear path in the absorber (see Figure 5.14), in effect disappearing from the emerging beam. This process is discussed in Section 5.2.1.2, Scatter. Scatter dominates attenuation for all atomic numbers at energies from 0.7 to 4.5 MeV (see Figure 5.10). At 3.5 MeV, scatter dominates attenuation, and there is only a slight dependence on atomic number from Li ($Z = 3$) to U ($Z = 92$), as shown in Figure 5.20.

In pair production, photons with energy greater than 1.02 MeV passing close to atomic nuclei can give their energy to creating and imparting kinetic energy to two charged particles, an electron (β^-) and a positron (β^+):

$$X \text{ or } \gamma \text{ photon} > 1.02 \text{ MeV} \rightarrow \beta^- \text{ and } \beta^+.$$

This is an example of conversion of energy to matter in accordance with Einstein's equation:

$$E = mc^2, \quad (5.29)$$

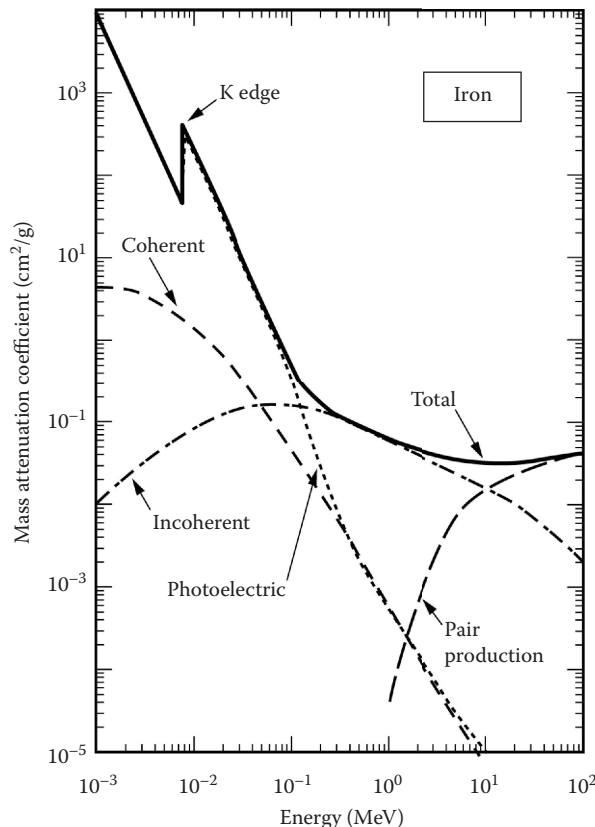


FIGURE 5.17 Mass attenuation coefficients of iron. Shown are the separate mass attenuation coefficients for coherent and incoherent scattering, photoelectric absorption, and pair production. Also shown is the total mass attenuation coefficient. Note that coherent scatter never accounts for more than a few percent of the total. Also note that incoherent scatter is the dominant constituent of the total attenuation over only one decade (2×10^{-1} to 2×10^0 MeV) of energy range.

where E is energy (ergs), m is mass (g), and c is velocity of light (cm/s). If we let m be the rest mass of the electron, m_{β^-} be 9.11×10^{-2} g, and c be 3×10^{10} cm/s, and insert the conversion factor 1.6×10^{-6} erg/MeV, the equation gives the energy equivalent of the electron, 0.51 MeV. It follows that the threshold photon energy for pair production is 1.02 MeV since the electron and positron have the same mass. Pair production dominates attenuation for chemical elements iron through uranium at energies greater than 8 MeV (see Figure 5.10).

To summarize, of the principal phenomena that arise on attenuation of high-energy (x-rays, γ -rays, and annihilation radiation) photons in matter are

- X-ray-excited photoelectrons, characteristic x-rays, and Auger electrons arise from photoelectric absorption, μ^p .
- Unmodified and modified photon scatter and Compton recoil electrons arise from scatter, μ^s .
- Electron–positron pairs arise from pair production, μ^{pp} .

Total attenuation, individual photoelectric absorption, coherent and incoherent scatter attenuation, and pair production attenuation values are tabulated in reports (Cullen et al. 1989; Henke et al. 1993) and are available on the Internet. For example, see the Lawrence Berkeley National

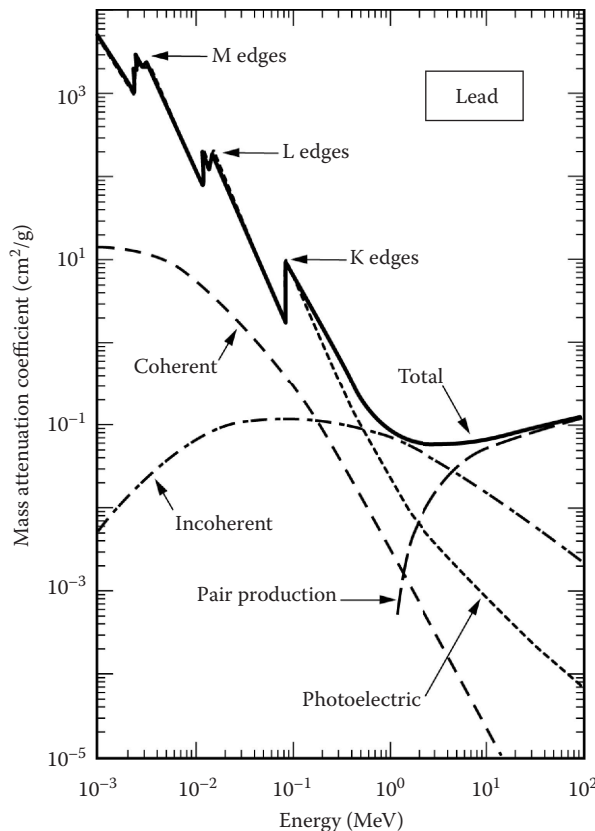


FIGURE 5.18 Mass attenuation coefficients of lead. Shown are the separate mass attenuation coefficients for coherent and incoherent scattering, photoelectric absorption, and pair production. Also shown is the total mass attenuation coefficient. Note that coherent scatter never accounts for more than a few percent of the total, that photoelectric domination extends to 3×10^{-1} MeV (i.e., hundreds of keV), and that considerable structure occurs for the L and M photoelectric edges while the K edge is a single jump. Incoherent scatter is the dominant constituent of the total mass attenuation over a very narrow energy range (5×10^{-1} to 3×10^0 MeV). Also note that in Pb, the total attenuation coefficient exhibits a pronounced minimum near 3 MeV. This means that 3 MeV photons are the most penetrating in lead. All other energies are less penetrating.

Laboratory (LBNL) Center for X-Ray Optics website (LBNLb 2015). NIST supports an online program called XCOM that provides attenuation tabulations and graphs for elements, compounds, and mixtures (NIST XCOM 2015).

5.4 REFLECTION

Following Hecht (2002, p. 86), the processes of transmission, reflection, and refraction are manifestations of scattering occurring on a submicroscopic level. Explanation of this statement is beyond the discussions of this text, but it is useful to describe the transmission of electromagnetic waves through a homogeneous medium as an ongoing repetitive process of scattering and rescattering (Huygens–Fresnel principle). When a beam of electromagnetic radiation or photons impinges on the surface of a transparent material, such as a sheet of glass for visible light, the wave “sees” a vast array of closely spaced atoms that will somehow scatter it. As shown by Hecht (2002), in the case of transmission through a dense medium, the scattered wavelets cancel each other out in all but the forward direction, and just the ongoing beam is sustained. But that can only happen if there

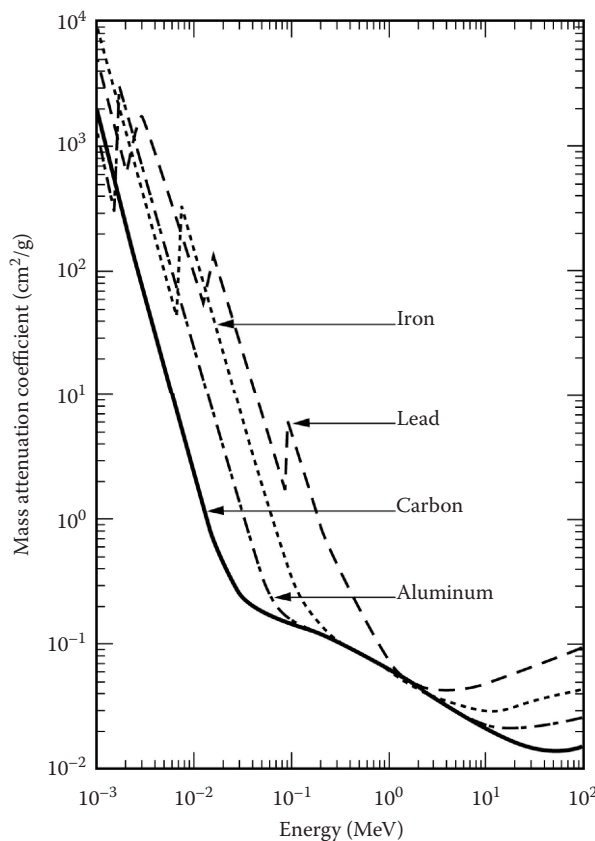


FIGURE 5.19 Total mass attenuation coefficients for the elements carbon, aluminum, iron, and lead. This is the same information presented in the previous four figures (Figures 5.15 through 5.18) for the totals of each element but plotted together. While it is generally true that higher-atomic-number elements have larger mass attenuation coefficients, there are energy ranges (1×10^{-3} to 2.5×10^{-3} and 7×10^{-3} to 1.5×10^{-2} MeV) where iron is more attenuating than lead. Similarly, at the lowest energies (1×10^{-3} to 1.6×10^{-3} MeV) shown, carbon is more attenuating than aluminum.

are no discontinuities. This is not the case at an interface between two different transparent media (for visible radiation such as air and glass), which is a big discontinuity. When a beam of radiation strikes such an interface, some radiation is always scattered backward, and we call this phenomenon *reflection*.

If the transition between two media is gradual—i.e., if the index of refraction (or the dielectric constant) changes from that of one medium to that of the other over a distance of a wavelength or more—there will be very little reflection. The interface essentially vanishes. On the other hand, a transition from one medium to the other over a distance of $1/4$ wavelength or less behaves very much like a totally discontinuous change.

A beam of *optical*, i.e., visible, radiation that reflects off a material in which the radiation travels from a less to a more *optically* dense medium is called *external* reflection (see Figure 5.21). In other words, the index of the incident medium (η_i) is less than the index of the transmitted medium (η_r), i.e., $\eta_i < \eta_r$. When visible radiation reflects backward from an incident beam on a medium whose index is more than the index of the transmitted medium, $\eta_i > \eta_r$, this is called *internal* reflection. It is important to note that these definitions do not always hold true for all electromagnetic radiation; for example, x-ray radiation that reflects off a material in which the radiation travels from a more

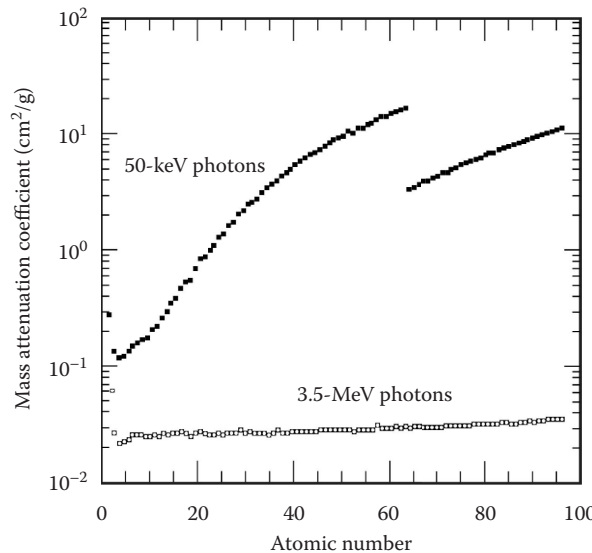


FIGURE 5.20 Plot of the mass attenuation coefficient as a function of atomic number for two photons energies: 50 keV and 3.5 MeV. At 50 keV from Li to Eu ($3 \leq Z \leq 63$) the mass attenuation coefficient increases with atomic number until gadolinium ($Z = 64$). This is mainly due to attenuation being dominated by the photoelectric effect. For gadolinium, 50 keV is no longer sufficient to eject an electron from the K shell, and the mass attenuation coefficient drops by a factor of about 5. For 3.5 MeV photons, the mass attenuation coefficient is fairly constant. For 3.5 MeV photons, the attenuation is dominated by Compton scatter for all elements. For Compton scatter, binding energies are unimportant, and the attenuation coefficient depends mainly on the electron density. Since to the first order, the number of electrons per unit mass is approximately constant, the mass attenuation coefficient varies only slightly with changing atomic number.

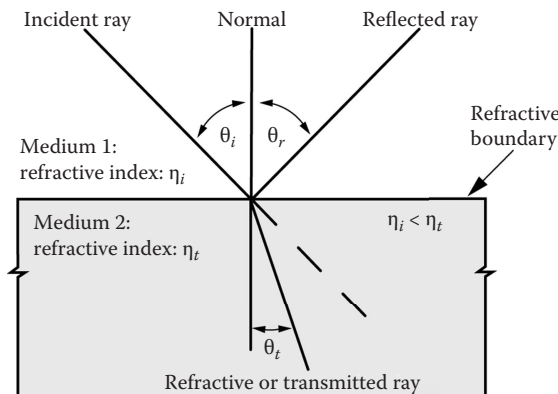


FIGURE 5.21 Diagram showing the reflection and refraction of a photon ray at an interface. If a photon travels from a medium of lower refractive index to a medium of higher index, $\eta_i < \eta_t$, the photon is refracted toward the normal. For reflection, note that $\theta_i = \theta_r$.

to a less refractive index medium is called *external* reflection even though $\eta_i > \eta_t$. This is discussed further in [Section 5.5.1.2](#), Total External Reflection of X-Rays.

Following Hecht (2002), there are two laws of reflection:

- The angle of incidence equals the angle of reflection (see [Figure 5.22a](#)), $\theta_i = \theta_r$
- The incident ray, the perpendicular to the surface, and the reflected ray all lie in a plane called the plane of incidence—this takes into account the third dimension (see [Figure 5.22b](#)).

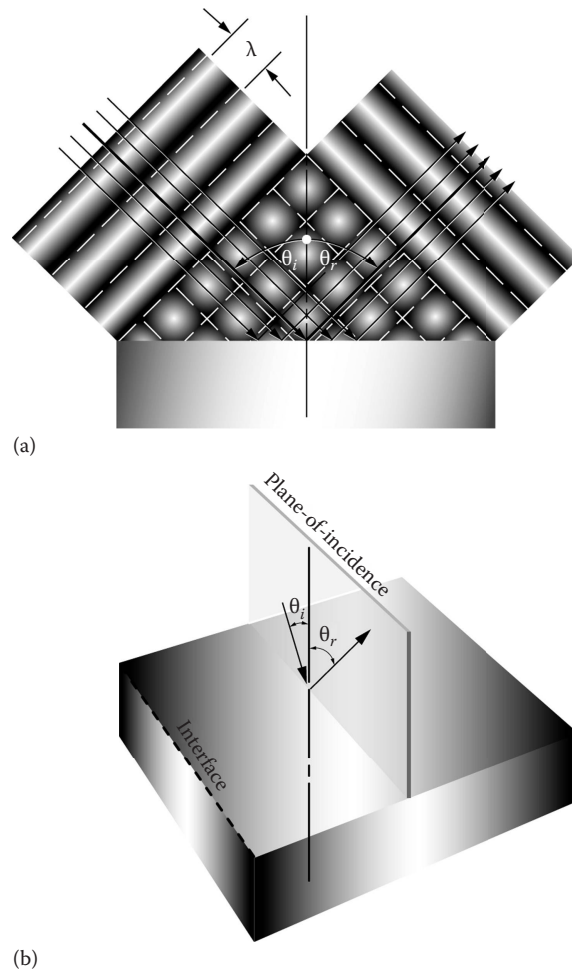


FIGURE 5.22 Select one ray to represent the beam of plane waves. (a) Both the angle of incidence, θ_i , and angle of reflection, θ_r , are measured from the perpendicular drawn to the reflecting surface. (b) The incident ray and the reflected ray define the *plane of incidence*, perpendicular to the reflecting surface. (Adapted from Hecht, E., *Optics*, fourth edition, Addison Wesley, San Francisco, 2002.)

In the case where the surface (peaks and valleys) of a medium is smooth (see Figure 5.23), that is, the irregularities are small compared to the wavelength, λ , the scattered wavelets will arrive more or less in phase when $\theta_i = \theta_r$. This is called *specular reflection*. *Specular* is from the word for a common mirror alloy in ancient times, *speculum*; thus, any mirror is a good example of a specular reflecting surface, just as a calm lake is a good specular reflector. On the other hand, when the surface is rough in comparison to λ , although the angle of incidence will equal the angle of reflection for each ray, the whole lot of rays will emerge every which way, yielding what is called *diffuse reflection*. The pages of this book are an example of a diffuse reflector, just as a rough lake is a diffuse reflector. Both of the conditions shown in Figure 5.23 are extremes; the reflecting behavior of most surfaces lies somewhere between them.

5.5 X-RAY PHASE EFFECTS

The contrast in conventional x-ray transmission images is formed by differences in the x-ray attenuation coefficients, and thus, structures are depicted in the images. For objects consisting of

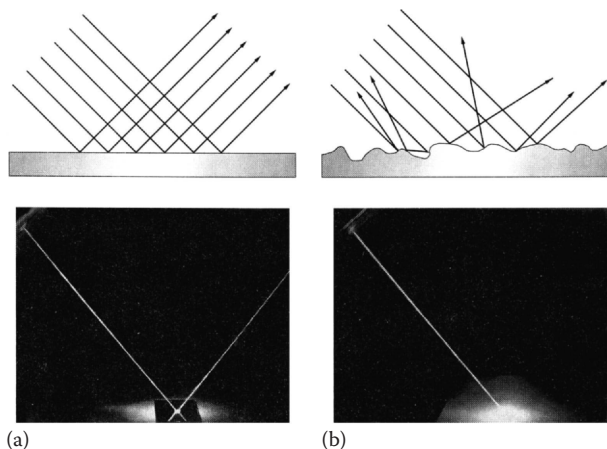


FIGURE 5.23 Schematic of (a) specular and (b) diffuse reflection. (Adapted from Hecht, E., *Optics*, fourth edition, Addison Wesley, San Francisco, 2002.)

low-atomic-number elements, such as biological soft tissues or plastics and/or very low-density materials, such as aerogels,* however, conventional x-ray imaging is not effective, because of the low x-ray attenuation coefficient.

Recently, research activity using phase information has been growing rapidly in the field of x-ray imaging. This is because the cross sections of the phase shift of low-Z elements are about 100 to 1000 times larger than those of attenuation at low (a few keV) energies. Therefore, x-ray phase contrast[†] can lead to a breakthrough in x-ray imaging, especially in biology. Often, phase contrast is not required for conventional industrial imaging; however, recent advances in small-spot-size (<20 μm) x-ray sources, called microfocus and nanofocus sources (see Chapter 8, Radiation Sources), and high-spatial-resolution (~10 μm) detectors (see Chapter 9, Radiation Detectors) have led to very high-spatial-resolution (~1 μm) imaging (Mayo et al. 2002; Donnelly et al. 2003; Yoshimura et al. 2003). In this regime, whether useful or not, phase effects are observed as bright and dark edges (see Figure 5.24). It is important to correctly interpret phase effects in such images, or they will generate dimensional errors (see Figure 5.25), fictitious gaps, and incorrect material identification.

Phase-contrast techniques (see Section 5.5.3, X-Ray Phase-Contrast Radiography) offer ways to augment or complement standard attenuation contrast x-ray imaging. Phase techniques can be understood using wave optics rather than ray optics. As mentioned in Section 5.2, given the electromagnetic nature of x-rays, they can be attenuated, scattered (see Figure 5.2), reflected (see Figure 5.3a), refracted (see Figure 5.3b), and diffracted (see Figure 5.4). X-ray phase effects are manifestations of mainly refraction and diffraction (see Figure 5.26). Thus, before we discuss x-ray phase-contrast radiography and computed tomography, we provide an overview of refraction and diffraction.

* Aerogels are the lightest of all solid substances. Chemically, for example, silica aerogels are identical to silica glass, but they have a very porous internal structure. They can have densities down to 2–20 mg/cm³, which leads to a number of interesting properties. They are excellent thermal insulators; they have a huge internal surface area; they are transparent to visible light; and they can absorb a large amount of kinetic energy.

[†] Here we refer to contrast in the sense of changes in irradiance due to phase shifts, not a direct measurement of the phase shift.

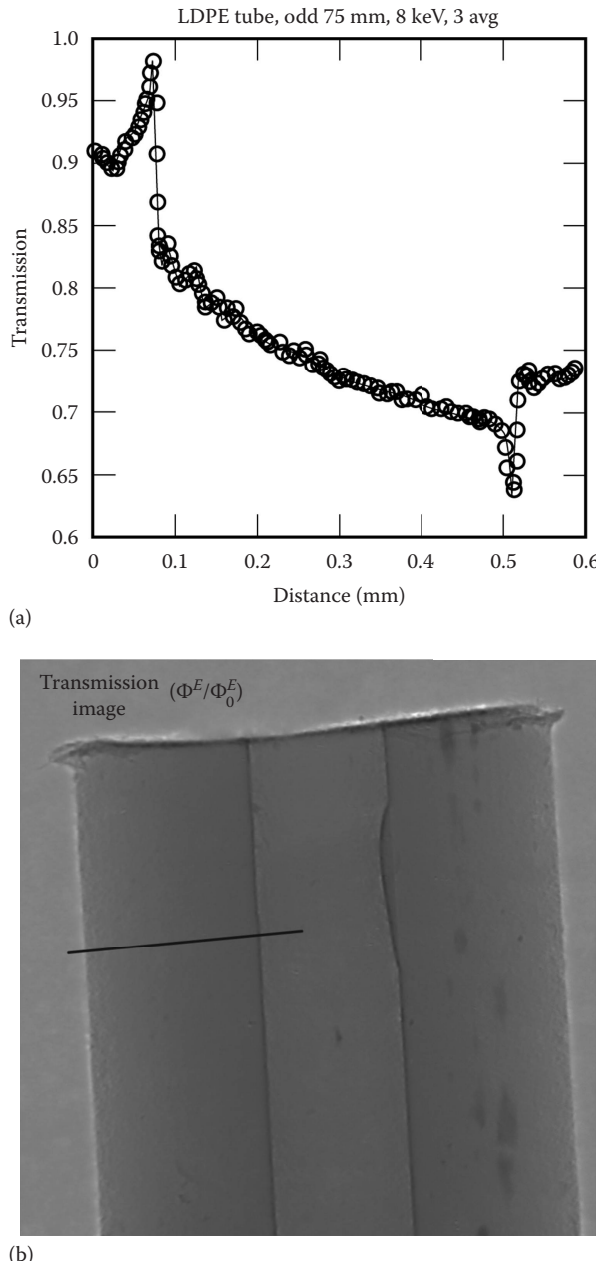


FIGURE 5.24 (a) A line out from the black line in (b) an x-ray digital radiograph of a low-density polyethylene (LDPE; 0.92 g/cm^3) tube of 1.1 mm outer diameter with a wall thickness of $\sim 0.35 \text{ mm}$ (Schneberk et al. 2004). These data show the telltale signs of phase contrast, i.e., bright and dark edges in (b) and the peak (at 0.08 mm) and valley (at 0.52 mm) in (a). The digital radiographs were acquired at 8 keV and object-to-detector distance of 75 mm using the Lawrence Berkeley National Laboratory Advanced Light Source synchrotron facility tomography beamline 8.3.2.

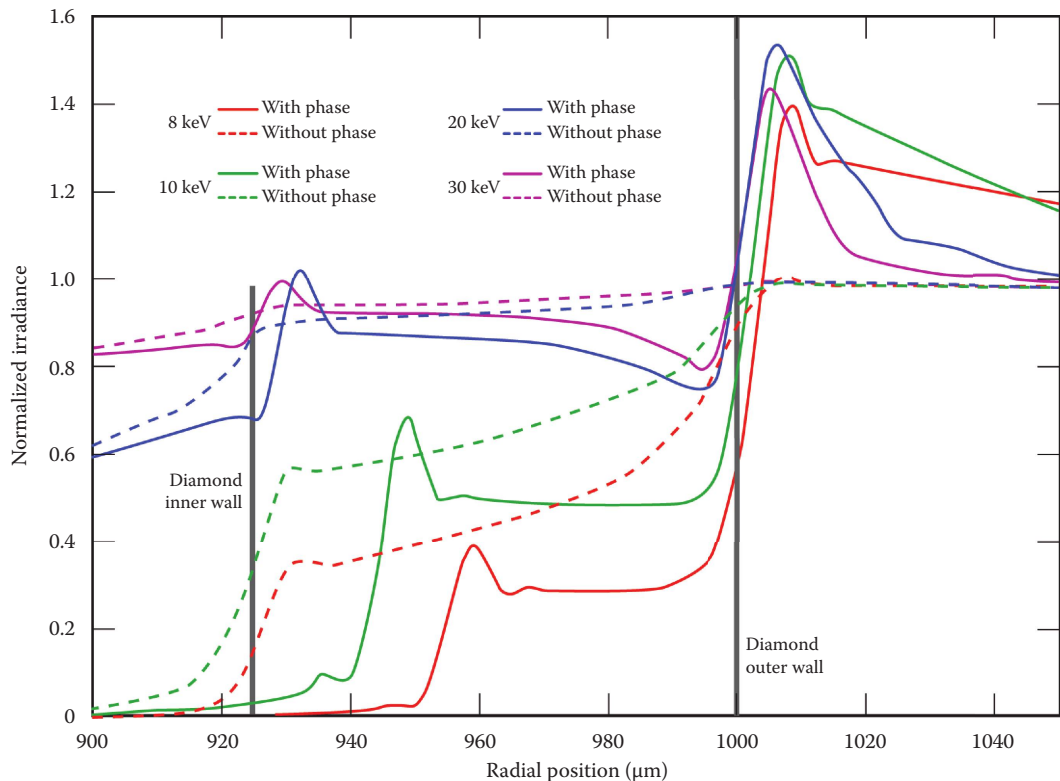


FIGURE 5.25 Simulated results for x-ray imaging of a 75- μm -thick chemical vapor deposition (CVD) diamond ($\rho = 3.3 \text{ g/cm}^3$) shell coated on a 925- μm -radius SiN ($\rho = 3.44 \text{ g/cm}^3$) mandrel. The object-to-detector distance is 200 mm. The object pixel pitch is 1 μm , convolved with a Gaussian blur with a sigma value of 2.0 μm . Results with phase effects included are given by the solid lines. The dashed lines give straight-ray results, i.e., no phase effects. Note the dramatic difference in the phase data as a function of energy (due to the change in refractive index) compared with the no-phase results. Bottom line, if you do not account for x-ray phase shifts, you can get incorrect dimensional measurements.

5.5.1 REFRACTION

As mentioned in [Section 5.4](#), Reflection, the processes of transmission, reflection, and refraction are manifestations of scattering occurring on a submicroscopic level (Hecht 2002). Explanation of this statement is beyond the discussions of this text, but it is useful to describe the transmission of electromagnetic waves through a homogeneous medium as an ongoing repetitive process of scattering and rescattering. Each event introduces a phase shift into the electromagnetic field, which ultimately shows up as a shift in the apparent phase velocity of the transmitted beam from its nominal value of c , i.e., the speed of electromagnetic radiation in a vacuum. That corresponds to an index of refraction for the medium equal to the velocity of electromagnetic radiation in a vacuum divided by the velocity in a medium or

$$\eta = \frac{c}{v}, \quad (5.30)$$

which is other than one, even though photons exist only at the speed of c . It is useful to show that a phase shift is indeed equivalent to a difference in phase velocity. In free space (a vacuum), the electric field disturbance at some point j may be written as

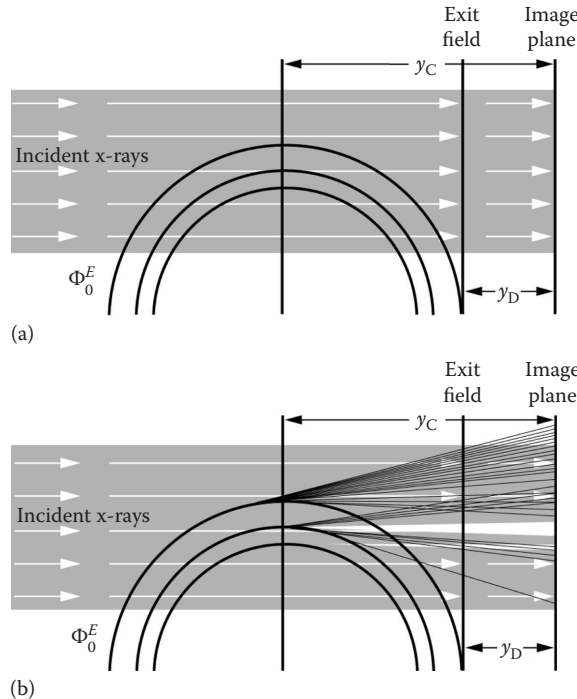


FIGURE 5.26 Schematic comparison between (a) conventional and (b) phase-contrast x-ray imaging. Conventional x-ray imaging (a) does not account for any bent rays, i.e., scatter, refraction, or diffraction (it is mainly a straight-ray method, while phase-contrast techniques (b) do account for bent rays, at least refraction and diffraction, within the object.

$$F_{E_j}(t) = F_{E_0} \cos \omega t, \quad (5.31)$$

where F_{E_0} is the electric field in a vacuum and ω is the angular temporal frequency and t is time.

$$\omega = 2\pi\nu = \frac{2\pi}{\tau}, \quad (5.32)$$

where ν is the temporal frequency and τ is the temporal period (or the amount of time it takes for one complete wave to pass a stationary observer). This is given by

$$\tau = \frac{\lambda}{v}, \quad (5.33)$$

where v is the wave velocity. If the point is surrounded by a dielectric, there will be a cumulative phase shift φ_j , which is built up as the wave moves through the medium to the point j . At ordinary levels of irradiance, the medium will behave linearly, and the frequency in the dielectric will be the same as that in vacuum, even though the wavelength and speed may differ. The disturbance at j in the medium is

$$F_{E_j}(t) = F_{E_0} \cos(\omega t - \varphi_j), \quad (5.34)$$

where the subtraction of φ_j corresponds to a phase-shift *lag*. An observer at j will have to wait a longer time for a given crest of the wave to arrive when he/she is in the medium than he/she would have to wait in a vacuum. That is, for two parallel waves of the same frequency, one in a vacuum and one in a medium, the vacuum wave will pass j at time φ_j/ω before the other wave. Thus, a *phase lag* of φ_j corresponds to a reduction in speed, $v < c$ and $\eta > 1$. Similarly, a *phase lead* yields an increase in speed, $v > c$ and $\eta < 1$. The scattering process is a continuous one and the cumulative phase shift builds as the photons penetrate the medium. In the vast majority of situations encountered in optics, $v < c$ and $\eta > 1$. The *important exception is the case of x-ray propagation, where $\omega > \omega_0$, $v > c$, and $\eta < 1$.* Since this text deals with x-ray and γ -ray radiation radiology, this difference is important to emphasize and is given in Panel 5.6.

PANEL 5.6 Important Insight

The fact that the index of refraction for x-rays is negative will be important later when one builds an x-ray lens (see Section 15.9, X-Ray Microscopy and X-Ray Optics). Instead of a convex lens to focus visible light, an x-ray focusing lens will be concave. X-rays impinging at normal incidence on any material are largely attenuated rather than reflected. Normal-incidence mirrors, like those used for optical telescopes, are ruled out. Also, since $\eta \sim 1$ at x-ray wavelengths, any refracting system (i.e., lens) must be sufficiently thin to transmit x-rays and must possess a long focal length; such a system would be highly impractical for use on a rocket or satellite. However, the property of the index of refraction being slightly less than unity at x-ray wavelengths offers the possibility of using *total external reflection* of x-rays incident on a surface near grazing incidence (see Section 5.5.1.2, Total External Reflection of X-Rays, and Section 15.9, X-Ray Microscopy and X-Ray Optics).

5.5.1.1 Snell's Law

Here it is useful to describe a law of geometric optics that defines the amount of bending (refraction) that takes place when an electromagnetic ray strikes a refractive boundary, e.g., an air–glass interface, at a nonnormal angle (see Figure 5.21). Snell's law* states that

$$\eta_i \sin \theta_i = \eta_t \sin \theta_t, \quad (5.35)$$

where

- η_i is the index of refraction of the medium in which the incident ray travels;
- θ_i is the angle, with respect to the normal at the refractive boundary, at which the incident ray strikes the boundary;
- η_t is the index of refraction of the medium in which the transmitted or refracted ray travels; and
- θ_t is the angle, with respect to the normal at the refractive boundary, at which the transmitted or refracted ray travels.

The incident ray and refracted ray travel in the same plane, on opposite sides of the normal at the point of incidence. Rather than going straight through, the ray entering a higher-index medium, $\eta_i < \eta_t$, bends toward the normal (see Figure 5.21). The reverse is also true: on entering a medium of a lower index of refraction, the ray, rather than going straight through, will bend away from the

* Snell's law, given in Equation 5.35, is the first portion of the law of refraction and is named after the man, Willebrord Snell van Royen, who proposed it in 1621.

normal. Notice that this implies that the rays will traverse the same path going either way, into or out of either medium.

If the incident ray travels in a medium of higher refractive index toward a medium of lower refractive index, $\eta_i > \eta_t$, at such an angle that Snell's law would call for the sine of the refracted ray to be greater than unity (a mathematical impossibility), i.e.,

$$\sin \theta_t = \frac{\eta_i}{\eta_t} \sin \theta_i > 1, \quad (5.36)$$

then the *refracted* ray in actuality becomes a *reflected* ray and is *totally reflected* back into the medium of higher refractive index, at an angle equal to the incident angle (and thus still "obeys" Snell's law). This reflection occurs even in the absence of a metallic reflective coating (e.g., aluminum or silver). This phenomenon is called *total internal reflection*. The smallest angle of incidence, with respect to the normal at the refractive boundary, which will support total internal reflection, is called the critical angle, θ_c , and is given by

$$\theta_c = \sin^{-1} \left(\frac{\eta_i}{\eta_t} \right), \quad (5.37)$$

where $\eta_i > \eta_t$. The incident ray is in the medium with a higher refractive index. If the incident ray is precisely at the critical angle, the refracted ray is tangent to the boundary at the point of incidence.

5.5.1.2 Total External Reflection of X-Rays

At x-ray wavelengths, for most materials, the index of refraction is slightly less than unity, i.e., $\eta_i = \eta_{air} > \eta_t$. Important consequences of this are mentioned in [Panel 5.6](#), Important Insight. This property offers the possibility of using *total external reflection** of x-rays incident on a surface near grazing incidence. The index of refraction at x-ray wavelengths may be written as

$$\eta = 1 - \delta - i\beta, \quad (5.38)$$

where δ and β depend on the material and the wavelength of the incident x-rays. If $\delta > 0$ and $\beta \sim 0$, and the incident x-rays are propagating in a vacuum (for which $\eta_{vacuum} = 1$), $\eta_{vacuum} > \eta_{mat}$ or $\eta_i > \eta_t$, then by Snell's law, x-rays will undergo *total external reflection* for angles $\theta < \theta_c$, where $\cos(\theta_c) = 1 - \delta$. Thus, $\theta_c \sim (2\delta)^{1/2}$ (Bertin 1978).

The visible-light analogy to this phenomenon is the *total internal reflection*, which, among other things, produces the glistening of a diamond. In that case, the index of refraction of the diamond is higher than air, $\eta_{Diamond} > \eta_{air}$ or $\eta_i > \eta_t$, so light within the diamond reflects efficiently off the various facets.

Generally, the dependence of δ , and thus θ_c , of a material is proportional to its atomic number, Z . Thus high- Z materials reflect x-rays more efficiently than low- Z materials. The most commonly used reflecting materials are gold and nickel, for which the critical angle at 1 keV is about 1 degree—sometimes referred to as grazing incidence. This is useful for grazing incidence x-ray optics.

* Given the definition for *internal* and *external* reflection in [Section 5.4](#), Reflection, this should be called *total internal reflection*; however, for x-rays, the definition is reversed. This may be due to the fact that the x-ray radiation is traveling from a less to a more mass-dense medium, but it just so happens that refractive index values go from a high value to a lower value.

5.5.2 DIFFRACTION

An opaque body placed midway between a screen and a point source casts an intricate shadow made up of bright and dark regions quite unlike anything one might expect from the principles of geometrical optics. The work of Francesco Grimaldi in the 1600s was the first published detailed study of this deviation of light from rectilinear propagation, something he called “diffracio.” The effect is a general characteristic of wave phenomena occurring whenever a portion of a wave front, be it sound, a matter wave, or electromagnetic radiation, is obstructed in some way.

If in the course of encountering an obstacle, either transparent or opaque, a region of the wave front is altered in amplitude or phase, *diffraction* will occur. The various segments of the wave front that propagate beyond the obstacle interfere, causing the particular energy density distribution referred to as the diffraction pattern. There is no significant physical distinction between interference and diffraction. It has, however, become somewhat customary, if not always appropriate, to speak of interference when considering the superposition of only a few waves and diffraction when treating a large number of waves. Even so, one refers to multiple-beam interference in one context and diffraction from a grating or crystal in another. It should be noted that the problem of determining an exact solution for a particular diffracting configuration is among the most troublesome to be dealt with in optics (Hecht 2002).

X-ray diffraction arises from interference of unmodified coherently scattered x-rays. One version of diffraction of x-rays by crystals is that of Laue, who regards the phenomenon in terms of scatter from the individual lattice sites of a crystal (Friedrich et al. 1913). For a collimated monochromatic x-ray beam of wavelength λ and frequency v is directed at angle θ on a set of crystal planes of interplanar spacing d (see Figure 5.27), the atoms in the crystal lattice are excited to oscillate at frequency v and act as spherical radiators of x-rays of the same wavelength as the incident x-rays. This is the coherent scatter process. In

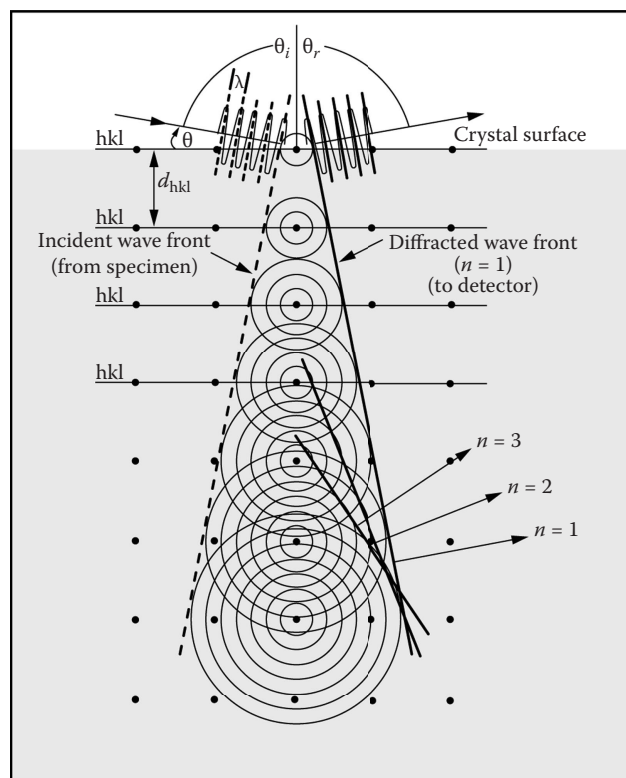


FIGURE 5.27 The Laue version of diffraction by atoms in a crystal. (Adapted from Bertin, E. P., *Principles and Practice of X-Ray Spectroscopic Analysis*, second edition, Plenum Press, New York, 1978.)

most directions, the scattered x-rays are out of phase and undergo destructive interference. However, in certain directions, they are in phase and mutually reinforce. The group of such reinforced rays in a given direction constitutes a diffracted x-ray beam. The conditions for diffraction are as follows:

- The angles made by the diffracting crystal planes with the incident and diffracted beams are equal.
- The directions of the incident and diffracted beams and the normal to the diffracting planes are coplanar.
- The waves emitted by individual atoms in the direction of a diffracted beam are in phase.

The condition for first-order ($n = 1$) diffraction of λ is shown in Figure 5.27. The first-order wave front consists of the first wave from the first (top) atom, the second wave from the second atom, etc., i.e., waves from successive atoms differ by 1. If θ is increased to appropriate discrete values, the crystal diffracts the second order ($n = 2$), where waves from successive atoms differ by 2, the third ($n = 3$), where they differ by 3, etc.

A more useful version of diffraction is that of Bragg (1912), who regards the phenomenon in terms of reflection from a stack of crystal planes (see Figure 5.28). A collimated monochromatic x-ray beam of wavelength λ is directed at angle θ on a set of crystal planes of interspacing d . Again, the incident beam is scattered in all directions from each plane, but only in certain directions does the scatter reinforce. The conditions for diffraction are the same as for the Laue version, but the third condition might be more appropriately restated as follows:

- Reflected rays from successive planes differ in path length by an integral number of wavelengths.

In Figure 5.28, rays 1 and 2 are directed on two successive planes and scattered in all directions. Rays 1 and 2 travel equal distances to AC, and rays 1' and 2' travel equal distances beyond AD. The path difference between rays 1A1' and 2B2' is then

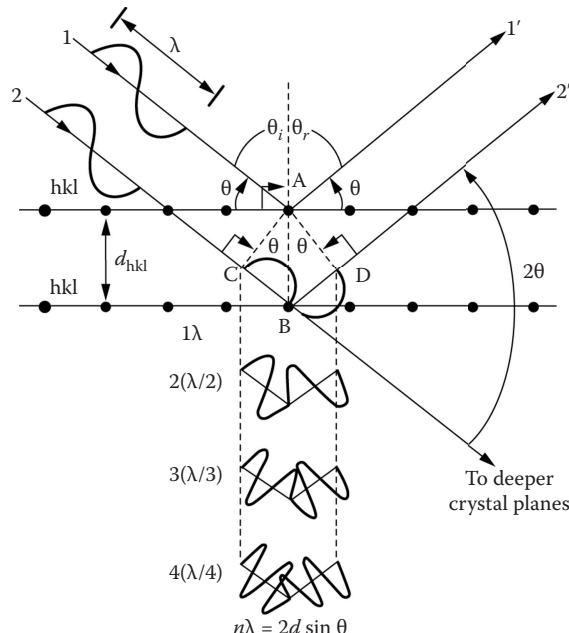


FIGURE 5.28 The Bragg version of diffraction by atoms in a crystal. (Adapted from Bertin, E. P., *Principles and Practice of X-Ray Spectroscopic Analysis*, second edition, Plenum Press, New York, 1978.)

$$CBD = CB + BD = 2AB \sin \theta = 2d \sin \theta. \quad (5.39)$$

If these rays are to be in phase, this path difference must be an integral number of wavelengths, that is,

$$n\lambda = 2d \sin \theta. \quad (5.40)$$

This is Bragg's law, where n is the order of the diffracted beam and is numerically equal to the path difference, in wavelengths, for successive planes; d is the interplane spacing of the diffracting planes; and θ , the Bragg angle, is the angle between the incident x-rays and the diffracting planes. Spectrometers are usually calibrated in terms of 2θ , the angle between the diffracted beam and the undeflected incident beam. The analogy of the Bragg version of diffraction with Snell's law of reflection is evident; however, it is important to note that the two phenomena are quite different. Optical reflection is a wholly surface effect and occurs at all incident angles greater than a certain small critical angle.

The phenomenon of diffraction orders is illustrated in [Figure 5.28](#). The same angle θ at which wavelength λ is diffracted in the first order ($n = 1$, one wavelength path difference between successive planes), wavelength $\lambda/2$ is diffracted in the second order ($n = 2$, two wavelengths path difference between successive planes), etc. Thus, the method of crystal diffraction cannot separate two wavelengths λ_1 and λ_2 related by

$$\lambda_2 = \frac{\lambda_1}{n}. \quad (5.41)$$

X-ray diffraction is not a common industrial imaging technique; thus, for specific x-ray diffraction methods—crystal dispersion, Laue, moving crystal, Debye–Scherrer, divergent beam, diffraction by gratings—we refer the reader to Bertin (1978), Hecht (2002), Cullity (1978), and Guinier (1963). Now that we have briefly described x-ray refraction and diffraction, we can discuss x-ray phase-contrast radiography.

5.5.3 X-RAY PHASE-CONTRAST RADIOGRAPHY

The behavior of x-rays as they travel through an object can be described using a complex index of refraction, just as in conventional optics. In the x-ray region, the index of refraction, η , deviates only slightly from unity. It can be written as

$$\eta = 1 - \delta - i\beta, \quad (5.42)$$

where δ ,^{*} the phase-shift term or index, incorporates refractive effects and β , the attenuation index,[†] describes the attenuation of x-rays. The real part, δ , of the refractive index, although small, is larger than the imaginary part β , for energies down to 1 keV or so, depending on the material. For light elements, $Z \leq 10$, δ exceeds β by a factor of ~ 100 for photon energies down to 8 keV (Momose and Fukuda 1995). Another advantage of phase contrast is that away from absorption edges, it falls off less quickly at higher energies than attenuation contrast:

$$\delta \propto E^{-2}, \text{ whereas } \beta \propto E^{-4}. \quad (5.43)$$

^{*} This should not be confused with the Dirac delta function given by $\delta(\cdot)$.

[†] What we refer to here as the *attenuation index* is often referred to as the *absorption index*. We use the former to keep with our nomenclature that only the photoelectric effect results in absorption.

A method for computing the δ and β indices is given in Panel 5.7, The δ and β Indices.

These are the reasons behind the promise of gaining additional information via x-ray phase-contrast imaging over conventional x-ray attenuation radiography. However, the realization and interpretation of phase-contrast radiography are less straightforward than for attenuation contrast radiography.

PANEL 5.7 The δ and β Indices

The δ and β indices can be computed from the real and imaginary atomic scattering factors f_1 and f_2 , respectively, as follows:

$$\delta = \frac{r_e \lambda^2}{2\pi} \rho N_A \sum_i \frac{X_i}{A_i} f_{1,i} \quad (5.44)$$

and

$$\beta = \frac{r_e \lambda^2}{2\pi} \rho N_A \sum_i \frac{X_i}{A_i} f_{2,i}, \quad (5.45)$$

where r_e is the classical electron radius (2.8179×10^{-13} cm), λ is the x-ray wavelength (cm), N_A is Avogadro's number (6.023×10^{23} atoms/mol), X_i is the mass fraction of the i th element, A_i is the atomic mass (g/mol) of the i th element, $f_{1,i}$ and $f_{2,i}$ are the first and second atomic scattering factors of the i th element, ρ is the density (g/cm³) of the compound, and the summation is over all i isotopes in the compound. The atomic scattering factor tables can be obtained from the LBNL Center for X-Ray Optics website (LBNLb 2015), which are modified tables based on the work of Henke et al. (1993). Additional scattering factors can be obtained at the website for the European Synchrotron Radiation Facility (ESRF 2015) and at the website for the Lawrence Livermore National Laboratory (LLNL) Physics Division (LLNL 2015). The latter provides calculated anomalous scattering factors up to 10 MeV, which are related to the f_1 and f_2 , and can be used to calculate δ and β .

The linear attenuation (coefficient), μ , and phase (shift), φ_p , are related to β and δ as follows:

$$\mu(E, Z, \rho, x, z) = \frac{4\pi}{\lambda} \beta(E, Z, \rho, x, z) \quad (5.46)$$

and

$$\varphi_p(E, Z, \rho, x, z) = \frac{2\pi}{\lambda} \delta(E, Z, \rho, x, z). \quad (5.47)$$

When x-rays pass an object, the change of the x-ray wave field is expressed by the complex x-ray irradiance

$$\Psi(E, Z, \rho, x, z) = e^{[i\varphi_p(E, Z, \rho, x, z)]} e^{\left[-\int \mu(E, Z, \rho, x, y, z) dy\right]/2}, \quad (5.48)$$

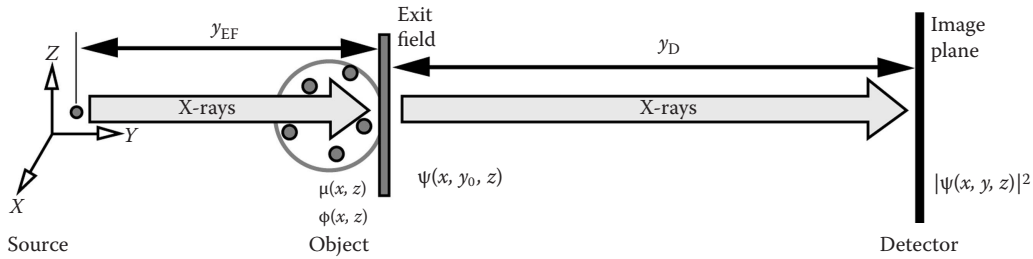


FIGURE 5.29 Geometry of x-ray phase-contrast radiography. Spatially coherent x-rays are generated by the source, pass through the object, and emerge as the exit field $\psi(E, Z, \rho, x, y_0, z)$. The field then propagates to y_D . For either case, the irradiance is given by $|\psi(E, Z, \rho, x, y, z)|^2$.

where $\mu(E, Z, \rho, x, y, z)$ is the linear attenuation coefficient, $\phi_p(E, Z, \rho, x, z)$ is the phase shift, and the x-ray propagation direction is parallel to the y -axis (see Figure 5.29). In quantitative measurements like digital radiography, at the exit plane ($y_D = 0$ or $y = y_{EF}$), the x-ray line integral or ray sum,*

$$\begin{aligned} g(x, z) &= -\ln \left\{ e^{-\int \mu(E, Z, \rho, x, y, z) dy} \right\} \\ &= \int \mu(E, Z, \rho, x, y, z) dy = -\ln \frac{\Phi^E(E, Z, \rho, x, z)}{\Phi_0^E(E, x, z)}, \end{aligned} \quad (5.49)$$

is evaluated, where

$$\Phi^E(E, Z, \rho, x, z) = |\psi(E, Z, \rho, x, z)|^2. \quad (5.50)$$

Thus, there is no phase contrast in the contact or “in-focus” radiographic image. Fresnel–Kirchhoff diffraction and other phase-contrast x-ray radiography methods are being explored by a number of researchers (White and Cerrina 1992; Hirano and Momose 1999; Iwata et al. 1999; Kotre and Birch 2002; Donnelly et al. 2003; Wu and Liu 2004; Momose 2005). In the Fresnel–Kirchhoff diffraction method (Snigirev et al. 1995; Cloetens et al. 1996), upon further propagation of the wave ($y_D > 0$), phase contrast is produced. This propagation is sometimes referred to as free-space propagation, a *phenomenon where Fresnel diffraction transforms phase shifts into intensity variations*. One can think of the object as a lens or diffracting object through and around which the wave propagates. In the paraxial approximation,[†] typically satisfied in most x-ray imaging cases, the wave function on planes $y_D > 0$ is given by the Fresnel integral:

$$\psi(E, Z, \rho, x, y, z) = \frac{i}{\lambda y} e^{-iky} \iint \psi(E, Z, \rho, x', y_{EF}, z') e^{\frac{i\pi}{\lambda y} [(x-x')^2(z-z')^2]} dx' dz', \quad (5.51)$$

* Line integral and ray sum are often used for computed tomography. Sometimes it is referred to as (x-ray) density. We avoid this term because most often, it is confused with mass density; they are very different, and this can often be misleading.

[†] The paraxial approximation is usually referenced in optical systems and is a thin region about the optical axis, which is so small that all the angles made by the rays may be set equal to their sines and tangents. At first, this concept seems useless; however, calculations of the performance of an optical system based on paraxial relationships are of tremendous utility (Smith 2000; Hecht 2002).

where y' is given by $y_D/(1 + y_D/y_{EF})$. y_{EF} is the source to the exit field distance, and y_D is the exit field to detector distance, as given in [Figure 5.29](#). This integral can be simplified by using the convolution form of the Fresnel integral:

$$\psi(E, Z, \rho, x, y, z) = -e^{iky'} \mathfrak{J}^{-1} \left\{ e^{\frac{-i\pi\lambda y' ii^2 + jj^2}{(N\Delta x)^2}} \mathfrak{J}\{\psi(x', y_{EF}, z')\} \right\}, \quad (5.52)$$

where \mathfrak{J} and \mathfrak{J}^{-1} are the Fourier and inverse Fourier transform, respectively; N is the number of pixels in the image; Δx is the size of each pixel; and ii and jj are the image indices. This form is useful because the wave function can be treated as a complex image and is computed quickly using fast Fourier transforms.

The phase shift $\varphi_p(E, Z, \rho, x, z)$ is given by

$$\varphi_p(E, Z, \rho, x, z) = \left(\frac{2\pi}{\lambda} \right) \int \delta(E, Z, \rho, x, y, z) dy, \quad (5.53)$$

where λ is the x-ray wavelength and $\delta(x, y, z)$ is the refractive index decrement from unity. Following Momose (2002), $\mu(E, Z, \rho, x, y, z)$ and $\delta(E, Z, \rho, x, y, z)$ can be written using atomic parameters as

$$\mu(E, Z, \rho, x, y, z) = \sum_k \rho_a^k(Z, x, y, z) \mu_a^k(E, Z) \quad (5.54)$$

and

$$\delta(E, Z, \rho, x, y, z) = \left(\frac{r_e \lambda^2}{2\pi} \right) \sum_k \rho_a^k(Z, x, y, z) (Z^k + f_1^k), \quad (5.55)$$

where ρ_a^k is the atomic density (atoms/cm^3), μ_a^k is the atomic attenuation coefficient (cross section), Z is the atomic number, f_1^k is the real part of the anomalous atomic scattering factor of element k , and r_e is the classical electron radius ($2.8179 \times 10^{-13} \text{ cm}$). The substitutions of Equation 5.54 into Equation 5.49 and Equation 5.55 into Equation 5.53 yield

$$g(x, z) = \int \sum_k \rho_a^k(Z, x, y, z) \mu_a^k(E, Z) dy \quad (5.56)$$

and

$$\varphi_p(E, Z, \rho, x, z) = \int \sum_k \rho_a^k(Z, x, y, z) p^k dy, \quad (5.57)$$

where

$$p^k \equiv r_e \lambda (Z^k + f_1^k), \quad (5.58)$$

which is defined for comparison with the atomic attenuation cross section μ_a^k ; that is, p^k by analogy corresponds to the cross section of the x-ray phase shift. By comparing Equations 5.56 and 5.58, it

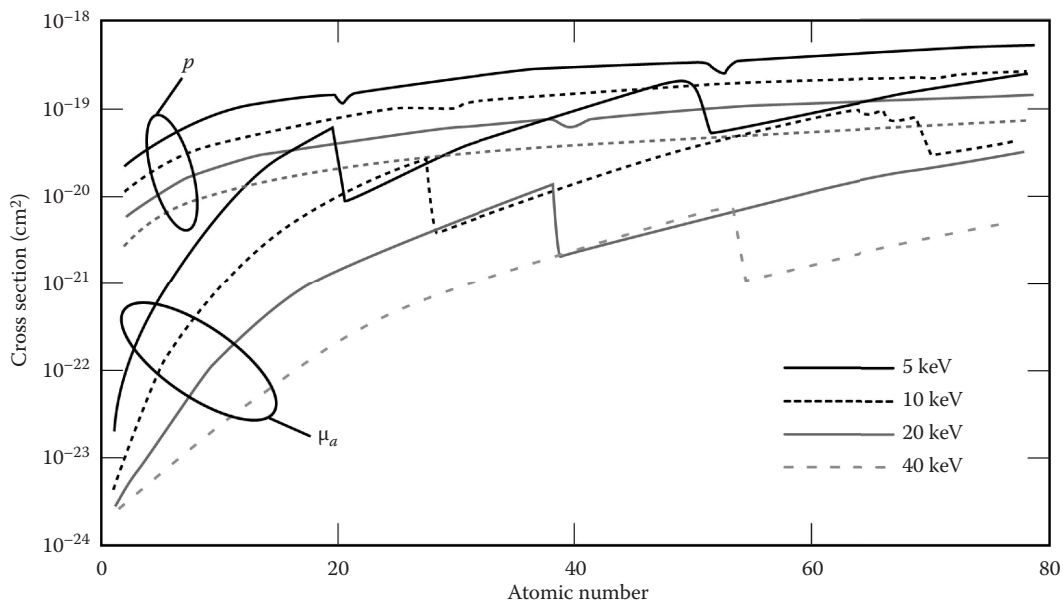


FIGURE 5.30 Plot of the x-ray phase (p) and atomic attenuation (μ_a) coefficients (or cross sections) as a function of atomic number for a selected set of energies. (Adapted from Momose, A., *J Synchrotron Rad.*, 9, 136–142, 2002.)

can be seen that the atomic density and composition contribute in the same manner, and the difference is attributed to p and μ_a . Therefore, the advantage of detecting the phase shift over detecting the attenuation is clear by graphing p and μ_a as functions of the atomic number, as shown in Figure 5.30.

It should be noted that p is always larger than μ_a and, especially for low-atomic-number elements, the ratio p/μ_a is about 1000. This means that remarkable improvement in sensitivity is achieved by using x-ray phase information in the imaging of materials with low- Z elements. In addition, high sensitivity contributes to reducing the x-ray radiation dose, which may be important, e.g., in biological specimens.

PROBLEMS

- 5.1 State or show why

$$E'_{\beta^-} < E_{p_0} - E_{B_{\beta^-}}$$

- 5.2 A company manufactures a shielding apron for use by physicians performing x-ray guided surgery. The shielding material is a fibrous form of metallic Pb. The aprons are heavy, and many users develop back injuries. The x-ray tube used for these procedures has a W anode and is operated at 150 kV tube potential. How could the apron be made with less mass but retain its shielding effectiveness? We are not asking for an exact analysis but for the student to recognize the design defect of the Pb apron.
- 5.3 A cross section is a measure of the interaction probability given by area per atom and sometimes given in units of b/atom. It is proportional to the mass attenuation coefficient (cm^2/g). Show the relationship between mass attenuation μ_m (cm^2/g) and cross section μ_a (b/atom).

5.4 Show that Equations 5.13

$$\ln\left(\frac{\Phi_0^E(E)}{\Phi^E(E, Z, \rho, y_\ell)}\right) = \mu(E, Z, \rho) y_\ell.$$

and 5.19

$$\ln\left(\frac{\int \Phi_0^P[S(E)] dE}{\Phi^P[S(E), \bar{Z}, \bar{\rho}, y_\ell]} \right) \approx \sum_i^n \mu_m^i(\bar{E}, Z_i) \rho_i y_\ell^i.$$

are essentially the same when accounting for a polyenergetic source and a material of more than one element. Hint: start by multiplying and dividing by ρ .

5.5 Show that Equation 5.21

$$\frac{d\Phi^E}{\Phi^E} = -\rho_a \mu_a dy_\ell$$

integrates to Beer's law.

- 5.6 Show that irradiance units, i.e., energy/(area \times time), are equivalent to power per unit area.
 5.7 Show that Equation 5.50

$$\phi^E(E, Z, \rho, x, z) = |\Psi(E, Z, \rho, x, z)|^2$$

reduces to a function of just attenuation and no phase.

- 5.8 A master brewer adds 5 g of calcium chloride per liter of water to improve the taste of her product. She wants to design an inspection device to measure uniformity of her feedstock. She will use thin plastic windows and a fluid stream thickness of 5 cm. What fraction of x-ray attenuation for 50 keV x-rays occurs because of the dissolved CaCl_2 ?
 5.9 Use the NIST program XCOM to obtain coefficients for total attenuation, photoelectric absorption, scatter, and pair production from 10 keV to 4 MeV for the explosive tri-aminotrinitrobenzene (TATB). Calculate the fraction of total attenuation arising from photoelectric absorption as a function of energy.
 5.10 You have an x-ray spectrum described by the polynomial $y = 57.132 + 3.9088E - 0.01819E^2$, from $E = 20$ keV to $E = 140$ keV. Plot this spectrum after filtering with 1 mm of Ta.
 5.11 What energy corresponds to 10% transmission through 1 in. of steel?
 5.12 Why is the x-ray mass attenuation coefficient most commonly used instead of the linear attenuation coefficient?

6 Radiation Transport Simulation

6.1 INTRODUCTION

In this chapter, we describe the types and methods of simulation of the passage of radiation through matter. This topic is usually referred to as radiation transport. We present names and sources of the major computer codes known for this purpose. We include a description of several applications where simulation proved important. This chapter begins by explaining the reasons and justifications for performing simulations.

After completion of this chapter, the student will have learned

- Situations in which radiation transport simulation is valuable or even essential
- Methods used for radiation transport simulation
- Computer codes that are applied to simulate radiation transport
- Representative applications of radiation transport simulation

6.2 WHY SIMULATE RADIOGRAPHY

To the novice, radiation transport simulation may seem unnecessary or frivolous. However, simulation is an essential tool for understanding actual radiographs and for computing aspects of the imaging system that are impossible to address experimentally. This enables better designs for detectors, sources, collimators, and enclosures. Less significantly, simulation is used for training and in establishing optimal radiographic variables with minimal experimental iteration. Examples where simulation is important include the following:

- To guide design of radiation enclosures, collimators, detectors, and sources
- To plan an expensive experiment or measurement, for example, a radiograph of a hydrodynamic implosion
- To understand a radiograph
- To understand sources of blur and scatter in a radiograph
- To design get-lost space for disposal of radiation once the image is captured
- To calculate energy deposit in estimating radiation absorbed dose (Chapter 7)
- To calculate energy deposit in detectors for derivation of the *point-spread function* (PSF)
- To change variables in physically difficult or impossible ways such as use of a point source, a monoenergetic source, or a source aimed in a specific direction
- To design test objects
- To teach radiographers and tomographers
- To explore effects of precisely known defects
- To determine the optimum radiographic view(s)

Next we discuss types, methods, codes, and radiation transport examples and reference publications illustrating some of these applications.

6.3 TYPES OF RADIATION COMMONLY TRANSPORTED IN SIMULATIONS

Our main interest is in photon transport, and for the most part, this discussion will be limited to high-energy x-ray and γ -ray transport. We learned in Chapter 4 that as high-energy photons interact

with matter, they produce energetic electrons and (in a few cases) neutrons. Thus, it is important to consider whether you should account for these secondary products in your simulation. Energetic electrons and neutrons can in turn produce photons. Some computer codes are capable of simulating coupled multispecies transport, but this should be approached cautiously.

Generally, when a simulation involves photons with energy less than 0.5 MeV, photon-generated electrons have a short enough range that it is not necessary to transport them. In this case, the electron energy is considered as deposited at the interaction site. In addition, at this photon energy (<0.5 MeV), neutrons are not produced by photon interactions or are produced in extremely small numbers.

In addition to photon radiation transport, proton and neutron transport can also be simulated. Neutrons and megaelectron volt protons are used for imaging (see Chapter 17). And, very high-energy, GeV, protons are used for imaging at Los Alamos National Laboratory (LANL) (Hogan et al. 1999; Morris et al. 2011).

6.4 METHODS OF SIMULATION

There are three main methods of radiation transport simulation that are relevant to x-ray and γ -ray radiography and computed tomography (CT). The three types are *discrete ordinates*, *ray tracing*, and *Monte Carlo*. All require a computer for practical problems.

6.4.1 DISCRETE ORDINATES

The discrete ordinates method is a deterministic method of solving radiation transport problems. It is a point-to-point solution and, in its basic form, accommodates neither time nor energy as a variable. This method lacks versatility in accommodating complex shapes and material variations. It is not useful for computing radiographs. But, it is the method of choice for so-called deep-penetration problems. This occurs in the design of shielding, where attenuation in the shield is often required to be 10^6 or more. In these problems, time dependence is not of interest. Energy dependence is easily incorporated by performing several calculations at different energies and then integrating them to simulate the source spectrum.

In the United States, the most easily available and widely used code suite of this type is DOORS3.2a: One, Two- and Three-Dimensional Discrete Ordinates Neutron/Photon Transport Code System. It is available from Oak Ridge National Laboratory's Radiation Safety Information Computational Center (RSICC). Their website describes the computational approach as follows (RSICC 2007):

The Boltzmann transport equation is solved using the method of discrete ordinates to treat the directional variable and weighted finite-difference methods, in addition to Linear Nodal and Linear Characteristic methods in TORT [author note, TORT is a computer code name] to treat spatial variables. Energy dependence is treated using a multigroup formulation. Time dependence is not treated. Starting in one corner of a mesh, at the highest energy, and with starting guesses for implicit sources, boundary conditions and recursion relationships are used to sweep into the mesh for each discrete direction independently. Integral quantities such as scalar flux are obtained from weighted sums of the directional results. The calculation then proceeds to lower energy groups, one at a time.

The publication by Odano et al. (2001) illustrates the classical problem type for applying the discrete ordinate method. In their application, the goal is design of shielding to meet specified dose rates at certain locations within the facility housing the national Spallation Neutron Source. The neutron source is described by Lisowski et al. (1990). This illustrates one type of radiation transport problem where it is impractical to arrive at an acceptable solution by trial and error since it would require pouring concrete and then destroying the facility to try the next geometry.



FIGURE 6.1 Example of a scene produced using a computer technique called ray tracing. This image illustrates reflection of the balls in the checkered surface, highlights on the balls from lighting, reflection of the highlights in the checkered surface, and shadows on the top of each ball.

6.4.2 RAY TRACING

Ray tracing has its roots in scene rendering and animation. In that case, the rays being traced are visible light. The hallmark of this method with visible light is the creation of realistic scenes with highlights, shadows, and surface subtleties (Glassner 1989). Imagery for video gaming is mainly created by ray tracing. Figure 6.1 illustrates a scene produced by ray tracing.

When applied to the simulation of an x-ray or γ -ray radiograph, rays being traced pass through surfaces and interact in the volume of objects in the scene. Generally, rays begin at the source and proceed through an object to an element (pixel) of the detector. This is depicted in Figure 6.2. Different ray-tracing codes present the computed radiograph in different units, but in each case, the magnitude represents the transmission of photons that occurs along each specific ray.

The overarching characteristic of ray tracing as a method of radiography simulation is that a projection through an object is produced. The characteristic that makes this practical is that computational complexity is modest compared to the Monte Carlo method (to be discussed in Section 6.4.3, Monte Carlo Method).

In ray tracing, the source is a point. Finite size sources can be generated by acquiring multiple points to represent the geometry required. Definition of the object model to be radiographed is accomplished by a variety of methods. Finite-element mesh models in various coordinate systems are one method. This is especially convenient when a mesh model is prepared for finite-element analysis, such as stress-strain, hydrodynamic, or thermal. Objects can be described as solids of common solid geometry shapes. Unions, intersections, and differences of solids enable complex objects to be defined. Lastly, an electronic file in the format used for computer-aided design (CAD) can serve to define the object. This is a powerful tool for testing the inspectability of a candidate design before any fabrication takes place. With this option, the file representing a trial design serves as input to the radiation transport simulation. In ray tracing, the detector can have a finite size and composition, the latter incorporating detector response.

6.4.2.1 XRSIM X-Ray Simulation

X-ray simulation (XRSIM) is a ray-tracing simulation code developed at the Iowa State University/Center for Nondestructive Evaluation. We could not find out if XRSIM is an acronym, perhaps it stands for x-ray simulation. In 1999, XRSIM was licensed exclusively to NDE Technologies* for

* <http://www.ndetechnologies.com/index.html>, NDE Technologies, Inc., 1785 Sourwood Pl., Charlottesville, VA 22911, phone: (866) 633-7461.

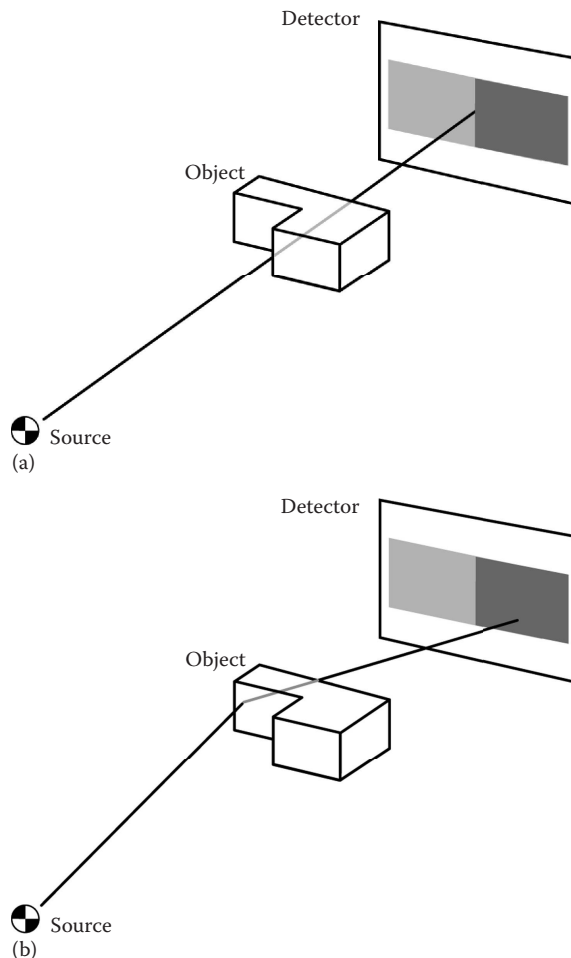


FIGURE 6.2 Schematic of the three major subsystems of an x-ray imaging system. Here we depict an object with two distinct thicknesses. (a) A single ray (in this case, it represents a primary photon) as may be computed in a ray-tracing code. (b) How a ray can be scattered (secondary or scattered photon) within the object. Scattered photons result in a degraded image. Thus, it is important to reduce nonprimary photons.

commercialization. Most of the details within XRSIM are proprietary and not discoverable by the user. The overview document (XRSIM 2015) describes the code as consisting of three base modules. The generator module creates the x-ray spectrum of the source that will be ray traced. Some versions of XRSIM claim capability for photons from 1 keV to 20 MeV.

The detector module contains the information regarding detector response. Eight x-ray films and one flat-panel detector are included. Because the details are hidden, we do not know if XRSIM contains the energy-dependent detector response and PSF or what approximation of these is made. The final module in XRSIM is the graphical user interface.

All versions of XRSIM are designed to be used with a CAD program. That is, XRSIM expects object model input in CAD format(s). XRSIM is strongly oriented toward film detection. Results are even produced as negative images like film. An example of positive and negative images of the same object is shown in [Figure 6.3](#).

XRSIM does have a response function for one flat-panel detector. We cannot determine from the manual or any publications what the output units are for the flat panel.

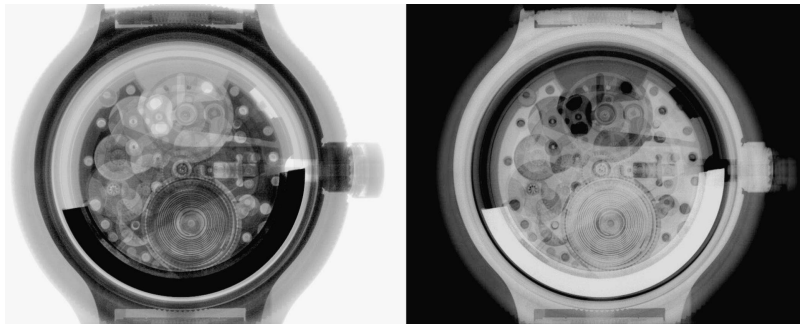


FIGURE 6.3 A positive digital radiograph of a watch is shown on the left. In this image, the brightness of the image increases with increased x-ray signal. This means that the areas of highest x-ray signal in the detector, such as the area outside the watch, are shown as white. This is typical of a digital detector. On the right, a negative image of the same watch is shown. This is the type of response that is produced by film. Black areas in film correspond to areas with the largest amount of energy deposited by x-rays. If the gray scale is inverted, a digital image will look the same as the image on the right. This is sometimes done to make the image look like film to radiographers who are used to looking at film images. For digital radiographers and tomographers, this is usually not done.

XRSIM is unique among ray-tracing codes in that it contains a scatter approximation within the basic ray-tracing package (Inanc and Gray 1997; Inanc 2002b, 2003). This makes a first-order approximation of object scatter arriving at the detector plane. We addressed scatter in detail in Section 5.2.1.2. Its importance can be appreciated by referring to Figure 6.2. Scattered photons arrive at the detector having traveled some path other than a straight ray. Inanc (2002a) shows that photons scattered in an object can exceed primary photons by several times in realistic imaging scenarios, as shown in Figure 6.4. It plots the scattered photons per unit area per unit time, Φ_s^P , divided by the primary photons per unit area per unit time, Φ_p^P (Inanc uses the term *uncollided*) at the center of the exit side of a 100×100 mm steel plate. The plate is flooded with monoenergetic x-rays normal to the surface. In Figure 6.4a, the plate is 10 mm thick, while in Figure 6.4b, the plate is 30 mm thick. Figure 6.4 shows that for 100 keV x-rays, there are more than 10 times as many scattered photons as there are (transmitted) primary photons for the 30-mm-thick plate. This makes for a difficult imaging environment since the primary photons carry the desired information and they are buried in a swamp of scattered photons. This is depicted schematically in Figure 6.5. Here, the line-outs separately depict the profiles of object scattered photons, primary photons, and total response at the detector for the geometry given in Figure 6.2.

6.4.2.2 HADES, a Radiographic Simulation Code

The second ray-tracing code we will address in some detail is HADES. Developed at Lawrence Livermore National Laboratory (LLNL), HADES is backward compatible with a predecessor code called XRAY (Aufderheide et al. 2001). While HADES's first capability is x-ray radiography from 1 keV to 100 MeV, it is now capable of simulating neutron radiography from thermal to 100 MeV and proton radiography in the 1 MeV to 100 GeV energy range (Aufderheide and Henderson 2004a; Aufderheide et al. 2005). Phase-contrast radiography is under active development (Aufderheide et al. 2004b). HADES can be shared with collaborators by contacting one of the authors.*

In HADES, the source can be at a point, or it can be distributed in space (in three dimensions if necessary). HADES always assigns a source angular distribution as required to fill the defined detector. When the source is spatially distributed, HADES is, in effect, running many point-source calculations and integrating the result. Similarly, calculating many single energies and integrating

* aufderheide1@llnl.gov; schach@llnl.gov.

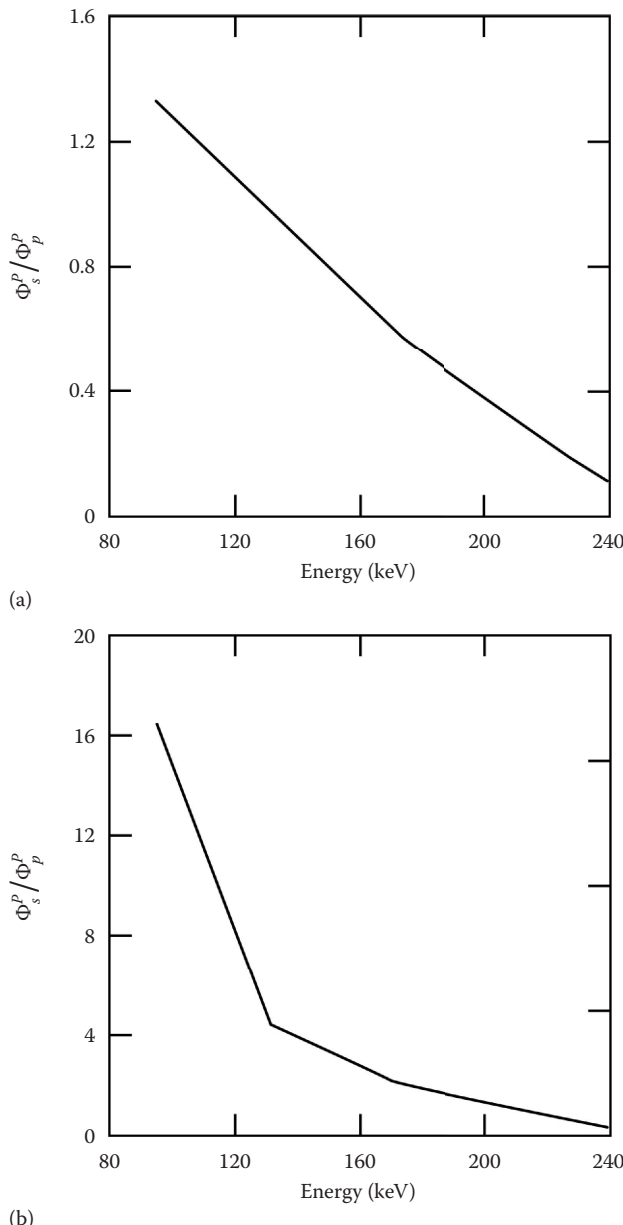


FIGURE 6.4 The ratio of scattered photons, Φ_s^P , to primary, Φ_p^P (direct from source without interaction), at the center of the exit side of a 100 mm square steel plate as a function of energy. This is calculated for mono-energetic x-rays incident normally to the plate over the entire surface. (a) The plate thickness is 10 mm. (b) The thickness is 30 mm. For the thicker plate and lower incident photon energies, there are more, by a considerable margin, scattered photons than primary photons. This makes it difficult to acquire a good image because only the primary photons contribute to the image. (Data are from Inanc, F., Impact of the Low Energy Scattering in the Radiography Simulations, *Review of Quantitative Nondestructive Evaluation*, 21, 582, AIP, 2002.)

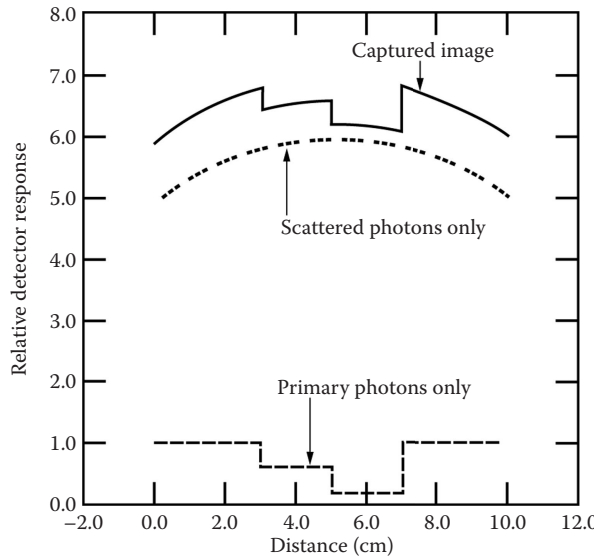


FIGURE 6.5 Notional profiles showing relative detector response as a function of position along the stepped object depicted in Figure 6.2. The lower dashed line represents the primary photons that are transmitted through the object. The middle line represents only scattered photons, while the top line is the total detector response, the sum of primary and scattered photons. In addition to the loss of contrast seen in the captured image profile, the scattered photons also contribute to image noise. In extreme cases, scatter can obliterate the desired image.

approximates a polyenergetic source spectrum. At present, HADES does not contain a source library or model. The user provides the source energy distribution as input.

Another way to account for a distributed source that requires less computational time than performing many point-source calculations is to do a single-point-source image and convolve the result by a source blur function. HADES provides this option.

The user defines the detector for HADES. This is usually a planar area detector of a certain overall size and dimension of each detector element (pixel). The energy dependence of detector response (magnitude) and the energy-dependent detector blur function (shape) are also provided as inputs. We often estimate the detector blur by performing a separate Monte Carlo simulation, which is then used as HADES input.

The object model is defined for HADES by some combination of meshes and solid objects. HADES is designed to be compatible with meshes of the type used for finite-element calculations. Solids of almost any geometry can also be defined.

For each pixel in a simulated radiograph, HADES computes attenuation times path length over the entire ray (potentially through many different materials). For a single material transmitted, irradiance is given by Equation 5.11, i.e.,

$$\Phi^E(E, Z, \rho, y_\ell) = \Phi_0^E(E) e^{-\mu(E, Z, \rho)y_\ell}, \quad (6.1)$$

where

$\Phi^E(E, Z, \rho, y_\ell)$ is the transmitted irradiance at monochromatic energy E through a thickness y_ℓ for a single material of atomic number Z with a density of ρ in energy per unit area per unit time;

$\Phi_0^E(E)$ is the incident irradiance in energy per unit area per unit time at monochromatic energy E ; y_ℓ is the thickness along the direction of x-rays of the single-material uniform absorber in cm; $\mu(E, Z, \rho)$ is the linear attenuation coefficient in cm^{-1} at energy E for a single material with atomic number Z and mass density ρ .

Rearranging Equation 6.1 yields

$$\ln\left(\frac{\Phi_0^E(E)}{\Phi^E(E, Z, \rho, y_l)}\right) = \mu(E, Z, \rho) y_l. \quad (6.2)$$

For an object with multiple materials, HADES computes the sum of all $\mu(E, Z, \rho)y_l$ for all materials that each ray passes through. This is the form (Equation 6.2) that most users chose for each pixel in a digital radiograph. HADES uses this form since it is oriented toward digital imaging. Note that digital radiography (DR) is quite different from film radiography. One key difference is that with film, there is no normalization by the incident irradiance, $\Phi_0^E(E)$.

6.4.2.3 Ray-Tracing Summary

The two codes XRSIM and HADES are not the only ray-tracing simulation codes. There are ample other examples in the literature (Duvauchelle et al. 2000; Ahn et al. 2003; Guillemaud et al. 2003; Mery et al. 2005).

6.4.3 MONTE CARLO METHOD

For five decades, the Monte Carlo method* has been applied to radiation transport problems of high importance (Metropolis 1987). It is helpful to think of this method as a computational analog of the actual physical process. For the sake of discussion, we will talk about simulations involving photons, though early applications were more focused on neutron simulations of fission.

When using the Monte Carlo method for photons, a source photon is created with energy and direction as specified or sampled from a source distribution. The “dice” are computationally rolled to determine where this photon first interacts in the specified geometry and then again to determine which interaction process takes place and what secondary radiation is produced, etc. Secondary photons and electrons are transported in a similar fashion. This is a powerful technique supported by compilations of probabilities (reactions,[†] attenuation coefficients, and angular distributions). It is the best method of treating scattered and secondary radiation. When the source photon and all its progeny have either escaped the problem or been absorbed, the calculation returns to the beginning, i.e., creation of another source photon, and the process is repeated until the statistical uncertainty is reduced to the desired level. The Monte Carlo technique suffers from the same statistical limitations imposed in nature. To get a precise answer, you have to run a lot of individual source photons. This makes Monte Carlo calculations computationally intensive.

A limitation of Monte Carlo is that it treats photons as particles. Because of this, any wave effects such as refraction and diffraction, are neglected. For example, this can be a significant omission when simulating low-energy (~keV) photons at very high spatial resolutions (~μm). For more on the wave nature of photons, see Section 5.5, x-ray Phase Effects.

The source in a Monte Carlo photon simulation is typically sampled from a probability energy distribution.[‡] The probability energy distribution is given by the number of photons versus energy. Additionally, the photon source can be directional (e.g., by specifying a limited solid angle). If one uses directionality, it needs to be used very carefully since it can yield inaccurate results. If you restrict source photons to a solid angle that fills the detector, you are not simulating scatter correctly. And the source can be any physical configuration imaginable to the person doing the simulation. This is one characteristic that makes simulation a powerful tool. A source can be configured as a

* The Monte Carlo method is a computational approach for simulating the behavior of physical systems. It is distinguished by being stochastic or nondeterministic and employs random numbers in repetitive calculations. The name comes from the city in Monaco where presumed random numbers appear on roulette wheels. It is capitalized by convention.

[†] Reactions for photons can include photoneutron (γ, n) and pair production. More are possible for neutrons.

[‡] It is difficult to accurately measure or simulate the energy distribution.

point, line, surface, or volume, and these can be combined. Keeping track of time is generally not of interest in high-energy photon (x-ray or γ -ray) radiography, but with neutrons, time is often an important variable.

Monte Carlo simulations are often used to better understand the interactions of high-energy photons and particles with detectors. For example, the user could input the geometry and material for a high-purity germanium (HPGe) detector and instruct the code to keep track of the pulse-height (related to energy deposited in the detector) spectrum* (covered in detail in Chapter 9, Radiation Detectors). In this case, the energy per photon interaction is recorded, also known as single-photon counting or energy discrimination detection. What is important to note is that the simulation needs to mimic the physics that is being measured. Another example would be the simulation of an ion-chamber measurement. In this case, you input the geometry and gas used in the detector and then instruct the code to keep track of the total energy deposited integrated over many photon interactions. This is known as current integration or non-energy discrimination and does not result in a pulse-height spectrum.

A new application of Monte Carlo is the simulation of imaging. Again, details for the detector are required. Let us assume that the detector is a flat photodiode panel with a gadolinium oxysulfide (GOS) scintillating screen; then all the components in the detector should be input into the Monte Carlo simulation. This includes the cover, empty spaces, conversion screen, conversion screen backing material, glass substrate for the photodiodes, backing plate, and whatever else is behind the detector. For this detector, the light output is proportional to energy deposited (non-energy discriminating) in the scintillator, and the panel electronics and signal processing have been adjusted to respond linearly to light. So, the Monte Carlo code should be directed to keep track of the sum of the energy deposited in the scintillating layer, which is proportional to the scintillator light output. If the user wants picture elements—pixels—for an image, then the detector model needs to be created with the necessary number, size, and geometry of the detector elements in order to simulate an image. For this imaging example, we would create pixels in the scintillator layer.

With Monte Carlo, any source, detector, or object model geometry that can be described can be computed. Most Monte Carlo codes accept input of solid bodies such as planes, spheres, cones, cylinders, and more complex shapes. Regions can be defined as unions, differences, etc. Mesh definition of input is also accommodated. This facilitates coupling of computation of dynamic phenomena such as fluid flow with simulation of the radiograph. Input in the format of popular CAD packages is also possible.

As mentioned earlier, the Monte Carlo technique suffers from the same statistical limitations imposed in nature. For this reason, Monte Carlo simulations are not often used to generate an image. We can see the issue if we consider a 1 megapixel image with an average transmission through the object of 1%. To achieve 1% statistical uncertainty in each detector element requires 10^4 transmitted (and counted) photons in each detector element. The number of source photons, S_γ , required is given by

$$S_\gamma = (\text{pixels})(\text{required photons/transmission})$$

or

$$S_\gamma = (10^6)(10^4/10^{-2}) = 10^{12}. \quad (6.3)$$

We estimate that a problem this large would require 20 to 100 days on a single desktop personal computer (PC) for just one radiograph. Simulation of CT data would take years.

Computing power is overcoming this obstacle to using the Monte Carlo method for imaging. Both Monte Carlo N-Particle (MCNP) (X-5 Monte Carlo Team 2003) and COG (Buck and Hall

* Sometimes referred to as a γ -ray spectrum.

1999) have imaging options under development. Buck and Hall report using 500 processors on some problems.

As computers have become faster and more capable, the number of problems that can be addressed using Monte Carlo has expanded. General-purpose Monte Carlo radiation transport codes are easily available; many versions can be run on an affordable computer such as a PC or Macintosh. A sampling of Monte Carlo codes and where to find them is presented in Table 6.1. We offer a note of caution. Monte Carlo radiation transport codes are plentiful. Be cautious about using them beyond their original intent. Many were written for a specific purpose and utilize omissions or approximations that were adequate for the original application but are inaccurate in a different application. Codes described in Table 6.1 have a wide user base and are intended to be general purpose. Even with these, however, coaching from a knowledgeable user is a great asset.

Monte Carlo simulations open a window for understanding that cannot be approached experimentally. Photons can be made perfectly monoenergetic and perfectly on axis. Scatter can be counted separately from primary radiation. Scatter contributions from collimators, detectors, objects, and even air can be separated. Density and composition in Monte Carlo simulations are input variables that are not constrained by room temperature and pressure. You can simulate many-times-normal density for a material if that is what you want to study. You can make a surface or volume a black hole for photons so that any photon that goes to a surface or inside a volume is eliminated.

6.4.3.1 Los Alamos National Laboratory Monte Carlo N-Particle (MCNP) Code

The roots of the Monte Carlo method of simulating radiation transport are at LANL, where the first neutron transport calculations using Monte Carlo were performed (Shultis and Faw 2005). It seems fitting that the most widely used (according to Google) Monte Carlo radiation transport code today is LANL's MCNP. LANL provides support for users in the form of classes, users groups, and consulting. The original motivation for the code was the study of nuclear weapon design technology.

Contemporary Monte Carlo simulation studies using MCNP include oil-well logging (Wielopolski et al. 2005), shielding (Kharrati et al. 2007), radiation detector design (Farsoni and Hamby 2005), radiation therapy (Konijnenberg et al. 2007), and dosimetry (Bohm et al. 2003). MCNP is available from the RSICC at Oak Ridge National Laboratory. The current version (2015) is MCNP6.

TABLE 6.1
General-Purpose Monte Carlo Radiation Transport Codes

Code Name	Motivation	Originating Organization	Reference
MCNP	Weapons physics	Los Alamos National Laboratory, USA	X-5 Monte Carlo Team 2003
Mercury	Modern C code/million processors	Lawrence Livermore National Laboratory, USA	Brantley et al. 2013
COG	Radiation detectors	Lawrence Livermore National Laboratory, USA	<i>COG User's Manual 2002</i> (http://cog.llnl.gov)
TART	Weapons physics	Lawrence Livermore National Laboratory, USA	Cullen 2003 (http://home.comcast.net/~redcullen1/)
Peregrine	Radiation dosimetry	Lawrence Livermore National Laboratory, USA	NOMOS 2001; Hartman Siantar 2001
GEANT	Particle physics	European Organization for Nuclear Research (CERN), border between France and Switzerland	Agostinelli et al. 2003 (http://geant4.web.cern.ch/geant4)
TIGER	Electron photon	Sandia National Laboratories, USA	Halbleib et al. 1992
EGS	High-energy physics	Stanford Linear Accelerator Center, USA	Nelson et al. 1985
EGSnrc	General purpose	National Research Council, Canada	Kawrakow and Rogers 2006 (http://www.irs.inms.nrc.ca/EGSnrc/EGSnrc.html)

The MCNP website describes the FORTRAN code as transporting photons by accounting “for incoherent and coherent scattering, the possibility of fluorescent emission after photoelectric absorption, absorption in pair production with local emission of annihilation radiation, and bremsstrahlung. A continuous-slowing-down model is used for electron transport that includes positrons, x-rays, and bremsstrahlung but does not include external or self-induced fields.” Therefore, MCNP cannot be used to simulate the interaction between electrons and electromagnetic fields. However, it does a good job of simulating the interaction of electrons with matter, and this is used to simulate spectra from linear accelerators (linacs) and x-ray tubes. This is useful since it is very difficult to measure linac and x-ray tube source spectra.

6.4.3.2 Lawrence Livermore National Laboratory TART, COG, Peregrine, and MERCURY Monte Carlo Codes

Development of the Monte Carlo method of radiation transport at LLNL also has a half century of history. TART (Cullen 2003) was developed to serve the nuclear weapon design community, and COG (COG 2002) focused on detector and diagnostics design. In the 1990s LLNL developed an all-particle Monte Carlo code named Peregrine aimed at planning for radiation therapy. It is exclusively licensed to North American Scientific.* It is used in five medical centers in the United States and Canada. This is the first application of the Monte Carlo method to radiation therapy planning.

Historically, LLNL codes have been less accessible to non-LLNL users, and less support is offered to users than has been the situation at LANL. LLNL offers no instructional classes in the use of TART or COG. In the 2000s, LLNL launched a major project to create a new code, called MERCURY (Procassini et al. 2005), that would be written from the beginning in C programming language. The historical codes were written in FORTRAN. MERCURY is now a highly capable Monte Carlo code for most radiation transport problems (Brantley et al. 2013).

6.5 EXAMPLE PHOTON TRANSPORT SIMULATIONS

We present in this section a series of examples where simulation of photon transport provided essential information or was a vital link in the interpretation of an experiment.

6.5.1 MCNP USED IN ANALYSIS OF ALBEDO FROM LEAD AND CONCRETE

In 1999, a Department of Energy laboratory asked us how close one could position the back wall of a radiography facility without serious ill effect on images when using a 9 MV linac bremsstrahlung spectrum and a flat-panel photodiode array detector. A companion question was whether it made any difference what material was used to construct the wall. This seemed like a straightforward measurement to perform, but the result surprised us. We measured that the albedo was higher than we expected and the albedo from concrete exceeded lead. In order to understand the result from these measurements, we turned to MCNP4B Monte Carlo modeling (Logan and Schach von Wittenau 2001).

The albedo measurements used a 50-mm-diameter, 150-mm-thick W cylinder (shield) to absorb x-rays from a 9 MV linac source and to create a 50-mm-diameter circle on the flat-panel photodiode array detector that was essentially free of primary radiation from the source. Any signal in this portion of the flat-panel photodiode array detector must come from scattered, not primary, radiation. The source was well collimated, so we had reason to believe that generalized room scatter should be small. Therefore, there could be but two sources of flat-panel photodiode array detector response behind the W shield: (1) scatter within the flat-panel photodiode array detector and (2) radiation scattering from behind the flat-panel photodiode array detector back into the detector, referred to as back-shield albedo. This configuration is shown schematically in Figure 6.6. We varied back-shield

* <http://www.nasmedical.com/page?id=1468>.

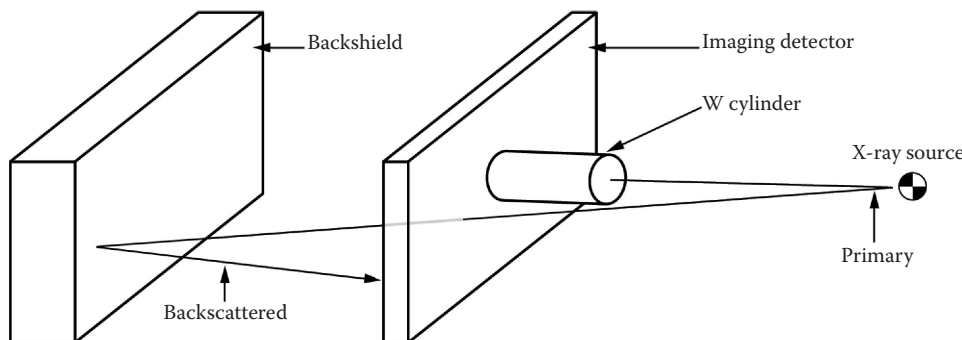


FIGURE 6.6 Schematic of the geometry used to measure internal detector scatter (not shown), secondary photons (not shown), and back-shield scatter returned to the detector as shown. The W cylinder is 50 mm in diameter and 150 mm long. A thickness of 150 mm is sufficient to limit transmission to $<10^{-6}$ for the spectrum from a 9 MV bremsstrahlung linac.

albedo by material (Pb and concrete). Each material was studied as a function of distance from the back of the detector. Note that albedo is only a function of material and incident spectrum (not varied in this study), while the amount measured by the detector is a function of material and distance away from the detector.

Our first surprise was that the response in the flat-panel photodiode array detector within the W shielded region was quite high, 8% of the radiation detected elsewhere in the detector, even when no back shield was in place. This response comes mostly from radiation that scatters within the flat-panel photodiode array detector. We revisited this issue and in [Section 6.5.3](#) describe scatter blur within a flat-panel photodiode array detector. In spite of the high level of scatter within the detector, the detector response to back-shield albedo could be observed when the back shield was at 1 m distance from the detector. The detector response from a concrete back shield at 1 m distance was 0.4% of the detector response in the unshielded region of the detector. The concrete albedo is about 3.3 times that of Pb.

We applied MCNP4B to this problem. Our first task was to verify that the concrete and Pb back shields we used experimentally were of sufficient thickness such that additional thickness would have no effect on the albedo. MCNP results show that photons backscattered from concrete arise from events no more than a few hundred millimeters into the back shield. Similarly for Pb, photons backscattered arise from events no more than a few dozen millimeters into the back shield. Our back shields were of sufficient thickness to represent back shields with greater thickness.

The result of an MCNP calculation with the 9 MV linac (bremsstrahlung) spectrum incident at 90° to the surface of the concrete back shield was that a photon emerged from the concrete surface once for every five photons incident. For Pb, the albedo was 1 in 23. Insight can be gained by examining the energy spectrum of backscattered photons shown in [Figure 6.7](#). Most of the backscattered photons have been Compton scattered (energy is a few hundred keV) or arise from positron annihilation (energy of 511 keV) or fluorescence (in Pb at 75 keV). Because of its higher photoelectric attenuation coefficient, Pb is more effective at preventing the escape of these photons than is concrete. In summary, for the flat-panel photodiode array detector, no material should be placed within 6 m, and Pb is always preferred over concrete.

6.5.2 MCNP APPLIED TO COLLIMATOR DESIGN FOR A 9 MV LINAC

The LLNL 9 MV linac facility has massive collimators made of Pb for digital imaging. The entire imaging system is shown in [Figure 6.8](#). A flat-panel photodiode array is mounted on an Al frame in the foreground. Three Pb collimators are painted black and mounted on the blue stand. Each lead

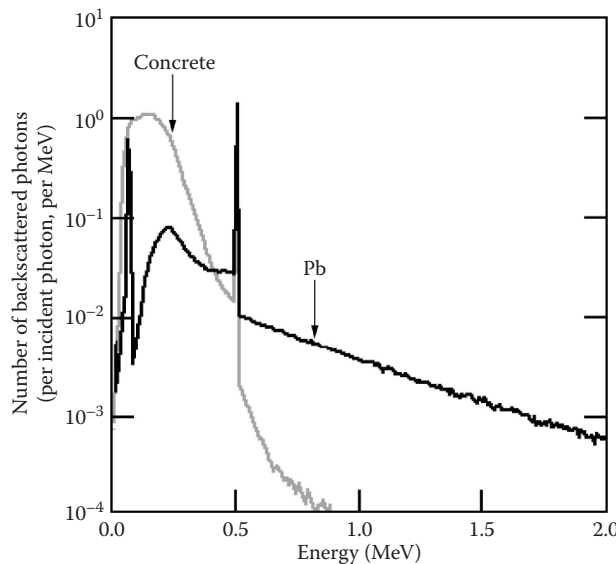


FIGURE 6.7 Calculated result of albedo photon spectra from concrete and Pb using MCNP4C. Incident x-rays were a 9 MV bremsstrahlung spectrum in each case. Considerably greater numbers of photons (and irradiance) return from concrete than from Pb, mainly at energies below 0.400 MeV. The peak at 0.511 MeV is due to pair production and is higher for Pb than concrete. At energies greater than 0.511 MeV, Pb has larger albedo than concrete, but these higher-energy photons account for a small portion of the total albedo.



FIGURE 6.8 Photograph of the 9 MV facility at LLNL showing the linac suspended from an overhead crane in the background and flat-panel photodiode array detector (gray color) visible in the foreground. In between on the blue stands is the collimator system (black) known as StonehengeII. Each of the collimators is made of Pb and is 100 mm thick.

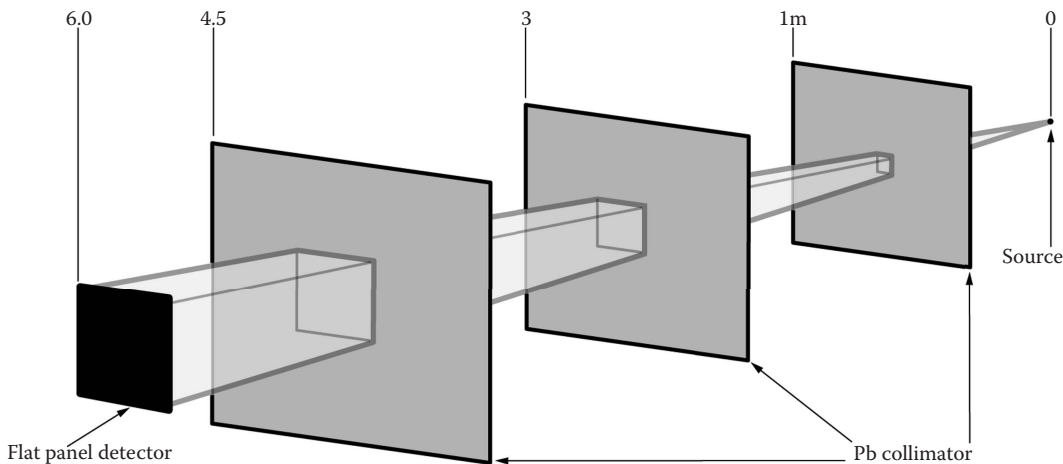


FIGURE 6.9 Schematic of the source, detector, and StonehengeII collimators shown in the photograph in Figure 6.8. Each collimator position and the flat-panel detector are labeled with the distance from the source. The object is typically placed on a motion platform (not visible) at about 5.8 m from the source (just in front of the detector). This experimental bay is configured so that 14 m of air-filled space exists behind the detector before x-rays enter the back concrete wall. This distance reduces x-rays scattered from the back wall into the detector to a negligible amount.

collimator is 1.2×1.2 m and 0.1 m thick. The 9 MV linac is mounted from an overhead crane with the source 6 m from the imaging panel. This system is shown schematically in Figure 6.9.

When collimators are not present between the linac source and the flat-panel photodiode array detector, two bad things happen: (1) primary radiation scatters from the walls, floor, ceiling, and air, creating an intense scattered-radiation field at the flat-panel photodiode array detector, and (2) primary radiation destroys electronic components in the flat-panel photodiode array detector after a few images are acquired. The flat-panel photodiode array detector is designed with sensitive electronics in the “frame” surrounding the active imaging area.

During the design of these collimators, we used MCNP4B to estimate the effect of collimator material and spacing on performance as measured by scattered photons at the flat-panel photodiode array detector location. We considered steel, Pb, and depleted uranium (DU) as candidate collimator materials. DU is essentially ^{238}U and the best collimator material for this application. It causes the fewest scattered photons into the imaging area of the flat-panel photodiode array detector. The US government has 700,000 tons of unwanted depleted UF_6 (ANL 2015), so incorporating a ton or two into this collimator should be a welcome application. However, because of DU’s mild radioactivity and toxicity, DU collimators must be canned with thin stainless steel. This stainless steel can must cover the inside of the collimator bores. MCNP simulations reveal that when the stainless steel can is included, DU has no advantage over Pb. Pb is also a toxic material, but a thin layer of paint (black in this case) is sufficient covering to protect personnel. The black paint has a little effect on performance.

6.5.3 MCNP TO DETERMINE SCATTER BLUR WITHIN A FLAT-PANEL PHOTODIODE ARRAY DETECTOR

Flat-panel photodiode array detectors were developed for medical imaging, but as soon as they became available, nondestructive evaluation (NDE) groups began using them for industrial applications. They have large active areas and nearly perfect geometry (flat and exact pixel pitch) that lends itself to high-quality DR and CT, and are easy to use.

These panels have a serious drawback for industrial use above an x-ray tube voltage of 200 kV. They are relatively massive and become the source of considerable scatter. We examined this in detail (Schach von Wittenau et al. 2002b) for imaging with a 9 MV linac x-ray source.

As part of this study, we examined the relative contribution to flat-panel photodiode array detector response from a variety of sources. This work utilized MCNP4C. It is our opinion that the LLNL 9 MV facility is the best there is for imaging. The original facility design is excellent and spacious, thereby minimizing scatter from walls.* Collimation has been investigated and improved over the last two decades as DR replaced film. A full description of the room, collimator construction, and results are given by Schach von Wittenau et al. (2002b). We found that 97% of the detector response comes from primary photons directly from the linac source. For the LLNL system, the 3% scatter (not primary) response comes from the collimator within the linac (1.7%), room walls, ceiling and floor (0.7%), air (0.4%), and the Pb collimator assembly affectionately known as StonehengeII (0.2% if we assume perfect alignment).

The response of the flat-panel photodiode array we studied[†] to x-rays arises solely from energy deposited in the scintillating layer. This energy deposit produces light in proportion to energy deposited, which is then sensed by the light-sensitive photodiodes making up the array.

The flat-panel photodiode array detector we studied presents an areal density to the x-rays of 2.61 g/cm². The single most massive layer in the panel contains 26% of the overall detector mass and is located 25 mm behind the scintillating layer. Here we use *behind* to indicate the direction away from the x-ray source. This massive layer is an Al plate whose purpose we presume to be structural. For megavoltage radiography, this amount of mass and the location have significant deleterious impact on image quality. The dominant photon interaction mechanism at these energies is Compton scattering, which is approximately proportional to electron density.

The scintillator in this flat-panel photodiode array detector system is only 1.4% of the electron density of the total detector assembly. So, about 99% of the photon interactions occurring in the flat-panel photodiode array detector take place somewhere other than in the scintillator. Further, the flat-panel mass is distributed over 37 mm thickness, causing scattered photons to deposit energy in the scintillator several centimeters from their original primary path. This causes an extreme form of blurring. In visible-light optics, the term *veiling glare* is applied to stray light at an image plane. This term has been adopted to describe a similar effect in image intensifiers (Seibert et al. 1985). Flat-panel photodiode array detectors have similar characteristics.

We used MCNP4C to direct a pencil beam of photons normal to the center of the flat-panel photodiode array detector. We performed 46 separate MCNP calculations for 46 separate monoenergetic photon energies ranging from 10 keV to 10 MeV. The photon energies calculated were spaced logarithmically with about 14 values per decade of energy. We used 11 separate layers to represent the flat-panel photodiode array detector. From the front (x-ray side) to the back of the flat-panel photodiode array detector, our model included a protective cover of carbon fiber composite, followed by an air gap. The scintillating screen has four layers: a protective coating on the front and one on the back, a substrate, and the scintillator. The scintillator consists of Gd₂O₂S plus urethane binder. We neglected the thin Si-based electronics but modeled the glass substrate. Behind the glass is a polypropylene pad, an aluminum support plate, an air gap, and an aluminum back cover. Complete details of layer thicknesses, compositions, and densities are published (Schach von Wittenau et al. 2002b).

We desired to get two things from each monoenergetic simulation. The first is the shape of the distribution of energy deposited in the scintillator by primary x-rays and all secondary (nonprimary) photons arising in the flat-panel photodiode array detector. This is the detector PSF. The second object of our simulation was the amount of energy deposit over the entire area (integrated over all detector elements) encompassed by the PSF.

* Legend has it that Dick Bossi was the reason this facility was constructed to be the best. It even had access for a fully loaded tractor/trailer. We owe you, Dick.

[†] Varian Paxscan 4030. <http://www.varian.com/xray/prd002.html>.

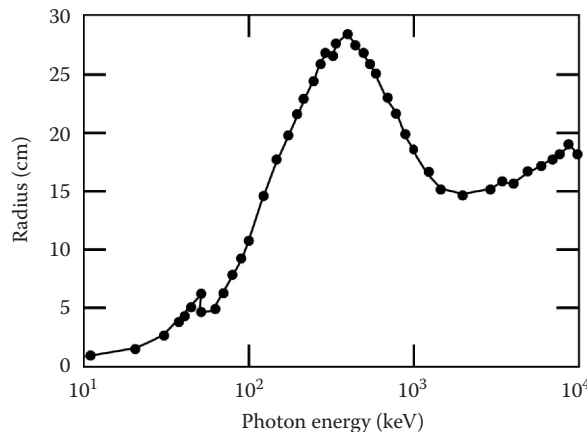


FIGURE 6.10 For monoenergetic x-rays incident on a flat-panel photodiode detector, the plot is the radius of the circle needed to account for 99% of the detector response as a function of energy. Many incident monoenergetic x-rays at a fixed location (at 0.0 radius) on the detector are transported and averaged to produce this plot.

For each of the 46 different monoenergetic simulations, we determined the energy deposition (both primary and scattered) in the scintillator (irradiance times the scintillator response) as a function of radius from the normal incident photon. This approach is a direct computation of the PSF. The results can be expressed several ways, but one of the most graphic is the radius required to contain 99% of the energy deposited in the scintillator. This is plotted as a function of monoenergetic photon energy in Figure 6.10. This is a stunning result! For the photons used in producing images with a 9 MV source, one has to include a circle of radius 15–30 cm to account for 99% of the flat-panel photodiode array detector response. Internal scatter in the flat-panel photodiode array detector at lower energy, ≤ 100 keV, is reduced compared to ≥ 200 keV energies. At 100 keV photon energy, one has to include a circle of ~ 8 cm radius in order to include 99% of the energy deposited in the scintillator. Such poor spatial resolution system performance is often missed if an improper measurement of the PSF is obtained. This is discussed in more detail in Chapter 14.

From each of the same 46 monoenergetic simulations, we computed the average energy deposited in the entire flat-panel photodiode array detector. This average energy (per source photon) is shown in Figure 6.11. The light produced in the scintillator is proportional to the photon energy deposited. The photodiode response is proportional to the light produced in the scintillator. The jump at 50.2 keV is the result of the K absorption edge of Gd, which is in the scintillator ($\text{Gd}_2\text{O}_2\text{S}$). The oxygen and sulfur K edges are below 3 keV and thus not shown in Figure 6.11. From Figure 6.11, it is evident that the average detector response per incident photon drops steadily from 50 keV to about 500 keV. For the novice, this behavior is probably not expected. It occurs because the interaction probability drops with increasing energy.

We took this simulation result another step by incorporating the flat-panel photodiode array detector response and the flat-panel photodiode array detector PSF into HADES (discussed earlier) and then comparing simulation to experiment for step wedges made of Cu. Agreement is within 2% (Schach von Wittenau et al. 2002b).

6.5.4 HADES PROTON RADIOPHGRAPHIC SIMULATIONS TO STUDY HYDRODYNAMICS

This simulation example is from a study of metals under hydrodynamic shock. We have the ability to acquire a proton* radiograph of a static (initial condition at time = 0) metal assembly containing

* This example uses a proton radiograph. Photons could also have been used for this type of study.

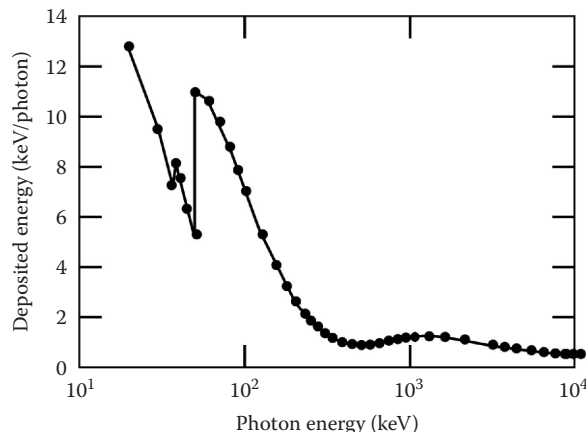


FIGURE 6.11 The average energy deposited in the scintillator of a flat-panel photodiode detector per incident photon as a function of photon energy. The scintillator used in this detector is Kodak Lanex fine. The scintillating material is gadolinium oxysulfide. The jump at 50 keV is the K absorption edge of Gd.

an explosive. This study is to investigate the constitutive properties* of Sn. The assembly as shown in Figure 6.12 can also be proton-radiographed at an arbitrary time after initiation of the explosive. The explosion moves material and changes their densities. This process can be computed by a hydrodynamic simulation.[†] By simulating the hydrodynamics of a model of the assembly at a set time ($t > 0$), then using HADES to simulate a proton radiograph of the model (in mesh format) at that time, we can create in a two-step simulation (hydrodynamic then radiographic) a simulated proton radiograph to compare to the experimental proton radiograph.

Two results (at $t = 0$ and 12.26 μ s) from a HADES simulation are given at the bottom of Figure 6.12. The initial ($t = 0$) model is given at the top left of Figure 6.12. The assembly has an axis of symmetry as shown. The color represents density, and in the initial (time = 0) state, the materials are as labeled. An 800 MeV proton radiograph was acquired 12.26 μ s after initiation of the explosive. In order to understand the acquired radiographs, Aufderheide and coworkers performed hydrodynamic simulations. Because the explosive assembly has an axis of symmetry, a mesh in radius and elevation is adequate to describe the problem. The resulting model as simulated at time equal to 12.26 μ s is then used as input to a HADES proton radiographic simulation, and the resulting simulated proton radiograph is produced, as shown in Figure 6.12. This figure also has the experimentally acquired proton radiograph for comparison.

While this agreement is not proof that the hydrodynamic and radiographic simulations are accurate, it is pretty strong evidence. We must recognize that it is possible for the hydrodynamic simulation to be inaccurate, and then for there to be a compensating inaccuracy in the radiographic simulation. Even though this is possible, it is highly unlikely. This coupling of hydrodynamic and radiographic simulations has been used to determine the accuracy of competing hydrodynamic simulations (Aufderheide, M.B., pers. comm., 2015).

* Constitutive properties and models for polycrystalline materials subjected to high-strain-rate loading over a range of temperatures are needed to predict the response of engineering materials to in-service-type conditions (foreign object damage, high-strain-rate forging, high-speed sheet forming, deformation behavior during forming, response to extreme conditions, etc.). To account accurately for the complex effects that can occur during extreme and variable loading conditions requires significant and detailed computational and modeling efforts. These efforts must be closely coupled with precise and targeted experimental measurements that not only verify the predictions of the models but also provide input about the fundamental processes responsible for the macroscopic response.

[†] For example, an LLNL code for this type of simulation is ALE3D.

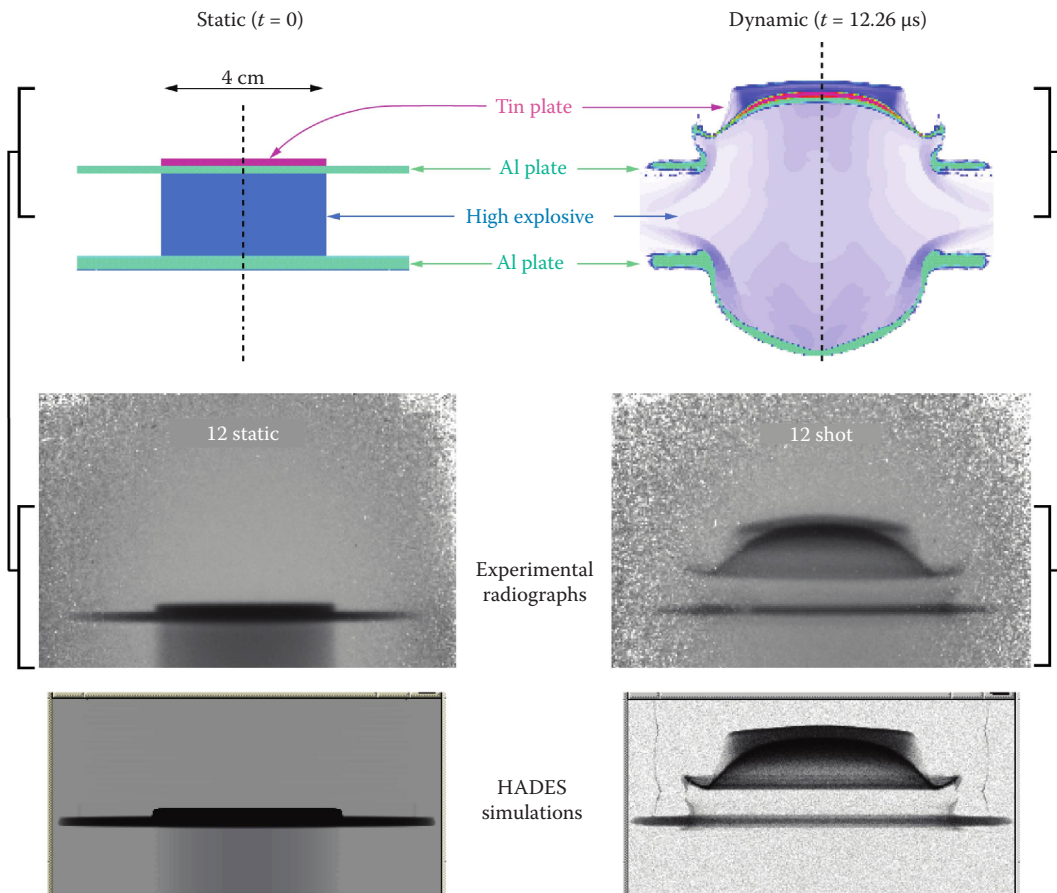


FIGURE 6.12 Comparison of HADES proton radiography simulations to experimental radiographs obtained from a hydrodynamic experiment. The top row shows cross sections of the static test piece and the configuration calculated by the hydrodynamic computer code at $12.26 \mu\text{s}$ after detonation. The middle row shows experimental radiographs of the static test object and of the exploding test piece at $12.26 \mu\text{s}$. The bottom row shows the equivalent HADES simulations.

6.5.5 COG SIMULATION APPLIED TO CARGO INTERROGATION

The example in this section is not imaging, but it does illustrate two important features of Monte Carlo simulation: (1) simulating time dependence and (2) coupled neutron/photon transport simulation. Additionally, this is applied to a problem of considerable importance, i.e., cargo container inspection for special nuclear materials (SNM), particularly Pu and U.

The detection of SNM hidden in large ($2.4 \times 2.4 \times 12 \text{ m}$) cargo containers used in ocean transport is an internationally recognized concern. Passive detection of radiation emitted by the fissionable material has limited utility because of the large container size and the presence of shielding cargo (Prussin et al. 2006). One group has proposed the interrogation of such containers with 14 MeV neutrons followed by detection of delayed γ -rays (Norman et al. 2004). The variety of cargo and packing methods makes experimental testing of all interesting configurations (various combinations of cargo and packing) impractical. Prussin and coworkers (2006) have developed a COG (see Section 6.3.3.2, Lawrence Livermore National Laboratory TART, COG, Peregrine, and MERCURY Monte Carlo Codes) Monte Carlo simulation of this problem and have experimentally tested it against three cargo configurations for validation.

Two characteristics drive the choice of Monte Carlo for this simulation: (1) The geometry is complex multimaterial and fully 3-D, and (2) the essence of the problem is time dependence. Time dependence here is due to the slow nature of neutrons and because the method detects delayed gammas. So, as neutrons are transported, time must be accounted for.

The COG simulations produced results in agreement with experiment, and additional simulations are therefore useful to test different configurations and source variations (Prussin et al. 2006).

PROBLEMS

- 6.1 What is the reason that radiographs have traditionally been presented as negative images?
- 6.2 Since the ratio of scattered photons, Φ_s^P , to primary, Φ_p^P (direct from source without interaction), drops with increasing energy (see [Figure 6.4](#)), why not use the highest energy available for all radiographs?
- 6.3 If one is concerned about albedo from a shielding wall for a 9 MV linac, which is the preferred material, concrete or Pb?
- 6.4 The Monte Carlo calculation of a flat-panel photodiode detector response presented in [Figure 6.10](#) shows that even at modest photon energies, there is a huge blur circle *caused by the flat panel itself*. Why does this happen?
- 6.5 Describe an experiment that could generate the information of Figure 6.10 without using a computer simulation.
- 6.6 In Figure 6.10, what causes the dip at ~55 keV?
- 6.7 The average energy deposited in a Lanex Fine scintillating screen in a flat-panel photodiode detector by a 1 MeV photon is about 1 keV. Why is this so small (only 0.1%)?

7 Radiation Dosimetry, Safety, and Shielding

7.1 INTRODUCTION

We address here radiation dose and effects in humans. You will become acquainted with the varied measures of radiation as related to human absorbed dose. We define and explain *radiation exposure*, *radiation absorbed dose*, *dose equivalent*, and *effective dose*.

Radiation protection and regulation through most of the world is based on the concept that effects observed at moderate dose can be linearly extrapolated to low dose. This is called the *linear no-threshold* (LNT) model. We cite key literature on this subject, including some by authors who do not subscribe to the LNT model. We describe the risk to humans from radiation dose. The instrumentation used to monitor and document human radiation is described in detail. We then describe the natural and man-made sources of human dose.

We close with a discussion of shield design and materials of construction. We explain *half-value layer* (HVL) and *tenth-value layer* (TVL) as measures of shielding material effectiveness.

Upon completion of this chapter, you will be familiar with

- Dose measurement metrics
- Instruments used to measure
 - Radiation exposure
 - Radiation absorbed dose
- High and low *linear energy transfer* (LET) radiation and *radiation weighting factor*
- Dose equivalent
- Effective dose
- The LNT model and low-dose effects in humans
- Natural and man-made radiation dose
- Radiation shielding

7.2 METRICS OF RADIATION EXPOSURE, ABSORBED DOSE, DOSE EQUIVALENT, AND EFFECTIVE DOSE

The radiation we consider here is called ionizing radiation, so called because it can eject electrons from atoms (or molecules), thereby creating an ion. Ionizing radiation typically requires between 1 and 30 eV to eject an electron. The x-ray and γ -ray energies (a few keV up to several MeV) used in industrial imaging have many times the energy required to eject an electron. In metals and salts, ionization produces no damage because free electrons soon replace ejected electrons and no lasting change occurs. But in biological material, ionization breaks molecular bonds, producing damage that can have adverse biological effects. Sometimes, the damage can be repaired, but sometimes, radiation may cause cellular mutations or even cause the cell to die. We limit our discussion to the effects in humans of absorbed dose from ionizing radiation. There is a large set of specialized vocabulary employed in radiation protection science and regulation.* We will introduce the basic vocabulary in this text.

* See, for example, <http://www.euronuclear.org/info/encyclopedia.htm#r>. This site contains a glossary of radiation terms.

Irradiation of an individual taking place within a duration of 1 week or less and not recurring is called *acute irradiation*. Long-term or continuing irradiation is called *chronic irradiation*. Effects of ionizing radiation limited to the irradiated individual (not genetically transmitted) are called *somatic effects*. *Teratogenic effects* are a special case of somatic effects in which an embryo or fetus is irradiated during gestation. *Genetic damage* may also affect subsequent generations.

7.2.1 RADIATION EXPOSURE

As word of Röntgen's discovery of x-rays spread, the need to specify a quantity of radiation became apparent. X-rays cause ionization as they interact with matter, and the first radiation measurements were based on the amount of ionization in air. The unit assigned to the amount of ionization in air was *Röntgen* (R), and it is called *exposure*. Exposure as a unit of ionization in air is very specific, while the English definition of exposure is quite general. The Merriam-Webster online dictionary lists four main meanings for exposure but never mentions ionization in air (Merriam-Webster OnLine 2005). Adding to the confusion is the fact that the word *exposure* is used in the context of recording an image (using photons of any energy or wavelength) with a sensitive coating on a film backing.

The term *exposure* used for ionization in air leads to much bad usage and confusion. When *exposure* is written or stated, the reader is often left to guess whether the English meaning is the intent or whether the author means radiation exposure (in Röntgen). In this text, we will use the term *radiation exposure* when the meaning is exposure to ionizing radiation. The exposure unit of Röntgen is defined as the quantity of x or γ radiation that produces 2.08×10^9 ion pairs in 1 cm^3 of dry air at standard temperature (0°C) and pressure (1 atm at sea level). There has been no special SI unit (SI: International System of Units) assigned. Radiation exposure is of limited use in radiation protection, but it is the easiest measurement to make as it uses an inexpensive instrument with an imposed voltage on an air-filled ionization chamber. Exposure is widely misunderstood, often incorrectly taken to mean *absorbed dose*. Exposure is, by definition, a descriptor of *only* x or γ radiation. It is not related to charged-particle or neutron irradiation.

7.2.2 ABSORBED DOSE

Absorbed dose (D) is defined as absorbed energy per unit mass in any absorber. Any form of ionizing radiation (e.g., γ -rays, α , neutrons, and β) can cause it. The traditional unit is the *Röntgen absorbed dose* (rad), which is defined as 100 erg/g. The SI unit of absorbed dose is the gray (Gy), which is defined as 1 J/kg. The traditional and the SI units of absorbed dose are related as follows:

$$1\text{ Gy} = 100\text{ rad.} \quad (7.1)$$

There is no simple relationship between absorbed dose and radiation exposure. Different materials exposed to the same ionizing radiation absorb different amounts of energy and thus have differing values of absorbed dose. Absorbed dose is meaningless unless a material is specified. In the special case of soft tissue, radiation exposure in *Röntgen* (R) and absorbed dose in rad are numerically similar (within 5%). While this is convenient, it also leads to confusion and sloppiness.

7.2.3 LINEAR ENERGY TRANSFER AND RADIATION WEIGHTING FACTOR

At this point, we need to introduce the concept of *linear energy transfer* (LET). LET refers to the energy density along the path of radiation (J/m) as it interacts in tissue. The biological response to absorbed dose from ionizing radiation is found to depend on LET. Absorbed dose with high LET is more damaging than absorbed dose with low LET. The reasons for this dependence are complex, but low-LET damage is thought to be more likely to be repaired than high-LET damage. You can think of this as high-LET damage having a greater fraction of broken bonds within the affected

volume than low-LET damage. It seems sensible that this might be the case. This concept (high LET worse than low LET) is consistent with the general acceptance that chronic radiation dose is less damaging than the same absorbed dose given acutely.

Charged particles such as α radiation (${}^2\text{He}^+$ or ${}^{++}$) have the highest LET. Neutrons have an intermediate LET that varies depending on neutron energy, and photons have the lowest LET. The variation in effect for various radiation sources is expressed as *radiation weighting factor* (w_R). High LET corresponds to high radiation weighting factor and leads to higher radiation effects. Photons and β^- are assigned a radiation weighting factor value of 1.0. The radiation weighting factor for neutrons ranges from 2.5 to 20. Thermal (mean energy of 0.025 eV) neutrons have w_R of 2.5. Protons have w_R of 2.5, while α particles (and other heavy ions) have a radiation weighting factor of 20 at all energies. Ions passing through tissue lose energy to electrons. The highest-LET portion of their track through tissue is near their stopping point. All ions have this high-LET behavior as they come to rest. The end effect is that w_R is the same for all ions except protons (ICRP 103 2007).

In the past, *radiation weighting factor* was known as *quality factor*.

7.2.4 Dose Equivalent

Dose equivalent (H) accounts for the biological response to absorbed dose. So dose equivalent is proportional to the biological effect that can be expected from radiation absorbed dose. The traditional unit of dose equivalent is the *Röntgen equivalent man* (rem). Again, the choice of names seems unfortunate. It employs the unit of radiation exposure (Röntgen) with modifiers for dose equivalent. The relationship between radiation exposure and dose equivalent is tortuous and almost never known in real applications. The SI unit of dose equivalent is *Sievert* (Sv). The traditional unit (rem) and the SI unit (Sv) are related as follows:

$$1 \text{ Sv} = 100 \text{ rem}. \quad (7.2)$$

Dose equivalent equals the absorbed dose in a particular material times the radiation weighting factor for the radiation:

$$H = (D_r)(w_R). \quad (7.3)$$

7.2.5 Effective Human-Equivalent Dose

The International Commission on Radiological Protection (ICRP) went beyond dose equivalent and defined *effective human-equivalent dose*, often called effective dose (ICRP 60 1990). Different parts of the body have a different response to radiation dose. Effective human-equivalent dose puts these differences on a common basis by generating a number that represents the whole-human-body equivalent of a dose equivalent. The ICRP defined 15 body parts, each with a *tissue weighting factor* (w_T). The effective human-equivalent dose, H_E , is the sum over each irradiated body part i of the product of dose equivalent and the appropriate tissue weighting factor, w_T .

$$H_E = \sum_T (w_T)(H_T). \quad (7.4)$$

Values of tissue weighting factors are given in [Table 7.1](#). The sum of the tissue weighting factors over the official 15 parts of the body is 1.0. So, for instance, the ICRP concept allows one to compare (conceptually) a dose of 1 mSv to the gonads with a dose of 1 mSv to the brain to a dose of 1 mSv to the entire body. ICRP defined the unit of effective human-equivalent dose as Sv, the same as is used for dose equivalent. From the unit name, you cannot tell whether a quantity is dose equivalent or effective human-equivalent dose. A dose equivalent of 1.0 mSv only to the breast (such as a

TABLE 7.1**Tissue Weighting Factors, w_T , Used for Calculating Effective Human-Equivalent Dose**

Tissue	Tissue Weighting Factor, w_T
Red bone marrow	0.12
Colon	0.12
Lung	0.12
Stomach	0.12
Breast	0.12
Other tissues ^a	0.12
Gonads	0.08
Bladder	0.04
Esophagus	0.04
Liver	0.04
Thyroid	0.04
Bone surface	0.01
Brain	0.01
Salivary glands	0.01
Skin	0.01
Total	1.00

^a Other tissues are adrenals, extrathoracic region, gall bladder, heart, kidneys, lymphatic nodes, muscle, oral mucosa, pancreas, prostate (for males) or uterine/cervix (for females), small intestine, spleen, and thymus.

TABLE 7.2**Hypothetical Radiation Situations and Their Corresponding Conversion among the Various Radiation Metrics**

Radiation	Body Part	Exposure (R)	Absorbed Dose (mGy)	Radiation Weighting Factor	Dose Equivalent (mSv)	Tissue Weighting Factor	Effective Human-Equivalent Dose (mSv)
X-ray	Breast	Not relevant	0.20	1.0	0.20	0.12	0.024
γ -ray	Whole body	Not relevant	0.010	1.0	0.010	1.0	0.010
Thermal neutron	Brain	Not defined	100	2.5	250	0.01	2.50
β^-	Skin	Not defined	1.0	1.0	1.0	0.01	0.010
β^- and γ (^{131}I)	Thyroid	Not defined	10	1.0	10	0.04	0.40

mammogram) results in an effective human-equivalent dose of 0.12 mSv because the tissue weighting factor for breast tissue is 0.12. Several hypothetical radiation situations and their corresponding conversion among the various radiation metrics are illustrated in Table 7.2.

7.3 RADIATION EFFECTS IN HUMANS

As Strom (1996) points out, radiation effects in humans is a complex issue. He states, “Dose as a surrogate for risk is simplistic: It’s a 16×4 dimensional problem.” This complexity is somewhat reduced for acute (short-duration) effective human-equivalent dose above 0.03 Sv. Below this level, no effects in humans can be observed. There may be increased cancer risk (see [Section 7.3.2](#)).

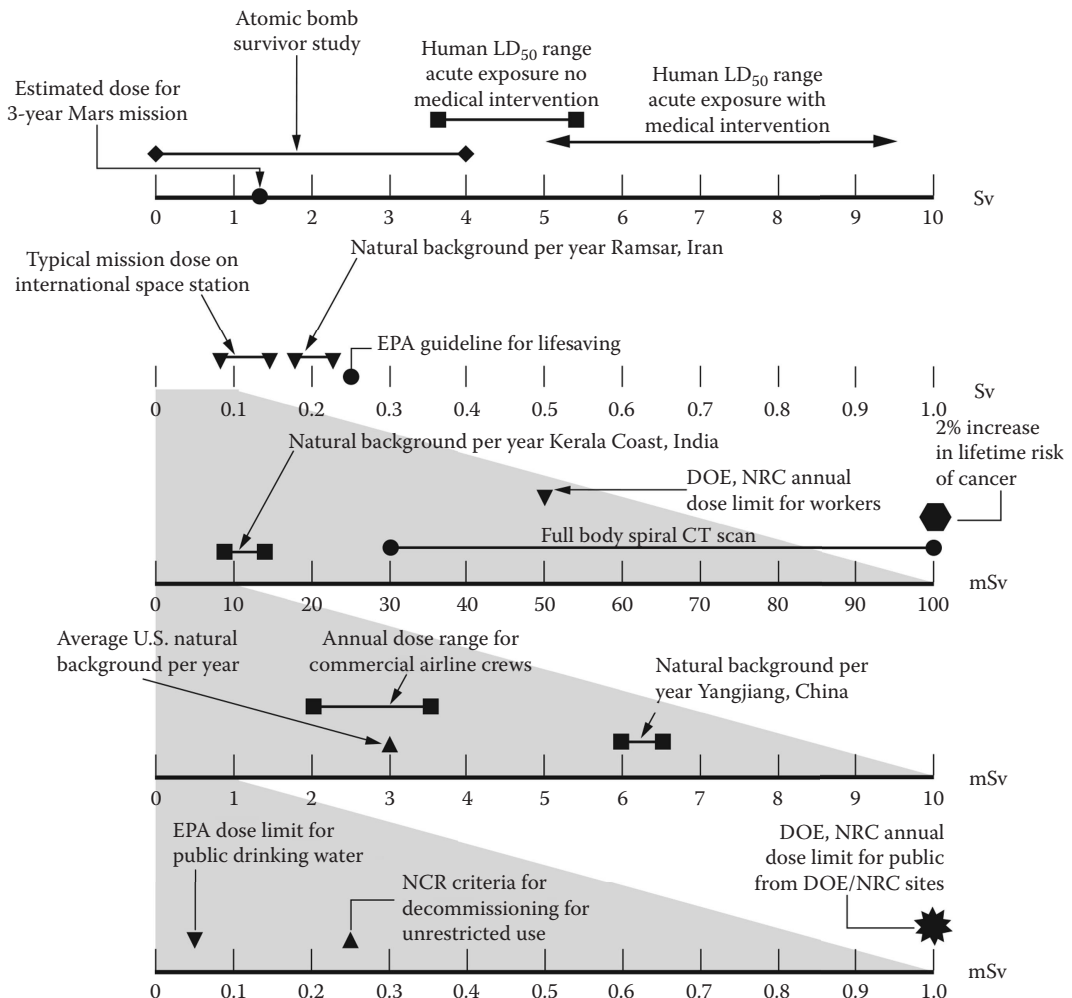


FIGURE 7.1 Effective human-equivalent dose for a wide range of limits, procedures, and situations. This chart was prepared using data from the BEIR VII report (BEIR VII 2005), a journal publication (Ghiassinejad et al. 2002), a Lawrence Livermore National Laboratory (LLNL) training document (LLNL 2005), and a chart by the US Department of Energy (Metting 2005). LD₅₀ means “lethal dose 50%” or the dose that will kill 50% of the people exposed for the specified conditions.

However, an acute effective human-equivalent dose of 3 Sv causes death within 60 days in 50% of the irradiated individuals. At a 10 Sv acute effective human-equivalent dose, death is certain in all humans irradiated. The effects and possible sources of acute dose equivalent over five orders of magnitude effective human-equivalent dose are shown in Figure 7.1.

The human effects of chronic (over an extended time period) dose equivalent are less than for acute dose equivalent. For humans, it is less harmful to get radiation dose equivalent a little at a time than all at once.

7.3.1 LINEAR NO-THRESHOLD (LNT) MODEL

There exists a long-running debate on the effects of radiation at low doses that hinges on the assumption that radiation effects are linear with no threshold. This is referred to as the *linear no-threshold* (LNT) model. It is in general use by regulatory bodies worldwide. In the United States,

the task of advising the government on regulation of radiation falls to the National Academy of Sciences (NAS). NAS was created with the signature of President Abraham Lincoln in 1863 and currently has a sitting committee on the Biological Effects of Ionizing Radiation (BEIR). In 2000, the US House of Representatives* requested a “reexamination of the scientific basis for the linear no-threshold model of low-dose radiation.” The BEIR VII “report in brief” (BEIR VII 2005) and the full BEIR VII report (BEIR VII 2006) are their latest position on the effects of low effective human-equivalent dose radiation. In the judgment of BEIR VII, the LNT model is justified. Flipped around, the LNT model means that there is no safe dose. Among those who disagree with LNT, there are two competing models: (1) Low doses are more harmful (Gofman 1999; Gould and Goldman 1993; Mangano 2004) than predicted by the LNT model. (2) There is no effect at low dose, or low dose is beneficial (Cameron 2001, 2002; Kauffman 2003). For a balanced discussion of the LNT model, we refer the student to D. J. Strom’s lecture (Strom 1996). See also Strom’s (2003) report, and the short book by Lapp (1995) and another by Walinder (2000).

7.3.2 HUMAN RISK FROM LOW EFFECTIVE HUMAN-EQUIVALENT DOSE

The main risk (perhaps the only one) from low effective human-equivalent dose is an increased risk of cancer. Since cancer is very common, it is impossible to observe a small increase in cancer incidence even in a large population. This is true for two main reasons: (1) the statistical variation swamps any small effect, and (2) other environmental and hereditary effects are nearly impossible to eliminate. The report BEIR VII estimates that in a population of 100, the average lifetime cancer incidence is 42. If 100 people are given 100 mSv of low-LET effective human-equivalent dose,[†] one additional cancer is the expected result. There are many environmental and genetic factors that influence cancer incidence so that in any random group of 100 people, the number of lifetime cancer cases varies widely.

As for risk from disease other than cancer from low effective human-equivalent dose, BEIR VII says that “there is no direct evidence of increased risk of non-cancer diseases at low doses, and data are inadequate to quantify this risk if it exists.”

Genetic diseases are another possible concern. Again, we turn to the BEIR VII report, which states that “genetic risks are very small compared to the baseline frequencies of genetic diseases in the population.” No increase in genetic diseases has been observed in intensive study of 30,000 children born to Japanese nuclear-weapon survivors.

7.4 RADIATION MEASUREMENTS FOR MONITORING RADIATION EXPOSURE AND ABSORBED DOSE

Our interest in this section is instruments used to measure radiation for the purpose of protection of personnel. In most cases, these are designed as handheld or even very small wearable units. The more sensitive of these are also called radiation survey meters. Some are designed to measure radiation exposure (ionization in air), while some indicate absorbed dose (D_p) in soft tissue, and some just count pulses induced by radiation in a sensitive volume within the meter.

7.4.1 GEIGER–MÜLLER COUNTER

The *Geiger–Müller* (G-M or sometimes Geiger) counter is a pulse-counting instrument that measures counts per unit time. It does not measure either radiation exposure or absorbed dose. It is the most common handheld radiation-measuring instrument. A G-M counter operates so that any

* Subcommittee on Energy and Environment, Committee on Science.

[†] An effective human-equivalent dose of 100 mSv is a very large value compared to established regulations and actual experience. At Lawrence Livermore National Laboratory in 2004, 0.6% of the employees received an effective human-equivalent dose greater than 1 mSv (LLNL 2005).

radiation interaction in the sensitive volume over a threshold produces a pulse. The threshold-level setting is performed in a calibration laboratory and is not intended to be adjusted by the user. The nature of the instrument is that all pulses are alike regardless of the energy deposited in the initial event. It counts an event in which 1 MeV is deposited the same as an event in which 2 MeV is deposited. This is shown in Figure 7.2. The output meter always reads in counts per minute (cpm), and G-M counters are almost always equipped with an audible indicator clicking for each pulse. A representative G-M counter is shown in Figures 7.3 and 7.4.

G-M counters indicate cpm. This is the function of a G-M counter. Unfortunately, they are often equipped with a scale that reads mR/h or something similar. The one shown in Figure 7.5 has an mR/h scale. Do not be misled by this! A G-M counter cannot be used to measure radiation exposure or absorbed-dose rate just because the manufacturer put an incorrectly labeled scale on the meter readout face. Since every radiation interaction is counted as a pulse, this instrument response is not directly related to radiation exposure rate or to absorbed-dose rate (Knoll 2000).

G-M counters are sensitive, robust, inexpensive, lightweight detectors of radiation. Because of these attributes, they are the tool of choice for radiation surveys. In a radiation survey, the operator is looking for the escape of any amount of radiation into the lab or other workspace or is confirming shielding enclosure effectiveness. If radiation is detected, then a different instrument (e.g., an ionization chamber meter as described in Section 7.4.2, Ionization Chamber Radiation Meter) should be used to quantify the amount of radiation present.

G-M counters are gas filled, usually with an inert gas because inert gases have low electron affinity. Different geometries can be used, but the simplest has a wire on axis in a cylinder containing the detection gas. High voltage is imposed between the wire and the outer shell. Any event that causes ionization, either in the walls or in the gas fill, starts a cascade in which charge is multiplied by the acceleration of the ions and electrons produced. This cylindrical geometry gives rise to the common expression *G-M tube*. The G-M counter shown in Figure 7.4 is equipped with a cylindrical chamber with height less than the radius, usually called a pancake probe. As can be seen from the electrical connector in the figure, this probe is interchangeable with others of different geometry via a simple connector. Most chambers

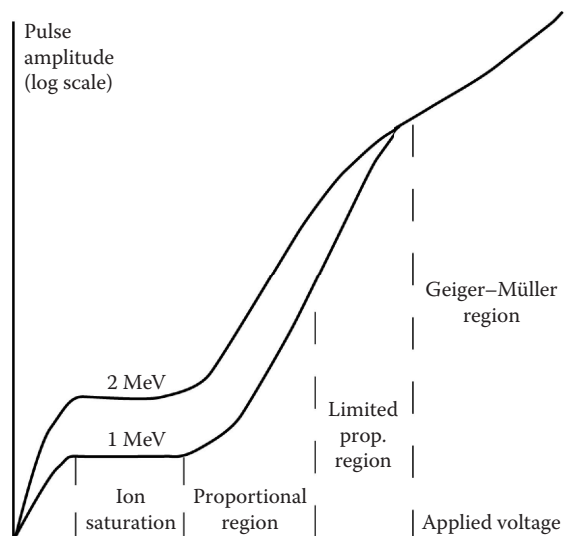


FIGURE 7.2 The different regions of operation of gas-filled radiation detectors. The pulse amplitude is plotted for energy deposits of 1 and 2 MeV, each as a function of applied voltage. Ionization chambers operate in the ion saturation region. Geiger–Müller counters operate in the Geiger–Müller region. Detectors operating in the proportional region are used for spectroscopy but not usually for radiation safety. (Knoll, G. F.: *Radiation Detection and Measurement*, third edition. 2000. Copyright Wiley-VCH Verlag GmbH & Co. KGaA. Reproduced with permission.)

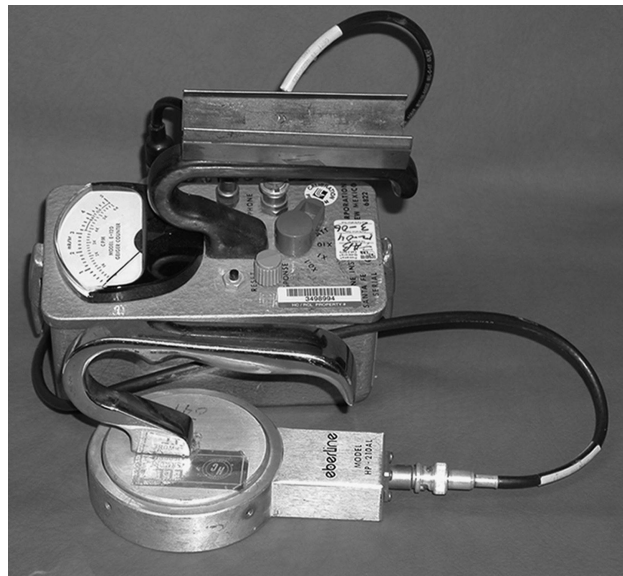


FIGURE 7.3 A G-M counter, the Eberline E-120, with a pancake probe attached. This instrument can be fitted with various probes. It has been manufactured since the 1970s and is very commonly found in NDE facilities.



FIGURE 7.4 The entrance window for the pancake probe used with the Eberline E-120. The purpose of the coarse wire mesh is to protect the thin foil window from puncture. Also note the optional speaker on the side of the main instrument body. When switched on, this provides an audible indication of the count rate.



FIGURE 7.5 The meter face for the E-120 G-M counter. A G-M counter detects counts and displays the rate as counts per minute (cpm). Note that the instrument provides an additional scale in units of mR/h. Do not be misled by this mR/h scale. Counts per minute in a G-M counter are not directly related to radiation exposure rate (mR/h) or to dose rate.

for G-M counters have a thin window for low-penetrating radiation to enter the active detector volume. This is necessary for detection of, for example, β^- and low-energy (<3 keV) x and γ radiation.

Everyone who uses G-M counters must be aware that they have some dangerous characteristics. We have already mentioned that cpm is not a good indication of radiation exposure or absorbed-dose rate. A second, more serious, characteristic arises because a G-M counter requires a certain recovery time after a pulse. If another radiation interaction occurs before the tube recovers, no discharge takes place, and the event passes undetected. When the rate of interactions becomes too high, the G-M counter does not recover. It will indicate nothing in the presence of a high radiation field. This is a very dangerous situation. Normally, a G-M counter will indicate a few cpm in a location with only background radiation present. If it is equipped with a speaker, this will be accompanied by a click every few seconds. If you are holding a G-M counter that suddenly goes silent and indicates 0 cpm, leave the area immediately!

7.4.2 IONIZATION CHAMBER RADIATION METER

Another type of radiation detector that uses ionization in a gas is referred to as an *ionization chamber* (sometimes called an ion chamber). An ionization chamber can be designed to measure radiation exposure or absorbed dose. This instrument has a gas-filled chamber with a voltage applied between the chamber wall and internal electrode. The applied voltage is much lower than used in a G-M counter (see Figure 7.2), so that no multiplication occurs. This amount of applied voltage collects the charge produced by the ionizing interaction in the fill gas. This operating region is called *ion saturation* in Figure 7.2. A photograph of a handheld ionization chamber is shown in Figure 7.6. Charge produced by radiation interaction is collected and measured as a current that is proportional to the energy deposited by the radiation interaction. The display and controls for this instrument are shown in Figure 7.7.

Early ionization chambers had a large active volume, and surface effects are not significant in this instance. For portable instruments, the chamber dimension is insufficient to collect all of the ionization produced by the initial energetic electron. Making the chamber walls of a material similar to the chamber gas circumvents this problem. For example, if the fill gas has composition similar to tissue (called *tissue equivalent*), then the walls will be coated with a plastic of similar composition. The walls and the fill gas then exist in electron equilibrium, and the instrument signal is proportional to absorbed dose in tissue. If the gas is air and the radiation is x-rays and γ -rays, current is proportional to radiation

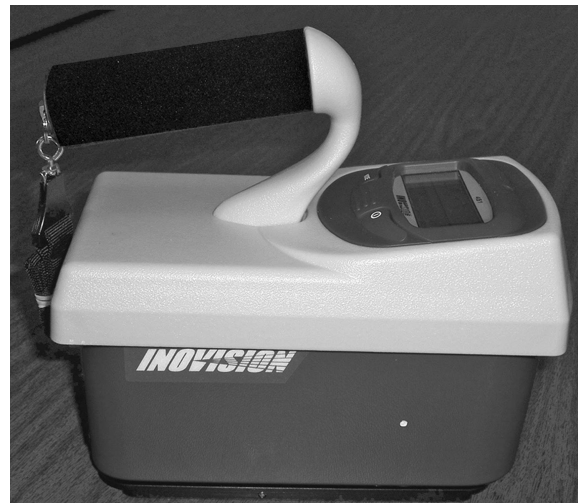


FIGURE 7.6 An example of a survey meter employing an ion chamber. This instrument is the Inovision model 451B. Display is LCD with autoranging (see Figure 7.7). The only user controls are on/off and mode selection, either the rate mode (e.g., R/h) or integrating (e.g., R). The instrument can be ordered to indicate radiation exposure (R/h or R) or absorbed dose (Sv/h or Sv).



FIGURE 7.7 The liquid crystal display of the Inovision 451B ion chamber radiation meter. The two user controls (mode and on/off) are visible below the display. The mode button toggles between operation as a rate meter (e.g., $\mu\text{R}/\text{h}$) and operation in integrating mode (e.g., μR). Here, the scale is correct, that is, when it states $\mu\text{R}/\text{h}$, it is a measure of radiation exposure rate.

exposure. Recall that exposure is defined in terms of ionization produced by x-rays and γ -rays in dry air. Pressurizing the gas in the ionization chamber increases sensitivity to higher-energy x-rays and γ -rays but generally makes the instrument insensitive to β^- because the window must be thicker to support the higher gas pressure and the β^- particles typically cannot penetrate such thick windows.

7.4.3 PERSONAL DOSIMETER

The final class of radiation-safety detectors we will consider in this chapter is the type designed to monitor accumulated radiation absorbed dose over a period of time that may extend to several months or more. The most common use for this type of detector is as a personal dosimeter—usually worn on the torso by workers. A visitor to a radiation work area will generally be issued a personal dosimeter for the duration of the visit. It is also used to monitor a set location such as a perimeter fence or a specific location in a laboratory. We have also found them useful for determining the amount of radiation in various shielding configurations and to compare to Monte Carlo shielding calculations.

Personal dosimeters are also used to monitor over short periods of exposure to high radiation fields, such as may be appropriate for repair or emergencies. For example, one of the authors (Logan) surveyed the radiation leakage through the ceiling of an enclosed space. This was done by crawling around in the space above the ceiling with approval and concurrence of health physics personnel. Of course, the radiation had to be turned on in order to perform a meaningful survey. I wore a separate dosimeter (in addition to the usual dosimeter changed quarterly) for the few hours of this exercise so that the radiation dose for this activity could be determined. The results of this survey provided guidance for design changes to decrease leakage through the ceiling.

The earliest wearable dosimeter that became widely used was the *film badge*. It is called this because the radiation recording is accomplished by activation of AgBr grains in a film similar to the AgBr grains used in black-and-white photographic film. Film badge dosimeters must be developed (chemically processed). The darkening of the film is related to the absorbed dose received by the film badge, and if worn correctly, it is related to the absorbed dose received by the wearer (Pradhan 1981).

Film badges have been largely replaced by *thermoluminescent dosimeters* (TLDs). TLDs use a material (for example, calcium sulfate, lithium fluoride, or lithium borate) that stores energy in metastable states (Pradhan 1981). The energy is released in the form of light when the irradiated TLD material is heated. This characteristic allows TLDs to be erased and reused. Their small size (mass of a few milligrams) makes them practical to wear on fingers or the face to monitor specific locations. A typical dosimeter package contains more than one TLD. The example shown in 7.8 uses the Panasonic UD-802 dosimeter containing four TLD pellets (Shachar et al. 1989). One $\text{Li}_2\text{B}_4\text{O}_7$ TLD has minimal packaging material so that it will respond to β^- radiation. This is the purpose of the hole in the plastic cover in [Figure 7.8](#). Another $\text{Li}_2\text{B}_4\text{O}_7$ TLD is behind a thin piece of plastic that shields it from β^- radiation. A third TLD is CaSO_4 and packaged in heavier plastic. The final TLD is another CaSO_4 that is filtered with 900 mg/cm^2 of Pb. This makes it insensitive to photons with energy less than 200 keV and to β^- (Stanford 2002). Filtering combined with the different TLD materials' inherent response to photons as a function of energy enables determining radiation absorbed dose in radiation situations with both β^- and photon radiation present.

TLDs containing natural boron and lithium are somewhat sensitive to slow ($<1 \text{ eV}$) neutrons (Kralick et al. 1986). Their sensitivity can be enhanced or suppressed by isotopic enrichment (Paic 1988).

Personal dosimeters that give real-time indication of absorbed dose or absorbed-dose rate are available in many different configurations. The oldest type used discharge of a charged capacitor to indicate absorbed dose. These were usually shaped like fat pens. The dose received by such dosimeters is read by looking through a lens at the deflection of a fiber along a mrem scale.

The newest personal dosimeters are credit card sized and give real-time absorbed-dose rate as well as recorded absorbed dose integrated over specific time periods. The system shown in [Figure 7.9](#) employs a Si sensor. This unit combines the function of a real-time radiation indication and a recording integral dosimeter.



FIGURE 7.8 Photograph of a thermoluminescent dosimeter (TLD). The TLD crystals are within the plastic housing. The TLD shown is designed to be worn with a photo identification badge. The circular hole is present to allow β^- radiation to access one of the TLD crystals.



FIGURE 7.9 The Dosicard dosimeter marketed by Canberra. Dosicard employs a silicon detector and has nonvolatile memory, an LCD display, and audio/visual alarms. (Photo by authors. With permission of Canberra.)

Other types of radiation detectors not mentioned here are not generally employed for personnel safety/protection. Those used for radiography and computed tomography (CT) are covered in detail in Chapter 9.

7.5 SOURCES OF HUMAN ABSORBED DOSE

We live in a radioactive environment. The earth, our food, and the sky all bathe us in natural *background radiation*. In industrialized countries, there is an additional radiation dose from *man-made*

sources. A third category of radiation dose that is important for regulatory control is *occupational dose*. We define occupational dose to consist of all dose received because of a person's occupation without regard to whether the source is natural or man-made.

7.5.1 NATURAL BACKGROUND RADIATION

The average worldwide background radiation is 2.4 mSv/year effective human-equivalent dose (BEIR VII 2005). The distribution of sources of this radiation is shown in Figure 7.10.

7.5.1.1 Radon

The largest component of background radiation arises from inhalation of the naturally occurring radioactive gas radon. The most significant radioactive isotope of radon is $^{222}_{86}\text{Rn}$, which is in the decay chain of $^{238}_{92}\text{U}$. Since uranium is found nearly throughout the earth's surface, radon is present in almost all rock, soils, water, and air. Radon does not pose a significant external radiation concern, but when inhaled, radon and its decay (daughter) products directly irradiate lung tissue with α particles (Shapiro 2002). In addition, there is a synergistic effect between exposure to radon and cigarette smoke. The combination is a more powerful carcinogen than the sum of the individual effects (EPA 2003). In most situations, indoor exposure to radon is greater than outdoor exposure. Radon from soil below structures infiltrates homes through basements or other surfaces in contact with soil or rock. Since radon

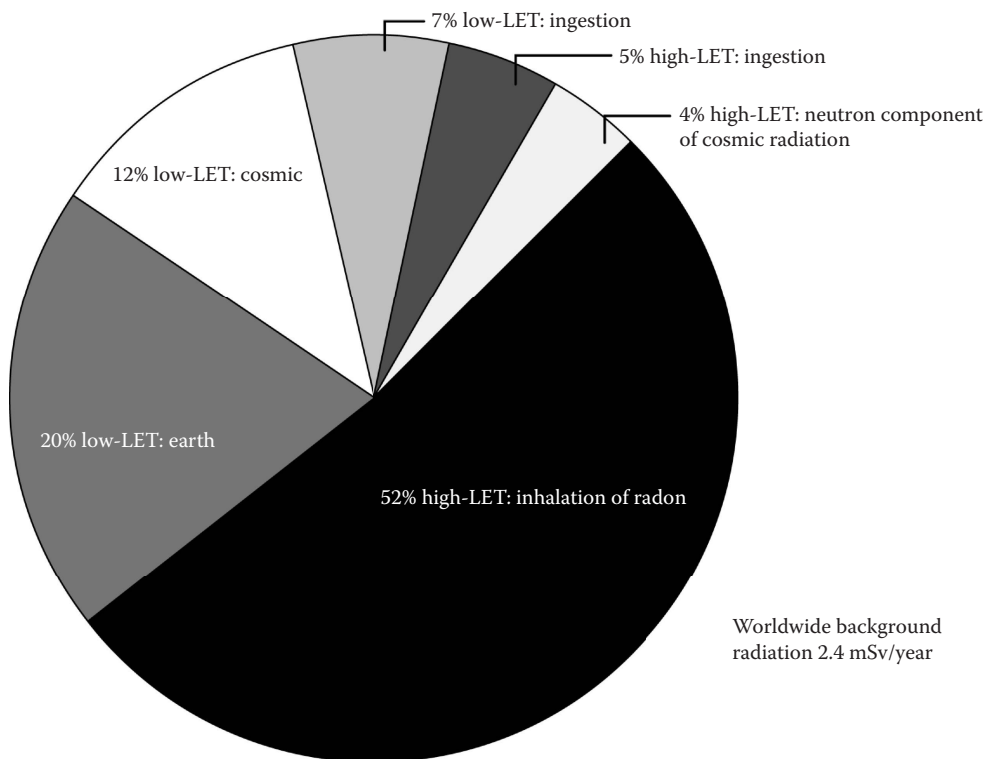


FIGURE 7.10 Average worldwide natural background radiation sources. Linear energy transfer (LET) is a measure of energy density (energy/length) along the interaction track where energy is deposited by ionizing radiation. X, β , and γ radiation are considered low-LET radiation. Their LET is a few keV/ μm . Neutrons and ions have higher LET, exceeding 100 keV/ μm . LET is discussed further in Section 7.2.3, Linear Energy Transfer and Radiation Weighting Factor. (This figure was created using data from BEIR VII, *Health Risks from Exposure to Low Levels of Ionizing Radiation, Report in Brief*, National Research Council, June, 2005.)

and its decay products are heavier than air, they tend to accumulate in basements and crawl spaces where they enter. Levels of airborne radon vary widely depending on local geology and construction methods. In the United States, average airborne concentration is ~ 0.4 pCi/L. The US Environmental Protection Agency recommends mitigation if indoor levels exceed 4 pCi/L. There are areas with much higher radon concentrations than average. Ramsar, Iran, has some inhabited areas with background levels of more than 40 pCi/L (Ghiassi-nejad et al. 2002). In Ramsar, this comes primarily from $^{222}_{86}\text{Rn}$ carried to the surface by hot springs. In the United States, a home in Pennsylvania had measured levels of 2700 pCi/L. This home was sited on natural granite containing uranium (see Panel 7.1).

PANEL 7.1 Discovery of a Home with High Levels of $^{222}_{86}\text{Rn}$

In Pennsylvania, USA, a home was discovered to have exceedingly high levels of radon. In 1984, Stanley Watras worked at the Limerick Nuclear Power Plant in Pottstown, near Reading. This facility had a portal monitor through which people passed while entering or exiting the plant. Of course, its purpose was to prevent workers from carrying radioactivity *out* of the plant. Watras repeatedly triggered the alarms on the detector going *into* work. Investigating, Limerick staff measured radiation levels in the Watras home that were very high. This turned out to be arising from radon and radioactive decay products. A concentration of 2700 pCi/L was reported. The radon source was the earth beneath the Watras home, which contained a substantial deposit of uranium (Honacherfsky 1991; Hunter 2004).

7.5.1.2 Terrestrial X and γ Radiation

Natural radioactivity in the earth, e.g., thorium, uranium, and potassium, also irradiates us with x and γ radiation. This is the 20% low-LET earth component of earth irradiation in [Figure 7.10](#).

7.5.1.3 Radioisotopes in Food and Beverages

Radioactive isotopes are present in our food and beverages and are thus ingested. Some of these pass through with little effect, but some are incorporated into tissue. Tritium (^3_1H), carbon-14 ($^{14}_6\text{C}$), and potassium-40 ($^{40}_{19}\text{K}$) are isotopes with a high likelihood of incorporation into tissue. Environmental tritium is nearly always in the form of water with one tritium in place of protium (^1_1H). Tritiated water freely mixes with body water. Potassium is a required nutrient with 0.0118% in the radioactive form, $^{40}_{19}\text{K}$, with a half-life* of 1.3×10^9 years. Any food containing potassium (notably bananas) contains $^{40}_{19}\text{K}$. Most people ingest these isotopes at a fairly constant rate and have a nearly stable body inventory of these isotopes but may be exposed to pulse intake by occupational tasks or consumption of a case of bananas. The estimated mass, activity, and ingestion rate of seven natural radioisotopes found in the average 70 kg adult are shown in [Table 7.3](#) (ANL 2015; UMICH 2005).

Some ingested radioactivity turns over by dilution exchange at a faster rate than it decays. For example, if one ingests a single dose of tritium, the concentration decreases as fresh (low concentration of tritium) liquid is ingested and excreted. This drop in body concentration by dilution is called biological half-life. The biological half-life of water varies considerably with lifestyle but is usually taken to be about 10 days. One of the authors (Logan) dropped his personal biological half-life to <5 days by increased fluid intake on one occasion. Logan measured this by tritium concentration in daily urine samples. Among people who work with tritium, it is often said that the treatment for tritium ingestion is a case of beer. Of course, this does not work very well if the tritium concentration in the beer is similar to excreted liquids.

* The *half-life* of a radioisotope is defined as the time required for the number of radioactive nuclei to be reduced by one-half. (For more on a radioisotope's half-life, see Section 4.2.2, The Nucleus and γ -Ray and X-Ray Generation.)

TABLE 7.3**Estimated Mass, Activity, and Daily Intake of Seven Radioisotopes Found in the Body from Natural Sources**

Nuclide	Mass in Average Body (μg)	Activity in Average Body (Bq)	Average Daily Intake (μg)
Natural uranium	90	1.1	1.9
Natural thorium	30	0.11	3
Potassium-40	17,000	4.4	390
Radium	31×10^{-6}	1.1	2.3×10^{-6}
Carbon-14	95	15,000	1.8
Tritium	60×10^{-9}	23	3×10^{-9}
Polonium-210	200×10^{-9}	37	0.0–0.6 ^a

Source: UMICH, Radioactivity in Nature, <http://www.umich.edu/~radinfo/introduction/natural.htm>, 2005; ANL, <http://web.ead.anl.gov/uranium/mgmtuses/storage/index.cfm>, 2015.

^a We find widely differing numbers for intake of Polonium-210.

An interesting result of natural radioactivity in the human body is that sleeping with a bed partner increases one's personal background radiation by 2 mrem/y effective human-equivalent dose (PBS 2005).

7.5.1.4 Cosmic Radiation

Cosmic radiation or cosmic rays are energetic particles, primarily protons, which originate in the sun and other stars, and from the far reaches of space. Cosmic rays interact with the earth's upper atmosphere and produce showers of lower-energy particles. Cosmic radiation increases with higher elevation, varies with latitude, and depends on solar activity. Denver, Colorado, USA, has about twice the cosmic background radiation of a sea-level location. Air travel involves increased absorbed dose from cosmic radiation. Airline flight crew members receive an occupational absorbed dose about twice that of nuclear power plant workers (LLNL 2005).

7.5.2 MAN-MADE RADIATION ABSORBED DOSE

In industrialized nations, the man-made radiation absorbed dose is 22% of that received from natural background (BEIR VII 2005). In the United States, it is almost half and increasing rapidly (NCRP 2009). Most (80%) man-made radiation dose comes from medical procedures. The dose from medical procedures is concentrated in a small fraction of the population. The most widespread medical radiation use is for diagnostic imaging, ranging from extremities to abdominal CT. Nuclear medicine techniques using radioactive material (single-photon emission computed tomography [SPECT] and positron emission tomography [PET]) account for some of the dose from medical procedures. The third type of medical exposure (after diagnostic imaging and nuclear medicine) is that from radiation therapy. Effective human-equivalent dose for some medical procedures is provided in Figure 7.1.

Nuclear weapons and nuclear energy production receive great attention but contribute only 3% of the man-made radiation dose.*

* BEIR VII lumps nuclear energy and nuclear weapons together. Nuclear energy production is a negligible contributor. Per unit of energy produced, coal combustion causes 100 times the US population effective human-equivalent dose as energy production from nuclear fission. This is from release of radioactive materials in coal. In addition, more than twice as much electrical energy is produced from coal in the United States as is produced from nuclear reactors.

TABLE 7.4
US Nuclear Regulatory Commission Allowable Limits for Annual Effective Human-Equivalent Dose per Specific Populations

Population	Annual Limit, Effective Human-Equivalent Dose
Radiation workers	50 mSv
Embryo/fetus of a declared pregnant worker	5 mSv
Minors and general public	1 mSv

7.5.2.1 Occupational Dose Limits

Occupational radiation dose is regulated in most industries worldwide. In the United States, the main regulatory agency is the US Nuclear Regulatory Commission (NRC). Regulatory compliance is a complex topic, which we will only touch upon. The most important occupational dose limits are given in Table 7.4. In addition, regulatory agencies worldwide subscribe to the concept that radiation dose to humans should be *as low as reasonably achievable (ALARA)*. This rule requires reasonable people to effectively implement. Ultimately, in many instances, it will boil down to how much money to spend in order to eliminate a person-Sv (the product of the number of persons and the dose equivalent eliminated in each). ALARA clearly means that no human radiation dose equivalent is acceptable if there is no benefit.

7.5.2.2 Marketing Radiation Dose

Some businesses promote high background radiation as healthful. Guarapari, Brazil, has radioactive black sand beaches that have a reputation for healthful effects. An approximate English translation of one travel website claims, “The most famous beach of Guarapari. Its sands are dark and rich in monazite, with medicinal properties from radioactivity. Tourists and patients come seeking to benefit themselves by the radiation from monazite, containing thorium and actinium in the black sand. These radiations act on the place of pain, increasing the cellular metabolism” (Turismo 2005). Radon Health Mine in Boulder, Montana, USA, is an example of a facility selling radon therapy (Radon Mine 2015). They claim benefits for chronic pain and 27 other afflictions. Customers lounge in old mine caverns inhaling the natural radon gas.

7.5.2.3 Mining Legacy

Worldwide, there is a legacy of dangerous residue from uranium mining (IAEA 2004b). For example, in the United States, there is a 12-million-ton pile of uranium mill tailings on the bank of the Colorado River near Moab, Utah (DOE 2005a). This represents about 10% of the US total of uranium mill tailings and only 1% of the world total (IAEA 2004b). The site is known as the Atlas mine tailings and is named after the bankrupt company that put the pile at this location. The pile leaks arsenic, radium, radon, and ammonia into the adjacent Colorado River, which is used for municipal water over a wide region of the arid southwest United States. In September 2005, the US Department of Energy issued a Record of Decision (DOE 2005b) to remove the pile to a site 30 mi. away. About 17% of the tailings had been removed at the time of the photo in Figure 7.11. At first glance, you might think that uranium tailings should not be all that dangerous. After all, it is just rock that has been crushed and had 90% of the uranium removed. What makes it more dangerous than the original mineral deposit is the fact that it has been crushed and then placed inappropriately. It has often been used for earthen dams and occasionally for fill beneath occupied buildings (IAEA 2004b). Since water is used for extraction and transportation, tailings are often left beside rivers. These tailings typically contain arsenic, heavy metals, radium, radon, and the residual uranium that is not removed by the extraction process. The chemical form of the



FIGURE 7.11 Photograph of the Atlas mine tailings near Moab, Utah, USA. At the time of this photograph on November 18, 2010, 2 million short tons had been removed to the disposal site. The Colorado River is near right center in the photograph. The town of Moab is on the opposite side of the Colorado River from the tailings. (Courtesy of the USDOE.)

residue may have been altered by the extraction process, making it more susceptible to distribution throughout the environment. Radium and radon from the decay of uranium easily leach or percolate through the rubble.

7.6 BASICS OF RADIATION PROTECTION

Radiation sources used for industrial nondestructive evaluation (NDE) are covered in detail in Chapter 8. These sources provide sufficient radiation to be very dangerous. Radiation sources can be divided into two main categories, radioisotopes and electrically powered electron accelerators. The two most common types of electrically powered electron accelerators are the constant-potential x-ray tube and the radiofrequency linear accelerator (linac). Linacs are used to accelerate electrons to >1 MeV. Electron energies below 1.0 MeV are typically provided by x-ray tubes.

You might assume that machines with higher electron energies deliver the highest radiation dose equivalent rates. This is the case. A typical electron linac, accelerating electrons to 9 MeV, will deliver a lethal dose in one second if a person is standing 100 mm from the machine surface. Machines with lower electron energy produce less radiation per unit current in the device but may operate at significantly higher currents, so the radiation hazard may still be substantial. Figure 7.12 presents a plot of the approximate dose equivalent rate 1 m from an x-ray-producing device as a function of the electron energy. For a constant-potential x-ray tube, the electron energy in keV is numerically the same as the applied tube potential in kV. A tube with a constant applied potential of 100 kV will accelerate electrons to 100 keV. Note that the plot in Figure 7.12 is given for 1 mA

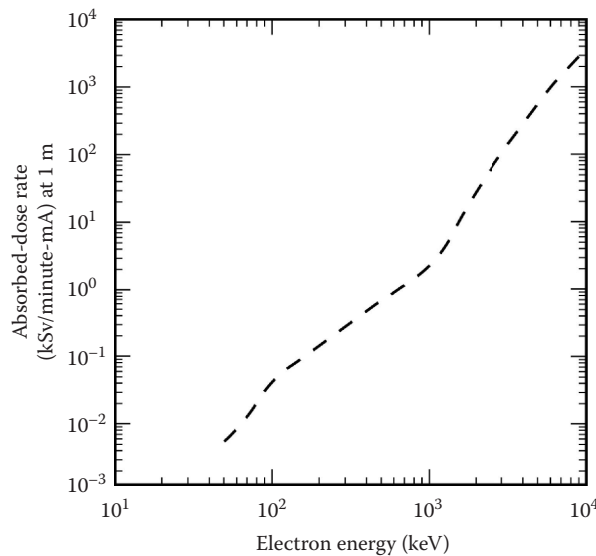


FIGURE 7.12 Plot showing the absorbed-dose rate at a distance of 1 m from an x-ray tube or electron linac with a W anode and no intentional filtering. Absorbed-dose rate is given in kSv/min for 1 mA of tube current.

of tube current. Industrial tubes in the range of a few hundred kV may have currents approaching 100 mA depending on the spot size.

Since the use of radioisotopes for industrial radiation applications is not so common today, for those interested, we refer to radiation dose equivalent rates from radioisotopic sources treated in the literature by Bossi (2002), and we do not address them here except as they apply to shielding such sources.

7.6.1 INTERNAL RADIATION DOSE

We will first mention protection against *internal radiation dose* and then cover *external radiation dose* in more detail. We exclude from this discussion internal radiation dose arising from naturally occurring radioisotopes. This was addressed in [Section 7.5.1.3](#), Radioisotopes in Food and Beverages.

Internal radiation dose comes about as a result of ingestion, inhalation, puncture, or absorption. In these cases, the radioactive material resides within the body. It may be incorporated into tissue (for example, radioactive Sr substitutes for Ca in bone). Or, it may pass through fairly quickly (for example, radioactive uranium oxide is not digested and passes in feces). Internal radiation absorbed dose is seldom encountered with radioactive isotopes used for industrial imaging. Industrial imaging radiation sources are typically doubly sealed to prevent the spread of radioactive material. In normal use, there is no direct contact between radioactive material and either the laboratory or the occupants. Anyone using radioactive sources should have a procedure in place for actions in the event of an accident. Radioisotopic source transportation is high risk and a well-regulated activity. Physical security of radioisotopic sources is also essential as they make attractive material for terrorist weapons. They present no explosive possibility but could cause terror if dispersed by other means. Radioisotopic sources require a plan for disposition. Some of the world's worst inadvertent exposures have resulted from abandoned radiation therapy (medical) sources that were purloined (Vincente et al. 2004). Dose equivalent assessment from internal radiation is a specialized area that should only be undertaken by a qualified person. Whole-body counting and bioassay of tissue or excreta are used to determine amounts of internal radioactivity.

7.6.2 EXTERNAL RADIATION DOSE

The external radiation human absorbed dose arises from radiation penetration through (or around) shielding or from an accident. Radiation penetrating or leaking through shielding can always be reduced and often should be under *ALARA*. *ALARA* principles include

- Shielding
- Time
- Distance
- Administrative controls

In other words, shielding, time, distance, and administrative controls can keep radiation human absorbed dose to a minimum level and can be used to meet *ALARA*.

Shielding is described in more detail in [Section 7.6.3](#), Shielding, from a personnel safety point of view, while shielding (or collimation) from an imaging point of view is discussed in Chapter 10.

One should minimize the time spent in an area with known radiation above normal background levels. In other words, if an area has an elevated radiation level, one should not linger in this area. Performing a required task may be acceptable, but it makes no sense to eat one's lunch there.

Distance can also be an effective radiation protection method since the absorbed dose is reduced as the square of the distance. For example, increasing your distance from the radiation source by a factor of two reduces the absorbed dose by a factor of four.

Some field radiography can be done without shielding if administrative access control is possible. Physical interlocks, key control, and training/procedures can reduce the potential for accidental radiation dose to a very low level. The authors' experience has been mainly with large walk-in bays. In these facilities, there is the potential for people other than the operator (e.g., a janitor) to be in a dangerous place when radiation commences. These facilities must be designed to facilitate a visual sweep, setting interlocks along the sweep that can assure no occupancy before radiation begins. Cabinet x-ray units present a different safety challenge. They are often located within high-occupancy areas and may be accessible to people ignorant of the potential danger. These systems have mechanical or electrical interlocks that operate in a fail-safe mode to insure that no person is accidentally irradiated. Effective key control and interlocks are the primary administrative controls or safety tools in these instances.

7.6.3 SHIELDING

Shielding, whether in a room or a cabinet, must be capable of attenuating the primary beam and scattered radiation to acceptable levels for any possible orientation of the tube head. In the United States, federal standards require the radiation exposure be less than 0.5 mR at any point 50 mm from the enclosure surface. The standard for exposure at the outside of an enclosure includes all six sides of the room or cabinet. Even when surrounding space is not usually occupied, radiation enclosures must meet the standard. It is the law, and it protects against inadvertent occupancy of a high-radiation area. Note that this standard is in units of exposure. This is unfortunate because it makes it impossible to accurately relate it to radiation dose equivalent. As we noted in [Section 7.2.2](#), Absorbed Dose, radiation exposure in Röntgens is approximately numerically equal to absorbed dose in soft tissue with units of rad. Since exposure is defined only for x-rays and γ -rays, we can consider the radiation weighting factor to be 1.0, leading to dose equivalent equal to absorbed dose. So, for this case, radiation exposure (R) approximately equals dose equivalent (rem). This leaves only the conversion from rem to Sv to get to the units of radiation protection limits given in [Table 7.4](#).

Penetrations through shielding for utilities, etc., must not follow straight lines since they allow direct or scattered radiation to easily escape. Air ducts are a particular issue because they frequently have large cross sections. Flat-stacked bricks are ineffective because radiation penetrates through the

cracks. Thus, special interlocking lead and concrete bricks are used for shielding. Doors must overlap or have matching nonplanar shapes at mating surfaces or a maze. Even an open sky can be a problem at MeV energies. The authors are familiar with a very expensive facility that was badly designed with open-topped bays to allow overhead crane access. Scattered radiation from overhead air, called skyshine, into areas outside the enclosure was so intense that the facility could not be operated.

Almost any material can be used for shielding. Cost often is a large factor in the final choice. Materials with high atomic number tend to have higher linear attenuation coefficients in the 10 to 500 keV energy range and therefore make effective shields. Pb is often the material of choice. It is high in atomic number (Z of 82), high in mass density (11.3 kg/m^3), easily formed, easily cast, and reasonable in cost. Disadvantages of Pb are that it is easily deformed and is a toxic material. The former can make joints difficult to fit and require extensive external support. Because of this, it is frequently laminated with a supporting material. A wide variety of manufactured products are available, including gypsum board and plywood bonded to a Pb sheet. Since Pb is toxic, it should be coated or covered to prevent worker ingestion. Disposal cost can equal initial cost, though it is easily recycled in most cases. For photon energies below 100 keV, steel is often chosen. It is cheap and easily welded. Reasonable thicknesses of <15 mm are usually sufficient. At energies in excess of 500 keV, the dominant attenuation mechanism is Compton scatter (see Section 5.2.1.2.1, Incoherent [Compton] Scatter). Compton scatter depends mainly on electron density, which in turn is proportional to mass density. So for shielding x-ray and γ -ray energies in excess of 500 keV, areal density, mass per unit area (kg/m^2), is the metric of merit, and concrete wins on a cost basis. It is important to note that for MeV x-ray and γ -ray energies, concrete returns more radiation to the enclosed space than higher- Z materials (Logan and Schach von Wittenau 2001), so for scatter control, it is preferable to have the surface within the radiation enclosure be of high- Z material. In situations where compactness is critical, *depleted uranium* (DU) can be used. DU is what is left over after removal of most of $^{235}_{92}\text{U}$ from natural uranium. DU is nearly all $^{238}_{92}\text{U}$. It is the material of choice for *exposure devices** using radioisotopes. Small containers made of DU are smaller, lighter, and more fire resistant than Pb of equal attenuation. See Panel 7.2 for a simple example of the potential weight savings. DU is radioactive and may interfere with low-level radiation measurements. It should not be stored or used where such measurements are performed.

Two other high- Z (atomic number) materials are used for shielding in some situations. W and Ta are both dense, relatively nontoxic, and not radioactive but expensive.

PANEL 7.2 Pb or DU?

We present here a simple example in which the additional cost and complexity of using DU rather than Pb for a shield is justified. Suppose we need a spherical storage shield/container for a $^{137}_{55}\text{Cs}$ source (γ -ray emission of 662 keV). The internal radius must be 5 mm. We know by experiment that 18 mm of Pb provides sufficient shielding to meet the desired dose equivalent of 1 mrem/h at a distance of 50 mm from the surface of the container. Voss (2001) states that the TVL thickness of DU is 52% of Pb in this energy range. This makes sense since DU (19 g/cm^3) is almost twice as dense as Pb (11 g/cm^3) and attenuation of the 662 keV γ -ray photons will be mostly from Compton scattering. Compton scattering depends on electron density, which is nearly proportional to mass density. So we conclude that the wall thickness of a DU sphere will have to be 9.4 mm. Calculating the mass of each reveals that the mass of the DU container can be less than 25% of the mass of a Pb container. This facilitates handling and transport. Analyzing the cost of this shield/container is more difficult than calculating the mass required.

* *Exposure device* is the name used for the entire assembly of a shield, guide tube, cable, and other minor elements used to store and deploy radioactive sources for radiography. The term is incorporated into standards by the American National Standards Institute (ANSI).

The material cost for either Pb or DU* is insignificant. Most of the cost is for fabrication. Both must be encased/coated since they are both toxic materials. It is significant to note that most commercial *exposure devices* (SPEC 2005) are DU shielded.

7.6.3.1 Half-Value and Tenth-Value Layer Thickness

Two measures of shielding effectiveness are often given in reference works as *half-value layer* (HVL) and *tenth-value layer* (TVL) thickness (Bossi 2002; NCRP 2004). HVL and TVL thickness are the thickness of a specified material that is required to reduce the dose rate by either a factor of 2 or a factor of 10, respectively. They are usually given for broad-beam geometry, meaning that scatter is included in the measured transmission. For this reason, HVL and TVL thicknesses are different than what you would calculate based on mass attenuation coefficients (see Section 5.3.2, Mass Attenuation Coefficient μ_m). Broad-beam geometry is almost always the geometry in which shielding is applied. For polychromatic spectra, the beam hardens (becomes more penetrating) as increasing shielding thickness is applied. This is always the case for x-ray tube and linac spectra and is most often the case for radioisotopes because they often emit multiple x-rays and γ -rays. For this reason, you will not achieve an attenuation of 10^3 by simply applying three TVL thicknesses. When designing a shield, you must make the shield thicker than seems necessary and measure the final result. An alternative is to perform a detailed radiation transport calculation such as described in Chapter 6. For x-ray tube sources with a W anode, TVL thicknesses of Pb and concrete are given in Figure 7.13 as a function of the voltage applied to the tube (Bossi 2002). Concrete composition and mass density can vary considerably, so the TVL thicknesses should be used with caution. TVL thicknesses for five common isotopic sources shielded with Pb or concrete are presented in Table 7.5 (Bossi 2002).

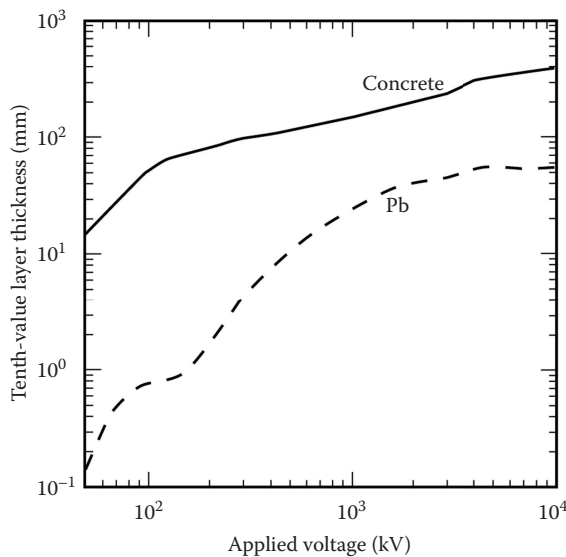


FIGURE 7.13 The tenth-value layer thicknesses of Pb and concrete for spectra from x-ray tubes with a W anode versus the voltage applied to the tube. (This graphic was created using data from the NDE Handbook: Bossi, R. H. et al., *Nondestructive Testing Handbook*, third edition: volume 4, *Radiographic Testing*, American Society for Nondestructive Testing, Inc., Columbus, 2002.)

* There is an ample supply of DU. The US government has 704,000 metric tons of depleted UF₆ in storage.

TABLE 7.5

Concrete and Pb Shielding Tenth-Value Layer (TVL) Thicknesses for Common Radioisotopic Sources

Isotope	Pb TVL (mm)	Concrete TVL (mm)
²²⁶ Ra	16	69
⁶⁰ Co	12	66
¹³⁷ Cs	6	48
¹⁹² Ir	6	41
¹⁹⁸ Au	3	41

Source: Bossi, R. H. et al., *Nondestructive Testing Handbook*, third edition: volume 4, *Radiographic Testing*, American Society for Nondestructive Testing, Inc., Columbus, 2002.

PROBLEMS

- 7.1 There is a distinct plateau for the TVL thickness of Pb near an applied tube voltage of 110 kV. Why is this? Why is there not a similar feature in concrete?
- 7.2 The TVL thickness for Pb flattens at an applied tube voltage of 6–7 MV. Why does it not continue to rise like concrete?
- 7.3 What organ is damaged by high exposure to naturally occurring radon? What disease may be initiated by radon exposure?
- 7.4 For equal absorbed dose, which causes larger radiation effects: chronic irradiation or acute irradiation?
- 7.5 Is there any direct evidence of increased risk of noncancerous disease in humans from low doses of radiation?
- 7.6 What are the main two reasons that it is difficult to observe increased risk of cancer in a human population as a result of low-level radiation exposure?
- 7.7 Does a G-M counter measure ionization?
- 7.8 What should you do if you are opening the door of a cabinet x-ray unit and your G-M counter begins to click and then suddenly becomes silent?
- 7.9 Airline crews receive radiation dose from flying above much of the earth's atmosphere. Is this *occupational dose*?
- 7.10 What does the acronym TLD stand for?

8 Radiation Sources

8.1 INTRODUCTION

In this chapter, we will explore the attributes of x-ray and γ -ray sources, especially as they apply to using sources for imaging. First we paint an imaginary picture of what a perfect source would be. Then we describe sources as they exist along with some historical descriptions of earlier technology upon which today's sources rely. We address the design of major tube components and key auxiliary systems used with x-ray tubes. Then we address the x-ray spectrum emitted by an x-ray tube. We close out the coverage of x-ray tubes with two sections describing new x-ray source technology research.

We discuss the common electron accelerators that are used for generation of x-rays, describe pulsed sources, address research using laser-driven Thomson/Compton-scattered sources, and close the chapter with a brief overview of radioisotopes.

Upon completion of this chapter, the student will be familiar with

- All important attributes of x-ray or γ -ray sources
- Design features of currently available x-ray sources
- Various tube configurations for specific applications
- X-ray spectra created by sources
- Common continuous and pulsed sources
- New source technology under development
- Radioisotopic sources

8.2 THE PERFECT SOURCE

Before we begin the discussion of demonstrated technologies for producing x-rays, it is useful to think about what characteristics we might wish for in a source meant for imaging. A perfect source would be/have the following parameters:

- A point directed along a ray with selectable direction
- Tunable from 1 keV to 10 MeV with energy spread $\Delta E/E$ of 10^{-6}
- Phase coherent
- Selectable position
- Temporally pulsed with pulse width selectable from 1 attosecond (as, 10^{-18} s) to 1 s and duty factor from 10^{-3} to 1.0 (where 1.0 is continuous)
- Source strength selectable from 10^3 to 10^{100} photons/pulse
- Response time of near 0 s to changes in any of the above characteristics
- Operate only when turned on by an authorized user and present no safety risk when turned off

Let us examine each of these parameters of the perfect source. A point source has no source image blur, while a finite source size (greater than a point) causes a type of image blur, usually called source unsharpness (see Panel 8.1).

PANEL 8.1 Source Unsharpness

A simple method to visualize the effect of finite x-ray source size is to use a visible-light analogy. Imagine the effect of a point light source casting a shadow of a common machine screw on

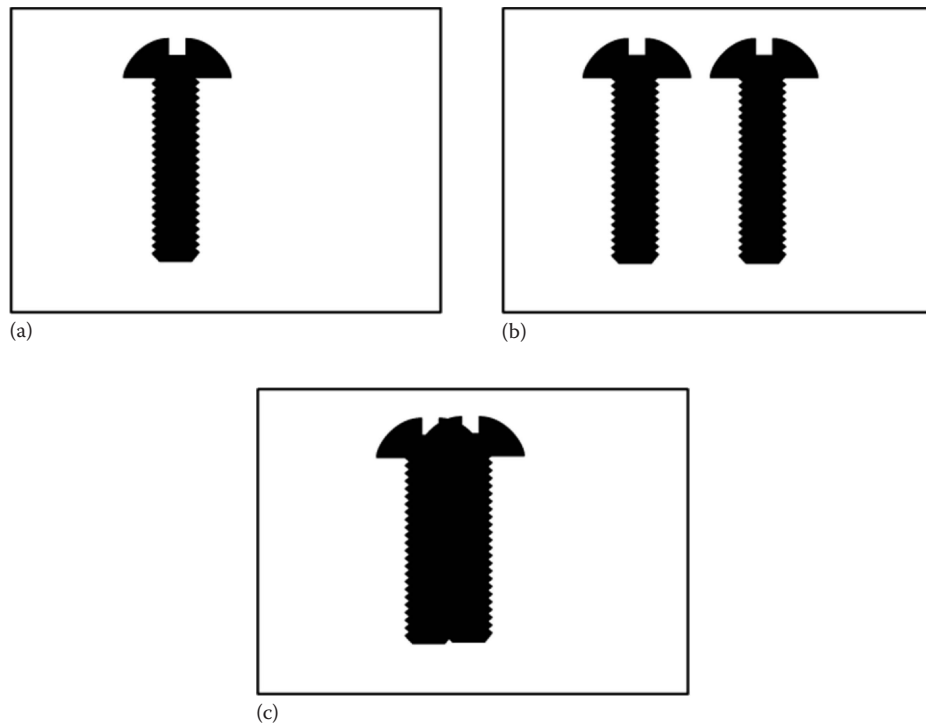


FIGURE 8.1 An illustration of x-ray source unsharpness using an optical analogy. (a) The shadow cast by a machine screw from a single-point light source located far from the object (screw). (b) If you have a second light source that is spatially separated from the first, you get a second shadow. (c) If the two sources are moved together, at some point, you would get the shadow shown in (c). The x-ray source produced by a tube is, in effect, the summation of many point sources of varying irradiance, each originating from a slightly different spatial position.

a blank wall. It would look like the image in Figure 8.1a. Simultaneously, casting shadows of a single screw onto a blank wall from two point light sources produces two shadows, as shown in Figure 8.1b. Each source produces a shadow on the blank wall. Now if the two sources are close enough to each other, the shadows begin to overlap, as in Figure 8.1c. When they are very close, the two shadows become only slightly out of register. The edges are blurred.

The typical x-ray image uses a source that is disk shaped. This produces an image similar to a multitude of images superimposed one on the other. Such an image is said to have source unsharpness or blur.

When source unsharpness occurs because of a finite x-ray source, the shadow on the image plane is said to have a *penumbra*. This is shown schematically in Figure 8.2. Comparing Figure 8.3a–b reveals the effect of source unsharpness on an image. Figure 8.3a is a digital radiograph acquired with the object on the detector so that source unsharpness did not contribute significantly to total image blur (simulates a point source). Figure 8.3b is the image of Figure 8.3a that has been numerically blurred using a Gaussian blur equivalent to taking the radiograph with a source 0.5 mm in diameter and the object midway between the source and detector. The two images in Figure 8.3 simulate the result of placing the object midway between the source and detector, acquiring

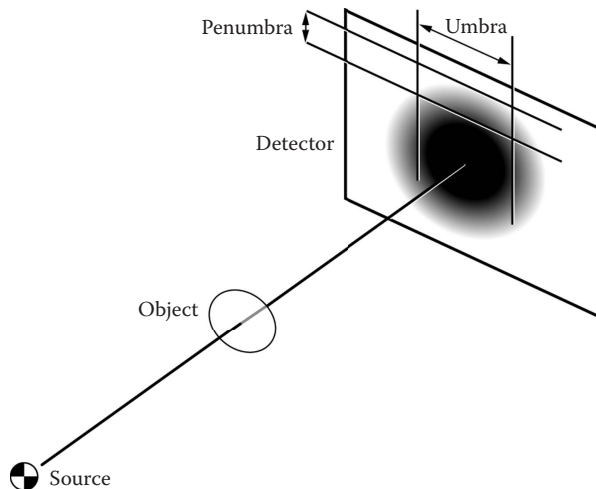


FIGURE 8.2 When a source is finite in size, the image formed of an object at the image plane has a penumbra, a region where only a portion of the finite source illuminates the detector without passing through the object. Sharp edges in the object appear blurred at the detector. The part of the image that is completely shadowed by the object is called the *umbra*.

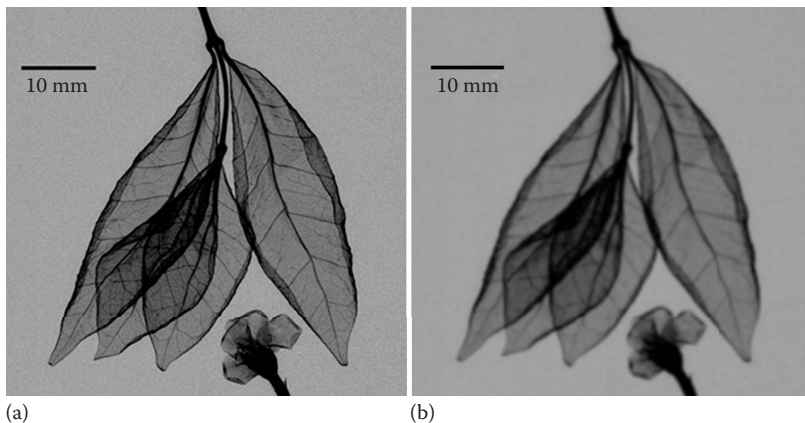


FIGURE 8.3 (a) A digital x-ray radiograph of a leaf and blossom taken in a geometry in which source unsharpness is negligible compared to detector element size. (b) The radiograph has been digitally blurred to simulate the effect of a Gaussian source casting a penumbra with a width of 0.5 mm. (Courtesy of Bioptics, Inc., Tucson, Arizona. With permission.)

a radiograph with a point source (Figure 8.3a), and then acquiring a radiograph with a 0.5 mm Gaussian source (Figure 8.3b). Clearly, small source size is desired.

We desire that a source have the ability to be pointed in any direction and that it have the ability to be positioned anywhere. This provides the capability to acquire radiographs from different angular directions and with different object views without physical movement of either source or object.

We have seen in Chapter 5 that the photon energy used to produce a radiograph should be chosen so that transmission is 0.5–20%. For our ideal tunable source, we have chosen the minimum energy to be 1 keV. This energy provides 11% transmission through $1 \mu\text{g}/\text{mm}^2$ of C. The areal density of

plastic kitchen wrap is about $10 \text{ }\mu\text{g/mm}^2$. One-tenth of this seems like a reasonable lower bound of industrial applications. We chose 10 MeV as the upper end of the range because to go higher introduces issues of activation with little benefit. Most often, high energies are sought to penetrate dense ($\sim 19 \text{ g/cm}^3$) materials. Maximum penetration for these materials is achieved with photons around 4 MeV (see Figure 5.18, Chapter 5).

We also ask that our ideal source be monoenergetic. This eliminates beam-hardening artifacts in computed tomography (CT, covered in Chapter 13) and enables elemental analysis of composition in three dimensions (Section 15.3).

We want the ideal source to be phase coherent so that the potential of diffractive and refractive effects can be fully realized.

Temporal control of an x-ray source opens the door to the study of dynamic events, such as impact, detonation, moving machines, gears, engines, implosions, and explosions. Temporal control is also used to capture images at the same point in repeating phenomena such as rotation. For example, one might image a specific blade in the turbofan of an operating jet engine and repeat the image every rotation as the rotational speed changes.

A lower limit for source strength is 10^3 photons/pulse for our ideal source. Fewer than this is just not very useful for imaging, even a single detector measurement. This is based on counting statistics. If we have 20% transmission through an object and perfect detection, then we are counting 200 of the original 10^3 photons. From this, we can expect the standard deviation of the counts to be $\sqrt{200}$. At the upper limit of 10^{100} photons/pulse, the energy deposited by the x-rays would destroy the test object.

The source is most useful if changes (for example, in position and energy) can be made quickly so there is minimal time lost while changing position or energy. Lastly, this imaginary x-ray source should be easily put in a safe configuration and present no radioactivity concerns.

8.3 SOURCE ATTRIBUTES: BRIGHTNESS, BRILLIANCE, IRRADIANCE, PHOTON FLUX DENSITY, PHOTON ENERGY SPECTRUM, AND SOURCE SIZE

One term describing an x-ray source is *brightness*. Most often, brightness is used in describing accelerator-based sources such as synchrotrons (see [Section 8.4.2.2](#)). Brightness is a very useful metric, but it is not the last and only important source descriptor and can be misleading if that is the only metric used. It encompasses the rate of photon production within a specified energy band, the effective source area, and the angular divergence of the source. The usual units are $\frac{\text{photons}}{\text{s} \cdot \text{mm}^2 \cdot \text{mrad}^2}$.

For synchrotrons, the energy band, ΔE , is usually specified as a percentage of E . The literature also uses the term *brilliance*. It is synonymous with brightness.

We caution you to not get caught up in the idea that higher brightness makes a better source. It all depends on the task at hand. A synchrotron source with high brightness is not much good for doing CT on a baseball. The energy is too low to penetrate the baseball, and the beam is too small to image the entire object. The lack of penetration cannot be overcome, while the small beam area can be overcome by rastering the beam over the baseball; sometimes, this is referred to as *tiling*.

Brightness is not usefully applied to x-ray tubes and radioisotopes. Purveyors of microfocal tubes will sometimes claim high brightness. This is advertising fluff. For x-ray tubes and radioactive sources, the photon flux density (photons/s mm²) varies inversely as the square of the distance from the source at distances greater than a few source diameters. Rather than brightness, it is far more useful to know the source size, the photon spectrum, and the irradiance or the photon flux density at a stated distance from the source. The source size defines the source unsharpness. The photon spectrum reveals the suitability for imaging with desired levels of transmission through the object. And the photon flux density at a stated distance tells you how long this image is going to require. Remember that it is not unusual to require 1000–4000 radiographic images for CT.

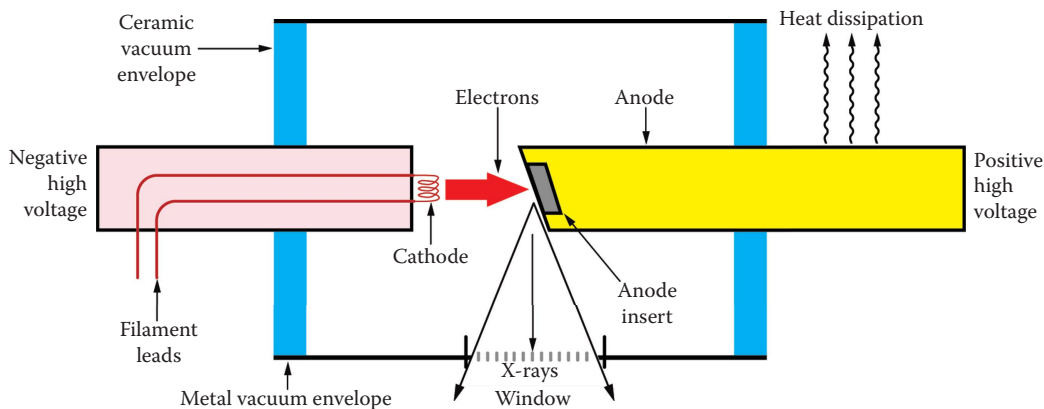


FIGURE 8.4 A schematic of an x-ray tube. Electrons are produced at the cathode and impinge on the anode or on the anode insert (if used). The insert is most often an alloy of W that has been brazed into a Cu piece to conduct heat away from the region where electrons impinge on the anode. Industrial tubes of this type are designed for continuous operation. They are usually cooled by air, oil, or water.

8.4 ELECTRICALLY POWERED X-RAY SOURCES

8.4.1 X-RAY TUBES

We traced some of the history of x-ray tube development in Chapter 2. The earliest tubes were based on establishing a gas discharge in a partial vacuum. These were temperamental and unstable devices. They relied on ion transport in the partial vacuum to produce electrons that then subsequently were accelerated and impacted the anode to make x-rays. In 1913, William Coolidge invented a tube that had the essential components of contemporary x-ray tubes. The Coolidge tube was thoroughly evacuated, used W for the anode* material, and had a heated W filament. Figure 2.10 (Chapter 2) is a photograph of a Coolidge tube. The heated filament serves as the source of electrons. It operated stably and was quickly adopted by the x-ray community.

8.4.1.1 Common Design Elements and Subsystems of X-Ray Tubes

The essential features of an industrial x-ray tube are shown in Figure 8.4. There is a vacuum envelope to exclude air, thus permitting the unobstructed flow of electrons from the cathode to the anode. The cathode is held at negative high voltage (kV) with respect to the anode. Different designs may have ground potential at the anode or at the cathode or be “center grounded.” In every case, the potential of the cathode is –10 to –500 kV with respect to the anode. This potential is the accelerating force on electrons liberated from the cathode. Electrons are produced at the cathode by passing a current through a filament, thereby heating it to incandescence. Electrons are then accelerated by the voltage gradient between cathode and anode.

8.4.1.1.1 Anode

An anode insert provides the material for stopping the electrons and converting ~1% of their energy into x-rays. The remaining energy, ~99%, appears as heat that must be conducted through the anode to a coolant to avoid melting or vaporization of the anode and destruction of the x-ray tube. Use of an insert allows using Cu for most of the thermal and electrical conduction path and a W anode insert or some other material (see the next paragraph for the usual choices) for producing x-rays. In some tubes, the coolant flows directly through the anode structure. In others, the tube is encased in

* Throughout this book, we use the term *anode* to describe the item upon which electrons impinge to produce x-rays. Another common term for the same item is *target*. We prefer *anode*.

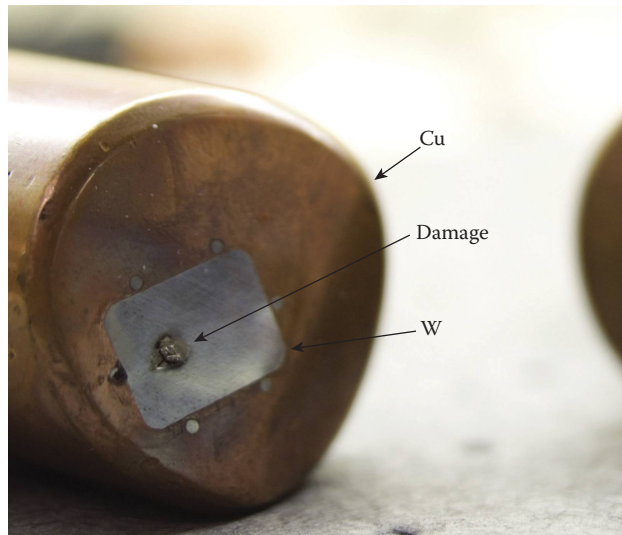


FIGURE 8.5 An anode taken from an industrial x-ray tube after it was destroyed by an electron beam with power density in excess of the tolerance of the anode insert. The main body of the anode is made of Cu. The anode insert is made of W.

a tank and the interstitial space filled with oil coolant. Some tubes with low total power, especially *microfocus* tubes and portable systems, may convect heat directly to room air.

The anode insert must make x-rays, conduct electrons, conduct heat, and not melt or be unduly sensitive to abuse by energetic electrons. W is by far the most common anode material. It has a high melting point (3422°C) and good conductivity (1.74 W/cm K). It produces intense bremsstrahlung, and its K lines are at an energy that is often useful. Mo and Rh are also used, especially for mammography (breast-imaging) tubes. Cu is used for lower-energy spectra needed in x-ray diffraction, and Rh is often used for x-ray tubes devoted to x-ray fluorescence because Rh is rare in nature and, therefore, its characteristic lines do not interfere with elements present in the sample being analyzed.

The type of tube shown in Figure 8.4 is a metal–ceramic tube. The ceramic serves as a vacuum envelope and electrical insulator. Most modern industrial x-ray tubes are of this type. Earlier designs used glass envelopes.

The anodes of x-ray tubes are susceptible to overloading. If too much power (power in watts is the product of tube current in mA and tube voltage in kV) is contained in the electron beam for a given diameter, then the anode will overheat, causing excessive vaporization of anode material or even melting. Figure 8.5 is a photograph of a tube anode that has been melted by the incoming electron beam. Clever cooling design may stretch the boundary, but an electron beam can always be made that will damage any anode. Electron beam welding provides sufficient evidence that this is true. X-ray production in an x-ray tube is proportional to tube current but not to tube power. This is because of the approximate voltage-squared dependence on applied tube voltage, as discussed in Chapter 4, Physics of X-Ray and γ -Ray Sources.

Heat transport within the anode is complex. The paper by Pankratov and Chkhalo (2006) is an example of the attention this receives from theoreticians. Their simplified equation for maximum power fills half a journal column. For the person who wants to use x-ray tubes, it is more useful to look at actual results. Each point plotted in Figure 8.6 represents a tube available for purchase in 2007 from the manufacturers listed in the figure key. All have stationary* W anodes. The tubes are

* Rotating anode tubes are covered in Section 8.4.1.2.3. These are seldom used for industrial applications because most are not suitable for continuous use.

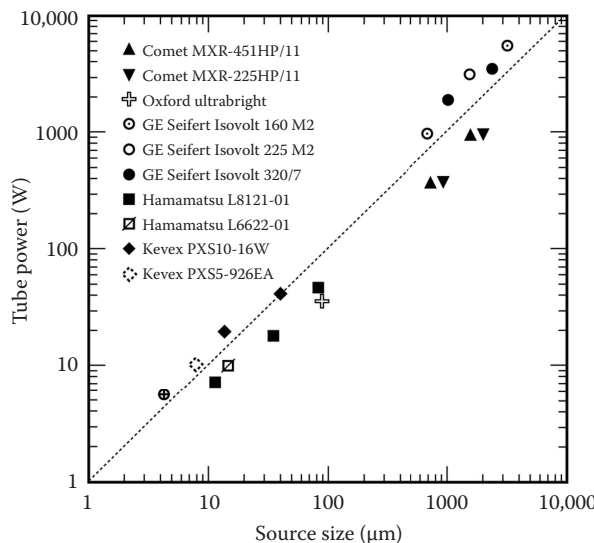


FIGURE 8.6 The allowable power in the electron beam for x-ray tubes as specified by their manufacturer (Comet 2007; GE 2007; Hamamatsu 2007; Kevex 2007; Oxford 2007). All are a stationary W anode. Most tubes offer variable source size and applied voltage with consequently different allowable power. Only the maximum power is plotted for each tube. The Comet series offers MXR-160HP/11 and MXR-320HP/11, which have the same values of tube power and source diameter as MXR-225HP/11. Only one of these is plotted, for clarity.

rated in the range from 60 to 450 kV. For each tube, the maximum allowable power is plotted versus the source size. The data were collected from the manufacturers' websites. In every case, the spot size is reported as measured by the method specified in one of the series of Deutsches Institut für Normung e.V. (DIN) EN 12543 standards (DIN EN 12543-1 1999; DIN EN 12543-2 1999; DIN EN 12543-3 1999; DIN EN 12543-4 1999; DIN EN 12543-5 1999). These standards address several different methods, discussed in the next paragraph. The line shown in Figure 8.6 is not a fit to the data but is simply an old rule of thumb for tubes with small source size that they will withstand 1 W for every 1 μm of beam diameter. It turns out that the rule is a reasonable approximation of achievements over four orders of magnitude in beam diameter and without regard to applied voltage.

The DIN EN 12543-[part number] standards referenced in the preceding paragraph warrant a description. In this paragraph, we use words from the DIN standards that may not be exactly as we would define them. We denote such words with **. Before these standards were issued, manufacturers were free to specify any spot size they wanted to market. Part 1 of the standard covers the DIN scanning method. In this method, a square collimator with variable opening is used to measure radiation **intensity** as the collimator and detector are scanned across the source in orthogonal directions. The collimator opening is specified based on spot size. The detector is specified as a thick scintillator/photomultiplier system, so **intensity** is equivalent to what we define as irradiance. This is then scanned and converted to an **isodose** contour plot, which in turn is used to interpret the spot size. DIN EN 12543-2 defines a pinhole method in which film is used to image the spot, and manual interpretation defines the dimensions of the spot image. DIN EN 12543-3 is a slit collimation method using film and manual interpretation. DIN EN 12543-4 is an edge method using film and measured optical density profiles. DIN EN 12543-5 is a method specific for spot sizes between 5 and 300 μm using a ball or crossed wires to produce sharp edge(s), film, and optical density profiles.

8.4.1.1.2 X-Ray Window

The most versatile industrial x-ray tubes are equipped with a Be window. This permits the passage of x-rays of the lowest energies. A 1-mm-thick Be window (most are thinner than this) transmits

90% of 10 keV x-rays. Some tubes are sold with considerable material in the x-ray path. It may be the metal vacuum envelope, i.e., it has no special x-ray window. There may also be coolant and an outer container in the path. Manufacturers lump this into something called *inherent filtration*. If you purchase a tube of this type, you are stuck with stuff in the beam forever. You can always add external filtration to a tube with a Be window, but you cannot remove inherent filtration. One final note about Be windows. Be is a toxic material and must not be scrapped indiscriminately.

8.4.1.1.3 Vacuum

X-ray tubes can either be evacuated and sealed or have active vacuum systems. The advantages of sealed tubes are their simplicity, lower cost, and lower maintenance. But the disadvantage with sealed tubes is that the entire unit must be replaced when any internal component fails or when performance degrades to an unacceptable level. A tube with an active vacuum allows components such as filaments, anodes, and windows to be replaced.

8.4.1.1.4 High-Voltage Power Supply

The earliest power supplies* for x-ray tubes were *self-rectified*. They supplied high-voltage alternating potential to the tube, and the tube served as a rectifier. A rectifier allows electrons to flow in only one direction. Using the tube for the rectifying function was convenient because high-voltage alternating potential can be easily produced from conventional utility power using a transformer. Electrons are produced at the cathode by heating the filament. These are accelerated to the anode by the applied potential. Current then flows from cathode to anode in the tube every half cycle of the alternating potential. No current flows during the alternate half cycle when the tube is operating correctly. These systems self-destruct if the anode becomes hot enough to emit electrons that then flow from anode to cathode within the tube, destroying the cathode and other stuff.

8.4.1.1.5 High-Voltage Power Supply Waveforms

Rectifiers in the high-voltage power supply eliminate the problem of reverse current flow within the tube and were quickly adopted.

Rectifiers simply blocked the reverse current flow, so that the applied waveform is as shown in Figure 8.7a. This type of system is called *half-wave rectified*. Clearly, the x-ray output from a tube supplied with this applied voltage will be pulsed, and the spectrum will be time dependent, according to what voltage is being applied. Power supplies of this type were described by the peak voltage applied to the tube, denoted kV_p . This is pronounced “kay-vee-pea.” This was a useful descriptor but incomplete. It does correspond to the maximum possible energy of x-rays produced, but the tube spends most of the power cycle time at lower applied voltage producing lower-energy x-rays. Tubes with this type of power supply produce x-rays in pulses corresponding to the frequency supplied by the power supply.

The addition of a more sophisticated rectifier produces a *full-wave rectified* waveform, as shown in Figure 8.7b. If the power is supplied with three phases, then six pulses per power cycle can be produced in this manner. The waveform is then best described by the average voltage and the “ripple,” usually expressed as a percentage of the average voltage. A waveform with 10% ripple is shown in Figure 8.7c.

Contemporary power supplies rectify and smooth input alternating current power and then chop and invert the waveform to produce higher-frequency (up to 100 kHz) square-wave voltage. A voltage transformer increases the voltage (still alternating), and rectifiers convert to high voltage with low ripple. These designs are called *medium frequency* or *high frequency*. The term used depends on the author or marketing department, not on the frequency. In any case, it is ripple that matters. With this type of supply, ripple is rarely more than a few percent and is often less than 1%. Medium-frequency power supplies are smaller, lower mass, and less expensive than older designs. They are better in every way than the technology they replaced.

* The word *generator* is often used in the x-ray business rather than *power supply*.

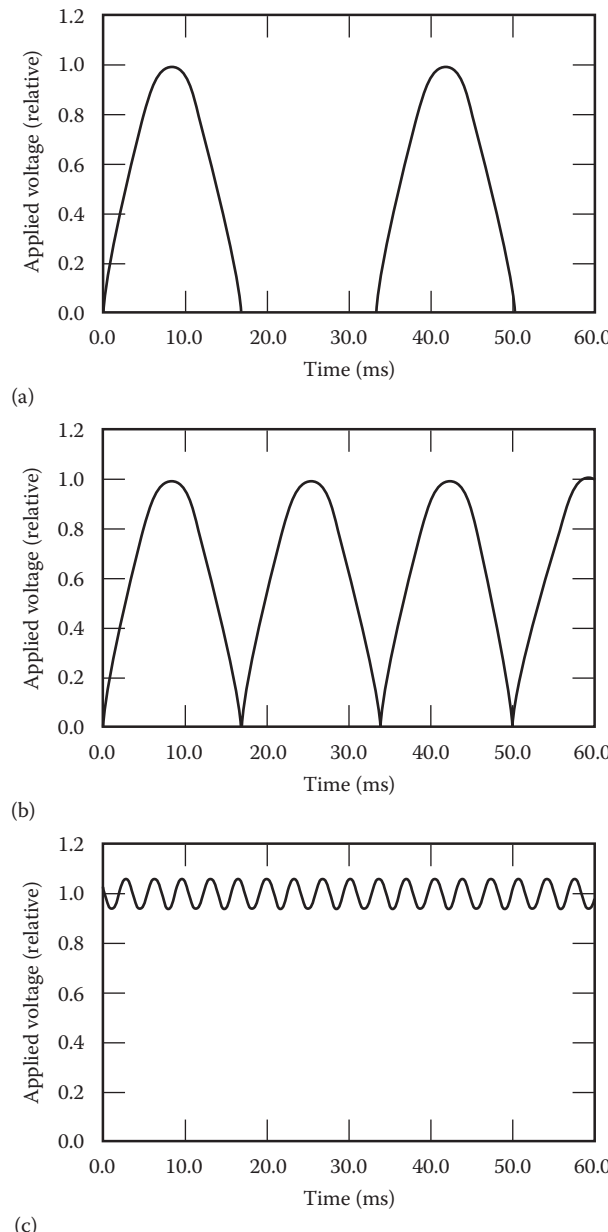


FIGURE 8.7 (a) The temporal shape of a half-wave rectified voltage is shown. (b) Full-wave rectified power. (c) The waveform of a power supply with 10% ripple. Contemporary power supplies typically have ~1% ripple.

Older machines with half- and full-wave rectified power are still in service. Our advice is to avoid them. They often have poor voltage and current control. We have personally attempted to use equipment in which the irradiance actually *decreased* with increased current. We discovered that the high voltage dropped under the demand of higher current.

8.4.1.1.6 kV versus kV_p

We return here to the term kV_p , which we introduced earlier. It was introduced to indicate the peak voltage applied to an x-ray tube by a power supply with large temporal variation. Unfortunately, it

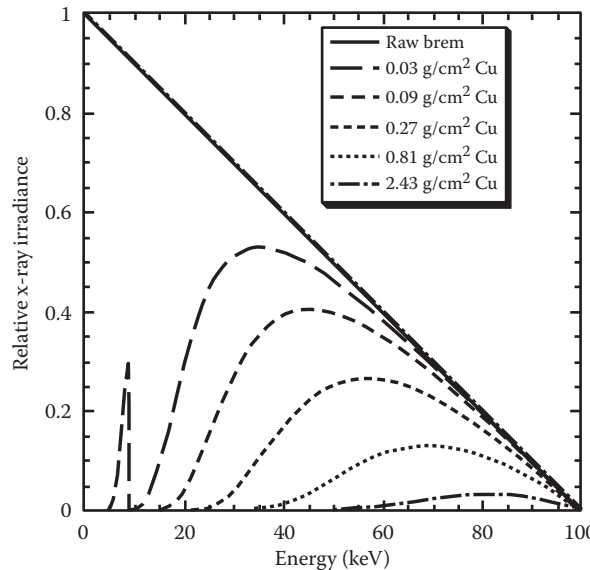


FIGURE 8.8 Plot of the effects of x-ray filtration. The solid line represents the spectrum generated by slowing down of electrons. This is the spectrum as it is created. It is not the spectrum that is emitted from the anode after absorption within the anode. The dashed lines represent the shape of the x-ray spectrum after being filtered, as given in the key.

entered the lexicon of the profession and continues to be (mis)used, even when the power is essentially constant potential. We think kVp should be reserved for antique equipment and that kV should be used to describe power supply voltage on modern equipment.

8.4.1.1.7 Spectra

In Chapter 4, Physics of X-Ray and γ -Ray Sources, we discussed the production of bremsstrahlung and characteristic x-rays by energetic electrons. The physics discussed in Chapter 4 has been incorporated into software packages named SpecCalc, TASMIP, and Spektr (Boone and Seibert 1997; Siewersen et al. 2004; Poludniowski et al. 2009). These have been developed by and for folks devoted to medical imaging and limited to anode materials and tube configurations relevant to medical imaging.

In Figure 8.8, we present a bremsstrahlung spectrum created by 100 keV electrons and show how it is modified by Cu filtration. The most obvious trait of bremsstrahlung radiation is that the maximum possible energy corresponds to the energy of the incident electron. Industrial tubes most often have a W anode, and the L and K lines of W will be superimposed onto the bremsstrahlung continuum.

Figure 8.9 presents the spectrum from a tube with substantial inherent filtration.* The tube inherent filtration removes the W L lines near 10 keV and nearly all the bremsstrahlung x-rays below 20 keV. Absorption within the W anode has also influenced this spectrum. Some of the absorption below 20 keV is attributable to the anode. More evident is the drop in x-rays due to absorption that occurs at the W K edge, at the high-energy side of the K_{β} line. The resulting drop in the spectrum is noted in Figure 8.9. The specific conditions for this spectrum are 1 m distance in air from an x-ray tube with a W anode, 20° takeoff angle, and 2.5 mm Al equivalence of inherent filtration. The two W K lines are clearly evident. The takeoff angle is the acute angle between the x-ray trajectory and the anode surface. It is labeled θ_{TO} in Figure 8.10.

* Inherent filtration is filtration caused by tube components such as cooling jacket and window. Windows are not always Be.

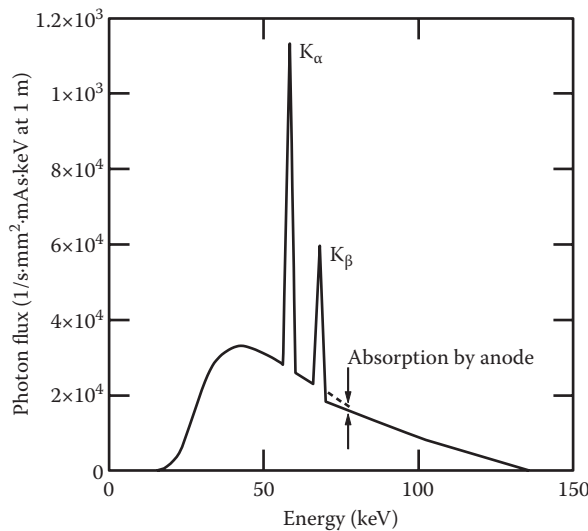


FIGURE 8.9 This plot presents the calculated spectrum at 1 m distance from an x-ray tube operating in air. The anode is made of W, and the takeoff angle is 20° (see Figure 8.10). The inherent filtration of the tube as specified by the manufacturer is equivalent to 2.7 mm of Al. The K edge of W occurs just above the K_β characteristic line. The increased absorption in the anode above the K_β line is evident in the figure. The drop in photon flux labeled “absorption by anode” is caused by the abrupt increase in the mass attenuation coefficient of W at 70 keV.

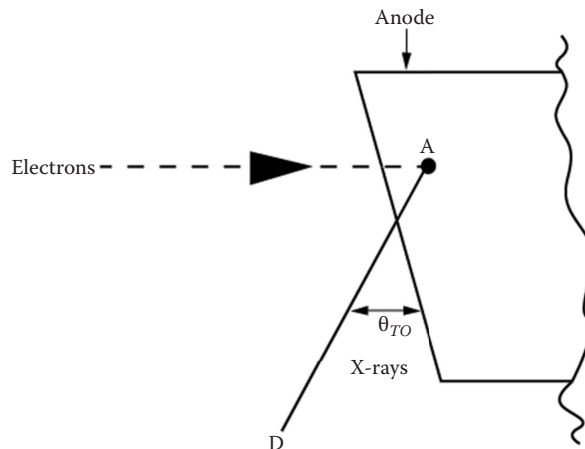


FIGURE 8.10 The angle θ between the anode surface and the x-ray path is called the *takeoff angle*.

Filtration can be applied to modify the output spectrum of an x-ray tube. In the simplest case, the softest (lowest-energy) x-rays are selectively absorbed. This was covered in detail in Chapter 5, High-Energy (X-Ray and γ -Ray) Photon Interactions with Matter. But be aware that spectrum modification by filtration reduces the number of photons. You can make a spectrum that is very narrowly peaked, but you may not have enough photons left to do anything useful. Figure 8.11 shows the effect of filtering with an additional 0.5 mm of Au. We chose this filtration to illustrate spectral features. The filtered spectrum is nearly all between 50 and 80 keV. The sharp cutoff near 80 keV is caused by the Au K edge. We have created a spectrum with three sharp peaks and a high-energy hump. You are advised to use a spectrum like this with caution. To emphasize that

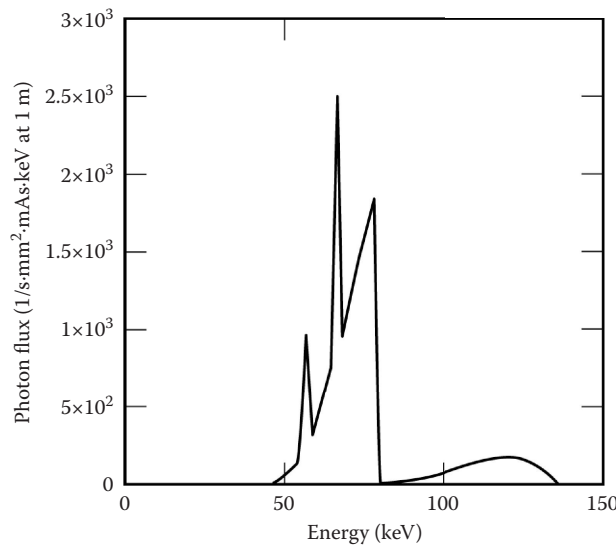


FIGURE 8.11 The spectrum resulting if you filter the spectrum from Figure 8.9 with an additional 0.5 mm of Au. The total x-rays of all energies are reduced by a factor of 62 by filtering. While the resulting spectrum is fairly narrowband, it is decidedly bizarre with three distinct peaks.

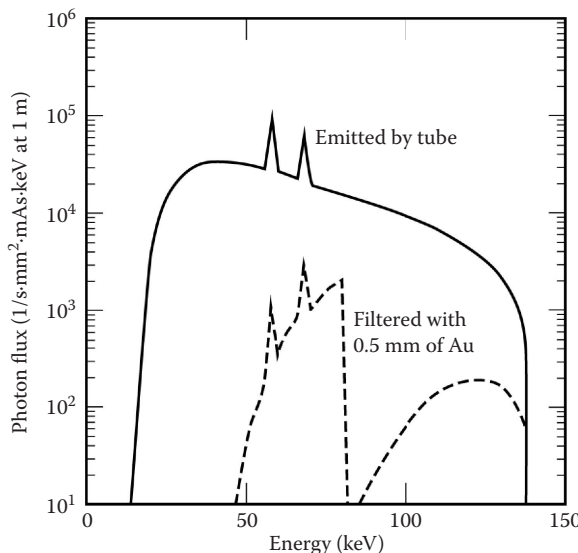


FIGURE 8.12 The spectra of Figures 8.9 and 8.11 plotted together in semilog format. The additional Au filtration both alters the spectrum shape and diminishes the irradiance.

filtering depletes the photon flux in a spectrum, the spectra from Figures 8.9 and 8.11 are shown together in Figure 8.12.

8.4.1.1.8 Heel Effect

The term *heel effect* is used to refer to the positional variation in x-ray irradiance and spectrum that is present in x-rays emitted from x-ray tubes. There are several causes for this variation. X-ray production is not isotropic. In addition, x-rays are produced at different depths within the anode,

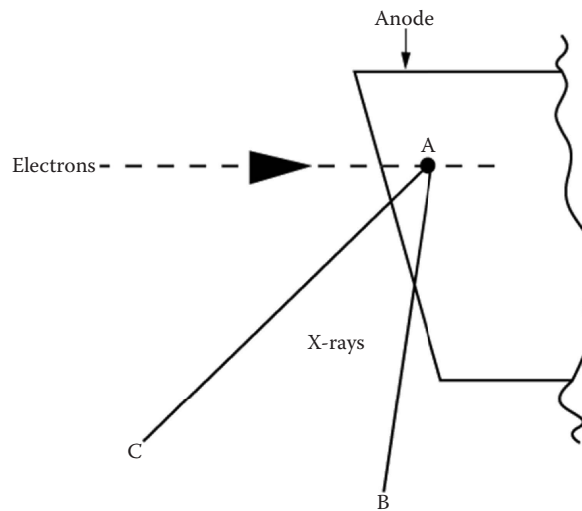


FIGURE 8.13 In an industrial x-ray tube, electrons penetrate some distance into the anode before producing an x-ray. This is shown schematically here as point A. This point of origin can lie anywhere along the electron path. Electrons produce x-rays with varying spectra and irradiance depending on the angle to the electron path. In addition, an x-ray traveling along ray AB passes through more anode material than an x-ray traveling along ray AC. There is more attenuation and more spectral modification along the path with more material, path AB. This gives rise to irradiance variations and spectral variations within the area of an image captured with an area detector. In addition, the distance from source to detector can vary over the image plane, giving rise to additional variation. The combined effects are called the *heel effect*.

the maximum depending upon the anode material and the energy of the incident electrons. Once an x-ray is produced, it must penetrate through some distance of anode material before it can escape the anode and be on its way to a useful purpose. This distance depends on the depth of origination and the takeoff angle. This effect is illustrated in Figure 8.13. The attenuation that occurs in the anode reduces irradiance and hardens the spectrum (removes lower-energy x-rays more than the higher-energy x-rays). In addition to the attenuation that takes place in the anode, the window and flight path also influence the x-ray spectrum.

The heel effect is very evident in the fine-art image shown in Figure 8.14. This is an x-ray image of an orchid produced by Meyers (2010).

One note of caution: in the literature, you can find plots purporting to quantify the heel effect. These are mostly nonsense. The magnitude and shape of the heel effect clearly depend on the details of the electron beam, detector, window, anode, and x-ray beam geometry. You could determine the positional variation of irradiance and spectrum if you had all the tube details and did an extremely complex analysis.

The heel effect is a three-dimensional problem, but the variation is substantially greater in the plane defined by the electron beam and the normal to the anode surface than it is in the orthogonal direction. Notice in Figure 8.14 that the heel effect from lower left to upper right is greater than in the orthogonal direction. This means that correctly arranged linear detectors can be subject to a much-reduced heel effect compared to area detectors.

8.4.1.2 X-Ray Tube Configurations and Tube-Like Sources

8.4.1.2.1 Metal–Ceramic X-Ray Tube

The x-ray tube depicted in Figure 8.4 is the most common design used in nondestructive evaluation (NDE) applications. X-rays typically emerge from the anode at 90° to the electron beam axis. They then pass through an x-ray window. The axis of the x-ray beam is typically $20\text{--}45^\circ$ from the anode surface. This angle is called the takeoff angle (see Figure 8.10). The inclination of the anode with respect to the



FIGURE 8.14 A radiograph of orchid blossoms. Note that this is a negative image (high irradiance corresponding to black). This fine-art image incorporates the heel effect as an integral contributor to the composition. The irradiance from the tube is highest in the lower left corner and diminishes at the top right. (From Steven N. Meyers, <http://www.xray-art.com>. With permission.)

incident electrons spreads the thermal loading somewhat. Ceramic insulators prevent current flow from the anode or cathode except within the tube. One or the other (anode or cathode) may be grounded.

8.4.1.2.2 Transmission-Anode X-Ray Tube

An x-ray tube can be configured so that the usable x-rays are transmitted through the anode assembly to the exterior of the tube. This places the x-ray beam along the same axis as the incident electron beam, as shown schematically in Figure 8.15. This offers the significant advantage that a specimen or sample can be placed very close to a small source for geometric magnification or x-ray fluorescence. For example, common tubes (see Figure 8.4) have a distance of 40–60 mm between the spot where electrons hit the anode and the outside of the window. With transmission-anode tubes, this distance can be <2 mm. The transmission-anode design results in very compact tubes that are typically low power (Jensen et al. 2004). Hamamatsu model L-10711 (Figure 8.16) in the standard configuration uses a W anode material put on a Be window. A specimen can be placed less than 1 mm from the source. This tube also features 140° beam coverage.

Transmission-anode geometry has a second attribute that can be useful. Because of the axial symmetry, the spectral and irradiance variation (heel effect) are very much less than in a common tube (see Figure 8.13 and Section 8.4.1.8, Heel Effect) in which the x-ray beam is not normal to the anode surface.

Of course, for every advantage, there are disadvantages. A transmission anode must be thin for x-rays to escape. This limits the thermal capacity and heat transport capability of the anode, restricting its use to low power. Secondly, even though thin, spectral alteration takes place in passage through the anode and window. This may be slight but must be considered. This configuration is not generally useful for x-rays of <10 keV energy.

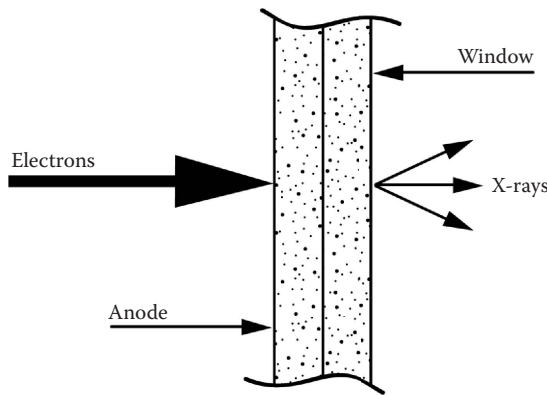


FIGURE 8.15 A schematic of the tube configuration for a tube in which the x-rays pass through the anode before exiting the tube.



FIGURE 8.16 Hamamatsu transmission-anode x-ray tube. This tube has an active vacuum. The pump is on the right in this photo. X-rays exit at the top of the tube in the orientation shown. A specimen can be placed within 1 mm of the x-ray source with this tube. (Photograph courtesy of Hamamatsu Photonics K.K., Iwata Shizuoka, Japan and Hamamatsu Corporation, New Jersey, USA.)

8.4.1.2.3 Rotating-Anode X-Ray Tube

Rotating-anode x-ray tubes are not generally used in industrial imaging applications, but they are used extensively in medicine (Pifferi 2005) and in x-ray diffraction work. The main reason for this is that they are usually designed for very intense tube loading (high power density) for short times. They need cool-down time between short exposures. This fits the traditional medical workload where a patient is repositioned and a new film cassette is put in place between each radiograph. Longer pauses occur with patient changes, allowing for more cool-down time.

The purpose of rotating the anode is to spread the heat load from the interaction of the electron beam with the anode over a larger area, thus permitting the use of higher power density in the electron beam. In addition to rotation, a small takeoff angle for x-rays is employed. This is done so that the heating can be further spread over more material while maintaining the apparent source dimensions. The combined effect of rotation and shallow takeoff angle is a source with an apparent irradiance at the desired energy region that is ~20 times that of a continuous-duty industrial tube. Operation at this irradiance is limited to less than 1 s duration. The shallow angle foreshortens the apparent beam in one direction. The electron beam is elliptical or oval in cross section so that the apparent foreshortening in one direction produces a source that is approximately circular as viewed from the direction of the radiograph.

It is useful to interject at this point that this apparent reduction in source size without penalty in irradiance occurs with x-ray sources because the emission of x-rays is nearly isotropic (at $E < 1$ MeV). X-ray sources employing electrons slowing in material emit with equal irradiance in all directions. Folks steeped in the lore of visible-light sources find this strange indeed. In that world, light sources are surface emitters and are approximately *Lambertian sources*. Lambertian sources emit with greatest irradiance normal to the surface and diminish as the cosine of the angle from the normal.

The anode of a rotating-anode tube is typically about 100 mm in diameter and rotates up to 10,000 rpm. The anode is mounted on a shaft, and the rotor component of the drive motor is integral with the shaft, as shown in Figure 8.17. The bearings must operate in a vacuum and conduct high voltage while rotating at high temperature. This is a complex engineering task. The stator portion of the drive motor is outside of the vacuum envelope. Everything that rotates is inside the vacuum envelope. The portion of the anode where x-rays are produced, the anode insert, is W (general medical imaging), Mo (mammography and some nano-CT systems), Rh (mammography), or Cu (diffraction). The bulk of the mass of the anode consists of material chosen for its heat capacity and ability to endure high temperature. The entire 100-mm-diameter rotating anode becomes incandescent under repeated periods of x-ray production. The most common thermal sink materials are Mo (heat capacity = 0.25 J/g K) or C (heat capacity = 0.71 J/g K) (Chemix 2010).

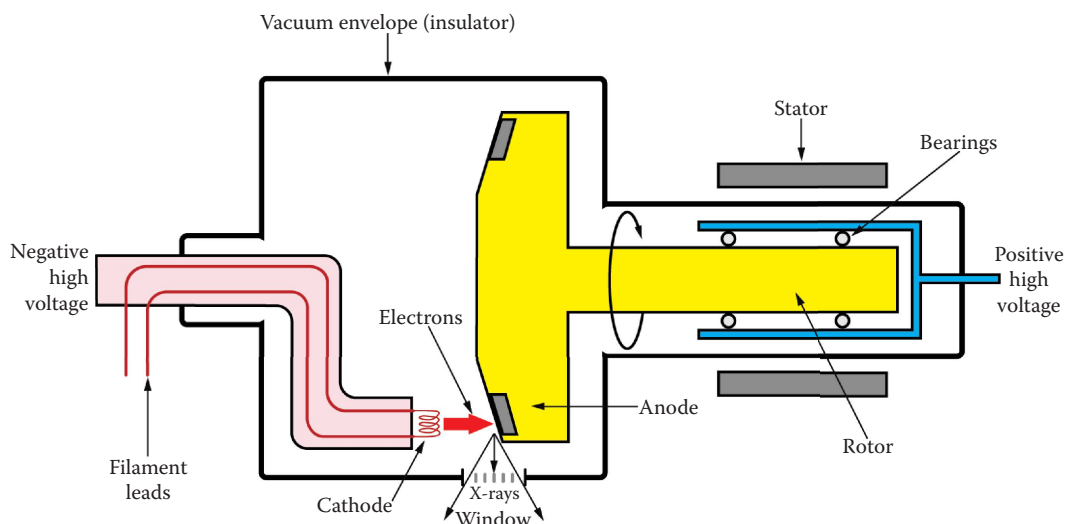


FIGURE 8.17 A rotating-anode x-ray tube is shown schematically. The anode rotates so as to distribute heat from the electron beam over more material. These tubes are designed for brief periods of use during which the rotating components rise in temperature. Longer recovery periods are required for the anode to radiate the stored heat to the surroundings. The bearing must operate at 10,000 rpm in a vacuum at elevated temperature while conducting high voltage.

During the subsecond time that x-rays are being produced in a rotating-anode tube, heat is conducted over a short distance (<1 mm). Over a period of tens of seconds, this heat is conducted to the thermal sink portion of the anode. With repeated use, the entire rotating anode becomes hot enough to radiate the absorbed heat to the tube housing. The housing may be cooled or filled with coolant. Some rotating-anode tubes have special coatings on bearings that are claimed to conduct some heat from the thermal sink to the housing.

8.4.1.2.4 Microfocus X-Ray Tube

There is no standard or specification that defines *microfocus* as it applies to x-ray tubes. The industry convention is to use that descriptor for tubes with source size less than ~100 μm . By this convention, about half of the commercial tubes represented in Figure 8.6 are microfocus. These tubes allow the use of geometric magnification. Most are configured to permit placing an object within 25–35 mm of the source. This makes it possible to resolve structure within an object that is much smaller than the detector element size.

8.4.1.2.5 Reverse-Geometry X-Ray Source

The most conventional geometry for radiography is with a fixed source at a distance of 1–3 m from the object and with the detector close (few mm) to the object. This became the convention because it minimizes the blur caused by finite source size and it makes the best use of the inherent high spatial resolution of x-ray film when used without a scintillator or screen. It is not necessarily optimal with the advent of microfocus x-ray tubes and electronic detectors. In *reverse geometry* (also called *inverse geometry*), the source is positioned as desired within a surface, and the object is placed near the source. One or a few detectors are placed some greater distance from the object (see Figure 8.18). Digiray was an early developer of this configuration (Albert and Albert 1993; Vossoughi et al. 2007). Their source uses an electron beam that can be steered over a large-surface-area transmission anode analogous to a cathode ray tube. The usable x-rays must pass through the anode stopping material and a vacuum window. The vacuum window is typically made of aluminum alloy.

Recently, a conceptually similar design has been commercialized for medical applications (Heanue et al. 1999; Solomon et al. 1999; Speidel et al. 2001, 2006a,b; Nett et al. 2004; Schmidt et al. 2006). In this source, coolant is circulated through the layered structure containing the anode, vacuum window, and collimation (for dose reduction in medical application).

Reverse geometry has three main advantages. It decreases the deleterious effects of object scatter by increasing the distance from the object to the detector (see Figure 8.19). It distributes

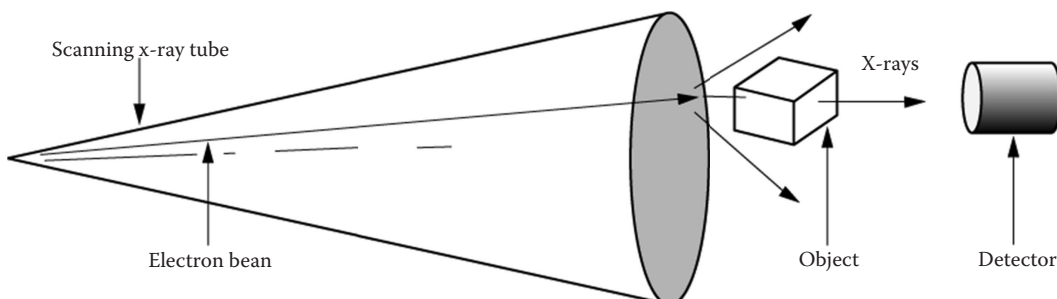


FIGURE 8.18 A schematic of reverse geometry. The name is loosely derived by contrast with the more conventional geometry with a stationary source. Digiray Corp. pioneered this geometry, in which the x-ray source tube employs a scanning electron beam resembling the configuration of a cathode ray tube. The position of the source is time variant. The spot size of the source is typically small compared to conventional tubes. The detector is a point detector that is typically spatially fixed. The object is usually placed near the source.

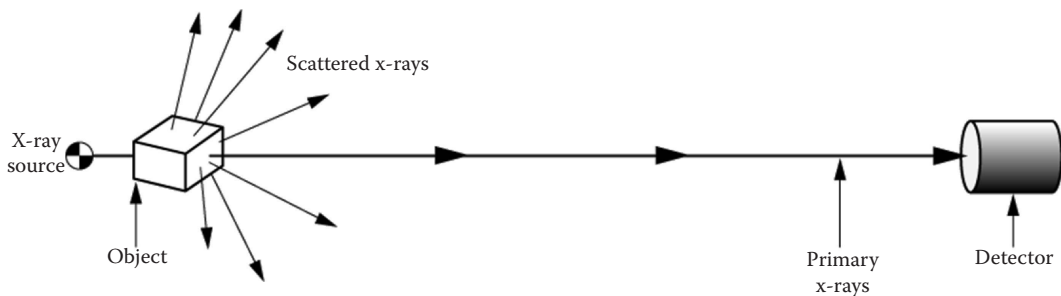


FIGURE 8.19 When the object is located far from the detector, x-rays scattered from the object are less likely to reach the detector and degrade the image. The primary x-rays transmitted through the object contain the image information. Scattered x-rays muddle the image.

the heat from electron bombardment over a surface much larger than the source area, thus allowing continuous operation without circulating coolant. And the detector(s) is laterally small, making it immune to scatter within the detector itself. Because of this, the detector can be made with sufficient areal density and appropriate composition so that it detects most of the x-rays that enter the detector. Reverse geometry also is adapted to stereo imaging (two detectors), laminography (5–50 detectors), and CT with few degrees of object motion (array detectors).

8.4.1.2.6 Contemporary Cold Cathode X-Ray Tube

Very early x-ray tubes generated electrons by bombardment of a cold cathode with ions created by a gas discharge in the tube. In Section 2.7, we described how the Coolidge x-ray tube using a heated cathode was a big step toward practical application of x-rays. Recently, x-ray sources have been developed that once again use a cold cathode (Yue et al. 2002; Cheng et al. 2004; Liu et al. 2006). The tips of a carbon nanotube can be made to emit electrons by the application of a sufficient voltage gradient. These sources can be exquisitely timed, and they can be compact (Liu et al. 2006). This leads to source assemblies containing arrays and to applications imaging objects with periodic motion (Cao et al. 2009a,b; Merali 2009). This type of source can also be made to have extremely small source size. Yabushita and Hata (2006) report an electron beam diameter of 50 nm and x-ray images with 700 nm spatial resolution.

Carbon nanotube field emission can be configured so that multiple sources are positioned almost as desired. Xintek (Merali 2009) is developing systems for medical and industrial applications employing multiple sources in a configuration that is reminiscent of reverse geometry but with much greater flexibility in source placement and with higher temporal and spatial precision than is possible with scanning electron beam sources. A carbon nanotube source x-ray CT system was designed and built for luggage scanning as described in Section 16.5.4.3.

8.4.1.2.7 Liquid-Anode X-Ray Tube

Two research laboratories have published work toward development of an anode consisting of flowing liquid. Most work has been done with metals and alloys of moderate melting point. The Philips group (Harding et al. 2003a,b) has worked with metal flowing in a closed conduit. They confined the liquid with a very thin window. The Swedish group (Otendal et al. 2004, 2005, 2007, 2008; Tuohimaa et al. 2007) uses unconfined liquid jets in vacuum.

These devices employ the same principle as rotating-anode x-ray tubes. They limit the temperature of the anode by distributing the heat deposited by the electron beam over more material than is possible by conduction in a static anode. However, with a liquid anode, turbulence assists heat transport, and the flowing liquid transports heat to a heat exchanger.

8.4.2 ELECTRON ACCELERATOR-BASED SOURCES

X-ray tubes are limited by voltage-holding considerations to about 450 kV. To perform megavoltage radiography, the NDE community needed a different type of source.

8.4.2.1 Electrostatic Generator

The first machine to break the megavolt barrier was the Van de Graaff, invented by Robert Van de Graaff in 1930. Van de Graaff was motivated by the desire to accelerate atomic nuclei for the study of nuclear physics (Van de Graaff et al. 1933). His first machine did not achieve 1 MV, but he demonstrated 1 MV at the 1933 meeting of the American Institute of Physics. The same month, a machine he built at the Massachusetts Institute of Technology (MIT) produced 7 MV between two Al spheres, each 15 ft. in diameter (Fufari 2005). This machine was a very large device, as is evident in Figure 8.20. It stood 43 ft. tall.

Van de Graaff's BS and MS degrees were in mechanical engineering, and mechanical wizardry is at the heart of his invention. A moving belt transports charge to the high-voltage terminal, and pressurized gas is used as insulation in later versions. Acceleration of charged particles is achieved by passage through a column in which the voltage gradient is carefully maintained.

These electrostatic machines were quickly applied to accelerating electrons for use as x-ray sources for radiography and cancer therapy. By the time the United States entered World War II (WWII), many machines existed that could achieve 2 MV, and they saw use in ordnance radiography (Fufari 2005). Van de Graaffs now have been largely retired from NDE service. They tended to be large and heavy. Belt maintenance was always a challenge, and high-pressure gas transfer is nice to avoid.

8.4.2.2 Synchrotron X-Ray Source

A type of charged particle accelerator called a synchrotron can be used to produce a large flux density (or high brightness) of x-rays. Synchrotrons used in this way circulate electrons at nearly

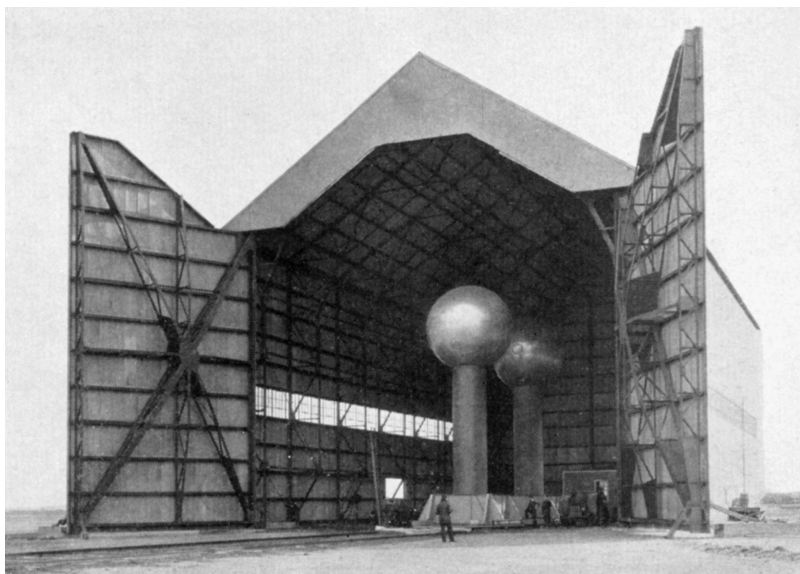


FIGURE 8.20 A large Van de Graaff electron accelerator designed by R. J. Van de Graaff, K. T. Compton, and L. C. Van Atta. This machine was built in a privately owned building, loaned to the Massachusetts Institute of Technology, whose original purpose was a large airship dock. The aluminum alloy spheres are 15 ft. in diameter. This machine operated at 7 MV in air despite the unfavorable foggy location of Round Hill, Massachusetts (now Dartmouth). It is now located at the Museum of Science in Boston, Massachusetts, USA. Though derived from a 1937 publication, this photo was probably taken in 1932 or 1933. (From AIP Emilio Segré Visual Archives, Brittle Books Collection, 1937.)

the speed of light around a loop made of multiple straight sections. Acceleration of electrons associated with bending the beam or intentionally introduced by *wigglers* or *undulators* produces copious x-rays.

These are large expensive machines that are owned by nations or groups of nations. The online encyclopedia Wikipedia maintains a list (Wikipedia 2015) with web links of the synchrotron sources in the world. In 2015, they listed 64 facilities. Imaging is a relatively small part of the experimental program on synchrotrons.

Synchrotrons emit a broad spectrum of x-rays that tends to peak around 1 keV. It is rare to see synchrotron work using x-rays greater than 40 keV. In most cases, a monochromator is used to pass a selected portion of the broad spectrum. This is feasible because the synchrotron source emits sufficient x-rays such that even a portion of the output can have useful irradiance. Because the direction of radiation emission is highly correlated with the direction of electron motion, the x-ray beam is limited in width to a few millimeters at the sample location.

8.4.2.3 Betatron

Professor Donald Kerst developed a device for accelerating electrons in 1940 that he named *betatron*. The betatron circulates electrons in a circular orbit. It was the first magnetic induction accelerator and was sited at the University of Illinois (Illinois 2010a). The first betatron accelerated electrons to 2.3 MeV (Bossi et al. 2002). It was made to produce x-rays by inserting a tungsten wire into the electron beam. In 1944, H. William Koch used this machine to make the first measurements of photofission in U and Pu (Illinois 2010b). This work was done in secret, but Koch was cleared to publish the uranium results in his thesis (Koch 1944). Kerst took leave from his university work to spend 1943–1945 at the Manhattan Project Los Alamos site. There, he built two betatrons for use in imaging implosions (Sessler et al. 1997).

Betatrons circulate electrons in orbit, where they gain energy on each trip around. Electrons are extracted to impinge on the anode. These machines were made and sold for radiation therapy and for industrial radiography. They are heavy and not well suited to mounting in a gantry as is required for radiation therapy. Most of the radiography machines built in the 1950–1980 period were designed to operate at 24 MV maximum (Bossi et al. 2002). More recently, JME* has brought to market a series of smaller betatrons that operate from 2 MV up to 10 MV (Stein et al. 2004). With betatrons, the beam can be extracted at certain fixed fractions of the maximum beam energy, so a 6 MV betatron may provide the option of a beam at 2 MeV. In the energy range from 2 to 10 MeV, betatrons are competitive with linear accelerators (linacs) in weight and cost, though with lower output. Betatrons are inherently pulsed and have an elongated source spot. The source spot on the JME model MIB-6 is 0.25×3.0 mm (Stein et al. 2004). Leidos has built nonintrusive imaging systems, e.g., IP6500, that use a betatron to screen cargo in sea/land/air containers for special nuclear materials and contraband, e.g., drugs and currency. For more on the Leidos system see Section 16.5.6.

8.4.2.4 Linac

Klystrons and magnetrons were both invented prior to WWII and each was intensely developed as a component of radar (Stanford 2007). After the war, these devices were employed as the radio-frequency (RF) power sources for linacs, which were initially research machines. The first use of an electron linac in London to treat a cancer patient was in 1953 (Thwaites and Tuohy 2006). By 1960, a collaboration between Varian and the Stanford Department of Radiology had produced a commercial electron linac configured as an x-ray source for cancer therapy (Varian 2014). By 1969, the University of California Radiation Laboratory[†] had completed a facility dedicated to industrial radiography using electron linacs.

* JME Ltd., Lowestoft, UK.

[†] Now known as the Lawrence Livermore National Laboratory.

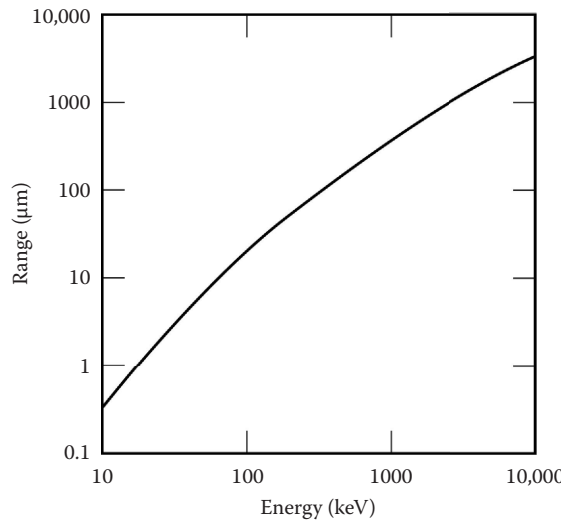


FIGURE 8.21 The approximate range of electrons in W as a function of electron energy. This is calculated using the online National Institute of Standards and Technology (NIST) computer program called ESTAR (NIST ESTAR 2017). The ESTAR computer program calculates continuous-slowing down approximation (CSDA) range. For purposes of our discussion, this equals the average range.

Linacs accelerate electrons using RF electric fields that are applied with precisely the correct phase as the electron passes through the machine. The electrons experience a series of accelerations. Linacs for industrial radiography have been manufactured that produce electrons with an energy of 1 MeV up to 16 MeV (Bossi et al. 2002). The current product line of Varian* ranges from 3 to 15 MV accelerating potential, with the 9 MV machine producing an exposure rate[†] of 30 Gy/min 1 m from the source.

The converter target in a linac is analogous to the anode in an x-ray tube. It is usually made of W and is water cooled. It is most often arranged as a plate positioned perpendicular to the electron beam. X-rays produced in the converter are transmitted through, and the usable beam is in the same direction as the electron motion. The beam from linacs is inherently pulsed at the microwave frequency. In addition, the beam is delivered in bursts. Typically, linacs are *on* only about 10^{-3} of the time.

A linac-based x-ray source is usually intended to produce multi-MeV x-rays. To minimize production of unwanted lower-energy x-rays, the converter target in a linac is usually made thinner than the range of the incoming electrons. Electrons slow down in a solid by many individual interactions. Considering the process to be continuous can approximate this. The range of electrons as a function of energy in W is given in Figure 8.21. We see from this that the converter target in a 9 MV linac is likely to be about 2 mm thick.

Linacs have become the dominant radiography source for nonflash systems operating above 4 MeV. Recently, a new CT system employing a 9 MV electron linac made by Varian was installed at The US Department of Energy (DOE) National Nuclear Security Administration (NNSA) Pantex Plant (LLNL 2009). This system is shown in Figure 8.22.

8.4.3 PULSED SOURCES

Pulsed x-ray sources can be used to freeze the motion of dynamic events. This technique is usually called *flash radiography*. The pulse duration required depends on the velocity of the object of

* <http://www.varian.com/sein/lm000.html>.

[†] Exposure is discussed in detail in Section 7.2.1.

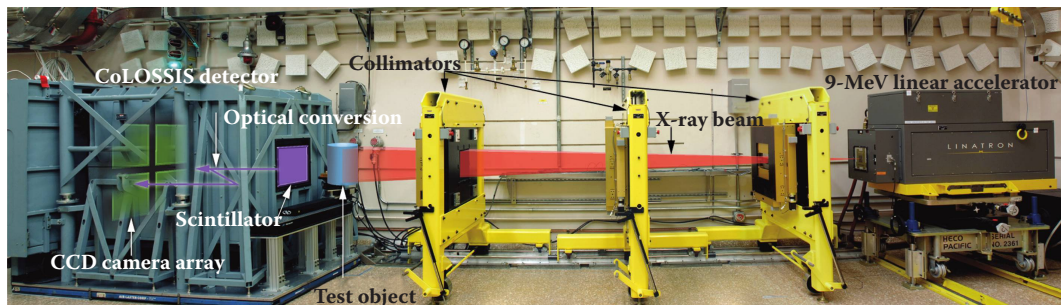


FIGURE 8.22 This CT system utilizes a 9 MV electron linac as the x-ray source. It was developed in order to image small features in nuclear weapons at the US DOE NNSA Pantex Plant. The distance from source to object is 6.5 m.

interest and the motion blur that is acceptable. Studies of machine dynamics, ballistics, and impact require submicrosecond exposure times (Grabarek and Herr 1966; Johnson and Mitchell 1972; Green and Rabinovich 1984; Molitoris et al. 2006; Tringe et al. 2009). Generally, longer exposures can be used for studies of fluid flow, casting, and welding. Femtosecond exposures are needed for some extreme events (Hau-Riege et al. 2007).

8.4.3.1 Pulsed X-Ray Tube

Flash-radiography tubes are similar in concept to those designed for continuous operation. They are driven by power supplies of a different nature from those for continuous high-voltage output. Pulsed supplies typically deliver multiple joules in 20–40 ns. Current is several kA. Commercial sources are available with voltage as high as 1.2 MV (Scandiflash 2010). Since most of the applications for these systems place them near explosions and impacts, they must be designed with greater robustness than standard x-ray tubes.

8.4.3.2 Accelerators as Pulsed Sources

We described electron linacs in [Section 8.4.2.4](#). These are usually used for static radiography, but they are inherently pulsed devices. This can be exploited to generate a stroboscopic x-ray image of a rotating or cyclic machine. These machines have insufficient output for high-fidelity imaging with a single burst, but by synchronizing the bursts with a machine position, a quality image can be acquired by time integration. At the Lawrence Livermore National Laboratory (LLNL), we once triggered a 9 MV Varian electron linac from the rotation of an operating V8 automotive engine.* In this way, we built up an image of a piston at a particular rotation point through successive rotations in an operating engine.

Nations with nuclear weapons programs have constructed large machines to perform flash radiography of weapon mock-ups and other explosive-driven hydrodynamic events (LLNL 1977, 2007; Scarpetti et al. 1997; Ekdahl 2002; Cunningham and Morris 2003). These machines must penetrate a substantial amount of heavy metal, so they tend to accelerate electrons to about 20 MeV. Current is 1–5 kA with a duration of ~50 ns. They are part of large fixed facilities and require a staff of tens or more. Several different machine types have been developed. Ekdahl (2002) reviews their history and presents a world inventory. Since their review paper, China added DRAGON-I to the list (Kaizhi et al. 2004). Some of these machines provide multiple radiographic views and/or multiple exposures.

* The most difficult and time-consuming aspect of this project was getting an emissions permit for a stationary engine from the Bay Area Air Quality Management District.

8.4.3.3 Plasma X-Ray Sources

Since the 1960s, there have been scattered groups of physicists working with devices that produce a dense plasma focus. These machines use electromagnetic compression to achieve a plasma sufficiently hot and dense that it emits x-rays. They are within the budget of universities and can be found in that setting worldwide. Dense plasma focus has been touted as the answer to fusion energy (Chang 2007) and inspection of bridges, roads, and buildings (Lawrenceville 2010). They can be used for industrial radiography (Di Lorenzo et al. 2007; Castillo et al. 2008), but no commercial source exists in spite of 50 years of research.

8.4.4 LASER-DRIVEN X-RAY SOURCES

Generating x-rays that have the properties of laser light has been a long-standing goal for experimental science. Here we describe a few different types of laser-driven x-ray sources.

8.4.4.1 K alpha (K_{α}) X-Ray Sources

A newer laser-driven source, and one of growing popularity, is what is generally referred to as a K_{α} source (Guo et al. 2001; Reich et al. 2001; Serbanescu et al. 2009). The name comes from the fact that the spectrum generated is that of the K_{α} line of the target material. These are systems in which an ultrashort-pulse laser is focused onto a metal, creating a plasma. The intense laser field then accelerates the electrons in the plasma to energies up to 100 keV and the electrons travel back toward the metal, and when they interact, they give off a bright flash of x-rays. The duration of this x-ray burst is similar to the duration of the laser pulse and therefore can be as short as tens of femtoseconds. These pulses have allowed for numerous useful experiments (Rischel et al. 1997; Siders et al. 1999; Cavalleri et al. 2000, 2001a,b, 2002; Kinoshita et al. 2001; Rousse et al. 2001a,b; Sokolowski-Tinten et al. 2001).

This occurs because the energy is deposited faster than the target is destroyed by hydrodynamic expansion. Solid targets are destroyed in a single shot (Goldstone et al. 1987). More recently, liquids (Ivanov et al. 2011) and gas (Chen et al. 2010) targets have been used. Liquid targets can be self-healing and withstand tens of thousands of shots even operating at a frequency of 1 kHz. The significant downside is the fixed energy of the x-ray pulse. Since the energy is defined by the K_{α} line of the target material (e.g., 8 keV for copper), changing the energy requires replacing the target material, which is generally not something that could be done during the course of an experimental run.

8.4.4.2 Free-Electron Laser (FEL) X-Ray Source

Another laser-driven x-ray source is an x-ray free-electron laser (FEL), such as the Linac Coherent Light Source (LCLS) built at the Stanford Linear Accelerator Center (SLAC) (Arthur et al. 1995; https://portal.slac.stanford.edu/sites/lcls_public/Documents/lcls_factsheet_2_2014_v6_0.pdf). LCLS produces pulses of x-rays more than a billion times brighter than the most powerful existing synchrotron sources, which are also based on large electron accelerators. The ultrafast x-ray pulses are used much like flashes from a high-speed strobe light, enabling scientists to take stop-motion pictures of atoms and molecules in motion, shedding light on the fundamental processes of chemistry, technology, and life itself. The downside here is again the low energy limit, plus this source also suffers one of the other significant drawbacks of synchrotrons—the large-scale facility investments required limit the number of available sources. Also see Zholents (2012) paper on next generation free electron lasers.

8.4.4.3 Thomson/Inverse Compton Scattering X-Ray Source

For the Thomson source, a high-intensity laser light is scattered from relativistic electrons, and the Doppler shift induced in the scattered light transforms the laser photons into x-ray photons. This process is referred to in the literature variously as *Thomson scattering* (Lau et al. 2003), because

that is typically the scattering process involved in the rest frame of the electron since the laser photon energy is below the rest-mass energy of the electron; *Compton scattering* (Panek and Ehlotzky 2002), a more general name when the Thomson condition is not met; *inverse Compton scattering* (Sakai et al. 2003), due to the transfer of energy and momentum from the electron to the photon, the opposite of the effect Compton first observed; and *laser synchrotron radiation* (Sprangle et al. 1992), due to the parallels between this source and synchrotron radiation. We will refer to this type of source as Thomson scattering.

Thomson scattering from relativistic electrons was first studied in depth in the 1940s, when it was postulated as a slowing mechanism for intergalactic electrons (Feenberg and Primakoff 1948). It was not until the invention of the laser in the 1960s, however, that the first Compton sources were proposed (Arutyunian and Tumanian 1963; Milburn 1963) and demonstrated (Fiocco and Thompson 1963; Bemporad et al. 1965). After the initial demonstrations, interest in producing Compton sources waned due to the low brightness of the x-rays produced—a consequence of the low cross section for Compton scattering ($\sigma\tau = 6.65 \times 10^{-25} \text{ cm}^2$; see Rischel et al. [1997]). In recent years, however, powerful lasers, photoinjectors, and high-quality accelerators have become commonplace, and the possibility of producing high photon and relativistic electron densities, and consequently high x-ray fluxes, has renewed interest in the field. A variety of theoretical research into proposed sources was performed (Sprangle et al. 1992; Kim et al. 1994; Pogorelsky 1998), and in 1996, the first subpicosecond hard x-ray source was demonstrated at Lawrence Berkeley National Laboratory (Schoenlein et al. 1996). This produced 5×10^4 photons/pulse with a peak energy of 30 keV. Similar results have been obtained by others.

Thomson scattering-based x-ray radiation sources are being developed by several groups around the world to enable studies of dynamic material properties that require temporal resolution on the order of tens of femtoseconds to tens of picoseconds. These sources offer pulses that are shorter than available from synchrotrons, more tunable than available from so-called laser-driven interactions with matter (or sometimes referred to as K_a) sources, and more penetrating and more directly probing than ultrafast lasers. Furthermore, Thomson scattering sources can scale directly up to x-ray energies in the few-MeV range, providing peak brightness far exceeding any other sources in this regime. Such a source was developed at the LLNL. This Thomson source is called the Picosecond Laser-Electron InterAction for the Dynamic Evaluation of Structures (PLEIADES). It was designed to target energies from 30 to 200 keV, with a peak brightness on the order of $10^{18} \text{ photons s}^{-1} \text{ mm}^{-2} \text{ mrad}^{-2} 0.01\% \text{ bandwidth}^{-1}$ (Kuba et al. 2003).

A new compact x-ray source has been developed by Lyncean Technologies Inc.; it has a small electron storage ring with a circumference of less than 5 m and is filled with electron bunches at an energy of 25–45 MeV by a linac of about 5 m length, as shown in Figure 8.23 (Esarey et al. 2009; Achterhold et al. 2013; Ghebregziabher et al. 2013). The orbital frequency is 65 MHz. The electron bunches are focused to about 40 mm diameter (rms) in a spot where the counterpropagating laser beam of a bow-tie, high-finesse laser cavity is also focused. The laser has a wavelength of about 1 mm. The electrons oscillate in the electromagnetic field of the laser light like in the undulator field of an insertion device at a synchrotron beamline. Due to the short period of this laser field, radiation in the keV energy regime is produced even by electrons of some MeV energy (Schwoerer et al. 2006; Esarey et al. 2009; Phuoc et al. 2012; Ghebregziabher et al. 2013). Note that in the synchrotron case, an undulator with some centimeter field period needs electrons in the GeV regime to produce keV radiation. With a beam divergence of 4 mrad and an energy bandwidth of 3% in the energy range of 15–36 keV, the radiation is perfectly suitable for high- and medium-resolution radiographic and tomographic x-ray imaging applications.

Fundamentally, the efficiency of laser Thomson scattering is limited by the small magnitude of the Thomson cross section (~ 0.6 barns) and the inability of electron beams to be focused to spots on par with minimum laser spot dimensions. In 1994, LLNL scientists recognized (Barty and Hartemann 2004) that the Thomson scattering brilliance should increase rapidly as a function of electron beam energy and beam quality. To the first order, this occurs because at higher electron

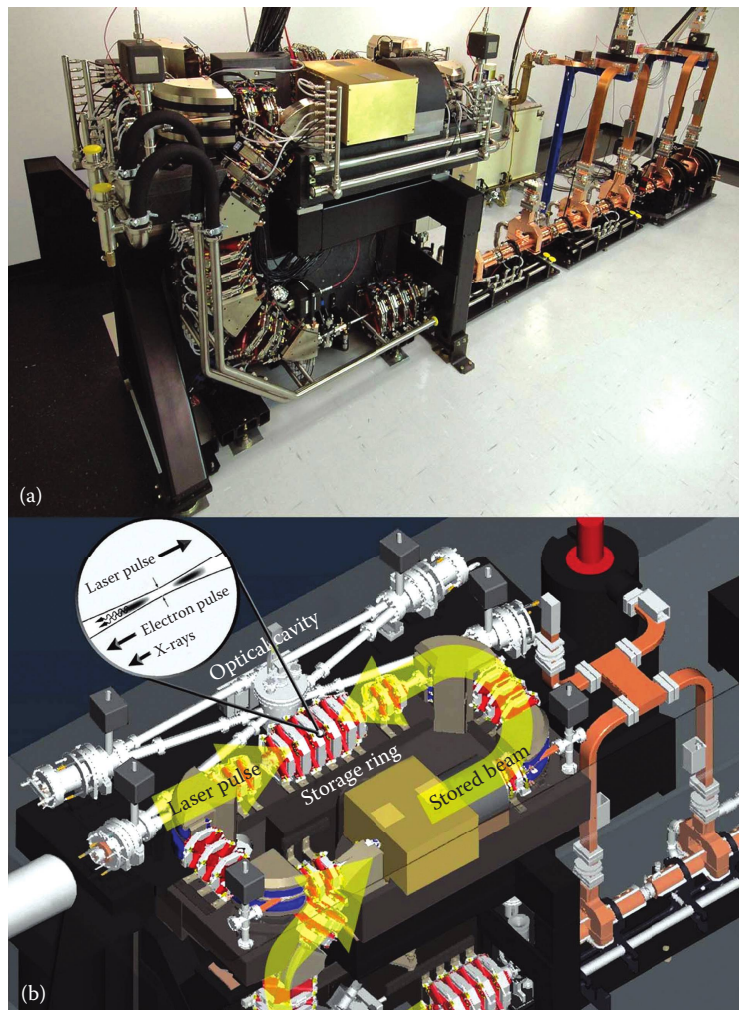


FIGURE 8.23 Overview of the Lyceum Compact Light Source (CLS). (a) Front view of the CLS showing the injector (on the right), the transport line (on the left), and the electron storage ring (at the top). The length of the CLS is about 5 m. (b) Computer-aided design (CAD) drawing of the CLS with the electron storage ring and the optical cavity of the infrared laser system. The interaction point of the laser pulse and the electron pulse is emphasized. (From Achterhold, K. et al., *Sci. Rep.*, 3, 1313, 2013. US DOE public domain.)

beam energy, it is possible to overcome electrostatic repulsion and focus the electron to smaller spot dimensions. Roughly, the electron spot dimension is proportional to its beam energy, and thus, the peak brilliance (photons s^{-1} 0.1% band width [BW] mrad $^{-2}$ mm $^{-2}$) of the laser Thomson source increases as a function of electron beam energy somewhere between the second and fourth power. This rapid increase in peak brilliance is in stark contrast to the trends of alternative sources, such as large-scale synchrotrons. In the nuclear excitation region above 100 keV, the peak brilliance of third-generation synchrotrons decreases faster than exponentially. Above 2 MeV, the peak brilliance of a monoenergetic γ -ray (MEGa-ray) source produced via laser–Thomson scattering can exceed that of the largest synchrotrons by more than 15 orders of magnitude. It is important to note that for many nuclear applications and especially for those related to management of nuclear materials, it is the bandwidth of the Compton source and not the pulse duration that is of foremost importance.

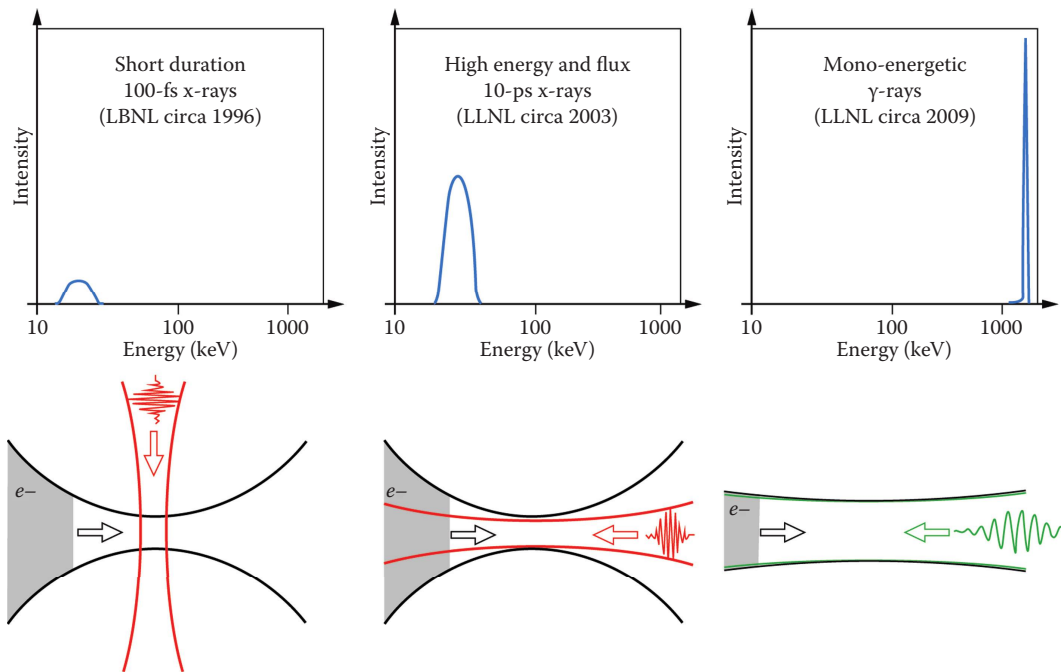


FIGURE 8.24 Schematic of laser Compton optimization for different applications. (Left panel) Femtosecond x-ray configuration. (Middle panel) High-efficiency x-ray configuration. (Right panel) Narrowband MEGA-ray configuration. (From Barty, C. P. et al., Overview of MEGA-ray-based Nuclear Materials Management Activities at the Lawrence Livermore National Laboratory, *Proceedings of Institute of Nuclear Materials Management 52nd Annual Meeting*, LLNL Report LLNL-CONF-515893, 2011. US DOE public domain.)

The optimization of laser Thomson scattering to produce femtosecond x-rays, high-efficiency x-rays, and narrowband x-rays is given in Figure 8.24. The narrowband x-ray design developed by LLNL MEGA-ray involves a different approach to machine design than that pursued for short-duration x-ray sources. The bandwidth of the Thomson source is driven by three effects; the energy spread of the electron bunch, the bandwidth of the laser photons, and the spread due to the angle correlation in the interaction region. Bandwidth can be minimized with high-quality (low-emittance) electron beams, 10 ps or longer laser pulses, and near-collimated laser-electron interaction geometries. Fractional bandwidths of $10^{-3} \Delta E/E$ or ~ 2 orders of magnitude less than that have been demonstrated from short-duration lasers (Gibson et al. 2010; Barty et al. 2011). Therefore, Thomson x-ray sources are possible with careful design.

8.5 RADIOISOTOPIC X-RAY AND γ -RAY SOURCES

Radioactive isotopes are unstable. They become more stable by emission of particles or radiation, an event called disintegration. Many natural and man-made materials spontaneously emit photons, either γ -rays or x-rays. We covered radioactivity and the presented example decay spectra in Section 4.2.2, The Nucleus and γ -Ray and X-Ray Generation. X-rays emanate from electronic orbital transitions, whereas γ -rays arise from proton or neutron orbital (protons and neutrons have energy orbital analogues to electrons) transitions. X-rays are produced from radioactive materials when a nucleus decays by electron capture or when primary decay radiation ejects an orbital electron, leaving an excited atom. The subsequent filling of an inner-shell electron orbit results in the emission of characteristic x-rays (Section 4.2.1.2). Similarly, the filling of an inner proton or neutron orbit results in the emission of characteristic γ -rays. In general, radioactive isotopes that decay by

emission of an α particle also emit characteristic x-rays produced by the α particle as it interacts with electrons in the material.

In this text, we give an introduction to radiography with radioisotopes. This subject is covered in detail in other literature (Halmshaw 1995; Bossi et al. 2002; Kodak 2014), and radioisotopes are seldom used for digital radiography and CT, our primary emphasis in this text.

For industrial applications radioisotopic sources offer the advantages of portability and no power requirements. The source capsule is typically smaller than an x-ray tube, thus permitting insertion of the radioactive source into locations where a tube cannot be used. Without radioisotopic sources, many field applications such as pipelines, petroleum storage tanks, and ship welds could not be inspected using radiography.

The primary disadvantage of radioisotopic sources is their low photon emission rate per unit of source volume. In order to get a useful source, a relatively large focal spot size (actual size of the source) must be employed. Secondary disadvantages of radioisotopic sources are that they cannot be turned off and that they present a contamination hazard if containment is accidentally breached. Also, since radioisotopic sources decay, they must be regularly replaced.

A given radioisotope usually emits at multiple energies, e.g., ^{192}Ir emits γ -rays at 24 different energies. These are shown in the spectrum of Figure 8.25. Although many materials are radioactive, only a few are commonly used in industrial NDE. Table 8.1 lists five radioactive isotopes that are commonly incorporated into sources for γ radiography.

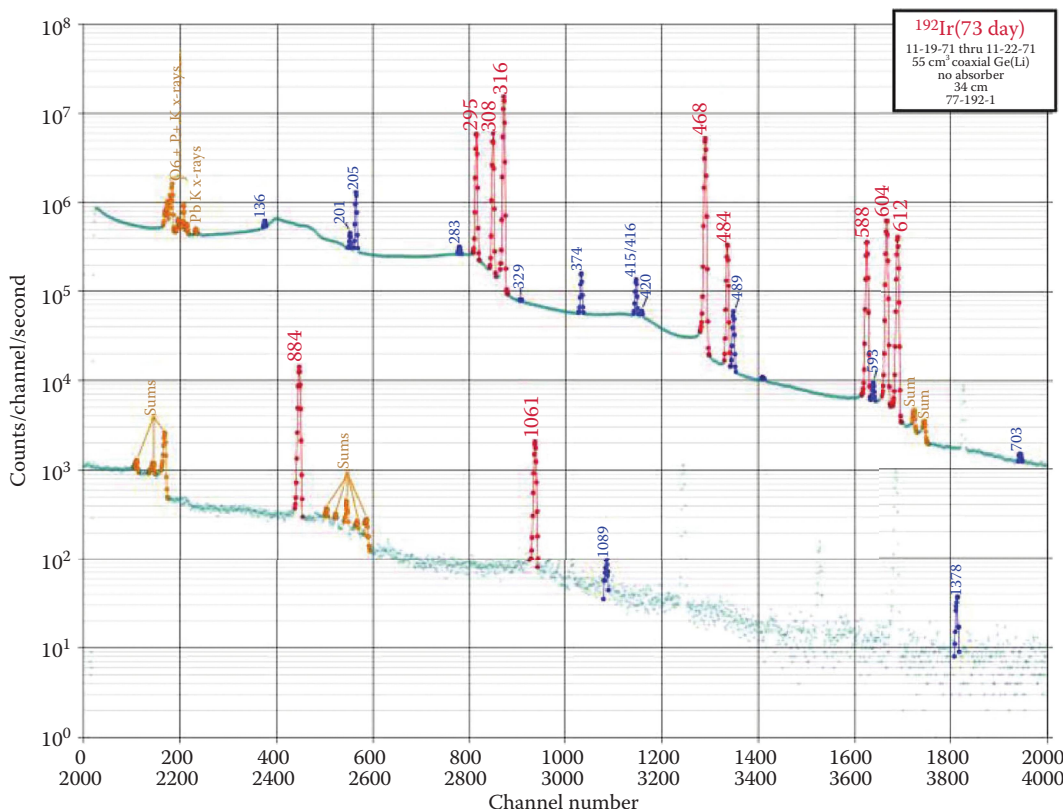


FIGURE 8.25 The pulse height spectrum from ^{192}Ir taken with a high-purity Ge(Li) detector. The most prominent peaks are shown in red. Labels on peaks are in units of keV. Gold peaks are not γ -ray peaks. (From Heath, R. L., *Gamma Ray Spectrum Catalogue; Ge and Si Detector Spectra*, fourth edition, Idaho National Laboratory, Gamma Ray Spectrometry Center, 1998, available at <http://www.inl.gov/gammaray/catalogs/catalogs.shtml>, 1998. US DOE public domain.)

TABLE 8.1
Important Characteristics of Five Radioisotopes and Radioisotopic Sources Used for Radiography

Isotope	^{60}Co	^{137}Cs	^{192}Ir	^{75}Se	^{170}Tm
Half-life	5.3 years	30 years	74 days	120 days	129 days
Chemical form	Co	CsCl in glass or ceramic	Ir	H ₂ Se	Tm ₂ O ₃
Specific activity ^a					
TBq/g	42	3	339	537	220
Ci/g	1130	87	9141	14,500	5950
γ -ray energies (keV), x-rays as noted	1173, 1332	662	^b	121, 136, 265, 280, 304, 401 ^c	Yb K x-rays, 84
γ -rays/disintegration (for each γ -ray listed)	1.0, 1.0	0.85	^b	0.17, 0.58, 0.59, 0.25, 0.01, 0.11	0.03
Maximum source activity readily available					
TBq	1.2	2.8	5.6	2.2	1.8
Ci	33	75	150	60	50
Diameter of source for listed activity (mm)	3	10	3	3	3
Photon emission rate per unit of source vol. (photons s ⁻¹ μm^{-3})	170	5	852	270 ^d	4
Al mass attenuation coefficient (for each γ -ray listed) (cm ² /g)	0.0568, 0.0532	0.0748	N.A.	0.153, 0.144, 0.109, 0.107, 0.104, 0.0927	0.194
Fe mass attenuation coefficient (for each γ -ray listed) (cm ² /g)	0.0553, 0.0518	0.0736	N.A.	0.266, 0.223, 0.119, 0.115, 0.109, 0.0939	0.533
Pb mass attenuation coefficient (for each γ -ray listed) (cm ² /g)	0.0619, 0.0562	0.111	N.A.	3.44, 2.57, 0.525, 0.466, 0.392, 0.231	2.14

^a Specific activity is defined as activity per unit mass of the radioactive isotope *only*. It is a function of the isotope mass and half-life.

^b ^{192}Ir has 24 γ -rays. The decay spectrum of ^{192}Ir is shown in Figure 8.25. There are 2.17 γ -rays emitted per disintegration.

^c ^{75}Se has 11 γ -rays. Only six of the most abundant γ -rays are listed.

^d The emission rate for ^{75}Se is given including only the six listed γ -rays.

The industrial radioisotopic sources listed in Table 8.1 span a range of energies that implies a range of penetrating ability. Of those listed, ^{60}Co has the highest energy of 1.33 MeV, and ^{170}Tm has the lowest at 0.052 MeV (52 keV). If the energy is too low for inspection of a given object, the photons will be absorbed within the object and will not create a response in the detector. On the other hand, if the energy is too high, very few of the photons will be absorbed within the object, and there will be no discrimination (*contrast*) of the density or material variations within the object; the object would look nearly transparent to the radiation. Therefore, the radiation energy must be matched to the material (elemental) composition, density, and thickness of the object being inspected. Many radioisotopes emit at multiple energy levels, as indicated in Table 8.1. The table gives the mass attenuation coefficients in cm²/g for Al, Fe, and Pb for each of the listed γ -rays for each radioisotope.

While the energy of the emitted photons must be appropriate for the elemental composition, density, and thickness of the object, such that a reasonable fraction (~80%) of the energy is absorbed, we also want the length of time required to expose the detector to be as short as possible. For a given

radioisotope and detector, exposure time is determined by the rate at which photons are emitted by the source and the attenuation caused by the object. Making the source physically larger in diameter increases the emission rate but degrades image sharpness via the penumbra effect, as discussed earlier in [Section 8.2](#). For radioactive sources, the source size is defined by the lateral dimensions of radioactive material or, if a collimator is used, by the dimensions of its opening (or aperture). Because of the generally low photon emission rate of NDE radioisotopic sources, the source size is typically at least several millimeters (see [Table 8.1](#)). This is larger than is typical of x-ray tubes.

Radioisotopic sources used for NDE are encapsulated. A bare source could slough radioactive debris into the lab and working environment. This is not good. Usually, the source pellet(s) is placed into a stainless steel capsule and a lid is welded in place (Bossi et al. 2002). This may be inserted into a second capsule with a welded cap and a connecting feature. A short section of drive cable is attached to the source capsule. This source subassembly is often called a *pigtail*. At the other end of the pigtail is a connector used to attach a longer drive cable used to move the source out of the storage pig and position it for exposures.

Because the radiation from a radioisotopic source cannot be turned off, special storage, handling, shipping, and operating equipment is required to maintain safety. One type of device to serve these functions is shown in Figure 8.26. This manufacturer uses the term *exposure device* for this item.

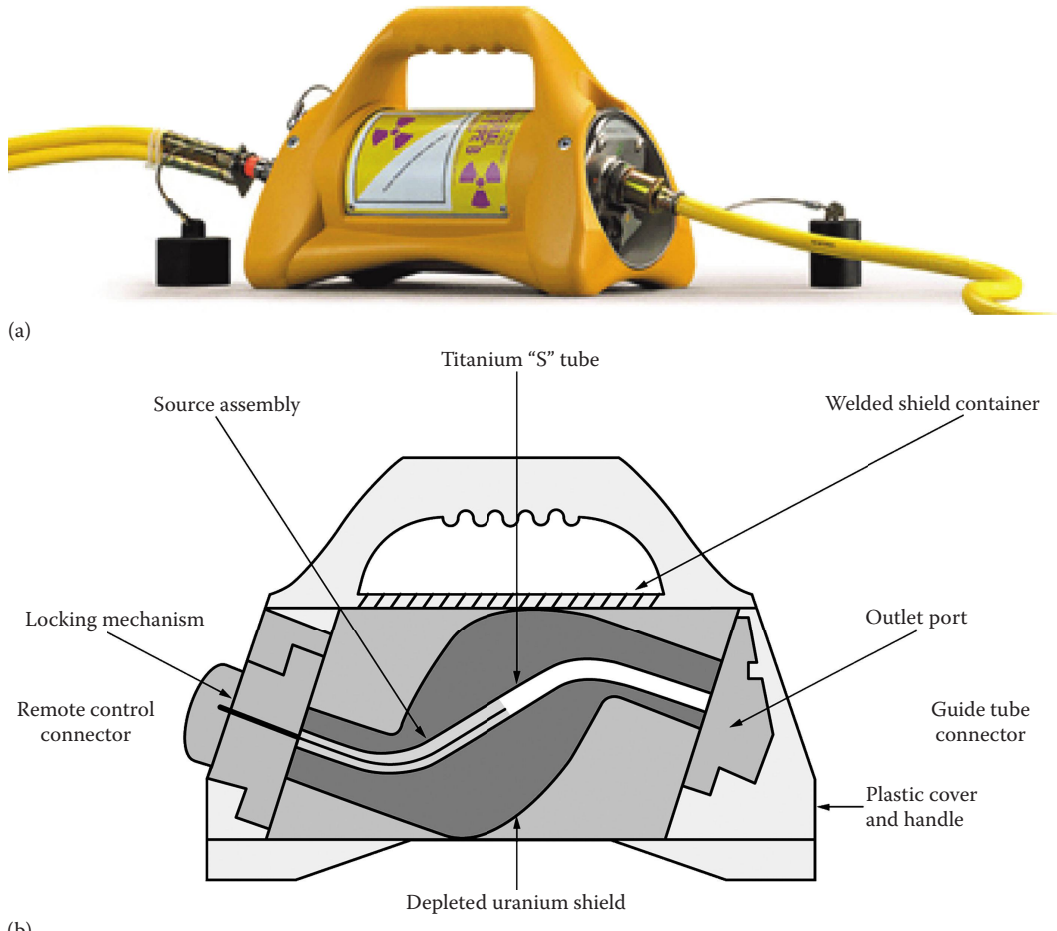


FIGURE 8.26 An example of an exposure device designed to be used with a radioactive source for radiography. (a) A photograph. (b) A cross-sectional schematic showing major internal features. (Adapted from advertising brochure, AEA Technology.)

Within the NDE literature, one also finds the terms *camera* and *projector*, meaning very similar devices (Raj and Venkataraman 2004). Some of these devices leave the source within a shield and open a window or rotate a shutter to expose the source and project γ -rays in one direction.

When not in operation, the device shown in [Figure 8.26](#) surrounds the source with a radiation shield made from depleted uranium. Other components of the exposure device are shown in sectional view in [Figure 8.26b](#). In operation, a drive cable is attached to the pigtail and used to remotely push the source out of the outlet port into a guide tube to the desired location for use.

Care is required in using radioisotopes. They must be recycled or disposed of under strict regulatory and environmental guidelines. When control is lost, serious incidents can result. We pointed out in Section 2.10, Radiation Accidents, that in industrial settings, radioisotopic sources account for nearly all injury and death from radiation accidents. This happens from poor use practices, and it happens when control of the material is lost, sometimes to theft.

PROBLEMS

- 8.1 If you were to perform CT twice on a W wire using the two spectra in [Figure 8.12](#), which scan would have the greatest beam hardening assuming no correction is applied?
- 8.2 The spectrum shown with a dashed line in [Figure 8.12](#) has been filtered by 0.5 mm of Au. What alternative filter is likely to be more appropriate for imaging a W wire?
- 8.3 Imagine you have selected an x-ray tube for purchase. You intend for this tube to serve as a general-purpose source in your NDE lab. The tube has a W anode, is of the sealed design, operates from 10 kV to 160 kV, and is equipped with a 200- μm -thick Be window. Just as you are about to sign the order, the salesman makes a counterproposal. He will discount the price \$1000 if you will take an identical tube with a 0.5-mm-thick stainless steel window. He points out that you will save another \$1000 when the time comes to dispose of the tube with Be. Should you take the salesman's offer?
- 8.4 The highest-power (thermal load) tube in [Figure 8.6](#) is a GE Seifert Isovolt 160. Would this tube be a good choice for imaging 100 μm inclusions in Al?
- 8.5 In [Figure 8.8](#), why does the spectrum filtered with 0.03 g/cm² of Cu have a peak at ~8 keV?
- 8.6 Siemens sells a rotating-anode x-ray tube that can operate at 150 kV with an electron beam power of 78 kW. If the anode is capable of storing 260 kJ and the maximum tube heat dissipation rate is 1.2 kW, how long can the tube be operated at maximum power before reaching the thermal capacity of the anode?
- 8.7 If you worked in the NDE section of a large research laboratory and the beam deposition group came to you and asked you to NDE a new method they have developed to apply W coating onto Cu substrates, what two NDE methods should you apply before digital radiography?

9 Radiation Detectors

9.1 INTRODUCTION

Chapter 9 explores the types, technologies, modes, and configurations of radiation detectors used for imaging with γ -rays and x-rays. First we explore an imaginary perfect detector. Then we describe detectors as they exist today. We consider those operating in pulse mode versus integrating mode. We cover dimensionality of detectors, address efficiency, discuss the most important imaging scintillators, and conclude with flat-panel imagers and scintillator/charge-coupled device (CCD) systems.

When you are finished with this chapter, you will have the basic foundation for understanding the operating principles of modern digital radiation imaging detectors. You will have been introduced to

- Pulse detectors and energy-discriminating detectors
- Integrating detectors
- Scintillation converters
- Detection of visible scintillation light
- Storage phosphors
- Point detectors
- Linear detectors
- Area detectors

9.2 THE PERFECT DETECTOR

Before we delve into the demonstrated suite of x-ray detection methods and configurations, let us first imagine what we would wish an imaging detector to look like. A perfect detector would have the following characteristics.

- An area detector with tunable detector element or pixel size* from $10\text{ }\mu\text{m}$ up to 1 mm
- Overall size scalable up to 1 m^2
- Less than 0.1% cross talk between adjacent detector elements
- Read time of $<10^{-9}\text{ s}$ with no measurable read noise
- Capable of energy discrimination with energy resolution of one part in 10^6 over the energy range of 1 keV to 10 MeV
- Operable in photon counting mode with energy discrimination at a rate of $10^5\text{ photons s}^{-1}\text{ pixel}^{-1}$
- Less than 0.01% persistence from one image to the next
- Efficiency $>50\%$ for incoming 3 MeV x-rays
- Fill factor of $>90\%$
- Directionality such that acceptance angle of each pixel can be pointed toward the source with acceptance angle $\leq 1^\circ$
- Detection surface deformable to planar and spherical shapes

The student who read Chapter 8 should notice that if we had the perfect source, we could relax the characteristics of the perfect detector, and vice versa.

* Often people use detector pixel to mean the single detector either in a linear or area-array detector.

9.3 FUNDAMENTAL STATISTICAL CONSIDERATIONS

Consider a window in space through which a “uniform” irradiance of photons passes. Mentally divide this window into detector elements or pixels and reconsider just how uniform the irradiance really is. The probability distribution of photons/pixel is well described by the *Poisson probability distribution* (Dainty and Shaw 1974). Suppose we have 9×10^6 photons pass through our hypothetical window and further that we have 3×10^6 pixels. Thus, the average number of photons/pixel (κ) is 3.0. The probability $P(x)$ of a pixel being illuminated by x photons according to Poisson is given by

$$P(x) = \frac{e^{-\kappa} \kappa^x}{x!}. \quad (9.1)$$

We see from this that the probability of a pixel having 0 photons pass through it is quite finite. The evaluation of Equation 9.1 for x from 0 to 7 is 0.050, 0.149, 0.224, 0.224, 0.168, 0.101, 0.050, and 0.022. [Figure 9.1](#) depicts 100 pixels with a Poisson distribution and a mean value of 3.0. The color scale runs from 0 to 8 (9 levels). We see that 5 pixels have 0 value. In our hypothetical window with 3 million pixels, we have 150,000 pixels that see no photons whatsoever when $\kappa = 3$. The Poisson distribution (Equation 9.1) for $\kappa = 15$ is shown in [Figure 9.2](#).

It is illustrative to ask ourselves the following question: what would κ have to be in order to expect all pixels to have at least one photon with a window made up of 3×10^6 pixels? Following the development by Rose (1974) shows that we need to be about six times the standard deviation value away from the mean before a random event is unlikely* in one of 3×10^6 pixels. Evaluating Equation 9.1 for an area with 3 million pixels shows that we must have a mean value of 35 photons/pixel to have <1% chance of a single empty pixel.

There are additional sources of noise once we consider the detector. All electronic detectors exhibit dark current. Dark current is not a single value but a noisy set of values unique for each pixel and each exposure. The mean offset from dark current is corrected pixel by pixel during processing, but there is an additional noise component that is introduced in the process. Examples of dark-current images are presented in [Figure 9.3](#).

Even if we had a monoenergetic source of x-rays, they would deposit a spectrum of energies in a detector. Swank (1973) analyzed this circumstance for scintillators. We quote here from his abstract.

When the signal in an x-ray image system is formed by integrating the scintillation pulses rather than by counting them, the signal-to-noise ratio is reduced by a factor which depends on the shape of the pulse-height distribution. The signal-to-noise cannot be related directly to either quantum absorption or energy absorption.

Swank cemented his legacy with this publication. This form of noise is called *Swank noise*. Note that while Swank considered scintillators, the same phenomenon occurs in detectors in which electrons are produced and collected (Kim et al. 2012).

Further, most x-ray imaging utilizes a polyenergetic spectrum of x-rays. This causes an additional effect similar to Swank noise due to modification of the distribution of electrons produced.

Noise is also added to the image by absorption and scatter of light in scintillators. Even though a large pulse of light is created, only a variable portion arrives at the sensor.

Finally, scatter is spatially variant with noise.

We refer the student who desires the full mathematical treatment of noise to Chapter 6 of Macovski (1983).

* The probability of a single pixel with a value six times the standard deviation below the mean is 2×10^{-9} . With 3×10^6 pixels, that leads to a probability of ~1% of a single pixel with 0 photons (Rose 1974).

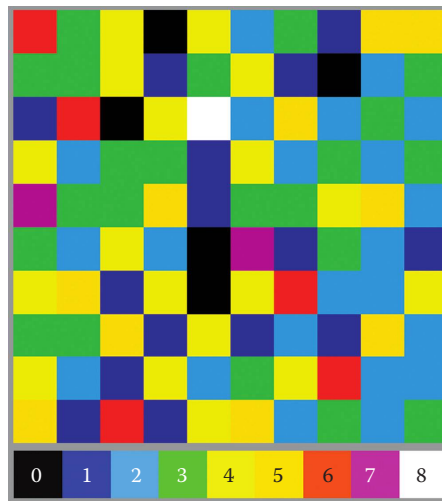


FIGURE 9.1 A 100-pixel image with a mean of 3, obeying Poisson statistics. The numerical value for each color is indicated by the color bar at bottom of the figure. (For the idea for this figure, we acknowledge Dainty, J. C., and Shaw, R., *Image Science—Principles, Analysis and Evaluation of Photographic-Type Imaging Processes*, ACADEMIC Press, 1974. Their figure depicts photon count with dots.)

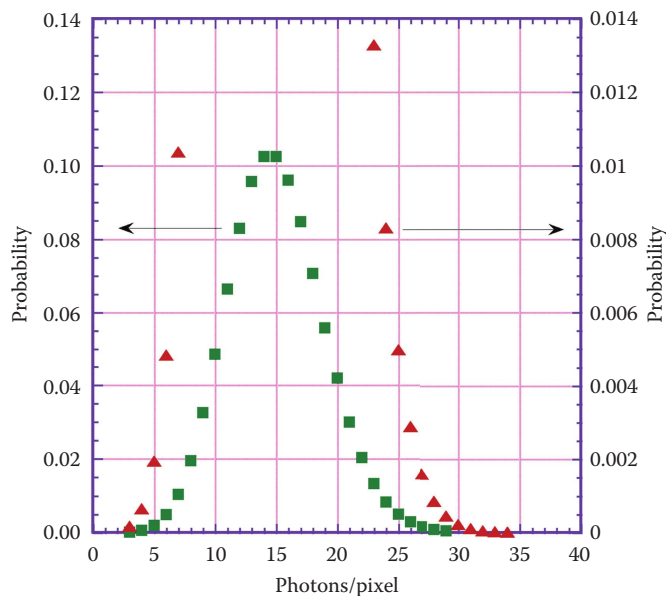


FIGURE 9.2 This plot shows the distribution of counts for a Poisson distribution with a mean of 15. The central portion of the distribution is read on the left probability scale. The points in the tails of the distribution can be read on the right probability scale.

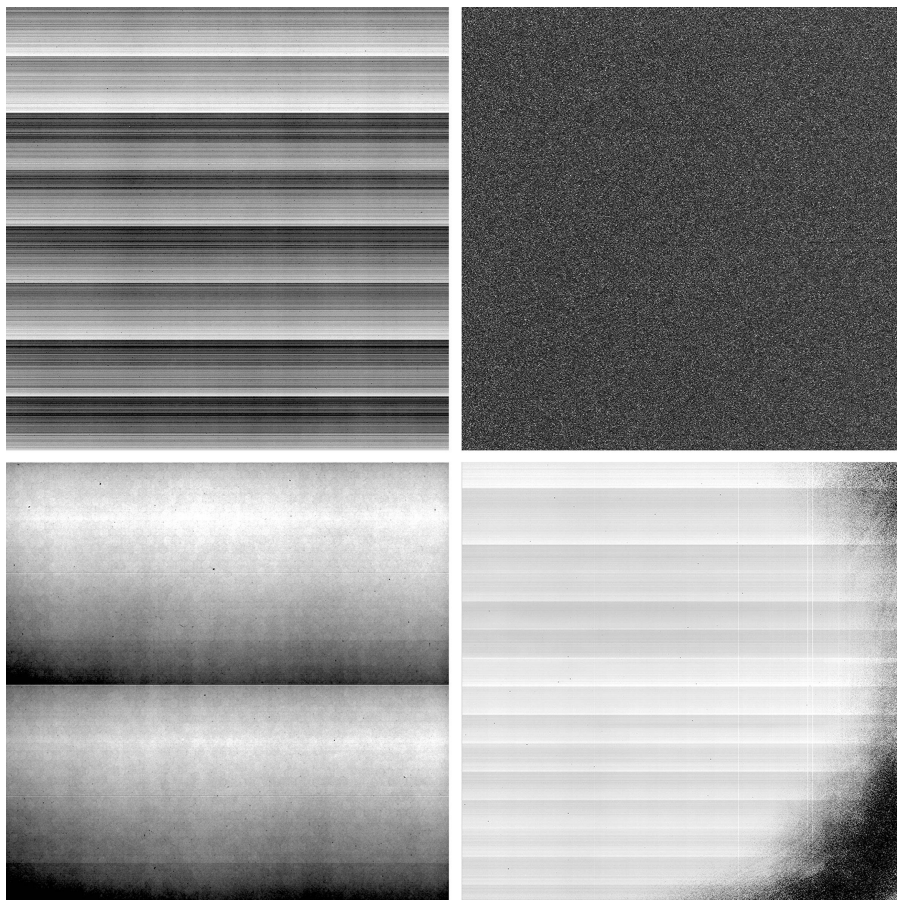


FIGURE 9.3 Dark-current images of four different visible-light detectors widely used in x-ray imaging. Each image has been extracted from a larger image so that the size presented is $1k \times 1k$. In the top row reading left-to-right is the dark image from an amSi photodiode area array and a cooled CCD area array. In the bottom row, left-to-right, are images from a CMOS area array and a different amSi photodiode area array that has been damaged by extensive use. The lower-right portion of this dark-current image was proximate to a source of scattered radiation. In all four of these images, there is Poisson noise in addition to the fixed pattern noise that is visually obvious.

9.4 DETECTION PRINCIPLES

In every case, detection of an x-ray or γ -ray begins with an electron interaction. The various types of interaction were covered in detail in Chapter 5.2.1. Each interaction creates an energetic electron. It may also create an excited atom that emits characteristic x-rays, or the photon may scatter and move off in a new direction with less energy. Finally, the interaction may produce an electron–positron pair. Both carry kinetic energy, and the positron will subsequently decay, emitting two annihilation photons. The annihilation photons may be detected some distance from the original interaction. This has a profound effect on detector response.

Once an energetic electron is produced, it moves through the detector material, sharing its energy with other electrons. To the first order, the number of progeny electrons is proportional to the parent electron energy. If the detector material is a semiconductor or a gas, the electron family can be induced to migrate to an electrode for collection. If the detector material is a scintillator, light is promptly emitted and subsequently collected for measurement. If the detector is photographic film or photostimulable phosphor, the latent image is stored for subsequent development.

9.5 DETECTOR TYPES

X-ray detectors can be classified in many different ways. Each of the short subsections that follow describes a specific detector type or characteristic and gives the major features. Any specific detector may belong to several of these types. That is, it might be an energy-integrating, linear, indirect, CCD detector. But any specific detector can only belong to one of the types forming each subsection. A detector *cannot* be energy discriminating and integrating.

9.5.1 PULSE DETECTION, ENERGY DISCRIMINATION, OR INTEGRATING DETECTION

A detector employing pulse detection counts individual x-ray interactions. This requires that it be sensitive enough to deliver a measureable pulse from a single interaction.

In an energy-discriminating detector, each pulse arising from an interaction with an x-ray is analyzed. The magnitude of the pulse is used to infer the energy of the incoming x-ray. Detectors of this type may be configured as point detectors, line detectors, or area detectors. They either employ a semiconductor such as Si(Li), CdTe, or high-purity germanium (HPGe) or employ a scintillator and a photodetector to sense the magnitude of the light pulse. The most common scintillator for this purpose is Tl-doped NaI, NaI(Tl). Photomultiplier tubes are the usual photodetector for detection of light pulses.

We refer the student to the text by Glenn Knoll (2000) for a thorough treatment of γ spectroscopy, including counting statistics and error propagation.

Integrating detectors sum the effect of multiple x-ray interactions before readout.

9.5.2 POINT, LINE, OR AREA DETECTION

The beauty of a point detector is that this geometry allows for scatter rejection collimation at both the source and the detector. By collimating to a single beam, scatter from the object is nearly eliminated. When combined with energy discrimination, this leads to the purest, most artifact-free computed tomography (CT) that is possible. The detector element, HPGe for example, can be thick enough to stop most x-rays, and it can be large enough in lateral dimension to assure that the secondary photons and electrons come to rest in the active detector.

The ugly characteristic of a point detector is that it is slow. One measures a single ray at a time. We once built a point-detector CT scanner, Pencil Beam Computed Axial Tomography (PBCAT) shown in Figure 9.4 to answer a multimillion-dollar problem that had eluded solution for several years. This machine used a radioisotope and an HPGe energy-discriminating detector. It took 5 days of continuous scanning to generate a single $1k \times 1k$ CT slice by translate and rotate motion. This is referred to as first generation CT. See Section 13.3 CT Data Acquisition and Processing. It was painful, but we nailed it.

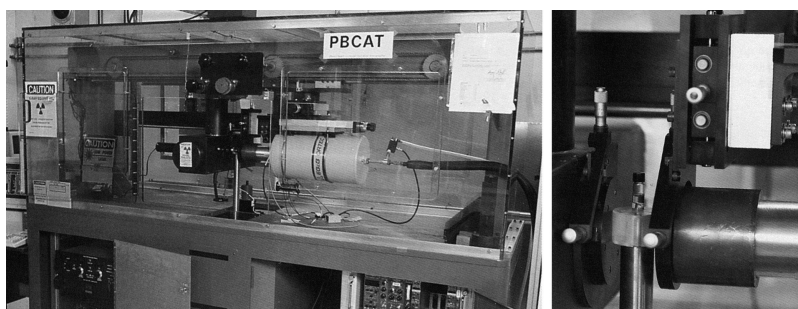


FIGURE 9.4 An example of a point-detector CT system. The overall system is shown on the left. The image on the right shows just the vicinity of the object being imaged. A small fluid-filled vial is visible on the object stage.



FIGURE 9.5 A photograph of a linear detector array.

The preceding example should serve as a reminder to the reader that data for 2-D (radiographs) and 3-D (tomographic reconstructions) can be acquired with a point detector. Done carefully, it is the highest-quality data that can be obtained.

Linear detectors, also called linear detector arrays, arrange detector elements in a straight or a curved line. One example is shown in Figure 9.5. They generate a 2-D projection image by moving the object* perpendicular to the line of detector elements. The motion is controlled so that the object moves 1 pixel between detector read cycles. They are naturally suited to imaging an object moving on a conveyor or assembly line. The length of the array can be tailored to the application.

Linear arrays are also used for CT imaging. If 3-D imaging is required, data may be acquired either slice by slice by rotating the object or in a series of 2-D radiographs by translating and rotating the object. When using a linear detector, the source can be collimated into a planar fan beam. This nearly eliminates object scatter since only scatter in the illuminated plane can reach the detector. This can then be reduced even more by collimation at the detector. The sensitive area of individual pixels in linear detectors is typically less than the square of the pixel pitch. This results in a *fill factor* somewhat less than unity. Some linear detectors are designed with low fill factors in order to incorporate shielding septa between detector elements. Thick septa block some of the (desired) primary photons. Stages can be used if necessary to acquire the data blocked by septa.

Area detectors contain two-dimensional arrays of detector elements. The most common geometry is for the array to be planar. For CT, data are typically acquired as a series of 2-D radiographs. Flat panels are available with up to 3 million pixels at the time of this writing. CCDs with 4 million pixels are readily available. One system designed by the Lawrence Livermore National Laboratory (LLNL) utilizes four CCDs to achieve 16 million pixel radiographs (LLNL 2009).

There is a mode of operation for CCDs (Davis et al. 2015) and complementary metal oxide semiconductors (CMOSs) (Rushton et al. 2015) that creates images of nearly arbitrary length. In this mode, charge is transferred along a line of pixels (let us call it the length) while also being accumulated until the end of the chip. At this point, a line of data is read. This line of data contains the integration of all the charge added pixel by pixel during the transfer. This mode of operation is called *time-delay integration* (TDI). Now if a matching motion is imposed on the object being imaged, each pixel on the sensor represents a pixel at the object. This can be most easily envisioned by thinking of one of the earliest applications of this technology—aerial photography from a moving aircraft. Imagine a setup where each pixel represents 1×1 cm on the ground. As the aircraft moves 1 cm, the charge is transferred to the next pixel and continues to accumulate. If you are using a $1k \times 1k$ chip, you will have an integration time that corresponds to the time it

* With a linear detector, the most common motion is to move the object. However, the source and detector can be moved instead if motion of the object is impractical.

takes the aircraft to move 1000 cm. This is especially valuable in low light conditions. In the case of x-ray imaging, TDI can be used to image a linearly moving object (production line) or for CT of a rotating object.

9.6 DETECTOR TECHNOLOGY

The earliest detector for x-ray and γ -ray images was film coated with a photon-sensitive layer. Energy storage phosphor technology was later applied to develop a commercial imager called *computed radiography (CR)*, and several different forms of photosensors were adapted for use with scintillators. Just as energy storage could serve as an imager, semiconductors were likewise adapted to imaging.

9.6.1 FILM

We stated at the onset that this text would give but brief note to x-ray film. Commercial industrial film consists of a polyester base coated on both sides with a Ag–halide mixture. X-rays produce a latent image. The image is developed by a chemical bath with subsequent chemical treatment to stop developing and fix the image. Film is almost always used as an area detector. Film is flexible and so can be used in curved geometry. It is highly portable, lending itself to field usage. It must be stored carefully at all stages of use. The cost of storing film is a significant burden, especially if retention is required for the lifetime of the product. The US government intends to fly B-52s for 80 years. Temperature and humidity must be controlled during storage. Filing and retrieval are unreliable processes. We worked with one medical facility that had a failure rate of 15% on attempted retrievals and considered that to be a great achievement.

The sensitive emulsion on film is very thin, and consequently, film only interacts with a small fraction of the x-rays that impinge upon it. To overcome this limitation, *intensifying screens* are often used. These can be of three types. The first is a foil of dense metal, usually Pb, W, or Ta. The metal emits electrons that expose the film. The second is a scintillating material, often granular, that emits visible light that exposes the film. The third type of intensifying screen combines a metal with a scintillator. Electrons emitted by the metal cause the scintillator to glow and expose the film.

The most definitive reference for film use in industrial radiography is that by Kodak (2014), *Radiography in Modern Industry*. Film waste is hazardous and toxic. Film does not lend itself to CT.

9.6.2 COMPUTED RADIOGRAPHY

Computed radiography (CR) is the name assigned by the medical imaging community (and now widely used in industrial imaging) for an imaging method using a photostimulable storage phosphor to record the image. It was developed by Fuji and introduced into the market in the early 1980s (Sonoda et al. 1983). The phosphor is bonded to a flexible base and covered by a clear protective coating. This is referred to as a *CR plate*. A CR plate is flexible but, for many applications, is packaged into a rigid, lighttight cassette. The packaging may include Pb intensifying screens depending on the application.

When exposed to x-rays, the photostimulable phosphor traps electrons at elevated energy levels (Rowlands 2002). This energy is released as blue light when the phosphor is interrogated with red laser light in a scanner. The laser is scanned over the phosphor plate, and the emitted light is detected with a photomultiplier tube. The resulting signal is clocked and digitized to form a digital image. The photostimulable phosphor is erased by exposure to intense light, usually by the scanner doing the reading. While reusable, the imaging plates are vulnerable to damage and contamination due to handling. They can become fatigued by overexposure or repeated exposure of repetitive objects. These defects create image artifacts. With CR, there is neither a dark image nor an open-field image for use in subsequent processing.

The latent image stored within the phosphor degrades with time and must be read within a few hours (or less). The spent plates are hazardous waste because of Ba content. CR does not lend itself to CT.

9.6.3 SCINTILLATORS

The topic of scintillators fills books and is a very active research area. Scintillators exist as gases, liquids, and solids. Solids can be further subdivided as crystalline, ceramic, glass, and granular. We limit our consideration to the most important scintillators employed for x-ray and γ -ray imaging.

The scintillator properties of most interest are light output (photons), linear attenuation coefficient versus energy (mm^{-1}), optical clarity, decay time for light, afterglow, and color spectrum of the emitted light.

9.6.3.1 Clear Crystals, Glass, or Ceramic Scintillators

Clear scintillators are used with optical coupling to light-sensitive detectors. The most common means of optical coupling is with a lens. This is depicted in Figure 9.6. We address this in more detail in [Section 9.6.4](#).

CsI(Tl) produces copious photons that are well matched to the sensitivity of Si photodiodes, CCD chips, and CMOS chips. It can be grown in single crystals with lateral dimensions of 10 cm and thickness as desired. It is slightly hygroscopic and so cannot be used in a high-humidity or condensing atmosphere. Skin contact should be avoided because of moisture damage to the CsI(Tl) . It does not cleave and is soft and somewhat plastic. CsI(Tl) has the highest afterglow (Greskovich and Ducas 1997) of the scintillators we discuss here.

CdWO_4 is the other single crystal used for area imaging in lens-coupled systems. It has lower light yield than CsI(Tl) and is slightly more green, making it less well suited to photodiode sensitivity. Its high density and atomic number produce good stopping power for x-rays. CdWO_4 has very little afterglow. It is limited in physical size by crystal growing capacity.

In the early 1990s, Industrial Quality, Inc., brought to market a family of dense scintillating glass. It was manufactured in several slightly different formulations. We will describe IQI 301 as

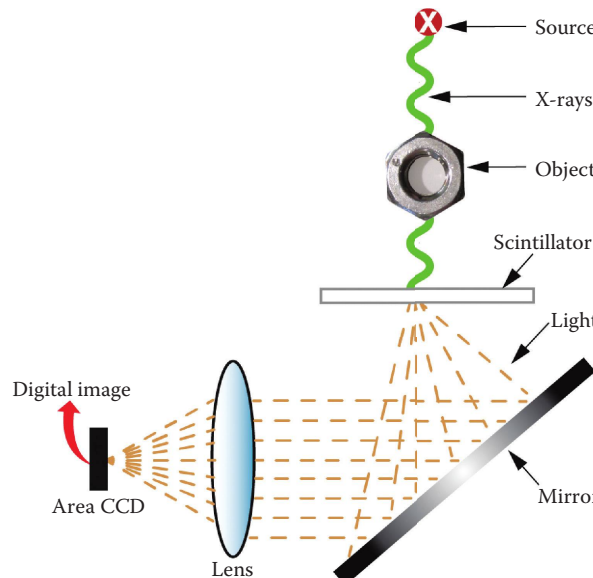


FIGURE 9.6 Schematic representation of a detector system employing a scintillator and a CCD for image acquisition. A turning mirror is often used in order to protect the CCD chip from direct irradiation.

a representative dense glass scintillator. IQI 301 is a Tb-activated silicate glass with a density of 3.8 g/cm³ and emits green light (Placious et al. 1991). It was readily available in sizes up to 10 in. × 10 in. and thickness to 12 mm, although availability in 2015 is uncertain. IQI 301 is relatively slow to emit its light, 3 ms for the main component, but this is seldom an issue when used with lens-coupled CCDs. It has complex afterglow behavior that must be evaluated for a specific application. This was a very large step forward for CT with sources operating at voltages greater than 250 kV since it was available in large area and thickness. IQI glass offered significant gains in stopping power over competing granular composites (Section 9.6.3.2).

GE developed HiLight for use in their medical CT scanners (Greskovich and Duclos 1997). It is a ceramic scintillator emitting red light. Other key attributes are included in Tables 9.1 and 9.2. We include it here because it seems, at first look, like a very attractive possibility for industrial CT scanning. HiLight has never been utilized in an industrial CT scanner. When used in medical scanners, HiLight is in the form of discreet bars. In this configuration, small amounts of light scatter from residual porosity are not of concern. When imaging a plate of HiLight using a lens, these scatter sites reflect light and become hot spots in the image that destroy the utility of the image.* Since these pores do not significantly impact performance of the GE scanners, GE was not interested in eliminating them.

A new scintillator (*GLO*) tailored for MV radiography is being developed at LLNL (Seeley et al. 2011a,b, 2012, 2013; Cherepy et al. 2015a,b). GLO is a huge step up in performance compared to IQI 301. It has a linear attenuation coefficient for 4 MeV x-rays that is 2.7 times higher than IQI glass. The LLNL group has produced GLO with an 11 in. diameter. GLO produces more than twice as much signal in a photodiode sensor per unit of energy deposited, and its primary emission time constant is shorter than IQI glass. Best of all, it shows improved spatial resolution.

9.6.3.2 Granular Composite Scintillators

The medical imaging industry created the demand for scintillating screens to use in conjunction with film for capturing x-ray images. There are now many choices. These products have been honed over decades. They are highly engineered. Medical products have been adopted for industrial use, especially with flat-panel detectors. We will describe here one of these screens that we evaluated extensively, Lanex Fine by Eastman Kodak. The scintillator in Lanex Fine is gadolinium oxysulfide, $\text{Gd}_2\text{O}_2\text{S}$. This is often referred to as *gadox* or *GOS*. Lanex Fine is has four distinct layers. It is built on a polyester base. The gadox is contained between two very thin protective layers of plastic, probably polyester. Scanning electron microscope images of a fractured Lanex Fine screen are shown in Figure 9.7. We chilled a piece of Lanex Fine in liquid nitrogen and then broke it. This separated the gadox layer from the polyester base. The images shown in Figure 9.7 are edge views of the broken scintillator screen without the base layer. The higher magnification view on the right reveals the granular nature of the product. This layer contains binder and light-absorbing dye. The function of the dye is to reduce the spreading of light, thereby improving spatial resolution. Clearly, this is a delicate balance since it also absorbs some of the desired light. It is somewhat selective because of the longer path traversed by light traveling off normal to the surface. Dimensions and mass details are given in a paper by Schach von Wittenau et al. (2002b).

9.6.3.3 Structured Scintillators

We address in this section several methods that introduce a columnar effect in order to reduce or eliminate spreading of light as it propagates from its origin to the sensor.

Scintillating glass can be fabricated into fiber-optic scintillator plates. These are commercially available[†] up to 200 mm × 200 mm and 20 mm thick. These scintillators are complex objects and

* Personal unpublished work by the authors.

[†] Collimated Holes, Inc., Campbell, California.

TABLE 9.1
Important Properties of Optically Clear Scintillators

Material	Form	Density (g/cm ³)	Emission λ (nm)	Relative Photodiode Signal (%)	Primary Decay Time (μs)	Afterglow ^e (%)	Radiation Effect ^{f,b} (%)	FWHM for 140 keV Photons ^{d,g} (μm)	Comment
CsI(Tl)	Single crystal	4.51	550	100	1	0.3	+13.5	147	Slightly hygroscopic
CdWO ₄	Single crystal	7.99	530	30	14	0.02	-2.9	87	
LLNL/GLO	Ceramic	9.00	610	85	1–2 × 10 ³	Unknown	Unknown	65–75	Gd _{0.3} Lu _{1.6} Eu _{0.1} O ₃
IQI Tb glass	Glass	3.75	540	30	3000	^b	+2 to -5%	^g	^a
GE/HiLight ^c	Ceramic	5.92	610	70	1000	<0.01	<1.0	N.A.	Y _{1.34} Gd _{0.6} Eu _{0.06} O ₃

^a IQI and Collimated Holes are secretive regarding the composition of their scintillating glass. We reverse-engineered from patents and publications to arrive at the following estimate, where the numbers in parentheses are mass fraction: Ba (0.353), Si (0.176), Na (0.013), Mg (0.023), K (0.019), Sr (0.006), Gd (0.026), Tb (0.097), O (0.286).

^b The authors observed afterglow in IQI glass under different irradiation conditions than the other entries in this table. IQI glass exhibits very long-term afterglow after sustained irradiation from a 9 MV linear accelerator (linac). After 30 min of irradiation followed by 30 min of glow time, we observed afterglow of 0.1%. This glass also exhibits complex gains and losses when irradiated. When irradiated continuously, it increases in brightness, yet when exposed sufficiently, it exhibits diminished output and turns visibly brown. The brown can be removed by annealing. It is possible that the gain in light output reported by others is buildup of long-life afterglow.

^c HiLight is not truly optically clear. First, it appears red to the naked eye. More importantly, it has internal voids that behave badly when observed with a lens. The voids reflect light and appear as stars with a brightness that depends on light created elsewhere and scattering around. It is like looking at stars through clouds. We include it here for comparison. Data for HiLight is from Greskovich and Duclos (1997). HiLight is a huge success in medical CT. It is not used in industrial CT to our knowledge.

^d From Heemskerk et al. (2012). These measurements were made by imaging a slit. All scintillators were at a thickness such that interaction probability was 66% for 140 keV photons. Range of full width at half maximum (FWHM) for GLO is from Heemskerk's published measurements for two similar scintillators; Lu₂O₃:Eu and Gd₁L₁O₃:Eu.

^e From Greskovich and Duclos (1997). Measured at room temperature 100 ms after pulse excitation from a tube at 140 kV potential. They state that HiLight has a small amount of mystery sauce to control afterglow.

^f From Greskovich and Duclos (1997) except for IQI glass. Observed after 450 Röntgens from a tube operating at 140 kV potential.

^g We measured resolution of IQI glass and GLO both at a thickness of 2.2 mm using a depleted uranium edge and the spectrum from a 9 MV electron linac. IQI exhibits 5% modulation at 5.8 lp/mm, while GLO exhibits 7.8 lp/mm at 5% modulation. The difference would be even greater if thicknesses were adjusted for equal interaction probability.

TABLE 9.2**Linear Attenuation Coefficients (mm^{-1}) of the Scintillators of Table 9.1**

Scintillator	Energy			
	50 keV	150 keV	500 keV	4000 keV
CsI(Tl)	5.80	0.329	0.0442	0.0163
CdWO ₄	4.89	0.803	0.0916	0.0297
LLNL/GLO	4.50	1.100	0.1100	0.0346
IQI Tb glass	2.09	0.184	0.0356	0.0127
GE/HiLight	2.69	0.356	0.0574	0.0208

Note: Generated using composition from Table 9.1 and XCOM (NIST XCOM, Available at <http://www.nist.gov/pml/data/xcom/http://physics.nist.gov/PhysRefData/Xcom/html/xcom1.html>, 2015).

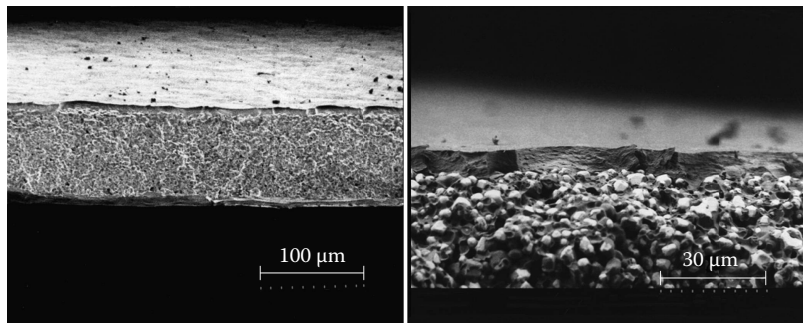


FIGURE 9.7 Cross-sectional scanning electron microscope (SEM) image of a fractured Kodak Lanex Fine screen. The substrate is not shown here. The granular nature of the gadox is evident. The thin coatings are for protection.

are consequently more expensive than monolithic scintillating glass plates. Their advantage is that light that meets the requirement for total internal reflection is guided toward the light-sensitive detector. In some instances, the fiber-optic plate may be placed directly in contact with or may be bonded to a CCD or other light detector.

Thallium-doped CsI can be induced to grow in long slender crystals. A photograph of a fractured piece of CsI(Tl) is shown in Figure 9.8. The seed pattern upon which the crystals are grown is a substrate designed for that function, or the crystals can be grown directly on the pixels of a photo sensor (Sabet et al. 2012). The image of Figure 9.9 was acquired with a CMOS sensor and a columnar CsI(Tl) scintillator.

Yet another method for producing pixelated scintillators is to dice a monolithic plate of scintillator using a saw (Fujita et al. 2014; Kataoka et al. 2015). This approach has been aimed at modest resolution with pulse height analysis. First applications are likely to be in medicine and in improved gamma cameras for environmental safety surveys. Kamada et al. (2012) are working with a crystalline Ce-doped Gd₃Al₂Ga₃O₁₂ scintillator (Ce:GAGG).

Structured scintillator assemblies can be fabricated with intricate septa. One of the authors (Logan) commissioned Tecomet to produce an array made of W for use in a gamma camera being developed by a startup. It has square cells in an offset pattern shown by the photograph in Figure 9.10. Each cell is 0.9 mm × 0.9 mm. The septa are 0.1 mm thick. These provide the function of stopping secondary photons and electrons from entering neighboring scintillators. This device is 17 mm in length. The holes are parallel and were filled with bars of CsI(Tl) after the photo in Figure 9.10.

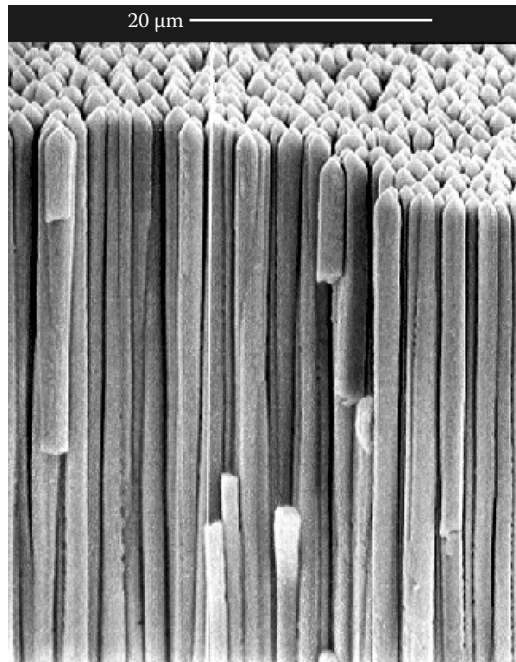


FIGURE 9.8 Scanning electron micrograph showing CsI(Tl) grown in columns. (Image provided and permission for use granted by Applied Scintillation Technologies.)

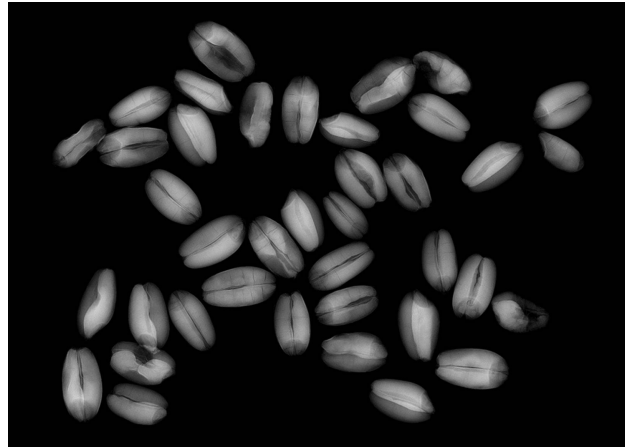


FIGURE 9.9 This image of wheat kernels was acquired with a CMOS detector fitted with a columnar CsI(Tl) scintillator coupled to the CMOS with a fiber-optic coupler. (Image by A. Basal. Used with permission.)

9.6.4 CCD-BASED AREA DETECTORS EMPLOYING A SCINTILLATOR

Many industrial radiography and CT systems are based on a scintillator to convert the x-ray projection into visible light and optics to deliver the visible light to the CCD. The CCD then converts the light into a digital image that can be up to 16 million or more pixels. A schematic of this type of system is shown in [Figure 9.6](#). In nondestructive evaluation (NDE), this type of system is used over a range of photon energy from 5 keV to 5 MeV.

A turning mirror is often necessary in order to remove the CCD from direct irradiation with transmitted x-rays. Direct hits in the active part of a CCD make bright pixels and cause permanent

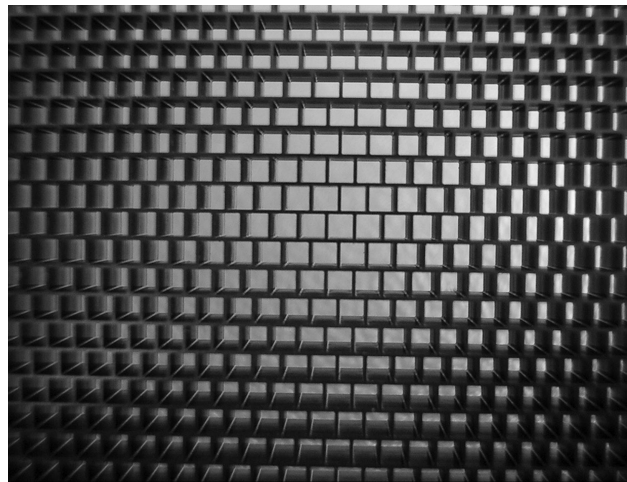


FIGURE 9.10 An array made of W for use in a gamma camera. Cells are $0.9\text{ mm} \times 0.9\text{ mm}$ and 17 mm deep and have a pitch of 1 mm. (Personal photograph by Clint Logan.)

damage to the CCD. In Figure 9.6, we show a mirror followed by a lens. In some systems, this order is reversed (Doshi et al. 2015). Some systems use a fiber-optic coupler rather than a lens. The fiber-optic material serves as a shield for the CCD while transmitting light from the scintillator to the CCD. In one LLNL design, we used a sheet of leaded glass between the scintillator and the camera lens. In this system, the microfocus tube has a maximum operating potential of 75 kV. This makes it possible to shield the camera with the leaded glass. A photograph of this system is shown in Figure 9.11. At higher potential (450 kV), a mirror is required, as can be seen in Figure 9.12.

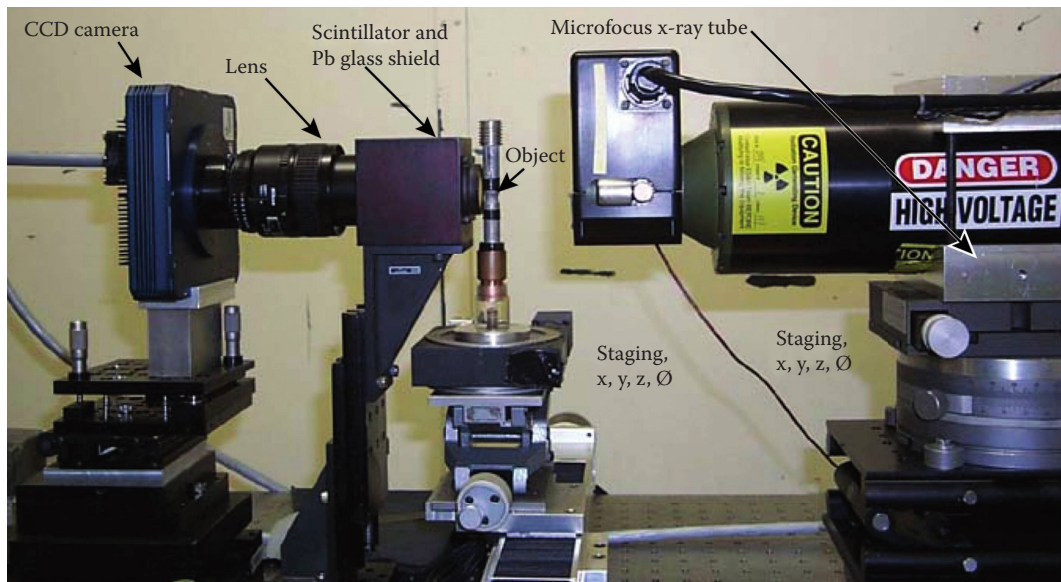


FIGURE 9.11 A photograph of an LLNL-built CT system utilizing a straight-line configuration. The object being imaged is a tensile specimen that has undergone some plastic deformation. There are 12 translation/rotation stages, 4 each for camera, object, and x-ray tube. A sheet of glass containing PbO is placed between the lens and the scintillator in order to shield the camera from x-rays.



FIGURE 9.12 This CT system uses a turning mirror within the L-shaped Al box to remove the CCD camera from the direct x-ray beam emitted by a 450 kV tube (yellow). This LLNL system, called PCAT, is located in a large shielded room with the tube mounted on an overhead system for position control.

In detectors that use a lens, the lens can magnify the image from the scintillator, or it can demagnify the image to provide a field of view larger than the CCD chip. When a fiber-optic coupler is used, it may be tapered to provide magnification or demagnification.

X-ray imaging systems of the type shown in Figure 9.6 are the most versatile method of acquiring digital radiographs. By changing the lens and distances between components, it is possible to change the field of view over a wide range. This permits examining objects of vastly different sizes and made of a wide range of materials. The turning mirror gets the radiation-sensitive components out of the direct beam path. At LLNL, we reconfigure these systems often when the job calls for doing something unfamiliar.

One consideration when selecting and using a lens for this purpose is distortion. If the purpose of the imaging is precise dimensional analysis of an object, then distortion should be minimal and perhaps corrected (Goldberg 1992). You also need to very carefully align all the individual components. A second consideration is focusing of the lens and its depth of field. Be aware that with a thick clear scintillator, light is produced through the entire thickness. The optimum focus is somewhere within the thickness. It is *not* at either surface. A third consideration with thick scintillators and large fan or cone angles is that light is produced over a volume shaped like an elongated blob. The blob axis is from the blob centroid to the source spot. Since the lens views this shape off axis, the blob shape and orientation affect the blob image on the CCD or CMOS sensor (Goldberg 1992).

9.6.5 CMOS-BASED AREA DETECTORS EMPLOYING A SCINTILLATOR

CMOS is a technology that can be used to make visible-light sensor arrays. This type of sensor is now widely used in consumer cameras. The sensor array can be made larger than is conventional with CCD sensors. This simplifies or eliminates optical demagnification in many instances.

Flat-panel CMOS x-ray area arrays are commercially available with pixel size ranging from 24 to 75 μm . The CMOS chip can be manufactured with active pixels very near to the edge on three edges. This facilitates butting individual arrays together to produce a larger detector array. CMOS imaging arrays can be coupled to a scintillator using a fiber-optic plate (no magnification or demagnification). The fiber-optic plate relays the image and shields the CMOS sensor from transmitted x-rays. A scintillator is placed in contact with the x-ray side of the fiber-optic plate.

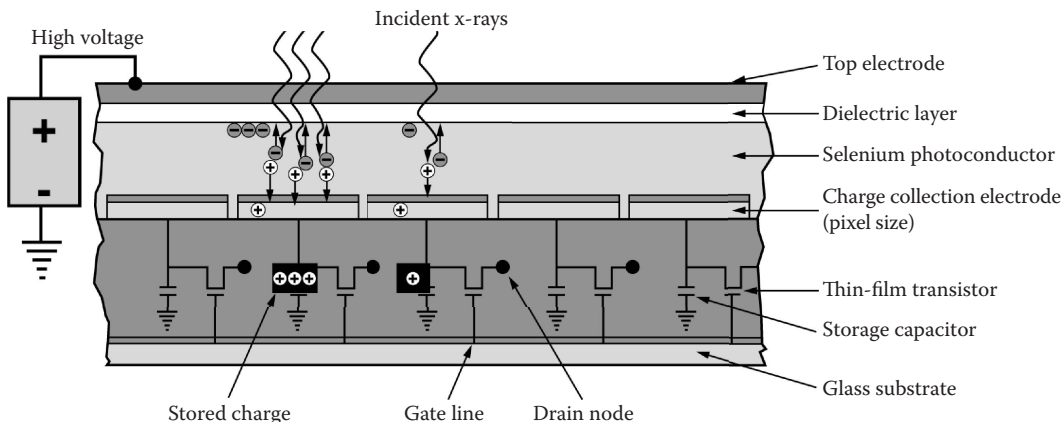


FIGURE 9.13 Schematic of a portion of a direct-imaging flat panel. Incident x-rays interact in a Se layer producing electrons and holes. This charge is attracted to the nearest electrode (pixel) by an imposed voltage. The charge is collected in a storage capacitor and then read out via a thin-film transistor array.

9.6.6 DIRECT-DETECTION FLAT PANELS

The term *direct detection* was adopted first by the medical imaging industry. It indicates that the electrons arising from interaction with x-rays are collected and measured using a thin-film transistor array. Amorphous selenium (amSe) is the most highly developed material employed in the semiconductor layer in which charge is produced. This layer has a bias voltage applied across it so that charge produced is collected and measured pixel by pixel. This is depicted in Figure 9.13. When the panel is configured normal to the incident x-rays, the imposed voltage moves the charge parallel to them. Electrode designs move charge to collector elements, minimizing fill-factor losses. Direct-detection flat panels have a tendency to trap charge, resulting in ghosting from previous exposures. This is similar to the effect called afterglow in scintillating screens. This severely limits application to industrial CT, where small rotation angles cause ghosting to mess with edges. For a review of direct detection flat panels, see Kasap and Rowlands (2000).

9.6.7 INDIRECT-DETECTION FLAT PANELS

The process for *indirect detection* involves an additional step compared to direct detection. Incident x-rays interact in a scintillator, producing visible light. This light is emitted isotropically and so spreads in all directions. In a granular screen such as Lanex Fine, shown in Figure 9.7, the light scatters, and some is absorbed (intentionally). This is shown schematically in Figure 9.14. The scintillator is placed in contact with a photodiode array with the pixel structure. The photodiodes convert light to charge that is stored until read out using a thin-film transistor array analogous to the direct-detection case.

Structured scintillators, such as shown in Figure 9.8, avoid much of the spreading inherent in granular or monolithic scintillators.

While most indirect-detection flat panels are oriented to the incident radiation, as depicted in the opening paragraph of this section and in Figure 9.14, Fujifilm has reported improved results from reversing the orientation of the panel (Sato et al. 2010). X-rays pass through the thin-film transistor and photodiode arrays before entering the scintillator. This configuration results in the most intense light originating near the light-sensitive array. This reduces light spreading and absorption, thereby improving spatial resolution and sensitivity. They call this system CALNEO.

Indirect-detection flat panels are available in sizes up to 400 mm × 400 mm and pixel size as small as 100 µm. The space required for the components to store and actively read out the image

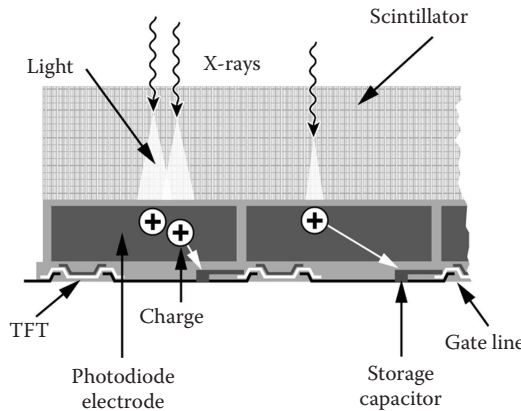


FIGURE 9.14 Schematic of a portion of an indirect-imaging flat panel. Incident x-rays interact in a scintillating layer producing visible light. This light is emitted in all directions. Some reach the light-sensitive photodiode pixel, allowing electrons to charge a storage capacitor. The charge is then read out via a thin-film transistor array.

is essentially independent of pixel pitch (center to center spacing of the detector elements). Pixels pitch smaller than 100 μm have rapidly diminishing fill factor. For technology and applications of amorphous silicon, see the book by Street (2000).

PROBLEMS

- 9.1 Say you owned a small NDE shop and a company approached you with a sample of a new metallic alloy they want evaluated for mass density uniformity and compositional uniformity without destroying the sample. The sample is a solid 3-cm-diameter cylinder. The atomic number is about 28, and the density is 7.0 g/cm^3 . If you use x-rays, what type of detector is the best choice?
- 9.2 For the situation of Problem 9.1, describe the test phantom you would use to certify your process. Shape? Material? Source?
- 9.3 For the situation of Problem 9.1, what non-x-ray NDE can you suggest?
- 9.4 For the collimator shown in Figure 9.10, what test method do you suggest for evaluating the uniformity of light output from each cell if the cell is filled with CsI(Tl)?
- 9.5 If your radiography firm wins the bid for inspection of a small component of the new long-range bomber for the US Air Force, you must retain the images for 75 years. You estimate that if you take film images, it will require 10,000 sheets of 20 cm \times 30 cm film. What protective measures must you take for storage if you retain film?
- 9.6 Which would cost less: (1) storage as digital images or (2) storage of x-ray film?
- 9.7 For the best CT data collection with minimum artifacts what detector would you employ?

10 Imaging System Components

10.1 INTRODUCTION

This chapter continues the progression from fundamentals of radiation interactions with matter and radiation transport to the elements of fielded systems. Further, this chapter finishes the description of the elements of fielded systems in the discussion of motion control, motion hardware, and computers for control and acquisition. In many ways, the material in this chapter is an application of the fundamentals presented earlier. First, the principles for radiation interaction apply to each component of imaging systems in the source–detector envelope. Second, the detector does not always discriminate between different sources of irradiance (through the object or scatter from the detector itself); rather it is the design of the entire system (including collimation) that substantiates the connection between the counts you measure and the object you are inspecting. Third—for tomosynthesis/laminography and CT—the measurements of the geometry of the system and the accuracy of the motion control effectively limit the accuracy for the inspection data.

From the fundamentals presented earlier in Chapter 5, the energy used in a system or inspection (monochromatic or polychromatic) makes a difference and impacts all aspects of system/collimator design. In particular, for medium- and high-energy x-ray systems, the effects of scatter in the object, in the x-ray facility, and in the detector impact the inspection performance of an imaging system. Well-designed collimation is the most widely used and, in some sense, the *best* tactic for countering the effects of x-ray scatter on spatial resolution and contrast sensitivity. As is canonical in all aspects of x-ray imaging, this is not without costs. Collimation decreases the amount of x-ray source irradiance available for performing inspection and can dramatically increase total scan time. Implementing collimation schemes is always more costly, at least in materials and setup, more in maintenance, with the warning that incorrectly positioned collimation can markedly decrease system performance.

The approach to managing the intrinsic trade-offs employed here involves an accounting of the types of signal involved in the inspection, an understanding of the principles for designing collimators, some access to a modeling capability, and a commitment to carefully acquired experimental data. The principles for designing collimators will build upon the fundamentals of radiation transport, but will be placed in context with the different factors accounting for signal impinging upon a detector element for a certain type of inspection.

In spite of the importance of collimation on spatial resolution, it should be mentioned here that well-known area detector techniques (i.e., film radiography) exist for the high-energy regime that can provide unmatched spatial resolution, as compared to highly collimated systems. The specifics of high-energy radiographic techniques will be covered more in Chapter 12, and Sections 15.3.1.2 and 16.3.3; it is hoped that the material in this chapter equips the reader with the tools for explaining both the value of collimation and the reasons why some area detector techniques can perform so well in certain contexts.

Lastly, x-ray radiation interactions are less important for motion control systems and the computers used for control and acquisition, that is, until you inadvertently compromise the operation of the motion hardware by direct exposure to a high-energy beam of radiation. Desired properties of the motion control hardware follow from the type of scanning for the system. However, each type of system configuration and the expected targeted spatial resolution/contrast puts more or less emphasis on a single system component. For example, microfocal systems put the emphasis on the size and integrity of the source spot size. For CT systems, the accuracy, precision, and reliability

of the motion control system are critical components for 3-D inspection performance. Rotational positioning errors cumulate—so later views are impacted by earlier views—and the entire data set can be compromised from the position of the first error. Further, computers for control and acquisition should be capable of supporting the installation/alignment of x-ray hardware, estimation/troubleshooting of system performance, and measurement of key geometric parameters, and should fully support the operation of the system at its designed performance. In this chapter, we will develop some guidelines for determining requirements for motion control equipment and connected computers.

Upon completion of this chapter, you will be able to understand

- Properties of the different sources of signal in fielded x-ray systems
- Strategies for countering/controlling the effects of x-ray scatter
- Principles for designing collimation systems for different energy regimes and different scanning modalities
 - How to measure the impact of collimation, good and bad
 - How to measure the relative contribution of scatter in the detector
 - How to obtain some measure of detector efficiency
- Principles for configuring motion control hardware
 - Types of motion control hardware for different scanning modalities
 - Motion control hardware for different energy regimes
 - How the properties of the motion control hardware support a level of inspection performance
- Principles for selecting computers and display hardware for acquisition and control

One additional comment for this chapter is that the emphasis here is on accounting for the impact of all components in the x-ray imaging system. While we have used detailed Monte Carlo modeling to identify and count these sources of irradiance (see Chapter 8), we also advocate certain experimental measurements to gain some measure of the effects occurring in your targeted system. Since access to x-ray systems to perform *off-normal* experiments may be difficult to obtain, we still recommend that the reader choose a system to objectify some of the suggestions made in this chapter.

10.2 SOURCES OF DETECTED SIGNAL IN X-RAY IMAGING

Up to this point, we have made a lot of comments about the importance of x-ray energy for determining the type and proportions of the interactions between radiation and matter. This information has a direct practical value in the design of collimation. The relative importance of different x-ray attenuation mechanisms and their proportional change with energy is given in [Table 10.1](#). For a variety of reasons, x-ray inspection applications sort themselves into four separate energy regimes: (1) very low energy, 20 keV or lower; (2) low energy, 20–160 keV; (3) medium energy, 160–600 keV; and (4) high energy, 600 keV to 15 MeV (please regard these as loose groupings and not strict regimes).

In this discussion, we will make reference to *primary* and *scattered* photons (irradiance). In this context, *primary* photons are defined primarily by geometry, that is, those photons that proceeded from source to detector on a straight-line trajectory. In previous chapters, primary photons were defined in terms that make sense if you are using energy discrimination for detecting the emitted spectrum. However, in this section, we are more oriented to mostly non-energy discriminating detectors to measure irradiance and assume in part integrating over the entire energy spectrum that makes it to the detector.

In principle, the primary irradiance talked about here is the source of signal that most closely corresponds to the ray-sum model at the foundation of CT reconstruction, or tomosynthesis algorithms

TABLE 10.1
X-Ray Attenuation^a for Selected Materials at a Single Energy

Energy (keV)	Carbon (1.6 g/cm ³)	Lucite (0.9 g/cm ³)	Teflon (2.16 g/cm ³)	Magnesium (1.738 g/cm ³)	Steel (7.8 g/cm ³)	Tungsten (17.25 g/cm ³)
20	45.4	54.2	73.03	87.58	97.5	96.7
	38.9	32.6	15.9	5.4	0.45	0.11
	0	0	0	0	0	0
	0.658897	0.482291	2.003853	4.621758	199.9842	1154.473
60	2.7	4.03	9.94	26.7	80.6	86.2
	91.67	90.3	81.4	61.05	11.6	2.8
	0	0	0	0	0	0
	0.279171	0.172282	0.403158	0.435757	9.143435	62.95239
100	0.58	0.89	2.4	7.75	54.3	93.84
	96.96	96.56	93.5	85.1	35.5	2.33
	0	0	0	0	0	0
	0.241996	0.147573	0.323763	0.291315	2.858425	76.38129
200	0.08	0.124	0.34	1.2	16.85	81.85
	99.1	99.06	98.3	96.3	76.18	11.87
	0	0	0	0	0	0
	0.196733	0.119562	0.256827	0.216242	1.141662	13.41445
400	0.0126	0.02	0.06	0.205	3.54	53.2
	99.7	99.72	99.5	98.9	93.7	39.8
	0	0	0	0	0	0
	0.152741	0.092771	0.19841	0.164879	0.734233	3.244022
1000	0.0016	0.003	0.007	0.027	0.507	18.5
	99.9	99.9	99.88	99.8	98.8	78.1
	0	0	0	0	0	0
	0.101809	0.061827	0.132061	0.10936	0.467193	1.123441
2000	0	0.002	0.002	0.011	0.204	7.6
	99.2	99.26	98.96	98.46	96.33	81.1
	0.7	0.72	1.0	1.46	3.2	9.94
	0.071101	0.043169	0.092463	0.076877	0.332584	0.75272
4000	0	0	0	0.006	0.0997	2.9
	94.9	95.03	93.2	90.5	81.46	58.4
	5.07	4.95	6.8	9.49	18.35	38.4
	0.048789	0.029591	0.06443	0.054912	0.258221	0.688295

Source: Cross-section information obtained from Cullen, D.E. et al., Tables and graphs of photon-interaction cross sections from 10 eV to 100 GeV derived from the LLNL evaluated-photon-data library (EPDL), Report UCRL-50400, Vol. 6, Rev. 4, Lawrence Livermore National Laboratory, Livermore, California, 1989.

^a Proportions in percent of total linear attenuation from top to bottom for the photoelectric, Compton, and pair production cross sections, and total linear attenuation in 1/cm. All values calculated using the mixture rule formula implemented in the LLNL-TPORT code. The percentages do not add up to 100 since we do not include the percentage of Rayleigh scattering.

to be covered subsequently (more about this in Chapters 11, 13, and 15). Practically, whenever you see the details of a processing algorithm represented as straight lines between a source and a detector, think ray-sums. The detected signal that is not in straight lines from the source to the detector (not primary) can be divided into further subcategories: the source of scattered signal that is connected to interaction with the object, and that source of signal that originates from some other part of the system (more about this in [Sections 10.2.2](#) and [10.2.3](#)).

For the very-low and low-energy regimes, photons counted at the detector have not resulted from scatter events, most are primary photons and collimation is a less critical component of the imaging system. Most of the attenuation at these energies is due to photoelectric absorption and Rayleigh or *coherent* scattering. In the very-low-energy case, the photons at the detector may be refracted or phase-shifted by the object. Of necessity, most of the parts to be inspected or characterized in the very-low-energy regime are small or have very low density (or you get no penetration of the x-rays—and no signal for inspection). Consequently, very-low- to low-energy systems can include small length scales with target spatial resolution on the order of nanometers and micrometers to tens of micrometers. Collimators are used sometimes to protect equipment, or provide a certain size beam for a detector, but are not an integral part of what accounts for the imaging fidelity of the imaging system. In the very-low-energy regime, factors like source spot size (see Chapter 8), intrinsic scintillator resolution/brightness properties, or imaging optics (see Chapter 9) are the key factors responsible for the achieved spatial resolution and contrast. X-ray refraction and phase effects can be significant contributions to recorded signal, but x-ray incoherent scatter is a small component in this particular regime.

In the low- to medium-energy regimes, x-ray scatter is a significant component of x-ray attenuation, especially as the energy is in the 100 keV range or above and the atomic number of the materials is low. The relative decline of photoelectric absorption depends somewhat on the type of material; higher-Z materials retain significant photoelectric absorption into the medium-energy ranges, while lower-Z materials make the transition to a scatter-dominated attenuation at lower energy (as discussed in Chapter 5 and illustrated in Figure 10.1 and [Table 10.1](#)). This property is one of the reasons why high-Z materials are the best choice for collimator materials in the lower-energy range; all the photons are stopped in relatively short material thicknesses with minimal scatter. Inspections of substantial object thicknesses of lower-Z materials can contain substantial scatter fractions. The combination of high- and low-Z materials in the same object/assembly can likewise result in images with troublesome scatter fractions, especially in the interface region between the different materials (e.g., plastic and metal interfaces and bone–tissue interfaces). Inspections of these kinds can directly benefit from some improved collimation. In particular, antiscatter grids,

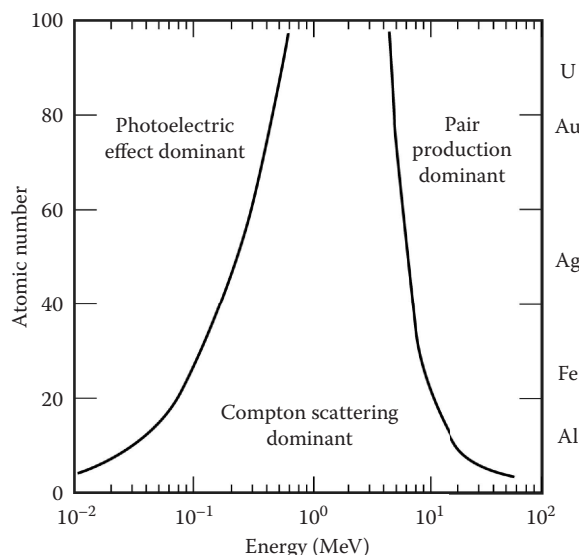


FIGURE 10.1 Photon attenuation between 10^{-2} (10 keV) and 20 MeV is dominated by one of three processes: photoelectric, Compton scattering, or pair production. The plot identifies the regions in atomic number and photon energy space where the three processes dominate (contribute >50% of the photon interactions). (Adapted from Evans, R.D., *The Atomic Nucleus*, McGraw Hill, New York, 1955.)

composed of thin but precisely made high-Z materials, can be an important collimation technique in this regime (more about this in [Section 10.4](#)).

In the medium- to high-energy regimes, Compton or incoherent scatter is more important in every part of system design and impacts system performance directly. Especially in the high-energy regime, all of the objects intersecting even small solid angles of source irradiance generate x-ray scatter. For instance, in the 9 MeV bay at Lawrence Livermore National Laboratory (LLNL), scatter from objects within 3 m of the back of the amorphous silicon x-ray detector find their way into the recorded image, reducing contrastive performance (Logan and Schach von Wittenau 2001) for the inspection. In this energy regime, every physical part of the imaging context needs to be taken into account and evaluated for scatter production and impact on the acquired data. Uncontrolled scatter and/or a lack of collimation will impact every part of the imaging and inspection performance. It is important to emphasize that the impact of x-ray scatter is both spatial and contrastive. The detected scattered x-rays create features that can further clutter the radiograph (or CT measurement), providing no inspection value, while detector elements are filled with digitized counts that may have little to do with the object/region to be inspected.

A single look at a DR/CT system housed inside a radiation enclosure (a cabinet) or bay (see Figure 10.2) can produce a list of scatter sources: (1) pre-object (or upstream) collimators and/or cabinet hardware; (2) the object; (3) references, object fixtures, and staging; (4) post-object (or downstream) collimators; and (5) the detector (including hardware behind the detector). For the x-rays, everything is just a material to interact with, and all of the elements of the scanner can and do participate to some extent. Figure 10.2 also includes some of the strategies used to ameliorate the impact of scatter. Pre-object collimation ensures that you have some control for the paths of the x-ray incident on the object and/or references. Post-object collimation can reduce the scatter cross-talk between detector elements due to the object, and shield the detector from scatter due to cabinet, motion hardware, or fixtures used to hold the part.

Referring back to Chapter 5, another reason why source energy is so important is that the angular distribution of scattered photons varies significantly with energy. The most probable trajectories are more forward peaked at the higher energies as shown in [Figure 10.3](#). Oftentimes this encourages

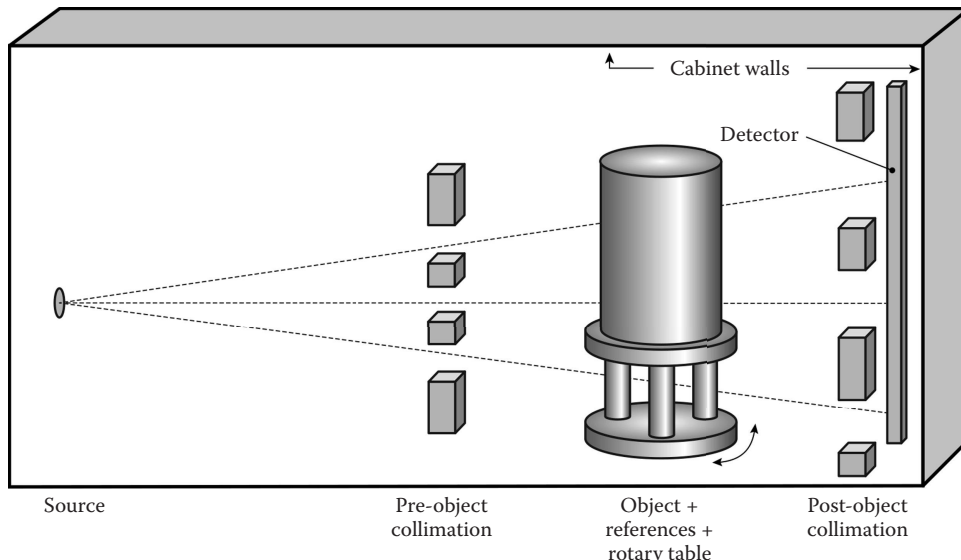


FIGURE 10.2 Reference cross-sectional sketch of a generic x-ray system within a radiation enclosure or cabinet. Note that there are several different sources of scatter, e.g., collimation, cabinet walls, object, and references in an x-ray system.

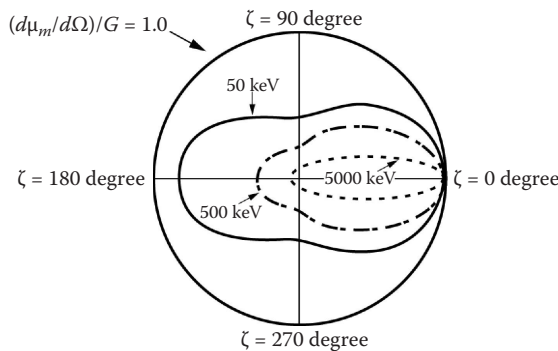


FIGURE 10.3 Angular distribution of Compton scattered x-rays. This is just a polar plot of the Klein-Nishina formula in units of $\text{cm}^2/(\text{g steradian})$ (Equation 5.6) for three incident x-ray energies.

modelers and analysts to employ single scatter approximations for dense objects. The rationale here is sensible: most of the energy of scattered photons is carried forward; if the path of the x-rays is long in an object, etc., the irradiance is progressively winnowed down, and only the last couple of scatter events emerge from the object, i.e., single scatter events. While results of these analyses generate intriguing and useful processing kernels for deconvolution/image processing schemes, they can incorrectly simplify the imaging context for high-energy imaging. Even pencil-beam collimated systems can include sources of photons, which are not just single scatter. We will identify some artifacts (see Chapter 13) present in medium- and high-energy CT images, to be evidence of a source of signal, which does not match simple models but reflects the variety of mechanisms that occur in the x-ray interaction with the object and with the system components as a whole. This is especially true for situations of low transmission (5% or less) in DR and/or CT where even small effects can emerge as proportionately significant (5% transmission is a μy_t of 3; 3% transmission is a μy_t of 3.5).

Consider the following comparison between two scans acquired from an area detector scanner: one without and one with pre-object collimation. In this example, the detector is a THALES Amorphous Silicon detector equipped with a KODAK Lanex fine scintillator. The object under inspection is composed of three cylindrical samples: aluminum, graphite, and Delrin, the physical properties of which are given in Table 10.2. In total, four CT scans were acquired, two of the scans at two different kilovolts and x-ray source or beam filter combinations: 100 kV, 2-mm aluminum filter and 160 kV, 2-mm copper filter, each energy acquired with and without collimation. Figure 10.4 shows an image from the collimated 160 kV, 2-mm copper beam filter CT scan with the different materials identified. The resultant x-ray attenuation values measured for the four scans are given in Table 10.3.

First, notice the measured attenuation of all the materials increase once collimation is applied, regardless of the material. This occurs using the same spectrum and the same scanning technique.

TABLE 10.2
Properties of Materials Used in Collimation Study

Sample Properties	Delrin	Graphite	Aluminum
Height (cm)	13.27	13.528	13.66
Diameter (cm)	2.547	2.717	2.543
Weight (g)	95.427	126.952	187.070
Density (g/cm^3)	1.41	1.62	2.7
Chemical formula	$\text{H}_6\text{C}_3\text{O}_2$	C	Al

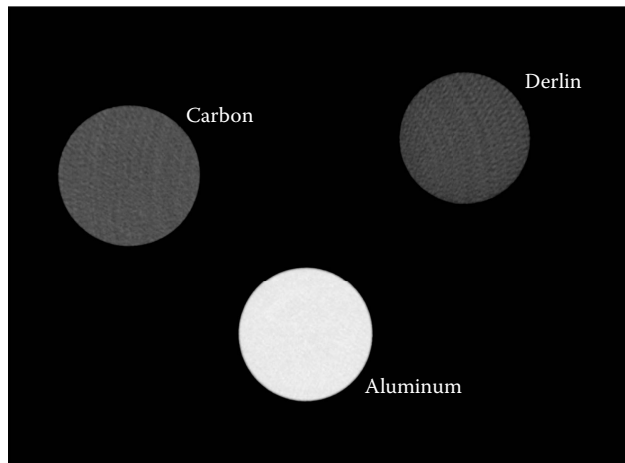


FIGURE 10.4 Example x-ray CT cross-sectional image using a 160 kV, 2-mm Cu filter x-ray source with pre-object collimation and an amSi flat-panel detector.

TABLE 10.3

Measured X-Ray Attenuation Values for Three Materials at Two Energies with and without Collimation

Material	Linear X-Ray Attenuation (mm^{-1})			
	100 kV: 2-mm Al Filter, No Collimation	100 kV: 2-mm Al Filter, with Collimation	160 kV: 2-mm Cu Filter, No Collimation	160 KVP: 2-mm Cu Filter, with Collimation
Aluminum	0.092534	0.102528	0.037886	0.044998
Delrin	0.026487	0.029224	0.01822	0.020994
Graphite	0.026199	0.028851	0.019343	0.022165

Also, notice the small changes in the ratios of the measured attenuation for different materials when collimation is introduced. It should be mentioned that, for both energies, the radiographic attenuation is relatively small: $\mu_{\text{eff}} = 1.8$ for the 100 kV scan, and $\mu_{\text{eff}} = 1.4$ for the 160 kV scans (μ_{eff} is shorthand for attenuation times path length). We are in the regime of robust transmission for this object. For the moment, ignore the change in attenuation order between graphite and Delrin. This is to be expected since at low energies, the higher atomic number (Z) makeup of Delrin is more significant and thus the total attenuation is greater, while the higher-density property of the graphite results in more attenuation at the higher energies when photoelectric absorption is less prominent in total attenuation (more about this in dual-energy techniques in Chapter 15). From these results, what is it about the addition of collimation that results in an increase in attenuation for each of these materials and what about the ratio between the measured attenuation values for the different materials? A main point is when you introduce collimation, the attenuation values change even though you did not change anything else. How can we explain what causes such results?

We propose a different categorization of the acquired signal in x-ray imaging to describe the observed results and their origins. In general, independent of the detector, the interaction of the source irradiance with the object generates an image in three-dimensional space. A detector element at a certain position and with a certain size will sample a specific part of this irradiance

regardless of detector type. For any detector position, \mathbf{d}_a^* (some 3D position on the other side of the object \mathbf{O} from the x-ray beam with some area), on a line \mathbf{l} from the x-ray source $\mathbf{S}(E)$, the detected x-ray photons intersecting this solid angle are divided into three different types of irradiance:

$$\Phi[\mathbf{S}(E), \mathbf{O}, \mathbf{d}_a, \mathbf{l}] = \Phi_p[\mathbf{S}(E), \mathbf{O}, \mathbf{d}_a, \mathbf{l}] + \Phi_s[\mathbf{S}(E), \mathbf{O}, \mathbf{d}_a, \mathbf{l}] + \Phi_{rf}[\mathbf{S}(E), \mathbf{O}, \mathbf{d}_a, \mathbf{l}], \quad (10.1)$$

$$\Phi_s[\mathbf{S}(E), \mathbf{O}, \mathbf{d}_a, \mathbf{l}] = \Phi_{sbk}[\mathbf{S}(E), \mathbf{d}_a] + \Phi_{sobj}[\mathbf{S}(E), \mathbf{O}, \mathbf{d}_a, \mathbf{l}], \quad (10.2)$$

$$\Phi_0[\mathbf{S}(E), \mathbf{d}_a, \mathbf{l}] = \Phi_{p0}[\mathbf{S}(E), \mathbf{d}_a, \mathbf{l}] + \Phi_{sbk}[\mathbf{S}(E), \mathbf{d}_a]. \quad (10.3)$$

The schema represented by these equations decomposes the photon output from an x-ray source, $\mathbf{S}(E)$, for the solid angle subtended by detector area \mathbf{d}_a , into primary irradiance, Φ_p , scattered (both coherent and incoherent, Compton) and pair production irradiance, Φ_s , and refracted photons, Φ_{rf} . The irradiance is from source $\mathbf{S}(E)$ (polychromatic), undergoing x-ray interactions with object function \mathbf{O} , along path \mathbf{l} (a line from source to detector). Furthermore, there are two types of scattered photons: background scattered, Φ_{sbk} , and object scattered, Φ_{sobj} . It should be mentioned that Φ_{sbk} can be decomposed further into scatter from the detector, from collimators, and/or from the fixtures/hardware within physical proximity to the detector, but determining this gets system dependent. Φ_0 , a measurement of the radiation field without the object, is fundamental to many x-ray measurements and is included here. Typically this measurement contains some background scattered photons from the supporting fixtures in the x-ray system or in the detection hardware, in addition to the photons launched by the x-ray source. In some instances, the incident irradiance, Φ_0 , can contain an image of, for example, a safety or containment device, say a cylinder around the object, but is not part of the object, that is, if it is left in the field of view after the object is removed. One additional source of signal is the result of the digitization of the received signals $\mathbf{D}(\Phi)$ and $\mathbf{D}(\Phi_0)$, and while the magnitude of this input depends upon the amount of signal to be digitized, it does not depend directly on the source-detector geometry or object, so we have left out the subscripts. This signal component is comparatively small but again can be important in some contexts when transmission is low, and can frustrate the best-designed deconvolution schemes. Since the amount of digitization noise usually varies with the different detector types, we relegate this to the discussion after which a detector is selected.

This particular taxonomy of the sources of signal impinging on a detector emphasizes the impact of the geometry of the x-ray paths from the source to the detector element, some intersecting the object, and less to the interaction mechanism of the x-rays in the object (again some detected irradiance can be Compton scatter that is in lines of sight to your detector). As expected, the ways in which photons from different attenuation mechanisms populate these types of detected photons vary with the energy level of the inspection. Not all of these types of signal are populated at every energy regime or for every scanner configuration. As indicated above, lower-energy inspection regimes generate less scatter, especially from surrounding materials; medium- to high-energy regimes include more scatter; and longer part lengths through low-Z materials can result in scatter effects at surprisingly low energies. Each of these sources of signal has certain characteristic properties. Consequently, evaluating and measuring the proportions for

* In this description, we have collapsed a lot of information into the symbol represented by \mathbf{d}_a , which is meant to signify both 3-D position, x,y,z , and an area with width and height. It was decided to represent this 5-tuple as just \mathbf{d}_a for brevity, since the notation is substantial already. Also, when we get to CT image reconstruction algorithms and analysis, the position of the detector and the area of the detector get parcelled out to different sets of equations connected to already established algorithms. Consequently, we ask the readers' indulgence and request that the focus be on the concept at this point and not all of the notation details.

these different types of signal is important for planning, implementing, and troubleshooting any collimation scheme.

10.2.1 PROPERTIES OF Φ_p

The primary radiation is the idealized path from the source to a detector element, called a ray-sum, part of the signal counted by the detector. This source of signal at the detector was launched by the x-ray source and arrived at the detector along straight lines. For this source of signal, the transmission on that line through the object is the result of interactions on that particular line and not from other x-ray paths or lines, i.e., to interactions from adjacent materials. Whichever energy regime is particularly significant, and systems can include hardware elements that work to reduce, if not eliminate, all sources of signal except the primary radiation. The purest realization of this ray-sum model is the highly collimated, pencil-beam, single-energy detector system (see Chapters 11 and 12). At the other end of the continuum are the area detector systems equipped with a multispectral source and minimal collimation.

A single-energy x-ray source, pencil-beam-collimated, energy-discriminating detector is a primary irradiance only system. All other sources of signal have been eliminated in the structure of the system. Data from this type of system are the most quantitative, and results should equal the tabled attenuation quantities (Cullen et al. 1989). If the entire signal arriving at the detector is primary radiation, a number of important possibilities for quantitative radiography follow. Dividing by Φ_0 , taking the natural logarithm, and multiplying by minus one is a direct measurement of attenuation multiplied by path length (Martz et al. 1991a,b). If the thickness of the sample is known, then the changes in the radiograph are changes in electron density and composition and may be quantitatively determined from a single radiograph. If radiographs can be acquired at two energies, the ratio between transmissions or attenuation values can be used to estimate the chemical formula of the material (Martz et al. 1991a,b). All the data for every transformation have a quantitative interpretation for defect recognition or materials characterization as discussed further in Chapter 11.

The CT system at the advanced light source (ALS) Synchrotron (ALS 2010) combines a single-energy source with a camera-scintillator based area detector. Synchrotron x-ray beams are both monochromatic and very close to parallel (especially for small fields of view). Data from this system will not include the effects of beam hardening, but will include scattered irradiance due to the scatter interactions in the material (depending on the energy). Data are quantitative, and reconstructed CT data contain a quantitative significance for the materials in an object under inspection; for more on this, see the high explosives inspection application given in Section 16.4.4.

Results from multispectral x-ray tube sources and current integrating detectors are a bit more difficult to interpret. All of the possible sources of signal identified in Equations 10.1 to 10.3 are populated at some level. Calculations of transmission and attenuation are integrated over the energy spectrum launched from the x-ray source. In this experimental context, only relative comparisons make sense on such a CT system, and by scanning a set of pure materials on a particular scanner, a table of relative relationships can be built; but this process must be replicated for each scanner and for each set of scanner conditions, e.g., x-ray filtering the source, and thus changing the spectral content of the beam can dramatically change scanning properties. Beam hardening is the preferential attenuation of the lower-energy photons, more than higher-energy photons, and results in an artifact. Separate data must be acquired to measure the extent of this effect and to provide data for its remediation. This further compromises the quantitative aspects of the acquired data. Say you acquire an interesting CT image, but you are just not sure what is accounting for the precise change in the voxel-to-voxel magnitudes. For polychromatic sources and area detectors, the important point is that you do not measure the primary radiation but measure the result of all the scattered photon processes occurring in the radiation field, and this results in less quantitative data/images. Methods are being developed to overcome this as given in Azevedo et al. (2016).

PANEL 10.1 Scatter-to-Primary Measurements Panel

To get an idea of the difference between the primary x-ray radiation and the signal you measure, perform the following measurement. Acquire an image of a single-material, simple-geometry, e.g., a cylinder, object that substantially attenuates the x-rays, say less than 10% transmission. Second, use a collimator, e.g., some long blocks of an opaque material, to construct a pre- and post-object collimated pencil beam. Acquire a single trace by translating the object laterally in between the two pencil beam collimators, (make sure that the collimator acceptance [C_w/C_l ; see [Section 10.2.1](#)] is small enough to ensure elimination of a wide scatter path, say 1° [a 50:1 collimator length-to-width aspect ratio]). Compare the results; this is the amount of the signal that is not part of the primary radiation; you just determined the scattered radiation getting to the detector. A scatter-to-primary ratio can be calculated from these data.

The point of the discussion for the different systems mentioned above is that the primary radiation can be difficult to measure, since it depends upon the system configuration. One method used to measure primary and scattered radiation is given in [Panel 10.1](#). The primary radiation is the detected component that proceeds in straight lines from the source through the object to the detector. It includes substantial spatial resolution and is the closest realization of the ray-sum model upon which CT reconstruction algorithms are built. Unless you employ some hardware mechanism to isolate the primary radiation component, all you can do is hope that you have a lot of primary radiation for good data/images. For area detectors and polychromatic x-ray sources, the properties of the primary radiation are directly affected by the geometry of the source and the x-ray magnification of the object. As an aside, without considering anything but the primary irradiance, a number of trade-offs have emerged, and more will follow.

10.2.2 PROPERTIES OF BACKGROUND OR SYSTEM SCATTER, Φ_{Sbk}

The fundamental engine for the production of scatter is the Compton scattering mechanism detailed in the Klein–Nishina formula presented in [Chapter 5](#) and shown in [Figure 10.3](#). Rayleigh scattering is also part of these signal components, but is comparatively much smaller at energies greater than 40 keV. A couple of details from this previous discussion are worth highlighting. Overall, the amount of scatter produced is a joint function of attenuation and density. First, if a photon does not interact in a material, it cannot scatter. Second, the constitutive materials in the object are important; scatter production is proportional to the electron density of the material. Third, Compton scatter is somewhat forward peaked, and more so as energy gets higher as given in [Figure 10.3](#). However, at higher energies, the scattered photons, even at larger angles, can penetrate many different types of object lengths, generate more scatter events, and then be more likely to be directed toward and be stopped by the detector. It is useful to note that many detectors are thin and stop a much greater proportion of the lower-energy irradiance.

The Φ_{Sbk} signal originates in the surrounding hardware, collimators, possibly in the detector hardware in the case of some flat-panel detectors (Logan and Schach von Wittenuau 2001), or in the veiling glare exhibited by some image intensifiers (Seibert et al. 1985). This source of signal has no direct relationship to the object and is only indirectly produced by scattered irradiance from the object and/or the production of radiation from the object itself (in the instance where the object is radioactive). The size of Φ_{Sbk} can be proportionally largest for high-energy scanning and is not entirely accounted for by the Φ_0 measurement. The hardware remedies for Φ_{Sbk} are to measure and inventory the surrounding hardware for possible scattering contributions. The contributions may be performed by strategically placing detectors in the system and, where possible, collimate and shield these sources of scattering to prevent them from reaching the detector. An important measurement that measures the magnitude and structure of the scatter signal reaching the detector is given in [Panel 10.2](#).

PANEL 10.2 Background or System Scattered Photons Measurements

Radiographically opaque objects fulfill a key experimental role in determining photons scattered from the x-ray system, also referred to as background scatter, that reach the detector, Φ_{Sbk} . Referring to Equations 10.1 through 10.3, the detected signal behind a radiographically opaque object is entirely the background scatter contribution at that physical location. To obtain a measure of this component, place the opaque object in front and on the detector (eliminating the possible influence of x-ray magnification), and acquire an image at the parameters (e.g., same energy, integration time, and detector settings) used to acquire the inspection data. Record the number of counts behind the opaque object; let us call this measurement S1. Now change the collimation or the hardware surrounding the detector, acquire another image, and/or change another piece of hardware. In this way, for the configuration of an x-ray cabinet, or x-ray bay that you can change, you can obtain a minimum (optimum) value for S1 (Logan and Schach von Wittenau 2001). To investigate the structure of S1, make a set of opaque objects of different sizes to place on the detector and record the minimum value. This sequence of values/images can be used, and have been used, to construct system-specific processing kernels implemented in deconvolution schemes for improving spatial resolution and contrast (Boone and Seibert 1988). The deconvolution can be considered spatially invariant and thus make FFT-based techniques convenient choices.

Measurements of S1 (see Panel 10.2) can guide future design of x-ray bays or cabinets, can directly inform subsequent processing procedures, and can define certain limits on contrastive performance for a particular scanning technique. The bad news about S1 is the loss in dynamic range. At best, if S1 has no particular structure, the bit depth of the detector is compromised, i.e., loss of dynamic range, but in an equivalent way throughout the image. In this circumstance, S1 can be treated like *dark current* in a charge-coupled device detector, an offset that can be subtracted from each image. This is a common practice in some medical and industrial scanners. However, it is always true that S1 occupies a number of counts in nearly every pixel and has little to do with the object, and the counts involving the object that you are interested in sit on this scatter background. If there is structure from some collimator or hardware piece in the cabinet, the situation is worse; care must be taken to ensure that this feature is included in the Φ_0 image to enable the elimination in the transmission/attenuation processed image. If not, the artifacts that result from a structured Φ_{Sbk} will be a part of the detected image, and somehow must be accounted for or ignored if possible by the analyst.

10.2.3 PROPERTIES OF OBJECT SCATTER, Φ_{Sobj}

Φ_{Sobj} refers to photons that are detected from paths through the object, not on the particular line from the source to the detector, not occupied by the primary radiation. These photons have interacted in the object through Compton scattering and have arrived at a particular detector element as the detector aperture to the object permits. For a current-integrating detector, it can be true that a certain number of the primary photons are in the straight lines through the object but have scattered in the object within the aperture of the detector width. The issue here is the correlation between changing lengths of the object and the production of scatter. Objects with complicated geometries generate equally complicated scatter effects. Objects do have localized features, and x-ray scatter can have areas where scatter is more prominent, and thereby compromise the inspection in that region. As indicated above and shown in many tests, source and pre-object collimation, yes two collimators between the source and the object, always reduce the amount of scattered photons.

10.2.4 X-RAY SCATTER CORRECTIONS AND THE SUBTLETIES OF RADIOGRAPHIC IMAGING

With the above schema given in Equations 10.1 through 10.3 in hand, let us return to the results from scanning at two energies with and without collimation. The first question was, why do the materials at each energy appear to be less attenuating when no collimation is present as opposed to when pre-object collimation is applied? An examination of the radiographs shows that there are simply more digitized counts, for the same integration time, in the uncollimated images. Consider this situation: for the same chord length through the same object, using the same energy spectrum, there are more digitized counts. It is proposed here that the majority of these extra counts do not interact with the object but interacted with the pre- and/or post-object collimators, or interacted with the object and some other part of the system and all of which reach the detector. The act of restricting the radiation to a smaller solid angle has reduced the number of photons detected from sources other than the object, such as scattering from fixtures, long-tail scatter from adjacent components in the detector, and possibly backscatter from other constituent components behind the detector. Processing the uncollimated data in the standard fashion, it would appear that the objects are less attenuating relative to the incident irradiance due to the extra photons counted by the detector. When the scattered photons are removed through collimation, the proportion of the primary to scattered radiation increases, the measurements have more to do with the object, and the attenuation ratios between different materials are more consistent with expectations. The cost of the collimation is in the size of the field of view and ultimately scanner efficiency. That is, for a collimated x-ray pencil-beam system, we will have to translate the object through the collimated pencil beam (or translate the source–collimator across the object) to cover the same number of ray sums when compared to a linear-array detector (see Figure 10.5). On the other hand, for an x-ray fan-beam system, we would

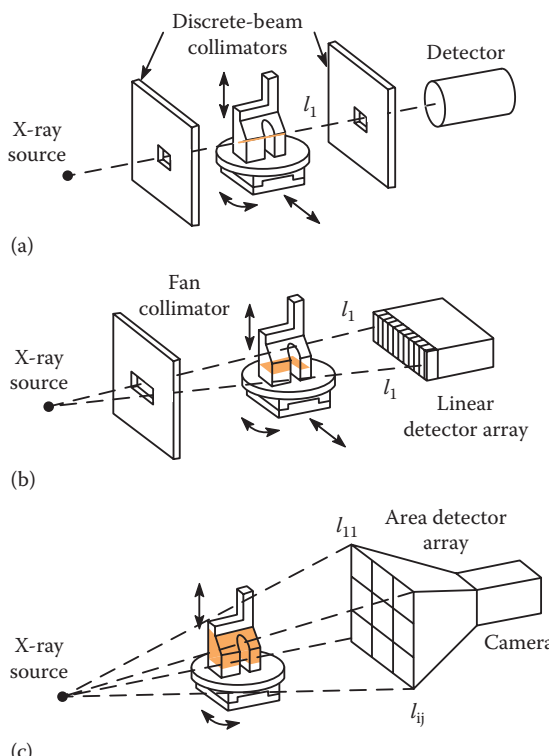


FIGURE 10.5 (a) A pencil-beam collimated x-ray source and single detector, (b) fan-beam collimated x-ray source and linear-array detector, and (c) a cone-beam collimated x-ray source and area-array detector DR and/CT system.

have to translate the object across the fan beam to cover the same number of ray sums when compared to an area-array detector. For more on this comparison, see Chapters 11 and 12.

For area-array detector systems, x-ray scatter correction algorithms intend to fix this dilemma and apply a correction to the images to remove the deleterious effects of scatter. Two necessary tasks are included in the correction effort: (1) estimating the correction function and (2) performing the correction. From here, the proposals for estimating the scatter correction divide into three approaches: (1) estimate the correction function from some set of specialized radiographs of particular test objects; (2) estimate the correction function from a section of the acquired inspection data (via some collimated portion of the radiograph or with the use of a *beam blocker*); and (3) estimate the correction function from a model of the scatter or from a Monte Carlo estimation of the scattered radiation.

Applying the correction function also includes various choices and can introduce new artifacts. If the correction function is characterized as a point-spread-function (PSF) blur, then some kind of Weiner filtering procedure is appropriate (Kak and Slaney 2001). A Wiener filter minimizes the mean square error between the estimated random process and the desired process (Kak and Slaney 2001). A number of authors have shown ways to handle the usual problems with noise amplification and possible oversharpening associated with inverse filtering (Seibert and Boone 1988). Since it is well known that x-ray scatter from the object can be spatially variant, some approaches perform the correction differently for different chord lengths through the object (Kak and Slaney 2001). This can result in improved images where more detail is evident and less noise is included in the image. However, if the correction function is estimated from similar data and includes noise that is correlated with the noise in the images you are correcting, other artifacts can result. In the cases where the correction function is a map of the scattered radiation, the map is subtracted from the acquired image and further calculations or reconstruction proceed from the corrected data/image.

For medical scanning, applying these techniques consistently improves image quality, edges of features are better defined, attenuation values are more in line with models, and noise is often reduced (Zhao et al. 2015). Difficulties arise when applying these methods in industrial contexts. Industrial objects can be much more varied, i.e., they can be more heterogeneous in terms of x-ray attenuation (e.g., an object that includes steel, aluminum, and plastic). Energy ranges can be much higher than employed in medical x-ray imaging systems with different proportions of x-ray attenuation mechanisms inherent in the scanning. Perhaps the most important aspect of the medium- to high-energy regimes is that the detector stopping power is a small fraction of the total irradiance. Using the multicomponent model presented above in Equations 10.1 through 10.3 as a reference,

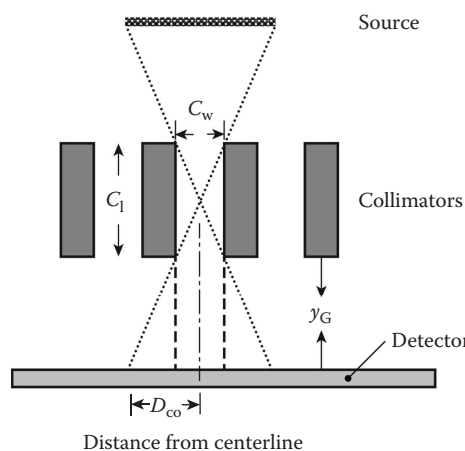


FIGURE 10.6 Diagram of relationships impacting collimator properties due to solid-angle considerations.

when only a small fraction of the irradiance is stopped and counted by the detector, some fraction of the rest of the irradiance contributes to detected scatter in unknown ways.

The model for scattered photons in x-ray transmission systems presented here partially favors correction schemes calculated from some artifice placed in the field of view such as a collimator leave or a beam blocker (see [Figure 10.6](#)). The model underscores the multiple types of physical mechanisms that result in some digitized signal. Further, everything interacts with the x-rays, and if some condition changes in the system or the modeled correction schemes, the PSF distributions have to be recalculated and/or the correction schemes are hard-pressed to reflect the current state of the object, the source, the detector, and the collimation/shielding. According to the schema we have presented, it is just difficult to model all the sources of signal with one singular measurement of *scattered photons*. This problem gets worse as the energy increases. We consider this the fundamental reason why the general-purpose scatter-correction scheme is inherently elusive.

All this says for complicated industrial object geometries involving high-aspect ratios and/or large changes in materials modeling the entire scatter field is a larger job. Small changes in the highest attenuating materials can result in large changes in the scatter field with the added complication that the transmitted signal is low, and the scattered signal will be a higher fraction of the signal measured. Further, it may be true that a certain technique can work for a part that includes a single material and a simple geometry, and not work for an object that is multiple material and that includes a complicated geometry (high aspect ratios and complicated geometric arrangements for the interfaces). This further begs the question of what it means for a scattered photon correction to *work*. It may be true that the edges of the material are not *sharp*, but the edge is averaged over the pixel or voxel size and making the image sharper may be fictitious. Also scattered photons can result in loss of contrast. For a measure of contrast sensitivity see Panel 10.3.

PANEL 10.3 Contrast Sensitivity Measurements

Test objects consisting of different thicknesses or steps can be used to assess the x-ray penetration capabilities, can be used to assess the contrastive performance of systems through real material lengths, and are important for assessing the usefulness of image processing schemes employing single-scatter approximation schemes. Obtain a step wedge of material that spans the useful range of the detector in transmission. Place ASTM pennies (ASTM 2012) of the same material at each step, constituting a 2% or 4% thickness change of the step, and place the step wedge as close as possible to the detector, close enough to eliminate source unsharpness. Acquire one radiograph with the pennies facing the x-ray tube, and acquire one image with the pennies facing the detector. The step at which the features of the pennies are no longer detectable is one limit of the penetrating power of the source and detector configuration. Second, the size of the smallest detectable feature is a measure of the spatial/contrastive performance at a particular path length. Lastly, the difference between the image with the pennies facing the source and the pennies facing the detector is an additional measure of the tractability of scatter corrections as applied to your problem. The larger the difference is, the less tractable the scatter will be.

In summary, x-ray transmission images can include a variety of spatially varying effects, some due to scatter in the object, some due to scatter in the detector, and some due to scatter in the surrounding structures of the system. The proportional magnitudes of these effects depend on energy, object constituent materials, and object geometry. Digital radiography (DR) applications can devise schemes for placing the feature to be inspected in a region in which these effects are muted or result in specific and identifiable patterns that can be read around, e.g., a radiographic signature of a defect can be identified in the midst of these and other effects. Algorithms developed for tomosynthesis

and computed tomography (CT) based on the ray-sum model work best when the dominant signal is the primary radiation. Consequently, imaging configurations that include substantial amounts of nonprimary signal tend to be nonquantitative and can include substantial artifacts. The point of an accounting model of the contributions to the detected x-ray signal is to acknowledge the different types of irradiance populating the signal acquisition of a detector and how each type can impact inspection performance. We recommend some measurement of the relative magnitudes of the different signal components obtained from the techniques suggested here be performed. By acquiring these measurements, you then have a baseline for assessing any next changes in collimation or to evaluate the effects of a scatter correction procedure however implemented.

10.3 SHIELDING AND COLLIMATION

Shielding has three aspects: for personnel safety, to increase equipment operational lifetimes, and to improve imaging performance. In the first aspect, shielding must contain the radiation and eliminate unsafe levels of human exposure. Secondly, x-rays can have long-term deleterious impact on some electronic components; shielding can effectively reduce this impact. Lastly, the impact of shielding can find its way into the acquired measurements, especially in the medium- to high-energy regimes where Compton scatter is the dominant attenuation mechanism (see the high-energy collimation example in Section 6.5.2).

Collimators can be organized by the type of detector: area collimators for area detectors, slit collimators for fan-beam detectors with and without septa, and pencil-beam collimators restricting the source solid angle into the area of a single detector. Of course, you can constrict the cone-beam geometry irradiance into a fan beam even for an area detector, effectively reducing the detector to a slit. But this begs the question of why you purchased an area-array detector. Formally, the mechanics for designing collimation are the most rigorous for the construction of pencil beams; slit collimation relaxes collimation in one dimension, with collimation for area detectors somewhat less strict. The goals for the different collimators are different according to type and result in different considerations for their design. Area detector collimators are meant to restrict the total irradiance for the solid angle covered by the detector area, which covers the object or the region of interest in the object.

A second property of collimation pertains to the number of collimators in a system. It is often the case that the collimators are configured in sequence along the direction of the beam—the intention being to act in concert to remove scatter (for example, see [Figure 10.2](#) with pre- and post-object collimation). This is often the most beneficial for x-ray sources with MeV end-point energies where the amount of scatter is large, and it is not clear that you have really stopped the primary beam. At high energies, additional collimators act to clean up scattered x-ray photons from interactions with the collimators closer to the x-ray source. One consequence of collimation is fundamental: a number of source photons are blocked by the collimators, so there is less irradiance per time at the detector. Highly collimated scanners can require substantially more time to scan the same object due to the lower source efficiency. Of course, loss of scatter from supporting structures with no relation to the object is not a loss. However, for time-sensitive inspections, the impact of slower scanning can be significant.

The mechanics for designing collimation and shielding are similar. X-rays interact with elements of collimation or shielding with the principles outlined in Chapter 5. Weight and space considerations for these structures result in the use of the same materials—high Z and high density. In both cases, the goal of the collimator/shield is to put the radiation where you want it and prevent the irradiance from going where you do not want it.

The general model for the source-detector envelope is the landscape for designing a collimation strategy and assessing its impact. For fielded DR and CT systems, source irradiance has two aspects: (1) the deposited energy due to geometry, i.e., for a flat detector, the detector elements that are at a larger fan/cone angle will detect less irradiance with the greater distance, and (2) for multispectral sources, spectral changes with the fan/cone angle. A cosine-cubed distribution is a

reasonable description of the emerging source irradiance. Following the development in Barrett and Swindell (1981), for a square detector element area, d_a , at a radius r_{det} from the center of the detector, and ϕ_{det} , the angle subtended by the normal to the detector element plane and the line connecting the center-of-source to the center-of-detector element, let y_{sod} be the source-to-object distance (measured at the center of the object) and y_{odd} be the object-to-detector distance (see Figure 10.5); solid-angle considerations lead to a \cos^3 distribution, with

$$R = (y_{\text{sod}} + y_{\text{odd}})/\cos \phi_{\text{det}}, \quad (10.4)$$

$$d\Omega = [\cos^3 \phi_{\text{det}}/(y_{\text{sod}} + y_{\text{odd}})^2] d^2 r_{\text{det}} \quad \text{and} \quad (10.5)$$

$$\text{XS}(r_{\text{src}}) d\Omega/(4\pi K) = (\cos^3 \phi_{\text{det}}/[(y_{\text{sod}} + y_{\text{odd}})^2 4\pi K]) d^2 r_{\text{det}}, \quad (10.6)$$

where K is a source geometry factor, representing the restricted angular dispersion of the source (most sources do not emit into a complete sphere but into some fraction of the total 4π steradians around the source), $\text{XS}(r_{\text{src}})$ denotes the x-ray output at position r_{src} , and $d\Omega/(4\pi K)$ denotes the solid-angle field of view for the irradiance. A few relationships follow from the above expression and are worth mentioning.

Source irradiance decreases or increases in the aggregate by the square of the distance between the source and the detector. Smaller detector sizes decrease the solid angle from the source by the area of the detector, and this decreases or increases in a geometric scaling (a 0.2 mm \times 0.2 mm detector is four times the area of a 0.1 mm \times 0.1 mm detector).

For a flat detector, the detector elements away from the centerline lose intensity by the greater distance from the source (the intensity decreases as the square of the distance to the detector) and will have less intensity due to the structure of the irradiance from the source (many sources include an intensity and energy fall-off independent of the fall-off with r -squared, i.e., some sources have a *heel effect* discussed in Chapter 8). For curved detectors, the detector elements are all at a single radius from the source, and can measure a more uniform intensity from the x-ray source over the same source envelope, but do not compensate for the energy drop-off.

As mentioned above, spectral changes in source output also have a spatial component, but this is somewhat source dependent. For instance, *end-window* x-ray tubes have a different spectral distribution than standard x-ray tubes. Also, linac sources include their own characteristic spectral fall-off.

From the solid-angle relationships alone, source efficiency is best served by curved detectors at close distances from the source (the canonical setup for most medical CT scanners). Also, it is important to ensure that the detectors are placed at the position of highest irradiance from the source; this is the midplane for the irradiance of the source. Smaller detector element sizes can make this task more difficult requiring more precision in the positioning of the detector, in the motion control, and in alignment measurements. From this vantage point, it can be understood why Chesler et al. (1977) stated, “CT system difficulty increases to the 4th power of the decrease in spatial resolution.” Higher spatial resolution requires more irradiance and better accuracy and precision for everything in the system.

10.3.1 COLLIMATORS

For the collimator, the aperture of a collimator carves out a portion of source irradiance characteristic of the collimator shape at some point in the source to detector envelope as shown in Figures 10.6 and 10.7. For rectangular collimators, acceptance angle from a position D_{co} at some distance from the centerline of the detector results in a trapezoidal (2D) see Figure 10.7 or prismaticoidal (3D) shape, the exact properties depending upon collimator aperture width, C_w , collimator thickness in the direction of the beam, C_l , distance to the source y_{sc} , and air gap to the detector y_G . The exact solid-angle relationships depend on the particulars of collimator placement in the source-detector

envelope: at the source, at the midline between the source and the object, after the object but not flush against the detector, and after the object and flush on the detector (the values determined for y_{sc} and y_G). As shown in other treatments (Barrett and Swindell 1981; Wang et al. 2005a), a key quantity for collimator design is the aperture ratio (C_w/C_l): the ratio of the width of the collimator aperture to the length of the collimator. This ratio figures importantly in the solid-angle relationships for any of the configurations mentioned above. Consider a collimator with a 0.015 in. aperture and a 4-in. thickness. Figure 10.7 shows plots of different fractions of irradiance varying by the distance from the centerline of the collimator at some air gap away from the front of the collimator. Notice the enlargement of the tails for the acceptance of this high-spatial-resolution collimator from the change in air gap, y_G .

Following Wang et al. (2005a) and from Figure 10.6, we develop the solid-angle distribution for a rectangular collimator for distance D_{co} from the collimator center as

$$\begin{aligned} & 1 \text{ when } |D_{co}| < C_w/2, \\ & 1 - [(|D_{co}| - (C_w/2))/[(C_w/C_l)y_G]] \text{ when } C_w/2 < |D_{co}| < C_w/2 + [(C_w/C_l)y_G], \\ & 0 \text{ elsewhere.} \end{aligned}$$

The plots in Figure 10.7 show the more sharply defined collimator acceptance angles for a smaller air gap, y_G . This same kind of relationship follows from small values of (C_w/C_l) where the width of the collimator is small relative to the length. Only the x-ray photons that are close to the centerline of the collimator make it through the aperture. For the impact of air gap, a collimator or a collimator grid on the detector results in the most scatter rejection due to the acceptance angle where photons arriving at small angles relative to the centerline are stopped in the collimator and not counted in the detector. For large detectors, this kind of (C_w/C_l) acceptance angle performance can be obtained in a number of ways. Figure 10.8 includes a couple of alternatives for large detector areas. Small

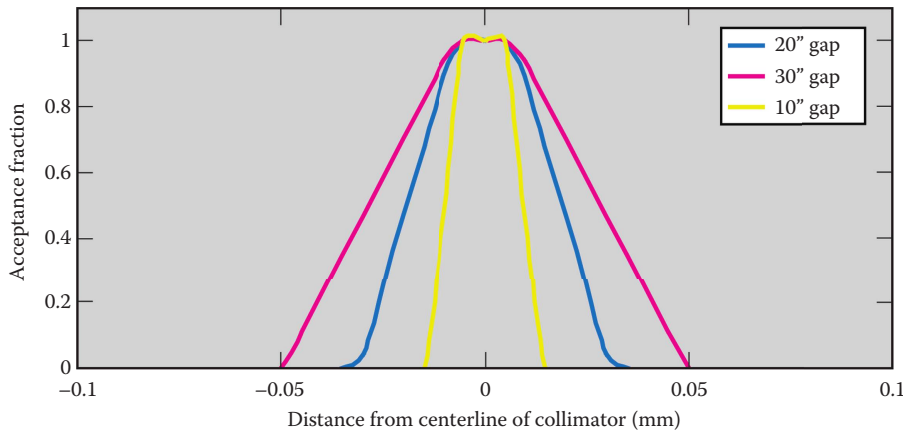


FIGURE 10.7 Plots of collimator acceptance fraction for different collimator configurations.

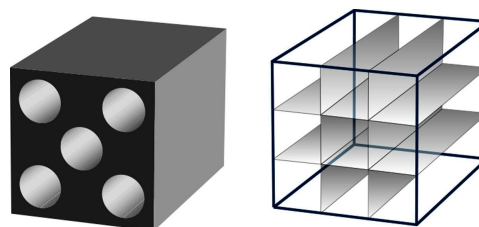


FIGURE 10.8 Examples of collimators fabricated with small holes in larger lengths.

apertures are fabricated into larger slabs of collimator material resulting in low (C_w/C_l) for a large detector area, even for small collimator widths with relatively small thicknesses.

Consider a post-object collimator with small through-holes. In this case, the (C_w/C_l) ratio is small. Most of the detected signal is on the designed collimated path. More scatter has been rejected. Even if the air gap is substantial, the overall geometry of the x-rays impinging on that detector element is good. Consider the case where we remove the air gap and put the small collimator holes with the small (C_w/C_l) ratio right on the detector. In this case, the collimator acceptance is a near rectangle. Arrays of small-hole or small-grid collimators placed right on the detector, sometimes called septa, are a part of many medium- to high-energy DR/CT systems.

This approach can be extended to arrays of collimators, aligned in series between the source and the detector. For arrays of collimators, the system acceptance angle is built up from calculating the distance between collimator centerlines for any particular position on either side of the collimator array, or from all collimators for any particular position on either side of a collimator array. Other variables held constant, large air gaps between the collimator arrays or the collimator and the detector increase the solid-angle overlap between collimator apertures. Thicker collimators decrease the overlap.

For a pre-object collimator, source unsharpness or blur in the image due to the finite size of the x-ray source spot is an additional consideration. Pre-object collimators will be imaged as a magnified object and are subject to source-spot blur. Depending on the source-spot size, the edges of the projection of the collimator will be more or less blurry. You can reduce or collimate out some of this blur with additional downstream (close to the detector) collimation in the source-detector envelope. As the collimators are positioned closer to the detector, the amount of source blur at the collimator edge is reduced. For area arrays, some blur is usually left in the sides of the collimation; for pencil-beam collimation or slit collimators that are positioned down the length of the beam path, the impact of the source spot can be negligible.

Graded collimation, the implementation of a series of inline sequential pre-object collimators, can prove useful in medium- to high-energy contexts (see Figure 10.9). Both the experimental results and the Monte Carlo modeling for the LLNL 9 MV DR/CT system and the Confined Large Optical Scintillator Screen and Imaging System (CoLOSSiS) are given in Section 6.5.2. Both cone-beam, area-array detector DR/CT systems attested to the improvement in imaging performance due to the implementation of graded collimation. In this type of collimation, the collimators are positioned along the source-detector beam line in such a way that they mutually contribute to carving out a directionally cleaner quaternion of x-rays. While the aperture size was fixed by the

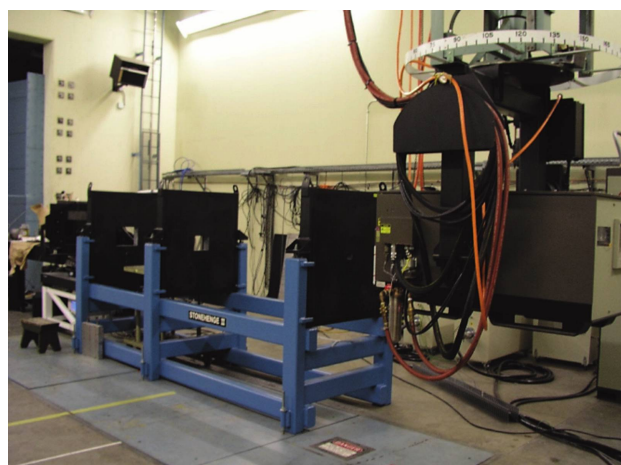


FIGURE 10.9 Picture of a three-panel graded collimation (Stonehenge II) fielded at LLNL 9 MV bay in Livermore, California. The collimation was developed for a system called CoLOSSiS.

size of the field of view at the detector, the position of the different panels along the source–detector beam line was determined by experiment and modeling.

A Thales amSi flat panel area detector is used to acquire the images from the DR/CT system shown in [Figure 10.9](#). Consequently, a substantial amount of object scatter is digitized by the detector. However, for each introduction of a collimator panel, we observed an overall increase in imaging performance. Further, the field of view was maximized by aligning different collimator panels, which are beveled to match the divergence of the x-rays, and this contributed to better imaging performance throughout the field of view.

Aligning arrays of collimators has an impact on the success of the collimation and source efficiency of the system. Considering the low- to medium-energy cases where you really stop many of the x-rays at the collimator, you will want the regions with the collimator acceptance fraction of 1 to fit into the subsequent collimator aperture, ensuring that only the radiation traveling down that path carved out by the many collimators is being counted by the detector. Building some adjustment of the collimator array into the design of the system is useful, and the adjusted position with the greatest irradiance for a downstream (detector side) collimator is the best position.

Alignment considerations for post-object collimation right at the detector can be a bit relaxed since at this position, you are just trying to reject photons that are arriving from scatter events many detector widths lateral or vertical from that detector position. In this case, you can put a grid array in place or perhaps a collimator with a number of holes in the material. In summary, the alignment considerations are more important as the collimator is closer to the source and are more relaxed as the x-ray geometric magnification of the system is lower with the limit at the detector.

With respect to x-ray scattered photons from the object, for medium- and high-energy systems, the object can generate considerable scatter and can significantly widen the collimator distribution (Light et al. 2000). Source-side collimation narrows the tails of the distribution impinging on the object, and the amount of scatter within the acceptance angle of the detector is reduced. Post-object collimation can reduce side-scattered x-rays from the x-ray signal reaching the detector; however, some forward scattered x-rays will of course get counted at the detector. Ultimately, systems with pre- and post-object collimation include the best primary-to-scatter ratio. Across all systems, the total collimator acceptance response is the product of all the acceptance angle distributions in the scanning system (for more on this, see the problems at the end of this chapter). For highly collimated systems, the entire chain of collimators accounts for the spatial resolution and contrast of the system and needs to be included in any calculation of expected performance or in an assessment of the impact of misalignment between collimator apertures.

At this point, let us take a moment to consider the costs of collimation. First, you have less source irradiance detected for the time of inspection. In medical contexts, you have irradiated the patient with dose, and in the industrial contexts, you have taken more time, which increases cost. Second, with some collimators, which effectively block the irradiance to certain detectors, you will have to scan twice, that is, change the position of the object or source–detector to fill in the missing area. Third, you purchased and installed the collimator material, which is heavy, had to be aligned, and increases the overall weight and footprint of the system. Fourth, the selected collimator chain and their placement in the source–detector envelope creates a set of trade-offs for scanner design. The envelope for scanning techniques is reduced; with the collimators in place, there are all kinds of places you cannot put the object. This may lead to limitations on the size of the objects that can be scanned.

As mentioned above, collimators with small acceptance angles (C_w/C_i) are more difficult to align, and directly reduce the available source output for imaging, but can result in higher spatial resolution, better contrast and more quantitative and accurate data/images. For high-energy systems, thick detectors can be employed to increase detector efficiency, making up for the loss in source irradiance. Collimator materials can be expensive and are heavy, and it may be more advantageous to position a few arrays of thinner collimators than to position one thick collimator. The different design considerations are not all equal; moving the detector back to fit more collimators in the envelope still reduces the output by r^2 , which is substantial.

In summary, complications for designing collimation and shielding owe to the fact that every material placed in the source-detector envelope can impact the total number of photons impinging on a detector element. Scatter effects need not be spatially invariant, which is certainly true for multimaterial, complex-shaped objects, and this makes many software fixes problematic. A three-fold strategy is recommended to obtain the best results: (1) design the system with close attention to Monte Carlo modeling; (2) make strategic measurements of the scatter production and impact of individual components (these measurements are described in [Panels 10.2](#) and [10.3](#)); and (3) design and implement methods for system performance measurements that incorporate the imaging performance targets you are planning to achieve.

10.4 ANTISCATTER GRIDS

When x-rays pass through an object, some are absorbed and some are scattered. Those that are scattered may reach the detector and degrade the desired image. This is especially prevalent when the detector is placed near the object. Under radiographic conditions where the scattered x-rays have scattered a few times, they arrive at the detector with nearly uniform spatial distribution and degraded energy. The lower energy usually increases the likelihood that they will stop in the detector and become a part of the detector signal. Scatter can then resemble a background that increases the overall signal and noise. Contrast is reduced in the acquired image since the dynamic range of the detector is spent on digitizing scatter and not primary photons that best define features in the object. It becomes a great concern when the object is large and is close to the detector for an area-array detector. In addition, when the detector is film, loss of contrast and dynamic range may be critical.

A grid placed between the object and the detector can remove some scattered radiation. Hollis Potter and others at the University of Chicago developed the first grids. Gustav Bucky is thought to have recognized that scatter was the critical problem, and Potter found the solution (Kevles 1997). The first grids consisted of parallel layers of radiolucent and radiopaque material as shown in [Figure 10.10](#). For example, paper and lead were used for the radiolucent and radiopaque material, respectively. These were arranged perpendicular to the film surface so that the Pb layers preferentially blocked scattered x-rays. An additional refinement was the manufacture of focused grids with the layers aligned toward the x-ray source. This increased the area that could be imaged, but these grids still produced stripes on the image corresponding to the separate septa of the grid. Sometime around 1920–1925, Potter and Bucky developed a grid that moved during the procedure and thereby blurred the grid image while still serving the original purpose. These moving grids became known as *Potter–Bucky* grids or even just Buckies.

In the last decade, fabrication methods have advanced so that it is possible to make focused grids that are two-dimensional (Logan, U.S. patent, 1995; Logan and Lane, U.S. patent, 1995). These have individual cells that align to the x-ray source at a predetermined distance. The W grid shown in [Figures 10.11](#) and [10.12](#) is an example that has parallel openings. Some grids have air as the spacer material and some use leaded glass, Ni, or Cu–Be alloy for the radiopaque material.

Grids are widely used in medical radiology and seldom used in industrial radiography. There are many complex reasons for this practice. The leading reasons why grids are not generally used in industrial radiography are as follows:

- Grids cause artifacts.
- Commercial grids are not available at 20 lp/mm (spatial resolution of 0.025 mm or 25 μm) required for much industrial nondestructive evaluation (NDE).
- Grids are most useful with film of low-dynamic range. In this instance, contrast cannot be adjusted even if noise is negligible. In other words, contrast, *per se*, is not important unless one is imaging low-contrast objects using film. Contrast to noise is important in digital imaging.

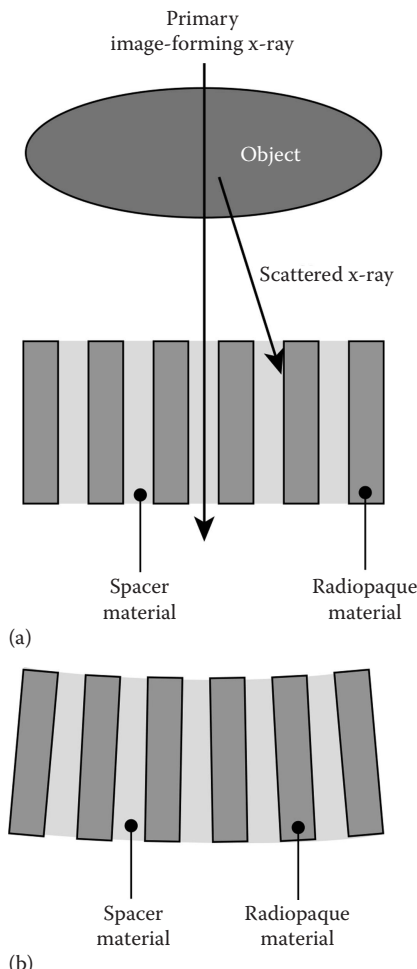


FIGURE 10.10 Diagram illustrating the concept of grids. (a) The layers are parallel, which can be made by stacking strips of radiopaque material (usually Pb or Ta) and spacer (paper, wood, or Al). (b) A focused grid is shown schematically. The layers are aligned to a distant point where the x-ray source is to be positioned.

- Industrial applications usually need not be concerned with radiation dose to the object; therefore, more radiation can be used to reduce noise and overcome low contrast.
- Distance between the object and the detector can usually be increased to reduce scatter.
- In critical radiographic, not generally CT cases, the incident beam can be collimated to a small area to reduce scatter.
- Commercial grids are not available for tube potentials greater than 120 kV.
- At higher energies, Compton scatter becomes more forward-peaked and grids become ineffective.
- At higher energies, the grid itself becomes an intolerable source of scatter.
- At higher energies, common in industrial NDE, the radiopaque layers must be thicker in order to attenuate scatter. This reduces grid effectiveness and increases artifacts. In the medical world, Pb is much more attenuating than the object. In the industrial world, this is often not the case.
- Grids are fragile.

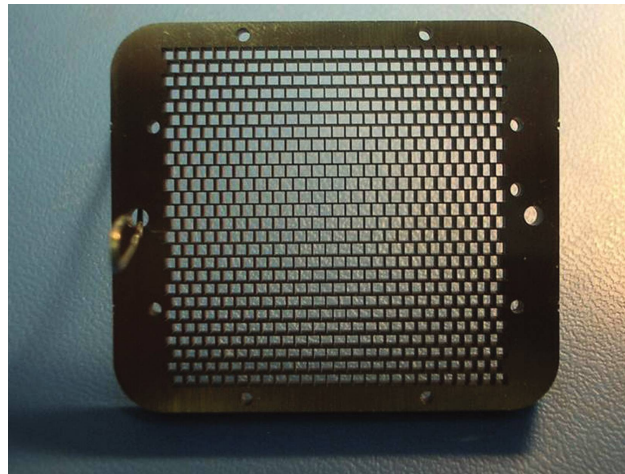


FIGURE 10.11 Photograph of a parallel-beam x-ray source grid.



FIGURE 10.12 Close-up photo of the parallel-beam grid shown in Figure 10.11. Note that the magnification makes the grid appear to be a focused grid, which it is not.

The use of grids in medical imaging is discussed in a medical imaging book by Bushberg et al. (1994). Their use in mammography is addressed by Barnes and Frey (1991) and Boone et al. (2001).

10.5 LIMITING APERTURES

A number of important imaging techniques employ specialized apertures placed between the source and the detector. One particularly useful configuration is for pinhole imaging of the x-ray source. This technique can result in an explicit image of the x-ray spot at the detector. Another case is the strategic use of an array of pinholes to image the source spot for high-energy radiation sources in a small space.

Figure 10.13 includes a schematic of two pinhole imaging techniques combining a source, an area detector, and a pinhole in a sheet of radio-opaque material somewhere between the source and the detector. It is important to note that the material into which the pinhole is fabricated should be completely opaque to the x-rays. For us, completely opaque is typically 10^{-6} reduction in the incident irradiance photons. The introduction of the pinhole has important consequences for the

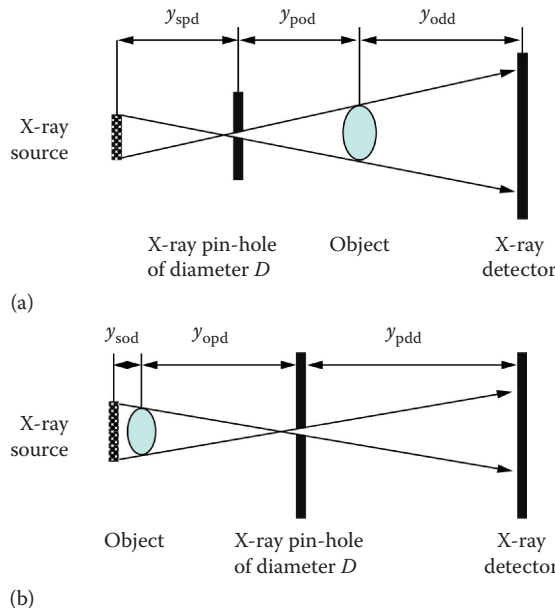


FIGURE 10.13 Schematic of distances and relationships involved in two different pinhole imaging methods. (a) A pinhole projection geometry DR/CT system and (b) a pinhole camera.

mapping between the distances of features in the source plane and the detected distance at the detector plane. For an alternate presentation, see Barrett and Swindell (1981). As shown in the diagram in Figure 10.13, introduction of the pinhole restricts the rays for exposing a view of the source or the detector, and relative magnification of features is a product of the relative distances between the source to pinhole (y_{spd}) and pinhole to the detector (y_{pdd}). When $y_{spd} = y_{pdd}$, the distances of features at the source and the detector plane are equal. Otherwise, features at the source are imaged in a magnified M_y or reduced size according to the ratio of y_{pdd}/y_{spd} . A feature with height R_{source} at the source will have size $(y_{pdd}/y_{spd})R_{\text{source}}$ at the detector or $R_{\text{Det}} = (y_{pdd}/y_{spd})R_{\text{source}}$, where $R_{\text{Det}} = M_y R_{\text{source}}$.

A particularly useful pinhole imaging application is to image an x-ray source and use this image to measure the size of the x-ray source, sometimes referred to as the spot size of an x-ray source. Figure 10.14 illustrates one configuration used to measure the spot size of a multi-emitter cold-cathode x-ray source manufactured by XinRay. The source-detector beam line was rotated to measure the spot size for each emitter. In this configuration, the 0.1 mm pinhole aperture was positioned at 131 mm from the source emitter surface (SES) with the detector positioned at 572 mm from the SES. Notice that the entire measurement apparatus is less than 600 mm long and could be engineered to require less total distance.

Digital images of a few x-ray source spots obtained from this pinhole imaging configuration are given in Figure 10.15. In this case, the y_{pdd}/y_{spd} ratio is 4.7. Consequently, features at the source will be magnified by 4.7 at the detector. The pinhole size was fabricated to be a diameter of 0.1 mm. The detector employed in this imaging is a 2 in. 14-bit complementary metal-oxide semiconductors (CMOS) detector with $0.05 \text{ mm} \times 0.05 \text{ mm}$ pixels. In this case, an approximately 1 mm source spot is now 4.7 mm on the CMOS detector allowing analysis of shape and intensity for further evaluation.

In a different fashion, an array of pinholes is used to image the source spot on a Varian Linac. The array of 0.025 mm pinholes drilled in 3 mm tantalum plates is assembled and aligned to obtain a 15 cm column of tantalum with small holes penetrating all the way through the column of tantalum. A representation of this pinhole array is given on the left in Figure 10.8. This assembly of tantalum is then attached to the source, close to the source spot. A detector (usually film) is placed at the other side of the column of tantalum. The effect of this pinhole collimator is that it eliminates

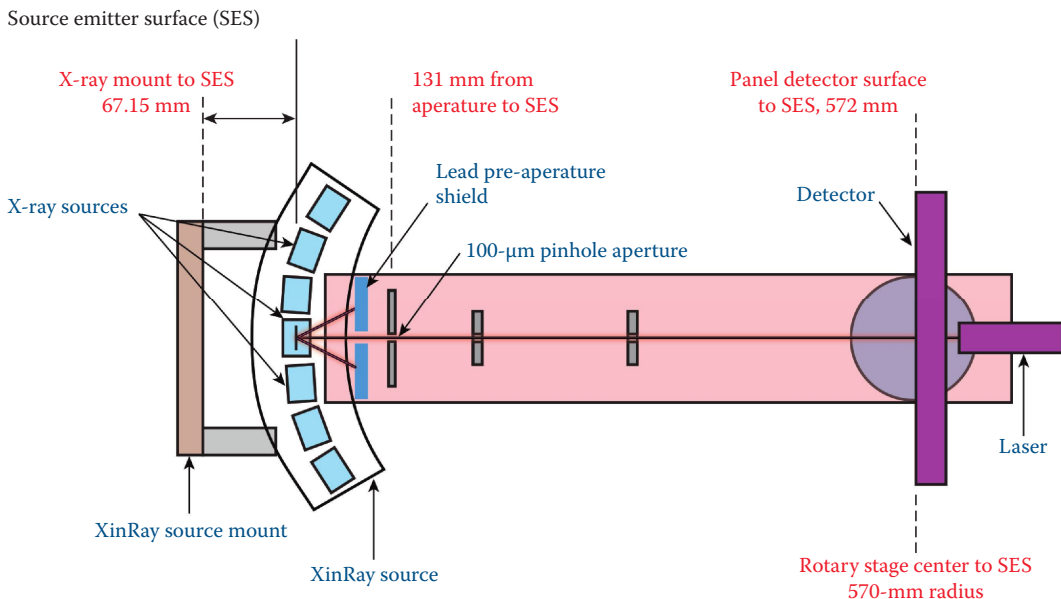


FIGURE 10.14 Sketch of pinhole measurement used to measure the x-ray spot size for an early version of a XinRay multielement cold-cathode x-ray source.

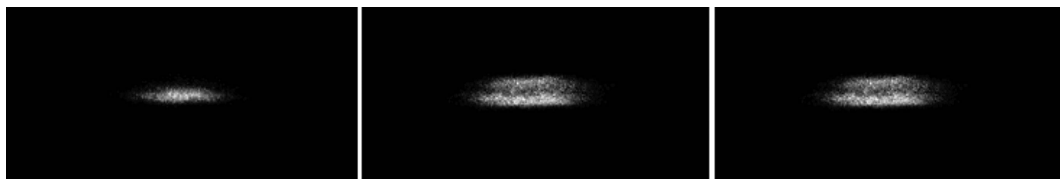


FIGURE 10.15 X-ray spot images from different source emitters for an early version of a XinRay x-ray source. The data were acquired using the pinhole imaging technique sketched in Figure 10.14.

all divergent x-rays enabling a view of the source spot down the parallel ray lines of the holes in the tantalum. This image can then be used to measure the size and intensity distribution of the source spot. In this case, the pinholes are not used for magnification but as parallel viewing ports on a feature that would not be viewable due to the penetration of most materials at this energy. Another important property of this technique is that no x-ray magnification is involved. Consequently, this measurement can be made in a small space unlike other techniques for measuring spot size that require long source-to-detector distances. This feature can be useful for saving heavily shielded space in linac manufacturing contexts.

10.6 STAGING FOR OBJECT POSITIONING AND CONTROL

Motion control hardware is one of the key components of some automated radiography, and all CT systems, and must meet certain requirements to adequately support the target spatial resolution of the system. A good rule is that the precision of the motion control hardware should be better than the target spatial resolution. One-half the target resolution is what we strive for. This is not a necessary rule, but it needs to be emphasized; all x-ray equipment degrades in the field. Motion control errors are some of the most subtle and hardest to correct and can result in data with limited application for comparison to previously acquired radiography or CT reconstruction. Inconsistent

or imprecise angular movements are one of the subtle errors that can void the acquired data. More importantly, these are errors you are not in the habit of checking, but just trusting the encoder counts is not always sufficient. It is important to consider the impact; you can take the results from a good detector and a robust source, and turn them into junk by cutting the precision of the motion control too close. Also, be advised that just because it works at that precision once does not mean it will work all the time, and for CT scanners, it needs to work all the time. The best strategy is to take a skeptical view of any claim by any motion-control manufacturer/integrator and test the equipment once received. Get a piezo-probe gauge better than the resolution of the stage, move the stage to the limit or home position and back to the desired position, record the value of the gauge, do it at least 30 times, and calculate the average and standard deviation from the measured positions. The difference in the value of the average position from the target position is the accuracy, while the value of the standard deviation is the precision of the stage.

Calculating the requirements for stage accuracy varies with the type of acquisition whether for radiography or CT. In radiography, the precision may be important only for a single axis. For instance, sometimes it is not that crucial that the part is in exactly the same place in the field of view, but that the region of interest be close (say within 1 cm) to the center of the field of view. At the same time, the rotational angle for viewing that particular location in the object may be critical and requires accuracy and precision.

For CT scanning, the requirements are more explicit. The accuracy of the rotational stage for rotational-only scanning or translation and rotational stages for translate-rotate scanning is integral to the reconstructed image and, by implication, the imaging performance of the system. Requirements for the accuracy of the rotational stage derive from the horizontal resolution of the detector and the radius in the object space of the feature you are evaluating. Following the discussion in Barrett and Swindell (1981) or Kak and Slaney (1998), the number of rotational views, N_θ , required to get all of the spatial resolution of your detector into the reconstructed image at radius R is when the radian distance of the angular increment for the rotational views is on par with the spatial resolution of your detector. In general, for a 360° scan, this works out to be

$$N_\theta = 2\pi N(R),$$

where $N(R)$ is the number of spatial resolution distances at the radius of interest. For instance, consider a detector with resolution at 0.3 mm (but a pixel size of 0.2 mm) to be scanned with a 360° technique and the feature you are interested in is 60 mm from the center of the field of view. A 360° scan of 1200 views will result in a reconstructed image with the 0.3 mm spatial resolution instantiated in the reconstructed image ($N_\theta = 2\pi 60/0.3 = 1256$).

It is important to appreciate the significance of this result. First, if you can put the feature of interest in the center of the rotational table, you do not have to acquire many views to obtain a good reconstructed image of that region. For example, see the reconstruction algorithm techniques featured in Brokish and Bresler (2007). Second, if the spatial resolution of your technique is relatively large, you need not acquire many views to get all the resolution from your technique into your reconstructed image. Third, if the spatial resolution requirements of the inspection are not substantial and it just so happens you have more resolution in the technique, you can acquire less views or you can resample the detector. The point is that this is another variable you can adjust to obtain the best inspection for the object in that region of interest in the shortest time.

The choices for the type of and the control protocol for the stages are large, and some of the distinctions are not consequential for system performance but can impact scan time. For the most part, there are three types of motor operation: stepper motor, AC servomotor, and DC servomotor. A stepper motor or step motor or stepping motor is a brushless DC electric motor that divides a full rotation into a number of equal steps. The motor's position can then be commanded to move and hold at one of these steps without any feedback sensor (an open-loop controller), as long as the motor is carefully sized to the application with respect to torque and speed. A servomotor is a

rotary or linear actuator that allows for precise control of angular or linear position, velocity, and acceleration. It consists of a suitable motor coupled to a sensor for position feedback. It also requires a relatively sophisticated controller, often a dedicated module designed specifically for use with servomotors.

All three motors can be reasonably precise, depending on the intended weight of the load and the requirements of the motion. AC and DC servomotor-operated stages can produce very smooth movement and, coupled with DSP-based controllers, can produce tightly controlled velocity profiles. DSP is a digital signal processor. It is a specialized microprocessor with its architecture optimized for the operational needs of digital signal processing. The goal of DSPs is usually to measure, filter, and/or compress continuous real-world analog signals. Both of these types of stages require some tuning, usually a proportional-integral-derivative (PID) algorithm where the user (or the factory) sets the PID gain settings to result in quick response to move commands, smooth operation, and resolute holding current to maintain a selected position.

Stepper motors operate by responding to step pulses and generally include less smooth operation, but require no tuning (which means you cannot tune it wrong). For point-and-shoot CT systems, i.e., where you move the object to a position and acquire a transmission measurement, there is little practical difference between stepper or servo stages, assuming you have tuned the PID control correctly and the stage does not chatter. For constant motion CT systems, which rely on tightly controlled velocity of motion, servomotor stages are usually a better choice.

In general, the bigger the weight is, the greater the accuracy and precision becomes, and the more expensive the motion control equipment will be. For CT, three kinds of stages are involved: rotational stages, translational stages, and elevational stages. For elevational stages, we prefer the scissor-type elevation stage and not the reconfiguration of a translational stage, i.e., put on end to result in vertical movement. Rotational stages can move/hold lots of weight for on-center loads. A 120 to 160 mm diameter table can rotate hundreds of kilograms and is available in a large variety of table sizes. Translational stages vary greatly in length, width, accuracy, and precision.

Exceeding weight limits for these types of stages can result in severe penalties, warping the lead-screw mechanism and permanently damaging the stage. For all vertical stages, some braking mechanism is useful to control stage movement in the event of power outage. Stage alignment is important when configuring a number of stages into a coordinated motion system, say xyz or xyz-theta. We have found it useful to spend time aligning stages (or assign the task to a trusted contractor). Lastly, inasmuch as possible, build head room into the design of multiple-axis motion systems. The stages themselves can be heavy, and it is really important to leave a large place in the scanning system for objects with a wide variety of sizes and weights. We recommend obtaining stages with greater precision and that can hold greater loads. In our applications, the extra cost of the stage is small compared to the cost of tearing the system up and replacing a stage because the part you want to inspect is too heavy or that the stage has seized up or failed.

The constant position/velocity checking required by some CT scanning techniques can argue for an upgraded motion-controller option. For constant motion CT, or even point-and-shoot CT, reporting the position of the stages in a timely fashion is an important ingredient to high-fidelity timely scanning. It is just critical to know where the object is in three-dimensional space as measured by the encoders on the stages. The reconstruction code takes these measurements as including substantial accuracy and precision (usually 32 bits) and acts as if there are no errors at all. It is best to get as close to this rather unreal standard as possible. Three types of controllers are in focus here: (1) smart stages connected by Ethernet that you directly command and query; (2) standalone controllers; and (3) controllers that are interfaced into a computer (for example, a card on a PCI bus). Conventional PCI, often shortened to PCI, is a local computer bus for attaching hardware devices in a computer. PCI is the initialism for peripheral component interconnect and is part of the PCI Local Bus standard. All of these types can include DSP-based operation for very fast velocity control and very fast position reporting. Communication to standalone controllers is usually over some serial communication standard such as RS-232, GPIB, USB, or

100 Base/T Ethernet. We prefer the faster serial communication protocols, say GPIB, USB, or Ethernet, which result in quicker, more responsive position reporting. Controllers interfaced to a computer bus, or passive standalone bus, can support very fast position reporting with almost no central processing unit (CPU) or input/output (I/O) overhead. For standard scanning applications, especially point-and-shoot scanning, nearly any motion controller will do. However, it is advantageous to have the capability to implement more exotic scanning regimes, which require more constant checking for position in coordination with acquisition for hard-to-inspect objects/assemblies.

Implementing stages using half of the target spatial resolution rule for DR/CT systems will result in higher up-front costs. The cost differential can be a factor of 2 or sometimes 3 for more accurate and quicker reporting stage systems, especially if requirements for inspection also include the need for velocity profiling and control. If the system is dedicated to the scanning of a particularly costly object, then the additional costs are justified, since the impact and cost of passing one bad part due to hardware malfunction can pay for the better hardware. Again, for the general purpose scan-anything-that-you-can scanner, we have been uniformly rewarded for paying more up-front for stages since down the road you will not regret it. The real payoff occurs when encountering some troublesome artifact in the reconstructed data, and you know you can definitely rule out motion control errors.

10.7 DR/CT ACQUISITION, PROCESSING, CONTROL, AND DISPLAY

All DR/CT scanners process the same data in roughly the same steps. For DR imaging, the results are one or more radiographic images of your part. In CT, several hundred to thousands of DR images are reconstructed into a 3D volume image. If acquired, processed, and reconstructed correctly, a CT reconstructed image volume is a dimensionally correct, quantitatively accurate image of the internals of objects and assemblies. The volume is suitable for measuring internal dimensions, material identification, defect recognition, and/or geometry acquisition of the entire object or assembly. In some respects, the volume of data is 4D; there is a voxel at each 3D position, and this voxel is a measurement of the product of density and atomic number.

The computer resources for acquiring these data are significant but easy to acquire. For CT, there are a lot of data at every step of the process, and you can end up with a lot of intermediary data. So there are many ways to mess it up. Computer capabilities have improved to the point where most, if not all, reasonable desktop computers include the speed and resources for DR/CT acquisition. Also, the additional good news is that the hardware in most computers is getting better, less expensive, and more available for every DR/CT task even including complex image processing and reconstruction.

DR/CT systems involve at least four components: (1) a source of penetrating radiation; (2) a motion control capability for moving the object (and/or the source and the detector); (3) a computer for scan control and data acquisition; and (4) computer capability for processing, reconstruction, and

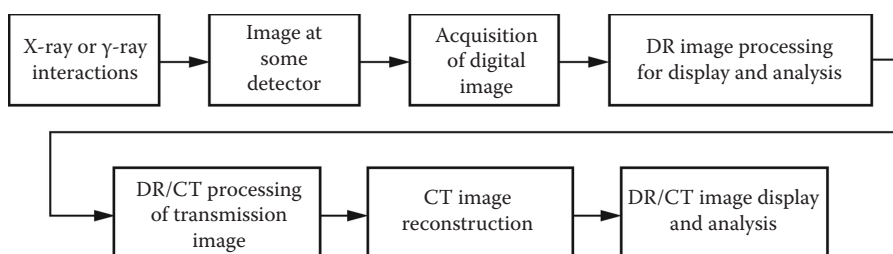


FIGURE 10.16 Flow diagram of the different steps involved in the DR/CT image acquisition, processing, and reconstructing. The latter is only for CT data. DR/CT display and analysis.

display. Sometimes only one computer may be used for data acquisition, processing, and reconstruction. A flow diagram of the different steps involved in the DR/CT process is given in [Figure 10.16](#).

Processing CT data in preparation for CT reconstruction can be a compute-intensive task and is always a disk-intensive task. The acquired data for CT reconstruction are large. Processing CT data includes applying a background correction, outlier removal, beam hardening correction, and ring removal. Each requires that all of the acquired data be read before being processed. In some cases, this requires a couple of passes through the acquired data. For some deconvolution schemes, the preprocessing can rival CT reconstruction in the amount of processing. If the decision is made to keep all intermediate data, the disk space requirements can become very large. This implies that every operation applied to the data generates another copy of the data, and the result is multiple copies of the data (sometimes three copies). Lots of disk space, preferably fast disk space, is recommended.

10.7.1 HOW BIG ARE THE DATA SETS?

Recent interest in high-spatial-resolution inspections, combined with the introduction of new flat panel-type (e.g., amorphous silicon, amorphous selenium, and CMOS) detectors, has led to increases in detector sizes. The impact of this change for the amount of data flowing through the process represented in Figure 10.16 is profound. Consider a 2000×2000 pixel area-array detector system, for a rotation-only scan, digitized at 16 bits (8 Mb per view). Each of these 2000×2000 images when combined with the Φ_0 image results in a corrected radiograph, sometimes referred to as an attenuation radiograph of around 16 Mb per radiograph or view or angle acquired (if the images are in floating point). The reconstructed volume results in a 32 Gb cube of data (again if we reconstruct into floating point numbers). Depending on whether the intermediary files are kept around or not, about 100 Gb of disk space and about 64 Gb of memory are nice to have. The latter assumes that the entire cube of data need to be held in memory and the operating system needs some room to work, and you may want to keep copies of the volume or versions of the input data around for reference. While as little as 2 years ago, 2013, this resource may have been difficult to configure. These requirements are straightforward to obtain on different types of computers.

The interest in still higher-spatial-resolution scanning, such as developments in CT range-extension scanning or larger field of view scanning, is driving these numbers even higher. Camera-based and small-pixel amorphous-silicon detectors can be 3072×2048 or 4096×4096 . So consider a 4096×4096 detector, another factor of 4 per radiograph, and another factor of 8 per reconstructed volume. What happens if we start manipulating $6k \times 6k \times 6k$ or $8k \times 8k \times 8k$ volumes?

10.7.2 ON SCREEN AND INTERACTIVE TOOLS OF VALUE FOR CT

Acquiring radiographic data intended for CT reconstructed volumes results in a different focus for interactive analysis of raw and processed images. The quantitative values of the pixels in the image are of key importance. Throughout the process depicted in Figure 10.16, the results of the next step are critically dependent on the particular values of the pixels in the images in the preceding step. Consequently, we distinctly prefer interactive toolsets and toolbars that enable the quantitative evaluation of image data, or the easy viewing of the pixel values in the acquired image in a particular pixel, group of pixels, or along a line or for an area, etc. drawn by the analyst. Further, it is important that the values of the pixels be accessed in their full dynamic range and in the units appropriate to that particular step in the process, since you are very interested in the low and high ends of the digitization spectrum for all kinds of reasons.

Interactive image enhancement techniques are usually provided in toolbars, which can be accessed on the desktop display of the control information for the software package. There are three types of toolbars, which are important in this discussion: (1) point-processing toolbars; (2) color manipulation toolbars; and (3) image modification, drawing, or text annotating toolsets.

Point-processing toolsets at a minimum should include pixel value query, line-out extraction, region-of-interest extraction, and image. With these tools, the values of the images can be directly examined. The pixel query tool allows you to click on a position in the image and see the values or a neighborhood of values. The line-out extraction tool enables you to draw line across a position in the image, extract the values along that line, and view the extracted signal as a vector plot. These two tools provide a direct viewing of the values in the image and enable you to directly view the change in attenuation along the line of interest. Image zoom tools display resampled or pixel replicated versions of an image or region of the image. In images with a lot of details, these kinds of tools can verify the nature of the attenuation change in the image. Related to these tools is some statistics capability, which can calculate the means and standard deviations of small or selected areas. It is advantageous if the software allows for archiving some extracted part of an image for later comparison. Lastly, a loop tool (a means of quickly setting the display minimum and display maximum to the minimum and maximum of a selected region of interest) is important for quickly adjusting the smaller number of colors or gray scale of 8 bits on the monitor to the sometimes large pixel depth of the detector, which can be in excess of 16 bits.

10.7.3 COMPUTERS FOR CT DATA ACQUISITION

Acquisition of CT data requires enough processing power to handle multiple tasks and multiple interfaces. Acquisition computers focus on five main functions: (1) reading the detector; (2) commanding the motion control to move to the correct position; (3) ensuring that the sequence of moves and acquisition events are performed correctly; (4) possibly controlling the x-ray source; and (5) communicating with the operator. Of these different functions, the last, communicating with the operator, admits the most variability usually in direct relation to the type of the DR/CT system. The first three functions emphasize the I/O capabilities of the control computer. By I/O, that means fast disk transfer speeds, preferably large amounts of disk space, fast memory, and fast bus speeds. CPU speeds, the need for dual or more processing capability, are not as important for computers dedicated to scan control and data acquisition. The fourth function, controlling the x-ray source, requires very few resources; an RS-232 interface is sufficient since very little information is exchanged for command and control. This interface requires that the source can be turned on; set to the correct kV, mA, and spot size; turned off; monitored for operational messages; and possibly turned back on in a coordinated way should the source unexpectedly turn itself off.

The exception to this rule are the large-area-array, cone-beam, general-purpose systems. Verifying alignment and, in the case of camera-based scanners, ensuring best focus are additional tasks for the acquisition and control computer. For cone-beam scanners, two alignment tasks are fundamental: (1) aligning the area detector to the beam divergence and (2) aligning the rotational stage to the beam-detector envelope. While there are many ways to evaluate the state of this alignment, most, if not all, of the strategies involve multiple acquisitions of the large format detectors for certain test objects, calculations applied to the images acquired, and interactive or automated image analysis. Consequently, good display capabilities become important, as do large video memory and interactive image analysis software. Recently, we designed, developed, and built a phantom that is scanned and has greatly reduced the alignment process.

Panel detectors require gain calibration schemes requiring two or three calibration images be acquired to enable the calculation of a gain-corrected image. The corrected image accounts for the many small but significant variations in detector response across the x-ray detector, results in an image proportional to the x-ray irradiance, and is independent of detector idiosyncrasies. Determining the state of system alignment requires the cleanest possible images for evaluation. Faster CPU-memory speeds become important for area-array detector systems. Regardless of how long the exposure time is for the detector or how long it takes to digitize the image, any wait for the calibration step to complete is too long. Easy-to-obtain desktop computers are reasonable choices for the acquisition and control computer. If detector sizes get large, a high-end desktop computer

TABLE 10.4
Comparison of Computer-Based Operations by Scanner Type

Step	DR/CT System Configuration		
	Single	Linear	Area
Restoring ray-sum geometry			X
Corrections for detector blur			X
Corrections for dark current		X	X
Detector linearity corrections		X	X
Individual detector response corrections		X	X
Normalizing Φ_0	X	X	X
Calculating ray sums	X	X	X

with large disk space (500 Gb or greater), 1 Gb of memory, ample video memory (256 MB or greater), and a large display monitor is a good choice.

10.7.4 COMPUTER REQUIREMENTS FOR DR/CT PROCESSING

The functions involved in DR/CT processing vary with the type of system used. Area-array detector systems constitute the maximal case with regard to functions required, since they require the most processing for each pixel on each image acquired. A list of different operations applied to DR/CT data sorted by the type of system is given in Table 10.4. The details of the operations identified in the table will be described in Chapters 12 and 13. Suffice it to say here that these operations taken together require a couple of passes through the radiographic data. For area detectors, this constitutes a substantial amount of I/O, calculation, and processing. Perhaps more importantly, some of these calculations need to be adjusted if the source or detector changes (more about this in Chapter 13).

Computing resources for accomplishing these tasks can assume a few different forms. First, everyday multicore desktop computers will accomplish this task in a reasonable time. The speed of the disk access and limitations for disk space are usually the drawbacks to greater speed and easier processing. Computer clusters, connected by a high-speed network, can perform this task in a much shorter time, proportional to the number of processors gathered together to perform this work (Brancaccio et al. 2011). In this circumstance, the different corrections applied to the raw and processed data are parceled out to the different computers. For instance, consider the case of 360 views for an area detector scanner and six processors/computers. In this case, each processor would apply corrections to 60 radiographs. At the same time, currently configured multicore computers can serve as a cluster-in-one-box provided that the software can be parallelized or has a multithreaded capability.

One configuration of a multicomputer reconstruction resource is regular workstations or rack-mount computers, connected to a RAID array, which contains the data. RAID arrays are getting more affordable, even for the dual-controller higher-reliability models. Dual controllers basically ensure that if one controller malfunctions, the second one can operate the unit. In some cases, a head node computer is employed, and the other computers access the RAID array through that computer. With large data sets, the network speed connecting the computers to the central disk resource can quickly become a bottleneck, which is a recommendation for the fastest network interconnections that one can afford (Brancaccio et al. 2011).

10.7.5 COMPUTERS FOR CT RECONSTRUCTION

Choices for computers dedicated to this task are divided into three categories: (1) general-purpose desktop computers; (2) computers with specialized processors or specialized software that accesses

microcode instruction sets or firmware for a particular chipset; and (3) computer clusters of the variety mentioned in [Section 10.7.4](#). The first choice, general-purpose desktop computers, provide a lot of versatility at low cost, but large cone-beam CT reconstructions can easily require days to be completed on single processor computers. The second alternative, specialized processors, can provide significant increases in reconstruction speed. The number and type of these processors have increased steadily from the introduction of CELL and graphics processing chips (GPUs) to the now widespread use of GPUs for CT reconstruction. Cell processor (also called CELL) is a microprocessor chip with a multicore, parallel processing architecture and floating-point design.

In recent years, GPUs have become much more available and can be obtained at a reasonable cost (a Tesla personal supercomputer, which includes 448 cores, can be purchased for \$10,000). Many GPU implementations have demonstrated speed increases of $110\times$ (Zhao et al. 2009). Perhaps more important, software support and accessibility has become less of an issue. Both scientific software packages (MATLAB®) and C/C++ compilers include extensions and packages for GPUs. Converting the code from CPU to GPU computing is getting less arduous with time. Of course, CPU technology has not stood still; recently introduced CPUs can include many more cores than previous versions. Further, software packages for multithreading and parallel computing such as Open MP and message passing interface (MPI) are commonplace.

It is still true that a poorly implemented GPU computation can be no faster than a CPU-based calculation. For large data sets, the problem will of necessity be split up into smaller pieces and then fed to the specialized processor in pieces, respecting the memory capacities of the specialized processor. CT processing and reconstruction is still a substantial task for both calculations and I/O, and care must be observed for where the data are, i.e., on the GPU or CPU or disk. Regardless of the details, CT reconstruction is now much more tractable on any modern platform computer.

The last alternative, computer clusters, can reconstruct arbitrarily large volumes with speeds about linearly proportional to the number of processors. One strategy for CT reconstruction on a computer cluster is to pass all the radiographs through the cluster where each cluster node reconstructs a contiguous portion of the total reconstructed cube. This strategy has the disadvantage of requiring each processor/computer read every acquired radiograph. For a $2k \times 2k$ radiograph, with 720 views, some 11.5 Gb of data is circulated throughout the network. As mentioned in [Section 10.7.4](#), this puts more emphasis on the system network speed, but adding capacity is straightforward as shown by Brancaccio (2011), in which large CT reconstruction can be processed quickly. Also, as indicated above, computer clusters can be used for other tasks, and individual computers can be used to process and analyze data independently of the other members of the computer cluster. This means that a loosely configured cluster can serve as individual computers for everyday analysis and report writing when it is not used for computationally intensive tasks.

One alternative feature that has proven to be important is configuring reconstruction resources for reconstruction on the fly. In this type of configuration, the acquired data are reconstructed as it is acquired. Consequently, it can be the case that the 3D reconstructed volume is ready for viewing and analysis once the scan is complete. High-volume inspections and automated analysis inspections can certainly benefit from this type of arrangement. Unfortunately, one result of this type of system is the rapid accumulation of data. ISO-9001 requirements of saving data for 2 weeks or 1 month can require substantial disk resources (10 Tb or greater).

At this point in time, a variety of different configurations of computer resources for CT volume reconstruction are possible. Each choice has different costs, advantages, disadvantages, and consequences. While increases in detector size seem to be running just ahead of the abilities of a single computer, the improvement in computers is relentless. From experience, a particularly hard choice involves what to do with the data, how much of them to keep around, and for how long. This is particularly strategic with the introduction of ISO-9001 concerns in production settings and the requirements for retaining quality records for long periods of time. Other issues are just how to analyze all of this information and what methods can be used to sort important aspects for an inspection from the large quantities of data in the CT volume, most of which may not be of interest. The usual

refrain applies here: the more you know about your inspection, your object, and the goals of the inspection, the better you will do at navigating these choices.

10.7.6 DISPLAYING CT DATA

A variety of 3D rendering software packages exist for displaying CT volumetric data. These packages enable complete control of transfer functions for determining the opacity of different materials and components in the 3D volume. Further, most 3D data viewing and analysis packages include a variety of browsing tools for displaying slices from different orientations in the CT volume. Packages differ on the type of operations provided for obtaining dimensional measurements. This is partly due to the large number of different types of measurements possible from 3D volume measurements of contours, measurements from a particular 3D surface, etc. Further, a number of extensions to these software packages exist for specialized segmentation, stereolithography (STL) file generation, and generation of input data to finite-element method (FEM) and finite-element analysis (FEA) packages. STL is a file format native to the stereolithography CAD software created by 3D systems. FEM is a numerical technique for finding approximate solutions to boundary value problems for partial differential equations. It is best understood from its practical application, known as FEA. FEA is a computational tool for performing engineering analysis. It includes the use of mesh generation techniques for dividing a complex problem into small elements, as well as the use of software program coded with FEM algorithm.

At some level, detailed, quantitative, exhaustive analysis of 3D CT data may be the most challenging task for computers. As we've described in [Section 10.7.1](#), large data-set sizes make all of this work more difficult. Most 3D analysis software packages require the entire volume of CT data be read into computer memory. At this point, $2k \times 2k \times 2k$ volumes are tractable; $4k \times 4k \times 4k$ volumes are a tougher task; and $8k \times 8k \times 8k$ volumes are still quite difficult. The strategy for very large volumes is to resample the data down in volume or in intensity (rescale to 1-byte pixels perhaps). If there is a focus to the inspection, some area, or region of special interest, and you can just extract that chunk from the volume, the data-set size problems are reduced.

The toughest job for display analysis tools is the general perusal of a volume, searching for some yet to be discovered anomaly, some problem with a dimension, or anomalous gap in the assembly. This brings up somewhat separate uses of CT scanning, exploratory and focused or confirmatory. While we will discuss this again in Chapter 13, exploratory CT scanning is the toughest job to do well. As mentioned throughout this section, CT volumes are large and can be unwieldy, and if you are just looking for something untoward, you can just miss it. Just as in viewing radiographs, it is important to build some model of what the good part should look like, and for CT, a physical model or one you can visualize in your mind that can be rotated and viewed from any direction to compare to the data you are viewing. This task gets more difficult as the object geometry and constituents are more varied and the interfaces more complicated.

Specialized processing hardware is available for 3D rendering in many video cards. These are the same GPU engines that you can use for CT reconstruction. For volumes that fit into the local memory of these processors, 3D rendering can keep pace with the refresh rate of the screen. Changes in opacity for rendering different materials are implemented instantaneously. Furthermore, fast slice-by-slice viewing and even animation can be performed with this hardware to assist in the analysis of 3D volumes. Most of these processors can be added to desktop computers, can contain a lot of local memory, and generate high-quality graphics for high-end displays. In this same connection, entire workstations are available with embedded 3D rendering engines and custom software.

In summary, robustly configured multicore computers and/or computers with multiprocessors can perform all of the tasks for CT acquisition, processing, reconstruction, and display. If the data sets get large, and they can be large, the reconstruction will take time. In production settings, this may be an issue. For R&D settings or CT systems that acquire data for parts with a lot of different sizes and compositions, the time constraints may not be as severe. One comparison worth keeping

in mind is that, if you can process the data in the time it takes to acquire, you have met an important processing goal. One consideration for planning the minimum configuration is usually having two computers. Another computer is used for image data acquisition and one for processing, reconstruction, and display. It is useful for both computers to include two monitors and to be on the same network. The advantage of this arrangement is that you can be processing one data set while acquiring the next data set. Lastly, for analysis, it is good to think about how you are going to use the scanner and then how much re-reconstruction you are going to support. CT reconstructions include a lot of variables and knobs, and changing the values changes the reconstructed data. Providing access to another reconstruction/analysis workstation or purchasing an additional workstation is usually a good idea.

PROBLEMS

- 10.1 Consider a high-energy flat (non-curved) LDA with 1024 elements, 2 cm thickness, and a 1.2-mm pixel pitch. How would you configure the collimation and septa to maximize the primary-to-scatter ratio? At what source-to-detector distance would you put the detector? What are the sizes of the collimators? How thick are they? Will you use septa or a bucky grid? What C_w/C_l did you achieve?
- 10.2 Consider the same detector but configured in a circular orientation. What is the source-to-detector distance? Where would you put the collimators? What are the sizes of the collimators? How thick are they? Did you use septa? What C_w/C_l did you achieve?
- 10.3 How much total data can be generated from a 1024×1024 detector, digitized at 16 bits, using 720 views? How big is the reconstructed volume? How does this change for a 3072×3072 size detector?
- 10.4 For a 4096×4096 detector acquiring 2000 views, how many computers/processors would you configure for processing? For reconstruction?
- 10.5 X-ray hits on the detector are usually taken care of with outlier-removal techniques. Should you perform outlier removal on the radiographs or on the sinograms? Justify your answer.

11 Imaging-System Configurations

11.1 INTRODUCTION

Considerable differences exist between the physical architectures of fielded digital radiographic (DR) and computed tomographic (CT) systems. In this chapter, we present these differences and will make use of the material in the previous chapters to indicate how the differences in architecture impact performance. The focus here is not on the detectors used (see Chapter 9) or their practical use (see Chapter 12) but on the impact of the physical setup used for scanning (data acquisition). Also, we discuss how these differences in architecture are connected to particular applications. A number of typologies have arisen in the CT literature for classifying CT systems. We mention these categorizations here, but our focus is on how the configuration of the imaging components lends itself to certain applications. In particular, we seek to relate differences in fielded systems, types of sources, detectors, and collimation to the equations developed in previous sections. Hopefully, this will shed light on why there are many different types of sources, detectors, collimation, and source-detector configurations, and provide a background for the techniques and applications to be described in Chapters 15 and 16.

At the end of this chapter, you will be able to

- Identify the different configurations of DR/CT systems
- Compare the advantages/disadvantages due to physical structure
- Identify the limiting factors or components for each type of system
- Mathematically represent the measurements obtained by each system

In Chapter 10, we unpacked the content of the irradiance subtended by a pixel from a free-flight ray path through the object into different types of signals, highlighting how the different signal proportions are impacted by different types of collimation. We repeat the schema here since we will refer to the quantities throughout this chapter. Independent of the detector, the source interaction with the object generates an image in 3-D space. A detector element at a certain position and with a certain size will sample a specific part of this irradiance.

For any detector position, \mathbf{d}_a^* (some 3-D position on the other side of the object \mathbf{O} from the x-ray beam and includes an area), on a line \mathbf{l} from the x-ray source $\mathbf{S}(E)$, the detected x-ray photons intersecting this solid angle are divided into three different types of irradiance:

$$\Phi[\mathbf{S}(E), \mathbf{O}, \mathbf{d}_a, \mathbf{l}] = \Phi_p[\mathbf{S}(E), \mathbf{O}, \mathbf{d}_a, \mathbf{l}] + \Phi_s[\mathbf{S}(E), \mathbf{O}, \mathbf{d}_a, \mathbf{l}] + \Phi_{\text{Rf}}[\mathbf{S}(E), \mathbf{O}, \mathbf{d}_a, \mathbf{l}] \quad (11.1)$$

$$\Phi_s[\mathbf{S}(E), \mathbf{O}, \mathbf{d}_a, \mathbf{l}] = \Phi_{\text{Sbk}}[\mathbf{S}(E), \mathbf{d}_a] + \Phi_{\text{Sobj}}[\mathbf{S}(E), \mathbf{O}, \mathbf{d}_a, \mathbf{l}] \quad (11.2)$$

$$\Phi_0[\mathbf{S}(E), \mathbf{d}_a, \mathbf{l}] = \Phi_0^p[\mathbf{S}(E), \mathbf{d}_a, \mathbf{l}] + \Phi_{\text{Sbk}}[\mathbf{S}(E), \mathbf{d}_a]. \quad (11.3)$$

The schema represented by these equations decomposes the photon output from an x-ray source, $\mathbf{S}(E)$, for the solid angle subtended by detector area \mathbf{d}_a , into primary irradiance, Φ_p , scattered (both coherent and incoherent, Compton) and pair-production irradiance, Φ_s , and refracted photons, Φ_{Rf} .

* In this description, we have collapsed a lot of information into the symbol represented by \mathbf{d}_a , which is meant to signify both a 3-D position, x, y, z , and an area with width and height. It was decided to represent this 5-tuple as just \mathbf{d}_a for brevity, since the notation is substantial already. Also, when we get to CT image reconstruction algorithms and analysis, the position of the detector and the area of the detector get parcelled out to different sets of equations connected to already established algorithms. Consequently, we ask the readers' indulgence and request that the focus be on the concept at this point and not all of the notational details.

The irradiance is from a polychromatic source, $S(E)$ (which reduces to E for a monochromatic source), undergoing x-ray interactions with object function O , along path ℓ (a line from source to detector). Furthermore, there are two types of scattered photons: background scattered, Φ_{Sbk} , and object scattered, Φ_{Sobj} . For a variety of reasons, Φ_0 , a measurement of the radiation field without the object, is fundamental to many x-ray measurements and is included here. Typically this measurement contains some background scattered irradiance from the supporting fixtures in the x-ray system or in the detection hardware, in addition to the primary irradiance launched by the x-ray source.

As mentioned in Chapter 10, fundamental to all x-ray transmission systems is the primary irradiance, Φ_p , the most interpretable and the most quantitative data. We will describe x-ray systems in terms of how the schema in Equations 11.1 through 11.3 changes according to the physical structure of the system components. Some applications will be mentioned in passing, but the focus will be upon the way in which the configuration of the system impacts performance. If not registered already, it is our position that each of the system choices necessarily involves certain trade-offs between spatial resolution, contrast, energy resolution, and system speed. As we cover the different systems, we will continue to focus on trade-offs between different configurations.

11.2 1-D X-RAY GAUGING SYSTEMS

This scanning modality employs extensive hardware to physically realize a detected signal consisting of primary-only irradiance. The system usually combines a monochromatic energy source (some gauging systems include a polychromatic source), with an energy-discriminating detector and collimation at both the source and the detector. Figure 11.1 contains a sketch of the elements of a gauging system, which is the architecture behind the CT system called Pencil-Beam Computed Axial Tomography (PBCAT) (Martz et al. 1991a), shown in Chapter 9, Figure 9.4. This system combines an isotopic source of γ -rays, an intrinsic-germanium detector, and source-side and detector-side collimation to carve out a pencil beam of penetrating radiation. The spectra from the germanium detector are analyzed to obtain a number of counts in a peak of the energy spectrum due to the absorption of the x-rays by the sample in that pencil beam at that energy. The same measurement is acquired for the beam without the sample, a measurement of $\Phi_0[E, d_a, \ell]$, and the attenuation can be calculated according to Equation 5.13, reproduced here for convenience

$$\ln\left(\frac{\Phi_0^E(E)}{\Phi^E(E, Z, \rho, \ell)}\right) = \mu(E, Z, \rho)\ell. \quad (11.4)$$

Notice how the schema for the distribution of photons is simplified for the single-energy gauging system. First, all of the references to a spectrum $S(E)$, reduce to a single energy E . Also, due to

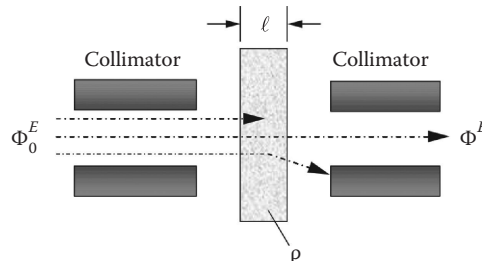


FIGURE 11.1 Arrangement for x-ray or γ -ray attenuation. The source is on the left, the object is in the middle and the detector is on the right. The top, center, and bottom photons undergo photoelectric absorption, transmission, and scatter, respectively. (Adapted from Bertin, E. P., *Principles and Practice of X-Ray Spectroscopic Analysis*, second edition, Plenum Press, New York, 1978. With permission.)

both the collimation and the detection mechanism, $\Phi_s[E, \mathbf{O}, d_a, I]$ is all but eliminated. The beam from the source and the beam emanating from the object are directionally collimated to a specific location, along a specific line. Secondly, the signal from the germanium detector is a pulse-height spectrum, as shown in Figure 11.2, and from an analysis of the spectra, only that irradiance at the source energy peak or close to the source energy peak is counted. Consequently, scattered photons that emerge from the object at a different angle are absorbed in the collimator or not counted by the detector. Note that direct scattered photons at or close to the source energy peak are counted. Scattered irradiance from the source collimator is stopped in the second collimator. If any background scattered irradiance makes its way into the center of the detector aperture area, it is more probable that the irradiance is at a reduced energy and will not occupy the peak. The measurement of $\Phi_0[S(E), d_a, I]$ is also similarly simplified. In this measurement, there is no absorber and therefore no object scatter. As in the case with the object present, the amount of possible background scatter from the sides of the collimator is eliminated by analysis of the spectra (only *counting* or *digitizing* the irradiance at the source energy). Consequently, for a highly collimated system like PBCAT, Equation 11.2 is eliminated, and Equations 11.1 through 11.3 reduce to

$$\Phi[\mathbf{E}, \mathbf{O}, d_a, I] = \Phi_p[\mathbf{E}, \mathbf{O}, d_a, I] \quad (11.5)$$

$$\Phi_0[\mathbf{E}, d_a, I] = \Phi_{p0}[\mathbf{E}, d_a, I]. \quad (11.6)$$

The results from a 1-D gauging system, that is, acquiring the measurements in Equations 11.5 and 11.6, is a single measurement of attenuation multiplied by the thickness, $\mu(E, Z, \rho)\ell$ or $\mu(E, Z, \rho)\ell$, loosely referred to as $\mu\ell$ (“mew-el”). The estimate of this quantity can be obtained by using Equation 11.4 on the quantities in Equations 11.5 and 11.6. If the material and density are known, this is a measure of the thickness of the absorber at this position. Alternatively, if the thickness is known, this is a measurement of the attenuation. In this way, gauging systems can be used for in-line monitoring of thickness for a single material, or they can be used to detect material impurities due to changes in material or density or both. However, for a single energy, notice the fundamental indeterminacy of the system. The measurement depends on both length and attenuation; without additional data, you do not know if variation in the attenuation measurement is the result of changes in thickness or changes in attenuation.

Gauging systems that acquire measurements of Φ and Φ_0 for two energies provide more information on what is accounting for observed variations in attenuation multiplied by path length, $\mu\ell$,

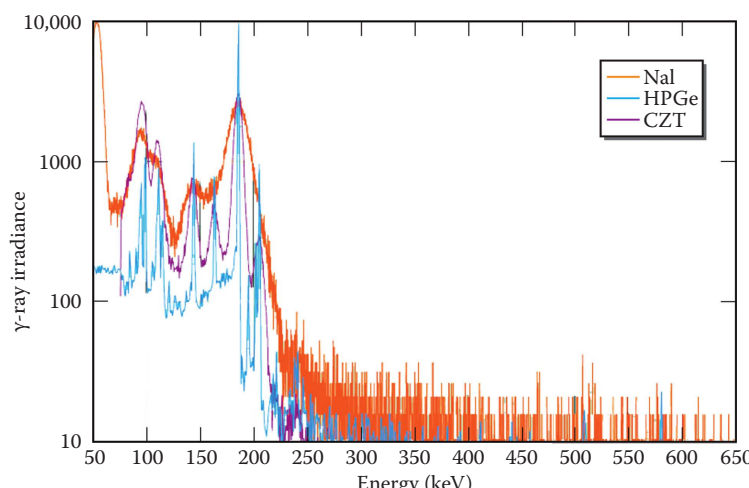


FIGURE 11.2 Plot of γ -ray irradiance as measured by three different energy-discriminating detectors.

from position to position in the object. For some pairs of energies and some materials, the changes in material attenuation, μ , can be separated from changes in length, l . Consider the variables and structure of two 1-D gauging measurements at different energies:

$$\ln(\Phi_0^P)[E_1, \mathbf{d}, l]/\Phi_P[E_1, \mathbf{O}, \mathbf{d}_a, l]) = \mu(E_1, Z, \rho)l \quad (11.7)$$

$$\ln(\Phi_0^P)[E_2, \mathbf{d}, l]/\Phi_P[E_2, \mathbf{O}, \mathbf{d}_a, l]) = \mu(E_2, Z, \rho)l \quad (11.8)$$

$$R(E_1, E_2) = \mu(E_1, Z, \rho)/\mu(E_2, Z, \rho). \quad (11.9)$$

From these two measurements, we can calculate the ratio of attenuations, $R(E_1, E_2)$, and the thickness divides out of the result. Further decomposing the total attenuation in Equations 11.7 and 11.8 into their photoelectric and Compton components enables a further analysis of the characteristics of the material constituents of the object (Macovski 1983; Ying et al. 2006; Azevedo et al. 2016). If you know that the material is not changing, the thickness can then be recovered from any single equation. In this same way, if the system can acquire data for three energies, estimates of mass absorption coefficient or effective Z can be further separated from density (Schneberk et al. 1991). The limits implicit in this multiple-energy approach involve the necessary requirement that good statistical transmission data are obtained at each energy level and that the energy is not so high that there is perfect transmission, i.e., no attenuation and thus no information, which effectively places a bound on the energy range available for dual- or multiple-energy configurations. For more on this, see discussion of multienergy techniques in Section 15.3.

The inherently quantitative character of the 1-D gauging measurements results in well-defined distributional properties of the measured data. Variation in the gauging measurements depends directly on the amount of irradiance contained per measurement or the counting statistics of the measurement. X-ray or γ -ray attenuation conforms to Beer's law, or exponential attenuation. The other side of this mechanism is that the measured counts are Poisson random variables (Barrett and Swindell 1981; Ross 2009) with mean N , variance $1/N$, and standard deviation $\sqrt{1/N}$, where N is the number of digitized counts. Consequently, for constant source strength, the precision of a 1-D gauging measurement is improved with greater measurement time. Also, if you can increase the output of the source, you can acquire the same or better data in the same or less time.

Given this characterization of noise in 1-D gauging, the signal-to-noise ratio can be composed and used to calculate an optimum energy. This argument, detailed by Grodzins (1983), reaches the somewhat surprising result that the optimum energy for gauging a sample thickness is when attenuation multiplied by thickness, μl , equals 2, or when transmission equals 13%. Various CT designers have argued that this transmission value is optimum for polychromatic sources as well. Other analysts have argued for a value of 1 for inspections focused on measuring object geometry, while others consider values closer to 3 to be a good choice for inspections focused on obtaining the maximum contrast in the object. The point here is that the quantitative nature of gauging data provides an analytic foundation for all DR and CT systems.

The cost of the quantitative character of the data for the single-energy, single-detector configuration is a dramatic reduction in system speed. A gauging system produces a single measurement of attenuation multiplied by thickness at a particular object position. To match the output of a radiograph with dimensions of 512×512 would require 262,144 gauging measurements. Also, from a source-efficiency standpoint, the gauging system uses very little of the available source output since the dual collimation severely restricts the solid angle and the analysis of spectra further reduces source output to the energy range used or counted in the measurement. The trade-off exemplified by the 1-D gauging configuration is that as you improve energy resolution and contrastive performance by eliminating sources of scatter, you will sacrifice system speed.

The exception here is the use of synchrotron radiation, which provides very high levels of source irradiance at a selectable single energy. When applicable, inspection data acquired at synchrotron facilities can be quantitative and acquired in short order. Also, current synchrotron facilities provide in-house gauging, radiography, and CT hardware (see Chapter 16). However, for large-scale industrial inspections of lots of objects, transporting samples to synchrotron facilities can be problematic. In addition, the maximum energy available is a few tens of kilovolts (or 100 kV max), limiting object size and attenuation.

One-dimensional gauging systems can be configured with polychromatic sources and current-integrating detectors. In this case, the $S(E)$ is inserted back into Equations 11.4 through 11.6. In this case, attenuation is the integration over a number of different energies, and the ability to eliminate all scatter is more difficult. Irradiance at lower energies at the detector can result from scattered irradiance at higher input energies or from the source, and from the detector measurement, it is difficult to know the exact nature of the digitized spectra. Calibration of different thickness samples can be used to develop automated measurements of material thickness, but all of the other algebra for using multiple energies to unravel attenuation and density have to be adjusted for the spectrum from the x-ray source. Tuning a detector to energies corresponding to the spectrum at the position of characteristic lines from different source targets, called Ross filtering, provides interesting opportunities for near-single-energy acquisition and analysis (Kirkpatrick 1939; Khutoretsky 1995). Also, as indicated in Chapter 10, strategic use of septa and/or antiscatter collimation can significantly reduce the probability of scattered irradiance intersecting the detector element. However, all of these applications include the single-point geometry, and system speed is compromised. For a gauging application, see Section 16.2.

11.3 RADIOGRAPHY SYSTEMS

At this point, we review radiography systems for this same physical typology of scanners: single, linear, and area detectors. In many CT references, radiography is only presented as a stepping-stone to CT inspection. We take exception to this as it is still true that more radiographic inspections are performed than CT. Also, it is important to emphasize that the properties of the CT volume inherit the signal-to-noise ratio of the transmission measurements (radiographs) acquired. In addition, each component radiograph in a CT data acquisition is useful for an inspection and can contribute to further radiographic work if the goals of the inspection change. For all these reasons, we have chosen to cover radiographic systems separately in this section.

11.3.1 RADIOGRAPHY WITH A LINEAR-DETECTOR ARRAY

A gauging system produces a single measurement, collimated in both width and height and corresponding to a single pixel in a radiograph. As mentioned in the previous discussion on gauging, if acquisition time is not important, an entire radiograph could be built up of single gauging measurements, generating a no-scatter, highly quantitative image of the internals of an object. However, calculations show that the time required can be very long. The next most quantitative alternative is to employ multiple detectors and, in varying magnitudes, relax the collimation in a single dimension. This can be accomplished in different degrees. First, multiple detectors can be configured in a line, referred to as a linear array. In the same time it takes to acquire a single gauging data point, measurements from all the detector elements of a linear detector array (LDA) can be acquired. Some additional collimation can be provided, first in the collimation of the source down to a slit, in the array from the introduction of septa. Septa are small strips of collimator material placed in between adjacent detectors to reduce detector-to-detector cross talk from scattered irradiance. The amount of x-ray source used in any one acquisition has increased from a single (small-area) point-like measurement by a multiple that is equal to the number of detectors in the linear array. An illustration of an LDA detector DR/CT system is given in [Figure 11.3](#).

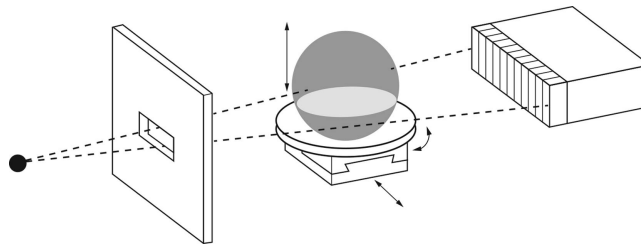


FIGURE 11.3 Illustration of a digital radiographic and computed tomography system employing slit collimation and a linear detector array (LDA).

From each acquisition of the linear array, transmission data from an entire planar projection through the object can be obtained. The speed-up for the data acquisition is a direct multiple of the single gauging measurement, i.e., 512 detectors are about 512 times faster if their efficiencies are the same. If the multiple detectors are energy discriminating, the same quantitative data obtained in the 1-D gauging system can be obtained for the LDA. Radiographs can be built up by translating the source and detector over the source solid angle subtended by the object or by translating the object through the fan beam of radiation detected by the LDA. In Figure 11.3, notice that the collimation on the source is similar to the collimation employed in the gauging system (see Figure 10.5), but the source collimator opening is fabricated to match the solid angle subtended by the line of detectors. The object is only irradiated in the slit or horizontal strip intersecting the detector sensitive area, in this case a line with some height. Detected scatter is reduced in two ways; only a certain slit section of the object is irradiated so the total number of scatter sources (out of the plane or fan beam) is reduced, and the collimation at the detector not shown in Figure 11.3 also restricts the solid angle for the detection of scattered irradiance (see Figure 11.4).

For the LDA with energy discriminating detectors, the interpretation of the measured signal is the same as in the 1-D gauging example. An example of this type of detector is an LDA built up of cadmium zinc telluride (CZT) elements, where each detector records the energy of the photon detected

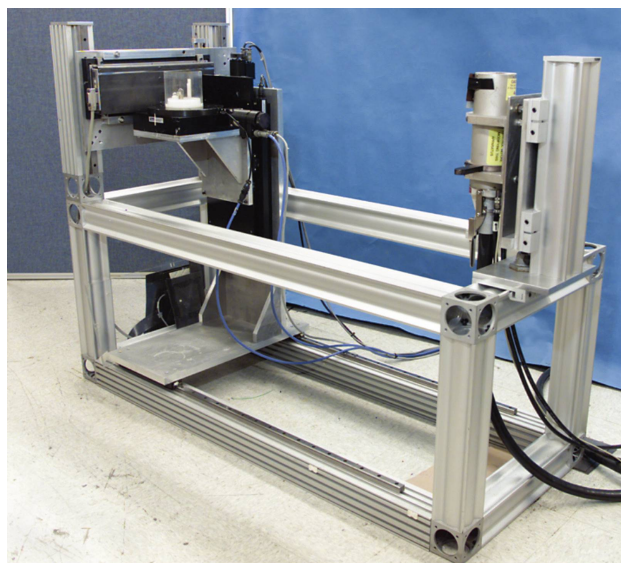


FIGURE 11.4 Picture of an Lawrence Livermore National Laboratory (LLNL) fan-beam collimated x-ray source (right), linear-array detector (left) DR/CT configuration system called linear computed axial tomography (LCAT).

(see Chapter 9). For some choice of energy bins, the detected signal integrated over some period of time records a spectral distribution of the source with or without the object. Each of the bins can be treated as a single energy, within limits, and the array of energy bins can be treated as a multiple-energy data acquisition system. All of the algebra available from the use of multiple energies applies, as well as the quantitative nature of the interpretation of the data, direct application of the optimum energy criteria, etc.

A common configuration for LDA-based radiographic systems is to employ a polychromatic x-ray tube source with a current-integrating (no energy resolution) detector (for more on different detectors, see Chapter 9). As discussed in Chapter 8 on x-ray sources, machine sources can be operated over a range of x-ray tube potentials and incorporate x-ray source or beam filtering to better select the energy range of interest. Matching the source with a detector that can stop most if not all of the irradiance results in a system with substantial acquisition speed and short integration and read times, in spite of the fact that only a limited portion of the object is being examined in any one acquisition. The acquisition times can be so short as to provide the opportunity for acquisition while the object is continuously moving (or equivalently, the source and detector are moving). Figure 11.4 includes a picture of the Lawrence Livermore National Laboratory (LLNL)-configured linear computed axial tomography (LCAT) system, which couples a slit-collimated flat linear array with a slit-collimated tube x-ray source.

The introduction of the polychromatic source and the current-integrating detector substantially changes the interpretation of the measured data. Instead of Equation 11.4, the analysis of the acquired signal for transmission, T , and attenuation multiplied by path length is the result of integrating over the energy spectrum given by Equations 5.18 and 5.19, reproduced here for convenience:

$$T[S(E), \bar{Z}, \bar{\rho}, \ell] = \frac{\Phi^P[S(E), \bar{Z}, \bar{\rho}, \ell]}{\int \Phi_0^P[S(E)] dE} \approx e^{-\sum_i^n \mu_m^i(\bar{E}, Z_i) \rho_i \ell_i} \quad (11.10)$$

$$\ln = \left(\frac{\int \Phi_0^P[S(E)] dE}{\Phi^P[S(E), \bar{Z}, \bar{\rho}, \ell]} \right) \approx \sum_i^n \mu_m^i(\bar{E}, Z_i) \rho_i \ell_i. \quad (11.11)$$

Notice that we have replaced the equal signs with approximations and average energy. Or let us agree that this notation represents an integral over some numerical dimension, and we are using a sufficient statistic as a proxy for this distribution. The system measures attenuation similarly to the monochromatic case but with important differences. The detector counts every bit of irradiance it can for the state of the spectrum along that ray path to the detector. It reflects both the particulars of the object along those ray paths as well as the detection efficiency or stopping power of the detector. For an alternate representation of these quantities see the work of Whiting et al. (2006).

The stopping power of a detector is a key component in the overall efficiency/system speed of an x-ray inspection system, as well as determining the energy that is actually used in the inspection. As indicated in Chapter 9, LDAs can be built up of scintillator-photodiode or direct-detection elements, but both include a stopping power or the proportion of the irradiance at a particular energy that the detector will stop. As can be shown from a review of the fundamentals, this quantity is 1 minus the x-ray transmission or the proportion of the irradiance that did not make it through the detector (Whiting et al. 2006). As an example, consider a scintillator-based system with 1-mm deep CsI detector elements. The W-anode source is separated at 220 kV with 2 mm of Cu filtration. Using tools for estimating transmission, Figure 11.5 includes a plot of the stopping power of 1 mm of CsI over the range of potentials from 10 to 200 kV. Figure 11.6 shows a comparison between the spectrum launched from the x-ray source, 220 kV filtered with 2-mm Cu, and that same spectrum

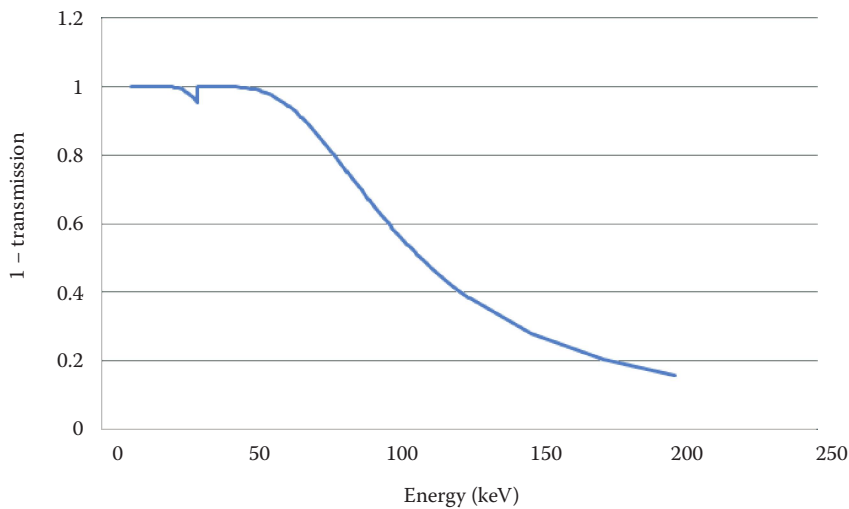


FIGURE 11.5 Plot of the modeled results for the stopping power ($1 - \text{transmission}$) of a 1-mm-thick (in the direction of the x-ray incidence) thallium-doped CsI scintillator.

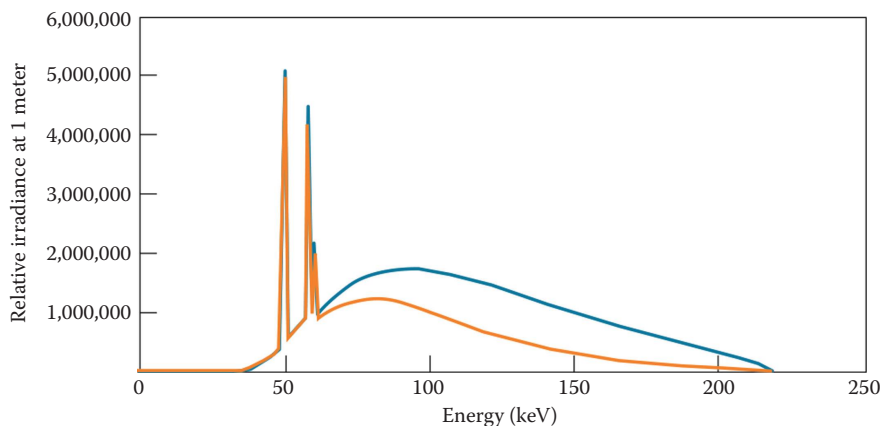


FIGURE 11.6 Modeled 220-kV W-anode x-ray spectrum filtered with 2 mm of Cu (blue curve) and the filtered spectrum as detected by 1-mm-thick thallium-doped CsI scintillator (orange curve).

as stopped by 1 mm of a CsI(Tl) (thallium-doped cesium iodide). Notice that the average energy of the *stopped* spectrum is lower than the spectrum emitted from the filtered source.

For scintillator-based x-ray detectors, changing the thickness of the scintillator is one of the ways in which the stopping power of a detector can result in a different part of the x-ray source energy spectrum being accessed. Consequently, the thickness of the scintillator introduces another variable for CT system design that impacts the effective energy used in an inspection and affects system performance for large fan/cone angles. In single-detector systems, the source irradiance is the result of collimation in both height and width; consequently, the geometry (thickness) of the detector in the direction of the beam is less significant, although more stopping power still equates to faster scanning. Certainly, you want to count all of the meager irradiance that makes it past the collimation, but once you have enough thickness to obtain a usable spectrum for analysis, you are done. All this says is that for a single-detector system, there is no real consequence beyond acquisition time for differences in detector stopping power.

For linear and area detectors, the introduction of detector geometry results in an interaction between detector geometry and source geometry, and this increases the impact of scintillator thickness more so than with a well-collimated, single-detector DR/CT system. First, the detector element in a flat LDA that is at some distance from the center of the beam divergence is at a greater source-to-detector distance than the detector element at the closest distance to the source center line or spot (the geometric center of the beam). If the fan angle is small, say less than 4°, the irradiance at the farthest distance is better than 99% of the irradiance at the center. However, for a 14° fan angle, the irradiance is approximately 94% of the centerline detector element, and for a 22° fan angle, the irradiance is approximately 86% of the centerline detector element. Second, if the detector element is thick, the divergence can result in cross talk between detector elements, that is, the diverging x-rays detected in one element include irradiance from a neighboring detector element. This is especially true if the inspection energy is high (MeV range) and you do not stop most of the irradiance. Depending on the construction of the detector elements (in particular, the use of septa in the detector element), this can reduce detected irradiance and/or reduce spatial resolution in the outer detector elements (see example problem at the end of this chapter).

Curved detector arrays eliminate all the issues with decreased irradiance and detector aperture at higher fan angles. That is, when the detector element is thick and the detector is flat, the photons counted for an element at a large fan angle include photons from other elements that the ray has passed through, or if you have septa, you have unnecessarily decreased the irradiance to the detector element. For curved detector arrays, all of the detectors are at one source-to-detector distance, and since each element points to the source, there are no issues with septa possibly interfering with some irradiance. Detectors can include robust stopping power (increased thickness) with impunity. The cost of the curvature is that the curved detector can only be used at a single source-to-detector distance. Therefore, the source-detector envelope and object size are determined by your selected distance. For fixed-scanning envelope systems (baggage scanning is one example), or medical systems, the gains in overall scanning efficiency outweigh other considerations. As a result, virtually all baggage-scanner CT systems include a curved detector array.

It would appear from Equations 11.10 and 11.11 that the analysis and multiple-energy options available in single-energy scanners for decomposing attenuation into an effective atomic number and electron density are not available for LDA systems with x-ray tube sources and current-integrating detectors. A number of strategies have been developed to address these issues; some are presented in Chapter 15. For multiple-energy applications, two strategies have been developed to perform the same quantitative inspections produced by single-energy gauging systems. First, the strategic scanning of different single materials at different energies can be accumulated, tabled, and used in a basis material schema to produce material identification and density estimation from multiple scans at different energies. This is referred to as basis material decomposition (BMD) (Alvarez and Macovski 1976; Sukovic and Clinthorne 1999; Liu et al. 2009). In this way, the ratio of attenuation data from two different energies for a particular system has been used for material identification, within limits. At the same time, novel applications of nonlinear constrained optimization have been used to generate estimates of Z-effective and density without the table of scans of pure materials but from models of the output spectra of different tube sources. This method is referred to as photoelectric and Compton decomposition (Ying et al. 2006; Azevedo et al. 2016). Both of these approaches have successfully performed material identification and characterization for multiple-material contexts.

Returning to the schema presented at the start of this chapter, for the LDA-based, slit-collimated scanner with septa and a current-integrating detector adjusted to stop most to all of the irradiance, some of the terms in the equations are gone. For both the object, Φ , and the Φ_0 signals, background scatter is at or near 0. This means that the estimated values identified in Equations 11.10 and 11.11 reflect more of the interactions going on in the object and less in the system, i.e., collimation, detector scatter, etc. We consider this the fundamental way in which the estimated values from the collimated versus noncollimated CT are improved. At the same time, the data are not as quantitative as the single-detector, single-energy (monochromatic) data. The ability to reject scatter from the

object is compromised. With this detector, there is no spectrum to analyze and no way to distinguish lower-energy x-rays scattered from the object along that ray path from low-energy x-rays that are emitted from the source. The collimator configuration can reduce this type of irradiance by restricting the angle, but it is not reduced to 0. Unlike 1-D gauging systems, the array of equations (see Equations 11.1 through 11.3) describing the constituent parts of the acquired signal for this type of system includes a scatter term. Consequently, certain artifacts due to object scatter are regular parts of the radiographs acquired with this type of system. The object geometry, e.g., parts with a high aspect ratio or objects with high- and low-attenuating components in very close proximity, can lead to certain artifacts. Such artifacts are covered in Chapter 13.

11.3.2 RADIOGRAPHY WITH AN AREA-DETECTOR ARRAY

The next system is the closest analog to the free-flight detection of irradiance depicted in the equations presented in the first part of this chapter and schematically represented in Figure 11.7. All of the scatter terms in Equations 11.1 through 11.3 are nonzero, and no alternate or simpler equations are forthcoming in this physical configuration. From the point of view of any particular type of area detector, these different sources of detected signal are difficult to distinguish. In addition to the sources of signal, the spatial properties of the x-ray source are important for the analysis of the radiographic results.

The radiograph is formed from the irradiance emanating from the source to the detector. Unlike the single-detector or the slit-collimated LDA, the radiograph more clearly reflects all of the complex interactions occurring between the geometry of the x-ray source, the geometry of the object, and the sampling operation performed by the detector. Further, this sampling operation occurs in energy, in space, and somewhat in time, if the detector includes some residual signal (for scintillator detectors, afterglow). The result of the interactions impacts both the spatial distribution of the attenuation and the energy distribution of the irradiance detected by the area-array detector.

The results of the properties of each of the system components are present in the area-detector radiograph. The impact on imaging performance due to the physical size of the source spot or source unsharpness (Bossi et al. 2002) is more significant for area detectors. Scattered radiation is detected from both the object and the system (referred to as scattered background). System scattered photons can come from the cabinet for a cabinet system, walls in a room or bay installed system, and elements in the detector construction, depending on the state of the area collimation and the particulars of the x-ray cabinet or x-ray bay. At the same time, the area detectors excel at acquisition speed and source utilization. An entire array of detectors is read in one acquisition, and the larger solid angle illuminating the detector is used for the inspection, as opposed to a single ray, or a single line. Inspections using this geometry are usually considerably faster, sometimes on the order of 5–10 times faster depending on the target spatial resolution.

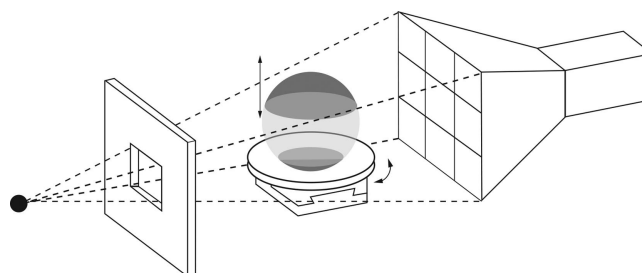


FIGURE 11.7 Pictorial diagram of an area-array detector DR/CT (rotate and elevate) data acquisition configuration.

At another level, obtaining higher spatial resolution image data can be more tractable with area detectors. First, there are a variety of means for configuring detectors with smaller detector elements such as amorphous silicon (amSi) and complementary metal oxide semiconductor (CMOS) flat panels, camera-scintillator configurations, computed radiography plates, or digitized film. Furthermore, the complications of aligning septa or aligning septa to additional slit collimators inherent in progressively smaller LDA systems are eliminated. The area detector can be treated as a single plane in 3-D space, and proper alignment can be achieved by aligning the center of the source to the center-perpendicular of the area detector. This alignment operation can be made more tractable by laser attachment accessories designed for x-ray sources and front-surface mirrors. We and others also have used alignment phantoms to help in the alignment of the source to the area-array detector. The many different types of area detectors described in Chapter 9 serve to make this option even more attractive.

Using a detector that eclipses the entire radiographic plane puts more emphasis on the accuracy, precision, and properties of the area-array detector, but this is not an issue for many area-array detectors. Manufacturing processes for charge-coupled device (CCD) chips and flat panels include high precision for repeatable detector widths and detector-to-detector spacing. This is not necessarily the case for image intensifiers, which can include well-known pincushion distortion and troublesome hot spots. In this case, it can be hard to separate the effects of the detector from the divergence properties of the source and a possible misalignment of the detector to the normal from the x-ray source.

The main advantage of the area-array detector system is speed, but it is at the cost of a lower primary-to-scatter ratio and greater dependence on the physical attributes of the x-ray source spot. Area detectors usually have low stopping power and, as will be discussed, a greater reliance on calibration and preprocessing. There are ways to remediate these effects for area-array detectors. For instance, it is still true that the imaging performance of some mature film techniques is better by far than any image acquired from any digital, area-array detector. This assumes all the adjustments in film type and possible filtering at the film or film/screen combinations. The robust imaging performance of x-ray film versus digital detectors is even more dramatic at high energy (see Chapter 9).

An additional property emerges for certain scintillator-based area-array detectors: the intrinsic spatial properties of the scintillator itself. In CCD camera-based radiography, the camera acquires an image formed by the x-ray interactions with the scintillator, which result in a visible image at a certain wavelength of the scintillator used. Similarly, with amSi or CMOS flat panels, the scintillator itself has a certain impact on the spatial resolution obtained in a certain inspection. As in the case with LDAs, the chemical formula and density of the scintillator material are fundamental to the stopping power of the scintillator; however, for area-array detectors, the fabrication methods can alter the intrinsic spatial resolution. If the detector element size of the detector is much less than the intrinsic spatial resolution of the scintillator screen, the image will appear blurry regardless of the other geometric factors. [Figure 11.8](#) contains a comparison plot of the intrinsic spatial resolution of different scintillator screens. Particulars of different scintillators were covered in Chapter 9 and will be discussed in measuring imaging quality in Chapter 14.

Lastly, all of the alignment considerations possible are present for area-array detectors. The beam divergence in both height and width must be accounted for, as must the plane of the detector relative to the center of the divergence. The x-ray magnification of the object is present in the image in two dimensions, so the size of the area detector needs to support the full size of the projected image in both dimensions. Inserting septa in detector elements is difficult, except at low cone angles. Thicker scintillators are more prone to cross talk as the beam divergence occurs in height and width, and this puts limitations on the stopping power that can be obtained for area-array detectors.

One advantage for digital, area-array detectors is the resident expertise in reading their images that has been developed for film-based inspections. This expertise is deep, mature, and without parallel for other detector modalities. However, the properties of film-based images can be difficult to produce from digital detectors, and the difference can be significant for human readers.

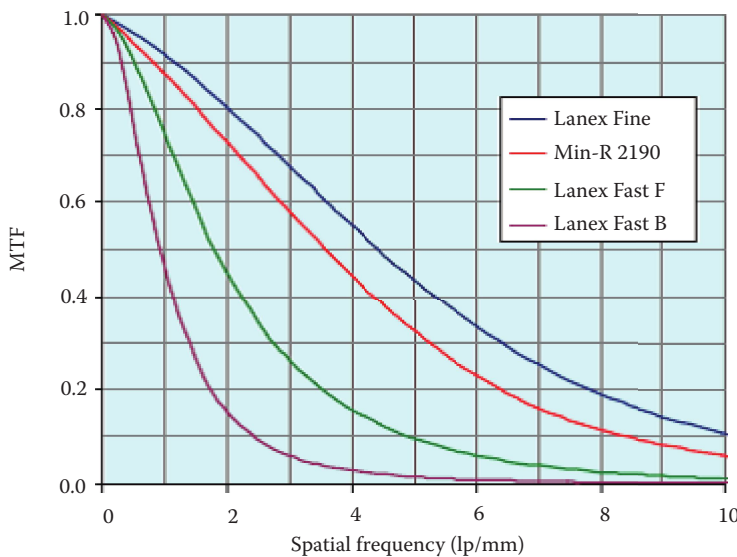


FIGURE 11.8 Comparison modulation transfer function (MTF) plot for different commercially available scintillator screens. lp, line pair. (Courtesy of Rad-icon Imaging Corp.)

11.4 3-D COMPUTED TOMOGRAPHY

In the previous scanning modalities, whether 1-D gauging or radiography, the result is a measurement of attenuation multiplied by path length. Both of these properties of the object function, the attenuation of the material components and their path length with respect to the angle of the source emanation, are in every detector element. The goal and product of the data acquisition, processing, and reconstruction techniques involved in CT is to generate an in-plane measurement of the object function per volume element or voxel. It can be true that when properly acquired and processed, CT reconstructed images include a dimensionally correct, quantitatively accurate image of the object internals. A pictorial illustration of the data acquisition process for rotate-only scanning and highlights of the differences between projection data and 3-D reconstructed images is given in Figure 11.9.

As indicated in the Figure 11.9 illustrations, CT acquisition involves some means for obtaining different transmission rotational views of the object and, through some subsequent process, results in a 3-D image composed of voxels (instead of pixels). As illustrated in Figure 11.10, the entire CT reconstructed volume can be thought of as a 4-D data set where each 3-D object position contains a voxel quantity that is proportional to x-ray attenuation, which in turn is the result of chemical or elemental composition and density. As such, the changes in the voxel values can be used to identify boundaries of object components and dimensions of object features and/or find anomalous changes in voxel intensities due to different defect or material component configurations. If the entire object function is eclipsed in the CT-scanned volume, a number of quantitative measures can be produced, total object volume, volume fraction for certain cavities or certain components, volume fraction of voids/porosity, etc. The richness of a CT data set also results in a certain complexity, e.g., boundaries and defect conditions can get intertwined. There is an averaging process occurring within a voxel, which impacts the identification of edges and the error variance for any of the quantities that can be calculated, known as partial volume artifacts. In fact, there is always a fundamental indeterminacy, at the level of a voxel, between the edges of a feature and the voxel boundaries. In the worst case, you are always averaging the position of the edge in space into a voxel quantity (Bulaevskaya 2015). More troublesome still is the presence

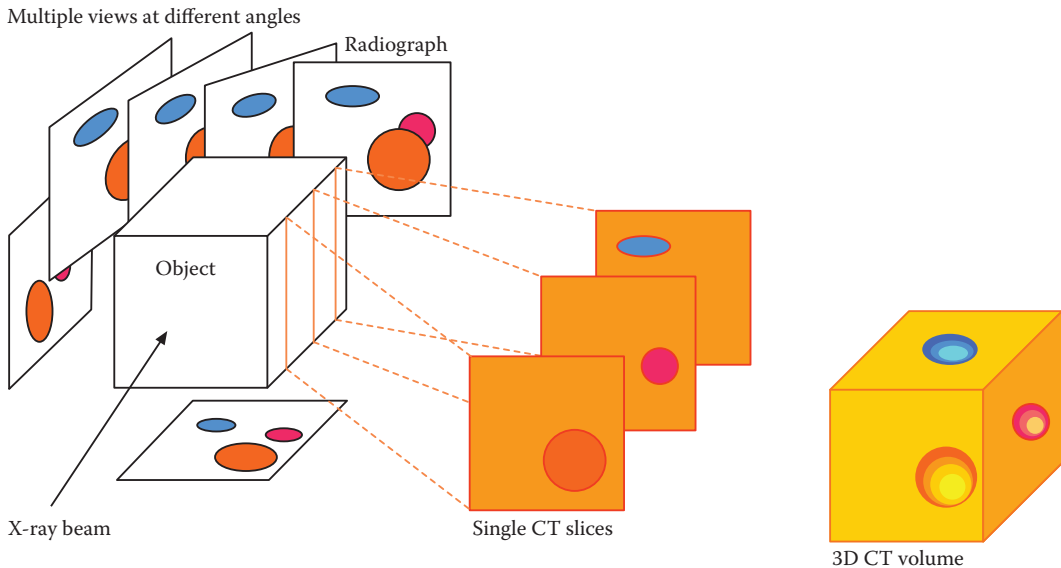


FIGURE 11.9 Pictorial illustration of rotate-only CT acquisition for area-array detectors.

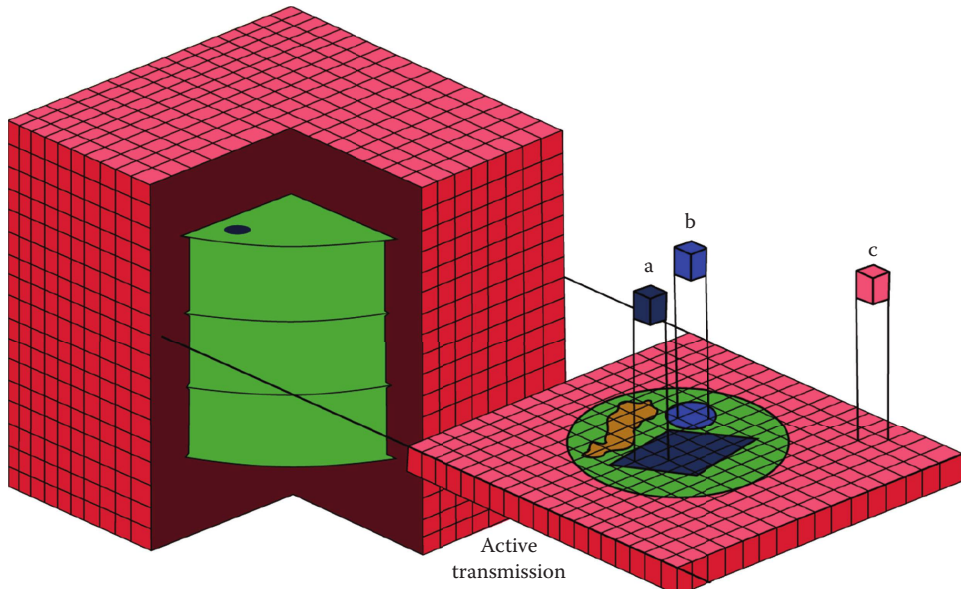


FIGURE 11.10 Pictorial of 3-D CT reconstructed volume.

of artifacts, which result in local voxel values that are simply incorrect and impact every further calculation in unpredictable ways.

All of the source-detector modalities mentioned can provide the foundation for CT scanning. All CT scanners include four subcomponents: (1) source of radiation, (2) detector, (3) object fixtures and motion control, and (4) a computer for scanning control, processing, reconstruction, and display. For each modality, the physical configuration of source and detector and the motion of the source or detector need to result in a complete CT data set. At this point, we identify a complete data set in terms of four properties: (1) The constituent transmission measurements include some attenuation and some transmitted signal for every pixel with a ray path intersecting the object.

- (2) The measurements include data over an angular range commensurate with the beam geometry.
- (3) The measurements include complete object coverage (one example of this criterion would be that the outside edges of the part are included in each rotational view).
- (4) The measurements include enough data for all of the voxels in a particular plane of the object to reconstruct the data with equal information content (more about this later).

For CT, the position of the object (or object function) and the rotational angle with respect to some nominal 0 position is now an important part of the description of the ray sum. For a radiograph or small number of radiographs, the position of the object is important, and the preferred orientations are critical elements for many radiographic techniques. However, the focus of the inspection is often on a particular section of the object or assembly. In contrast, for CT, the description extends to a description and measurement of the entire object function. Consequently, the x-ray transform or radon transform of the entire object function at each rotational or translational position is required, as is an accounting of how the different processing steps combine to impact the measurement of object details.

11.4.1 CT SCANNING WITH 1-D GAUGING SYSTEMS

A CT scanner built upon a 1-D gauging measurement system requires motion capability for translating and rotating the object. A single gauging measurement results in one ray-path or pixel. For such a system, to obtain coverage of the object at a particular plane within the object, the CT data set is built up from acquiring a ray sum or pixel of data, translating by one ray sum width (or less), and acquiring another ray sum, until just beyond the width of the part is spanned. The object is then rotated and translated as before, i.e., a ray sum or width (or less) at a time for just beyond the width of the object. This process is repeated until the intended number of rotational views is acquired. As hinted at previously, if the motion control is sufficiently precise, translating the object one-half of a ray sum or pixel and interleaving the resulting data can improve spatial resolution (Martz et al. 1991a).

The overall result of this operation for one plane through the object is what is referred to as a sinogram, one line of data for each angle, over enough angular range for the beam geometry. It is referred to as a sinogram since any ray sum or pixel off the center axis of rotation traces out a sin wave from 0 to 2π . [Figure 11.11](#) illustrates this operation for an object with three internal ellipsoids. The figure shows the transmitted irradiance resulting from a single projection line of data, an example sinogram, and the resulting reconstructed image.

For the case of the 1-D gauging system described here, the beam geometry is parallel, as depicted in [Figure 11.11](#). The object is translated across the same source and detector collimated ray of irradiation. The physical location of the ray of penetrating radiation is the same at each point of measurement; only the object position has changed. As illustrated in the figure, for any one line of data, all of the rays through the object are parallel to one another. Also, as indicated in the figure, there is a relationship between the quality of the reconstructed image and the number of acquired rotational views.

While this will be covered in more detail in Chapter 13, performing CT requires an explicit knowledge of the location of the source and detector (ray sum) position with respect to the center of rotation for the scan. For the 1-D gauging system, this criterion requires knowing the size of the translational displacements of the object as it is translated through the 1-D ray path and also the position in which the 1-D ray path intersects the center of rotation (in this case, usually the center of the rotational table on which the object sits). CT systems depend upon the precision of the positioning subsystem, for the object or the source detector, or both. At this point, considering [Figure 11.11](#), what do you suppose would happen to the reconstructed image of the three ellipsoids if the error variance for the motion system were on the order of the width of the ray sum or path? This is given as a problem at the end of this chapter. We will return to motion errors in [Section 13.7, Artifacts in CT Reconstructed Data](#).

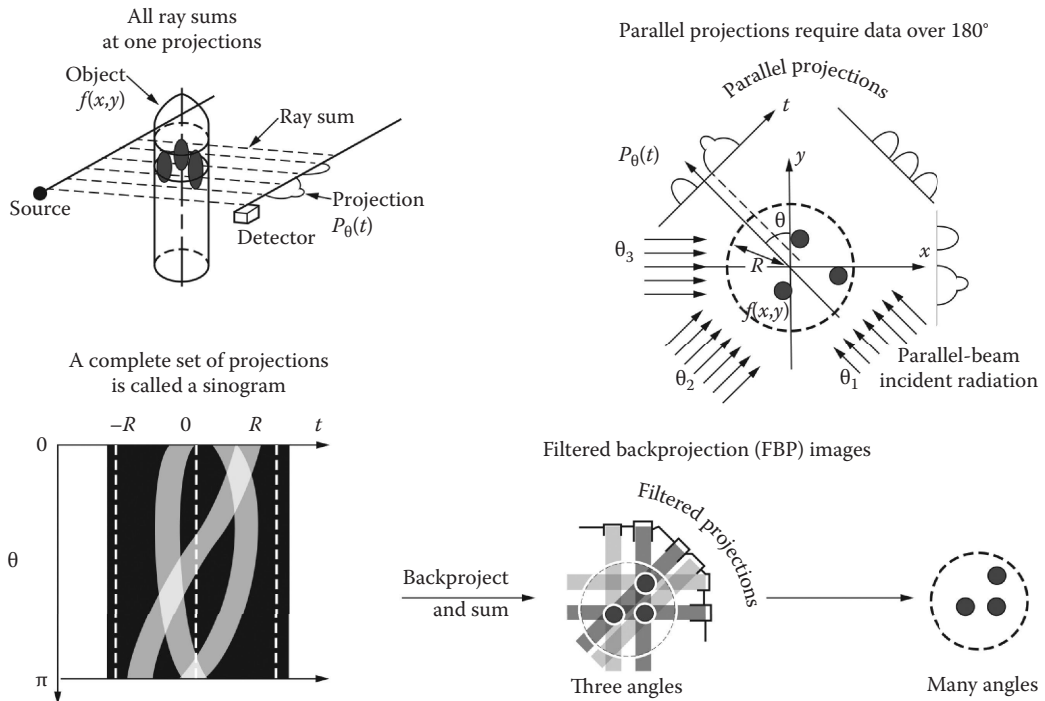


FIGURE 11.11 Illustration of parallel-beam data acquisition (top two illustrations) and image reconstruction (bottom three illustrations).

Quantitatively describing a ray sum through an object requires some definitions. For this 1-D system, a description is adequate for representing the key aspects of the interaction between object function and scanning. Make no mistake, though; the CT reconstructed slice from these 1-D data are 3-D data. The data are obtained one cross section or plane of the object function at a time. Define a coordinate system in space with center in between the source and detector (x_0, y_0), and let the position of the source be represented as (x_s, y_s) and the position of the detector as (x_d, y_d) . Since there are multiple detector positions we replace x_d with iw_x , (iw_x, y_d) , where w_x represents the horizontal detector width at the detector and n is the n th detector position counting from the left.

Given these definitions, we can define a line from source to detector as the points $(x_{sd}, y_{sd}) = (x_s, y_s) + l(x_{dc}, y_{dc})$, where x_{dc} equals the direction cosine in x : $(x_d - x_s)/l$; y_{dc} equals the direction cosine in y : $(y_d - y_s)/l$; and l equals the distance between (x_s, y_s) and (x_d, y_d) for that particular detector position. Depending on the measurement of the values for (x_s, y_s) and (x_d, y_d) relative to the center position (x_0, y_0) , we can convert all of these positions to be relative to another center position (x_0, y_0) , representing (x_s, y_s) and (x_d, y_d) as $(x_s - x_0, y_s - y_0)$ and as $(x_d - x_0, y_d - y_0)$. While there are many ways to represent the coordinates at the detector and the projection lines drawn back to the x-ray source (Barrett and Swindell 1981; Kak and Slaney 2001), the point is that once you have multiple detectors (or multiple detector positions), you have to account for a line drawn from source to detector, and this can be defined by the horizontal and/or vertical angles, or the two points that define the line.

For parallel-beam data, there is no beam divergence and no x-ray magnification; consequently, all of the y coordinates for the detector positions are the same value from the center of the space, which we define here as the object-to-detector distance, y_{odd} . Define the center of the space to be the center of the rotational table in the scanning hardware (or if the source and detector rotate, the center of rotation for the source-detector arc path). The successive translate motion performed by this scanner results in an equal shift to both the x_s and x_d coordinates, so x_{sd} equals x_s , the value of the shifted distance from the center of the rotational table (or isocenter). The family of lines traversing

the object in the parallel-beam geometry are distinguished only by the change in x coordinate, and all lines have the same length, $y_{\text{sdd}} = y_{\text{sod}} + y_{\text{odd}}$, where y_{sdd} is the source-to-detector distance. Rotating the projection through the object is equivalent to rotating the coordinates of all the lines through the object space by θ , or equivalently, by rotating each point in the space with a 2×2 rotation matrix $[\cos \theta, \sin \theta | -\sin \theta, \cos \theta]$. For any angle θ , the equation of the line for the parallel-beam geometry can be represented as the set of points $(t, s) = (x \cos \theta + y \sin \theta, -x \sin \theta + y \cos \theta)$, where t is the distance from center to the detector position (at each rotation) and s is the position along the ray sum or path measured from the center of the space, y_0 .

Following Kak and Slaney (2001), the numerical integral of the intersection between the ray sum and object function is the sum of all the material x-ray attenuation on that ray sum or path, indexed by t , at that rotational angle θ , and it can be represented as $P_\theta(t)$. Using the delta function to identify the intersection between one of the parallel lines traversing the object function and the volume elements of the object function results in

$$P_\theta(t) = \iint f(x, y) \delta(x \cos \theta + y \sin \theta - t) dx dy. \quad (11.12)$$

Notice that we have made use of the fact that the s variable does not vary in this geometry, so we can uniquely identify the different ray sums through the object by only the variable t and the rotation angle θ .

The polar-coordinate version of this integral can be particularly convenient. Make the canonical change of variable with $x = r \cos \phi$, $y = r \sin \phi$ with $r = \sqrt{x^2 + y^2}$, and $\phi = \tan^{-1}(y/x)$ results in

$$P_\theta(t) = \iint f(r, \phi) \delta(r \cos(\theta - \phi) - t) |r| dr d\phi. \quad (11.13)$$

Note that $f(x, y) = f(r, \phi)$ and $t = x \cos \theta + y \sin \theta = r \cos(\theta - \phi)$.

This integral (and its variations) is referred to in many texts as the Radon (1917) transform of the function $f(x, y)$ (or $f(r, \phi)$) and is the fundamental description of the projection through the object for the development of reconstruction algorithms. For parallel-beam CT systems, a set of measurements of $P_\theta(t)$ distributed over 180° angular range covers the entire object function. As will be covered in more detail in Chapter 13, the point of the reconstruction algorithm is to recover or estimate the values of the object function from a set of ray-sum measurements. It is important to note that the units of the object function determine the physical significance of the projection measurements. Also, notice that this is a general relationship between an object function and the ray sums or line integrals through the function and could be applied to a variety of different physical circumstances.

Provided there is enough time for acquisition, a 1-D gauging system can acquire a complete CT data set for an object by translating through the object, rotating, and translating through the object again. Once completed at one level or plane, the object is elevated to the next plane, repeating the data acquisition all over again. It is a matter of indifference whether the source detector is translated across the object width or the object is translated across a single-detector ray sum or beam path. As shown in Chapter 12, Digital Radiography, the equations for the measurements are simpler and more quantitative, and this extends to CT. Parallel-beam reconstruction is the simplest, and the CT reconstructed data are composed of per-voxel measures of attenuation at the particular source energy (if the source is monochromatic). Consequently, acquiring multiple energies results in per-voxel measures of chemical formula and density (Schneberk et al. 1991).

11.4.2 CT SCANNING WITH LINEAR-DETECTOR ARRAYS

Configuring CT scanning with a linear-array detector and fan-beam source geometry introduces a number of additional variations. First, in terms of the notation mentioned previously, there are two

centers of interest, the center of the beam divergence for the linear array and the line intersecting the rotational table containing the object. In what is called the aligned case, the two centers are collinear. Every detector position includes some reference to at least one of these two centers. In some texts, such as that by Kak and Slaney (2001), these two centers are on the same line. Figure 11.12 contains a drawing that identifies these two centers and some notation for their description.

Linear-array x-ray detectors can have a flat or curved configuration. For CT with a flat linear array, obtaining a complete set of projections pertains to the coverage of the projection of the object relative to the size of the linear array. If the projection of the object fits within the width covered by the detector, you have the option of rotate-only scanning. If the array is narrower than the object, obtaining a complete data set requires both translation and rotation. The translation can be a minimal shift to fill in the detector space occupied by the septa or a larger motion to cover the width of the part, or both. The different configurations of linear arrays, in combination with possibly different scan motions, converge upon essentially the same data as acquired for the CT system built up from the 1-D gauging hardware, i.e., a sinogram. However, the acquired data include a difference in the beam geometry, i.e., the definition of the ray paths through the object and possible variations in detector geometry (e.g., curved versus flat detector arrays).

For all fan-beam geometry CT scanning, the sinograms for each illuminated plane or slice through the object are reconstructed into slices, and they are combined to result in a 3-D volume image data set. To obtain out-of-plane coverage of the object, either the object must be moved through the fan beam of radiation or the fan beam of radiation is moved down or up the length of the object in the direction orthogonal to the plane of the fan beam. A full 3-D scan of the object is built up from the illuminated fan beams. Translating the object or source-detector in this way can also be used to acquire single radiographs. Without rotation, as mentioned, this out-of-plane motion can be used to build a fan-beam or slit-collimated digital radiograph. In this same connection, digital radiographs could be acquired at each rotational angle and then subsequently reshuffled into sinograms.

Layered upon these differences in scanning motion is the possibility of scanning with constant motion or step and shoot. Depending upon the application, it can be of some advantage, e.g., it is usually faster to move the object or source-detector at a constant velocity without stopping and

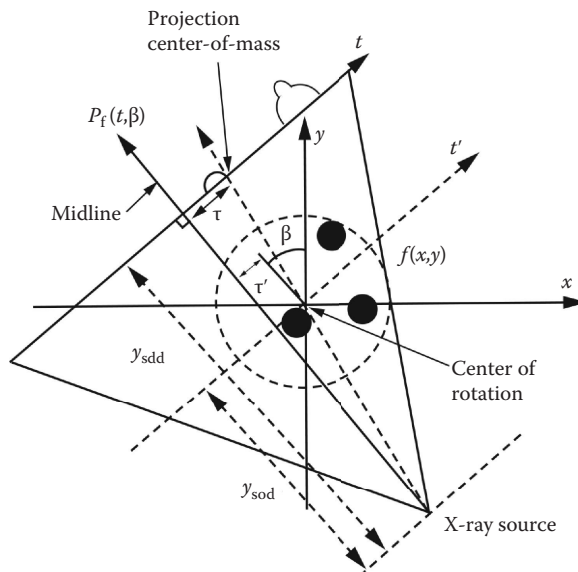


FIGURE 11.12 Pictorial of linear-array detector and fan-beam x-ray source projection CT and associated alignment relationships.

acquire the transmission data in a particular timing sequence. This type of scanning can be particularly strategic for pulsed x-ray sources, where the x-rays are generated for short periods of time and data acquisition can be synced to the x-ray pulse. The result is a data set that can include the effects of scanning motion, and accounting for these effects requires some strategy in the data acquisition hardware or in the processing of the data. Also, constant-motion systems can benefit from curved detector geometries where all of the motion takes place at a certain radius from the object center, not at different radii as in the case of a flat LDA.

Step-and-shoot data acquisition describes the process of moving the object to a particular angle or translational position, acquiring an image with the object still, and then moving to the next position. This type of data acquisition does not include any motion errors by design and can be easily combined with small translations for subsequent interleaving. Further, this type of data acquisition can be combined with other source trajectories for more sophisticated reconstruction algorithms.

CT systems based on fan-beam geometry, LDAs, and polychromatic sources have been the most common configuration for explosives detection in checked luggage at airports and medical CT. From all the previous discussion, it can be argued that the slit-collimated linear-array detectors result in x-ray transmission data with the highest primary-to-scatter ratio per throughput. The same relationship between the precision of the positioning system or the accuracy with which you know the position of the ray path (in the coordinates that describe the object) and the reconstructed image is true for the 1-D gauging measurement. However, in this case, the precision needs to extend to every element of the linear array. If the system is designed to put the detector elements on a certain radius, the data need to be on that radius to within the target spatial resolution. Or for a flat detector, the detector width and spacing need to be as designed, again with the detector-to-detector error less than one-half the target spatial resolution. For most flat LDAs, manufacturing tolerances well exceed many, if not all, of these criteria. Furthermore, since there is a dimension that is not collimated, it is important to know the beam characteristics of the x-ray source divergence, where the center of the divergence is located on the array, and if there is an asymmetry in the intensity from the source (a heel effect) or not. If the system includes an upstream or source-side collimator, the alignment between the source-side collimation and the detector elements needs to be adjusted to fully illuminate the array elements that will be used. The point is that an LDA results in faster data acquisition than a 1-D pencil-beam gauge system for the same sinogram, but new alignment considerations follow, and the opportunities for artifacts increase. Thus, additional processing of the data is required to minimize the artifacts.

Equations for describing the ray sums or paths through the object function are different for the fan beam with a linear-array detector as compared to the parallel beam with a single detector. First, for the fan-beam geometry system, the rays travel along the lines of the beam divergence to the different detector element positions. Instead of one detector and source position, (x_d, y_d) and (x_s, y_s) , d that is translated across the object function, all the ray sums are measured in one projection data acquisition. The notation for the detector position can be modified to (x_{di}, y_{di}) , where i indexes the detector position. Following this, the lines traversing the object function are the points (x_{sdi}, y_{sdi}) on the lines between the same source position (x_s, y_s) and the different detector positions (x_{di}, y_{di}) . The set of ray paths taken together constitutes a fan-beam projection through the object function. For what we shall call the aligned case, the central ray of the fan intersects the center position (x_0, y_0) and is the position of the shortest distance between the source and the detector or the line perpendicular to the detector array and intersecting the x-ray source. In this geometry, we can label the distance on the central ray to be the source-to-detector distance, or y_{sdd} , and the distance from the center of the space to the detector to be the object-to-detector distance, or y_{odd} . All of the other rays corresponding to the detector positions in the array can be defined by their individual fan angles, $\gamma_i := \text{atan}(x_{di}/y_{sdd}) = \text{atan}(n/l)$, measured as the arctangent of the ratio of the distance of this detector from the central ray, and y_{sdd} , the source-to-detector distance on the central ray, where x_{di} is measured at the distance from the central ray. In terms of the general equation for lines presented earlier, this ratio is the direction cosine in the x -axis.

The fan-beam projections resulting from the x-ray projection of an object onto an LDA spanning the object generates substantially different data than a parallel-beam projection system. The central ray for the source-detector envelope and the fan-angle positions of the different detector elements are now important geometric properties of the system. Further, the x-ray magnification of an object and its features is included in the projection of the object function. The projected size of a feature will be smaller or larger depending upon whether the feature is closer or farther away from the detector. This effect gets less important as the source-to-detector distance gets large with respect to the object size, as the object gets close to the detector, and at small magnification. At the same time, by considering the detector plane translated to the center of the object space, a complete set of projections over a large angular range for the fan-beam data can be sorted (or interpolated) into a parallel-beam data set. The accuracy of this sorting depends strongly upon how well all the values of the fan-beam geometry are known (source-to-detector distance, object-to-detector distance, and detector spacing). Fan-beam systems are more complicated, and using them for CT scanning requires more measurements of the system geometry (we will return to this in Chapter 13).

A number of other relationships are important in the fan-beam geometry coverage of the object function. For the flat-detector case, equations can be represented with the detector array at its physical geometric position (behind the object) or translated to the center of the space (the center of the rotational table). The fan angles are the same since the denominator for the direction cosines is y_{sod} , not y_{sdd} , and the detector spacing is smaller, the inverse of the x-ray magnification multiplied by the physical detector spacing at the detector. The intersection between a line to a detector position and some arbitrary x, y position in the object function can be solved for either the physical detector position ($x_{\text{di}}, y_{\text{sdd}}$) or the translated detector position, i.e., translated to the center axis of rotation, ($x'_{\text{di}}, y_{\text{sod}}$). For a single point (x, y) or, equivalently, ($r \cos \phi, r \sin \phi$), the intersection of the line with a detector element provides a quantitative comparison of the difference between the parallel and fan-beam geometries:

$$x'_{\text{di}} = y_{\text{sod}} [(r \cos (\theta - \phi)) / (y_{\text{sod}} + r \sin (\theta - \phi))], \quad (11.14)$$

dividing both the denominator and numerator by y_{sod} yields

$$x'_{\text{di}} = (r \cos (\theta - \phi)) / [1 + (r \sin (\theta - \phi) / y_{\text{sod}})], \quad (11.15)$$

so x'_{di} is the virtual horizontal detector position with the detector translated to the center of the space or at y_{sod} , and x_{di} without the ' is at the detector or y_{sdd} .

A fan-beam geometry converges to parallel-beam geometry as the source-to-object distance gets large with respect to the extent of the object function (that is, $r \sin (\theta - \phi) / y_{\text{sod}}$ goes to 0). This relationship contains an aspect of the differences in the projection images of an object over a large angular range. In fan-beam x-ray projection geometry (not parallel beam), features closer to the detector are projected smaller than the same features when they are rotated 180° and are close to the x-ray source. As the source-to-object distance gets larger, this difference gets small to insignificant, and data can be regarded as parallel beam. One test for the appropriateness of parallel-beam techniques is to compare the size of the same feature at different source-to-detector distances for the full rotation of the object.

Consider the relationship between the set of ray sums in the parallel-beam and fan-beam geometry, over all the rotational angles. In this discussion, we index the rotational angles for the parallel data by θ and the rotational angles for the fan beam by β . The central ray in the fan-beam geometry case is the same as the central ray in the parallel-beam geometry; both rays are perpendicular to the detector and intersect the center of the space. A similar correspondence can be derived between ray sums or paths from fan-beam and parallel-beam ray paths. The parallel-beam path through a detector element can be found in the set of fan-beam ray paths where the parallel rotational angle is the rotation for the fan-beam geometry plus the fan angle. The detector location for the parallel-beam data can be found by multiplying the fan-beam detector distance by the cosine of the fan angle. In general, also see the work of Kak and Slaney (2001):

$$t = (x'_{\text{di}} y_{\text{sod}}) / \sqrt{y_{\text{sod}}^2 + y'_{\text{sod}}^2 + x'^2_{\text{di}}}, \text{ and } \theta = \beta + \tan^{-1}(x'_{\text{di}}/y_{\text{sod}}). \quad (11.16)$$

For a curved LDA, the positions of the detectors differ only by angle and not by distance, so the correspondence to parallel-beam rays is a bit closer. Some extra calculations are required, and you have to acquire at least 180° plus two maximum fan angles (Parker 1982). You can rebin the fan-beam data into parallel-beam data, and this gets easier or harder depending on the shape of the linear array (more about this in Chapter 13).

A number of options are possible for acquiring CT scan data with an LDA detector. Also, these options change a bit whether the detector is flat or curved. Processing and reconstructing LDA detector data can be performed in a number of ways, and there are correspondences to the parallel-beam case that can be important. In practical terms, you need to know more about the geometry for fan-beam data—curved or flat—as compared to parallel-beam data. First, you need to know the source-to-detector distance, the source-to-object distance, and the pixel size at the detector. Second, it is advantageous if the center of the rotational table is on the centerline of the beam divergence. For parallel-beam data, there was no beam divergence, no x-ray magnification, and the only parameter to be measured was the center of rotation and source/detector or object translation step size.

11.4.3 CT SCANNING WITH AREA-DETECTOR ARRAYS

A quick review of the mathematical texts and papers on 3-D tomographic reconstruction will yield many different notations for representing x-ray projections and 3-D object space. It is hoped that the notation presented here does not become a distraction. The point of the notation is to show how the situation gets more complicated with the physical form of the detector, now an area instead of a point or line, and it is only a means for identifying key quantities and relationships for work to be presented subsequently. You are encouraged to pick or develop a notation that you are most familiar with and translate the added complexity into your chosen algebra.

Area-detector arrays introduce further variations into CT-scanning modalities and options. This type of detector records an entire array of measurements in a single acquisition, sampling the entire emanation of the x-ray irradiance for the solid angle subtended by the detector. One of the common configurations utilizing this detector is rotation-only cone-beam geometry scanning. In this modality, the object usually fits into the field of view of the detector, and the scan is performed by acquiring irradiance measurements from the array, rotating the object, acquiring a next array of image data and so on. [Figure 11.13](#) includes a picture of the LLNL cone-beam geometry CT system called Clint's Computed Axial Tomography (CCAT), which combines a FeinFocus 225 kV microfocus x-ray source with a 40 × 30 cm Thales amSi area-array detector placed at a 1 m source-to-detector distance. With this system, x-ray magnification of up to 18× is employed to obtain high-spatial-resolution digital radiographs and 3-D CT volumes to support inspections of objects and assemblies.

This type of system can also be employed in tiled-scan CT inspections where the object is larger than the field of view (see Section 16.4.2.2 describing the scan of a National Aeronautics and Space Administration [NASA] Stardust Reentry Capsule). A virtual detector size is constructed by successively moving the detector in height and width to different positions, thereby filling in the entire detector area. The virtual detector is assembled later by stitching the individual radiographs together.

As mentioned in Chapter 10, the options for collimating the x-rays in this modality are somewhat restricted. Antiscatter grids have shown some performance at lower energy but are difficult to configure at medium- to high-energy regimes. Secondly, aligning the collimation with the horizontal and vertical divergence of the x-ray beam is not without issues (see collimator design for a 9 MV linac in Section 6.5.2). Again, medium- to high-energy techniques are challenging especially in the case of linear accelerator (linac) energies, where the propensity to scatter is high and a small misalignment of the beam divergence and the collimator can result in significant scattered irradiation in the object and the detector.



FIGURE 11.13 Photograph of the LLNL cone-beam geometry CT system called CCAT. Shown from left to right are the Thales amSi flat-panel area-array detector, object staging (just beneath the source), and the FeinFocus 225 kV microfocal x-ray source.

Using an area-array detector for CT scanning, referred to as cone-beam CT, requires the measurement or estimation of a few more geometric relationships than already measured with a fan beam into a linear-array detector. With area-array detectors, an entire plane of image data is acquired, and both the fan-beam or horizontal aspect of this detection plane and the cone-beam vertical aspect of divergence are important. Additionally, like the fan-beam case, it is important to know the relationship between the axis of rotation of the rotational table and the vertical center of the beam divergence.

The equations for ray sums in this modality include x , y -, and z - (height) axes. The source position is (x_s, y_s, z_s) , with detector positions (x_{di}, z_{dj}) , with the detector positions varying over indexes i and j . Each detector position can be identified by two angles; γ_i , the fan angle, and ζ_j , the vertical cone angle for that (x_{di}, z_{dj}) position. The center ray for the cone-beam projection is perpendicular to both the x - and z -axes and is the center of the divergence for both width and height of the detector. Following the fan-beam case, the center of the coordinate space is on the center axis of rotation of the rotational table (or isocenter when the source and detector rotate). In an aligned cone-beam CT system, the midplane of the x-ray source should be aligned with a single row in the detector, preferably the center row. Also the axis of rotation should be in a single column in the detector, preferably the center column. Since we are in 3-D space, it is more convenient to represent the radon transform of the object function onto a point on the detector \mathbf{d} with vector notation, with $\mathbf{x} \rightarrow (x, y, z)$ the points in the object space, $\mathbf{n} \rightarrow (n_x, n_y, n_z)$ the direction cosines for the line between source and detector, and $\mathbf{d} \rightarrow (x_{di}, y_{di}, z_{di})$ the coordinates of the detector. For the case of aligned cone-beam geometry, the entire detector plane is at one distance from the center of the space, y_{odd} , the object-to-detector distance and the 3-D projection is given by:

$$P_\beta(\mathbf{d}, \mathbf{n}) = \int \int \int f(\mathbf{x}) \delta(\mathbf{x} \cdot \mathbf{n} - \mathbf{d}) dx dy dz. \quad (11.17)$$

The intersection between the ray paths between source/detector and the object function now includes both the horizontal and vertical divergence. In the same fashion as in the fan-beam case, we can translate the plane of the detector into the center of the space. The x , y , z coordinates of the space intersect the detector fan angle corresponding to the y -axis direction cosine for the line through that voxel and at that height. We can divide up the different rows except the midplane row

of the detector into sets of tilted fan beams, spanning the height of the detector. In this same connection, the intersections between the object function and the detector data can be organized into a set of sinograms at tilted fan-beam locations, with the height interpolated along the length of the tilted fan. The source-to-detector distance on this fan is longer than the distance at the midplane by $\sqrt{1 + \tan(\zeta_j)}$.

The connection to the 3-D parallel-beam projection through an object can be established as before (Kak and Slaney 2001), but the correspondence has to be extended to both the x - and z -axes. However, for the rotation-only data acquisition regime, we consider difficulties arising in the completeness of the acquired data set. A difficulty for cone-beam geometry systems is missing data. The data perpendicular to a voxel at a specific height are not acquired; rather, only the data at the tilted angle is acquired for reconstructing that voxel value (Grangeat 2001). As expected, the degree of incompleteness of the data increases with the cone angle, and the artifacts grow with the degree of incompleteness. More about this is discussed in Section 13.7, Artifacts in CT Reconstructed Data.

11.5 SUMMARY

The variety of applications for x-rays has resulted in a number of DR and CT system configurations for inspections. These different systems can be organized by type of source (monochromatic and polychromatic) and source and detector geometry, from single detectors through linear-array to area-array detectors. Each type of system includes different advantages and disadvantages for performing DR/CT inspections. The highly collimated single-detector, monochromatic source system is the most quantitative, with the loosely collimated area-array detector with a polychromatic source the least quantitative.

CT systems built upon the different source and detector configurations include the added component of motion staging and inherit the strengths and weaknesses inherent in that scanning modality. The number of geometric parameters of importance increases proceeding from single detectors to linear-array and area-array detectors, as does the complexity for describing the projected features of the object. For the single-detector parallel-beam system, processing/reconstruction depends only on knowing the center of the rotational table and the detector-to-detector spacing. The effects of x-ray magnification are included in the linear-array system, so source-to-detector and source-to-object distances are added to the list of required parameters for subsequent processing. For area-array detector systems, both the horizontal and vertical detector spacing are required, as well as the position of the center of the beam in height. In addition, alignment conditions are usually required such that the vertical central column of the detector is colinear with the axis-of-rotation of the rotational table. The gains from the added complexity in system configuration are dramatic increases in system speed and source efficiency.

After reviewing all of these details, perhaps the best question here is why choose one system over another? In our opinion, managing the trade-offs inherent in the different DR/CT system choices—and there are always trade-offs—is best performed from an in-depth understanding of the inspection application.

PROBLEMS

- 11.1 How many detected counts are required to satisfy a noise requirement of 0.01% for a 1-D gauging system?
- 11.2 Describe the process for calibrating a current-integrating LDA detector for measurement, and describe a process for material identification with two different applied electron accelerating voltages.
- 11.3 Do you need the same number of rotational views to image with a single-detector as with an LDA?
- 11.4 Describe how motion errors propagate through a CT reconstruction algorithm. Do this in words.

- 11.5 Describe how you would spot collimator misalignment.
- 11.6 Propose an alignment scheme for a 1-D detector, an LDA, and an area-array detector. Do you need a test object? How would you verify that you are aligned?
- 11.7 Consider a single-detector iridium radioisotopic-source x-ray system, in which you can acquire data at one or all of the three highest-keV energy lines. Which one would you use to scan a sample equivalent to 2.54 cm of copper? Why? Which line would you use to scan a sample equivalent to 5 cm of copper? Why?

12 Digital Radiography

12.1 INTRODUCTION

In this chapter, we turn to the more practical considerations for acquiring and processing digital radiographs (DR) for inspections. Chapter 9 included descriptions of an ideal detector and detailed descriptions of particular detectors in which the emphasis was on the physical mechanisms involved in the capture and digitization of the source irradiance. We directly build upon the material presented in Chapter 9 (a quick review of Chapter 9 might be good idea). Looking forward, in Chapter 14, we cover the tools for the evaluation of acquired data from DR systems, and some of the material presented there is connected to Chapter 9 and the material presented here. It is our position that consistent and effective use of digital detectors involves understanding the source irradiance (discussed in Chapter 8), the detection mechanisms (Chapter 9), the different acquisition modes (Chapter 11), processing of the image data (this chapter), and application of methods for analysis of the inspection performance of the image (Chapter 14).

Beyond the specific mechanisms for counting/digitizing x-rays, digital detectors include a variety of properties that figure prominently in the task of producing an image with spatial resolution and contrastive performance sufficient to support the goals of an inspection. Furthermore, a number of different detectors include idiosyncratic features that need to be factored into the analysis of data used in inspections and into their use in the design of inspections. In some ways, this chapter is an answer to the following question: What about using this detector at this energy, in this way, for the inspection of this object? At the end of this chapter, the goal is to equip the reader with the ability to provide some answers to these questions and some practical understanding of how the acquisition and analysis would be performed.

Upon completion of this chapter, you will be aware of

- The process of data acquisition for different types of detectors
- Some of the data processing methods applied to raw digital data and their impacts on the image used in the inspection
- Image calibration, physical image format (raw/transmission/attenuation), and the importance of the Φ_0 (reference irradiance) image
- Artifacts in DR
- Test objects or phantoms and image quality indicators (IQIs)
- Some options for signal and data analysis and interpretation

12.2 PHYSICAL STRUCTURE OF DIGITAL RADIOGRAPHIC DETECTORS

The point of departure for DR is the transmitted image in space. As mentioned in Chapters 5, 8, and 10, this image is generated by the interactions between the x-ray irradiance and the object, as the x-rays are focused or collimated, and the image has been formed in space whether or not you put a detector in the mix. All this just says that everything we mentioned about the x-ray interactions with matter in Chapter 5, the properties of the source in Chapter 8, and the properties of collimators in Chapters 10 and 11 is effective.

One first consideration here is the structure of the x-ray detection. As discussed in Chapters 8, 10, and 11 source-detector geometry includes many impacts for area-array systems and fewer for linear-array systems, and is not impactful for single-detector systems. Following previous chapters, we unpack digital detectors first into their physical structure: single, linear-array, and area-array

TABLE 12.1**Comparison of Computer-Based Operations by Type of DR/CT System**

Step	DR/CT System Configuration		
	Single	Linear	Area
Calculating ray sums	X	X	X
Normalizing Φ_0	X	X	X
Individual detector-response corrections		X	X
Detector linearity corrections		X	X
Corrections for dark current		X	X
Corrections for detector blur			X
Restoring ray-sum geometry			X

detectors. The difference between these three modalities is, in some sense, just collimation, but the options for detection and how you handle the data are so significant that we continue to treat them separately. A summary of the data handling or possible corrections that are applied to process DR or projection data is given in Table 12.1.

12.2.1 SINGLE-DETECTOR SYSTEMS

As mentioned in Chapter 11, fielded, single-detector systems are usually presented as x-ray gauging systems or γ -ray gauging systems depending on the type of source. Digitizing the image or obtaining some measure of counts in this context can be more complicated than simply posting a read on the detector and receiving counts. In the case of energy-discriminating detectors (intrinsic-germanium detectors a case in point), a spectrum of measured irradiance is the result of a read of the detector over an energy range for a certain integration time. Plots of a γ -ray source measured using three different energy-discriminating detectors—(1) sodium iodide (NaI), (2) high-purity germanium (HPGe), and (3) cadmium zinc telluride (CZT)—are provided in Figure 12.1.

From these spectra, a number of types of counts can be determined. First, there are the counts under the photopeak, or peaks if you choose to average over an energy range. Second, there are

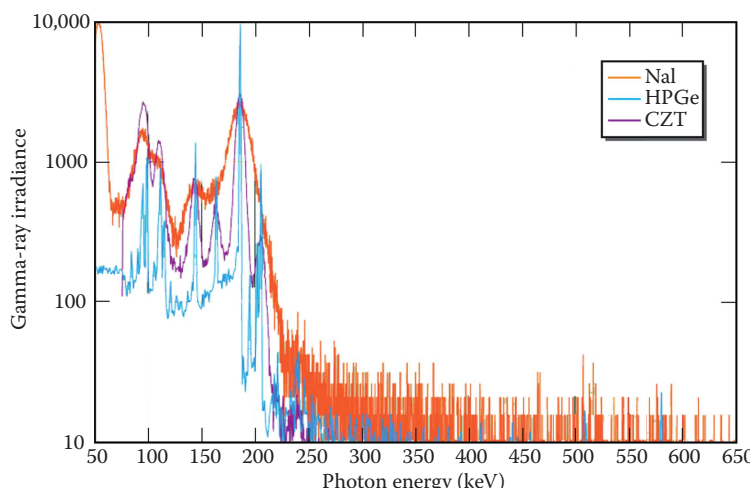


FIGURE 12.1 Plot of γ -ray irradiance as measured by three different energy-discriminating detectors.

the counts in the baseline or background. Notice that all the peaks in the 50–250 keV range sit on an envelope of measured irradiance. Third, there are the somewhat noisy counts at the higher-keV range. Now, do the counts in the peaks include the counts in the baseline or not, and if they are subtracted, how is this operation performed? How would the variation in the choice of a baseline impact the variation in the measurement of counts? For the counts in the peak at 147 keV, a baseline of 100 seems reasonable. However, notice that the peak at about 160 keV looks like it is sitting on a slope, and picking a single value is kind of tricky. In this case, you should at least fit the baseline to a line or some other function to account for the slope in the baseline. One last consideration: What is the state of the detector at the time the data are read? What is the temperature of the detector at the time the detector is read, and does it make a difference? With all these considerations given and after the operations are performed, you get digitized counts at some energy or integrated over some energy range.

With single-detector systems, a number of important types of counts have been introduced that are common to the detectors to be discussed subsequently. First, you have some kind of baseline counts that will be read that reflect the state of the detector or some property of the detector or the mechanism employed to obtain a read of the detector data. For some detectors, these types of counts are usually referred to as dark-current or offset counts. For cameras or amorphous silicon (amSi) detectors, as the temperature of the detector increases, the number of counts of this type increases. This baseline load or counts can increase in absolute value with integration time, which limits the value of taking longer to obtain more counts in the event of low source irradiance.

Single-detector gauging systems include two methods for scatter rejection. First, the systems are collimated, sometimes with both pre-object and post-object at or near the detector. Second, you can further eliminate scatter by processing the spectra, i.e., restricting the counts to a single peak or peaks that correspond to the energies in the source emission since the scattered counts will be at a different energy. Be advised that not all of the scatter is rejected through an analysis of the spectrum. The forward scatter that is at the same energy as the source is counted. However, as mentioned in Chapter 11, this type of detector can be considered to be the best realization of the ray-sum model. The source irradiance along a line is attenuated according to the appropriate x-ray mechanisms, which measure the amount of thickness, material composition, and density along that ray sum or ray path. This is not to say that the entire spectrum does not contain a rich source of information about the object constituents and include opportunities for many different types of inspections. All of the peaks in the aforementioned plot contain some information about the x-ray interactions with the object and are available for or related to many different types of measurements. In many ways, the use of spectroscopy hardware to acquire DR and computed tomography (CT) data only accesses a small part of the application horizon for this kind of acquisition.

One important consideration here is that in single-detector systems, the spatial–physical properties of the x-ray source are not significant. The spot size per se is not a key contributor to the overall spatial resolution; rather, the spatial properties of the acquired data are more a result of the size of the collimation and the step size used to translate the part through the single-detector ray path. A number of options are available, e.g., (1) adjacent spacing of the object, i.e., where each measurement is one detector width and the translation step is one detector width; (2) half-step spacing, where the translation step is 1/2 detector width and the data are interleaved for more spatial resolution; and (3) combinations of translation step sizes to acquire more resolution where needed and interpolating in the event of more sparse sampling (Martz et al. 1991a,b). The spatial resolution obtained in this modality has everything to do with the step size and the collimator aperture and little to do with the spatial properties of the x-ray source or detector.

12.2.2 LINEAR-DETECTOR ARRAYS

With linear detector arrays (LDAs), you acquire measurements from many detectors in a read of the detector. Also, you have the option of choosing the detector array to be in a flat or curved

configuration. The flat configuration includes the added issues of geometric falloff with distance from the center of the beam divergence, but you can position the flat detector at a range of source-to-detector distances, or equivalently, at a variety of fan angles, and perform inspections. Limits for the different fan angles supported by a flat linear detector array depend on the angular irradiance properties of the source and on the thickness of the scintillator (see Chapter 11). In the first instance, if the linear detector array acceptance fan angle is larger than the divergence of the source, some part of the array includes little or no irradiance. Secondly, if the thickness of the scintillator, relative to the pixel pitch, results in substantial cross talk between adjacent scintillators, the acquired spatial resolution is compromised as the fan angle increases. It should be mentioned here that DR with substantial fan angles does change the position of projected features depending upon the position of the feature relative to the center of the beam divergence (more about this on area-detector arrays).

Curved detector arrays are configured to obtain a constant source-to-detector distance at each detector. Further, since each detector looks at the source with the same acceptance angle, further collimation can be applied to each ray sum in the array. Also, septa and small grids can be used in the fabrication of the detector to provide additional rejection of scatter in the object. Unlike flat detectors, a curved detector array is designed to operate at a single source-to-detector distance where the divergence of the source matches the curvature of the array. This physical arrangement puts additional requirements on source-to-detector alignment, with the center of the divergence required to be in the center of the curvature of the array. Flat detectors do not include this requirement, as the choice of where to put the center of the beam divergence is not as critical—only that you make the best use of the source irradiance—depending on the details for the scanning geometry. Adding some slit collimation to the scanner, pre-object and post-object at or near the detector, is common to LDAs. Since you are only acquiring data on one plane, you might as well match the acquisition with the irradiance. Most often, a fan-beam source geometry is coupled to a linear-array detector. However, sometimes it is useful to do this even with an area-array detector.

Additional issues with using linear detector arrays pertain to the individual response of detectors. It is rarely true that all the detectors in the array include the exact same digitization properties. In particular, the digital value that represents zero for each detector element is a little different, and the inherent gain of the detector or how each detector responds to varying amounts of irradiance is a little different. Make no mistake; it is the goal of the detector manufacturer to fabricate the detectors similarly, and the response of detector elements in the same array are usually close, just not exactly the same, especially since detectors are sensitive to small differences in temperature. As a result, linear detector arrays provide for some means to acquire an offset or dark correction (establishing the numerical state of no x-ray irradiance) and a gain correction, a way of accounting for the small differences in the digitization characteristic of that particular detector. In some cases, the detector manual will lay out a procedure for obtaining a set of correction data and some options for utilizing those data to generate data that are free of the idiosyncratic features of these detector elements in this linear array.

While there are few real differences in the procedures for obtaining a detector's offset and gain-correction images, it is important to consistently practice some form of calibration and to perform the procedure consistently. Secondly, it is important to record these images for later review. These images contain information on the health of the detector. Comparing these images over time measures the degradation of the detector. A degraded detector can effectively void any inspection. This further emphasizes the importance of consistency in the acquisition of the correction and calibration images and their use.

12.2.3 AREA-DETECTOR ARRAYS

The use of area-array detectors includes some of the same issues mentioned for both the single-detector and linear-array detector modalities, but with a bit more complexity and somewhat fewer opportunities for collimation. As in the case of linear arrays, reading the detector results in a lot of

pixels, and not all of the counts from those pixels are the result of the interaction between the x-rays and the object. For many of the current integrating detectors, you have the same task of subtracting off the dark or offset counts and balancing the inherent gain of the detector. This makes sure that your measured results reflect the input irradiance to the detector element and are independent of the state of that detector (e.g., temperature) and/or how that detector counts quantum inputs (i.e., gain). Example dark-current images from four different area-array detectors are shown in Figure 12.2. Also, following linear arrays, area-array detectors can be somewhat curved, or you can configure a multirow curved detector, acquiring many rows at a time so that it is basically an area detector, but in many ways, it acts like a linear-array detector. In this subsection, area-array detectors considered operate like flat screens that acquire a frame of image information in a single acquisition without any part movement.

As indicated in Chapter 11, with area detectors, the beam divergence takes place in both the vertical and horizontal directions. The detector intersects with the full cone of irradiance from the x-ray source. So scanners with area detectors of this type are referred to as performing cone-beam scanning. Also, as indicated in Chapter 11, this type of detector makes the best use of the source irradiance—capturing the largest solid angle of the source emission. For a variety of reasons, some related to basic material fabrication issues in making that many detector elements in a compact package, area detectors include bad detector elements. This class of detector elements is considered not salvageable by performing offset and gain corrections, and you need to develop a method for replacing the value of that pixel with something else. Additionally, you need a method for identifying bad detector elements in a reasonably dynamic way so that if pixels go bad over time, you can

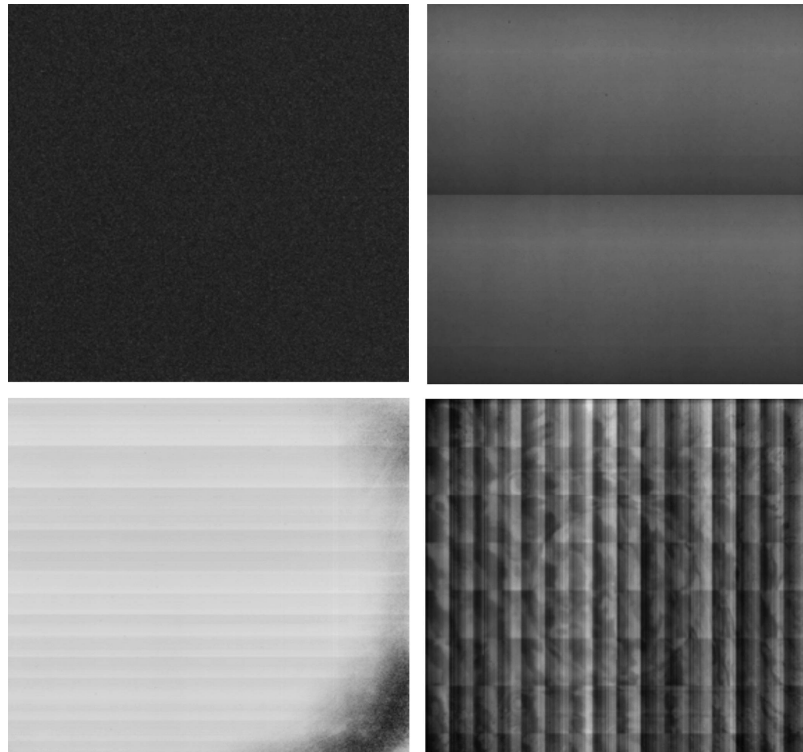


FIGURE 12.2 Example dark-current (x-ray source is off, i.e., no x-rays are impinging upon the detector) images from different area-array detectors. From the top left clockwise are an Apogee camera, a Radicon CMOS panel, a Perkin-Elmer amSi flat panel, and a Thales amSi flat panel. Note that the Thales flat-panel detector has radiation damage as observed by the dark regions in the upper right and lower right of the Thales panel image.

treat them accordingly. Also, at birth, the number of bad detector elements is usually related to the grade of the detector or is a stated property of the detector included in the specifications upon purchase. It is important to have a bad-detector-element correction method to perform this measurement at birth and throughout the useful life of the detector, whether the bad detector elements are static or change over time.

The definition of a bad detector element (sometimes referred to as detector pixel) can vary, as can the procedure used to remedy or fix the values of these errant measurements. One category of bad pixels corresponds to a detector element that does not change with an exposure; the digital value is always really low or really high independent of the source irradiance or the integration time. This type of bad pixel is included in nearly every definition. One definition in use for charge-coupled device (CCD) cameras would say that for an average dark-current value of K (dependent somewhat on the integration time), any pixel that is greater than $1.2K$ or less than $0.8K$ is bad and needs to be put on the bad-pixel list for specialized processing. Another definition of bad pixel emerges from the inherent gain behavior of the detector, that is, for some base level of uniform irradiance, say K' , if a pixel digitizes a value greater than $K' + E$ or less than $K' - E$, that pixel can be considered bad. This criterion is used at the Lawrence Livermore National Laboratory (LLNL). In this case, the value of K' need not be uniform throughout the area detector but could be some area average used for comparison. Implementing this second type of bad-pixel definition related to the gain of a detector is a bit tricky with x-rays since some scatter x-rays can result in a saturated pixel, so the pixel looks bad, but that is because it sustained an x-ray hit, and the next read of that pixel will likely be OK. We will discuss this later in the section on artifacts and corrections. For x-ray imaging with area-array detectors, there are pixels that are inherently unreliable all the time and pixels that are intermittently unreliable, and this means some processing decisions and the possibility of specialized processing for some inspection data sets.

Fixing or remediating bad detector elements unpacks into two operations: finding the bad detector elements (pixels) and replacing that value with some estimated value. While the basis for finding bad pixels follows from the definitions mentioned earlier, a question remains as to when you should look for bad pixels or refresh the list. The implementation of a definition of bad pixels results in a list of bad-pixel locations, which can be kept track of in a bad-pixel list. If you believed that the detector elements/pixels in the detector at birth will basically not change, then saving the bad-pixel list at any time prior to deploying the detector is sufficient. If you believe that x-ray detectors degrade over time, and a lot of them do, you will refresh the bad-pixel list at some interval related to the absorbed dose. In the limit, you refresh a bad-pixel list before and after every scan, and you can compare the results to see if the list was stable for the acquisition.

The second operation, estimating the value to be used to replace the bad detector element or pixel, usually involves calculating some local average or median. One strategy would be to obtain an average of a 3×3 kernel of neighbor pixels excluding other bad-pixel neighbors and use that average for replacement. A second strategy would be to use the median of the nonbad neighbor pixels. The differences in strategy are less important if the spatial resolution is not very good or on the order of 2–3 pixels. In this case, the differences due to changes in the object are spread over many pixels, and using the average or the median is near-equivalent. If it happens that the imaging includes significant modulation at a pixel, the median-based techniques will do better in preserving the transmission/attenuation from the object. Be advised that bad pixels can be part of the high-spatial-frequency content of the image and so are imaged edges of a part or assembly. It can be true that smoothing or median filtering options used to obtain local averages for identifying bad pixels can modify the projected edges in inspection data, and this is information you do not want to perturb or modify.

Another practical consideration in using area detectors is alignment with the source. X-ray sources often include an irradiance and spectrum that varies with the angle from the beam center. This is captured in the digitized view of the area-array detector. In DR, the part may be tipped or tilted to obtain a particular view of the object to inspect that particular location in the object or

assembly. In this case, you can articulate either the object or source detector to get the best intensity of the beam on the region of interest at that angle. With CT, measurements of the source-detector geometry are in order. In particular, you need to measure the location of the center of the beam divergence in the vertical and horizontal directions and measure the source-to-detector distance. Further, in the standard aligned case, (1) the plane of the detector is perpendicular to the source center ray or line (2) the source centerline through the rotation axis of the rotational table is on the center of the beam divergence, and (3) it is advantageous when the rotation axis of the rotational table is on one row or column of the area detector. All this says that when you are deploying area detectors, it is nice if you include some mechanical adjustments with the installation of the detector and/or source. Typically at LLNL, we fix the x-ray source and align the object stages and detector to the source central ray.

The last practical consideration for area-array detectors intersects with the scanning regime. It is now common for area-detector systems to include a range-extension mode, where either the source or object is translated across the field of view of the detector or the detector is positioned across a larger field of view to enable scanning of an object larger than the detector. In the latter case, it will be important to think through the changes in the calibration operations for the different positions of the detector or possibly for different operating parameters for the source.

12.3 ROLE OF IMAGE CALIBRATION AND IMPORTANCE OF THE Φ_0 MEASUREMENT

In the previous section, we mentioned the offset and gain properties of linear-array and area-array detectors. In this section, we discuss the process of calibration that uses metadata and some kind of calculation to generate calibrated image data. The calibrated image data are then used as the basis for the inspection. The goal of the calibration process is to separate the counts that are a result of the transmitted irradiance from the counts that are due to the characteristics of that detector element(s). As indicated previously, you want every detector to have the same zero and also digitize the input irradiance with the same gain. Another way of looking at this operation is to institute a set of estimated adjustments so that each detector response is the same for the same input. Stepping back, it is useful to point out that for all of these approaches, you will (1) have to acquire the metadata for the dynamic range of the detector, (2) estimate some gain-coefficient with these calibration data, and (3) apply these corrections to every acquired view. Consequently, the signal-to-noise ratio of the data will be strongly impacted by the noise properties of the calibration data. Therefore, it is best to acquire the calibration data with care.

As mentioned in the section on LDAs, the zero of a detector represents the number of counts in the detector with no irradiance and presumably at some steady and constant physical state. Establishing the same zero for each detector element involves three operations. They are (1) implementing some hardware to control the environment around the detector, (2) acquiring an image that contains the best estimate of offsets for that particular detector, and (3) performing the correction. The last step is the most straightforward. Subtract the dark-current (offset) counts from the acquired image. Notice that we have acknowledged some process or at least some awareness of the operating conditions of the detector. We consider it important to recognize that when you subtract a dark-current or offset image from another acquired image, you are assuming that the conditions under which you acquired the dark current are the same conditions under which you have acquired the inspection image data. At LLNL, it is routine to acquire a dark-current image prior to and after each acquisition of a CT sequence or at the beginning and end of a series of radiographs. On occasion, the differences between the image at the start and at the end may be significant.

Four dark-current images from four area-array detectors are shown in [Figure 12.2](#) to illustrate the characteristic patterns and variations in the offset or dark-current images characteristic of typical area-array detectors. Notice that the difference in the structure of the pattern noise is connected to the type of detector. Also, the dark-current image from the Thales amSi flat panel detector, in the lower left of

the figure, includes some impact or damage due to prolonged irradiance. This detector has been used for 2-plus years of regular operation in a MV linear accelerator (linac) bay with a certain beam shape and scatter profile. In itself, this is an argument for periodic inspection of the dark-current image.

To evaluate the impact of subtracting the dark current, it is useful to consider the absolute level of the dark-current image data compared to the full irradiance for an inspection. In the case of the inspection using the Thales panel (shown in the bottom left of [Figure 12.2](#)), the average for the dark-current counts was about 1000 not including the damaged section of the panel. The full-irradiance image was about 14,000 counts. In the case of the inspection with the Perkin-Elmer panel (also shown in [Figure 12.2](#)), the average for the dark-current counts was 4800, with the average for full irradiance at about 20,000 counts. Consider the case where the conditions in the room heat up and by the end of the inspection, the dark-current counts have increased by 5% or 10%. For both detectors, you use the dark-current image acquired at the start of the acquisition. The result is that a significant number of counts are left unsubtracted in the acquired signal, and they have nothing to do with the object. By not accounting for the dark-current change, in essence, you treat the increase in dark-current counts as if they have something to do with the object. This results in lower attenuation since you have more counts where the object is. This problem becomes more impactful in the regions with low transmission (high attenuation). Consider a location in a radiograph with 5% transmission, which, for the dark-subtracted Perkin-Elmer panel inspection, translates to 760 [0.5(20,000–4800)] counts. In this location, you have, say, 200 counts of dark current that is in the radiograph due to changes in the detector, so the measurement is 960 counts. Nine hundred and sixty counts is close to a 25% [100(200/760)] change in transmission or an 10% change in attenuation, and again, this increment in the measurement has nothing to do with the object. There is more about this in the homework problems.

Estimating the correction factors or adjustments necessary to equalize the differences in inherent gain for each detector element will require more data acquisition and more processing. As in the case of dark current, there are at least two tasks for estimating the correction and applying the correction. One way to look at this is that you have a model of a virtual detector response for this ensemble of detector elements. This model of detector response pertains to the number of counts each detector should measure as a result of a certain irradiance input. You know that the detector elements are not precisely equal in detector response. The task, then, is to acquire data that enable you to convert the raw measurements for each detector element into the response for this virtual detector.

A number of different calibration calculations are employed in current practice:

1. *Single-gain corrections.* At some level of irradiance, preferably not close to saturation, an image is acquired of the field of view without the object (if there is substantial collimation affecting the detector elements in the image, you will want to handle these pixels a bit differently); call this the Gain-image(x,z). For each pixel, an average or nominal digitized value is generated. After dark-current or offset correction, a gain-correction factor is calculated, which, when multiplied into each detector element, equilibrates the digitizing behavior of each detector element. The gain-correction factor is the ratio between what the pixel measures and what the nominal value of the detector element should be according to the calibration approach (or your model of the detector response). One estimation of the gain-correction factor for a fixed nominal or average value is as follows:

Calculate the gain image as

$$\text{Gain-factor}(x,z) = \text{Average}/[\text{Gain-image}(x,z) - \text{Dark}(x,z)].$$

Apply the gain-factor image to raw images to obtain processed images, where

$$\text{Processed}(x,z) = [\text{Raw}(x,z) - \text{Dark}(x,z)][\text{Gain1}(x,z)].$$

In the case of the linear array, the z goes away.

2. *Multiple-gain corrections.* For multiple-gain corrections, more than one gain image is acquired, and the acquisition is performed at some prescribed level of irradiance. In the

case of Thales flat panels, two Gain-images(x,z) are acquired: one at two-thirds of full irradiance (midfield) and one at full irradiance (light field). The level of full irradiance can be automated or determined by the operator. For each level of irradiance image, a nominal or average value is determined, and a set of gain-factor coefficients or corrections are calculated per detector element or pixel in the image and applied to the range of irradiance covered by that gain image. The gain-factor corrections are then applied to the raw (after dark-current subtraction) counts, Raw-image (after dark-current subtraction) values below the average midfield value use the midfield gain-factor corrections; those image values between midfield and light-field values use a linear combination of the midfield and light-field corrections. Raw (after dark-current subtraction) images with counts at or above the light-field average value will access the light-field gain corrections. One version of this calculation would be as follows:

$$\text{Gain2}(x,z) = \text{MidFieldGain}(x,z) \text{ when}$$

$$[\text{Raw}(x,z) - \text{Dark}(x,z)] \leq \text{Nominal-Mid-Field} \text{ or}$$

$$\text{Gain2}(x,z) = \text{LightFieldGain}(x,z) \text{ when}$$

$$[\text{Raw}(x,z) - \text{Dark}(x,z)] \geq \text{Nominal-Light-Field} \text{ or}$$

$$\text{Gain2}(x,z) = k1[\text{MidFieldGain}(x,z)] + (1 - k1)[\text{LightFieldGain}(x,z)] \text{ when}$$

$$\text{Nominal-Mid-Field} < [\text{Raw}(x,z) - \text{Dark}(x,z)] < \text{Nominal-Light-Field},$$

where $k1$ represents the weights for interpolating between the two gain-correction images as a function of the intensity of the dark-subtracted raw image.

$$\text{Processed}(x,z) = [\text{Raw}(x,z) - \text{Dark}(x,z)][\text{Gain2}(x,z)],$$

In the case of LDA z goes away.

3. *Multiple-gain pixel response fit routines.* In this case, a series of gain images are acquired at specified levels of irradiance, and a polynomial is estimated for the acquired values for each detector element or pixel. Using the estimated function for each pixel, a transformed function is generated that effectively linearizes the digitized value of each pixel.

$$\text{Processed}(x,z) = \text{Gain3}[\text{Raw}(x,z) - \text{Dark}(x,z)],$$

where Gain3 is the estimated gain-correction.

The impact of this processing is illustrated in Figure 12.3, which contains a raw image from a Thales amSi panel and the same image after processing with a two-gain correction or calibration applied.

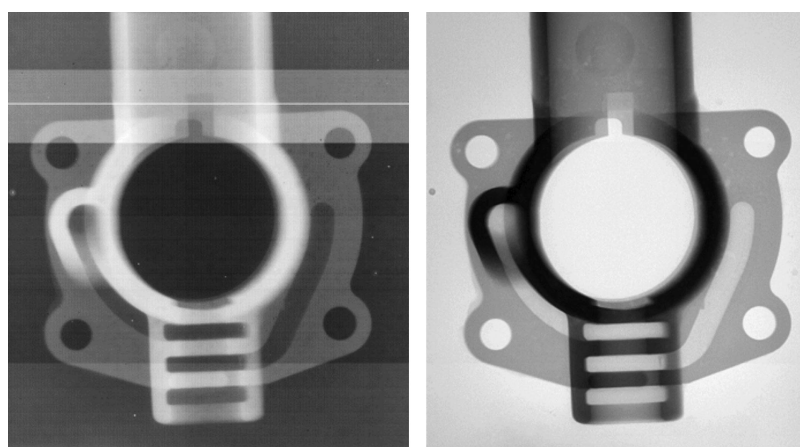


FIGURE 12.3 On the left is a raw minus-dark-current image from a Thales amSi flat-panel detector of an aluminum casting, and on the right is the same image processed using a two-gain image correction technique. Note how the gain-corrected image has fewer artifacts. It is interesting to point out that the raw image on the left is opposite what you would expect in a digital detector in that with no irradiance the panel is close to 16,500 counts and it digitizes into fewer counts with greater irradiance. The gain corrected image fixes this.

Some detectors do not require elaborate gain correction or calibration schemes. X-ray detectors that include CCD cameras only require a dark-current correction (e.g., the Apogee CCD camera image in [Figure 12.2](#)). The digitization is sufficiently linear to enable a single division by the Φ_0 image (or Φ_0 measurement) to equilibrate the possible small differences in the per-pixel digitization behavior. For CT, dividing by Φ_0 and taking the natural log of the result is a regular part of the conversion to attenuation multiplied by path length to create $\ln(\Phi_0)/\Phi = \mu y_t$. In some ways, dividing by Φ_0 is another way of performing a gain correction. The acquisition of the Φ_0 is necessary for performing the transformation to attenuation multiplied by path length— $\ln(\Phi_0)/\Phi = \mu y_t$ —a prerequisite for CT image reconstruction.

12.4 DR/CT ACQUISITION AND USE OF THE Φ_0 IMAGE

In every equation representing the acquired attenuation times path length image values ($\ln(\Phi_0)/\Phi = \mu y_t$) in previous chapters, a reference is made to the Φ_0 image or the acquired irradiance without the object in the field of view. In detail, this is the level of the irradiance to be used for the inspection of the object, but without the object in the field of view. Now, from the simplest model presented in Chapter 5, the value of Φ_0 is that of irradiance impinging on the object. For linear-array and area-array detectors, we want that value of the irradiance, per-pixel, at the object for that position of the object. CT scans can involve the acquisition of many views at different rotational angles. Ultimately, in CT, it is of course difficult or time-consuming to acquire the irradiance with, Φ , and without, Φ_0 , the object in the field of view for every view. It is also known that the source irradiance can vary over the course of the scan. The issue is the possible difference between the Φ_0 or incident irradiance image acquired at some previous time and the state of the incident irradiance at the time you acquired that Φ view of the object. A number of possible strategies have been developed to account for these small changes that can occur over time to ensure that the value of the incident irradiance used to transform the image is the closest proxy for that value impinging on the object.

The different options in current use employ some aspect of the detection hardware that is available or can be made available to track the level of the incident irradiance over time. One option is to employ a reference detector. This detector will always have an unobstructed view of a portion of the incident irradiance. Another possibility is to define as a reference region a part of the detector that does not contain the object, and you make sure the projection of the object will never intersect with this portion of the detector. A third strategy is to acquire a number of Φ_0 images at periodic intervals throughout the scan. This can be useful when the source spot or source properties are changing during the scan. With any of these methods, you can track the changes in the digitized incident irradiance and adjust the level of the Φ_0 portion of the Φ image data prior to calculation of the attenuation multiplied by path values, $\ln(\Phi_0/\Phi)$.

From a practical point of view, the reference detector or reference portion of the Φ image are critical data for the inspection. If the reference detector malfunctions or something untoward occurs, for the reference portion of pixels used for a reference region in the Φ_0 image or the Φ_0 image as a whole, the processed images will be compromised. Perhaps this goes without saying, but CT scanning gets better when the properties of the acquisition of Φ_0 match the settings used in the acquisition of Φ , such as the integration time, the source settings, the operation of the detector, the state of the calibration data, and hopefully the physical environment. If the Φ_0 is compromised in some way, our experience argues that it is a better idea to simulate or generate a repaired Φ_0 image than to forge ahead with a Φ_0 measurement that is problematic. Particularly notable artifacts result from the use of a bad Φ_0 measurement, and in many cases, the inspection data are unusable. Lastly, it is a good idea to evaluate the Φ_0 image and apply some processing routines to remediate measurement issues of various types; more about this later, prior to discussion of use in processing the Φ image data.

12.5 OPTIONS IN DATA PROCESSING OF DIGITAL RADIOGRAPHIC IMAGE DATA

In the earlier discussions, we have mentioned a number of operations routinely applied to digital detector image data. Many of the operations enable a way to isolate that part of the raw measurement from the detector that best corresponds to our model of a ray sum. The digitized counts measure the amount of the irradiance at that detector or pixel position, which is on a straight line from the detector element to the source and nothing else, little to no scatter. While offset-gain corrections or other calibration corrections provide a means for this measurement, certain transient data events can occur. Additionally, other processing routines are applied to data that remediate persistent issues with some acquired data and serve to reduce the artifacts that can be traced to those components of the measured signal.

A summary of the possible corrections that are applied to process DR or projection data is given in [Table 12.1](#). The table starts with the kinds of operations that are common to every type of DR/CT system and proceeds downward to the more complicated procedures for deconvolving or subtracting scattered radiation from the detected image, etc. Functions involved in DR/CT processing vary first according to the type of system. Area-array detector systems constitute the maximal case in this regard, requiring the most processing for each detector element/pixel on each image acquired. Notice also that the number of operations to be applied is inversely correlated to the amount of collimation applied to the scanning. Lastly, it should be mentioned that if you do apply all of these corrections, it is a substantial amount of input/output (I/O) and computations.

Proceeding from the top down in [Table 12.1](#), the first two operations involve the acquisition and use of the Φ_0 image to create $\ln(\Phi_0)/\Phi = \mu_t$, or radiographs of attenuation multiplied by path length. The next three operations shown in [Table 12.1](#) are individual detector-response corrections, detector linearity corrections, and corrections for dark current can be eclipsed by the offset and gain corrections described previously. However, it can be the case that another operation specifically related to CT ring artifacts (see Chapter 13) is applied to further normalize the individual detector response of adjacent detectors. This is an additional detector-calibration adjustment that should and can be scaled with the amount of attenuation in the scan.

The last two operations in [Table 12.1](#) are corrections for detector blur and restoring ray-path geometry involving the class of sophisticated techniques for removing veiling glare (Lazos and Williamson 2012) or backscatter from the detector components, and the scatter removal techniques (Zhao et al. 2015) mentioned in Chapter 10. In both of these operations, more metadata is usually required. For instance, to estimate the detector blur as a point-spread function (PSF) for use in a Weiner filter deconvolution, a series of specific images is acquired as the basis for the estimation. The estimated Weiner filter (using the PSF as the kernel) is then applied to every DR to restore the contrast and resolution loss due to blur from the detector. As indicated in Chapter 10, the scatter-removal routines include the acquisition of some metadata or the use of a beam blocker in the field of view to estimate the amount of scatter in the radiograph. Once the estimate of the scatter field (or PSF) for that radiograph is obtained, the subtraction or deconvolution is performed for every radiograph.

12.6 ARTIFACTS IN DIGITAL RADIOPHYSICS

In spite of the calibration and processing applied to DRs, certain artifacts are a part of the DR images; a list of some of these artifacts, their symptoms, and remedies is given in [Table 12.2](#). Perhaps the most common and the easiest to remediate are outliers, usually either x-ray hits and/or dropouts during a scan, damage to a detector element or an area of elements in a detector. This damage can affect the digitization behavior of these elements so that their response is different. In the end, you have more bad pixels at this point in the radiograph than you did when you last refreshed the bad-pixel list. The bad-pixel list is for detector elements that are always bad. Outliers refer to detector elements that are temporarily bad. It should be mentioned here that a pixel can be distorted to read high or low when

TABLE 12.2
Summary of Some of the Artifacts in Digital Radiographs, Their Symptoms, and Remedies

Type of Artifact	Symptoms	Remedy
X-ray hits or outliers	Pixel value too high or the value has dropped out	Use bad-pixel removal techniques or update the list
Dark current or calibration drift	Pixel values have shifted in intensity with no change in the source parameters	Redo the calibration with current measurements from the detector
Collimator blur or detector blur from collimator	Blur drifts into the image and obscures a portion of the irradiance	Reposition the part with respect to the collimator or realign collimator to source
Light leaks in camera-scintillator detectors	Bright spots in the image that do not change with the changes in the x-ray source	Inspect the camera mounting hardware for issues
Image distortions characteristic of image intensifiers	Image includes some eyeball and keystone distortions	From an image of a known fixed pattern of features (say a ball grid) un warp the image back to rectilinear grid spacing

damaged (see lower-right part of the Thales flat panel dark current image shown in [Figure 12.2](#)). An x-ray hit that is the pixel receiving and digitizing the exceptional x-ray energy deposited in the detector element usually becomes highly saturated or results in a lot more counts. Further, depending on the energy and the type of radiation, the x-ray hit can be a single pixel, or it can be a blob where the deposited energy impacts a group of pixels. This type of effect is more common for neutron imaging and/or high-energy (MeV) imaging. [Figure 12.4](#) contains a raw (dark-current-subtracted) and an outlier processed neutron DR images. The images are from a neutron DR/CT system located at the University of California (UC) Davis McClellan Nuclear Research Center (MNRC).

The methods for remediating the effect of outliers involve the same techniques used for fixing bad pixels. For a single radiograph, usually, more than one radiograph is acquired, referred to as frames, and the frames are averaged to reduce noise and other issues like bad pixels. You find the bad pixels and replace their digital value with the average or median of its neighbors. However, the average or median value is not robust with respect to outliers. This operation is more problematic if it is a group of pixels, as shown in [Figure 12.5](#), but similar techniques have been developed for this instance (Li et al. 2006). The difficulty here is that it is possible that the correction will blur or erode the edges of the object in the effort to find and remove outliers. This may impact the inspection results. [Figure 12.6](#) includes two pairs of images (top and bottom) showing different outlier removal routines applied to the same DRs that have outliers. Notice that the bottom right difference image includes some of the edge of the object; this means you have compromised the features of the object to process outliers. This is the trade-off that needs to be managed when postprocessing digital radiographic image data to remediate the impact of outliers. Also, notice that the processed images are quite similar even though some of the edge content of the image in the lower set has been lost. A better strategy would be to implement some other kind of filter, such as a Min-D filter, and remove the outliers while acquiring the data. This is, of course, difficult if you do not have control of the data acquisition software.

A description of the Min-D filter is warranted. In multiframe-per-view image acquisition, Min-D filtering refers to the practice of retaining the per-pixel minimum over the acquired frames for a single radiograph. That is, instead of calculating the average per-pixel value for each detector element over the frames acquired, you retain the minimum value, thereby eliminating the x-ray hits that can result in a pixel with more counts. Another way to explain the Min-D method is as follows. We acquire multiple frames; we place all the measurements for the same pixel in a vector, which is as long as the number of frames you acquired; and we find the minimum value for that pixel.

A more subtle type of artifact is due to dark current or calibration drift. This occurs when you do not recalibrate your detector for a substantial period of time and the dark-current and gain behavior

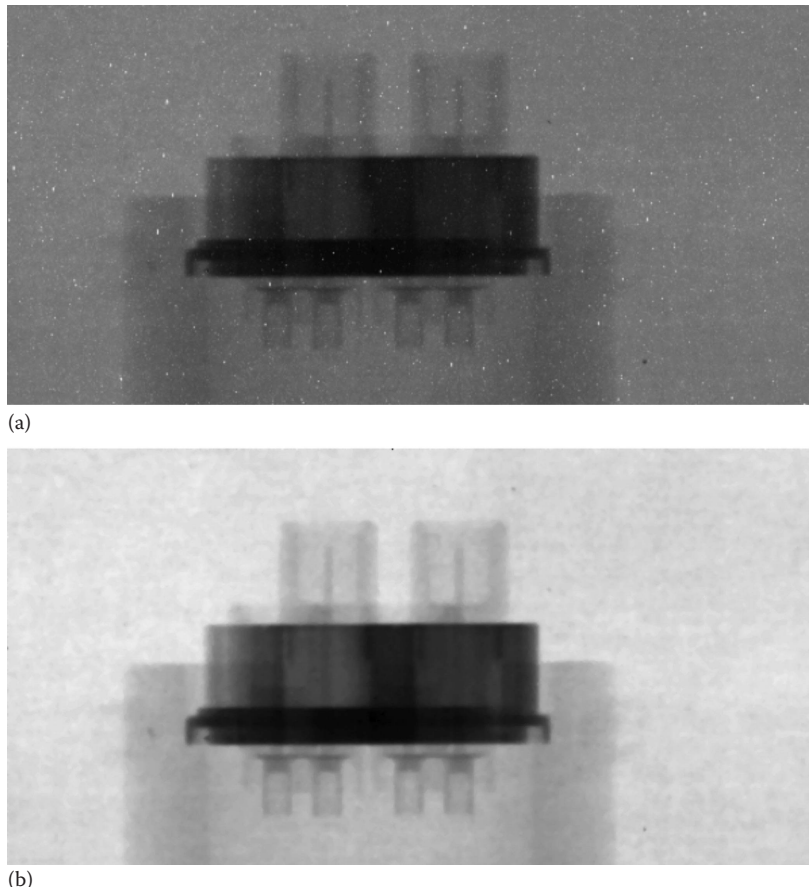


FIGURE 12.4 Dark-current subtracted DR images from a camera-scintillator detector coupled to a neutron reactor source fielded at the MNRC. (a) A raw image containing outliers or hits (white pixels), and (b) a processed image with outliers identified and replaced with a local median. MNRC is the McClellan Nuclear Research Center at the University of California, Davis.

of your detector changes over time. Consequently, you are using the wrong value for zero, and your detector elements are not being digitized in the same fashion. As a result, there may be more counts where there should be no counts, and there is more noise in the image due to the difference in gain-correction values, which has nothing to do with the projection of the object onto the detector. The remedy for this situation is straightforward. Reacquire the dark-current and gain-correction images to better reflect the state of the detector, and reacquire the data set.

A less common artifact in DRs occurs when the blur from the collimator edge intersects with features of interest. This kind of artifact is more common in high-energy DR (see Figure 12.7), where the tail from the blurred edge of collimators can be of substantial length (on the order of a centimeter or larger). Also, since the blur tail is longer, the impact is more difficult to identify in the image. The contrastive performance of the system in the shadow of the collimator or in the collimator tail is less than the unperturbed section of the beam. This can impact the shape of certain features, which can confound visual and/or automated detection. Sometimes, this can be remedied by repositioning the part (or the collimator) so that the blur tail does not intersect with the feature(s) of interest.

Camera-scintillator detectors are not as common in industrial contexts as in experimental scanning or research and development (R & D) facilities. Consequently, the installed base of this type

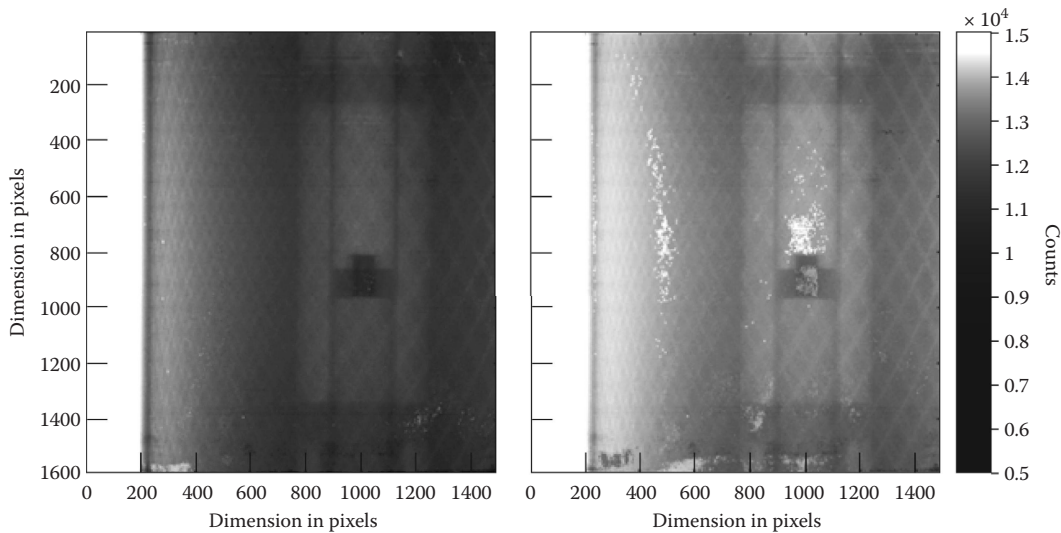


FIGURE 12.5 Two 9 MV Φ radiographic images for a CT scan acquired over about 4 h, 1800 views, 360° , 1.5 s integration time with 4 frames averaged. The first and last Φ images are on the left and right, respectively. The two Φ images are separated by 0.2° . Note the many grouped outlier pixels in the last acquired image. Removing these outlier pixels is difficult.

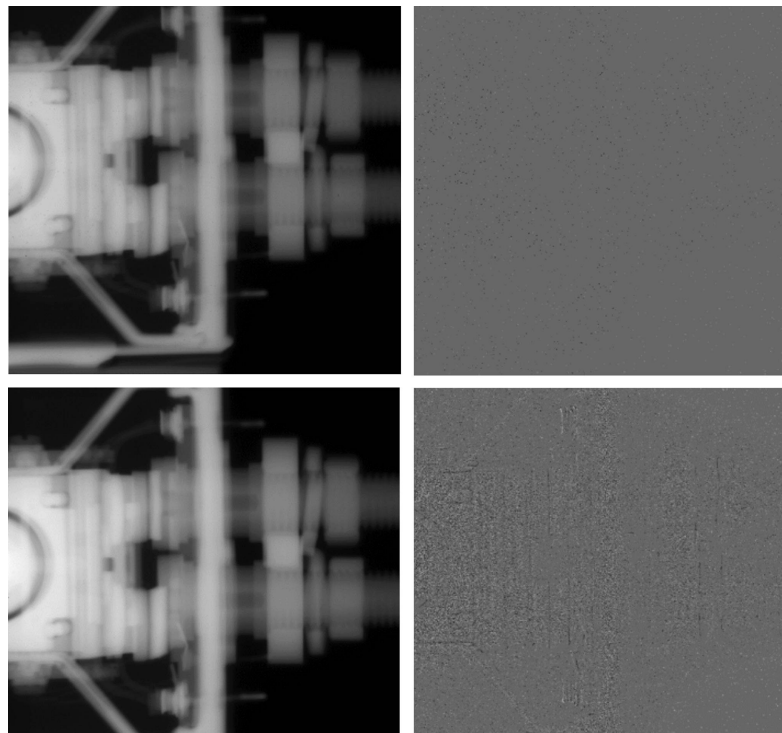


FIGURE 12.6 On the left are different outlier removal processed images, and on the right are difference images of processed minus original. The top row shows the results using one outlier removal method, while the bottom row shows the results for another outlier removal method. The difference images show the impact of applying different outlier removal methods. For example, the outlier removal method used in the bottom image removes some of the edges in the part, this is bad.

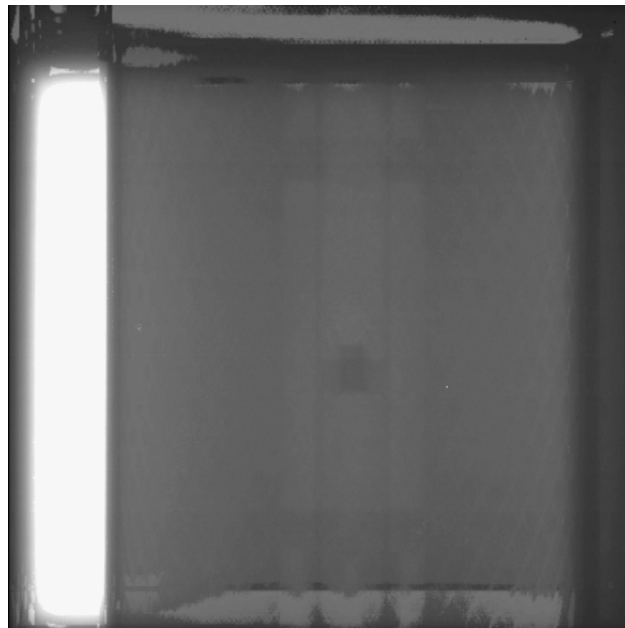


FIGURE 12.7 A 9 MV source and Perkin-Elmer amSi flat-panel detector digital radiographic image of a munition that shows poor use of a collimator. This is revealed by the light gray pixels along the top and bottom of the radiograph.

of system is not large. Camera-scintillator detectors include a digital CCD or complementary metal oxide semiconductor (CMOS) camera focused into the scintillator. If the camera housing is not entirely lighttight, the errant light is digitized as transmission signal. Sometimes, this errant light source can include some structure, and sometimes, it is a broad, nonstructured component as it is out of focus for the camera. The less structure, the less pronounced the artifact will be. Another troublesome feature of this errant light source is that it will not divide out using the Φ_0 image, as the component depends on other factors besides the irradiance of the x-ray source. Dark-current images are usually acquired with the shutter closed and so are not affected. Determining if you have this type of artifact is straightforward. Compare the acquisition of a dark-current image with the shutter closed to the dark-current image with the shutter open. To the extent that they are different, you have a light leak. The best remedy is better light shielding with some textured material and perhaps some light-absorbing baffles.

Image intensifiers (IIs) include a set of artifacts that may not be important for your application. As has been shown in detail in Chapter 9, IIs, by the nature of the imaging chain from input to output phosphor, can result in eyeball and keystone artifacts in the acquired image. Oftentimes, IIs are employed for visual inspection of a part, and the inspector can identify anomalies in the midst of the image distortions typical of IIs. Sometimes, this is not the case. If the inspection task includes the quantitative determination of the size of a feature or an object, acquiring additional metadata to verify the physical distances measured and/or to be used to generate a correction map for the images acquired from an II are very important (Lazos and Williamson 2012). A ball-grid or etched-grid image can be useful to correct the eyeball geometric distortions. The grids usually have features made of some high-contrast material, often embedded into plastic, that help in measuring the distortions. The procedure consists of acquiring an image of the grid- or ball-calibration piece and using the physical locations of the grid or balls to calculate a from-to correction function that generates a new image with the pixel values in locations that are physically correct. This correction-map function is applied to every acquired image.

12.7 PHANTOMS/TEST OBJECTS AND IMAGE QUALITY INDICATORS (IQIs)

The intended goal of the processing described previously is to reduce or eliminate all components of the acquired signal that have little to do with the x-ray interactions with the object or that cause artifacts. What is problematic about all of these procedures is that you are manipulating both parts of the signal, i.e., those you want to correct for and those you do not want to correct for, such as information about the object. If it so happens that you overcorrect or undercorrect, you will process that change in transmission or attenuation space as if there was some change in the object function, and you may interpret the results as significant for the inspection. The more complicated and involved the procedures, the more difficult it is to sort out what is a possible artifact and what is a change in the object function.

The use of phantoms, test objects, and IQIs is fundamental for establishing a physical connection to the object you are scanning. The idea here is for the phantom or test object to physically resemble the object, but with a change in the material (perhaps a void or a high attenuating inclusion) or a change in the object for that material and for that feature size. Thus, verify that you can detect and/or observe that change in the acquired and processed data. The more closely you match the object and features of interest, the more confidence you will have in the relationship between your inspection technique and the state of the object. The means by which you configure the change in the object varies with the object under inspection and the type of DR data acquisition.

For radiographic inspections, IQIs of different types are necessary. Two types of general-purpose IQIs are notable: (1) the wire and (2) the penny. Figure 12.8 shows photographs of four wire IQIs where the wires are encased in plastic, with the array of wires spanning a range of wire diameters.

The plastic packs are flexible and can be attached to the outside of an object with tape or adhesive. If the type of wire matches the object material, you have added a small change in object length, due to the diameter, and cords of the wire. This is observed in the radiograph of the object at that orientation. Detecting a change in the DR for a certain diameter wire verifies that you have contrastive and spatial performance to detect that change in thickness, usually as a percentage of change relative to the local transmission or attenuation.

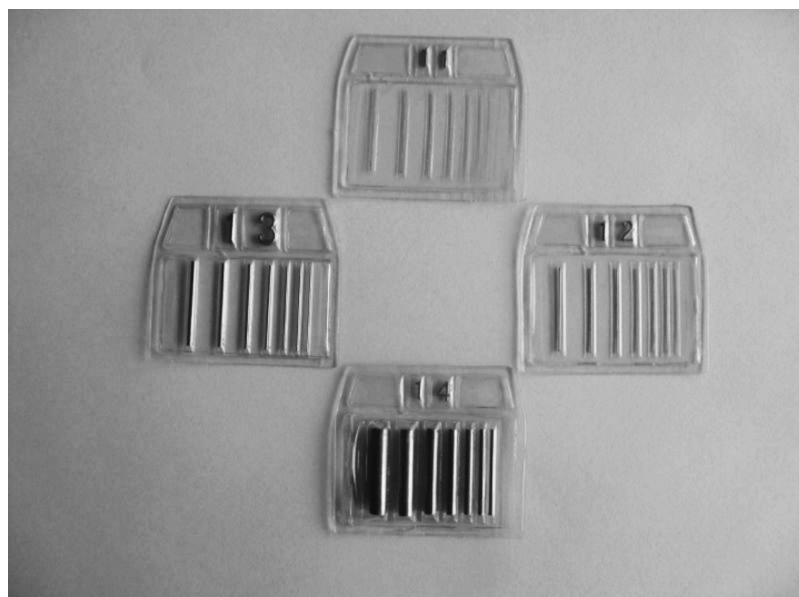


FIGURE 12.8 Examples of an Al wire image quality indicator (IQI) used for radiography system characterization.

The penetrometer-type IQI includes additional features for measuring contrast and spatial resolution for a particular radiographic technique. Figure 12.9 includes a photo of an assortment of aluminum and steel penetrometers. These are often called “pennies.”

As in the case with the wire IQIs, the penetrometer of the same material as the object is attached to the object with the flat aspect of the penny perpendicular to the direction of the x-rays. The thickness of the material and the amount of detail in the acquired and processed image are measurements of the spatial and contrastive performance of the radiographic technique, that is, for that thickness, what size holes can you resolve. Two types of information are included in the penny. If you can see the outlines of the penny, as in the case of the wires, you can calculate a local measure of contrast, as shown in Figure 12.10. If you can resolve all the holes, you can conclude more about the spatial resolution for that change in thickness. For either type of IQI, it is useful to calculate a common measure of contrast, illustrated in Figure 12.10.

While not shown in the figure, it is useful to calculate the local noise for each level of thickness, say D1 and D2 in the figure. One measure of noise is the average standard deviation for D1 and D2. Notice that you can attach either the wire IQI or the flat penetrometer to the object you are inspecting, thereby measuring the contrastive performance of the technique for all of the acquisition and processing procedures. In many cases, production radiography routinely makes use of IQIs for every radiograph acquired.

A third type of IQI, or really, an analysis tool to evaluate a particular technique, is a step wedge, as shown in [Figure 12.11](#). A step wedge is a machined object with a set of steps with different measured

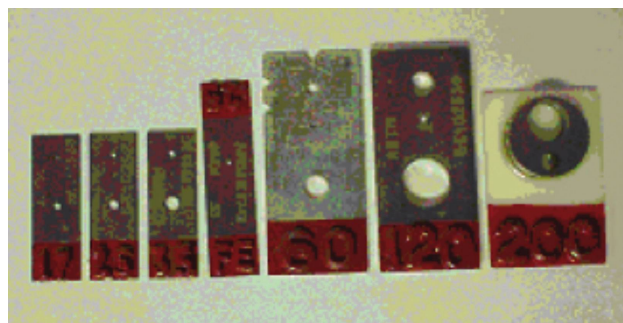


FIGURE 12.9 Photograph of different penetrometers. They differ in thicknesses of aluminum and steel and have different-sized machined holes and notches. They are identified by lead letters in red paint.

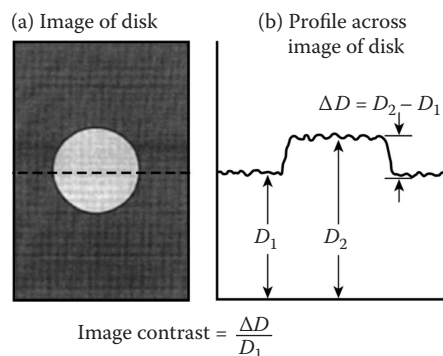


FIGURE 12.10 (a) Illustration of a digital radiographic image for a contrast penetrometer, a thin disk on a large plate. (b) A drawing illustrating 1-D profile from the dashed line on the left and the calculation of local contrast for the change in the disk's radiographic attenuation from the background plate attenuation. This calculation is referred to as contrast.

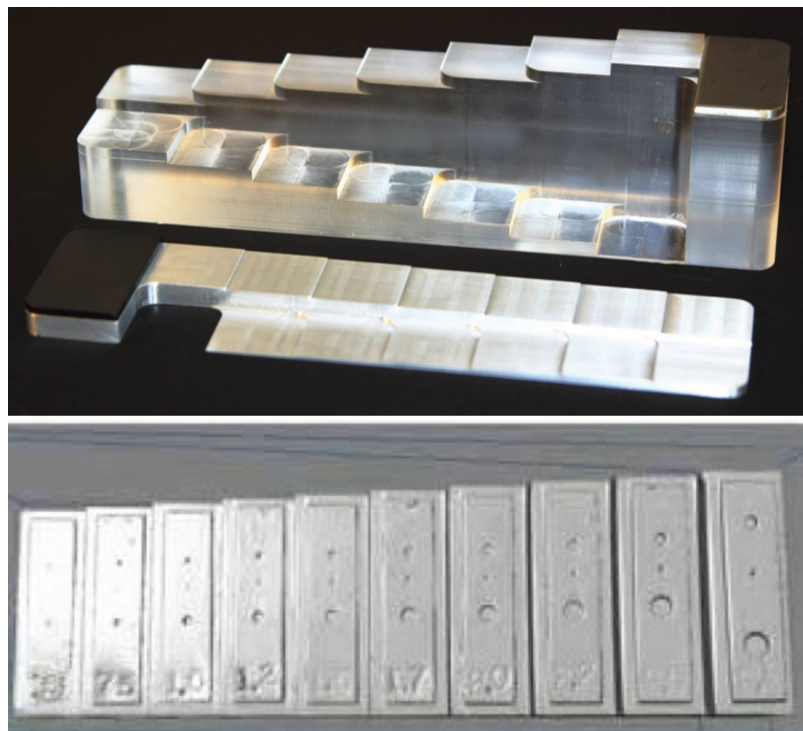


FIGURE 12.11 Photographs of three machined step wedges comprised of different materials. From top to bottom are wedges made of aluminum, polymethyl methacrylate (PMMA), and aluminum. The step wedge in the bottom photo includes Al penetrometers. These test pieces are used in evaluating different radiographic techniques.

thicknesses. A step wedge can be used in three ways: (1) to measure the amount of transmission or attenuation in each step; (2) to measure the amount of local noise per step thickness (it should change as the thickness increases—see Section 9.3, Fundamental Statistical Considerations); and (3) combined with wire or penetrometer IQIs, to estimate the contrastive performance (as measured earlier) per thickness. In many ways, the analysis of a well-prepared step wedge can address most of the issues connected to a radiographic technique. At one and the same time, you can estimate the dynamic range (in material terms), the local noise per thickness, and the per-thickness limits of contrastive performance (more about this in Chapter 14).

Some practical difficulties can arise in the use of IQIs. In the case of the penetrometer, if you cannot get the flat aspect of the penny in the direction of the x-rays, then you are not changing the thickness in the radiograph by the precise thickness of the penny. This can happen with objects that include a lot of curvature or some other particularly complicated geometry. Wire IQIs have the advantage of more flexibility in these circumstances. However, for multimaterial objects where the radiograph is to be acquired at an angle and the region to be inspected is an internal interface or seam, inserting or attaching an IQI to an internal component is not tractable, i.e., without modifying the object, and a step-wedge is a better choice. The best type of step wedge is made of the material in the object to be inspected, but this can be difficult for expensive materials. Also, it can be difficult to orient a wedge to be at the precise angle used in the technique. Consequently, step wedges are made in all kinds of shapes to match the important aspects of the inspection, circular, cylindrical, etc. The key aspect is to get an object with known changes in thickness that span the properties of the object under inspection.

For more complicated inspections, e.g., inspection of a particular region with multimaterials orientated at a certain angle, the fabrication of a phantom or test object may be the best option. In

this case, the phantom, just like the object to be inspected, is fabricated, but with known size features embedded in the object/assembly. Instead of including the IQI with every radiograph, this test object can be radiographed periodically within the inspection cycle for the objects being inspected. Consequently, the inspection of the objects includes a measure of inspection performance periodically for this group of objects. If you can always detect the embedded feature, then it makes sense that you had sufficient inspection performance for the objects being inspected.

A number of issues arise for the task of fabricating phantoms and test objects. It is often the case that their fabrication and inspection can be expensive. It can be hard to manufacture a complicated test object with precise defects. It can be harder to precisely measure the defects by some other technique. However, it hardly makes sense to build a test object without a verified set of defects of precise sizes and locations. In the face of this expense, it can make sense to configure a test object of generic utility. For instance, you put together a slab or cylinder of the object material with the same length, and insert defects in this more simple shape, where access and measurement by another technique are more straightforward. If you detect the defects in these simple objects, you have achieved a level of contrast and spatial resolution that is necessary to inspect the actual objects for that type of feature. The difficulty here is that you have not matched the scatter properties of the object you are inspecting and you have not really accounted for issues with the articulation of the objects. The latter can be important if a radiograph is to be acquired at that particular angle or aspect. Both types of test objects are in use, but one fundamental remains: the more closely your test object matches the object to be inspected, the more confidence you have in the results of your inspection.

Once you have decided on a strategy for using a penetrometer, a step wedge and/or a test object, the question arises as to what to calculate from their images and what you do when calculations from the images of these test pieces show that the system has degraded. We expect this since x-ray detectors have a tendency to degrade with dose. First, some measurement of local image noise is useful. The acquired counts in the DR are the result of multiple stochastic processes, each with its own type of uncertainty. The measurement of local noise monitors the joint product of all of these processes. Second, if the requirements for detection are defined in terms of three-sigma criteria or a certain probability of detection, the estimate of local noise is a central quantity in these requirements. Lastly, it is important that the estimate of local noise be calculated from the processed image, which includes all the calibration corrections, metadata, and processing routines, since this yields the images used in the inspection.

In summary, the use of IQIs and phantoms or test objects provides critical information on the inspection of the object to be examined. This information gets more important as the number of processing operations is applied to the acquired raw data prior to viewing or analysis. Tracking the radiographic operation with the regular use of IQIs and test objects can readily detect when some aspect of the inspection technique is not working correctly and you are simply not inspecting the object as you expect. Also, once you have worked out how to make use of IQIs and test objects, this will help you better understand the inspection, and evaluating any change needed in the acquisition hardware or processing procedures is straightforward. A last point is that advances in x-ray inspection technology are, many times, by-products of an advancement in some other inspection modality. It can easily be true that a detector is mature or obsolete at the point at which the useful life of the detector is reached. The only resource you really have in hand is a thorough knowledge of your system and the inspection required.

12.8 DATA ANALYSIS AND INTERPRETATION

All of the calibration procedures, artifact reduction techniques, IQIs, and test objects notwithstanding, the goal of most radiographic data acquisition is to measure some property of the object (see Chapter 16 for examples). It is at this point that the amount of data analysis applied to a DR varies with the accuracy, precision, and depth of the inspection claims about the object. For instance, a

large, easily detected void in an object is immediately identified by a visual inspection of a radiograph. This may be all that is required to conclude the inspection. The object/assembly is defective, and no further analysis is needed. Notice in this case what does not need to be measured: the dimensions of the void, possibly the inner texture of the void, and/or the possible changes in the material in the vicinity of the void.

Alternatively, if the goal of the inspection is to quantify the void, quantify the material changes in the bulk of the object or at the void interface, then the properties of the acquired data need to include the spatial and contrastive properties required to support the inspection claims. If the analysis is performed by an automated routine, certain signal-to-noise requirements must be met, or the analysis is of no value. Further, additional data may be required, perhaps a radiograph of known different mixtures of different materials, i.e., a test object of sorts, so that a correspondence can be made between the material mix in the object and the known mixtures. A still different set of questions arises if you want to state something about the accuracy and precision of the measurement with the implication that if you perform this measurement many times, all the data are likely to fall within a certain uncertainty.

A different type of radiographic inspection is supported by sophisticated image transforms: wavelet-based transforms, image segmentation algorithms, multiscale multiresolution transforms, and/or specialized transforms intended to eliminate some intensity component in the radiographic image, i.e., scattered radiation (Bossi et al. 2002). For this type of inspection, the important piece of data is the transformed image, not the original image, with the understanding that the properties of the transformed image are sufficient to support the inspection claims. Now, the analysis applied to this type of inspection can be further complicated by various unknowns concerning the internals of the transform algorithm, which may be embedded in an application or in the system software. The point here is that the focus should be on the transformed image and, next, on the way in which changes in the raw data impact the transformed image.

For either type of inspection, evaluating any data analysis process or developing custom data analysis for the DRs unpacks into at least three tasks. First, perform a detailed review of the goals of the inspection and the dependencies on the properties of the image. For instance, if the goal of the inspection is the detection of porosity of a certain size in a certain region of the object, the contrastive performance of the system should detect voids that are slightly smaller than that change in the material chord length for that radiographic view of the object.

Second, before you measure the system performance, we suggest that you write down the system properties that would do well and the ones that would do poorly, relative to the goals of the inspection. Define a radiographic system with the spatial resolution and the contrastive performance that will detect or measure the features in the object 99% of the time. Also, define a system that will just make the inspection requirements with a substantial risk of measuring key features with substantial error. Calculate a probability of detection when things are not so good, to see how bad it can get. Our experience has been that even with bad signal-to-noise ratio, you can do well on some days, and then it falls apart. Third, the analysis should include a list of the individual dependencies on the system components; for example, the properties of the source, spot size, source spectral output and irradiance, properties of the detector, energy response, stopping power, integration time, and digitization noise. These can also include properties of the system geometry, the tolerance for the position of the object, etc.

From an analysis of the goals of the inspection, the first task, perhaps, is that a set of samples or test objects is determined to be required and should be used to generate key properties of the object to be inspected. This can be accomplished in a couple of ways. Fabricate coupons that, when applied to an object to be scanned, effectively generate a defect. This is similar to adding an IQI to an object. Another approach is to sacrifice a couple of objects and embed an array of defects or features for the inspection. Using either method, you have fabricated test objects that are from

the population of objects to be inspected and can be radiographed. For any type of inspection, images of these test objects will include enough differential counts in the acquired pixels to detect the defect or feature, or it will not. The same is true of the transformed image. The defect/feature can be identified/segmented, or it cannot. It is recommended that the features be made for a range of graduated sizes so that a number of defects/features will not be detected. In this manner, the spatial resolution and contrast limit can be established for this technique and this level of system noise.

A next step would be to acquire sample data for the range of thicknesses spanned by the object or for a set of objects with known problems. At the same time, it is vital to measure the properties of the source and the spatial resolution of the DR system of the technique at the object. Acquiring the sample data for a precise range of thicknesses in question can be somewhat straightforward for single-material objects, but finding known mixtures of objects to match the attenuation of multimaterial objects can be challenging, and approximations are necessary. Another useful task, measuring the x-ray source spot size and the spatial resolution of the DR system at the key location(s) in this acquisition, is covered in Chapter 14. The goal of this task is to convert the pixel values and their differences into differences in object length or attenuation or both, and to measure the modulation transfer function (MTF) to establish that there is enough modulation at the spatial frequencies required for making the measurements of interest. Data acquired in this connection can also be used to further correct for other artifacts, such as beam hardening.

The result of these tasks is a verified physical significance for the values in the radiograph and the test data to show how you did this going forward. At the end of this process, you should know, for example, what noise level, what change in spot size, what error in positioning will void the inspection. At the same time, from the test data, you know the likelihood that you will detect a change in thickness of a particular size for the object being inspected.

One aspect of the radiographic data analysis program outlined here has been a preference for performing calculations on radiographs in attenuation units rather than in some raw state. X-ray machine sources include both spectral falloff and spatial distributions impacted by heel effects. Analyzing radiographs that include both effects can get problematic. How is the feature you are analyzing impacted by either of these effects? How prominent are these effects in this particular radiograph? Acquiring a Φ_0 image and dividing out by this image neutralizes both of these effects (taking the natural log of the result only changes the scale). Analyzing radiographs that have been Φ_0 corrected enables the analyst or analysis routine to focus on the differential values due to changes in the object, which is independent of the issues with the x-ray source and detector. This does not say you cannot detect or dimension defects without acquiring and normalizing by a Φ_0 image. It is our opinion that the Φ_0 processed radiographic image tells you more about the object than the unprocessed image.

At this point, it is useful to reflect on all the operations that have gone into the DR that is the subject of analysis: (1) It is acquired for some integration time. (2) The raw images are usually processed by a dark-current and/or offset correction. (3) The processed Φ images can then be divided by the processed incident irradiance image, Φ_0 , and log-transformed or alternatively processed by some further multigain calibration protocol to remove fabrication differences for different parts of the detector. (4) The pixels can be further processed if it is determined that the counts include the result of an x-ray hit or the pixel has drifted out of calibration. With these operations in play, a coupon or IQI attached to the object enables the verification that the changes in a radiograph reflect the changes in the object.

The data analysis task for radiographs requires that some distinction be made for the types of features of interest in the inspection. We propose three levels of features in images as a guide for making claims about the state of the object. For the applications to be presented later and for the concepts presented in Chapter 14, we have summarized these differences in [Panel 12.1](#).

PANEL 12.1 Definition of Three Detection Terms

Feature is observable. The first level of identification is observing. This indicates that you visually observe an unusual pattern in the pixels in a radiograph. Consider the case where you acquire a line-out of pixels across this observed feature, and the changes in values do not clearly emerge from the local noise variation. It may be true that this image is indicating the presence of a feature, but you cannot say you can be sure that you will observe this feature in the next radiograph. For example, small changes in source output, object positioning, the feature could be on the order of a pixel, and a different partial volume position may mask the observation of this feature or noise may cause the impression of something real.

Feature is detectable. The second level of identification is detection, in this case, when you acquire a line-out of values across a feature; the center intensity in the feature is at least one local variation width greater than the average value. The section on automated defect recognition in Section 15.6 includes examples of features detectable above the local noise threshold. For a CT example, Figures 12.12 and 12.13 illustrate an observable and detectable feature.

Feature can be measured. The third level of detection includes a feature that is large enough to measure a dimension. In this case, the intrinsic contrast of the feature is larger than the local noise variation, and the size of the feature is greater than the modulation limit for the spatial

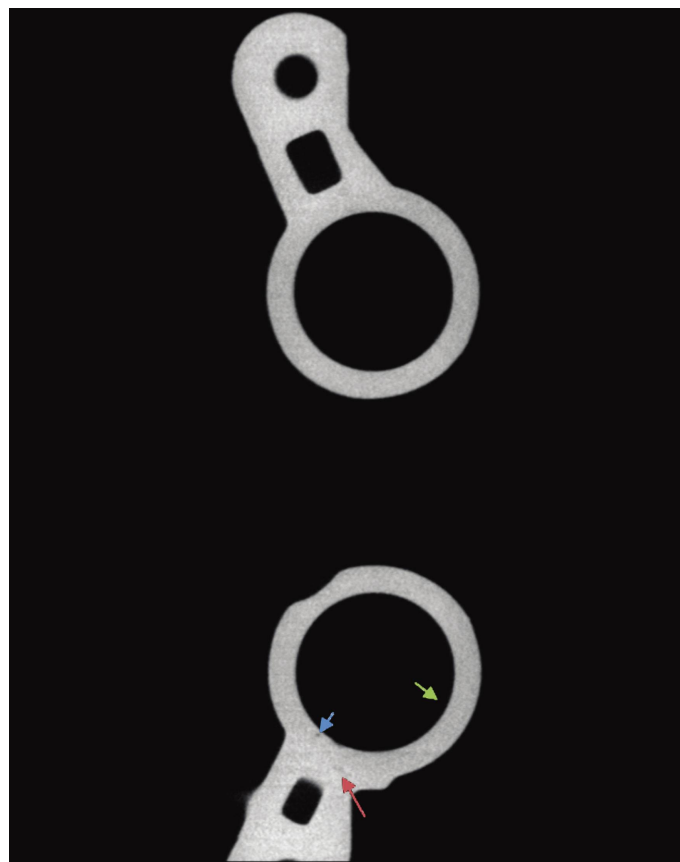


FIGURE 12.12 CT cross-sectional image of an aluminum casting. The locations are identified for a detectable void feature, highlighted by a blue arrow, and an observable feature, highlighted with a red arrow. 1-D profiles or lineouts for these features are shown in [Figure 12.13](#). The line-out for the wall shown in [Figure 12.14](#) is located by the yellow arrow.

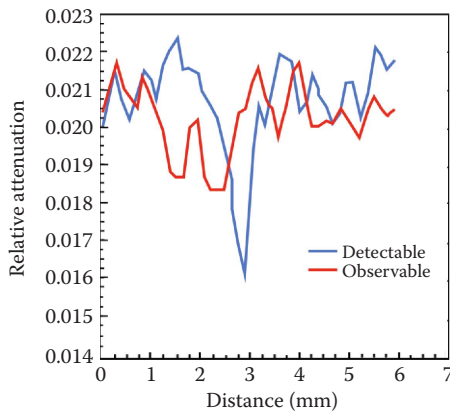


FIGURE 12.13 Resultant 1-D profiles or line-outs for a detectable and an observable feature as highlighted in Figure 12.12.

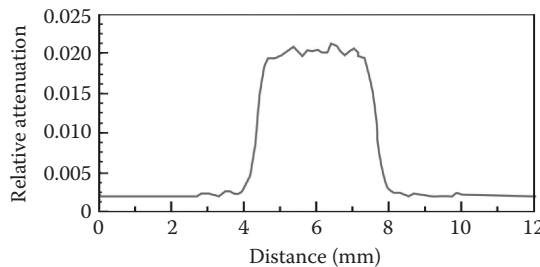


FIGURE 12.14 Resultant 1-D profile or line out across a wall from the aluminum casting shown in Figure 12.12.

resolution of this acquisition. Consequently, you can measure when the feature starts and stops and develop protocols for consistent measurement of such features. For example, the dimension of the Al casting wall can be measured. A 1-D profile or line-out across one of the walls (see green arrow) for the Al casting shown in Figure 12.12 is given in Figure 12.14.

Dimensional measurements highlights an important difference between DR and CT. In DR, you never really know the thickness of the dimension in the direction of the x-rays without some supporting assumptions. Even after extensive calibration, it can always be true that the change in attenuation could be a change in thickness or a change in the material attenuation, i.e., the presence of some impurity. Of course, if you know that the object cannot have any impurities, then the attenuation is due to a change in thickness or density, or vice versa. Or if you can effectively divide out or neutralize the change in attenuation due to thickness, the goal of some multiscale multiresolution transforms, then you can make the measurement of the changes in the material composition and/or density. The point is that with DR, you assume something about the state of the object to make a dimensional measurement or about the dimension to make a material measurement.

In summary, data analysis for DR involves substantiating claims connecting the changes in the acquired pixel values to the changes in the thickness, shape or composition of the object. This task needs to navigate, or take into account, the particular chain of calculations used to process raw data into the data used in the inspection. It is recommended that additional physical testing tools be developed to guide the analysis and measurements be acquired to determine performance. Lastly, analysis may require some method or criteria for describing what you consider to be detected

or observed or what you consider to be an artifact. In each inspection, you have to make some decision(s) or develop a guide about what you consider to be a detection, what you consider to be a likely or observable feature of the object, what can be measured and what you consider to be an artifact. The point is to be as clear as possible about the decisions and criteria used to make those determinations.

PROBLEMS

- 12.1 How much cross talk is there for an LDA whose detector elements have a thickness of 1 cm, a width of 2 mm, a height of 4 mm and a fan angle of 2° , 4° , or 8° ?
- 12.2 Why should the noise increase in locations with thicker chords of a material? Be specific and characterize the different-thickness chords with probability distributions mentioned in this chapter.
- 12.3 You are inspecting for voids as small as 0.127 mm, in 50.8 mm of aluminum. What tungsten energy spectrum would you recommend? What beam filtering, if any, and why?
- 12.4 For the circumstance in Problem 12.3, what kind of area-array detector would you recommend, with what scintillator? Include the scintillator material and thickness.
- 12.5 In Problem 12.4, for all the choices you have made, what level of contrast ($\Delta D/D_1$) do you calculate?
- 12.6 For the inspection described in Problem 12.3, assuming no detector noise, what does the local noise sigma have to be to be able to perform the inspection? What if the requirements of the inspection are to detect a change in thickness with three-sigma reliability? How does this impact your choices?
- 12.7 Consider a radiograph with an average level of counts of 15,000 outside the object, with a minimum of 600 counts through the thickest portion of the radiograph. What kind of outlier removal technique would you recommend? Why?
- 12.8 After acquiring many DRs for a CT scan, you discover a large difference in the number of bad pixels by subtracting the dark current that you acquired at the start of data acquisition from the dark current you acquire at the end of data acquisition. What do you do? What if you discover this difference between two dark-current images acquired a week apart?
- 12.9 What pixel size would you choose for digitizing an image acquired with a DRZ-Enhanced screen? How about for DRZ-Fast? DRZ-Standard? or DRZ-Fine? Why did you make your choice? Compared to DRZ-Fast, what are the implications for scanning speed from the scintillator-pixel-size combinations you have selected for each of these scintillators? (Use a 100-kV spectrum, 5 mA, filtered with 2 mm of aluminum as your source.)

13 Computed Tomography

13.1 INTRODUCTION

In this chapter, we present the key ideas involved in computed tomography (CT) reconstruction algorithms and the basics of CT data acquisition and discuss sources of artifacts in CT reconstructed images. In passing, we will point out the significance and range of application for CT reconstructed voxels. This last topic will be covered quickly in this chapter since it is elaborated in detail in the sections on applications given in Chapter 16, where the use of CT voxel data for inspections is demonstrated. In this chapter on CT algorithms, we will focus on components and concepts in CT algorithms and will describe the important dependencies for specific routines. The point of this description of algorithms is not to present a rigorous treatment of the mathematics of CT reconstruction, but to set up the discussion of artifacts in CT reconstructed images. It is our experience that the difference between the inner loops of CT reconstruction algorithms across vendors or systems is surprisingly small. Most of the differences in the implemented algorithms reside in the preprocessing methods for the raw data and/or specifics related to the particular type of scanning (see Chapters 11 and 12) and/or hardware idiosyncrasies.

Regardless of the specific issues and alternatives for processing CT data, the user of CT data should be able to identify and understand the source of different artifacts and be acquainted with methods for lessening their effects where possible. Ultimately, the ability to inspect an object with CT reconstructed data depends on the measurement accuracy of acquired data and the details of the way in which the acquired data are used to estimate the CT voxel values. Often with CT inspections, it is also important to identify CT artifacts and separate the changes in voxel values connected to a source of artifacts from real changes in the object/assembly. The importance of a claim about the state of the object depends on both knowing and sorting the artifacts from the object features. Since CT reconstructed images are a strong function of the properties of the acquired data, much of the material presented in earlier chapters will be used throughout this chapter.

A number of excellent texts exist detailing the mathematical basis for CT reconstruction, such as that of Natterer (2001), and a particularly accessible description of reconstruction algorithms can be found in the books by Kak and Slaney (2001) and Barrett and Swindell (1981). The book by Kak and Slaney is the coordinate system basis for the treatment in this book. The reader is encouraged to access these texts or others for investigation of details of interest in CT reconstruction mathematics as well as algorithms. As indicated above, this description of CT reconstruction will focus more on key steps in CT processing and reconstruction and how each step impacts the calculation of the volumetric data. As such, less time will be spent on the details of the inner loops of CT reconstruction algorithms.

At the end of this chapter, the reader should understand

- The basic ideas and operations involved in CT reconstruction
- Data acquisition for CT reconstruction
- Types of CT reconstruction algorithms and some appreciation of their differences
- Artifacts in CT reconstructed images
- Sources of artifacts in CT reconstructed images and strategies for remediating or removing the artifacts

13.2 FOUNDATIONAL IDEAS FOR CT IMAGE RECONSTRUCTION

Fundamentals of CT image reconstruction begin with the radon transform (Radon 1917), considered here to be the integration of the values through an object function along the lines from a source to a detector from a particular direction. A sketch of this integration or projection operation for a parallel-beam geometry system applied to three solid disks with the same attenuation is shown in Figure 13.1. Also in this figure are the results for three different angles around the object function.

Reviewing the material from Chapter 11 and referring to Figure 13.1, the vector of values resulting from the integration over the object function depends on the object constituents and the particular angle defining the direction of the integration relative to the object. Consistent with the previous discussion, values of the vector resulting from the integration are referred to as ray sums, which are the sum of all the object function elements along those ray paths. In this context, the point of a CT reconstruction algorithm is to recover the object function from some set of ray-sum measurements.

Referring back to Figure 13.1, it can be noticed that each view from each rotational angle conveys more information about the object. From one view, it can be surmised that there are at least three distinct objects. From that same view, it can be surmised that the objects are roughly of the same material or have at least the same projection value. Other features of the object require more views, for instance, the exact shape of each object and their precise juxtaposition. A few questions at this point might be as follows: how many ray-sum measurements are required to recover the object function? Is there some lower limit? With what precision do we want to measure the object function? What precision is required to perform dimensional measurements of the object internals?

Answering the above questions, that is, determining a measure of the necessary data for object function recovery, depends somewhat on the goals of the inspection. If you only want to know how many big objects are there, a few views may be sufficient. If you want to make detailed dimensions with lots of accuracy over the entire region spanned by the object function, a much larger number of views are required. Also, what about the scanning regime? Can you acquire a lot of views in a small angular range corresponding to a region of interest or do you always have to acquire equally over the entire angular range, or do you need to just acquire at a distinct set of angles? Answers to these questions are covered in Section 15.5, which includes a discussion on tomosynthesis and comparison to CT, but as indicated, the goals of the inspection and the shape of the object are fundamental.

Another important consideration at this point is that nothing has been mentioned about the physical mechanisms accounting for the integration through the object function. This is one reason why CT image reconstruction algorithms have found application in a wide variety of scientific

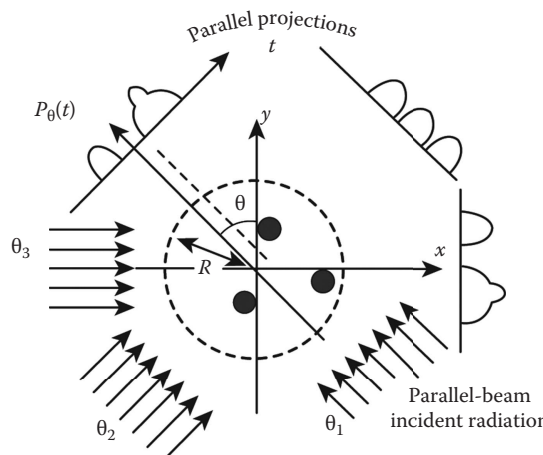


FIGURE 13.1 Illustration of parallel-beam system ray-sum projections for three different angular positions around the three solid disks.

measurements. It can be used for all circumstances in which some energy penetrates an object or is transmitted through the object or emitted from the object with the result of the interaction recorded by some detector. For example visible light, electrical resistance, etc. can be cast into the CT image reconstruction mechanics with more or less success.

General circumstances aside, our discussion is focused on x-rays. The object function is composed of per-voxel x-ray attenuation (in most cases, the total attenuation integrated over energy). In turn, we consider ray sums to be physically realized at each detector element or as individual pixels in x-ray transmission acquisition acquired with various detectors, converted to attenuation units, and are described by Equation 5.13 (see Chapter 5) for a monochromatic source and by Equation 5.19 for a polychromatic source. Measured ray sums and their components are best represented as instances of Poisson random variables Whiting et al. (2006) and subject to the kinds of issues and limitations presented in Dainty and Shaw (1974). As pointed out in Dainty and Shaw, if the average for the ensemble of ray sums is close to saturation, you likely have some saturated pixels in the mix. Also, if you do not have enough transmission to get past the threshold for digitization, the measurements are simply unreliable.

In CT reconstructed images, voxel values are in units of attenuation per voxel; the length of materials (y_ℓ) in Equation 5.19, reproduced here for convenience,

$$\ln\left(\frac{\int \Phi_0^P[S(E)]dE}{\Phi^P[S(E), \bar{Z}, \bar{\rho}, y_\ell]}\right) \approx \sum_i^n \mu_m^i(\bar{E}, Z_i) \rho_i y_\ell^i, \quad (13.1)$$

for example, is gone and is now

$$\mu_m^i(\bar{E}, \bar{Z}_i(\bar{E})) \bar{\rho}_i(x, y, z), \quad (13.2)$$

where we have labeled E , Z , and ρ to represent averages over energy, materials, and densities, respectively, in the voxel. If data are from a monochromatic source, then it is just E , but the averaging over materials and densities remains. Lastly, voxels include the 3D location coordinates (x, y, z) . It is important to notice the different types of averaging going on: (1) over energy and (2) over attenuation and density within a voxel. The additional significance of this voxel value unpacks into the relative proportions of the x-ray mechanisms resulting in the total mass attenuation and just how that particular ray sum when combined with other ray sums contributes to the measurement of the content of the object function. [Figure 13.2](#) contains an illustration of the definition of a voxel value from the sketch of a CT volume generated from the scan of a waste drum.

A review of CT data shows how quickly things get more complicated than in the above illustration. Consider the CT scan of a single material object with a polychromatic source. An image of a CT reconstructed slice through the object function of a cylindrical test object and a constituent digital radiograph—from that acquisition—with the direction of the x-rays indicated is given in [Figure 13.3](#). This object is made up of a single material (Delrin), and the features of the object are fabricated to be in a particular pattern. In particular, this object was made to support two of the common methods for calculating the modulation transfer function (MTF) from CT data (more about this in Chapter 14). The interpretation of the voxels is straightforward: the voxel value corresponds to the value of the total attenuation at that energy or for that energy spectrum as recorded by the measurements from the detector as obtained by a reconstruction. A CT voxel is a sum over the projection data. Voxels in this case are measurements of Delrin attenuation. There should be no other materials except for air and/or possible anomalies in the Delrin. However, by looking more closely at the CT slice in [Figure 13.3](#), there is an apparent decrease in voxel attenuation value from the outside of the cylinder to the center. Also, notice a few ring-like features in the CT reconstructed

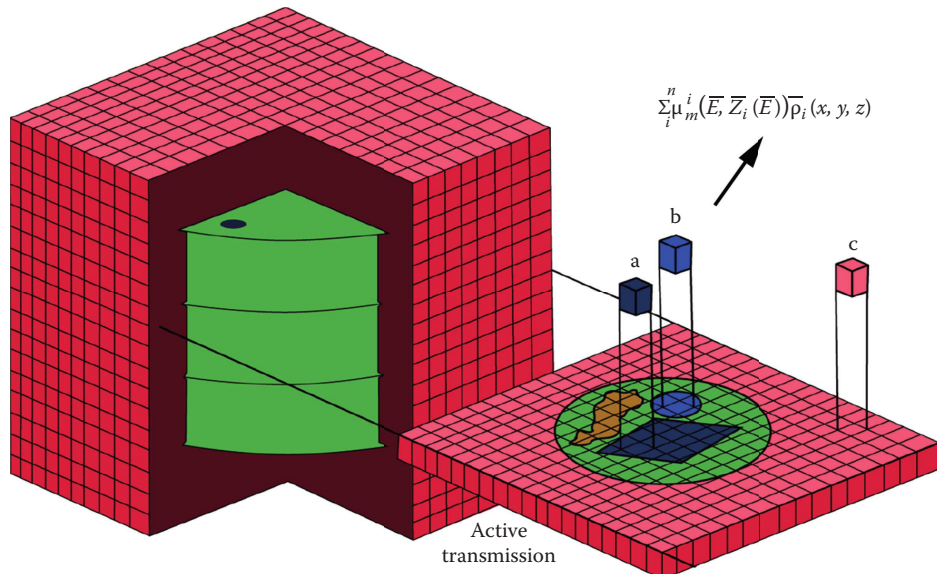


FIGURE 13.2 Illustration and definition of a voxel value in a CT volumetric scan of a waste drum, for three different materials in locations a, b, and c. Note that the density, ρ , is moved outside the parentheses since we are using the mass attenuation, μ_m .

slice. Are these features part of the fabric of the Delrin MTF test object or are they a result of some other mechanism?

For x-ray transmission data, interpreting the content of ray sums via Equation 5.19, reproduced in Equation 13.1, introduces a number of complexities for the measurement of the object function. First, the elements of the object function are in terms of total attenuation. As discussed in Chapter 5, the particular mechanism constituting the majority of the x-ray attenuation changes with energy and so does the significance of the measurement of the object function. For instance, at high energies ($E > 400$ keV), the majority of the x-ray interactions are primarily Compton events, and the total attenuation is more of a measurement of electron density than the atomic number of materials. Second, since Equation 13.1 represents the measurement from a polychromatic source, the ray sum is an integration over two dimensions: the geometric ray path and energy. For many machine sources, the shape of the incident energy spectrum is not a simple function as shown in [Figure 13.4](#). Third, if the object function is complicated, i.e., multiple materials with a complicated geometry, the radiograph will reflect all of that complexity and may hide some of the complexity if the energy is not sufficient to penetrate that part of the object. Alternatively, things get simpler if the object is composed of just one material and simpler still if the beam is monochromatic to reduce the complexity of the input spectrum to a single energy (see Equation 5.13 and compare it to Equation 5.19).

These comments are meant to further emphasize the contrast between the rather simple model of the ray sum for a monochromatic vs. a polychromatic source as well as a single vs. multiple element object function. The differences are important and will come up in the discussion of artifacts. Secondly, and more important, the best interpretations of CT reconstructed images are built upon the knowledge of the image-forming context: what energy was used, what detectors, what geometry, and what likely artifacts. Third, there may be no substitute for knowing a lot about the object, but this is often embedded in the goals of the inspection.

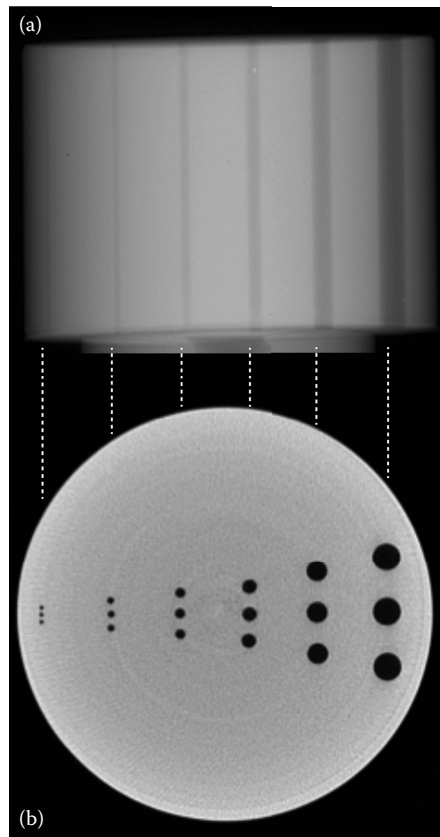


FIGURE 13.3 (a) X-ray attenuation multiplied by path length digital radiograph from an MTF test object. (b) Cross-sectional (transverse) CT slice. These data can be used to calculate the MTF of a CT system.

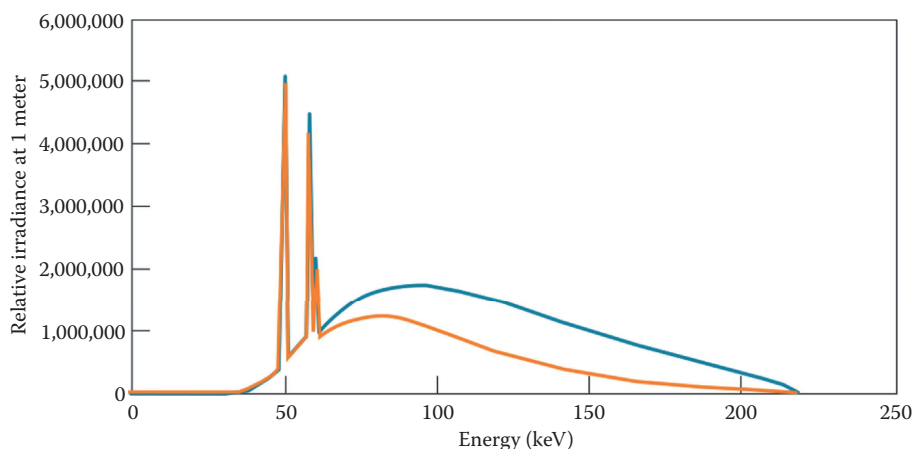


FIGURE 13.4 Modeled 220 kV W-anode x-ray spectrum filtered by 2 mm of Cu (blue curve) and the filtered spectrum as detected by 1-mm thick thallium-doped CsI scintillator (orange curve).

13.3 CT DATA ACQUISITION AND PROCESSING

For a variety of reasons, acquiring a complete data set for CT reconstruction of an object function can be done in a variety of ways. Considerations for completeness follow from the mathematical foundations for CT image reconstruction (see, for example, Kak and Slaney 2001; Natterer 2001), but are also impacted by many practical considerations. One complete set of ray sums is the integration/projection through an object function, with no missing pixels, with complete coverage of the projected object. In complete coverage, the entire object must be within the field of view with space or air around the object for the entire scan, and the projection data are acquired at many angles over a 180° angular range for a parallel-beam source–detector geometry. Three conditions have been mentioned here: (1) pixels contain measures of positive attenuation where the ray sum traverses some part of the object function, i.e., data are positive definite; (2) the entire object is within the field of view, i.e., finite extent; and (3) the scanning of the object covers the correct angular range for the beam geometry; for completeness or Tuy's condition, see Natterer (2001). Given these conditions, obtaining this data set requires a synchronized operation of measuring or recording the transmitted irradiance after the object, reading the detector, and moving to the next angular position for the next recording/measurement/reading or data acquisition. It is not important whether the object rotates and the source–detector stays fixed or the object stays fixed and the source–detector is rotated about the object. The acquired data set will be the same. Additionally, the object or source–detector can be operated at some constant speed; the only consequence of this operation is motion blur that can result from interaction of the measurement and the motion. However, if the amount of motion blur per measurement/read time/distance is less than the spatial resolution of the system, the impact will be small to insignificant.

Given this interplay of acquisition and motion, it may be clear why all CT systems involve four components: (1) x-ray source, (2) detector, (3) motion control, and (4) computers. Computers are used for acquisition, processing, reconstruction, analysis, display, and reporting. The operation of all the components has to be coordinated to obtain the data set, and the details of that acquisition need to follow the raw data to put all the views in their proper order. The components work as a system to obtain the ray-sum data with different specific hardware and for different geometries. Two different typologies have emerged for the description of CT data acquisition: one that emphasizes differences in system design developed chronologically, and the other emphasizing the differences in source–detector geometry.

In the first typology, the types of CT scanner acquisition have been described in different generations as shown in [Figure 13.5](#). First generation is the simplest and the most time consuming, since only one ray sum is acquired and read out at a time and the source/detector or object is translated to a different position for the next adjacent ray sum. Once the entire object has been covered plus a few ray sums on both sides of the object (or a line across the part has been covered), the object is rotated and another projection is acquired. This context matches the parallel-beam gauging example described in [Chapter 11](#). In second-generation scanning, the detector is a multidetector element array, but often does not span the entire width of the object, and as in first-generation scanners, both translate and rotate motions are executed to obtain the types of projection of the entire object function. The second-generation scan time is shorter, as you acquire data from many detectors with each acquisition, and it is a smaller number of translation steps to cover the object. For third-generation scanning (or rotate-only), the detector is wide enough to cover the object with extra space on both sides of the object, and the object/source–detector only needs to be rotated to acquire the data over the angular range. In fourth-generation scanning, there is a large stationary ring of detectors, and only the x-ray tube is rotated about the object. The next type of CT is called helical CT. In helical CT, an alternate strategy is used to continuously rotate and continuously acquire data as the object is smoothly moved though the source–detector rotating gantry; the resulting trajectory of the x-ray tube and detectors relative to the object traces out a helical or spiral path.

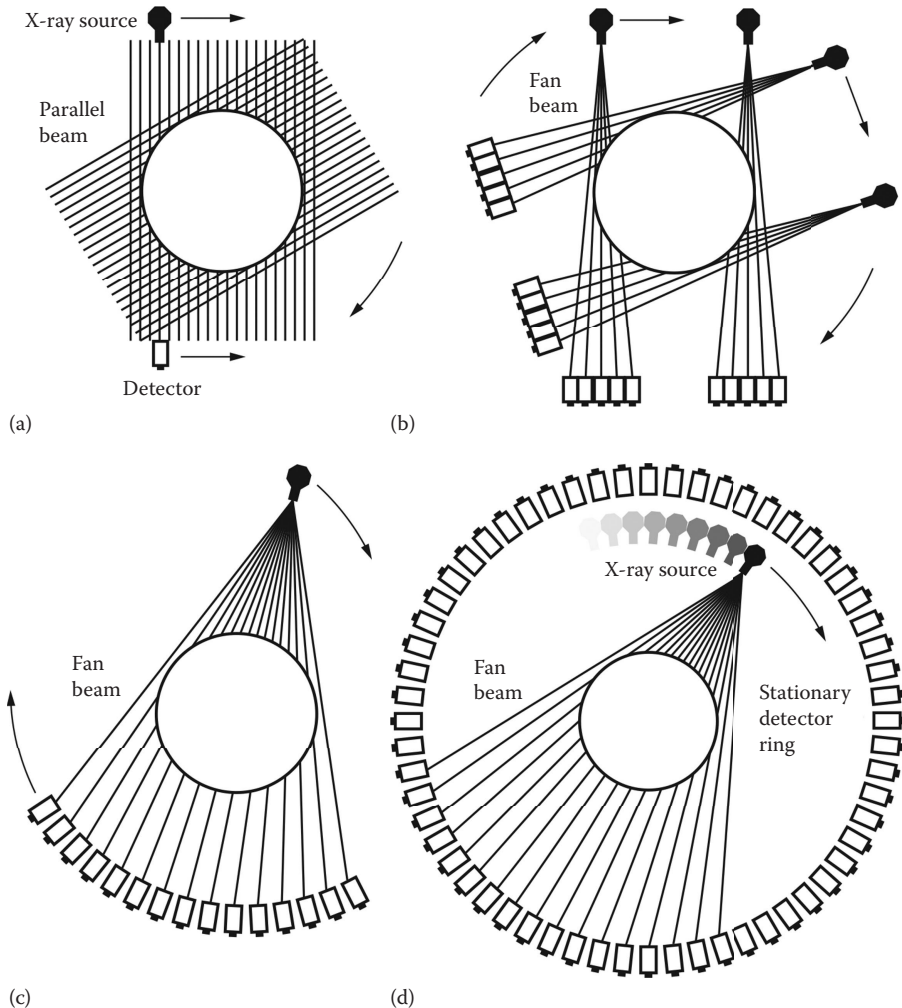


FIGURE 13.5 First- through fourth-generation CT scanning geometries. (a) First generation uses a single well-collimated source and detector, and the object or source/detector pair is translated and rotated. (b) Second generation uses multiple detectors but does not cover the entire object so the object or source/detector is translated and rotated. (c) In third generation, the entire object fits within the multiple detectors and only requires rotation of the object or source/detector. (d) Fourth generation has a ring of detectors and only the source needs to be rotated.

Fifth-generation CT uses a scanning-electron-beam x-ray source and is referred to as electron-beam CT or EBCT. It was developed by Boyd and Farmer (1986) in the mid-1980s to minimize motion blur during cardiac CT. The cardiac EBCT scanner has a partial (semicircular 210°) anode and opposing detectors. It is not shown in Figure 13.5, since it is not commonly used in industrial or NDE CT. An even newer generation CT scan geometry uses a stationary gantry in which there is a ring of both sources and detectors. The sources are fired individually or some combination of multiple sources firing at the same time. The result is obtaining different angles for CT. Common to all of the scanning types present in the generation typology is an element of source-detector collimation, where the source is reduced to a point, a line, or a cone. For more on the different CT generations, see the article by Goldman (2007).

A second typology for CT scanning overlaps with the generation categories, but emphasizes the differences in the physical source–detector geometry and was covered previously in Chapter 11. Figure 13.6 contains illustrations of the three different types: (1) single-detector pencil-beam; (2) linear-array detector fan-beam; and (3) area-array detector cone-beam scanning. In this typology, the single-detector system closely resembles the first-generation-type scanning requiring translating for each ray sum and the rotation. Both the second- and third-generation scanners include multielement detector arrays, usually in the form of a line to capture a slit of radiation from the source and could be used to scan with translate-rotate or rotate-only depending on whether the detector spans the object width. The area-array detector introduces a new modality into this typology. In this type of scanning, a cone of radiation is used to illuminate a large solid angle of the object, and a large region of the object is covered in each acquisition.

It should be noted here that the data sets acquired from these different systems can be very similar, since they can be reshuffled into the same format independent of the sequence of operations used in acquiring the data. Consequently, the same reconstruction algorithm can be configured to service data from a variety of different scanners. Also, notice that you find many of the same ray sums between the different geometries whether parallel, fan, or cone beam. In particular, you can re-bin the ray sums from one geometry into another geometry (Kak and Slaney 2001). The general acquisition goals for all the different systems are the same. Acquire ray sums that cover the entire object function, and acquire a certain number of views around the object. Also, acquire enough of the projected area to cover the entire object, or, as we shall discuss, we need just over half of the object and the projected center of rotation must be in the acquired field of view for the entire data set. This is referred to as a half or offset scan.

The goal of the processing steps applied to CT data is to obtain the best measured estimate of the ray sum, the integration of the transmitted irradiance at that particular rotational angle between

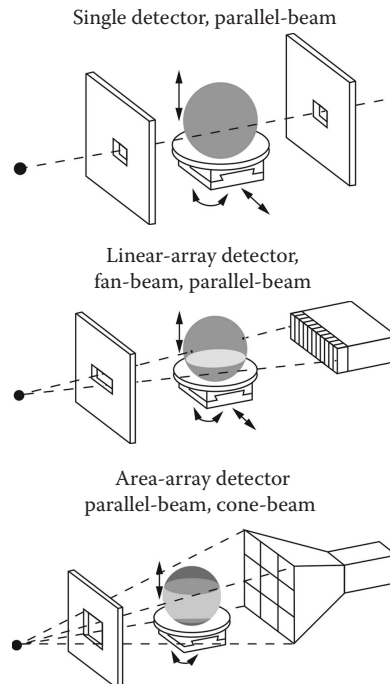


FIGURE 13.6 Different types of CT source–detector geometry. At the top is a first generation parallel-beam CT system. In the middle is either second- or third-generation parallel- or fan-beam CT system. At the bottom is either a second- or third-generation CT parallel- or cone-beam.

the source and the detector. As depicted above, and represented in textbooks, this somewhat fictional quantity is perfectly digitized at a rotational angle known to very high accuracy and with the attributed coordinates reflecting a perfect alignment of the source, the object stage, and the detector. Also, considering this idealized quantity, every part of the quantity of the ray sum and the variations in ray sums is due to the object, not to scatter from the cabinet, room, or stage platform; scatter in the detector; or individual gain-offset behavior for that particular detector. The nonidealized, actually acquired ray sums can of course include a variety of troublesome signal components not related to the object function (as mentioned in Chapters 10–12). However, as shown in Chapter 12, data or metadata acquired before or after the sequence of rotational views can assist in isolating or estimating a measured quantity like ray sums (Whiting et al. 2006).

Restating the results from Chapters 10–12, different CT scanner and acquisition types include important differences at the pixel (a digitized ray-sum value) and at the scanner level. Radiometric pixels can include primary and scatter components, and a portion of the detected scatter signal component can arise from interactions in the object. X-ray scatter can be very small at low (approximately tens of kiloelectron volts) energies and high at high (megaelectron volts) energies. Also, the scatter contribution can arise from the detector, the room, etc. As scan data include more collimation, they are more quantitative (better primary-to-scatter ratio), but data acquisition times can be slower. For the same reasons, highly collimated data can require less preprocessing. For example, for a single-detector system, all data are equivalently digitized; for multiple-detector systems, differences between detectors are commonplace but can be remediated with additional corrections to ensure that measurements acquired at different detectors are comparable. As indicated in Chapter 12 and shown here, the types and nature of the preprocessing follow from the different physical types of scan data as given in Table 13.1.

Two preprocessing steps in Table 13.1, normalizing by Φ_0 and calculating ray sums, are foundational for all subsequent processing and CT image reconstruction. Both of these steps involve the acquisition of the values of the source irradiance without the object in the field of view (the Φ_0 image), referred to as incident irradiance. Consequently, unlike acquiring data for radiographic inspection, acquiring CT data always includes acquisition of Φ_0 regardless of the detector. The exact detail of the Φ_0 values can vary with the detector, but the protocol for scanning requires the acquisition of a Φ_0 signal or some way of accounting for Φ_0 from a calibrated detector. Some flat-panel detectors require a calibration operation from which a measure of Φ_0 can be obtained. With a measurement of Φ_0 in-hand raw ray-sum data, Φ , can then be converted to the attenuation units required before CT reconstruction algorithms can generate an estimate of the object function.

Notice from Table 13.1 that a number of other preprocessing steps are identified in addition to the Φ_0 normalization and attenuation calculation. At this point, notice the number of preprocessing steps corresponding to the type of system and the type of detector. As mentioned in Chapters

TABLE 13.1
Comparison of Compute-Based Operations by Type of DR/CT System

Step	DR/CT System Configuration		
	Single	Linear	Area
Calculating ray sums	X	X	X
Normalizing Φ_0	X	X	X
Individual detector response corrections		X	X
Detector linearity corrections		X	X
Corrections for dark current		X	X
Corrections for detector blur			X
Restoring ray-sum geometry			X

10 through 12, all of these steps are corrections intended to account for small differences between multiple detectors that do not have anything to do with the object or the x-rays, and to account for the polychromatic character of the x-ray source. Performing these corrections substantially reduces image artifacts. We will show the impact of some of these effects in [Section 13.7](#), Artifacts in CT Reconstructed Data, but the precise effects on a reconstructed image vary with the acquisition method and the reconstruction machinery.

13.4 CT DATA PROCESSING AND THE IMPORTANCE OF Φ_0

Notable in the list in [Table 13.1](#) is the Φ_0 normalizing step. The acquisition of a Φ_0 image is particularly fundamental for CT systems. Notice that this operation is applied to every acquired pixel. Consequently, whatever artifact or idiosyncrasy is present in the Φ_0 image is written into every pixel in the acquired radiographic data. Consider the physical effects included in the Φ_0 measurement for a CT system (see signal components covered in Chapter 10). For the single-detector highly collimated system, the value of Φ_0 represents the irradiance at that energy impinging on the front face of the object. For the linear detector array system, the value of Φ_0 , for all the multiple detectors, represents the same quantity, but at the particular location of that detector and subject to the particulars of the digitization for that detector. Lastly, for area-array detector systems with loosely configured collimation, the detectors can include a scatter component from the particular configuration of the cabinet or room containing the CT system, which does not have any connection to the object.

The fundamental experimental principle here is to acquire Φ_0 by only removing the object from the field of view. Consequently, whatever was in the cabinet/room during the acquisition of the CT data should be left in place for the Φ_0 measurement. For instance, in some applications at Lawrence Livermore National Laboratory (LLNL), we are required to surround high-value objects with a seismic shield. The shield is usually a cylinder of acrylic material to ensure that the object stays on the stage should an earthquake occur during scanning. In these cases, we simply remove the object and leave the seismic shield in the field of view for the measurement of Φ_0 (see Problems).

As the measurement of Φ_0 is a key part of calculating the value of the ray sum, it is important to remove any part of the acquired Φ_0 signal that is unique to the acquisition of that pixel in the Φ_0 signal. In particular, some multiple detector configurations are susceptible to hot pixels or direct x-ray hits, which can occur at random occasions and in random locations in the detector array. If at all possible, these values should be remediated by singularly processing the Φ_0 image prior to combining the values of Φ_0 with the x-ray transmitted data through the object, Φ . As mentioned in Chapter 12, experience has shown that it is better to estimate or model a likely value of Φ_0 rather than include an erroneous value into the reconstruction process. Any one of the different outlier removal techniques mentioned in Chapter 12 can be used for this operation.

Different techniques for normalizing by Φ_0 to adjust to the effects of source drift and/or detector buildup, which increased digitized values for the same irradiance, are important tools for producing quality data across the different applications of digital radiography (DR)/CT. It is common at LLNL to normalize the entire Φ_0 image from a comparison between the acquired view of Φ and the values of the Φ_0 image on a small region (referred to as a postage stamp at LLNL) in the acquired Φ image. Many commercial scanners include a reference detector for this same purpose. Consequently, the value of Φ_0 applied to that rotational view is scaled so that the measured irradiance matches the postage stamp or reference detector in the acquisition. In this same connection, buildup, i.e., increased digitized values for the same irradiance over time, in the detector can occur in the course of scanning, and the measurement of Φ_0 at the end of the scan is sometimes the most reliable estimate of Φ_0 , since it reflects the thermal equilibrium achieved among the room, the detector, and possible active cooling mechanisms; thus, it can be the most representative Φ_0 . An example of detector buildup is given in [Figures 13.7](#) and [13.8](#). However, the added buildup of the signal can result in saturated pixels or close to saturated pixels, which for digital detectors is equivalent to no information. In this case, it is better to reacquire the Φ_0 measurement at a lower

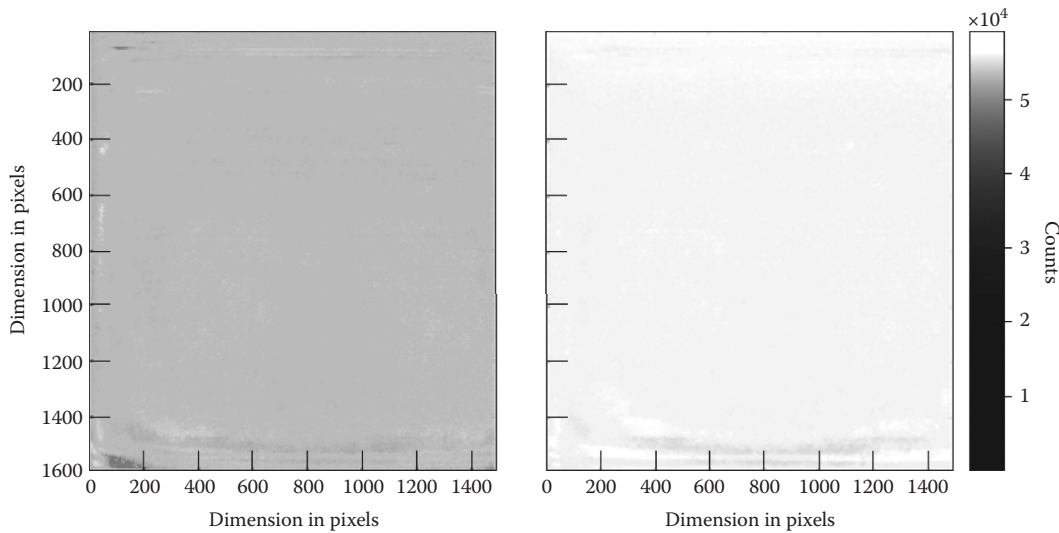


FIGURE 13.7 Two 9 MV Φ_0 radiographic images for a CT scan acquired over about 4 hours, 1800 views, 360° , and 1.5 s integration time with 4 frames averaged. Note the increase in the measured Φ_0 from the start to the end of the data acquisition represented by the image on the left and right, respectively. 1-D line out plots for each image are shown in Figure 13.8.

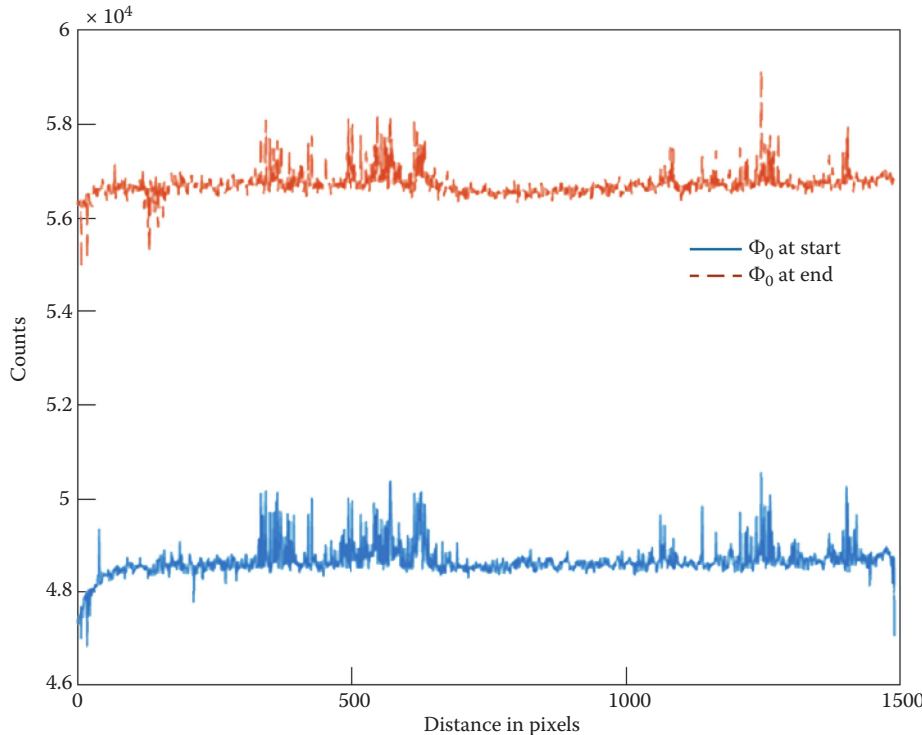


FIGURE 13.8 1-D profile plots for the two 9 MV Φ_0 radiographic images shown in Figure 13.7. Note that the counts increased from around 48 k to 57 k over the 4 hours CT scan.

source current or, for some detectors, this is equivalent to acquiring Φ_0 with less integration time to obtain a saturation-free Φ_0 image. In this case, the postage stamp or reference detector measurement can be used to adjust the Φ_0 value to track with the irradiance in the acquired rotational view. The reader is reminded of the fundamentals for transmission measurements presented in Dainty and Shaw (1974).

The measurement of Φ_0 from polychromatic sources can also include drift in the spectral content of the beam. Also, for some machine sources, the x-ray source energy spectrum is not uniform over the entire field of view. In this instance, it is advisable to position a reference such as a metal strip in the field of view to measure the kV drift (Ying et al. 2006) from view to view or across the field of view. In this way, variability in the measured attenuation from a change in the spectrum can be distinguished from real change in the material attenuation. This last aspect of polychromatic sources emphasizes the difficulty of performing quantitative scanning with current-integrating area-array detectors and polychromatic sources. It can be the case that for small differences in source energy and thus attenuation at the object result in artifacts. The detector is measuring what the x-ray spectrum is producing (e.g., the source spot moves and splits into two spots or the energy spectrum changes), scatter-vignetting from incorrect collimator placement and what passes through the object. The apparent difference in attenuation can be a property of the source, the collimation, and not just a property of the object. As mentioned in Chapters 10, 11 and especially 12, scanning regularly with known test objects, phantoms, or standards may be the only reliable way to determine the extent to which the reconstructed data are accurately measuring properties of the object and not reflecting the variation in the source spectrum or detector response.

13.5 CT RECONSTRUCTION ALGORITHMS

The ray-sum measurements reflect the integration of the x-rays along rays or lines at some angle for some source-detector and object geometry. For back-projection-based algorithms, the attenuation content in the projections is summed into the voxels. Referring to Chapter 11, consider the case of the parallel-beam geometry. Following the development in Kak and Slaney (2001), and with respect to [Figure 13.9](#), the line defining the object function, $f(x,y)$, at detector position t , in a parallel-beam geometry at rotational angle θ , is $t = x \cos \theta + y \sin \theta$. In this equation, x and y are the coordinates of the object function, and t and θ are the coordinates in the projected space. Converting x and y to polar coordinates: $x = r \cos \phi$, $y = r \sin \phi$, for r and ϕ , the same line can be described as $t = r \cos(\theta - \phi)$. The integral of this line indexed by t can be represented as the integral of the convolution between the delta function $\delta(x \cos \theta + y \sin \theta - t)$ and the object function defined as $f(x,y)$ where

$$P_\theta(t) = \iint f(x,y) \delta(x \cos \theta + y \sin \theta - t) dx dy = -\ln \left[\iint [S(E)] e^{-\mu(E,Z,\rho)\ell} dE d\ell \right]. \quad (13.3)$$

The above equation defines $P_\theta(t)$ as the Radon (1917) transform (Kak and Slaney 2001) through an object function at angle θ , and we have added that we are interpreting this Radon transform through the object function to be the x-ray exponential attenuation through the object along those lines through the object. Rays traversing the object encounter a set of per-voxel attenuation elements and are attenuated according to the energy of the spectrum and the atomic number and density comprising the attenuation in the voxels. The total attenuation is composed of the different physical attenuation mechanisms (Rayleigh, photoelectric, Compton, and pair production).

The Fourier slice theorem contains the key mathematical relationship between the object function, $f(x,y)$, and the projection through the object function, $P_\theta(t)$, foundational for CT reconstruction algorithms. While there are many forms of this theorem (Barrett and Swindell 1981; Kak and Slaney 2001; Natterer 2001), one way to describe this result is showing the equivalence between a

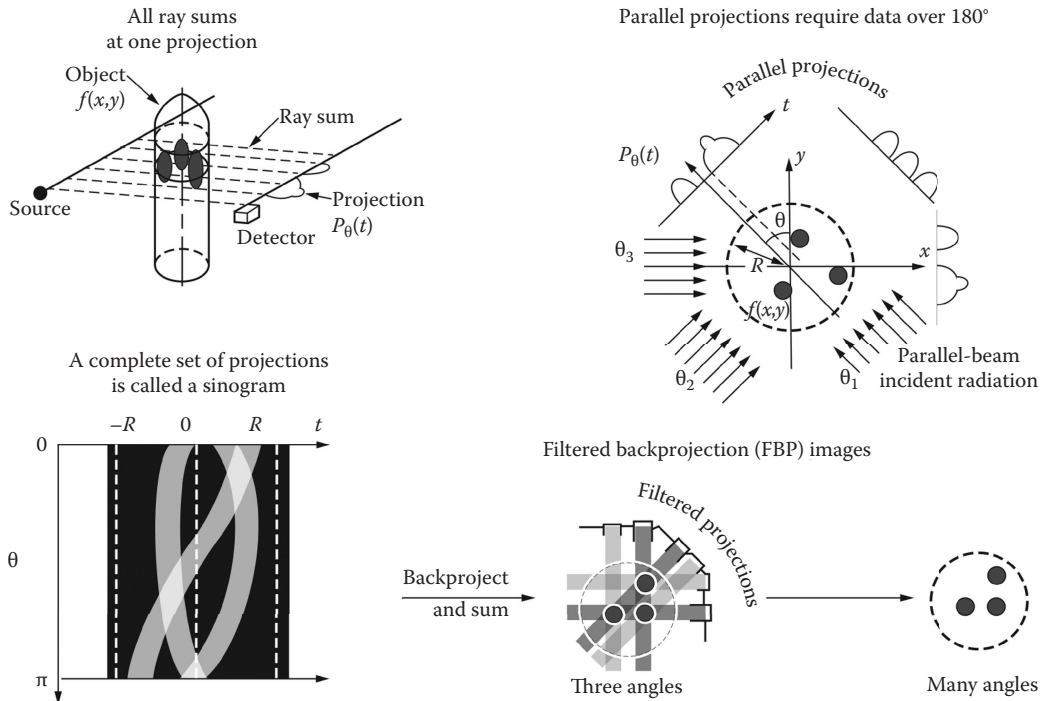


FIGURE 13.9 Illustration of parallel-beam data acquisition (top two illustrations) and image reconstruction (bottom three illustrations).

line through the 2D Fourier transform of the object function at angle θ and the Fourier transform of the projection at angle θ . We start by defining a 2D Fourier transform of the object function, $F(\omega, \theta)$, with polar coordinates ω and θ . Again, following the development in Kak and Slaney (2001), consider the object function expressed as the inverse Fourier transform and switching the integral into polar coordinates in frequency space yields

$$f(x, y) = \int \int F(\omega, \theta) e^{[j2\pi\omega(x\cos\theta + y\sin\theta)]} \omega d\omega d\theta. \quad (13.4)$$

Substituting t for $x \cos \theta + y \sin \theta$ and employing some parallel-beam geometry symmetry relationships between 0–180° and 180–360° in a 2D Fourier transform, the above expression can be reduced to

$$f(x, y) = \int \int F(\omega, \theta) e^{[j2\pi\omega t]} |\omega| d\omega d\theta. \quad (13.5)$$

From Kak and Slaney (2001), the Fourier slice theorem is stated as follows: the Fourier transform of the parallel projection of an image $f(x, y)$ taken at an angle θ gives a slice of the two-dimensional transform at an angle θ from the horizontal axis u in Fourier space. Consequently, we can substitute the Fourier transform of projection $P_\theta(t)$, $S_\theta(\omega)$, for the transform $F(\omega, \theta)$, again where ω and θ represent the polar coordinates in the frequency domain,

$$f(x, y) = \int \int S_\theta(\omega) e^{[j2\pi\omega t]} |\omega| d\omega d\theta. \quad (13.6)$$

The consequence of this development is that the object function can be composed as the sum over a set of filtered projections. The form of the filter function is described in the innermost integral in Equation 13.6. Labeling the filtered projections as $Q_\theta(t)$ and substituting the value of t back into Equation 13.6 yields

$$f(x, y) = \int Q_\theta(x \cos \theta + y \sin \theta) d\theta. \quad (13.7)$$

We have substituted back for t , so the filtered projection is in terms of $x \cos \theta + y \sin \theta$, that is, we sum all of the contributions from $t = x \cos \theta + y \sin \theta$ into the correct locations in x and y in the object function. The algorithm we are describing here is to iterate over x and y , and find all the contributions from the filtered detector measurements at t that intersect with a ray sum (or line integral through the object function at the detector positions t). In this process, we are putting back or back-projecting the irradiance measured by the detector elements, filtered by the filter function, to the points they traversed in the object function. Consequently, for filtered back-projection or convolution back-projection algorithms, the key point is that every voxel in a CT reconstructed volume is a sum over the filtered projection data.

Substituting the polar coordinate representation into Equation 13.7 can further illuminate the relationship between points in the reconstructed image and acquired projection data given by

$$f(x, y) = \int Q_\theta(r \cos(\theta - \phi)) d\theta, \quad (13.8)$$

where points in the image are identified by $r \cos \phi$, $r \sin \phi$. For any fixed point voxel at (x, y) for a parallel-beam geometry (Figure 13.9), the projection data summed into that voxel sweep out a sinusoidal path through the projection data with maximum amplitude r and phase ϕ , and the center of mass of the sinusoid is the center of rotation (Azevedo et al. 1990). The significance of this result has importance for a variety of alignment tasks (Gullberg et al. 1990).

As a sum over acquired measurements, which are Poisson random variables, the same expectations for variances and precision apply, i.e., more measurements in the sum are better than less. However, in the case of this sum, the measurements added together are not repeated trials of the same experimental conditions; rather, the measurements are somewhat different detector measurements acquired from different angular positions around the object function. The number of measurements in the sum is the number of projections acquired; each measurement has two aspects, a particular geometric relation to the object function, which covers the object function, and it is an additional measurement from the same object.

As shown in Chapter 11 and in Kak and Slaney (2001), we can develop algorithms for other source-detector geometries in this same way, fan-to-flat detector or fan-to-curved detector, by relating the ray-sum measurement back to the parallel-beam position and integrating over a sufficient angular range. The necessary angular range has to be larger for fan and cone-beam data acquisition. For a system using a fan-beam geometry and flat-panel detector, the substitutions

$$t = \left((x'_{di} \ y_{sod}) \sqrt{(y_{sod}^2 + x'^2_{di})} \right) \text{ and} \quad (13.9)$$

$$\theta = \beta + \tan^{-1}(x'_{di}/y_{sod}) \quad (13.10)$$

are significant. From Chapter 11, x_{di} is the distance from the central ray at the detector, and x'_{di} is the distance from the central ray with the detector translated to the center of the object. The details of

the substitution vary with the exact geometry of the detector. For example, a curved detector would be different from a linear detector.

The required angular range also varies with the scan geometry. For parallel-beam geometry, 180° angular range is a complete data set for recovering the object function. For fan-beam data, flat or curved detector, 180° + 2 fan angles is sufficient for a complete CT reconstruction (Parker 1982). For any of this scanning, an angular range of 360° certainly satisfies the requirements but, as indicated, has more data than absolutely necessary.

For an area-array detector system, the x-ray geometry is cone beam, which introduces an additional level of complexity for image reconstruction algorithms. The Feldkamp (FDK) 3D cone-beam algorithm (Feldkamp et al. 1984) can be employed to reconstruct area detector data from rotation-only scanning. This algorithm reconstructs the volumetric data on tilted fans for each line of the detector in height. As shown in Yang and Ning (2006), FDK can be modified with same machinery developed in Parker (1982) to produce volumetric CT reconstruction data acquired over 180° + 2 fan angles. The data at the midplane of the cone beam is a fan beam, and the data acquired at the appropriate angular range mentioned above are complete for the reconstruction. However, for rotation-only scanning, the data acquired off the midplane are incomplete to some extent (Grangeat 1987, 1991, 2001). The degree of incompleteness or the percentage of missing data grows with the cone angle. This missing data can be acquired or filled in by rescanning the object with some change in the source angle (Grangeat 1991) and then obtaining another set of rotational views, but this time, the object is tilted in some known and precise way (say with a goniometer).

The problem of missing data is made more complicated by the compliance of certain geometries with the tilted-fan approach. Cylindrical object geometries with small or gradual changes in attenuation with cone angle implicitly include a smoothing of the missing data or cone-beam artifacts. The lack of change in material attenuation with height is compliant with the implicit mechanics of reconstructing on tilted fans. Consequently, results from cone-beam scanners can be somewhat confusing; some objects appear to reconstruct without artifacts, while the reconstruction of other objects includes substantial artifacts that are really not a part of the object at all. We will mention this again in [Section 13.7](#). Objects with large changes in attenuation with moderate cone angles (3–4°) elicit substantial missing data artifacts.

Helical cone-beam scanning as given by Katsevich is schematically shown in Figure 13.10. Katsevich's approach is an exact cone-beam reconstruction algorithm (Katsevich 2002, 2004).

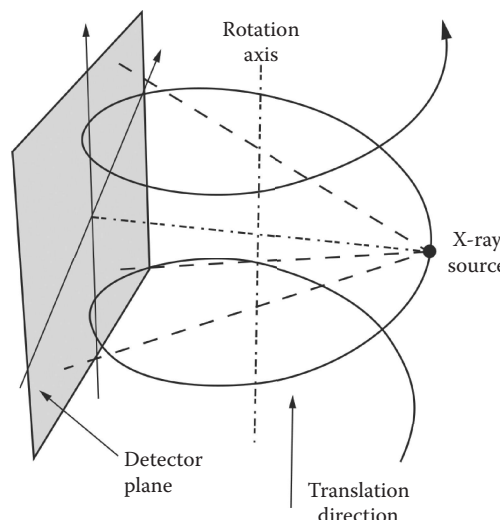


FIGURE 13.10 Pictorial of helical cone-beam scanning.

Properly acquired, the projections of the object include a helical path for the source-detector pair around the object, which includes both elevation and rotation. The helical cone-beam scanning method does not result in the missing data characteristic of the rotate-only cone-beam scanning acquired for FDK. The only difficulty here is the added complexity for the data acquisition. The Katsevich-type data acquisition requires accuracy and precision for both movements in height along the object coordinated with object rotation. This difficulty is amplified somewhat by added expense of an accurate and precise vertical translating stage. This method gets more expensive if the object you want to scan is heavy. The added complexity may certainly be justified if your application requires cone beam and the object includes large changes in attenuation with height.

13.5.1 REGION OF INTEREST AND CT FIELD-OF-VIEW EXTENSION TECHNIQUES

A number of scan geometries have been mentioned to this point: parallel beam, fan beam to a flat detector, fan beam to a curved detector, cone beam to a flat detector with only object rotation, and cone beam to flat detector (or curved detector) with coordinated movements in height (helical cone beam). In all of these cases, the projection of the object fits into the field of view. A somewhat different set of techniques applies for region-of-interest (ROI) scanning geometries where you want to focus on a smaller part of the object, and field-of-view or range-extension techniques where the projection of the object is bigger than the field of view of the detector and you want to scan the entire object. Figure 13.11 contains illustrations of these different techniques. For the half-scan, tiled-CT, and translate-rotate CT scanning, the acquired data can be processed to conform to the requirements for the algorithms mentioned above.

The two types of ROI scanning pictured in Figure 13.11 do not satisfy the finite-extent requirement for CT scanning mentioned above. In both of these cases, the area of interest is in the field of view for all the acquired views, but the other parts of the object outside of this selected region sweep

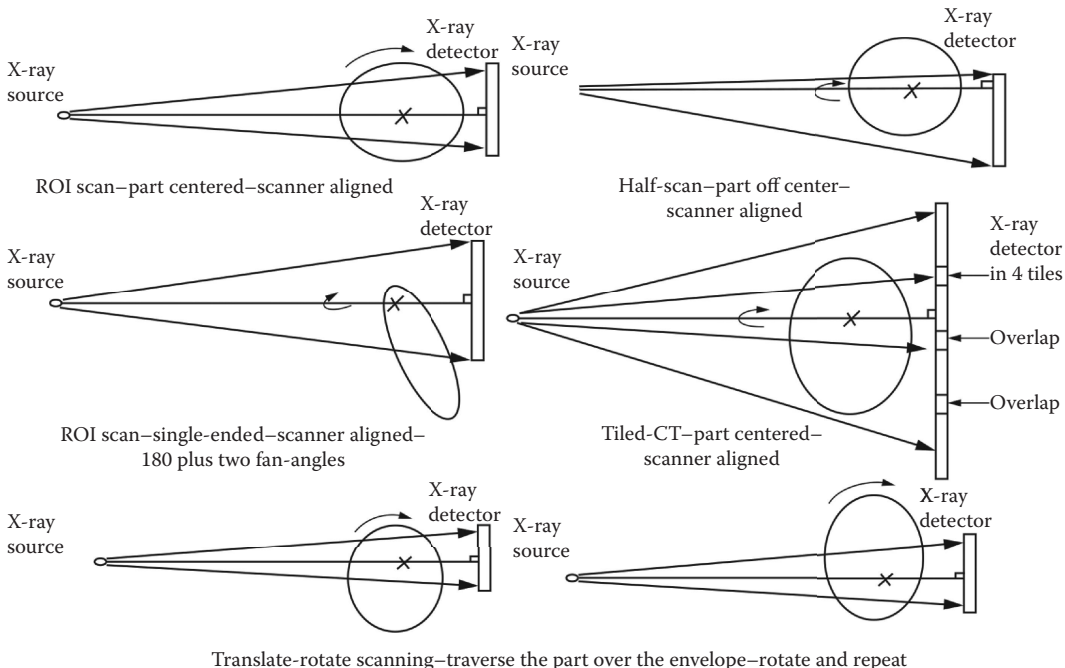


FIGURE 13.11 Illustration of ROI and CT field-of-view or range extension scan geometries used in CT.

into and out of the projection. For the ROI technique, the acquired projection only captures a portion of the object projected attenuation, in the acquired view. When the features are close to the detector, the features are sharply imaged, while in other parts of the angular range, those features are not in the projection at all. The result is some background streaking and some attenuation sometimes referred to as (mass) at the outside of the reconstruction circle. The reconstruction circle is the reconstructed area that can be supported by the acquired data when finite-extent criterion is met. CT reconstruction algorithms intend to put all the projected attenuation somewhere in the reconstructed image; since these features are at a radius that is not supported by the acquisition, the attenuation builds up at the outer radii and is another cupping-like artifact. This artifact confounds the data analysis. This is similar to the previously mentioned beam-hardening artifact.

However, some objects are more suited to ROI scanning than others. For instance, the values of the artifacts at the outer edge of the reconstruction are proportional to the attenuation that has swept out of the field of view. If there is very little attenuation outside the region of interest, say a low-attenuating thin membrane, the effect can be negligible. Also, if the goals of the inspection are to look for anomalies and the relative quantitative scaling of the voxels is not important, the cupping-like artifact can be remediated by processing after reconstruction.

The field-of-view or range-extension technique shown in the upper right of [Figure 13.11](#) called half- or offset scanning is a complete scan for fan beam for either flat or curved detectors. For rotational-only scanning, this technique will produce results on par with full-scan FDK and will include the missing data artifacts mentioned above for the larger cone angles. Acquiring a full 360° scan is required for half-scanning, since you are only viewing half of the object in a single projection. Therefore, you only will see features in the object once over the angular range of the acquisition. Half-scans include less data about the object, so the calculated voxels include less data, and the reconstructed data will include more noise relative to a full scan, i.e., 360 in which you obtain both sides (Schneberk et al. 2016). This particular scanning modality can be combined with enhanced collimation to improve the primary-to-scatter ratio, as just more than half the projection of the object is viewed, since just less than half of the object can be blocked by collimation.

The tiled CT and second-generation scanning presented in the lower sections of [Figure 13.11](#) are ways of building a full projection from acquisitions of the smaller field of view in the detector. In this modality, the detector is translated to cover the necessary field of view, possibly a half- or offset scan, and the different acquisitions are joined to compose a full view of the object. The scanning of the Stardust Shield presented in Chapter 16 was a tiled CT, offset-scan acquisition of a 76.2 cm object with a 40.6 cm wide detector. The particulars of this scanning are covered in the description of this application.

13.6 THE SINOGRAM

For parallel- or fan-beam data (flat or curved detector), or equivalently, for fan-beam data at the midplane of a cone beam, a particularly useful view of the data emerges in what is referred to as a sinogram. A sinogram is a 2D data structure encompassing all the data on one line of detectors, for all of the acquired rotational angles. In a sinogram image, the horizontal axis indexes detector positions spanning the object function, while the vertical axis indexes the angular positions in the data acquisition. A point within an object off the center of axis of the rotation traces out a sine function from 0 to 2π or 0–360°, hence the name sinogram. For a point in the object that is on the center of rotation, a vertical line in the sinogram is traced out (ASTM E 1441 2011). An image of a sinogram from a simulation of an LLNL MTF test object (shown in [Figure 13.12](#)) for a rotation-only scan of 360 views over 360° is given in [Figure 13.13](#). Also shown in this figure is a Wallis transform (sinogram on the right) of the sinogram on the left to better show the sinusoidal traces of the holes in the MTF test object. Notice the relationship between the holes in the test object and the sinusoidal patterns in the sinogram (and this is the explanation for the name). Referring back

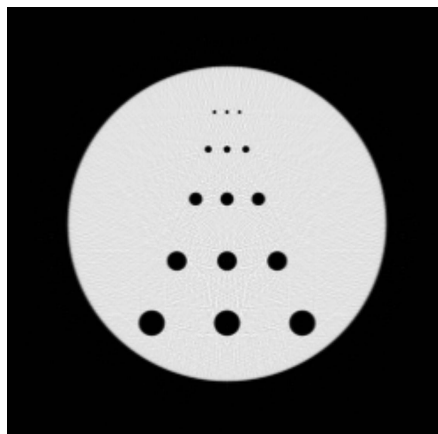


FIGURE 13.12 A simulated cross-sectional image of an LLNL MTF test object.

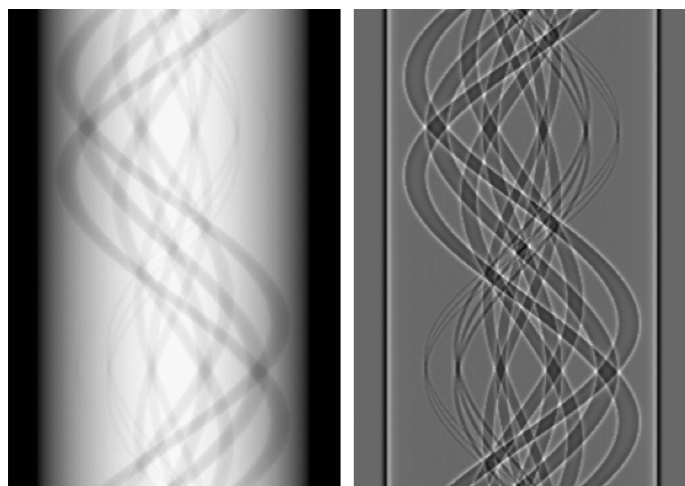


FIGURE 13.13 Two x-ray CT sinograms of an MTF test object. On the left is a simulated sinogram of the LLNL MTF test object shown in Figure 13.12. On the right is the Wallis transform of the sinogram on the left.

to the sketch of algorithms mentioned previously, the image of the test object and the sinogram is a graphic example that every voxel in a CT reconstructed image is a sum over the projection data.

The sinogram image can be a particularly useful means for spotting problems with the acquired data. Consider any one of the holes in the test object for parallel data or near-parallel data; the sinusoidal trace includes the maximum amplitude equal to the distance of that hole from the center of rotation. The equation for the projection of a single point within an object includes information on the center of rotation and, for fan-beam data, information on possible midline offset, τ , given in Figure 13.14. The difference in the size of the projected holes as they are closer to the detector or further away over the scan measures the x-ray magnification. A number of algorithms for estimating the best center of rotation and x-ray magnification parameters have been developed using single features or regions in a test object as given in Azevedo et al. (1990) and Gullberg et al. (1990). The test objects referred to in these papers are pin test objects or phantoms, a base material with a small number of pins or small cylinders extending throughout the field of view. Other algorithms have

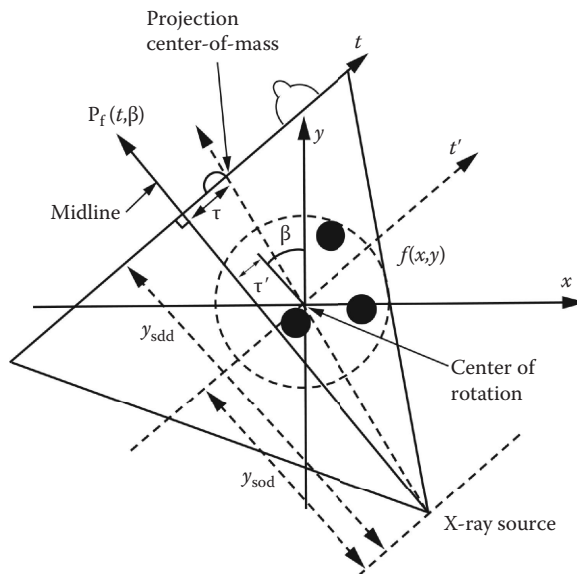


FIGURE 13.14 Illustration of fan-beam CT geometry and various parameters, including the offset, τ , between the center of rotation and the midline.

been developed for estimating the geometrical parameters of cone-beam scanning, including that by Ford et al. (2011).

The point here is that the sinogram is a particularly useful and compact view of the CT scanning operation and results from the values of the key data acquisition parameters such as center of rotation and magnification. Troubleshooting CT scans usually involves creating and manipulating sinograms. We will make use of the sinogram view of CT data to showcase artifacts in Section 13.7.

13.7 ARTIFACTS IN CT RECONSTRUCTED DATA

Artifacts are features in a CT reconstructed image that are not in the object function or result in distortions of the object function being recovered. Artifacts arise when there is a fundamental difference between the requirements of the algorithm and the state of the acquired/processed data. Some of these artifacts can be easily remediated by reprocessing and re-reconstructing the same acquired data. Other artifacts are more serious and may require some change in the scanner and/or scanning parameters and then a rescan. Much of the material in this section assumes you can get to the raw, unprocessed data. In some cases, the data have already been calibrated or processed, and a secondary reconstruction or re-reconstruction capability may be needed. It should be mentioned here that many secondary reconstruction software packages are available. Most include a number of options for specifying the parameters in an image reconstruction calculation and/or performing iterative reconstructions with the implementation of constraints or principles for guiding the calculation. For more on CT artifacts, see for example Boas and Fleischmann (2012).

We organize the factors that result in the emergence of artifacts into three groups: (1) geometric parameters, (2) physical issues or issues with ray-sum values, and (3) scanner/technique issues. As indicated above, every voxel in a CT reconstructed image is a sum over the filtered projection data. The details of the sum depend first on a few independently measured geometry variables where the number of independent variables changes with the source-detector geometry. The set of parameters required for each of the three geometries described in Chapters 11 and 12 and illustrated in

TABLE 13.2
Critical Independent Parameters for CT Reconstruction Algorithms

Acquisition Geometry	Critical Geometry Parameters	Angular Range (Degrees)
Parallel beam	Center of rotation, angular range, and number of views	180 or 360
Fan beam—Flat detector	Center of rotation, angular range, number of views, source-to-detector distance (y_{sdd}), source-to-object distance (y_{sod}), and pixel width at the detector ^a	180, 180 plus 2 fan angles or 360
Fan beam—Curved detector	Same as flat detector, but also angular spacing between detectors	
Cone beam—Flat detector	Center-of-beam divergence in height, pixel height at the detector, ^a and fan beam—flat-detector parameters	180, 180 plus 2 fan angles or 360

^a If the pixel width and the pixel spacing are not uniform, then center-to-center pixel spacing would have to be added to this list.

Figure 13.6 is given in Table 13.2. Notice that the parameter list grows with the choice of acquisition geometry; i.e., from parallel- to cone-beam. Algorithms assume that you know these parameters at the accuracy and precision of the reconstruction calculation, but the effective accuracy and precision is somewhat limited by the spatial resolution of the system. If the system radiographic spatial resolution is much less than the CT volume you are reconstructing into, then working to obtain a precision better than your spatial resolution is difficult to justify.

Second, as described in Chapters 10 and 12, algorithms assume that the values of the ray sums acquired include a consistency in the measurements of the physical irradiance independent of the detector, detector position, or rotational position of the object. Only a weak standard of consistency is used here: that a ray sum records the same value for the same integral over a particular length and materials through the object function. A third category of artifacts is due to certain physical mechanisms endemic to certain types of x-ray systems and scanning regimes, for example, cupping artifacts that include beam hardening for polychromatic and object scatter for medium- to high-energy systems. This last type of artifact occurs in the best calibrated and aligned systems across all source—detector geometry types. We will start with the geometry parameters and those artifacts common to all scan geometries, then those specific to fan- and cone-beam geometries. We will cover artifacts due to beam hardening and scatter last since the artifacts are usually overlaid on top of other artifacts already present in the scanning and surface in the context of other physical mechanisms emerging at different energy regimes. Also, more than one type of artifact may be present in any CT scan, and until you really clean up the geometric acquisition parameters, it is difficult to develop a strategy to remediate the other artifacts. We will discuss the list of artifacts and the scan geometries connected to the artifacts, and the suggested remedies are summarized in **Table 13.3**.

Throughout this chapter, we use test objects to illustrate the characteristics of the different types of artifacts. The test objects used repeatedly in this section are: MTF, contrast test object assembly (CTOA), and vertical alignment cylinder (VAC). Photographs of four test objects are shown in **Figure 13.15**. One of two MTF test objects is not shown in the photograph. Both MTF test objects are made of the same material, but they have different diameters and holes. All of these objects are of a simple design, with features located at strategic positions for measuring artifacts. The features in the MTF and CTOA test objects span the height of the object, making the positioning of these test objects at a particular height not important. The VAC test objects were designed to evaluate and measure cone-beam misalignments and will be used only in those contexts. In addition, we will make use of simulations of these test objects when this is strategic to illustrate a particular error or

TABLE 13.3**Summary of Types of Artifacts and Suggested Remedies**

Type of Artifact	Scan Geometry	Possible Remedies
Centering	Parallel, fan, cone	If system is aligned, can fix with correct center
Bad or hot pixels	Parallel, fan, cone	Outlier removal, may need to extend to many bad pixels for MeV image data
Ring artifacts	Rotation-only scanning for any geometry	Calculate per-detector element gain/offset with standard object and correct projection data
Angular positioning errors	Parallel, fan, cone	Estimate the correct angular position for each projection and re-reconstruct
X-ray magnification	Only fan or cone geometry	Get better measurement of y_{sod} and y_{sdd} and re-reconstruct
Horizontal or in-plane midline offset	Fan or cone geometry	Can estimate/measure the offset and reconstruct with a modified algorithm
Vertical centering	Cone-beam geometry	Estimate/measure a new value of the vertical center of the beam and re-reconstruct
Vertical midline offsets	Cone-beam geometry	Estimate/measure a new value of the vertical midline offset and re-reconstruct
Beam hardening	Parallel, fan, cone	From a standard object, acquire a measurement that enables the calculation of a beam-hardening correction
Scatter	Parallel, fan, cone	In combination with beam-hardening correction, try a scatter-deconvolution correction, or rescan with different collimation



FIGURE 13.15 Photo of four different test objects. From left to right: CTOA, MTF, and large and small VACs used to illustrate artifacts in CT images. These test objects are also the templates to generate simulated data. The square is used for scale.

artifact independent of any other effect in acquired data. Lastly, we will add scans of objects from different CT systems to further illustrate the impact of an artifact in a more realistic context.

To prepare for the images of reconstructions with artifacts, we thought it prudent to record the reconstruction of these objects when all the parameters are correct for reference going forward. Such reconstructed images are given in Figures 13.16 through 13.18.

The choice of whether to use simulated data or acquired data depends on whether we can singularly capture a particular artifact independent of other artifacts. As indicated above, oftentimes CT reconstructed images can include several artifacts. Referring to the schema presented in Chapter 10, acquired x-ray data include different sources of detected irradiance, and each includes different impacts on noise and spatial resolution. For many geometry parameters, it is more illustrative to show the exact impact of an artifact with simulated data, where the only error introduced is the one being discussed. However, in the case of the MTF test object, we have acquired several data sets and will provide examples with the acquired as well as simulated data.

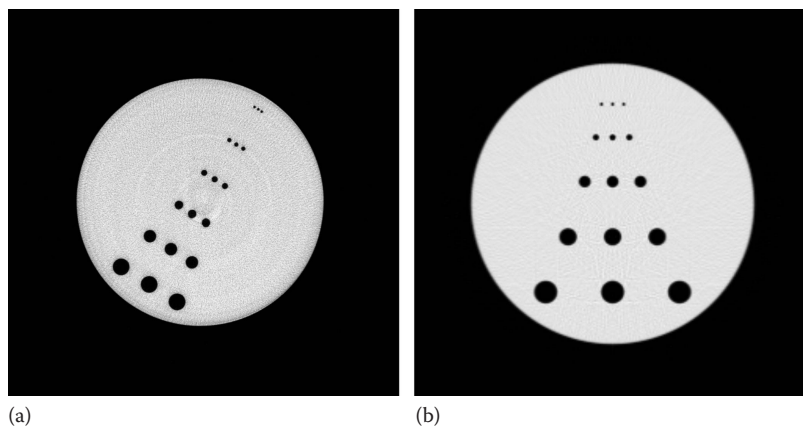


FIGURE 13.16 X-ray CT acquired (a) and simulated (b) reconstructed. Note that they are for slightly different MTF test objects.

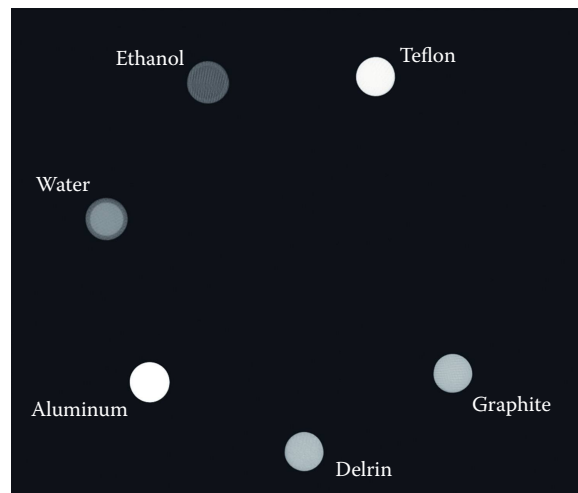


FIGURE 13.17 Reconstructed image from acquired x-ray CT data of the CTOA with all corrections applied.

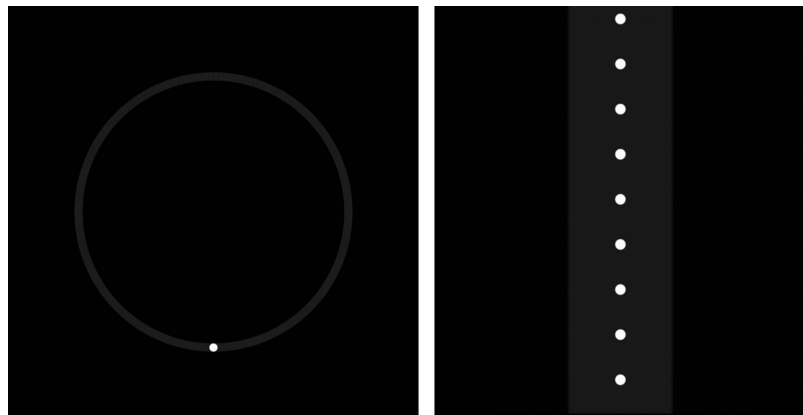


FIGURE 13.18 Reconstructed images from simulated data of the large VAC test object with all corrections applied. The image on the left is a cross-sectional CT slice in the x,y -plane. A cross-sectional CT slice for the x,z -plane is on the right. Note that the plastic hollow cylinder (light gray) used to suspend the metal spheres (white) is barely visible in the grayscale used.

13.7.1 CENTERING ARTIFACTS

As indicated in Chapter 11, the quantitative description of projection data from any geometry includes the specification of a center of the reconstructed space, in either 2D or 3D. We included the specification of the center value in the description of the ray sums, rather than assume that you can shift-tilt the projection to put the acquired and processed data into a fixed relationship relative to the center of the space. Centering artifacts occur when the specification of the center of the reconstructed space does not match the value inherent in the acquisition. The incorrect specification of the center of reconstruction (sometimes called the center axis of rotation) results in artifacts of a certain pattern dependent on the angular range of the scanner, and they grow with the size of the centering error relative to the spatial resolution of the scan.

For CT data acquired at an angular range of 180° (or 180° plus two fan angles), incorrect specification of the center results in tuning fork artifacts in the reconstructed image. The pattern of the tuning fork artifacts indicates the amount and direction for changing the value of the center in the reconstruction. For example, when the center error becomes larger, this results in tuning fork artifacts that are thicker with more structure. For CT data acquired over 360° , centering artifacts emerge as a double or blurred edge inundating the features in the reconstructed image. Reconstructed images with two incorrect specifications of the center for an MTF test object from simulated data acquired over 180° plus two fan angles are shown in Figure 13.19. In Figure 13.20, we show the results for simulated data acquired over 360° for the same two values of error for the specification of the center as given in Figure 13.19.

As shown in these two figures, an incorrect specification of the center impacts every voxel in a CT reconstructed image. For both 180° and 360° data, dimensional measurements of features are substantially impacted. The material features for the 180° data are substantially distorted, whereas the blurred or double edges in the 360° data are not as obvious; but this artifact can directly impact the location of an edge for dimensional measurements. The signature of incorrect center specification type of artifact is fundamentally the same regardless of the scan geometry, parallel, fan, or cone beam. Some differences emerge for the shape of centering artifacts in half- or offset scans. As can be seen by comparison to the correct reconstructed image on the right in Figure 13.16, centering artifacts are easy to fix and can use the already simulated or already acquired data.

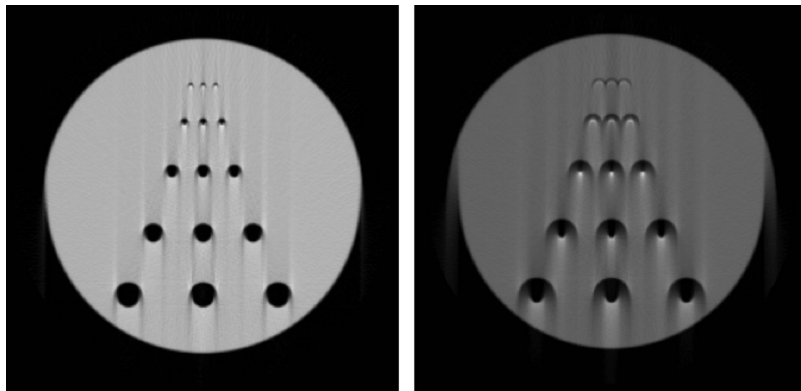


FIGURE 13.19 Centering artifacts in LLNL simulated data of an MTF test object. On the left and right are 1 and 4 pixels, respectively, off the correct center-axis-of-rotation for projections over 180° plus two fan angles. Note the characteristic tuning fork artifact in both images.

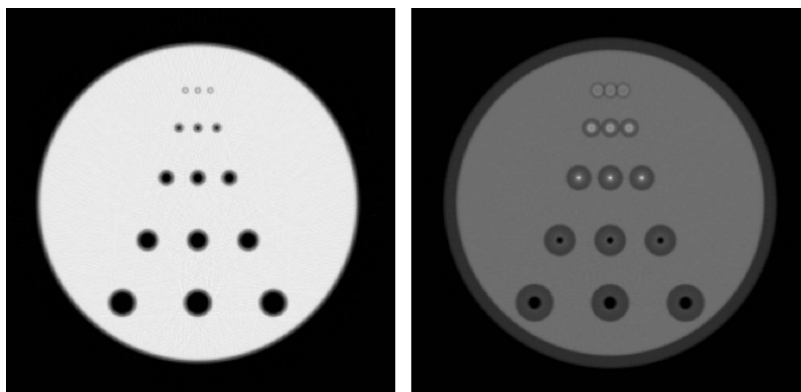


FIGURE 13.20 Centering artifacts in LLNL-simulated data of an MTF test object. On the left and right are 1 and 4 pixels, respectively, off the correct center-axis-of-rotation for projections over 360° . Note that it is difficult to tell the center is off for the image on the left.

13.7.2 RING ARTIFACTS

Ring artifacts occur in multiple detector systems when the measurements from all of the detector elements are imbalanced, that is, they do not produce the same results for the same irradiance. In particular, there is some additional component to the acquired signal that is unique to that detector element, and this usually small but persistent signal component is not a feature of the object. In the sinogram, this imbalance is observed as vertical lines as shown in Figure 13.21, and when reconstructed, they produce a circle or ring artifact as shown in the image on the left in Figure 13.22, hence the name. Figure 13.22 contains two reconstructed images: one with ring artifacts and one with the rings mostly remediated. Note that the reconstructed images also include beam-hardening artifacts, which we will discuss later. The data with the ring artifacts are an example of the inner workings of the back-projection operation referred to above. The data on a single radius from the center of reconstruction can be traced back to the acquisition from a single detector.

A number of techniques have been developed for remediating ring artifacts. First, from detailed scanning of uniform attenuation test objects, gain-offset adjustments can be estimated to remove the unique characteristic of the digitization from that detector element and thereby minimize or remove

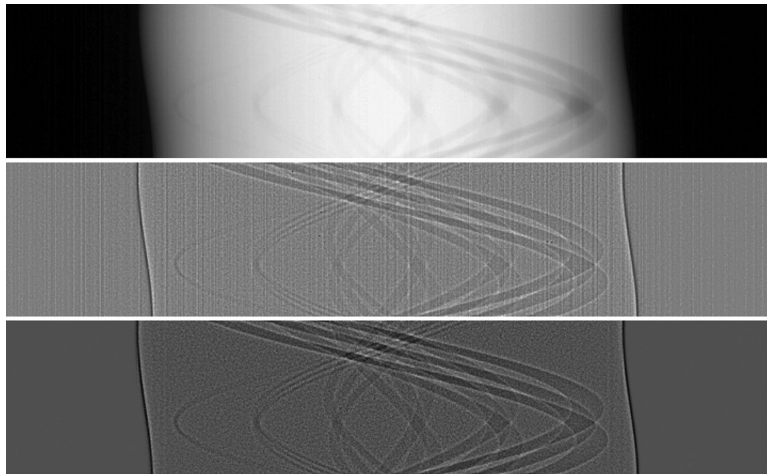


FIGURE 13.21 On the top is an acquired μ_y sinogram for an MTF test object with no additional processing. The middle sinogram has been Wallis transform–processed and shows vertical lines due to imbalanced detectors. The vertical lines in the sinogram reconstruct into CT ring artifacts as shown on the left in Figure 13.22. The bottom sinogram has vertical line, often referred to as ring removal, applied to the middle sinogram. Note that many of the vertical lines are removed as shown in the sinogram as well as the image on the right in Figure 13.22.

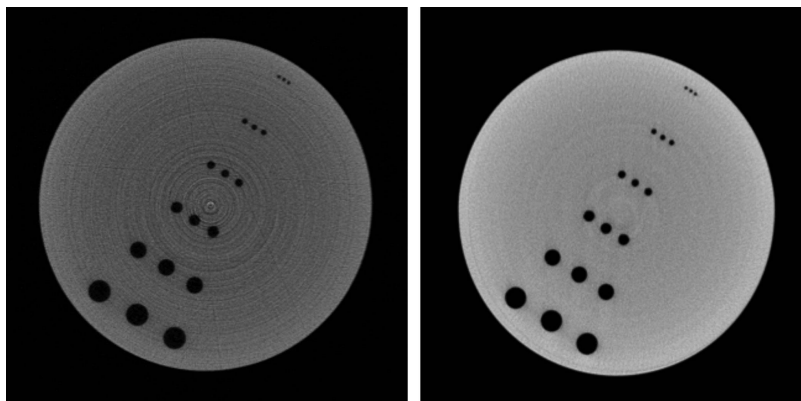


FIGURE 13.22 CT reconstructed images for x-ray acquired data of an MTF test object (left) without and (right) with ring or outlier artifact correction applied to the same data. The rings are due to imbalanced detectors.

the ring artifacts. Second, a class of techniques exist that can be applied after scanning, which attempt to identify and remove the impact from a particular detector (Kowalski 1978; Munch et al. 2009). These techniques are tunable, but are not without risk, and can generate their own artifacts; but they can be applied without acquiring any new data.

13.7.3 BAD-PIXEL ARTIFACTS

Single-point streak artifacts arise from bad pixels or hot pixels in the acquired data. In either case, the digitized value from that detector element is somehow voided, i.e., the detector did not work or an x-ray saturated the detector element or the digitized value for that detector at that rotational angle

is within range, but just erroneous, for a particular radiographic acquisition. This results in no useful information. A single bad pixel in a CT data set for a single view gets reconstructed into a single line, often referred to as a streak artifact as shown in Figure 13.23. In the single bad-pixel case, the digitized value is incorrect for that particular acquisition at that angle; often the detector element recovers and is OK or good at other acquisition angles. This differs from ring artifacts where the digitization from that particular detector element is always or most of the time inconsistent with the digitization from other detector elements.

A number of different outlier removal techniques have been developed to remediate this type of artifact (Li et al. 2006; Munch et al. 2009). At LLNL, we use techniques based on comparing the acquired radiographs to a median filtered, 3×3 , 5×5 , or 7×7 radiograph. The kernel size depends on the radiograph. Next we employ a user-defined threshold, and selectively replace the pixels in the acquired radiograph with the pixel from the median-filtered radiograph when the difference is larger than the threshold. Figure 13.24 contains a reconstructed image with outlier and ring removal applied. Note how the rings and streaks are remediated as compared to those in Figure 13.23.

The MTF example supplied here is taken from a low-energy regime; in the high-energy regime, or when scanning with neutrons, other mechanisms result in a different signature of voided detector

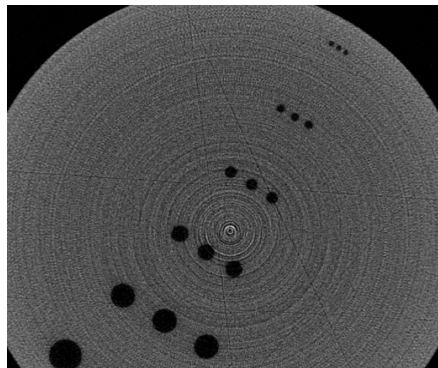


FIGURE 13.23 CT reconstructed image for x-ray acquired data of an MTF test object. Note the ring and streak artifacts. The streaks are due to individual outlier detector elements (pixels) for a particular projection.

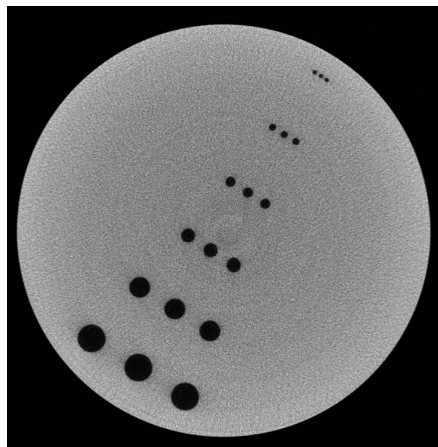


FIGURE 13.24 CT reconstructed image for an MTF test object with ring removal and outlier removal applied to the same acquired data as in Figure 13.23. Note the difference between this image and that without artifact corrections shown in Figure 13.23.

elements and can result in groupings of bad pixels. A high-energy (9 MeV) example of several bad pixels is shown in Figure 13.25. These larger clumped bad pixels arise in high-energy imaging from scatter in the scintillator or detector and are different from the single pixel hits occurring at low to medium energy. A digital radiograph and an image showing the pixels that were corrected by an LLNL outlier removal technique are shown in Figure 13.26.

As stated in Chapter 12, outlier removal routines replace singular bad pixels or bad-pixel clusters with estimates from the surrounding good pixels. Sometimes one has to resort to model data to determine good surrounding pixels to replace the bad ones. The problem is you are making up or estimating data that you wanted to acquire. If your system is measuring spatial resolution or modulation at a pixel, then you probably compromised the resolution somewhat by removing outliers. Also, if tuned poorly, the process of outlier removal can remove the sharpness of edges and ultimately compromise dimensional measurements.

Fundamentally, the pixels you estimated and inserted were not the measurements you should have obtained from a scan of the object function. Figure 13.26 includes an outlier-processed image of an acquired radiograph of an LLNL MTF test object and the difference image showing what was taken out of the image. Notice in the image on the right the outlines of the part geometry and some of the

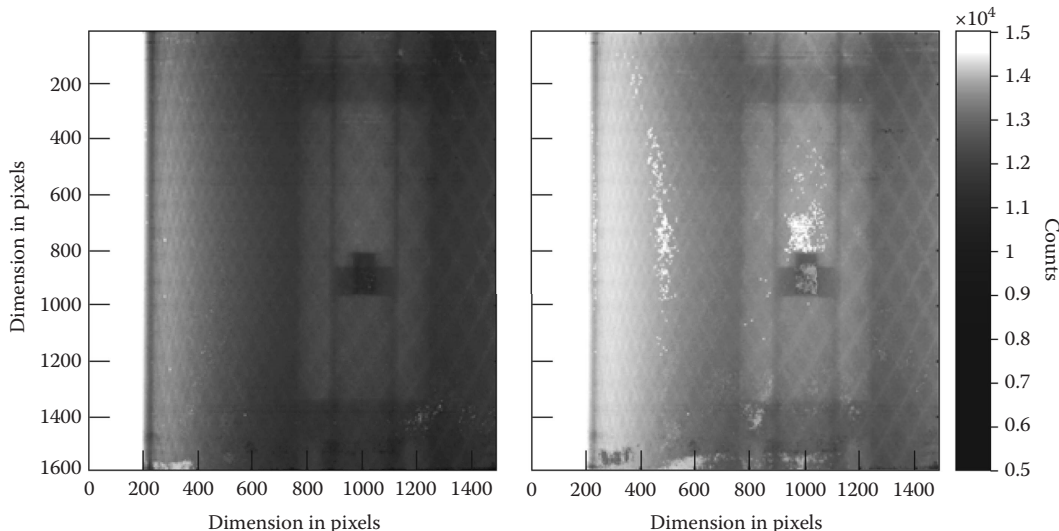


FIGURE 13.25 Two 9 MV Φ radiographic images for a CT scan acquired over about 4 hours, 1800 views, 360°, and 1.5 s integration time with 4 frames averaged. The first and last images are on the left and right, respectively. The two images are separated by 0.2°. Note the many grouped bad pixels in the last acquired image. Removing these bad pixels is difficult.

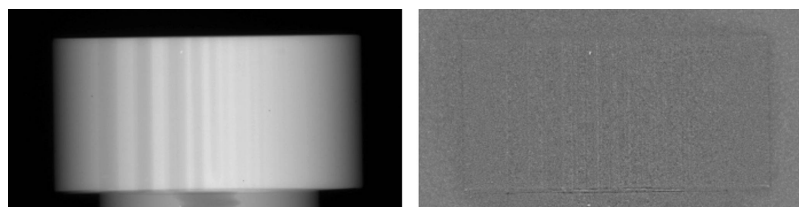


FIGURE 13.26 Example of bad-pixel (or outlier) processing and assessment on the impact for a radiographic image for an MTF test object. On the left is a bad-pixel corrected attenuation digital radiograph. On the right is a difference image from the noncorrected radiograph. This shows the impact.

other features in the outlier removal. We consider this as evidence of too much outlier processing. It is to the point where the spatial resolution and ability to detect features will be compromised.

This example of checking or accounting for what you have removed and what you have let remain in the data by examining the difference between the original and processed data is an important tool in evaluating the subsequent inspection. Notice a small, but brighter, feature in the upper part of the difference image. This is a location that includes a small inclusion in the plastic material, which in this object is of no consequence, but is a real feature of the object and not an outlier. The brighter pixel values in the difference image indicate that we have changed the value of the radiograph of this feature by outlier-processing the data. The pixel value of this inclusion in the outlier-processed reconstructed image is lower as a result of the processing. The difference is not large, but it could lead to an incorrect identification of a material and subsequently an error in the inspection if detecting these features is important to this inspection. All of this recommends an awareness of the processing steps applied to radiographic and CT image data.

13.7.4 ANGULAR POSITIONING ARTIFACTS

Two types of artifacts can be found in angular position errors. One is a difference between the assumed position of the object relative to the source and the detector, and the actual position. The second is errors in the specification of the direction of the angular movement, positive or negative. Errors in the angular position can occur in a variety of ways. One is due to a problem with the mounting of the object, i.e., the object rotationally slips while on the stage. Another is in mechanical positioning, i.e., the position determined from the encoder counts is not accurate. Figure 13.27 includes a reconstructed image of a simulation of the CTOA with two types of angular position error. Two angular positions are recorded incorrectly. One is intermittent throughout the scan. The other is due to cumulative drift in rotational position. The latter can happen when the object is not properly secured onto the rotational stage.

For the cylindrical objects of mostly a uniform material, as shown in Figure 13.27, artifacts emerge at the boundaries. For the two angular error cases, the edges do not meet at the position at which the error occurs, in this case at angles of 50° and 150° . In between those positions, a consistent boundary is reconstructed, but the boundaries do not meet for the angles of the missing or incorrect measurement projections. For a slow angular position drift, the boundaries are smooth in the direction of the error, which is a simulation of a pure rotation error. One should be reminded that if there were features in the cylinder material, they would be reconstructed with the same inconsistent boundaries; in essence, they would be blurred and some features may be missed.

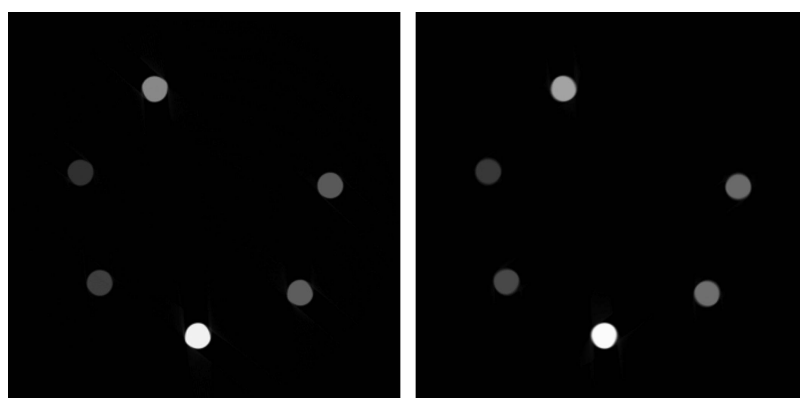


FIGURE 13.27 X-ray CT reconstructed images of simulated CTOA data sets with different angular errors. On the left are the results of two angular errors, and on the right is the result of a drift in the angular position. Notice that the cross sections of each material are not round, as they should be.

Fortunately, rotational artifacts are rare since they are difficult to find and fix. It is usually the case that objects are securely attached to the manipulation stages, and the encoder counts are read with every view acquired. Motion systems usually stop when errors are reported, e.g., the target position could not be reached or that the reading of the encoder failed. Consequently, it is usually the case that the scan stops and you fix the problem. Once fixed, the data need to be reacquired. However, if you get a complete data set when the stages are malfunctioning, determining the correct angular position is challenging. The missing angular position can be difficult to determine in actual data, which includes noise of all kinds. Also, it is difficult to estimate all the different ways in which an object can move when pulling away from a fixture inadequate for securing the object to the stage. Usually, when you see an artifact of this type, it is most expedient to secure the part to the stage, possibly add some more diagnostics on encoder reads from the rotational stage, and rescan.

The error that occurs when there is a mismatch between the direction of the readout of the detector and the direction of the angular range is one of the easiest errors to fix. This type of error usually occurs when reconstructing data acquired by a scanner that has been recently reconfigured or when reconstructing data from a scanner about which little is known. Further, this type of error only really emerges for nonparallel-beam data, since for parallel-beam data, the direction of rotation does not impact the reconstructed image. The features in the object are not more or less magnified by the x-rays, since in a parallel-beam geometry CT system, there is no x-ray magnification. Figure 13.28 shows what happens when you have a nonparallel-beam CT system and you use the wrong rotation direction. The simulated data acquisition is for 360 views over 360° with a fan angle of 3.34°. The image on the left is with the incorrect direction of rotation, while the one on the right is with the correct rotation direction. Figure 13.29 contains two reconstructed images of the CTOA. These data were simulated using 400 views over 200°. The reconstructed image on the left uses +200°; the one on the right uses -200°.

The reconstructions of the MTF test object (see Figure 13.28) show the kind of effect mentioned as you get closer to the center of the beam, i.e., the center of the reconstruction; the artifacts are smaller and this is due to the smaller fan angle. The data in the center of the reconstruction are almost a parallel geometry. As the voxel positions start to include a larger fan angle, the artifacts increase. The effects are a little more pronounced for the scan of the CTOA in Figure 13.29 which is 180 plus 2 fan-angle data, and all of the cylinders are positioned at a fan angle of about 4°.

As mentioned earlier in this section, the incorrect direction of rotation artifact is easy to fix. All you need to do is reconstruct with the angular direction matching the direction of rotation relative to the order of the detector readout. It is best to use a test object to look for this type of artifact. However, as seen in the images, this kind of error is easy to spot.

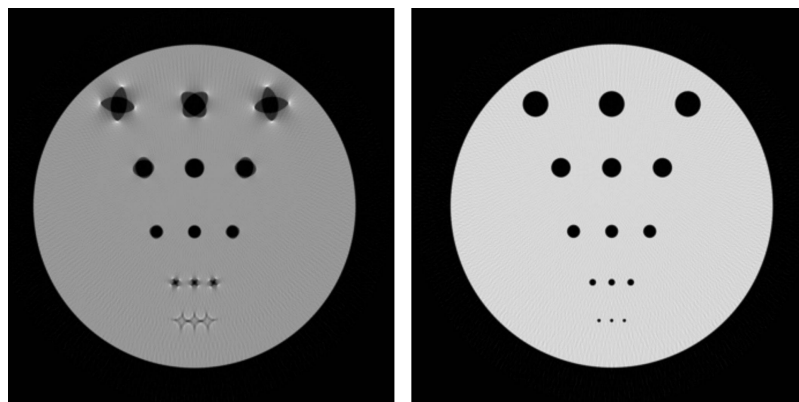


FIGURE 13.28 Example of wrong direction of rotation for a simulated fan-beam CT data acquisition of an MTF test object. On the left is the wrong rotational direction. The correct rotation direction is on the right.

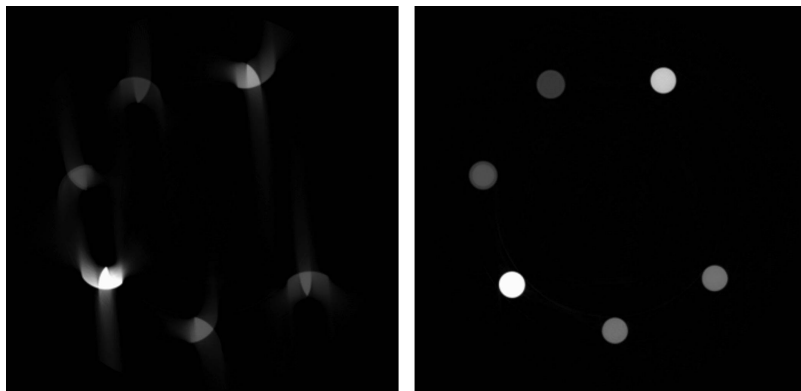


FIGURE 13.29 Example of wrong direction of rotation for an acquired fan-beam CT data acquisition of the CTOA. On the left is the wrong rotational direction. The correct rotation direction is on the right.

13.7.5 X-RAY MAGNIFICATION ARTIFACTS

Artifacts of this type also apply only to nonparallel-beam data. Errors in the measurement of y_{sdd} and y_{sod} , and in the pixel size at the detector, have more impact for the reconstructed image as the fan-angle increases. This is really tautological since you measure the fan angle from the arctangent of the ratio of the distance from the center position in the detector array from the values of y_{sdd} and the voxel size at the center of the object using y_{sod} . Referring back to Section 11.4.2, CT Scanning with Linear-Detector Arrays, for any particular voxel position in the reconstructed image, Equation 13.11 can be used to calculate the error involved in treating fan- or cone-beam data as parallel beam, instead of accounting for the beam divergence:

$$x'_{\text{di}} = (r \cos(\theta - \phi)) / [1 + (r \sin(\theta - \phi) / y_{\text{sod}})]. \quad (13.11)$$

The amount of error is in some fashion an upper bound for x-ray magnification errors, that is, what would the image look like if reconstructed for a parallel-beam geometry. To further illustrate these types of errors, Figure 13.30 contains the simulated image of the MTF test object, 360 views over 360° and a fan angle of 3.34° , reconstructed with a parallel- and fan-beam reconstruction

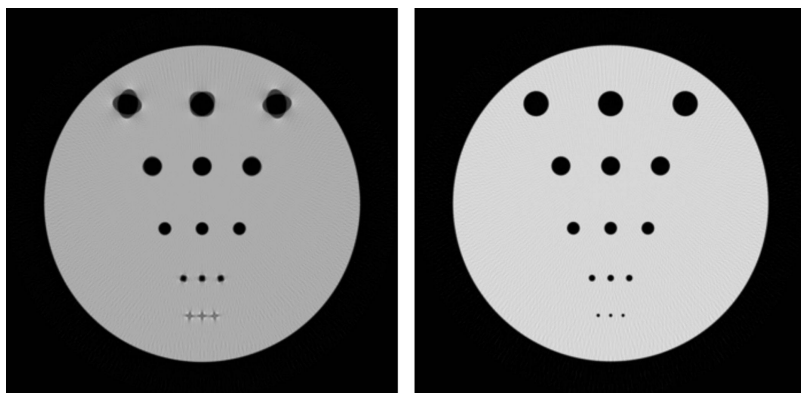


FIGURE 13.30 Impact of getting the fan angle and/or the x-ray magnification wrong. On the left is a parallel-beam CT reconstructed image for a simulated 3.34° fan-beam geometry CT system of an MTF test object. On the right is the result for a correct reconstruction, i.e., a fan-beam reconstruction using a fan-beam reconstruction algorithm with the correct fan angle (magnification).

algorithm. In this case, the fan angle of 3.34° at the edge of the detector is moderate to small. For larger fan angles, the artifacts get worse.

Considering the comparison of the two images, a number of important points emerge. First, notice the outer boundaries of the MTF cylinder for both reconstructions; the parallel- and fan-beam algorithm resultant images look like they have the same outer-boundary shape. There is a difference, but it is small relative to the total diameter. Second, notice the differences between the holes reconstructed with the correct (fan as fan) and the incorrect (fan as parallel) algorithms. The holes in the center of the reconstructed image include less fan angle, and consequently there is less error. That is, the impact of x-ray magnification errors varies per voxel with the fan angle of the voxel. Lastly, notice the shape of the errors; the edges of the holes come apart since the parallel algorithm assumes that the projected size of the hole will be the same regardless of the angular position. In some respects, the outer boundary of the larger holes contains a measure of the accuracy of the fan-beam parameters relative to the center of the beam divergence, around the circumference of the hole. If the pattern was asymmetric, the asymmetry points to the largest departure from the expected fan angle, the angular view where the difference between the fan angle you specify and the true fan angle is greatest. All this says in diagnosing these types of errors is that you can get fooled by axially symmetric objects, e.g., an annular ring being a good case in point. The errors vary with the fan angle, that is, you need to build test objects that measure the angle range required to cover the object, and that actual shapes of the artifacts tell you about the real position of the center of the beam and possible problems with the detector array.

The presentation of artifacts in acquired vs. simulated data will of course be subtler, since you will have measured y_{sdd} and y_{sod} with some uncertainty, and then there are all the other sources of noise in the reconstructed image that may suppress the artifacts. To illustrate this, we present a comparison of a reconstructed image with a 7% error in the measurement of y_{sdd} ; we used 1288 mm instead of the actual value 1388 mm. For a fixed object location, this incorrect y_{sdd} value results in an x-ray magnification error. The reconstructed images are shown in Figure 13.31. The data were acquired with a flat-panel detector, 400 views over 200° , and a pixel size of 0.1905 at the detector, resulting in a fan angle of 5.41° . The test object is the CTOA that has cylinders of different materials positioned at roughly the same radius from the center of the assembly.

As expected, the consequence of this error is not large, and the artifacts resemble a centering error for 180 plus fan-angle reconstructed images. For example, see Figure 13.19 and compare the outer boundary of the MTF test object to the CTOA cylinder outer boundaries. However, this error will not be fixed by a respecification of the center. That is, there is not a single value of the center that will fix magnification artifacts.

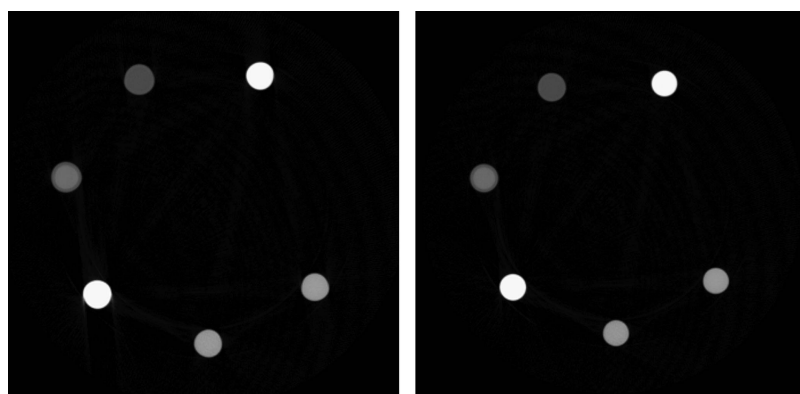


FIGURE 13.31 X-ray CT reconstruction showing the results of an incorrect y_{sdd} that yields a magnification artifact. The CT image on the left uses an incorrect y_{sdd} of 1288 mm instead of the correct value of 1388 mm as shown in the image on the right.

The remedy for magnification artifacts is to correctly measure y_{sdd} and y_{sod} and subsequently fan angle. This measurement can be performed from two radiographs of a well-known size test object such as a cylinder or sphere, acquired at two different known locations along the beam centerline, i.e., two distances along y . The test object must be accurately made and its dimensions verified with an accuracy at least one-half of the voxel size determined at the center of the object. If this is not true, you will simply encrypt the measurement error for the part of the test object into the measurements for your scanner. As a cautionary note, this has happened more than once where the presumed accuracy of a test object was not as advertised.

Using two radiographs to measure y_{sdd} is as follows. Place the object at the center of the rotational table at a known y value, acquire the radiograph, and measure the diameter of the cylinder in pixels call it x_{M1} . Place the object at a different known distance along y (an optical rail is real useful for this operation). Acquire a radiograph and measure the diameter as before in pixels, x_{M2} . The estimate of y_{sdd} can be calculated in a number of ways: one is from the difference in magnification in pixels and the known diameter (or radius) of the machined object:

$$y'_{\text{sdd}} = \frac{y_{\text{MD}} M_1}{[1 - (M_1/M_2)]}. \quad (13.12)$$

where

y_{MD} is move distance between magnification 1 and 2;

M_1 is the object magnification at position 1;

M_2 is the object magnification at position 2.

The accuracy of the estimate y'_{sdd} is dependent on the measured accuracy of the distance moved along the beam line (Move-Dist) and the known diameter of the cylinder. As can be seen from Equation 13.12, the error in either of these measurements translates directly into the error for the estimate of y_{sdd} (for more on this, see Problems). As expected, this measurement becomes more difficult with higher target spatial resolution. However, the combination of acquiring measurements and scans with test objects usually provides enough data to produce an estimated value that is consistent with the target spatial resolution for the CT system.

13.7.6 MIDLINE OFFSET ARTIFACTS

Artifacts that resemble centering artifacts can occur when the projection center of attenuation or mass, also known as the center of the rotational table, and the midline of the beam are not collinear. An example when they are not collinear is illustrated in [Figure 13.14](#). The point is when the central ray of the beam is not the same as the center of the rotational table (for our geometry, the default center of the object space), the fan-beam relationships contained in the back-projection operation are not correct, and the reconstruction of features is wrong. This type of artifact only occurs when there is a diverging x-ray beam, that is, for a fan or cone beam. [Figure 13.32](#) contains reconstructions for 2 pixel midline offsets for projections over 360° and 180 plus 2 fan angles.

This type of artifact resembles the centering artifacts presented earlier (see [Figures 13.19](#) and [13.20](#)). However, in this case, the change in center value does not entirely fix the problem. The difficulty here is estimating the value of the midline offset. A few strategies have been proposed involving nonlinear fitting applied to scans of the object or a pin test object (Azevedo et al. 1990; Gullberg et al. 1990). From the nonlinear fit to the scan of the pin test object, you can estimate all of the x-ray magnification parameters including the center and midline offset. An alternate strategy is to measure the position of the beam midline with a two-pin test object or a cylinder, and then put the center of the rotational table on that line. Experience at LLNL favors the latter strategy. While the offset values can be estimated with a nonlinear fit code or simply by trial and error by plugging

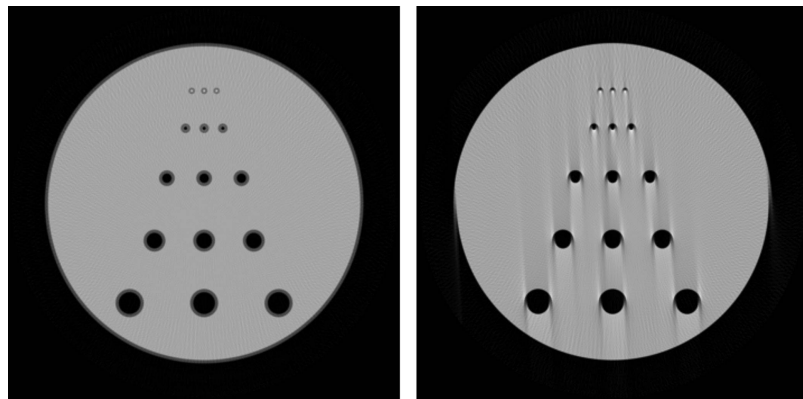


FIGURE 13.32 Reconstructed images from the simulated MTF data with midline offsets. On the left is a 2 pixel midline offset for projections over 360° . On the right is the same offset but for projections over 180° plus two fan angles.

in values and reconstructing, estimating the correct values can be laborious. Realigning the scanner eliminates this trial and error, and the added variance from including another parameter, the midline offset, in the estimation of voxel quantities.

13.7.7 INCORRECT VERTICAL CENTER CONE-BEAM ARTIFACTS

The last couple of geometry-based artifacts mentioned above for fan-beam contexts apply to the midplane for cone-beam acquisition. For cone-beam data, the beam divergence in height requires the specification of another geometry parameter for estimation of the 3D volumetric data. As in the case with the horizontal midline of the beam, the vertical center of the beam can be measured in a couple of different ways. A particular useful test object to confirm the measurement of the vertical beam height is a cylinder with metal spheres. This object can be a hollow or solid cylinder of a low-attenuating material that is easy to penetrate for the selected energy range and has several small metal spheres inserted on a line along the cylinder height. The metal spheres are small but can be larger than the spatial resolution of the system. We refer to the one we use as the VAC. A photograph of the VAC test object is shown in [Figure 13.15](#). A radiographic simulation of the VAC test object is shown in Figure 13.33, and reconstructed images are shown in [Figure 13.18](#).

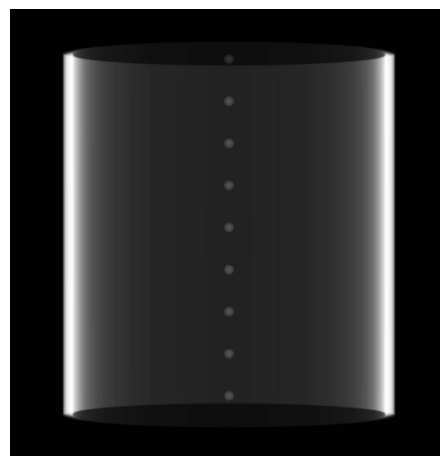


FIGURE 13.33 Simulated attenuation radiograph of the VA test object.

For cone-beam geometry systems, the projection of the center-of-mass vertical central plane should be coplanar with the central ray plane of the cone beam and the middle detector column. If they are not coplanar, the equations used to back-project the acquired data along the ray lines from the x-ray source to the detector are incorrect and will result in artifacts that extend along the height of the reconstructed image. Images of the reconstructed vertical plane containing the spheres in the VAC test object are shown in Figure 13.34. The simulation of this object was generated with 360 views over 360° and reconstructed using the Feldkamp (FDK) 3D cone-beam algorithm (Feldkamp et al. 1984). Notice the spheres get blurred with increasing displacement between the specified vertical center of the beam and the correct center.

A good estimate of the vertical center of the beam can be obtained from a scan of the VAC test object (Gullberg et al. 1990). Visually, a first-cut estimate can be obtained from the sum of the radiographs from a scan of the VAC test object. Figure 13.35 shows the result of summing 90 radiographs of the VAC test object simulated scan. The 90 radiographs are for 360 equal angles over 360° .

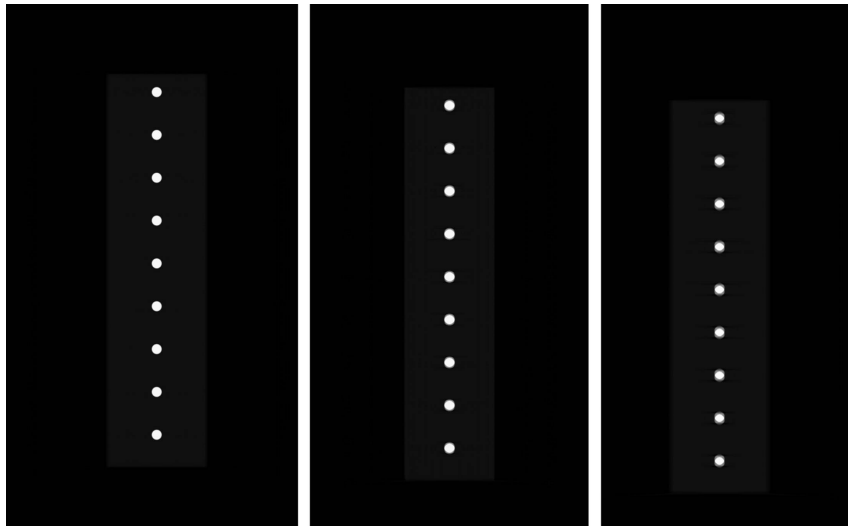


FIGURE 13.34 Comparison of vertical slices containing the spheres in the VAC test object. From left to right are simulated reconstructed images for the correct, 25, and 50 pixel offsets from the vertical center.

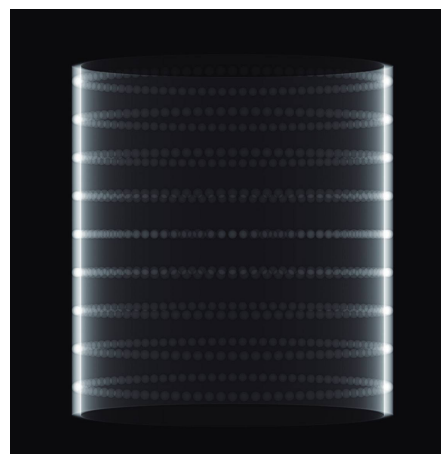


FIGURE 13.35 Sum of 90 simulated radiographs of the VAC test object.

Notice the middle horizontal location where the trajectory of the spheres is close to level, i.e., their summed projection is a line. This is the location of the vertical center of the beam or what is referred to as the midplane. As indicated above, algorithms have been developed for a more precise estimate of these parameters. No matter how the estimates are obtained, it is a good idea to verify that the value of the vertical center is correct by reconstructing a vertical plane in the volume intersecting the VAC spheres, i.e., a vertical plane similar to the location shown in [Figure 13.34](#).

For scanners with rotational tables, an additional alignment issue can arise. As indicated in Chapter 11, the center of the rotational table is the center of the object space for reconstruction. For cone-beam systems, the aligned case is when the center axis of rotation of the rotational table is on one line of the area detector and the axis of rotation is parallel with the plane of the detector. When this is not the case, the reconstructed volume will contain artifacts. These artifacts only impact the reconstructed voxels that are higher or lower than the midplane. The reconstructed voxels along the vertical center of the beam are correct, while the voxels off the vertical center are incorrect. As expected, the artifacts get more dramatic as the distance from the vertical center to the particular voxel gets larger.

There are modifications to the Feldkamp algorithm that incorporate the tilt between the axis of rotation and the detector plane into an accurate reconstruction of the object function. The difficulty here is the same as in the case of the midline offsets; estimating the values of this tilt is nontrivial, and it is difficult to measure. Again, an indication of the size of the tilt can be visually obtained from the sum of a relatively small number of views, as shown in [Figure 13.35](#). Experience at LLNL has shown that realigning the scanner to eliminate the tilt is a good policy.

13.7.8 CONE-BEAM MISSING DATA ARTIFACTS

Missing data artifacts occur in scans under two conditions: (1) cone-angle geometry of greater than 10° and (2) object geometry with sharp changes in path length in height. From the analysis by Grangeat (2001), missing data artifacts can occur due to a preponderance of missing data, that is, for large-cone angle rotation-only systems.

Cone-beam artifacts are generated by two types of sources: the size of the cone angle and the amount of change in the attenuation of the object function with height. Cone-beam artifacts can be combined with scatter and beam-hardening artifacts in subtle and untoward ways. Representative simulated radiography and FDK CT reconstructed images for a 6° cone-angle, rotation-only CT scan of a stacked-plates test object is shown in [Figure 13.36](#). To better determine the impact of cone-beam artifacts, we further investigate the stacked plates test object, since this is the kind of object most susceptible to this type of effect.

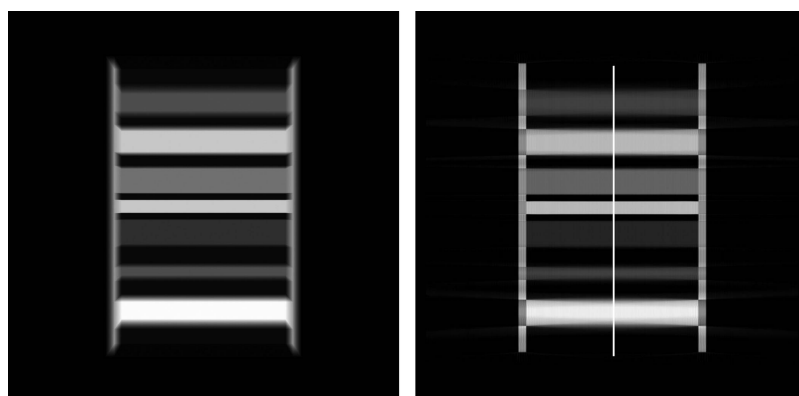


FIGURE 13.36 On the left is a simulated attenuation radiograph of a synthetic stacked-plates test object. On the right is a vertical CT slice image of this object. The 1D profile or lineout in the CT slice image is given in [Figure 13.37](#).

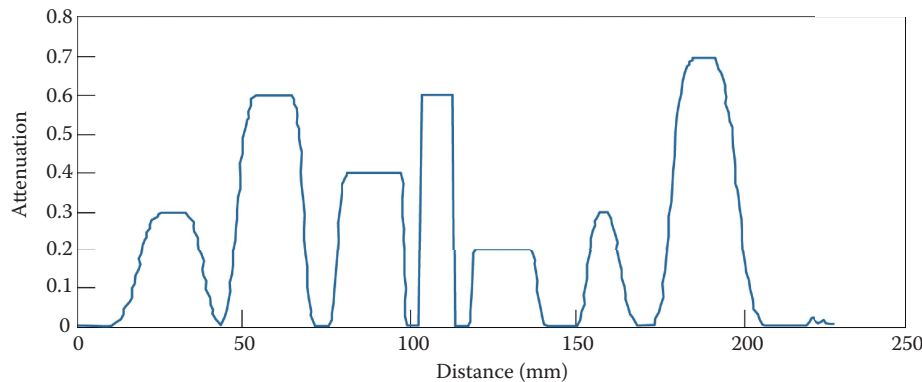


FIGURE 13.37 Lineout through a vertical CT slice from a simulated CT scan of vertical stack of plates shown in Figure 13.36.

Analysis of the vertical CT image in Figure 13.36 and a 1D profile along this image as shown in Figure 13.37 reveals a number of important features. First, notice how the values in the 1D lineout are not step functions with a maximum at the correct attenuation values. As the cone-angle increases, the edges of the material become smoother. Also, the extent to which the spaces in between the plates do not reach zero is proportional to the cone angle. It should be reiterated that these artifacts are due solely to acquiring large-cone angle CT data with rotation-only techniques.

13.7.9 BEAM-HARDENING ARTIFACTS

Beam hardening, as it has been referred to in other treatments, e.g., Kak and Slaney (2001), can arise when polychromatic sources are used in an inspection, and this implicates the commercial x-ray tube sources used in the majority of x-ray inspections. The output of tube sources is a spectrum, not a single energy, as shown in Figures 13.4. As the spectrum penetrates the specimen, the lower-energy part of the spectrum is absorbed preferentially over the higher-energy portion of the

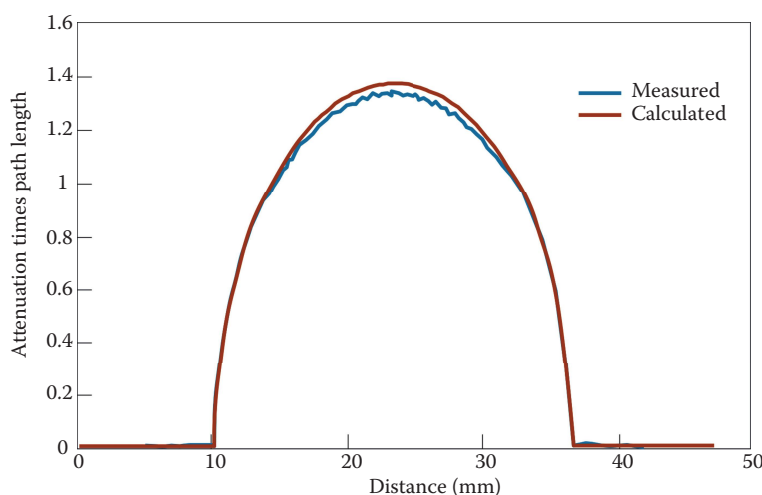


FIGURE 13.38 Plot of the measured projection through a 2.54 cm diameter Teflon cylinder from a 100 kV potential x-ray source with a 2 mm aluminum filter as given by the blue curve. A calculated projection without beam hardening is shown by the red curve.

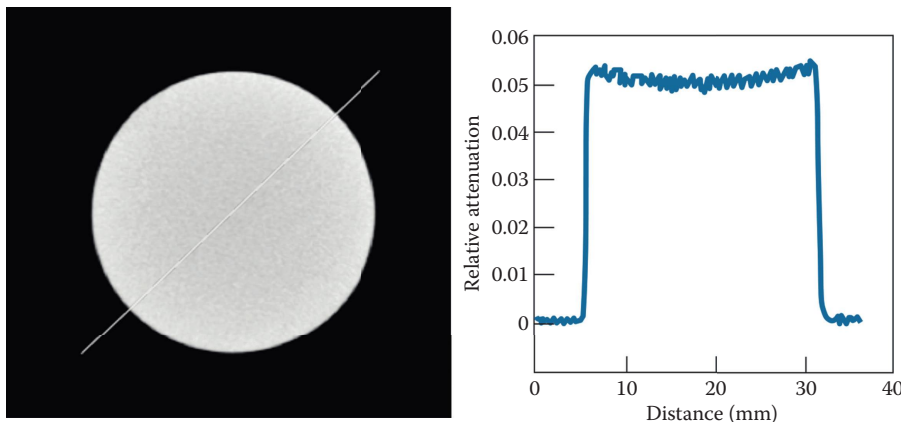


FIGURE 13.39 On the left is a CT slice through a 25.4 cm Teflon cylinder with 100 kV, 2 mm Al filtered spectrum. On the right is a 1D profile or lineout showing the cupping effect of beam hardening.

spectrum; this is referred to as beam hardening. In essence, as the polyenergetic beam penetrates an object, the spectrum effectively shifts to higher energy as the lower-energy portion is attenuated. As an example, consider the projection of a 2.54 cm diameter Teflon cylinder as shown in Figure 13.38. Notice that the measured projection is less than the calculated projection. The data were acquired using a tungsten anode tube source at 100 kV with a 2 mm aluminum filter coupled to a Thales amorphous-silicon detector with a Lanex fine screen.

For CT, the consequence of this difference is a cupping (beam hardening and scatter) artifact in the regions with substantial material attenuation, in this case the region in the center of the cylinder. A reconstructed CT image of the Teflon cylinder is shown in Figure 13.39. A 1D profile across the CT image is also shown in Figure 13.39. Notice the change in measured relative attenuation from the outside to the inside of the cylinder. The reason for the dip or cupping is due to beam hardening and scatter and not a nonuniform cylinder.

The canonical remedy for beam hardening is to estimate and apply a beam-hardening correction. For instance, for the Teflon cylinder, we fit a polynomial between the measured and calculated projections. In this case, we ended up with a second-degree polynomial with coefficients 0, 0.944, and 0.0684, respectively. Second, apply that polynomial to correct the measured projection data and then

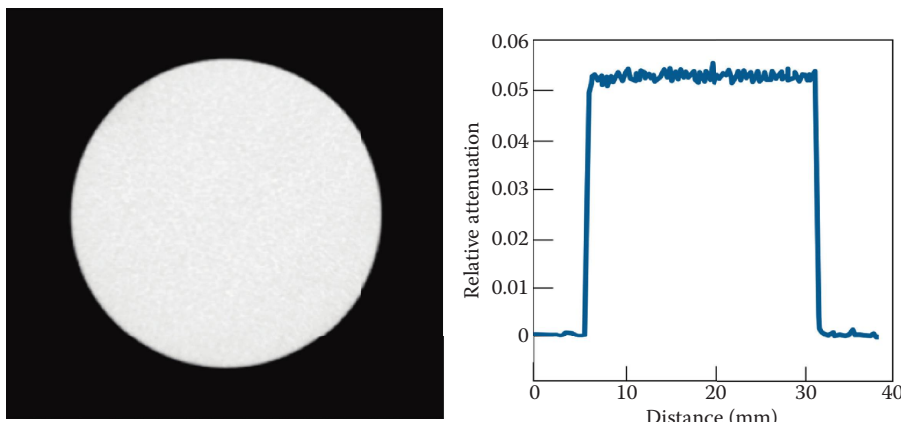


FIGURE 13.40 Image (left) and 1D profile or lineout (right) of a CT slice through the 2.54 Teflon cylinder with beam-hardening correction applied.

re-reconstruct. The beam-hardened compensated reconstruction is shown in [Figure 13.40](#). Notice that the 1D profile across the CT image is now flat. However, in the beam-hardening correction process, we have multiplied every pixel in the projection data (see [Figure 13.38](#)) by two constants and squared the projection data for the application of the second constant. So, we have changed the noise spectrum of the reconstructed data. Notice that the profile is now flat but includes more noise since multiplying a random variable by a constant is the variance of the random variable times the constant squared.

The beam-hardening correction remediated the cupping artifact but increased the voxel-wise noise in the center of the CT slice. Depending on contrastive requirements of your inspection, this may or may not be of any consequence. More about this potential impact is given in Chapter 14.

13.7.10 SCATTER ARTIFACTS FOR HIGH-ASPECT RATIO OR HIGH-ATTENUATING OBJECTS

Another type of artifact occurs with high-aspect ratio or high-attenuating objects. This results in a lowering of the apparent attenuation of the material along the long chords of the object. Representative examples of these types of artifacts are given in Figures 13.41 and 13.42. Two CT images from a CT scan of a turbine blade using a GE v-tome cone-beam CT system are shown in Figure 13.41. The image on the left illustrates the severity of artifacts caused by a high-attenuating turbine blade. The GE v-tome has an option called scatter correct, and when applied to the turbine-blade data set, it results in an artifact-free image as shown on the right in Figure 13.41. The image looks much better, but one should wonder what is real and what is fake. A similar effect is present in the scan of a NASA Space Shuttle 20 cm niobium thruster scanned at LLNL using a 9 MV linac source and a Thales aSi flat-panel detector. A representative digital radiograph and a CT image are shown in [Figure 13.42](#). Notice that small features are still visible in both the turbine blade and the NASA part. For example, the small holes in the inner edge of the turbine blade as well as the notch in the niobium thruster and the dis-bond in the NASA T-seal are shown in [Figure 13.43](#). However, it looks as if there is a change in the attenuation of all these objects, in line with the long chords of the objects, and this is fictitious.

The source of the artifacts in these three objects is the joint product of the lack of penetration through the long chords of the object, the meager stopping power of the detector, and the presence of background scatter resulting in counts on the detector that have no relationship to the object. The proportion of counts recorded behind the long chords of the object should be next to nothing, but

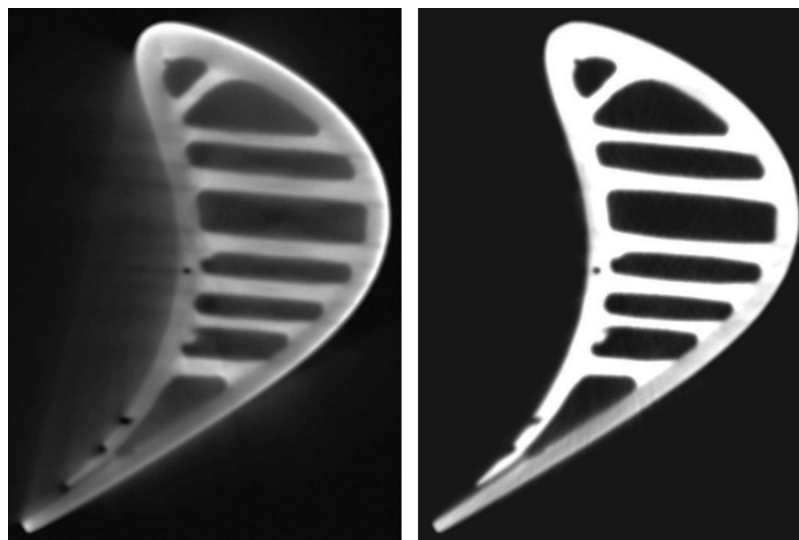


FIGURE 13.41 GE v-tome CT images of a turbine blade. On the left is an example of scatter-radiation artifacts, and on the right are the results when a GE scatter correction is applied.

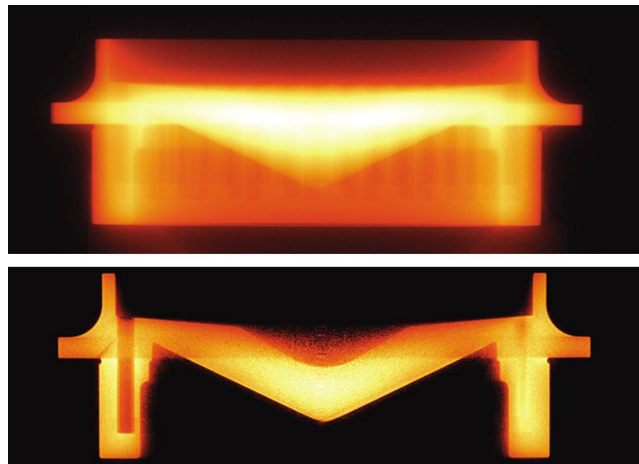


FIGURE 13.42 On the top is a digital radiograph and on the bottom is a vertical CT image of a NASA Space Shuttle 20 cm pure niobium thruster. The data were obtained using an LLNL CT system with a 9 MV linac and an amSi panel detector.

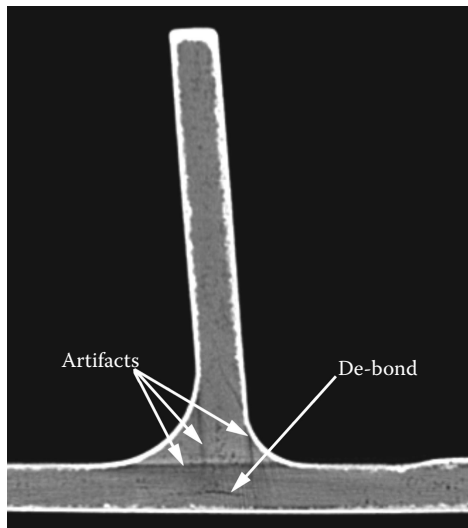


FIGURE 13.43 A vertical CT image from the inspection of a T-seal. The CT image reveals a de-bond and a few artifacts. The artifacts are due to long chords from the T-seal's high-attenuating ceramic outer coating. The indicated de-bond has a width of 8.0 mm, a total de-bond curvature of 0.75 mm, and an estimated de-bond void size of 0.43 mm.

as is the case with amorphous silicon flat panel and other detectors, the back of the detector can generate counts and the sides of the cabinet can result in counts from scatter (Schach von Wittenau et al. 2002b); the reconstruction routine reconstructs these few counts as if they were on straight lines through the object.

As shown in the GE images in Figure 13.41, there are calculation-based remedies for these types of artifacts. Another remedy is thicker beam filtering, scanning at a higher energy, and/or use of more collimation. However, in the case of the scan of the niobium thruster, the source was a 9 MV linac, filtered with 6 mm of tantalum, which results in a high-average energy spectrum. Still 20 cm of niobium is a lot to penetrate, and the Lanex fine screen cannot stop even a meager fraction of the

4 MeV average-energy photons at the exit face of the long chord in the niobium. This is a circumstance where iterative codes and additional calculations can play an important role in using the best CT system and to help in artifact reduction.

13.8 TEST PHANTOMS AND TEST OBJECTS FOR SYSTEM EVALUATION

Up to this point, we have identified three functions for test objects: (1) to validate an inspection technique, (2) to diagnose scanner problems, and (3) to determine the performance of different systems. In the first and second functions, the construction of a test object is closely connected to the inspection to be performed, with the constituent materials matching the materials of the object under inspection. Also, the inserted features should match the spatial and contrastive targets for the inspection. For scanner comparison purposes, the construction of phantoms can be more controlled. With the prevalence of medical CT systems, the need to evaluate performance has given rise to the fabrication of medical CT performance test objects such as those shown in Figures 13.44 and 13.45.

The variety and structure of CT test objects are oriented to the intended inspection targets and goals. The medical test objects and test object pieces in the figures include a range of different materials of different sizes. They are similar to the types of features in the MTF test objects, but of different materials other than just air. The total path length matches the attenuation of the objects to be inspected, and the different inserts include different features, defects, or anomalies to be detected in the overall material matrix. For CT, as opposed to radiography, the CT test object includes features that have aspects in three dimensions.

CT test objects enable the estimation of key performance parameters for a CT system. Two properties identified in the ASTM E 1695 standard (ASTM E 1695 2013) are the contrast discrimination function and the MTF. The first is a measure of the range of detection for materials in medical

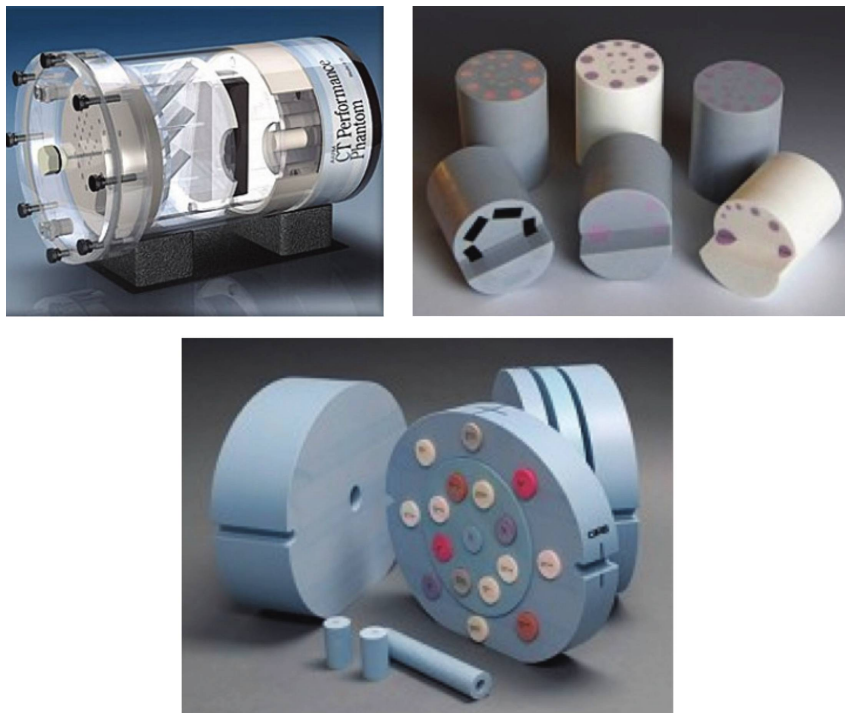


FIGURE 13.44 CT performance test objects and internal components used to evaluating CT systems.



FIGURE 13.45 Photograph of the American Association of Physicists in Medicine (AAPM) test object 610.

inspections. The second is a measure of the spatial resolution for the scanner that connects to the limits in size of what can be detected. Properties of system performance and their estimation are covered in Chapter 14.

In industrial contexts, the range of materials is larger, the chord lengths can be longer, and the target inspection sizes can be larger or smaller than medical. Also, the particular object and materials under inspection may not have a ready-made test object of similar material lengths with contrastive features and spatial properties matching the goals of the inspection. Consequently, the task of fabricating a test object can be a part of the inspection effort. Principles for constructing a test object were mentioned in Chapter 12; in summary, fabricate an object of the same materials, with the same geometry, and insert a range of known defects into the test object that span the size and material changes that capture the goals of the inspection.

13.9 DATA ANALYSIS AND INTERPRETATION

Referring back to Figure 13.2, a CT volumetric scan is a particularly rich data set for use in inspections. When acquired and reconstructed correctly, a CT reconstructed volume is a voxelized image of the object, where the value of each voxel occupying some 3D position in the object is dependent upon the elemental composition and density. As such, CT data sets include data to support a large variety of inspection tasks such as defect identification, assembly verification, measurement of dimensions of components and structures, estimation of volumes of cavities, and extraction of key contours and boundaries. For example see the paper by De Chiffre et al. (2014). A number of commercial packages are available for viewing, re-viewing, and analyzing the features in CT reconstructed volumes; examples include VG Studio MAX, Avizo 3D software, GE-v-tome, and 3D-DOCTOR. In addition, there are a large number of user-developed scripts and command files

for MATLAB and IDL. All of these options can generate interesting and important views and analyses of 3D volumetric data. For this section, the more important question is, are these views and analyses supported by the data and how does the analyst know this? Chapter 16 includes a variety of CT inspections with a description of analysis tools used in the application.

Stepping back from these options, it has been our experience that review and analysis of CT volumetric data falls into two general tasks. One is exploratory analysis of volumes where you are looking for anything untoward, e.g., a void or a component that is the wrong size or some incorrect orientation of an internal assembly. The other is confirmatory or a more focused analysis of the inspection data that you are inspecting a particular section of an object for this problem or defect and you have done the background work to know the correct dimensions and the correct fit-up between the components. For complicated multimaterial assemblies, the first task can be difficult and time-consuming, and it can be difficult to know when you are done. This task is of course more complicated when there are artifacts and you re-reconstruct the volume to remediate the effects, and now you have two volumes for inspection instead of one. In the second task, things are much better defined. You know where to look and what to look for. Once this task is better known, you may be able to automate the analysis or take steps to semi-automate the inspection. For either task, the following groups of tools are important:

Data query tools—Some means for slicing, extracting, or rotating to view any plane in the volumetric data set. In viewing these planes, the tool must have the ability to view a 1D profile or lineout, easy access to the values of the voxels and obtain a local standard deviation or variance. Add to this the usual window/level operations for viewing images on a monitor. See Section 16.4.12 for an example.

Visualization tools—Some means for performing volume rendering of the CT volume or parts of the CT volume, with the usual controls for the transfer functions to control the opacity of the different parts of the volume. Keep in mind that you are setting up a false light source and reilluminating the volume to show certain features. This viewing need not be quantitative but tuned to show a particular component vis-à-vis other components in the volume. See Section 16.4.10.

Dimensional measurement tools—These tools include, at a minimum, some means for obtaining a thickness of a wall or component either by pointing to the feature or drawing a line across the dimension. The next level of sophistication would be a boundary-dimensioning tool that can adapt to curved surfaces in 3D space and then generate drawings or surfaces of the estimated boundary. See Section 16.4.12.1.

Segmentation and volume estimation tools—One particularly strategic operation that can be useful for analysis of CT data is segmenting the voxels into larger bundles; presumably these bundles correspond to distinct materials or a component in the CT volume. These bundles of voxels are then treated as distinct pieces of the volume, and statistics can be generated from each of the segmented bundles. This operation is performed routinely in airport luggage scanning, where the CT volumetric data are segmented into objects that are then evaluated as a threat or nonthreat (see Section 16.5). The package of software for segmenting volumes into constituent bundles should provide some controls for defining the thresholds directing the work, substantial statistical reporting on the segmented bundles, and the ability to export the segmented volume, independent of the input CT volume for use in other analyses. See Section 16.5.2.

Advanced analysis tools—This category of tools is a bit open ended and is the place where different packages differ. For instance, some packages allow for animating the CT volume, showing how something would move as the function of the object is exercised. Another package includes advanced contour extraction tools: to extract the adaptive boundaries of objects, then extract the voxel values of some number of pixels from that material boundary and view those voxels as a sheet or layer. For an example, see Section 16.4.7.1.

All of these tools are important for the two tasks mentioned above, more so for the open-ended exploratory analysis and less so for confirmatory-focused data analysis. It might be argued that all data analyses should be of the focused variety, since you should know a lot about the object before you acquire a scan and have a plan for looking at the CT volume before you even turn on the x-rays. However, this would miss many of the important findings uncovered from exploratory analysis of CT volumes. The data sets are large and there is a lot to inspect. While difficult and time consuming, looking through the entire volume with lots of different tools has proven to be a good idea.

In the analysis of CT volumes, two questions are central: (1) Do these voxel data include the spatial and contrastive properties to support the inspections I want to perform? (2) When and how do you decide against making a claim from the CT volumetric data or how do you select between the features you have imaged reliably and those that while interesting are beyond the properties of these data?

In the analysis of CT volumes, it is important to begin with the fundamentals:

1. The quantitative value of the voxel varies with the energy used in the inspection and the materials in the object. For example, if the inspection is in the megaelectron volts range, the total attenuation is more dependent on density than Z .
2. The voxel values are in themselves an average over the individual voxel volume. A component in the object can be smaller than a voxel and/or can span a couple of voxels. There is always a fundamental indeterminacy about features that are smaller than a voxel to those on the order of a few voxels and the claims you can make about those small features.
3. The baseline noise in the region of the image you are inspecting is a real limit on the reliability of the claims you can make about the inspection data. At this point, we know that this noise is multicomponent and includes some impact from the object scatter at this location. The projection from a slightly different angle may include more or lesser noise than the previous projection, and you may just miss this feature.

Given these considerations, we reiterate the same threefold detection terms mentioned in Chapter 12: Panel 12.1, i.e., feature is observable, feature is detectable, and the feature can be measured. Making claims for features in the first two categories involves considerable risk.

In summary, more uses for CT volumetric data are being developed as shown in Chapter 16. As computer capabilities increase, it gets easier to manipulate the entire 3D CT volume. This situation just invites new ways to view, review, and analyze CT data. Further, it is now possible to directly calculate important physical quantities from CT volumetric data, examples of which are given in Chapter 16. The difficulty now may be a problem with the inability of the CT data to truly support the many sophisticated operations applied to the inspection volume. You must ensure that you are producing measurements reliably and with the accuracy and precision needed. In this context, CT artifacts just make the inspection problems harder. It is often the case that remediating artifacts includes re-reconstructing the data, which then has impacts for image noise or, in the case of model-based iterative reconstructions, just makes the data look like the model. As in the case with digital radiography, well-constructed test objects, scanned periodically, are the best strategy for validating the data and operations applied to the CT data. Lastly, some kind of re-reconstruction capability may be critical to getting the best reconstructed image for analysis.

PROBLEMS

- 13.1 From two images of a 50 mm diameter cylinder, the projected diameters are 75 and 60 mm, and the move distance between the two images is 200 mm. Estimate the value of y_{sdd} and one of the positions of y_{sod} for either of the measurements. What is the expected error in y_{sdd} if it turns out that the measured diameter for one of the positions is actually 72 mm instead of 75 mm? If you have a measurement accuracy of 1 mm, what is the average

expected error for an estimate of y_{sdd} ? How can you reduce this error and/or better verify your estimate?

- 13.2 Using Equation 13.1 as a starting point, show under what circumstance removing the inner part of an assembly, leaving other components as the Φ_0 for the inner part of an assembly, is OK? What is the data acquisition strategy that makes this work?
- 13.3 If you have access to data, from the image of a sinogram of a test object, and the point and click tools in ImageJ, come up with an estimate of the center of rotation. How close were you? How did you determine how close you were?
- 13.4 How much total data can be generated from a 1024×1024 detector, digitized at 16 bits, using 720 views? How big is the reconstructed volume? How does this change for a 3072×3072 size detector?
- 13.5 Can you acquire, process, and reconstruct data on the same single desktop computer?

14 Image Quality

After reading this chapter, you will be able to identify and evaluate components of image contrast, resolution, and noise for transmission images. It is the goal of this chapter to unpack the components underpinning the inspection performance properties of an image, and detect when one or more of these components are the cause of some issue for using this image for that inspection. The properties of image quality we are considering here are to be distinguished from *image artifacts*, which can degrade overall image quality but are more the result of specialized features of the imaging process. Further, understanding the components constituting image performance can serve as a basis for suggesting the next improvement to the current technique and/or can supply the machinery for modeling *probability of detection* and *false alarm rate* for proposed techniques.

Part and parcel of this evaluation process is the use of tools for the measurement of image quality. These tools can be used in a variety of ways: (1) as a basis for comparison between images and (2) as a way of measuring the properties of the image compared to the goals of the inspection. An added complication here is, for transmission images, each measurement is statistical in nature (independent of detector, transmission measurements are Poisson random variables), and so the measurement of image quality includes an inherent variability. Also, this results in some inherent limits to the accuracy of different estimated quantities in different contexts. The key to navigating this complexity is measurements of *line-spread functions*, *point spread functions*, *edge spread functions*, *modulation transfer functions*, *detective quantum efficiency*, and *receiver-operator characteristic curves*. It is our goal to equip the reader with a working knowledge of these concepts and their utility for assessing images—and image-based inspections.

14.1 INTRODUCTION

The fundamental properties of digital radiography (DR) and computed tomography (CT) images constitute the support for claims of an inspection and define the limitations for the scope of the measurements. As mentioned in Chapters 10 through 13, DR and CT images include a few distinctive subtleties characteristic of the properties of *transmission imaging* that are not a part of reflected light or reflected sound images. In general, components and properties of transmission images can be sorted into three headings: (1) factors impacting contrastive performance, (2) factors affecting spatial resolution, and (3) sources of image noise. It is fundamental to understand that these properties are intrinsically related to each other and involve all the aspects of the image-forming process: the source properties, the particulars of the detector, and the configuration of the object in the source-detector envelope; they also combine in any one image to constitute the *sharpness* or *contrast* for the revealed features of an object.

In addition, for x-ray transmission imaging, these composite properties of images can be variable throughout the image. For instance, a feature in one part of an object is sharply imaged, while other object features in a different part of the image include a greater amount of blur, or include edges of that feature that are not crisply defined. A number of questions can follow, sometimes beginning with the following: is the imaging system operating correctly? Or perhaps this is just the object—it is just true that the object includes some small mottling or surface feature that results in a blurry edge; the image is faithfully reflecting the properties of the object function. Alternatively, it could be true that the differing *sharpness* in the image could be a product of the technique—the spot size of the source is not small enough to produce sufficient sharpness for the magnification of that part of the object, positioned at that part of the source-detector geometry (or the spot could have bloomed on that particular image). Again, perhaps the energy is not sufficient to adequately penetrate the

object for that thickness, and the scatter proportion is greater relative to the primary x-ray content for that region of the object, resulting in fuzzy edges. Lastly, perhaps the detector is simply degraded in that region and we need to get a new one. Just how you use this image to inspect the object can depend on answers to these questions, and for some responses to the above questions, you simply acquire another image, maybe on a different system.

Given the multiple factors upon which the *sharpness* and *contrast* of a transmission image depend, comparing images acquired from multiple systems gets complicated, and usually you need more gear—software and hardware. For both medical and industrial systems, ASTM standard methods for calculating and measuring image performance have been defined, and software packages are available (some of which will be demonstrated here). Also, for assessing image quality between and across systems, the role of *image quality indicators* or *test objects* can demonstrate how the variability of properties of images connects to the performance of that system acquiring data for objects of that type. The caveat here is the test objects and test object features need to be made with accuracy and precision, and are constituted of known materials with known thicknesses, holes, or features. The ASTM defines just such objects, *pennies** or *step wedges*, for just this purpose.

Addressing the questions mentioned above has identified three sets of tools for assessing image quality: (1) a background familiarity for the factors involved in image formation and how these factors impact the image, (2) software for calculating measured image properties, and (3) test objects or image quality indicators designed to demonstrate the system response of a critical feature of interest for an object inspection and provide a complimentary capability for assessing image quality. If performed correctly, a measured property from an image should predict the imaging performance for a test object or image quality indicator, and vice versa.

To describe the components of image contrast, spatial resolution, and noise, we will need to utilize some of the equations and schemas presented in previous chapters. Up to this point, we have presented descriptions of x-rays, x-ray interactions (Chapter 5), x-ray signals (Chapter 10), and properties of x-ray transmission for supporting algorithms and algorithm development (Chapter 13). The description of the interaction between x-rays and matter focuses attention on the type of source energy (monochromatic or polychromatic) and the kinds of interactions that take place in the object—and how those change the interpretive context for the detected signal. The taxonomy of signal components presented in Chapter 10 is an attempt to account for the different types of detected signal and how different systems result in different relative proportions of signal components. Fundamentally—in addition to the object—all the materials in the system and surrounding the detector will react to the x-rays by absorption or scattering, and these sources of signal can find their way to the detector. In this chapter, we will discuss the different signal components and attenuation mechanisms and how they account for image contrast, spatial resolution, and noise. We summarize from earlier chapters the relevant concepts, notation, and equations in Panel 14.1.

PANEL 14.1 Review of Equations and Key Concepts

Following Beer's law,

$$\Phi^E(E, Z, \rho, y_\ell) = \Phi_0^E(E) e^{-\mu(E, Z, \rho)y_\ell}, \quad (14.1)$$

where

$\Phi^E(E, Z, \rho, y_\ell)$ is the transmitted irradiance at monochromatic energy E through a thickness y_ℓ for a single material of atomic number Z with a density of ρ in energy per unit area per unit time

* Penny is a widely used slang term for penetrometer.

$\Phi_0^E(E)$ is the incident irradiance in energy per unit area per unit time at monochromatic energy E

y_ℓ is the thickness along the direction of x-rays of the single material uniform absorber in centimeters

$\mu(E, Z, \rho)$ is the linear attenuation coefficient in units per centimeter at energy E for a single material with atomic number Z and mass density ρ

Equation 14.1 can also be rewritten as

$$T(E, Z, \rho, y_\ell) = \frac{\Phi^E(E, Z, \rho, y_\ell)}{\Phi_0^E(E)} = e^{-\mu(E, Z, \rho)y_\ell}, \quad (14.2)$$

where $T(E, Z, \rho, y_\ell)$ is the transmission.

In other words, $\Phi^E(E, Z, \rho, y_\ell)$ is the photon irradiance after traveling distance y_ℓ in the uniform absorber with linear attenuation coefficient μ . From Equation 14.1, *monoenergetic* x-rays are exponentially attenuated when passing through matter. Another useful quantity is the attenuation times path length (sometimes referred to as the radiographic attenuation), which is given by

$$\ln\left(\frac{\Phi_0^E(E)}{\Phi^E(E, Z, \rho, y_\ell)}\right) = \mu(E, Z, \rho)y_\ell. \quad (14.3)$$

Sometimes $\mu(E, Z, \rho)y_\ell$ is abbreviated to $\mu\ell$.

For a single energy, $\Phi^E(E, Z, \rho, y_\ell)$ can be replaced by $\Phi^P(E, Z, \rho, y_\ell)$, i.e., the photon flux density (number of photons per unit area per unit time):

$$\Phi^P(E, Z, \rho, y_\ell) = \Phi_0^P(E)e^{-\mu(E, Z, \rho)y_\ell}. \quad (14.4)$$

Again, it is important to emphasize that Equations 14.1 through 14.4 are for a single (mono-chromatic) photon energy (E) interaction with a single uniform material.

For a polyenergetic source and single material, this expands to

$$\Phi^P[S(E), Z, \rho, y_\ell] = \int \Phi_0^P[S(E)]e^{-\mu[S(E), Z, \rho]y_\ell} dE, \quad (14.5)$$

where $S(E)$ is the x- or γ -ray source spectrum (photon flux density vs. energy). $S(E)$ refers to a family of source functions, each specific source function depending upon the type of source and its operating parameters, for example, a tungsten-anode x-ray tube source at an operating voltage of 150 kV or a 100 mCi ^{109}Cd radioisotope (for more details on this source, see Chapter 8). Each source has a particular source function that must accurately be represented by the function $S(E)$. Further expanding this to multiple materials (1, ..., n) results in

$$\Phi^P[S(E), \bar{Z}, \bar{\rho}, y_\ell] = \int \Phi_0^P[S(E)]e^{-\sum_i^n \mu_m^i[S(E), Z_i] \rho_i y_\ell^i} dE, \quad (14.6)$$

where $\mu_m^i(E, Z_i) = \mu_i(E, Z_i, \rho_i)/\rho_i$ is the mass attenuation coefficient with density and atomic number for the i th material, and \bar{Z} and $\bar{\rho}$ are the average or effective atomic number and average density, respectively.

Components of acquired signals are given by

$$\Phi[S(E), \mathbf{O}, \mathbf{d}, \mathbf{I}] = \Phi_p[S(E), \mathbf{O}, \mathbf{d}, \mathbf{I}] + \Phi_s[S(E), \mathbf{O}, \mathbf{d}, \mathbf{I}] + \Phi_{rf}[S(E), \mathbf{O}, \mathbf{d}, \mathbf{I}], \quad (14.7)$$

$$\Phi_s[S(E), \mathbf{O}, \mathbf{d}, \mathbf{I}] = \Phi_{Sbk}[S(E), \mathbf{d}] + \Phi_{Sobj}[S(E), \mathbf{O}, \mathbf{d}, \mathbf{I}], \quad (14.8)$$

$$\Phi_0[S(E), \mathbf{d}, \mathbf{I}] = \Phi_{P0}[S(E), \mathbf{d}, \mathbf{I}] + \Phi_{Sbk}[S(E), \mathbf{d}]. \quad (14.9)$$

Source unsharpness is given by

$$\delta_{spotx} = D_x(M_x - 1), \quad (14.10)$$

where

$$M_x = \frac{y_{sdd}}{y_{sod}}. \quad (14.11)$$

14.1.1 COMPONENTS OF IMAGE CONTRAST

All sources of detected signal impact the image contrast you obtain for a single view or for a sequence of views in DR and/or CT. Consequently, both the description of the interactions with materials presented in Chapter 5 and the taxonomy of sources of signal presented in Chapter 10 are implicated. Following previous practice, we will present the components of image contrast with a focus on how these constitute the means for an inspection. Part of this section constitutes a review of the materials in Chapters 9, 12, and 13, but we attempt here to bring them all together for the analysis of inspection data.

The first component for image contrast is usually referred to as *intrinsic contrast* or *object contrast*. This refers to the differences in x-ray attenuation that are resident in the object when viewed from that angle with that energy or energy spectrum, or in the case of CT, the contrast in the object function for that system. This is depicted in Figure 14.1. In many ways, this is the contrast one would obtain independent of the detector, or if you would be able to perfectly capture all the irradiance at some fixed distance beyond the exit face of the object. Most importantly, this component of image contrast is the substance for the inspection and supports the claims you make about the object features. The magnitudes for this type of contrast are determined by the x-ray interactions in the material at the energy used in the inspection. The energy used is critical: at low energies where photoelectric absorption is significant, the attenuation difference between two materials can be very large; at higher energies where total attenuation is proportionately more Compton scattering, the differences in material attenuation are less and are more of a result of differences in density than the type of material. So, at a given single energy or energy spectra, the *intrinsic* contrast is the difference in x-ray properties between material(s) on different chords through the object.

It is important to mention here that for polychromatic sources, image contrast is impacted by the stopping power and gain characteristics of the detector, which act as a weighting function on the source spectrum, thus effectively changing the energy used in the inspection. To account for or estimate *stopping power*, D_{sp} , the x-ray properties of the detector have to be known, and are accounted for as,

$$D_{sp}(E) = 1 - T(E, Z, \rho, y_\ell), \quad (14.12)$$

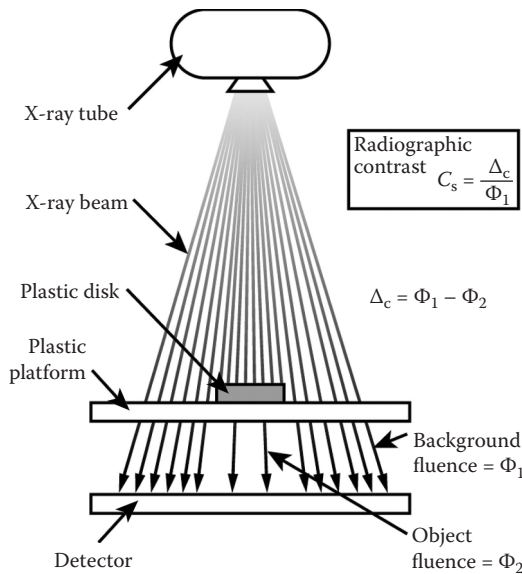


FIGURE 14.1 Illustration of the definition of Δ_c .

or equivalently

$$D_{sp}(E) = 1 - e^{-\sum_i^n \mu_m^i(E, Z_i) p_{ti} y_{ti}^i}, \quad (14.13)$$

where the list of materials in the exponent corresponds to the characteristics of the detector. To show the impact of the detector on the energy used in the inspection, consider two scintillator-based detectors: one using Lanex Fine (0.085 mm of Gd_2O_2S , with binder and a plastic base) and one using 1.0 mm of CsI(Tl). Consider two tungsten spectra, 100 kV applied potential filtered with 2 mm of Al, and 220 kV applied potential filtered with 2 mm of Cu. Figure 14.2 contains the 100 kV spectra, and the spectra with stopping power applied, while Figure 14.3 plots the same values for the 220 kV spectrum. Notice the large changes in the shape of the 220 kV spectra for the Lanex Fine and CsI(Tl) scintillators. In terms of average energy, for 100 kV voltage, average energies are 46.7 no detector, 45.8 (CsI(Tl)), and 40.6 (Lanex Fine); and for 220 kV voltage, average energies are 117.3 no detector, 100.2 (CsI(Tl)), and 96.2 (Lanex Fine). Notice the larger change when Lanex Fine is used as compared to CsI(Tl).

Reviewing the two sets of plots, it is shown that the losses incurred from a loss of stopping power in the detector include multiple impacts. First, the number of photons effectively used in the inspection is substantially lower with the Lanex Fine screen, especially with the 220 kV spectra. The consequence is less photon statistics for the same time, or conversely, if you want to get the same signal-to-noise ratio (SNR) with the thinner screen, you will have to take more time to acquire measurements. Second, the average energy is lower and the shape of the spectrum is more weighted to the lower-energy photons. The result here is more significant beam-hardening artifacts, since the higher-energy photons are not stopped, and only those photons make it through the long chords of the object. In the same connection, the photon statistics in the long chord regions will be meager—and increasing the milliamperes (tube current) for the inspection does not help as much, especially if there are regions in the image where the low-energy photons are detected in a robust way. It is likely that those regions in the detector will be saturated before you gain much more precision in the hard-to-penetrate regions. Regardless of the exact mechanism, detector stopping power changes

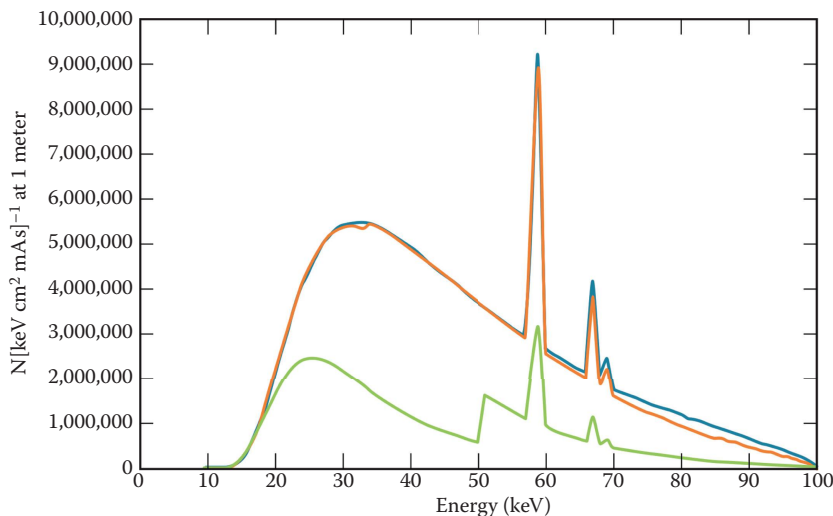


FIGURE 14.2 Comparison stopping power of CsI(Tl) with thickness of 1 mm (red) to that of Lanex fine (green) for an x-ray spectrum (blue) from a W-anode tube operated at 100 kV and filtered with 2 mm of Al.

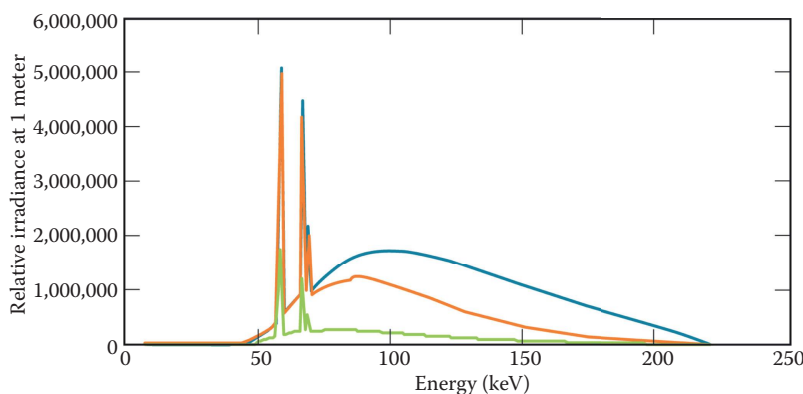


FIGURE 14.3 Comparison stopping power of CsI(Tl) with thickness of 1 mm (red) to that of Lanex fine (green) for an x-ray spectrum (blue) from a W-anode tube operated at 220 kV and filtered with 2 mm of Cu.

the intrinsic contrast in an inspection, lowering the average energy, and often, changing the noise for hard-to-penetrate materials, thereby compromising overall contrast in the inspection.

Scatter from the object is part of the intrinsic contrast and most often degrades the contrast that could be achieved without the presence of object scatter. This component has two impacts. The first impact is that the scattered irradiance from an object feature can affect the imaging of adjacent object features. This can be observed in medium- to high-energy inspections, when imaging low-attenuating object features that are located directly next to high-attenuating object components. In DR, the object contrast for the low attenuation region is compromised, the region includes more blur, and the magnitudes for the low-attenuating material are artificially higher due to the presence of object scatter. In CT, the scattered irradiation is deposited on the interior edges of the high-attenuating materials with the result being additional blur—and this is problematic if this is the most important part of your inspection. The second impact of object scatter is that it can convolve

with *beam-hardening* effects to result in image artifacts (scatter streaks) that likewise degrade the measured contrast between materials in the object.

Following Chapter 10, two sources of signal are important here: scatter from the surrounding components of the system and scatter within the detector package. These sources of signal are components of image contrast that are not directly related to the object function. Scatter from the system is identified as that source of signal that is due to scatter from the surrounding system components—upstream collimation, scatter from side walls, and scatter from object mounting or object-fixture hardware. In particular, for high-energy inspections, collimators positioned close to the source, or midstream, often include an intensity roll-off, where the detected intensity is lower due to the lower-energy content of the scatter photons in close proximity to the collimator edges (this effect is also convolved with the source unsharpness from the size of the source spot). Scatter in the detector package results in counts added to the measured signal, which are not part of the primary or direct irradiance. In both cases, the measurement of intrinsic contrast is degraded, and a proportion of the digitized counts for the pixel are occupied by these two sources of scatter. As a result, instead of the measured contrast between two chords corresponding to the intrinsic difference in the x-ray attenuation, the difference is diluted by the proportion of the signal counting these two sources of scatter. This effect on contrast is further complicated by the presence of these signal components in the Φ_0^P image. Consequently, the detected differences are less, and it can be more challenging to detect and dimension the features in the object.

For DR, the geometry for the inspection, the orientation and position of the object in the source-detector envelope, is important for determining the expected *intrinsic contrast*. Part of the art of radiographic inspections is picking just the correct view through a certain orientation of the object function that focuses on those properties of the object. For tomosynthesis and CT, the orientation of the object relative to the scanning motion (object or source-detector) can impact the magnitudes for the intrinsic contrast obtained in a scan. Scan geometry has an impact in this connection as well—fan and cone-beam geometries mollify the impact of object scatter (Light et al. 2000) (more about this in [Section 14.3](#)). For CT, a choice of energy that does not provide adequate penetration through the most attenuating orientations of the object can result in artifacts that decrease or mask the intrinsic local contrast. The effects of not penetrating a certain section of an object function and then letting the detector and surrounding scatter sources fill in the blanks is a component of the intrinsic contrast.

In summary, intrinsic contrast, the expected differences in the magnitudes in the image, either pixels or voxels, is the combined result of object components, energy and detector used in the inspection, and the orientation of the object relative to the source-detector envelope. The energy used determines the proportional contributions of each attenuation mechanism to the total attenuation (the amount of object scatter). Detector stopping power plays a role here as it filters the energy of the irradiance emerging from the exit face of the object. Object scatter is just problematic and the orientation of the object relative to the source-detector impacts all of the above. The most important point for x-ray absorption-based inspections *object* or *intrinsic* contrast is the base or fundamental contrast in the system—and it is just the information connected to the state of the object that you are interested in measuring.

14.1.2 COMPONENTS OF SPATIAL RESOLUTION

Components that account for spatial resolution in a transmission image can be divided into those factors that impact the image independent of the detector: x-ray source unsharpness, scatter from the object, scatter from cabinets, and collimators (those not connected to the detector); and those factors that are connected to the detector package: scintillator effects, detector internal scatter/blur, and detector pixel pitch. This division of factors reflects the situation of the experimenter—the factors in the geometry of the technique are with you even if you change detectors—but sometimes changing the detector is a really good idea.

In the first category, for tube sources, the size and shape of the x-ray spot results in a penumbral blur for object constituents according to their position in the source-detector envelope. This is illustrated in Figure 14.4.

In particular, for a uniformly emitting disk spot, the size of the penumbral blur is the joint product of the spot diameter and the x-ray magnification (Bossi et al. 2002), as given in Equations 14.10 and 14.11.

As can be seen from the *pinhole* image of the source spot usually provided with the reference materials for the x-ray source, source spots are not uniformly emitting disks. However, we consider this equation a useful approximation that is easily calculated for your x-ray source.

The significance of the source-spot blur is a bit different for DR and CT. For DR images, the effects can sometimes be directly observed as features close to the detector are imaged more sharply than the features farther away from the detector and at higher magnification. For CT, the impact of source-spot blur is *averaged* out over the different positions of the feature imaged by the set of views that constitutes a scan (in particular, the distance of the feature from the source). In both cases, if the spot size blooms, or is simply larger due to some impact of source filtering, spatial resolution is degraded for both DR and CT images. With DR, the magnitude of the impact is more acute if the feature is at magnification where the spot blur is large compared to the size of a pixel.

Object scatter has an impact on spatial resolution according to the amount of scatter for that feature at that energy, and the adjacent materials in the object. As shown in Chapters 5 and 10, Compton scattered photons distribute into an angular distribution, with the angle at which the photon is scattered corresponding to a different energy relative to the incident energy. As the energy increases, the overall scatter distribution is more forward-peaked; this still means that the input *ray size* is enlarged by the scatter width. From the point of view of the pixel looking at the object, this means recording the irradiation from adjacent pixels. For algorithms, this means that recorded counts at adjacent pixels are more *correlated* than before, and routines that assume the pixels are independent and identically distributed random variables will likely produce some untoward artifacts. This will

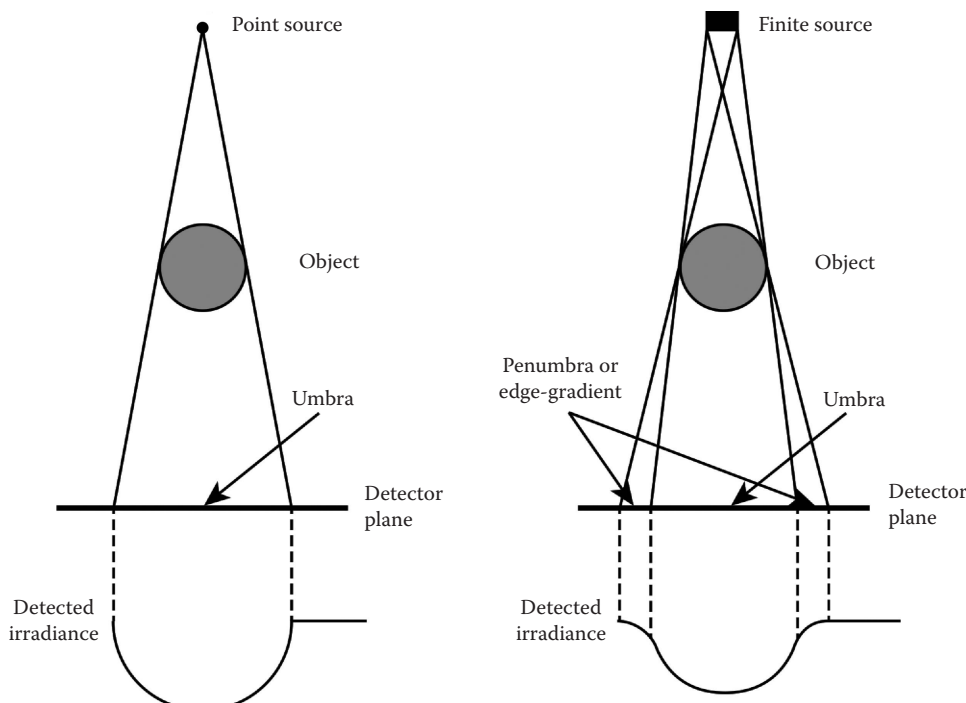


FIGURE 14.4 Schematic showing how blur arises from finite source spot size.

also frustrate statistical tests based on counts of voxels as the number of degrees of freedom. As indicated in other treatments, pixel-wise distributions of irradiance from object features are narrower, and thus less correlated when the object is farther away from the detector plane—but this is not without cost—increasing the spot-size blur. When possible, and the spot-size blur is small enough, we have found object-to-detector distances of 1–2 part diameters to result in a decrease in scatter width.

One added consequence of spot-size blur and increased blur due to scatter from the object is the relative loss of *spatial invariance* for the features in transmission images. Both effects are generated from local properties of the object and scan geometry: (1) the distance of the feature from the source relative to the source-to-detector distance and (2) the local scatter properties of the ensemble of materials with the angular scatter distribution for that feature. As a result, when the x-ray magnification of a feature puts spot-size blur at magnitudes greater than a pixel or local scatter effects are present, parts of the image just include more blur compared to other regions in the image. Applying spatial filtering schemes that require spatial invariance to remove this or that image component will be frustrated—resulting in a local increase in noise or artifacts in the region where the chosen filter is at a mismatch with the underlying process of image formation.

The construction and components of the x-ray detector capture the image in space and, in the process, effectively account for the spatial resolution of the image. Two types of indirect (employing scintillators) detectors are covered here: area- and linear-array detectors (with and without septa). Area detectors include a few components, the scintillator, the array of pixels (their pixel pitch and well depth), and possibly some mechanisms for intensifying the light from the scintillator. In [Section 14.1.1](#), we discussed the importance of the stopping power of the scintillator. In addition, there are circumstances where the *inherent* resolution of the scintillator includes a direct impact for the spatial resolution. Scintillators for area detectors can be fabricated into different formats: (1) unstructured scintillating screens (the scintillating compound is mixed with some binding element and support), plastic, glass, or ceramic, or (2) structured scintillators where the scintillator is arranged in columns (sometimes these columns of crystals are directly deposited onto the array of photodetector pixels). The two key properties of scintillators in either of these formats, the material in the scintillator and the thickness, combine to produce an *inherent* resolution, the spatial resolution of the transmission image on the exit face of the scintillator.

Measuring the inherent resolution of scintillators can be performed with detectors that include the capability to change out or switch scintillators. At Lawrence Livermore National Laboratory (LLNL), we have used camera-lens scintillator configurations and panel detectors that support scintillator change-out capability. [Figure 14.5](#) contains a plot of the modulation transfer functions (MTFs) for a variety of scintillators that can be used with the Perkin–Elmer detectors, each curve representing the *inherent* resolution of that scintillator screen. One caveat here is that, to make sure you are measuring the properties of the scintillator screen and not the spot size, it is advantageous to use a *line-pair* gauge, or other IQI measurement piece attached to the scintillator. Further, to ensure your signal is robust, you will want to pick an energy that is favorable for the stopping power of the screen.

Notice the large range of modulation values at the 1 lp/mm location: spanning a range from 0.05 to 0.5 modulation. As a first introduction to what this means, if you have a feature that is 0.5 mm (1 line pair per millimeter is two lines per millimeter so the width of the line is 0.5 mm), the Lanex Fine screen will image that feature at 0.5 of the input modulation, as opposed to imaging with the AST INSPEX M screen which will only image 0.05 of the input modulation of the same feature (see [Section 14.4](#)). As one might expect, there are large differences in stopping power and scintillator screen light output connected to these two screens. Also, we are only discussing the impact of the choice of scintillator screen, which is a fractional part of a fielded system. The point here is the choice of screen is significant, and MTF curves are many times available and should be studied.

For linear-array detectors, with or without septa, the scintillator material is usually deposited on the array element. Consequently, the *inherent* spatial resolution of the scintillator does not figure

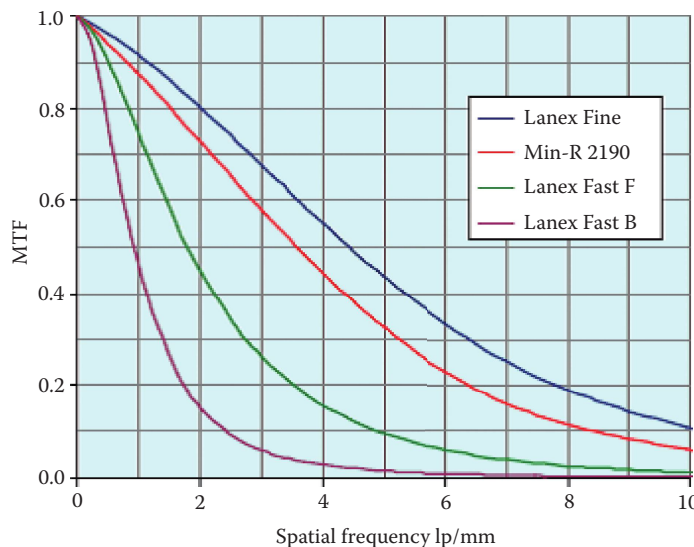


FIGURE 14.5 Intrinsic MTFs for different commercial scintillator screens. Many of which can be used in amSi detectors. This was measured RadEye2 CMOS photodiode detector. (Copyright 2012 by Feledyne Rad-icon Imaging Corp. Reprinted with permission.)

into the resolution achieved by this type of a detector. The use of septa in the detector package further rejects the irradiation that is diverging within the solid angle spanned by the detector by restricting the photons impinging on the detector according to direction including scattered ones. The detection samples the output of the scintillator by restricted collimation and does not access the *inherent* resolution properties of the scintillator. Spatial resolution for linear array detectors is determined largely by the pixel size or pixel pitch of the array elements.

For any detector, one key property is pixel pitch or the size of the pixel in both width and height. This is the fundamental limiting factor for spatial resolution—even if the scintillator presents an image with better resolution than the pixel size of the array; you are hard-pressed to improve much on the pixel pitch of the detector. You can dither the array in one or both directions and interleave the multiple acquisitions into a larger array, but this is hard to justify if a smaller pixel-pitch detector of the same type exists. Two straightforward impacts follow from the choice of pixel pitch: (1) resolution impact, an MTF bounded by $\sin x/x$ (Dainty and Shaw 1974) and (2) partial volume limits.

The *partial volume* limits for an inspection introduce an additional variability into the task of detecting features at the length scale of a pixel or smaller than a pixel (more about this in Section 14.4). Partial volume effects work out into the imaging performance a bit differently for DR and CT. In DR, if the feature is a small component of the ray sum through the object at that pixel size—lower than the local contrast—you do not see the feature. For CT, the many different views of the object can include that particular view, which enables the best contrast for that feature for the view of the object function. The issue for CT is the voxel value, which is an average over the voxel volume, though the small portion of the voxel occupied by that material will necessarily be imaged at a reduced contrast. The detectability of the material depends on the difference in attenuation corresponding to the amount of the volume of that voxel occupied by that feature—convolved with the blur functions operating in that location. These effects can result in surprising performance for detecting large differences in attenuation for small amounts of material within a larger voxel of contrasting material. For example, CT might reveal a steel BB in a pumpkin using voxels that are five times the BB diameter when the BB is not discernable in any single radiograph.

In summary, radiation area detector arrays can be in a variety of formats: (1) amorphous silicon, (2) complementary metal–oxide semiconductor (CMOS), (3) charge-coupled device (CCD), or

(4) amorphous selenium. It is customary to match the size of the pixel in the arrays to the scintillator and the scintillator format. This means that the inherent resolution includes some spatial resolution at the pixel size of the detector. If this is not the case, the images are artificially large, and a resampled smaller image (larger pixels and shorter scan times) would convey the same information in a more economical way. This is typically not the case for linear-array detectors.

The important consideration here is that the detector package combines three components in the task of x-ray detection—some x-ray stopping/conversion mechanism, a pixel-array size for digitizing that solid angle of irradiance, and the scatter consequences of the package. The three components all figure into the spatial resolution of the detector, independent of the source and the object. Considerations for how the spatial resolution impact of detector properties factors into overall performance depend on the other aspects of the system. It is usually a principle of system design to configure the detector package at just less than the impact of source blur and object magnification. A detector with too small a pixel size relative to the other system components will spend extra time on digitizing, and possibly more time obtaining sufficient counts (if there is no way to bin or combine the content of detectors in the detector package), which means the system runs slower for no gain in spatial resolution.

14.1.3 COMPONENTS OF TRANSMISSION IMAGE NOISE

Following [Section 14.1.2](#), we group the components of noise in transmission images into the factors that are independent of the detector: photon statistics from the source, and photon attenuation in the object, and the effects that are a consequence of introducing a detector: photon absorption in the detector, electronic or dark current noise, structure noise in the detector, and quantization noise (the noise that results from the act of digitization).

In transmission imaging, independent of where you place the object, the source, what detector you use—and how long you take to acquire an image—the input to the pixels in the image, and the linear array are Poisson-distributed random variables and include a variability characteristic of the stochastic process that is behind the equations for exponential attenuation ([Ross 2009](#)). In this sense, all x-ray measurements include *noise*. It is expected that acquiring the same image multiple times will result in images with some variation, and some variation will exist between different pixels exposed to identical irradiance. This noise component is the fundamental photon statistics of the measurement or the noise you would get if you measured everything to perfection (more about that in [Sections 14.2](#) and [14.5](#)).

Transmission imaging has the added complication that the incident signal has been reduced by the attenuation in the object. The consequence is that some parts of the object will include more noise than others. For DR, this can be remediated by increasing the irradiance of the x-ray source, the x-ray current or the x-ray energy or both, or taking longer to acquire the measurement. In some cases, this results in some part of the radiograph being saturated (one of the virtues of x-ray film is the gradual way in which the film slowly approaches saturation). It is good to reiterate here that saturating a digital detector results in no information for that region. Also, as shown in numerous treatments, e.g., [Dainty and Shaw 1974](#), teasing saturation limits for detectors will exhibit some nonlinear behavior in detectors for Poisson processes.

For CT, every measurement in every rotational view needs to include some measurable signal, and the signal must not be saturated. In particular, every voxel in a CT reconstructed image is the massaged sum of the set of Poisson random variables across the projections that intersect the voxel to be reconstructed. Consequently, the local noise in a CT scan can include variable amounts of scatter—or the combined effects of source unsharpness, object scatter, and detector scatter for high-aspect-ratio objects. The local effects on CT images are sometimes referred to as *scatter streaks* or *attenuation inconsistencies* ([Ying et al. 2006](#)) or just local noise. The point here is that the source of these effects is the high aspect ratio of the object function. Some views are too strongly attenuated, while others drive the detector to near saturation.

The differences in photon attenuation across a particular view of the object, or for the ensemble of views of the object acquired in a CT scan, are impacted by the stopping power of the detector—effectively reweighting the spectrum for each ray sum through the object function. When the stopping power of the detector is meager, ray sums through high-attenuating portions of the object include even fewer counts. In DR, this just results in a lack of detectability for the features in that region of the image. In CT, this can result in more troublesome artifacts in the image—some of them effectively masking important features in the image (see Section 13.7 on CT artifacts).

Sources of noise connected to the detector—or the task of measuring the irradiance incident on a detector pixel—include a number of components. In this treatment, *electronic* noise is that variation due to the *dark current*—or some other electronic mechanism that results in a certain number of *counts* present when you read the detector when there is no x-ray irradiance. Physically, the counts measured can be dependent on the temperature of the detector or some other mechanism. For instance, silicon-based detectors often have a dark current that increases with temperature, and that is the reason why many are actively cooled. Further, this source of noise is statistical. It has a mean and a variance that depend on temperature and the characteristics of the detector. This source of noise gets more important for regions with slight x-ray penetration since their lower counts are close or in the noise. This source of noise—both the signal level and the variance—must be small compared to the number of counts in the image used for an inspection. For example, noise can impact dynamic range. Dynamic range is the difference between the smallest and largest usable signals. Dynamic range is usually calculated as the ratio of Φ_{\max}/Φ_{\min} , where Φ_{\max} is the value just below detector saturation, e.g., in a 12-bit detector, it would be near 4096, and Φ_{\min} is the minimum value above the noise, e.g., dark current, threshold of the detector.

Detector *structure* noise is idiosyncratic with the type, construction methods, and read-out methods of the detector. Figure 14.6 contains raw images from an Apogee Camera, Radicon CMOS panel, a Thales amorphous silicon panel, and a Perkin–Elmer amorphous silicon panel. Notice the differences in structure for each of these *raw* images from the detector arrays, all acquired with no irradiance on the detector. For instance, the Spectral Instruments camera (not shown in Figure 14.6) is read in a *multiported* fashion—so each quadrant includes a separate *gain* and there can be a small difference in the signal level between the quadrants of the image (user-settable gain coefficients can be adjusted to minimize this effect). The amorphous silicon detectors include pattern noise that follows the properties of their manufacture. On top of the pattern noise characteristic of the detector, digitization noise is the small increment in the noise in the image, which occurs as a result of reading/converting to digital counts. This source of noise is usually included in the *structure* noise for a detector.

X-ray scatter from the system, e.g., the detector package (the detector backing) or from collimator roll-off, can figure into the noise for a pixel or an ensemble of pixels (Schach von Wittenau et al. 2002b). In this case, the digitized irradiance is the result of x-ray interactions. The problem is that the counts are not only from the interactions in the object. The result is that the contrast for the material difference you are trying to measure is diluted by the overall signal level of the noise source. Secondly, there is an additional variation in the signal—the variance is larger and smaller features are more difficult to detect. To assess the extent of this source of signal, we recommend measurements with *opaque* objects, say a series of different size disks. The amount of signal measured behind the opaque object is a measure of the magnitude of this source of signal (Seibert et al. 1985).

Noise in transmission images begins with the pattern noise in the detector, with the signal components of interest sitting on top of that base signal level. All of the signal components are the product of random processes, but as digital signals are bounded by a certain lower threshold required to register counts, and as the irradiance reaches detector saturation, where the noise changes in nonlinear ways as an ensemble of detector elements approaches saturation. Many instances of transmission imaging include scatter: from the detector, possibly from the collimator, and/or from the surrounding hardware. For low transmission ray sums, paths, or chord lengths, the relative proportion of nonprimary photons is larger and artifacts in the image result. In DR, this is shown by greater noise and lack of contrast; in CT, the result can be troublesome streaks that are difficult to

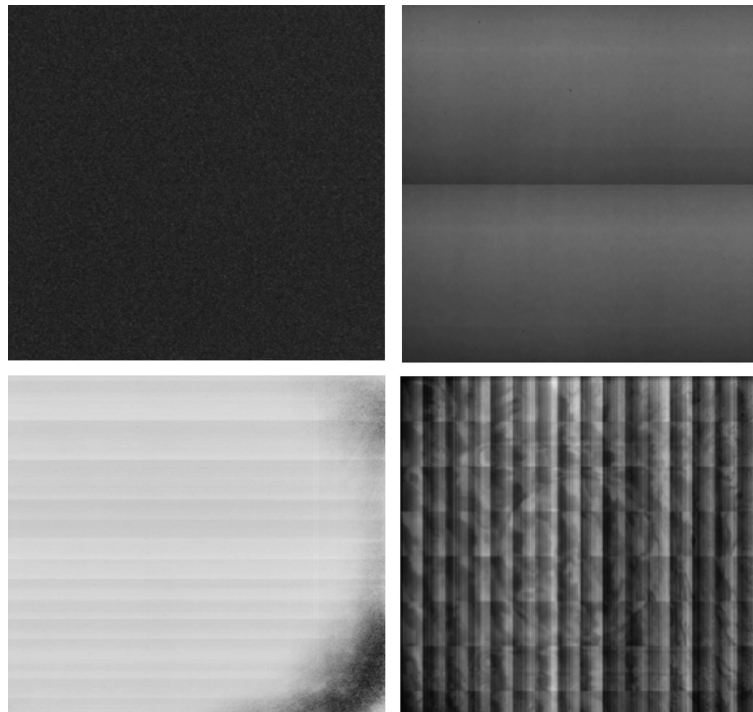


FIGURE 14.6 Dark current images from different area detectors. Upper left is an Apogee CCD camera. Upper right is a RadIcon CMOS panel. Lower left is a Thales amSi panel, and lower right is a Perkin–Elmer amSi panel.

connect to any property of the object. A good practice to assess the extent of these effects is a series of measurements with opaque objects mentioned in Chapter 10.

14.1.4 X-RAY TRANSMISSION IMAGING ARTIFACTS

At this point, we have mentioned many different components that comprise the contrastive and spatial resolution in an image. We have mentioned the different ways in which noise and scatter impact contrastive performance, whether scatter from the object, from the detector, or from the surrounding hardware in the inspection. Also, we have mentioned how these problems change with the selection of energy. All of these sources of signal can result in *artifacts* found in the inspection images. These *artifacts* are changes in the image that are not connected to the object—or are not measuring some property of the object—and are thus a distraction for the inspection. So, in an important sense, we have been discussing *artifacts* in Sections 14.1.1 through 14.1.3 as well as Chapters 12 and 13.

Beam hardening has consequences for both image contrast and spatial resolution. In particular, for features in the center of long chords, detection is difficult unless there is some treatment of the effects of the *cupping* or a decrease in attenuation in the region of the feature. Second, while the sharpness of the image is not impacted by the cupping artifact, the same issue arises for small features in the middle of long chords of the object. If the pixel-to-pixel change in the attenuation is on the order of the modulation attributed to that feature, you miss it. This is an artifact of the source irradiance, not a property of the object.

One additional complication is the change in relative attenuation for different materials in the object. Applying a beam-hardening correction changes the values of the attenuation, either in the projection data or in the case of CT in the voxel values. According to the nature of the beam-hardening artifact, the correction is performed on the total detected irradiance, which then impact the values

of the smaller component materials. One remedy to this circumstance is the application of expected attenuation informed by models of the spectra and the object. The difficulty here is how to distinguish when applying the model is *doing too much*. The process of *correcting* the data may adjust the intensities to values that are not in the object but were assumed to be there.

A beam-hardening correction may remove the artifacts connected to beam hardening—but the result is more noise—which can then degrade contrast and resolution in another way. The good news for this type of effect is that you can easily apply a correction and not apply a correction and assess the changes. For CT, many different types of iterative reconstructions have demonstrated good results for removing this effect with the input being some model of the source output. Good models of source output are easily obtained (Ying et al. 2006). As mentioned above, in this case, being able to distinguish the effects of the model from the data can get tricky—and it is possible to just *make up* data to fit what it should have been all along, which kind of defeats the point of the inspection.

14.2 PHOTON STATISTICS

The process of x-ray emission and transmission is a thoroughly statistical process. For x-ray tube sources, photons are produced from the interaction between an electron beam and an anode material; radiation emerges as the electrons *brake* into the material. On average, the total spectrum of photons will sort into the convolution of the bremsstrahlung radiation with the characteristic lines of the x-ray anode material. On the transmission side, x-ray photons will interact with the components in the object function corresponding to the x-ray attenuation cross section for that mechanism at the energy of that photon. The x-ray detector will count the receipt of a photon depending on its own attenuation or stopping power and characteristics for its own counting efficiency, which can change over time, i.e., scintillator browning. The act of counting or digitizing the incoming signal then includes an additional variation, e.g., silicon detectors usually include some noise due to digitization. Now it is usually the case that the operation of the source is stable. Large numbers of photons are produced by the source, so the averages are stable, and the repeatability for source spectra is then reasonable; except for instances of very low transmission, or in the case of a mismatch between the energy used and the detector stopping power, measured transmission values are stable. It is reasonable to expect the variation in measurements from acquisition to acquisition for the same geometry, object, and detector to be small. At the same time, it is important to emphasize the stochastic properties of the signal at each stage of the measurement, regardless of the detector, or with the detector factored into the mix.

It is traditional to model x-ray detectors as instances of Poisson counting processes, see for example, Ter-Pogossian (1967), Barrett and Swindell (1981), and Whiting et al. (2006), to mention only a few. The reasons for this choice begin with the general requirements for Poisson counting processes; following Barrett and Swindell (1981), for some time t and some *rate* of counts denoted as a , the three requirements for a Poisson process can be stated:

1. The number of photons detected in any time interval is statistically independent of the number detected in any other non-overlapping interval.
2. The probability of detecting one photon in a decreasingly small time interval is directly proportional to the interval time.
3. As the interval time approaches zero, the probability of more than one photon being detected is zero, so that for sufficiently small interval time, the photon count is either 1 or 0.

When these three conditions exist for a counting process, the probability density function for the number of counts in a certain time interval is Poisson, or

$$P(N) = \frac{e^{-\Phi_D} \Phi_D^N}{N!}, \quad (14.14)$$

where $P(N)$ is the probability of a pixel being illuminated with N photons and Φ_D is the mean number of photons. (An alternative development of this result can be found in Ross [2009].)

In the fabric of the above-stated conditions are the key properties of Poisson counting processes: the probability that some number of counts detected in a time interval are independent of other time intervals. While these assumptions are not strictly satisfied in some x-ray detection scenarios, x-ray response is not necessarily constant for some detectors in some energy regimes, or for source operation during idiosyncratic ramp-up; the ways in which the assumptions are not satisfied can be shown to still resemble a Poisson distribution for the average counts over continued operation (Barrett and Swindell 1981).

The significance of this result for the discussion here is in the properties of Poisson random variables, and the definition of signal-to-noise ratio (SNR) and root mean square (RMS) accuracy and going forward to the characterization of the variance of measurements we use in DR and CT. A distinctive feature for Poisson random variables is that the mean and the variance are equal. This means that the variance for a given pixel can be estimated at the value of that pixel. Consequently, representing the SNR of a Poisson random variable, the ratio of the mean to the standard deviation is $N/\sqrt{N} = \sqrt{N}$. The inverse of the SNR, sometimes referred to as the RMS accuracy, or the precision of the distribution around the mean, is $1/\sqrt{N}$. All of this fits with experience in transmission imaging; all things held constant (no part motion, no change in energy), the more the detected counts, the lower the noise in the image.

Additional properties of Poisson random variables are notable. First, sums of Poisson random variables, say N_1 and N_2 , with expectations a_1t and a_2t result in a Poisson distribution, with expectation $(a_1t + a_2t)$. Second, as t gets large, Poisson random variables are increasingly close to Gaussian distributions. Third, when Poisson random variables are conditional on binomial random variables, or are in combination with binomial random variables, the resulting distribution is Poisson. Also, a Poisson distribution can be derived as the limiting case for the binomial distribution as the number of trials gets large, and the expected number of successes remains fixed. All of this emphasizes the important role Poisson random variables play in processes where the outcome involves counting of some event, or when some event that counts *successes* is combined with other random variables.

An example of how detector properties are modeled as Poisson random variables is shown in Whiting et al. (2006). In this treatment, the probability density function for an *x-ray quantum (or photon) counter detector* is modeled as a Poisson random variable with the form

$$P(N, \Phi_D) = \frac{\Phi_D^N e^{-\Phi_D}}{N!}, \quad (14.15)$$

where Φ_D is the mean of the total number of x-rays of all energies measured, and N is the discrete (integer) number of photons measured for that input.

Also, for an energy integrating detector, where each photon contributes a random amount of energy, the distribution takes the form of

$$P(\Phi, \lambda) = \sum_N \frac{\Phi_D^N \Omega(\Phi/G)^{\otimes N} e^{-\Phi_D}}{N!}, \quad (14.16)$$

where Φ is the measured signal, G is an energy weighting factor, and $\Omega(\Phi/G)^{\otimes N}$ is the N -fold convolution of the energy spectrum and λ is the mean. Notice that this takes the form of a compound Poisson distribution.

The ubiquity of the Poisson and compound Poisson distributions notwithstanding, attenuation measurements used in CT (and sometimes when attenuation radiographs are used for inspections) are a sum of Poisson random variables, and a combination of incident and transmitted counts, both transformed by the natural log function. From the equations mentioned above, the attenuation radiograph is calculated in Equation 14.3 and when rearranged, yields $\mu(x,z)l = \ln \Phi_0(x,z) - \ln \Phi(x,y)$, where Φ_0 is the incident counts at pixel location (x,z) , and $\Phi(x,z)$ are the transmitted counts.

The impact of applying the natural log function to counts from the detector can be evaluated with techniques presented by Ross (2009) and Bevington (1989), or followed in the development in the work of Kak and Slaney (2001). Following Ross (2009), for any discrete random variable,

$$Y = g(X), E(g(X)) = \sum p(x)g(x), \text{ where } p(x) \text{ is the probability of } X = x \text{ for the possible values of } X.$$

So for the case of $g(N) = \ln(N)$, $E(\ln(at))$ and $E(\ln(N)) = \ln(E(N))$. {Make sure to check for the case where $p(x = 1)$ and $\ln(1) = 0$; so for N small (less than 5), there could be issues here.} Also, for the variance of $g(N) = \ln(N)$, where $\sigma_{g(N)} = \sigma_N/N$, this can be shown directly by working through the expectations or in a more compact way using the development from Bevington (1989) since the derivative of $\ln x = 1/x$. Using the property of Poisson random variables that the mean and variance are both estimated as the mean number of counts, the variance for the natural log of the Poisson distributed counts is $1/\bar{N}$, or 1 over the mean number of counts. The standard deviation is $1/\sqrt{\bar{N}}(N)$, or 1 over the square root of the number of counts, the same value as the RMS accuracy for the counts.

The significance of this result applies at a couple of different levels: for evaluating radiographs or CT images, for use in designing the next radiograph or CT acquisition, or for designing an inspection and calculating estimates of probability of detection. At the most fundamental level, the noise in the ray-sum measurements is inversely related to the detected counts. If you can obtain more counts, through longer acquisition times or through increasing the source current, the noise in the image will decrease. This is true for DR or CT. Within a particular radiographic image, locations with higher local noise can be a result of meager x-ray transmission, that is, a lower number of detected counts, and this is the case when the detector is working completely to specification. If this is the case, you need to take more time for acquisition or find a hotter source. For CT, the incident irradiance, Φ_0^P , image is also a part of the acquisition. The above development says that the number of counts on a pixel without the part in the way should be large—and so the variance of the log of the counts should be small. It is expected then that the noise in the incident irradiance image is smaller than the noise in the image with the object in the field of view, since each Φ_0^P pixel has the advantage of all the counts that the source can produce at that location. One indication of a problem with a particular CT acquisition technique or acquisition equipment is that the incident irradiance signal is noisy—and so that noise will find its way into every ray-sum measurement used in the subsequent calculations.

As mentioned above, voxels in CT reconstructed images are sums over the projection data. As shown in Chesler et al. (1977), Kak and Slaney (2001), and Barrett and Swindell (1981), the first contribution to the variance of the reconstructed voxel is the variance of the individual ray sums that constitute the voxel. Each of these components is $1/N(\theta,t)$ for that ray sum at position t along the detector at that angle θ . For a region in a CT scan of a uniform material in a cylinder, the variance of the voxel reflects the overall amount of transmission from all the views in the object. When transmitted counts are particularly meager, the local noise in the reconstructed image can be large compared to its neighbors with more transmitted counts. Further, the combination of meager transmitted counts, combined with a certain number of scattered counts from the other positions in the object or from the detector package itself, can result in untoward artifacts.

The above results facilitate back-of-the-envelope calculations for improving or designing inspections. For example, at the end of failure analysis, it is determined that a void that is roughly 1% of the thickness of a certain component is enough to make the probability of component failure unacceptable. One way to interpret this criterion is that the local standard deviation for the image needs to be less than 1%; in fact, if you subscribe to 3-sigma or 3-standard-deviation type practices, then you may want the noise in the image less than or equal to 0.3%, or at a fraction of 0.003. Consider the requirements for a single transmission radiograph; by implication, this says that the SNR needs to be in the 100 to 1 or 333 to 1 range, and since $\text{SNR} = \sqrt{N}$, that factors into photon statistics in the 10,000 to 110,000 range, e.g., if the only change you have available is increasing irradiance. CT measurements can benefit from the position of the void in the entire object function; since not all chord lengths are necessarily the same, the voxel benefits from the summation of the transmission

measurements through shorter chords from different angular orientations (of course, the opposite can be true as well if all the other chords are longer). The limiting case here is the single void at the very center of a cylinder or sphere. This is likely the reason Barrett and Swindell (1981) chose this particular geometry for characterizing the variance of voxels in CT reconstructed images.

Notice the large spread in the range of detected photons needed to detect a small change in thickness from a single radiograph with some confidence; this reflects the trade-off between accuracy in the transmission image and acquisition time and/or money spent on a high-output x-ray source. It may be daunting to consider that each increase in SNR goes to a square of the detected counts, and the result can be a 10-fold increase in acquisition time, which is sometimes just unacceptable. It is hoped that the above discussion has pointed to how spatial resolution might figure into the mix. For instance, if you increase the detector size by 2 (height and width), you increase the area by 4, and for detector average counts of 10,000 on the smaller size, you now have 40,000 counts. Increase the detector size by 3 and you have 90,000 counts, enough to move from an SNR of 100 to an SNR of 300. Perhaps you only need the spatial resolution in a single dimension, say in the width of the detector. So, increase the height of the detector element by a factor of 5, and you move from an SNR of 100 to something close to 220. We will cover this in detail again later when discussing the *Rose criterion* and detectability.

14.3 MEASURING COMPONENTS OF IMAGE CONTRAST

The measured contrast in an image reflects the properties of the object, the technique, and the properties of the system components. The impact from the multiple constitutive factors depends on their mutual relationship, in particular, the factor with the greatest limitation will be the most significant. Following others, we sort the factors into three groups: (1) the characteristics of the object for that energy (intrinsic contrast); (2) the properties of the chosen technique; and (3) with this object, and with this technique, the specific properties/limitations of the detector.

For transmission imaging, fundamental observed contrast is the difference in the measured irradiance between chords (possibly adjacent). In the simplest case, we have

$$C_s = (\Phi_0^E - \Phi^E) / \Phi_0^E.$$

In this case, Φ_0^E is the irradiance of the source that does not intersect the object (preferably at some adjacent location), and Φ^E represents the transmitted irradiance through the object. Often the numerator is represented as Δ_{Obj} , representing the difference in irradiance due to the object. Alternatively, these concepts can be generalized further into two multicomponent idealized chords, each encompassing the same list of material components, but differing in the absence of one component, or in the length of a single component. Now define Δ_c as the difference due to some defect or change in material in the local region of the object. [Figure 14.1](#) is an illustration of these concepts.

When imaging materials whose mass density is constant, the fundamental limit on contrast is the difference in the material composition between chords in that direction of the object. For this discussion, we are considering x-rays as the energy source for this inspection, and so the material properties of interest are the x-ray attenuation values for the constituent parts of the object and the length of the material component in the direction of beam propagation. The values for total x-ray attenuation change with energy, as do the proportions of the different x-ray attenuation mechanisms. For radiography or CT, the orientation of the object or object features configured in the object geometry within the source-detector envelope determines the *object-based* or *intrinsic* contrastive performance.

To illustrate the factors mentioned here, consider an object with three rectangular embedded minislabs as depicted in [Figure 14.7](#). The dimensions of the object are (l_1, l_2, l_3) , centered at (oc_1, oc_2, oc_3) . The object attenuation is μ_{obj} . We use the three dimensions of the object to identify the three orientations for transmission imaging—along l_1 , l_2 , or l_3 . Transmission measurements for a single energy source, for this object, with total x-ray attenuation, μ_{obj} , and for these three orientations

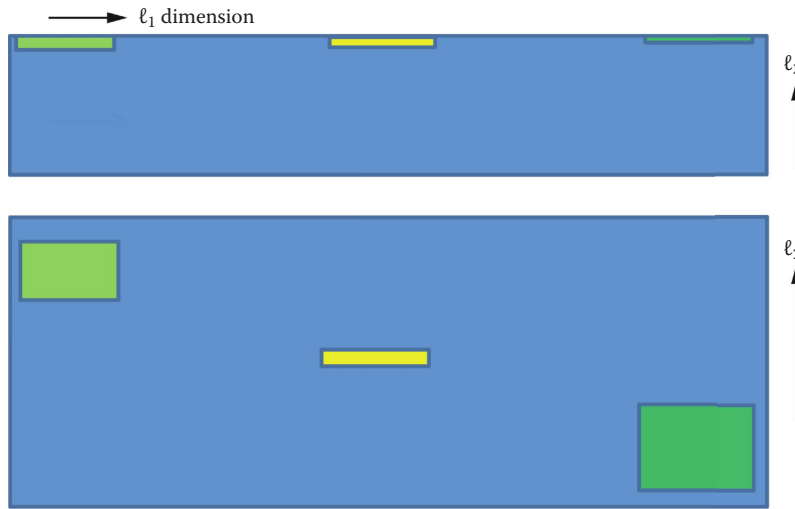


FIGURE 14.7 Synthetic object with three embedded minislabs viewed from two different orientations of the object.

will be the difference in path length or $\mu_{\text{obj}}l_1$, $\mu_{\text{obj}}l_2$, and $\mu_{\text{obj}}l_3$. Now, insert three rectangular minislabs in this object, all close to the top of the slab, considered from the l_3 dimension as shown in Figure 14.7. Minislab 1 is 5% of the thickness ($0.05l_3$). Minislab 2 is 3% of the thickness ($0.03l_3$). Minislab 3 is 1% of the thickness ($0.01l_3$). Again, all of these thicknesses are considered with respect to the l_3 dimension of the object. As considered from the l_1 direction, each minislab is 10% of the thickness of the l_1 dimension.

We will investigate three cases of transmission measurements for this synthetic object. Consider first the minislabs as voids. The direction of the x-rays is in the l_3 dimension, so a single radiograph includes the smallest change in path-length material in this object function. Consequently, all the expected values for C_s are calculated from the lengths of the object minus the lengths of the minislabs in the direction of the beam propagation divided by object length size, the attenuation μ drops out. For this simple case, a number of expected values can be performed independent of the material and the energy used in the inspection. These are depicted in a synthetic radiograph of Figure 14.8. For the second case, the minislabs are made of different materials from the object. In this case, let the object consist of Delrin, with minislab 1 made of Lucite, minislab 2 made of nylon, and minislab 3 made of Teflon. In this case, we will simulate measurements at 30 keV: $\mu_{\text{delrin}}(30) = 0.0435617$, $\mu_{\text{lucite}}(30) = 0.0263461$, $\mu_{\text{nylon}}(30) = 0.0299697$, and $\mu_{\text{teflon}}(30) = 0.0839752$. For the third case, the geometry and materials are the same as case 2, but we use 300 keV as the energy for simulating the measurements: $\mu_{\text{delrin}}(300) = 0.0164327$, $\mu_{\text{lucite}}(300) = 0.103650$, $\mu_{\text{nylon}}(300) = 0.125134$, and $\mu_{\text{teflon}}(300) = 0.221924$. Table 14.1 contains the expected values for the simulated μl measurements for the three cases.

Notice the difference in μl for the chords that intersect the minislabs (Lucite, nylon, Teflon), relative to the chords that intersect only Delrin. Also, notice the value of μl for the adjacent object chord and the chord through a minislab. For the first case, only thickness matters, and detecting component minislabs 3 will be the most challenging, since the intrinsic contrast is smaller. For the second case, the situation is different, since minislab 3 includes the greatest material difference from Delrin; moreover, the difference in the attenuation coefficient is larger at the relatively low energy of 30 keV, and the intrinsic contrast for minislab 3 is relatively larger than minislab 2. For the 300 keV inspection, photoelectric absorption is less of a component of total attenuation; the difference in component minislab density has a more significant impact on attenuation, and the size of the *intrinsic* contrast tends more toward the first case, where only thickness was a factor in constituting the expected difference.

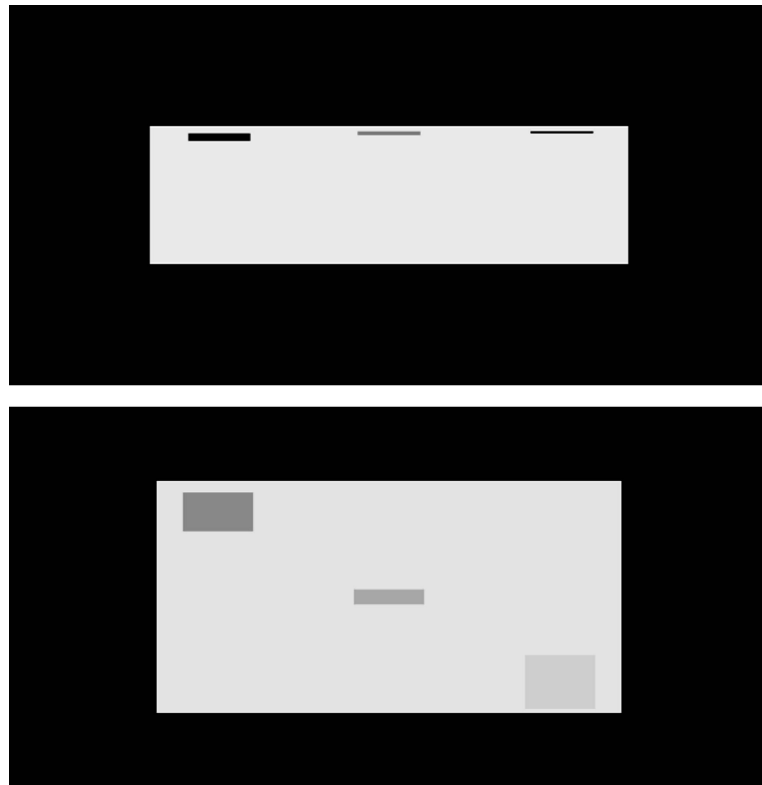


FIGURE 14.8 Synthetic radiographs of the slab object drawn in Figure 14.7. Orientations are the same as those in Figure 14.7.

TABLE 14.1

Expected Attenuation Values for the Object Constituents for the Slab Object for Single Material and Multimaterial Object Definitions

	Object Matrix—Delrin	Minislabs 1—Lucite	Minislabs 2—Nylon	Minislabs 3—Teflon
Case 0: 30 keV μl	1.568323	1.489923	1.521175	1.552651
Minislabs are voids		$C_s = 0.050$	$C_s = 0.030$	$C_s = 0.010$
Case 1: 30 keV μl	1.568323	1.537353	1.553542	1.582886
Minislabs are materials		$C_s = 0.020$	$C_s = 0.0094$	$C_s = 0.0093$
Case 2: 300 keV μl	0.591615	0.580701	0.587344	0.593695
Minislabs are materials		$C_s = 0.018$	$C_s = 0.0072$	$C_s = 0.0035$

Across these three cases, we see object lengths, material, and the energy used for inspection, all having an impact on the *intrinsic* contrast. It is important to emphasize the significance of these calculations or simulations, i.e., if you do everything well (all the equipment works correctly), these are the numbers you should obtain. Conversely, if the inspection configuration you are using—source, detector, geometry—does not result in a contrastive performance that exceeds the intrinsic contrast for that object component, do not expect to detect that feature. For instance, if your system noise is on the order of 1% of the signal, detecting a void of size minislabs 3 is just at the edge of your system's performance. Moreover, if you are operating at a higher energy, it will be difficult to detect

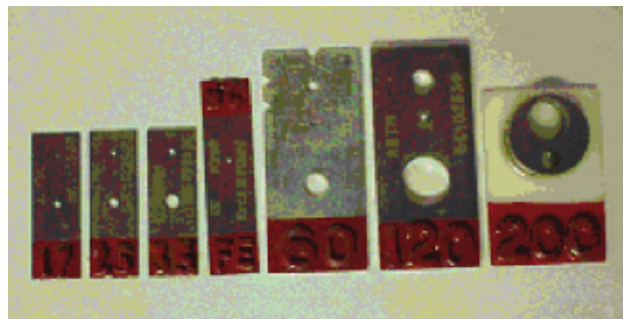


FIGURE 14.9 Picture of different penetrometers, of different thicknesses of Al and steel, with different sized machined holes and notches (and lead letters in red paint).

this feature at all, which is similar for the case of minislab 2 when using higher energy, where the differences are all due to density and less to chemical formula.

As mentioned in Sections 14.1.1 and 14.1.3, detector stopping power effectively filters the irradiance emerging from the exit face of the object at that angle. The important concept here is “you only count the x-rays you can stop”; in many cases, this means the average energy of the inspection is less than the average energy of the incident spectrum. Consider cases 2 and 3, but consider the impact of using an amorphous silicon panel that employs a Lanex Fine screen, 0.085 mm thick, in the direction of the beam, and a chemical formula of GdSO_4 with a density of 4.2 g/cc. For single-energy sources, at 60 keV, we only stop 0.7 of the transmitted photons; if you want to obtain better photon statistics, you have to increase the time of the inspection. This is not without costs. For the third case, 300 keV, the Lanex screen only stops 0.2 of the transmission, a fivefold decrease in photon statistics—and a fivefold increase in noise from what could be obtained if you stopped every transmitted photon.

While it can be straightforward to configure a system for an inspection and just acquire some data, we recommend these *back-of-the-envelope* type calculations as a companion to the measurements. The role of these expected contrastive performance calculations can be extended to the use of ASTM *pennies* or *image quality indicators*. Figure 14.9 includes a photograph of a set of aluminum ASTM pennies of different thickness. If you are expecting a change in contrastive performance, use the expected values to find a thickness in this array that is just greater than and just less than the expected value, acquire an image, and evaluate the results.

At this point, nothing has been considered except the materials and the x-ray attenuation. For this energy, all of the calculations of attenuation contrast or transmission contrast are independent of the detector or the geometry of the source and the detector. As mentioned before, intrinsic contrast of the materials is the best you can do, and taking care to pick the correct energy, a detector that counts the photons of interest, and a context in which other sources of noise are within limits of the contrast targets is important.

14.4 MODULATION TRANSFER FUNCTION

The MTF is a fundamental measurement of the composite properties of an image that includes both the spatial sharpness of an image and its contrastive performance. The point of the MTF is to quantitatively measure the *transfer* properties of an imaging system or imaging component by comparing the output amplitude of a feature to the input amplitude for that same feature. The MTF is the answer to the question, “If I have a feature with this size and this relative contrastive amplitude, how well will the imaging system represent that size and amplitude in the output image?” Implicit in this concept is this idea that there is an input object with some properties and feature space, an imaging process, and an output image with measurable properties. The point of the MTF is to measure the impact of the imaging process relative to the input object.

Measuring and displaying MTFs are commonplace for characterizing the performance of an optical lens. The use of the lens can change the properties of the output image. Consider the following example taken from an optical evaluation of a lens: the line-outs (in C and D) and the images (A and B) in Figure 14.10. The black and white bars of decreasing size displayed horizontally across the figure are the input image to the lens, image A, and image B represents the image from the output of the lens. The scale on the bottom of the line plot in D represents the size of the black bars. Each number (1.0, 0.8, 0.5, and 0.1) corresponds to the physical width of the black bars directly above the numbers in the A and B images. The line-out in C is obtained from the bars represented in A. Notice the steep climb to the maximum pixel level around 255—and the corresponding steep descent to 0—or the region covering the black bars. Now consider the B image—the edges of the black bars are now fuzzy; the intensity represented in the line plot in D reflects the loss in the sharp edges. Notice that as the size of the bar gets smaller, the intensity change in the plot in D does not reach the full height (or modulation) shown in the C line plot. In particular, for the plot in D, notice the intensity change for the bars directly above the 0.1 scale marker, which barely show much change in intensity at all.

The operation of the lens is embedded in the properties of the B image and in the companion D line-out. Notice how the operation of this lens transferred or changed the modulation from the input image to the output image. In particular, two changes occurred for the output image: all edges became less sharp, and for smaller features the contrast between features was lower—to the point where small figures were barely distinguishable from the background.

Define the MTF for the operation of the lens shown in line-out D, for the different size features, q , in line-out A of Figure 14.10 as

$$\text{MTF}_{\text{lens}}(q) = \frac{\nabla_{\max}(q) - \nabla_{\min}(q)}{\nabla_{\max}(q) + \nabla_{\min}(q)}, \quad (14.17)$$

where ∇ is the intensity.

Note that this function is defined for each feature size and is defined across the range of sizes for which there is a measurement, relating the change in intensity to the size of the feature.

So using some interpolation from plot D in Figure 14.10, $\text{MTF}(1.0) = (255-0)/(255+0) = 1$, whereas $\text{MTF}(0.5) = (167-87)/(167+87) = 0.31$ and $\text{MTF}(0.1) = (131-123)/(131+123) = 0.031$. Using this lens, with features 1.0 or greater, the change in brightness will be negligible in the output image. However, for features half that size, only a fraction of 0.3 of the input change will make its way into

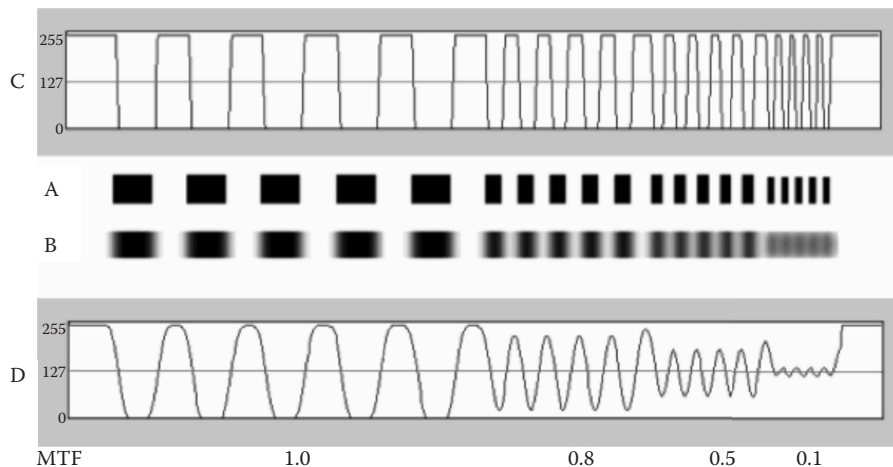


FIGURE 14.10 Images and line-outs showing the impact of the use of a specific lens. Line-out C is taken through object row A, while line-out D is taken through object row B.

the output image. For features of size 0.1, only 0.031 of the input modulation will be measured in the output image, and features smaller than 0.1 will be difficult to detect. Two things are important here: MTFs measure the transformative action of some imaging component, and this measurement is expressed as a function of the spatial size in the image.

The bar pattern in [Figure 14.10](#) captures the key design element for one type of physical device used to measure MTFs, usually referred to as a line-pair gauge or a test-pattern fiducial. These are made with alternating bars and space, which range in size in some graduated way. In many instances, the input image is not an image at all, but rather the expected change in intensity assuming that the line-pair gauge was manufactured with precision. Line-pair gauge dimensions can be verified optically with great precision. The line-pair gauge is made with some area covered by Pb that is substantially larger than the alternating lines. This provides an indication of the modulation at zero spatial frequency. Figure 14.11 is a visible-light image of three different radiographic line-pair gauges. Each of these gauges is constructed with different size pairs of alternating plastic and lead—the plastic being considerably more transparent than the lead; the resulting transmission

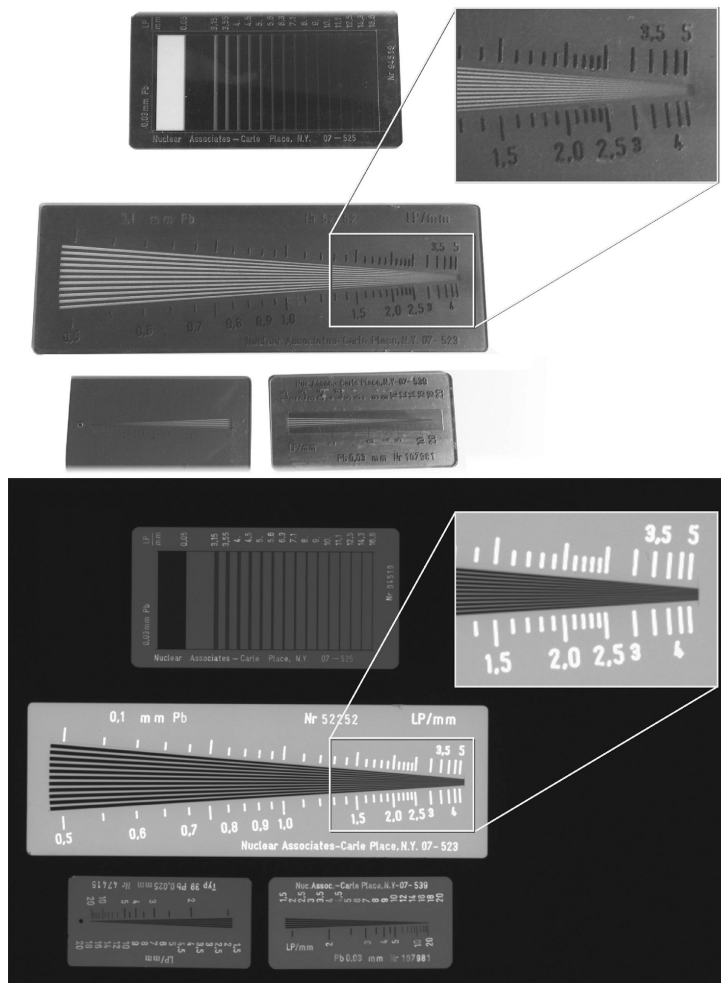


FIGURE 14.11 At the top is a photograph and the bottom a digital radiograph, μl , of four x-ray line-pair gauges. To see more details, a portion of one of the line-pair gauges is expanded in both images. In each image, the line-pair gauges are top: 16.6, middle: 5, and bottom: 20 lp/mm gauges. The design style is varied among these gauges, but the function is the same.

image consists of light and dark bars resembling the optical image in Figure 14.10. The three line pair gauges include different patterns with the same basic characteristic—the lines of plastic and lead get smaller for a region of the gauge, with the size of the line corresponding to the number of line pairs per millimeter displayed on the side of the gauge.

Figure 14.12 is an x-ray image of the 10 lp/mm gauge of Figure 14.11, converted to attenuation (μ) times path length (ℓ). Figure 14.13 is a line-out from end to end showing the declining change in $\mu\ell$ with size of the bars extending across the gauge. Unlike the image from the lens, the image in Figure 14.12 and the corresponding line-out in Figure 14.13 are from an x-ray image of a line-pair gauge. Like the image for the lens, the line-pair gauge is made from low- and high-attenuating materials (plastic and lead) in smaller and smaller widths to enable the same measurement. Notice the same pattern: as the widths of the lines get smaller, the amplitude difference between the low- and

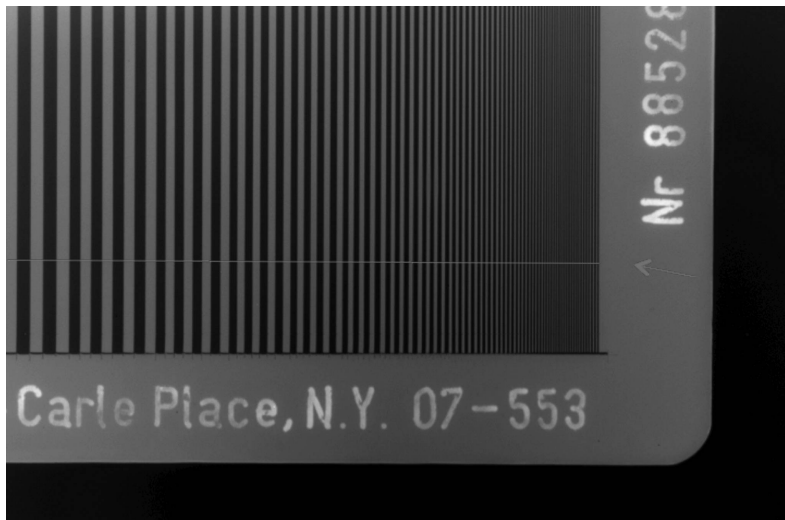


FIGURE 14.12 Attenuation ($\mu\ell$) radiograph of a 10 lp/mm gauge. The white horizontal line shows the location of the line-out in Figure 14.13.

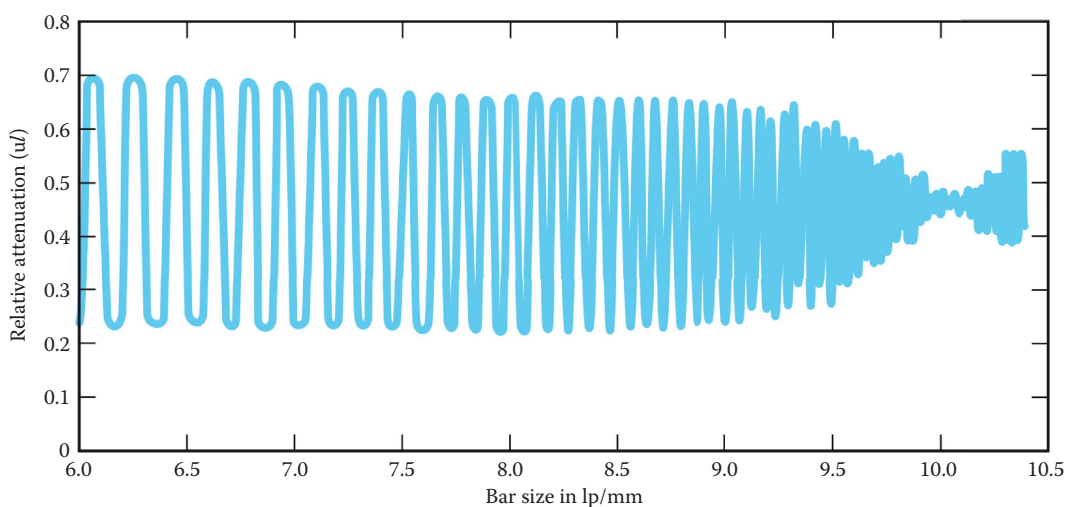


FIGURE 14.13 Line-out from a radiograph of the 10 lp/mm gauge in Figure 14.12 ending at the highest resolution (narrowest bars) region.

high-attenuating regions gets smaller—up to the point where there is meager modulation at all. The 10 lp/mm means 20 lines in a millimeter or the size of each line is 0.05 mm. The x-ray image above was acquired with a camera-scintillator system focused to obtain 0.051 mm pixel size at the scintillator, and the line-pair gauge was taped to the front of the scintillator (very small x-ray magnification involved in this image, so no source unsharpness to speak of). It is possible that the line-pair gauge can be oriented in such a way that the smallest lines (0.05) lie directly on the 0.051 pixel boundaries, but this was not the case in this image as the gauge is just slightly tilted in the vertical dimension. Also, notice that for this gauge, the smallest spatial width is not at the very end of the series of bars, but at a position close to the end of the pattern. This occurs because of aliasing between the pixel pitch and the line-pair gauge pitch. It is not useful modulation.

For the x-ray line-pair gauge, we can make the same measurement of the MTF, but from the assumed properties of the gauge, not from some better image of the modulation of the gauge. This is a typical circumstance; you do not have an input image, but only the designed properties of the object being imaged (in this case, the line-pair gauge), and you make the measurements of the MTF against the nominal properties of the gauge. In this case, we have close to full modulation up to 6–7 lp/mm, and then the modulation falls off from there to 10 lp/mm. One can trace a line on the top of the sinusoidal trace from the line-pair gauge, which will pretty much trace out the value of the MTF for the feature sizes in this gauge.

In general, measuring the change in contrast for feature sizes in an image connects to two concepts in signal and image processing: (1) transforming images into their spatial frequency representation (Fourier transforms of images) and (2) representing operations in an imaging chain as the *convolution* of an input image with the mathematical model of the operation in the imaging chain (which by the way can also be represented as an image). The first concept—transforming images into their component spatial frequencies—is a key piece of machinery that provides the basic grid for the measurement of MTF. If every image can be transformed into the amplitudes on its component spatial frequencies, then every image can be compared on the same scale. Related to this transform of images into their amplitudes for spatial frequencies, the convolution operation is a quantitative means for representing the impact of a particular function applied to every element of the grid spacing or every feature size in the image.

While it is assumed in this text that the concepts of Fourier transform and mathematical convolution (Papoulis 1997) are not foreign to the reader, we will spend a little time motivating the ideas in the following, as they are key to the practical use of the MTF in various contexts. It is especially important to understand the assumptions behind calculating Fourier transforms, and what is the impact of considering the results to be representative of the imaging process you are using. Further, it is important to recognize how these assumptions might not apply in certain circumstances with x-rays.

In the above lens example shown in [Figure 14.10](#), the object was constructed of perfectly transparent and opaque strips of material that were certain fixed distances apart in order to examine the operation of the lens for smaller and smaller features. We calculated a value for the MTF at the separate distance spacing points between the bar-like features. Now consider that a *transform* of an image exists, which can decompose an image into the different amplitudes for each possible feature size in the image. That is, the transform generates a companion image with each element of the transformed image indexed to the amplitude of an intensity transition, at some size. That is, in the transform image, the component elements relate to the intensity transition at a set of feature sizes. In an important sense, this is the machinery that the Fourier transform of an image provides.

A fundamental property of a digital image is the detector element or pixel size. In an important sense, the pixel size is a key limiting property of digital images. Object features that are less than a pixel will get averaged into the area covered by a pixel. Or if the object feature is at the size of a pixel, it may sit on a pixel boundary and be spread over up to four different pixels, in 3D up to 8 pixels. If the relative amplitude of the feature is small relative to the surrounding pixels, and the noise in the image is larger, the feature will not be detectable. However, if the relative amplitude of the feature is large compared to the surrounding material (for instance, a small piece of metal in a

matrix of explosives imaged by low-energy x-rays), you may see evidence of the material even when the size of the material is much less than a pixel.

The idiosyncrasies of object contrast notwithstanding, for an MTF calculation, we are looking for a measurement of the change in contrast (modulation) versus spatial frequency. Consequently, you will only measure amplitude differences up to the spatial frequency that the pixel size can support. Frequencies that are smaller than a pixel are all averaged into a pixel and are not measurable. Another way of saying this is that you can only assess the impact of the imaging operation on the feature size you can reliably measure, not a feature that could be measured if the input contrast were 300 to 1, and it is only 1/10 of a pixel. It is not important that you can detect very small high contrast features; rather, for measuring MTF, we want to measure the impact on feature sizes in fully filled pixels in a repeatable way (for features smaller than a pixel, there is always some indeterminacy regarding where the feature sits in the pixel). Further, from the formula above, we want to measure the impact as a percentage of the full change in intensity or attenuation from minimum to maximum.

Given these constraints for the measurement of the MTF, we restrict our measurement to the range of spatial frequencies that support a full transition from maximum and minimum intensity; the limit of this is 2 pixels, or a spatial frequency of $1/2w$, where w is the size of the pixel per distance. For instance, consider an x-ray imaging system with a pixel size at the object of 0.1 mm, or 10 pixels/mm. For the full change in minimum to maximum intensity, only five min-max transitions per millimeter can be supported by this pixel size. It may be true that the imaging device includes spatial resolution that is greater than the maximum spatial frequency of $1/2w$, but including these higher frequencies would include the transitions from the higher spatial frequencies that are aliased into those measurements—the minimum and maximum for all the greater frequencies all averaged into a single pixel. This emphasis on measuring the extent of a full intensity transition, and the goal of comparing spatial frequencies calculated on the same footing, is tantamount to the Nyquist-Shannon rule for determining the maximum time or spatial frequency that can be independently measured in a Fourier transform. The range of 2π cycles of a Fourier transform and the number of line pairs per unit distance are referring to the same spatial frequency.

Now let us consider another approach to defining sharpness and another means for comparing images on this basis. In the lens example above in [Figure 14.10](#), all of the edges were impacted by the operation of this particular lens. In the input image, image A, the edges are almost perfectly sharp for this spatial scale. That is, in the line-out represented in C, in [Figure 14.10](#), the number of points traversed from an intensity of 0 to full intensity (255) is at least 2 and at most 3. After the operation of the lens ([Figure 14.10 B and D](#)), the number of pixels required to go from minimum to maximum intensity is considerably larger, 6 or 7. For this discussion then, the quantitative definition of *sharp* edges relates to the number of pixels required to represent an edge, and the smaller the number of pixels required, the sharper the image up to the limit for this pixel size—1 pixel. In particular, we can consider the definition of a perfect edge to be equivalent to a *step* function, or also known as the Heaviside step function, $HS(y_\ell)$, which is defined as $HS(y_\ell) = 0$ when $y_\ell < 0$, and $HS(y_\ell) = 1$ for $y_\ell > 0$. Notice that, for digital images, this function is defined in discrete terms. For this definition, we can make any image *sharp* provided that we increase the pixel size to cover the distance for a transition from minimum to maximum intensity.

Now consider the series of steps diagrammed in the ASTM standard for measuring MTF for a CT system (ASTM 1441 2011). Specifically, consider step b shown in [Figure 14.14](#). This represents a single transition from maximum to minimum intensity like those in plot b in [Figure 14.14](#) called the edge response function (ERF). To evaluate the state of this transition of the image, calculate the derivative, $d\mu/dx$, of the ERF, that is, calculate a tangent to the line trace at every point along the plot represented in [Figure 14.14c](#), the edge-spread function (ESF). [Figure 14.15](#) shows this operation applied to two different edges, one sharper than the other. Notice the differences in the derivative values calculated from the two line traces of two different edges. Also, notice that the edge-spread function resembles a probability density function in statistics. The mean or central value in the distribution occurs at the point of inflection for the distribution, and in [Figure 14.14c](#), the distribution

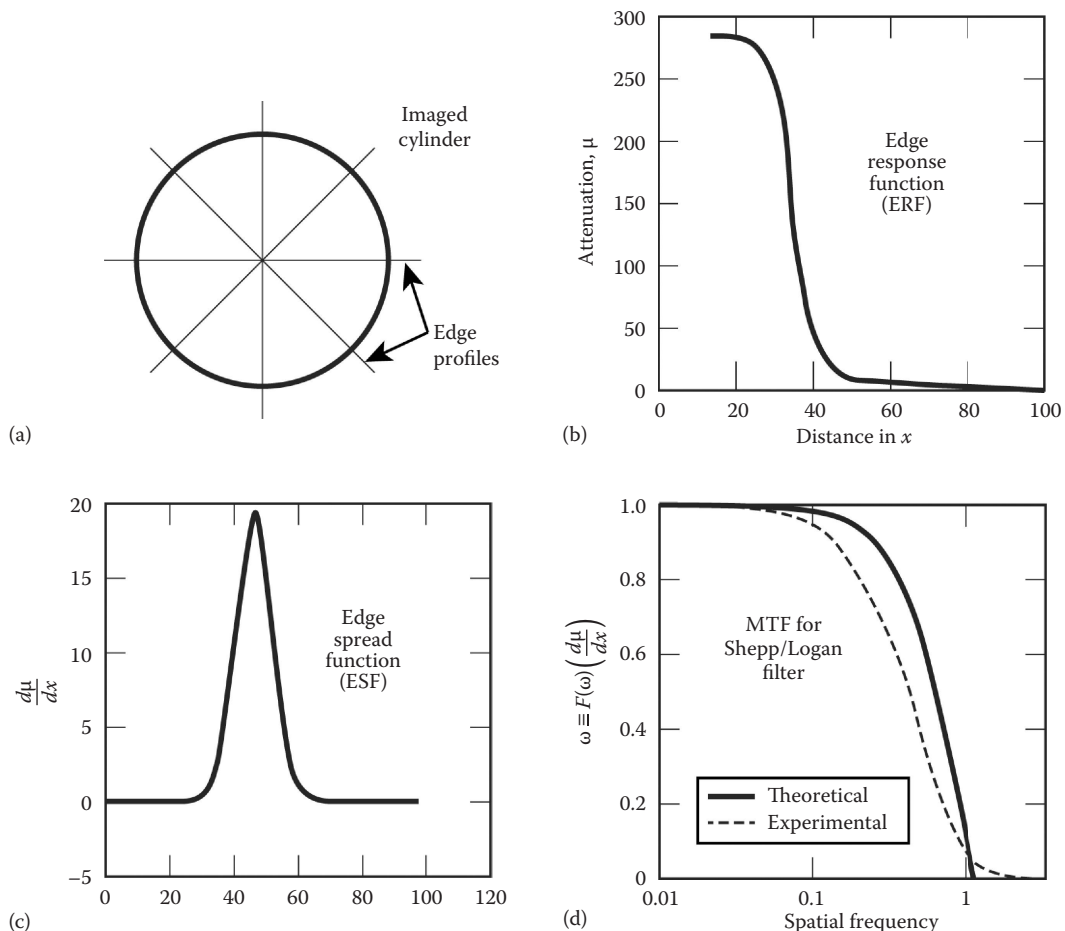


FIGURE 14.14 Diagram illustrating the procedure specified in ASTM 1441 (2011) for determining MTF in a CT reconstruction. (a) Location of edge profiles or 1D line outs is specified. (b) Plot of an edge profile is also known as an edge response function. (c) Derivative of the ERF with respect to x . (d) Fourier transform is also known as the MTF of the ESF, i.e., the derivative of (c). Exclusive use of an outside edge is a limitation of this procedure.

is symmetric. In reverse then, the edge spread functions resemble the cumulative probability functions, which are the integral of the density function across the possible values for the probability density function. Also, the width of the distribution obtained from calculating the derivative is larger as the edge is blurrier, and less as the edge is sharper as shown in Figure 14.15.

Application of these operations is demonstrated for a very high-spatial resolution imaging system in Figure 14.16 (Schneberk et al. 2004; Brown and Martz 2006). In this example, we are comparing the MTF measured from line-outs for the outer and inner edges of an Au tube scanned at high-spatial resolution. The MTF in Figure 14.16a calculates the MTF directly from the numerical derivatives of the edge response function, and in Figure 14.16b, the MTFs are calculated from the Gaussian fit to the derivatives of the ERF of an inner and outer wall of the tube. In general, the MTF values are close, whether you transform the derivative of the line trace (which includes the noise in the image) or transform the Gaussian fit to the derivative of the line trace—the overall picture is the same. The inner edges of these Au tube CT images include much less sharpness or spatial resolution than the outer edge. Note that 10% modulation happens at 30 lp/mm for the inside surface, while 10% modulation on the outside surface is at about 60 lp/mm. It is important to note here that

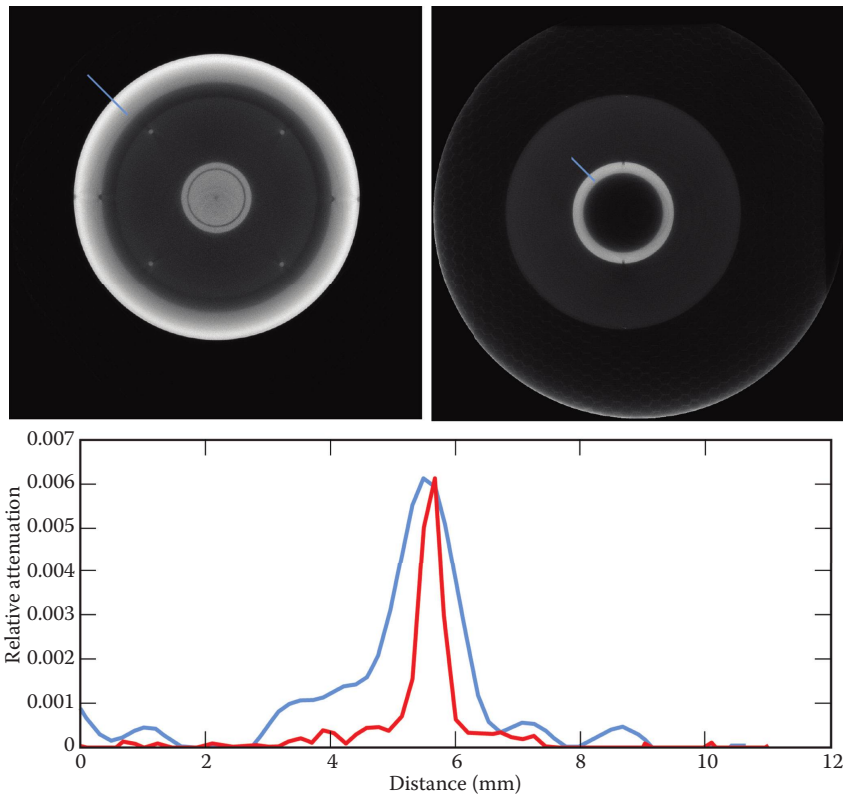


FIGURE 14.15 Comparison of derivatives from two different edge response function locations in the CT inspection data of a NASA compression pad. The red line is from the outer edge shown in the left image. The blue line is from the outside edge of an internal location. This is typical in CT images that internal details are less sharp than external details or surfaces.

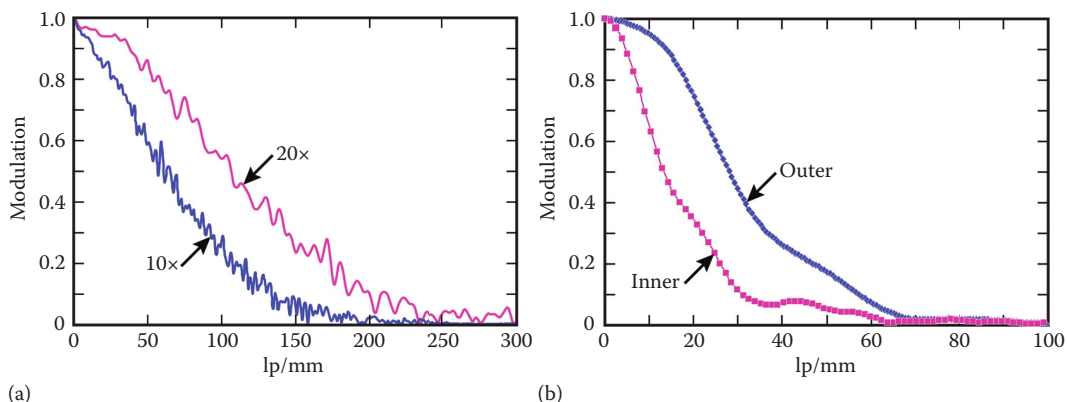


FIGURE 14.16 MTFs calculated in two ways for measuring the difference in resolution of a CT system using a W edge and for inner and outer edges of an Au tube: (a) MTFs calculated from the derivative of the edge response function (noise included) for the same DR and CT system using 10 and 20x (as labeled) optical magnification with a scintillator lens coupled to a CCD camera; and (b) MTFs calculated from edge response functions but from the Gaussian fit to the derivative of the ERF. Comparison shows a large difference between the resolution for the inner and outer edges of the tube imaged at high-spatial resolution.

these data were acquired in the 60–100 keV range, where Compton scatter is relatively low (unlike high-energy scanning where you can also get even larger differences in sharpness between inner and outer edges). Also, at these length scales, *phase effects* operative from the exit face of the object to the detector face-front can figure into the image (see Sections 5.5 and 15.9). We consider this another x-ray imaging context where assumptions of spatial invariance do not apply. At the very least, when you perform CT inspections for a customer, it is incumbent on you to convey that sharp outside edges do not always translate to internal results.

Consider an operation between two functions where we combine the integrals of the product of the two functions, and each point is the integral of the product of two functions, but the values at which the two functions are multiplied are displaced by a fixed value. Figure 14.17 represents this type of operation where two step functions are combined. This operation is the convolution of the two functions. Another way of looking at this operation is if we took one of the functions and centered it in different positions proceeding from left to right over the range of values, integrating the result at each point.

Now consider the convolution of a step function and one of the symmetric blur functions that we calculated above by taking the derivative of the line-out. Figure 14.18 includes the convolution of a step function and a Gaussian distribution with a full width at half-maximum (FWHM) of 5 pixels. As the width of the Gaussian gets smaller, the impact on the step function gets smaller, and as the width gets bigger, the impact on the step function is larger.

Now stepping back a bit further, we can consider every edge-spread function to be the convolution of a step function and a blur function. At the same time, we can estimate or obtain the blur function by calculating the derivative. Consequently, we can measure the width of the transition from minimum to maximum intensity by the width of the blur function convolved with the *perfect* step function. We can compare the sharpness of edges by the line-outs (by the number of pixels to traverse from minimum to maximum intensity) or by the widths of the blur functions that arise from taking derivatives from the line-outs.

Now consider the Fourier transform of the blur function estimated by calculating the derivative of the edge-spread function. Figure 14.19 contains a series of Gaussian distributions and the MTFs calculated from each of the Gaussian distributions. As shown in various texts, the Fourier transform of a Gaussian is a Gaussian. Also, as the width in the spatial domain gets smaller, the width in the frequency domain gets larger. Applying this relationship to our examples above, as an edge gets

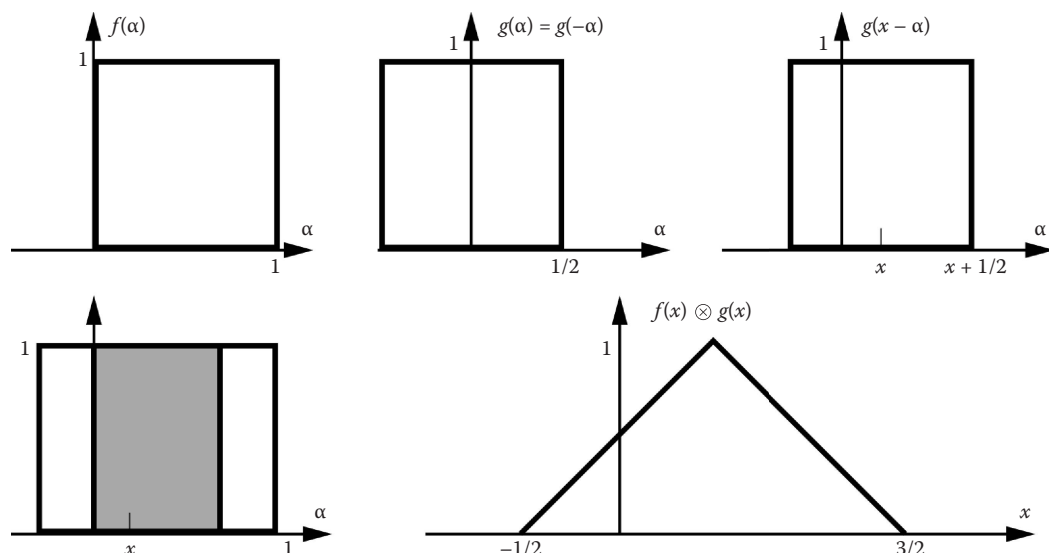


FIGURE 14.17 Pictorial of the convolution of two step functions.

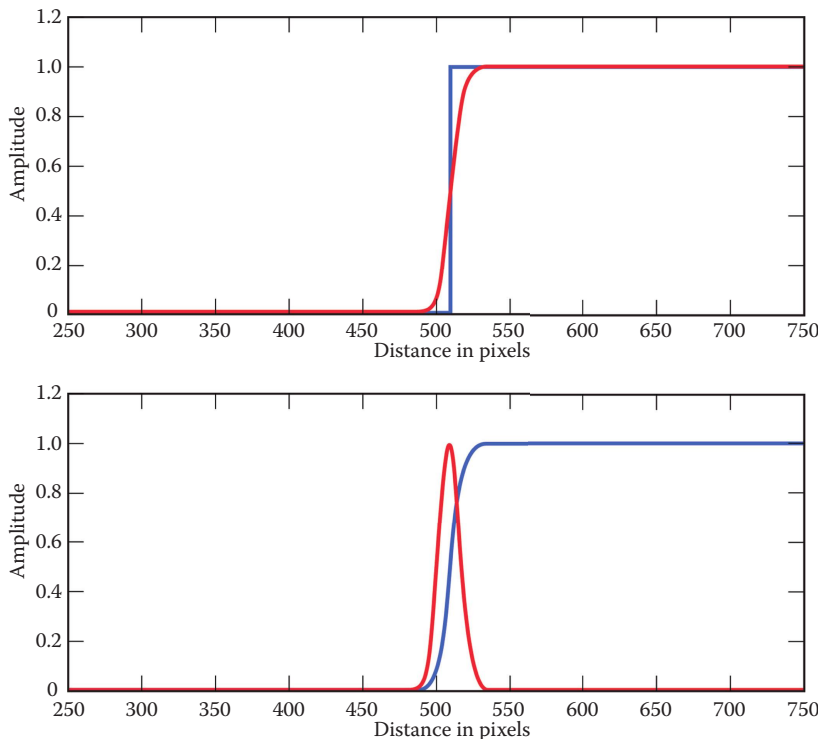


FIGURE 14.18 Close-up look at a step function and the effects of the convolution with a Gaussian blur function.

sharper, the width of the blur function gets smaller, and the width of the Fourier transform of the blur function gets larger. Another way of stating this result is that sharper edges will include more amplitude on the higher spatial frequencies. Relating this back to the MTF, an imaging system with sharper edges can measure more amplitude on the smaller features in the line-pair gauge. Consequently, the sharper the edges, the higher the modulation for the smaller features in the image, or put differently, the greater the amplitude for the higher spatial frequencies in the image. In summary then, we can consider the Fourier transform of the edge spread function to be a measure of the MTF since it is a measure of the amplitude per spatial frequency that constituted that edge.

At this point, it should be clear that there are at least two different ways of measuring MTFs. First, you put a designed object constituted of features with alternating x-ray opacity, and you measure the change in signal for decreasingly smaller feature sizes. Knowing the size of the features on the gauge, you can calculate the modulation versus spatial frequency by the procedure above. The second procedure is you scan an object with a known *sharp* edge (the change in x-ray opacity for this edge is smaller than a pixel), acquire the edge response function and then calculate/estimate the edge-spread function, and estimate the MTF from the Fourier transform of the line-spread function (Boone 2001). Both of these methods measure the *sharpness* of the imaging for this pixel size. Also, both methods obtain a measurement of sharpness or resolution at position(s) in the imaging field of view.

The critical step is to assert from either of these approaches that this measurement of MTF is a property of the *imaging system*, in particular, that this is the resolution/contrast you can expect at any place in the field of view—or for any other object you scan with this system. Proceeding further, you can use this estimate of the MTF in a subsequent probability of detection calculation to predict the performance of an imaging system (see Section 14.6). Two assumptions are involved here: (1) whether the imaging conditions you used to acquire data for calculating the MTF typical of the system operation and (2) for any object feature of particular size put anywhere in the field of

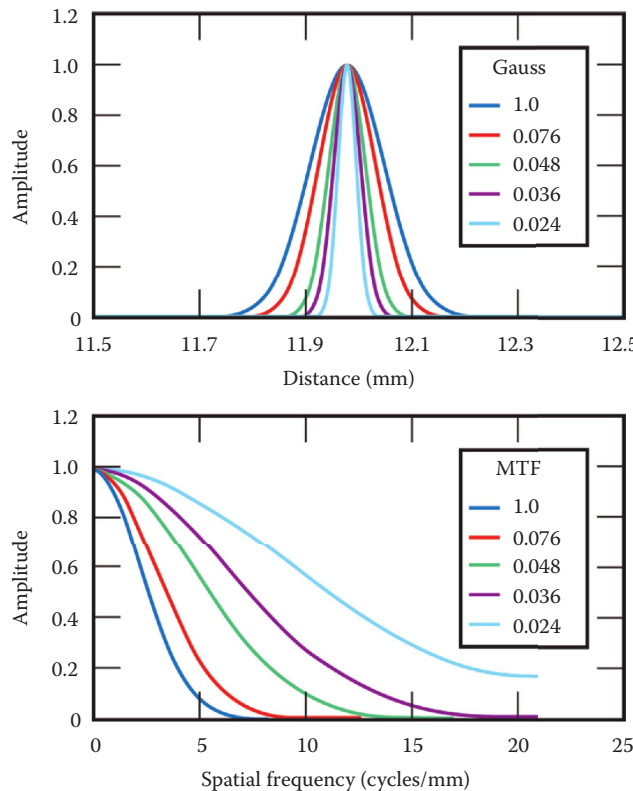


FIGURE 14.19 Comparison of Gaussian distributions (top) and their corresponding MTFs (bottom).

view of the system, we get the same sharpness. The validity of the first assumption can be assessed from a review of the experimental conditions, but the second is subtler.

The second assumption involves the concept of *spatial invariance*, and this is the glue that connects the two methods for calculating the MTF. The MTF calculated from a line-pair gauge involves a few assumptions; you image the gauge and calculate the MTF. Also, by putting the high-frequency part of the line-pair gauge in different positions throughout the field of view, you can verify that the MTF is the same in every part of the scanner. The second technique (edge response function, edge-spread function, and then Fourier transform to obtain the MTF) more critically depends on the assumption of spatial invariance. The procedure of calculating a Fourier transform decomposes an image into the characteristic Fourier frequencies, which is a *basis set* for the entire line trace, and/or for the entire 2D image if you use this as the representation of the imaging system. Now you can take line-outs from the same *edge* placed in different positions in the imaging field of view and see if you get the same MTF at different locations in the image; but this assumes that you have the same physical edge at each position in the field of view.

The added complexity for applying the assumption of spatial invariance in x-ray imaging is the different mechanisms that result in local changes in the edge response function. First, source unsharpness varies throughout the object; when a feature is closer to the source, the source unsharpness is larger than when the feature is closer to the detector. Second, greater proportions of object scatter will represent edges with more blur, and this is the dual result of the energy used in the inspection and the materials in the object from that orientation. Third, in circumstances with meager penetration, either due to inadequate source energy or a lack of stopping power in the detector, the object-edge transition is close to the noise floor or close to the amount of background scatter in the system at that position. All of these three mechanisms are part of the x-ray imaging but are

masked over by procedures that rely heavily on Fourier transforms, which enforce spatial invariance in terms of the Fourier frequencies, for that pixel size.

X-ray transmission images are the composite result of a number of subprocesses in the overall image-forming process. Not all of the mechanisms are spatially invariant. However, knowing the mechanisms and taking experimental precautions can produce images that are generally spatially invariant. For instance, low-energy images, where the source unsharpness is on the order of a pixel, there is minimal scatter, the cone-angle is low, and the stopping power of the detector is substantial (0.9 or better), can produce images with similar resolution throughout the image. Also, MTFs can be calculated to evaluate the resolution in some extracted portion of the image where the resolution is pretty much the same in this region. The point is to review these aspects of the imaging technique along with making the measurements and be strategic with either method for calculating MTFs.

It should not be surprising at this point to find that the inner edges of features are not as sharp as the outer edges (Brown and Martz 2006). This result has been documented in both low- and high-energy contexts for scans of the inner walls of tubes, cylinders, and turbine blades (see [Figure 14.16b](#)). The accumulated blur in a CT scan can vary by region impacted by local scatter sources, size, and variation of the source spot throughout the scan, or issues with the detector. This effect is many times referred to as the impact of *scattered radiation* (see artifacts in Chapter 13). This emphasizes that the MTF, the edge sharpness of the image, is not constant throughout the image. Consequently, it is a good idea to check the operation of any automated routine for performing dimensional measurements in the high-attenuating sections of the CT volume.

A case in point is a recent comparison of scintillator screens by calculating their MTFs. Now in order for this comparison to be valid, all aspects of the experimental technique are held constant—and only the scintillator screen is changed. Also, the pixel size for the measurement is smaller than the highest resolution for the highest-resolution screen. See [Figure 14.5](#) for the plots of the scintillator screen MTFs.

The relative importance of scintillator MTFs depends upon the inspection goals and the system geometry. Given a target spatial resolution, or a critical flaw size, and an x-ray magnification less than the pixel at the object, the resolution of the system depends on the inherent resolution of the scintillator, sampled by the pixel pitch. In this case, [Figure 14.5](#) provides a means for choosing and eliminating scintillator screens that will not provide adequate performance.

Lastly, measuring MTFs can include some computational variations that impact the measured magnitudes per spatial frequency. Consider the ASTM approach, in particular, calculating the derivative, transforming the line-out from an edge response function to an edge-spread function. A number of possibilities exist for calculating the derivative; however, all of the methods that calculate the derivative by calculating a tangent (fitting a line to the curve at a local point) actually use up some of the spatial frequency information in the image. Whenever you apply an operation that sums 2 or 3 pixels together, you have compromised the higher spatial frequencies. Consequently, the MTF from an edge-spread function calculated in that way will have lower modulation on the higher spatial frequencies than it would if you did not estimate the edge-spread function in that way. Another way of calculating the MTF involves nonlinear fitting of a Gaussian cumulative distribution function to the edge response function, and the fast Fourier transform (FFT) of that Gaussian is the MTF. An MTF calculated in this manner always results in a Gaussian-shaped MTF and will usually include more modulation on the higher spatial frequencies than techniques that calculate a tangent by adding pixels together or averaging. If this image does not include any modulation at say 3 pixels, then the two methods will likely be the same.

An argument can be made for both types of techniques. For the type that involves estimating a tangent, consider most if not all of the imaging operations applied to an image, and you usually end up adding a couple of pixels together in a weighted or unweighted fashion. Consequently, the MTF calculated in this way will correspond to the image as transformed by the various operations you will apply to the image. Also, the MTF calculated in this way is not necessarily Gaussian. It can reflect the modulation on the lower spatial frequencies that may not have a Gaussian fall-off, and you can see the impact of the image noise on the modulation.

On the other hand, why should the estimated MTF include the choice of processing options? Are we interested in the MTF for this application with all of the processing included? Or are we trying to measure the MTF of this imaging system, which should reflect the *best* performance you can obtain? Estimating the MTF without any calculation of a tangent or any kind of averaging can provide a better measure of the MTF for the higher spatial frequencies and can identify the *best* you can do with this equipment. Also, there is no real variation per technique here; you find the best-fit Gaussian, defined by two parameters, and the MTF is measured.

ASTM E 1695 (2013) attempts to take the variability out of the estimation of the MTF by controlling the interpolation schemes for obtaining and processing the line-out. Explicit steps are prescribed, and if followed, control this source of variability. Unfortunately, without some control on beam hardening, this ASTM standard rewards scanners with beam-hardening artifacts with higher MTFs, which is certainly not intended. This is more problematic as these scanners are then used for dimensional measurements to that *accuracy*, which is likely not the accuracy for inner edges and features.

At LLNL, for inspection data we pass on to customers, we prefer the non-Gaussian techniques. This means that we knowingly compromise the highest spatial frequencies by calculating a simple two-point tangent and can estimate an MTF in the midst of the noise in the image. Admittedly this has a tendency to report a more conservative estimate of the spatial resolution in an image, and it is true that imaging systems can include more resolution and contrast than an MTF calculated in this way. If the technique we have chosen includes some beam hardening in the scanning, we simply report it and issue caution about the inner and outer edges. Our belief is that we do not see much practical value in reporting levels of resolution that customers cannot access or realize in operations for detecting features or dimensioning objects. Further, our customers, who usually evaluate the inspection images themselves, have appreciated the conservative numbers, so that when something is detected and the MTF values justify this as a true detect, the destructive results have been in line with these claims. As mentioned before, highly attenuating features can be detected even if they are some part of a pixel. This is not a measurement of resolution, and our experience has justified a healthy suspicion of claims of resolution based on imaging with small high attenuating objects.

The last point here is that image evaluation techniques for calculating edge-spread functions and MTFs are a tool to understand your inspection image. Whether assumptions are strictly observed or not, taking care to apply the same techniques in the same fashion builds a basis of comparison. Correlating these measurements with measurements of inspection performance builds the empirical connection to the kinds of probability of detection and error in dimensional measurements that one can expect from a measured MTF. This is the kind of correlation that results in better designs for inspections and better inspections, which is ultimately the goal of this work.

14.5 SIGNAL-TO-NOISE RATIO AND DETECTIVE QUANTUM EFFICIENCY

A still more composite measurement of system performance is *detective quantum efficiency* (DQE). The concept behind this measurement is similar to the MTF: comparing the content of the input image to the content of the output image. The underlying assumption here is that the inspection images are the product of multiple processes in an imaging chain usually represented as some kind of sequential or nested set of convolutions. So, the focus is on tracking the impact of a process, or processes, on the inspection image. Also, as in the case of the MTF, the input can be some idealized representation of the input image or a quantitative measure of what the input should be and not an actual image.

One way to motivate the definition of DQE is to consider what is missing in the measurement of the MTF: some measure of image noise. It is tacitly true that detecting features in the sharpest images (large comparative modulation for small features) can be undone by some quantity of image noise. So to assess the impact of an operation, we want to compare the relative amount of noise in the output image to the amount of noise in the input, but not just the raw amount of noise, since the absolute level of variation changes with the average value of the signal. So, we would need to compare the noise relative to the mean signal before the operation and after the operation. At this

point, we have implicated the concept of SNR mentioned previously, and also we have let the measure of SNR be defined as the ratio of the mean signal for a feature to the standard deviation of the background noise. However, other definitions have been proposed, which are important to review.

Classically, DQE has been used to compare detectors or detection schemes against some idealized or measured input for the source irradiance. One such classic development can be found in Chapter 1 of Dainty and Shaw (1974). The concept of DQE or *comparative noise level* was developed for ideal digital detectors with a Poisson source, exposed to an average number of quanta or photons, resulting in an average number of counts, each detector including the same threshold for detection and a level of saturation. The best case for a detector in this scheme is unity, that is, the process of detection generated no additional noise relative to the signal detected. Taking this development further, it was shown that this concept is applicable to a wide variety of detectors, since the comparison is between the noise input to the detector and the output from the same detector, which are always on the same scale.

The actual name *detective quantum efficiency* was proposed by Rose (1946) in his analysis of detectability of features in any image. The *Rose criterion* (as it is referred to in the current literature) was introduced in this paper and is simply described as follows: to detect features in images, the SNR for the feature must be greater than 5. For this criterion, the SNR is the mean difference in signal for the feature, relative to the standard deviation of the local background. Remarkably, this particular criterion has demonstrated widespread utility for feature detection and is still used as a standard for evaluating proposed and extant image detection schemes. As has been shown, and will be used later in an example, fixing the level of the SNR at a value of 5, or at any level for that matter, is useful for all kinds of system design tasks: generating requirements for source output, limits on detector noise, estimates of system speed, etc.

To unpack the measurement of DQE, and prepare for some different methods for performing this calculation, we will spend some time on the concept of *SNR*—its significance and methods for measurement. On the face of it, the SNR is a way of parsing the measured intensity levels for signals or images (which can just be considered as signals). This concept recognizes that the measured values are the result of a stochastic process, or are the results of a cascade of stochastic processes each contributing some random variation. In general, we want the SNR to be the ratio of the expectation for the signal to the measure of variation around that expectation, reflecting the noise in the signal. For the Rose model, SNR is calculated as the mean difference for the feature, as a fraction of the average local signal. This is depicted in Figure 14.20. Now due to the properties of Poisson distribution, the mean value is also functionally the variance, and the ratio of the difference to background signal over the background signal is a ratio of the difference to the expected variation.

The key aspect of the Rose criterion is in how the machinery connects contrastive or SNR performance with *counts* or, as referred to in this volume, *irradiance*. The result is a way of calculating the source output necessary for a certain contrastive performance. This calculation can be made from an evaluation of a system. This model fits exactly with an evaluation of a radiograph with an

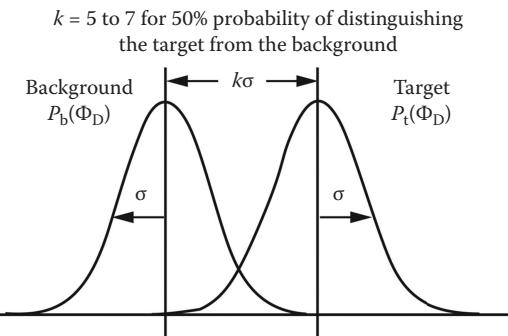


FIGURE 14.20 Graphical representation of the Rose (1946) model for calculating DQE.

IQI penny attached to a thickness, or from the expected properties of a system still at the design stage. From either context, the evaluation of a system or a designed system, this calculation quickly generates a measure of what needs to be done to get robust contrastive or SNR performance for the identification of a feature. While it may be true that an SNR of 5 is a good number for robust identification of features, it is not always clear that more source output will improve the situation. The model behind the criterion does not include treatment of other factors that impact measured contrast besides source output; to the extent that other noise sources are significant (control of scatter, digitization noise, etc.), calculating a level of source output may not be very important.

Alternatively, SNR can be calculated as the ratio of the local average signal to the standard deviation for the image or some region of the image that is relevant for the inspection. In particular, we can reduce the Rose criterion to this calculation: if the ratio of the mean to the standard deviation is not larger than the difference in transmission for that feature, the probability of detection are problematic. In some circumstances, it can make sense to substitute the mode or median from the histogram for the mean of a local region in the calculation of the SNR. Utilizing nonparametric measures of central tendency can be strategic for medium- to high-energy inspections where the presence of x-ray hits or other bad pixel outliers can increase the calculated mean value beyond its normative value. It should be true that the standard deviation will be higher, thereby lowering the SNR accordingly, but we reiterate a point made earlier that saturated pixels have no information. Also, pixels that include an x-ray hit are bad measurements, and their number and magnitude change with each acquisition. These bad pixels have little to do with the object, so they should not be used.

As shown in the types of analysis directed by the *Rose criterion*, the SNR is both a measurement of performance and a prediction for system performance going forward. Consider an inspection for porosity or voids that are 2% of a 0.5 in. thickness you are inspecting. Now a 2% void is 1/50 of the thickness. If the SNR is less than 50, the chance that you can reliably detect this kind of difference is low, since the magnitude of the intensity of the noise is larger than the change in thickness you are looking to detect (Problem 14.3). From a system design point of view, if you are looking to detect a 2% change in thickness, it is a good idea to have an SNR of at least 100, or where the standard deviation for the noise is one-half of your target detection limit. If the goal for the inspection involved 3-sigma-type requirements, you might want the SNR to measure something on the order of 150 or 200.

The comparison of the average signal for a region to the standard deviation for that same region establishes a metric for inspections. In this same connection, a single radiograph of a step wedge covering the range of thicknesses of interest to an inspection generates a set of SNR values measuring the performance of the system. Figure 14.21 contains a raw image of an eight-step aluminum step wedge (the image is in counts from the detector). The steps are in increments of 0.25 in., with the maximum thickness of the wedge being 2 in. The radiograph was acquired at 100 kV applied potential, with a Thales amSi detector employing a Lanex Fine screen. We obtained an SNR for each thickness in the step wedge, extracting a 20×20 patch from a location in each step. Also attached to this step wedge are aluminum penetrometers, each with thickness less than the step it is placed on, with the thickness displayed in thousandths of an inch (the lead letters), and each includes two holes. It should be mentioned that the smaller regions were extracted at locations that do not intersect the penetrometers. Regions were extracted that only include the multiple noise sources in



FIGURE 14.21 Digital radiograph of a step wedge. The step sizes from left to right are given from bottom to top in [Table 14.2](#). The object is an Al step wedge with Al penetrometers. The penetrometer thickness is given by the Pb letters in thousandths of an inch.

the system for that singular thickness in the step wedge to produce measures of SNR using mean/standard deviation.

Table 14.2 contains the results of the SNR calculation for the extracted regions for the raw image. Notice that the relative SNR values follow the photon statistics relationships you expect from thinner to thicker steps in the step wedge. As the step wedge gets thicker, the SNR gets worse.

Figure 14.22 contains the same image as Figure 14.21 but converted to μl . The beam divergence and intensity in the background image have been divided out, and the transmission has been transformed by the natural log function. These transformed data are both a different scale and include somewhat different noise properties. The act of dividing out the incident irradiance, Φ_0 , signal remediates some of the digitization bias in the acquired signal. Notice in Table 14.3 that the SNR is different in this transformed scale in part due to the dividing out by Φ_0 and in part due to the

TABLE 14.2
Calculated SNR for Each of the Values of the Step Wedge in the Raw Image from Figure 14.21

Step Thickness (in.)	Mean	Standard Deviation	SNR
2.00	165.5008	5.928596	27.91568
1.75	209.7156	6.489204	32.31761
1.50	273.9029	6.638568	41.25934
1.25	362.2791	6.723339	53.8838
1.00	489.8365	7.33482	66.78234
0.75	694.1932	7.784596	89.17524
0.50	1023.521	10.18276	100.5152
0.25	1669.588	11.92289	140.0321



FIGURE 14.22 Attenuation, μl , image derived from the radiograph of Figure 14.21. The object is an Al step wedge with Al penetrometers (thickness in lead letters).

TABLE 14.3
Calculated SNR for Each of the Values of the Step Wedge in the Attenuation, μl , Image of Figure 14.22

Step Thickness (in.)	Mean	Standard Deviation	SNR
2.00	2.953588	0.017685	167.0083
1.75	2.728148	0.016311	167.2604
1.50	2.478728	0.013301	186.3615
1.25	2.206776	0.010179	216.795
1.00	1.907431	0.007795	244.6946
0.75	1.564862	0.007049	221.9961
0.50	1.180655	0.006573	179.6138
0.25	0.70083	0.006177	113.4582

transform to the natural log scale. This is the input contrast to CT processing and reconstruction. Notice that the SNR peaks close to the $\mu l = 2$ range, a level where the change in attenuation signal peaks in the trade-off with the Poisson and system noise as expected.

Without any other processing, a measure of SNR calculated in this fashion can be used to predict the expected detection performance for an inspection with this hardware and this technique. For the 0.5 in. step and the 0.012 in. penetrometer, the change in thickness constitutes a 2.4% ($(0.512 - 0.500)/0.500$) difference, or at least an SNR of 41.667.

We consider the evaluation of a technique with step wedges and penetrometers of great value. In this way, you get the actual performance of the system. This is made better by obtaining/fabricating step wedges of the material you are inspecting, which then can be used as a measure of system performance going forward. Further, once a system has been characterized in this way and documented, the same measurement can be performed subsequently, which is then a measure of system stability or the change in system performance. If a connection can be made between this measurement and the probability of detection, a criterion has then been established for system readiness for this task (see [Section 14.6](#)).

One problem with SNR is the omission of spatial resolution as a factor in measured contrastive performance. Object features, voids, or inclusions have a size that is part of their definition. The previous section documented the impact of the sources of spatial blur and how those sources can be measured with ESF and MTF. It may be true that you have good contrastive performance at 1% (say a 2-sigma criterion, an SNR of 200, for that size change of thickness over that path length). However, if the feature you are trying to detect is smaller than the 5% modulation point on the MTF, the measured difference is only an SNR of 10 for that size feature. The sources of blur in the system have reduced the measured contrast of that small feature by spreading out all that hard-earned performance into adjacent pixels, and now the feature is *in the noise*.

Consequently, we need to put *size* or alternatively *spatial frequency* into the measurement of SNR. In frequency space, the ratio of $MTF(f)/NPS(f)$ is the analog to the SNR in the spatial domain where NPS is the noise power spectrum. This ratio measures the modulation—relative to full modulation—over the noise at that frequency, or the signal at that frequency to the noise at that frequency. This ratio can then be used in combination with the average signal, measures of the fluence, and x-ray source to produce the definition of fractional DQE at a spatial frequency or *high-dose* DQE:

$$\begin{aligned} DQE = DQE(f, \infty) &= \frac{SNR_{out}^2}{SNR_{in}^2} = \frac{|MTF(f)|^2}{NPS(f)SNR_{in}^2} = \frac{|MTF(f)|^2 at}{NPS(f)\Phi_D^2} \\ \text{for } SNR_{in}^2 &= \frac{\Phi_D^2}{at}, \end{aligned} \quad (14.18)$$

where a is the count rate, t is time and Φ_D is the average signal in the region of interest used for the NPS in detector counts.

The above formula is called the *high-dose* DQE since the measurement implicitly assumes that you are not lacking x-ray irradiance as the $NPS(f)$ is in part a function of the fluence times x-ray exposure. In circumstances of low dose and high $NPS(f)$, this measurement gets problematic. It should be mentioned here that this frequency space measurement does not supplant the analysis using the images of a step wedge. Knowing the kind of penetration you are obtaining through lengths of material similar to the object is critical for understanding the limits of the inspection. Further, if you have taken care to ensure that the feature of interest is large compared to the spatial resolution of the system, all of the conclusions from the analysis using the Rose model or taking the ratio of SNRs are entirely valid.

In summary, we have described measures of DQE from the Rose model, from a data-driven measurement of SNR, and from the ratio of the MTF to the NPS. For all of these measurements, the fundamental idea is the same: compare the change in counts or attenuation for the feature to some measure of noise in the surrounding pixels in the radiograph. It is significant for Poisson process

measurements that the mean and the variance for the measurement are the same, and dividing by the signal level is tantamount to dividing by the average variation. Second, when Poisson process considerations are not the dominant impact on contrast, or other sources of noise are more significant, basing SNR and DQE measurements on calculated quantities from the image or the image of a step wedge can provide good estimates of contrastive performance.

DQE or the components for the measurement of DQE can serve a number of important functions. First, the results include a quantitative measurement of the contrastive performance of the system. If calculated using the step wedge, you have the probability that a feature will be detected for a thickness through the material. If the critical feature of interest is that change in thickness for that total path length, you can calculate the chances that you do not detect that feature and calculate the risks and benefits of the system. Second, if you can determine the detection requirements, you can use the step-wedge measurement to ensure that your system is capable of detecting the critical feature to that confidence. Third, once you have the measurements, you can compare this measurement to other systems and/or calculate the impact of change of one or more components of the system.

14.6 PROBABILITY OF DETECTION AND ROC CURVES

Given all the measurements and methods for evaluating image contrast and spatial resolution, it is important to show how these properties impact more practical metrics of system performance, e.g., probability of detection, system viability, and system cost. To get some traction on these practical issues, we need to present some ideas from the framework for and the calculation of receiver operator characteristic (ROC) curves. With these concepts, we can connect the measures of image contrast and spatial resolution to more practical questions. Is this inspection viable? Does it accomplish the intended purpose? What are the total costs of this inspection? What are the costs if the inspection is not performed? Obtaining a good measurement of the probability of detection for an inspection enables a number of important calculations: estimating the limits for a viable inspection; evaluating the usefulness of an inspection before you field it; in the same connection, the impact of an improvement or change to the system; and an important input to the different *cost* functions for an inspection.

It is the point of view of this section that the issues and the questions around these issues can be best viewed through the framework behind ROC curves. Consider a population of objects to be inspected; a certain percentage of the population includes a certain condition (will be considered positive [P] for the condition); the rest of the population does not include the condition (will be considered negative [N] for the condition). To sort this population, you institute a test, which reports a “T” if the measurement indicates a true *detect* and “F” otherwise. One additional property about this test is that it is not a *perfect* classifier. That is, the measurement includes some stochastic components or some measurement variability, or whatever, and a certain percentage of the time it will be wrong: missing some objects in the population with the condition (classifying them as not having the condition), and classifying some objects in the population that do not have the condition as having the condition.

Figure 14.23 represents the different alternatives and the totals for the actual value and the test.

The different cells correspond to a variety of different well-known statistical components. The upper right-hand cell or FP is equivalent to *Type I errors* in statistical testing. The results of the test say that this object has the condition when in fact it does not (you rejected the *null* hypothesis of no relationship, but it is really that there is no relationship; the null hypothesis was true). The lower right cell, the false negatives, corresponds to a *Type II error*. This is just a miss; you claim the *null* hypothesis is true, no relationship, and this object really has the condition.

The ratio of different combination of cells to the totals corresponds to various canonical test properties. First, the ratio of the upper left-hand cell to the total positive in the population is sometimes referred to as the probability of detection. There are so many with that condition in the population, and for that number, the ratio of upper left to total positive is the probability that if you have the condition, it will be detected by the test. The false positive rate (FPR) is often calculated as the ratio of the upper right-hand cell to the total number of negatives or N, which is the rate at which those who do not have

		Actual value		Total
		<i>p</i>	<i>n</i>	
Test results	<i>t</i>	True positive	False positive	T
	<i>f</i>	False negative	True negative	F
Total	P		N	

FIGURE 14.23 Table distribution of outcomes against the true condition for objects being tested.

the condition in the population are classified incorrectly as having the condition. Two other quantities of interest are the *accuracy* $((TP + TN)/(P + N))$ and *specificity* (TN/N) or $1 - FPR$.

The importance of the ROC curve is the way the relation between the true positive rate (TPR) and the FPR is configured to enable an evaluation of the usefulness of the test, and can provide a detailed accounting of the *cost* of the test. In particular, there are at least two costs for a *test*—the cost of implementing the test and the cost of what to do with the misclassified items from the test. If the TPR and the FPR are the same, it is hard to justify implementing the test as you are just as likely to classify correctly as to classify incorrectly. Figure 14.24 contains the axes of a ROC curve plot with some annotations. As shown in the figure, the dotted line is the result you would get if you implemented a random test involving no measurement at all.

Both the ROC curve and the different quantities calculated to compose a ROC curve enable a more detailed accounting of the *cost* of a test or inspection. Consider the case of a part inspection, where true positive means you found a part with a defect, and when you find a part with a defect, you scrap the part. In this case, a large number of false positives means that you are throwing away

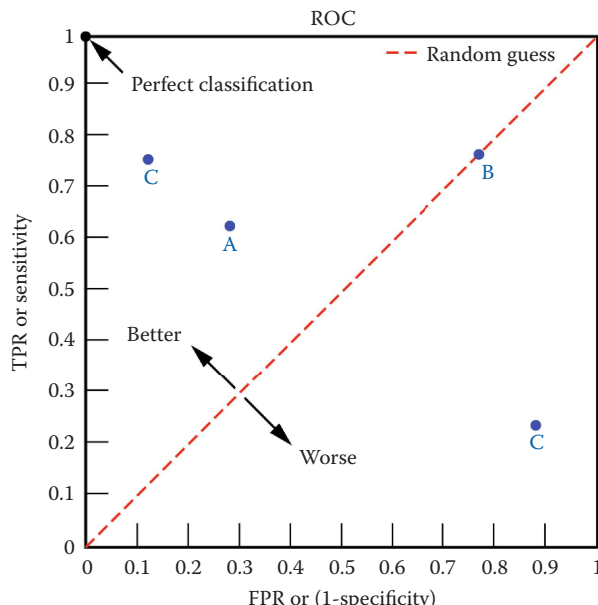


FIGURE 14.24 Axes and areas of a ROC curve.

a large number of perfectly good parts. On the other hand, false negatives may be more costly since you let a part into the good part pool, and it is likely that the part will return to you as a warranty repair (or a lawsuit); connected to that repair is often a dissatisfied customer (which is not without a certain cost). In this case, there are three items to the cost of inspection: the cost of performing the test, the cost of the *false positives* that you threw away, and the costs associated with warranty repairs, assuming a certain rate of return for the parts that include the defect but were missed by the inspection.

In many cases, in radiography, the defect condition and the no-defect condition represent two separate distributions, each with some mean value determined by the object material and the properties of the test. Consider the case of detecting a highly attenuating anomaly in a certain location in a single projection through a part, so the value for a *clean* section of the part is a certain attenuation value, measured with some uncertainty (the width of the distribution); furthermore, the value for an *anomaly-present* section is an attenuation value that is a certain amount greater or lower depending on the defect than the clean section, again measured with a certain uncertainty. Putting the two distributions on the same graph enables the identification of the different cells in Figure 14.23. Figure 14.25 contains a pictorial of the two distributions with the cells in the table labeled on the graph within the two distributions.

Notice that this plot was presented earlier in the development of the Rose criterion (see Figure 14.20) and is also a representation of the concepts in the *difference of means* statistical test. There are different ways to obtain these distributions. First, make a test object and obtain measurements of the value for the *clean* part and for the *anomaly-present* part of the test object. Even better, you make a test object with different amounts of the anomaly so when you apply the threshold, you have some idea of the amount of the defect you are passing in the inspection. Second, from the results of a different but similar inspection, you estimate a new set of distributions for *clean* and *anomaly-present* measurements. Third, from first principles, some estimate of the intrinsic contrast for the materials in the *clean* and *anomaly-present* chords through the object, an estimate of the *effective energy* for the source and the detector, and some estimate of the spatial resolution for the system given the pixel size, spot size, and intrinsic resolution of the detector, you construct these distributions. In our opinion, the best numbers can be obtained from measurements; however, good estimates of source spectra can be found and paired with known properties of materials, and good estimates of system performance and cost can be obtained.

The strengths or weaknesses of an inspection are rooted in the factors that affect these two distributions. From the plot in Figure 14.25, the amount of incorrect classification (FP and FN) depends on the amount of overlap between the two distributions. There are two ways to decrease the amount of overlap: increase the difference between the mean values of the two distributions and/or decrease the width of the distributions. For x-ray inspections, affecting any of these changes requires some change to the inspection and/or some component of the measurement. For single-view radiography, changing the distance between the averages implicates the value of the x-ray attenuation times path

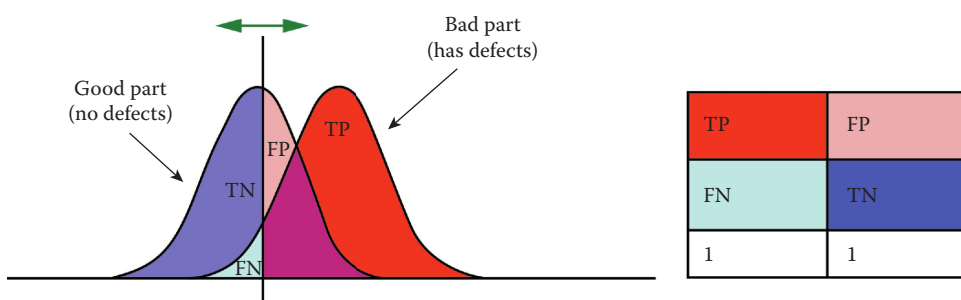


FIGURE 14.25 Pictorial of the cells of the fourfold table labeled for two distributions of the two conditions and a threshold identified by a vertical line.

length or μl for the *clean* and *defect* condition and the choice for effective energy (the choice of source energy coupled with a detector). The width of the distributions gets smaller with better photon statistics, which means a source with more output or longer inspection times, or, if the feature is small, a smaller x-ray source spot size, a detector with better spatial resolution, or an inspection configuration with better collimation. The DQE of the system, measured as the modulation at a spatial frequency smaller than the defect size relative to the noise power spectrum at that spatial frequency, or just to the noise at that μl level, should be a certain factor greater than the noise, or once the system degrades even slightly (and all x-ray systems degrade in the field), the accuracy ($TP + TN$) of the system degrades and the cost of the system increases. It should be mentioned here that regular scanning of a well-designed *test object* can measure the distributions and provide an accurate window into the state of the inspection system.

An analysis of the dependencies between system components as they combine to constitute these two distributions is the landscape for implementing system changes to obtain greater system speed, or greater system accuracy, or possibly to increase the range of the inspection to include the detection of some other conditions.

In summary, the components of an inspection system combine to produce a measurement distribution for the *clean* or *no-condition* and *defect* or *condition-present* objects. The state of these imaging components can be measured with the techniques mentioned in this chapter: measurement of contrast, spatial resolution, noise, and the types of composite measurements—SNR, MTF, and DQE. Each system will include dependencies on properties of system components that account more or less for the performance of the system. This type of analysis leads to the best design of test objects useful for establishing system performance and monitoring system maintenance. Using these tools to compose distributions that can result in good estimates of the elements in ROC curves provides windows into system performance, system cost, and quality of the inspection method.

PROBLEMS

- 14.1 How many detected counts are required to satisfy a noise requirement of 0.01% for a 1D gauging system?
- 14.2 Describe the process for calibrating a current-integrating LDA detector for a measurement.
- 14.3 Describe a process for material identification using two different applied tube potentials.
- 14.4 Consider a scan of a hollow cylinder that includes a large change in the MTF for the inner and outer edges? If this scan is acquired at 60 kV, what are the possible mechanisms that could lead to the change in these two MTFs? What if the pixel sizes are 0.05 mm? Or 0.5 mm? What would be the mechanisms for the change in these two MTFs if the scan were acquired at 6 MV? What changes would you make to the scanning parameters to remedy this so you can do better dimensional measurements?
- 14.5 Apply the Rose model and analysis to the labeled distributions in [Figure 14.25](#). Create two cases. Case 1 is where $k = 7$ and Case 2 is where $k = 2$. Plot the resultant ROC curves for comparison.

15 Special Techniques

15.1 INTRODUCTION

Here we address special techniques. We consider techniques that are not as commonly used as digital radiography (DR) or computed tomography (CT). Techniques to be discussed include contrast agents imaging, dual energy for effective atomic number, active and passive CT, x-ray topography, x-ray backscatter, phase-contrast imaging, and x-ray optics. You will become acquainted with these techniques as related to industrial imaging.

Upon completion of this chapter, you will be familiar with the following imaging techniques:

- Contrast agents
- Dual energy for effective atomic number
- Active (transmission) and passive (emission both single-photon emission CT [SPECT] and positron emission tomography [PET])
- Depth information without CT
- Computer defect recognition
- X-ray backscatter
- Topography
- Phase contrast
- X-ray microscopes and optics (pinholes, Fresnel zone plates, and Wölter optics)

15.2 CONTRAST AGENTS

Situations arise in industrial x-ray imaging where the result can be improved by adding a fluid to the object. This is usually done by filling a void or channel with a fluid selected for its x-ray attenuation properties. This filling material is called a *contrast agent*. Less frequently, the contrast agent may surround the object.

A typical example in which a contrast agent may prove useful is the inspection of internal cooling channels in a high-value turbine blade made of Inconel. These channels are low in contrast because of their small size. When filled with Hg, the channels become much higher in contrast and are readily imaged.

Sulfur hexafluoride (SF_6) is a gas that is sometimes used as a contrast agent. It is 5.0 times the density of air and has a mass attenuation coefficient 5.5 times that of polyethylene at 20 keV. Also, water-soluble compounds (Brunetti et al. 2004) offer great flexibility in adjusting attenuation properties.

Performing CT on the blade of a spatula is an example where an external contrast agent is likely to be useful. The high aspect ratio of the blade presents a challenge because of the very large difference between attenuation through the long chord and attenuation through the blade thickness. This can be diminished by immersing the spatula in a thin tube filled with an appropriate fluid.

15.3 DUAL ENERGY FOR EFFECTIVE-ATOMIC NUMBER

The purpose of x-ray inspections using multiple energies is to obtain some measurement of the material composition of the object or assembly under inspection. This type of application usually employs two different energy ranges: (1) low energy (20–200 keV) and (2) high energy (2–9 MeV). Security applications have recently become the chief application for these types of techniques.

Various dual-energy methods have been used in a variety of characterization contexts for some time: materials characterization for food inspection and specialized studies when using synchrotron radiation. Recently, low-energy security applications have shown good performance for characterizing the items in checked baggage and carry-on luggage. High-energy applications attempt to find nuclear materials and contraband in large shipping containers, the type hauled by big diesel trucks on highways. Both of these applications include a means of distinguishing items on the basis of their material composition somewhat independent of density. For more on security applications, see Section 16.5. These two applications notwithstanding, multiple-energy techniques have been used whenever there has been an interest in unraveling the identities of components parts/materials in objects/assemblies.

15.3.1 PHYSICAL BASIS FOR MULTIPLE-ENERGY APPLICATIONS

In many of the low-energy applications, a measure of *effective-atomic number* (Z_{eff}) is explicitly calculated. For the high-energy applications, one focus is on how to find high- Z materials in containers; the other is to find contraband, such as drugs, currency, and explosives. In both cases, the basis for the measurement of the material composition arises from the changes in the relative proportions of the different attenuation mechanisms in different materials, which constitute the total attenuation of the object/assembly. The physical basis for the lower-energy dual-energy application is the particular way in which the amount of x-ray attenuation from photoelectric absorption changes with the atomic number of the material as energy increases. Alternatively, the high-energy application is driven by the way in which *pair production* emerges as a significant attenuation mechanism in higher- Z materials. The percentage of photoelectric, Compton, and pair production in the total attenuation for a few selected materials (carbon, Lucite, Teflon, magnesium, steel, tungsten) and for a few selected single energies ranging from 20 to 4000 keV are provided in Table 15.1 (all entries in this table are calculated with the LLNL-TPORT code and cross-section information obtained from Cullen et al. [1989]).

Notice the change in the proportion of photoelectric attenuation for carbon and for tungsten as energy increases. At 60 keV, for carbon, the amount of photoelectric attenuation is 2.7%, and at 100 keV, it is less than 1%. For tungsten, photoelectric absorption is still 18.5% of the total attenuation at 1000 keV, and is the dominant attenuation mechanism at 400 keV and below. Total x-ray attenuation depends on material composition and density, but the magnitude of photoelectric attenuation scales with atomic number to the fourth or fifth power (see Chapter 5). Consider the photoelectric absorption for Teflon, which includes only 10% of total attenuation at 60 keV and 2.4% of total attenuation at 100 keV. Now, compose ratios of the total linear attenuation for 60 keV divided by 100 keV for carbon (1.15), Teflon (1.25), magnesium (1.5), and steel (3.2). The difference in ratio between two materials, e.g., carbon and Teflon, is due entirely to composition as density is *divided out* of the ratio. Composing more ratios, notice how the total linear attenuation or sensitivity to x-ray attenuation for a given atomic number is greater as the energy is smaller. For example, 20–60 keV total linear attenuation ratios are more dramatic: carbon (2.4), Teflon (5.0), and magnesium (10.6). The significance here is that a small amount of a higher- Z versus lower- Z material in a volume, or along a chord length, has a marked impact on changes in attenuation and the sensitivity changes as the energy is lower.

15.3.1.1 Low-Energy Dual-Energy Techniques

For low-energy dual-energy applications employing CT, the sensitivity to changes in composition is enhanced by the voxel-wise comparison at different energies, whereas with radiographic inspections, the comparison is an integral of the attenuation times path length. The result is that voxel-wise data can make use of small differences in energy to unravel attenuation effects due to material attenuation as opposed to changes in density. A 12.7 mm outer diameter high-explosive material was scanned using two monoenergetic spectra, 20 and 25 keV. The data were acquired at

TABLE 15.1
X-Ray Attenuation^a for Selected Materials at a Single Energy

Energy (keV)	Carbon (1.6 g/cm ³)	Lucite (0.9 g/cm ³)	Teflon (2.16 g/cm ³)	Magnesium (1.738 g/cm ³)	Steel (7.8 g/cm ³)	Tungsten (17.25 g/cm ³)
20	45.4	54.2	73.03	87.58	97.5	96.7
	38.9	32.6	15.9	5.4	0.45	0.11
	0	0	0	0	0	0
	0.658897	0.482291	2.003853	4.621758	199.9842	1154.473
60	2.7	4.03	9.94	26.7	80.6	86.2
	91.67	90.3	81.4	61.05	11.6	2.8
	0	0	0	0	0	0
	0.279171	0.172282	0.403158	0.435757	9.143435	62.95239
100	0.58	0.89	2.4	7.75	54.3	93.84
	96.96	96.56	93.5	85.1	35.5	2.33
	0	0	0	0	0	0
	0.241996	0.147573	0.323763	0.291315	2.858425	76.38129
200	0.08	0.124	0.34	1.2	16.85	81.85
	99.1	99.06	98.3	96.3	76.18	11.87
	0	0	0	0	0	0
	0.196733	0.119562	0.256827	0.216242	1.141662	13.41445
400	0.0126	0.02	0.06	0.205	3.54	53.2
	99.7	99.72	99.5	98.9	93.7	39.8
	0	0	0	0	0	0
	0.152741	0.092771	0.19841	0.164879	0.734233	3.244022
1000	0.0016	0.003	0.007	0.027	0.507	18.5
	99.9	99.9	99.88	99.8	98.8	78.1
	0	0	0	0	0	0
	0.101809	0.061827	0.132061	0.10936	0.467193	1.123441
2000	0	0.002	0.002	0.011	0.204	7.6
	99.2	99.26	98.96	98.46	96.33	81.1
	0.7	0.72	1.0	1.46	3.2	9.94
	0.071101	0.043169	0.092463	0.076877	0.332584	0.75272
4000	0	0	0	0.006	0.0997	2.9
	94.9	95.03	93.2	90.5	81.46	58.4
	5.07	4.95	6.8	9.49	18.35	38.4
	0.048789	0.029591	0.06443	0.054912	0.258221	0.688295

Source: Cross-section information obtained from Cullen, D.E. et al., Tables and graphs of photon-interaction cross sections from 10 eV to 100 GeV derived from the LLNL evaluated-photon-data library (EPDL), Report UCRL-50400, Vol. 6, Rev. 4, Lawrence Livermore National Laboratory, Livermore, California, 1989.

^a Proportions in percent of total linear attenuation from top to bottom for the photoelectric, Compton, and pair production cross sections, and total linear attenuation in 1/cm. All values calculated using the mixture rule formula implemented in the LLNL-TPORT code. The percentages do not add up to 100 since we do not include the percentage of Rayleigh scattering.

the Lawrence Berkeley National Laboratory (LBNL) Advanced Light Source (ALS) using a synchrotron x-ray MicroCT system. Representative CT results for both energies and their ratio are shown in Figure 15.1; see Section 16.4.4 for more information on this application. This particular high explosive includes two dominant features: the higher-attenuating (light gray) web-like structure and the lower-attenuating (dark gray) cells that are called prill. There is also the occasional high-attenuating (white) anomaly shown at about 3 o'clock in Figure 15.1. Notice that all of the

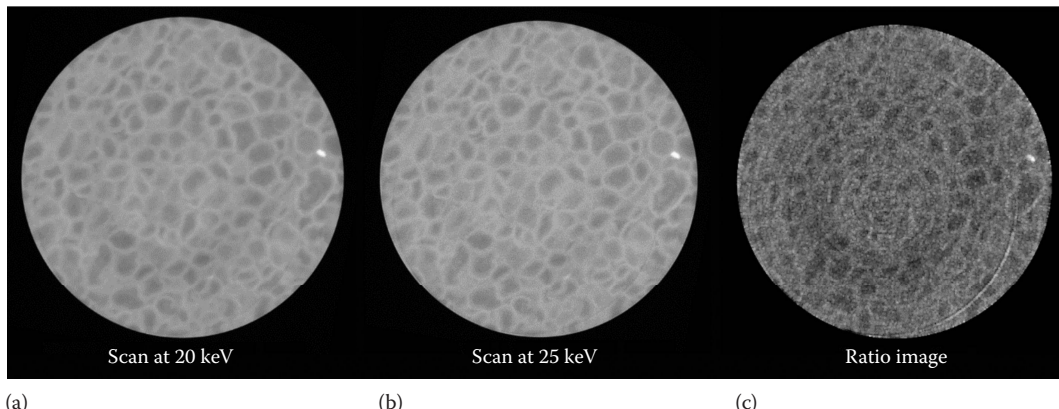


FIGURE 15.1 CT images of a 1.27 cm diameter high-explosive material acquired at the LBNL ALS at (a) 20 keV, (b) 25 keV, and (c) their ratio 20 keV/25 keV.

features are present in the ratio image—with the difference in ratio as compared to the single energy results indicating the web-like regions include a different material composition than prill among the webs. The higher-attenuating anomaly is likely a *chunk* of a higher-Z material, as the voxel-wise ratio between the two scans is a lot higher than the web or prill.

The above example showed that the differences in energy need not be large to distinguish changes in composition from changes in density for dual-energy CT inspections. However, access to a synchrotron is not always readily available. Also, this high-explosive inspection was performed with small samples (12.7 mm outer diameter cylinders). Objects packed in bags are often larger; the bags that the items are packed in are certainly larger, so the field of view (FOV) will of necessity be larger and the energy used for inspection higher. In addition, the overall inspection needs to be timely. One of the limitations for this type of dual-energy inspection is front and center: you have to choose energies that penetrate the object/assembly at both energies or the entire inspection is compromised. At the same time, if you go too high in energy, you lose the ability to distinguish low-Z materials of the same density, which defeats the goals of the inspection. Another way to state this is that the problem you have with dual-energy scanning is you have to pick both energies carefully or the dual-energy inspection could be useless, e.g., if the low energy is so low as to not penetrate the part, then you will not be able to do dual energy.

Until portable synchrotrons are available, x-ray tube/machine sources are the best alternative. Their emitted irradiance is a spectrum and not a single energy level, which impacts the inspection sensitivity further. Filtering the beam, that is, placing some slab of material close to the x-ray source, can considerably restrict the energy delivered to the object, from the low end, and this can increase the difference in energy for two spectra. A number of specialized inspection techniques have been developed with different filter combinations to take advantage of certain characteristic lines in various types of x-ray sources with different anodes (Ross filtering is one example) (Kirkpatrick 1939; Bol 1967). However, for baggage inspection, DR or CT, high throughput is a requirement, which can disqualify a number of filtering schemes. In most security applications, a sandwich detector is employed instead of different endpoint voltages and source filters.

Combining data from two filtered spectra can result in good sensitivity to changes in total x-ray attenuation. Consider two spectra from a tungsten-anode x-ray source, one using 90 kV filtered with 2 mm of aluminum, and the second using 140 kV filtered with 1 mm of copper. The spectra were estimated using SpekCalc (Poludniowski et al. 2009) and are shown in Figure 15.2. As discussed earlier and as can be surmised from the plots, the average energy for these two spectra is substantially different from their maximum energy, with the average energy for the 90 kV potential spectrum at 43.9 keV, and the average energy for the 140 kV potential spectrum at 81.3 keV. Assuming

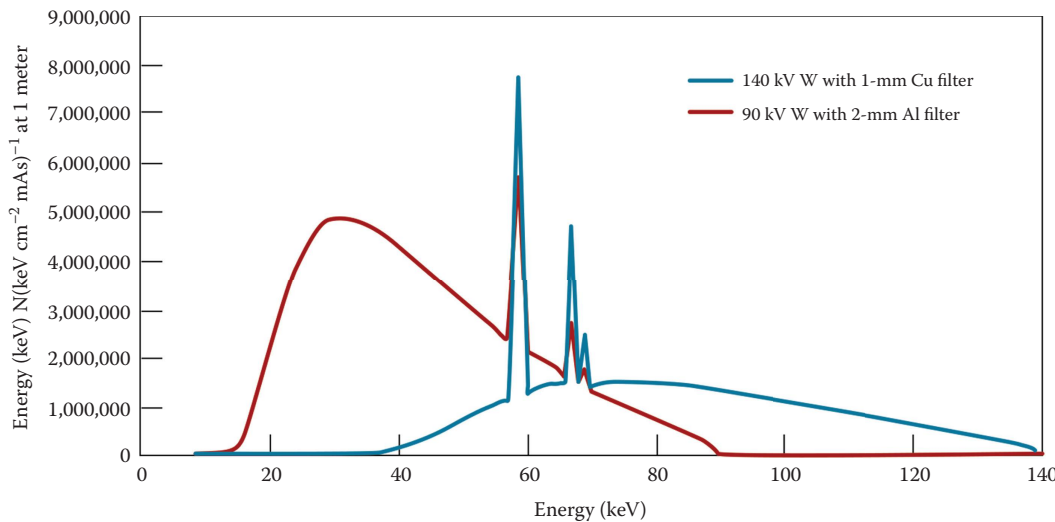


FIGURE 15.2 SpekCalc results for two different x-ray spectra. One spectrum (red) is the result of a tungsten anode source with 90 kV potential filtered with 2 mm of aluminum. The other spectrum (blue) is from a tungsten anode source with 140 kV potential filtered by 1 mm of copper.

a detector with perfect efficiency (all of the photons that make it through the material are counted), the polyenergetic total attenuation 90 kV/140 kV ratios for carbon, Teflon, and magnesium are 1.37, 1.94, and 3.29, respectively. These values are different from the single-energy 44 keV/81 keV total attenuation ratio values of 1.22, 1.45, and 2.0 for carbon, Teflon, and magnesium, respectively. The polyenergetic compared to the monoenergetic spectra include more low-energy irradiance, where the difference in photoelectric absorption between materials is greatest. Now, it is not clear that if you had the advantage of single-energy radiation, you would pick 44 and 81 keV as the two candidate single energies for the objects you are inspecting; however, it is true that the filtered polyenergetic spectra can include more sensitivity than particular combinations of single-energy spectra.

It is important to point out that the polyenergetic spectra are nonlinear. In the 20–200 keV energy range, the attenuation mechanisms are principally photoelectric and Compton (incoherent) scattering. A number of approaches have been developed to account for the nonlinear properties of the x-ray spectrum (Ying et al. 2006; Azevedo et al. 2016). In these approaches, a model of the x-ray spectrum is explicitly included in the processing of the input data in combination with some parameterization of the distribution of attenuation into photoelectric and Compton. From this point, nonlinear fitting techniques can be *trained* to solve for the relative proportions of photoelectric and Compton scattering. The processing is often adjusted to a particular scanner and for a battery of sample materials covering the range of atomic number and density. In the paper of Azevedo et al. (2016), they take this one step further and convert to electron density, ρ_e , and a new effective atomic number based on the x-ray cross section called Z_e .

Using two somewhat different spectra, Table 15.2 contains results from one implementation of these techniques on an LLNL in-house developed CT scanner (Smith et al. 2009) for a selection of relatively low-Z (Zs from 6 to 20) materials. In this case, the two spectra were chosen to obtain robust attenuation through the selected ~12.7 mm outer diameter objects using both spectra, and scanning did not include a strict time requirement (CT data sets could be acquired in an hour). From Table 15.2, A_c represents a measure of the Compton attenuation, and A_p a measure of the photoelectric component (these are in units internal to the algorithm). The results in Table 15.2 show how good this technique can be at measuring the atomic number or Z-values of materials in this case under well-controlled conditions in a lab.

TABLE 15.2
**Measurements of Z-Value from an R&D CT Scanner Using
 100 and 160 kV Potential Spectra**

	A_c	A_p	Z-Estimated	Z-Value
Ethanol	0.134	1240.0	6.61	6.53
Graphite	0.234	1600.0	6.11	6.0
Water	0.163	2380.0	7.53	7.54
Delrin	0.224	2724.3	7.16	7.11
Teflon	0.309	6862.0	8.45	8.5
Magnesium	0.2708	18224.3	11.53	11.0
Aluminum	0.412	45800.0	13.16	13.0

The reliance on nonlinear fitting techniques has advantages and consequences. First, the calculation will adjust to small changes in the output and can be trained with the assistance of some reference measurements, say the transmission measurements through a slab of a pure material, to produce robust calculations from scanner operation. Sometimes there are unintentional consequences, for instance, a range of materials for which you do not do well (Ying et al. 2006; Azevedo et al. 2016). Further, it has happened in some applications that improving the accuracy in one material range is at the cost of another material range.

These low-energy techniques, which identify materials according to the amount of photoelectric attenuation in the material, are the substance of materials-based contraband detection in all CT-based and DR-based baggage scanners at airports. The added item to the approach illustrated here is that separating out the photoelectric absorption from Compton scattering provides a way to measure density independent of material composition. Consequently, you have a means for identifying low-Z, high-density materials with considerable accuracy, which is one of the central goals for high-explosive detection and explosive detection in luggage. Examples of such systems are given in Chapter 16.

Notice that all of the aspects of the system are relevant here: the choice of energy spectrum and beam filtration, the methods for accounting for spectrum variations, the means for tracking system stability, the type of collimation used, the type of detector used (the stopping power), the number of views and/or angles acquired to make the measurement, and the expected speed/resolution/contrast for scans from each energy spectrum. For other dual energy efforts, see Engler et al. (1989), Haghghi et al. (2011), Heismann et al. (2003), Iovea et al. (2007), Park and Kin (2011), Semerci and Miller (2012), Szczykutowicz et al. (2011), and Braz et al. (2000).

15.3.1.2 High-Energy Dual-Energy Techniques

As mentioned above, an additional contraband inspection method has been developed for MeV energies. Table 15.1 shows the emergence of pair production as an important component of the total attenuation for high-Z materials. Referring back to Table 15.1, notice the change in the proportion of attenuation due to pair production that arises for steel and tungsten. The empirical result of this physical phenomenon is that for high-Z materials, inspected with MeV energies, more energy does not necessarily result in higher transmission. Figure 15.3 includes plots of transmission for energies ranging from 20 to 10,000 keV for slabs of various materials. Notice that the transmission for lead reaches a plateau at 3.5 MeV. The effect that the next increment in energy does not result in an increase in transmission for this material does not occur for steel and Inconel until 7–8 MeV.

The distinctiveness of the pair production at energies greater than 1.022 MeV for high-Z materials can be formulated into a detection scheme for finding particularly sensitive materials especially nuclear materials and shielding materials such as uranium and plutonium, and lead and tungsten, respectively, in large (12.2 m long, 2.44 m wide, and 2.6 m high) cargo containers. To the extent that a particular assembly includes substantial amounts of high-Z material, the change in transmission with increasing

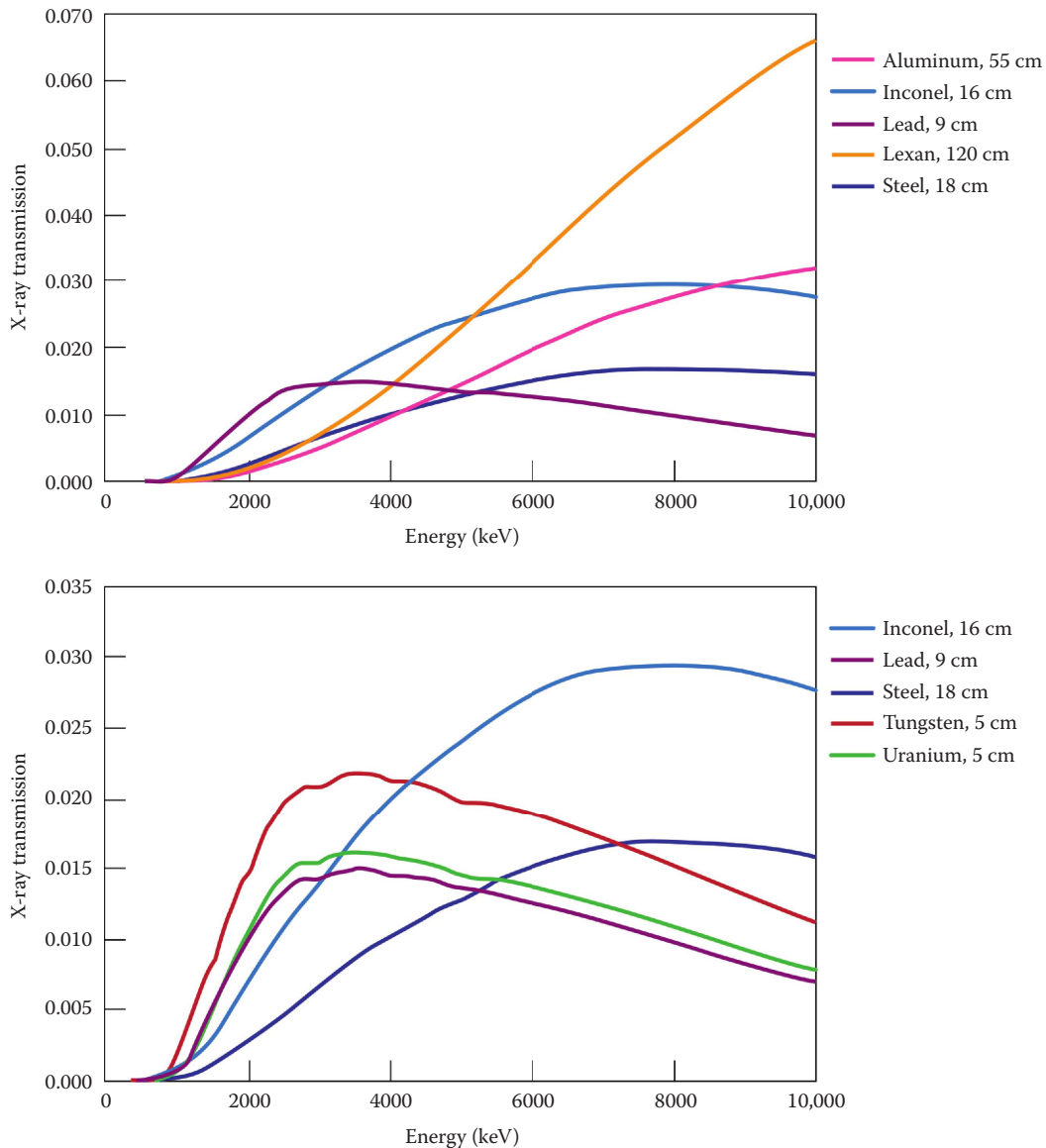


FIGURE 15.3 Plots of x-ray transmission as a function of an x-ray energy. Source data were calculated using LLNL-TPORT and made use of the Cullen et al. x-ray tables. (From Cullen, D.E. et al., Tables and graphs of photon-interaction cross sections from 10 eV to 100 GeV derived from the LLNL evaluated-photon-data library [EPDL], Report UCRL-50400, Vol. 6, Rev. 4, Lawrence Livermore National Laboratory, Livermore, California, 1989.)

photon energy is less. Consider the following experiment to study a complex assembly using 5 and 9 MV potential linac spectra. A description of the assembly is given in Figure 15.4. This assembly was also used in the comparisons between 9 and 16 MV linac scanning as discussed in Section 16.4.8. We acquired two sets of DRs of this object at 5 and 9 MV, one set of 5 and 9 with and without a lead cylinder in the assembly.

Plots of 1D profiles or line-outs from a 9/5 MV transmission ratio image (transmission at 9 MV potential divided by transmission at 5 MV potential) are given in Figure 15.5. Notice the decrease in the 9/5 MV transmission ratio values when the lead cylinder is present. More importantly, the

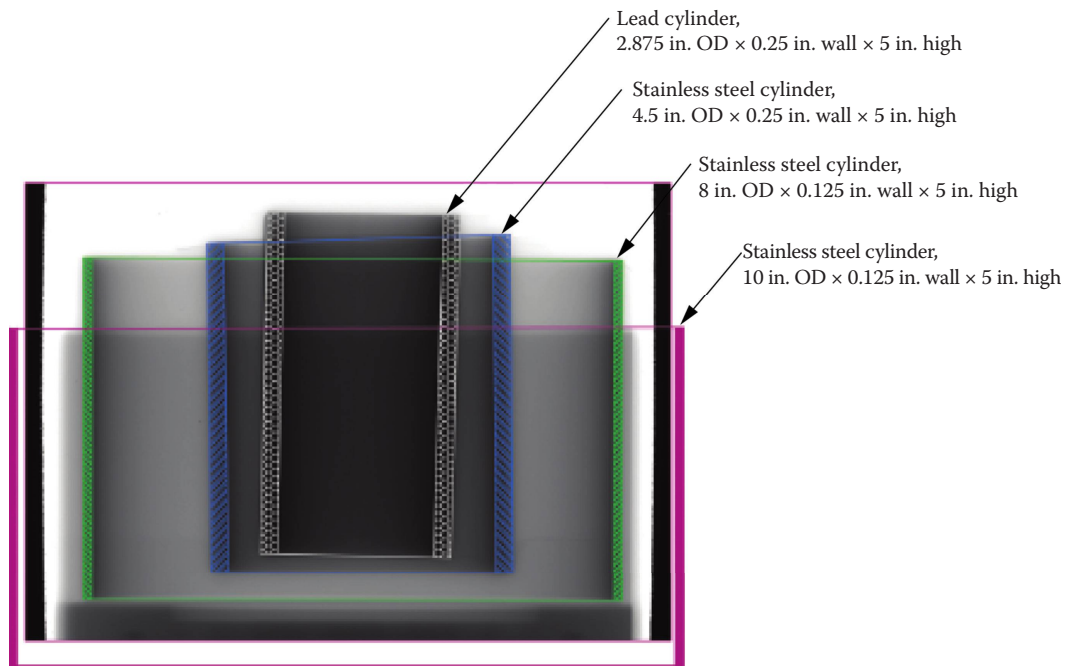


FIGURE 15.4 Annotated drawing of a composite assembly used to evaluate high-Z detection capability using 5 and 9 MV potential linac spectra.

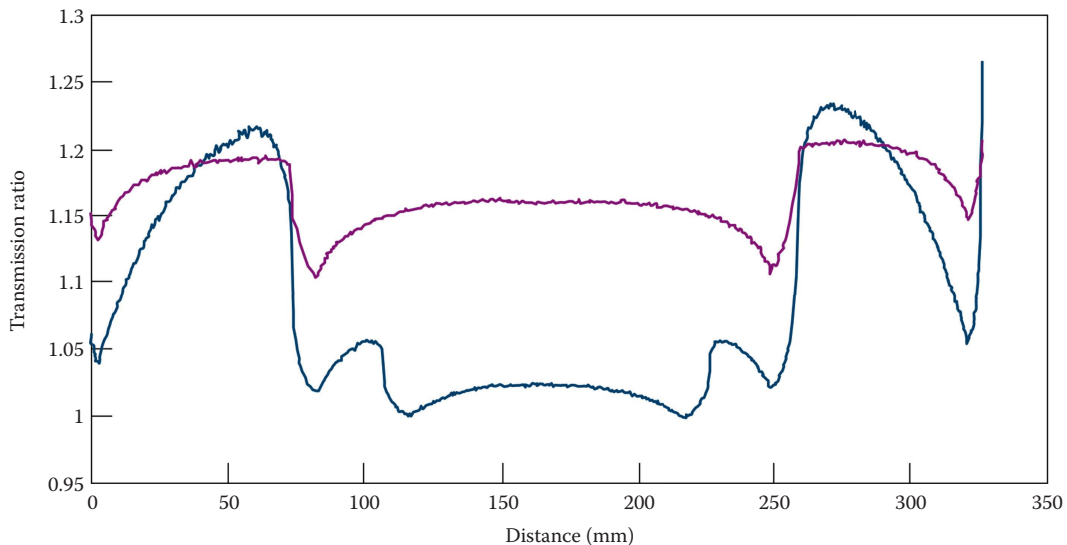


FIGURE 15.5 Plot of x-ray transmission ratios (9/5 MV) for the same locations in the high-Z composite assembly shown in Figure 15.4; with (dark blue line) and without (magenta line) the lead cylinder.

presence of the lead cylinder results in a great deal more variation in the transmission ratio for the 1D profile across the multiple materials in the assembly, and considerably lower differences in transmission in the regions with the lead present.

A word of caution here: in this assembly, the introduction of a lead ring is a relatively large change in the overall amount of attenuation for this assembly. On the one hand, this may not be

realistic for some concealments of high-Z material in large cluttered cargo loads. Alternatively, this spectrum at 5 MV may be too low, as transport of high-Z, radioactive materials usually includes substantial shielding and that usually means substantial amounts of steel, tungsten, and/or lead (or else the radioactive material whether special nuclear materials [SNMs] or radiological dispersal devices [RDDs] may be detected by passive radiation detection sensors called radiation portal monitors [RPMs]). The overall concealment package will likely be quite heavy and require the smaller type of container, and the 5–9 MV radiographic data will show that there is a lot of high-Z stuff in the cargo.

Alternatively, the 5–9 MV inspection technique clearly identifies low-Z materials. Referring back to [Table 15.1](#) again, notice the relatively small proportion of pair production for carbon, Lucite, Teflon, and magnesium even up to 4 MeV. The measured increase in transmission for 9 MV spectra as opposed to 5 MV spectra will enable the operator to clear this cargo load as low-Z with confidence. As shown in the ROC curve discussion in Chapter 14, this inspection capability can be as important as finding contraband (e.g., currency, drugs, and/or guns) or SNMs and RDDs.

15.3.1.3 Summary of Dual-Energy Measurements

In summary, inspection systems employing multiple energies enable the possibility of identifying the types of materials constituting the total attenuation measured in an object. The additional discriminating capability from the use of multiple energies can be applied for both DR and CT. At low energies, <300 keV, the focus is on measuring the relative amount of photoelectric and Compton attenuation and sorting organic from inorganic, such as explosives from metals. At high energies, >1 MeV, the goal is to measure pair production to identify high-Z, $Z \geq 72$, i.e., materials or regions in a cargo where the transmission does not increase proportionately with energy. Note that for $Z \geq 72$, pair production is the most dominant attenuation at ~ 5 MeV.

For both low and high dual-energy methods, the cost of this additional detection capability is in scanner complexity. First, if either of the two energies does not penetrate the object, the dual-energy method will fail. This gets more difficult when you are trying to get a measurement at a lower energy to access more sensitivity. Alternatively, if the difference in energy is small, the ability to discriminate may be compromised, bounded by the noise for each of the measurements taken together. On the scanner hardware side, for example, you need at least two detectors (more hardware and more maintenance) and/or you have to take twice the number of measurements, i.e., dual energy usually takes more time.

15.4 ACTIVE AND PASSIVE (EMISSION) CT

In the 1990s, there was a need to clean up over 1 million 55-gallon drums of transuranic and low-level waste that were at 50 sites throughout the United States. Sites included Hanford, Idaho National Engineering Laboratory, Nevada Test Site, and LLNL (GAONUCWASTE 1990). Various state and federal regulations required that the amount of radioactivity in each waste barrel be determined in order to properly dispose of the barrel. Methods existed that could nondestructively radioactively assay waste barrels such as segmented gamma scanning (SGS) developed at LANL. In SGS, the drum is rotated and scanned segment by segment along its height (Parker 1991). A two-pass measurement—one for transmission and one for emission—results in two spectra for each segment that was used to estimate the radioactivity in the barrel nondestructively. Unfortunately, SGS resulted in an inaccurate determination of the radioactivity within a 55-gallon waste drum.

In the late 1980s, we considered developing a CT-based technique to overcome SGS's main limitation, i.e., the assumption that the contents of the waste and its radioactivity distribution were homogeneous. Our method was to use both transmission and single-photon emission CT (SPECT), which is shown schematically in [Figure 15.6](#). Transmission CT (TCT) is used to measure the highly attenuating homogeneous or heterogeneous waste drum content (matrix). SPECT is used to determine the radioactive isotopes present as well as their location within the waste drum. SPECT was a well-known

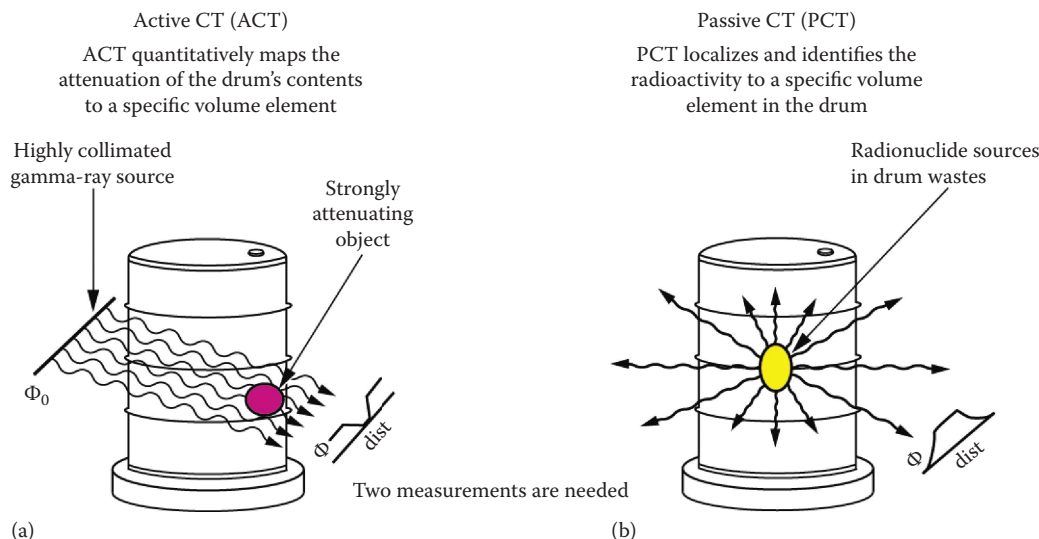


FIGURE 15.6 Schematic diagram showing the (a) active and (b) passive CT concepts. Active CT quantitatively maps the attenuation of the container contents to a specific volume element (voxel). Passive CT localizes and identifies the radioactivity to a specific voxel in the container.

medical technique but was not used for industrial applications. To account for the attenuation of the radioactive isotopic data acquired in SPECT, we combined TCT and SPECT to measure the heterogeneity and yield more accurate actinide activity. At LLNL, we decided to apply this technology to the waste drum nondestructive radioactive assay problem (Martz et al. 1990). Our method is a decidedly quantitative technique, measuring quantities of materials and their locations. Alternatively, medical CT and SPECT were relative measurements (not quantitative). To distinguish our methods from the medical methods, we decided to name this type of scanning active and passive CT or A&PCT.

We started out to prove the A&PCT method by using a 1.4 L juice can as a small-scale 55-gallon drum. We loaded the juice can first with simple square slabs of known materials, such as aluminum, Lucite, and copper and two passive radioactive sources: $\sim 95 \mu\text{Ci}^{133}\text{Ba}$ and $\sim 74 \mu\text{Ci}^{228}\text{Th}$ (Martz et al. 1992). The slabs are simple-shaped attenuators, and the ^{133}Ba and ^{228}Th are of known activity. This enabled us to determine how well we can determine the x-ray attenuation (linear attenuation coefficients) of the slabs and the ^{133}Ba and ^{228}Th radioactivity. The results were promising enough to go on to more complex attenuators in the juice can as shown in Figure 15.7. This was useful in developing our method as well as getting internal research funds for a full-scale 55-gallon drum system called IMPACT (Isotope Measurements by Passive and Active Computed Tomography). The IMPACT waste barrel nondestructive assay system is shown in Figure 15.8. Representative results for IMPACT are shown in Figure 15.9. Eventually this technology was transferred to BioImaging Research (now Varian) and was located in a mobile tractor trailer (Figure 15.10) (Bernardi and Martz 1995; Bernardi 1997; Camp et al. 2002). It is instructional to mention that the waste drum nondestructive assay CT objective was to optimize the spatial resolution required to assay the drum vs. data acquisition time. Poorer spatial resolution, i.e., the larger the voxel, results in faster data acquisition times. As shown in Figure 15.9, the resultant spatial resolution was low, $50 \text{ mm} \times 50 \text{ mm} \times 50 \text{ mm}$. However, the spatial resolution was sufficient to meet the WIPP transuranic waste requirements for accuracy, precision, and throughput. Most applications require high spatial resolution, while for the A&PCT case, it was the opposite. The reason for this is that the end result is a single number, effective Pu, not an image for defect, etc. detection. To speed up data acquisition, a multiple HPGe detector system was developed, shown in Figure 15.11 (Roberson et al. 1997). Other CT radioactive waste barrel assays include efforts by Estep et al. (1994), Robert-Coutant et al. (1999), Mason et al. (2003), Savidou et al. (2007),

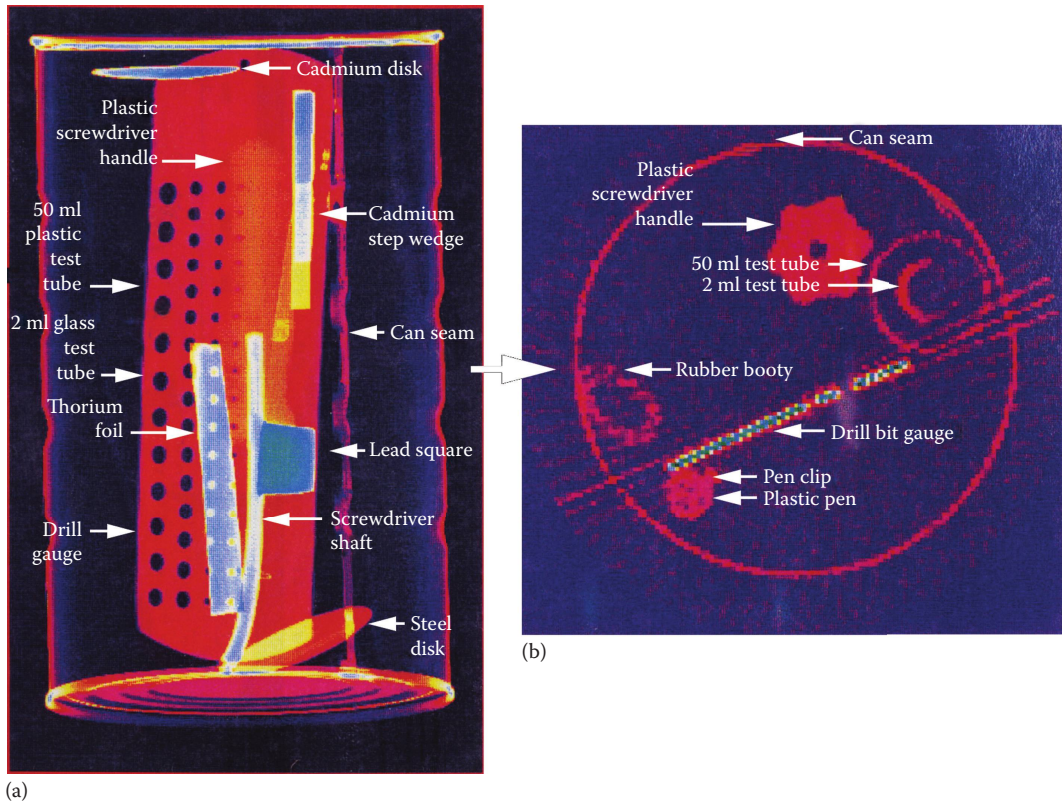


FIGURE 15.7 (a) Digital radiograph of a juice can with various items inside as labeled. (b) TCT cross-sectional image of the juice can contents at the location of the middle arrow.

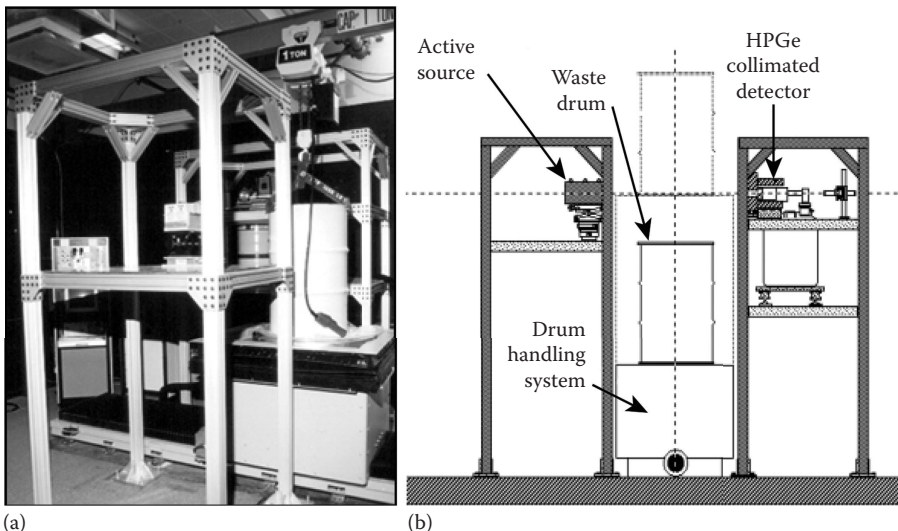


FIGURE 15.8 A (a) photograph and (b) a schematic of one of the full-scale 55-gallon drum A&PCT systems built at LLNL. It was called IMPACT (Isotopic Measurements by Active and Passive CT). It consisted of one >90% HPGe detector, an ~3 mCi ^{166m}Ho radioactive source, and a drum manipulator that can handle ≤ 110 gallons over pack or 1 m o.d. and 1.5 m high and up to 500 kg.

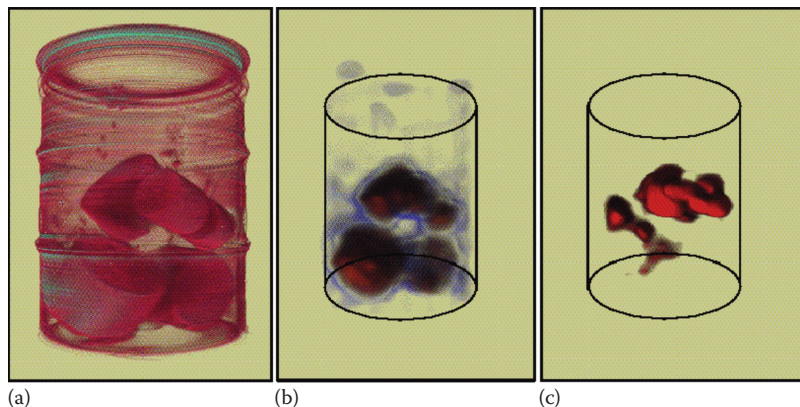


FIGURE 15.9 (a) 3D rendering from a high-spatial resolution TCT system data set of a 55-gallon waste drum. (b) 3D rendering from the low-spatial resolution ACT system data set of the same 55-gallon waste drum. (c) 3D rendering from the low-spatial resolution PCT system data set of the same 55-gallon waste drum. From left to right are x-ray, gamma-, and gamma-ray images, respectively.

and Roy et al. (2015). Another nondestructive assay technique is imaging of the γ -ray emissions from irradiated fuel (Caruso 2007; Caruso et al. 2008).

15.5 TOMOSYNTHESIS—DEPTH INFORMATION WITHOUT CT

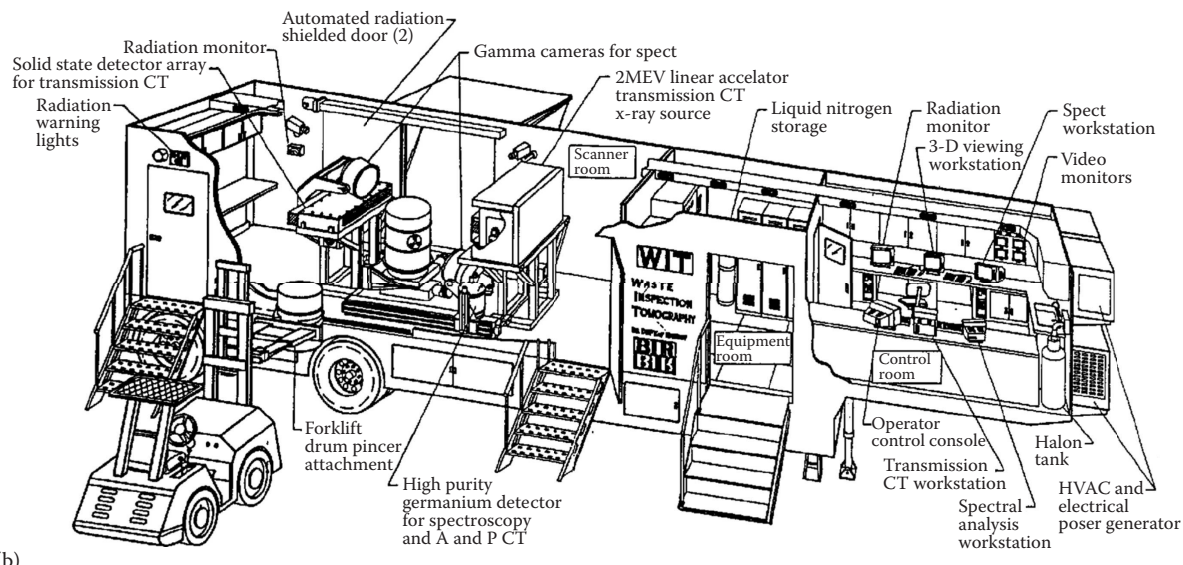
Tomosynthesis scanning techniques enable the 3D imaging of features in objects and assemblies (Gondrom and Schröpfer 1999). Tomosynthesis was developed by Kaufman in 1936 and des Plantes in 1938 well before CT became practical in the early 1970s, about the time when computers became available. Tomosynthesis data acquisition is less restrictive in the number and angular range of views required as compared to CT. Typically, CT entails anywhere from 180° views for parallel-beam geometry or 180° plus two fan-angle views for fan-beam geometry data acquisition. Sometimes even 360° angular views are acquired for CT. The scanning protocol for tomosynthesis requires fewer angular views around the object and includes a variety of different movements of source–object–detector that usually enable the imaging of a particular plane in the object volume, or some series of *planes* that is of particular interest to the inspection. Tomosynthesis is an imaging technique especially suited for flat samples and is a generalization of CT that uses a rotation axis tilted by less than 90° with respect to the incident beam. Thus, tomosynthesis avoids using projections from angles closest to the sample surface and is useful for planar objects. It is also referred to as laminography. Laminography is an image-forming method that yields images of object slices by a simple linear translation of the object relative to the source–detector system. In this book, we will use tomosynthesis for both methods.

Tomosynthesis began as a specialized film (analog) technique, where an x-ray source and film are moved with respect to a pivot point in such a way that the features of a certain plane are progressively *summed* into the film, while features in other planes fade (are blurred) into the background of the image. Once digital detectors became available, digital tomosynthesis became popular. With digital detectors, this technique can be unpacked as a series of acquisitions at different source–detector angles without moving the object or without moving the source and the detector and just moving the object; the results averaged into a final image with some registration informed by recorded positions from motion control hardware.

We can employ a simulation of the *slab* object that is described in Section 14.3 that is used to illustrate measures of radiographic contrast to illustrate one instance of laminography/tomosynthesis sometimes also referred to as planar tomography. A schematic of one of the operations involved in estimating a planar tomographic image at a certain depth by tomosynthesis is given in Figure 15.12.



(a)



(b)

FIGURE 15.10 (a) Photograph of BIR's mobile waste inspection trailer and (b) schematic of the equipment layout.



FIGURE 15.11 Two different photographic views of the six high-purity Ge (HPGe) ($>65\text{--}70\%$) detector system housed in a sea/land container (L 20', W 8', H 8'). The drum manipulator can handle ≤ 55 gallons overpack or 2'o.d., H 3' packages up to 800 lb.

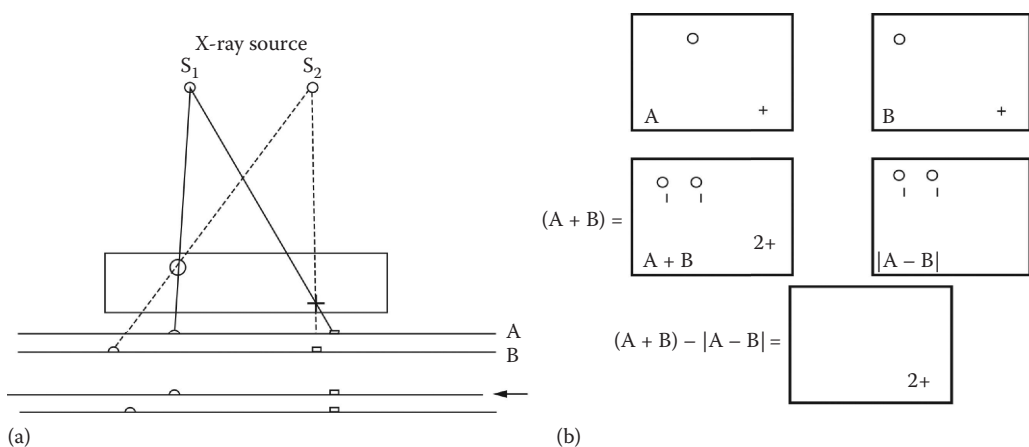


FIGURE 15.12 Diagram of the (a) data acquisition and (b) resultant calculations of summed planes for tomosynthesis inspection.

The simulated slab object presented in Section 14.3 has been altered to include different sized inclusions at three depths and is shown in Figures 15.13 and 15.14. Figure 15.13 is a simulated attenuation multiplied by path length radiograph of the modified slab object and Figure 15.14 is a simulated cross-sectional image of the slab object from the angle that shows the depths of the inclusions (white). Notice the difference in depth for each of the inclusions in the slab.

By changing the position of the x-ray source, as depicted in [Figure 15.12](#), from S_1 to S_2 , three synthetic radiographs were acquired; in each radiograph, a ray from the x-ray source perpendicular to the detector passes through one of the inclusions, and the other inclusions are at a much greater angle, and so project to a different location at the detector. Figure 15.15 includes two planar tomosynthesis images for two of the planes that contain the inclusions, calculated from the acquired radiographs. In each case, only the inclusions at that plane are included in that plane within the slab.

Of course, this example is exceptionally clean and contains none of the artifacts that may be a part of any real acquisition and calculation. Also excluded from this example is scatter and streak artifacts that will result from any large mismatch between the energy used and the materials and path lengths in an actual object and data acquisition. Regardless, the point is you can get depth information from a few radiographs using reasonably accurate positioning equipment.

Following the development in *ASNT Nondestructive Testing Handbook, Volume 4 Radiographic Testing*, Chapter 12 (Bossi et al. 2002), another way tomosynthesis can be characterized is by the size of the object-slice-plane imaged—smaller than radiography and larger than CT. [Figure 15.16](#) adapted from Bossi et al. (2002) illustrates the basis for this comparison of techniques.



FIGURE 15.13 Simulated attenuation (white is high attenuating and black is air) radiograph of a slab object.

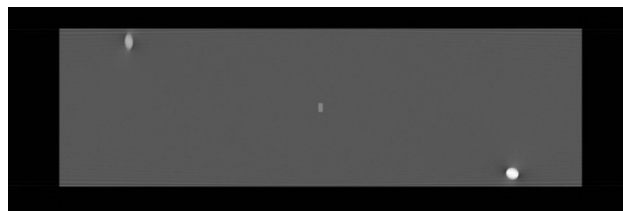


FIGURE 15.14 Cross-sectional slice of the simulated slab object with three inclusions (white) each at different depths in the uniform (gray) slab.



FIGURE 15.15 Two of the three calculated (summed images) tomosynthesis planes from an acquisition of three radiographs acquired at different angles appropriate to focus on the three specific planes that include the three inclusions within the slab.

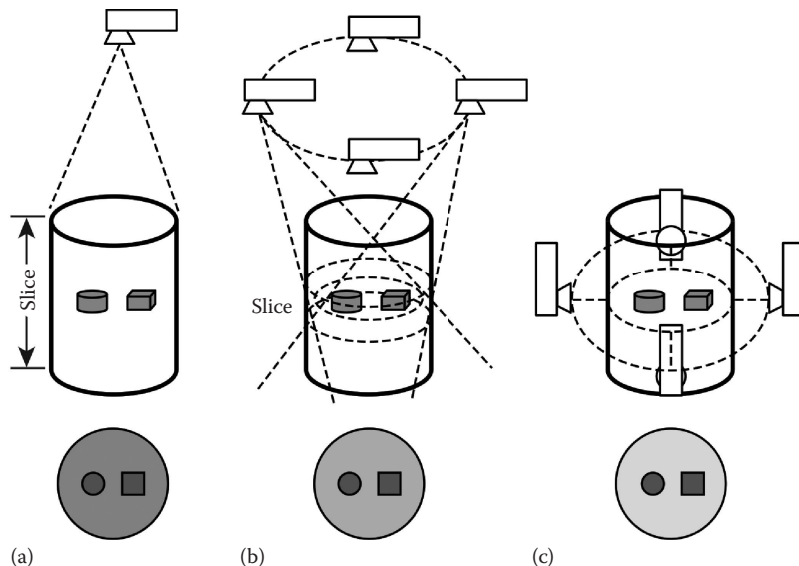


FIGURE 15.16 Comparison of (a) radiography, (b) tomosynthesis, and (c) CT data acquisition geometries.

From Figure 15.16a, radiography can be considered to include the whole part as the slice thickness. All the x-ray transmission interactions in the entire object are projected onto one plane. In the case of CT, as shown in Figure 15.16c, the slice thickness is defined by the source–collimator aperture and further determined by the scanner geometry. For tomosynthesis as shown schematically in Figure 15.16b, the slice thickness is determined by the angle of the data acquisition. The angles for acquisition in tomosynthesis carve out a slice thickness at the pivot points for the different views considered as a whole.

The number of different scanning regimes for tomosynthesis is large, and these techniques benefit from all the advances in computerized motion control and increased availability of faster computers with large amounts of local memory and disk space that make CT more tractable. As indicated in Figure 15.16, the two types of scanning (tomosynthesis and CT) have a lot in common and are in many ways on a continuum. The key questions are as follows: (1) How much 3D information do you need for the inspection? (2) Do the data in all three dimensions need to be equally precise? (3) Will good imaging of a few planes in 3D suffice? Example tomosynthesis applications are shown in Sections 16.4.10 and 16.4.11.

15.6 AUTOMATED DEFECT RECOGNITION

A substantial number of systems have been developed and deployed to perform automated defect recognition (sometimes referred to as computer-aided inspection or automated flaw detection) (Bossi et al. 2002). The principal feature for these types of applications is the full automation of the inspection for that particular defect or flaw. That is, the image is acquired and specialized software is applied to the acquired data in an automated way, with the analysis resulting in some particular determination of part integrity. At the very least, the computerized analysis of the image of the object/assembly is used to sort the population into groups: pass, fail, or no decision. Alternatively, the automated inspection results in a report detailing the number of flaws found, their location, and size.

The following is an example of an automated inspection applied to the detection of voids in titanium tube welds. The acquisition and processing method proceeds as follows. Four radiographs are acquired at different rotational angles for each tube (each image is processed into attenuation multiplied by path length). The inner edge of each tube is segmented out of the image, and the double-wall profile (without defects) is subtracted from the extracted center of each image. The results of this method to the inspection of titanium tube welds are given in [Figures 15.17](#) and [15.18](#).

In Figure 15.18, the image on the far right shows the result of the automated processing. In this processing, the objective is to subtract out the projected profile of metal with no voids. In this case, this profile is obtained by a low-order polynomial fit to each row of the radiograph. The image in the middle shows the result of subtracting the polynomial fit from the original image. The image on the right is obtained by applying a 2σ (2 standard deviations) threshold to the image, thereby isolating all pixels that are 2 standard deviations less than the mean value (represented by the fit). From here, a number of calculations can be performed: the number of void locations, the total area of the voids, the area of the largest void, etc. The importance of any one of these measurements for object *acceptability* or *failure* depends on the goals of the inspection and the functional requirements for the object.

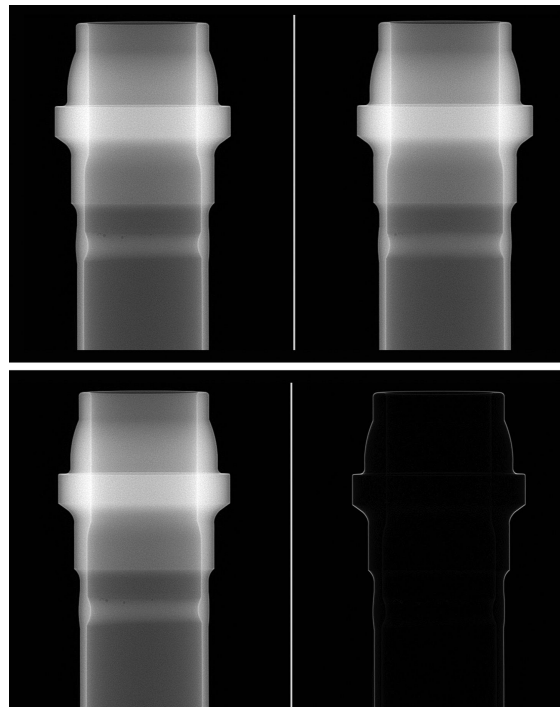


FIGURE 15.17 Digital radiographic views of a titanium tube with a weld. At top left is a 120° view, top right is a 60° view, and bottom left is a 0° view. At bottom right is a processed boundary image of the tube.

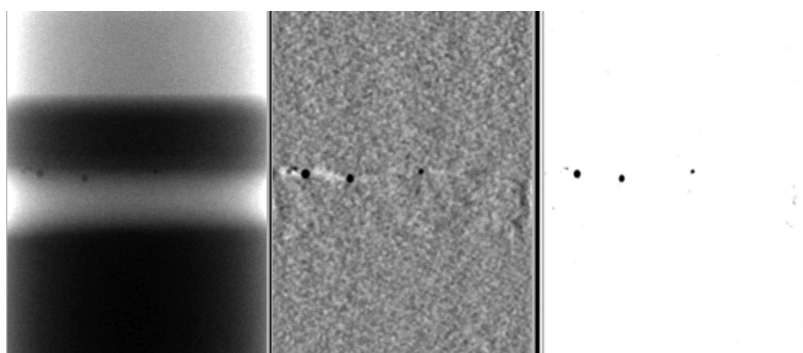


FIGURE 15.18 On the left is an extracted portion of the titanium tube weld radiograph. In the middle is the result of subtracting out a polynomial fit to the horizontal lines in the radiograph, and on the right is the result of applying a two-sigma (two standard deviations) fixed threshold result showing voids (black regions) inside the weld.

The design of x-ray-based automated defect recognition inspections can be divided into four different efforts. First, from an analysis of the functional requirements for the object, identify the properties of a critical flaw, its size, and the likely incidence in the population. Second, perform an analysis of this flaw in the object geometry to obtain a set of possible fielded x-ray techniques. Third, based on modeling and experimental data, develop a prototype inspection for each of the possible x-ray techniques. Fourth, perform a cost–benefit analysis for each of the fielded techniques against the costs for passing objects with this flaw into the field. Once these steps are in hand, it is now possible to proceed with the estimation of the receiver operator characteristics (ROC) curve for this inspection. For further details, see Section 14.6.

15.7 X-RAY FORWARD AND BACKSCATTER

In Chapter 5, on photon interactions with matter, a number of different scatter mechanisms were described, and as might be expected, most provide a basis for backscatter imaging. The four processes that form the basis for backscatter imaging include (1) coherent or Rayleigh scattering, (2) incoherent or Compton scattering, (3) photoelectric fluorescence, and (4) high-energy resonance fluorescence. Coherent scattering is a forward scattering method while Compton can be either forward or backscattered photons. While the latter two processes mentioned here are not listed in the fundamentals section as strictly scattering processes, each does involve photon–electron interactions, and they result in x-rays being emitted and thus are a measurable output for backscatter imaging. The common property of backscatter imaging techniques discussed here is that they are one-sided, i.e., the source and the detector are on the same side of the object. This can be a distinct advantage for inspections of large objects or objects with a high aspect ratio, where positioning anything on the other side is hard if not impossible; not to mention that penetrating some of the large objects with long path lengths changes the overall system complexity of the source, detector, and collimator.

As described in Chapter 5, coherent scattering involves no energy loss, so the wavelength of the scattered photon is known. Consequently, if the wavelength is on par with atomic dimensions, diffraction effects result from the scatter process. Material composition of thin films can be measured from the diffraction patterns, as crystalline materials will diffract in a way that is characteristic of that material. In addition, noncrystalline materials can be evaluated by analyzing the x-ray spectra arising from the coherent scatter, the composition being embedded in the small-angle scattering spectra. In addition, small changes in the small-angle scattering from materials provide information on the residual stresses in the material; this information can be particularly important in the evaluation of fabricated materials (Longo et al. 2009; Odén et al. 2009).

The limitations for coherent or Rayleigh scattering applications relate to the energy regime for this mechanism, which is significant in the 5–20 keV range. Consequently, inspections are generally restricted to prepared samples or thin films.

Another application of scattered x-rays is x-ray diffraction. X-ray diffraction imaging measures coherently (elastically) scattered x-rays to construct diffraction profiles of materials that can provide molecular signature information about the material. Until recently, the Rayleigh scattering process has largely been ignored as an imaging technique. One reason is that penetrating photon energies for Rayleigh scattering is confined to the forward direction of the x-rays. Here we discuss how x-ray diffraction can be used to improve the identification of explosives in luggage. Applications include inspection of checked passenger luggage at airports and cruise ships. The angular dispersive technique generally used in materials analysis (crystallography), with variation of the scatter angle θ and the use of a mono-energetic source, can be replaced by an energy dispersive method. In this case, the polychromatic bremsstrahlung spectrum of an x-ray tube serves as the source, and the scatter radiation is measured at a small fixed angle using an energy-resolving detector as shown in Figure 15.19 (Strecker 1998). The resulting scatter spectra provide information on the crystallographic structure of the scattering materials and objects within luggage.

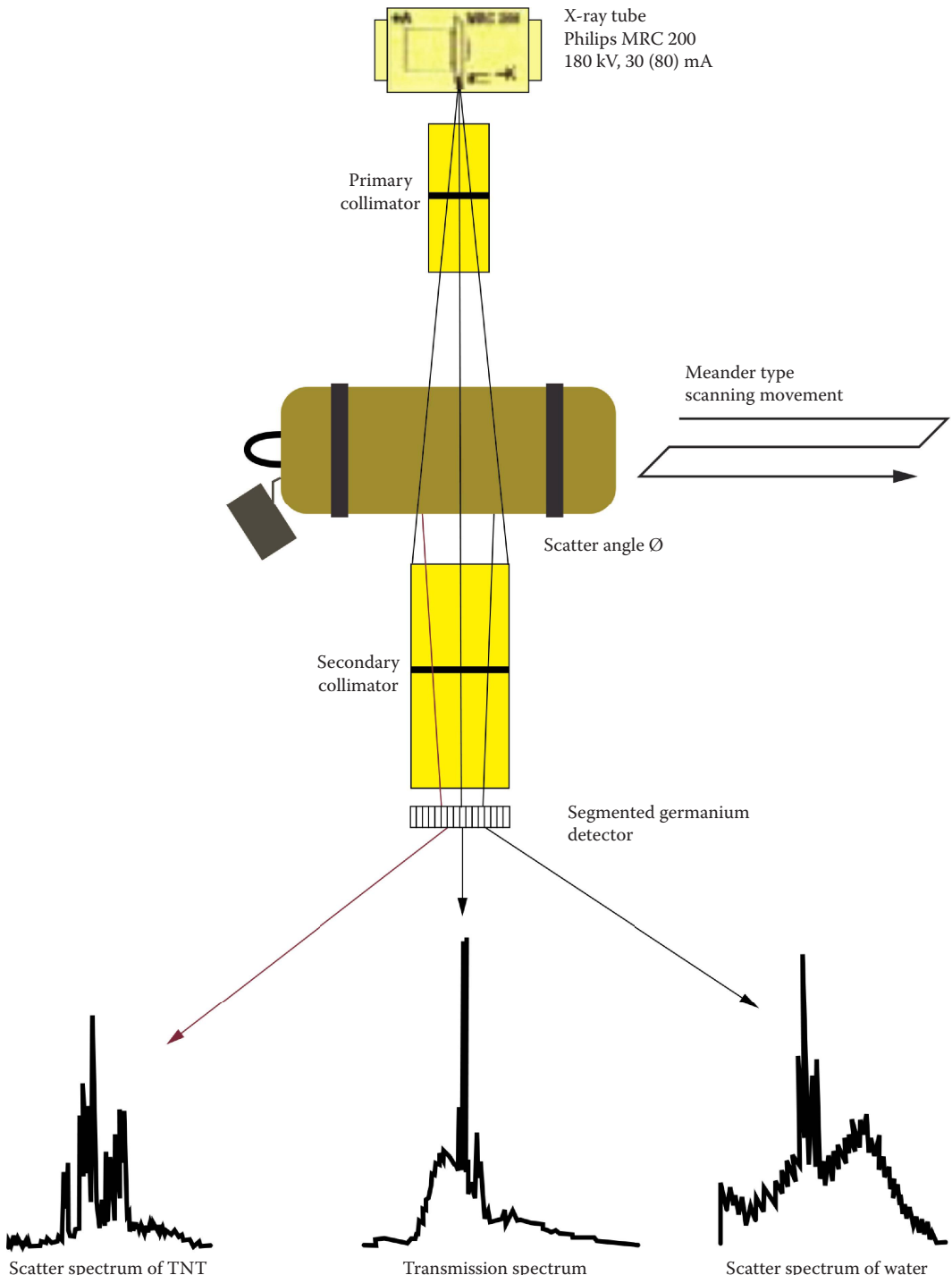


FIGURE 15.19 Schematic for the measuring geometry of a system for automatic detection of explosives in airline baggage. Scatter spectra are measured at a small angle \emptyset via an energy-resolving high-purity germanium detector.

There are major limitations in x-ray diffraction systems. First, there is a need to localize the coherent scatter to regions so that the signatures can be associated with specific objects inside luggage. Second, the resulting scattered signals from different volumes inside the suitcase undergo complex absorption and secondary scatter on the way to detectors, which must be compensated for. Third, the measured signals are relatively weak, as a fraction of scattered photons are spread over volumetric angles in a frequency-dependent manner, so that the signals collected by each detector are limited. Given these limitations, typically x-ray diffraction images are not displayed or used; often a high-spatial resolution (~1 mm) image of the bag is obtained by digital x-ray radiography. For applications to luggage screening, see Section 16.5.3.

The bulk of NDC materials applications considered here involve incoherent or Compton scatter. As shown in Chapter 5, Compton scattering results in a scattered signal for a distribution of energies at or less than the incident energy depending on the scatter angle. From Chapter 5, Equation 5.4,

$$E'_p = \frac{E_{p_0}}{1 + \alpha_p(1 - \cos \zeta)}, \quad (15.1)$$

where E'_p is the scattered photon energy in kiloelectron volts, and E_{p_0} is the incident photon energy in kiloelectron volts. The term α_p is the ratio of the incident photon energy to the rest mass energy of the electron (511 keV). The scattering angle is ζ . Also, following Chapter 5, the angular distribution of the Compton photons can be expressed as

$$\frac{d\mu_m}{d\Omega} = 2\pi G'' \left[\left(\frac{E'_p}{E_{p_0}} \right)^2 \left(\frac{E'_p}{E_{p_0}} + \frac{E_{p_0}}{E'_p} - \sin^2 \zeta \right) \right] \sin \zeta. \quad (15.2)$$

Detecting the backscattered signal requires that the scattered photons emerge from the object in the solid angle covered by the detector and penetrate the material chord length on the path from the scatter event to the detector. Designing Compton backscatter systems includes recognition of this round-trip property—the detected signal depends on both the depth at which the scatter event occurred and the surrounding materials in the path back to the detector. This can be seen in an expression developed in Chapter 14 of the ASNT NDE Handbook, Vol. 4 (Bossi et al. 2002); the expected amount of scatter detected at a particular location from a volume element of thickness l , with probability of Compton scatter σ , where y is the distance to the surface of the material with attenuation μ , can be represented as

$$\text{Scattering} = \Phi_0 (\mu^s l) \exp(-2\mu y), \quad (15.3)$$

where the “2” reflects the attenuation of the x-rays on the way in and the way out of the object and μ^s is the linear scattering coefficient. This is a key property when considering backscatter techniques for possible inspections, e.g., thick sections of a material can be effectively hidden from an x-ray backscatter inspection even though you measure a lot of signal.

A number of different sampling processes are in the fundamentals of backscatter imaging. First, you only generate scattered signal proportional to the Compton scattering cross section, a single component of the total attenuation, which depends both on the material and the source energy. For instance, from [Table 15.1](#) for energies around 60 keV, the Compton scattering component is low for steel (less than 12% of the total linear attenuation) and very low for tungsten (2.8%), but is the largest component of attenuation for Lucite and Teflon. Second, you will only detect those photons in the solid angle of the detector. The scattered irradiation is generated in three dimensions, but you will only collect the photons that exit the object and in the solid angle subtended by the detector. This can have distinct advantages, since multiple detectors pitched at an angle will see different

parts of the angular distribution of scatter—you can obtain some measure of the depth at which the scatter occurs (see application in the following paragraph). Alternatively, as energy increases, Compton scatter gets more forward-peaked, and there is proportionately less irradiance channeled into the detectors on the same side as the source of the x-rays. Third, if the detector is on the same side as the source, you are not measuring forward scatter, and all the scattered irradiation generated is at a lower energy than the source. The probability of penetration through the materials in the path back to the detector is less due to the lower energy; moreover, the detected signal will be less robust, and at some depths, or when next to certain materials, you will get no signal. Perhaps more interesting in this connection is the significance of the signal you do acquire, which does contain some depth information that may be made more precise with the aid of additional measurements.

An acquired image from a checkpoint baggage inspection system illustrates some of the properties of backscatter systems. The attenuation multiplied by path length radiographic image of a mock bag and the backscatter image of the same bag acquired at the same time is given in Figure 15.20. The mock bag is reasonably cluttered and includes a number of distinct objects with the combined digital radiograph and backscatter measurements revealing the identity of some of the objects and their relative position in the bag.

Consider the metal-rod handles (white bars in the left image of Figure 15.20) for the exercise weights (top of both images; a white disk in the left image and black in the right image). All of these items are highly attenuating, as indicated by the relatively high attenuation multiplied by path length value (white) in the radiograph. At the same time, since there is little (if any) transmission, there is little (if any) scatter, all of the radiation is stopped, and few scattered photons emerge from the metal, the values in the backscatter image are small (black) for the exercise weight.

Another factor here is the energy used, which is likely around 100 keV, so photoelectric absorption is high for metal parts, and Compton scatter is lower. Also, notice in the backscatter image that the darker values of only one of the metal handles are observed; this shows that this one handle is on the side of the backscatter detector, and the other handle is behind the shoes, which stop all of the signals than can make the round-trip back to the detector before the metal rod is encountered within the thickness of the bag. Next, notice the shoe soles, which are prominent in the backscatter image and harder to distinguish in the radiograph. Again, this indicates that the shoe soles are on the side of the bag closest to the backscatter detector.

Also notice the robust signal from the shoe soles; this is due to the lower-atomic number composition of the sole of the shoe accounting for the significant Compton scatter attenuation component. The scattered photons are sufficiently energetic and the sole is low attenuating, such that the photons emerge from the shoe sole, hence the detail in the backscatter image. Lastly, notice one of the liquid

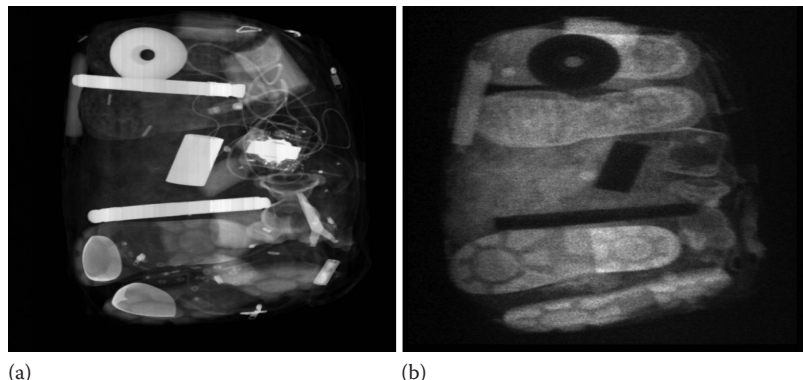


FIGURE 15.20 (a) Digital radiograph converted to attenuation times path length, μl , (black is no attenuation and white is high attenuation) of a bag. (b) An x-ray backscatter image (black is no backscatter and white is large backscatter) from one side of the same bag.

bottles (center-right in the radiographic image) and the tube of gel (upper left in the radiographic and backscatter image). Using the same thought process, the tube is on the side closest to the detector (and in front of one of the metal handles), while the liquid bottle is on the other side of the bag and is obscured by the other objects in the bag volume.

A number of conclusions follow from the results of this application. The backscatter signal from an object contains some information on material composition. The metal parts include a distinctive signature at this energy. Second, there is a critical attenuation limit in backscatter imaging. This has two impacts: (1) Opaque objects quench the backscatter signal. (2) For object layers that include a significant scatter component, there is a critical inspection depth where the materials at that depth or larger are hidden from the backscatter inspection (the liquid bottle in this case). Alternatively, if the contraband you are interested in includes a scatter component and is close to the detector, the inspection signal is robust. Third, for objects that are in the *material-depth* window for that backscatter signal at that incident energy, ample detail is available. In the above example, the pattern of the shoe sole can be measured. If some additional measurements can be supplied, the thickness of the shoe sole could be estimated with some accuracy. For more bag backscatter results, see Section 16.5.1. Companies have also developed high-potential 450 kV x-ray backscatter for cars, vans, and cargo inspection (Callerame 2006; Adams et al. 2007).

The next application is detection of threats and contraband concealed on people under their clothes. Examples of people x-ray backscatter systems are shown in Figure 15.21. The incident radiation is tuned to effectively remove the apparel, allowing the inspector to observe the presence of concealed objects under the clothes or in body cavities. Figure 15.22 includes examples of backscatter systems and backscatter images of test subjects with concealed items underneath clothing.

As seen from these images and numerous tests, backscatter systems can detect concealed metal items or, for that matter, items that are substantially more (black such as the gun) or less attenuating (lighter than flesh such as the rectangular plastic block on the persons belly in the image on the left image on the left in Figure 15.21) than fat (0.9 g/cm^3), muscle (1.06 g/cm^3), and bone (1.85 g/cm^3) (the comparison to bone is muted by the covering layer of fat/muscle). It may seem contradictory to be more or less attenuating; but it is the difference or contrast that one is looking for. As can be seen from the backscatter images of human subjects, and similar to the results of the scan of the baggage, metal and even high-density composites can be easily detected from the difference in backscatter signal relative to the surrounding materials. For this type of inspection, if the shape of the contraband is anomalous in some way, detection can be substantial. This is true even if the material is similar in density and composition to human tissue, i.e., the shape of the concealed item is not smooth, the item



FIGURE 15.21 Photographs of three x-ray backscatter systems used to screen people for items concealed under their clothes.

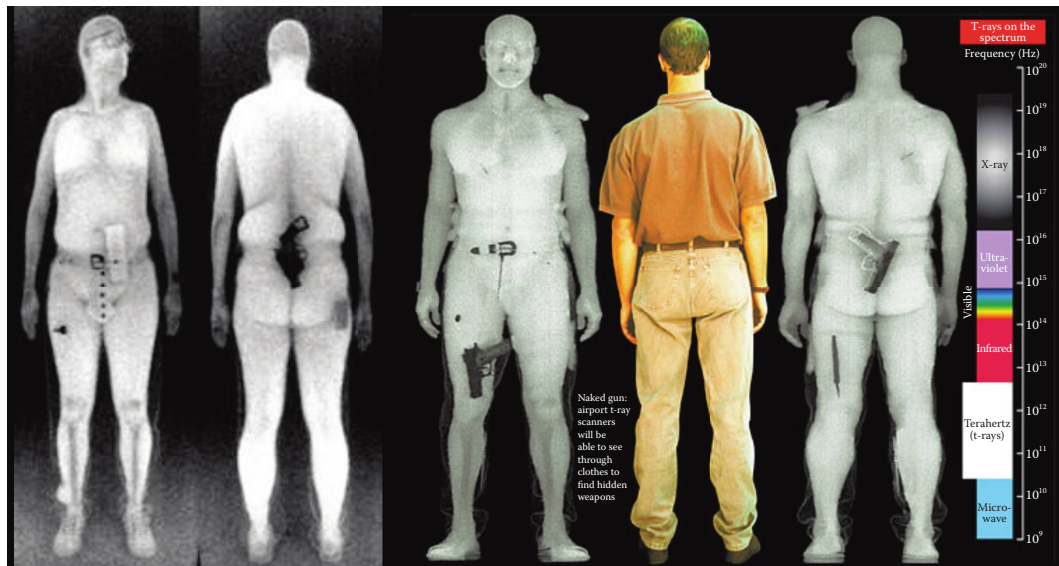


FIGURE 15.22 X-ray backscatter images of subjects with concealed items. (From Vijayalakshmi, P., Sumathi, M., *IOSR Journal of Computer Engineering (IOSR-JCE)*, 13, Issue 2, 25–32, 2013.)

has an irregular shape compared to the local tissue, or the item is protruding from the skin (and then is closer to the backscatter detector). It is important also to be clear about the limits of the inspection. Small differences in density for materials are difficult to detect and can easily be confused with differences in position with respect to the detector, especially for concealed items where you do not know the object or the materials. For additional information on passenger screening, see Section 16.5.5.

Another class of inspections with backscatter x-rays applies to industrial objects and assemblies. A number of inspection techniques have been developed for munitions, and airplane wing sections and panels, where the ability to image from a single side is particularly advantageous. In these circumstances, the point of the inspection is the detection of anomalies in the material or assembly. Alternatively, Compton backscatter process tomography employs backscatter techniques to perform one-sided material characterization and, in certain circumstances, generates estimates of material density. Figure 15.23 contains a sketch of the backscatter-scanning apparatus.

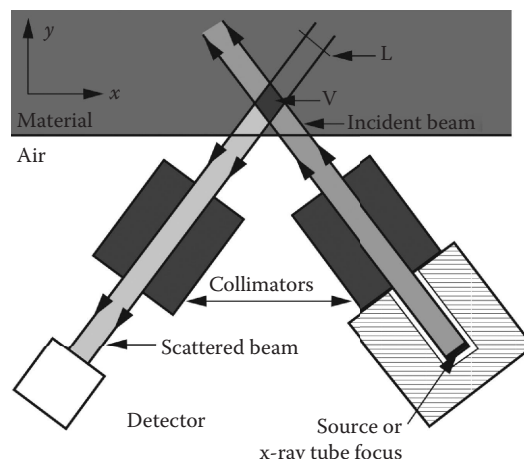


FIGURE 15.23 Illustration of a setup for x-ray backscatter process control tomosynthesis measurements.

A number of aspects of this physical setup for this measurement are important and further illustrate the kinds of information contained in the backscatter signal. First, collimation is implemented for both the source and the detector. The material volume under measurement is defined by the intersection between the source and detector collimation given by V in [Figure 15.23](#). The angle and the energy of the tube define the location of the volume to be measured in the depth of the material. As indicated in the figure, the collimation is substantial; the integrity of the scatter measurement depends strongly on the assumption that the measurements at the detector are from no stray position in the volume. Varying the different aspects of the apparatus and scanning in the horizontal direction (the x and y directions in the material) enables scatter measurements to be obtained from different parts of the 3D volume, somewhat like tomography. Further, with proper calibration and some assumptions concerning the material under test, estimates of material and/or density can be obtained.

X-ray backscatter applications have been developed for a variety of different types of objects and assemblies, for example, aerospace parts as given by Kolkoori et al. (2015). The techniques are important whenever aspects of a material that can be measured with x-rays are of interest, and two-sided imaging is problematic. Techniques have been developed to find contraband, look for defects, and examine the density profile of materials at a certain depth.

15.8 X-RAY DIFFRACTION TOPOGRAPHY

X-ray topography is not primarily concerned with the study of surfaces. The full title, x-ray diffraction topography, is much clearer since it indicates that the topography being studied is that of diffracting planes within a crystal, not the topography of the exterior features. The contours of the crystal surfaces are important in determining the contrast on x-ray topographs, but it is somewhat secondary in importance to the contours of the crystal lattice planes. When used to observe dislocations, topography is used to study the lattice planes around defects. The irradiance of the x-rays diffracted from the deformed planes differs from the irradiance diffracted by a perfect crystal forming an image of the defects. Topography is not a point probe, and the interpretation of the observed contrast is not trivial.

Consider a perfect crystal set to diffract monoenergetic x-rays of wavelength λ from a set of lattice planes spaced by d . For a strong diffracted beam to emerge at angle 2θ to the incident beam, the well-known Bragg relation applies, i.e.,

$$\lambda = 2d \sin \theta. \quad (15.4)$$

This is Bragg's law; note that this is slightly different from Equation 5.40 given in Chapter 5, where n (the order of the diffracted beam) is not in this equation. For more on x-ray topography, see the textbook by Tanner (1976).

Applications for x-ray topography include observing dislocation motion in early stages of plastic deformation in single crystals of ice (Ahmad and Whitworth 1988); characterization of crystal growth (Venkataraman et al. 1995; Raghathamachar et al. 2003); and microstructure, composition, and etching of dental ceramics (Della Bona and Anusavice 2002).

An overview of the various synchrotron white-beam x-ray topography (SWBXT) imaging techniques and their basic principles for characterization of silicon carbide (SiC) crystals is given in a paper by Dudley et al. (2003). SiC is a prominent material for various high-temperature and high-power electronics technologies due to its large bandgap, thermal conductivity, and breakdown voltage, among other outstanding properties. The past decade has seen rapid advances of SiC technology, mainly led by steady improvement in the quality and size of SiC crystals. Despite these achievements, however, the overall crystalline quality of SiC is still far inferior to Si or GaAs. SiC crystals generally contain various defects, such as dislocations, stacking faults, inclusions, etc., among which *micropipes* and closed core threading screw dislocations have been the most severe problem as they affect almost every aspect of SiC technology. These dislocations are called *superscrew*

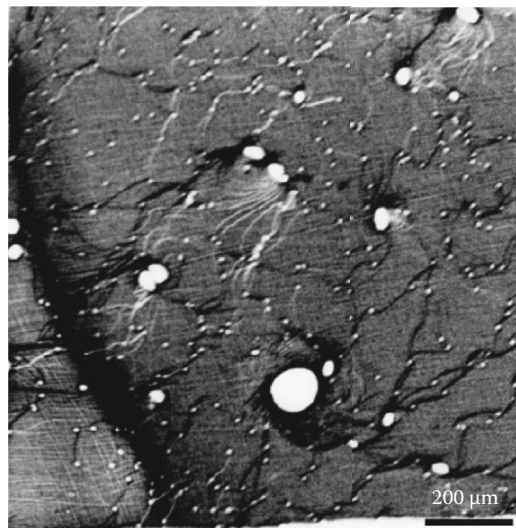


FIGURE 15.24 Back-reflection image recorded from a 6H SiC (0001) wafer thinned to around 30 μm . The circular images (black rings surrounding white circles) correspond to SSD images. (From Dudley, M. et al., *J Phys D: Appl Phys*, 36, A30–A36, 2003.)

dislocations (SSDs). Although the density of hollow-core SSDs has been somewhat reduced, they still are not low enough for almost all commercial SiC wafers. In addition, SSDs severely degrade the crystalline quality and can trigger the formation of other defects during growth. For this reason, crystal characterization is an indispensable step for SiC growth, epitaxy, and many other processes. SWBXT, with its high strain sensitivity and suitable spatial resolution, is the technique of choice for this aim. In fact, SWBXT has played a very strong role in the progress of SiC growth by providing a thorough understanding of the nature and origins of SSDs and other studies of defects in SiC. It has been, to date, one of the most accurate and reliable methods for discerning both the distribution and character of SSDs in SiC wafers, and has been widely adopted by the SiC community. A representative SWBXT image is given in Figure 15.24.

15.9 X-RAY MICROSCOPY AND X-RAY OPTICS

The earliest description of enlarged x-ray images was reported in 1897 (Heycock and Neville 1898), only 2 years after the discovery of x-rays by Röntgen, and well before the physical properties of x-rays were known. In that case, radiographs were simply enlarged photographically. By the 1950s, the spatial resolution had exceeded that of the light microscope and today reaches close to 10 nm. However, it is the unique properties of x-ray imaging in regard to penetration, depth of focus, and contrast mechanisms, rather than simply resolution, that make x-ray microscopy an important tool in structural research. An x-ray microscope denotes an instrument that produces an enlarged image of an object.

Once it was generally understood (ca. 1912) that x-rays have wave properties, use of lenses to focus x-rays was considered. There are two main principles of microscopes to be distinguished: full-field microscopes and scanning microscopes. In full-field microscopes, the whole FOV is imaged to a detector plane at the same time. In scanning microscopes, the sample is illuminated with a bright well-focused spot scanning over the sample. The detector then measures the total irradiance versus time coming from the currently illuminated spot on the sample, and the image is calculated from these data when the scanning process is finished. We will only describe full-field microscopes in this book. For scanning x-ray microscopes, see Rarback et al. (1988) and de Smit et al. (2008).

X-ray lens, mirror, or optic microscopes that enlarge an image of an object typically have better spatial resolution (~ 10 nm) than x-ray microfocus source point projection microscopes that do not use x-ray optics. Point projection microscopes spatial resolution is ~ 1000 nm (~ 1 μm). The point projection microscope technique uses no lenses in the x-ray optics, but relies on a point source of x-rays projecting the object onto a detector, originally a photographic emulsion that is now a digital detector, which is located at some distance from the object. The challenge is to make the source small, for high spatial resolution, and bright, for a reasonable data acquisition time.

What are the advantages of x-ray microscopes over other types of microscopes? X-rays penetrate matter far deeper than visible light and electrons. So x-ray microscopes can image the inside of samples opaque for visible-light or scanning electron microscopes. X-ray microscopes can achieve higher optical resolution than microscopes using visible light. The wavelength of x-rays is much shorter than the wavelength of visible light, so the limit of the optical resolution (caused by diffraction) of x-ray microscopes is far below the diffraction limit of microscopes working with visible light. Scanning electron microscopes, in comparison, have a higher image resolution, but they need vacuum-proof samples with metallic or metallized surfaces, and they cannot image the inside of a sample. A comparison of x-ray, visible, and electron microscopes is summarized in Table 15.3.

In the context of this section, the term *x-ray microscope* denotes an instrument in which an enlarged image of an object is formed by an x-ray lens, mirror or optic. In the literature, however, the term is also used to describe contact or projection microradiography systems. The main emphasis in this section will be on the overview of the field and recent developments. There are a few good books on this topic including those by Cosslett and Nixon (1960) and Poen (1959), a chapter by Stuart (1980), a keynote by Parish (1986), and proceedings of the X-ray Microscopy International Conferences (Warwick and Attwood 1999; Susini et al. 2003).

The essential function of the optical system of any *microscope* is to produce an image of an object at a magnification such that the observer's ability to resolve detail in the object is not limited by lack of resolving power in the detection system. For high-quality microscopy in the visible wavelength region, two distinct optical systems are normally needed:

- One set of lenses to produce the magnified image of the object
- Another set of lenses (condenser) to provide adequate illumination by concentrating light from a source onto the object

Likewise, x-ray microscopes require an optical system, even if it is only a small pinhole, to perform the first function. Unless the object is self-luminous, such as a laser compressed fuel capsule in a nuclear fusion experiment, an x-ray condenser may also be required for the external source

TABLE 15.3
Comparison of Three Different Types of Microscopes

	Microscope		
	X-Ray	Visible Light	Scanning Electron
Wavelength range (nm)	$\sim 0.03\text{--}50$	400–800	$\sim 0.06\text{--}3$
Resolution (nm)	~ 20	~ 200	~ 2
Imaging	Inner and surface	Inner and surface	Surface
Relative depth of field	Medium to high	Low	High
Samples	X-ray transparent	Optically transparent	Vacuum proof; metallic or metallized
Imaging modes	Full field/scanning	Full field/scanning	Scanning

Source: Adapted from http://www.x-ray-optics.de/index.php?option=com_content&view=article&id=118&Itemid=131&lang=en.

to fully illuminate the object. X-ray microscopes with magnifications as large as 100 \times have been developed.

Visible-light microscopes almost invariably employ refracting optics. At x-ray wavelengths, however, this is extremely challenging because the refractive index of most materials is less than, but very close to, unity, often differing from unity by only a few parts per million (see Section 5.5.1). The difference between the angle of incidence and the angle of refraction at a lens surface would thus be extremely small, and the focal length of a lens of normal shape would therefore be extremely long. Furthermore, the attenuation coefficient of x-rays in solid materials is usually far greater than that of visible light in optical quality glass, so a refracting lens of normal thickness would be effectively opaque to x-rays. Although some researchers have successfully built and tested refractive optics (Snigirev et al. 1996), practical constraints usually require alternative methods including

- Pinhole optics
- Reflection optics
- Diffraction optics

A pinhole for x-rays is used in a similar fashion to a pinhole for visible light. Reflection involves a change in the direction of waves when they bounce off a barrier such as an optical mirror; refraction of waves involves a change in the direction of waves as they pass from one medium to another; and diffraction involves a change in the direction of waves as they pass through an opening or around a barrier in their path. Each of these optics techniques has been considered for x-ray microscopes, and they are briefly described in Sections 15.9.1, 15.9.2, 15.9.2.1, 15.9.2.2, 15.9.3, and 15.9.4.

15.9.1 PINHOLE MICROSCOPES

A pinhole microscope (or camera) is shown in Figure 15.25c. Imaging is provided by a pinhole placed between the irradiated object and the detector. The source size by simple geometry must be at least as large as the object dimensions. An image of magnification, M_x , will be formed on the detector where

$$M_x = \frac{y_{\text{pdd}}}{y_{\text{opd}}}, \quad (15.5)$$

y_{pdd} is the pinhole-aperture-to-detector distance, and y_{opd} is the object-to-pinhole distance as shown in Figure 15.25. The main virtue of a pinhole microscope is its simplicity. It is simple to construct, simple to use, and relatively free of aberrations. However, it has two serious disadvantages. First, only a very small portion of the x-rays leaving the object is used to form the projection image, and second, the spatial resolution is severely limited by penumbra and diffraction effects (Attwood et al. 1977; McCall 1977). It is useful to point out that these two effects are related in that they are really an issue of solid angle. The solid angle is proportional to the pinhole diameter. Thus, if the spatial resolution is increased by a factor of 2, this decreases the solid angle/aperture by a factor of 4 for a given magnification/geometry.

The spatial resolution of a pinhole (camera) microscope is determined by both geometry and wavelength. However, with large pinhole diameters compared to the wavelength, as is generally the case for x-rays, a simple consideration based on limiting cases is appropriate as discussed by Attwood et al. (1977). With reference to Figure 15.25c, consider a pinhole of diameter D , a wavelength of λ , an object-to-pinhole distance y_{opd} , and a pinhole-to-detector distance y_{pdd} . An optimum pinhole size D_{opt} will provide the best spatial resolution for the parameters λ , y_{opd} , and y_{pdd} . In the limit of a large pinhole size, $D \gg D_{\text{opt}}$, diffraction is not important; spatial resolution is governed

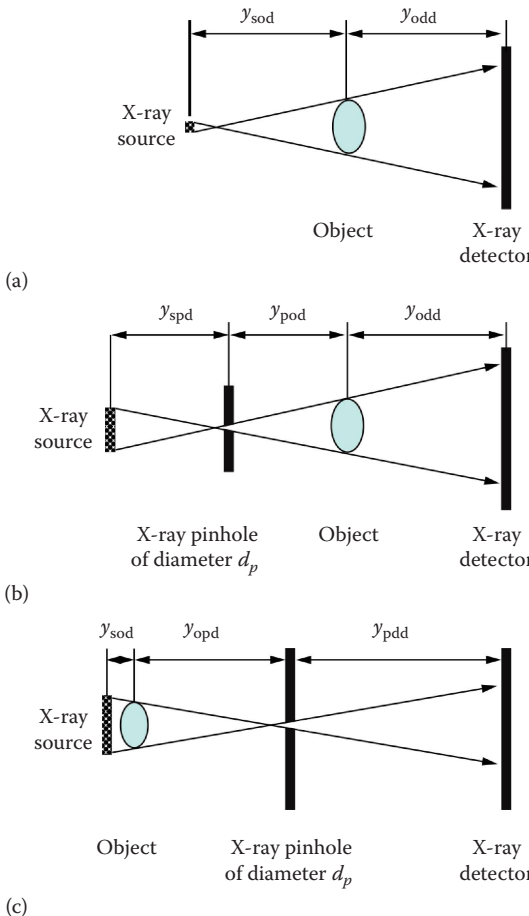


FIGURE 15.25 Schematic of x-ray projection configurations: (a) point projection using a point x-ray source spot size; (b) pinhole projection using a large x-ray source spot size with a pinhole (similar to a); and (c) pinhole x-ray camera. Note that (a) and (b) are quite similar, while (c) is quite different from (a) and (b).

by simple geometric considerations and is directly proportional to the pinhole diameter. For the geometrically limiting case, the width of the penumbra, P_g , will be

$$P_g = D \left[\frac{(y_{pdd} + y_{opd})}{y_{opd}} \right] = D(M_x + 1). \quad (15.6)$$

Alternatively, a point on the detector plane projects back on the object plane as a circle of diameter D_o

$$D_o = \frac{[D(M_x + 1)]}{M_x}. \quad (15.7)$$

If, as is usually the case, $M_x \gg 1$, then the resolution expressed in terms of object detail is approximately equal to the pinhole diameter.

On the other hand, for very small pinholes, diffraction effects dominate, and the spatial resolution is inversely proportional to D . With respect to diffraction effects, one can use the diameter of

the central disk, D_F^d , of the Fraunhofer diffraction pattern at the detector plane (Jenkins and White 1976) as an indicator of the limiting spatial resolution. The diameter D_F^d is given by

$$D_F^d = \frac{[(2y_{\text{pd}})(1.22\lambda)]}{D}. \quad (15.8)$$

The corresponding central disk diameter, D_F^o , diffraction pattern at the object plane is

$$D_F^o = \frac{[(2y_{\text{pd}})(1.22\lambda)]}{D}. \quad (15.9)$$

As given by Stuart (1980), a rough estimate of the spatial resolution, R_s , can be obtained by adding the penumbral and diffraction terms in quadrature to give

$$R_s = \sqrt{D^2 + \left[2.44\lambda \left(\frac{y_{\text{pd}}}{D} \right) \right]^2}. \quad (15.10)$$

This is a minimum when $D = \sqrt{2.44\lambda y_{\text{pd}}}$, in which case the corresponding resolution is

$$R_{s_{\text{min}}} = (4.88\lambda y_{\text{pd}})^{1/2} \approx 2.2(\lambda y_{\text{pd}})^{1/2}. \quad (15.11)$$

If, for example, the object-to-pinhole distance, y_{pd} , is 10 mm and the wavelength is 0.6 nm (2 keV), then $R_{s_{\text{min}}}$ is 5.4 μm , and the corresponding optimum pinhole size would be approximately 4 μm .

Another method is described by Attwood et al. (1977), and in this case, he states that a reasonable estimate of the optimum pinhole size is obtained by equating the two limiting cases (geometric and diffraction), i.e.,

$$\left(1 + \frac{1}{M} \right) D_{\text{opt}} = \frac{2.4\lambda y_{\text{pd}}}{D_{\text{opt}}} \quad (15.12)$$

or

$$D_{\text{opt}} = 1.6 \left[\frac{\lambda y_{\text{pd}}}{[1 + (1/M_x)]} \right]^{1/2}. \quad (15.13)$$

For large magnifications, this reduces to

$$D_{\text{opt}} \approx 1.6(\lambda y_{\text{pd}})^{1/2}. \quad (15.14)$$

For an object distance y_{pd} of 1 cm and λ of 0.6 nm (2 keV), the best spatial resolution is obtained with a pinhole diameter of $\sim 4 \mu\text{m}$. Note that this is somewhat similar to that derived by Stuart as given in Equation 15.11 and provides about the same pinhole diameter, $\sim 4 \mu\text{m}$. For larger or smaller pinholes, the obtainable resolution will be impaired. For larger pinholes, one enters the

geometrically limited region, diffraction plays a reduced role, and resolution is essentially equal to the pinhole diameter (see Equation 15.7).

Producing an aperture of this size can be quite a problem since the aperture material must be thick enough to be essentially opaque* to x-rays; this becomes more and more difficult as the x-ray energy increases. Attwood et al. (1977) developed a method to make pinholes for ~2.5 keV x-rays. The pinholes were constructed from 66% (tungsten by weight) tungsten phosphate glass 9 μm thick. Their glass measured absorbance of 10^6 at ~2.5 keV. A ruby laser was used to drill a 7 μm diameter hole in the glass. The glass being transparent to visible light facilitated optical alignment of the microscope.

It is useful to point out that, at higher energies, the thickness of the material required becomes a driver in making a useful pinhole. For example, consider the National Ignition Facility (NIF) at LLNL; pinhole experiments are planned at 40 keV, and the desired spatial resolution is in the 1–10 μm range. Diffraction will not be the limiting factor. What will be, however, is making a small hole through a thick piece of tantalum or other high-Z material. Even if you do not plug the hole with debris (a NIF-specific problem), you will still have an impaired FOV due to the high-aspect ratio (radius/thickness) of the pinhole.

Some variants of the pinhole microscope are worthy to note. In the scanning pinhole x-ray microscope (camera), a source, an aperture, a mechanically scanned object, a second aperture, and a detector are all placed in line. An image is built up on a cathode ray tube, the spot of which is scanned in synchronism with the movement of the object and the brightness of which is modulated in proportion to the detector output. A second variant of the pinhole microscope replaces the single pinhole with many pinholes or apertures; this was initially referred to as a multiaperture *scatter hole* x-ray camera (Dicke 1968). This method helps to overcome the principal drawback to using the simple, single-aperture, pinhole camera as an x-ray microscope, i.e., only a very small proportion, ~0.01–0.1%, of the radiation passing through the object is able to reach the detector. The efficiency can be increased by several orders of magnitude without loss of spatial resolution if the plate containing the pinhole is replaced by a plate containing many pinholes. Today this variant is known as the coded aperture camera (Barrett and Swindell 1981; Haboub et al. 2012; MacCabe et al. 2012). The coded aperture camera produces an image that is the superposition of those produced by the individual pinholes. The detected projection has to be subsequently decoded and the single image synthesized.

Often pinhole cameras or coded aperture cameras are used to image radioactive material or sources whether in an object, a room, or a person. For a single point radioactive source, a coded aperture camera improves the signal-to-noise ratio by the square root of the increase in photon collection efficiency. Unfortunately, not very many interesting radioactive objects consist of a single point source. For distributed radioactive source scenes, coded aperture cameras suffer loss in signal-to-noise ratio in the decoded image compared to a point source image. And like all synthetic aperture imaging approaches, coded aperture systems also suffer from limitation in dynamic range. For example, coded aperture cameras generally perform worse than a single pinhole camera for situations with scenes filling the FOV and where faint objects may be near bright objects (Barrett and Swindell 1981).

One advantage of coded aperture cameras in some applications is that depth information is encoded into the image along with the other two image dimensions. This means that the 3D location of a source can be decoded from a single image with a coded aperture camera. Two situations where this is potentially useful are in nuclear medicine applications (Meikle et al. 2002) and materials science (Haboub et al. 2012; MacCabe et al. 2012).

* One author (Martz) prefers to use 10^{-6} as the x-ray attenuation to be considered opaque.

15.9.2 REFLECTION OPTICS MICROSCOPES

A comprehensive survey of x-ray reflection optical systems can be found in the review paper by Franks (1977). We discuss in some detail x-ray reflection in Section 5.4. For recent work on reflection optics microscopes, see Hignette et al. (2003). Reflection optics, unlike pinhole optics, are suitable for both magnification and condenser systems.

The x-ray reflectance of a material varies as a function of the grazing angle of incidence, i.e., 90° minus the angle of incidence relative to the surface normal, and intimately depends on the density and the atomic number of the material, as well as its surface finish (or micro-roughness). It is desirable that the x-ray reflectance be as high as possible, especially when multiple reflections are involved. The transition between high (i.e., near unity) and low ($\ll 1$) reflectance for a given material at a particular energy occurs at a graze angle called the critical angle θ_c , defined as the square root of twice the real part of the index of refraction. In the x-ray energy band of ~ 0.1 – 10 keV (wavelengths of ~ 10 to 1 nm), typical values of the critical angle range from 0.5° to 5° . Dependence of x-ray reflectance on grazing angle and the surface roughness of the material is given in Figure 15.38. In this case, reflectivity versus graze angle is plotted for a thick iridium coating at an energy of 8.048 keV. Surface finish values range from 5 to 25 Å, in 5 Å steps. A calculated variation of critical angle with wavelength of six materials commonly used as x-ray reflectors is shown in Figure 15.26. For a given application, the higher the critical angle, the greater the working grazing angle of incidence and, consequently, the greater the aperture of the system. Thus, from considerations of maximizing the x-ray-collecting aperture, reflecting materials having high density and high atomic number are favored. On the other hand, in order to avoid loss of image contrast due to scatter, it is necessary to use materials that can be polished to such a degree that the amplitude of the residual surface roughness (sometimes referred to as the finish) is less than that of normal optical finishes by a factor of at least 10 . Surface roughnesses of < 4 Å have been achieved (Marshall et al. 1998). This latter requirement favors the use of high-quality vitreous (resembling glass) optical materials.

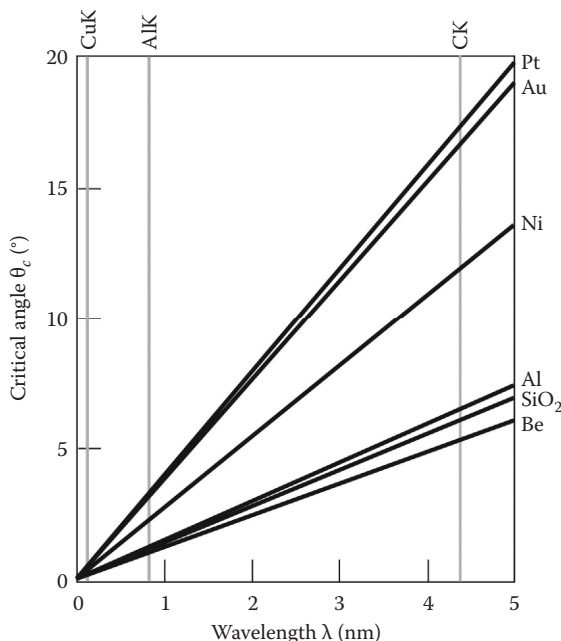


FIGURE 15.26 Dependence of the critical angle for x-ray reflection upon wavelength of the incident radiation as calculated for six materials used in the construction of x-ray mirrors. (From Stuart, P.R., Towards the ultimate X-ray microscope, in *Microfocal Radiography*, Ely, R.V., ed., Academic Press, London, 1980. With permission.)

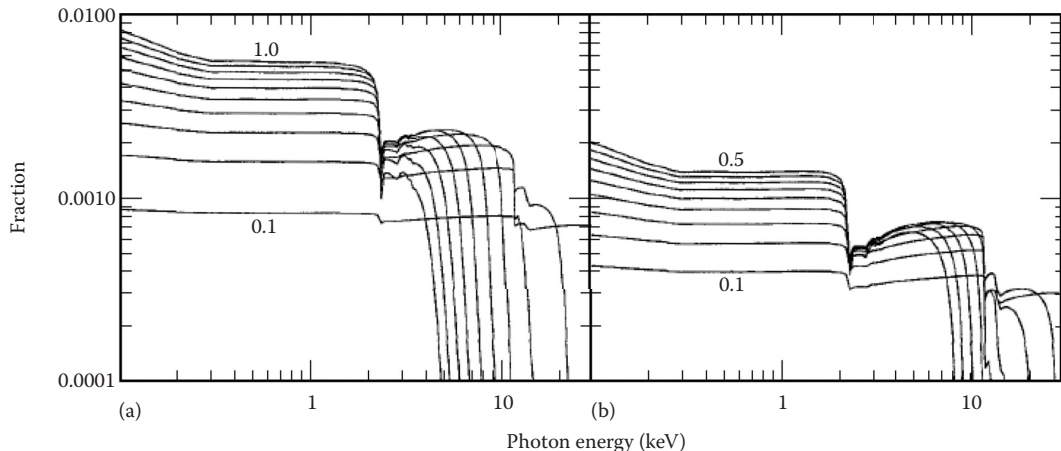


FIGURE 15.27 Efficiency of a gold surface as used in (a) two and (b) four reflection foil mirrors at indicated grazing angles in degrees. (From Serlemitsos, P.J. and Soong, Y., *Astrophys Space Sci*, 239-2, 177–196, 1996.)

Typical x-ray optics are made by depositing a thin film of a dense metal such as nickel, gold, or iridium on a strong, stable, polished substrate such as fused silica or nickel. If possible, the material chosen for the reflective coating should not have absorption edges in the working wavelength range, since such edges would cause a reduction of reflectance in the region of their wavelengths as shown in Figure 15.27. Fraction is the fraction of the Au reflecting area, which is effective in imaging in a two- or four-reflection mirror.

The plot in Figure 15.27a also reveals a problem immediately faced, that is, reflection at grazing incidence is a very inefficient process. Note that, in the range of a few keV, the fraction never exceeds about 0.0025. Putting it differently, for every 1 cm^2 of effective area, you need in excess of 400 cm^2 of actual reflector area, regardless of how the mirror is designed. Since mirror weight is roughly proportional to gross reflector area, the figure shows that both of these increase disproportionately as the mirror response is extended to include the iron K band. Four reflections present an even more prohibitive situation, as seen in Figure 15.27b.

There are many types of reflective x-ray optics using curved mirrors. They can be distinguished by the geometry and arrangement of the mirror substrates used, e.g., Kirkpatrick–Baez optics, Wölter optics, Schwarzschild optics, and Montel optics. In Sections 15.9.2.1 and 15.9.2.2, we describe two of them, i.e., Kirkpatrick–Baez and Wölter optics, respectively.

15.9.2.1 Kirkpatrick–Baez Reflection Optics Microscopes

In one type of reflection optics microscopes, the beam is first focused in one direction by reflection from a cylindrical mirror; the reflected beam then passes to a second cylindrical mirror, the axis of which is orthogonal to the first mirror, and this produces focus in the other direction (see Figure 15.28a). This is known as the Kirkpatrick–Baez (KB) type microscope named after the inventors (Kirkpatrick and Baez 1948). A KB x-ray microscope has the two mirrors instead of a pinhole (see Figure 15.25), and they are centered along the y -axis at the location of the pinhole.

There are two ways of obtaining cylindrical mirrors suitable for x-ray microscopes of the KB type. One is by the elastic bending of plane mirrors in specially designed bending jigs (Franks 1958; Franks and Breakwell 1974; Haselgrove et al. 1977). These bending jigs were designed for use with rectangular mirrors, in which case the surfaces of the bent mirrors are sections of right cylinders, and the images exhibit coma and spherical aberration. Researchers have demonstrated that it is possible to produce lower aberration mirrors, with more desirable elliptical surface profiles, by elastically deforming plane mirrors having appropriately curved sides, i.e., mirrors that are wider in the middle than at the ends (Underwood and Turner 1977; Stedman 1978).

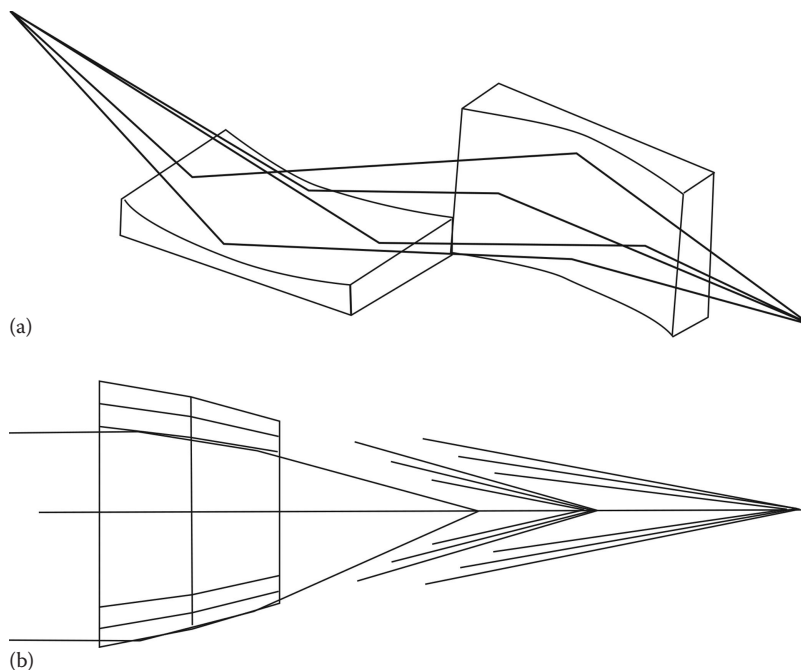


FIGURE 15.28 Schematic diagrams for two common reflective optics. (a) KB x-ray optical mirror. (b) Wölter x-ray optical mirror. Notice that the KB is a portion of a cylinder while the Wölter is conical, and both require two reflections.

The second method used to produce cylindrical mirrors for KB x-ray microscopes is to grind, lap, and polish them to the required shape. Several low-magnification ($3\times$) microscopes of this type have been constructed for use in the observation of laser fusion targets (Seward and Palmieri 1975; Boyle 1977). The FOV of these microscopes is $\sim 500 \mu\text{m}$, and the spatial resolution of the object at the center (the resolution falls off away from the center) of the FOV is $5 \mu\text{m}$ or less. This performance is obtainable only by keeping the magnification small and by using a small aperture to reduce the significance of the aberrations. Although the solid angular aperture of the system is approximately that of a pinhole x-ray microscope of the same resolution, for laser fusion studies, the KB x-ray microscope is experimentally more convenient, since it need not be positioned so close to the object for comparable performance.

Advances in KB microscopes optics include using two pairs of hyperbolic and elliptic mirrors to avoid spherical aberration and field obliquity (Kodama et al. 1996; MacDowell et al. 1997). The spatial response of the microscope has been measured by x-ray imaging (sometimes called back-lighting in the laser fusion business) a fine grid with laser-plasma x-rays. A spatial resolution of better than $3 \mu\text{m}$ has been obtained with 2.5 keV x-rays over the field of $800 \mu\text{m}$ at a magnification of $25\times$. This microscope has been applied for laser implosion experiments, resulting in high-spatial-resolution images of compressed cores from a plastic shell target as shown in Figure 15.29. More recent results have obtained high-spatial-resolution 3D imaging of heterogeneous metals using KB focusing optics, achieving voxel sizes of $50\text{--}60 \text{ nm}$ (Requena et al. 2009).

15.9.2.2 Wölter Objective Reflection Optics Microscopes

In order to obtain higher spatial resolutions and larger apertures, it is necessary to employ conichoidal (a quadric surface such as a hyperboloid, paraboloid, or ellipsoid) mirror systems. A single conichoidal mirror, i.e., part of an ellipsoid, hyperboloid, or paraboloid of revolution, violates the Abbe sine rule and thus has poor off-axis performance. Instead, practical imaging systems employ

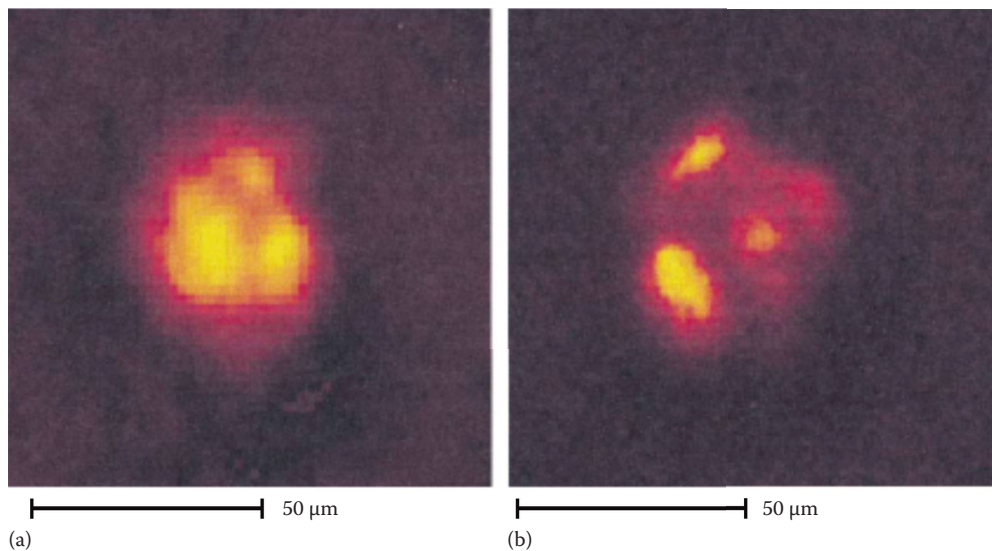


FIGURE 15.29 X-ray images of a core plasma of a laser-imploded plastic shell target obtained with (a) a $15\text{ }\mu\text{m}$ x-ray pinhole camera and (b) the advanced KB (AKB) microscope, observed from different directions. The AKB microscope clearly resolves the small structure in the x-ray image of the core plasma, whereas they are poorly resolved with the x-ray pinhole camera. (From Kodama, R. et al., *Opt Lett*, 21, 1321–1323, 1996. With permission.)

at least a single pair of coaxial, confocal, and conichoidal mirrors (Wölter 1952) (see Figure 15.28). In 1952, Hans Wölter outlined three ways that such practical imaging systems could be built. He mentioned an x-ray telescope using a glancing (or grazing) incidence mirror applying three different designs. They are called Wölter telescopes of types I, II, and III as shown in Figure 15.30. Each has different advantages and disadvantages.

For microscopes, a preferred combination is a hyperboloid followed by an ellipsoid as shown in Figure 15.31. The central beam stop screens the detector from direct radiation from the source. The conichoidal mirrors used in microscopes are normally complete 360° figures of revolution, as typically the case for x-ray astronomical telescopes. However, this is not essential, as it is possible to use only sectors of the complete figure of revolution, though as sectors, their aperture and FOV would be less than a complete optic.

Some of the first uses of an axisymmetric, hyperboloid–ellipsoid, microscope has been described by Hudec et al. (1999), Chase and Silk (1975), Boyle (1978), and Boyle and Ahlstrom (1978). The Chase and Silk x-ray imaging system employed ellipsoid and hyperboloid mirrors that are confocal and coaxial. Spatial resolutions between 1 and $3\text{ }\mu\text{m}$ were obtained. The useful FOV was hundreds of micrometers, and the geometrical collecting solid angle is $3.2 \times 10^{-3}\text{ sr}$ corresponding to a geometrical area of 1.3 cm^2 at 20 cm . The Wölter microscope was $\sim 10^3$ times more efficient (a larger solid angle) than that of a pinhole microscope. The instrument has application for diagnostics of laser–pellet interactions. Diagnostic measurements using the emitted x-rays from the spatially small microballoons that contain the deuterium–tritium (DT) fuel of typically $50\text{--}80\text{ }\mu\text{m}$ outer diameter with multilayer walls approximately $1\text{--}10\text{ }\mu\text{m}$ thick and high-temperature products of laser–pellet interactions provide valuable insights into the heating and compression processes.

The Boyle and Ahlstrom x-ray microscope was also designed for laser fusion research. It has a magnification of $9\times$. The length of the hyperboloid–ellipsoid mirror pair is about 35 mm, and the mean internal diameter is $\sim 19\text{ mm}$. The FOV at the object is approximately 1.5 mm in diameter, and the resolution in the center of the field was estimated to be $4\text{ }\mu\text{m}$, which is similar to that of a typical KB microscope. However, the solid angle for radiation acceptance is $4.2 \times 10^{-4}\text{ sr}$, which is

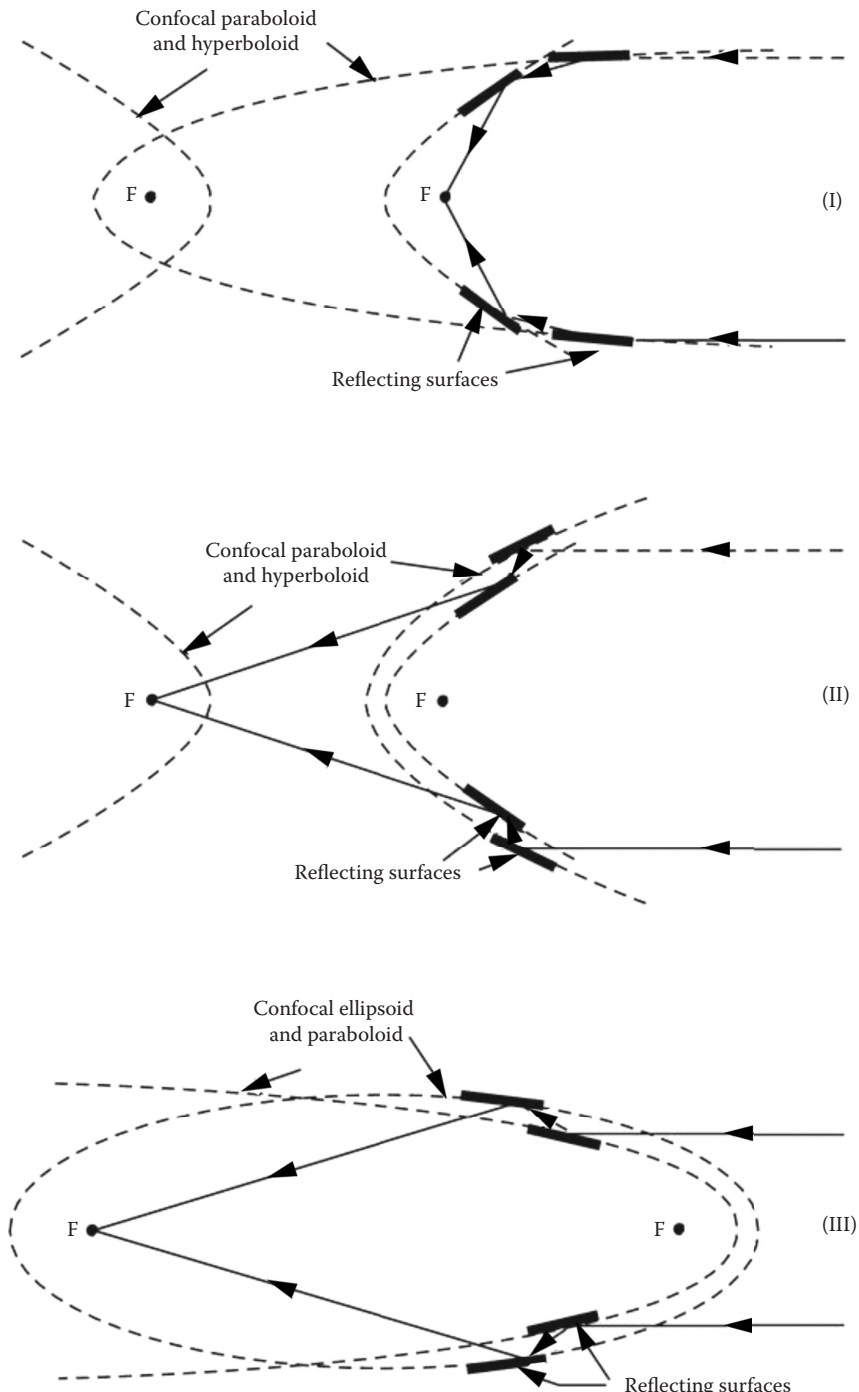


FIGURE 15.30 In 1952, Hans Wölter outlined three ways an x-ray telescope could be built using a glancing (or grazing) incidence mirror. These are called Wölter telescopes of types I, II, and III. Each has different advantages and disadvantages.

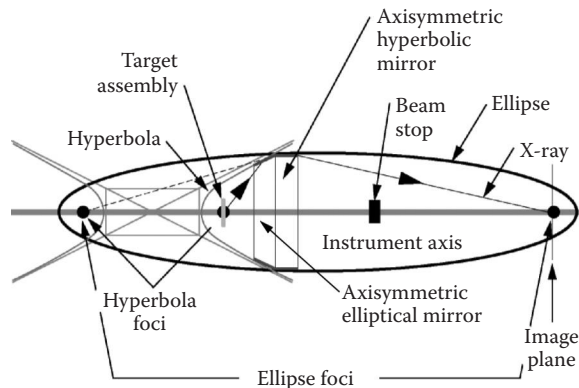


FIGURE 15.31 Schematic diagram of the optics of a hyperboloid–ellipsoid x-ray microscope (axial dimensions greatly foreshortened).

several thousand times higher than the KB microscope (see Figure 15.32). Thus, the main advantage exhibited by the Wölter microscope is that the data acquisition times can be significantly shorter. This can be important when carrying out time-resolved measurements.

Following the theoretical analysis of Sakayanagi (1976), he and Aoki (Sakayanagi and Aoki 1978) constructed a microscope using two toroidal mirrors in tandem. The magnification was about 20 \times , the resolution in the object plane about 3 μm , and the FOV approximately 0.15 mm. In 1992, Aoki et al. developed a sub-100 nm resolution grazing incidence soft (4–9 nm) x-ray microscope using a laser-produced plasma source (Aoki et al. 1992). The x-ray microscope consists of an axisymmetric toroidal condenser mirror and Wölter 20 \times objective mirror. The total length of the system is less than 3 m as shown in Figure 15.33.

At LLNL, we researched the development of a Wölter x-ray microscope for characterization of laser fusion targets. Our design goals for the microscope were to image 8 and 59 keV x-rays with

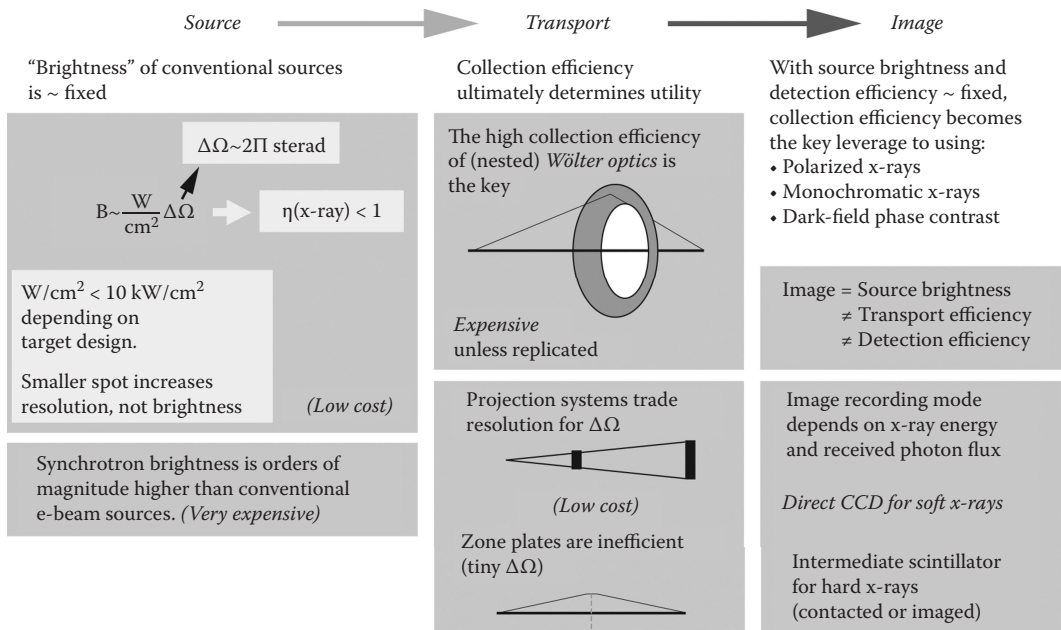


FIGURE 15.32 Increased x-ray collection efficiency at adequate resolution is the key to using low-cost x-ray sources for advanced microscopy.

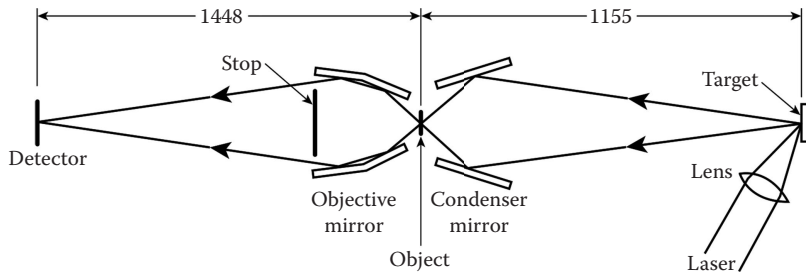


FIGURE 15.33 Schematic diagram of the optical system of the grazing incidence Wölter objective x-ray microscope with a laser-produced plasma x-ray source. (From Aoki, S. et al., *Jpn J Appl Phys*, 31, 3477–3480, 1992. With permission.)

1 μm spatial resolution at the edge of a 1–2 mm FOV (Nederbragt 2002, 2003). The final design does not include an x-ray condenser mirror as shown in a schematic of the system provided in Figure 15.34. The overall length of the designed microscope was about 6 m. The mandrel and Wölter optic fabricated are shown in Figure 15.35. The LLNL Wölter x-ray optic was fabricated as summarized in Figure 15.36. This Wölter x-ray microscope was developed to image 1–5 mm sized laser targets before ignition (Martz and Albrecht 2003).

Ray-tracing calculations show that the spatial resolution of present-day x-ray microscopes is limited by inaccuracies arising in the fabrication and alignment of their mirror systems. In order to achieve 1 μm object resolution, it is necessary that all parts of the mirror system should be made and aligned to a tolerance of well under 1 μm and that the figure of the mirrors should be correct to well under 1 arcsec (see Figure 15.37). For a single-material optic, the surface roughness, or finish, is on the order of tens of angstroms as shown in Figure 15.38. For multilayered material optics, the finish is even more stringent. The multilayered material Wölter optic we designed required a finish of better than 5 Å and a figure with an angular resolution of 0.1 arcsec. We were unsuccessful in making an x-ray Wölter optic with this figure and finish (Pivovaroff et al. 2004). These requirements put great demands on fabrication technologies. Some of the problems encountered in the production of supersmooth x-ray reflective surfaces have been reviewed by Lindsey and Penfold (1976) and Spiga and Raimondi (2014).

Lastly, it is of interest to note that Mosher and Stephanakis (1976) have produced x-ray light pipes over a meter long. X-rays are channeled through the bores of bundles of fine glass or nickel tubes. Further work on x-ray light pipes has been described by Pantell and Chung (1978) and more recently by Kukhlevsky et al. (1997).

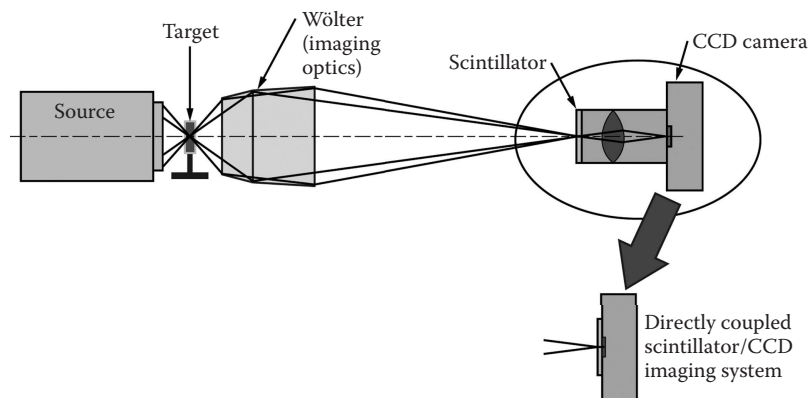


FIGURE 15.34 Schematic drawing of a Wölter optic x-ray microscope.



FIGURE 15.35 Photograph of a multilayer (alternating layers of tungsten carbon and boron carbide) (a) Wölter optic and (b) the mandrel from which it was created. The mandrel is nickel coated on an aluminum substrate.

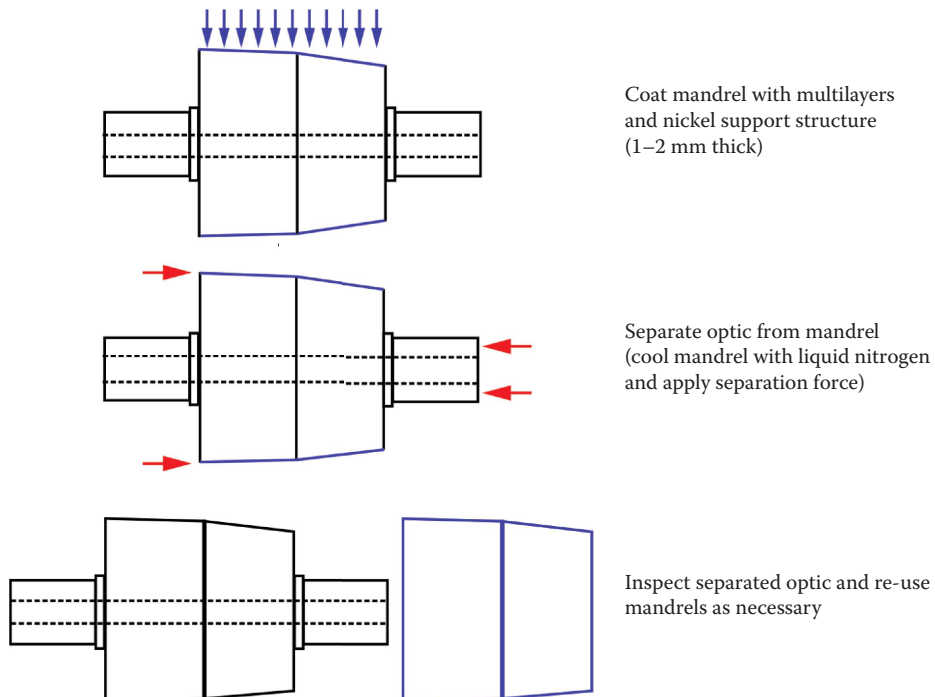


FIGURE 15.36 The LLNL Wölter optic was fabricated using the optical replication method. This method involves coating the outside surface of a high-accuracy super-polished mandrel and separating the coating (i.e., the optic) from the mandrel.

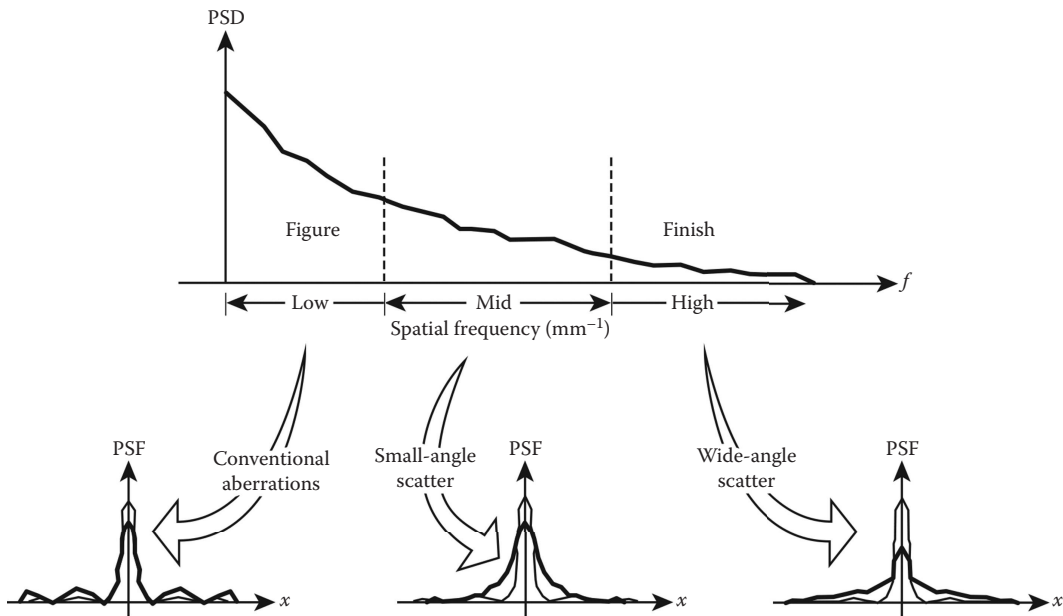


FIGURE 15.37 There are three spatial frequency regimes that are important in the fabrication of an x-ray mirror/optic: (1) low spatial frequencies (LSF): length scales longer than 1 mm often called figure; (2) midspatial frequencies (MSF): length scales 1 μm to 1 mm; (3) high spatial frequencies (HSF): length scales shorter than 1 μm ; often called finish or micro roughness.

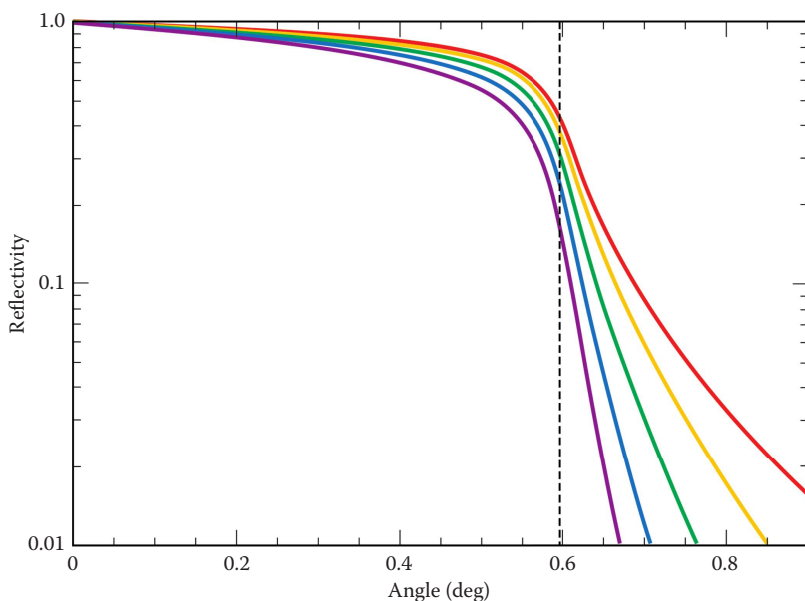


FIGURE 15.38 Dependence of x-ray reflectance on grazing angle and the surface roughness σ_{sr} of the material. In this case, reflectivity versus graze angle is plotted for a thick iridium coating at energy of 8.048 keV. Surface finish values range from $\sigma_{sr} = 5$ to 25 \AA , in 5 \AA steps. The dashed line indicates the value of the critical angle $\theta_c = 0.59^\circ$ for iridium at this particular energy.

15.9.3 REFRACTIVE LENS MICROSCOPES

We discussed in some detail x-ray refraction in Section 5.5.1. Here we discuss how it is used to focus x-rays for use as an x-ray microscope. Refractive lenses, which are used extensively in visible-light optics, are generally not appropriate for focusing x-rays because x-ray refractive effects are extremely small and x-ray absorption is high. This has led to alternative approaches based on reflective optics using bent crystals and x-ray mirrors (see Section 15.9.2), Fresnel and Bragg–Fresnel zone plates (see Section 15.9.4), and capillary optics (Kumakhova et al. 2014). In microscopes with refractive optics, x-rays are guided by refraction at surfaces between different materials. This effect is described by Snell's law (see Equation 5.38 in Section 5.5.1.2). The index of refraction at x-ray wavelengths may be written as

$$\eta = 1 - \delta - i\beta, \quad (15.15)$$

where δ and β depend on the material and the wavelength of the incident x-rays. δ is the phase-shift term or index and incorporates refractive and diffractive effects, and β is the attenuation index and describes the attenuation of x-rays. For x-rays, the difference of the refractive index to a value of 1 is sometimes called the index decrement. With the refraction being very small (δ is typically between 10^{-5} and 10^{-7}), attempts to build refractive lenses have not been very successful. In the late 1990s and early 2000s, discussions about refractive lenses were revived (Michette 1991; Suehiro et al. 1991; Yang 1993; Snigirev et al. 1996). To overcome the problem that the index decrement for x-rays for all materials is only slightly below 1 and the high attenuation effects, researchers have decided to use low atomic number materials and multiple lenses instead of one refractive lens. Multiple refractive lenses are referred to as compound refractive lenses in the literature. So hundreds of well-aligned lens elements with very small radii of curvature are used to form a refractive x-ray lens with a focal length in the range below 1 m as shown in Figure 15.39. For visible light, the index of refraction is larger than 1 for lens materials, and focusing lenses are thicker in their center than at their edges, resulting in their typically biconvex shape. Due to the fact that the index of refraction is smaller than 1 for x-rays, focusing lenses are thinner at the center than at their edges, giving a biconcave shape. A parabolic geometry of the refracting surfaces is well suited to focus x-rays hitting the lens parallel to the optical axis. Often researchers drill several holes in a material such as boron, carbon, aluminum, or a polymer (Snigirev et al. 1996). Compound refractive lenses are easy to make. An important feature of focusing optics is the irradiance gain in the focal spot compared with the irradiance that would be obtained without a lens using a pinhole or slit. One set of holes focuses in one direction; to get a point, you need another set of holes at 90° to the first set.

As an example of a refractive lens system, Snigirev et al. (1996) built an aluminum lens for a 14 keV x-ray source. δ is 2.8×10^{-6} using $300 \mu\text{m}$ diameter holes. A single lens results in a focal length of 54 m, while for 30 lenses (30 holes), the focal length is only 1.8 m (Snigirev et al. 1996).

In 2002, Schroer et al. developed a 3D compound refractive lens microscope with a spatial resolution of $\sim 400 \text{ nm}$ in a FOV of about $200 \mu\text{m}$ (Schroer et al. 2002c). In their x-ray microscope, a sample is imaged by an aluminum parabolic refractive lens onto a high-spatial-resolution position-sensitive detector. Like in classical optics, a sharp image is formed at a distance

$$L_2 = L_1 F / (L_1 - F), \quad (15.16)$$

behind the lens, where L_1 is the object to lens distance and F the focal length of the lens. The magnification is L_2/L_1 . While the focal distance and effective aperture, D_{eff} , of the objective lens determines the imaging properties of the microscope, its transmission determines the data acquisition times. The lateral resolution is given by $0.75\lambda/2NA$, where λ is the wavelength of the x-rays and $NA = D_{\text{eff}}/(2L_1)$ is the numerical aperture. The numerical aperture typically lies in the range

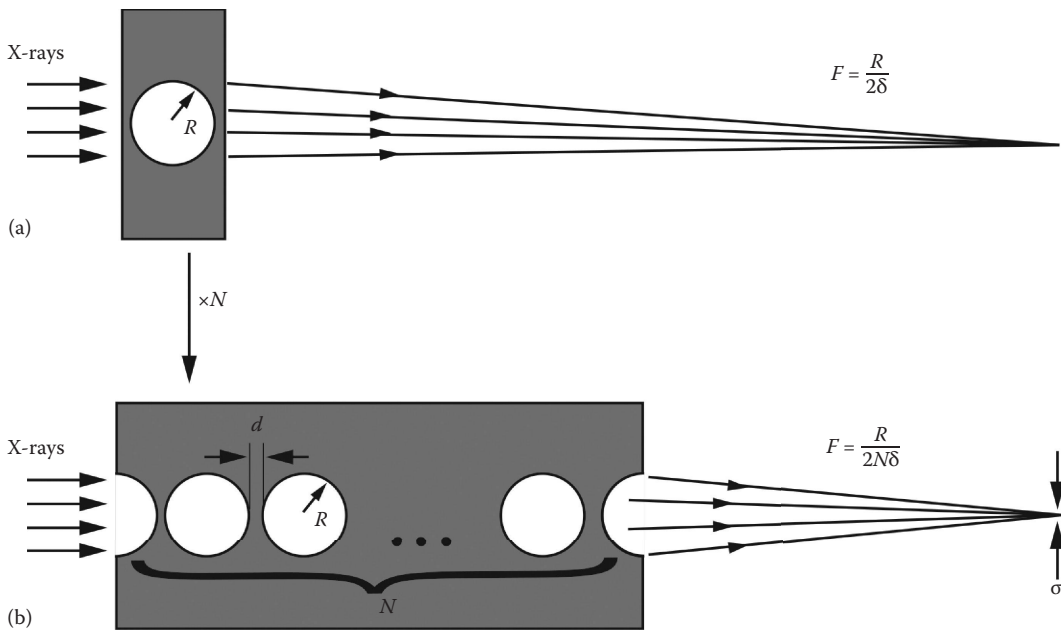


FIGURE 15.39 Schematic diagram showing the x-ray focusing by a single and compound refractive lens. (a) A simple concave lens fabricated as a cylindrical hole in a material. (b) A compound refractive lens consisting of a number, N , of cylindrical holes placed close together in a row along the optical axis focuses the x-rays at a distance N times shorter than a single refractive lens. R is the hole radius, d is the spacing between the holes, λ is the wavelength, F is the focal distance for a parallel beam x-ray source, and δ is the decrement of the refractive index. (From Snigirev, A. et al., *Nature*, 384, pp. 49–52, 1996.)

from 10^{-4} to 10^{-3} , resulting in a depth of field $d_t = 64\lambda/(NA)^2$ of several millimeters. Therefore, the x-ray radiographs of samples with a thickness of up to several hundred micrometers have sharp projections.

The high degree of spatial coherence at 40–60 m from a third-generation undulator source made it possible to image in both absorption and phase contrast. Phase-contrast images cannot be interpreted directly as projections but require phase retrieval prior to tomographic reconstruction (Schroer et al. 2002a). Schroer et al. (2002b) suppressed the phase contrast by introducing a rotating diffuser (2.5 mm B_4C powder between two thin glass plates) that reduces the spatial coherence before the sample. For the absorption contrast images obtained this way, tomographic reconstruction is straightforward.

They performed some imaging experiments at the European Synchrotron Radiation Facility (ESRF) in Grenoble, France, of a fragment of an AMD K6 microprocessor (see Figure 15.40). At a photon energy of 24.9 keV, an aluminum objective lens with 120 single lenses results in a focal length of about 1 m. The image of the sample located $L_1 = 1098$ mm before the lens was projected onto a 2D position-sensitive detector $L_2 = 23.02$ m behind the lens. In this geometry, the magnification is 20.93, resulting in an effective pixel size of 131 nm in x-ray micrographs. For ideal aluminum parabolic lenses, the resolution of this setup is limited by a Gaussian Airy disc with d_t equal to 230 nm full width at half-maximum (FWHM).

15.9.4 DIFFRACTION OPTICS MICROSCOPES

Diffracting elements can be used to focus x-rays provided that the radiation is monochromatic. We discuss in some detail diffraction of x-rays in Section 5.52. Diffraction optics for x-ray imaging

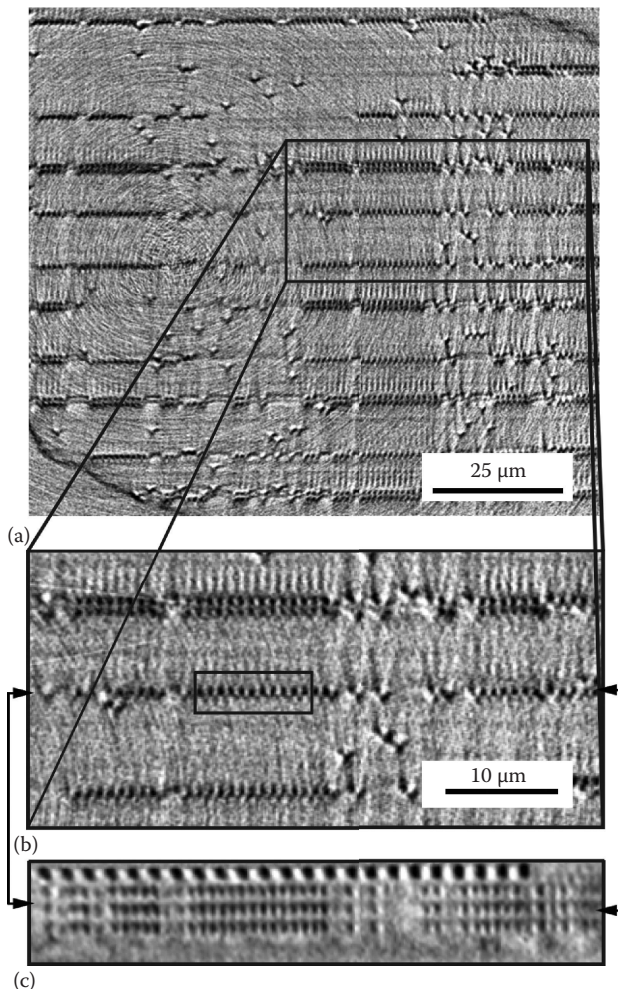


FIGURE 15.40 (a) Tomographic (horizontal) slice through the second layer of tungsten plug vias in an AMD K6 microprocessor. (b) Magnification of the rectangular region shown in (a). (c) Vertical section through the processor along the line of plug vias marked by arrows in (b). (Reproduced with permission from Schroer, C.G. et al. 2002c. Copyright 2002, AIP Publishing LLC.)

falls into two categories: Fresnel zone plates and diffraction gratings (Stuart 1980). We will only describe the Fresnel zone-plate microscopes since diffraction gratings are not commonly used for x-ray imaging. For CT systems that use diffraction gratings, see Pfeiffer et al. (2006) and Momose et al. (2006).

A Fresnel zone plate consists of a series of concentric annular rings, capable of absorbing the incident irradiation, separated by annular gaps of approximately the same widths as the rings as shown in Figure 15.41. If the widths of the rings and gaps are inversely proportional to their diameters, then monochromatic radiation diffracted at the gaps will produce a series of foci on the axis, corresponding to the various orders of diffracted radiation (Jenkins and White 1976). The foci length, f , for first-order diffraction is given by

$$f = \frac{r_1^2}{\lambda} \text{ or} \quad (15.17)$$

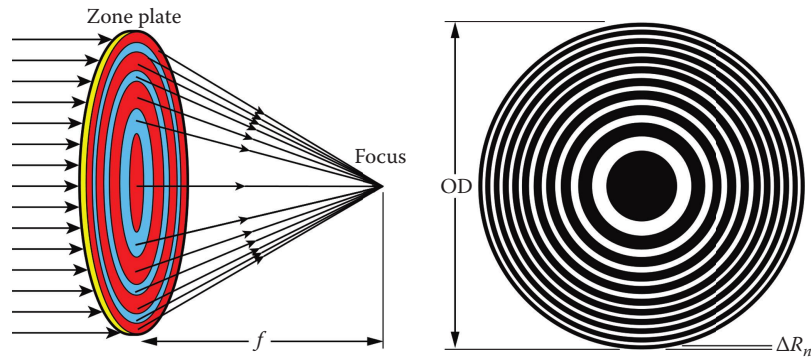


FIGURE 15.41 A Fresnel zone plate. (From Xradia web site, available at http://www.xradia.com/pro_zpl.htm. With permission.)

$$f = \frac{OD\Delta R_n}{\lambda}, \quad (15.18)$$

where λ is the wavelength, r_1 is the radius of the central zone, OD is the zone-plate outer diameter, and ΔR_n is the outermost zone width (see Figure 15.41):

$$r_1^2 = OD\Delta R_n. \quad (15.19)$$

If one wanted to make a zone plate with a focal length of 50 mm at a wavelength of 4.5 nm (0.28 keV), then the radius of the central zone would be 15 μm . According to the Rayleigh criterion, the spatial resolution, R_s , of a zone plate is given by

$$R_s = \frac{(1.22\lambda f)}{OD}. \quad (15.20)$$

In the example given above, if the diameter of the outermost zone is 1 mm, then the number of zones would be about 1100 and the resolution should be about 0.3 μm .

The fabrication of a Fresnel zone plate with the structure of this nature is a formidable task. Baez constructed a somewhat larger and coarser zone plate for use with ultraviolet radiation and showed that it performed better than the optimum-sized pinhole by a factor of ~ 6 in resolution and 40 in speed. One common method to make zone plates is by a photofabrication process; in one stage, a layer of photosensitive lacquer is illuminated with the required zone pattern generated in an optical interferometer. A zone plate constructed by Niemann et al. (1976) and for use with an x-ray of wavelength 4.6 nm (0.27 keV) from a synchrotron resulted in a microscope with a spatial resolution of 0.5 μm . More recently, Wang et al. (2005b) at Xradia have fabricated Fresnel zone-plate x-ray nanoscopes (see Figures 15.42 and 15.43) with tens of nanometers spatial resolution. A representative x-ray microscope image of an electronic circuit using the Xradia nanoscope is shown in Figure 15.44. Also shown for comparison purposes are optical and scanning electron microscope (SEM) images.

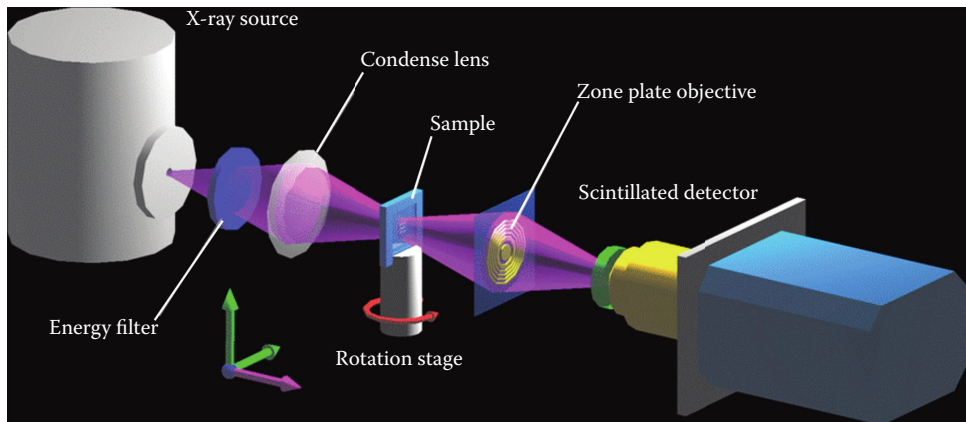


FIGURE 15.42 Schematic diagram of the Xradia Fresnel zone-plate nanoscope called XTM. (From Xradia. With permission.)

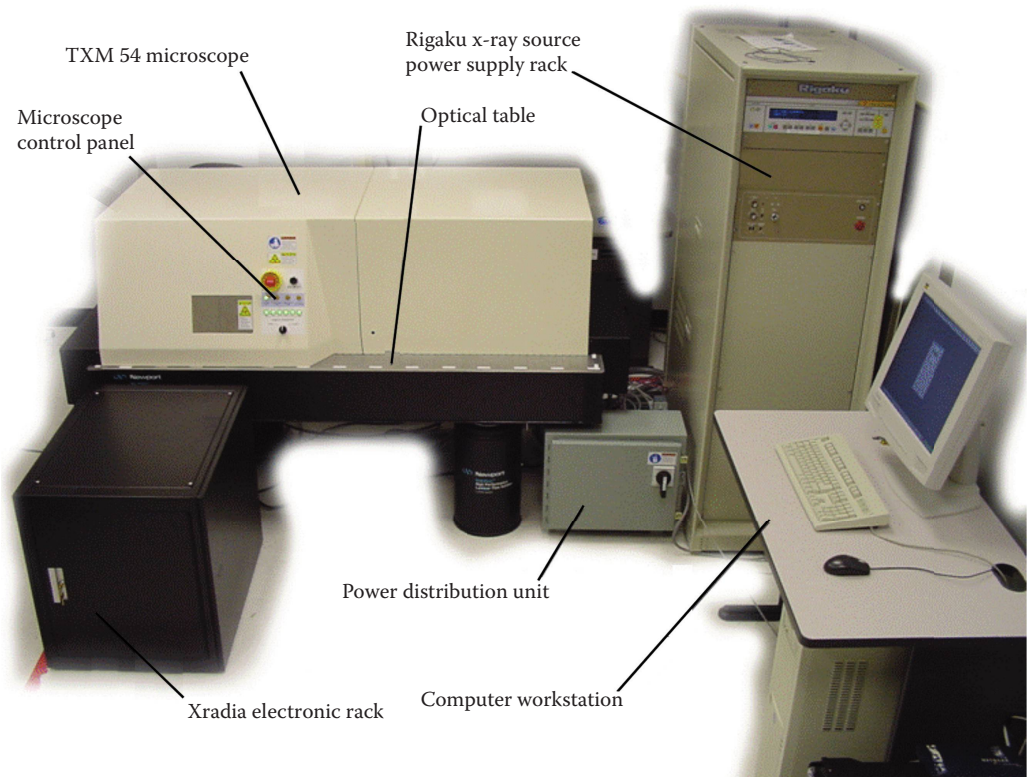


FIGURE 15.43 Photograph of the Xradia TXM-54 system. (From Xradia. With permission.)

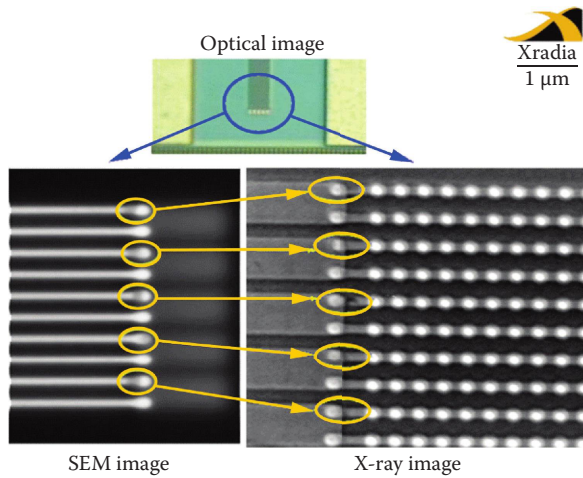


FIGURE 15.44 Three images of an electronic circuit reveal the usefulness of high spatial resolution imaging of the Xradia TXM-54-80 system. Note that defects highlighted by the circles in the x-ray image reveal defects not observable in either the optical or SEM (scanning electron microscope) images. (From Xradia. With permission.)

PROBLEMS

- 15.1 You have to scan a cylindrical part that is three times larger than the FOV of your DR/CT system. You want to do CT of this part to find internal defects. Can you still scan this part? If yes, how? If no, why not? Specify in detail the technique that you would choose including the generation, geometry, etc.
- 15.2 You have a part that is spherical in shape and just smaller than twice the size of your FOV of your DR/CT system. You want to do CT of this part to verify that it was assembled correctly. Can you do CT of this part? If yes, how? If no, why not? Specify in detail the technique that you would choose including the generation, geometry, scanning protocol, etc.
- 15.3 You have a complex, high-aspect ratio part and need to inspect it for internal flaws such as voids and inclusions. What method would you use to scan the part? Justify the answer you choose. Specify in detail the system that you choose including the technique, geometry, source, detector, etc.
- 15.4 A customer gives you a rock the size of a baseball. They tell you that it is heterogeneous, highly attenuating, and radioactive. They want to identify the radioisotopes and their distribution within this rock. What method would you use to answer their question? Specify in detail the system that you choose including the technique, geometry, source, detector, etc.
- 15.5 A customer has a high-value material and they want to know if it has a density gradient. What system would you design and build to measure whether the material has a density gradient? Justify the selection you make.
- 15.6 A new customer has a large $50\text{ cm} \times 50\text{ cm} \times 0.5\text{ cm}$ Al sheet and they want to know the areal density of the sheet. How would you perform such a measurement? Specify the design of your system, geometry, source spectrum, detector, etc.
- 15.7 A materials research lab approaches your NDE firm with a sample of a new open-cell Ti foam material. They need to know that all void space within the foam is connected to the surrounding environment. How would you perform this inspection using x-rays?

16 Selected High-Energy Photon Applications

16.1 INTRODUCTION

The applications presented here are in some sense the *payoff* for the material presented earlier. As mentioned several times throughout this book, the choices involved in determining a particular inspection technique involve trade-offs. Each of the applications presented here represents a set of choices, against alternatives, for performing an inspection. It will be left to the reader to decide if the choices are appropriate—or if a different set of parameters would result in a better inspection (this will be the substance of exercises at the end of this chapter).

The selected applications by no means eclipse the scope of inspections employing penetrating radiation in the 10 keV to 10 MeV regime. Rather the selection shown here should be viewed as a few of the current uses of a particular inspection modality. Also, we chose these applications because we know them best.

Upon completion of this chapter, you will have reviewed applications utilizing 1D transmission measurements, 2D transmission images, and 3D computed tomography (CT) reconstructed images. Applications range from laser fusion targets of millimeter size, DoD munitions, automotive parts, Archaeopteryx, David's (Michelangelo) ankle, to a few meters size NASA heat shield. In the concluding section, we present several methods in which x-rays are being applied in defense of the US homeland. The authors hope we will have inspired at least one instance where you are amazed at the imaging possible with x-rays.

16.2 1D APPLICATIONS

One-dimensional applications consist of an x-ray transmission measurement along a single ray. These are often referred to as *x-ray gauging*. The geometry of gauging is usually pencil beam, meaning a circular beam profile whose diameter is selected according to the spatial dimension desired. The beam diameter is defined by appropriate collimation. The source may be a radioactive isotope or a tube. The detector may be energy integrating or discriminating.

Many gauging applications are closely coupled to manufacturing or process control. For example, if a process stream carries a two-phase mixture of steam and coal, transmission through a pipe carrying this stream reveals the relative amounts of steam and coal.

Gaging is often used on continuous sheet manufacturing as a thickness measurement (Artemiev 2014; Thermo 2014). In the paper industry, gaging measures moisture and clay content.

A Lawrence Livermore National Laboratory (LLNL) program is desired to assay sheets of synthetic material made up of a plastic impregnated with heavy metal. The manufacturing process assured that only two materials were present. At x-ray energies applicable to this product, the heavy metal accounted for about 95% of the attenuation but little of the mass. Weighing and measuring established the areal density of the sheets. Radiography defined the uniformity of the heavy metal. The final link in the characterization puzzle was to nondestructively determine the areal density of heavy metal at a few discreet locations on each sheet.

We chose ^{109}Cd as the radioisotopic source. ^{109}Cd decays by electron capture leaving excited ^{109}Ag . The isotope emits Ag characteristic x-rays as shown in [Figure 16.1](#) at 22.1 and 24.9 keV. The silver decays with an 88 keV γ -ray also apparent in Figure 16.1. ^{109}Cd has a half-life of 463 days

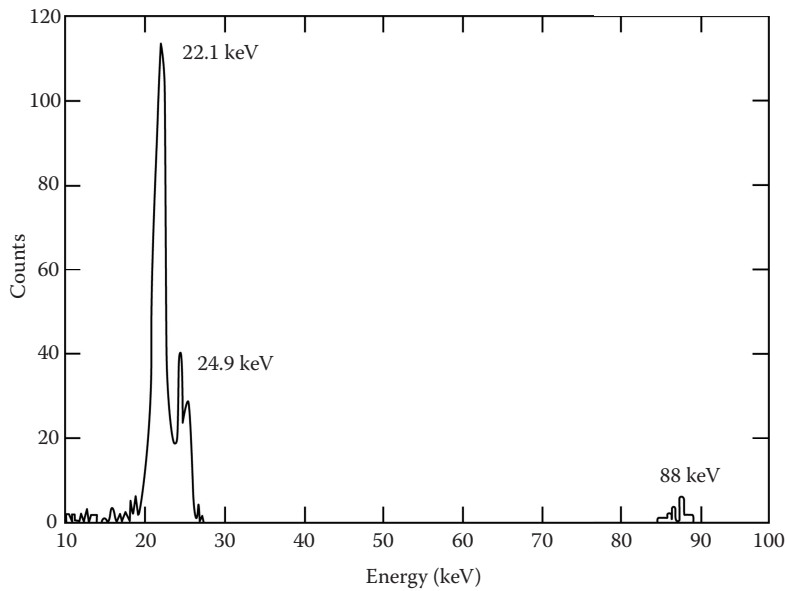


FIGURE 16.1 Emission spectrum from ^{109}Cd as recorded with a SiLi detector.

resulting in convenient irradiance and reasonable service lifetime. We based our assay on attenuation of the 22.1 keV characteristic line.

We chose a lithium-drifted silicon detector. This is usually shortened to SiLi detector and pronounced “silly.” SiLi detectors tally energy deposited by x-ray interactions in the SiLi material (Knoll 2000). This permits the cleanest transmission measurement possible. Scattered x-rays lose some energy and generally deposit less energy in the detector than pure transmitted x-rays. These low energy scattered photon counts are rejected.

This characterization system had to process several thousand sheets per month to accommodate manufacturing schedules. This required implementation of a computer-controlled translation stage and data acquisition system.

Having determined the total areal density and x-ray attenuation of the sheets, we had two equations and two unknowns. We could solve for the areal densities of the constituent ingredients as follows.

Let A_m and A_p be the areal density of metal and plastic, respectively. Also, let μ_m^m and μ_m^p be the respective mass attenuation coefficients. The measured transmission, ψ , is given by

$$\psi = e^{(-A_m \mu_m^m)} \times e^{(-A_p \mu_m^p)}, \quad (16.1)$$

or

$$\ln \psi = A_m \mu_m^m - A_p \mu_m^p$$

We also know that

$$A_m + A_p = B, \quad (16.2)$$

where B is the total areal density of the sheet, obtained by measuring the weight and area. Solving Equation 16.2 for A_p and substituting into Equation 16.1 gives

$$\ln \Psi = A_m \mu_m^m - [B - A_m] \mu_m^p, \quad (16.3)$$

and solving for A_m yields

$$A_m = \frac{\ln \Psi + B \mu_m^p}{\mu_m^p - \mu_m^m}. \quad (16.4)$$

The precision of this system is limited only by counting statistics. The operator is free to count longer or repeatedly to improve precision at the cost of throughput. Accuracy is primarily determined by the accuracy of the theoretical attenuation coefficient employed for the heavy element. This is generally good to better than 1%. We separately removed whole sheets from the process stream for destructive chemical analysis. This was mostly for quality control but occasionally resulted in some interesting conversations between analytical chemists and x-ray experts.

This x-ray gauge was so successful that we were asked to develop a similar machine that could analyze materials containing more than two known compounds. For this, we chose to employ a Cr-anode x-ray tube for the source. By using Cr, we avoided having anode characteristic lines (Cr K-lines are at 5.41 and 5.95 keV) near absorption edges of elements we wished to analyze. We used the continuum portion of the Cr anode output spectrum.

We achieved energy discrimination with a SiLi detector. Because the count rate for the detector is limited to a few thousand counts per second, the appropriate source was low power (50 kV, 100 μ A). An example is given in a paper by Lewis et al. (1992) for analysis of a material consisting of Th, Pb, C, and H.

16.3 2D APPLICATIONS

Once a decision is made to employ x-ray imaging on an object, the usual course is to first perform radiography and then, if necessary, proceed to CT if the situation seems to warrant the extra effort and resources required by CT. We selected the applications presented in this section because they are familiar to us and we found them interesting.

16.3.1 X-RAY DIGITAL RADIOGRAPHY OF 40 MM GRENADES

The 40 mm grenade launcher can be mounted on a tripod, vehicle, or helicopters. Forty-eight grenades are linked together to form an 8-ft. belt and are fed through the launcher. The Navy identified potential low-propellant and or missing copper cup enclosures that would keep the propellant from transferring to the pressure chamber. Both conditions could cause the projectile not to exit the launcher before another round was fired. This could cause destruction of the launcher and risk to personnel.

The Navy developed a digital radiography (DR) system to inspect 100% of the suspected grenades. The system consisted of a 160 kV source and a scientific grade charge coupled device (CCD) camera optically coupled to a gadolinium oxysulfide (GOS) scintillator as the detector and a motion control system to advance the grenade belt between the source and the detector. The system was housed in a safe x-ray shielded structure. The CCD was used in time delayed integration (TDI) mode such that the transfer of charge from one column of the detector to the next was at the same rate as the belt was travelling through the system. This allowed for one DR image of each belt.

Software was developed to segment out the propelling charge area from the image and this was presented to the operator for inspection. A DR image of a single belt run through the x-ray radiography system is shown in [Figure 16.2](#). The top four rows show propellant levels that range from too much (top row) to too little (row 4). Two white lines barely visible in Figure 16.2 are used to

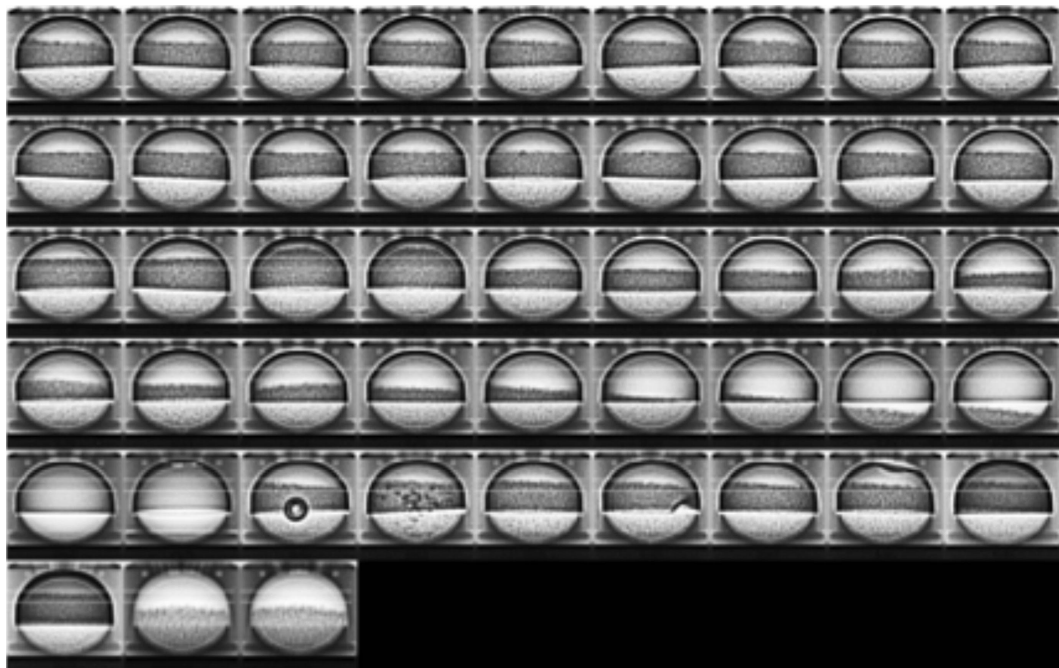


FIGURE 16.2 Representative DR image of a 40 mm grenade belt with each of the propelling charges segmented and presented to the inspector. The inspector reviews each propelling charge for low propellant, missing components, damaged components, and foreign material.

aid the inspector in determining the minimum and maximum acceptable propellant levels. Row 5 contains foreign material in the propelling charge (from left, image numbers 3 and 4) and damaged copper enclosure cups (from left, image numbers 6 and 8). Row 6 contains an image with two copper enclosure cups (from left, image number 1) and missing copper enclosure cups (from left, image numbers 2 and 3).

16.3.2 AUTOMATIC TRANSMISSION

DR and CT scanning in the MeV range enables inspections of large objects with highly dissimilar and dense high Z materials. Linacs accelerating electrons to 2–15 MeV are the dominant source for work at these energies (see Section 8.4.2.4). Scans of this type can provide remarkable sensitivity for the light low-density materials in an assembly containing heavy high-density material. Referring back to the fundamentals as discussed in Chapter 5, the total attenuation for materials using MeV energies is primarily based on the density of the material. The dominant attenuation mechanism is Compton scatter (see Figure 16.3), which is a function of electron density and is a linear function of mass density. Consequently, the attenuation differences among steel, aluminum, and plastic are much less than the differences observed at energies in the 100–200 keV range where the photoelectric effect (and therefore the atomic number) plays a significant role. Using MeV energies, you can penetrate the entire assembly, yet the differences among materials are still distinctive but much less than at lower energies. This has distinct advantages for imaging complex assemblies. This is part of the reason why scans from MeV energy systems are often used for reverse engineering and 3D geometry applications.

At the same time, the dominance of Compton-scatter-based attenuation has disadvantages. Every part of the object and the scanner is generating scattered irradiance that can be counted by the detector as transmission through the object—which will then be reconstructed into artifacts within the reconstructed volume. This complicates interpretation.

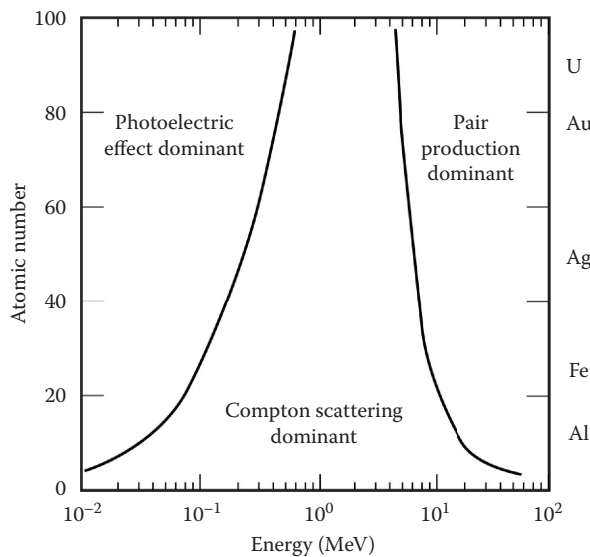


FIGURE 16.3 Plot showing that x-ray interaction process accounts for more than 50% of the interactions occurring as a function of x-ray energy and atomic number.

Two types of detection systems are in use across the different MeV inspection facilities: (1) area detectors and (2) highly collimated linear detector arrays. The two types of detector systems represent different approaches to handling the prevalence of scattered x-rays. Both approaches employ extensive collimation. For area detector systems, the majority of the collimation is on the source side of the object. And the materials around and behind the detector are kept to a minimum beyond what is required to shield detector electronics. For the linear-array systems, collimation is employed before and after the object to restrict the detected irradiance to *pencil-beam* rays through the object. Spatial resolution for area detector systems is dependent on the intrinsic properties of the detector and the spot size of the linac source. For LDA systems, the resolution is more dependent on the size of the collimated rays and how well the pre-and post-object collimation is aligned. The results are as expected: area detector systems can deliver high spatial resolution with less contrastive performance than LDA systems. This is primarily due to meager stopping power of the higher-resolution scintillators and to the uniform fog of scattered radiation. Scatter also makes it impossible to do quantitative determination of attenuation with area detectors at MeV energies. The increased contrastive performance (stopping power) and superior scatter rejection of the LDA systems enable scanning of larger assemblies than the area detector scanners but with longer data acquisition times for equal CT volume.

While there are differences in the details, either of the linac-based DR/CT scanning systems can perform quality inspections for a large range of complicated assemblies. Figure 16.4 contains two digital radiographs of an automobile transmission acquired with a flat-panel area detector. Notice the detail for the various sections of the transmission assembly.

16.3.3 DUAL-MEV RADIOGRAPHY FOR HIGH-Z MATERIAL DISCRIMINATION

The Department of Homeland Security (DHS), Domestic Nuclear Detection Office (DNDO), and Cargo Advanced Automated Radiography System (CAARS) program* aimed to utilize advanced radiographic systems to detect radiological and nuclear (R/N) threats. More about DNDO and the use of nondestructive characterization (NDC) to defend the US Homeland is given in Section 16.5.

* Work was also performed under the Joint Integrated Non-Intrusive Inspection (JINII) program.



FIGURE 16.4 Two 9 MV flat-panel area detector digital radiographic views of an automatic automobile transmission.

DNDO asked LLNL to determine whether dual-MeV radiography for W, Pb, and/or depleted (^{235}U) uranium (DU) is distinguishable from special nuclear materials (SNMs), i.e., highly enriched uranium (HEU) and/or weapons-grade Pu (WGPu). If any or all of them, W, Pb and/or DU, are not distinguishable from SNMs, they could be used as surrogates (sometimes referred to as simulants or mocks) of SNMs. This is useful for development and testing since use of SNMs is restricted. We also investigated if dual-MeV radiography can be used to distinguish high-atomic number, Z, from low-Z materials; the CAARS program defines high Z as $Z \geq 72$. This is to be expected; however, DNDO wanted more data to show that these two cases are correct.

To meet both of these requests, we performed several dual-MeV radiography experiments at LLNL. The sample matrix studied was designed to match the thickness of a cube of SNM with a nominal volume of 100 cm^3 . To take advantage of existing LLNL SNM manufacturing capabilities, the test was performed using cylindrical samples. The nominal DU cube dimension ($100^{1/3} = 4.64 \text{ cm}$) was used as the length of a WGPu cylinder. The diameter of the WGPu cylinder, 2.6 cm, was chosen to ensure that a single WGPu sample does not exceed the 400 g Category III limit on individual WGPu parts for the LLNL x-ray facility used to acquire the DR images.

Two sample sets of right circular cylinders were fabricated (Pincus et al. 2011). Each set contains three nuclear materials: DU, HEU, and WGPu, and four other metals: Fe, Sn, W, and Pb. Both sets have the same outer diameter: 2.6 cm. The lengths of the two sets differ. Sample set 1 had sample cylinder lengths chosen such that the product of the density multiplied by length (ρy_ℓ or areal density) was equal for all samples in this set. Sample set 2 are machined to a cylinder length of 4.64 cm to match the nominal length of the WGPu samples.

Samples were placed in a crossed plate aluminum holder, sealed in a polyvinyl chloride bag, approximately 0.33 mm thick. A sketch and a photograph of the can configuration are shown in Figure 16.5. Each sample and bag was placed in a sealed steel paint can, approximately 0.23 mm thick, which is approved for transport of SNMs. The can has an inner diameter of 164 mm, inside height of 178 mm, and a volume of 3.76 L. The holder was designed to have *transmission windows* through the holder both longitudinally and laterally, for axial and radial measurements of the samples, respectively. Foam rubber spacers, placed at the top and bottom of the paint can, keep the holder in position inside the can. The position of the holder relative to the can was marked on the outside of the can.

X-ray radiography measurements were acquired at LLNL using a Varian M9 dual-energy Linatron at 5.4- and 9.6-MeV endpoint energies. Two detector systems were employed. The first was a Thales amorphous silicon (amSi) flat-panel area array (2D) detector with 127 μm detector element pitch. The second was a Varian linear (1D) detector array with a 4 mm detector element pitch. The source and LDA detector used are very similar to fielded cargo x-ray nonintrusive inspection (NII) systems that are used by Customs and Border Protection (CBP) to acquire radiographic images of cargo containers.

The sample paint cans were placed at the front of the amSi detector and measured one at a time. The characteristics and size of the LDA allowed us to place two paint cans, side by side, at a distance halfway between the source and the detector. Measurements were made with samples oriented so that the direction of beam travel is either in line with the cylindrical axis (0°), as shown on the left of Figure 16.6, or perpendicular to the cylindrical axis (90°), as shown on the right of Figure 16.6. Representative amSi DR images are shown in Figure 16.7. The LDA DR image data are more quantitative than the amSi detector image data, and we only show the LDA results here.

The ratio of the x-ray linear attenuation coefficient multiplied by the path length, μy_t , at 5.4 MeV, to μy_e at 9.6 MeV is a metric for atomic number-based discrimination of materials. The measured



FIGURE 16.5 Sketch (left) and photograph (right) of package containing sample and holder inside can. Note that the SNM samples needed to be wrapped in plastic, so all, even non SNM samples, were wrapped in plastic.

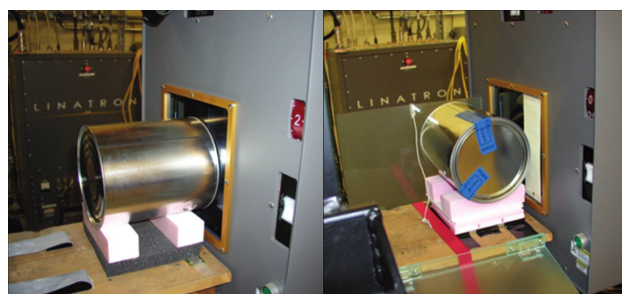


FIGURE 16.6 Paint cans positioned close to the linac x-ray source for axial or 0° (left) and radial or 90° (right) measurement of samples using the amSi flat-panel detector (not shown).

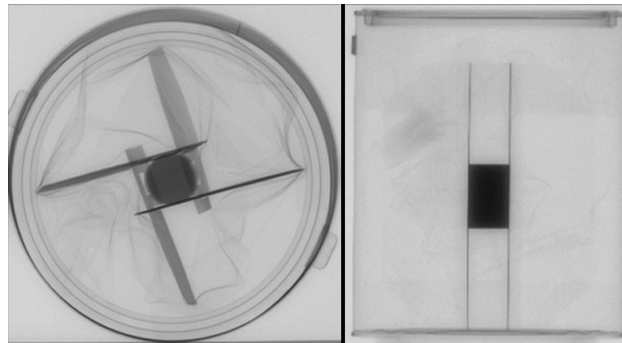


FIGURE 16.7 Axial (0° , left) and radial (90° , right) amSi flat-panel digital radiographs of samples in paint cans. Direction of beam travel is normal to image plane. Images produced with paint cans near the amSi panel detector.

TABLE 16.1

Measured and Computed LDA Ratio of Material $\mu\gamma_\ell$ Values of 5.4/9.6 MeV Endpoint Energies for Samples with Areal Density of 73.4 g/cm²

Material	Measured Ratio	Computed Ratio	Z
WGpu	1.059 ± 0.005	1.080	94
HEU	1.062 ± 0.004	1.080	92
DU	1.059 ± 0.005	1.081	92
Pb	1.060 ± 0.005	1.079	82
W	1.062 ± 0.005	1.081	74
Sn	1.097 ± 0.006	1.112	50
Fe	1.183 ± 0.008	1.187	26

ratios were compared with computed values based on LLNL photon cross-section data (Cullen et al. 1989) and LLNL developed models of x-ray detector characteristics (Schach von Wittenau et al. 2002). The measured and computed ratio values are presented in Table 16.1 and Figure 16.8. The LDA ratio values demonstrate that it is hard to distinguish W, Pb, and DU from SNM. It also shows the feasibility of using a threshold for the ratio to discriminate low-Z ($Z < 72$) from high-Z ($Z \geq 72$) materials (as defined by DNDO CAARS specification). In the case of our test system, a threshold ratio value of 1.08 would be suitable based on the measured results. Note the little difference for these materials in the lab without clutter. In the field, adding clutter (the cargo) makes the measurements much more difficult.

As expected, the results of this study revealed that W, Pb, and DU are valid surrogates for SNM in the CAARS Advanced Technology Demonstration (ATD) performance field tests of dual-MeV transmission radiography systems. Dual-MeV transmission measurements of W, Pb, and DU are nearly identical to SNM and are distinct from lower-Z materials, provided that the samples are matched to equal areal density. Results from an alternative method, using samples of equal thickness, showed sample discrimination by material density, rather than by atomic number (Z) (Pincus et al. 2011).

16.3.4 PHASE CONTRAST RADIOGRAPHY OF A DEUTERIUM–TRITIUM SOLID-LAYER SINGLE-SHELL FUSION TARGET

Inertial confinement fusion (ICF) and high-energy density physics (HEDP) research is being conducted at large laser facilities, such as the University of Rochester's Laboratory for Laser Energetics OMEGA facility and the LLNL's National Ignition Facility (NIF). At such facilities,

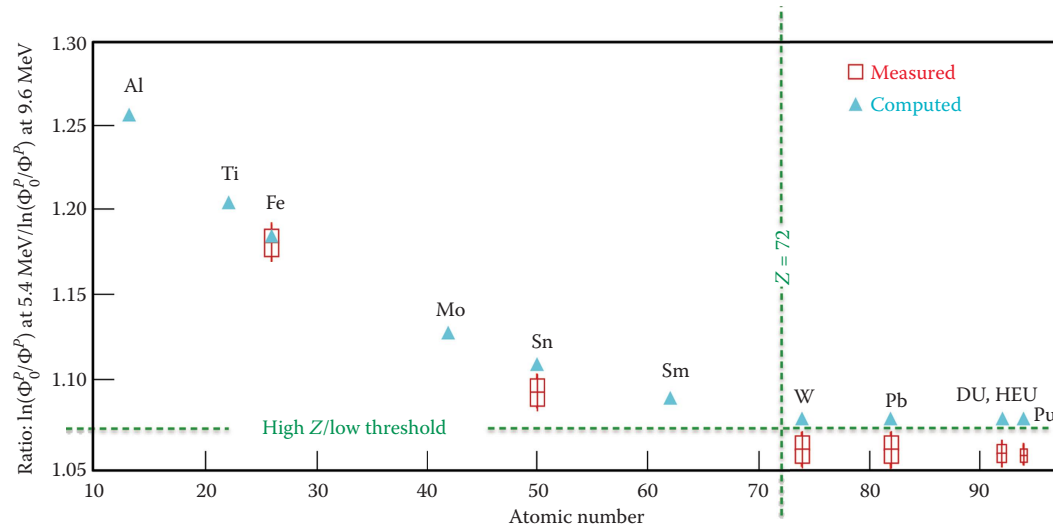


FIGURE 16.8 Ratio of material $\ln(\Phi_0^P/\Phi^P) = \mu_{\gamma_\ell}$ values of 5.4/9.6 MeV endpoint energy for a linac x-ray source and LDA, measured (red square) and computed (blue triangles) for set 1 (constant areal density) samples, oriented axially. Dotted green lines denote $Z \geq 72$ threshold for high- Z vs. low- Z materials (as defined by DNDL CAARS specification).

millimeter-sized targets with micrometer structures are studied in a variety of hydrodynamic, radiation transport, equation-of-state, ICF, and high-energy density experiments. The extreme temperatures and pressures achieved in these experiments make the results susceptible to imperfections in the fabricated targets (Lindl 1998; Haan et al. 2004). Targets include materials varying widely in composition ($\sim 3 < Z < \sim 82$), density (~ 0.03 to ~ 20 g/cm 3), geometry (planar to spherical), and embedded structures (joints to subassemblies). Fabricating these targets with structures to the tolerances required is a challenging engineering problem that the ICF (Sater et al. 1998) and HEDP (Hibbard et al. 2004) communities are currently undertaking. NDC provides a valuable tool in material selection, component inspection, and the final pre-shot assemblies' inspection (Martz and Albrecht 2003). X-rays are a key method used for the NDC of these targets.

NIF is the world's largest and most energetic laser facility. It also has a very precise and reproducible laser as well as a very large optical instrument. NIF is the size of a sports stadium—three football fields could fit inside. One hundred ninety-two lasers can be focused on a few-millimeters outer-diameter target. There are two competing deuterium-tritium (D-T) laser ICF target designs—single and double shells—that are being investigated. We discuss x-ray phase-contrast radiography characterization for single-shell targets in this section. In Section 16.4.9, we discuss x-ray absorption CT characterization for double-shell (DS) targets.

There are many other targets that are investigated in NIF. In Section 16.4.1, we provide the characterization results for a laser target called low-temperature Raleigh–Taylor target, referred to as LoRTT. This target is used to produce dynamic, shockless compression of materials for studying the properties of matter at high pressure and density, but at low temperature.

Absorption (the imaginary part of the refractive index; see Section 5.5) x-ray radiography or CT cannot be used for the single-shell targets because the opacity of the D-T is four orders of magnitude lower than that of the Be Cu-doped {Be(Cu)} single outer shell. However, the difference from vacuum in the real part of the refractive index for solid D-T at x-ray wavelengths is within a factor of 10 of that of Be(Cu) (Henke et al. 1993; Montgomery et al. 2004). The real part of the refractive index can be determined by phase-contrast enhanced x-ray imaging. Phase-contrast enhanced imaging methods have been demonstrated for other materials with similar characteristics (Cloetens et al. 1996; Nugent et al. 1996; Wilkins et al. 1996; Paganin and Nugent 1998; Gureyev et al. 1999;

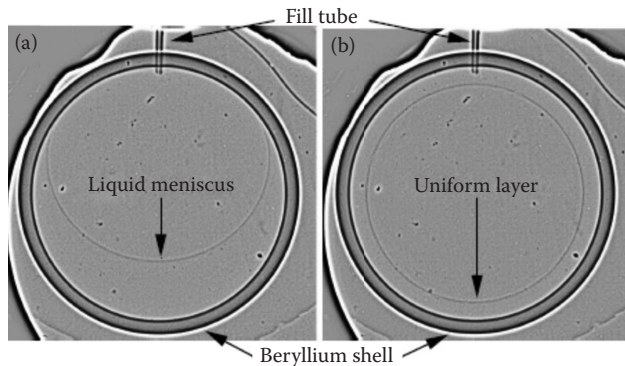


FIGURE 16.9 X-ray image with (a) liquid D-T and (b) solid D-T in the Be(Cu) shell. The image was processed with a band-pass filter to enhance the contrast of the D-T surfaces. In both cases, gravity is down. The liquid is slowly cooled to solid, and as the tritium beta decays, the solid D-T layer results in a uniformly thick spherical shape.

Allman et al. 2000; Suzuki et al. 2002; Kozioziemski et al. 2005a). Advances in phase-contrast enhanced x-ray imaging using laboratory x-ray sources make x-ray imaging of the solid D-T layer possible (Pogany et al. 1997; Gureyev and Wilkins 1998; Gbur et al. 2005).

The data acquired in the single-shell target were collected using an LLNL-designed and -built CT system called KCAT (Waters et al. 2004; Martz et al. 2005). This is a modular point projection x-ray CT microscope that can acquire DR and tomography data. KCAT employed a 150 kV tungsten anode Kevex sealed-tube x-ray source. The x-ray tube was operated at 60 kV voltage and 0.082 mA current. The x-ray spot size is between 10 and 20 μm full width at half-maximum (FWHM) given these operating parameters (Kozioziemski et al. 2005b).

The x-ray detector consists of an Industrial Quality, Inc. terbium oxide-doped scintillating glass plate that converts x-rays to visible light. The scintillator was optically coupled by a Nikon 60 mm Micro-Nikkor lens to a cooled 3072 \times 2048 Quantix CCD camera. The camera has 14 bit dynamic range and a detector pitch of 9 μm . The distances between the source to the center of the single-shell target, and the shell to the scintillator, were chosen consistent with the phase-contrast imaging theory. The source-to-shell distance was 70 ± 5 mm. The shell-to-scintillator distance was 205 ± 5 mm, giving a geometric magnification of 3.9 \times . The pixel size at the shell is 2.3 μm . X-ray images of D-T in a Be(Cu) shell that have been processed with a band-pass filter are given in Figure 16.9 (Kozioziemski et al. 2005b). The left image shows the Be(Cu) shell partially filled with liquid D-T. The right image shows solid D-T after the Be(Cu) shell was cooled to 19.3 K (0.4 K below the triple-point temperature of D-T) and held at a constant temperature for 4 h. In both cases, a light-to-dark transition inside the single-shell target as shown in Figure 16.9 indicates the inner D-T surface. The projected image through the spherical, solid D-T shell is circular in shape, as expected based on previous experiments with optically transparent shells. The exposure time for these images was 30 min. The system has been optimized over the years. Recent work is given by Koch et al. (2009).

16.4 3D APPLICATIONS

The 3D applications presented in this section range from very small (~ 1 mm) materials characterization and part inspection through automotive parts to a large (1 m sized) NASA ablator shield.

16.4.1 LoTRT TARGETS

LoTRT targets are used in a new laser-driven technique to produce dynamic, shockless compression of materials for studying the properties of matter at high pressure and density, but at low

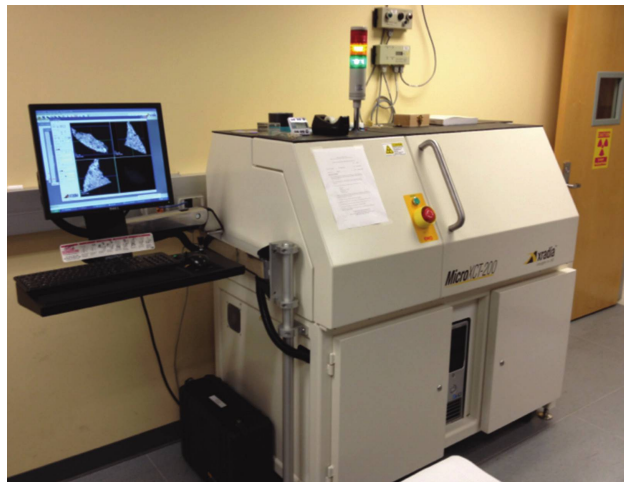


FIGURE 16.10 Photograph of the Xradia (now Zeiss) MicroXCT.

temperature (Edwards et al. 2004). This work is based on the conversion of kinetic energy into thermal pressure. This is applicable to planetary science, i.e., measurement of solid-state dynamics at ultrahigh strain rates relevant to meteor impact and crater formation studies, and for equation of state studies and interstellar dust dynamics.

A LoTRT target consists of a number of solid and hollow disks with various materials including a Au shield, a LiF window, an Al coating, a CH ablator, a Br-doped CH reservoir, and a gradient-density SU8 reservoir. The gradient-density SU8 reservoir was a newly developed subassembly component that was very difficult to fabricate and characterize (Aufderheide et al. 2007). The SU8 reservoir contains 60 layers of SU8 photoresist with density varying roughly from 0.2 to 1.2 g/cm³.

We employed an x-ray point-projection system developed by Xradia Inc. called MicroXCT. A photo of the MicroXCT is given in Figure 16.10 (XRADIAXCT 2015). The Xradia MicroXCT system at LLNL used a Hamamatsu tungsten-anode source with a nominal spot size of 5 μm at 4 W and a maximum potential of 150 kV. The detector is a 25 μm CsI scintillator with a microscope (10× and 20×) lens coupled to a 16-bit Andor CCD camera. The CCD chip is 2048 × 2048, with a detector-element pitch of 13.5 μm × 13.5 μm. It was operated at -50°C in these experiments. Source-to-object and object-to-detector distances of ~61 and ~14 mm, respectively, were employed resulting in a pixel pitch of 0.6 μm at the object center. To characterize the SU8 density gradient, both DR and CT were acquired with 100 kV potential and 0.04 mA current and data acquisition times of ~2 min per DR (or projections); 720 projections were acquired for CT image reconstruction (Brown and Martz 2006).

Due to the system setup, the DR (Figure 16.11) and CT (Figure 16.12) data contain x-ray refraction or phase-contrast effects (see Section 5.5.3) at each boundary as well as the conventional x-ray attenuation effects. X-ray phase effects are revealed in the images as bright and dark regions at each layer interface. For this application (unlike that of the D-T single shell target discussed in Section 16.3.4), the phase-contrast effects interfere with the x-ray attenuation data and make it difficult to measure the density gradient in the SU8 material. The SU8 reservoir was modeled with phase effects to better understand the gradient density in the SU8 material as discussed in Aufderheide et al. (2007).

16.4.2 INSPECTION OF JOINERY

Joining is often one of the final manufacturing steps. Whether joining is done by welding, brazing, gluing, or diffusing, it is one of the most difficult manufacturing steps to perform well and is often the point at which failure begins. This leads to the need to inspect joinery with care.

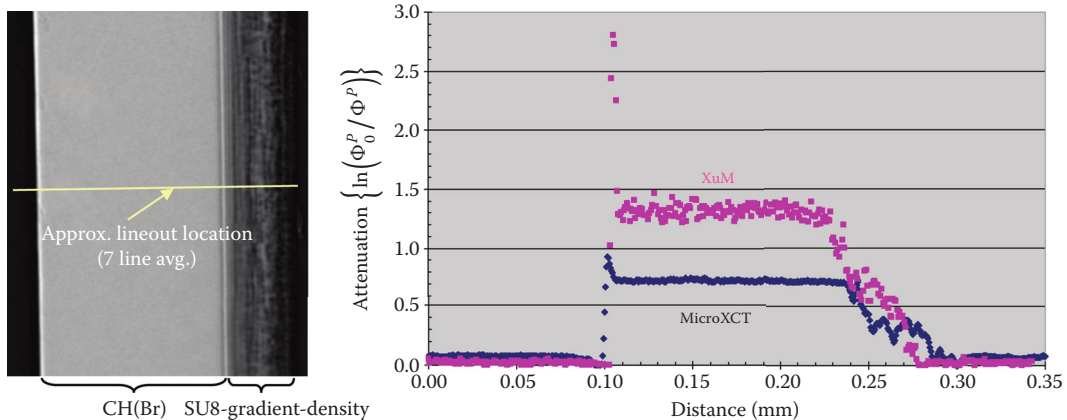


FIGURE 16.11 Representative MicroXCT attenuation DR (left) and profiles (right blue data points) of the CH(Br) and SU8-gradient-density reservoirs. The magenta data points are from the XuM. XuM is an x-ray ultra-microscopy system developed by XRT Limited.

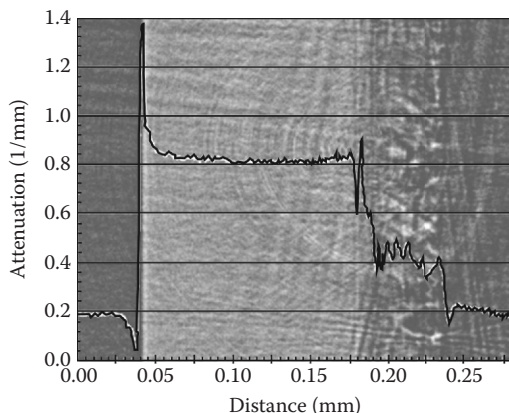


FIGURE 16.12 CH(Br) and SU8-gradient-density reservoirs MicroXCT CT x,y cross section with a 1D profile overlay.

16.4.2.1 Metal Weldment

Modern auto and aircraft manufacturing involves many types of fabrication and joining techniques. Inspecting the results of these processes is currently performed with a variety of modalities including ultrasonics, infrared, as well as x-rays. Inspection criteria for weldments vary by the specific application. The application of *automated defect recognition* covered in Section 15.6 is an example where 2D DR was used to detect voids in the welded region of titanium tubes.

Another configuration that can recommend x-rays is the case of a weld performed in a layered assembly. In this instance, access to the weldment is limited making ultrasound, dye penetrant, and eddy current techniques not applicable. Figure 16.13 shows an example of a component that is uniquely appropriate for CT-based weld inspection. Only a single cross-sectional slice is needed to evaluate weld integrity.

Notice the void space (dark partial ring) in the CT slice at this particular weld location. One additional feature of the CT reconstruction is the ability to quantify the void volume. In this case, the object is several inches in diameter, and the scan was performed with a 9 MV linac source. The object was placed 4.6 m from the source and a Thales amSi detector ~4.9 m from the source.

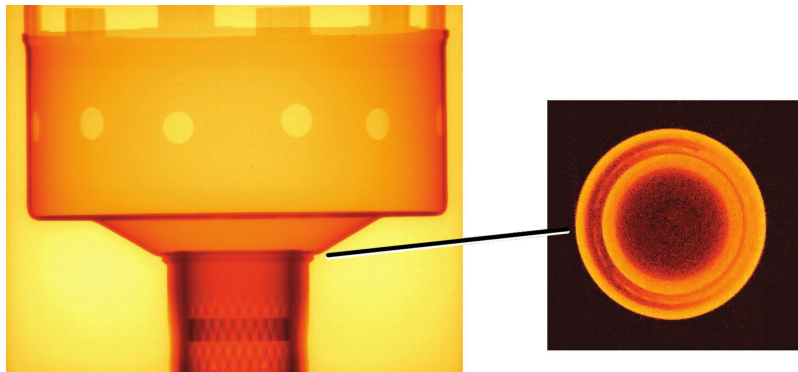


FIGURE 16.13 A 2D digital radiograph (left) and a single CT slice (right) through a weld region of an automobile transmission component. In the radiograph, the more opaque regions are of darker color. The color scale is reversed in the CT slice.

16.4.2.2 Stardust Reentry Capsule Bond

Welds are but one means for joining two different components of an assembly. In some cases, the joining process is performed with an adhesive. The Stardust reentry capsule is a NASA vehicle for reentry into the Earth's atmosphere from space (McNamara et al. 2010). The ablator heat shield is a subassembly that is sacrificed during reentry to protect the remainder of the Stardust reentry capsule. The different components of the Stardust ablator shield are joined by means of an adhesive. CT was used in this case to inspect the properties of the adhesive layer. Photographs of the Stardust capsule are presented in [Figure 16.14](#). CT slices of the capsule are shown in [Figure 16.15](#) with layers identified.

By extracting layers of the material according to measured contours, we isolated the adhesive bond layer from the rest of the CT inspection volume. [Figure 16.16](#) presents an interior contour extracted from the reconstructed volume of the ablator shield showing just the region constituting the bond between the layers.

Notice the pattern of incomplete adhesive fill (dark area) shown in the image of [Figure 16.16](#) extracted from the CT reconstructed volume. The Stardust ablator shield performed without incident for the effective lifetime of the unit, yet there is considerable void space in the adhesive. This information is applicable to the criteria used to evaluate current bonding techniques. Notice the hole toward the top of the image, a place where a destructive sample was taken from the shield. By pure chance, destructive analysis of the cutout region revealed a continuous fill of adhesive. Without CT, the conclusions drawn from this sample would be to reject parts that do not have a continuous fill of adhesive. From the CT result, it is clear that complete fill is not required for adequate performance of the shield.

16.4.3 AVIATION SAFETY: DR AND CT OF PITOT TUBES

Recent events in commercial airplane operation resulted in concern regarding the integrity of *pitot tubes*. This resulted in inspection and reinspection of these sensors. [Figure 16.17](#) presents two selected attenuation radiographs (of 760 taken for CT) of one of the tubes we inspected. Notice the darker features (crack) in the region of the inner tube radius. Also, realize that the crack was first found using CT, and then the appropriate DR was identified. A radiograph or two would not likely capture the view in which these cracks are apparent. This region is the focus of this inspection, especially the material in the inner tube. [Figure 16.18](#) contains two cross-sectional CT slices through this region showing the extent of the cracking in the inner tube. [Figure 16.19](#) contains two shell extractions from the 3D CT reconstruction. These are extractions of the data within the inner tube concentric with



FIGURE 16.14 (a) Men recovering the capsule after test. (b) The capsule on a rotary table in position for CT at Johnson Space Center in Houston, Texas.

the outer surface of the inner tube. The two extractions are at slightly different radii. Notice the clear identification of the cracks in the upper right of these extractions from within the inner tube.

16.4.4 CHARACTERIZATION OF LX-17 HIGH EXPLOSIVE

As covered in [Sections 16.5.1](#) and [16.5.2](#), dual-energy methods are used in nearly all fielded x-ray scanners for inspecting carry-on and, in a few scanners, checked-in baggage prior to air travel. However, multiple-energy techniques have other applications for investigating materials. In this application, we combine the unique x-ray choices available at synchrotron facilities with more commonplace and accessible laboratory-based x-ray tube source DR/CT systems.

Plastic-bonded explosives are a blend of explosive and plastic binder. At LLNL, detailed characterization of plastic-bonded high explosives (HEs) is an important inspection task. One such HE is LX-17: a compound made up of 91% TATB (triaminotrinitrobenzene— $C_6H_6N_6O_6$), the explosive, and 9% Kel-F ($C_8H_2C_{13}F_{11}$), the plastic binder, and some small amount of air (porosity). The overall density of LX-17 is close to 1.9 g/cm³. Measuring the physical properties for both bulk materials and for local regions is important for understanding the limits of HE performance in assemblies. Tensile strength as a function of the temperature of LX-17 varies with the local variation in density. HE performance is strongly influenced by local density, i.e., porosity.

A number of CT scans of 12.7 mm diameter cylinders of LX-17, acquired at various x-ray tube-based scanners at LLNL, showed a cell-like structure in the HE material as shown in [Figure 16.20](#). This cell-like structure resembles prills surrounded by walls or a foam-like structure. These data were acquired at an LLNL microfocus CT scanner called CCAT using a 225 kV W-anode source.

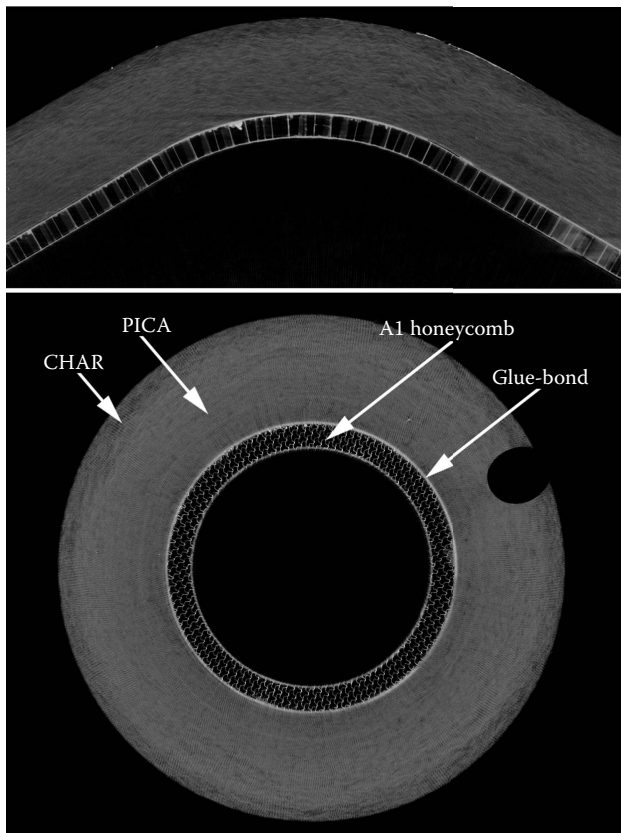


FIGURE 16.15 CT slices from the reconstructed volume of the Stardust ablative heat shield. The component layers are identified. PICA; phenolic impregnated carbon ablator. The outer char layer exhibits a slight darkening in the CT slices. NASA destructively sampled this shield by cutting the circular hole at 2 o'clock in the lower image.

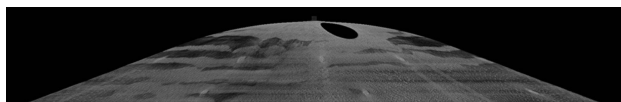


FIGURE 16.16 Extracted image of the adhesive used between the aluminum honeycomb and outer PICA material. The circular hole near the top is the location where NASA extracted a destructive sample (also observed in Figure 16.15).

Modern synchrotron radiation facilities usually enable a choice of a mono-energy or a way for selecting a specific portion of the broader energy spectrum for use in a particular inspection. The result is that one can acquire CT data at several discreet single (or monochromatic) energies and apply the methods of Chapter 11 given by Equations 11.7 through 11.9, thereby computing information about the material voxel-by-voxel. This is a powerful technique to apply to understanding the segregation of constituents in LX-17.

To investigate the compositional variation in LX-17, we scanned the 12.7 mm diameter cylindrical LX-17 samples at 17, 20, and 25 keV on the Lawrence Berkeley National Laboratory (LBNL or sometimes LBL) Advanced Light Source (ALS) MicroCT beamline 8.3.2. Results from three energies taken together enable the calculation of weight fraction for the two major components of LX-17: TATB and Kel-F. Figure 16.21 is from a scan acquired at the ALS using 20 keV. Figures 16.22 and 16.23 contain two processed images where we have segregated those voxels with Kel-F

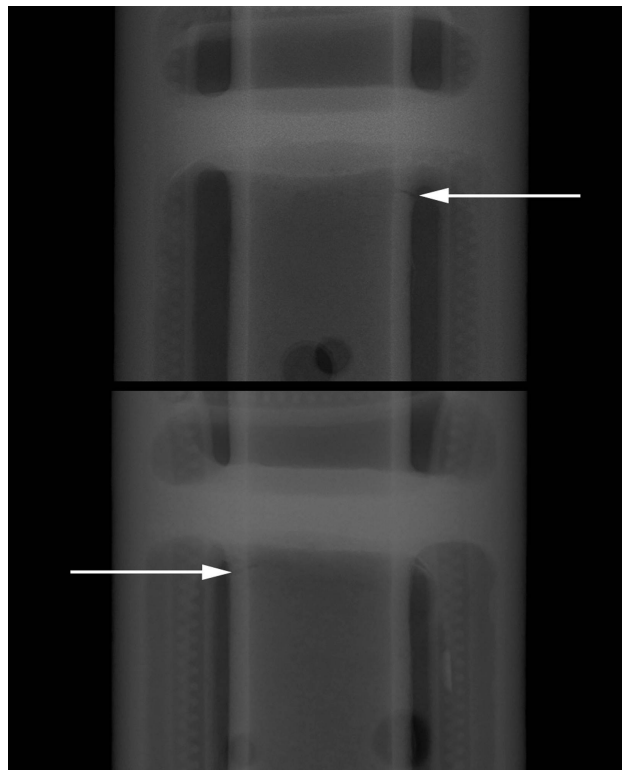


FIGURE 16.17 Two attenuation radiographs selected from a set taken for CT. These two views show a single crack in a pitot tube. Arrows identify the crack. The crack is not visible in radiographs at other angles. An attenuation radiograph is expressed as the natural logarithm of the ratio (detector response with no object/detector response with object present) or $\ln(\Phi_0^P/\Phi^P) = \mu y_c$.

weight fraction greater than 7.5% from those voxels with weight fraction less than 7.5%, respectively. Notice the greater concentration of Kel-F in the cell walls of the cell-like structure. In Figure 16.23, on the other hand, notice the prills in the cell-like structure. The highly attenuating cluster on the image in Figure 16.21 (white spot at 3 o'clock) is off the scale we used to calculate weight fractions. This cluster is neither Kel-F or TATB but probably a metallic impurity.

The results of these scans confirm the expectation that the cell-like structure of LX-17 is due to the segregation of Kel-F plastic binder into the cell walls. Kel-F is a thermoplastic that softens under increased temperature as occurs during pressing operations. We expect that formation of this cellular structure occurs during pressing. Since raising the temperature may have introduced the structure observed, we expect that additional changes could occur when LX-17 undergoes thermal cycling. Further, we expect the cellular distribution of Kel-F to result in high strength for the material when put under mechanical load and for the cell-like structure to remain intact.

CT results from three samples: a baseline sample, one subjected to load testing and thermal cycling, and one subjected to load only are given in Figure 16.24. Thermal cycling of the LX-17 sample impacted the distribution of the cell-like structure. Load cycling decreased the overall x-ray attenuation of the samples as revealed in Figure 16.25. Combined load and thermal cycling has a slightly larger effect. Careful inspection of Figure 16.24 reveals that the diameter of the specimen at the midpoint of length is increased in specimens that have been thermally and/or load cycled.

We found a few highly attenuating clusters in every sample we scanned. One is apparent in Figure 16.21 that is located at the 3 o'clock position near the outside. Using the techniques described in Sections 15.3.1.1 and 15.3.1.2, we scanned a number of samples at a tube potential of 100 kV with

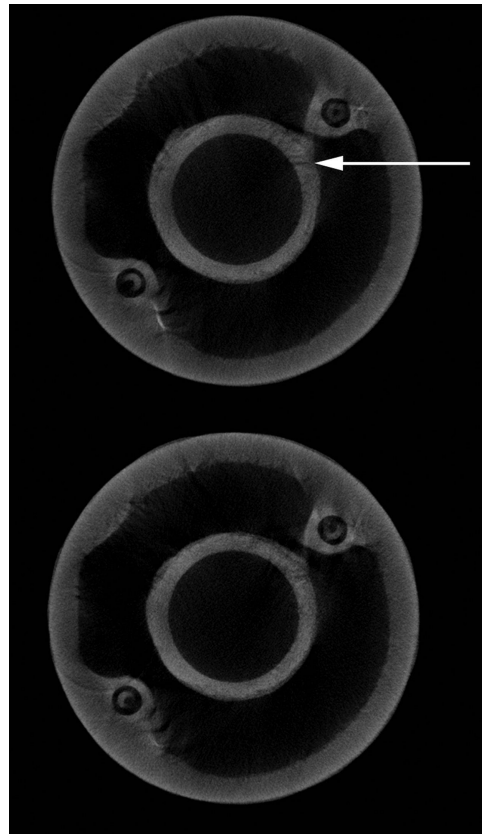


FIGURE 16.18 CT images through the pitot tube in Figure 16.17. These slices are at different heights. The crack is at the location shown in the top slice. The lower CT image or slice is at a location where the crack is very subtle.

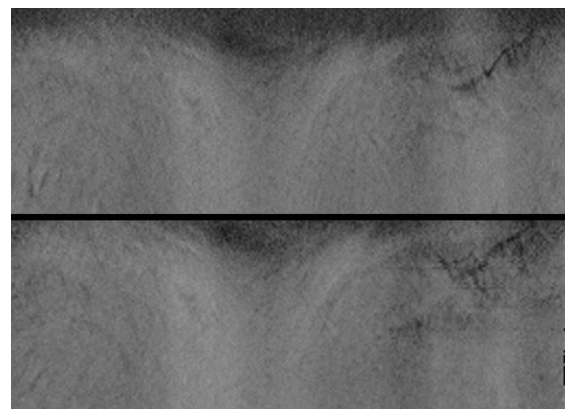


FIGURE 16.19 Two shell extractions of the cracked inner pitot tube. These shells follow the surface of the tube at different radii. The crack is evident at the upper right in both extracted images.

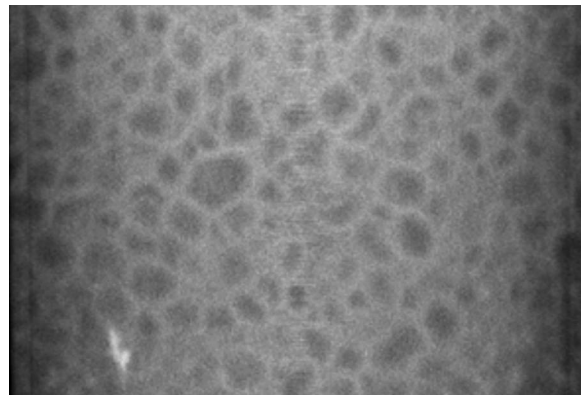


FIGURE 16.20 Vertical CT slice of a 12.7 mm diameter LX-17 pellet from the CCAT scanner at LLNL. Note the *prill* structure—nearly spherical particles such as those made by solidifying droplets while falling.

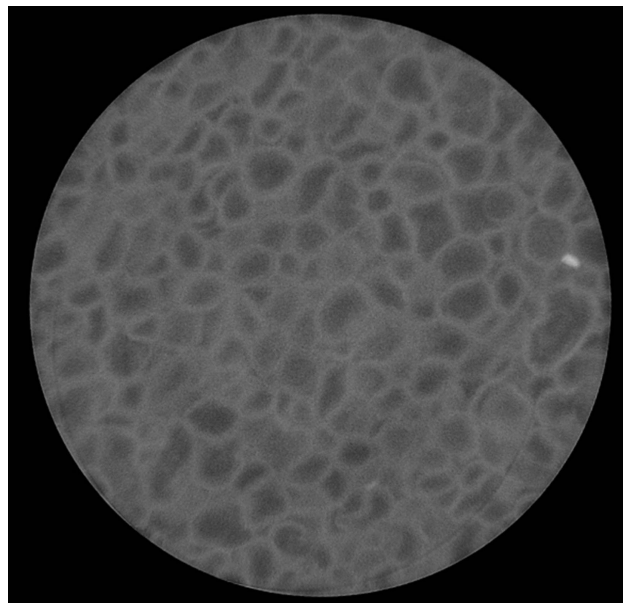


FIGURE 16.21 20-keV cross-sectional CT slice from the same LX-17 pellet as shown in Figure 16.20. Note similar *prill* structure as shown in Figure 16.20. (Data taken at the LBL Advanced Light Source [ALS].)

2 mm of Al filtration and 130 kV with 1 mm of Cu filtration. When combined, the data can be sorted into two groups: those with very high attenuation (probably metallic) and those with attenuation somewhat higher than Kel-F (probably nonmetallic).

In this application, monoenergetic CT scanning using three energies at ALS was used to confirm a hypothesis concerning LX-17, and this information was used to interpret scans from tube-spectra scanners where larger amounts of HE can be scanned using simpler x-ray equipment than ALS.

16.4.5 AUTOMOTIVE APPLICATIONS

The automotive industry was among the first to adopt widespread nondestructive testing (Zuuk 2014). The use of diagnostic radiography was minimal until World War II demanded higher performance

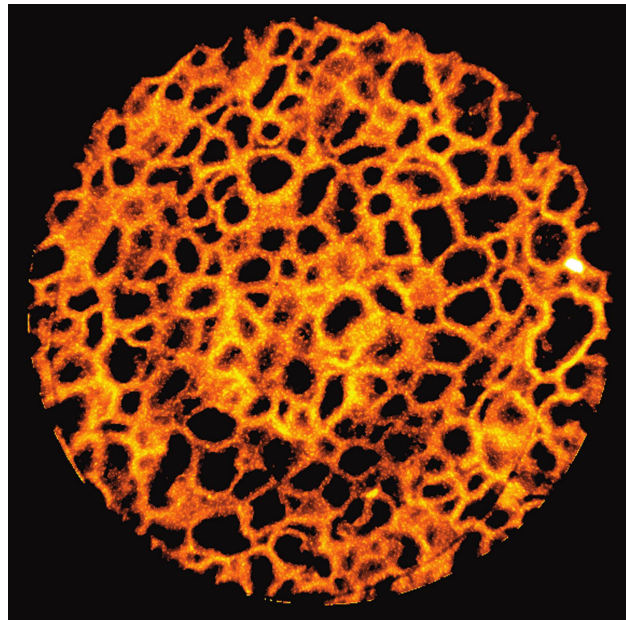


FIGURE 16.22 Cross-sectional CT slice with orange color depicting LX-17 voxels with Kel-F mass fraction greater than 7.5%. Data computed from ALS scans at 17, 20, and 25 keV.

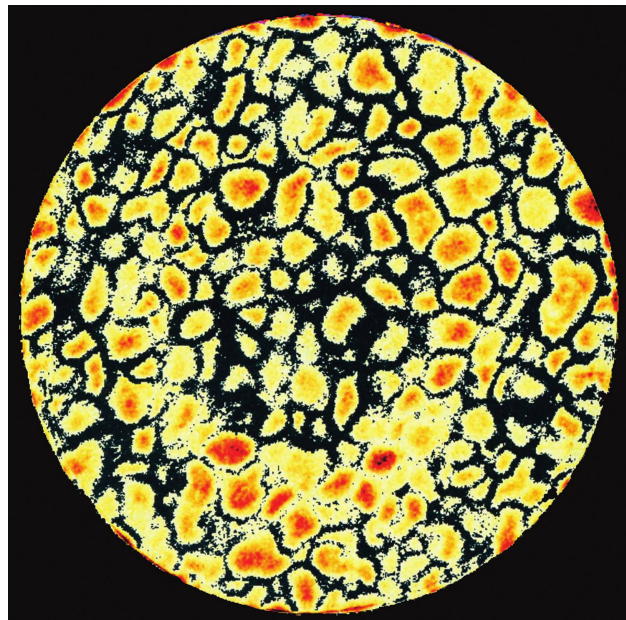


FIGURE 16.23 Cross-sectional CT slice of LX-17 pellet with voxels containing less than 7.5% Kel-F depicted as colored blobs referred to as prill.

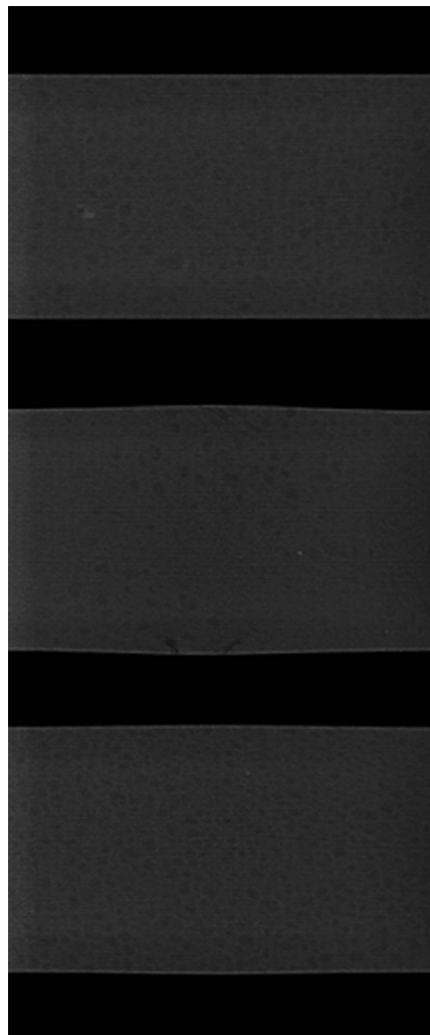


FIGURE 16.24 CT slices, using a common grayscale, along the axis of three cylindrical LX-17 pellets. The top pellet is for baseline comparison. The center pellet was subjected to both load and thermal cycling. The lower pellet was subjected to load only. Bulging at the midplane is apparent in the lower two images.

for military applications, and their use continues to this day as shown in [Sections 16.3.1](#) and [16.4.10](#). As recent events have shown, failure of a very minor component can cost a major automotive company billions of US dollars. This raises the incentive for good inspections. Some examples are given in the next few sections.

16.4.5.1 Metal Castings

Makers of components manufactured by metal casting in its different forms (pressure die casting is one example) often employ penetrating radiation for inspections. In general, x-ray inspections for metal castings can be classified into four types: (1) individual part inspection to ensure part integrity; (2) in connection with individual part inspections, some sampling of the entire part population for process monitoring and feedback; (3) detailed x-ray inspection to uncover different failure modes or in lieu of destructive disassembly (since you destroy the part); and (4) R&D inspections of part under load, or of the central core of new materials as a means to measure key constants and variables in models of materials and failure modes.

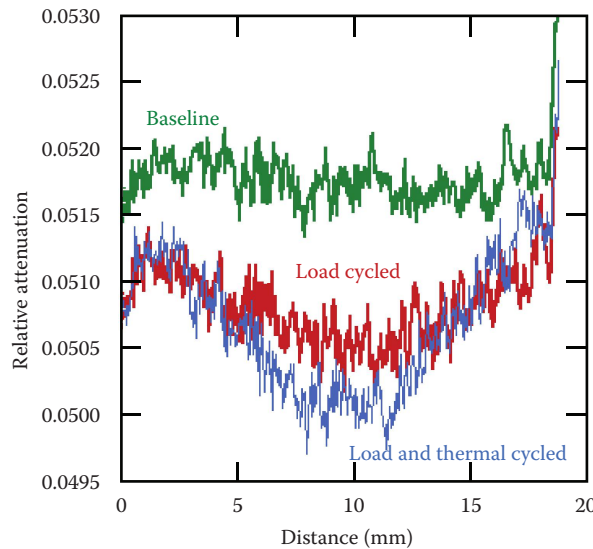


FIGURE 16.25 Relative attenuation from end to end for the three pellets shown in [Figure 16.24](#). The change in attenuation induced by load and temperature cycling at the pellet midplane is only about 2%, below the edge attenuation but is clearly above the voxel-to-voxel variation. The standard deviation of the data from the baseline pellet is 0.2%.

A large number of Al castings are inspected with DR to image the location of porosity and to ensure component integrity. For many inexpensive cast components, some porosity is acceptable, provided that the porosity is confined to certain locations in the volume. Inspections of Al cast parts with 1 to 2 in. chord lengths constituting the region of interest can be inspected with systems at near medical energies (60–100 keV but without the constraints of limiting dose).

In [Figure 16.26](#), a digital radiograph of a specific region within an Al casting and a transformed image of the same region are displayed to show how radiography can be used to detect the location

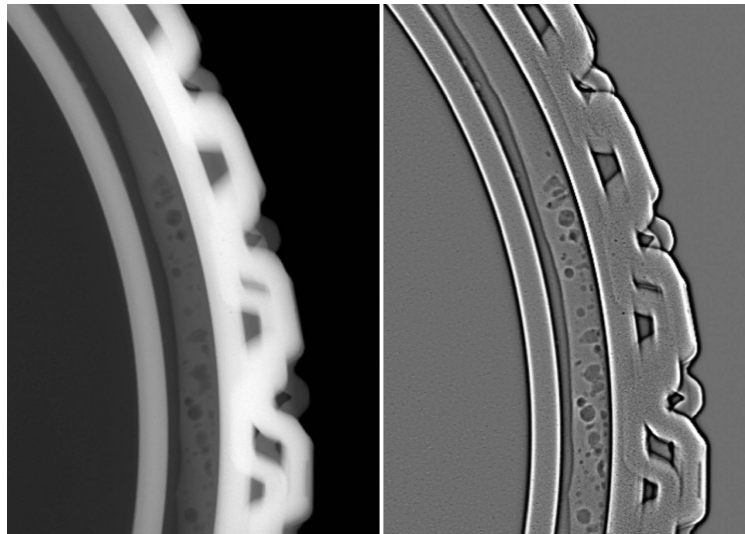


FIGURE 16.26 Digital radiograph (left) of a cast Al component containing porosity. The right image has been transformed by a variation of a Wallis transform to show that radiography can capture the needed information about the amount and location of porosity in this part.

and extent of porosity. Figure 16.27 contains a number of small Al cast parts all inspected with DR. Notice that the parts in the bottom locations of the digital radiograph are inspected with the overflow metal attached to the casting. With some casting techniques, porosity in the overflow metal is expected, even desired. Since porosity often occurs, the process is designed to capture it in the overflow. This porosity is evident in the processed image of [Figure 16.28](#). If porosity is not present in the overflow, then it is more likely in the casting.

While CT is more work (more views, more processing and reconstruction, and then more inspection data to analyze and review), it identifies the location and extent of porosity within the object in 3D. A digital radiograph of a cast Al fuel pump housing containing a significant void is shown in [Figure 16.29](#). In a part that is this complex it is nearly impossible to spot a void. A CT slice through the same fuel pump housing reveals locations of the porosity within that part is shown in [Figure 16.30](#). In some parts with this complexity, porosity is nearly impossible to pinpoint with any single radiographic view, and CT therefore is required.

Porosity in the overflow metal of an Al casting sometimes leaves a track of porosity back into the Al component. Full CT of a casting and the overflow metal can be applied to track porosity from the overflow metal back into the metal component. [Figure 16.31](#) contains selected CT images of a cast

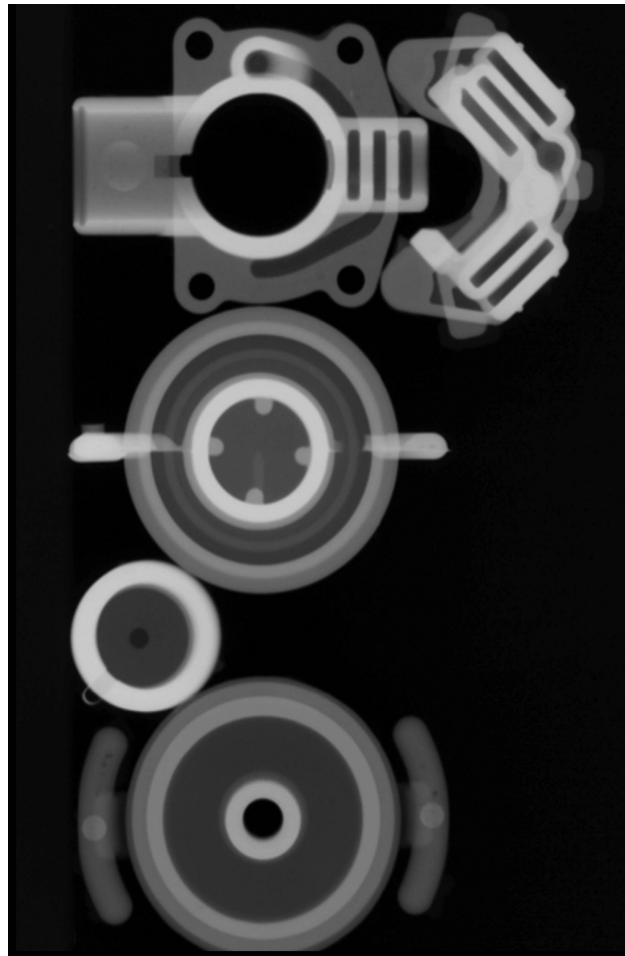


FIGURE 16.27 Digital radiograph of several small cast Al parts. Some have the overflow metal still attached to the part. This can provide a useful indication of the part quality.

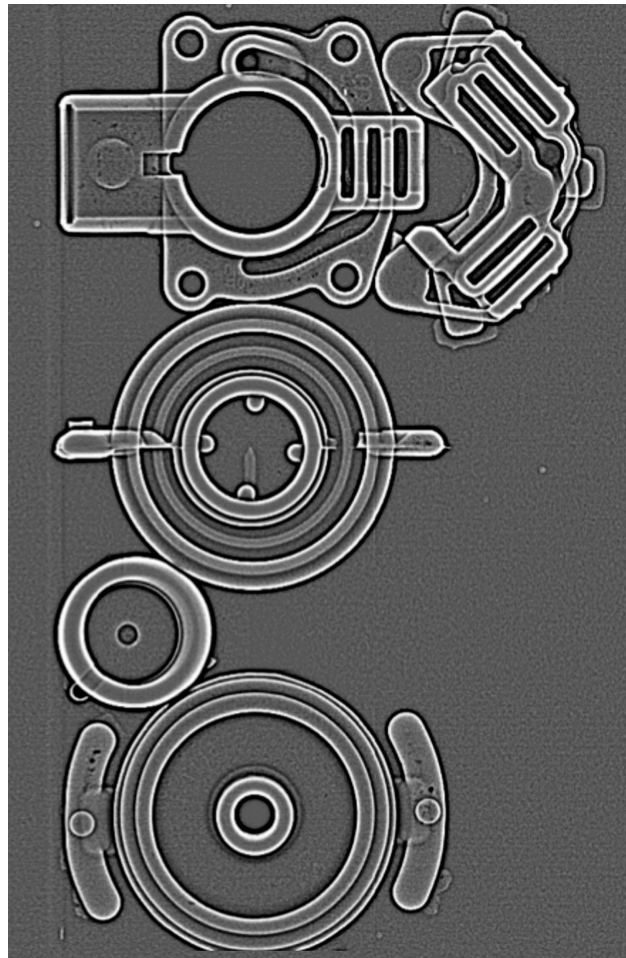


FIGURE 16.28 Digitally processed image derived from the radiograph shown in [Figure 16.27](#). This processing makes porosity and edges more apparent. This is especially helpful in the overflow regions of the casting.

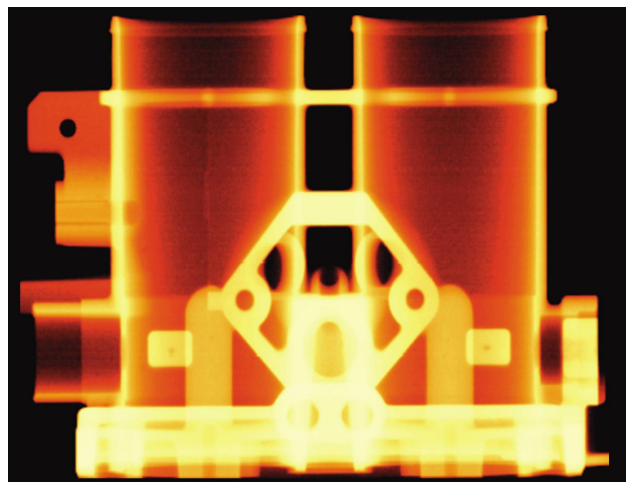


FIGURE 16.29 Digital radiograph of a cast Al fuel pump housing.

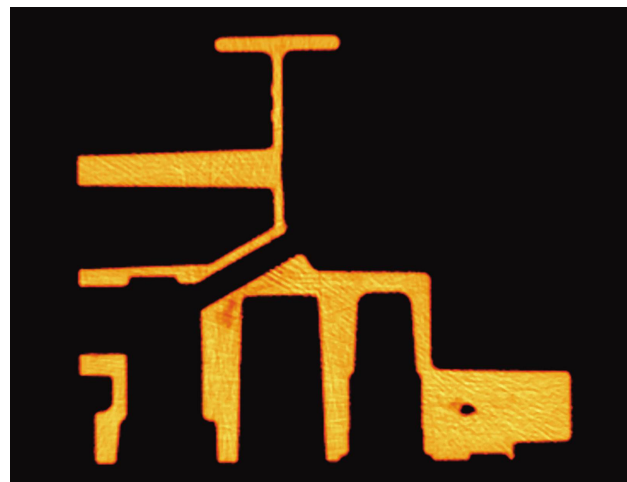


FIGURE 16.30 CT slice through a large internal void within the Al fuel pump housing depicted in Figure 16.29.

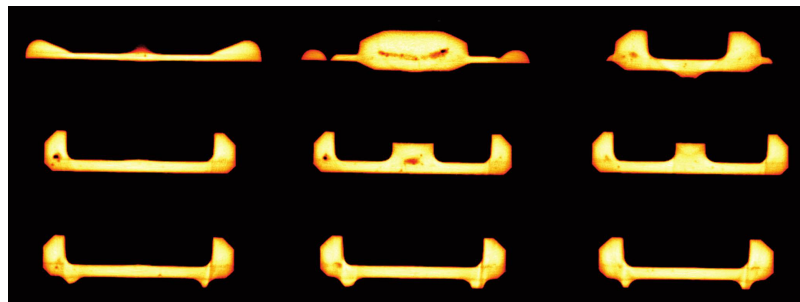


FIGURE 16.31 Selected CT slices through a cast Al part showing porosity.

Al part with porosity. Figure 16.32 plots data derived from the CT data set for this part. It shows relative porosity as a function of position along the length of the part.

For complicated castings, CT is more powerful than destructive analysis for pinning down the source of a failure. An example of this is a developmental cast Al fuel rail that leaked from an unexpected location. Figure 16.33 is a digital radiograph of the entire fuel rail. The part is too complicated to determine the leakage path from a radiograph. Destructive sectioning would risk

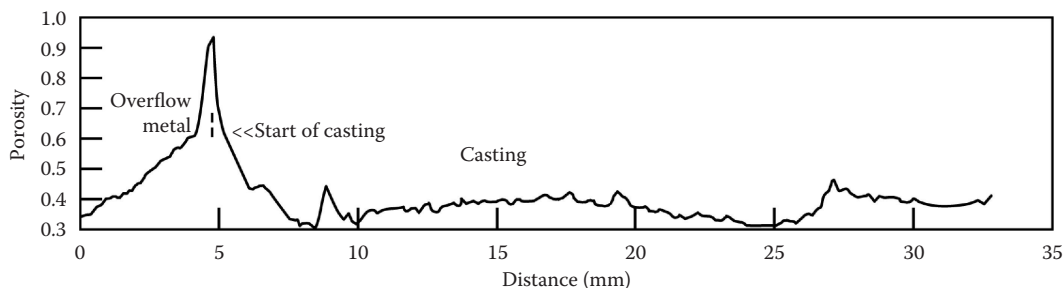


FIGURE 16.32 The plot presents fractional porosity along the length of the part from the CT data shown in Figure 16.31.

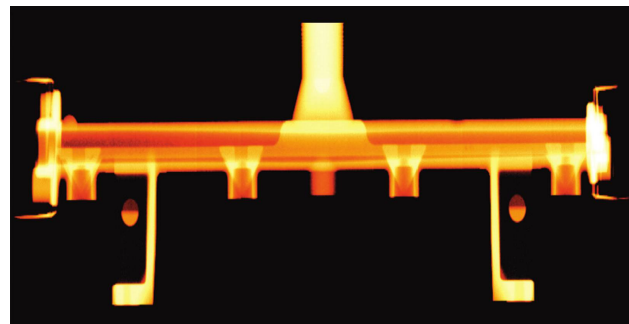


FIGURE 16.33 Digital radiograph of a fuel rail that leaks. The function of a fuel rail is to deliver fuel to injectors on engines employing fuel injection.

obscuring or missing the faulty region. Rather than destroying the part, we employed CT to image the entire rail.

A series of CT slices down the length of the fuel rail are shown in Figure 16.34. The middle slices in the casting reveal sponge porosity. Sponge porosity is a defect type that contains many pores that are too small to be revealed in these images but cause an overall decrease in mass density apparent with CT. The cylindrical passage through which fuel flows has a crack called *cold crack porosity*. CT of the entire unit showed how the sponge porosity connected to the cold cracks. This provided a continuous path for fuel that accounted for the leak. The defect geometry is consistent with the observation that leakage increased at higher pressure. Employing CT enables a better

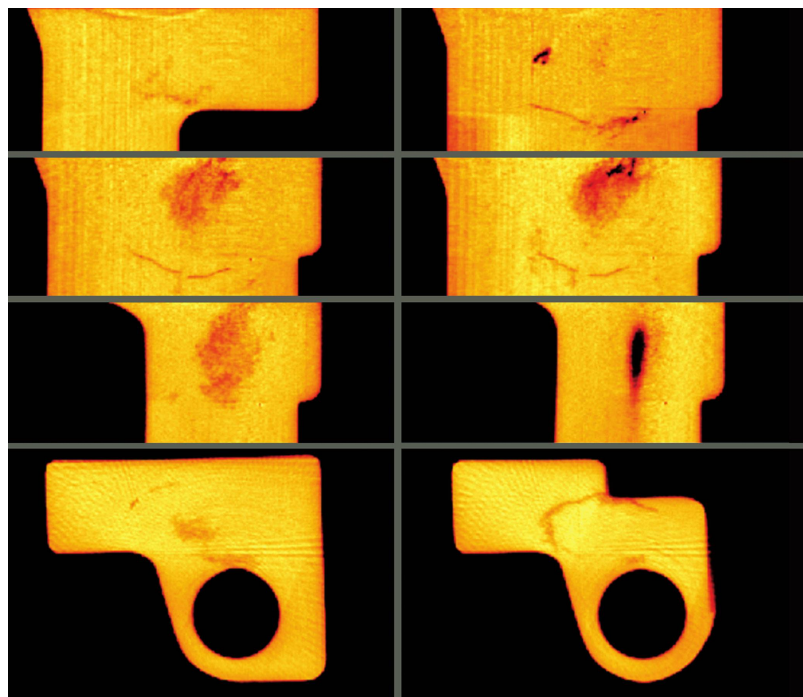


FIGURE 16.34 Selected CT slices from the leaking fuel rail depicted in Figure 16.33. Sponge porosity is revealed as darker orange regions in the the middle set of images. A crack is visible in the lower images. The CT data show that this crack extends from the fuel passage into the sponge porosity creating a leakage path.

targeted approach to subsequent destructive analysis. Analytical resources can be concentrated on regions that impact part performance. This might include metallurgical analysis and evaluation for impurities in the faulty regions.

16.4.5.2 Windshield Wiper Motor

Many automotive subsystems are complicated assemblies of dissimilar objects and materials configured under load with spring tension and/or torque required to support the functions of the assembly. Differing materials and subsystem complexity provide a rich opportunity for CT, e.g., a windshield wiper motor.

CT slices from a windshield wiper motor that includes powdered steel components enclosed in an Al housing are shown in Figure 16.35. We acquired these data with a W-anode tube at 400 kV potential. We applied substantial filtering (3 mm brass) and used a 10 mm thick IQI terbium oxide glass fiber scintillator plate that was lens-coupled to an Apogee AP6 camera with a KAF-1001 chip 1024 by 1024 detector elements with a 0.024 mm × 0.024 mm pixel pitch and 300,000 electrons full well CCD camera for detection. This resulted in an effective energy of ~250 keV. Under these conditions, Compton scattering is the dominant attenuation mechanism, and differences in attenuation are due principally to differences in density of the materials (see [Figure 16.3](#)).

With respect to Figure 16.35 notice the difference in attenuation in the powdered metal gear and teeth (light orange) as distinct from the denser steel (white) backing for the teeth. This is as expected, although the difference along the teeth was a bit surprising. Slices from the volume enable dimensional analysis of all internal pieces and cavities. Also, notice the modest porosity in the outer Al housing (dark orange). The porosity (black) in the housing is not an issue as the housing is completely functional.

16.4.5.3 Planetary Transmission Gear Assembly

The robust irradiance from a 9 MV linac can penetrate complicated high-value metal assemblies. We used the same system that we used for scanning the NASA rocket booster nozzle (see [Section 16.4.7.2](#)) to image a planetary transmission gear assembly and a turbomolecular vacuum pump (see [Section 16.4.6](#)). [Figure 16.36](#) contains a photograph of the planetary gear assembly along with two CT sections through the gear assembly. The diameter of this assembly is about 8 in.

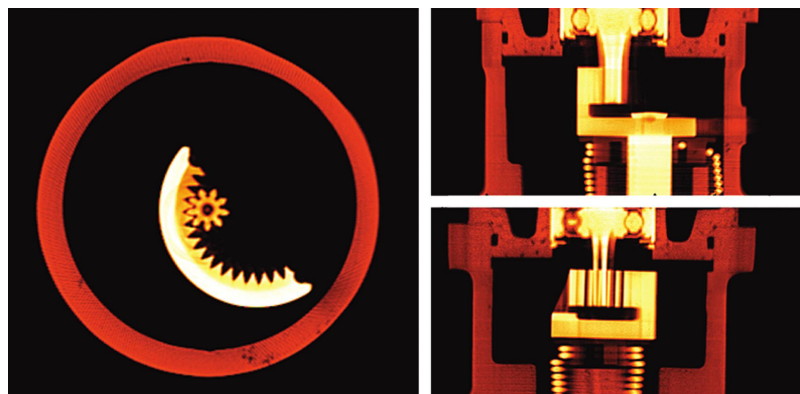


FIGURE 16.35 Three orthogonal CT slices through a windshield wiper motor made of steel (white) and aluminum (red-orange). Porosity (black) in the Al housing (dark orange) does not impair function. The CT scan was performed using radiographic conditions so that mass attenuation coefficients for steel and aluminum are quite similar.

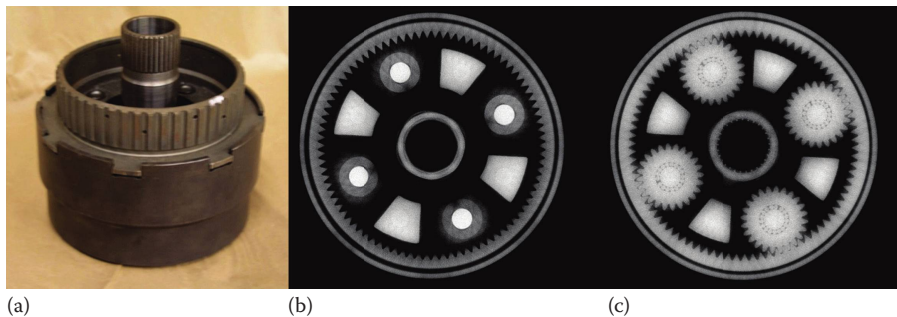


FIGURE 16.36 (a) Photo and (b and c) CT sections of an automotive transmission planetary gear assembly. Notice the detail. Even in this reproduction, it is quite easy to verify the number of balls and intact cage for each of the ball bearings on the planet gears.

16.4.5.4 Fuel Pump

The ability to capture precise dimensions of dissimilar parts in an assembly can be a powerful tool during development. Figure 16.37 contains two CT slices from a developmental automotive fuel pump demonstrating the imaging of the internal parts made of different materials. This object was scanned with the same techniques as the windshield wiper motor (see [Section 16.4.5.2](#)), 400 kV potential, W-anode, 3 mm brass filtration, and a 10 mm thick IQI glass fiber scintillator lens coupled to an Apogee AP6 CCD camera. In this case, we applied segmentation techniques to the left image in Figure 16.37 in order to generate drawings for the as-built structure of this part. Examples of the resulting segmented image and resulting edge enhanced image are presented in [Figure 16.38](#).

16.4.6 TURBOMOLECULAR VACUUM PUMP

Turbomolecular vacuum pumps are one of a class of assemblies that must be precisely assembled and are of high value. A photograph of a turbo pump along with a digital radiograph and an axial CT slice is shown in [Figure 16.39](#). This pump has an 8 in. diameter inlet. This type of pump is made of alternating rotor blades and stator blades. The rotor includes an axial spindle that supports the blades. The rotor must turn at an angular velocity that results in a blade velocity similar to molecular velocity in order for the pump to function. Rotation rates up to 90,000 revolutions per minute are employed (Wikipedia 2014). Such an assembly tolerates no assembly error.

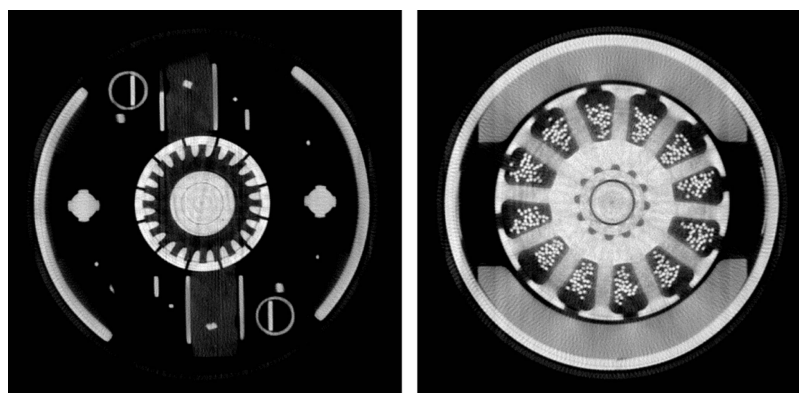


FIGURE 16.37 Two CT slices through a developmental fuel pump for an automotive application.

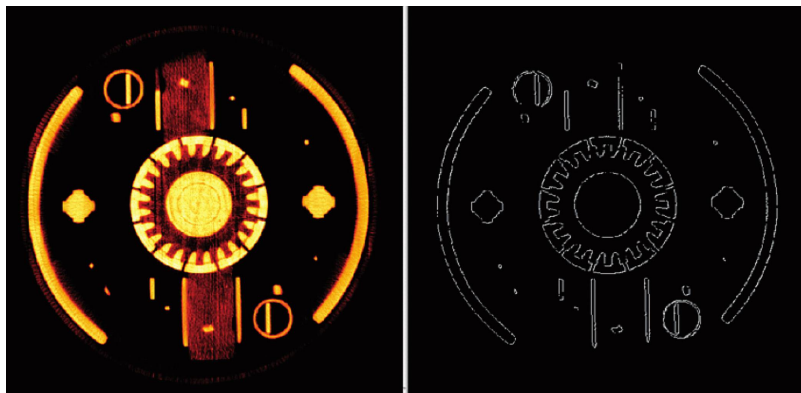


FIGURE 16.38 Two processed images derived from the left image of [Figure 16.37](#). These were segmented (left) then edge enhanced (right).

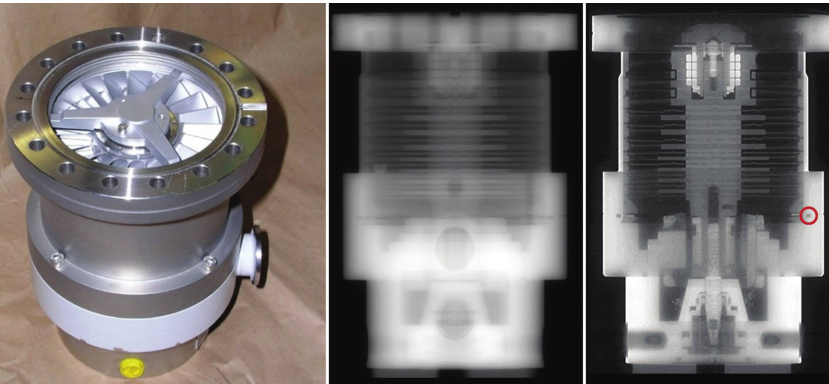


FIGURE 16.39 A photograph (left), digital radiograph (middle), and an axial CT slice (right) through a turbomolecular vacuum pump. Note the groove (encircled in CT slice) for the seal between upper and lower sections of the pump body.

16.4.7 NASA SPACE HARDWARE

The scope and variety of inspections performed by NASA and NASA contractors in support of space-related missions are large in every respect. Compared to automotive manufacturing, the number of parts and assemblies is modest, but since many parts are critical to support human space flight, or other expensive scientific data-gathering missions, the standards for part integrity are high, and the inspection regime is necessarily rigorous. X-ray inspections, DR, and CT are employed and have been employed on rocket motor components (nozzles, check-ball valves, explosive bolts), space shuttle parts (leading edge wings and T-seals, fuel cells, and fuel pumps), ablator shields and components, new materials that have been developed in the course of different missions, inspection of materials after return-from-flight, and International Space Station (ISS) parts and assemblies. In this section, we present only a few of the different inspection applications.

16.4.7.1 NASA Advanced Ablator Materials

Ablator heat shields are a necessary part of any spacecraft that transits through the atmosphere of a planet. NASA has developed and is developing a number of ablator shield materials (examples

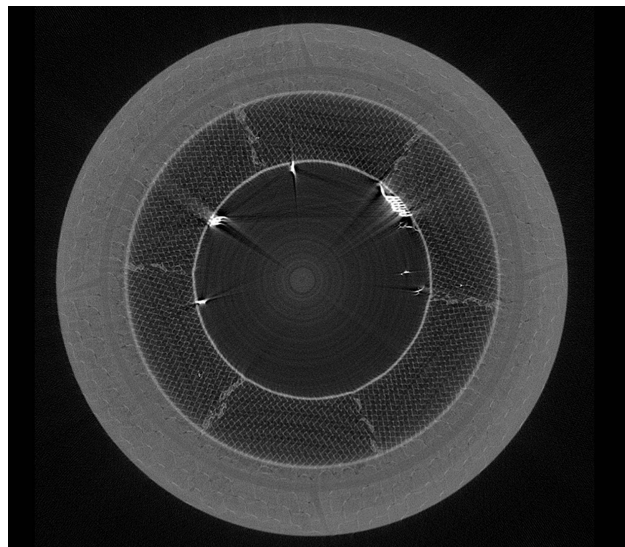


FIGURE 16.40 CT slice through the ISPT program aeroshell prior to thermal testing showing components in the TPS.

are AVCOAT* and PICA†) for various probes and spacecraft. Numerous CT scans of old and new ablator materials have been performed for materials analysis (Empey et al. 2012). As indicated in [Section 16.4.2.2](#), CT was used to inspect the Stardust shield (McNamara et al. 2010), which traveled in space for some 5 years and returned to earth with the fastest recorded reentry speed. A number of important measurements were performed including depth of char layer, mass loss, and detailed inspection of the adhesive or bond layer between the aluminum honeycomb and the outer PICA shield material.

Given the data obtained from Stardust, NASA has elected to use CT to capture the state of an ablator shield before a thermal test, then again post-test to determine differences. A 70° sphere-cone aeroshell test article, developed by the ARA Ablatives Laboratory‡ for the In-Space Propulsion Technology (ISPT) Program at NASA, was CT-scanned at LLNL before and after thermal testing at the Sandia National Laboratories (SNL) Solar Power Tower (National Solar Thermal Test Facility) in Albuquerque, New Mexico. We employed a Yxlon 450 kV x-ray source (1.5 mm spot) and a Perkin–Elmer 1621 2k × 2k amorphous silicon detector with 0.200 mm pixel size. To image the 1 m aeroshell with a 0.41 m (16 in.) detector, we used a tiled, half-scan geometry. Two tiles were enough to include over half of the object. We acquired 1440 views over 360° in two sequences. With the source spot for the Yxlon tube of 1.5 mm, we elected to place the object in a moderate magnification, a source-to-detector distance of 3048 mm, and an object-to-detector distance of 578 mm. We resampled the radiographs post-acquisition by a factor of 2 resulting in a pixel size on the detector of 0.400 mm and a voxel size of 0.324 mm at the object. A CT slice through the ISPT aeroshell showing components in the thermal protection system (TPS) is given in Figure 16.40.

The ISPT aeroshell was then tested at the Sandia National Labs Solar Power Tower in Albuquerque, New Mexico. [Figure 16.41](#) shows the article under test. After testing, the aeroshell was returned to LLNL for a repeat CT inspection identical to the pretest effort.

Comparing pre- and post-thermal test results for the aeroshell revealed expected and unexpected results. Vertical CT slices from the center of the pre- and post-thermal test volume are given in [Figures 16.42](#) and [16.43](#). [Figure 16.44](#) includes an extracted region around the pole of the aeroshell

* Ablative heat shield made using a fiberglass honeycomb that is filled with epoxy resin.

† Phenolic impregnated carbon ablator.

‡ ARA is a private company with the Ablative Laboratory located in Centennial, Colorado, USA.

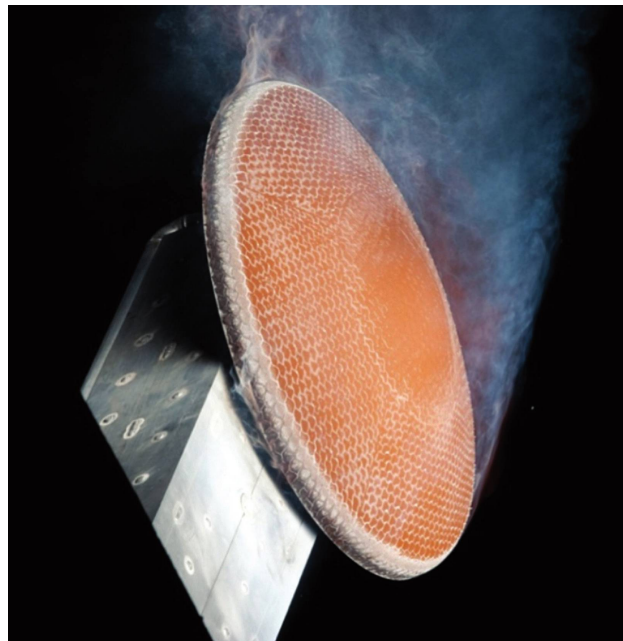


FIGURE 16.41 ISPT aeroshell under test at the SNL Solar Power Tower.

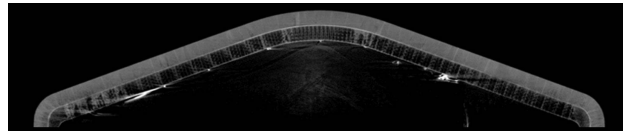


FIGURE 16.42 Pre-thermal test vertical CT slice along the axis of the ISPT aeroshell.

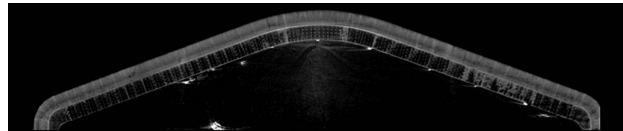


FIGURE 16.43 Post-thermal test vertical CT slice from the same location as Figure 16.42.

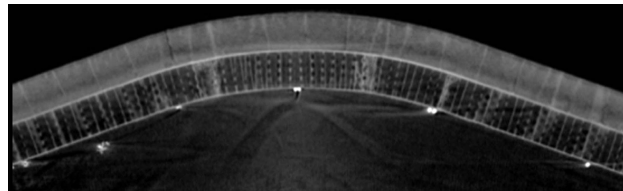


FIGURE 16.44 Polar region of Figure 16.43 shown with expanded scale to reveal more details.

for a close-up view of the slice from the post-test data. In the original data (but not well reproduced at this scale), it is possible to see a thin but relatively uniform char layer on the very outside of the aeroshell. In addition, there are a few cracks in the aeroshell, but this is likely due to idiosyncrasies of the Solar Power Tower heating. Also, notice a decrease in attenuation (dark gray band) in the outer material closer to the Al honeycomb. [Figure 16.45](#) compares pre- and post-thermal test cross-sectional slices through the region near the top of the aeroshell at the peak of the Al honeycomb.

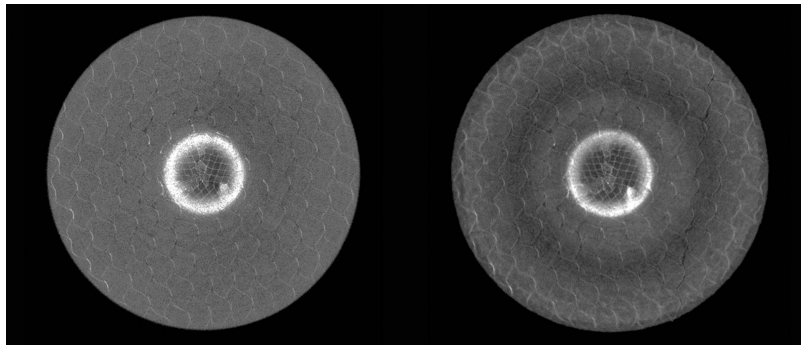


FIGURE 16.45 Cross-sectional CT slices using pre- (left) and post-thermal (right) test data from Figures 16.42 and 16.43, respectively. These slices are taken near the tip of the Al honeycomb. The honeycomb structure is clearly visible in the center of the two images. Note that the thermal test reduced x-ray attenuation (darker annular ring) compared to the pretest attenuation.

As expected, the *char* layer was thinner 1.5–3.0 mm for the current aeroshell than the char layer measured for the Stardust shield (McNamara et al. 2010), 8 mm. The thinner char layer probably is a result of the lower thermal loading in this test as compared to the Stardust shield. Also, the char layer in the recently fabricated unit is not symmetric around the aeroshell, but this is likely due to the experimental characteristics of the Sandia National Laboratory Solar Power Tower. One unexpected result in the post-test data is the decrease in density some 18 mm inward from the outside edge of the 1 m diameter aeroshell compared to the pre-test data. NASA is currently considering the mechanisms for this result.

16.4.7.2 NASA Rocket Booster Nozzle

Figure 16.46 contains results from a scan of a NASA rocket booster nozzle that had been sectioned in half. In this case, the nozzle fit within the field of view of a Thales amorphous silicon panel and was scanned with a 9 MV linac using rotation only. The CT inspection volume identifies a number of voids in the synthetic material around the nozzle’s metal housing and shows the density difference in the different components of the nozzle.

16.4.7.3 Diagnosis of Failure in Spare NASA Fuel Cell Pump

The NASA Space Shuttle Program procured a robust pool of spare parts to maintain shuttle operation throughout the lifetime of the shuttles. On-the-shelf aging was not considered a potential issue at the time the parts were procured. However, some off-the-shelf fuel cell pumps failed routine tests prior to use in the Space Shuttle. CT scanning of these units at 9 MV showed the issues to be voids and cracks in the aged epoxy filler resulting in failure of some of the wiring for the pump motor. Figures 16.47 and 16.48 include a number of CT slices showing the issues in the epoxy filler. In this case, the higher energy enabled superior imaging of the epoxy contained in an assembly of high-Z components.

16.4.8 EXPLORING THE LIMITS OF MeV IMAGING—9 MV AND 15 MV LINACS

To evaluate the limits for detecting changes and flaws in low-attenuation materials in assemblies with high-attenuation components, we conducted a series of experiments. We developed a challenging test object, conducted CT scanning using a 9 and a 15 MV linac with the same detector, and analyzed the results. The 9 MV linac is at LLNL, and the 15 MV linac is at the Hill Air Force Base. The object was a specially configured assembly of aluminum, steel, tungsten, lead, and polyethylene, named JAMDAN, a sketch of which is shown in Figure 16.49. The center of JAMDAN is a polyethylene insert. This insert consists of two hemicylinders that fit together. Figure 16.50 presents

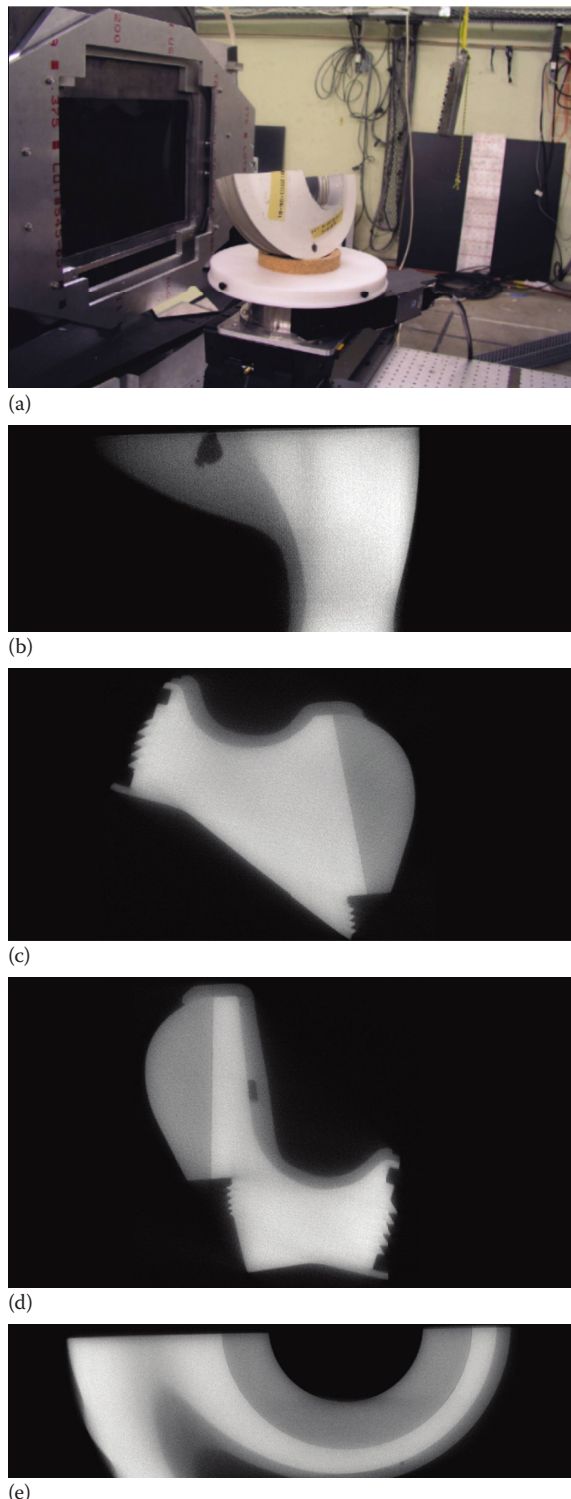


FIGURE 16.46 (a) At the top is a photograph of a sectioned NASA rocket booster nozzle in position for a CT scan at LLNL's 9 MV linac. (b–e) CT slices selected from the full-volume reconstructed data set. These CT slices reveal voids and the different materials of construction.

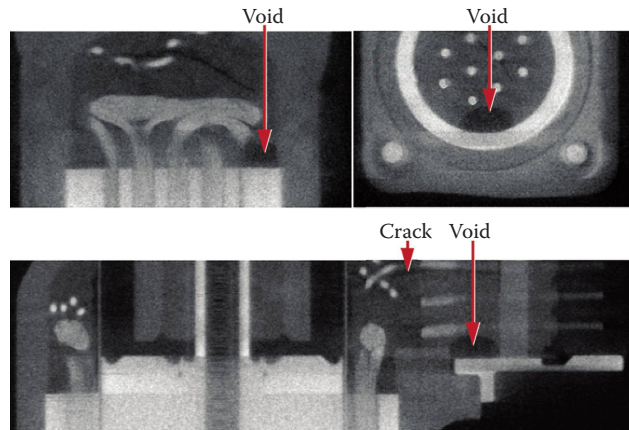


FIGURE 16.47 CT slices of a stored fuel cell pump showing voids and cracks in aged epoxy filler. These defects cause the pump to fail when used after prolonged storage.

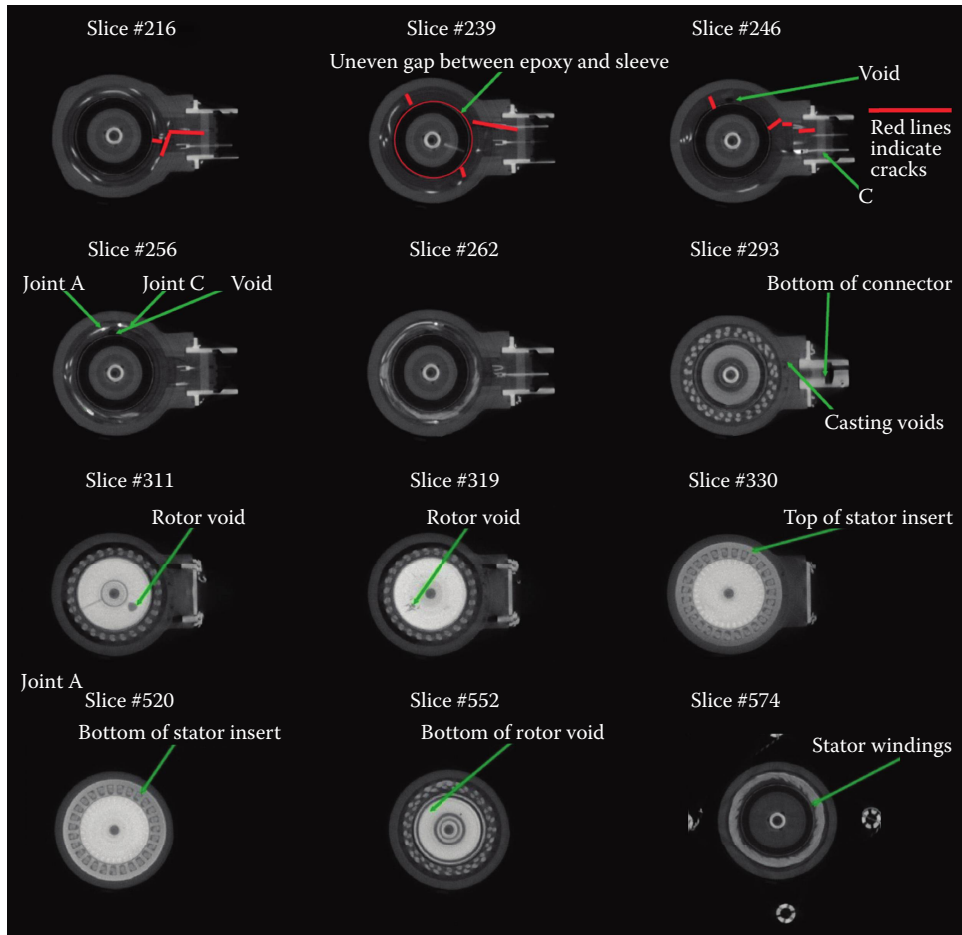


FIGURE 16.48 Multiple slices from a spare Space Shuttle fuel cell pump showing defects in a portion of the epoxy filler used in the pump. These defects cause the fuel cell pump to fail when used after prolonged storage.

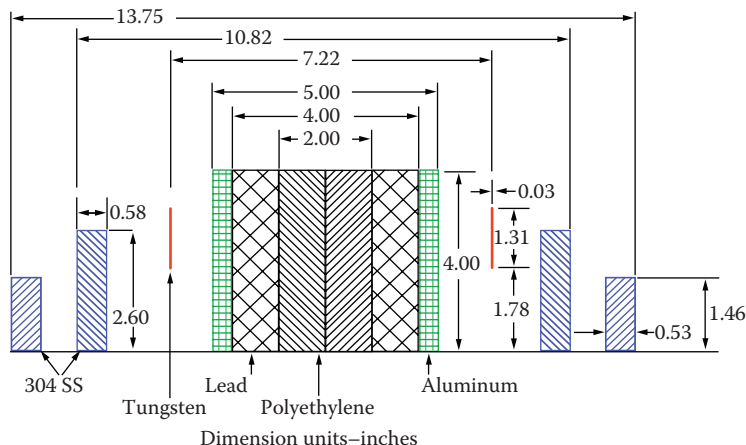


FIGURE 16.49 Test object, named JAMDAN, designed to test the limit of MV x-ray imaging of complex assemblies of heavy metals and light plastics.

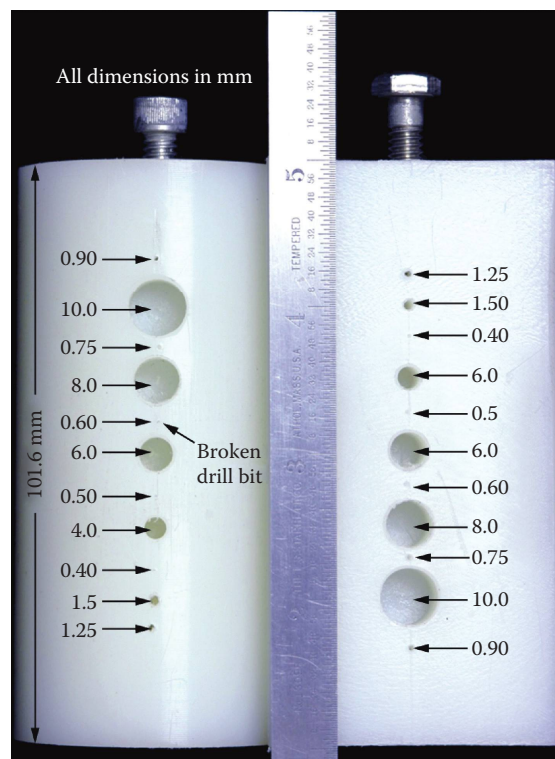


FIGURE 16.50 Photograph of the centermost portion of the test object called JAMDAN. This insert is made of two polyethylene hemicylinders, each with multiple drilled holes. The left hemicylinder in this photograph has holes on the curved surface. The right hemicylinder has holes on the planar surface. The two planar surfaces are placed in contact for insertion.

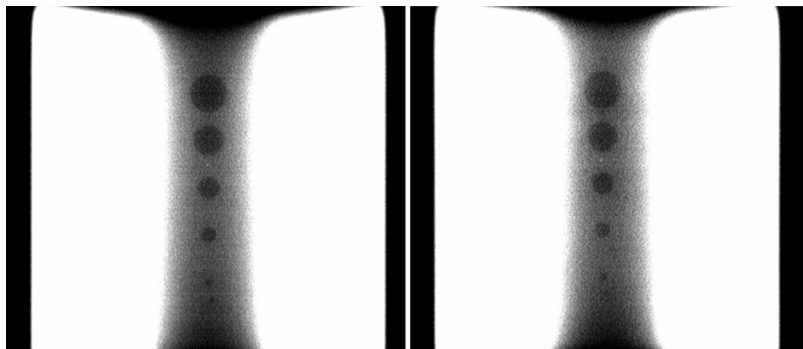


FIGURE 16.51 Comparison of 9 (left) and 15 MV (right) axial (parallel to, but off, axis) CT slices through the outside holes of the polyethylene inserts in JAMDAN.

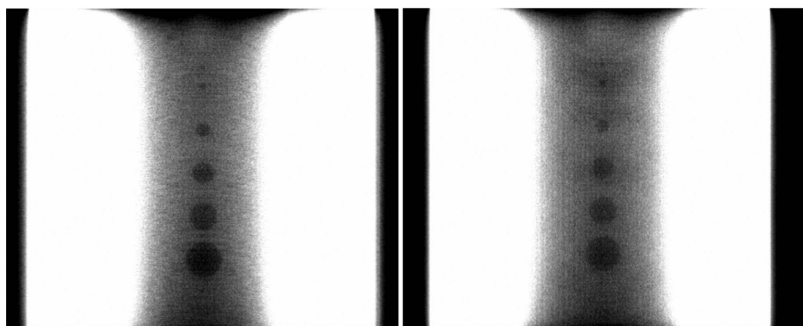


FIGURE 16.52 Comparison of 9 (left) and 15 MV (right) axial (slightly off axis) CT slices through the inside holes of the polyethylene inserts in JAMDAN.

a photograph of both halves of the centermost polyethylene insert. These inserts contain a carefully chosen set of drilled holes that are labeled in Figure 16.50. Notice that one set of holes on the flat surface of one hemicylinder rests near the central axis of JAMDAN, while a second set is in the curved side (25 mm from the JAMDAN axis) of the other polyethylene hemicylinder insert.

Results (see Figures 16.51 through 16.53) show that both the 9 and 15 MV scanning can image low-Z internal features with accuracy in the submillimeter range. Further, the data show that the 15 MV scanning delivers greater contrast sensitivity in this test object. Photons from both 9 and 15 MV potential linacs penetrate highly attenuating assemblies of dissimilar materials.

The significance of these results points to an advantage for MeV techniques for the geometry-acquisition application of CT. At MeV energies, the differences between the attenuation of materials are mostly differences in density (see Figure 16.3). Also, issues connected to *lack of penetration* are much less. The result is fewer artifacts when imaging assemblies for generating drawings from the 3D CT volume. This can be strategic for both developmental assemblies and/or parts at the end of service lifetimes. In particular, the drawing generated from the CT volume is *as-built* and/or *as-is* as opposed to *as-designed*. The CT data are therefore realistic input to finite-element analysis and modeling codes (Kokko et al. 2006).

16.4.9 DS LASER ICF TARGETS

As given in more detail in Section 16.3.4, ICF and HEDP research is being conducted at large laser facilities, such as the University of Rochester's OMEGA facility and the LLNL's NIF.

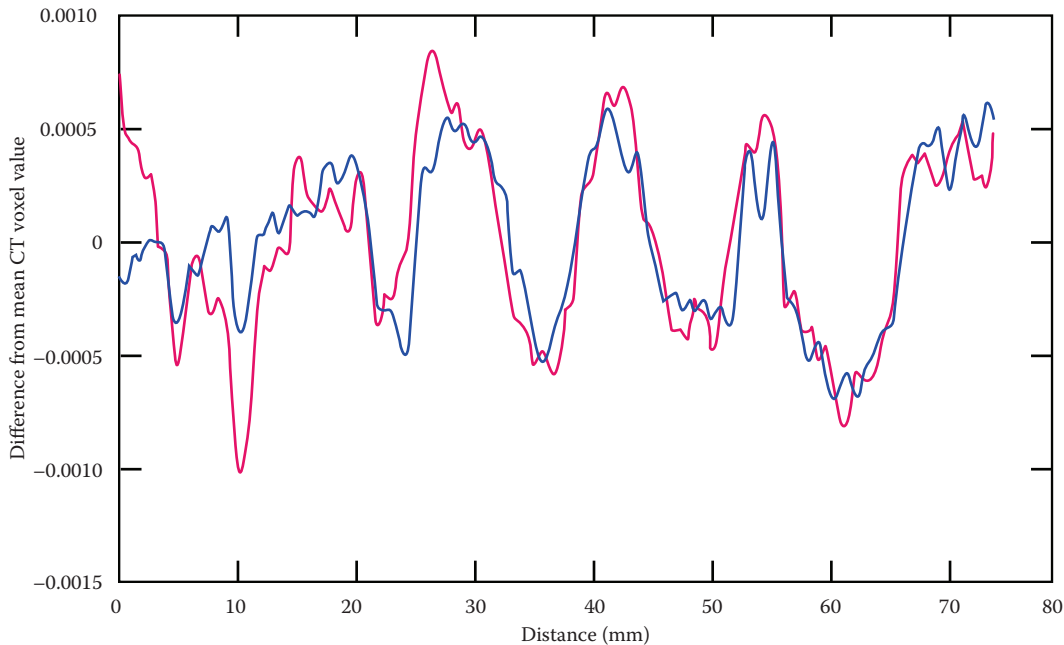


FIGURE 16.53 Line-outs plotted for the inside the hemicylinder inset holes of the JAMDAN assembly from 9 (red) and 15 MV (blue) linac CT data sets.

Millimeter-sized targets with micrometer structures are studied in a variety of hydrodynamic, radiation transport, equation-of-state, ICF, and high-energy density experiments.

A complementary approach to cryogenic deuterium-tritium filled single-shell targets (see Section 16.3.4) for demonstrating ignition uses noncryogenic DS targets (Amendt et al. 2005). The DS target ignition tolerance to interface instabilities is rather low; thus, the characterization requirements are particularly strict. For example, in a DS target, the outer spherical shell is assembled from two hemi-shells with a glued step joint that requires mating within a few hundred nanometers and an inner and outer delta radius of less than 1.0 μm (Hibbard et al. 2004). Concentricity of inner and outer shells needs to be within 3 μm . The sphericity and wall thicknesses of each shell, material uniformity, and wicking of glue into foams are other issues that must be characterized, since they can affect the hydrodynamics of the as-built target. A schematic of a DS target and characterization issues and methods are summarized in Figure 16.54. A photograph of a DS laser ICF target is given in Figure 16.55.

A DS target consists of two concentric shells. In one DS campaign the outer shell is a CH(Br-doped) ablator with inner and outer diameter of 444 and 550 μm , respectively. The inner shell is made of glass with an outer diameter of 216 μm and wall thickness of 8 μm . The inner shell is held in place within the outer shell by 50 mg/cm³ SiO₂ aerogel (see Figure 16.55). In the first DS target-manufacturing campaign, the aerogel was machined as two hemi-shells with a cavity to house the inner shell concentric to the outer. The outside diameter of the aerogel was machined slightly less than the inner diameter of the ablator. To construct the DS target, the lower aerogel hemi-shell was placed in the lower ablator hemi-shell, and the glass shell was mounted in the machined cavity of the lower aerogel hemi-shell (see Figure 16.55). The upper aerogel hemi-shell is then placed on the lower aerogel hemi-shell, and the upper ablator hemi-shell was placed over the lower assembly and glued. A final machining of the outer diameter ablator was performed to meet specifications. During the first campaign (December 2004 and January 2005), a total of six DS targets were fabricated.

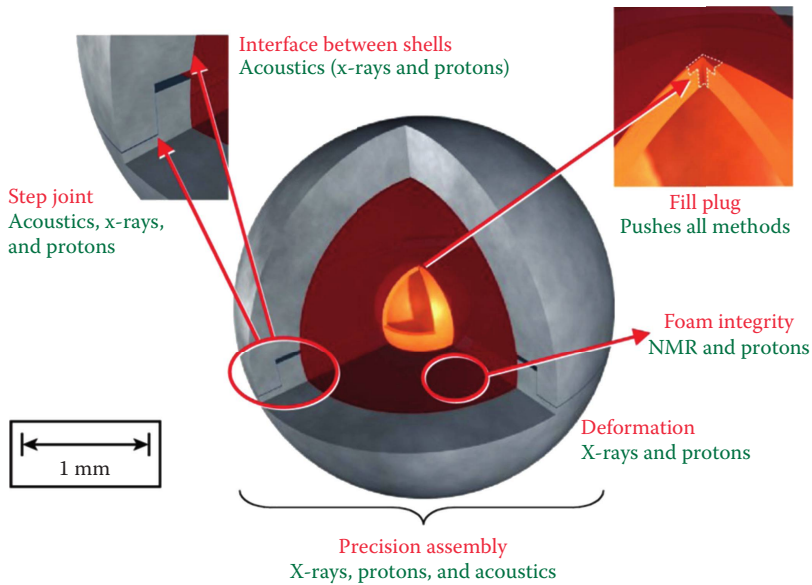


FIGURE 16.54 This schematic shows how a notional millimeter-scale DS laser target requires complementary NDC methods to adequately characterize its materials and assemblies. The inner shell is typically a full-density metal or plastic, the outer shell may be plastic or Be, and a low-density (tens of mg/cm³) aerogel is used to support the inner shell. The various characterizations required (top red text) are met by the technologies shown (bottom green text).

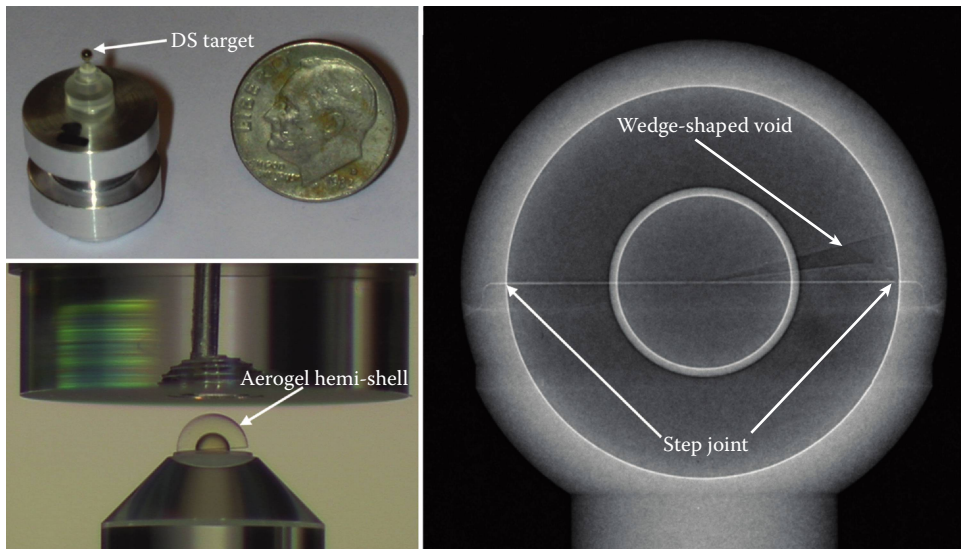


FIGURE 16.55 (Top left) DS target final assembly photograph, (bottom left) a photograph during assembly, and (right) MicroXCT radiograph showing the wedge-shaped void/gap and the glued step joint in the outer ablator shell.

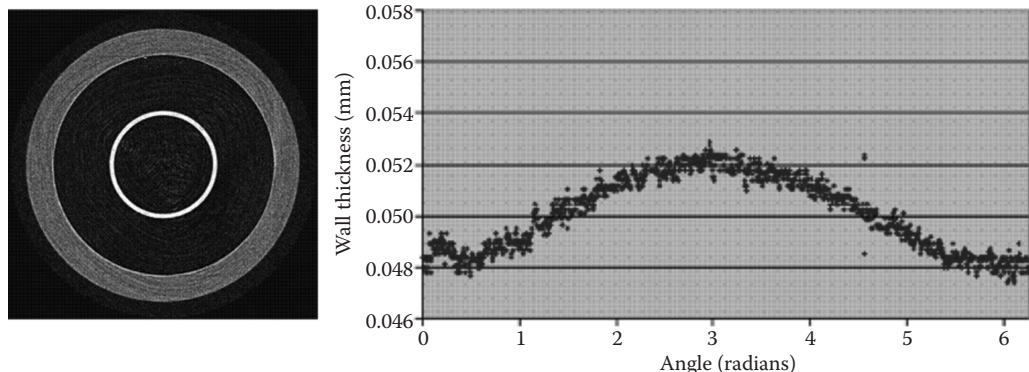


FIGURE 16.56 (Left) DS target Xradia (now Zeiss) MicroCT image and (right) wall thickness vs. angle measurement for the CT image on the left.

We employed an x-ray point-projection system developed by Xradia Inc. called MicroXCT (see Figure 16.10) (XRADIAMXCT 2015). This system uses a Hamamatsu tungsten-anode source with a nominal spot size of 5 μm at 4 W and a maximum potential of 150 kV. The detector is a 25 μm thick CsI scintillator microscope (10 \times and 20 \times) lens-coupled to a 16-bit Andor CCD camera. The CCD chip is 2048 \times 2048 with a detector-element pitch of 13.5 $\mu\text{m} \times$ 13.5 μm . It was operated at -50°C in these experiments. Typical source-to-object and object-to-detector distances of ~119 and ~12 mm, respectively, were employed resulting in a pixel pitch of ~0.6 μm at the object. The data were with a tube voltage of 60 kV and resulted in data acquisition times of 60 s per DR; 360 DRs or views were acquired for the CT image reconstruction.

Both DR (Figure 16.55) and CT (Figure 16.56) were used to characterize the DS targets (Brown and Martz 2006). During review of the DRs, a void between the upper and lower aerogel hemi-shells was detected (Figure 16.55). The void appeared to be wedge-shaped in the digital radiographs and this was confirmed in some of the CT images. Characterization of all six targets revealed similar wedge-shaped voids. CT revealed that the six targets had inner- to outer-shell concentricity ranging from 0.5 to 1.7 μm (Sain et al. 2006) well within the 3 μm specification. Three of the six targets had ablator wall thickness uniformity (see Figure 16.56) that met the physicist's specification of 1 μm or better. The other three targets ranged from 1.7 to 3.9 μm and thus were out of specification. DR also revealed step discontinuities in excess of 1 μm on the inner surface of the ablator for a few of the targets. Consequently, the manufacturing process had to be changed for future DS targets (Bono et al. 2007).

16.4.10 CT AND TOMOSYNTHESIS OF DoD ORDNANCE

Nondestructive testing of military ordnance is carried out to ensure that the ordnance will perform safely and as expected. Military ordnance is a broad term that includes conventional warheads, rocket motors, gun ammunition, propelling charges, cartridge-actuated devices (CADs), propellant-actuated devices (PADs), and their components. One thing common to all ordnances is that they contain explosives. DR, CT, and tomosynthesis are used at various stages of the life of the ordnance. After military ordnances are built, NDC techniques are used to inspect for flaws in the final build. This reduces the possibility that an unsafe or malfunctioning ordnance will reach the stockpile. As the ordnance ages over time, NDC is used on a small sampling of items in the field to help determine the effects of aging on the safety and operation of the ordnance. If there is a malfunction in the field, nondestructive techniques can be used to determine the cause. The inspections can include a small sampling for nonsafety malfunctions (see WDU-17/B example in Section 16.4.10.1) to 100% screening of all ordnances for safety issues (see the 40 mm grenade example in Section 16.3.1). Below are NDC examples for a few different military ordnances.

16.4.10.1 CT of a WDU-17/B Conventional Warhead

The WDU-17/B conventional warhead is an air-to-air ordnance that contains 20 lb. of HE and is considered a fragmenting warhead. When the warhead is detonated, explosive gasses fragment the metal case and Ti bars damaging the enemy aircraft in their path. The warhead is part of the US Navy surveillance program that inspects a portion of these warheads in the stockpile to determine potential aging issues. CT data were acquired on the warhead using an LLNL developed CT system (see Figure 16.57). The CT parameters included a 450 kV x-ray source operated at 325 kV and 2.75 mA. The detector was a Thales amSi flat panel with 127 μm elements. The data were acquired with 900 views over 360°. The warhead components are shown in Figure 16.58. The main interest of the inspection was the initiating components, which include the explosives in the booster plate and the detonator cord that initiates the explosive in the booster plate and the main charge.

The warhead is mounted on a turntable for CT data acquisition as shown in Figure 16.57. The amorphous silicon detector can be seen directly behind the warhead. In front of the warhead is an

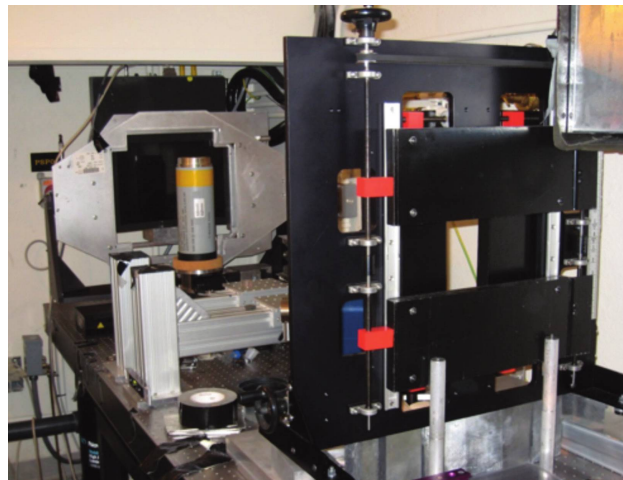


FIGURE 16.57 LLNL-built x-ray CT system used to acquire the DR and CT image data of a DoD WDU-17/B conventional warhead (the yellow and gray cylinder).

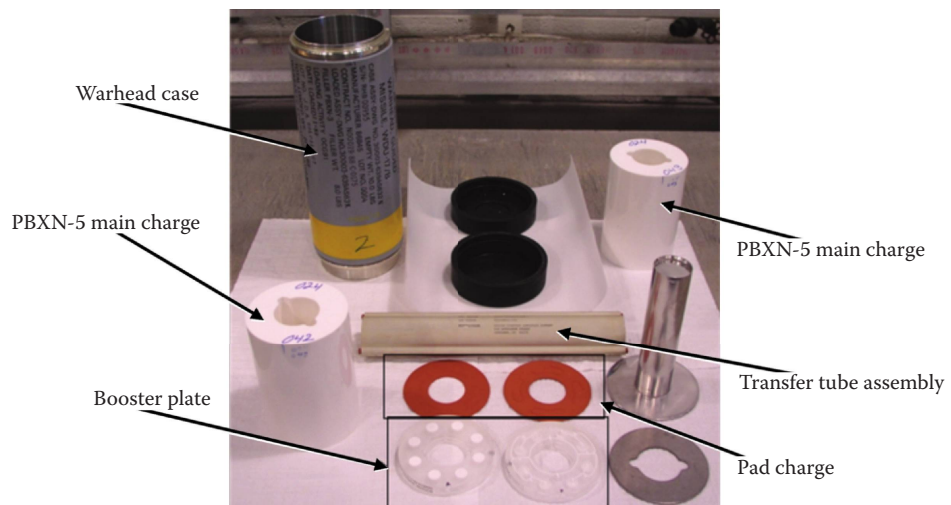


FIGURE 16.58 Photograph of the parts that make up the DoD WDU-17/B conventional warhead.

adjustable x-ray collimator that is used to remove unwanted x-rays that may cause x-ray scattered photons impinging on the detector. The x-ray source is not visible in this image. A digital radiograph of the warhead and two CT images is given in Figure 16.59. The center CT image shows titanium bars that provide the fragmentation and the transfer tube, which contains the detonator cord used to initiate the booster.

The CT image on the right in Figure 16.59 is a vertical (along the cylindrical axis) slice showing the transfer tube and one of the booster pellets. Figure 16.60 shows a vertical CT cross section of the transfer tube and components inside the tube. The ignition begins in the acceptor ferrule,

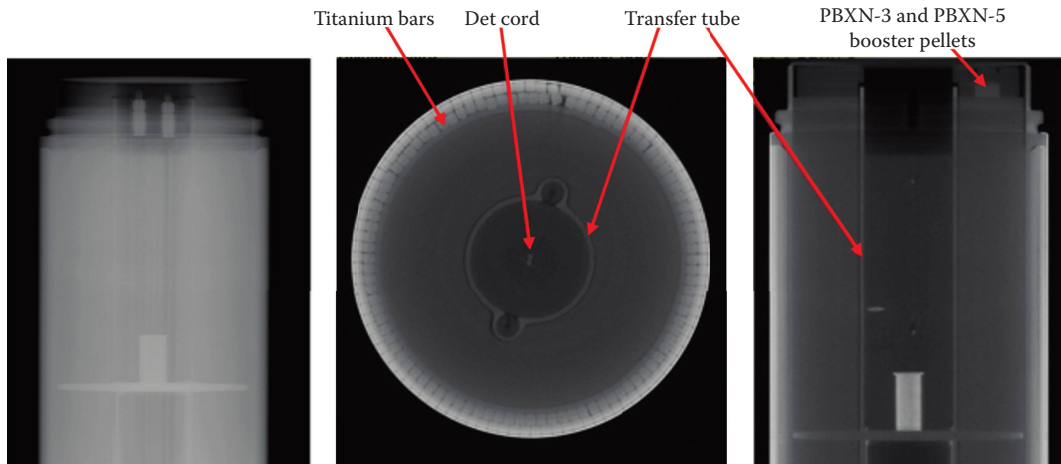


FIGURE 16.59 (Left) Digital radiograph and (middle) horizontal and (right) vertical CT cross sections of a DoD WDU-17/B conventional warhead. For a higher contrast image of the vertical CT cross section, see Figure 16.60.

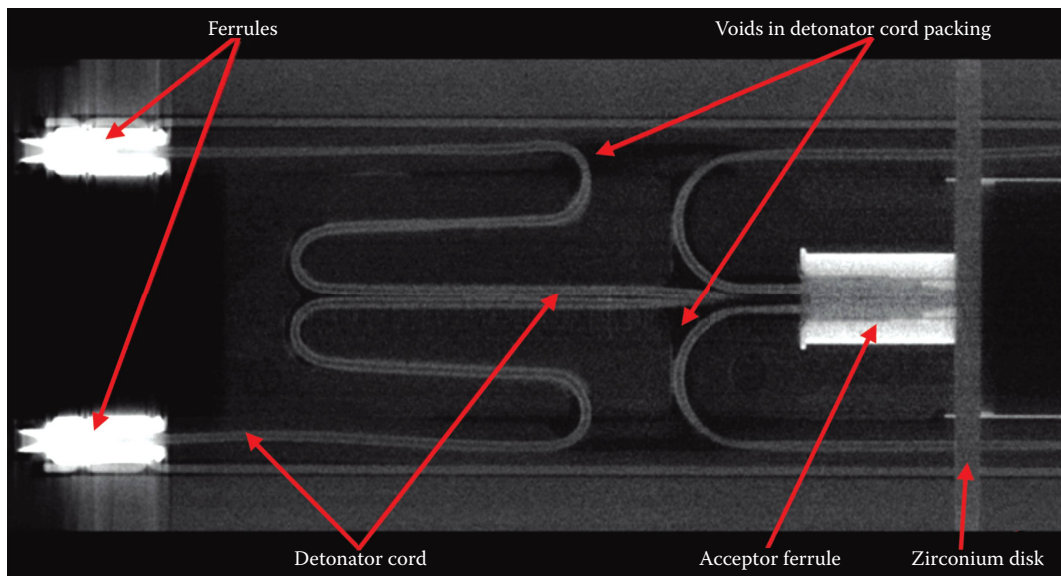


FIGURE 16.60 Vertical CT image showing various components of the warhead including the detonation cord and voids in the low-density packing that is used to hold the detonation cord in place. We have adjusted the level and contrast so that the ferrules on the left are saturated in order to reveal internal voids within the packing material.



FIGURE 16.61 A 3D rendered low-opacity (translucent) image of the transfer tube with detonation cord inside.

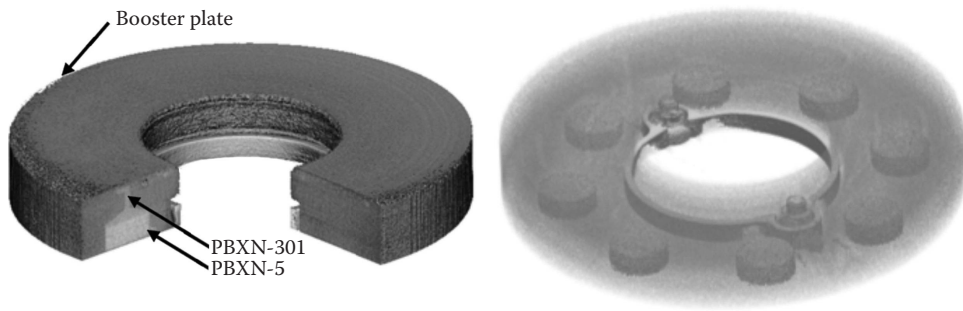


FIGURE 16.62 (Left) High- and (right) low-opacity rendered images of the warhead booster. On the left, a cutout is used to highlight one of the eight boosters. Note that eight boosters (look like pellets on the right image) are contained in a plastic booster plate, and each booster consists of two different explosives.

which ignites the detonator cord. The detonator cord carries the explosive chain to the booster pellets through the forward and aft ferrules (the aft ferrules are not seen in this cross section). The booster pellets ignite the main charge, which fragments the titanium rods and the warhead case. A 3D rendered image from the CT data of the transfer tube and the components inside is shown in Figure 16.61. The rendering shows the detonator cord that supplies the energy to the forward and aft booster pellets and the acceptor ferrule near the base that is the starting point of the detonator cord ignition.

A high-opacity 3D rendered CT image of the booster portion of the warhead is given on the left in Figure 16.62. The rendered image shows a cutout of the booster plate and two different types of explosive making up the booster pellet. The image on the right in Figure 16.62 is a low-opacity rendering of the booster plate and the booster pellets that are housed in the eight indentations seen in the plate shown in Figure 16.58.

16.4.10.2 CT and Tomosynthesis of a Multifunction Fuze

The multifunction fuze (MFF) military ordnance is used with a Navy 5 in. projectile and is used to initiate the HE in the projectile. The MFF allows for selectable operational modes (i.e., air proximity, electronic time, point detonate, etc.) depending on the target. The Navy required 100% radiographic inspection of each fuze after it was manufactured to verify that the safe and arming (S&A) device was in the safe position to forbid accidental initiation.

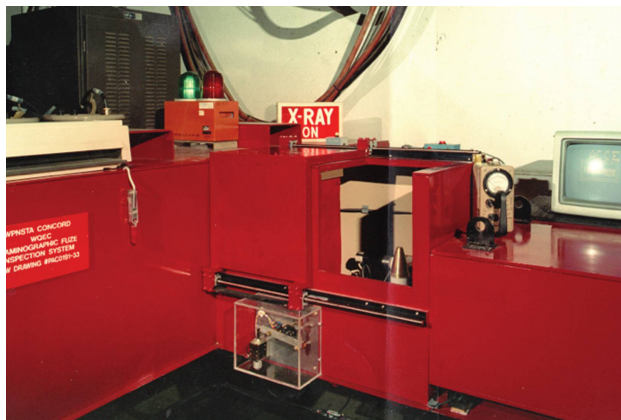


FIGURE 16.63 Photograph of a Naval Weapons Station, Concord, California, x-ray system that was used to acquire either CT or tomosynthesis data.

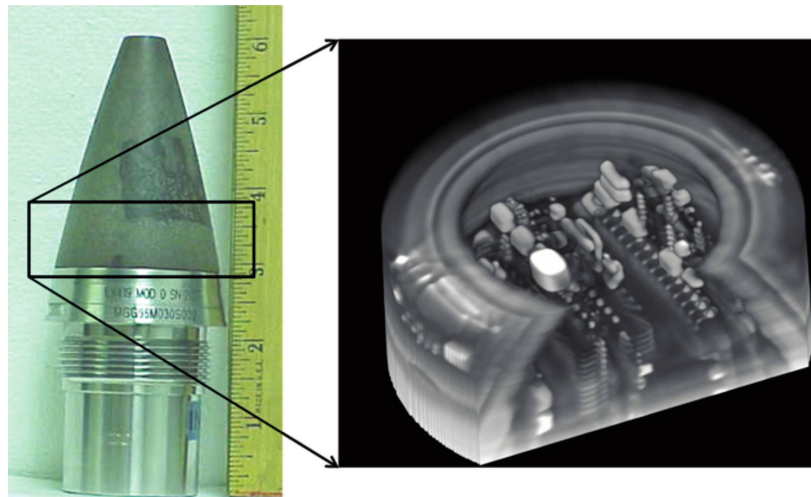


FIGURE 16.64 (Left) Photograph of a MFF used on a 5 in. projectile and (right) CT rendered image of the electronics in the nose cone.

Naval Weapons Station, Concord, California,* developed a single-slice tomosynthesis technique and manufactured two systems to verify that the S&A device was in the safe position. The system was also capable of acquiring full 3D volume CT data if additional inspection requirements warranted. The system included a 320 kV source, motion control for CT and tomosynthesis data acquisition, and a scientific-grade CCD camera optically coupled to a gadolinium oxysulfide (GOS) scintillator as the detector. Special features of the system included an automatic x-ray shutter that blocked the x-rays to allow the operator access to the fuze without turning off the source and a computerized *salting* program that would randomly present a stored armed S&A device image to test the operator's ability to detect defects.

A photograph of the Naval Weapons Station system with the MFF housed in the inspection well is given in Figure 16.63. A photograph and 3D rendered CT image of the electronics in the nose cone and MFF are given in Figure 16.64. DR and tomosynthesis images of the S&A MFF are given in Figure 16.65.

* Note that in 2005 the Naval Weapons Station in Concord, California, was closed during the DoD base closings.

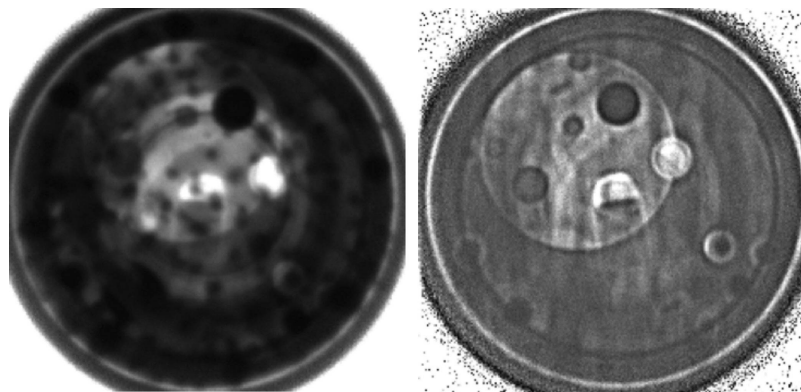


FIGURE 16.65 Representative (left) DR image and (right) a tomosynthesis image of a MFF used on a 5 in. projectile. Both images show the S&A device.

16.4.11 TOMOSYNTHESIS OF AN *ARCHAEOPTERYX* FOSSIL

In 1859, Charles Darwin published *On the Origin of Species*, providing a body of evidence that the great variety of life forms evolved through means of natural selection. However, one big criticism was that the fossil record had *missing links*—an absence of intermediate forms showing a transition from one major group to another. Yet just two years after the book was published, fossils from a 150-million-year-old, crow-sized creature were discovered in southern Germany that had a mosaic of both reptilian and bird-like features. Dubbed *Archaeopteryx* (*ancient wing*; von Meyer 1862), this animal had avian feathers, but also had clawed fingers on its wings, teeth in its mouth, and a long bony tail. Indeed, these fossils seemed to capture a special moment in time, representing a previously missing evolutionary link between two groups of animals: dinosaurs and birds. Thus, *Archaeopteryx* quickly became an icon of evolution and was generally considered to be the earliest flying dinosaur and true bird known—and arguably the most important fossil in the world. Over 150 years later, *Archaeopteryx* is now known from a total of 11 skeletons and a black wing feather (Carney et al. 2012) and still remains a key piece of evidence for unraveling the mysteries surrounding the evolution of birds and avian flight. For more about *Archaeopteryx*, see the book *Archaeopteryx: The Icon of Evolution* by Wellnhofer (2009), articles by Zimmer (2011) and the nature article by Callaway (2014).

At LLNL, we scanned the best-preserved skeleton of the *Archaeopteryx*, known as the *Thermopolis specimen* (collection number WDC-CSG-100) (Mayr et al. 2005), through generous access provided by the Wyoming Dinosaur Center in Thermopolis, Wyoming. The Thermopolis *Archaeopteryx* specimen is a slightly dissociated skeleton on a single plate of pure limestone. The work in this section was done in collaboration with paleontologist Ryan Carney (Carney et al. 2014) and was funded by a National Science Foundation grant to Yale University. A photograph and x-ray radiograph of the Thermopolis specimen are given in Figure 16.66. Labels indicating the various parts of the Thermopolis *Archaeopteryx* specimen are shown in Figure 16.67.

Carney is interested in examining and reconstructing the fossil in 3D in order to gain unprecedented access to its anatomy and potentially answer some long-standing controversies, e.g., from how well the animal was able to fly to its exact position within the dinosaur–bird family tree. Results from this x-ray imaging project will also provide opportunities to create educational content for the teaching of evolution and avian anatomy.

We acquired both CT and tomosynthesis (see Section 15.5 for a description of tomosynthesis methods) data on the fossil. The CT data set was acquired using an LLNL designed and built CT system. The parameters for CT acquisition were 225 kV, 3.6 mA, and 720 projections over 360°. A radiograph from the CT data acquisition is shown in Figure 16.66. The CT results were not very useful due to the lack of penetration through the long axis of the limestone plate and are not shown.



FIGURE 16.66 (Left) Photograph of the Thermopolis *Archaeopteryx* specimen (Courtesy of the Wyoming Dinosaur Center.) and (right) radiograph of the same specimen acquired at LLNL. The dashed red ellipses locate the *Archaeopteryx* skull in both images.

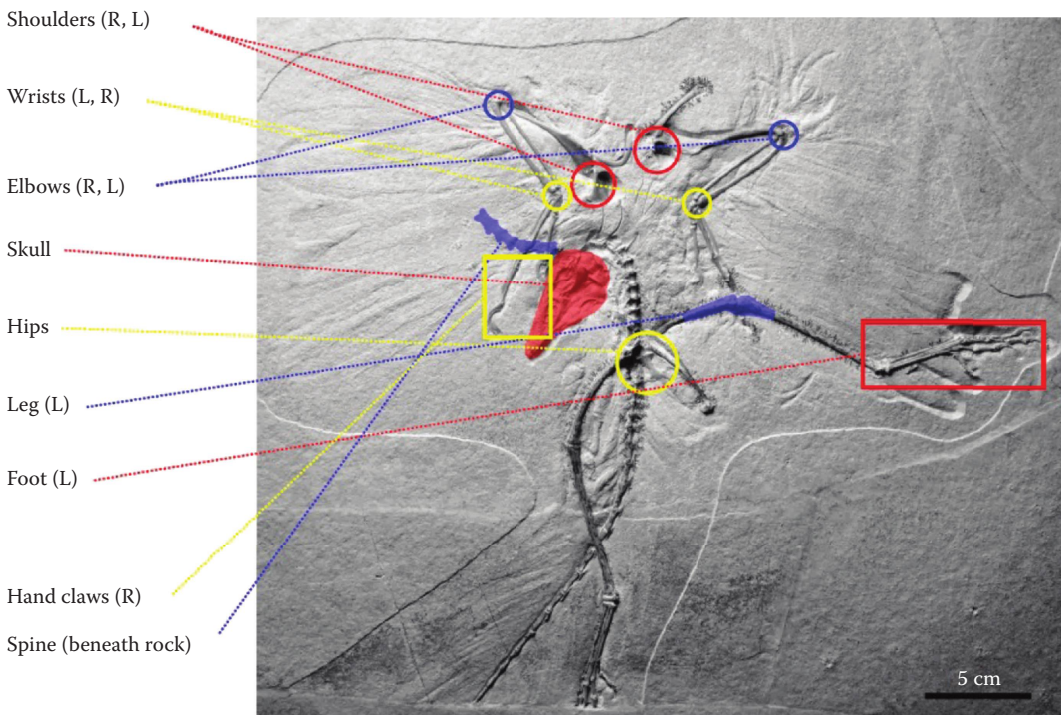


FIGURE 16.67 Photograph with labels indicating the various parts of the Thermopolis *Archaeopteryx* specimen.

Given this, LLNL designed and built another system to acquire the tomosynthesis data (setup is shown in Figure 16.68). The tomosynthesis data were acquired at 130 kV and 0.27 mA, in 720 projections over 360°. Note that the tomosynthesis (as opposed to CT) data acquisition technique used the source and the detector at about a 45° angle with respect to the limestone plate, and thus the x-rays only needed to penetrate the thin (not the long axis) portion of the limestone plate as shown in Figure 16.68. The tomosynthesis technique is optimal for acquiring 3D data of large aspect ratio and thin plates. The tomosynthesis radiographs were converted to sinograms, and ring removal was performed. Next, the ring-removed sinograms were converted back to radiographs and processed to

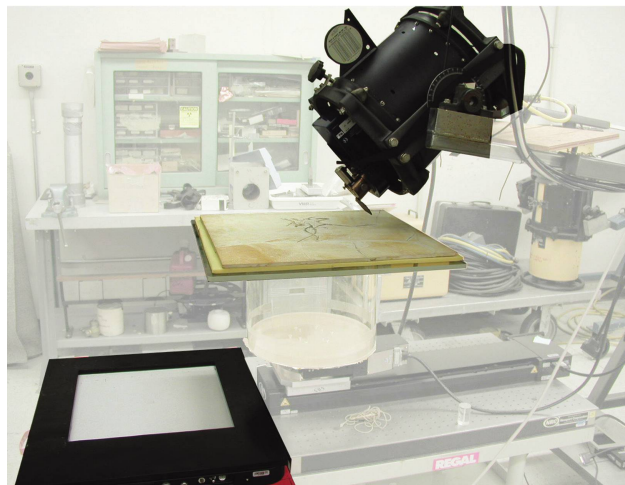


FIGURE 16.68 Photograph of the tomosynthesis setup for the *Archaeopteryx*. From bottom left to top right are the flat-panel detector, the Thermopolis *Archaeopteryx* specimen, and the x-ray source. The specimen was rotated while the source and detector were fixed.

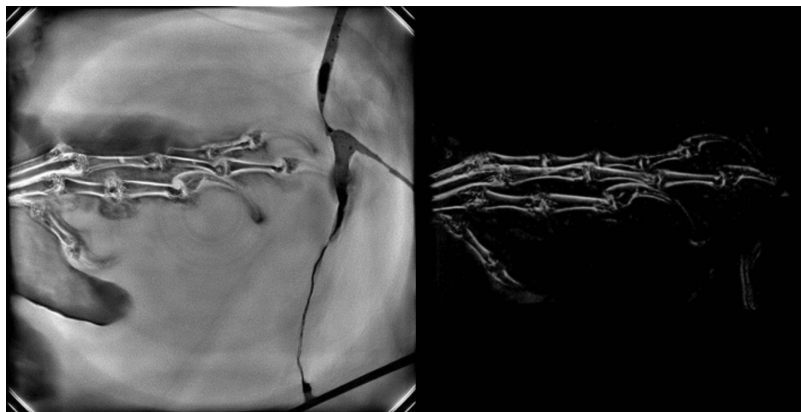


FIGURE 16.69 (Left) Tomosynthesis image of the Thermopolis *Archaeopteryx* specimen's left foot after reconstructing and focusing. (Right) Tomosynthesis image after thresholding and rendering the image on the left.

create the tomosynthesis results. The last step was 3D filtering, with a clipped high-pass kernel of the entire set of slices at one time.

Tomosynthesis results are given in Figures 16.69 and 16.70. A tomosynthesis stack image was generated by averaging the maximum and minimum 32 bit grayscale values per pixel as shown in Figure 16.71. In Figure 16.71, the top view of the skull and partial view of the right hand is shown. Also at the top left, the underlying vertebrae completely enclosed by the limestone is visible.

16.4.12 DR AND CT OF ART AND OBJECTS OF CULTURAL SIGNIFICANCE

DR/CT inspection of works of art and other objects of significance to cultural heritage has emerged as an important tool in restoration efforts (Casali et al. 2009). The government of Italy (through the National Institute for Nuclear Physics [INFN] and some universities) has employed a variety of techniques for the inspection of paintings, sculptures, and period furniture to answer questions about how works of art were constructed. As the work in maintenance and restoration progresses, the use of DR/CT has increased resulting in scanners operating at the Universities of Bologna and Turin.

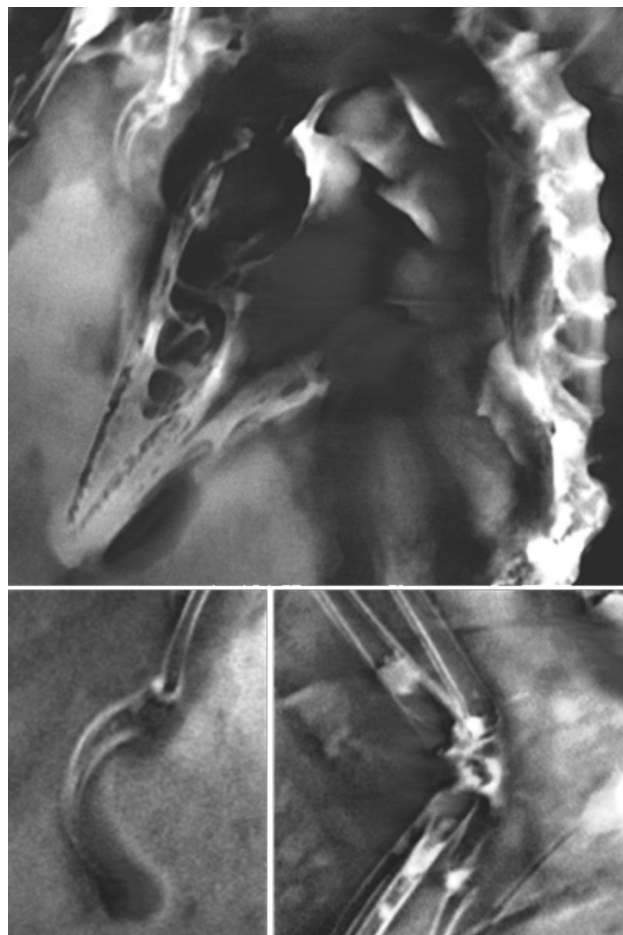


FIGURE 16.70 Three tomosynthesis images of the *Archaeopteryx* specimen. The top image reveals from left to right a claw, skull, and vertebrae. The bottom left image shows a claw. The bottom right shows a wrist.

One application for DR/CT inspection of artwork is to answer questions related to how objects were made, with what construction techniques, and with what materials. The value of CT is illustrated in the scans performed on old Japanese wooden statues of Tamon Ten and Kongo Risiki (Morigi et al. 2010). The details of the joined wood block technique can be viewed down to the rings in the cypress wood.

Of more immediate importance is what the CT inspection volume can tell you about the state-of-the-art object and how to implement a strategy for repair/restoration that will address the issue with minimum impact on the art object. Many of the priceless period furniture articles, as those in the Venaria Reale in Turin (Italy) contain some damage due to age and to insect infestation. The photo at the upper right in Figure 16.72 shows a “Doppio Corpo” by Piffetti (insured for 1.2 million dollars) with walls inlaid with ivory, tortoiseshell and golden wood. The CT was able to highlight the condition of internal structure, not visible from the outside, and the damage created by time and xylophagous insects. While the insects have been eradicated, the impact on structural members of the furniture was unknown. The CT allowed the restorer to act properly on the structure without causing additional damage (Re et al. 2014). Also shown in Figure 16.72 upper left and bottom are a photo and CT images, respectively, of another period piece. The CT data reveals damage to the wood caused by xylophagous insects. The damage results in voids (black voxels in the CT images at the bottom) within the wood structure (white to gray voxels).

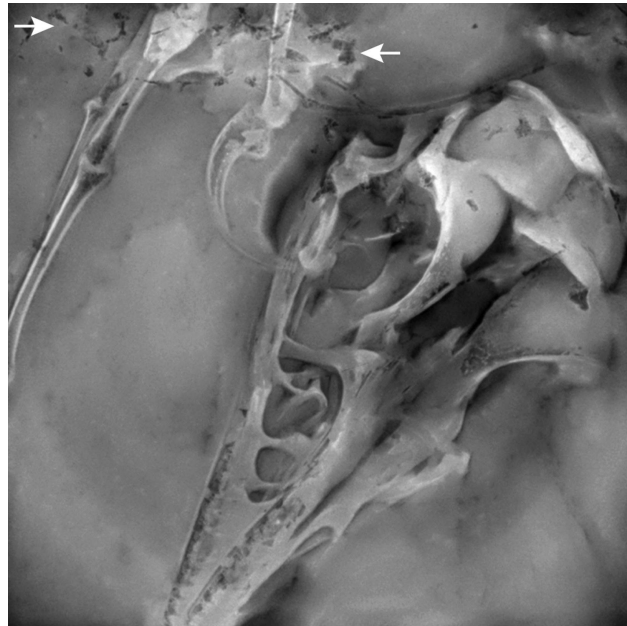


FIGURE 16.71 Tomosynthesis stack image showing the top view of the skull and partial view of the right hand, as well as underlying vertebrae completely enclosed by limestone (top left arrows).



FIGURE 16.72 Pictures of period furniture accompanied by representative CT slices.



FIGURE 16.73 Photographs of two Japanese statues that were CT-scanned at the Venaria Reale in Turin, Italy. The statue on the left is Kongo Rikishi and on the right is Tamon Ten (for CT results, see Figure 16.74).

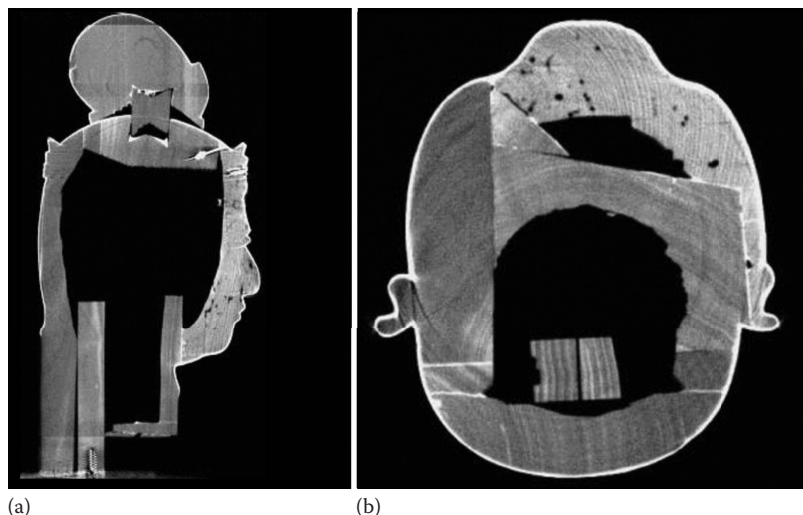


FIGURE 16.74 CT slices through the head of the Tamon Ten statue shown in Figure 16.73. (a) Vertical slice through the midplane of the head. (b) Horizontal slice through the ears. Note the (black) joined-block construction technique used. Also note the facial block has heavy perforation (black) from insects while others were spared. The various blocks were apparently taken from different trees as the density (different gray levels) varies considerably.

Another example of applying CT to the study of ancient art is shown in Figures 16.73 and 16.74. The first shows the outward appearance of two Japanese statues, while the second reveals the internal methods of construction and areas of insect damage. The CT data also reveal insect damage as shown by the voids (black) within some of the different pieces of wood used to build the Tamon Ten statue.

The scans of the wood sculptures and furniture led to another application for CT. The state of the tree rings in the wood can be used to establish the year the tree was cut, leading to the approximate year of construction of the art pieces. An evaluation of this application is ongoing.

16.4.12.1 Concerns with Michelangelo Buonarroti's Statue of David

Recently, a number of cracks have been observed in the ankles near the base of Michelangelo Buonarroti's statue of David, on display at the Accademia in Florence, Italy. The statue of David



FIGURE 16.75 Statue of David with an arrow pointing to cracked regions in his ankles. (Courtesy of Rico Heil/CC-BY-SA-3.0, Wikipedia.)

is shown in Figure 16.75. A number of important questions follow. How deep are the cracks? How do the cracks affect the strength of David and his ability to remain upright in an earthquake? Are the cracks getting worse? All of these questions can be addressed by a detailed inspection of the internals of David's ankles.

To evaluate the value of DR/CT for the inspection of David, a cylindrical test object made of Carrara marble (the marble used by Michelangelo to carve out David), supplied by the Department of Physics, University of Bologna, was prepared for scanning as shown in Figure 16.76. X-ray CT and ultrasonic techniques were applied at LLNL to establish the ability to discern cracks in the

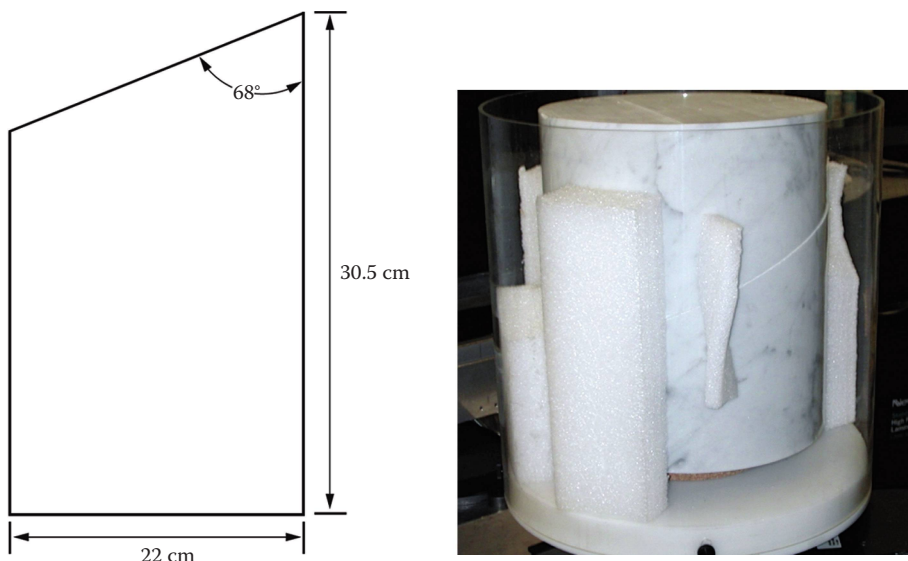


FIGURE 16.76 Sketch and photograph of Carrera marble test object used to evaluate the ability to detect simulated cracks in David's ankles. Simulated cracks were machined in the angled face of the cylinder test piece, and it was married to a second similar angled face of the cylinder without simulated cracks. In the photograph, the test piece is braced inside a plastic tube ready for CT.

cylindrical test object. The test object was CT scanned at LLNL using 9 MV x-rays and an amorphous silicon flat-panel detector. Images in Figures 16.77 through 16.79 summarize the x-ray results from the CT scans.

The acquired and analyzed CT volume showed promise for detecting cracks in David's ankle. This combination of source and detector employed resulted in an inspection volume that imaged all



FIGURE 16.77 Digital radiograph of the marble test object made to evaluate crack detection using x-ray CT. This radiographic view is aligned with the diagonal mating surface (faint black line) of the two marble pieces.

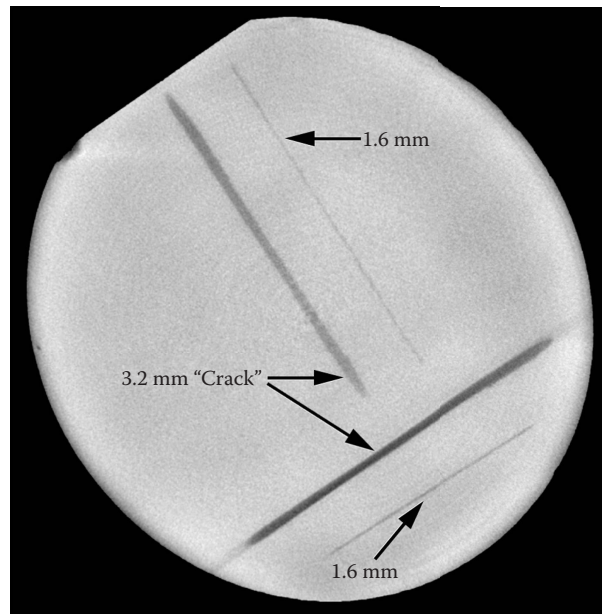


FIGURE 16.78 A CT slice, extracted at an angle through the simulated cracks. The width of the different simulated cracks is given in the figure. Note that these are not what is expected of a real crack.

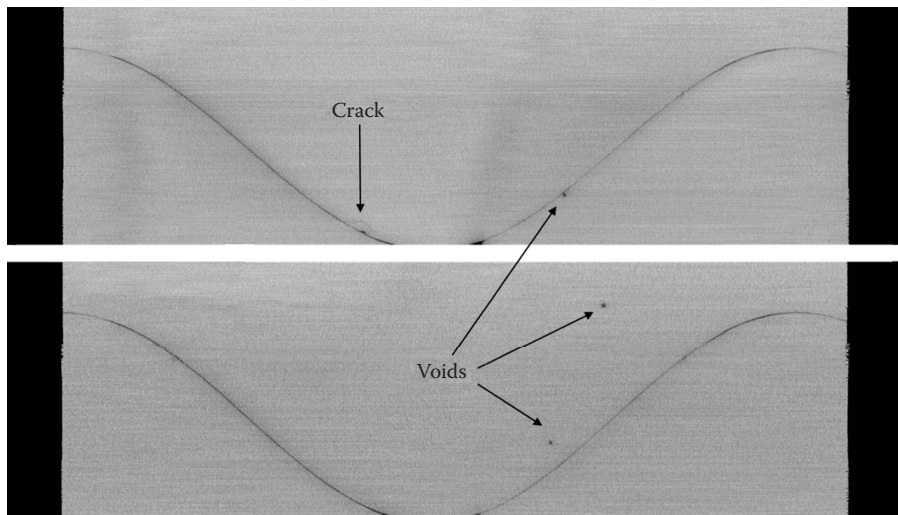


FIGURE 16.79 Two shell extractions from just inside of the outer surface of the Carrera marble test object. The sinusoidal features are the mating planes of the two halves of the test object. Natural voids in the marble are apparent in this view of the data taken with a 9 MV linac source and amSi panel detector.

the machined features in the crack plane made in the Carrara marble test object (see Figure 16.78). Also, shell extraction techniques were able to show the ability to detect small voids and microcracks close to the outer surface of the marble test piece. However, one important side effect of 9 MV scanning became apparent. The Carrara marble changes color with increasing x-ray dose, but this happens at a dose five times greater than that necessary for the ankle-CT as obtained by the measurements done at LLNL. Research is ongoing for the development of a compact x-ray source that can be rotated around the legs of the statue.

16.4.13 CT OF STRUCTURES MADE BY ADDITIVE MANUFACTURING

Since the 1980s, there have been manufacturing processes under development in which material is added rather than being removed, as is the more common manufacturing practice. It is useful to point out that *additive manufacturing* (AM) methods are known under various names, including *3D printing*.

One thing that distinguishes AM methods is the freedom to design a material and structure. The material or structure need not be isotropic in properties nor need it be full density. Polymer foams with custom properties are an active research area (LLNL 2014). We are applying CT to understanding the structure and properties of stainless-steel trusses made by AM (Martz et al. 2014). These structures deliver high stiffness with low density. The trusses we report here were made by laser melting of metal powder.

We used an LLNL-designed cone-beam CT system called CCAT. This system is equipped with a FeinFocus microfocus tube with a W-anode. For these scans, we operated CCAT at 200 kV with 250 μm of Cu filtration. The detector is a Thales amSi flat panel with 127 μm detector element pitch. Figure 16.80 is a photograph of CCAT.

The computer rendering in Figure 16.81 depicts one AM truss of interest to us. This truss is composed of repeating cells of struts, where each strut is aligned at a 45° angle to two of the main axes and 90° to the third. The cell geometry is the sum of an octahedral cell combined with a tetrahedral cell. The as-built structure built by AM will ideally have equal-diameter struts that are straight and complete.

Figure 16.82 presents a CT slice of an AM truss made of 316 stainless steel. This slice is taken through the plane depicted in orange in Figure 16.81. It is apparent that some struts are broken, and nodes have a hollow center. Notice also that this AM process has preferred directions. All of the incomplete struts are horizontal in Figure 16.82. The hollow center nodes may be artifacts.

We have compared CT results to sectioning and optically imaging the exposed surface. The astounding similarity is shown in Figures 16.83 through 16.85. CT is being used by the developers of AM methods to manufacture better parts. See for example Léonard et al. (2016) and Karmea et al. (2015).

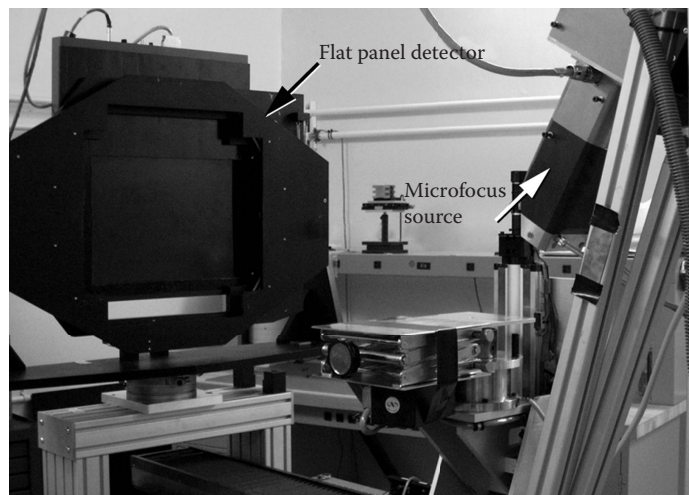


FIGURE 16.80 Photograph of LLNL-designed cone-beam CT system called CCAT.

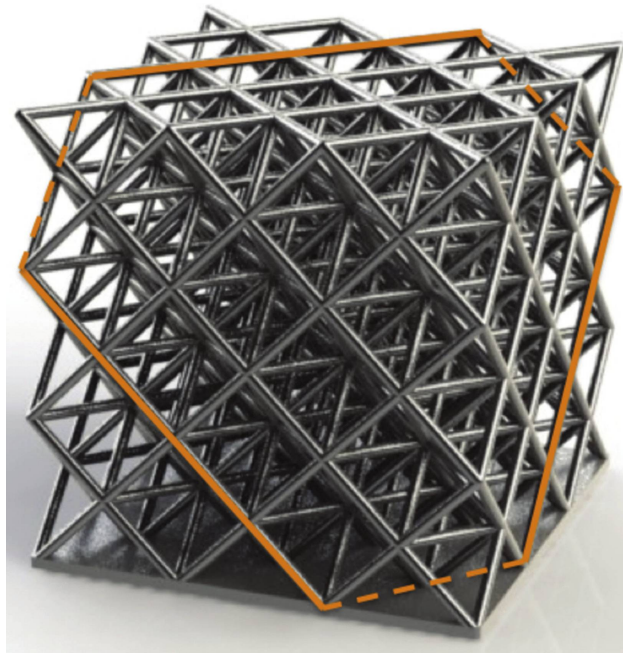


FIGURE 16.81 Structure shown in gray is a computer rendering of a desired AM component. A CT cross section given by the orange hexagon is shown in Figure 16.82.

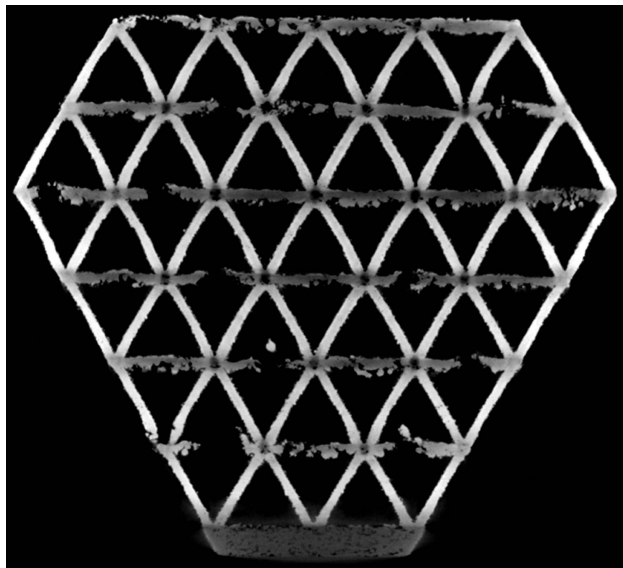


FIGURE 16.82 CT slice through the orange hexagon plane depicted in Figure 16.81. White is solid 316 stainless steel while black is air. Gray-shaded voxels are a combination of lower density struts and CT artifacts.

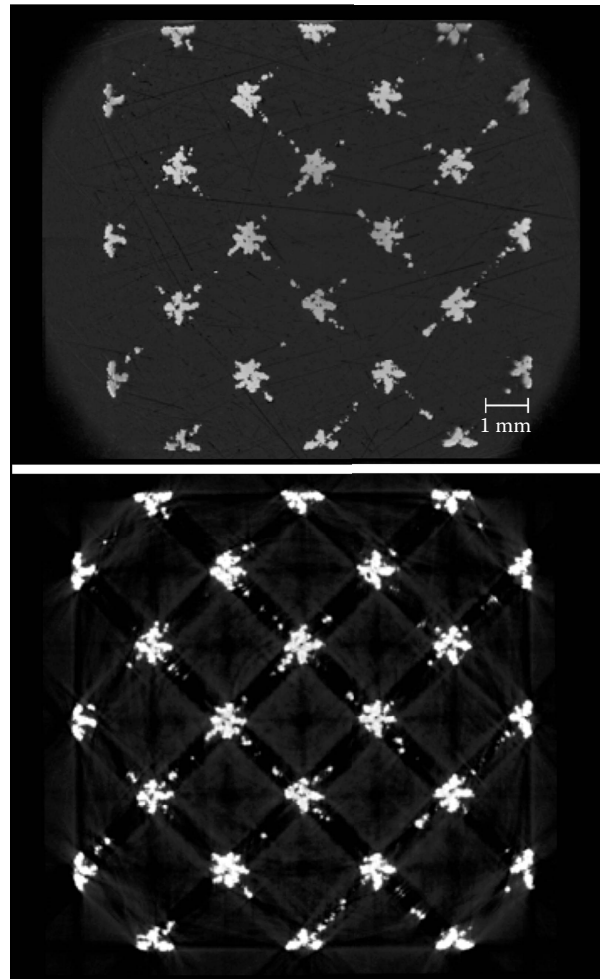


FIGURE 16.83 Comparison of (top) an optical micrograph through nodes of an AM truss to (bottom) a CT section through the same region.

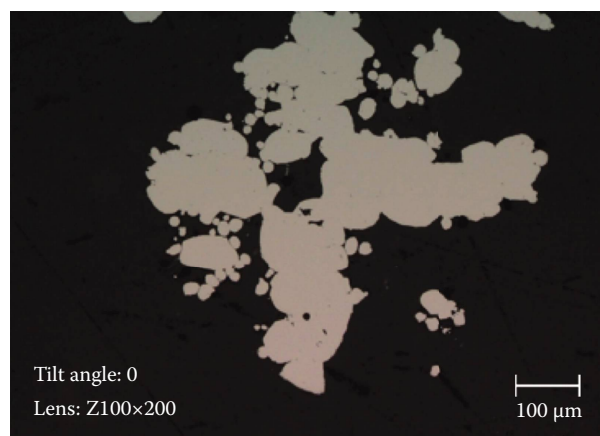


FIGURE 16.84 Optical micrograph of one node from the top of Figure 16.83. This image is about 100 \times the magnification of the image shown in Figure 16.83.



FIGURE 16.85 X-ray CT image taken from the bottom of [Figure 16.83](#). It is at equal scale to [Figure 16.84](#) and is of the same node.

16.5 X-RAY IMAGING TO DEFEND THE US HOMELAND

The attack on the United States by Islamic terrorists on September 11, 2001 brought increased awareness of the impact of terrorism (see Figure 16.86). One result was establishing the US DHS. DHS is a cabinet department of the US federal government, created in response to the September 11 attacks, and with the primary responsibilities of protecting the territory of the United States and protectorates from and responding to terrorist attacks, man-made accidents, and natural disasters. Whereas the Department of Defense (DoD) is charged with military actions abroad, DHS works in



FIGURE 16.86 Photos of terrorist attacks against the United States. From top left clockwise are the Boston Marathon bombing, twin towers, and U.S.S. Cole guided missile destroyer. (Courtesy of CC-BY-2.0 Aaron Tang, CC-BY-SA-2.0 Robert, U.S. Marine Corps Public Domain.)

the civilian sphere to protect the United States within, at, and outside its borders. Its stated goal is to prepare for, prevent, and respond to domestic emergencies, particularly terrorism. One aspect of the DHS and the 9/11 terrorist attacks is increased private- and government-sponsored research and development aimed at reducing this toll. Over time, US government programs included two objectives. One is making air travel safer, and the other is preventing entry into the country of special nuclear materials (SNM) and radiological dispersal devices (RDDs). In either case, the US government needs to protect all ports of entry (see Figure 16.87) into the United States.

The domestic nuclear detection office (DNDO) is a jointly staffed office established in April 15, 2005 by the United States to improve the nation's capability to detect and report unauthorized attempts to import, possess, store, develop, or transport nuclear or radiological material for use against the nation, and to further enhance this capability over time. DNDO coordinates US federal efforts to detect and protect against nuclear and radiological terrorism against the United States. DNDO, utilizing its interagency staff, is responsible for the development of the global nuclear detection architecture, the underlying strategy that guides the US government's nuclear detection efforts. DNDO conducts its own research, development, test, and evaluation of nuclear and radiological detection technologies, and is responsible for acquiring the technology systems necessary to implement the domestic portions of the global nuclear detection architecture. DNDO also provides standardized threat assessments, technical support, training, and response protocols for federal and nonfederal partners. Systems developed by DNDO are deployed and operated by the US Customs and Border Protection (CBP).

CBP is the largest federal law enforcement agency in the United States. It is charged with regulating and facilitating international trade, collecting import duties, and enforcing US regulations, including trade, customs, and immigration. CBP's primary mission is preventing terrorists and terrorist weapons from entering the United States.

The Transportation Security Administration (TSA) is an agency of the US DHS that has authority over the security of the traveling public in the United States. TSA was created as a response to the September 11, 2001 attacks. The agency's proponents, including Transportation Secretary Norman Mineta, argued that having a single federal agency charged with domestic aviation safety

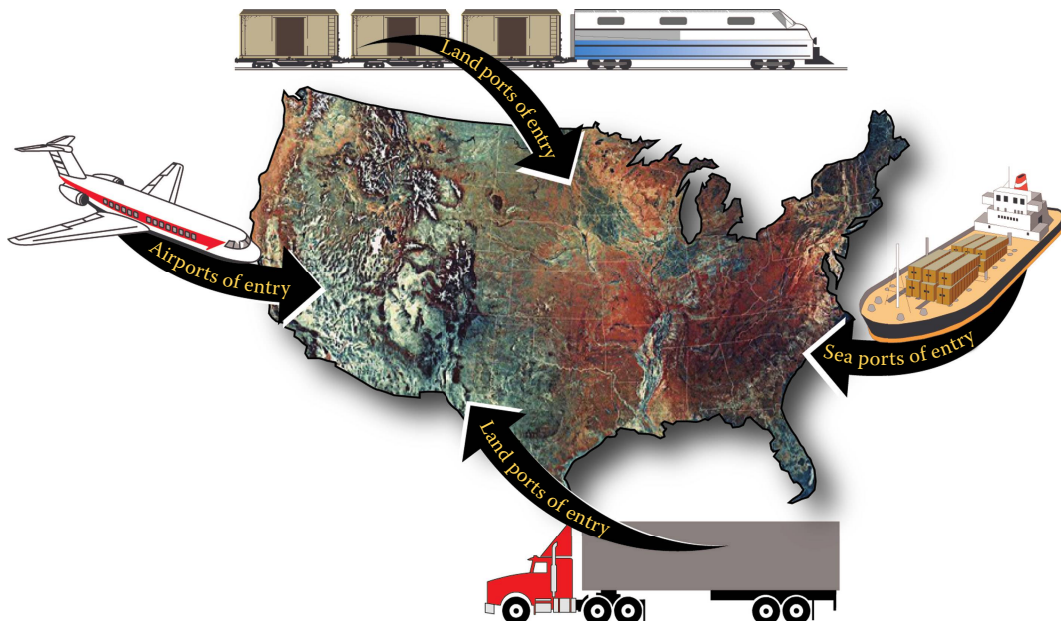


FIGURE 16.87 The US government needs to protect all ports of entry into the United States.

would better protect air travelers than private companies who operated under contract to single airlines or groups of airlines that used a given terminal facility. The organization was charged with developing policies to protect US transportation, especially in airport security and the prevention of aircraft hijacking. TSA administers the governmental programs to improve commercial aircraft security. Examples of the threat vectors to aviation security are given in Figure 16.88.

Explosives can be military, commercial, or homemade. The latter, homemade explosives, can be made by materials that are easily obtained from a grocery store, nursery, or hobby shop (Schubert and Kusnetsov 2008). SNM is defined by Title I of the Atomic Energy Act of 1954 as plutonium or uranium enriched in the isotopes ^{233}U or ^{235}U . RDD, also known as *dirty bombs*, consist of radioactive material combined with conventional explosives. They are designed to use explosive force to disperse the radioactive material over a large area, such as multiple city blocks.

Visual inspection of x-ray radiographs is one of the simplest security tools and is very efficient when single objects of small size like a briefcase are to be nondestructively inspected. The complexity of inspection increases when large *boxes* and/or when several objects are packed into a closed space, as in checked luggage, pallets for air cargo, or even in larger volumes like shipping containers or trucks.

We review and describe in separate sections through the remainder of this chapter some of the x-ray systems that are deployed or may be deployed to help defend the US homeland. We do not

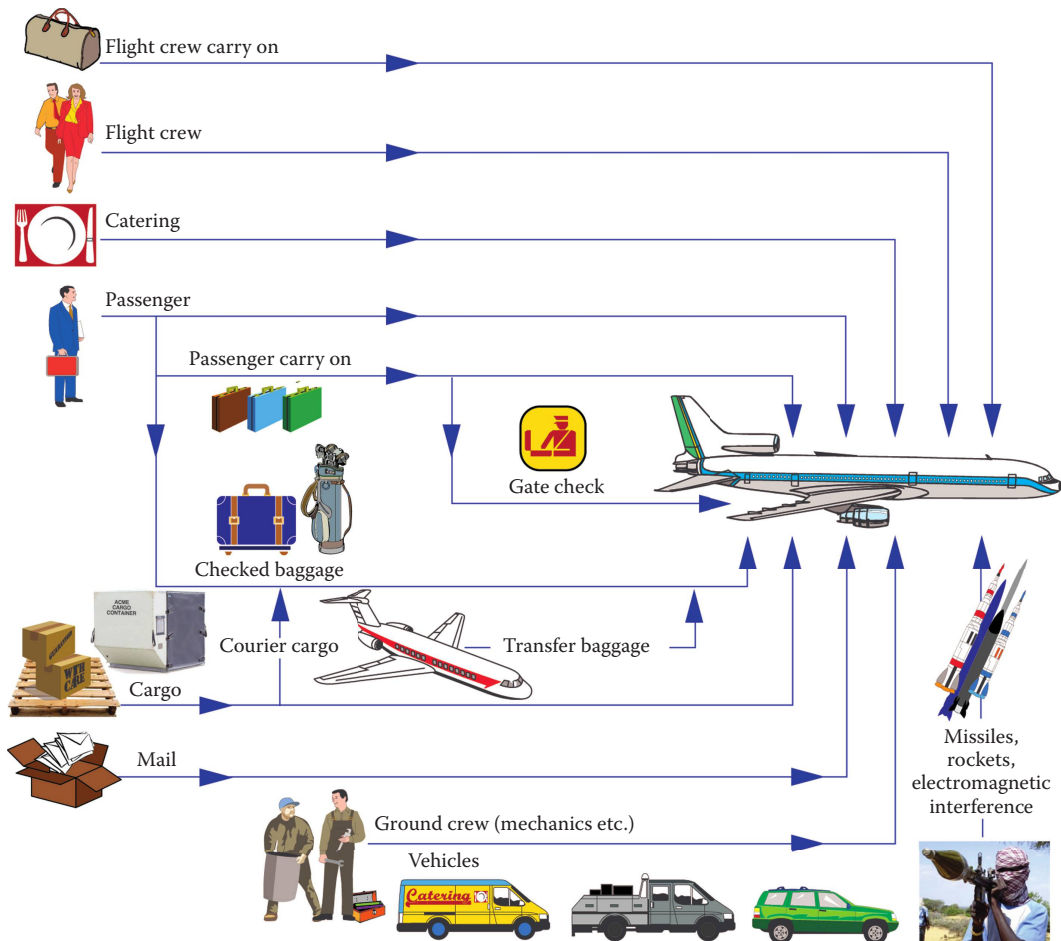


FIGURE 16.88 Some threat vectors in civil aviation.

include other than x-ray technologies except in some cases for comparison purposes. In Section 16.5.1, we describe how x-ray DR and x-ray backscatter are used to inspect carry-on luggage. In Sections 16.5.2 and 16.5.3, we discuss the use of x-ray CT, DR, and diffraction to inspect checked luggage. Emerging nonrotating (stationary) gantry CT systems are described in Section 16.5.4, while in Section 16.5.5, we show how x-ray backscatter is used to reveal what may be concealed on a passenger. See Singh and Singh (2003) and Sun (2010) for reviews of explosive detection systems for aviation security. In Section 16.5.6, we describe some x-ray systems that are used to inspect land and sea containers for SNM and RDDs before the containers leave a non-US port or enter the country through a US port.

16.5.1 X-RAY DR AND X-RAY BACKSCATTER TO INSPECT CARRY-ON LUGGAGE

The security focus for civil aviation has shifted from hijacking in the 1980s toward deliberate sabotage. One aspect of the DHS TSA is to manage aviation security policies and programs based on evolving threats to commercial airlines. TSA has helped develop x-ray imaging systems as a major tool in luggage, passenger, and cargo inspection. These x-ray systems are used to determine the form and density of items within luggage as well as other material-dependent parameters, such as effective atomic number. The US DHS TSA has requirements for future explosives scanners that include dealing with a larger number of threats, higher probability of detection, lower false alarm rates, higher throughput, and lower operating costs. In this section, we describe a few representative x-ray systems that are used to inspect carry-on baggage/luggage for explosives, knives, and guns.

Up to this time, the x-ray systems developed and some deployed to inspect carry-on luggage for knives, guns, and explosives use or used one of the following x-ray radiography systems:

- Single energy, single view
- Single energy, dual view
- Dual energy, dual view
- Dual energy, four views

Some carry-on luggage systems may also have included x-ray backscatter capability. CT has not yet been deployed at airports for carry-on screening. However, it appears that CT may be used in the near future.

Carry-on luggage security scanners operate at an approximate tube potential of 140–160 kV and have about 1 mm spatial resolution. A representative dual-energy, dual-view x-ray radiography system is shown in Figure 16.89. As shown in Figure 16.90, the system can show one or two views



FIGURE 16.89 Representative Rapiscan 620DV carry-on luggage system. (Courtesy of Rapiscan Systems.)

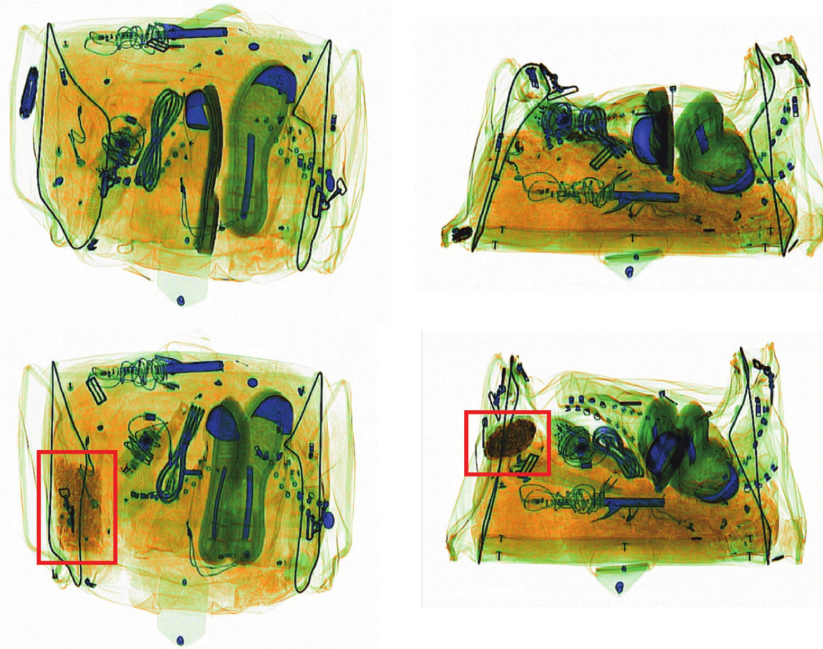


FIGURE 16.90 Representative images from the Rapiscan 620DV carry-on luggage digital x-ray radiographic system. The images on the left are a bottom-up view and on the right are for a side view of a carry-on bag. The images on the top are without an explosive simulant, while those on the bottom are with a simulant (highlighted by red rectangles). The colors are used to highlight low-Z organic (orange), intermediate-Z glass or Al (green) and high-Z metal (blue) objects within the luggage or bin. (Courtesy of Rapiscan Systems.)

and uses the two energies to color the image as to low-Z organic (orange), intermediate-Z glass or aluminum (green), or metallic (blue) content. So far, the images are reviewed by a human using the orange organic part of the image to look for explosives, green part to look for glass and Al, and blue part of the image to look for metallic threats such as knives and guns. Rapiscan and other manufacturers are exploring the use of automated operator assist and automated threat detection (ATD) or recognition (ATR) algorithms and software to identify threats such as explosives, guns, and knives. These algorithms rely on machine vision to identify distinct objects with the image and machine learning to classify these as a potential threat or benign objects based on atomic number, mass, size, and other properties of the scanned materials. However, it is ultimately up to the operator to decide if the bag should be cleared or if it contains a threat.

Examples of a carry-on luggage system that uses both single-view dual-energy x-ray radiography and x-ray backscatter images are shown in Figure 16.91. This figure shows AS&E (American Science and Engineering) GEMINI 6040 dual-energy x-ray radiography and x-ray backscatter (which AS&E calls Z Backscatter) images. On the left in Figure 16.91 is a dual-energy x-ray radiography image showing the contents within a briefcase. On the right is an x-ray backscatter image of the same briefcase. Note how the x-ray (Z) backscatter image helps reduce clutter in the image and clearly shows a gun and a bottle of liquid, which are not easily observed in the dual-energy radiography image. It is important to point out that x-ray backscatter is a near-surface imaging technique, and that the gun and bottle of liquid shown are near the edge of the briefcase on the x-ray backscatter side of the AS&E system and thus are easily revealed. However, if the bag were turned over, the gun and bottle of liquid would most likely be obscured in the backscatter image.

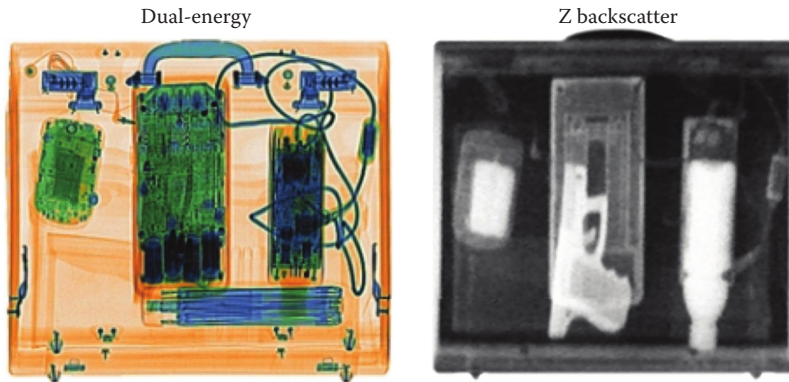


FIGURE 16.91 Representative images from the AS&E GEMINI 6040 x-ray system. On the left is a dual-energy x-ray radiography image showing the contents within a briefcase. The colors are used to highlight organic (orange), inorganic (green) and metal (blue) objects with the luggage or bin. On the right is an x-ray backscatter (called Z Backscatter by AS&E) image of the same briefcase. (Available at <http://www.as-e.com/products-solutions/parcel-inspection/checkpoint-mailroom-small-parcel/product/gemini-6040>.)

16.5.2 X-RAY CT TO INSPECT CHECKED LUGGAGE

In this section, we describe some representative x-ray CT systems that are used to inspect checked luggage for explosives. X-ray CT security scanners are deployed worldwide to detect explosives in checked luggage. The security scanners are very similar to CT scanners used today in medical imaging. For each bag scanned, the resulting reconstructed images are processed to identify (or segment) individual objects within the checked luggage and then sorted into threats and nonthreats by ATD algorithms to screen for explosives and shielding (a high-opacity object). Human operators review the images only when these automated algorithms report the presence of a possible threat or shielding. For a review of x-ray explosives detection techniques see Wells and Bradley (2012).

The term explosive detection system (EDS) is used by the TSA to describe equipment that is certified to detect explosives in checked luggage. Systems are tested by the DHS's Transportation Security Laboratory (TSL) in Atlantic City, New Jersey, and certified by the TSA. An EDS must consist of a device for automatically interrogating checked luggage and automatically determining if a threat is present. A schematic drawing of a CT-based EDS is shown in Figure 16.92. To become certified, an EDS must meet TSA requirements for detection of threats, false alarms, and conduct of operations. Several manufacturers have passed the TSA's certification testing.

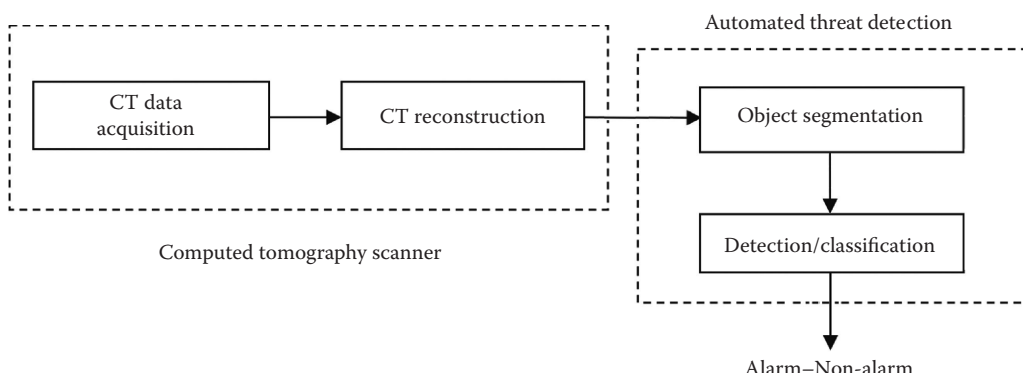


FIGURE 16.92 Schematic diagram of a CT-based EDS including ATD.

Some EDSs combine selected planar cross-sectional CT with a digital radiographic scanner. The images from the DR are automatically used to determine where selective cross-sectional images should be acquired (sometimes referred to as step-and-shoot CT). Such systems were the first certified EDSs and were developed and manufactured by InVision Technologies, Inc. (Peschmann and Harmann 1993). Since then, InVision was bought by GE Security and GE Security was bought by Safran and is now called Morpho Detection.

An example EDS is shown in Figure 16.93. An EDS's result may include a selected number of CT cross-sectional to 3D volume rendered images of checked luggage. A representative 3D rendered image of a mock checked luggage is given in Figure 16.94. The red area in the image specifies a potential threat (alarmed object or objects) generated by an ATD. These results are presented on a display so that the operator may confirm or override the decision of ATD and declare the alarm to be a non-alarm. The latter process is denoted as clearing. EDSs operate at a fairly wide range of tube potentials (up to 180 kV, typically), have from 1 to 9 mm³ voxels, and can now scan more than 1000 bags/h.

EDSs are deployed in a number of configurations (Martz and Crawford 2009). Inline means that the EDSs are fed with checked bags by a bag-handling system. An example of inline EDS deployment is shown in Figure 16.95 and schematically depicted in Figure 16.96. Stand-alone EDSs means that checked bags are fed manually. Standalone systems can be in front or behind the check-in counter.

Recently developed EDS CT scanners are typically volumetric. Examples include EDSs manufactured by Morpho Detection, Reveal (bought by SAIC and now called Leidos), and L-3 Security & Detection Systems. Most volumetric CT scanners are single-energy and therefore only produce measurements of one linear attenuation coefficient, which is used to estimate density. The Leidos CT EDS obtains dual-energy measurements and is used to produce estimates of effective atomic number and density. It is useful to point out that as the number of x-ray features for a material or object increases, the threat detection may increase while the false alarm rate may decrease.

The advantage of two measurements is schematically shown in Figure 16.97. For example, for a single-energy CT system, one feature is obtained, which is representative of density. So for a single-energy system to detect say the threat (red blob) on the left in Figure 16.97, this would result in several false alarms due to many nonthreats (green blobs) just above and below the threat. On the other hand, for a dual-energy system, there are two x-ray features, e.g., effective atomic number and density. In this case, for the same threat on the left in Figure 16.97, the resulting overlap between the two features is smaller than the single-energy density feature, and to detect this threat would result in fewer false alarms since there are fewer nonthreats within the two features' overlapped window.



FIGURE 16.93 Photo of an inline Safran Morpho CTX9800 EDS. (From Morpho, <http://www.morpho.com>, 2015. Courtesy of Morpho Detection.)



FIGURE 16.94 Representative images from Morpho Detection’s CTX9800 explosives detection system. The top left image is a 3D rendering of a bag with potential threats shown in red. The top right image is a CT cross section taken from the 3D CT data with one potential threat highlighted. The lower pair of images is of another bag. (Courtesy of Morpho Detection.)

Many if not all of the single-energy EDS manufacturers have dual-energy CT systems, though the approach taken to generating dual-energy information can vary widely.

At LLNL, we have a very broad range of x-ray CT capability. This was used by DHS and, at the time, Reveal (now Leidos) to investigate methods to reduce streak artifacts and to help reduce false alarms for highly attenuating checked bags. Some example DR and CT images were acquired at LLNL for a set of DHS luggage with and without explosive simulants. An LLNL-developed CT scanner was used for this study. The LLNL CT scanner has a Comet 450 kV x-ray source and an amorphous-silicon flat-panel detector (detector pitch of 127 μm in both axes) with a gadolinium oxysulfide (Lanex Fine) scintillating screen. A photograph of the scanner is shown in Figure 16.98. It is useful to point out that the images are representative of security scanner images, except that they are about three orders of magnitude (voxel volume of 10^{-3} mm^3 vs. 1 mm^3) better in spatial resolution than the security scanner images, and some CT data were acquired at higher potential (up to 300 kV) than a typical security CT scanner, 140 kV. Representative LLNL x-ray CT images for bags are shown in Figures 16.99 and 16.100. In the bottom right image in Figure 16.99, there are

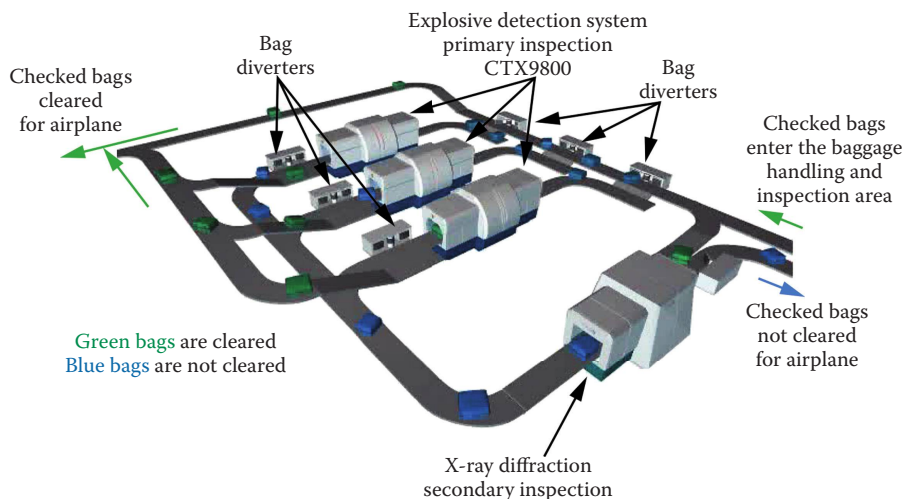


FIGURE 16.95 Diagram of three EDSs and an x-ray diffraction imaging system deployed in an example inline configuration. (Adapted from an image and courtesy of Morpho Detection.)

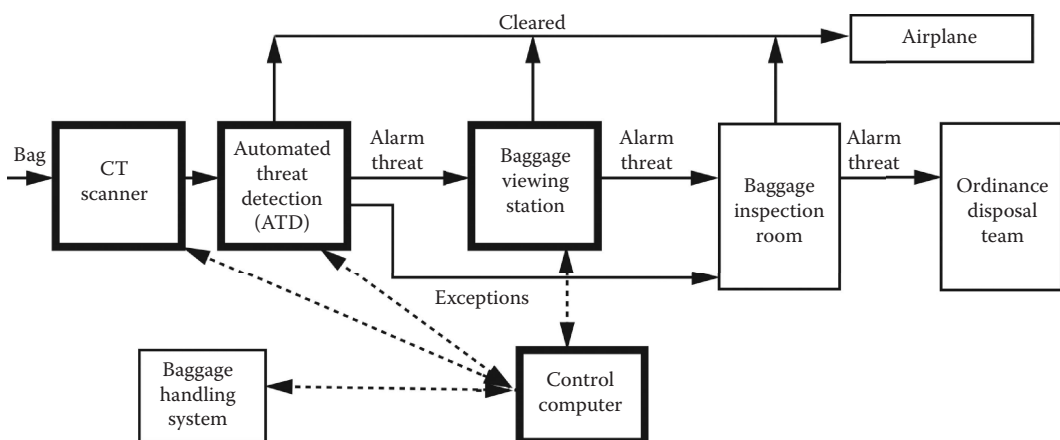


FIGURE 16.96 Schematic diagram of an inline EDS. Wide-lined boxes are components of an EDS. Narrow-lined boxes are subsystems used in conjunction with the EDS. Solid connecting lines show flow of bags and/or images of the bags. Dashed connecting lines show the flow of control and information.

several CT streak artifacts that result in poorer performance. Several researchers are investigating methods to reduce such artifacts and to increase performance (for example see Karimi et al. 2015). For other researchers efforts for explosive detection see Wells and Bradley (2012) and Iovea et al. (2007). One of the authors (Martz) has been active in getting others involved in explosives detection research (Martz et al. 2011) also see ALERT (2016).

Recently, manufacturers have developed explosives detection CT scanners that employ multiple sources and detector arrays to eliminate the mechanical rotation of a CT gantry (Morton et al. 2009; Gonzales et al. 2013, 2014). Others have been developing multiple sources and photon-counting detectors for spectral imaging and a limited number of views (US Patent 1998). A third type uses x-ray diffraction (Strecker and Harding 1993; Harding 2009). Some examples of such systems are given in Section 16.5.4.

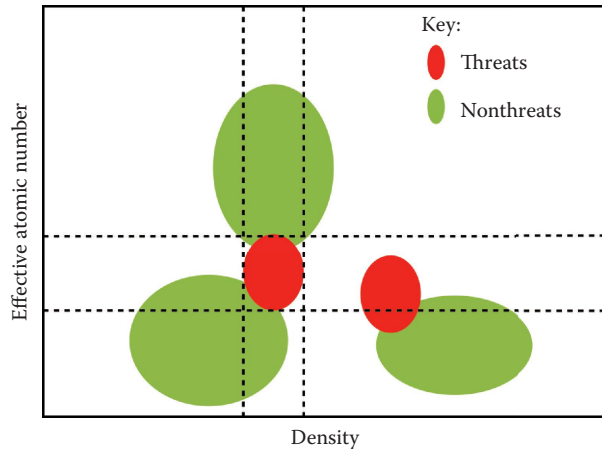


FIGURE 16.97 Notional plot showing threats (red) and nonthreats (green). As the number of x-ray features increases, the detection rate increases and/or the false alarm rate decreases.

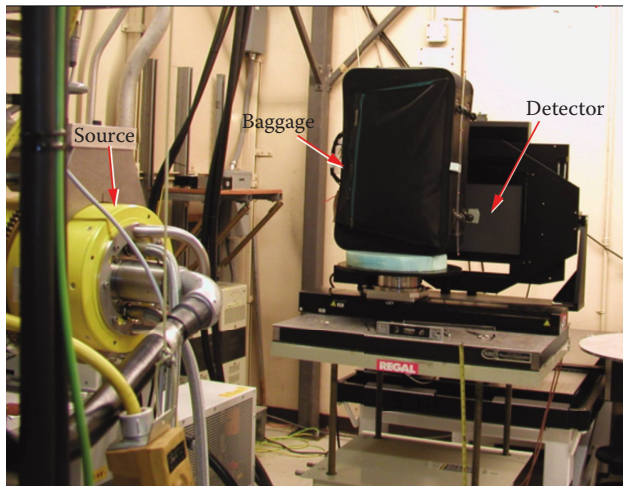


FIGURE 16.98 Photograph of the LLNL-developed CT scanner that is used to acquire DR and CT data. Shown is one of several mock bags that were scanned for a DHS explosives detection program.

16.5.3 X-RAY DR AND DIFFRACTION TO INSPECT CHECKED LUGGAGE

In addition to x-ray CT systems that have passed the checked luggage TSA certification process, at this time, only one x-ray diffraction system has also passed the certification process. The x-ray diffraction system that passed certification is a pencil-beam system that scans up to 10 bags/h. These x-ray diffraction systems are manufactured by Safran's Morpho Detection. X-ray diffraction systems are being developed for higher throughput. A schematic diagram and x-ray diffraction spectra are given in Figure 16.101. Representative radiographic images are shown in Figure 16.102. These DR images are used to guide x-ray diffraction data acquisition. Although the x-ray diffraction image is of much lower spatial resolution than the DR or CT images, the spectral information from diffraction provides greater material specificity. X-ray diffraction systems for explosives detection in luggage were initially developed by Philips (Strecker and Harding 1993;

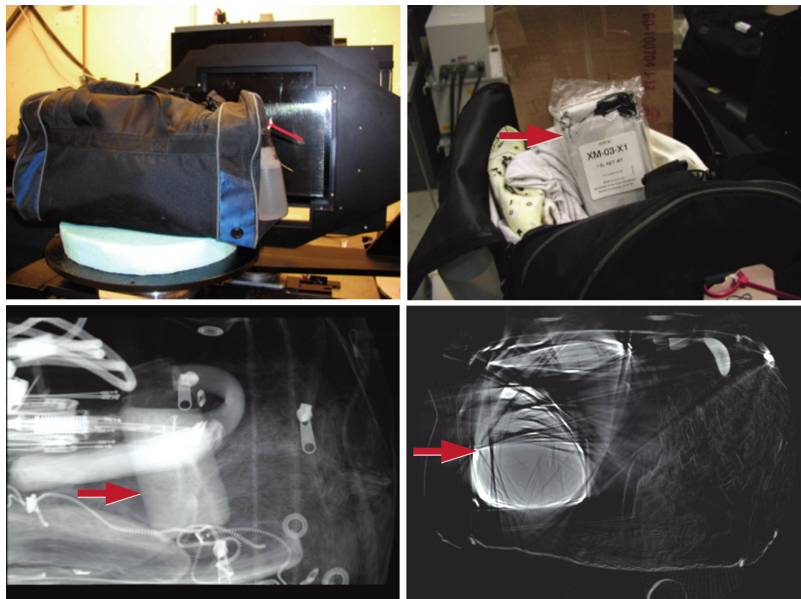


FIGURE 16.99 Top left: A photograph of luggage being scanned in an LLNL-developed CT scanner. Top right: Photo of a bag showing a bulk explosive simulant (highlighted by the red arrow) inserted into the luggage between some other items within a mock bag. Bottom left: A 2D DR image of a part of the luggage showing the simulant explosive (highlighted by the red arrow) along with the other items in the bag. Bottom right: A CT cross section of the luggage with the bulk explosive simulant (highlighted by the red arrow).

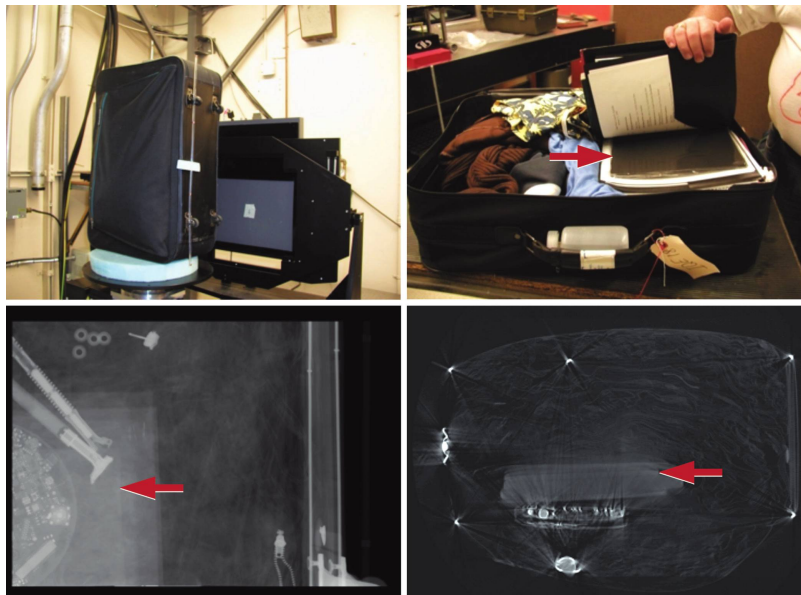


FIGURE 16.100 Top left: A photograph of luggage being scanned in an LLNL-developed CT scanner. Top right: Photo of a bag showing a sheet explosive simulant (highlighted by the red arrow) inserted into the luggage between some other items within a mock bag. Bottom left: A 2D DR image of a part of the luggage showing the simulant explosive (highlighted by the red arrow) along with the other items in the bag. Bottom right: A CT cross section of the luggage with the sheet explosive simulant (highlighted by the red arrow).

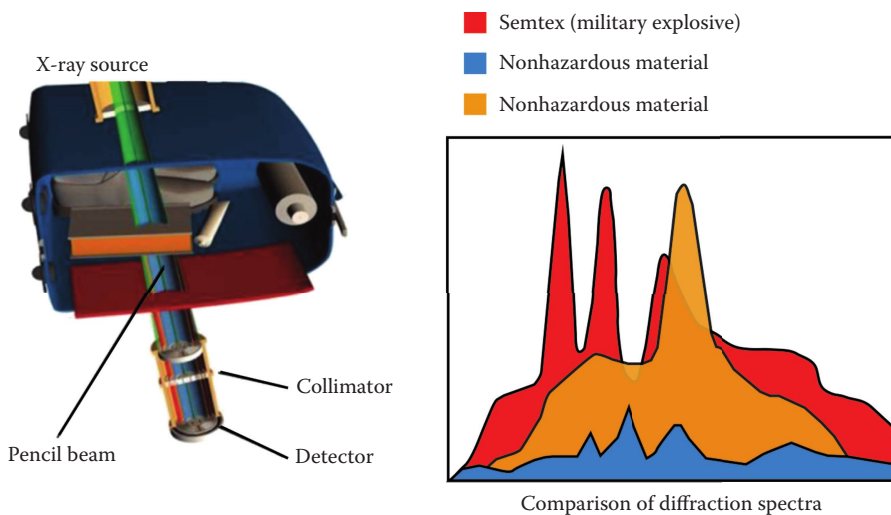


FIGURE 16.101 On the left is a schematic drawing of Morpho Detection’s XRD 3500 x-ray diffraction imaging system. A pencil beam of x-rays is rastered over the bag to generate a 3D volume of x-ray diffraction spectra similar to what is shown schematically on the right. Each material exhibits a unique diffraction spectrum. (Courtesy of Morpho Detection.)

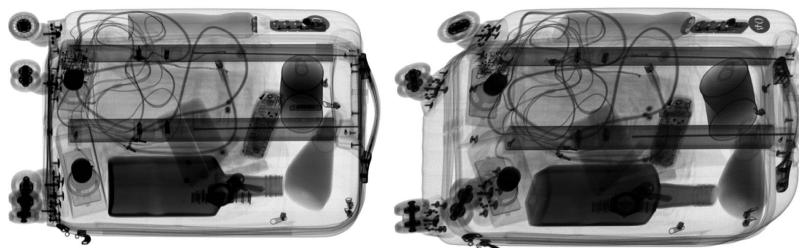


FIGURE 16.102 Two representative different radiographic views of a mock bag from Morpho Detection’s XDi x-ray diffraction imaging system for carry-on luggage. (Courtesy of Morpho Detection.)

Harding 2009). Their system was acquired by GE Security, which became Morpho Detection. Morpho Detection developed an x-ray diffraction system called *XDi* to detect liquid explosive threats inside carry-on luggage at the checkpoint. Others are working to advance x-ray diffraction, e.g., Brady et al. (2013).

16.5.4 NONROTATING GANTRY SECURITY CT SYSTEMS

Conventionally, medical and security x-ray tomographic imaging systems have used a single x-ray source and an array of detectors, which together rotate around the object of interest to form a set of x-ray projections through the object (see Chapter 13). These projections can be reconstructed to form an image of the object in 2D or 3D. Due to the mechanical motion involved in this scanning process, scan rates are restricted to only a few source revolutions per second. The latest dual-source medical CT scanners are able to perform just over 3 per second (Krauss et al. 2011); this gives a reconstructed image frame rate of less than 10 per second. In some applications, such frame rates are too slow to provide the required temporal resolution, for example, in the visualization of the flow of liquids in pipes.

The main factor limiting the speed of conventional rotating gantry cone-beam CT scanners is the physical rotation of the source (Kalender 2006). To address this problem, it is necessary to eliminate the mechanical scanning motion, replacing this with an electronic equivalent comprising a circular array of x-ray sources, which can be selected individually under computer control. Through the choice of a suitable source scanning sequence, the impression of movement can be generated without physical motion of any component of the system. Several manufacturers are investigating stationary or nonrotating CT systems for aviation security. Some are discussed in the following three sections.

16.5.4.1 SureScan Nonrotating Gantry CT System

SureScan designed and built a nonrotating, stationary gantry, CT system called SureScan x1000. It is based on 28 fixed switching x-ray sources, spectral photon-counting detectors, and iterative image reconstruction at speeds up to 50 CT images/s. In April 2014, the SureScan system was the first nonrotating CT gantry system to pass TSA's certification test. A photograph of the SureScan x1000 CT checked luggage scanning system is shown in Figure 16.103. A schematic drawing and representative images are given in Figures 16.104 and 16.105, respectively.



FIGURE 16.103 Photograph of the SureScan x1000 checked luggage CT scanner. (Courtesy of SureScan.)

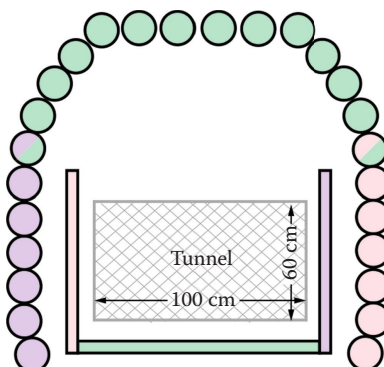


FIGURE 16.104 Schematic diagrams of the SureScan x1000 stationary gantry CT system. The multiple x-ray sources (colored circles) are imaged by three LDAs (colored rectangles). The matching colored source/detector show which sources are imaged by which detector(s). (Courtesy of SureScan.)

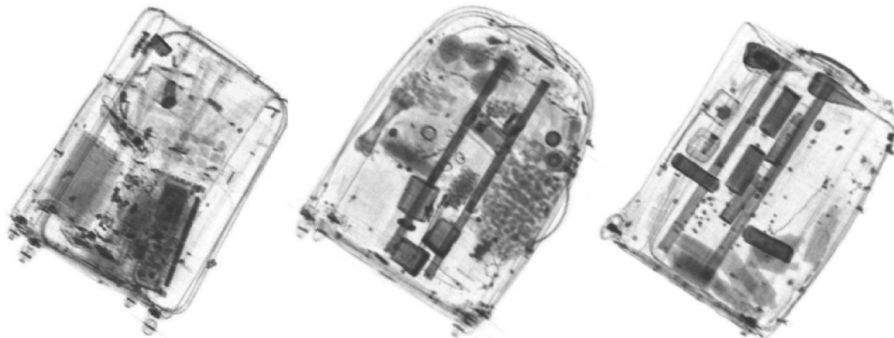


FIGURE 16.105 SureScan.x1000 3D rendered x-ray CT views of three different bags. (Courtesy of SureScan.)

16.5.4.2 Rapiscan Nonrotating Gantry CT System

Rapiscan Systems Laboratories developed a nonrotating gantry CT system, known as the real-time tomography (RTT) system, to solve this technological rotating gantry and CT throughput problem (Morton et al. 1999; Morton 2009). The RTT passed TSA certification in early 2015. Rapiscan uses a 360° circular array of x-ray sources, and the source array is matched with a corresponding circular array of x-ray detectors to provide a no-moving-parts besides the belt moving the luggage x-ray tomographic scanning system. The plane containing the x-ray sources is offset from the plane containing the x-ray detectors to avoid attenuation of the primary beam before it is transmitted through the object under inspection.

The x-ray sources comprise an array of electron guns, each of which is controlled by an independent electronic switching circuit. These switching circuits can be pulsed in microsecond timescales. The electron beam from a given source is accelerated through a high potential difference to a tungsten anode to produce x-rays. A single distributed anode is arranged in a circular manner such that each electron gun irradiates a different region of the anode around the circumference of a circle or polygon. The electron gun control electronics can be programmed to irradiate the electron guns in any given sequence. Therefore, this is a flexible data acquisition platform and is capable of generating tomographic scan data at practical source rotation rates of 30 revolutions per second.

RTT has been developed to look at luggage (Morton et al. 2009) as well as imaging of high-speed dynamic processes, such as moving fluid flows (Thompson et al. 2012). The Rapiscan RTT is designed to accurately detect an increased range of explosive threats and prohibited items, including liquid explosives. The stationary gantry design allows RTT to provide detailed 3D images at a throughput of about 1800 bags/h. Photographs of an RTT system and its operator consoles are given in [Figure 16.106](#) and [16.107](#), respectively. A representative RTT image of a bag is given in [Figure 16.108](#).

16.5.4.3 XinRay Laboratory Prototype Nonrotating Gantry CT System

XinRay Systems Inc. has developed a laboratory prototype CT system that utilizes an advanced carbon nanotube (CNT) multibeam tube to create a nonrotating gantry CT imaging system designed specifically for airport baggage screening (Gonzales et al. 2014). Conventional x-ray tubes are thermionic or hot sources, meaning that the cathode, a metal filament in this case, is heated up to produce electrons, which are subsequently accelerated toward the anode to produce x-rays. An alternative to thermionic sources is field emission sources or cold sources. In field emission tubes, electrons are extracted from the tip of the object through a process called quantum tunneling (Fowler and Nordheim 1928). Recently, CNTs have been developed for use as field emitters in field emission x-ray sources (Cheng and Zhou 2003; Calderón-Colón et al. 2009). Due to their large aspect ratios, and thermal and conductive stability, CNTs make ideal field emitters.

Most conventional CT systems are constrained to a circular imaging geometry ([Section 16.5.4.1](#) describes a system where this is not true and this is not the only one) due to the need to physically



FIGURE 16.106 Photograph of the Rapsican Systems stationary gantry RTT 110 security system. (Courtesy of Rapiscan Systems.)

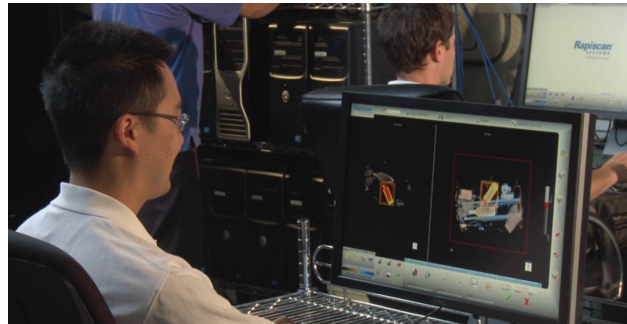


FIGURE 16.107 Representative Rapiscan RTT system console used to view scanned luggage. (Courtesy of Rapiscan Systems.)

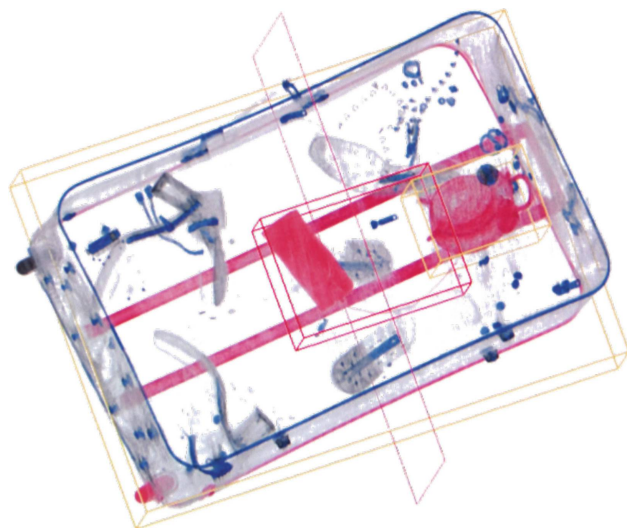


FIGURE 16.108 Representative 3D rendered image of a mock checked bag from the Rapiscan RTT luggage scanner. (Courtesy of Rapiscan Systems.)

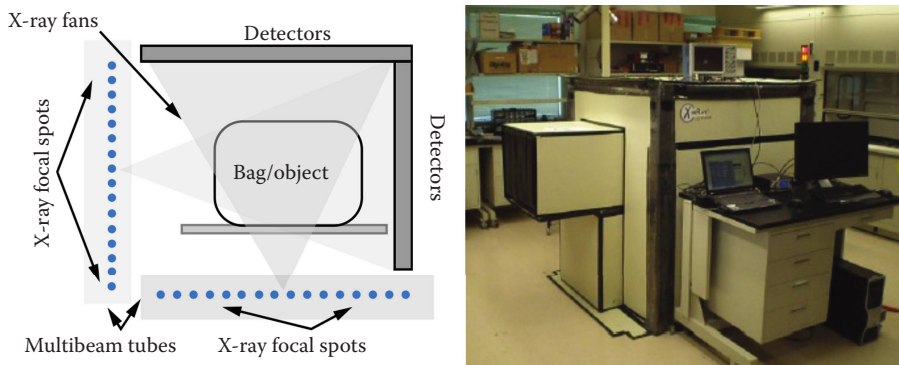


FIGURE 16.109 XinRay Systems Inc. laboratory prototype fixed gantry rectangular CT system for airport checkpoint carry-on baggage screening. On the left is a schematic representation of imaging geometry with linear arrays of focal spots arranged opposite LDAs to form a rectangular scan around a tunnel with a conveyor belt to move baggage through the CT scanner. On the right is a photograph of a prototype in XinRay's laboratory. (Courtesy of XinRay Systems Inc.)

rotate an x-ray source and detector (typical for medical and security CT systems) or object (typical for industrial or NDC CT systems) to acquire tomographic data. CNT multibeam tubes provide an array of fixed x-ray focal spots that can be arranged in any geometry. Using CNT multibeam tubes, a CT system can be designed with an imaging geometry tailored to a specific imaging problem. XinRay used the multibeam CNTs to design a rectangular CT imaging geometry for an airport carry-on baggage screening system. A schematic and photograph of their laboratory prototype is shown in Figure 16.109. At the airport checkpoint, space is limited and a full-sized rotating gantry CT does not fit into existing screening lanes. To reduce the size of the imaging system, XinRay arranged the x-ray focal spots and detectors to match the rectangular shape of the imaging tunnel used by airport baggage screening systems. The system is an example of using CNT multibeam tubes to create a CT imaging geometry around a specific application rather than trying to fit an imaging application into a circular geometry.

The XinRay laboratory prototype CT system has sparse angular sampling; a number of angles are undersampled or not sampled at all. The angular sparsity is due to both the rectangular geometry and the total number of x-ray focal spots used in the CT scan. XinRay uses a compressed sensing-based reconstruction method applying a total variation minimization algorithm to account for the sparse angular sampling. The reconstruction method is based on a modification of the adaptive-steepest descent projection onto convex sets method developed by Pan et al. (2009). For another reconstruction method that could be used see Champlay et al. (2016).

To demonstrate the laboratory prototype CT with a more realistic object, XinRay scanned a suitcase filled with a number of objects of interest and clothing. In Figure 16.110, a 3D rendering of the reconstructed suitcase is shown. Additionally, the 3D rendering of a number of objects of interest are shown separately, isolated from the suitcase data. The objects of interest include bottles filled with liquid, a knife, a cell phone, a bottle of wine, a laptop, and a personal grooming kit. The objects are isolated to show that the detail in the different objects is accurately reconstructed.

16.5.5 X-RAY BACKSCATTER OF PASSENGERS

X-ray backscattered imaging of people has been developed and used to look for concealed items on people entering prisons, for military security checkpoints, and for people entering the secure areas of an airport. In 2008, TSA deployed the x-ray backscatter Rapiscan Secure 1000 manufactured by Rapiscan Systems. This advanced imaging technology (AIT) (also known as a whole body imager) system is based on the x-ray backscatter imaging device described by Smith (1993). In summary,

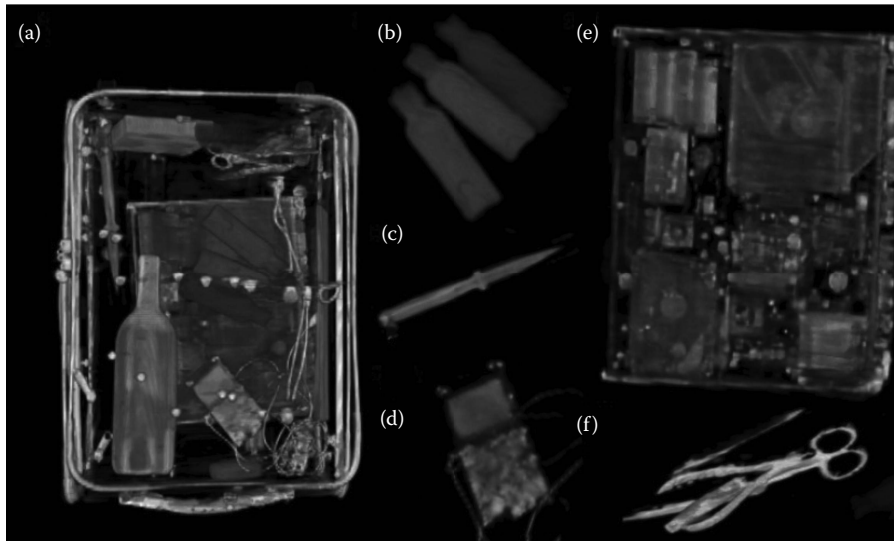


FIGURE 16.110 Representative 3D rendered images of a reconstruction of a mock suitcase scanned using the XinRay laboratory prototype CT system. The figure includes (a) full rendered image of the suitcase, as well as 3D segmented images of (b) multiple liquid-filled bottles, (c) a knife, (d) a cell phone, (e) a laptop computer, and (f) a personal grooming kit with multiple objects. (Courtesy of XinRay Systems Inc.)

a well-collimated pencil beam of x-rays is raster-scanned across an area in which a person is positioned, and the x-rays backscattered from a person toward the source are collected by large area detectors adjacent to and on the side of the x-ray source. The spatial resolution of the x-ray backscattered image is defined by the source collimator aperture and distance from the source to the person; the spatial resolution is not defined by the detector. A schematic of the interaction of the backscattered x-rays from a human is shown in Figure 16.111.

Since the technology was first developed, x-ray backscatter AIT systems have evolved, and several models with distinct characteristics are available today. For example, there are at least three x-ray backscatter manufacturers: Rapiscan Systems, American Science and Engineering, Inc. (AS&E), and Tek84 Engineering Group, LLC. Each of these manufacturers produces general-use x-ray security-screening AIT systems. The manufacturers use similar physics and differ mainly in their implementation of the physics and other aspects. Photographs for two x-ray AIT systems are

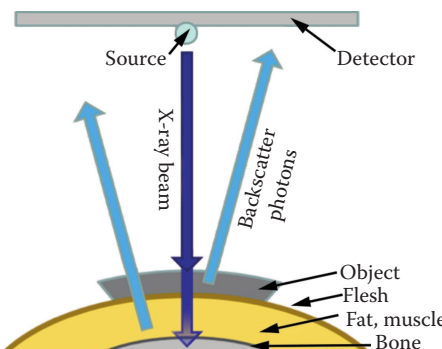


FIGURE 16.111 Schematic drawing depicting x-rays backscattered from a human. Backscattered x-rays are sensitive to elemental composition, i.e., atomic number, Z, and density. More x-rays are backscattered from low- than high-atomic number tissue and materials.

shown in Figure 16.112. Representative x-ray AIT images are shown in Figure 16.113a. Also shown in Figure 16.113b are millimeter-wave (MMW) AIT images for comparison. Tek84 is also combining through x-ray transmission and backscatter as shown in Figure 16.114.

TSA removed Rapiscan Secure 1000 AITs from all airports by June 2013 because of heightened privacy concerns (see Figure 16.113). US Congress set this deadline for deployment of software known as automated target recognition (ATR) or ATD, which eliminates the privacy issue since it displays ATD anomalies on a generic figure (see Figure 16.115) instead of an image of the individual's body. The AS&E SmartCheck x-ray backscatter AIT is under test and evaluation by TSA. It is to be determined if x-ray backscatter systems will be deployed in the future at airports. For a summary of x-ray AIT passenger dose see the National Academy of Sciences report (Martz et al. 2015).

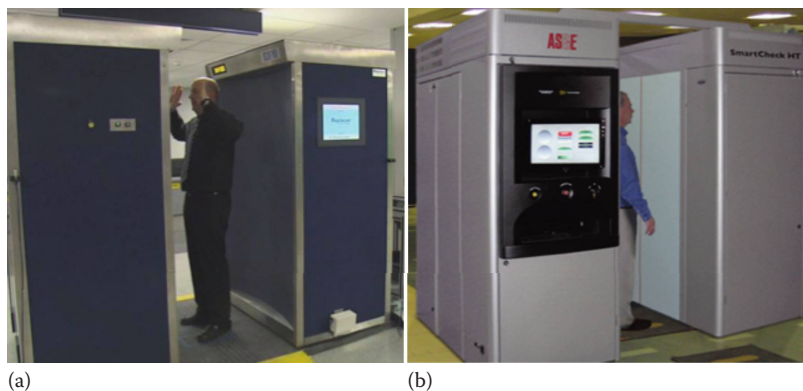


FIGURE 16.112 Example of two x-ray backscatter AIT systems used to screen people for concealed items. (a) Rapiscan Secure 1000 used to be deployed at airports and (b) AS&E SmartCheck under development for airport security. (From http://www.rapiscansystems.com/media/uploaded/products/126/rapiscan-secure-1000-sp-1__large.jpg and <http://www.as-e.com/uploads/images/SmartCheckHT.jpg>.)

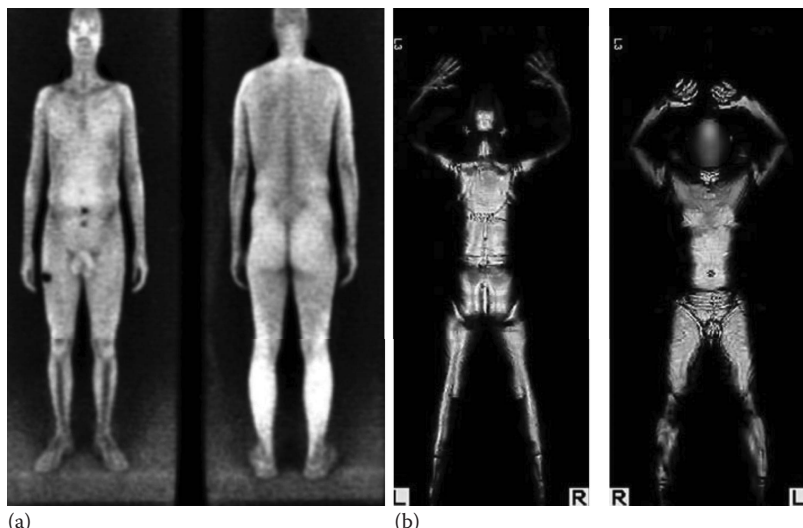


FIGURE 16.113 Backscatter images from advanced imaging technologies (AITs) not equipped with ATR: (a) Rapiscan Secure 1000 x-ray backscatter AIT and (b) L3 Safeview MMW AIT. Note that more x-rays are backscattered from low- (bright in a) than high-atomic number (dark in a) tissue and materials. (From <http://dcontscans.us/scans.html> and <http://www.sds.l-3com.com/advancedimaging/provision.htm>.)

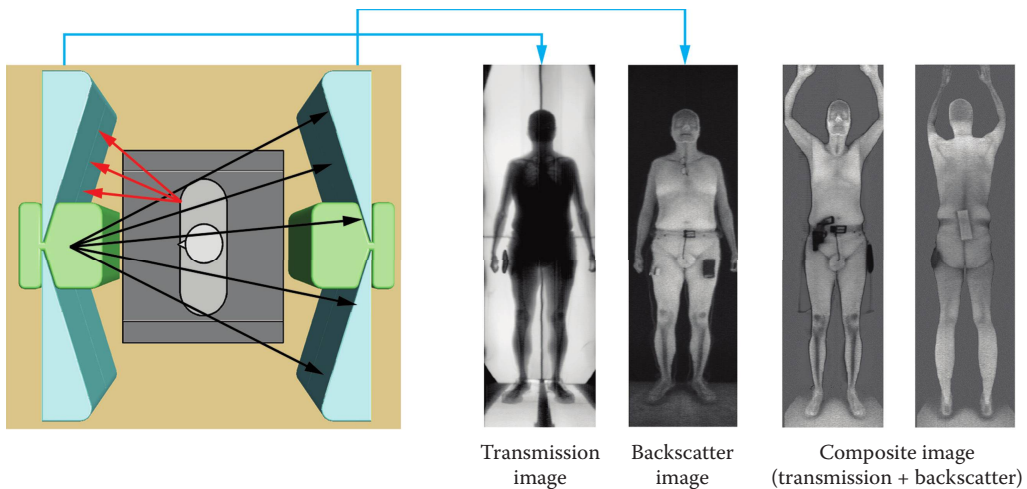


FIGURE 16.114 On the left is a schematic of the Tek84 AIT. On the right are representative images that their AIT generates. Note that the composite image is from a different person with different mock threats. (Courtesy of Tek84 Engineering Group, LLC.)

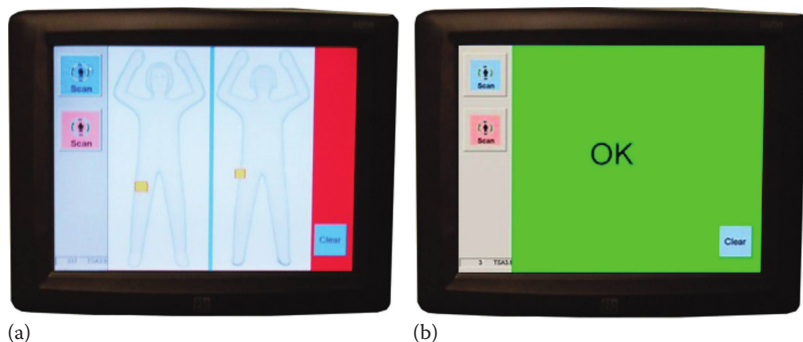


FIGURE 16.115 Images from a MMW AIT monitor equipped with ATR. Note: If potential threat items are detected on the person being scanned, they are indicated on a generic outline of a person that is identical for all passengers screened. (a) Areas identified as containing potential threats (yellow areas) will require additional screening. (b) If no potential threat items are detected, an "OK" appears on the monitor with no outline. X-ray backscatter systems will also need to have an ATR algorithm to provide similar monitor images.

16.5.6 X-RAY RADIOGRAPHY AND BACKSCATTER FOR CARGO NONINTRUSIVE INSPECTION

As mentioned above, since 9/11, there is a growing interest to improve the security of cargo shipping. Of particular concern to the US government is the illicit shipment of nuclear and other radioactive materials that are out of regulatory control. A homeland security Presidential Directive and the SAFE Port Act of 2006 mandated the creation of the Global Nuclear Detection Architecture and charged the DNDO with coordinating its development and implementing its domestic component.

DNDO has developed several systems to inspect cargo at various ports of entry. Programs within DNDO that have x-ray technologies as a key for nonintrusive inspection (NII) or nondestructive inspection include CAARS, Nuclear and Radiological Imaging Platform (NRIP), and Passive and X-ray Imaging Scanning (PAXIS). In the CAARS program, dual-energy radiography was developed, tested, and demonstrated to distinguish high atomic number ($Z \geq 72$) from lower Z ($Z < 72$) materials. A schematic diagram for a generic CAARS high-potential (3–9 MV) cargo inspection

system is given in Figure 16.116. An example of the use of dual-energy radiographs and processing to distinguish low- from high-Z materials is shown in Figure 16.117 and [Section 16.3.3](#). Manufacturers such as SAIC (now Leidos) and L3 have developed dual-energy x-ray radiography systems that take advantage of the pair production cross section to distinguish high- from low-atomic number materials. Photographs of two dual energy CAARS prototypes are shown in [Figure 16.118](#). Representative radiographs are shown in [Figure 16.119](#).

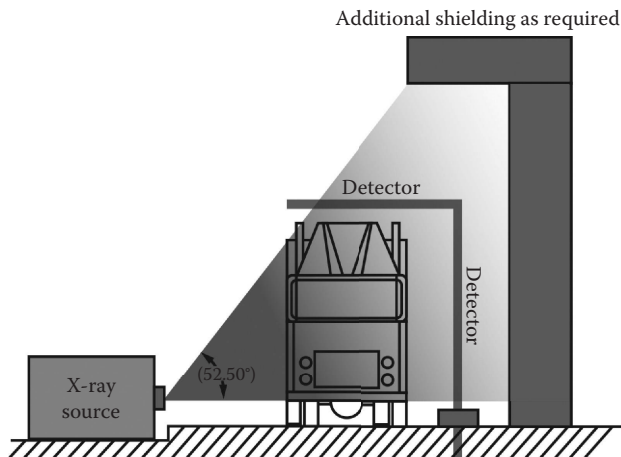


FIGURE 16.116 Schematic diagram for a generic CAARS high-potential (3–9 MV) cargo inspection system. These systems are typically referred to as NIIs.

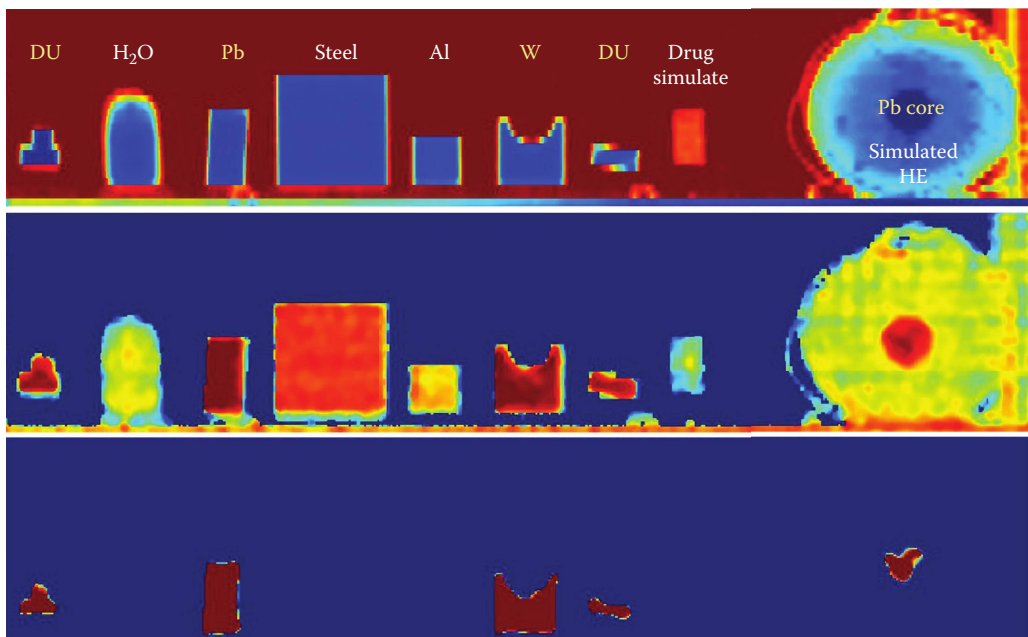


FIGURE 16.117 Images that show how dual-potential (6 and 9 MV) images can be used to sort low ($Z < 72$) from high ($Z \geq 72$) atomic number materials and objects. The top image is a 6 MV radiograph. The middle image is a Z map formed from 6 and 9 MV radiographs. High-Z detection radiography results obtained by an automated threshold for high Z are given at the bottom. Note that the image has no cargo. Once cargo is added to the radiographs, it becomes harder to detect high-Z materials and objects.



FIGURE 16.118 Two prototype CAARS dual-energy radiography systems. SAIC (now Leidos) is at the top and L3 is at the bottom.

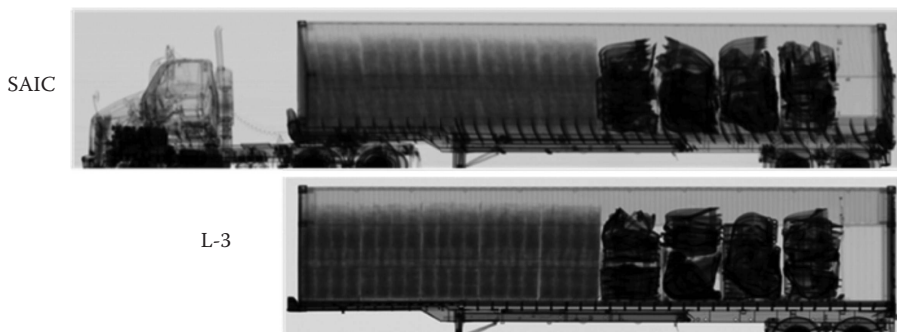


FIGURE 16.119 Representative SAIC (now Leidos) and L-3 CAARS prototype 9 MV x-ray radiographs of DNDO representative cargo. Near the front of the container are pallets of water bottles, and pallets of backhoe buckets are in the back.

The Leidos CAARS prototype used an interlaced dual-potential (6/9 MV) radiography approach. The system incorporated a new compact X-Band linac x-ray source, a new klystron power supply, and a low-neutron production target. SAIC also used a more efficient Cherenkov detector design, enabling use of lower photon flux in imaging, which results in less inadvertent occupant dose and a smaller radiation footprint. These features, combined with sufficient shielding for source and detectors, yielded a relatively small system footprint of 60 × 120 ft. The Leidos CAARS prototype was

gantry-mounted to enable inspection scanning of a stationary cargo conveyance, including tractor cab and engine compartment. A representative image is shown in [Figure 16.119](#).

The L-3 CAARS Prototype, uses a dual-energy radiography approach that uses two radiography systems. Their prototype has two Varian linac x-ray sources one operating at 6 MV and the other at 9 MV, each source has a two separate Bio-Imaging Research (now Varian) linear detector arrays. The 6 MV detector is tuned to the characteristics of the 6 MV linac. The other detector is tuned to the 9 MV linac. The L3 CAARS prototype is mounted on a gantry to enable inspection scanning of a stationary cargo conveyance including tractor. A representative image is shown in Figure 16.119.

The NRIP program is conducting the ATD of Performance Test Units (PTUs) and the benchmarking of existing systems. Testing performed by the NRIP program is intended to stimulate the R&D community to develop mature integrated prototypes that demonstrate improved methods to screen conveyances (tractor and cargo container) and/or passenger vehicles for R/N threats at land and sea ports of entry and ports of departure, as well as other checkpoint screening applications. The NRIP objectives are to characterize the performance of integrated R/N detection platforms and to compare that performance to currently deployed screening systems.

During the summer and fall of 2013, DNDN evaluated the capabilities of commercial cargo inspection systems for detecting R/N threats. Three representative commercial off-the-shelf systems were tested and evaluated the SAIC IP6500 FullScan, the SAIC SRPM-210 (a newer radiation portal monitor [RPM] only), and the Smiths Detection HCVP 6030. The SAIC IP6500 FullScan uses a NII x-ray radiography system with a Betatron single energy 6.5 MeV x-ray source and a linear detector array (LDA) colocated with a passive gamma/neutron RPM (see Figure 16.120). The Smiths Detection HCVP 6030 also uses both an NII with a single energy 6 MeV linac source and a LDA and an RPM and is the background in Figure 16.120. The SAIC SRPM-210 (the S stands for spectroscopy) is a newer RPM only—it is not colocated with an NII. All RPMs produce automated passive detection decisions by either detection of x- or γ -rays and/or neutrons.

Most of the NII systems including those in the NRIP program require humans to manually analyze radiographic images. ATD algorithms have been developed and are used on some NIIs such as the Rapiscan Eagle shown in [Figure 16.121](#) (Shaw et al. 2009). Representative x-ray radiographs and γ -ray RPM line traces for DNDN representative stream of commerce cargo are shown in [Figure 16.122](#). An x-ray radiograph of a stream of commerce cargo with two backhoes is shown in [Figure 16.123](#).

The NRIP program is also investigating two other systems. One is a multi-modal passive detection system (MMPDS) being developed by Decision Sciences International Corporation Inc. The



FIGURE 16.120 In the foreground is the SAIC (now Leidos) IP6500 FullScan system at the PNNL Test Track. The Betatron is at the bottom of the tower on the left side (driver side) of the lane; the x-ray linear detector array extends over the lane and down the right side (passenger side). The four-panel RPM system is just beyond the x-ray system; two of the panels can be seen on the left side. The operations booth is on the left in the front. The Smiths HCVP 6030 system (gray) can be seen in the background on the same truck lane.



FIGURE 16.121 Photograph of Eagle Portal 6 MV x-ray radiography system.

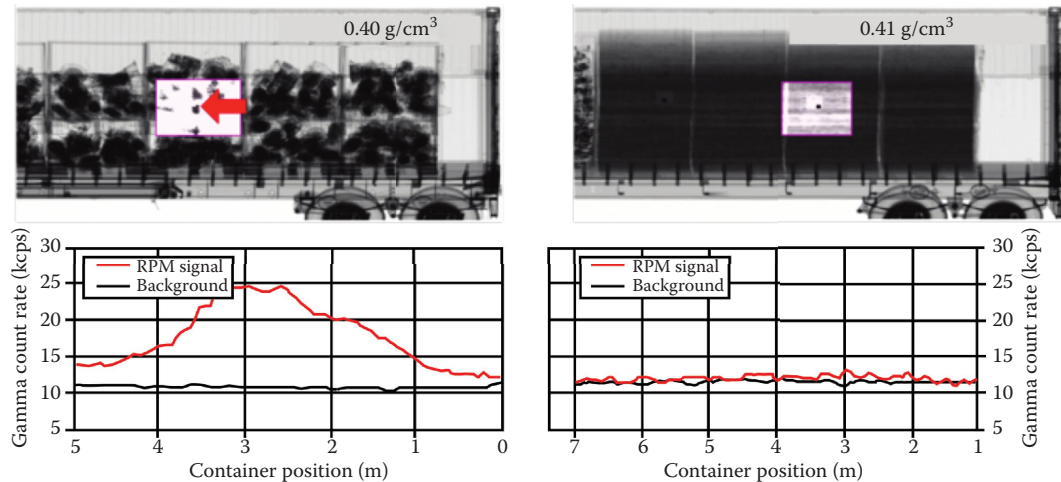


FIGURE 16.122 Smiths Detection HCVP 6030 representative (top) x-ray radiographs and (bottom) γ -ray RPM line traces for DNDI representative cargo.

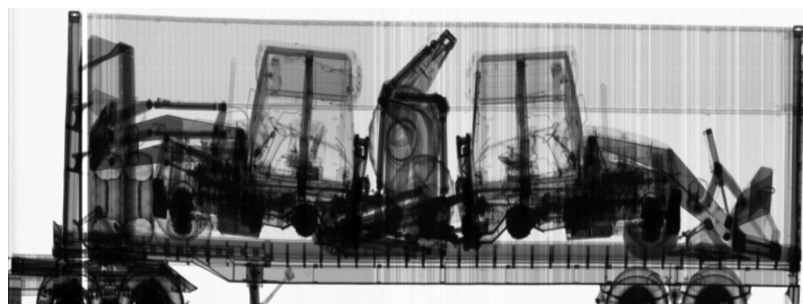


FIGURE 16.123 X-ray radiograph from a Smiths-Detection HCVM Mobile 4 MV NII system of a stream of commerce cargo with two backhoes.

MMPDS uses cosmic muons to detect high-Z materials and objects based on the scatter angle change of a muon as it traverses the contents of a cargo container (Blanpied et al. 2015). The second is under development by Passport Systems, Inc. The Passport NRIP system includes transmission radiography, x-ray backscatter (referred to as EZ3D), and prompt neutron photofission in primary scan mode and long dwell prompt neutron photofission and nuclear resonance fluorescence in secondary scan mode. Representative radiography and backscatter images are shown in Figures 16.124 and 16.125.

There is still considerable R&D in the area of cargo inspection; for example, see works by Saverskiy et al. (2015) on intrapulse multienergy method of material discrimination, Shaw et al. (2009) and Liu et al. (2008) on data fusion of x-ray radiography and neutron capture γ -ray spectroscopy, Clayton et al. (2007) on next-generation mega-voltage imaging system for inspection of cargo in large containers, Orphan et al. (2005) on enhanced γ -ray detectors for improved image resolution and Gilbert et al. (2014) on material discrimination using spectral radiography.

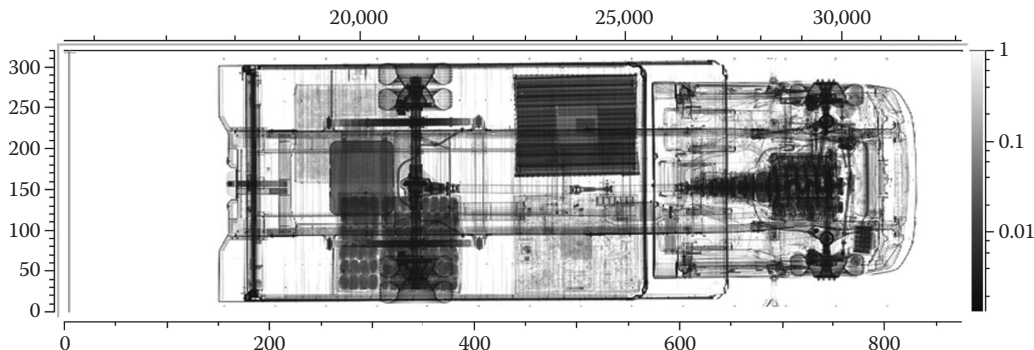


FIGURE 16.124 Representative Passport NRIP system 9 MV x-ray radiograph of a large van. The Passport NRIP system has the x-ray source on top of the vehicle, and the detectors are located under the vehicle, thus yielding a top-down view of the vehicle. From left to right in the image are the back of the van, cargo inside the van, the van's cab, and engine. (Courtesy of Passport Systems Inc.)

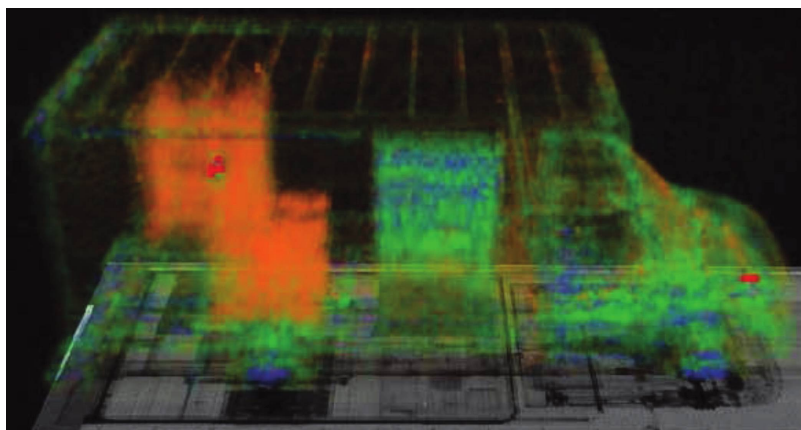


FIGURE 16.125 Passport x-ray backscatter 3D (EZ3D) rendered image of a large van. High-Z materials are automatically detected and are highlighted in red. Note that the battery at the front of the van is red since it has lead, $Z = 82$. The alarm in the cargo is a lead cube. Underneath the EZ3D image is a top-down radiograph. The radiograph is also shown in Figure 16.124. (Courtesy of Passport Systems Inc.)

PROBLEMS

- 16.1 In the x-ray gauging application described in [Section 16.1](#), suppose the sheet had a measured areal density of 1.02 g/cm^2 . The plastic substrate has an x-ray attenuation coefficient of $4.42 \text{ cm}^2/\text{g}$, while the heavy metal has an attenuation coefficient of $86.4 \text{ cm}^2/\text{g}$ for the line at 22.16 keV. The measured transmission is 55%. What are the areal densities of each component, plastic and heavy metal?
- 16.2 In a photon-counting detector, with perfect scatter rejection, how many detected counts are required to satisfy a noise requirement of 0.01% for a 1D gauging system?
- 16.3 If there are twice as many detected scatter counts as transmitted primary x-rays, how many detected counts are required to satisfy a noise requirement of 0.01% for a 1D gauging system? In a photon-counting detector, with perfect scatter rejection, how many detected counts are required to satisfy a noise requirement of 0.01% for a 1D gauging system?
- 16.4 Describe the process for calibrating a current integrating LDA to support quantitative transmission measurements.
- 16.5 Describe an x-ray-based inspection process whose goal is the identification of different component materials, and which utilizes at least two different energy values?
- 16.6 The CT image in [Figure 16.74b](#) has what look like rings. Are these rings in the different pieces of wood a CT ring artifact or different tree rings? Please explain what enables you to come to this conclusion.

17 Neutron and Proton Imaging

In this chapter, we give a brief introduction to radiation imaging methods that do not utilize photons. Neutrons and protons may be used to produce a single projection image or computed tomography (CT). The methods we address are attenuation transmission methods.

Here we will orient the reader as to the applications where radiography and/or CT using neutrons or protons is appropriate considering that sources for these are generally much more complex and expensive than x-ray sources. We restrict our considerations to two energy ranges for neutrons, thermal and megaelectron volt (MeV). Similarly for protons, we restrict our discussion to the MeV energy range.

Upon completion of this chapter, the student will be familiar with

- Type of applications where thermal neutron radiography and CT are most appropriate
- Unique attributes of MeV neutron imaging
- Imaging challenges best met with MeV protons
- Specific examples of applications employing these particles

17.1 IMAGING WITH THERMAL NEUTRONS

Thermal neutrons are second in importance only to x-rays and γ -rays in industrial imaging. *Thermal* refers to their energy. To attain thermal neutrons, neutrons of higher energy are slowed or *moderated* by scattering in certain materials. When they have slowed sufficiently that they are in equilibrium with the moderator, they have a spectrum of energies that is representative of the temperature of the moderator. For a room-temperature moderator, this corresponds to a mean energy of 0.025 eV.

Attenuation of thermal neutrons follows the same Beer's law (Section 5.3) relationship we covered for photons. For some materials, most of the attenuation arises from scatter with no energy loss. This can create substantial scatter contribution in the detected image.

Imaging with thermal neutrons is a valuable modality because their attenuation varies with material composition in a much different manner than that for x-rays. This results in situations where neutrons can image details not achievable with photons. Often, these applications require imaging a hydrogenous material shielded by a higher-Z material.

Thermal neutron mass attenuation coefficients (NIST Neutron 2015) are shown in [Figure 17.1](#) for the elements (natural abundance) and some important isotopes. The isotopes shown all have high mass attenuation coefficients and are technologically important for nuclear reactor control, for thermal neutron imaging and detection, and as *contrast agents* for thermal neutron imaging. Values for 70 keV and 3.5 MeV photons are given for comparison. Seventy kiloelectron volts is an important photon energy because it is near the K lines for the element tungsten, which is the material of most x-ray tube anodes. Thus, most x-ray tubes emit spectra rich in photons near 70 keV. Three and one-half megaelectron volts is the energy at which x-rays are most penetrating through high-Z material (NIST XCOM 2015).

Figure 17.1 provides clues to material combinations that may be effectively imaged with thermal neutrons. The mass attenuation coefficient for H is 1000 times that of Pb. So, it is possible to image a candle inside a Pb box. Fuels, elastomers, explosives, propellants, and plastics within various housings and containers make up a substantial portion of the applications for thermal neutron radiography (Berger 1965; Bossi et al. 2002).

The most important sources for thermal neutrons are nuclear reactors, ^{252}Cf , and accelerators. In each case, neutrons originate with higher energy and must be moderated to thermal energies. Nuclear reactors are nonportable facilities that provide the most intense sources of thermal neutrons.

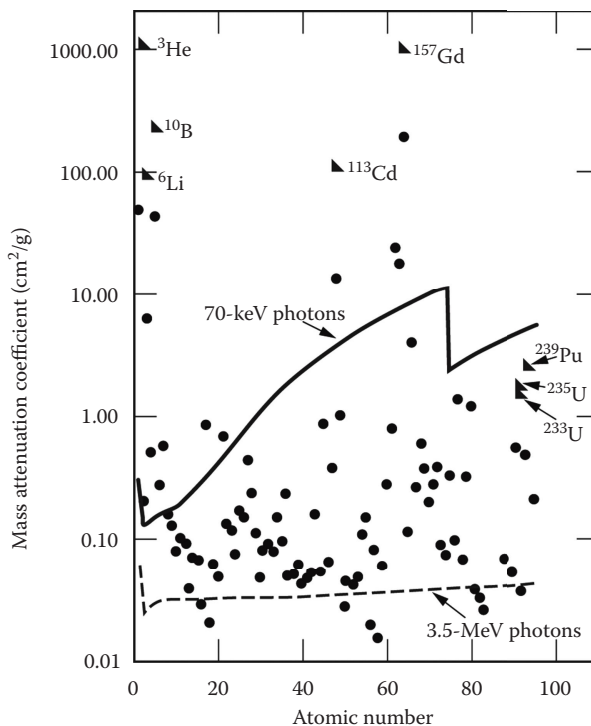


FIGURE 17.1 Mass attenuation coefficients of the elements and some important isotopes. The solid dots represent elements in their natural abundance. The isotopes (triangles) shown all have high mass attenuation coefficients for thermal neutrons and are technologically important for nuclear reactor control, thermal neutron imaging, and detection, and contrast agents for thermal neutron imaging. Values for photons at two energies are given for comparison. Seventy kiloelectron volts is an important photon energy because it is near the K lines for the element tungsten, which is the material of most x-ray tube anodes. Such tube spectra are rich in x-rays near 70 keV. (Plot created using data from NIST Neutron, <http://www.ncnr.nist.gov/resources/n-lengths/list.html>, 2015.)

Californium-252 decays (in part) by spontaneous fission. ^{252}Cf was first produced (Thompson et al. 1950) at the University of California (UC), Berkeley, in 1950, and was being used as a radiography source by 1968 (Reinig 1968). It is now produced by irradiation of heavy elements in fast reactors. Other Cf isotopes are also produced, so it must undergo an isotope separation to make useful sources. A ^{252}Cf source can be compact (see Figure 17.2), but for thermal neutrons to be produced, a considerable mass of *moderator* must be employed.

The third important type of thermal neutron source is accelerator based. These systems tend to be more portable than a reactor and less portable than a ^{252}Cf source. They typically accelerate protons or deuterons and employ different targets depending on the desired output. To deliver thermal neutrons, these systems are equipped with a moderator (Fantidis et al. 2013).

Thermal neutron sources are, by nature, diffuse sources. Using them for imaging requires collimation into a parallel or diverging beam. This collimation effectively defines the source size for a thermal neutron source. Collimation is usually described by the ratio of the distance from source to detector (L)* divided by the diameter of the collimator aperture (D) at the end nearest the source (see Figure 17.3). The L/D ratio is the parameter that defines the blurring in an image arising from the extent of the source. For large objects (in the direction of the beam), this is often the dominant cause of image blur.

* The source-to-detector distance is y_{sdd} in this book, but often it is common to use L in neutron imaging.

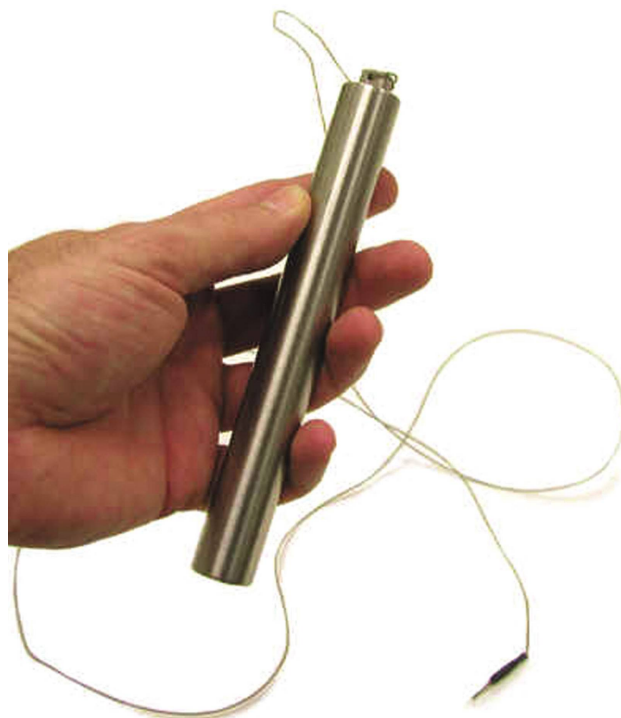


FIGURE 17.2 An early ^{252}Cf source capsule produced by Oak Ridge National Laboratory. This is a dummy capsule. (Courtesy of Oak Ridge Associated Universities, <http://www.orau.org/ptp/museumdirectory.htm>, 2015.)

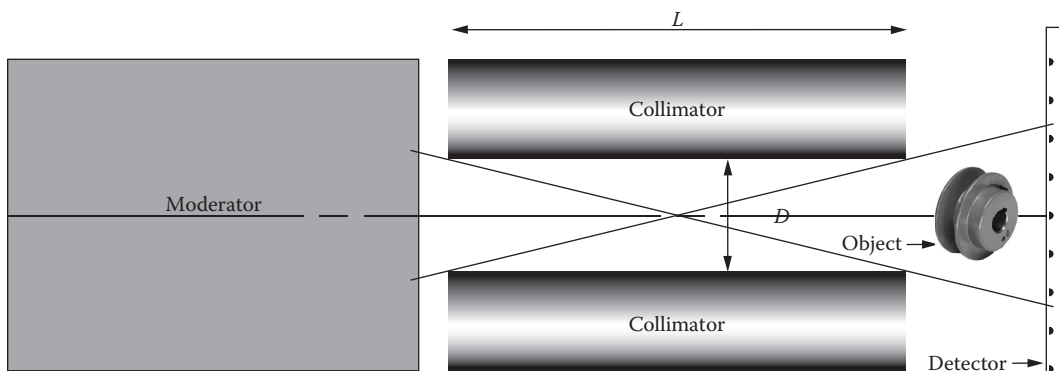


FIGURE 17.3 The effective source size of a thermal neutron source is determined by collimation. The ratio L/D determines the angular divergence of the beam. Making D larger generally results in higher neutron flux density at the object but increases the geometric blurring from source unsharpness.

The imaging detector used for most early work with thermal neutrons was film coupled with a conversion screen. Film alone has a slight response to thermal neutrons, so some conversion device (analogous to scintillation for photons) is required. Gadolinium metal foil is one effective conversion material. Gd emits conversion electrons after neutron capture. These electrons expose the film, usually single-emulsion x-ray film.

Photostimulable phosphors (PSP) are also used for thermal neutron imaging. These are similar to those used for photon imaging except that some material is added to undergo a neutron-induced reaction yielding an energetic electron or charged positive ion. One commercial PSP for thermal

neutron imaging (Andola et al. 2013) incorporates Gd that emits energetic electrons. As the electron slows and stops, it deposits energy in the PSP. The stored energy is released as visible light by scanning with a laser. The emitted light is detected, and position information is derived from the laser position. The PSP is then erased by intense light exposure and reused. Current PSP systems have a substantial response to photons, so this must be considered in their use. Their two main advantages over film are linearity and dynamic range. They also reduce waste, consume fewer resources, have no threshold exposure, have higher sensitivity than film, and once scanned, have all the advantages of digital images. As with film, PSPs are not practical detectors for CT, because at least several hundred accurately registered images are needed. Research and development (R & D) to develop improved PSPs is an active area. Goals include reduced γ response (Sakasai et al. 2004) and columnar structure (Nagarkar et al. 2001) to reduce light spread and scatter.

One detection method unique to neutron imaging is activation of a foil and then transferring the foil away from the neutrons and placing it in contact with an x-ray film. The image is recorded by the amount of activation in the foil. The film becomes an autoradiograph of the activated foil. In this manner, the film is not in the neutron beam and is not exposed to x and γ radiation present along with neutrons. The image retained by activation in the foil has essentially no photon response. This can be an especially important advantage for imaging radioactive objects. Imaging of irradiated fission fuel rods is one example where this method is uniquely suited.

Track-etch detectors also give immunity to photon radiation. A material is used that can be chemically etched to reveal the *tracks* left by a converter emitting an ion. The *track density* is proportional to the thermal neutron flux density delivered to the detector.

Electronic imaging of thermal neutrons usually employs a scintillator. Gadolinium oxysulfide screens have been highly developed for medical imaging with x-rays. This same screen is a useful detector of thermal neutrons via capture of neutrons by ^{157}Gd and subsequent electron emission. The emitted electron excites the scintillating gadolinium oxysulfide. ^{157}Gd is 16% of natural Gd. Other scintillators used with thermal neutrons combine an isotope that undergoes (n,α) reactions (^6Li or ^{10}B) in combination with a scintillator, such as ZnS(Ag). The emitted α -particle lights the scintillator. Light from the scintillator is imaged using lens and mirror coupling to a charge-coupled device (CCD) or direct contact with a photodiode array. Electronic detection enables CT and radiographic studies requiring reference images (for example, an empty container). At least one turning mirror is necessary when employing a CCD in order to remove it from the radiation field (Toops et al. 2013).

The first demonstration of thermal neutron imaging with a photodiode array fitted with a scintillating screen (Gibbs et al. 1999) was published in 1999. More recently, two groups report that photodiode arrays are being used (Claytor et al. 2004) or are under development (Lehmann et al. 2004) for thermal neutron imaging. Reported results with photodiode arrays have used scintillators developed for other purposes. Though some have used photodiode arrays with 127 μm pixel pitch, none have achieved a spatial resolution that is limited by the pixel pitch of the array.

From review of the literature, one can estimate spatial resolution for the various thermal neutron imagers. Table 17.1 presents our evaluation of the frequency at which modulation transfer is 10%.

TABLE 17.1
**Approximate Frequencies for 10% Modulation Transfer
for Various Thermal Neutron Detectors**

Imaging Detector	Frequency for 10% Modulation
Film w/ Gd screen	13 lp/mm
Track etch	13 lp/mm
PSP w/ Gd doping	6 lp/mm
CCD w/ scintillator	8 lp/mm
Photodiode flat panel w/ scintillator	2 lp/mm

One important application of thermal neutron radiography and CT is detection of corrosion in aircraft. Aluminum is frequently used as aircraft skin. Aluminum corrosion products contain OH. This is readily visualized with thermal neutrons. The UC Davis McClellan Nuclear Research Center (MNRC) was originally developed by the US Air Force largely to detect corrosion in military aircraft (MNRC 2013).

In some situations (Toops et al. 2013), materials of interest can absorb enough water to make them sufficiently contrastive to image.

Recently, two groups have reported assay of hydrogen content in metals. Richards et al. (2003) used CT to measure H in Ti alloy at concentrations ~200 ppm (wt). Lehmann et al. (2004) measured H in Zr down to 100 ppm (wt) using a radiographic technique.

Contrast agents are often useful in thermal neutron radiography. Occasionally, this can be as simple as filling cavities with water. In fact, one of the frequent applications is to visualize interconnected porosity in soil and stone (Middleton et al. 1999). If water offers insufficient contrast, boron can be added in solution. Boron can also be added to some metals to increase attenuation of thermal neutrons.

Thermal neutron radiography images materials with quite different contrast than photon radiography. Figure 17.4 is a thermal neutron radiograph of a camera with both silicon and boron glass elements in the lens system. With x-rays, these two materials would have similar attenuation. In the neutron radiograph, the boron (highly attenuating) glass elements are revealed in black. Notice that the metal lens ring is weakly attenuating.

The nondestructive evaluation (NDE) group at the Lawrence Livermore National Laboratory (LLNL) performed x-ray fluorescence (XRF), x-ray CT, and thermal neutron CT (at McClellan Nuclear Research Center) on two canisters of unknown composition and contents. The objective of this evaluation was to guide destructive disassembly. XRF revealed that the outer surface was mostly Pb. A photograph of one of these objects is shown in [Figure 17.5](#). A comparison of x-ray CT to neutron CT radiographs is shown in [Figures 17.6](#) and [17.7](#), respectively. We leave it as an exercise for the reader to identify the article in the neutron image that is missing in the x-ray image.

One of the most widely circulated thermal neutron images is shown in [Figure 17.8](#). This is a rendering of a kinked O-ring imaged at MNRC. This O-ring is contained within a stainless steel body and could not be imaged with photons. The image is rendered and presented so that the stainless steel is not revealed.

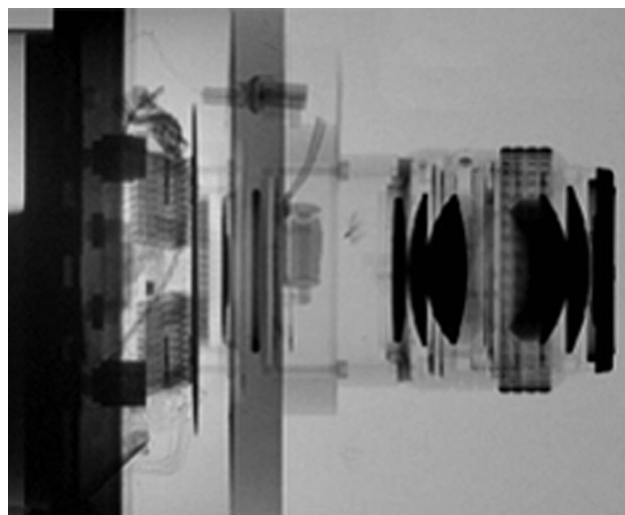


FIGURE 17.4 Thermal neutron radiograph of a camera and lens. The lenses containing boron are extremely attenuating. Other glass elements are seen faintly.

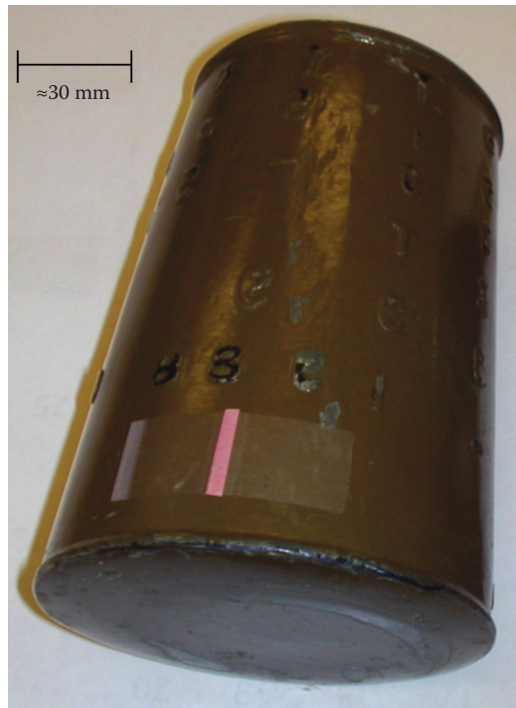


FIGURE 17.5 A photograph of canister with unknown contents.

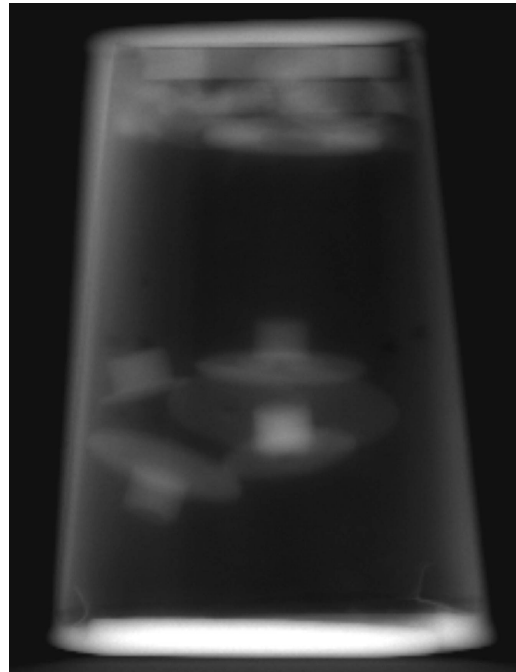


FIGURE 17.6 An x-ray radiograph of a Pb canister (see Figure 17.5) containing unknown material. The canister is 145 mm tall. The x-ray source was 9 MeV electron linac. The detector was an amSi photodiode flat panel. The data was acquired at LLNL.

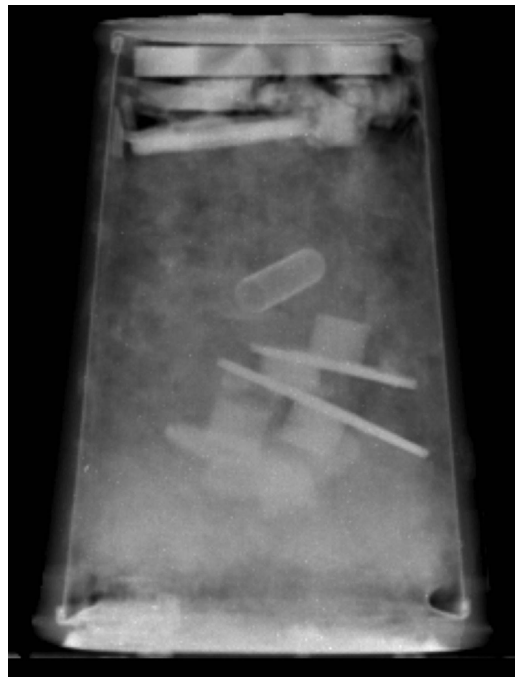


FIGURE 17.7 A thermal neutron radiograph of a Pb canister containing unknown material. This is the same canister as is shown in [Figures 17.5](#) and [17.6](#). Image was acquired at MNRC using their neutron CT facility.



FIGURE 17.8 Kinked O-ring. Rendering of 3-D attenuation data produced this image so that only the hydrogenous O-ring is shown. The O-ring is contained within a stainless steel valve housing that is not visible in this presentation. (Image courtesy of McClellan Nuclear Research Center.)

Finally, [Figure 17.9](#) is from a study of corn rootworms (Allee 2001). The opacity of the soil to x-rays would have obscured any information about the corn and insects in an x radiograph.

A numerical example is useful to demonstrate the difference between thermal neutrons and x-rays in imaging hydrogenous material shielded by higher-Z material. Consider the hypothetical case of a flange in a hydraulic line of the braking system for a locomotive. The flange assembly is

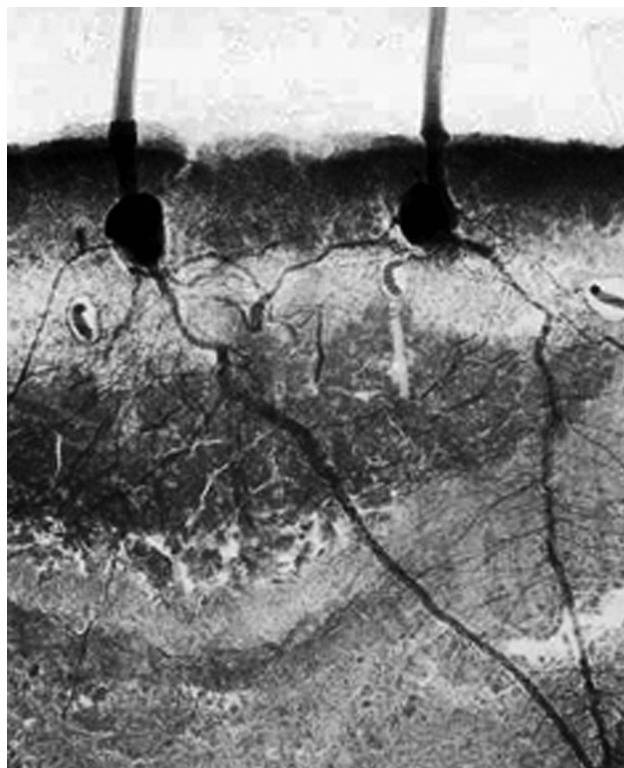


FIGURE 17.9 Thermal neutron radiograph of growing corn seedlings in soil. Corn rootworm pupae are present. Note also the revelation of the root structure. An x radiograph of these materials would reveal neither the corn roots nor the insects. (From Leslie Allee, using neutron radiography facilities at the Ward Center for Nuclear Studies (WCNS), Cornell. Allee, L. L., Corn Rootworm Ecology, Economics, and Behavior, PhD thesis, Cornell University, 2001.)

made of Inconel 625* with a Buna N elastomer O-ring seal compressed in a groove between two flanges. The dimensions are shown in [Figure 17.10](#). Since the locomotive pulls hazardous crude oil, the flange must be inspected to confirm the presence of the Buna N seal.

Let us compare the effectiveness of using x-rays versus thermal neutrons for this job. The composition of Inconel 625 for elements present in greater than 1 wt% is shown in [Table 17.2](#) (SMC 2015). Inconel's density is 8.44 g/cm^3 . The composition for Buna N is given in [Table 17.3](#). Its density is 1.25 g/cm^3 . Elemental attenuation coefficients in both tables are taken from a NIST database (NIST Neutron 2015).

If we use a W-anode x-ray tube, operate it at 75 kV, and filter with Yb, we can generate a spectrum that has an effective energy for this situation of 50 keV. Using online NIST data (NIST XCOM 2015) reveals that the mass attenuation coefficient for Inconel 625 is $2.80 \text{ cm}^2/\text{g}$ at an x-ray energy of 50 keV. Buna N is $0.20 \text{ cm}^2/\text{g}$. There are three “rays” of interest, through both flanges (ray A), through the region of the O-ring (ray B), and through the empty O-ring groove region (ray C).

The data in Table 17.2 lead to a thermal neutron attenuation coefficient of $0.173 \text{ cm}^2/\text{g}$ for Inconel 625. Similarly, for Buna N, the attenuation coefficient is $4.17 \text{ cm}^2/\text{g}$.

For neutrons, transmission through rays A, B, and C are 0.74, 0.176, and 0.386. For 50 keV x-rays, transmission through rays A, B, and C are: 0.00887, 0.0285, and 0.0289. There is only about 1% increase in transmission as a result of a missing O-ring when imaging with 50 keV x-rays! Neutrons

* Inconel 625 is a product of Special Metals Corporation, <http://www.specialmetals.com>.

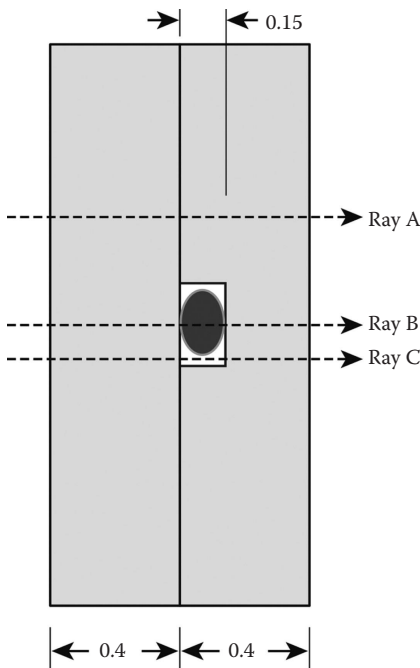


FIGURE 17.10 Flange configuration for hypothetical comparison of x-ray to thermal neutron imaging. Dimensions in centimeters.

TABLE 17.2
Composition of Inconel 625 and Thermal Neutron Attenuation of Constituents

Element	Wt%	Neutron μ_m (cm^2/g)
Ni	58	0.236
Cr	22	0.0757
Fe	5	0.153
Mo	9	0.0551
Nb	4	0.048
Co	1	0.437
Other (use Ti)	1	0.131

TABLE 17.3
Composition of Buna N and Thermal Neutron Attenuation of Constituents

Element	Wt%	Neutron μ_m (cm^2/g)
H	8	0.11
C	54	0.00015
N	38	0.048

provide excellent sensitivity to absence of the O-ring. Transmission increases more than 100% when the O-ring is not in the groove.

In almost every circumstance, thermal neutron radiography requires more effort and expense than x-ray radiography. It should be considered when the unique attenuation properties of thermal neutrons justify the cost. Many of the successful applications are in high-value components and in situations where the consequences of component failure are high.

17.2 IMAGING WITH MeV NEUTRONS

Neutrons of energy 5–15 MeV are more penetrating than x-rays, γ -rays, or thermal neutrons. This advantage is especially notable for penetration of dense high-Z material. In addition, they offer useful sensitivity for light low-Z material that is heavily shielded by dense high-Z material. This configuration exists in nuclear weapons; thus, this technique is being developed for this application (Hall 2001).

The system being pursued by Hall et al. (2007) uses an accelerator to produce ~7 MeV deuterons. A deuterium gas target is bombarded with this beam, thereby producing ~10 MeV neutrons via the $D(d,n)^3\text{He}$ reaction. The imager is a plastic scintillator that is mirror- and lens-coupled to a CCD camera.

Detection of contraband in baggage and cargo is an important worldwide problem. A large effort has been directed toward using MeV neutrons for this purpose. The deep penetration of neutrons and the fact that important elements exhibit resonance absorption for neutrons make this a tantalizing possibility. However, in spite of the effort devoted to this application, no neutron-based technology is in routine use for this purpose (Buffler and Tickner 2010).

17.3 IMAGING WITH MeV PROTONS

Protons in the energy range of 5–15 MeV interact in a material almost exclusively with electrons without regard to their location within an atom and, therefore, without regard to composition. The energy lost passing through a specimen is a measure of the integrated electron density along the ion path without regard to what material makes up the path. The incident energy is precisely known since it is determined by the accelerator producing the protons. The residual energy is measured with a solid-state detector.

The accelerator is also capable of delivering protons with positional accuracy that is submicrometer. This is accomplished with electromagnetic lenses and steering. The proton is slowed by a series of interactions with electrons. Each proton typically samples many billions of electrons, with each interaction causing a small energy loss and a negligible deflection. This enables knowing the ray followed by each proton to submicrometer accuracy. The ray is selected by stage motion combined with beam scanning.

Imaging with proton energy loss does not have the same statistical behavior that exists with photons. With x-rays, an individual x-ray is either detected or not detected. This means you have to detect a bunch of them in order to determine the transmitted fraction with some degree of certainty. With protons, the energy loss by one proton is sufficient provided that it did not undergo some unlikely event like a nuclear scatter. To guard against unlikely events, a few protons (five is good) are measured, and the median energy loss is taken.

These protons have a range of the order of 1 mm in material of density 1 g/cm³ and so are restricted to small specimens and/or low densities. Resolutions of 1 μm have been achieved.

This method is usually referred to as scanning transmission ion microscopy (STIM) when 2-D images are the result. When reconstructed into three dimensions, ion microbeam tomography (IMT) is the usual descriptive name (A.J. Antolak, pers. comm. 2013).

In their early work, the Sandia group (Pontau et al. 1989) imaged capillary tubes and low-density foams in three dimensions. Later, IMT was combined with proton-induced x-ray emission (PIXE)

(Antolak et al. 1992). In this manner, data were simultaneously acquired (for transmitted protons and emitted characteristic x-rays) that allowed 3-D reconstruction of total electron density and one or more high-Z components.

This imaging method is fundamentally a method taking data one ray at a time, so it is slower than x-rays and area detectors. It employs a large and expensive facility. Questions that can be answered by x-rays should be answered with x-rays. Protons should be reserved for the unusual cases, either in composition or the question being asked.

PROBLEMS

- 17.1 Describe the shape and location of the object revealed in [Figure 17.7](#) that cannot be seen in [Figure 17.6](#).
- 17.2 Find an estimate for the composition and density of fertile soil, corn roots, and rootworm pupae. Verify that the caption in [Figure 17.9](#) is accurate in stating that an x radiograph would not reveal the root nor pupae when viewed through 3 cm of soil.
- 17.3 Why does the side wall of the canister in Figure 17.6 appear thicker than in Figure 17.7?
- 17.4 What if you were asked to recommend a method for distinguishing borax-containing rocks from silicate rocks as they pass through a tunnel on a conveyor belt? The rocks are too big for penetration with x-rays from a linear accelerator (linac). Are thermal neutrons a possibility? Would this likely cost more than \$20 M if done in a third-world country where no approvals are required?
- 17.5 What would be the transmission of thermal neutrons along rays A, B, and C of [Figure 17.10](#) if the flange were made of aluminum and the O-ring were made of Viton A? How about 75-keV x-rays along the same rays?

Glossary

Absorbed dose: The amount of energy deposited by ionizing radiation per unit mass of irradiated matter. SI unit is the gray (Gy); $1 \text{ Gy} = 1 \text{ J/kg}$. The traditional unit is the rad, defined as 100 ergs/gram. Therefore, $1 \text{ Gy} = 100 \text{ rad}$.

Absorbed dose rate: The absorbed dose per unit time, Gy/s.

Absorption: The process whereby photons are reduced in number as they pass through a material in a dissipative process so that their energy is transferred locally to the material in the form of heat, this process is usually called the photoelectric effect.

Absorption edge: The location of a discontinuity in the energy-dependence of the photon attenuation coefficient for an element.

Accelerating potential: The electrical potential between the cathode and the anode in an x-ray tube through which electrons are accelerated; usually expressed in kV or MV.

Acoustic emission testing: The practice of testing or evaluating an object based on sound or ultrasound emitted by the object itself. Typically this is done as load is applied or relieved.

Acute irradiation: Irradiation taking place within one week or less and not recurring.

Acute radiation dose: Radiation dose occurring over a time period of one week or less.

Aeroshell: Heat shield.

ALARA: Acronym for as low as reasonably achievable. A regulatory concept that radiation dose to humans should be kept ALARA.

Alpha particle: A positively charged particle emitted by certain radionuclides. It consists of two protons and two neutrons, and is identical to the nucleus of a helium atom.

ALS: Acronym for Advanced Light Source, a synchrotron facility operated by Lawrence Berkeley Laboratory.

amSi: Acronym for amorphous silicon.

Analog image: An image produced by a continuously variable physical process (for example, irradiation of film).

Analog-to-digital converter (A/D): A device that converts an analog signal to a digital representation of the signal.

Angle of incidence: The angle that a light ray makes with the normal to a surface on which it is incident.

Angle of reflection: The angle that a light ray makes with the normal to a surface when it is reflected.

Angstrom (\AA): Measurement of length, $1 \text{ \AA} = 10^{-10} \text{ m}$.

Anode: The positive electrode of a discharge tube. In an x-ray tube, the anode carries the target.

Anode current: The electrons passing from the cathode to the anode in an x-ray tube, minus the small loss incurred by the back scattered fraction.

Areal density: In this book we use the term to mean the amount of mass per unit area along a path. It is the product of path length and mass density. The usual units are g/cm^2 . In the computer industry, the term areal density refers to the density of information (bits) per unit area on a storage device such as a hard drive.

Artifact: Spurious indication on a radiograph arising from, but not limited to, faulty manufacture, storage, handling, exposure, or processing. Also an indication on a computed tomography image arising from a faulty detector, high attenuation, imbalanced detectors, cupping, beam hardening, etc.

As low as reasonably achievable: See ALARA.

As-built modeling: Computational simulation of a physical process such as structural performance where the object model incorporates information about an object representative of the as-built

configuration as opposed to the as-designed configuration. The as-built information can include shape, flaws, dents, voids, etc. Most computational simulations are performed using the as-design, i.e., no flaws, configuration rather than the as-built configuration.

Atom: In physics and chemistry a unit of matter, the smallest unit of an element, having all the characteristics of that element and consisting of a dense, central, positively charged nucleus surrounded by a system of electrons. The entire structure has an approximate diameter of 10^{-8} cm and characteristically remains undivided in chemical reactions except for limited removal, transfer, or exchange of certain electrons.

Attenuation: The process whereby photons are reduced in number as they pass through a material. This includes photoelectric absorption, scattering and pair production losses.

Attenuation coefficient: Related to the rate of change in the intensity of a beam of radiation as it passes through matter.

Attenuation cross section: Similar to the mass attenuation coefficient only expressed in the physics units of barns/atom. One barn = 10^{-28} m²/atom.

Attenuation radiograph: A radiographic image where each pixel is expressed as the natural logarithm of the ratio (detector response with object present/detector response with no object).

Auger electron: The decay of an excited atom by the emission of an electron (instead of a photon) with an energy characteristic of the atom.

Automated defect recognition: A method of finding defects by employing a computer to analyze an image.

AVCOAT 5026-39: NASA code for a specific ablative heat shield material made by filling an aluminum honeycomb with epoxy.

Background radiation: That portion of the radiation present that arises from naturally-occurring sources.

Backscattered radiation: Radiation scattered by more than 90° with respect to the incident direction, that is, backward in the general direction of the radiation source.

Barn: A unit of area used for expressing the area of nuclear cross sections. 1 barn = 10^{-24} cm².

Becquerel (Bq): The SI unit of radioactivity. One nuclear transformation per second. The traditional unit is the Curie (Ci). 1 Bq = 2.7×10^{-11} Ci.

BEIR: Acronym for biological effects of ionizing radiation. A standing committee of the U.S. National Academy of Sciences that draws conclusions and recommends research on the biological effects of ionizing radiation.

Beta particle: An energetic electron or positron produced by radioactive decay.

Betatron: An electron accelerator in which acceleration is provided by a special magnetic field constraining the electrons to a circular orbit. This type of equipment usually operates at energies between 10 and 31 MeV. With a suitable target for the electrons a betatron can serve as an x-ray source.

Binding energy: The energy required to pull something apart. For an electron see electron binding energy.

Blooming: An undesirable attribute of some imaging devices in which all or part of the signal from a single photon or particle may appear at a considerable distance from the point where the radiation enters the imaging device. This may arise from several different effects, including readout characteristics.

Braze: A joining alloy generally of higher melting point than solder but lower than the pieces being joined.

Bremsstrahlung (white radiation): The electromagnetic radiation resulting from the retardation or deceleration of charged particles, usually electrons in a material.

Brightness: Here: A descriptor for an x-ray source. Brightness encompasses the rate of photon production within a specified energy band, the effective source area and the angular divergence of the source.

Brilliance: See brightness.

Broad-beam attenuation (absorption): The x-ray attenuation when contributions from all sources, including secondary radiation, are included.

Candling: The practice of examining the interior of a translucent object by passing light through it and observing either transmitted or reflected light.

Cassette: A light-tight container for holding radiographic recording media during an irradiation, for example, film, with or without intensifying or conversion screens.

Cathode ray: See electron.

CCAT: A microfocus cone beam CT system designed and built at LLNL.

CCD: Charged-coupled device.

Char: Solid material remaining after gases have been driven out of a carbonaceous material by heating.

Characteristic x-rays: X-rays emitted as a result of rearrangement of orbiting electrons. These characteristic x-rays are produced at specific energies (lines) that are characteristic of the emitting element.

Charge-coupled device (CCD): An electronic device with individual elements that are sensitive to visible light. Known as CCDs, these are often used as the sensor in digital cameras, for astronomy, and spectroscopy. When optically coupled to a scintillator, they are used as an x-ray imager.

Chronic irradiation: Irradiation delivered continuously or repeatedly over a period of time in excess of a week.

Cine-radiography: A time sequence of radiographs used to depict motion. Often used in the study of dynamic processing such as casting or forging.

CMOS: Complementary metal-oxide semiconductor.

Cold crack porosity: A type of crack that is formed by shrinkage during solidification.

Collimator: A device of radiation absorbent material with a hole or aperture intended for defining the direction and angular divergence of the radiation beam.

Compton scatter radiation: The scattered x-ray or γ -ray which results from the inelastic scattering of an incident x-ray or γ -ray on an electron. Since the ejected electron has short range in most materials, it is not considered part of the scattered radiation. The increase in wavelength of electromagnetic radiation, especially of an x-ray or a γ -ray photon, scattered by an electron.

Compton scattering: When a photon collides with an electron it may not lose all its energy, and a lower energy photon will then be emitted from the atom at an angle to the incident photon path.

Computed axial tomography (CAT) or computerized axial tomography (CAT) or computed tomography (CT): All refer to the same method. CAT was the earlier term used while now CT is more accepted.

Computed radiology (photostimulated luminescence method): A two-step radiological imaging process; first, a storage phosphor imaging plate is exposed to penetrating radiation; second, the luminescence from the plate's photostimulable luminescent phosphor is detected, digitized, and presented via hard copy or a CRT. Sometimes called CR.

Contrast agent: A material introduced into an object for the purpose of revealing internal structure in a radiograph. Usually a liquid or gas.

Contrast sensitivity: A measure of the minimum percentage change in an object that produces a perceptible density/brightness change in the radiological image.

Contrast stretch: A function that operates on the grayscale values in an image to increase or decrease image contrast.

Coolidge tube: A type of x-ray tube invented by William D. Coolidge. It used a heated cathode and operated much more reliably and consistently than earlier designs. Patent issued in 1913.

Cosmic radiation (or rays): Energetic particles arising in space.

Couplant: Material used to couple ultrasound energy from one object to another. This is usually from a transducer to an object under examination. Water is the most common couplant in NDE. Medical exams typically use a gel.

Critical flaw: Any flaw that is unacceptable.

Crookes tube: A sealed evacuated glass tube invented by Sir William Crookes in 1875. It was used in experiments to understand the properties of cathode rays (later shown to be electrons). Röntgen used a type of Crookes tube when he discovered x-rays in 1895.

Cumulative dose: The total amount of radiation received in a specified time.

Curie (Ci): That quantity of a radioactive isotope, which decays at the rate of 3.7×10^{10} disintegration (or decays) per second.

Densitometer: A device for measuring the optical density of radiograph film.

Density (film): A quantitative measure of film blackening when light is transmitted or reflected. See optical density.

Density gradient (γ) (G): The slope of the curve of density against log exposure for a film.

Depleted uranium (DU): Uranium left over after removal of most of $^{235}_{92}\text{U}$ from natural uranium. It is nearly all $^{238}_{92}\text{U}$. It is a very effective material for some types of x-ray shielding.

Developer: In film radiography, the chemical used to produce a visible image from the latent image recorded on the x-ray film. In dye penetrant inspection, the material that draws penetrant from flaws back to the surface and to causes it to spread thereby enhancing visibility of the flaw.

Diffraction: Interference effects giving rise to illumination beyond the geometrical shadow. This effect becomes important when the dimensions of the apertures or obstructions are comparable to the wavelength of the radiation, bending of waves around the edge of an obstacle. When electromagnetic radiation (light or x-rays) strikes an opaque body, for instance, a shadow forms on the side of the body that is shielded from the light source. Ordinarily light travels in straight lines through a uniform, transparent medium, but those light waves that just pass the edges of the opaque body are bent, or deflected. This diffraction produces a fuzzy border region between the shadow area and the lighted area. Upon close examination it can be seen that this border region is actually a series of alternate dark and light lines extending both slightly into the shadow area and slightly into the lighted area. If the observer looks for these patterns, he will find that they are not always sharp. However a sharp pattern can be produced if a single, distant light source, or a point light source, is used to cast a shadow behind an opaque body. Diffraction also occurs when light waves interact with a device called a diffraction grating. A diffraction grating may be either a transmission grating (a plate pierced with small, parallel, evenly spaced slits through which light passes) or a reflection grating (a plate of metal or glass that reflects light from polished strips between parallel lines ruled on its surface).

Diffuse reflection or reflector: The reflection of electromagnetic energy from an object where the reflected energy is scattered out-of-phase or in all directions. Diffuse reflectance occurs when the reflecting surface is rough relative to the wavelength of the incident energy; for example, a sheet of paper is a diffuse reflector.

Digital image: An image composed of discrete picture elements (pixels) each of which is characterized by a digitally represented luminance level.

Digital image enhancement: Any operation used for the purpose of enhancing some aspect of the original image.

Direct detection: A type of x-ray detection in which electrons are collected from the detector material without conversion to light.

Discharge tube: Is a closed insulating vessel containing a gas at low pressure through which an electric current flows when sufficient voltage is applied to its electrodes.

Dose equivalent: Used as a measure of the potential biological effects from a radiation field. The SI unit is the Sievert (Sv), numerically equal to the product of absorbed dose in Gy (D), times the radiation weighting factor (w_R).

Dye penetrant testing: A nondestructive method of detecting surface pits or cracks. The surface of the part is coated with a penetrant containing a dye. The penetrant is pulled into surface defects by capillary action. The excess penetrant is cleaned from the surface of the sample. A powder, called developer, is then sprayed or dusted over the part. The developer absorbs some of the dye from the defect thereby becoming visible either in white or UV light depending upon the type of dye used.

Dynamic range (for radiology): Ratio of the largest to the smallest usable inputs for an imaging system.

Eddy current testing: A method of NDT for near-surface flaws in conductive materials. Eddy currents are induced in the object being tested and flaws influence these currents.

Edge spread function (ESF): Representation of the spatial imaging performance of an imaging system. ESF is the response of an imaging system to area input as would arise from a parallel radiation beam with a perfect edge. This is often approximated in practice by imaging the (straight) edge of a highly attenuating material.

Effective dose, effective human-equivalent dose: A health physics term designed to express a radiation dose in terms of an equivalent whole body effect. Unit is Sievert (Sv).

Elastic scattering: Is one specific form of scattering. In this process, the energy of the incident photon or particle (e.g., electron, positron or neutron) is conserved and its propagating direction is changed by the potential of the target. (See also Rayleigh scattering.)

Electromagnetic (EM) radiation: Energy transmitted through space or material in the form of electromagnetic waves.

Electromagnetic spectrum: The entire wavelength, frequency and energy range of electromagnetic waves.

Electron: A stable subatomic particle in the lepton family having a rest mass of 9.109×10^{-28} grams and a unit negative electric charge of approximately 1.602×10^{-19} coulombs.

Electron binding energy: The net energy required to remove an atomic electron to an infinitely remote position from its orbit or the net energy required to remove an electron from an atom or a molecule.

Electron volt: The kinetic energy gained by an electron after passing through a potential difference of 1 V.

Element: In physics and chemistry a substance composed of atoms having an identical number of protons in each nucleus. Elements cannot be reduced to simpler substances by normal chemical means.

EMI number: The unit used to express linear attenuation in the first computed tomography scanner introduced by Electric and Musical Industries, or EMI. Later replaced by the Hounsfield unit (HU). See Hounsfield unit.

Energy flux density: See irradiance.

Equivalent IQI sensitivity: That thickness of an image quality indicator (IQI) expressed as a percentage of the section thickness radiologically examined in which a 2T hole or 2% wire size equivalent would be visible under the same radiological conditions.

Equivalent penetrometer sensitivity: That thickness of penetrometer, expressed as a percentage of the section thickness radiographed, in which a 2T hole would be visible under the same radiographic conditions.

Exposure: A measure of γ or x radiation based on the ionization caused in air. The SI unit is coulomb (C)/kg, which is not given a special name and is almost never used. The traditional unit is the Röntgen (R) defined as the exposure that results in the generation of one electrostatic unit of charge (2.08×10^9 ion pairs) per one standard cubic centimeter of dry air at STP.

Exposure device: A shielded container for a radioisotopic source that has a mechanism for moving the source into position for taking a radiograph.

Exposure range (latitude): The range of exposures over which a film can be employed usefully.

External radiation dose: Radiation dose arising from a source outside the body.

False positive: Incorrect identification of a non-existing critical flaw. False positive rate is (1-specificity).

Fill factor: The fraction of a sensor that is sensitive to radiation or light.

Film badge: An obsolete type of personal dosimeter that employs silver halide emulsion on a plastic film base to estimate radiation dose.

Film contrast: A qualitative expression of the slope or steepness of the characteristic curve of a film; that property of a photographic material which is related to the magnitude of the density difference resulting from a given exposure difference.

Film speed: A numerical value expressing the response of an image receptor to the energy of penetrating radiation under specified conditions.

Filter: A uniform layer of material placed between the radiation source and the object for the purpose of modifying the energy spectrum of x-rays.

Flash radiography: Radiography in which the source emits only briefly in order to “freeze” motion in dynamic events.

Flat-panel imager: An electronic device for capturing x-ray images. There are two main classes of flat panels: direct and indirect. Direct panels collect charge produced by ionizing radiation in each pixel. Indirect panels are sensitive to visible light and are used with a scintillator.

Fluorescence: The emission of light by a substance as a result of the absorption of some other radiation of shorter wavelengths only as long as the stimulus producing it is maintained.

Focal spot: For x-ray generators, that area of the anode (target) of an x-ray tube which emits x-rays when bombarded with electrons.

Fog: Any component of optical density of an x-ray film that arises from something other than exposure to the imaging radiation.

Fog density: A general term used to denote any increase in the optical density of a processed film caused by anything other than the direct action of the image-forming radiation.

Gamma (γ) radiography: A technique of producing radiographs using γ -rays.

Gamma-ray (γ -ray): High energy electromagnetic radiation that is generated by nuclear transitions.

Geiger–Müller counter, G-M counter, G-M tube: A type of radiation detector that detects and counts individual radiation interactions in the enclosed gas-filled volume of the detector. The most commonly used portable radiation detection instrument.

Genetic effects (of radiation): Hypothetical damage that could be genetically transmitted to offspring. Never observed in humans.

Geometric unsharpness: Geometric unsharpness refers to the loss of edge definition that is the result of geometric factors of the radiographic equipment and setup. It is also referred to as the penumbral shadow in a radiological image which is dependent upon (1) the radiation source dimensions, (2) the source to object distance, and (3) object to detector distance.

GHz: A frequency of 10^9 Hz.

GLO: An LLNL developed clear ceramic scintillator.

Graininess: The visual impression of irregularity of silver deposit in a processed film.

Gray (Gy): The SI unit of absorbed dose. $1 \text{ Gy} = 1 \text{ Joule/kg} = 100 \text{ rad}$.

Half-life: The time required for one half of a given number of radioactive atoms to undergo decay.

Half-value layer (HVL): The thickness of an absorbing material required to reduce the dose rate from a radiation source to one half of its original value.

Half-wave rectified: An obsolete type of high voltage power supply for an x-ray tube in which one half of an alternating potential has been removed by rectification. Sources with this type of power supply have pulsed x-ray output at the supply frequency.

HE: An acronym for high explosive.

Heel effect: The variation in irradiance and spectrum within the usable cone of x-ray emission from an x-ray tube.

High explosive (HE): A detonating (the front of the chemical reaction moves faster through the material than the speed of sound) explosive.

Hounsfield unit (HU): A unit of linear x-ray attenuation used for medical CT scans, each voxel being assigned a value on a scale on which air is -1000, water is 0, and compact bone is about 1000.

Hz: A unit of frequency equal to one cycle per second. Hertz.

Image quality indicator (IQI): A quality assurance test object for radiation imaging. Also known as a penetrometer. The image of the object provides visual or quantitative indication of the spatial and contrast performance of the imaging system.

In Space Propulsion Technology (ISPT): A NASA program.

Index of refraction: See refractive index.

Indirect detection: A type of x-ray detection in which electrons produce visible light which is then sensed with a photodetector.

Inelastic scattering: A fundamental scattering process in which the momentum of an incident photon or particle is not conserved. For photons, a scattering process in which the photon direction is changed and the photon energy is reduced.

Infrared radiation: Electromagnetic radiation in the wavelength range beginning just above human vision and extending to about 1 mm.

Inherent filtration: Filtration of the x-ray output that is inherent in the construction of an x-ray tube. It cannot be removed and always filters the x-ray output.

Insensitive high explosive: A high explosive that is resistant to detonation, e.g., by bullets, heat and shape charges.

Intensifying screen: A material that converts a part of the radiographic energy into light or electrons and that, when in contact with a recording medium during irradiation, improves the quality of the radiograph or reduces the irradiation time required to produce a radiograph, or both. Three kinds of screens in common use are:

(a) **Metal screen:** A screen consisting of dense metal (usually lead) or of a dense metal compound (for example, lead oxide) that emits primary electrons when exposed to x-rays or γ -rays.

(b) **Fluorescent screen:** A screen consisting of a coating of phosphors that fluoresces when exposed to x or γ radiation.

(c) **Fluorescent-metallic screen:** A screen consisting of a coating of a metallic foil (usually lead) coated with a material that fluoresces when exposed to x or γ radiation. The coated surface is placed next to the film to provide fluorescence; the metal functions as a normal metal screen.

Intensity: See irradiance. Intensity is a term used differently in different disciplines and this term is being replaced by the term irradiance within the x-ray community.

Internal radiation dose: Radiation dose in humans resulting from radioactive material within the body.

Inverse geometry: See reverse geometry.

Ion microbeam tomography (IMT): A tomographic imaging method utilizing data from scanning transmission ion microscopy (STIM) images.

Ionization chamber, ion chamber: A type of radiation detector using a gas-filled chamber with sufficient voltage imposed to collect the charge produced by an ionizing interaction in the gas.

Ionizing radiation: Particles or photons that have sufficient energy to produce ionization directly in their passage through material.

IQI sensitivity: In radiography, the minimum discernible image and the designated hole in the plaque-type, or the designated wire image in the wire type image quality indicator.

Irradiance: Energy flow defined by energy per unit area per unit time this is equivalent to power per unit area (in the past sometimes called intensity, but this term is being replaced by the term irradiance). Compare with photon flux density.

Irradiate: Here: The condition of directing or applying ionizing radiation to an object, flora, fauna or especially a human. (Noun) irradiation.

Isotope: One of two or more atoms having the same atomic number but different mass numbers, thus they differ only in number of neutrons.

Kel-F: A thermoplastic that is used as a binder in production of some plastic bonded explosives.

keV (kiloelectron volt): A unit of energy equal to one thousand electron volts, used to express the energy of x-rays, γ -rays, electrons, and neutrons.

Lambertian source: An emitter with the characteristic that the irradiance varies directly as the cosine of the angle between the observer's line of sight and the normal to the source surface. Common in visible light scattering. X-ray sources are NEVER Lambertian sources.

Laminography: The specimen and the detector move in step so that only one image plane only of the specimen remains relatively sharp on the detector, also known as tomosynthesis. See tomosynthesis.

Latent image: A condition produced and persisting in the image receptor induced by radiation and able to converted into a visible image by processing.

LBL advanced light source (ALS): A synchrotron operated by Lawrence Berkeley Laboratory in Berkeley, CA.

Line pair gauge or test pattern: A pattern of one or more pairs of objects with high contrast lines of equal width and equal spacing. The pattern is used with an imaging device to measure spatial resolution.

Line spread function (LSF): A representation of the spatial imaging performance of an imaging system. LSF is the response of an imaging system to a linear input such as would arise from a perfectly collimated thin plane of incident radiation. In practice, this is usually approximated by use of a narrow slit made of highly attenuating material.

Linear accelerator (linac): In radiography: An electron accelerator in which the acceleration of the electrons is achieved by propagation of a high-frequency field inside a linear waveguide. Used as an x-ray source.

Linear attenuation coefficient: A numerical value depending on energy that expresses the (linear) attenuation properties of a material at a specific density for photons or neutrons. For neutrons the linear attenuation coefficient depends on the specific isotope of the element. SI unit is m^{-1} . See mass attenuation coefficient.

Linear energy transfer (LET): A measure of energy deposited along the interaction track (energy/length) where energy is deposited by ionizing radiation. X, beta, and γ radiation are considered low LET radiation. Their LET is a few $\text{keV}/\mu\text{m}$. Neutrons and ions have higher LET, exceeding $100 \text{ keV}/\mu\text{m}$.

Linear no-threshold (LNT) model: The hypothesis that low dose radiation effects in humans can be estimated by linear extrapolation to zero (no threshold) from effects observable at higher doses.

Location marker: A number or letter made of lead (Pb) or other highly radiation attenuating material that is placed on an object to provide traceability between a specific area on the image and the part.

Low-energy γ radiation: γ radiation having energy less than 200 keV.

Magnetic particle testing: A method of nondestructive testing for ferrous metals in which a magnetic field is applied. Small magnetic particles are applied and these decorate the location of flaws. The particles may be colored and they may be coated with fluorescent dyes.

Man-made radiation source: A source of ionizing radiation that is produced by man. This can be made by machine or it can be radioisotopes produced by human activity. Most man-made radiation is produced and used for medical procedures.

Mass attenuation coefficient: A numerical value depending on energy that expresses the (mass-based) attenuation properties of a material for photons or neutrons. For neutrons the mass attenuation coefficient depends on the specific isotope of the element. SI unit is

m^2/kg . See linear attenuation coefficient. Attenuation of charged particles does not follow the same physical laws and cannot be described by either mass or linear attenuation coefficients.

Mean free path (MFP): The inverse of the linear attenuation coefficient. SI unit is m. Almost never used with photons. MFP is commonly used in physics for neutrons.

Microfocus x-ray tube: An x-ray tube having an effective focal spot (source) size less than 100 μm .

Micropower impulse radar (MIR): A device employing very low power broadband electromagnetic radiation. Developed at Lawrence Livermore National Laboratory and used for intrusion and level sensing.

Microscope: An optical instrument, consisting of a lens, or combination of lenses, for making an enlarged image of an object which is too minute to be viewed by the naked eye.

Microwaves: An electromagnetic wave having a wavelength between that of infrared and longer to radio (one millimeter to one meter).

Millimeter waves: An electromagnetic wave having a wavelength between one millimeter and one centimeter, corresponding to frequencies between 30 and 300 gigahertz.

Moderator: Neutron moderator is a medium that reduces the speed and energy of fast neutrons turning them into thermal neutrons.

Modulation transfer function (MTF): Representation of the spatial imaging performance of an imaging system expressed in the frequency domain. MTF is derived from any one of PSF, LSF or ESF.

Monochromatic photons: See monoenergetic photons.

Monoenergetic photons: Photon radiation composed of a single energy (wavelength). Contrasted with Polyenergetic photons.

Negative predictive value (NPV): The probability that a part is free of critical flaws given that NDE found none. NPV depends on the NDE system and on the population of parts being tested.

Net density: Total optical density less fog and support (film base) density.

Neutron binding energy: Energy required to remove a neutron from a nucleus.

Neutron radiography (NRT): A process of making an image of the internal details of an object by the selective attenuation of a neutron beam by the object.

Noise: In radiography: The data present in a radiological measurement that is not directly correlated with the degree of radiation attenuation by the object being examined.

Nondestructive evaluation (NDE): A nondestructive evaluation method in which detailed information is measured. Examples might be size and orientation distribution of internal voids.

Nondestructive testing (NDT): A nondestructive test characterized by a simple pass/fail result.

Nonintrusive inspection (NII): A non-destructive method of inspecting and identifying goods in transportation systems. It is often used for scanning of intermodal freight shipping containers.

Nuclear activity: The number of disintegrations occurring in a given quantity of material per unit of time. “Curie” is the traditional unit of measurement. One curie is equivalent to 3.7×10^{10} disintegrations per second. The SI unit of measurement is the becquerel (Bq) which equals one disintegration per second.

Nucleus binding energy: The minimum energy required to dissociate the nucleus into its component neutrons and proton.

Occupational dose: Human radiation dose that results from one's occupation.

Optical density: The degree of visible light removal in passing through a film or a filter. It is expressed as the negative base ten logarithm of transmission. So, a film that transmits 1% of visible light has an optical density of 2.0.

Pair production: The conversion of a photon into an electron and a positron. Requires a photon energy exceeding 1.02 MeV. If electrons are available, the positron will quickly annihilate, producing two 511-keV annihilation photons.

Pencil beam: A radiation beam that has small divergence, usually created by collimating a radiation source.

Penetrometer: See image quality indicator.

Penumbra: The shadow of an object with an appreciable size has two distinct regions; one of full-shadow, called the umbra, the other of half-shadow, called the penumbra shadow. The penumbra in a radiological image is dependent upon (1) the radiation source dimensions, (2) the source to object distance, and (3) object to detector distance.

Phase contrast: Contrast in a transmission radiograph that arises from phase shifts occurring in the object.

Phenolic impregnated carbon ablator (PICA): A material used in thermal protection shields on reentry vehicles.

Photodisintegration: The breakup of an atomic nucleus into two or more fragments as a result of bombardment by very energetic photons.

Photoelectric effect: A photon transfers its energy to an electron to eject it from the atom. As the electron slows down it loses energy to the lattice in the form of heat or by generating new x-rays called bremsstrahlung or braking radiation.

Photoelectron: An electron that is emitted from an atom or molecule by an incident photon.

Photofission: Nuclear fission as the result of the absorption of a high-energy photon (e.g., x- or γ -ray).

Photon: The name given to a small bundle or quantum of electromagnetic energy. It is used when describing the particle-like behavior of electromagnetic waves (including light waves).

Photon flux density: Photon flow defined by number of photons per unit area per unit time (in the past sometimes called intensity, which we do not use in this text). Compare with irradiance.

Photonuclear: Of or relating to a nuclear reaction induced by photons. See also photodisintegration.

Photostimulable luminescence (PSL): The physical phenomenon of phosphors absorbing incident ionizing radiation, storing the energy in quasi-stable states and emitting luminescent radiation proportional to the absorbed energy when stimulated by radiation of a different wavelength.

Photostimulable phosphors (PSPs): Imaging plates using photostimulable luminescence as a method to record a radiation image.

Phototransmutation: See photodisintegration.

Pigtail: Short cable attached to a radioactive source within a cable based radiography exposure device.

Pitot tube: A transducer used to measure air speed.

PIXE: Proton induced x-ray emission. An imaging method in which a beam of protons stimulates the emission of characteristic x-rays present in a specimen. Position is known from the beam location and the number of observed x-rays is a measure of the amount of the particular element present.

Pixel: Picture element. The smallest addressable (area) element in a 2D electronic image.

Pixel size: The length and width of a pixel.

Plastic bonded explosive (PBX): An explosive made of a mixture of explosive material and a plastic binder.

Point-spread function (PSF): Representation of the spatial imaging performance of an imaging system. PSF is the response of an imaging system to a point input as would arise from a small diameter parallel radiation beam. This is often approximated in practice by a pinhole in a sheet of highly attenuating material or a wire for CT.

Poisson probability distribution: A discrete probability distribution that expresses the probability of a given number of events occurring in a fixed interval of time and/or space if these events occur with a known average rate and independently of the time.

Polychromatic photons: See polyenergetic photons.

Polyenergetic photons: Photon radiation composed of more than one energy (wavelength). Contrasted with monoenergetic photons.

Positive predictive value (PPV): The probability that a critical flaw actually exists given that NDE has found a critical flaw. PPV depends on the NDE system and on the population of parts being tested.

Positron: Also called the positive electron or the antielectron, it is an elementary particle, the anti-particle of the electron. It has the same mass and spin as an electron, but has a positive charge (equal in magnitude to the charge of an electron).

Prevalence of critical flaws: The fraction of a population of parts that contain critical flaws.

Prill: Nearly spherical particles such as those made by solidifying droplets while falling.

Primary radiation: Radiation coming directly from the source.

Probability of detection (POD): For an NDE system, the probability of detection vs. flaw size. Usually presented as a curve.

Proton: A positively charged particle that is the nucleus of the lightest chemical element, hydrogen.

Proton binding energy: Energy required to remove a proton from a nucleus.

Quality factor (obsolete): The factor by which absorbed dose is to be multiplied to obtain dose equivalent. Denoted Q, quality factor is dimensionless. For x, beta, and γ radiation $Q = 1.0$, and is not energy dependent. For neutrons and ions, Q is energy and ion specific and can exceed 20. Replaced by radiation weighting factor.

Quantitative nondestructive evaluation (QNDE): The most quantitative and specific of NDE methods. Those that return quantitative measure of material properties.

Quantum noise: Is the noise associated with the finite number of x-ray photons forming the image. It is often the dominant noise and is governed by Poisson statistics. And is sometimes referred to as shot noise.

rad: The traditional unit of radiation absorbed dose. $1 \text{ rad} = 0.01 \text{ Gy}$.

Radar: An acronym for radio detection and ranging, the original and still principal application of radar. The name is applied to both the technique and the equipment used. Radar operates by transmitting electromagnetic waves into the surroundings and detecting waves reflected by objects or meteorological conditions such as rain.

Radiation: Here, generally used as shorthand for ionizing radiation.

Radiation absorbed dose: See absorbed dose.

Radiation exposure: See exposure.

Radiation weighting factor: Factors used to convert absorbed dose into equivalent dose. Used to place biological effects from radiation exposure on a common scale.

Radio waves: A type of electromagnetic wave whose wavelength is approximately from 1 m to 1 km. Radio waves are usually used for communication. Some wavelengths travel long distances around earth.

Radioactive decay: The spontaneous transformation of a nuclide into one or more different nuclides, accompanied by the emission of ionizing radiation. The amount of a radioactive substance may be specified by the SI unit of activity, the becquerel (Bq), defined as one disintegration per second. The traditional unit is the curie (Ci), defined as 3.7×10^{10} disintegrations per second.

Radiograph: The image produced by radiography.

Radiographic contrast: The difference in density between an image and its immediate surroundings on a radiograph.

Radiographic equivalence factor: That factor by which the thickness of a material must be multiplied in order to determine what thickness of a standard material (often steel) will have the same absorption.

Radiography: The process of imaging the internal details of an object using penetrating radiation, usually photons, neutrons, or charged particles.

Radiography camera: See exposure device.

Radiography projector: See exposure device.

Radon: A colorless, radioactive, inert gas formed by the radioactive decay of radium. A major contributor to natural background radiation dose.

Rayleigh scattering: Of an electromagnetic wave propagating in a material medium, scattering caused by refractive-index inhomogeneities that are small compared to the wavelength. (See also elastic scattering.)

Real-time radioscopy: Radiography that captures the motion of an object, usually at ~30 frames per second.

Receiver operating characteristic (ROC) curve: A graphical expression of the sensitivity vs. (1-specificity) for a binary classifier system such as a pass/fail NDE system. Also expressed as the rate of detection versus rate of false alarms.

Reflection: The backward scattered radiation from a beam incident upon an interface of two different media such as air and a mirror.

Refraction: The bending of electromagnetic waves as they pass between materials with different refractive indices such as air and water.

Refractive index: Refractive index (η): Of a medium, the ratio of the velocity of propagation of an electromagnetic wave in vacuum to its velocity in the medium. *Synonym* index of refraction.

Reverse geometry: Radiography configuration in which the source is sequentially at many known positions within a surface while the detector is normally single (or few) at fixed points.

Röntgen: Unit of exposure. One Röntgen (R) is the quantity of x or γ radiation that produces, in dry air at normal temperature and pressure, ions carrying one electrostatic unit of quantity of electricity of either sign.

Röntgen absorbed dose: The historical unit of absorbed dose, rad. Defined as 100 erg/g of absorbed energy. The SI unit is gray (Gy). 1 Gy = 100 rad.

Röntgen equivalent man (rem): The historical unit of dose equivalent used as a measure of potential biological effects from a radiation field. The SI unit is Sievert (Sv). Dose equivalent is the product of absorbed dose and quality factor (Q). 1 rem = 0.01 Sv.

Scanning transmission ion microscopy (STIM): An imaging method employing ions (usually protons) from an accelerator passing through a specimen. The energy lost by the ion reveals integral electron density along the ion path.

Scattered radiation: Radiation redirected away from the primary beam by scattering events.

Scintillating screen: A type of intensifying screen. Another name for fluorescent screen.

Scintillator: A material that emits visible light when excited by radiation. Used in conjunction with a light-sensing detector for radiation detection and imaging. Scintillators are often used in construction of energy discriminating (pulse counting) detectors. For imaging, scintillators are usually configured into some type of sheet structure that may contain other materials as well.

Scintillators and scintillating crystals: A detector that converts ionizing radiation to light.

Screen: A thin sheet of material that emits secondary electrons when exposed to x-rays or γ -rays of sufficient energy. This is used to “intensify” the interaction of radiation with the detector. Screens are usually made of a dense metal such as Pb or Ta. Screens generally alter the photon energy dependence of the detector.

Secondary radiation: Radiation emerging from an interaction between primary radiation and a material.

Segmentation: Partitioning digital data, 2D or 3D, into multiple separate sets according to some criterion.

Self-rectified: An obsolete means of applying high voltage to an x-ray tube in which the supplied voltage is alternating potential and the tube itself serves as a rectifier.

Sensitivity: The probability that a test will be positive given that a critical flaw exists. Also called true positive rate.

Shearography: An NDE method in which surface deformation is measured using an interferometric method. This is usually done with and without load.

Shot noise: See quantum noise.

Sievert (Sv): The SI unit of dose equivalent. The same unit is used for effective dose.

SiLi detector: Also written Si(Li). An x-ray detector formed by lithium compensation or drifting of p-type silicon. When paired with the appropriate electronics this system provides energy discrimination.

Sinogram: Is a 2D array or image of data for a single CT slice. It is the distance along the projection versus angle of the projection. Any pixel (except the center axis pixel) in the image traces out a sine wave over 2π .

Snell's law: Relationship between the path taken by a ray of light as it moves from one medium to another and the refractive indices of the two media. Discovered in 1621 by Willebrord Snell (1580–1626).

SNR: Signal-to-noise ratio.

Solar power tower: Common name for Sandia's National Solar Thermal Test Facility.

Somatic damage, somatic effects: Effects of radiation that are limited to the exposed individual; not genetically transmitted.

Sonic IR: A term applied to the NDE method in which high intensity sound is used to excite an object creating heat at certain types of flaws. These flaws are observed by the infrared radiation they emit.

Source: A machine or radioactive material that emits penetrating radiation.

Special nuclear material (SNM): Defined by Title I of the Atomic Energy Act of 1954 as plutonium, uranium-233, or uranium enriched in the isotopes uranium-233 or uranium-235.

Specificity: The probability that a test will be negative given that a critical flaw is not present. Also called the true negative rate.

Specular reflection (or reflector or reflectance): The reflection of electromagnetic energy from an object where the reflected energy is scattered in-phase or one direction. Specular reflectance occurs when the reflecting surface is smooth relative to the wavelength of the incident energy; for example, a mirror is a specular reflector.

Step wedge: A test object with known thickness steps used to test an imaging system.

Stereo radiography: A technique in which two images are produced from two different source positions within a plane parallel to the image plane.

Storage phosphor imaging plate: A flexible or rigid reusable detector that stores a radiological image as a result of interaction with penetrating radiation.

Submillimeter waves: An electromagnetic wave having a frequency from 300 to 1000 GHz.

Swank noise: Arises from variations in the pulse height distribution—the number of optical photons detected for each interacting x-ray. It has both radiation and optical components.

Take-off angle: The acute angle between an x-ray trajectory and the anode surface in an x-ray tube.

Target: That part of the anode of an x-ray emitting tube hit by the electron beam.

TATB: Triaminotrinitrobenzene. A high explosive.

TDI: Time delay integration. A mode of photodetector operation that compensates for motion of the object being imaged.

Tenth-value layer (TVL): The thickness of an absorbing material required to reduce the dose rate from a radiation source to one tenth of its original value.

Terahertz (THz): A frequency of 10^{12} Hz.

Terahertz radiation: Electromagnetic waves sent at terahertz frequencies, known as terahertz radiation, terahertz waves, terahertz light, T-rays, T-light, T-lux and THz, are in the region of the electromagnetic spectrum between 1 to 10 terahertz (1×10^{12} Hz to 10×10^{12} Hz), corresponding to the sub-millimeter wavelength range between one millimeter (high-frequency edge of the microwave band) and 100 micrometers (long-wavelength edge of far-infrared light).

Teratogenic effects: Here, radiation effects that arise from irradiation during gestation.

Thermal neutrons: Neutrons having energies ranging between 0.005 eV and 0.5 eV; neutrons of these energies are produced by slowing down fast neutrons until they are in equilibrium with the moderating medium at a temperature near 20 degrees C.

Thermography: An NDE technique in which an IR camera is used to measure the spatial and temporal variation in surface temperature of an object.

Thermoluminescent dosimeter (TLD): A type of personal dosimeter using a material that stores deposited radiation energy in metastable states. The energy is released in the form of light when the irradiated material is heated. They are a very common dosimetry system.

Tissue equivalent: A material whose composition is similar to tissue and that therefore has an absorbed dose similar to tissue. May be gas, liquid, or solid.

Tissue weighting factor: Factors designated for 13 body parts that are meant to convert equivalent dose to specific body parts to effective dose over the entire body. The sum of the 13 tissue weighting factors is 1.0.

Tomography: Any radiological technique that provides an image of a selected plane in an object to the relative exclusion of structures that lie outside the plane of interest.

Tomosynthesis: A method for producing limited angle tomography like data. A single plane is in focus while all other planes are blurred.

Total image unsharpness: The blurring of test object features, in a radiological image resulting from any cause(s).

Total internal reflection: The reflection that occurs when radiation, in a higher refractive-index medium, strikes an interface, with a medium with a lower refractive index, at an angle of incidence (with respect to the normal) greater than the critical angle.

Transmission densitometer: An instrument that measures the intensity of the transmitted light through a radiographic film and provides a readout of the transmitted film density.

Transmitted film density: The density of radiographic film determined by measuring the transmitted light. See optical density.

True positive: Correct identification of an actual critical flaw.

Tube current: The flow of electrons from the cathode to the anode target in an x-ray tube; usually expressed in unit of milliamperes.

Ultrasonic testing: An NDE technique that uses sound energy greater in frequency than the range of human hearing.

Ultrasound: Sound with a frequency above the range of human hearing. Most NDE with ultrasound uses frequencies from 50 kHz to a few GHz.

Ultraviolet radiation: Electromagnetic radiation shorter in wavelength than the range of human vision, but longer than x-rays.

Umbral: That portion of the radiation shadow of an object that has no direct view of any portion of an extended radiation source.

Undulator: A magnetic device to undulate the electron beam of a synchrotron and thus produce x-rays.

Unsharpness: A component of image blur. Usually referring to source unsharpness and/or motion unsharpness.

Vibrothermography: See sonic IR.

Voxel: The smallest addressable volume element (voxel) in a 3D electronic image.

Voxel size: The length, width and depth of a voxel.

Wavelength: The distance between corresponding points of two consecutive waves. For example, from crest to crest.

White radiation: See bremsstrahlung.

Wiggler: A device used to laterally deflect an electron beam at a synchrotron so that intense broad band x-rays are produced. Similar to undulator.

X-ray: High energy electromagnetic radiation that is generated by changes of electrons in an atom or by the acceleration or deceleration of charged particles such as electrons or protons.

X-ray fluorescence: The emission of characteristic x-rays by an element when excited by x-rays of sufficient energy.

X-ray gauging: An x-ray transmission measurement along a single ray, usually with source and detector collimation.

X-ray tube: The portion of an x-ray-producing machine that contains the anode, cathode and associated components.

List of Notations

a	count rate (counts/s)
A	atomic weight in (g/mole)
A_i	atomic weight of the i th element (g/mole)
A_w	atomic weight of the specific atoms (g/mole)
b	barn, a unit of area, equal to 10^{-24} cm^2
c	velocity of electromagnetic radiation in a vacuum ($2.998 \times 10^8 \text{ m/s}$)
C_l	collimator aperture length
C_w	collimator aperture width
C_s	radiographic contrast
d	interplanar spacing of a crystalline material
d_a	detector area and x, y, z location
D	diameter of a pinhole or aperture
$D(\Phi)$	digitized transmitted irradiance
$D(\Phi_0)$	digitized incident irradiance
D_C	dark current measured without radiation or light
D_{co}	distance from center line
D_x	diameter of an x-ray source
d_{hkl}	distance between crystal planes in diffraction
DQE	Detective Quantum Efficiency
D_r	radiation absorbed dose, (gray [Gy] defined as 1 J/kg)
D_{sp}	detector stopping power
e	electronic charge on an electron ($1.602 \times 10^{-19} \text{ C}$)
E	total energy (J or MeV)
E_i	energy of stationary states
E_k	kinetic energy (J)
E_{PE}	potential energy (J)
\bar{E}	effective energy
E_p	kinetic energy (MeV) of a photon
E'_p	kinetic energy (MeV) of a scattered photon
E_{p_0}	kinetic energy (MeV) of an incident-photon
E_B	binding energy (MeV)
$E_{B_{\beta^-}}$	binding energy (MeV) of an electron
E_{β^-}	kinetic energy (MeV) of an electron
E_{β^+}	kinetic energy (MeV) a positron
E'_{β^-}	kinetic energy (MeV) of a photon-scattered or recoil electron (sometimes called a photo electron)
EPS	equivalent penetrometer sensitivity
f	effective focal spot size, in CT object function
f_0	object function
f_1	real atomic scattering factor
f_2	imaginary atomic scattering factor
F_{E_j}	electric field disturbance at some point j in a material
F_{E_0}	electric field in a vacuum
F	the focal length of a lens
\mathfrak{J}	Fourier transform
\mathfrak{J}^{-1}	inverse Fourier transform

G, G', G''	constants in various forms of the Klein–Nishina formula
H	dose equivalent, and is used as a measure of biological effects expected from a radiation absorbed dose
H_i	dose equivalent delivered to the i th specific body part
H_E	effective human equivalent dose
h	Plank's constant (6.626×10^{-34} Js)
HVL	half-value layer, the thickness of a material required to reduce the irradiance by one half
K, L, M, N	electron shells or orbits
ℓ, l	defines a line or ray sum from source to detector
LET	<i>linear energy transfer</i>
LNT	<i>linear-no-threshold</i> ; an assumed model for extrapolating radiation effects to low absorbed dose where no effect has been observed
m	rest mass of a particle
m_{β^-}	rest mass of the electron (9.10×10^{-31} kg)
m_β	rest mass of the electron or positron (9.10×10^{-31} kg)
m_j	mass of the j th isotope
mfp	<i>mean free path</i> , units of length, inverse of the linear absorption coefficient
M_x	Geometric magnification of an object onto the detector
MTF	Modulation transfer function
n	an integer order of refraction that expresses the number of wavelengths in the path differences between rays scattered by adjacent crystalline planes with spacing d
n_a	number of atoms
n_t	the number of disintegrations occurring at time t
n_0	the number of disintegrations occurring at an earlier time $t = 0$
N	number of photons or counts
N_P	number of primary photons
N_S	number of scattered photons
N_A	Avogadro's number (the number of atoms per mole of material, 6.02×10^{23} atoms/mole)
N_0	number of radioactive nuclei at time, $t = 0$
N_t	number of nuclei remaining at a later time, t
N_θ	number of rotational angles or views or projections
n_q, l_q, m_q	quantum numbers: principal or primary, secondary, and magnetic, respectively
O	general object function
p	cross section of the x-ray phase shift
P	probability density function
P_g	width of the penumbra
P_0	line integral or ray sum, dimensionless
PSF	<i>point spread function</i>
$P(x)$	probability a detector element or pixel being illuminated by x photons
rem	röntgen equivalent man, an obsolete unit of effective radiation dose
R	Röntgen, a unit of radiation exposure. One R will produce one electrostatic unit of charge in 1 cm^3 of dry air at 0°C and 1.0 atmosphere pressure.
R_s	spatial resolution
r_e	classical electron radius (2.8179×10^{-13} cm or 2.8179×10^{-15} m)
r	radius
$r_{\text{Be}}, r_{\text{l}}, r_{\text{DT}}$	radii of interfaces in a capsule for laser implosion
$R(r)$	radial solution to the polar Schrödinger wave equation
\vec{r}	linear attenuation position vector

$R(\phi, y_r)$	Radon transform
s	in CT index along the ray sum or ray path
S	source strength (photons produced per unit time i.e., in an x-ray tube)
$S(E)$	X-ray or γ -ray source spectrum
S_γ	number of source photons
SNR	signal-to-noise ratio
t	time (s); in CT index along the detector
T	transmission
TVL	tenth value layer, the thickness required to reduce irradiance to 1/10 of the incident value
V	bias voltage
w_T	tissue weighting factor, used for calculating effective human-equivalent dose
w_j	fraction by weight of the j th element
w_R	<i>radiation weighting factor</i>
w_x	width of a detector in x
X_i	mass fraction of the i th element
x_0, y_0, z_0	the object axes center or origin
x, y, z	Cartesian coordinate axes, also DR/CT system axes where y is along the x-ray beam direction
x	vector x, y, z
y_{spd}	source-to-pinhole distance
y_{pdd}	pinhole-to-detector distance
y_{pod}	pinhole-to-object distance
y_{opd}	object-to-pinhole distance
y_{sc}	source-to-front-of-collimator distance
y_G	back-of-collimator-to-detector distance
y_p	penetrometer thickness
y_t	specimen or object thickness in the radiographic direction
y_{sdd}	source-to-detector distance (cm)
y_{sol}	source-to-center-of-object distance (cm)
y_{odd}	center-of-object-to-detector distance (cm)
y_C	object-to-image-(detector)-plane distance (cm)
y_D	exit-field-to-image-(detector)-plane distance (cm)
y_{EF}	source-to-exit-field distance (cm)
Z	the atomic number of the element
Z_{eff}	effective atomic number as defined by (Johns and Cunningham 1983)
\bar{Z}	effective atomic number for computing x-ray attenuation
Λ	<i>activity</i> of a radioisotope
Λ_s	specific activity of a radioisotope, activity per unit mass
Λ_{sp}^j	specific activity of the j th isotope
α	an alpha particle
α_p	ratio of the incident photon energy to the rest mass energy of the electron
β	the attenuation index that describes the attenuation of x-rays; in CT an angle
β^-	an electron (rest mass of 9.1066×10^{-28} g with a unit negative electric charge of $\sim 1.602 \times 10^{-19}$ coulombs)
β^+	a positron (positive electron or the antielectron)
δ	the phase-shift term or index and incorporates refractive and diffractive effects
δ_{spotx}	source unsharpness
η	index of refraction

η_i	index of refraction of i th medium
κ	average value of the probability function ($P(x)$) or average number of photons per pixel or detector element
λ	wavelength
λ_{\min}	wavelength corresponding to maximum energy radiated
λ_r	radioactive decay constant, λ_r , is the probabilistic decay rate
μ	linear attenuation coefficient (units of inverse length, for example, cm^{-1})
μ_m	mass attenuation coefficient (units of area/mass, for example cm^2/g)
μ_m^j	mass attenuation coefficient of the j th element
μ_a	atomic attenuation coefficient (units of area per atom, b/atom)
μ_M	molar attenuation coefficient (cm^2/mole)
μ^{pe}	linear photoelectric absorption coefficient (cm^{-1})
μ^{pp}	linear pair production attenuation coefficient (cm^{-1})
μ^s	linear scatter attenuation coefficient (cm^{-1})
v	particle or wave velocity (m/s) in a medium
\mathbf{v}_{β^-}	velocity of an accelerated electron
ν	temporal frequency (s^{-1} or Hz)
ν_0	temporal frequency (s^{-1} or Hz) of the incident photon
θ	angle in polar coordinate system
θ_c	reflection critical angle measured from the surface normal
θ_i	angle of incidence measured from the surface normal
θ_r	angle of reflection measured from the surface normal
θ_t	angle of transmission or refraction measured from the surface normal
θ_{TO}	takeoff angle, angle between the direction of x-ray beam and anode surface
θ_{null}	angle with zero diffracted irradiance
$\Theta(\theta)$	polar solution to the Schrödinger equation
ς	photon scattering angle relative to the primary photon direction; CT angle
ρ_a	atomic density atoms per unit volume (atoms/ cm^3)
ρ	mass density mass per unit volume (g/cm^3)
$\bar{\rho}$	effective mass density for computing x-ray attenuation
σ	standard deviation of a signal
σ_{sr}	surface roughness of a material
τ_{HL}	half life of a radioisotope defined as the time required for the number of radioactive nuclei to be reduced by one half
τ	temporal period
Φ_P	the phase path length
Φ_0^E	incident irradiance (also called energy flux density)
Φ^E	transmitted irradiance (also called energy flux density)
Φ_0^P	incident photon flux density (number of photons per unit area per unit time)
Φ^P	transmitted photon flux density (number of photons per unit area per unit time)
Φ_p^P	transmitted primary photon flux density (number of primary photons per unit area per unit time)
Φ_s^P	transmitted scattered photon flux density (number of scattered photons per unit area per unit time)
Φ_0	detected incident irradiance; irradiance without the object
Φ	detected transmitted (through an object) irradiance
Φ_D	mean of the total number of photons
Φ_P	detected transmitted primary irradiance
Φ_S	detected scattered and pair production irradiance
Φ_{Sbk}	detected background scattered irradiance

Φ_{Sobj}	detected object scattered irradiance
$\Phi(\phi)$	polar solution to the Schrödinger equation
ϕ	angle in polar coordinate system
Φ_j	phase lag
Ψ	amplitude that is a function of the Cartesian coordinates of that point
Ψ_i	amplitude that is a function of the polar coordinates of that point
Ω	solid angle (steradian, which is equal to radian ²)
ω	angular temporal frequency
\forall	optical intensity

References

- Abdul-Aziz, A., Challenges in integrating nondestructive evaluation and finite element methods for realistic structural analysis, *National Aeronautics and Space Administration, NASA/TM-2000-209952*, 2000.
- Achterhold, K., Bech, M., Schleede, S., Potdevin, G., Ruth, R., Loewen, R., and Pfeiffer, F., Monochromatic computed tomography with a compact laser-driven X-ray source, *Sci Rept*, **3**, 1313, 2013.
- Adams, W.L., Chalmers, A., Grodzins, L., Perich, L.W., and Rothschild, P., X-ray backscatter mobile inspection van, U.S. Patent US7218704 B1, 2007.
- Agostinelli, S., Allison, J., Amako, K., Apostolakis, J., Araujo, H., Arce, P., Asai, M. et al., GEANT4 A simulation toolkit, *Nucl Instr Meth A*, **506:3**, 250–303, 2003.
- Ahmad, S. and Whitworth, R.W., Dislocation motion in ice: A study by synchrotron X-ray topography, *Phil Mag A*, **57:5**, 749–766, 1988.
- Ahn, S.K., Cho, G., Yong, K.C., Kin, H.K., and Jae, M., A computer code for the simulation of X-ray imaging systems, *Nuclear Science Symposium Conference Record, 2003 IEEE*, **2**, 838–842, 2003.
- Albert, R.D. and Albert, T.M., Aerospace applications of X-ray system using reverse geometry, *Mater Eval*, **51:12**, 1350–1352, 1993.
- ALERT, <http://www.northeastern.edu/alert/transitioning-technology/adsa/>, 2016.
- Alessandro R., Albertin F., Avataneo C., Brancaccio R., Corsi J., Cotto G., De Blasi, S. et al., X-ray tomography of large wooden artworks: The case study of “Doppio corpo” by Pietro Piffetti, *Heritage Science*, **2**, No. 19, 1–9, 2014.
- Alfayez, L., Mba, D., and Dyson, G., The application of acoustic emission for detecting incipient cavitation and the best efficiency point of a 60 kW centrifugal pump: Case study, *Ndt Int*, **38:5**, 354–358, 2005.
- Allee, L.L., Corn Rootworm Ecology, Economics, and Behavior, PhD thesis, Cornell University, 2001.
- Allgaier, M.W. and Ness, S., *Nondestructive Testing Handbook*, second edition: Volume 8, *Visual and Optical Testing*, American Society of Nondestructive Testing, 1993.
- Allman, B.E., McMahon, P.J., and Tiller, J.B., Noninterferometric quantitative phase imaging with soft x rays, *JOSA A*, **17:10**, 1732–1743, 2000.
- ALS, http://www.als.lbl.gov/als/synchrotron_sources.html, 2010.
- Alvarez, R.E. and Macovski, A., Energy-selective reconstructions in x-ray computerised tomography. *Phys Med Biol*, **21:5**, 733, 1976.
- Amendt, P.A., Robey, H.F., Park, H.S., Tipton, R.E., Turner, R.E., Milovich, J.L., Bono, M. et al., Hohlraum-Driven Ignitionlike Double-Shell Implosions on the Omega Laser Facility, *Phys Rev Lett*, **94:6**, 065004, 2005.
- American Cancer Society, *Radiation Therapy Principles*, 2015. http://www.cancer.org/docroot/ETO/eto_1_3_Radiation_Therapy.asp.
- Andola, S., Niranjan, R., Shaikh, A.M., Rout, R.K., Kaushik, T.C., and Gupta, S.C., Characterization of pulsed (plasma focus) neutron source with image plate and application to neutron radiography, *AIP Conference Proceedings*, **1512**, 528–529, 2013.
- ANL, <http://web.ead.anl.gov/uranium/mgmtuses/storage/index.cfm>, 2015.
- Annis, C., False positives, http://www.statisticalengineering.com/false_positives.htm, 2007.
- Annis, C. and Erland, K., Measuring differences among probability of detection curves, *Review of Progress in Quantitative Nondestructive Evaluation*, Thompson and Chimenti, (Editors), New York, Plenum Press, 2229–2234, 1989.
- Antolak, A.J., Pontau, A.E., Morse, D.H., Weirup, D.L., Heikkinen, D.W., Cholewa, M., Bench, G.S., and Legge, G.J.F., Ion microtomography and particle induced X-ray emission analysis of direct drive inertial confinement fusion targets, *J Vac Sci Technol A*, **10:4**, 1164, 1992.
- Aoki, S., Ogata, T., Sudo, S., and Onuki, T., Sub-100 nm-resolution grazing incidence soft X-ray microscope with a laser-produced plasma source, *Jpn J Appl Phys*, **31**, 3477–3480, 1992.
- Artemiev, B.V., X-ray thickness gauges, http://www.ndt.net/article/ecndt2010/reports/1_04_31.pdf, 2014.
- Arthur, J., Materlik, G., Tatchyn, R., and Winick, H., The LCLS: A fourth generation light source using the SLAC linac, *Rev Sci Instrum*, **66:2**, 1987, 1995.
- Arutyunian, F.R. and Tumanian, V.A., The Compton effect on relativistic electrons and the possibility of obtaining high energy beams, *Phys Lett*, **4:3**, 176–178, 1963.
- AS&E, http://www.as-e.com/american_science_and_engineering/timeline.asp, 2006.

- ASNT, *Proceedings of ASNT Topical Conference on Industrial Computerized Tomography*, July 25–27, Seattle, Washington, American Society for Nondestructive Testing, Columbus, Ohio, 1989.
- ASTM E 1417, Standard practice for liquid penetrant examination, *American Society for Testing and Materials*, 1999.
- ASTM E 1441, Standard Guide for Computed Tomography (CT) Imaging, *American Society for Testing and Materials*, 2011.
- ASTM E 1742, Standard Practice for Radiographic Examination, *American Society for Testing and Materials*, 2012.
- ASTM E 1695, Standard Test Method for Measurement of Computed Tomography (CT) System Performance, *American Society for Testing and Materials*, 95, 2013.
- Attwood, D.T., Weinstein, B.W., and Wuerker, R.F., Composite X-ray pin-holes for time-resolved microphotography of laser compressed targets, *Appl Opt*, **16**, 1253–1259, 1977.
- Aufderheide, M.B. and Henderson, G., HADES, A code for simulating a variety of radiographic techniques, *IEEE Nuclear Science Symposium Conference Record*, 2004, UCRL-PROC-207616, 2004a.
- Aufderheide, M.B., Sloan, D.M., and Schach von Wittenau, A.E., HADES, A radiographic simulation code, *Review of Progress in Quantitative Nondestructive Evaluation*, **20A**, AIP Conf. Proc. #557, 507–513, 2001.
- Aufderheide, M.B., Barty, A., and Martz, H.E., Simulation of phase effects in imaging for mesoscale NDE, *Review of Progress in Quantitative Nondestructive Evaluation*, **24A**, AIP Proceedings 760, 663–670, 2004b.
- Aufderheide, M.B. III, Sloan, D.M., and Schach von Wittenau, A.E., *HADES user's manual*, Lawrence Livermore National Laboratory, UCRL-MA-151338, HADES version 3.0.1, 2005.
- Aufderheide, M.B., Brown, W.D., Hamza, A.V., Park, H.-S., Martz, H.E., Remington, B.A., Rogers, J.A., Jeon, S., and Nam, Y.-S., Analysis and modeling of phase contrast radiography of gradient density laser targets, *Nuc Inst Meth A*, **579**, 1, 223–226, 2007.
- Auld, B.A. and Moulder, J.C., Review of advances in quantitative eddy current nondestructive evaluation, *J Nondestruct Eval*, **18:1**, 3–36, 1999.
- Azevedo, S.G., Exploring the ultrawideband, *Science and Technology*, Lawrence Livermore National Laboratory, UCRL-TR-52000-04-9, 2004.
- Azevedo, S.G., Schneberk, D., Fitch, P., and Martz, H., Calculation of the rotational centers in computed tomography sinograms, *IEEE T Nucl Sci*, **37**, 1525, 1990.
- Azevedo, S.G., Martz, Jr., H.E., Aufderheide, III, M.B., Brown, W.D., Champley, K.M., Kallman, J.S., Roberson, G.P., Schneberk, D., Seetho, I.M., and Smith, J.A., System-independent characterization of materials using dual-energy computed tomography, *IEEE T Nucl Sci*, **63:1**, 341–350, 2016.
- Bar-Cohen, Y., In-service NDE of aerospace structures—Emerging technologies and challenges at the end of the 2nd millennium, *NDT.net*, **4:9**, 1999; <http://www.ndt.net/article/v04n09/bcohen/bcohen.htm>.
- Barnes, G.T. and Frey, G.D., (Editors), *Screen Film Mammography: Imaging Considerations and Medical Physics Responsibilities: Spring Symposium: Papers*, Medical Physics Publishing, Madison, WI, 1991.
- Barrett, H.H. and Swindell, W., *Radiological Imaging*, Academic Press, New York, 1981.
- Barty, C.P. and Hartemann, F.V., *T-REX: Thomson-Radiated Extreme X-Rays Moving X-Ray Science into the "Nuclear" Applications Space with Thompson Scattered Photons*, LLNL Technical Report UCRL-TR-206825, 2004.
- Barty, C.P., Albert, F., Anderson, S.G., Armstrong, P., Bayramian, A., Beer, G., and Cross, R., Overview of *MEGa-Ray-Based Nuclear Materials Management Activities at the Lawrence Livermore National Laboratory*, Proceedings of Institute of Nuclear Materials Management 52nd Annual Meeting, LLNL Report LLNL-CONF-515893, 2011.
- BEIR VII: *Health risks from exposure to low levels of ionizing radiation*, report in brief, National Research Council, June, 2005.
- BEIR VII: *Health risks from exposure to low levels of ionizing radiation, phase II*, National Research Council, June, 2006.
- Bemporad, C., Milburn, R.H., Tanaka, N., and Fotino, M., High-energy photons from Compton scattering of light on 6.0-GeV electrons, *Phys Rev*, **138:6B**, B1546, 1965.
- Berens, A.P., *NDE Reliability Data Analysis, Metals Handbook*, ninth edition, **17**, *Nondestructive Evaluation and Quality Control*, American Society for Metals, Metals Park, OH, 689–701, 1989.
- Berger, H., *Neutron radiography—Methods, capabilities and applications*, Elsevier, Amsterdam, 1965.
- Bernardi, R.T., Field test results for radioactive waste drum characterization with waste inspection tomography (WIT), *Proceedings of the 5th Nondestructive Assay and Nondestructive Examination Waste Characterization Conference*, Salt Lake City, Utah, Jan. 14–16, 1997, INEL CONF-970126, 107, 1997.

- Bernardi, R.T. and Martz, Jr., H.E., Nuclear waste drum characterization with 2 MeV X-ray and gamma-ray tomography, *Mat Eval*, **53:10**, 1995.
- Bertin, E.P., *Principles and Practice of X-Ray Spectroscopic Analysis*, second edition, Plenum Press, New York, 1978.
- Betz, C.E., *Principles of Magnetic Particle Testing*, Magnaflux Corp., Chicago, 1967.
- Bevington, P.R., *Data Reduction and Error Analysis for the Physical Sciences*, McGraw-Hill, Inc., New York, 1989.
- Birch, R. and Marshall, M., Computation of bremsstrahlung x-ray spectra and comparison with spectra measured with a Ge(Li) detector, *Phys Med Biol*, **24:3**, 505–517, 1979.
- Birks, A.S. and Green, R.E., (Technical Editors), P. McIntire (Editor), *Ultrasonic Testing, Nondestructive Testing Handbook*, Vol. 7, American Society for Nondestructive Testing, 1991.
- Blanpied, G., Kumar, S., Dorroh, D., Morgan, C., Blanpied, I., Sossong, M., McKenney, S., and Nelson, B., Material discrimination using scattering and stopping of cosmic ray muons and electrons: Differentiating heavier from lighter metals as well as low-atomic weight materials, *Nucl Instrum Meth A*, **784**, 352–358, 2015.
- Boas, F.E. and Fleischmann, D., CT artifacts: Causes and reduction techniques, *Imaging Med*, **4:2**, 229–240, 2012.
- Bohm, T.D., DeLuca, Jr., P.M., and DeWerd, L.A., Brachytherapy dosimetry of ^{125}I and ^{103}Pd sources using an updated cross section library for the MCNP Monte Carlo transport code, *Med Phys*, **30:4**, 701–711, 2003.
- Bohr, N., On the constitution of atoms and molecules, *Philos Mag*, **26**, 1–25, 1913a.
- Bohr, N. II., On the theory of the decrease of velocity of moving electrified particles on passing through matter, *Philos Mag*, **25:145**, 10–31, 1913b.
- Bol, W., The use of balanced filters in X-ray diffraction, *J Sci Instrum*, **44:9**, 736, 1967.
- Bono, M., Bennett, D., Castro, C., and Wallace, R.A., Fabrication of double shell targets with a glass inner capsule supported by SiO_2 aerogel for shots on the Omega laser in 2006, *Fusion Sci and Technol*, **51**, 611–625, 2007.
- Boone, J.M., Determination of the presampled MTF in computed tomography, *Med Phys*, **28:3**, 356–360, 2001.
- Boone, J.M. and Seibert, J.A., An accurate method for computer-generating tungsten anode x-ray spectra from 30 to 140 kV, *Med Phys*, **24:11**, 1661–1670, 1997.
- Boone, J.M. and Seibert, J.A., An analytical model of the scattered radiation distribution in diagnostic radiology, *Med Phys*, **15**, 721, 1988.
- Boone, J.M., Nelson, T.R., Lindfors, K.K., and Seibert, J.A., Dedicated breast CT: Radiation dose and image quality evaluation 1, *Radiology*, **221:3**, 657–667, 2001.
- Bossi, R.H., Iddings, F.A., Wheeler, G.C., and Moore, P.O., *Nondestructive Testing Handbook*, third edition: Volume 4, *Radiographic Testing*, American Society for Nondestructive Testing, Inc., Columbus, 2002.
- Boyd, D.P. and Farmer, D.W., *Cardiac Imaging and Image Processing*, S.M. Collins and D.J. Skorton. Eds. New York: McGraw-Hill. Ch. 4, 57–87, 1986.
- Boyle, M.J., Grazing incidence X-ray microscopy of laser fusion targets, In *1977 SPIE/SPSE Technical Symposium East*, International Society for Optics and Photonics, 86–92, 1977.
- Boyle, M.J. and Ahlstrom, H.G., Imaging characteristics of an axisymmetric, grazing incidence x-ray microscope designed for laser fusion research, *Rev Sci Instrum*, **49:6**, 746–751, 1978.
- Brady, D.J., Marks, D.L., MacCabe, K.P., and O'Sullivan, J.A., Coded apertures for x-ray scatter imaging, *Appl Optics*, **52:32**, 7745–7754, 2013.
- Bragg, W.L., Diffraction of short electromagnetic waves by a crystal, *P Camb Philos Soc*, **17**, 43–57, 1912.
- Brancaccio, R., Bettuzzi, M., Casali, F., Morigi, M.P., Levi, G., Gallo, A., Marchetti, G., and Schneberk, D., Real-time reconstruction for 3-D CT applied to large objects of cultural heritage, *IEEE Trans Nucl Sci*, **58:4**, 1864, 2011.
- Brantley, P.S., Dawson, S.A., McKinley, M.S., O'Brien, M.J., Stevens, D.E., Beck, B.R., Jurgenson, E.D., Ebbers, C.A., and Hall, J.M. Recent advances in the mercury Monte Carlo particle transport code. In *International Conference on Mathematics and Computational Methods Applied to Nuclear Science & Engineering (M&C 2013)*, pp. 5–9. 2013.
- Braz, D., Lopes, R.T., and Motta, L.M.G., Dual-energy computerized tomography in compacted soil, *Geotechnical & Geological Engineering*, **18:3**, 221–238, 2000.
- Britannica, http://www.britannica.com/nobel/macro/5005_7.html, 2005.
- Brokish, J. and Bresler, Y., Ultra-fast hierarchical backprojection for micro-CT reconstruction, In *Nuclear Science Symposium Conference Record, 2007. NSS'07, IEEE*, **6**, 4460–4463, 2007.
- Brown, W.D. and Martz, Jr., H.E., X-ray digital radiography and computed tomography of ICF and HEDP materials, subassemblies and targets, in *Digital Imaging IX, An ASNT® Topical Conference*, Mashantucket, CT, July 24–26, 2006, also Lawrence Livermore National Laboratory report, Livermore, CA, UCRL-PROC-221772, 2006.

- Browne, J.A., Koshy, M., and Stanley, J.H., On the application of discrete tomography to CT-assisted engineering and design, *Int J Imag Syst Tech*, **9**, 78, 1998.
- Brunetti, A., Princi, E., Vicini, S., Pincin, S., Bidali, S., and Mariani, A., Visualization of monomer and polymer inside porous stones by using X-ray tomography, *Nuc Instrum Meth B*, **222**, 235–241, 2004.
- Buck, R.M. and Hall, J.M., Applications of the COG multiparticle Monte Carlo transport code to simulated imaging of complex objects, *SPIE International Symposium on Optical Science Engineering and Instrumentation*, Denver, CO, 1999.
- Buckley, M.J., The future economic role of NDE, *IEEE T Son Ultrason*, **SU-23**, No. 5, 287–292, 1976.
- Buffler, A. and Tickner, J., Detecting contraband using neutrons: Challenges and future directions, *Radiat Meas*, **45**, 1186–1192, 2010.
- Bulaevskaya, V., *Probabilistic Characterization of Partial Volume Effects in Imaging of Rectangular Objects, LLNL report, LLNL-TR-670422*, May 8, 2015.
- Bushberg, J.T., Seibert, J.A., Leidholdt, E.M., and Boone, J.M., *The Essential Physics of Medical Imaging*, Williams and Wilkins, 1994.
- Calderón-Colón, X., Geng, H., Gao, B., An, L., Cao, G., and Zhou O., A carbon nanotube field emission cathode with high current density and long-term stability, *Nanotechnology*, **20:32**, 325707, 2009.
- Callaway, E., Rival species recast significance of ‘first bird’, *Nature*, **516:7529**, 18–19, corrected December 4, 2014.
- Callerame, J., X-ray backscatter imaging: Photography through barriers, JCPDS-International Centre for Diffraction Data ISSN 1097-0002, 2006. From http://www.icdd.com/resources/axa/vol49/v49_02.pdf.
- Cameron, J.R., Is radiation an essential trace energy? *Forum on Physics and Society* (A Division of APS), **30:4**, 2001.
- Cameron, J.R., Radiation increased the longevity of British radiologists, *Brit J Radiol*, **75**, 637, 2002.
- Camp, D.C., Martz, H.E., Roberson, G.P., Decman, D.J., and Bernardi, R.T., Non-destructive waste-drum assay for transuranic content by gamma-ray active and passive computed tomography, *Nuc Instrum Meth A*, **495**, 69–83 2002.
- Cao, G., Lee, Y.Z., Peng, R., Liu, Z., Rajaram, R., Calderon-Colon, X., An, L. et al., A dynamic micro-CT scanner based on a carbon nanotube field emission x-ray source, *Phys Med Biol*, **54**, 2323–2340, 2009a.
- Cao, G., Zhang, J., Zhou, O., and Lu, J., Temporal multiplexing radiography for dynamic x-ray imaging, *Rev Sci Instrum*, **80**, 093902, 2009b.
- Carney, R.M., Vinther, J., Shawkey, M.D., D’Alba, L., and Ackermann, J., New evidence on the colour and nature of the isolated Archaeopteryx feather, *Nature Comm*, **3**, 637, 1–6, 2012.
- Carney, R., Molnar, J., Updike, E., Brown, W., Jackson, J., Shawkey, M., Lindgren, J., Sjövall, P., Falkingham, P., and Gauthier, J., Archaeopteryx in 4D, *J Vertebr Paleontol*, Program and Abstracts, 103, 2014.
- Caruso, S., Characterisation of high-burnup LWR fuel rods through gamma tomography, Ph.D. Thesis, École Polytechnique Fédérale de Lausanne, laurea in ingegneria nucleare, Università degli studi di Roma, Italie et de nationalité italienne, Thesis No. 3762, 2007.
- Caruso, S., Murphy, M.F., Jatuff, F., and Chawla, R., Nondestructive determination of fresh and spent nuclear fuel rod density distributions through computerized gamma-ray transmission tomography, *J Nucl Sci Technol*, **45:8**, 828–835, 2008.
- Casali, F., Morigi, M.P., Brancaccie, R., Montefusco, L., Jerjen, I., Flisch, A., Sennhauser, U., Liritzis, I., and Tiseanu, I., X-ray computed tomography for damage assessment of cultural heritage assets, *Protection of Historical Buildings, PROHITECH09*, CRC Press, 847–851, 2009.
- Case, J.T., Robbins, J., Kharkovsky, S., Hepburn, F., and Zoughi, R., Microwave and millimeter wave imaging of the space shuttle external fuel tank spray on foam insulation (SOFI) using synthetic aperture focusing techniques (SAFT), *Quantitative Nondestructive Evaluation*, AIP Conference Proceedings, **820**, 1546–1553, March 6, 2006.
- Castillo, F., Gamboa-de Buen, I., Herrera, J.J.E., Rangel, J., and Villalobos, S., High contrast radiography using a small dense plasma focus, *Appl Phys Lett*, **92:5**, 051502, 2008.
- Cavalleri, A., Siders, C.W., Brown, F.L.H., Leitner, D.M., Tóth, C., Squier, J.A., Barty, C.P.J. et al., Anharmonic lattice dynamics in germanium measured with ultrafast X-ray diffraction, *Phys Rev Lett*, **85:3**, 586, 2000.
- Cavalleri, A., Siders, C.W., Rose-Petrucci, C., Jimenez, R., Tóth, C., Squier, J.A., and Von Der Linde, D., Ultrafast x-ray measurement of laser heating in semiconductors: Parameters determining the melting threshold, *Phys Rev B*, **63:19**, 193306, 2001a.
- Cavalleri, A., Tóth, C., Siders, C.W., Squier, J.A., Ráksi, F., Forget, P., and Kieffer, J.C., Femtosecond structural dynamics in VO₂ during an ultrafast solid-solid phase transition, *Phy Rev Lett*, **87:23**, 237401, 2001b.

- Cavalleri, A., Blome, C., Forget, P., Kieffer, J.C., Magnan, S., Siders, C.W., Sokolowski-Tinten, K., Squier, J.A., Tóth, C., and Vonder Linde, D., Femtosecond X-ray studies of photo-induced structural phase transitions, *Phase Transit*, **75:7 and 8**, 769–777, 2002.
- Champlay, K., Smith, J., Kallman, J., and Top, P., Automatic Threat Detection for a Dual-Energy Four-View X-ray Carryon Luggage Scanner. Lawrence Livermore National Laboratory, Livermore, CA, UCRL-LNL-ABS-681605, 2016, to be published in 4th International Congress on Image Formation in X-ray CT, 2016.
- Chang, K., Practical fusion or just a bubble?, *NY Times*, February 27, 2007.
- Chase, R.C. and Silk, J.K., Ellipsoid-hyperboloid x-ray imaging instrument for laser-pellet diagnostics, *Applied Optics*, **14:9**, 2096–2098, 1975.
- Chemix, <http://www.standnes.no/chemix/periodictable/specific-heat-capacity.htm>, 2010.
- Chen, L.M., Wang, W.M., Kando, M., Hudson, L.T., Liu, F., Lin, X.X., Ma, J.L. et al., High contrast femtosecond laser-driven intense hard X-ray source for imaging application, *Nucl Instrum Meth A*, **619**, 128–132, 2010.
- Cheng, Y. and Zhou, O., Electron field emission from carbon nanotubes, *Comptes Rendus Phys*, **4:9**, 1021–1033, 2003.
- Cheng, Y., Zhang, J., Lee, Y.Z., Gao, B., Dike, S., Lin, W., Lu, J.P., and Zhou, O., Dynamic radiography using a carbon-nanotube-based field-emission x-ray source, *Rev Sci Instrum*, **75**, 3264–3267, 2004.
- Cherepy, N.J., Payne, S.A., Seeley, Z.M., Thelin, P.A., Schneberk, D., Stone, G., Perry, R.L., Thompson, R., and Hunter, J.F., Transparent ceramic scintillator for radiography, to be submitted to *IEEE T Nuc Sci*, 2015a.
- Cherepy, N.J., Seeley, Z.M., Payne, S.A., Swanberg, E.L., Beck, P.R., Schneberk, D.J., Stone, G. et al., Transparent ceramic scintillators for gamma spectroscopy and MeV imaging, *Proc. SPIE 9593, Hard X-Ray, Gamma-Ray, and Neutron Detector Physics XVII*, 95930P, 2015b.
- Chesler, D.A., Riederer, S.J., and Pelc, N.J., Noise due to photon counting statistics in computed X-ray tomography, *J Comput Assist Tomo*, **1:1**, 64–74, 1977.
- Chua, H.S., Haigh, A.D., Obradovic, J., Gibson, A.A.P., and Linfield, E.H., Terahertz time-domain spectroscopy of wheat grain, *2004 Joint 29th Int. Conf. on Infrared and Millimeter Waves and 12th Int. Conf. on Terahertz Electronics, Spectroscopy and Material Properties*, ISBN:0780384903, 399–400, 2004.
- Clayton, J., Regentova, E., and Yfantis, E., Final Report Next-Generation Mega-Voltage Cargo-Imaging System for Cargo Container Inspection, UNLV Research Foundation, Las Vegas, NV 89113, 2007.
- Claytor, T.N., Taddeucci, T.N., Hills, C.R., Summa, D.A., Davis, A.W., McDonald, T.E., and Schwab, M.J., High-Energy and Thermal-Neutron Imaging and Modeling with an Amorphous Silicon Flat Panel, *Appl Radiat Isotopes*, **61**, 579, 2004.
- Cloetens, P., Barrett, R., Baruchel, J., Guigay, J.-P., and Schlenker, M., Phase objects in synchrotron radiation hard X-ray imaging, *J Phys D Appl Phys*, **29**, 133, 1996.
- COG <http://cog.llnl.gov/2007>.
- COG, *User's Manual*, fifth edition, *A Multiparticle Monte Carlo Transport Code*, Lawrence Livermore National Laboratory, UCRL-TM-202590, 2002.
- Columbia Accident Investigation Board Report, volume 1, August 2003. http://www.nasa.gov/columbia/home/CAIB_Vol1.html, 2003.
- Comet, <http://www.comet.ch/>, 2007.
- Compton, A.H. and Allison, S.K., *X-Rays in Theory and Experiment*, D. Van Nostrand, New York, 1935.
- Coolidge, <http://www.orau.org/ptp/collection/xraytubesc coolidge/coolidge.htm>, 2015.
- Cordell, T.M., NDE: A full-spectrum technology, in *Review of Progress in Quantitative Nondestructive Evaluation Volume 17B*, Thompson, D.O., and Chimenti, D.E., Eds., Plenum Press, New York, 1099–1107, 1998.
- Cormack, A.M., Representation of a function by its line integrals, with some radiological applications, *J Appl Phys*, **34:9**, 2722, 1963.
- Cormack, A.M., Representation of a function by its line integrals, with some radiological applications II, *J Appl Phys*, **35:10**, 2908, 1964.
- Cormack, A.M., Early two-dimensional reconstruction and recent topics stemming from it, Nobel Lecture, December 8, 1979. Available at <http://nobelprize.org/medicine/laureates/1979/cormack-autobio.html> 1979.
- Cosslett, V.E. and Nixon, W.C., *X-Ray Microscopy*, Cambridge University Press, New York, 1960.
- Crews, A.R., Bossi, R.H., and Georgeson, G.E., *X-Ray Computed Tomography for Geometry Acquisition*, Wright Patterson Air Force Base Material Command Report WL-TR-93-4036, 1993.
- Cullen, <http://home.comcast.net/~redcullen1/2007>.

- Cullen, D.E., *TART 2002 A Coupled Neutron-Photon 3-D, Combinatorial Geometry Time Dependent Monte Carlo Transport Code*, University of California Lawrence Livermore National Laboratory Report UCRL-ID-126455, Rev. 4 Code Release: UCRL-CODE-2003-043, 2003.
- Cullen, D.E., Chen, M.H., Hubbell, J.H., Perkins, S.T., Plechaty, E.F., Rathkopf, J.A., and J.H. Scofield, *Tables and Graphs of Photon-Interaction Cross Sections From 10 eV to 100 GeV Derived From the LLNL Evaluated-Photon-Data Library (EPDL)*, Report UCRL-50400, **Vol. 6**, Rev. 4, Lawrence Livermore National Laboratory, Livermore, CA, 1989.
- Cullity, B.D., *Elements of X-ray Diffraction*, Addison Wesley, Reading, MA, 1978.
- Cunningham, G.S. and Morris, C., The development of flash radiography, *Los Alamos Science*, **28**, 2003.
- Dainty, J.C. and Shaw, R., *Image Science—Principles, Analysis and Evaluation of Photographic-Type Imaging Processes*, Academic Press, New York, 1974.
- Davidson, N.C. and Chase, S.B., Radar tomography of bridge decks, *Proceedings of SPIE—Volume 3400, Structural Materials Technology III*, 250–256, 1998.
- Davis, G.R., Evershed, A.N.Z., and Mills, D., Characterisation of materials: Determining density using X-ray microtomography, *Mater Sci Tech*, **31:2**, 162–166, 2015.
- Davisson, C. and Germer, L.H., Diffraction of electrons by a crystal of nickel, *Phys Rev*, **30:6**, 705, 1927.
- De Chiffre, L., Carmignato, S., Kruth, J.-P., Schmitt, R., and Weckenmann, A., Industrial applications of computed tomography, *CIRP Annals Manuf Technol* **63**, 655–677, 2014.
- de Smit, E., Swart, I., Fredrik Creemer, J., Hoveling, G.H., Gilles, M.K., Tyliszczak, T., Kooyman, P.J. et al., Nanoscale chemical imaging of a working catalyst by scanning transmission X-ray microscopy, *Nature*, **456**, 222–226, 2008.
- Della Bona, A. and Anusavice K.J., Microstructure, composition, and etching topography of dental ceramics, *Int J Prosthodont*, **15:2**, 159–167, 2002.
- Di Lorenzo, F., Raspa, V., Knoblauch, P., Lazarte, A., and Moreno, C., Hard x-ray source for flash radiography based on a 2.5 kJ plasma focus, *J Appl Phys*, **102**, 033304, 2007.
- Dicke, R.H., Scatter-hole cameras for X-rays and gamma rays, *Astrophys J*, **153**, L101–L106, 1968.
- DIN EN 12543-1, *Non-destructive testing. Characteristics of focal spots in industrial X-ray systems for use in non-destructive testing. Scanning method*, 1999.
- DIN EN 12543-2, *Non-destructive testing. Characteristics of focal spots in industrial X-ray systems for use in non-destructive testing. Pinhole camera method*, 1999.
- DIN EN 12543-3, *Non-destructive testing. Characteristics of focal spots in industrial X-ray systems for use in non-destructive testing. Slit camera method*, 1999.
- DIN EN 12543-4, *Non-destructive testing. Characteristics of focal spots in industrial X-ray systems for use in non-destructive testing. Edge method*, 1999.
- DIN EN 12543-5, *Non-destructive testing. Characteristics of focal spots in industrial X-ray systems for use in non-destructive testing. Measurement of the effective focal spot size of mini and micro focus X-ray tubes*, 1999.
- Dobmann, G., NDE for material characterization of ageing due to thermal embrittlement, fatigue and neutron degradation, *Int J Mater Prod Tec*, **26:1–2**, 122–139, 2006.
- DOE, Moab, Utah UMTRA project, <http://gj.em.doe.gov/moab>, 2005a.
- DOE, Remediation of the Moab uranium mill tailings, Grand and San Juan counties, Utah, Final Environmental Impact Statement, DOE/EIS-0355, July, available at http://www.eh.doe.gov/nepa/eis/eis_0355/, 2005b.
- Donnelly, E., Price, R., and Pickens, D.R., Quantification of the effect of system and object parameters on edge enhancement in phase-contrast radiography, *Med Phys*, **30**, 2888–2896, 2003.
- Doshi, C., van Riessen, G., Balaur, E., de Jonge, M.D., and Peele, A.G., Characterization of an indirect X-ray imaging detector by simulation and experiment. *Ultramicroscopy*, **148**, 20–24, 2015.
- Dudley, M., Huang, X., and Vetter, W.M., Contribution of x-ray topography and high-resolution diffraction to the study of defects in SiC, *J Phys D: Appl Phys*, **36**, A30–A36, 2003.
- Dusaussay, N.J., Cao, Q., and Stanley, J.H., Image processing for CT-assisted reverse engineering and part characterization, *1995 International Conference on Image Processing, IEEE*, **3**, 3033, 1995.
- Duvauchelle, P., Freud, N., Kafandjian, V., and Babot, D., A computer code to simulate X-ray imaging techniques, *Nucl Instrum Meth B*, **170:1&2**, 245–258, 2000.
- Edwards, J., Lorenz, K.T., Remington, B.A., Pollaine, S., Colvin, J., Braun, D., Lasinski, B.F. et al., Laser-driven plasma loader for shockless compression and acceleration of samples in the solid state, *Phys Rev Lett*, **92:7**, 075002, 2004.
- Ekdahl, C., Modern electron accelerators for radiography, *IEEE T Plasma Sci*, **30:1**, 254–261, 2002.
- EMI, <http://www.emiarchivetrust.org/about/history-of-emi/>, 2015.

- Empey, D.M., Schneberk, D.J., Allen, Jr. G.A., and Venkatapathy, E., X-Ray computed tomographic investigation of thermal protection system materials, *50th AIAA Aerospace Sciences Meeting January 2012*, Nashville, TN, AAIA 2012–0593, 2012.
- Engler, P., Friedman, W.D., and Armstrong, E.E., Determination of material composition using dual energy computed tomography on a medical scanner, *Proc. of ASNT Topical Conf. on Industrial Computerized Tomography*, Seattle, WA, 142, July 1989.
- EPA, Assessment of Risks from Radon in Homes, EPA 402-R-03-003, 2003.
- ESRF, <http://www.esrf.eu/>, 2015.
- Esarey, E., Schroeder, C.B., and Leemans, W.P., Physics of laser-driven plasma-based electron accelerators, *Rev Mod Phys*, **81**:3, 1229, 2009.
- Estep, R.J., Prettyman, T.H., and Sheppard, G.A., Tomographic gamma scanning to assay heterogeneous radioactive waste, *Nucl Sci and Eng*, **118**:3, 145–152, 1994.
- Evans, R.D., *The Atomic Nucleus*, McGraw Hill, New York, 1955.
- Fantidis, J.G., Bandekas, D.V., and Vordos, N., The replacement of research reactors with a compact proton Linac for neutron radiography, *Radiat Phys Chem*, **86**, 74–78, 2013.
- Farmelo, G., The discovery of X-rays, *Sci Am*, **273**:5, 86, 1995.
- Farsoni, A.T. and Hamby, D.M., MCNP analysis of a multilayer phoswich detector for β -particle dosimetry and spectroscopy. *Nucl Instrum Methods Phys Res A*, **555**:1, 225–230, 2005.
- Favro, L.D., Han, X., Ouyang, Z., Sun, G., Sui, H., and Thomas, R. L., Infrared imaging of defects heated by a sonic pulse, *Rev Sci Instrum*, **71**:6, 2418–2421, 2000.
- Feenberg, E. and Primakoff, H., Interaction of cosmic-ray primaries with sunlight and starlight, *Phys Rev*, **73**:5, 449, 1948.
- Feldkamp, L.A., Davis, L.C., and Kress, J.W., Practical cone-beam algorithm, *J Opt Soc Am*, **1**:6, 612–619, 1984.
- Fiocco, G. and Thompson, E., Thomson scattering of optical radiation from an electron beam, *Phy Rev Lett*, **10**:3, 89, 1963.
- Fitzgerald, R., Phase sensitive X-ray imaging, *Phys Today*, **53**, 23–26, 2000.
- Ford, J.C., Zheng, D., and Williamson, J.F., Estimation of CT cone-beam geometry using a novel method insensitive to phantom fabrication inaccuracy: Implications for isocenter localization accuracy, *Med Phys*, **38**:6, 2829–2840, 2011.
- Fowler, R.H. and Nordheim, L., Electron emission in intense electric fields, *Proc Roy Soc London Ser A: Math, Phys and Engineering Sciences*, **119**:781, 173–181, The Royal Society, 1928.
- Frame, P., Oak Ridge Associated Universities, <http://www.orau.org/ptp/collection/radioluminescent/radioluminescentinfo.htm>, 2005.
- Franks, A., Some developments and applications of microfocus X-ray diffraction techniques, *Brit J Appl Phys*, **9**, 349–352, 1958.
- Franks, A., X-ray optics, *Sci Prog*, (London), **64**, 371–422, 1977.
- Franks, A. and Breakwell P.R., Developments in optically focusing, reflectors for small angle X-ray scattering cameras, *J Appl Cryst*, **7**, 122–125, 1974.
- Friedrich, W., Knipping, P., and von Laue, M., Interference phenomena with Röntgen rays, *Ann Phys-Berlin*, **41**, 971–988, 1913.
- Fufari, F.A., A history of the Van de Graaff generator, *IEEE Ind Appl Mag*, **11**, 10–14, 2005.
- Fujishiro, M., Tsujii, Y., Taniguchi, R., Okamoto, K., and Yoneda, K., A trial of quantitative estimation of Al-corrosion detected by neutron radiography, *Appl Radiat Isotopes*, **61**:4, 725–728, 2004.
- Fujita, T., Kataoka, J., Nishiyama, T., Ohsuka, S., Nakamura, S., and Yamamoto, S., Two-dimensional diced scintillator array for innovative, fine-resolution gamma camera. *Nucl Instrum Methods Phys Res A*, **765**, 262–268, 2014.
- GAONUCWASTE, Nuclear Waste: Storage Issues at DOE's Waste Isolation Pilot Plant in New Mexico, *Government Accounting Office Report: GAO/RCED-90-1*, 1990.
- Gbur, G., Anastasio, M.A., Huang, Y., and Shi, D., Spherical-wave intensity diffraction tomography, *JOSA A*, **22**:2, 230–238, 2005.
- GE, <http://www.geinspectiontechnologies.com/en/index.html>, 2007.
- GEANT4, <http://geant4.web.cern.ch/geant4/>, 2007.
- Georgiou, G.A., Probability of detection curves: Derivation, applications and limitations, Research Report 454, HSE Books, 2006.
- Georgiou, G.A. and Schneider, C.R.A., Radiography of thin-section welds, part 1: Practical approach, *Insight*, **45**:2, 116–118, 2003.
- Ghebregziabher, I., Shadwick, B.A., and Umstadter, D., Spectral bandwidth reduction of Thomson scattered light by pulse chirping, *Phys Rev Spec Top-AC*, **16**:3, 030705, 2013.

- Ghiassi-nejad, M. Mortazavi, S.M.J. Cameron, J.R., Niroomand-rad, A., and Karam, P.A., Very high background radiation areas of Ramsar, Iran: Preliminary biological studies, *Health Phys*, **82:1**, 87, 2002.
- Gibbs, K.M., Berger, H., Jones, T., Polansky, D., Haskins, J., Schneberk, D., and Brenizer, J., Flat Panel Imaging of Thermal Neutrons, *Westinghouse Savannah River Company report WSRC-MS-99-00655 (1999), Summary Proceedings of ASNT Fall Conference*, 140, 1999.
- Gibson, D.J., Albert, F., Anderson, S.G., Betts, S.M., Messerly, M.J., Phan, H.H., Semenov, V.A. et al., Design and operation of a tunable MeV-level Compton-scattering-based γ -ray source, *Phys Rev Spec Top-AC*, **13:7**, 070703, 2010.
- Gilbert, A.J., McDonald, B.S., Robinson, S.M., Jarman, K.D., White, T.A., and Deinert, M.R., Non-invasive material discrimination using spectral x-ray radiography, *J Appl Phys*, **115:15**, 154901, 2014.
- Glassner, A.S., Ed., *An Introduction to Ray Tracing (The Morgan Kaufmann Series in Computer Graphics)*, 1st edition, Academic Press Limited, San Diego, 1989.
- Goebbelz, K., *Materials Characterization for Process Control and Product Conformity*, CRC Press, 1994.
- Gofman, J.W., Radiation from medical procedures in the pathogenesis of cancer and ischemic heart disease: Dose-response studies with physicians per 100,000 population, *The Library*, **99**, 045096, 1999.
- Goldberg, N., *Camera Technology: The Dark Side of the Lens*, Academic Press, Chicago, 1992.
- Goldman, L.W., Principles of CT and CT technology, *J Nucl Med Technol*, **35:3**, 115–128, 2007.
- Goldstone, P.D., Goldman, S.R., Mead, W.C., Cobble, J.A., Stradling, G., Day, R.H., Hauer, A. et al., Dynamics of high-Z plasmas produced by a short-wavelength laser, *Phys Rev Lett*, **59**, 56–59, 1987.
- Gondrom, S. and Schröpfer, S., Digital computed laminography and tomosynthesis—Functional principles and industrial applications, *International Symposium on Computerized Tomography for Industrial Applications and Image Processing in Radiology, Berlin, Germany, Proceedings BB 67-CD*, 1999.
- Gonzales, B., Spronk, D., Cheng, Y., Spronk, D., Cheng, Y., Zhang, Z., Pan, X., Beckmann, M., Zhou, O., and Lu, J., Rectangular computed tomography using a stationary array of CNT emitters: Initial experimental results, *SPIE Medical Imaging*, 86685K, *International Soc Optics and Photonics*, 2013.
- Gonzales, B., Spronk, D., Cheng, Y., Tucker, A.W., Beckman, M., Zhou, O., and Lu J., Rectangular fixed-gantry CT prototype: Combining CNT X-ray sources and accelerated compressed sensing-based reconstruction, *Access IEEE*, **2**, 971–981, 2014.
- Goodman, P.C., The new light: Discovery and introduction, Penn State University College of Medicine, http://www.xray.hmc.psu.edu/rct/contents_1.html, 2005.
- Gould, J.M. and Goldman, B.A., *Deadly deceit: Low-level radiation, high-level cover-up*, Four Walls Eight Windows, New York, 1993.
- Grabarek, C.L. and Herr, L., *X-ray multi-flash system for measurement of projectile performance at the target*. No. BRL-TN-1634, Army Ballistic Research Lab Aberdeen Proving Ground MD, 1966.
- Grampp, S., Genant, H.K., Mathur, A., Lang, P., Jergas, M., Takada, M., Glüer, C.C., Lu Y., and Chavez, M., Comparisons of noninvasive bone mineral measurements in assessing age-related loss, fracture discrimination, and diagnostic classification, *J Bone Miner Res*, **12**, 697–711, 1997.
- Grangeat, P., Analyse d'un Système d'Imagerie 3D par Reconstruction à partir de Radiographies X en Géométrie Conique, Ecole Nationale Supérieure des Télécommunications, These de doctorat, 1987.
- Grangeat, P., Mathematical framework of cone beam 3D reconstruction via the first derivative of the radon transform, in *Mathematical Methods in Tomography, Lecture Notes in Mathematics*, G.T. Herman, A.K. Luis, and F. Natterer, (Editors), Springer-Verlag, Berlin, 66–97, 1991.
- Grangeat, P., Fully three-dimensional image reconstruction in radiology and nuclear medicine, *Enc Comp Sci Tech*, Kent, A. and William, J.G., Eds., **29–44**, 167–201, 2001.
- Green, R.E. and Rabinovich, D., Exploration of structural phase transformations by flash X-ray diffraction, *1984 Flash Radiography Symposium, ASNT*, 157–170, 1984.
- Greskovich, C. and Duclos, S., Ceramic scintillators, *Annu Rev Mater Sci*, **27**, 69–88, 1997.
- Grodzins, L., Optimum energies for x-ray transmission tomography of small samples: Applications of synchrotron radiation to computerized tomography I, *Nuc Instrum Meth A*, **206:3**, 541–545, 1983.
- Gros, X.E., *NDT data fusion*, Arnold, 1997.
- Guillemaud, R., Tabary, J., Hugonnard, P., Mathy, F., Koenig, A., and Glière, A., SINDBAD: A multipurpose and scalable X-ray simulation tool for NDE and medical imaging, PSIB, 2003.
- Guinier, A., *X-ray Diffraction in Crystals, Imperfect Crystals, and Amorphous Bodies*, W. H. Freeman & Company, San Francisco, 1963.
- Gullberg, G.T., Tsui, B.M.W., Crawford, C.R., Ballard, J.G., and Hagius, J.T., Estimation of geometrical parameters and collimator evaluation for cone beam tomography, *Med Phys*, **17:2**, 264–272, 1990.
- Guo, T., Spielmann, C., Walker, BC., and Barty, C.P.J., Generation of hard x rays by ultrafast terawatt lasers, *Rev Sci Instrum*, **72:1**, 41–47, 2001.

- Gureyev, T.E. and S.W. Wilkins, On x-ray phase imaging with a point source, *JOSA A*, **15:3**, 579–585, 1998.
- Gureyev, T.E., Raven, C., Snigirev, I., Snigirev, A., and Wilkins, S.W., Hard x-ray quantitative non-interferometric phase-contrast microscopy, *J Phys D Appl Phys*, **32:5**, 563, 1999.
- Guvenilir, A., Breunig, T.M., Kinney, T.H., and Stock S.R. Direct observation of crack opening as a function of applied load in the interior of a notched tensile sample of AlLi 2090, *Acta Mater*, **45:5**, 1977–1987, 1997.
- Haan, S.W., Amendt, P.A., Dittrich, T.R., Hatchett, S.P., Herrmann, M.C., Hurricane, O.A., Marinak, M.M. et al., Update on NIF indirect drive ignition target fabrication specifications, *Fusion Sci Tech*, **45:2**, 69–73, 2004.
- Haboub, A., MacDowell, A.A., Marchesini, S., and Parkinson, D.Y., Advances in X-Ray/EUV optics and components VII, Goto, S., Morawe, C., Khounsary, A.M., (Editors), *Proc. of SPIE*, **8502:850209**, 850209-1-10, 2012.
- Haddad, W.S., McNulty, I., Trebes, J.E., Anderson, E.H., Levesque, R.A., and Yang, L., Ultrahigh-resolution X-ray tomography, *Science*, **266**, 1213, 1994.
- Hagelstein, P.L., Senturia, S.D., and Orlando, T.P., *Introductory Applied Quantum and Statistical Mechanics*, John Wiley & Sons Inc., Hoboken, 2004.
- Hagemer, D.J., *Fundamentals of Eddy Current Testing*. American Society for Nondestructive Testing, Columbus, OH, USA, 1990.
- Haghghi, R.R., Chatterjee, S., Vyas, A., Kumar, P., and Thulkar, S., X-ray attenuation coefficient of mixtures: Inputs for dual-energy CT, *Med Phys*, **38:10**, 5270–5279, 2011.
- Halbleib, J.A., Kensek, R.P., Mehlhorn, T.A., Valdez, G.D., Seltzer, S.M., and Berger, M.J., *ITS Version 3.0: The integrated TIGER series of coupled electron/photon Monte Carlo transport codes*, Albuquerque, NM: Sandia National Laboratories; SAND91-1634; 1992.
- Hall, J.M., Uncovering hidden defects with neutrons, *LLNL Science and Technology Review*, May 2001.
- Hall, J.M., Rusnak, B., and Fitzsos, P.J., High-energy neutron imaging development at LLNL, *Proceedings of 8th World Conference on Neutron Radiography*, Gaithersburg, MD, 2006. (Also, UCRL-CONF-230835, LLNL, 2007.)
- Halliday, D., Resnick, R., and Walker, J., *Fundamentals of Physics*, sixth edition, extended, John Wiley & Sons, New York, 2001.
- Halmshaw, R., *Industrial Radiology: Theory and Practice*, second edition, Springer, The Netherlands, 1995.
- Hamamatsu, <http://sales.hamamatsu.com/en/products/electron-tube-division/x-ray-products/microfocus-x-ray-source-mfx.php>, 2007.
- Harding, G., X-ray diffraction imaging—A multi-generational perspective, *Appl Radiat Isotopes*, **67:2**, 287–295, 2009.
- Harding, G., Thran, A., and David, B., Liquid metal anode X-ray tubes and their potential for high continuous power operation, *Radiat Phys Chem*, **67**, 7–14, 2003a.
- Harding, G., David, B., and Schломka, J.P., Liquid metal anode X-ray sources and their potential applications, *Nucl Instrum Meth B*, **213**, 189–196, 2003b.
- Harris, E.L., *The Shadowmakers*, American Society of Radiologic Technologists, Albuquerque, NM, 1995.
- Harris, L.D., Bernardi, R.T., Hughes, Simon, H.C., and Slocum, R.E., Optimizing spatial resolution with mechanical design of an X-ray computed tomography scanner, *Review of Progress in Quantitative Nondestructive Evaluation*, **9A**, 423–430, Plenum Press, New York, 1990.
- Hartmann Siantar, C.L., Description and dosimetric verification of the PEREGRINE™ Monte Carlo dose calculation system for photon beams incident on a water phantom, *Med Phys*, **28:7**, 1322–1337, 2001.
- Hasagawa, B.H., *The Physics of Medical X-ray Imaging*, second edition, Medical Physics Publishing, Madison, WI, 1991.
- Haselgrave, J.C., Faruqi, A.R., Huxley, H.E., and Arndt, U.W., The design and use of a camera for low angle X-ray diffraction experiments with synchrotron radiation, *J Phys E Sci Instrum*, **10**, 1035–1044, 1977.
- Hau-Riege, S.P., Chapman, H.N., Krzywinski, J., Sobierajski, R., Bajt, S., London, R.A., Bergh, M. et al., Subnanometer-scale measurements of the interaction of ultrafast soft X-ray free-electron-laser pulses with matter, *Phys Rev Lett*, **98**, 145502, 2007.
- Heanue, J.A., Pearson, D.A., and Melen, R.E., CdZnTe detector array for a scanning-beam digital x-ray system, *Proceedings SPIE Medical Imaging* 1999, 1999.
- Heath, R.L., *Gamma-Ray Spectrum Catalogue Ge (Li) and Si (Li) Spectrometry*, third edition volume 2 of 2, Aerojet Nuclear Company, Reproduced by National Technical Information Service, U.S. Department of Commerce, Springfield, VA, 1974.
- Heath, R.L., *Gamma Ray Spectrum Catalogue; Ge and Si Detector Spectra*, fourth edition, Idaho National Laboratory, Gamma Ray Spectrometry Center, 1998. Available at <http://www.inl.gov/gammaRay/catalogs/catalogs.shtml>.

- Hecht, E., *Optics*, fourth edition, Addison Wesley, San Francisco, 2002.
- Heemskerk, J.W.T., Kreuger, R., Goorden, M.C., Korevaar, M.A., Salvador, S., Seeley, Z.M., Cherepy, N.J. et al., Experimental comparison of high-density scintillators for EMCCD-based gamma imaging, *Phys Med Biol*, **57**, 4545–4554, 2012.
- Heismann, B.J., Leppert, J., and Stierstorfer, K., Density and atomic number measurements with spectral x-ray attenuation method, *J Appl Phys*, **94**:3, 2073–2079, 2003.
- Henke, B.L., Gullikson, E.M., and Davis, J.C., X-ray interactions: Photoabsorption, scattering, transmission, and reflection at $E = 50\text{--}30000 \text{ eV}$, $Z = 1\text{--}92$, *Atomic Data and Nuclear Data Tables*, **54**:2, 181–342, 1993.
- Heycock, C.T. and Neville, F.H., Röntgen ray photography applied to alloys, *J Chem Soc Trans*, **73**, 714–723, 1898.
- Hibbard, R.L., Bono, M.J., Amendt, P.A., Bennett, D.W., and Castro, C., Precision manufacturing of inertial confinement fusion double shell laser targets for OMEGA, *Fusion Sci Tech*, **45**:2, 117–123, 2004.
- Hignette, O., Cloetens, P., Lee, W.-K., Ludwig, W., and Rostaing, G., Hard X-ray microscopy with reflecting mirrors status and perspectives of the ESRF technology, *J Phys IV*, **104**, 231–234, 2003.
- Hirano, K. and Momose, A., Development of an x-ray interferometer for high-resolution phase-contrast x-ray imaging, *Jpn J Appl Phys Part 2*, **38**, L1556–L1558, 1999.
- Hogan, G.E., Adams, K.J., Alrick, K.R., Amann, J.F., Boissevain, J.G., Crow, M.L. et al., Proton Radiography, Proceedings of the 1999 Particle Accelerator Conference, New York, 1999.
- Honachefsky, W.B., *Land Planner's Environmental Handbook*, Noyes Publications, Park Ridge, New Jersey, 1991.
- Hopkins, F., Morgan, I.L., Ellinger, H., and Klinkseik, R., Tomographic image analysis, *Mat Eval*, **40**:12, 1226–1228, 1982.
- Hounsfield, G.N., Computerised transverse axial scanning (tomography) I. Description of system, *Brit J Radiol*, **46**, 1016–1022, 1973.
- Hounsfield, G.N., Computed medical imaging, Nobel Lecture, December 8, 1979. Available at <http://nobelprize.org/medicine/laureates/1979/hounsfield-lecture.html>.
- Hudec, R., Pina, L., and Inneman, A., Replicated grazing incidence X-Ray optics: Past, present and future, Part of the SPIE Conference on X-Ray Optics, Instruments, and Missions II, Denver, Colorado, July 1999, *SPIE*, **3766**, 62–71, 1999.
- Hung, Y.Y. and Ho, H.P., Shearography: An optical measurement technique and applications, *Mater Sci Eng*, **49**:3, 61–87, 2005.
- Hunter, B.T., *Air and Your Health: Clean Air Is Vital to Your Health*, Basic Health Publications, 2004.
- IAEA, International Atomic Energy Agency, *The radiological accident in Cochabamba*, STI/PUB/1199, IAEA 04-00368, 2004a.
- IAEA, *The long term stabilization of uranium mill tailings*, IAEA-TECDOC-1403, Available at <http://www.iaea.org/programmes/ne/nefw/crp1/CRPL-TStabFinRepV31.pdf>, 2004b.
- ICRP103, The 2007 Recommendations of the International Commission on Radiological Protection. ICRP Publication 103. Ann. ICRP 37 (2–4), 2007.
- Illinois, <http://physics.illinois.edu/history/Betatron.asp>, 2010a.
- Illinois, <http://physics.illinois.edu/history/timelines/1940s.asp>, 2010b.
- Inanc, F., Impact of the low energy scattering in the radiography simulations, *Review of Quantitative Nondestructive Evaluation*, **21**, 582, AIP, 2002a.
- Inanc, F., Scattering and its role in radiography simulations, *NDT&E Int*, **35**:8, 581–593, 2002b.
- Inanc, F., Issues with high energy radiography simulations, *Review of Quantitative Nondestructive Evaluation*, **22**, 561, AIP, 2003.
- Inanc, F. and Gray, J.N., Scattering simulations in radiography, *Appl Radiat Isotopes*, **48**:10:12, 1299–1305, 1997.
- Iovea, M., Neagu, M., Dului, O.G., and Mateiasi, G., High accuracy X-ray dual-energy experiments and non-rotational tomography algorithm for explosives detection technique in luggage control, *Proc Intl Symp on Digital Industrial Radiology and Computed Tomography-Lyon*, 2007.
- Ivanov, K.A., Uryupina, D.S., Volkov, R.V., Shkurnov, A.P., Ozherodov, I.A., Paskhalov, A.A., Eremin, N.V., and Savelev, A.B., High repetition rate laser-driven $K\alpha$ X-ray source utilizing melted metal target, *Nucl Instrum Meth A*, **653**:1, 58–61, 2011.
- Iwata, K., Kikuta, H., Tadano, H., Hagino, H., and Nakano, T., Phase-shifting x-ray shearing interferometer, *Jpn J Appl Phys Part 1*, **38**, 6525–6539, 1999.
- Jackson, Jr. C.N., Sherlock, C.N., and Moore, P.O., *Nondestructive Testing Handbook*, third edition: Volume 1, *Leak Testing*, American Society of Nondestructive Testing, USA, 2000.
- James, D.R. and Carpenter, S.H. Relationship between acoustic emission and dislocation kinetics in crystalline solids. *J Appl Phys*, **42**:12, 4685–4697, 1971.

- JCISE Special issue on reverse engineering and computational metrology: Part I, surface reconstruction methods, *J Comput Inf Sci Eng*, **6:4**, 317–424, 2006.
- Jenkins, F.A. and White, H.E., *Fundamentals of Optics*, fourth edition, McGraw Hill, New York, 1976.
- Jensen, C., Elliott, S.M., Liddiard, S.D., Reyes-Mena, A., Moras, M., and Turner, D.C., Improvements in low power, end-window, transmission-target X-ray tubes, *Adv X Ray Analysis*, **47**, 64–69, 2004.
- Johns, H.E. and Cunningham, J.R., *The Physics of Radiology*, fourth edition, Charles C. Thomas, Springfield, IL, 1983.
- Johnson, Q. and Mitchell, A.C., First X-ray diffraction evidence for a phase transition during shock-wave compression, *Phys Rev Lett*, **29:20**, 1369–1370, 1972.
- Johnston, W.R., <http://www.johnstonsarchive.net/nuclear/radevents/index.html>, 2014.
- Kaizhi, Z., Bonan, D., Jianjun, D., Linwen, Z., Jinshui, S., Haucen, W., Guangsen, D. et al., Installation and initial results of the "Dragon-I" Induction Linac, *Proc. of APAC 2004*, 253–255, 2004.
- Kak, A.C. and Slaney, M., *Principles of Computerized Tomographic Imaging*, Society for Industrial and Applied Mathematics, Philadelphia, 2001.
- Kalender, W.A., X-ray computed tomography, *Phys Med Biol*, **51:13**, R29, 2006.
- Kamada, K., Yanagida, T., Endo, T., Tsutumi, K., Usuki, Y., Nikl, M., Fujimoto, Y., Fukabori, A., and Yoshikawa, A., 2 inch diameter single crystal growth and scintillation properties of Ce:Gd₃Al₂Ga₃O₁₂, *J Cryst Growth*, **352:1**, 88–90, 2012.
- Karacan, C.O., Grader, A.S., and Helleck, P.M., Mapping of permeability damage around perforation tunnels, *J Energ Resour-ASME*, **123:3**, 205–213, 2001.
- Karimi, S., Martz, H., and Cosman, P., Metal artifact reduction for CT-based luggage screening, *J X-ray Sci Technol*, **23:4**, 435–451, 2015.
- Karmea, A., Kallonen, A., Matilainen, V.P., Piili, H., and Salminen, A., Possibilities of CT scanning as analysis method in laser additive manufacturing, *Phys Proc*, **78**, 347–356, 2015.
- Kasap, S.O. and Rowlands, J.A., Review x-ray photoconductors and stabilized a-Se for direct conversion digital flat-panel x-ray image detectors, *J Mater Sci Mater Electron*, **11**, 179–198, 2000.
- Kataoka, J., Kishimoto, A., Fujita, T., Nishiyama, T., Kurei, Y., Tsujikawa, T., Oshima, T. et al., Recent progress of MPPC-based scintillation detectors in high precision X-ray and gamma-ray imaging, *Nucl Instrum Meth A*, **784**, 248–254, 2015.
- Katsevich, A., Analysis of an exact inversion algorithm for spiral cone-beam CT, *Phys Med Biol*, **47:15**, 2583, 2002.
- Katsevich, A., An improved exact filtered backprojection algorithm for spiral computed tomography, *Adv Appl Math*, **32:4**, 681–697, 2004.
- Katsuyama, K., Nagamine, T., Matsumoto, S.-I., and Ito, M., Measurement of central void diameter in FBR MOX fuel by X-ray computer tomography, *J Nucl Sci Technol*, **39:7**, 804–806, 2002.
- Katsuyama, K., Nagamine, T., Matsumoto, S.-I., and Ito, M., Application of X-ray computer tomography for observing the deflection and displacement of fuel pins in an assembly irradiated in FBR, *J Nucl Sci Technol*, **40:4**, 220–226, 2003.
- Kauffman, J.M., Radiation hormesis: Demonstrated, deconstructed, denied, dismissed, and some implications for public policy, *Journal of Scientific Exploration*, **17:3**, 389, 2003.
- Kawrakow, I. and Rogers, D.W.O., The EGSnrc code system: Monte Carlo simulation of electron and photon transport, ionizing radiation standards, National Research Council of Canada Ottawa, K1A OR6, 2006.
- Keane, A., Radioactive luminous paints, *Scientific American Supplement*, **84**, 126–127; August 25, 1917.
- Kevex, <http://www.thermo.com/com/CDA/Category/CategoryFrames/1,15080,00.html>, 2007.
- Kevles, B.H., *Naked to the Bone*, Basic Books, New York, 1998.
- Kharrati, H., Agrebi, A., and Karaoui, M.K., Monte Carlo simulation of x-ray buildup factors of lead and its applications in shielding of diagnostic x-ray facilities. *Med Phys*, **34:4**, 1398–1404, 2007.
- Khutoretsky, I.V., Design of an optimal Ross filter system for x-ray spectra measurements in the range of 8.98–88 keV, *Rev Sci Instrum*, **66:1**, 773–775, 1995.
- Kim, H.K., Lim, C.H., Tanguay, J., Yun, S., and Cunningham, I.A., Spectral analysis of fundamental signal and noise performances in photoconductors for mammography, *Med Phys*, **39:5**, 2478–2490, 2012.
- Kim, K.J., Chattopadhyay, S., and Shank, C.V., Generation of femtosecond X-rays by 90° Thomson scattering, *Nucl Instrum Meth A*, **341:1**, 351–354, 1994.
- Kinney, J.H., Stock, S.R., Nichols, M.C., Bonse, U., Breunig, T.M., Saroyan, R.A., Nusshardt, R., Johnson, Q.C., Busch, F., and Antolovich, S.D., Nondestructive investigation of damage in composites using X-ray tomographic microscopy (XTM), *J Mater Res*, **5:5**, 1123–1129, 1990.
- Kinoshita, K., Harano, H., Yoshii, K., Ohkubo, T., Fukasawa, A., Nakamura, K., and Uesaka, M., Time-resolved X-ray diffraction at NERL, *Laser Part Beams*, **19:01**, 125–131, 2001.

- Kirkpatrick, P., On the theory and use of Ross filters, *Rev Sci Instrum*, **10:6**, 186–191, 1939.
- Kirkpatrick, P. and Baez, A.V., Formation of optical images by X-rays, *JOSA*, **38:9**, 1948.
- Knoll, G.F., *Radiation Detection and Measurement*, third edition, John Wiley & Sons, Inc., New York, 2000. (A fourth edition of this text was published in 2010.)
- Koch, H.W., *Part I. The thresholds of photofission in uranium and thorium, Part II Experimental depth dose for 5, 10, and 20 million volt X-rays*, Thesis, University of Illinois, Urbana, Illinois, 1944.
- Koch, J.A., Landen, O.L., Kozioziemski, B.J., Izumi, N., Dewald, E.L., Salmonson, J.D., and Hammel, B.A., Refraction-enhanced x-ray radiography for inertial confinement fusion and laser-produced plasma applications, *J Appl Phys* **105:11**, 113112, 2009.
- Kodak, *Radiography in modern industry*, Eastman Kodak Co. <http://www.kodak.com/eknec/documents/87/0900688a802b3c87/Radiography-in-Modern-Industry.pdf>, 2014.
- Kodama, R., Ikeda, N., Kato, Y., Katori, Y., Iwai, T., and Takeshi, K., Development of an advanced Kirkpatrick-Baez microscope, *Opt Lett*, **21**, 1321–1323, 1996.
- Kokko, E.J., Martz, Jr., H.E., Chinn, D.J., Childs, H.R., Jackson, J.A., Chambers, D.H., Schneberk, D.J., and Clark, G.A., As-built modeling of objects for performance assessment, *J Comput Inf Sci Eng*, **6:4**, 405–417, 2006.
- Kolb, C.A., Wirth, E., Kaiser, W.M., Meister, A., Riederer, M., and Pfündel, E.E., Noninvasive evaluation of the degree of ripeness in grape berries (*Vitis vinifera* L. Cv. Bacchus and Silvander) by chlorophyll fluorescence, *J Agr Food Chem*, **54:2**, 299–305, 2006.
- Kolkoori, S., Wrobel, N., Zschepel, U., and Ewert, U., A new X-ray backscatter imaging technique for non-destructive testing of aerospace materials, *Nondestruct Test Eva*, **70**, 41–52, 2015.
- Konijnenberg, M., Melis, M., Valkema, R., Krenning, E., and De Jong, M., Radiation dose distribution in human kidneys by octreotides in peptide receptor radionuclide therapy. *J Nucl Med*, **48:1**, 134–142, 2007.
- Kotre, C.J. and Birch, I.P., Phase contrast enhancement of x-ray mammography: A design study, *Phys Med Biol*, **44**, 2853–2866, 2002.
- Kouris, K., Spyrou, N.M., and Jackson, D.F., Materials analysis using photon attenuation coefficients, in: *Research Techniques in Nondestructive Testing Vol. VI*, Sharpe, R.S. ed., Academic Press, New York, 1982.
- Kowalski, G., Suppression of ring artifacts in CT fan-beam scanners, *IEEE Trans Nucl Sci*, **NS:25**, 1111–1116, 1978.
- Kozioziemski, B.J., Koch, J.A., Barty, A., Martz Jr., H.E., Lee, W.-K., and Fezza, K., Quantitative characterization of inertial confinement fusion capsules using phase contrast enhanced x-ray imaging, *J Appl Phys*, **97:6**, 063103, 2005a.
- Kozioziemski, B.J., Sater, J.D., Moody, J.J., Sanchez, J.J., London, R.A., Barty, A., Martz, Jr. H.E., and Montgomery, D.S., X-ray imaging of cryogenic deuterium-tritium layers in a beryllium shell, *J Appl Phys*, **98:10**, 103105, 2005b.
- Kralick, S.C., Watson, Jr. J.E., and Croslin, S.W., Neutron dosimetry in the containment of a pressurized water reactor using a neutron-sensitive beta/gamma dosimetry system, *Health Phys*, **50:6**, 761, 1986.
- Krauss, B., Schmidt, B., and Flohr, T.G., Dual source CT, in *Dual Energy CT in Clinical Practice*, Johnson, T., Fink, C., Schonerg, S.O., and Reiser, M.F., (Editors), Springer Science and Business Media, New York, 11–20, 2011.
- Krautkramer, J. and Krautkramer, H., *Ultrasonic Testing of Materials*, English translation of the fifth revised German Edition, Springer-Verlag, Berlin, Heidelberg, New York, 1990.
- Kuba, J., Anderson, S.G., Barty, C.P.J., Betts, S.M., Booth, R., Brown, W.J., Crane, J.K. et al., PLEIADES: High peak brightness, subpicosecond Thomson hard x-ray source, *Optical Sci Tech, SPIE's 48th Annual Meeting*, 241–252, also UCRL-CONF-201565, 2003.
- Kuhl, D., Transmission scanning: A useful adjunct to conventional emission scanning for accurately keying isotope deposition to radiographic anatomy, *Radiology* **87**, 278, 1966.
- Kukhlevskyy, S.V., Lupkovics, G., Negrea, K., and Kozma, L., Guiding of femtosecond pulses by microcapillary light-pipes, *Pure Appl Opt*, **6**, 97–102, 1997.
- Kumakhova, A.A., Ibraimov, N.S., Zaitsev, D.V., Kumakhov, A.M., and Gruev, D.I., Analysis of extended focal area of polycapillary lenses, *Tech Phys+*, **59:11**, 1720–1722, 2014.
- Lagowski, J.J., *Modern Inorganic Chemistry*, Marcel Dekker, Inc., New York, 1973.
- Lapp, R.E., *My Life with Radiation: The Truth about Hiroshima*, Cogito Books, Medical Physics Publishing, Madison, Wisconsin, 1995.
- Lau, Y.Y., He, F., Umstadter, D.P., and Kowalczyk, R., Nonlinear Thomson scattering: A tutorial, *Phys Plasmas*, **10:5**, 2155–2162, 2003.
- Laugier, P., Challenges in quantitative ultrasound bone strength assessment: Status and perspectives, in *Computerized Tomography for Scientists and Engineers*, Chapter 6, P. Munshi (Editor), Anamaya Publishers, India, 2007.

- Lawrenceville, 2010, <http://lawrencevilleplasmaphysics.com/intense-x-rays-signal-breakthrough-for-non-destructive-inspection/> accessed 2015.
- Lazos, D. and Williamson, J.F., Impact of flat panel-imager veiling glare on scatter-estimation accuracy and image quality of a commercial on-board cone-beam CT imaging system, *Med Phys*, **39**:9, 5639–5651, 2012.
- LBNLb, http://henke.lbl.gov/optical_constants/, 2015.
- Lehmann, E.H., Vontobel, P., and Kardjilov, N., Hydrogen distribution measurements by neutrons, *Applied Radiation and Isotopes*, **61**, 503, 2004.
- Léonard, F., Tammas-Williams, S., and Todd, I., CT for Additive Manufacturing Process Characterisation: Assessment of Melt Strategies on Defect Population, 6th Conference on Industrial Computed Tomography, Wels, Austria, iCT, 2016.
- Lewis, D.L., Logan, C.M., and Gabel, M.R., Continuum x-ray gauging of multiple-element materials, *Spectroscopy*, **7**:3, 40–46, 1992.
- Li, H., Schillinger, B., Calzada, E., Yinong, L., and Muehlbauer, M., An adaptive algorithm for gamma spots removal in CCD-based neutron radiography and tomography, *Nuc Instrum Meth A*, **564**, 405–413, 2006.
- Li, X., A brief review: Acoustic emission method for tool wear monitoring during turning, *Int J Mach Tool Manu*, **42**, 157–165, 2002.
- Lienhard, J.H., *X-Ray Hair Removal*, Radio episode 1494 of Engines of our Ingenuity, University of Houston, 2005. <http://www.uh.edu/engines/epi1494.htm>.
- Light, G.M., Hudak, Jr. S.J., and McClung, R.C., Turbine engine inspection and life extension technology, *Final Report Southwest Research Institute, Project No. 15.02950*, Prepared for AFRL/MLLN, Wright-Patterson AFB, Ohio, October, 2000.
- Lindl, J.D., *Inertial Confinement Fusion: The Quest for Ignition and Energy Gain Using Indirect Drive*, American Institute of Physics, New York, 1998.
- Lindsey, K. and Penfold, A.B., Production and assessment of supersmooth optical surfaces, *Opt Eng*, **15**, 220–225, 1976.
- Lisowski, P.W., Bowman, C.D., Russell, G.J., and Wender, S.A. The Los Alamos National Laboratory Spallation Neutron Sources, *Nucl Sci Eng*, **106**:2, 208–218, 1990.
- Liu, X., Yu, L., Primak, A.N., and McCollough, Quantitative imaging of element composition and mass fraction using dual-energy CT: Three-material decomposition, *Med Phys*, **36**:5, 1602–1609, 2009.
- Liu, Y., Sowerby, B.D., and Tickner, J.R., Comparison of neutron and high-energy X-ray dual-beam radiography for air cargo inspection, *Appl Radiat Isotopes* **66**, 463–473, 2008.
- Liu, Z., Yang, G., Lee, Y.Z., Bordelon, D., Lu, J., and Zhou, O., Carbon nanotube based microfocus field emission x-ray source for microcomputed tomography, *Appl Phys Lett*, **89**, 103111, 2006.
- LLNL, Better flash radiography using the FXR, *Science and Technology Review, Report #UCRL-52000*, May 1977.
- LLNL, Radiation safety at LLNL: General Employee Radiological Training, UCRL-TB-104702 Rev. 6, 2005.
- LLNL, <http://www.llnl.gov/IPandC/technology/profile/announcement/CeramicCandlingInspectionSystem.php>, 2006.
- LLNL, Ramrods Shepherd Hydrodynamic Tests, *Science and Technology Review, Report #UCRL-52000*, September 2007.
- LLNL, 2009, <https://str.llnl.gov/JulAug09/pdfs/07.09.2.pdf>, A CAT scanner for Nuclear Weapon Components, *S&TR July/August, UCRL-TR-52000-09-78*, Lawrence Livermore National Laboratory, 2009.
- LLNL, 2014, <https://str.llnl.gov/content/pages/september-2014/pdf/09.14.pdf>, Additive Manufacturing Reshapes Foam Design, *S&TR September, UCRL-TR-52000-14-9*, Lawrence Livermore National Laboratory, 2014.
- LLNL, https://www-pls.llnl.gov/?url=about_pls-physics_division, 2015.
- Logan, C.M. and Lane, S.M., Air-core grid for scattered x-ray rejection, *U.S. Patent #5,455,849*, 1995.
- Logan, C.M., High-performance x-ray anti-scatter grid, *U.S. Patent #5,418,833*, 1995.
- Logan, C.M. and Schach von Wittenau, A.E., Effects of backshield albedo on imagery with a dpiX flashscan20 using a 9-MV bremsstrahlung spectrum, *Mater Eval*, **59**:5, 617–620, 2001.
- Longo, A., Giordano, F., Giannici, F., Martorana, A., Portale, G., Ruggirello, A., and Turco Liveri, V., Combined small-angle X-ray scattering/extended X-ray absorption fine structure study of coated Co nanoclusters in bis(2-ethylhexyl)sulfosuccinate, *J Appl Phys*, **105**, 114308, 2009.
- MacCabe, K., Krishnamurthy, K., Chawla, A., Marks, D., Samei, E., and Brady, D., Pencil beam coded aperture x-ray scatter imaging, *Opt Express*, **20**:15, 16310–16320, 2012.
- MacDowell, A.A., Celestre, R., Chang, C.-H., Franck, K., Howells, M.R., Locklin, S., Padmore, H.A., Patel J.R., and Sandler R., Progress towards sub-micron hard x-ray imaging using elliptically bent mirrors, *SPIE*, **3152**, 126–133, 1997.

- Macovski, A., *Medical Imaging Systems*, Prentice Hall, Englewood Cliffs, New Jersey, 1983.
- Madaras, E.I., Prosser, W.H., and Gorman, M.R., Detection of impact damage on space shuttle structures using acoustic emission, *Rev Prog Q*, **760:1**, 1113–1120, 2005.
- Maldague, X.P.V., *Nondestructive Testing Handbook*, third edition: Volume 3, *Infrared and Thermal Testing*, American Society of Nondestructive Testing, Columbus, OH, 2001.
- Mangano, J., Three mile island: Health study meltdown, *B Atom Sci*, **60:05**, 30, 2004.
- Marshall, F.J., Allen, M.M., Knauer, J.P., Oertel, J.A., and Archuleta, T., A high-resolution x-ray microscope for laser-driven planar-foil experiments, *Phys Plasmas*, **5:4**, 1118–1124, 1998.
- Martz, H.E., Roberson, G.P., Schneberk, D.J., Skeate, M.F., Perkins, D., and Azevedo, S.G., The role of non-destructive evaluation in life cycle management, in *Frontiers of Engineering: Reports on Leading Edge Engineering from 1997 NAE Symposium on Frontiers of Engineering, Third Annual Symposium on Frontiers of Engineering*, National Academy Press, Washington D.C. 56–71, 1998.
- Martz Jr., H.E. and Albrecht, G.F., Nondestructive characterization technologies for metrology of micro/mesoscale assemblies, in *Proceedings of Machines and Processes for Micro-scale and Meso-scale Fabrication, Metrology, and Assembly*, American Society for Precision Engineering, 131–141, 2003.
- Martz, Jr., H.E. and Crawford, C.R., Overview of Deployed EDS Technologies, *Report LLNL-TR-417232, Lawrence Livermore National Laboratory*, 2009.
- Martz, H.E., Robertson, G.P., Schneberk, D.J., Skeate, M.F., Perkins, D. and Azevedo, S.G., Computed Tomography of a Simulated Waste Canister, *Lawrence Livermore National Laboratory, Livermore, CA, UCID 21940*, February 1990.
- Martz, H.E., Robertson, G.P., Schneberk, D.J., and Azevedo, S.G., Nuclear-spectroscopy-based, first-generation, computerized tomography scanners, *IEEE Trans Nucl Sci*, **38:2**, 623–635, 1991a.
- Martz, H.E., Schneberk, D.J., and Azevedo, S.G., Lynch, S.K., Computerized tomography of high explosives, in *Nondestructive Characterization of Materials IV*, Ruud, C.O. et al. (Editors), Plenum Press, New York, 187–195, 1991b.
- Martz, H.E., Roberson, G.P., Robert-Coutant C., Schneberk D.J., and Camp, D.C., Quantitative waste assay using gamma-ray spectrometry and computed tomography, *Proceedings of the 14th Annual ESARDA Meeting, Salamanca, Spain*, 273, 1992.
- Martz, H.E., Crawford, C.R., Beaty, J.S., and Castanon D., Facilitation of third-party development of advanced algorithms for explosive detection using workshops and grand challenges, DSH Science Conference—Fifth Annual University Network Summit, Mar 30 through Apr 1, 2011, *Report LLNL-CONF-471533, Lawrence Livermore National Laboratory*, 2011.
- Martz, H.E., Divin, C., Panas, R.M., Brown, W.D., Burke, S.C., Rathbun, H., Alexander, P.A., Smith, J.A., and Taylor, J.S., *CT to Evaluate Distortions in Stainless Steel AM Structures*, Presented at 2014 ASPE Spring Topical Meeting, Lawrence Livermore National Laboratory report, LLNL-ABS-653163, 2014.
- Martz, Jr., H.E., Kozioziemski, B.J., Lehman, S.K., Hau-Riege, S., Schneberk, D.J., and Barty, A., Validation of radiographic simulation codes including x-ray phase-effects for millimeter size objects with micro-meter structures, *JOSA A*, **24:1**, 169–178, 2007; Lawrence Livermore National Laboratory, Livermore, CA, UCRL-JRNL-218242-DRAFT, December 2005. <http://www.opticsinfobase.org/josaa/fulltext.cfm?uri=josaa-24-1-169&id=119830>.
- Martz, Jr., H.E., McNeil, B.J., Amundson, S.A., Aspnes, D.E., Barnett, A., Borak, T.B., Braby, L.A. et al., Airport Passenger Screening Using Backscatter X-Ray Machines: Compliance with Standards, Committee on Airport Passenger Screening: Backscatter X-Ray Machines, National Materials and Manufacturing Board, Division on Engineering and Physical Sciences, and Nuclear and Radiation Studies Board, Division on Earth and Life Studies, ISBN 978-0-309-37133-9 and doi: 10.17226/21710, National Academy Press, Washington, D.C., 2016.
- Mason, J.A., Tolchard A.C., Towner, A.C.N., Burke, K., Price, R.A., Dittrich, S., Zurey, F., and Walraven, D., A tomographic segmented gamma scanner for the measurement of decommissioning wastes, *Proceedings of ICEM '03: The 9th International Conference on Radioactive Waste Management and Environmental Remediation*, icem03-4658, 2003.
- Matzkanin, G.A. and Yolken, H.T., *A Technology Assessment of Probability of Detection for Nondestructive Evaluation*, Nondestructive Testing Information Analysis Center, NTIAC-TA-00-01, 2001.
- Maxwell, K. and Johnson, G.N., Chlorophyll fluorescence—A practical guide, *J Exp Bot*, **51:345**, 659–668, 2000.
- Mayo, S.C., Miller, P.R., Wilkins, S.W., Davis, T.J., Gao, D., Gureyev, T.E., Paganin, D., Parry, D.J., Pogany, A., and Stevenson, A.W, Quantitative X-ray projection microscopy: Phase-contrast and multi-spectral imaging, *J Microsc-Oxford*, **207**, 79, 2002.
- Mayr, G., Pohl, B., and Peters, D.S., A well-preserved Archaeopteryx specimen with theropod features, *Science*, **310:5753**, 1483–1486, 2005.

- Mba, D. and Rao, R.B., Development of acoustic emission technology for condition monitoring and diagnosis of rotating machines; bearings, pumps, gearboxes, engines and rotating structures, *Shock Vib*, **38:1**, 3–16, 2006.
- McCall, G.H., X-ray imaging in the laser fusion program, *1977 SPIE/SPSE Technical Symposium East*, 2–7, 1977.
- McEwan, T.E., United States Patent 5,274,271, *Ultra-Short Pulse Generator*, 1993. See also a listing of 57 related McEwan patents at <http://www.getradar.com>.
- McNamara, K.M., Schneberk, D.J., Empey, D.M., Koshti, A., Pugel, D.E., Cozmuta, I., Stackpoole, M. et al., X-ray computed tomography inspection of The Stardust Heat Shield, *Proceedings of the 7th International Planetary Probe Workshop*, Barcelona, Spain, 2010.
- MCNP, <http://mcnp-green.lanl.gov/index.html>, 2007.
- Meikle, S.R., Kench, P., Weisenberger, A.G., Wojcik, R., Smith, M.F., Majewski, S., Eberl, S., Fulton, R.R., Rosenfeld, A.B., and Fulham, M.J., A prototype coded aperture detector for small animal SPECT, *IEEE Trans Nucl Sci*, **49:5**, 2167–2171, 2002.
- Merali, Z., Nanotubes sharpen x-ray vision, *Nature News*, online, July 28, 2009 <http://www.nature.com/news/2009/090728/full/news.2009.744.html> 2009.
- Mery, D., Hahn, D., and Hitschfeld, N., Simulation of defects in aluminum castings using CAD models of flaws and real x-ray images, *Insight*, **47:10**, 618–624, 2005.
- Merriam-Webster Online, <http://merriam-webster.com>, 2005.
- Metropolis, N., The beginning of the Monte Carlo Method, *Los Alamos Sci*, **15:584**, 125–130, 1987.
- Metting, N.F., http://www.lowdose.energy.gov/resources_pics/images/Dose-Ranges-pdf.pdf revised August 2005.
- Meyers, S.N., <http://www.xray-art.com>, 2010.
- Michette, A.G., No x-ray lens, *Nature*, **353**, 510, 1991.
- Middleton, M.F., Pázsit, I., and Solymar, M., Petrophysical applications of neutron radiography, *Proceedings of the Sixth World Conference on Neutron Radiography*, Osaka, Japan, 1999, 1999.
- Milburn, R.H., Electron scattering by an intense polarized photon field, *Phys Rev Lett*, **10**, 75, 1963.
- Miller, W.O., Darnell, I.M., Burke, M.W., and Robbins C.L., Defining the envelope of sonic IR: Detection limits and damage limits, *Thermosense XXV*, Orlando FL, 2003.
- MNRC, <http://mnrc.ucdavis.edu/tomography.html>, 2013.
- Molitoris, J.D., Andreski, H.G., Garza, R.G., Batteux, J.D., and Souers, P.C., An experimental investigation of detonation corner-turning using high resolution radiography, *13th Int Detonation Symposium*, 2006. Also available as LLNL Report UCRL-CONF-222997 2009.
- Momose, A., Phase contrast x-ray imaging based on interferometry, *J Synchrotron Rad*, **9**, 136–142, 2002.
- Momose, A., Recent advances in x-ray phase imaging, *Jpn J Appl Phys*, **44:9A**, 6355–6367, 2005.
- Momose, A. and J. Fukuda, Phase contrast radiographs on nonstained rat cellular specimens, *Med Phys*, **22**, 375, 1995.
- Momose, A., Yashiro, W., Takeda, Y., Suzuki, Y., and Hattori, T., Phase imaging with an x-ray Talbot interferometer, *JCPDS Int Centre Diffract Data*, 21–30, 2006.
- Montgomery, D.S., Nobile, A., and Walsh, P.J., Characterization of National Ignition Facility cryogenic beryllium capsules using x-ray phase contrast imaging, *Rev Sci Instrum*, **75:10**, 3986–3988, 2004.
- Morigi, M.P., Casali, F., Bettuzzi, M., Brancaccio, R., and Errico, V.D., Application of x-ray computed tomography to cultural heritage diagnostics, *Appl Phys A-Mater*, **100**, 653–661, 2010.
- Morpho, <http://www.morpho.com>, 2015.
- Morris, C.L., Ables, E., Alrick, K.R., Aufderheide, M.B., Barnes Jr., P.D., Buescher, K.L., Cagliostro, D.J. et al., Flash radiography with 24 GeV/c protons, *J Appl Phys*, **109**, 104905, 2011.
- Morton, E.J., X-ray monitoring, *US patent application US2006023961(A1)*, 2006.
- Morton, E.J., Luggar, R.D., Key, M.J., Kundu, A., Tavora, L.M.N., and Gilboy, W.B., Development of a high speed x-ray tomography system for multiphase flow imaging, *IEEE Trans Nucl Sci*, **46 III(1)**, 380–384, 1999.
- Morton, E., Mann, K., Berman, A., Knaup, M., and Kachelriess, M., Ultrafast 3D reconstruction for x-ray real-time tomography (RTT), in *Nuclear Science Symposium Conference Record (NSS/MIC)*, IEEE, 4077–4080, 2009.
- Mosher, D. and Stephanakis, S.J., X-ray light pipes, *Appl Phys Lett*, **29**, 105–107, 1976.
- Mowery, K., Wustrow, E., Wypych, T., Singleton, C., Comfort, C., Rescorla, E., Checkoway, S., Halderman, J.A., and Shacham, H., Security analysis of a full-body scanner, *Proceedings of the 23rd USENIX Security Symposium*, August 20–22, 2014, San Diego, CA, 369–384, 2014.
- Munch, B., Trtik, P., Marone, F., and Stampanoni, M., Stripe and ring artifact removal with combined wavelet—Fourier filtering, *Opt Express*, **17:10**, 8567–8591, 2009.

- Nagarkar, V.V., Tipnis, S.V., Gaysinskiy, V., Klugerman, Y., Squillante, M.R., and Entine, G., Structured LiI scintillator for thermal neutron imaging, *IEEE T Nucl Sci*, **48:6**, 2001.
- NAS, <http://www.nasmedical.com/page?id=1468>, 2007.
- National Academies of Science, Committee on Assessment of Security Technologies for National Research Council, O'Bryon, J.F., Chair, *Assessment of Millimeter-wave and Terahertz Technology for Detection and Identification of Concealed Explosives and Weapons*, ISBN:0309104696, National Academies Press, 2007.
- Natterer, F., *The Mathematics of Computerized Tomography*, SIAM, Philadelphia, 2001.
- NCRP Report # 147, Structural shielding design for medical x-ray imaging facilities, National Council for Radiation Protection, 2004.
- NCRP Report # 160, Ionizing radiation exposure of the population of the United States, National Council for Radiation Protection, 2009.
- Nederbragt, W.W., Wölter Instrument—Optical Design, *LLNL internal report, UCRL-ID-150702*, 2002.
- Nederbragt, W.W., Fabrication of a Precision Mandrel for Replicating Wölter X-ray Optics, 18th Annual Meeting of the American Society for Precision Engineering, Portland, OR, October, 26–31, 2003, *LLNL internal report, UCRL-JC-155073*, 2003.
- Nelson, W.R., Hirayama, H., and Rogers, D.W.O., *The EGS4 code system*, Menlo Park, CA: Stanford Linear Accelerator Center; SLAC-265; 1985.
- Nett, B., Chen, G.H., Van Lysel, M., Betts, T., Speidel, M., Rowley, H., Kienits, B.A., and Misstretta, C.A., Investigation of tomosynthetic perfusion measurements using the scanning-beam digital x-ray system, *Proc SPIE*, **5535**, 2004.
- New York Times*, C.M. Dally Dies A Martyr to Science, *New York Times*, October 4, 1904.
- Nicoletti, D. and Anderson, A., Determination of grain-size distribution from ultrasonic attenuation: Transformation and inversion, *J Acoust Soc Am*, **101:2**, 686–689, 1997.
- Niemann, B., Rudolph, D., and Schmahl, G., X-ray microscopy with synchrotron radiation, *Appl Opt*, **15:8**, 1883–1884, 1976.
- NIST ESTAR, <http://physics.nist.gov/PhysRefData/Star/Text/ESTAR.html>, 2007.
- NIST Neutron, data from <http://www.ncnr.nist.gov/resources/n-lengths/list.html>, 2015.
- NIST XCOM, <http://www.nist.gov/pml/data/xcom/http://physics.nist.gov/PhysRefData/Xcom/html/xcom1.html>, 2015.
- NOMOS, Peregrine Monte Carlo based dose calculation system, *Nomos Corporation, Report Peregrine 1001 1.5M*, 2001.
- Norman, E.B., Prussin, S.G., Larimer, R.-M., Shugart, H., Browne, E., Smith, A.R., McDonald, R.J. et al., Signatures of special nuclear material: High-energy gamma rays following fission, *Nucl Instrum Meth A*, **521**, 608, 2004.
- NRCCA, http://www.irs.inms.nrc.ca/EGS4/get_egs4.html, National Research Council Canada, 2007.
- NTIAC, *Non-destructive evaluation (NDE) capabilities data book*, 3rd ed., NTIAC DB-97-02, Non-destructive Testing Information Analysis Centre, November 1997.
- Nugent, K.A., Gureyev, T.E., Cookson, D.F., Paganin, D., and Barnea, Z., Quantitative phase imaging using hard x-rays, *Phys Rev Lett*, **77:14**, 2961, 1996.
- Obal, M., “Michelangelo’s David” by Obal, Licensed under Creative Commons Attribution-Share Alike 3.0 via Wikimedia Commons—http://commons.wikimedia.org/wiki/File:Michelangelo%27s_David.JPG#media_viewer/File:Michelangelo%27s_David.JPG. 2014.
- Odano, N., Johnson, J.O., and Lillie, R.A., Preliminary shielding analysis and design of the remote maintenance cells for the proposed National Spallation Neutron Source, Report Number P01-111448, Available at http://www.osti.gov/energycitations/product.biblio.jsp?osti_id=788526 2001.
- Odén, M., Rogström, L., Knutsson, A., Terner, M.R., Hedström, P., Almer, J., and Ilavsky, J., In situ small-angle x-ray scattering study of nanostructure evolution during decomposition of arc evaporated TiAlN coatings, *Appl Phys Lett*, **94-053114**, 1–3, 2009.
- Olin, B.D. and Meeker, W.Q., Applications of statistical methods to nondestructive evaluation, *Technometrics*, **38-2**, 95–112, 1996.
- ORAU, <http://www.orau.org/ptp/museumdirectory.htm>, 2015.
- Orphan, V.J., Muenchau, E., Gormley, J., and Richardson, R., Advanced γ ray technology for scanning cargo containers, *Appl Radiat Isot*, **63:5–6**, 723–732, 2005.
- Osiander, R., Spicer, J.W.M., and Murphy, J.C., Thermal nondestructive evaluation using microwave sources, *Mater Eval*, **53:6**, 942–948, 1995.
- Otendal, M., Tuohimaa, T., Hemberg, O., and Hertz, H.M., Status of the liquid-metal-jet-anode electron-impact x-ray source, *X-Ray Sources and Optics*, *Proc SPIE*, **5537**, 57–63, 2004.

- Otendal, M., Hemberg, O., Tuohimaa, T.T., and Hertz, H.M., Microscopic high-speed liquid-metal jets in vacuum, *Exp Fluids*, **39**, 799–804, 2005.
- Otendal, M., Tuohimaa, T., and Hertz, H.M., Stability and debris in high-brightness liquid-metal-jet-anode microfocus x-ray sources, *J Appl Phys*, **101**, 026102, 2007.
- Otendal, M., Tuohimaa, T., Vogt, U., and Hertz, H.M., A 9 keV electron-impact liquid-gallium-jet x-ray source, *Rev Sci Instr*, **79**, 016102, 2008.
- Oxford, <http://www.oxfordxgt.com/products/micro.htm>, 2007.
- Paganin, D. and Nugent, K.A., Noninterferometric phase imaging with partially coherent light, *Phys Rev Lett*, **80:12**, 2586, 1998.
- Paic, G., *Ionizing Radiation: Protection and Dosimetry*, CRC Press, Boca Raton, FL, 1988.
- Pan, X., Sidky, E.Y., and Vannier, M., Why do commercial CT scanners still employ traditional, filtered back-projection for image reconstruction?, *Inverse Probl*, **25:12**, 123009, 2009.
- Panek, P., Kamiński, J.Z., and Ehlotzky, F., X-ray generation by Compton scattering of elliptically polarized laser light at relativistic radiation powers, *Opt Commun*, **213:1**, 121–128, 2002.
- Pankratov, E.L. and Chkhalo, N.I., Thermal loads of x-ray tubes with a fixed anode under long-duration exposure, *High Temp+*, **44:5**, 766–772, 2006.
- Pantell, R.H. and Chung, P.S., Transmission of x-rays through curved waveguides, *IEEE J of Quant Electr*, **QE:14**, 694–697, 1978.
- Papoulis, A., *The Fourier Integral and Its Applications*, Electronic Science Series, McGraw-Hill College, Blacklick, Ohio, USA, 1962.
- Papoulis, A., *Signal Analysis*, McGraw-Hill College, Blacklick, Ohio, USA, 1977.
- Parish, R.W., Microfocus x-ray technology—A review of developments and applications, Keynote Address in *Review of Progress in Quantitative Nondestructive Evaluation*, **5A** AIP Proceedings, eds. D.O. Thompson, D.E. Chimenti, Springer Science+ Business Media, New York, 1986.
- Park, J.S. and Kin, J.S., Calculation of effective atomic number and normal density using a source weighting method in a dual energy x-ray inspection system, *J Korean Phys Soc*, **59:4**, 2709–2713, 2011.
- Parker, D.L., Optimal short scan convolution reconstruction for fan beam CT, *Med Phys*, **9:2**, 254–257, 1982.
- Parker, J.L., Passive nondestructive assay of nuclear materials, Chapters 4–6, Reilly, D. et al., (Editors), *Nucl Reg Comm doc. NUREG/CR-5550*, 1991.
- PBS, <http://www.pbs.org/wgbh/pages/frontline/shows/reaction/interact/facts.html>, 2005.
- Perez, N., *Fracture Mechanics*, Springer, 2006.
- Peschmann, K.R. and Harmann, J., Automatic concealed object detection system having a pre-scan stage, *Patent Pub No US 5182764 A* 1993.
- Pfeiffer, F., Weitkamp, T., Bunk, O., and David, C., Phase retrieval and differential phase-contrast imaging with low-brilliance x-ray sources, *Nat Phys*, **2**, 258–261, 2006.
- Phuoc, K.T., Corde, S., Thaury, C., Malka, V., Tafzi, A., Goddet, J. P., Shah, R.C., Sebban, S., and Rousse, A., All-optical Compton gamma-ray source, *Nat Photonics*, **6:5**, 308–311, 2012.
- Pifferi, A., X-Ray Sources, published in *Encyclopedia of Condensed Matter Physics*, Bassani, Liedl, and Wyder (Editors), Elsevier Academic Press, Oxford, 2005.
- Pincus, C., Chinn, D., Martz, H., Rodriguez, J., and Thompson R., Technical Advice and Support for the Cargo Advanced Automated Radiography System (CAARS) Program; Task 2.2 Transmission Digital Radiography (DR) Final Report, *Lawrence Livermore National Laboratory, Livermore, CA 94551, LLNL-TR-473131-Final*, 27 June 2011.
- Pivovaroff, M.J., Nederbragt, W.W., and Martz, H.E., Lessons learned on x-ray optics fabrication: Work completed as part of the ‘advancing the technology R&D of tabletop mesoscale nondestructive characterization’, Report UCRL-TR-208400, Lawrence Livermore National Laboratory, Livermore, CA, December 2004.
- Placius, R.C., Polansky, D., Berger, H., Bueno, C., Vosberg, C.L., Betz, R.A., and Rogerson, D.J., High density glass scintillator for real-time x-ray inspection, *Mater Eval*, **49:11**, 1419–1421, 1991.
- Poen, O.S., Microprecision with x-rays, *Practical X-Ray Microscopy*, Springer Science+ Business Media Dordrecht, 1959.
- Pogany A., Gao D., and Wilkins S.W., Contrast and resolution in imaging with a microfocus x-ray source, *Rev Sci Instrum*, **68**, 2774–2782, 1997.
- Pogorelsky, I.V., Ultra-bright x-ray and gamma sources by Compton backscattering of CO₂ laser beams, *Nucl Instrum Meth A*, **411:1**, 172–187, 1998.
- Poludniowski, G., Landry, G., DeBlois, F., Evans, P.M., and Verhaegen, F., *SpekCalc*: A program to calculate photon spectra from tungsten anode x-ray tubes, *Phys Med Biol*, **54**, N433–N438, 2009.
- Pontau, A.E., Antolak, A.J., Morse, D.H., Ver Berkmoes, A.A., Brase, J.M., Heikkinen, D.W., Martz, H.E., and Proctor, I.D., Ion microbeam tomography, *Nucl Instrum Meth B*, **40**, 646–650, 1989.

- Pontau, A.E., Antolak, A.J., and Morse, D.H., Some practical considerations for ion microtomography, *Nucl Instrum Meth B*, **45**, 503, 1990.
- Pradhan, A.S., Thermoluminescence dosimetry and its applications, *Radiat Prot Dosim*, **1:3**, 153–167, 1981.
- Procassini, R.J., Taylor, J., and Hagmann, S., Update on the development and validation of mercury: A modern Monte Carlo particle transport code, *Proceedings of International Topical Meeting on Mathematics and Computations, Avignon, France*, 2005. Lawrence Livermore National Laboratory Report UCRL-PROC-212722, 2005.
- Prussin, S.G., Descalle, M.-A., Hall, J.M., Pruet, J.A., Slaughter, D.R., Accatino, M.R., Alford, O.J. et al., Comparison of tests with 14-MeV neutrons to a Monte Carlo model for interrogation of thick cargos for clandestine fissionable materials, *Nucl Instrum Meth A*, **569**, 853–862, 2006.
- Radon, M., <http://www.radonmine.com> 2015.
- Radon, J., Über die Bestimmung von Funktionen durch ihre Integralwerte längs gewisser Mannigfaltigkeiten, *Berichte Sächsische Akademie der Wissenschaften Math.-Phys. Kl.* **69**, 262–267, 1917.
- Raghothamachar, B., Dudley, M., Rojo, J.C., Morgan, K., and Schowalter, L.J., X-ray characterization of bulk AlN single crystals grown by the sublimation technique, *J Cryst Growth*, **250**, 244–250, 2003.
- Raj, B. and Venkataraman B., *Practical Radiology*, Alpha Science International, UK, 2004.
- Rarback, H.D., Shu, D., Feng, S.C., Ade, H., Kirz, J., McNulty, I., Kern, D.P. et al., Scanning x-ray microscope with 75-nm resolution, *Rev Sci Instrum*, **59:1**, 52–59, 1988.
- Re, A., Albertin, F., Avataneo, C., Brancaccio, R., Corsi, J., Cotto, G., De Blasi, S. et al., X-ray tomography of large wooden artworks: The case study of “Doppio corpo” by Pietro Pifetti, *Heritage Science*, 2, No. 19, 1–9, 2014.
- Reich, Ch., Gibbon, P., Uschmann, I., and Förster, E., Yield optimization and time structure of femtosecond laser plasma K α sources, *Phys Rev Lett*, **84**, 4846, 2000.
- Reinig, W.C., Californium-252 A New Isotopic Source for Neutron Radiography, presented at the *National Conference of the American Society for Nondestructive Testing, Detroit, MI*, October 14–17, 1968.
- Requena, G., Cloetens, P., Altendorfer, W., Poletti, C., Tolnai, D., Warchomicka, F., and Degischer, H.P., Sub-micrometer synchrotron tomography of multiphase metals using Kirkpatrick–Baez optics, *Scripta Mater*, **61**, 760–763, 2009.
- Richards, W.J., Gibbons, M.R., and Shields, K.C., Neutron Tomography Developments and Applications, *University of California Scholarship Repository*, http://repositories.cdlib.org/ucd_mnrc/neutron_tomography_applications, 2003.
- Ricks, R.C., Berger, M.E., Holloway, E.C., and Goans, R.E., REAC/TS radiation accident registry: Update of accidents in the United States, *Oak Ridge Institute for Science and Education, Report T-21-2, P-11-238*, 1999.
- Rischel, C., Rousse, A., Uschmann, I., Albouy, P.A., Geindre, J.-P., Audebert, P., Gauthier, J.-C., Fröster, E., Martin, J.-L., and Antonetti, A., Femtosecond time-resolved x-ray diffraction from laser-heated organic films, *Nature*, **390:6659**, 490–492, 1997.
- Roberson, G.P., Martz, H.E., Decman, D.J., Johansson, E., and Camp, D.C., Preliminary A&PCT Multiple Detector Design, Upgrade of a single HPGe detector A&PCT system to multiple detectors, *Lawrence Livermore National Laboratory, Livermore, CA, UCRL-ID-128052*, 1997.
- Robert-Coutant, C., Moulin, V., Sauze, R., Rizo, P., and Casagrande, J.-M., Estimation of the matrix attenuation in heterogeneous radioactive waste drums using dual-energy computed tomography, *Nucl Instrum Meth A*, **422**, 949–956, 1999.
- Roberts, T.M. and Talebzadeh, M., Acoustic emission monitoring of fatigue crack propagation, *Journal of Construction Steel Research*, **59:6**, 695–712, 2003.
- Romero, C.E., Fast image reconstruction, FY05 engineering research and technology report, *Lawrence Livermore National Laboratory, UCRL-TR-219671*, 92–93, 2006.
- Röntgen, W.C., Über Eine Neue Art von Strahlen, *Sitzungsber. Würzburger Phys.-Medic. Gesellschaft* **137**, 1895.
- Röntgen, W.C., On a new kind of rays, English translation by Arthur Stanton, *Nature* **53**, 274, 1896.
- Rose, A., A Unified approach to the performance of photographic film, television pickup tubes, and the human eye, *J Society Motion Picture Engineers*, **47:4**, 273–294, 1946.
- Rose, A., *Vision Human and Electronic*, Plenum Press, New York, 1974.
- Ross, S.M., *Introduction to Probability Models*, tenth edition, Academic Press, New York, 2009.
- Rousse, A., Rischel, C., Fourmaux, S., Uschmann, I., Förster, E., Audebert, P., Geindre, J.P., Gauthier, J.C., and Hulin, D., Time-resolved femtosecond x-ray diffraction by an ultra-short pulse produced by a laser, *Meas Sci & Technol*, **12:11**, 1841, 2001a.

- Rousse, A., Rischel, C., Fourmaux, S., Uschmann, I., Sebban, S., Grillon, G., and Hulin, D., Non-thermal melting in semiconductors measured at femtosecond resolution, *Nature*, **410**:6824, 65–68, 2001b.
- Rowlands, J.A., The physics of computed radiography, *Phys Med Biol*, **47**, R123–R166, 2002.
- Roy, T., More, M.R., Ratheesh, J., and Sinha, A., A practical fan-beam design and reconstruction algorithm for active and passive computed tomography of radioactive waste barrels, *Nuc Instrum Meth A*, **794**, 164–170, 2015.
- RSICC, <http://rsicc.ornl.gov/>, 2007.
- Rushton, J., Holland, A., Stefanov, K., and Mayer, F., Characterisation of a CMOS charge transfer device for TDI imaging, *J Instrum*, **10**:03, C03027, 2015.
- Sabet, H., Prekas, G., Breen, M., Bhandari, H.B., Nickerson, P., Derderian, G., Robertson, F., Kudrolli, H., Cool, S., and Nagarkar, V.V., High-performance and cost-effective detector using microcolumnar CsI:Tl and SiPM, *IEEE T Nucl Sci*, **59**, 1841–1849, 2012.
- Sain, J.D., Brown, W.D., Martz, H.E., and Schneberk, D.J., Analysis procedures for double-shell target concentricity and wall thickness, UCRL-TR-220178, Lawrence Livermore National Laboratory, Livermore, CA, 2006.
- Sakai, I., Aoki, T., Dobashi, K., Fukuda, M., Higurashi, A., Hirose, T., and Iimura, T., Production of high brightness γ rays through backscattering of laser photons on high-energy electrons, *Phys Rev Spec Top-AC*, **6**–9, 091001, 2003.
- Sakasai, K., Katagiri, M., Matsubayashi, M., Nakamura, T., and Kondo, Y., Characteristics of SrBPO₅:Ce³⁺ based materials as a neutron storage Phosphor, *Nucl Instrum Meth A*, **529**, 378–383, 2004.
- Sakayanagi, Y., Theoretical approach to x-ray imaging by toroidal mirrors, *Opt Acta*, **23**:3, 217–227, 1976.
- Sakayanagi, Y. and Aoki, S., Soft x-ray imaging with toroidal mirrors, *Appl Opt*, **17**:4, 601–603, 1978.
- Sater, J., Kozioziemski, B., Collins, G.W., Mapoles, E.R., Pipes J., Burmann, J., and Bernat, T.P., Cryogenic D-T fuel layers formed in 1-mm spheres by beta-layering, *Phys Rev B*, **35**, 1482–1491, 1998.
- Sato, K., Nariyuki, F., Kubawara, T., Fukui, S., Okada, Y., Nabeta, T., Hosoi, Y., Enomoto, J., Sasao, M., and Seguchi, Y., Development of “CALNEO,” an indirect-conversion digital radiography system with high-conversion efficiency, *Fujifilm Res Dev*, **55**, 2010.
- Saverskiy, A.Y., Dinca, D.C., and Rommel, J.M., Cargo and container x-ray inspection with intra-pulse multi-energy method for material discrimination, *Phys Proc*, **66**, 232–241, 2015.
- Savidou, A., Tzika, F., and Stamatelatos, I.E., Characterization of radioactive waste drums by non destructive gamma spectrometry, *4th International Conference on NDT*, Hellenic Society of NDT, 11–14, Oct. 2007, Chania, Crete-Greece, 2007.
- Scandiflash 2010; <http://www.scandiflash.com>, accessed 2015.
- Scarpitti, R.D., Boyd, J.K., Earley, G.G., Griffin, K.L., Ken, R.G., Kihara, R., Ong, M.M., Sentler, J.-M., and Back, N.L., Upgrades to the LLNL flash x-ray induction linear accelerator (FXR), *Proc 11th IEEE Int Pulsed Power Conf*, 597–602, 1997.
- Schach von Wittenau, A.E., Logan, C.M., and Rikard, R.D., Using a tungsten roll bar to characterize the source spot of a megavoltage bremsstrahlung linac, *Med Phys*, **29**:8, 1797–1806, 2002a.
- Schach von Wittenau, A.E., Logan, C.M., Aufderheide, M.B., and Slone, D.M., Blurring artifacts in megavoltage radiography with a flat-panel imaging system: Comparison of Monte Carlo simulations with measurements, *Med Phys*, **29**:11, 2559–2570, 2002b.
- Schmidt, J.T., Skeie, K., and McIntire, P., (Editors), *Nondestructive Testing Handbook*, second edition: Volume 6, *Magnetic Particle Testing*, American Society of Nondestructive Testing, Philadelphia, PA, 1989.
- Schmidt, T.G., Star-Lack, J., Bennett, N.R., Mazin, S.R., Solomon, E.G., Fahrig, R., and Pelc, N.J., A prototype table-top inverse geometry volumetric CT system, *Med Phys*, **33**:6, 1867–1878, 2006.
- Schneberk, D.J., Azevedo, S.G., Martz, H.E., and Skeate, M.F., Sources of error in industrial computed tomography reconstructions, *Mater Eval*, **48**, 604, 1990.
- Schneberk, D.J., Martz, H.E., and Azevedo, S.G., Multiple-energy techniques in industrial computerized tomography, UCRL-JC-10376, *Review of Progress in Quantitative NDE*, University of California, San Diego, La Jolla, California, July 15–20, 1990, QNDE Proceedings, D. Thompson, D. Chimenti, and D. Miller, Eds, Sept. (Plenum Press, New York) 451–458, 1991.
- Schneberk, D.J., Martz, Jr., H.E., and Brown, W.D., Dimensional measurements of three tubes by computed tomography, Report UCRL-TR-207195, Lawrence Livermore National Laboratory, Livermore, Calif., 2004.
- Schneberk, D., Maziuk, R., Soyfer, B., Shashishekhar, N., and Alreja, R., Application of offset-CT scanning to the inspection of high power feeder lines and connections, *42nd Annual Review of Progress in Quantitative Nondestructive Evaluation*, 2016.

- Schneberk, D., Maziuk, R., Soyfer, B., Shashishekhar, N., and Alreja, R., Application of offset-CT scanning to the inspection of high power feeder lines and connections. In *42nd Annual Review of Progress in Quantitative Nondestructive Evaluation*, AIP Publishing, February 2016.
- Schoenlein, R.W., Leemans, W.P., Chin, A.H., Volfbeyn, P., Glover, T.E., Balling, P., Zolotorev, M., Kim, K.-J., Chattopadhyay, S., and Shank, C.V., Femtosecond X-ray pulses at 0.4 Å generated by 90° Thomson scattering: A tool for probing the structural dynamics of materials, *Science*, **274**, 236–238, 1996.
- Schroer, C.G., Benner, B., Gunzler, T.F., Kuhlmann, M., Lengeler, B., Rau, C., Weitkamp, T., Snigirev, A.A., and Snigireva, I.I., Magnified hard x-ray microtomography: Toward tomography with submicron resolution, *Proc SPIE 4503, Developments in X-Ray Tomography III*, 23, 2002a.
- Schroer, C.G., Leemans, W., Chin, A.H., Volfbeyn, P., Glover, T.E., Balling, P., Zolotorev, M., Kim, K.-J., Chattopadhyay, S., and Shank, C.V., High resolution imaging and lithography with hard x-rays using parabolic compound refractive lenses, *Rev Sci Instrum*, **73**:3, 1640–1642, 2002b.
- Schroer, C.G., Meyer, J., Kuhlmann, M., Benner, B., Gunzler, T.F., Lengeler, B., Rau, C., Weitkamp, T., Snigirev, A.A., and Snigireva, I.I., Nanotomography based on hard x-ray microscopy with refractive lenses, *Appl Phys Lett*, **81**:8, 1527–1529, 2002c.
- Schubert, H. and Kusnetsov, A., (Editors), *Detection of Liquid Explosives and Flammable Agents in Connection with Terrorism*, Springer, Dordrecht, 2008.
- Schwoerer, H., Liesfeld, B., Schlenvoigt, H.P., Amthor, K.U., and Sauerbrey, R., Thomson-backscattered x rays from laser-accelerated electrons, *Phys Rev Lett*, **96**:1, 014802, 2006.
- Seale, M.D. and Madaras, E.I., Ultrasonic measurements of stiffness in thermal-mechanically fatigued IM7/5260 composites, *J Mater Eng Perform*, **8**:4, 429–436, 1999.
- Seeley, Z.M., Kuntz, J.D., Cherepy, N.J., and Payne, S.A., Transparent Lu₂O₃:Eu ceramics, *Mater Res Soc Symp P*, **1341**, 2011a.
- Seeley, Z.M., Kuntz, J.D., Cherepy, N.J., and Payne, S.A., Transparent Lu₂O₃:Eu ceramics by sinter and HIP optimization, *Opt Mater*, **33**, 1721–1726, 2011b.
- Seeley, Z.M., Dai, Z.R., Kuntz, J.D., Cherepy, N.J., and Payne, S.A., Phase stabilization in transparent Lu₂O₃:Eu ceramics by lattice expansion, *Opt Mater*, **35**, 74–78, 2012.
- Seeley, Z.M., Cherepy, N.J., and Payne, S.A., Two-step sintering of Gd_{0.3}Lu_{1.6}Eu_{0.1}O₃ transparent ceramic scintillator, *Opt Mater Express*, **3**:7, 2013.
- Seibert, J.A. and Boone, J.M., x-ray scatter removal by deconvolution, *Med Phys*, **15**:4, 567–575, 1988.
- Seibert, J.A., Nalcioglu, O., and Roeck, W.W., Removal of image intensifier veiling glare by mathematical deconvolution techniques, *Med Phys*, **12**, 281, 1985.
- Semercl, O. and Miller, E.L., A parametric level-set approach to simultaneous object identification and background reconstruction for dual-energy computed tomography, *IEEE T Image Process*, **21**:5, 2719–2734, 2012.
- Serbanescu, C., Fourmaux, S., Kieffer, J.C., Kincaid, R., and Krol, A., A K-alpha x-ray source using high energy and high repetition rate laser system for phase contrast imaging, *Proc SPIE Int Soc Opt Eng*, **7451**, 745115, 2009.
- Serlemitsos, P.J. and Soong, Y., Foil x-ray mirrors, *Astrophys Space Sci*, **239**:2, 177–196, 1996.
- Sessler, A.M., Symon, K.R., and Donald William Kerst, in, *Biographical Memoirs*, **72**, 235–241, National Academy Press, Washington, D.C., 1997.
- Sevan'kaev, A.V., Lloyd, D.C., Edwards, A.A., Moquet, J.E., Nugis, V.Y., Mikhailova, G.M., Potetnya, O.I. et al., Cytogenic investigations of serious overexposures to an industrial gamma radiography source, *Radiat Prot Dosim*, **102**:3, 201–206, 2002.
- Seward, F.D. and Palmieri, T.M., A simple x-ray microscope for photographing laser produced plasmas, *Rev Sci Instrum*, **46**:2, 204–206, 1975.
- Shachar, B.B., Catchen, G.L., and Hoffmann, J.M., Characteristics of the panasonic UD-802 phosphors, *Radiat Prot Dosim*, **27**, 121, 1989.
- Shapiro, J., *Radiation protection: A Guide for Scientists and Physicians*, Harvard University Press, Cambridge, MA, 2002.
- Shaw, T.J., Strellis, D.A., Keeley, D., Yee, R., and Gozani, T., Improvement of SNM detection performance by fusion of data from multiple inspection systems, *IEEE Trans Nucl Sci*, **56**:3, 939–943, 2009.
- Shell, E.B., Buchheit, R.G., and Zoofan, B., Correlation of residual fatigue life with quantitative NDE measurements, *Int J Fatigue*, **27**:2, 105–112, 2005.
- Shoe, <http://www.orau.org/ptp/collection/shoefittingfluor/shoe.htm>, 2015.
- Shull, P.J. (Editor), *Nondestructive Evaluation, Theory Techniques and Applications*, Marcel Dekker, Inc., New York, 2002.
- Shultis, J.K. and Faw, R.E., Radiation shielding technology, *Health Phys*, **88**:4, 297–322, 2005.

- Siders, C.W., Cavalleri, A., Sokolowski-Tinten, K., Toth, C., Guo, T., Kammler, M., Horn von Hoegen, M., Wilson, K.R., vander Linde, D., and Barty, C.P.J., Detection of nonthermal melting by ultrafast x-ray diffraction, *Science*, **286:5443**, 1340–1342, 1999.
- Siegel, M. and Gunatilake, P., Remote technologies for aircraft skin inspection, *IEEE Workshop on Emergent Technologies and Virtual Systems for Instrumentation and Measurement*, IEEE, May 1997.
- Siewerdson, J.H., A.M. Waese, D.J. Moseley, S. Richard, and D.A. Jaffray, Spektr: A computational tool for x-ray spectral analysis and imaging system optimization, *Med Phys*, **31:11**, 3057–3067, 2004.
- Singh, S. and Singh, M., Review of explosives detection systems (EDS) for aviation security, *Signal Process*, **83:1**, 31–55, 2003.
- SMC, <http://www.specialmetals.com/index.php>, 2015.
- Smith, J.A., Schneberk, D.J., Kallman, J.S., Martz, Jr., H.E., and Hoey, D., Documentation of the LLNL and Tyndall Micro-Computed-Tomography Systems, *Lawrence Livermore National Laboratory report LLNL-TR-421377* 2009.
- Smith, S.W., X-ray backscatter detection system, *U.S. Patent 5181234*, issued January 19, 1993.
- Smith, W.J., *Modern Optical Engineering*, McGraw-Hill, New York, 2000.
- Snigirev, A., Snigireva, I., Kohn, V., Kuznetsov, S., and Schelokov, I., On the possibilities of x-ray phase contrast microimaging by coherent high-energy synchrotron radiation, *Rev Sci Instrum*, **66**, 5486, 1995.
- Snigirev, A., Kohn, V., Snigirev, I., and Lengeler, B., A compound refractive lens for focusing high-energy x-rays, *Nature*, **384:6604**, 49–51, 1996.
- Sokolowski-Tinten, Klaus, Blome, C., Dietrich, C., Tarasevitch, A., Horn von Hoegen, M., von der Linde, D., Cavalleri, A., Squier, J., and Kammler, M., Femtosecond x-ray measurement of ultrafast melting and large acoustic transients, *Phys Rev Lett*, **87:22**, 225701, 2001.
- Solomon, E.G., Wilfley, B.P., Van Lysel, M.S., Joseph, A.W., and Heanue, J.A., Scanning-beam digital x-ray (SBDX) system for cardiac angiography, *Proceedings SPIE Medical Imaging*, 1999.
- Sonoda, M., Takano, M., Miyahara, J., and Kato H., Computed radiography utilizing scanning laser stimulated luminescence, *Radiology*, **148**, 833–838, 1983.
- Spark, <http://www.sparkmuseum.com/GLASS.HTM>, 2015.
- SPEC, <http://www.spec150.com/history.htm>, 2005.
- Speidel, M.A., Wilfley, B.P., Heanue, J.A., Betts, T.D., and Van Lysel, M.S., Comparison of vessel contrast measured with a scanning-beam digital x-ray system and an image intensifier/television system, *Med Phys*, **28:2**, 232–240, 2001.
- Speidel, M.A., Wilfley, B.P., Star-Lack, J.M., Heanue, J.A., and Van Lysel, M.S., Scanning-beam digital x-ray (SBDX) technology for interventional and diagnostic cardiac angiography, *Med Phys*, **33:8**, 2714–2727, 2006a.
- Speidel, M.A., Wilfley, B.P., Star-Lack, J.M., Heanue, J.A., Betts, T.D., and Van Lysel, M.S., Comparison of entrance exposure and signal-to-noise ratio between an SBDX prototype and a wide-beam cardiac angiographic system, *Med Phys*, **33:8**, 2728–2743, 2006b.
- Spiga, D. and Raimondi, L., X-ray optical systems: From metrology to point spread function, *Advances in Computational Methods for X-Ray Optics III*, Manuel Sanchez del Rio and Oleg Chubar, (Editors) *Proc SPIE* 9209, 92090E, 2014.
- Sprangle, P., Ting, A., Esarey, E., and Fisher, A., Tunable, short pulse hard x-rays from a compact laser synchrotron source, *J Appl Phys*, **72:11**, 5032–5038, 1992.
- Sproull, W.T., *X-rays in Practice*, McGraw-Hill Book Co., New York, 615, 1946.
- Stanford, <http://www.stanford.edu/home/welcome/research/klystron.html>, 2007.
- Stanford, N., A new algorithm for the panasonic UD-802, Presented at the 47th annual meeting of the Health Physics Society, 2002.
- Stedman, M., A parabolic collimator of adjustable incidence angle and constant focal length, in: *Workshop on X-Ray Instrumentation for Synchrotron Radiation Research*, H. Winick and G. Brown, eds., *SSRL Report No. 78/04*, pp. VII142–VII147, Stanford Linear Accelerator Center, 1978.
- Stein, M., Kasyanov, V.A., Chakhlov, V.L., Macleod, J., Marjoribanks, P., and Hubbard, S., Small-size betatrons for radiographic inspection, *16th World Conference on NDT*, (available at <http://www.ndt.net>) Montreal, Canada, 2004.
- Stergiopoulos, S. (Editor), *Advanced Signal Processing Handbook*, Chapter 15, Industrial Computed Tomographic Imaging, CRC Press, 2001.
- Strecker, H., Automatic detection of explosives in airline baggage using elastic x-ray scatter, *Medica Mundi*, **42:2**, 30–33, 1998.
- Strecker, H. and Harding, G., Detection of explosives in airport baggage using coherent x-ray scatter, *Proc SPIE* **2092:48**, 399–410, 1993.

- Street, R.A. (Ed.), *Technology and Application of Amorphous Silicon*, Springer, New York, 2000.
- Strom, D.J., The linear, no-threshold dose-response model: Both sides of the story, Continuing Education Lecture Presented at the 41st Annual Meeting of the Health Physics Society, 1996. Available at <http://www.pnl.gov/bayesian/strom/strompub.htm>.
- Strom D.J., *Health Impacts from Acute Radiation Exposure*, PNNL-14424, Pacific Northwest National Laboratory, Richland, Washington, 2003.
- Stuart, P.R., Towards the ultimate x-ray microscope, in *Microfocal Radiography*, Ely, R.V., Ed., Academic Press, London, 1980.
- Suehiro, S., Miyaji, H., and Hayashi, H., Refractive lens for x-ray focus, *Nature*, **353**, 385–386, 1991.
- Sukovic, P. and Clinthorne, N.H., Basis material decomposition using triple-energy x-ray computed tomography, *Proceedings of the 16th IEEE Instrumentation and Measurement Technology Conference*, **3**, 1615–1618, 1999.
- Sun, Y., *Field Detection Technologies for Explosives*, ILM Publications, Glendale, AZ, 2010.
- Susini, J., Joyeux, D., Polack, F., Eds., International Conference on x-ray Microscopy (7th 2002 Grenoble, France), EDP Sciences, France, *Journal de Physique IV* (Proceedings), 104, 2003.
- Suzuki, Y., Yagi, N., and Uesugi, K., X-ray refraction-enhanced imaging and a method for phase retrieval for a simple object, *J Synchrotron Radiat*, **9**:3, 160–165, 2002.
- Swank, R.K., Absorption and noise in x-ray phosphors, *J Appl Phys*, **44**:9, 4199–4203, 1973.
- Szczykutowicz, T.P., Qi, Z., and Chen, G.H., A simple image based method for obtaining electron density and atomic number in dual energy CT, *SPIE Medical Imaging*, International Society for Optics and Photonics, **1967**, 79613A, 2011.
- Tanner, B.K., *X-Ray Diffraction Topography*, Pergamon Press, New York, 1976.
- Ter-Pogossian, M.M., The physical aspects of diagnostic radiology, *Am J Med Sci*, **254**:6, 918, 1967.
- Thermo, 2014, <http://www.thermoscientific.com/>.
- Thompson, M., Baker, M.D., Tyson J.F., and Christie, A., *Auger Electron Spectroscopy*, Wiley-Interscience, New York, 1985.
- Thompson, S.G., Street, Jr. K., Ghiorso, A., and Seaborg, G.T., The New Element Californium (atomic number 98), *Phys Rev*, **80**, 790, 1950.
- Thompson, A., Attwood, D., Gullikson, E., Howells, M., Kim, K.J., Kirz, J., Kortright, J., Lindau, I., Liu, Y., Pianetta, P. et al., *X-ray data booklet, rev. 3*, Center for X-Ray Optics and Advanced Light Source, Report LBNL/PUB-490, Lawrence Berkeley National Laboratory, University of California, Berkeley, California, 2009.
- Thompson, W.M., Lionheart, W.R.B., and Morton, E.J., Real-time imaging with a high speed x-ray CT system, *Sixth International Symp Process Tomography*, Mar 26–28, 2012.
- Thorium, <http://www.orau.org/ptp/collection/quackcures/elbowsupporter.htm>, 2015.
- Thwaites, D.I. and Tuohy, J.B., Back to the future: The history and development of the clinical linear accelerator, *Phys Med Biol*, **51**, R343–R362, 2006.
- Tonner, P.D. and Stanley, J.H., Supervoltage computed tomography for large aerospace structures, *Mater Eval*, **12**, 1434, 1992.
- Toops, T.J., Bilheux, H.Z., Voisin, S., Gregor, J., Walker, L., Strzelec, A., Finney, C.E.A., and Pihl, J.A., Neutron tomography of particulate filters: A non-destructive investigation tool for applied and industrial research, *Nucl Instrum Meth A*, **729**, 581–588, 2013.
- Tracy, N. and Moore, P., (Editors), *Nondestructive Testing Handbook*, third edition: Volume 2, *Liquid Penetrant Testing*, American Society of Nondestructive Testing, 1999.
- Trevert, E., *Something About X Rays for Everybody*, Bubier Publishing, 1896.
- Tringe, J.W., Molitoris, J.D., Smilowitz, L., Kercher, J.R., Springer, H.K., Henson et al., Time-sequenced x-ray observation of a thermal explosion, *APS, 16th APS Topical Conf on Shock Compression of Condensed Matter*, 2009.
- Tuohimaa, T., Otendal, M., and Hertz, H.M., Phase-contrast x-ray imaging with a liquid-metal-jet-anode microfocus source, *Appl Phys Lett*, **91**, 074104, 2007.
- Turai, I and Veress, K., Radiation accidents: Occurrence, types, consequences, medical management, and lessons to be learned, *Central European Journal of Occupational and Environmental Medicine*, **7**:1, 3, 2001.
- Turismo, <http://www.citybrazil.com.br/es/guarapari/turismo.htm>. 2005.
- UIUC, <http://www.physics.uiuc.edu/history/Timeline/1950s.html>.
- UMICH, Radioactivity in Nature, <http://www.umich.edu/~radinfo/introduction/natural.htm>, 2015.
- Underwood, J.H. and Turner, D., Bent Glass Optics, 1977 *SPIE/SPSE Technical Symposium East*, Proc SPIE, **106**, 125–135, 1977.

- U.S. NRC, *U.S. Nuclear Regulatory Commission, Release of Patients After Brachytherapy Treatment With Remote Afterloading Devices*, NRCB 93-01, 1993.
- U.S. Patent US6236709B1, *Continuous High Speed Tomographic Imaging System and Method*, Perry, J.L. and Gamble, T.D., 1998.
- USAF, *U.S. Air Force Aeronautical Systems Center, Military Handbook, MIL-HDBK-1823, Nondestructive Evaluation System, Reliability Assessment*, 1999.
- USGS, United States Geological Survey, *Minerals Yearbook: Volume I—Metals and Minerals*, U.S. Government Printing Office, 2004.
- Van de Graaff, R.J., Compton, K.T., and Van Atta, L.C., The electrostatic production of high voltage for nuclear investigations, *Phys Rev*, **43:3**, 149–157, 1933.
- Varian, *Varian Medical Systems 2013 Annual Report*, p. 13, 2014.
- Venkataraman V., Dhanaraj, G., Wadhawan, V.K., Sherwood, J.N., and Bhat, H.L., Crystal growth and defects characterization of zinc tris (thiourea) sulfate: A novel metalorganic nonlinear optical crystal, *J Cryst Growth*, **154**, 92–97, 1995.
- Vijayalakshmi P. and Sumathi M., Design of algorithm for detection of hidden objects from Tera hertz images, *IOSR J Comp Eng (IOSR-JCE)*, **13:2**, 25–32, July–August 2013.
- Vincente, R., Sordi, G.-M., and Hiromoto, G., Management of spent sealed radiation sources, *Health Phys*, **86:5**, 497, 2004.
- von Lenard, P.E., On cathode rays, Nobel Lecture, May 28, 1906, available at <http://nobelprize.org/physics/laureates/1905/lenard-lecture.html>.
- Voss, J.T., Los Alamos radiation monitoring notebook, LA-UR-00-2584, Revised 2001.
- Vossoughi, F., Ostertag-Paulo, C.P., Monteiro, J.M., and Albert, R., Damage characterization of concrete panels due to impact loading by motionless X-ray laminography, *J Mater Sci*, **42:9**, 2007.
- Walden, Jr. T.L., The first radiation accident in America: A centennial account of the x-ray photograph made in 1890, *Radiology*, **181**, 635, 1991.
- Walinder, G., *Has Radiation Protection Become a Health Hazard*, The Swedish Nuclear Training & Safety Center, Medical Physics Publishing, Nykoping, Sweden, 2000.
- Wang, L., Liu, Y., and Kang, K., Scatter considerations in ultra-high-resolution high-energy x-ray transmission imaging systems, *Nucl Instrum Meth A*, **538:1**, 747–755, 2005a.
- Wang, S., Duewer, F., Feser, M., Scott, D., and Yun, W., X-ray microscopy for NDE of micro- and nano-structures, in Geer, R.E., Meyendorf, N., Baaklini, G.Y., and Michel, B., Eds., *Proceedings of SPIE 5776 on Testing, Reliability, and Application of Micro- and Nano-material Systems III*, **40:48**, 2005b.
- Warwick, T. and Attwood, D., Eds., *X-ray Microscopy Proceedings of the Sixth International Conference*, Meyer-Ilse, American Institute of Physics, Melville, **507**, 1999.
- Waters, A.M., Three-dimensional analysis of voids in AM60B magnesium tensile bars using computed tomography imaging, Ph.D. Dissertation, Johns Hopkins University, Baltimore, MD, 2001.
- Waters, A.M., Martz, H.E., Logan, C.M., Updike, E.O., and Green, Jr., R.E., High energy x-ray radiography and computed tomography of bridge pins, *Proceedings of the Second Japan-U.S. Symposium on Advances in NDT*, Kahuku, Hawaii, 433–438, 1999a.
- Waters, A.M., Martz, H.E., Dolan, K.W., Horstemeyer, M.F., Rikard, R.D., and Green, R.E., Characterization of damage evolution in an AM60 magnesium alloy by computed tomography, *Nondestructive Characterization of Materials IX*, Green, Jr., R.E. (Editor), American Institute of Physics 1-56396-911-4, 616–621, 1999b.
- Waters, A.M., Martz, H.E., Dolan, K.W., Horstemeyer, M.F., and Green, Jr., R.E., Three-dimensional void analysis of AM60B magnesium alloy tensile bars using computed tomography imagery, Fellowship Award Paper, *Mater Eval*, **58:10**, 1221–1227, 2000.
- Waters, A., Martz, H., Logan, C., Gross, J., and Chinn, D., KCAT Performance Summary—Update, Lawrence Livermore National Laboratory, Livermore, CA, UCRL-TR-203519-REV-1, September 2004.
- Wei, L. and Lawn, B.R., Thermal wave analysis of contact damage in ceramics: Case study on alumina, *J Mater Res*, **11:4**, 939–947, 1996.
- Wellnhofer, P., *Archaeopteryx: The Icon of Evolution*, Verlag Dr. Friedrich Pfeil, 2009.
- Wells, K. and Bradley, D.A., A review of x-ray explosives detection techniques for checked baggage, *Appl Radiat Isotopes*, **70**, 1729–1746, 2012.
- White, V. and Cerrina, F., Metal-less x-ray phase shift masks for nonlithography, *J Vac Sci Technol B*, **10**, 3141–3144, 1992.
- Whiting, B.R., Massoumzadeh, P., Earl, O.A., O’Sullivan, J.A., Snyder, D.L., and Williamson, J.F., Properties of preprocessed sinogram data in x-ray computed tomography, *Med Phys*, **33:9**, 3290–3303, 2006.

- Wielopolski, L., Song, Z., Orion, I., Hanson, A.L., and Hendrey, G., Basic considerations for Monte Carlo calculations in soil. *Appl Radiat Isotopes*, **62:1**, 97–107, 2005.
- Wikipedia, 2014, http://en.wikipedia.org/wiki/Turbomolecular_pump, Turbomolecular pump, 2014.
- Wikipedia, 2015, https://en.wikipedia.org/wiki/List_of_synchrotron_radiation_facilities, 2015.
- Wilkins, S.W., Gureyev, T.E., Gao, D., Pogany, A., and Stevenson, A.W., Phase contrast imaging using polychromatic hard x-rays, *Nature*, **384**, 335, 1996.
- Wölter, H., Glancing incidence mirror systems as imaging optics for x-rays, *Annal Phys*, **10**, 94–114, 1952.
- World Federation of NDE Centers; <http://www.wfndec.org/2015>.
- Wouwer, A.V., Sauciez, P., and Schiesser, W.E., *Adaptive Method of Lines*, CRC Press, Boca Raton, 2001.
- Wu, X. and Liu, H., A new theory of phase-contrast x-ray imaging based on Wigner distributions, *Med Phys*, **31**, 2378–2384, 2004.
- X-5 Monte Carlo Team, MCNP—A general Monte Carlo n-particle transport code, version 5. Los Alamos, NM: Los Alamos National Laboratory; *LA-UR-03-1987* (Vol. I: Overview and theory); *LA-UR-03-0245* (Vol. II: User's guide); 2003.
- XRADIAMXCT, http://www.lao.cz/data/ke-stazeni/MicroXCT_200_eu_1_.pdf, 2015.
- XRSIM, <http://www.ndetechnologies.com>, 2015.
- Yabushita, R. and Hata, K., Development of high spatial resolution x-ray radiography system equipped with multiwalled carbon nanotube field emission cathode, *J Vac Sci Technol B*, **26:2**, 702–705, 2006.
- Yang, B.X., Fresnel and refractive lenses for X-rays, *Nuc Instrum Meth A*, **328**, 578–587, 1993.
- Yang, D. and Ning, R., FDK Half-scan with a heuristic weighting scheme on a flat panel detector-based cone-beam CT (FDK-HSCW), *Int J Biomed Imaging*, **2006**, 1–8, 2006.
- Ying, Z., Naidu, R., and Crawford, C.R., Dual energy computed tomography for explosive detection, *J X-ray Sci Technol*, **14:4**, 235–256, 2006.
- Yoshida, M. and Asano, T., A new method to measure the oxide layer thickness on steels using electromagnetic acoustic resonance, *J Nondestruct Eval*, **22:1**, 11–21, 2003.
- Yoshimura, H., Maeda, H., Hori, A., and Igarashi, K., Three-dimensional visualization in projection x-ray microscopy of biological specimens, in *Journal de Physique IV (Proceedings)*, *7th International Conference on X-Ray Microscopy ESRF*, Susini, J., Joyeux, D., Polack, F., Eds., EDP Sciences, France, **104**, 355–358, 2003.
- Yue, G.Z., Qiu, Q., Gao, B., Cheng, Y., Zhang, J., Shimoda, H., Chang, S., Lu, J.P., and Zhou, O., Generation of continuous and pulsed diagnostic imaging x-ray radiation using a carbon-nanotube-based field-emission diode, *Appl Phys Lett*, **81**, 355–357, 2002.
- Zernike, E., Phase contrast: A new method for the microscopic observation of transparent objects, *Physica*, **9**, 686, 1942.
- Zhao, W., Zhu, J., and Wang, L., Fast scatter artifacts correction for cone-beam CT without system modification and repeat scan, *arXiv:1501.04409v1*, [physics.med-ph] January 19, 2015.
- Zhao, X., Hu, J.J., and Zhang, P., GPU-based 3D cone-beam CT reconstruction for large data volume, *Int J Biomed Imaging*, **2009**, 2009. <http://www.hindawi.com/journals/ijbi/2009/149079/>
- Zholents, A., Next-generation x-ray free-electron lasers, *IEEE J Selected Topics Quantum Electron*, **18:1**, 1–10, 2012.
- Zimmer, C., Evolution of feathers: The long curious extravagant evolution of feathers, *National Geographic*, February, 2011; <http://ngm.nationalgeographic.com/2011/02/feathers/zimmer-text/1>, 2011.
- Zou, K.H., Receiver operating characteristic (ROC) literature research, <http://splweb.bwh.harvard.edu:8000/pages/ppl/zou/roc.html>, 2006.
- Zuuk, 2014, <http://www.zuukinspection.com/ndtnde/history-of-non-destructive-testing/>, History of Non-Destructive Testing, 2014.

Index

Page numbers followed by f, t, and n indicate figures, tables, and notes, respectively.

A

- Ablator heat shields, of spacecraft, 442–445, 443f, 444f
Absorbed dose; *see also Radiation dosimetry/safety/shielding*
 defined, 136
 radiation measurements for
 Geiger-Müller counter, 140–143
 ionization chamber radiation meter, 143–145, 144f
 personal dosimeter, 145–146
Absorption (photoelectric absorption); *see also Attenuation interactions*
 about, 77–81
 Auger effect and fluorescence, 81
Absorption by anode, 167f
Acceleration of electrons, 176
Accelerators
 as pulsed sources, 178; *see also Pulsed sources*
 source of thermal neutrons, 496
Acoustic emission, 16, 17–18
Acoustic energy
 acoustic emission, 17–18
 ultrasonic testing, 16–17
Acquisition computers, 231
AC servomotor, 227–228
Active CT, 377–380, 378f, 379f, 380f, 381f, 382f
Active thermography, 12, 13f
Activity of radioisotope, 69
Acute irradiation, 136
Additive manufacturing (AM), CT of structures, 466–469, 466f, 467f, 468f, 469f
Administrative access control, 153
Advanced analysis tools, 326
Advanced imaging technology (AIT), 484, 485–487, 485f, 486f, 487f
Advanced light source (ALS), 211, 371, 372
Aerogels, 100n
 DS target manufacturing, 450
Ahlstrom x-ray microscope, 402
Air ducts, 153
Albedo
 from lead and concrete, 125–126
 measurements, 125
Aluminum, in aircraft, 499
American Society for Nondestructive Testing (ASNT), 4
Amorphous silicon (amSi) detectors, 263, 421, 421f, 422t, 453–454, 466
Annihilation, 77
Annihilation radiation, 55, 57
 generation, 70; *see also High-energy photons*, types of
Anode, 27, 161–163; *see also X-ray tubes*
Antielectron, 56n
Antiscatter grids, 222–224; *see also Imaging system components*
Apertures, limiting, 224–226; *see also Imaging system components*
- Archaeopteryx* fossil, tomosynthesis of, 457–459, 458f, 459f, 460f, 461f
Area-array detector systems, 247, 271, 292
 x-ray scatter correction algorithms, 215
Area collimators, 217
Area detection, 191–193; *see also Radiation detectors*
Area-detector arrays
 about, 264–267; *see also Digital radiography (DR)*
 CT scanning with, 256–258; *see also 3-D computed tomography*
 radiography systems with, 246–248
Area detectors, 337, 338–339, 419
Area detectors employing scintillator; *see also Radiation detectors*
 CCD-based, 198–200
 CMOS-based, 200
Areal density, 92
Art and objects of cultural significance, DR/CT of, 459, 460, 462–465
 Kongo Risiki, statue of, 460, 462f
 Michelangelo Buonarroti's statue of David, concerns with, 462–465, 463f, 464f, 465f
 pictures of period furniture, 460, 461f
 Tamon Ten statue, 462f, 466
Artifacts
 beam-hardening, 341–342
 cupping, 341
 x-ray transmission imaging, 341–342
Artifacts in CT reconstructed data, 303–324
 angular positioning artifacts, 312–313
 bad-pixel artifacts, 309–312
 beam-hardening artifacts, 320–322
 centering artifacts, 307, 308f
 cone-beam missing data artifacts, 319–320
 incorrect vertical center cone-beam artifacts, 317–319
 midline offset artifacts, 316–317
 ring artifacts, 308–309
 scatter artifacts for high-aspect ratio or high-attenuating objects, 322–324
 X-ray magnification artifacts, 314–316
Artifacts in digital radiographs/symptoms/remedies, 272t
As low as reasonably achievable (ALARA) principle, 150, 153
Atom
 characteristics, 55n
 in excited state, 64
Atomic attenuation coefficient, 88–89; *see also Attenuation measurement units*
Atomic cross section, 88, 89
Atomic Energy Act, 471
Attenuation
 inconsistencies, defined, 339
 mass attenuation coefficients, thermal neutron, 495, 496f
 measurements, CT, 343
 photoelectric, for carbon and tungsten, 370, 373–374

- radiographic, 331
of thermal neutrons, boron, 499, 499f
x-ray, 345, 371t
- Attenuation interactions; *see also* [High-energy photon \(x-ray/γ-ray\) interactions with matter](#)
absorption (photoelectric absorption)
about, 77–81
Auger effect and fluorescence, 81
pair production, 85
photofission, 85–86
photonuclear absorption, 85
scatter
about, 81–82
coherent (Rayleigh) scatter, 84–85
incoherent (Compton) scatter, 82–84
- Attenuation measurement units; *see also* [High-energy photon \(x-ray/γ-ray\) interactions with matter](#)
atomic attenuation coefficient, 88–89
attenuation coefficients, relationship, 90
linear attenuation coefficient, 86–88
mass attenuation coefficient, 88
mixture rule, 90–92
molar attenuation coefficient, 90
total attenuation/x-ray and γ-ray attenuation phenomena, 92–96
- Auger effect and fluorescence, 81; *see also* [Absorption \(photoelectric absorption\)](#)
- Auger electrons, 65
- Automated defect recognition, 384–386, 385f, 426
- Automated flaw detection, *see* [Automated defect recognition](#)
- Automated threat detection (ATD) algorithm, 473, 474–478, 474f, 475f, 476f, 477f, 478f, 479f
- Automated threat recognition(ATR) algorithm, 473, 486
- Automatic transmission, high-energy photon application, 418–419, 419f, 420f
- Automotive applications, three-dimensional, 432–441
fuel pump, 441, 441f, 442f
metal castings, 434, 435–440, 435f, 436f, 437f, 438f, 439f
planetary transmission gear assembly, 440, 441f
windshield wiper motor, 440, 440f
- AVCOAT, 443
- Aviation safety, DR and CT of pitot tubes, 427, 428, 430f, 431f
- Avizo 3D software, 325
- B**
- Background or system scatter, Φ_{sbk} properties of, 212–213; *see also* [Signal \(detected\) in x-ray imaging, sources of](#)
- Background or system scattered photons measurements, 213
- Backscatter imaging, 386–392
baggage inspection system, 386–389, 387f, 389f
for cargo NII, 487–492, 488f, 489f, 490f, 491f, 492f
carry-on luggage, inspection, 472–474, 472f, 473f, 474f
concealed items underneath clothing, detection, 390–391, 390f, 391f
explosives in airline baggage, detection of, 386–389, 387f
incoherent or Compton, 386–392
of passengers, 484, 485–487, 485f, 486f, 487f
process control tomosynthesis measurements, 391, 391f
- Bad-detector-element correction method, 266
- Bad pixels, 266, 272
- Baggage, inspection, 386–389, 387f, 389f, 472–474, 472f, 473f, 474f
- Basis material decomposition (BMD), 245
- Beam blocker, 215
- Beam diameter, defined, 415
- Beam geometry, 250
- Beam hardening
effects, in image artifacts, 334–335
for image contrast and spatial resolution, 341
- Becquerel, Henri, 36
- Beer's law, 240, 330
- Betatron, 176; *see also* [Electron accelerator-based sources](#)
- Binding energy, 80
- Binomial random variables, 343
- BioImaging Research (BIR)
linear detector array, 490
mobile waste inspection trailer, 378, 381f
- Biological Effects of Ionizing Radiation (BEIR), 140
- Blur functions, step and, 356, 356f, 357, 357f
- Bohr orbits, 60
- Bohr–Sommerfeld atomic model, 57, 58f, 60
- Bohr theory, 57
- Boltzmann transport equation, 116
- Boron, attenuation of thermal neutrons, 499, 499f
- Boston Marathon bombing, 469f
- Boyle x-ray microscope, 402
- Brachytherapy, 42n
- Bragg's law, 108, 392
- Bragg version of diffraction, 107
- Bremsstrahlung (braking or decelerating electrons), 62–64; *see also* [Electrons and x-ray radiation generation](#)
- Bremsstrahlung radiation, 342
- Brightness, 160
- Brilliance, 160
- Buckles, 222
- Buna N elastomer O-ring seal, composition, 502, 503t
- C**
- Cabinet hardware, 207
- Cabinet x-ray units, 153
- Cadmium zinc telluride (CZT), 242, 262
- Calcium tungstate, 35
- Calibration drift, 272
- Californium-252 (^{252}Cf), source of thermal neutrons, 496, 497f
- CALNEO, 201
- Camera-scintillator detectors, 273, 275
- Candling, 10; *see also* [Optical testing with visible photons](#)
- Carbon, photoelectric attenuation for, 370, 373–374
- Carbon nanotube field emission, 174
- Carbon nanotube (CNT) multibeam tube, 482, 484, 484f, 485f
- Cargo advanced automated radiography system (CAARS) program, 419, 420, 487, 488–490, 488f, 489f
- Cargo NII, radiography and backscatter for, 487–492, 488f, 489f, 490f, 491f, 492f
- Carry-on luggage, security scanners, 472–474, 472f, 473f, 474f
- Castings, metal, 434, 435–440, 435f, 436f, 437f, 438f, 439f
- Cathode, 27
- Cathode rays, 75

- Cathode ray tubes (CRT), 27
CBP (Customs and Border Protection), 421, 470
Cell processor, 233
Center for Nondestructive Evaluation (CNDE), 4
Ceramic scintillators, 194–195, 196t
Characteristic x-rays, 64–65; *see also* [Electrons and x-ray radiation generation](#)
Characterization
 of DS targets, CT and DR, 451f, 452, 452f
 of LX-17 HEs, 428, 429, 430, 432, 432f, 433f, 434f, 435f
 NDC
 military ordnance, 452–457
 use of, 419, 420
Charge-coupled device (CCD) cameras, 40, 417, 425
Charged particles, 137, 175
Checked luggage, inspection
 CT for, 474–478, 474f, 475f, 476f, 477f, 478f, 479f
 DR and diffraction for, 478, 480, 480f
Chemical vapor deposition (CVD), 102
Chlorophyll fluorescence analysis, 11
Chronic irradiation, 136
Clear crystal scintillators, 194–195, 196t
Clint's Computed Axial Tomography (CCAT), 256
Coded aperture cameras
 advantage, 398
 defined, 398
Coherent (Rayleigh) scatter, 77, 82, 84–85; *see also* [Scatter](#)
Coherent scattering, 206, 386–392, 387f, 389f, 390f, 391f
Cold crack porosity, 439
Collimated monochromatic x-ray beam, 106, 107
Collimation, 496, 497f
 properties of materials used in, 208t
 shielding and, 217–222
Collimators, 126–128
 about, 163, 218–222
 design for 9 MV linac, 126–128
 use of, 206
Color manipulation toolbars, 230
Compact Light Source (CLS), 181f
Complementary metal oxide semiconductors (CMOS), 192, 225, 247, 275
Complementary metal-oxide semiconductors (CMOS), 41
Compton scattering, 79f, 82f, 154, 180, 207
 forward/backscatter imaging, 386–392, 387f, 389f, 390f, 391f
 material attenuation, 332
 photoelectric and, 373, 374
 photons, distribution, 336
Computed radiography (CR), 193–194; *see also* [Radiation detectors](#)
Computed tomography (CT), 39–40; *see also* [X-ray history](#)
 ablator shields, spacecraft, 443
 acquisition, designing, 344
 active and passive (emission), 377–380, 378f, 379f, 380f, 381f, 382f
 art and objects of cultural significance, 459, 460, 462–465
 Kongo Risiki, statue of, 460, 462f
 Michelangelo Buonarroti's statue of David, concerns with, 462–465, 463f, 464f, 465f
 pictures of period furniture, 460, 461f
 Tamon Ten statue, 462f, 466
 attenuation measurements in, 343
 checked luggage, inspection, 474–478, 474f, 475f, 476f, 477f, 478f, 479f
 data, display of, 234–235
 data acquisition, computers for, 231–232
 data acquisition and processing, 290–294
 data processing and the importance of Φ_0 , 294, 295f, 296
 DS targets, characterization, 451f, 452, 452f
 fundamental properties of, 329
 image reconstruction, 286–327
 imaging performance for, 338
 low-energy dual-energy applications, 370, 371, 372f
 metal castings, 434, 435–440, 435f, 436f, 437f, 438f, 439f
 nonrotating gantry security CT systems, 480–484
 overview, 480–481
 Rapiscan, 482, 483f
 SureScan system, 481, 481f, 482f
 XinRay laboratory prototype, 482, 484, 484f, 485f
 of pitot tubes, aviation safety, 427, 428, 430f, 431f
 reconstruction, computers for, 232–234
 source-spot blur for, 336
 spatial resolution for, 336
 of structures, by additive manufacturing, 466–469, 466f, 467f, 468f, 469f
 tomosynthesis
 of *Archaeopteryx* fossil, 457–459, 458f, 459f, 460f, 461f
 depth information without, 380, 382f, 383–384, 383f, 384f
 of DoD ordnance, 452–457
 of MFF, 455–457, 456f, 457f
 transmission imaging, 339
 of WDU-17/B conventional warhead, 453–455, 453f, 454f, 455f
Computed tomography (CT) reconstruction algorithms, 296–301
 region of interest and CT field-of-view extension techniques, 300–301
Computer-aided design (CAD), 117, 181
Computer-aided inspection, *see also* [Automated defect recognition](#)
Computer-assisted tomography (CAT), 40
Computer clusters, 233
Computers
 for CT data acquisition, 231–232
 for CT reconstruction, 232–234
 requirements for DR /CT processing, 232
 with specialized processors, 232
Concealed items underneath clothing, detection, 390–391, 390f, 391f
Cone-beam collimated x-ray source, 214f
Cone-beam CT system (CCAT), 428, 432f, 466, 466f
Cone-beam geometry CT system, 256, 257, 257f
Cone-beam scanners, 231
Confined Large Optical Scintillator Screen and Imaging System (CoLOSSiS), 220
Constituent transmission measurements, 249
Contemporary cold cathode x-ray tube, 174; *see also* [X-ray tubes](#)
Contrast, of images
 beam hardening for, 341
 components, 332–335, 333f, 334f
 intrinsic/object contrast, 332–334, 333f, 334f
 measuring, 345–348, 346f, 347f, 347t, 348f
 overview, 329–330

- Contrast agents
defined, 369
for thermal neutron imaging, 495, 499
- Contrast penetrometer, 277f
- Contrast sensitivity measurements, 216
- Contrast test object assembly (CTOA), 304
- Conventional x-ray imaging, 103f
- Convolution, of step and blur functions, 356, 356f, 357, 357f
- Coolidge tube, 38–39, 38f, 161; *see also X-ray history*
- Coolidge x-ray tube, 174
- Cormack, Allan, 39, 40
- Corn rootworms, study of, 501, 502f
- Correction-map function, 275
- Corrosion in aircraft, detection, 499
- Cosmic radiation, 149; *see also Natural background radiation*
- Cost of shielding, 154
- Coulomb forces, 57
- Couplant, 16
- Crack, 49, 50f
- Critical angle, for x-ray reflection, 399, 399f
- Critical flaw, 21
- Crookes tube, 27, 28f, 29f
- Cross-section, attenuating atoms, 88
- CsI(Tl), scintillator-based detector, 333, 334f
- CT, *see Computed tomography (CT)*
- Cultural heritage, DR/CT use, 459, 460, 462–465
Kongo Risiki, statue of, 460, 462f
Michelangelo Buonarroti's statue of David, concerns with, 462–465, 463f, 464f, 465f
pictures of period furniture, 460, 461f
Tamon Ten statue, 462f, 466
- Cupping artifact, 341
- Current-integrating detector, 213
- Curved detector arrays, 245, 264
- Customs and Border Protection (CBP), 421, 470
- Cyclotron, 65
- D**
- Dark current, 263
in charge-coupled device detector, 213
corrected pixel by pixel, 188
images of visible-light detectors, 190f
- Dark-current images, 265, 267–268, 275
- Dark-current subtracted DR images, 273f
- Data acquisition
angle of, 384
time, spatial resolution and, 378
tomosynthesis, 380, 382f, 383, 384, 384f
- Data analysis, 279–284; *see also Digital radiography (DR)* and interpretation, 325–327
- Data processing of digital radiographic image data, 271; *see also Digital radiography (DR)*
- Data query tools, 326
- Data sets, size of, 230
- 3-D computed tomography; *see also Imaging-system configurations*
about, 248–250
area-detector arrays, CT scanning with, 256–258
1-D gauging systems, CT scanning with, 250–252
linear-detector arrays, CT scanning with, 252–256
- DC servomotor, 227–228
- 3D-DOCTOR, 325
- Decay constant, 69
- Deceleration of electron charge, 62
- Decision Sciences International Corporation Inc., 490, 492
- Delrin, 287–288
- Delrin attenuation, 287
- Dental x-rays, 25
- Department of Defense (DoD)
ordnance, CT and tomosynthesis of, 452–457
MFf, 455–457, 456f, 457f
WDU-17/B conventional warhead, 453–455, 453f, 454f, 455f
US, 469–470
- Department of Homeland Security (DHS), 419, 420, 469–470, 472, 474
- Depleted uranium (DU), 154–155
- Desktop computers, general-purpose, 232
- Detectability of cracks/gaps, 53
- Detectable feature, 282
- Detection
ATD algorithm, 473, 474–478, 474f, 475f, 476f, 477f, 478f, 479f
automated flaw, *see Automated defect recognition*
concealed items underneath clothing, 390–391, 390f, 391f
corrosion in aircraft, 499
DNDO, 419, 420, 470, 487, 490
EDS, 474–478, 474f, 475f, 476f, 477f, 478f, 479f
explosives in airline baggage, 386–389, 387f
MMPDS, 490, 492
Morpho Detection, 475, 476f, 478, 480, 480f
probability, ROC curves and, 365–368, 366f, 367f
- Detective quantum efficiency (DQE)
definition, 360–361
measurement, 361–365
Rose model for, 361–362, 361f, 364
at spatial frequency, 364
step wedges, 362–364, 362f, 363f, 363t
SNR and, 360–365
- Detector pixel, 266
- Detector(s)
amSi, 421, 421f, 422t, 453–454, 466
area detectors, 337, 338–339, 419
concealed items underneath clothing, 390–391, 390f, 391f
corrosion in aircraft, 499
energy-resolving detector, 386, 387f
explosives in airline baggage, 386, 387f, 388–389
forward and backscatter imaging, 386–392, 387f, 389f, 390f, 391f
GOS scintillator as, 456
HPGe, 378, 379f, 382f, 387f
noise characteristic of, 340
Perkin-Elmer, 337
scintillator-based, CsI(Tl) and Lanex Fine, 333, 334f
SiLi, 416, 417
silicon-based, 340
source-object-detector, 380
spatial resolution for
area, 337, 338–339
linear-array, 337–338, 339
stopping power, 335, 340
temperature of, 340
Thales amSi flat panel, 453–454, 466
with thermal neutrons, 497–499, 498t

- track-etch, 498
XDi, for liquid explosive threats, 471
x-ray detectors, photon statistics, 342–343
- Deuterium-tritium (D-T) solid-layer single-shell fusion target, 76, 422–424, 423f, 424f
- Deutsches Institut für Normung e.V. (DIN), 163
- 1-D gauging systems, CT scanning with, 250–252; *see also* [3-D computed tomography](#)
- Differential scattering, 83
- Diffraction optics microscopes, 409, 410–413, 411f, 412f, 413f
- Diffraction system, x-ray
checked luggage, inspection, 478, 480, 480f
overview, 386–388, 387f
topography, 392–393, 393f
- Diffuse reflection, 99
- Diffraction, 106–108; *see also* [X-ray phase effects](#)
- Digital detector, 119f
- Digital radiograph, 45f
- Digital radiography (DR), 9, 122
of art and objects of cultural significance, 459, 460, 462–465
Kongo Risiki, statue of, 460, 462f
Michelangelo Buonarroti's statue of David, concerns with, 462–465, 463f, 464f, 465f
pictures of period furniture, 460, 461f
Tamon Ten statue, 462f, 466
- artifacts in, 271–275, 272t
carry-on luggage, inspection, 472–474, 472f, 473f, 474f
checked luggage, inspection, 478, 480, 480f
data analysis and interpretation, 279–284
data processing of digital radiographic image data, 271
DR/CT acquisition and use of Φ_0 image, 270
- DS targets, characterization, 451f, 452, 452f
fundamental properties of, 329
image calibration/ Φ_0 measurement, 267–270
imaging performance for, 338
40 mm grenades, 417–418, 418f
phantoms/test objects/IQI, 276–279
physical structure of digital radiographic detectors about, 261–262, 262t
area-detector arrays, 264–267
linear detector arrays (LDA), 263–264
single-detector systems, 262–263
- of pitot tubes, aviation safety, 427, 428, 430f, 431f
source-spot blur for, 336
spatial resolution for, 336
transmission imaging, 339
- Digital radiography (DR)/computed tomography (CT) system configuration, 262t
- Digital radiography (DR)/CT acquisition/processing/control/display
about, 229–230
computer requirements for DR/CT processing, 232
computers for CT data acquisition, 231–232
computers for CT reconstruction, 232–234
data sets, size of, 230
display of CT data, 234–235
on screen/interactive tools of value for CT, 230–231
- Digitization noise, 340
- Dimensional measurement, 283
tools, 326
- Direct-detection flat panels, 201; *see also* [Radiation detectors](#)
- Direct detectors, 41
- Dirty bombs, defined, 471
- Discharge tube, 75
- Discrete ordinates method, 116; *see also* [Radiation transport simulation](#)
- Discrimination, high-Z material
dual-MeV radiography for, 419, 420–422, 421f, 422f, 422t
- Display of CT data, 234–235
- Distance, as radiation protection method, 153
- Domestic nuclear detection office (DNDO), 419, 420, 470, 487, 490
- Dose equivalent, 137; *see also* [Radiation dosimetry/safety/shielding](#)
- Dosicard dosimeter, 146f
- Double-shell (DS) laser ICF targets, 449, 450, 451f, 452, 452f
- Double-shell (DS) target, 8, 9
- DS (double-shell) laser ICF targets, 449, 450, 451f, 452, 452f
- Dual energy
dual-MeV radiography, for high-Z material discrimination, 419, 420–422, 421f, 422f, 422t
for effective-atomic number, 369–377
high-energy, 374–377, 375f, 376f
low-energy, 370–374, 371t, 372f, 373f, 374t
physical basis for multiple-energy applications, 370–377
radiography, for cargo NII, 487–492, 488f, 489f, 490f, 491f, 492f
- Dye penetrant testing, 18; *see also* [Tracer, NDE methods with](#)
- E**
- Easy-to-obtain desktop computers, 231
- Eddy current testing, 20–21; *see also* [Nondestructive evaluation \(NDE\)](#)
- Edge response function (ERF), 353–354, 354f, 355f, 357, 358, 359
- Edge-spread function (ESF), 353–354, 354f, 356, 357, 358, 359, 360
- Edison, Thomas, 35
- Effective-atomic number, dual energy for, 369–377
high-energy, 374–377, 375f, 376f
low-energy, 370–374, 371t, 372f, 373f, 374t
physical basis for multiple-energy applications, 370–377
- Effective human-equivalent dose, 137–138, 138t; *see also* [Radiation dosimetry/safety/shielding](#)
- Elastomeric O-ring, 49
- Electrical conductivity, 20
- Electrically powered electron accelerators, 151–152
- Electrically powered x-ray sources; *see also* [Radiation sources](#)
electron accelerator-based sources
betatron, 176
electrostatic generator, 175
linac, 176–177
synchrotron x-ray source, 175–176
- laser-driven x-ray sources
free-electron laser (FEL) x-ray source, 179
K alpha (K_{α}) x-ray sources, 179
- Thomson/inverse compton scattering x-ray source, 179–182

- pulsed sources
 - about, 177–178
 - accelerators as pulsed sources, 178
 - plasma x-ray sources, 179
 - pulsed x-ray tube, 178
 - x-ray tubes
 - common design elements/subsystems of x-ray tubes, 161–169
 - x-ray tube configurations/tube-like sources, 169–174
 - Electric Power Research Institute (EPRI), 4
 - Electromagnetic acoustic transducers (EMAT), 16
 - Electromagnetic (EM) energy, 6
 - Electromagnetic radiation, 57, 70
 - Electromagnetic (EM) radiation methods; *see also Nondestructive evaluation (NDE)*
 - about, 9–10
 - Gigahertz-Terahertz waves (microwaves/millimeter waves), 14–16
 - optical testing with visible photons, 10–12
 - thermal or infrared (IR) imaging, 12–13
 - Electromagnetic spectrum, 74f
 - Electromagnets, 18
 - Electron, 55n
 - Electron accelerator-based sources; *see also Electrically powered x-ray sources*
 - betatron, 176
 - electrostatic generator, 175
 - linac, 176–177
 - synchrotron x-ray source, 175–176
 - Electron accelerators, 25
 - Electronbeam CT (EBCT), 291
 - Electron binding energies, 65n, 83
 - Electron capture (EC), 67
 - Electronic wave, 58
 - Electron microscopes, 394t, 395
 - Electron probability function, 62f
 - Electrons, 27
 - Electrons and x-ray radiation generation; *see also High-energy photons, types of*
 - about, 57–62, 60t
 - accelerating charge, 65
 - Bremsstrahlung (braking or decelerating electrons), 62–64
 - characteristic x-rays, 64–65
 - Electrostatic generator, 175; *see also Electron accelerator-based sources*
 - End-window x-ray tubes, 218
 - Energy conservation, 65
 - Energy dependence, 116
 - Energy-discriminating detectors, 262f
 - Energy discrimination, 191
 - Energy distribution, 122
 - Energy of incident photon, 77
 - ESTAR (computer program), 177
 - Etched-grid image, 275
 - European Synchrotron Radiation Facility (ESRF), 109, 409
 - Explosive detection system (EDS), 474–478, 474f, 475f, 476f, 477f, 478f, 479f
 - Explosives
 - checked luggage, inspection, 474–478, 474f, 475f, 476f, 477f, 478f, 479f
 - liquid explosive threats, XDi for, 471
 - LX-17 HEs, characterization of, 428, 429, 430, 432, 432f, 433f, 434f, 435f
 - military/commercial/homemade, 471
 - plastic-bonded, 428, 429, 430, 432
 - scanners, 386–388, 387f, 472–474, 472f, 473f, 474f
 - Exposure, 136
 - devices, 154, 154n
 - External radiation dose, 153; *see also Radiation protection*
 - External reflection, 97, 98
- F**
- False positive rate (FPR), calculation, 365–366, 367
 - Fan-beam collimated x-ray source, 214f
 - Fan-beam geometry CT scanning, 253
 - Farmelo, Graham, 32, 32n
 - Feldkamp (FDK) 3D cone-beam algorithm, 299, 318
 - Ferromagnetic material, 19f
 - Fiber-optic scintillator, 195
 - Film, 193; *see also Radiation detectors*
 - Film badge dosimeters, 145
 - Film for medical usage, 25
 - Film waste, 193
 - Φ_0 image, use of, 270
 - Finite-element analysis (FEA), 234
 - Finite-element mesh models, 117
 - Finite-element method (FEM), 234
 - Fixed-scanning envelope systems, 245
 - Flash radiography, 177
 - Flash-radiography tubes, 178
 - Flat detectors, 264
 - Flat-panel CMOS x-ray area arrays, 200
 - Flat-panel imaging detectors, 25, 41
 - Flat-panel photodiode array detectors, 126, 128–130; *see also Photon transport simulations, example*
 - Fluorescence, 81
 - Auger effect and, 81
 - Fluorescent yield, 81
 - Φ_0 measurement, 267–270
 - FORTRAN code, 125
 - 40 mm grenades, DR of, 417–418, 418f
 - Forward imaging, 386–392
 - baggage inspection system, 386–389, 387f, 389f
 - coherent or Rayleigh, 386–392
 - concealed items underneath clothing, detection, 390–391, 390f, 391f
 - explosives in airline baggage, detection of, 386–389, 387f
 - Fourier slice theorem, 296–297
 - Φ_p , properties of, 211–212; *see also Signal (detected) in x-ray imaging, sources of*
 - Fraunhofer Institute for Nondestructive Testing (Germany), 4
 - Free charged particle, 65
 - Free-electron laser (FEL) x-ray source, 179; *see also Laser-driven x-ray sources*
 - Fresnel–Kirchhoff diffraction, 110
 - Fresnel zone plates
 - diffraction optics microscopes, 410–411, 411f, 412f
 - refractive lens microscopes, 408
 - Fuel pumps
 - automotive, 441, 441f, 442f
 - cell pump, NASA, 445, 447f
 - Fujifilm, 201
 - Full-irradiance image, 268

G

Gadolinium metal foil, 497
Gadolinium oxysulfide (GOS), 195, 197f
scintillating screen, 123
scintillator, 417, 456, 498
Gain-correction factor, 268
Gantry security CT systems, nonrotating, 480–484
overview, 480–481
Rapiscan, 482, 483f
SureScan system, 481, 481f, 482f
XinRay laboratory prototype, 482, 484, 484f, 485f
Gap radiographs, 52f
Gauging, x-ray, 415
Gaussian distributions, MTFs and, 356, 357, 358f
Geiger-Müller counter, 140–143; *see also Radiation dosimetry/safety/shielding*
GEMINI 6040 dual-energy x-ray radiography, 473, 474f
Generator, 164
Genetic damage, 136
GE Security, 475, 480
GE-v-to-me, 325
Gigahertz (GHz)-Terahertz waves, 14–16;
see also Electromagnetic radiation methods
Glass scintillators, 194–195, 196t
Global Nuclear Detection Architecture, 487
Graded collimation, 220, 220f
Granular composite scintillators, 195
Graphics processing chips (GPU), 233
 γ -ray, defined, 66
 γ -ray imaging, 6–9; *see also Nondestructive evaluation (NDE); X-ray and γ -ray imaging*
 γ -ray irradiance, 262f
Grenade launcher, 40 mm, 417–418, 418f
Ground state, 64
Guns, inspecting carry-on baggage/luggage, 390–391,
390f, 391f, 472–474, 472f, 473f, 474f

H

HADES, radiographic simulation code, 119–112;
see also Ray tracing
HADES proton radiographic simulations, 130–132
Half-life of radioisotope, defined, 69, 148n
Half-value layer (HVL), 135, 155, 155f, 156t
see also Shielding
Half-wave rectified system, 164
Half-wave rectified waveform, 164
Hamamatsu transmission-anode x-ray tube, 171
Heat transport, 162
Heel effect, 168–169, 169f, 218; *see also X-ray tubes*
Helical cone-beam scanning, 299–300
Helical CT, 290
Helium detectors, 20
High-energy density physics (HEDP) research, ICF and,
422–423
High-energy dual-energy technique, 374–377, 375f, 376f
High-energy photon applications, 415–492
1D applications, 415–417, 416f
2D applications, 417–424
automatic transmission, 418–419, 419f, 420f
dual-MeV radiography for high-Z material
discrimination, 419, 420–422, 421f, 422f,
422t

40 mm grenades, DR of, 417–418, 418f
phase contrast radiography of D-T solid-layer
single-shell fusion target, 422–424, 423f, 424f
3D applications, 424–469
advanced ablator materials, NASA, 442–445, 443f,
444f
automotive, 432–441
aviation safety, DR and CT of pitot tubes, 427, 428,
430f, 431f
CT of structures, by additive manufacturing,
466–469, 466f, 467f, 468f, 469f
CT of WDU-17/B conventional warhead, 453–455,
453f, 454f, 455f
DoD ordnance, CT and tomosynthesis of, 452–457
DR and CT of art and objects of cultural
significance, 459, 460, 461f, 462–465, 462f,
463f, 464f, 465f
DS laser ICF targets, 449, 450, 451f, 452, 452f
exploring limits of MeV imaging, 9 MV and
15 MV linacs, 445, 448f, 449, 449f, 450f
fuel pump, 441, 441f, 442f
inspection of joinery, 425, 426–427
LoTRT targets, 424–425, 425f, 426f
LX-17 HEs, characterization, 428, 429, 430, 432,
432f, 433f, 434f, 435f
metal castings, 434, 435–440, 435f, 436f, 437f,
438f, 439f
metal weldment, 426, 427f
MF, CT and tomosynthesis of, 455–457, 456f,
457f
Michelangelo Buonarroti's statue of David,
concerns with, 462–465, 463f, 464f, 465f
NASA fuel cell pump, diagnosis of failure, 445, 447f
planetary transmission gear assembly, 440, 441f
rocket booster nozzle, NASA, 445, 446f
space hardware, NASA, 442–445
Stardust reentry capsule bond, 427, 428f, 429f
tomosynthesis of *Archaeopteryx* fossil, 457–459,
458f, 459f, 460f, 461f
turbomolecular vacuum pumps, 441, 442f
windshield wiper motor, 440, 440f
overview, 415
protecting US, x-ray imaging, 469–492
all ports of entry, 470, 470f
backscatter of passengers, 484, 485–487, 485f,
486f, 487f
CT to inspect checked luggage, 474–478, 474f,
475f, 476f, 477f, 478f, 479f
DHS, 469–470, 472, 474
DoD, 469–470
DR and backscatter to inspect carry-on luggage,
472–474, 472f, 473f, 474f
DR and diffraction to inspect checked luggage,
478, 480, 480f
nonrotating gantry security CT systems, 480–484
overview, 469–472, 469f, 470f, 471f
radiography and backscatter for cargo NII,
487–492, 488f, 489f, 490f, 491f, 492f
Rapiscan nonrotating gantry CT system, 482, 483f
SureScan nonrotating gantry CT system, 481, 481f,
482f
terrorist attacks, 469, 469f
threat vectors in civil aviation, 471, 471f
TSA, 470–471, 472, 474, 484, 486

- XinRay laboratory prototype nonrotating gantry
 CT system, 482, 484, 484f, 485f
- High-energy photon (x-ray/γ-ray) interactions with matter
 attenuation and phase contrast
 about, 73–76
 attenuation, see [Attenuation interactions](#)
 attenuation measurement units
 atomic attenuation coefficient, 88–89
 attenuation coefficients, relationship, 90
 linear attenuation coefficient, 86–88
 mass attenuation coefficient, 88
 mixture rule, 90–92
 molar attenuation coefficient, 90
 total attenuation/x-ray and γ-ray attenuation
 phenomena, 92–96
- reflection, 96–99
- x-ray phase effects
 about, 99–101
 diffraction, 106–108
 refraction, 102–105
 x-ray phase-contrast radiography, 108–112
- High-energy photons, types of
 annihilation radiation generation, 70
 characterizing and describing, 70–72, 71t
 electrons and x-ray radiation generation
 about, 57–62, 60t
 accelerating charge, 65
 Bremsstrahlung (braking or decelerating electrons), 62–64
 characteristic x-rays, 64–65
 nucleus and γ-ray/x-ray generation, 66–69
 overview, 55–57
- High explosives (HEs), LX-17, 428, 429, 430, 432, 432f, 433f, 434f, 435f
- High-purity Ge (HPGe) detector system, 378, 379f, 382f, 387f
- High-purity germanium (HPGe), 191, 262
 detector, 123
- High-voltage power supply, 164; *see also X-ray tubes*
 waveforms, 164–165
- High-Z material discrimination, dual-MeV radiography
 for, 419, 420–422, 421f, 422f, 422t
- High-Z materials for collimator, 206
- Hounsfield unit (HU), 40
- Human absorbed dose, sources of; *see also Radiation dosimetry/safety/shielding*
 man-made radiation absorbed dose
 about, 149
 marketing radiation dose, 150
 mining legacy, 150–151
 occupational dose limits, 150
 natural background radiation
 about, 147, 147f
 cosmic radiation, 149
 radioisotopes in food/beverages, 148–149
 radon, 147–148
 terrestrial x and γ radiation, 148
- Human risk from low effective human-equivalent dose, 140
- Huygens–Fresnel principle, 96
- Hydrodynamic shock, 130
- I**
- IDL, 326
- Image calibration, 267–270
- Image intensifiers (II), 275
- Image modification, 230
- Image quality, 329–368
 contrast
 components, 332–335, 333f, 334f
 measuring components, 345–348, 346f, 347f, 347t, 348f
 overview, 329–330
 indicators/test objects, role, 330
 measurement of, 329
 MTFs, 348–360
 ASTM approach, 359–360
 comparison of scintillator screens, 359
 convolution of step and blur functions, 356, 356f, 357, 357f
 ERF, 353–354, 354f, 355f
 ESF, 353–354, 354f
 for feature sizes, 352–353
 Gaussian distributions and, 356, 357, 358f
 high-spatial resolution imaging system, 354–356, 355f
 images and line-outs showing impact, 349–350, 349f
 line-pair gauge, 350–352, 350f, 351f, 357, 358
 measurement, 352–360, 354f, 355f, 356f, 357f, 358f
 for operation of lens, 349
 for scintillators, 337, 338f
 spatial invariance, 358–359
 overview, 329–332
 photon statistics, 342–345
 probability of detection and ROC curves, 365–368, 366f, 367f
 properties, 329
 SNR and DQE, 360–365
 measurement, 361–365
 Rose model, 361–362, 361f, 364
 spatial frequency, 364
 spatial resolution, omission of, 364
 step wedges, 362–364, 362f, 363f, 363t
 spatial resolution, components, 335–339, 336f, 338f
 tools for assessing, 330
 transmission image noise, components of, 339–341, 341f
 X-ray transmission artifacts, 341–342
- Image quality indicators (IQI), 276–279; *see also Digital radiography (DR)*
- Image reconstruction, 251f
- Image zoom tools, 231
- Imaging system components
 antiscatter grids, 222–224
 apertures, limiting, 224–226
 DR/CT acquisition/processing/control/display
 about, 229–230
 computer requirements for DR /CT processing, 232
 computers for CT data acquisition, 231–232
 computers for CT reconstruction, 232–234
 data sets, size of, 230
 display of CT data, 234–235
 on screen/interactive tools of value for CT, 230–231
- object positioning and control, staging for, 226–229
- overview, 203–204
- shielding and collimation
 about, 217–218
 collimator, 218–222

- signal (detected) in x-ray imaging, sources of about, 204–211
background or system scatter, Φ_{sbk} , properties of, 212–213
 Φ_p , properties of, 211–212
object scatter Φ_{obj} , properties of, 213
x-ray scatter corrections/subtleties of radiographic imaging, 214–217
- Imaging-system configurations
3-D computed tomography
about, 248–250
with area-detector arrays, 256–258
with 1-D gauging systems, 250–252
with linear-detector arrays, 252–256
1-D x-ray gauging systems, 238–241
overview, 237–238
radiography systems
with area-detector array, 246–248
with a linear-detector array, 241–246
- Incident irradiance, 293
- Incident ray, 98, 104
- Inclusions, 47
- Incoherent (compton) scatter, 82–84
- Incoherent scattering, 207; *see also Compton scattering*
- Inconel 625, composition, 502, 503t
- Index of refraction, 108
- Indirect detection flat panels, 201–202; *see also Radiation detectors*
- Indirect detectors, 41
- Industrial computed tomography, 40–41; *see also X-ray history*
- Industrial film, 25
- Industrial x-ray imaging contrasted with medical x-ray imaging, 24–25
- Inert heavy gas, 20
- Inertial confinement fusion (ICF)
DS laser ICF targets, 449, 450, 451f, 452, 452f
HEDP research and, 422–423
- Infrared (IR) imaging, 12–13; *see also Electromagnetic radiation methods*
- Inherent filtration, 164, 166, 166n
- Inline EDS deployment, 475, 477f
- In-service NDE of aerospace structures, 5–6
- In-Space Propulsion Technology (ISPT) Program, 443, 444f
- Inspection
cargo NII, radiography and backscatter for, 487–492, 488f, 489f, 490f, 491f, 492f
carry-on luggage, x-ray DR and backscatter, 472–474, 472f, 473f, 474f
checked luggage, x-ray CT, 474–478, 474f, 475f, 476f, 477f, 478f, 479f
of joinery, 425, 426–427
metal weldment, 426, 427f
Stardust reentry capsule bond, 427, 428f, 429f
- Intensifying screens, 193
- Interactive image enhancement techniques, 230
- Interferometric optical inspection methods, 11
- Internal radiation dose, 152; *see also Radiation protection*
- Internal reflection, 97
- International Commission on Radiological Protection (ICRP), 137
- Intrinsic contrast, 332–334, 333f, 334f
- Inverse Compton scattering x-ray source, 179
- Inverse geometry, 173
- InVision Technologies, Inc., 475
- Ionization chamber radiation meter, 143–145, 144f; *see also Radiation dosimetry/safety/shielding*
- Ionizing radiation, 57
- Ion microbeam tomography (IMT), 504
- Ion saturation, 143
- IQI, *see Image quality indicators*
- Irradiance, 59, 63f, 71, 121
defined, 361
- Irradiation, 136
- Isotope measurements by passive and active computed tomography (IMPACT), 378, 379f
- J**
- JAMDAN, 445, 448f, 449, 449f
- Joinery, inspection of, 425, 426–427
metal weldment, 426, 427f
Stardust reentry capsule bond, 427, 428f, 429f
- Joint Integrated Non-Intrusive Inspection (JINII) program, 419
- K**
- K alpha (K_α) x-ray sources, 179; *see also Laser-driven x-ray sources*
- Katsevich-type data acquisition, 300
- KCAT, 424
- K-characteristic radiation, 65
- Kel-F, plastic binder, 428, 429–430, 432, 433f
- Kinetic energy, 62n
- Kirkpatrick–Baez (KB) reflection optics microscopes, 400–401, 401f, 402f
- Klein–Nishina formula, 84
- Klystrons, 176
- Knives, inspecting carry-on baggage/luggage, 390–391, 390f, 391f, 472–474, 472f, 473f, 474f
- Kongo Risiki, statue of, 460, 462f
- L**
- Laboratory prototype nonrotating gantry CT system, XinRay, 482, 484, 484f, 485f
- Lambertian sources, 172
- Laminography, defined, 380
- Lanex Fine, scintillator-based detector, 333, 334f
- Laser-driven x-ray sources; *see also Electrically powered x-ray sources*
free-electron laser (FEL) x-ray source, 179
K alpha (K_α) x-ray sources, 179
Thomson/inverse compton scattering x-ray source, 179–182
- Laser synchrotron radiation, 180
- Laue version of diffraction, 106
- Lawrence Berkeley National Laboratory (LBNL), 371, 372, 429
- Lawrence Livermore National Laboratory (LLNL), 4, 294
achieving 16 million pixel radiographs, 192
bad pixel, 266
camera-lens-scintillator configurations, 337
CCAT system, 466, 466f
CT of WDU-17/B conventional warhead, 453, 453f
CT scanners, 373, 443, 476, 478f, 479f

- development of HADES, 119
 DR/CT for inspection of David, 463, 464, 464f, 465f
 dual-MeV radiography, 420–422
 KCAT, 424
 LLNL-TPORT code, 370
 LX-17 HEs, characterization, 428, 432f
 MV linac at, 445, 446f
 NIF, 398, 422–423, 449
 nondestructive evaluation group at, 499
 TART/COG/Peregrine/MERCURY Monte Carlo Codes, 125
 tomosynthesis of *Archaeopteryx* fossil, 457, 458, 458f
 training document, 139f
 waste drum nondestructive radioactive assay problem, 378
 Wölter x-ray microscope, 404, 405, 406f
 Xradia MicroXCT system at, 425
 L-3 CAARS prototype, 490
 L-characteristic radiation, 65
 Leak testing, 20; *see also* [Tracer, NDE methods with](#)
 Leidos (SAIC), 475, 488–490, 489f, 490f
 Lenard, Philipp E. von, 29
 Lenard tube, 29
 Life cycle management, NDE to, 6
 Linac, 176–177; *see also* [Electron accelerator-based sources](#)
 Linac Coherent Light Source (LCLS), 179
 Linear-array detectors, spatial resolution for, 337–338, 339
 Linear-array x-ray detectors, 253
 Linear attenuation coefficients, 86–88, 197; *see also* [Attenuation measurement units](#)
 Linear computed axial tomography (LCAT), 242, 243
 Linear detector arrays (LDA)
 CT scanning with, 252–256; *see also* [3-D computed tomography](#)
 in digital radiography, 263–264; *see also* [Digital radiography \(DR\)](#)
 radiography systems with, 241–246
 Linear detectors, 191–193; *see also* [Radiation detectors](#)
 Linear energy transfer (LET), 136–137, 147f
 Linear no-threshold (LNT) model, 139–140; *see also* [Radiation effects in humans](#)
 Line integral, 110n
 Line-out extraction tool, 231
 Line-pair gauge
 features in, 357
 line-out from radiograph, 351–352, 351f
 manufacturing, 350–351, 350f
 MTF, calculating, 358
 x-ray image, 351, 351f
 Liquid-anode x-ray tube, 174; *see also* [X-ray tubes](#)
 Lithium-drifted silicon detector (SiLi), 416, 417
 LLNL, *see* [Lawrence Livermore National Laboratory \(LLNL\)](#)
 Local noise measurement, 278
 Los Alamos National Laboratory (LANL), 9, 116
 Los Alamos National Laboratory (LANL) Monte Carlo N-Particle (MCNP) Code, 124–125
 Low effective human-equivalent dose, 140
 Low-energy dual-energy techniques, 370–374, 371t, 372f, 373f, 374t
 Low-temperature Raleigh–Taylor target (LoTRT)
 3D application, 424–425, 425f, 426f
 defined, 423
 Luggage, inspection, 386–388, 387f, 472–474, 472f, 473f, 474f
 LX-17 HEs, characterization of, 428, 429, 430, 432, 432f, 433f, 434f, 435f
- ## M
- Magnaflux, 18n, 19f, 51f
 Magnetic particle testing, 18–19; *see also* [Tracer, NDE methods with](#)
 Magnetrons, 176
 Mammography, 23, 25
 Man-made radiation absorbed dose; *see also* [Human absorbed dose, sources of](#)
 about, 149
 marketing radiation dose, 150
 mining legacy, 150–151
 occupational dose limits, 150
 Marketing radiation dose, 150; *see also* [Man-made radiation absorbed dose](#)
 Mass attenuation coefficient
 about, 88; *see also* [Attenuation measurement units](#)
 of aluminum, 94f
 of carbon, 93f
 of iron, 95f
 thermal neutron, 495, 496f
 Mass density, 110n
 Mass vs. linear attenuation coefficient, 90
 Material discrimination, high-Z
 dual-MeV radiography for, 419, 420–422, 421f, 422f, 422t
 MATLAB, 326
 Maxwell's equations, 57
 McClellan Nuclear Research Center (MNRC), 272, 499
 MCNP, *see* [Monte Carlo N-Particle \(MCNP\)](#)
 Measurement
 of dimension, 282–283
 DQE, 361–365
 image contrast, components, 345–348, 346f, 347f, 347t, 348f
 MTFs, 352–360, 354f, 355f, 356f, 357f, 358f
 SNR, 361–365
 Medical film, 25
 Medical x-ray imaging, industrial x-ray imaging contrasted with, 24–25
 Medium-frequency power supply, 164
 Medium- to high-energy techniques, 256
 Megaelectron volt (MeV)
 dual-MeV radiography, for high-Z material discrimination, 419, 420–422, 421f, 422f, 422t
 imaging
 exploring limits, 445, 448f, 449, 449f, 450f
 with MeV neutrons, 504
 with MeV protons, 504–505
 Megaelectron volt protons, 116
 Mercaptan, 20
 MERCURY (Monte Carlo code), 125
 Message passing interface (MPI), 233
 Metal castings, 434, 435–440, 435f, 436f, 437f, 438f, 439f
 Metal-ceramic x-ray tube, 169–170; *see also* [X-ray tubes](#)
 Metal welding, 426, 427f
 MeV (megaelectron volt)
 dual-MeV radiography, for high-Z material discrimination, 419, 420–422, 421f, 422f, 422t

- imaging
exploring limits, 445, 448f, 449, 449f, 450f
with MeV neutrons, 504
with MeV protons, 504–505
- MFF (multifunction fuze), CT and tomosynthesis of, 455–457, 456f, 457f
- Michelangelo Buonarroti's statue of David, concerns with, 462–465, 463f, 464f, 465f
- Microfocus tubes, 162
- Microfocus x-ray source, 41
- Microfocus x-ray tube, 173; *see also X-ray tubes*
- Micropower impulse radar (MIR), 14, 16f
- Microscopy, x-ray, 393–413
advantages, 394
diffraction optics microscopes, 409, 410–413, 411f, 412f, 413f
overview, 393–395
pinhole, 395–398, 396f
reflection optics microscopes, 399–407
critical angle for, 399, 399f
efficiency of gold surface, 400, 400f
Kirkpatrick–Baez, 400–401, 401f, 402f
overview, 399–400
Wölter objective, 401, 402–407, 403f, 404f, 405f, 406f, 407f
- refractive lens microscopes, 408–409, 409f, 410f
types, comparison of, 394, 394t
- Microwaves, 14–16; *see also Electromagnetic radiation methods*
- MicroXCT system, Xradia, 425, 425f, 452
- Military ordnance, CT and tomosynthesis, 452–457; *see also Ordnances*
- Millimeter waves, 14–16; *see also Electromagnetic radiation methods*
- Min-D filter, 272
- Mineta, Norman, 470, 471
- Mining legacy, 150–151; *see also Man-made radiation absorbed dose*
- Minislabs, rectangular embedded, 345–348, 346f, 347f, 347t
- Mixture rule, 90–92; *see also Attenuation measurement units*
- Mobile waste inspection trailer, 378, 381f
- Modulation transfer functions (MTF), 44, 281, 287, 348–360
ASTM approach, 359–360
comparison of scintillator screens, 359
convolution of step and blur functions, 356, 356f, 357, 357f
ERF, 353–354, 354f, 355f
ESF, 353–354, 354f
for feature sizes, 352–353
Gaussian distributions and, 356, 357, 358f
high-spatial resolution imaging system, 354–356, 355f
images and line-outs showing impact, 349–350, 349f
line-pair gauge, 350–351, 350f
features in, 357
line-out from radiograph, 351–352, 351f
manufacturing, 350–351, 350f
MTF, calculating, 358
x-ray image, 351, 351f
- measurement, 352–360, 354f, 355f, 356f, 357f, 358f
for operation of lens, 349
for scintillators, 337, 338f
spatial invariance, 358–359
- Molar attenuation coefficient, 90; *see also Attenuation measurement units*
- Monochromatic light, 11f
- Monoenergetic γ -ray (MEGa-ray) source, 181
- Monoenergetic x-rays, 87, 130f
- Monte Carlo method; *see also Radiation transport simulation*
LANL Monte Carlo N-Particle (MCNP) code, 124–125
LLNL-TART/COG/Peregrine/MERCURY Monte Carlo Codes, 125
overview, 122–124, 124t
- Monte Carlo N-Particle (MCNP); *see also Radiation transport simulation*
in albedo from lead and concrete, 125–126
to collimator design for 9 MV linac, 126–128
for scatter blur determination, 128–130
- Monte Carlo radiation transport codes, general purpose, 124t
- Morpho Detection, 475, 476f, 478, 480, 480f
- Motion control hardware, 226
- MTFs, *see Modulation transfer functions (MTF)*
- Multiframe-per-view image acquisition, 272
- Multifunction fuze (MFF), CT and tomosynthesis of, 455–457, 456f, 457f
- Multi-modal passive detection system (MMPDS), 490, 492
- Multiple-energy applications, physical basis for, 370–377
high-energy, 374–377, 375f, 376f
low-energy, 370–374, 371t, 372f, 373f, 374t
- Multiple-gain corrections, 268
- Multiple-gain pixel response fit routines, 269
- Multispectral x-ray tube sources, 211
- N**
- National Academy of Sciences (NAS), 140
- National Aeronautics and Space Administration (NASA)
space hardware, 442–445
advanced ablator materials, 442–445, 443f, 444f
fuel cell pump, diagnosis of failure, 445, 447f
rocket booster nozzle, 445, 446f
- National Bureau of Standards (NBS), 4
- National Ignition Facility (NIF), 398, 422–423, 449
- National Institute for Advanced Interdisciplinary Research (Japan), 4
- National Institute of Standards and Technology (NIST), 4, 92, 177
- National Science Foundation, 457
- Natural background radiation; *see also Human absorbed dose, sources of*
about, 147, 147f
cosmic radiation, 149
radioisotopes in food/beverages, 148–149
radon, 147–148
terrestrial x and γ radiation, 148
- Naval Weapons Station, 456, 456f
- Negative electrode, 27
- Negative predictive value (NPV), 21–23; *see also Nondestructive evaluation (NDE)*
- Neutron, 58, 66
- Neutron and proton imaging, 495–505
MeV neutrons, 504
MeV protons, 504–505
overview, 495
thermal neutrons, 495–504
accelerators, 496
boron, addition, 499, 499f
Buna N, composition, 502, 503t

- ²⁵²Cf source, 496, 497f
 collimation, 496, 497f
 corn rootworms, study of, 501, 502f
 CT radiographs, 499, 501f
 detection of corrosion in aircraft, 499
 detectors, 497–499, 498t
 flange configuration, 501, 502, 503f
 Inconel 625, composition, 502, 503t
 kinked O-ring, 499, 501f
 mass attenuation coefficients, 495, 496f
 nuclear reactors, 495
 photodiode arrays, 498
 PSP for, 497–498
 sources for, 495, 496
 XRF, 499, 500f
- Neutron imaging, 272
- Neutrons, 116
- Newton rings, 11
- 9/11 terrorist attacks, 469, 470, 487
- Noise
- digitization, 340
 - electronic, 340
 - sources of, 340
 - in transmission images, components, 339–341, 341f
- Nondestructive characterization (NDC), 1–6
- military ordnance, 452–457
 - use of, 419, 420
- Nondestructive evaluation (NDE), 128
- acoustic energy, using
 - acoustic emission, 17–18
 - ultrasonic testing, 16–17
 - Eddy current testing, 20–21
 - effectiveness and statistics of
 - positive predictive value/negative predictive value, 21–23
 - probability of detection, 21
 - receiver operating characteristic curve (ROC), 23–24
 - electromagnetic radiation methods
 - about, 9–10
 - Gigahertz–Terahertz waves (microwaves and millimeter waves), 14–16
 - optical testing with visible photons, 10–12
 - thermal or infrared (IR) imaging, 12–13
 - history of NDE/NDT/NDC, 1–6
 - industrial x-ray imaging contrasted with medical x-ray imaging, 24–25
 - to life cycle management, 6
 - necessity of, 24
 - using tracer
 - dye penetrant testing, 18
 - leak testing, 20
 - magnetic particle testing, 18–19
 - x-ray and γ -ray imaging, 6–9
 - x-ray tube and, 169
- Nondestructive inspection (NDI), 1
- Nondestructive testing (NDT), 1–6
- of military ordnance, 452–457
- Nondestructive Testing Centre Atomic Energy Establishment (England), 4
- Nonintrusive inspection (NII), 1
- Nonintrusive inspection (NII), cargo
- radiography and backscatter for, 487–492, 488f, 489f, 490f, 491f, 492f
- Nonrotating gantry security CT systems, 480–484
- overview, 480–481
- Rapiscan, 482, 483f
- SureScan system, 481, 481f, 482f
- XinRay laboratory prototype, 482, 484, 484f, 485f
- Nuclear and radiological imaging platform (NRIP), 487, 490, 492, 492f
- Nuclear energy production, 149
- Nuclear medicine techniques, 149
- Nuclear reactors, source of thermal neutrons, 495
- Nuclear Regulatory Commission (NRC), 150
- Nucleus and γ -ray/x-ray generation, 66–69; *see also High-energy photons, types of*
- Nyquist–Shannon rule, 353
- ## O
- Object contrast, 332–334, 333f, 334f
- Object positioning and control, staging for, 226–229; *see also Imaging system components*
- Object scatter
- impact of, 334–335, 336
 - presence, 334
 - proportions of, 358
 - on spatial resolution, 336
- Object scatter Φ_{subj} , properties of, 213; *see also Signal (detected) in x-ray imaging, sources of*
- Observation of feature/noise, 282
- Occupational dose limits, 150; *see also Man-made radiation absorbed dose*
- Offset counts, 263
- Offset-gain corrections, 271
- Offset scan, 292
- One-dimensional applications, high-energy photon, 415–417, 416f
- 1-D x-ray gauging systems, 238–241; *see also Imaging-system configurations*
- Optical fluorescence, 11; *see also Optical testing with visible photons*
- Optical interferometric NDE methods, 11–12; *see also Optical testing with visible photons*
- Optically clear scintillators, properties of, 196t
- Optical testing with visible photons; *see also Electromagnetic radiation methods*
- candling, 10
 - optical fluorescence, 11
 - optical interferometric NDE methods, 11–12
- Optics, x-ray, 393–413
- diffraction optics microscopes, 409, 410–413, 411f, 412f, 413f
 - overview, 393–395
 - pinhole, 395–398, 396f
 - reflection optics microscopes, 399–407
 - critical angle for, 399, 399f
 - efficiency of gold surface, 400, 400f
 - Kirkpatrick–Baez, 400–401, 401f, 402f
 - overview, 399–400
 - Wöltjer objective, 401, 402–407, 403f, 404f, 405f, 406f, 407f
 - refractive lens microscopes, 408–409, 409f, 410f
- Ordnances, DoD
- CT and tomosynthesis of, 452–457
 - MFF, 455–457, 456f, 457f
 - WDU-17/B conventional warhead, 453–455, 453f, 454f, 455f

P

- Pair production, 85; *see also* [Attenuation interactions](#)
Panel detectors, 231
Parallel-beam reconstruction, 252
Passengers, x-ray backscattered imaging of, 484, 485–487, 485f, 486f, 487f
Passive and x-ray imaging scanning (PAXIS), 487
Passive CT, 377–380, 378f, 379f, 380f, 381f, 382f
Passive detection of radiation, 132
Passive imaging detection techniques, 14
Passive thermography, 12
Pencil-beam collimated x-ray source, 214f
Pencil-Beam Computed Axial Tomography (PBCAT), 191, 238
Penetrometer (penny), 330
Penetrometer-type IQI, 277–278, 277f
Penny (penetrometer), 330
Penumbra, 158, 159f
Penumbral blur, for object, 336, 336f
Peregrine, 125
Perfect detector, 187; *see also* [Radiation detectors](#)
Perkin–Elmer detectors, 337
Perkin–Elmer panel, 268
Personal dosimeter, 145–146; *see also* [Radiation dosimetry/safety/shielding](#)
Phase-contrast radiography, 76
 of D-T solid-layer single-shell fusion target, 422–424, 423f, 424f
Phase-contrast techniques, 100
Phase-contrast x-ray imaging, 103f
Phase lead, 104
Phase-sensitive techniques, 74
Phase shift, 74, 100n, 108
Photodetector, 191
Photodiode arrays, 41
 thermal neutron imaging with, 498
Photodisintegration, 85
Photoelectric absorption, 77–81; *see also* [Attenuation interactions](#)
Photoelectric attenuation, for carbon and tungsten, 370, 373–374
Photoelectric mass attenuation coefficient, 92
Photoelectron, 80
Photofission, 85–86; *see also* [Attenuation interactions](#)
Photographic plates, 30n
Photomultiplier tubes, 191
Photons, 6
 angular distribution, 84
 attenuation, 206f
 characteristics, 55n, 70
 flux density, 64, 64f, 71, 160
 radiation transport, 116
 scattered, 216
 statistics, 342–345
Photon applications, high-energy, *see* [High-energy photon applications](#)
Photoneutron, 122
Photon transport simulations, example; *see also* [Radiation transport simulation](#)
 COG simulation for cargo interrogation, 132–133
 HADES proton radiographic simulations, 130–132
MCNP for scatter blur determination, 128–130
MCNP to collimator design for 9 MV linac, 126–128
MNCP in albedo from lead and concrete, 125–126
Photonuclear absorption, 85; *see also* [Attenuation interactions](#)
Photonuclear interaction of photons, 85
Photopeaks, 67
Photostimulable phosphors (PSP), 193
 for thermal neutron imaging, 497–498
Phototransmutation, 85
PICA, 443
Picosecond Laser-Electron InterAction for the Dynamic Evaluation of Structures (PLEIADES), 180
Pinhole imaging techniques, 224
Pinhole microscope, 395–398, 396f
Pitot tubes, DR and CT of, 427, 428, 430f, 431f
Pixels, 44n
 bad, 272
Planar tomography
 defined, 380
 image, estimating, 380, 382f, 383
Planck's constant, 58, 59, 70, 80
Planetary transmission gear assembly, 440, 441f
Plasma x-ray sources, 179; *see also* [Pulsed sources](#)
Plastic-bonded explosives, 428, 429, 430, 432
Point detection, 191–193; *see also* [Radiation detectors](#)
Point-processing toolbars, 230
Point-processing toolsets, 231
Point-spread function (PSF), 115, 271
Poisson counting processes, 342–343
Poisson probability distribution, 188
Poisson random variables
 CT reconstructed image, 339
 properties, 343–344
Polycrystalline materials, 131n
Polyenergetic source, 87
Polyenergetic spectra, 62
Porosity
 cold crack, 439
 sponge, 439
Positive electrode, 27
Positive electron, 56n
Positive predictive value (PPV), 21–23; *see also* [Nondestructive evaluation \(NDE\)](#)
Positron, 56n, 77
Positron emission tomography (PET), 149, 377–380, 378f, 379f, 380f, 381f, 382f
Post-thermal test vertical CT slice, 443, 444, 444f
Potassium, 148
Potter–Bucky grids, 222
Pre-object collimation, 207
Pre-object (or upstream) collimators, 207, 220
Pressurization, 20
Pre-thermal test vertical CT slice, 443, 444f
Prill, defined, 371
Primary irradiance, 204
Primary photons, 204
Primary radiation, 211
Primary x-ray radiation, 212
Probability of detection (POD), 5, 21, 280; *see also* [Nondestructive evaluation \(NDE\)](#)
 ROC curves and, 365–368, 366f, 367f
Properties
 image quality, 329
 of Poisson random variables, 343–344
 transmission imaging, 329

Proportional-integral-derivative (PID) algorithm, 228
 Proton-induced x-ray emission (PIXE), 504–505
 Protons, 68, 69
 MeV, imaging with, 504–505
 Pulse detection, 191
 Pulsed sources; *see also* [Electrically powered x-ray sources](#)
 about, 177–178
 accelerators as pulsed sources, 178
 plasma x-ray sources, 179
 pulsed x-ray tube, 178
 Pulsed x-ray tube, 178; *see also* [Pulsed sources](#)
 Pulse-echo method, 16
 Pyrotechnic devices, 48

Q

Quality, image, *see* [Image quality](#)

Quality factor, 137

Quantitative nondestructive evaluation (QNDE), 3, 4, 6

Quantum numbers, relationship, 60t

R

Radiant energy, 57

Radiation accidents, 41–42; *see also* [X-ray history](#)

Radiation detectors

- detection principles, 190
- detector technology
 - CCD-based area detectors employing scintillator, 198–200
 - CMOS-based area detectors employing scintillator, 200
 - computed radiography (CR), 193–194
 - direct-detection flat panels, 201
 - film, 193
 - indirect detection flat panels, 201–202
 - scintillators, 194–198
- detector types
 - point/line/area detection, 191–193
 - pulse detection/energy discrimination/integrating detection, 191
 - perfect detector, 187
 - statistical considerations, 188

Radiation dosimetry/safety/shielding

- absorbed dose, 136
- dose equivalent, 137
- effective human-equivalent dose, 137–138, 138t
- human absorbed dose, sources of
 - man-made radiation absorbed dose, 149–151
 - natural background radiation, 146–149
- linear energy transfer (LET)/radiation weighting factor, 136–137
- overview, 135
- radiation effects in humans
 - about, 138–139, 139f
 - linear no-threshold (LNT) model, 139–140
 - risk from low effective human-equivalent dose, 140
- radiation exposure, 136
- radiation exposure/absorbed dose, radiation measurements for
 - Geiger–Müller counter, 140–143
 - ionization chamber radiation meter, 143–145, 144f
 - personal dosimeter, 145–146

radiation protection

- about, 151–152
- external radiation dose, 153
- internal radiation dose, 152
- shielding, 153–155, 155f, 156t

Radiation effects in humans

- about, 138–139, 139f
- linear no-threshold (LNT) model, 139–140
- risk from low effective human-equivalent dose, 140

Radiation exposure, 136

Radiation portal monitors (RPMs), 377

Radiation protection

- about, 151–152
- external radiation dose, 153
- internal radiation dose, 152
- shielding, 153–155, 155f, 156t

Radiation Safety Information Computational Center (RSICC), 116

Radiation sources

- electrically powered x-ray sources
 - electron accelerator-based sources, 175–177
 - laser-driven x-ray sources, 179–182
 - pulsed sources, 177–179
 - x-ray tubes, 161–174
 - perfect source, 157–160
 - radioisotopic x-ray and γ -ray sources, 182–186, 184t
 - source attributes, 160

Radiation therapy, 38; *see also* [X-ray history](#)

Radiation transport simulation

- photon transport simulations, example
 - COG simulation for cargo interrogation, 132–133
 - HADES proton radiographic simulations, 130–132
 - MCNP for scatter blur determination, 128–130
 - MCNP in albedo from lead and concrete, 125–126
 - MCNP to collimator design for 9 MV linac, 126–128
- radiography, simulating, 115
- simulation methods
 - discrete ordinates method, 116
 - Monte Carlo method, 122–125, 124t
 - ray tracing, 117–122, 117f
 - types of radiation, 115–116

Radiation weighting factor, 137

Radioactive decay, 67, 69

Radioactive parent, 67

Radioactivity, discovery of, 36–37

Radiography, 49

- attenuation, defined, 331
- for cargo NII, 487–492, 488f, 489f, 490f, 491f, 492f
- defined, 415
- dual-MeV, for high-Z material discrimination, 419, 420–422, 421f, 422f, 422t
- phase contrast, of D-T solid-layer single-shell fusion target, 422–424, 423f, 424f
- tomosynthesis and, 384, 384f

Radiography systems; *see also* [Imaging-system configurations](#)

- with area-detector array, 246–248
- with a linear-detector array, 241–246

Radioisotopes

- in food/beverages, 148–149; *see also* [Natural background radiation](#)
- harmful use, 36
- radiation source, 41, 151
- and radioisotopic sources for radiography, 184t

- Radioisotopic source transportation, 152
Radiological dispersal devices (RDDs), 470
Radiometric pixels, 293
Radio waves, 10
Radon; *see also* [Natural background radiation](#)
 discovery of home with high levels of, 148
 radioactive gas, 147
RAID arrays, 232
Rapiscan nonrotating gantry security CT system, 482, 483f
Raw (after darkcurrent subtraction) images, 269
Raw-image (after dark-current subtraction) values, 269
Rayleigh scattering, 206, 212, 386–392, 387f, 389f, 390f, 391f
Ray sums, 110
 defined, 286
Ray tracing; *see also* [Radiation transport simulation](#)
 HADES, radiographic simulation code, 119–122
 X-ray simulation (XRSIM), 117–119
Real-time tomography (RTT) system, Rapiscan, 482, 483f
Receiver operator characteristic (ROC) curves, 23–24;
 see also [Nondestructive evaluation \(NDE\)](#)
 estimation of, 386
 probability of detection and, 365–368, 366f, 367f
Rectifiers, 164
Reflected ray, 104
Reflection, 96–99; *see also* [High-energy photon \(x-ray/y-ray\) interactions with matter](#)
Reflection optics microscopes, 399–407
 critical angle for, 399, 399f
 efficiency of gold surface, 400, 400f
 Kirkpatrick–Baez, 400–401, 401f, 402f
 overview, 399–400
 Wölter objective, 401, 402–407, 403f, 404f, 405f, 406f, 407f
Refracted ray, 104
Refraction; *see also* [X-ray phase effects](#)
 about, 102–104
 Snell's law, 104–105
 total external reflection of x-rays, 105
Refractive lens microscopes, 408–409, 409f, 410f
Resolution, spatial, *see* [Spatial resolution](#)
Reverse engineering, 47
Reverse geometry, 173–174, 173f, 174; *see also* [X-ray tubes](#)
Ring-removed sinograms, 458, 459
ROC (receiver-operator-characteristic) curves
 estimation of, 386
 probability of detection and, 365–368, 366f, 367f
Rocket booster nozzle, NASA, 445, 446f
Röntgen (R), 136
Röntgen, Wilhelm (discovery of x-rays), 29–33
Röntgen absorbed dose, 136
Röntgen equivalent man (rem), 137
Röntgenology, 32
Röntgen rays, 32
Röntgen's publication on x-rays, 75
Root mean square (RMS), SNR and, 343
Rose model, for calculating DQE, 361–362, 361f, 364
Ross filtering, 241
Rotating-anode x-ray tubes, 171–173; *see also* [X-ray tubes](#)
Russian Academy of Sciences, 4
- S**
- SAFE Port Act, 487
Safran, 475, 475f, 478
SAIC (Leidos), 475, 488–490, 489f, 490f
SAIC IP6500 FullScan, 490
Sandia National Laboratories (SNL), 9, 443, 444f, 445
Scanning electron microscope (SEM)
 CsI(Tl) grown in columns, 198f
 of fractured Kodak Lanex Fine screen, 197f
Scanning transmission ion microscopy (STIM), 504
Scatter; *see also* [Attenuation interactions](#)
 about, 81–82
 coherent (Rayleigh) scatter, 84–85
 incoherent (compton) scatter, 82–84
Scatter blur determination, 128–130
Scatter contributions, 124
Scattered irradiance, 239
Scattered photons, 204
Scattered radiation, 246
 impact of, 359
Scatter hole, defined, 398
Scattering loss, 77
Scattering method
 coherent or Rayleigh, 386–392
 incoherent or Compton, 386–392
Scatter streaks, defined, 339
Schrödinger, Erwin, 59
Schrödinger wave equation, 59
Scintillating screen, 25
Scintillator-based x-ray detectors, 244
Scintillator(s), 35, 129, 130; *see also* [Radiation detectors](#)
 for area detectors, 337, 338–339
 based detectors, CsI(Tl) and Lanex Fine, 333, 334f
 clear crystals/glass/ceramic scintillators, 194–195
 GOS, 417, 456, 498
 granular composite scintillators, 195
 inherent resolution of, 337–338
 properties of, 337–338
 screens, MTFs for, 337, 338f, 359
 structured scintillators, 195–197
Segmentation, 47
 and volume estimation tools, 326
Segmented gamma scanning (SGS), 377
Self-rectified power supply, 164
Sensitivity, 21, 23
Septa, 241
Servomotor, 227–228
Sharpness, of images, 329–330
Shearography, 12
Shielding; *see also* [Radiation protection](#)
 about, 153–155
 half-value layer (HVL)/tenth-value layer (TVL)
 thickness, 155, 155f, 156f
Shielding and collimation
 about, 217–218
 collimator, 218–222
Shoe-fitting fluoroscopes, 36
Siegbahn designation system, 65
Sievert, 137
Signal (detected) in x-ray imaging, sources of; *see also* [Imaging system components](#)
 about, 204–211
background or system scatter, Φ_{sbk} ; properties of, 212–213

- Φ_p , properties of, 211–212
object scatter Φ_{subj} , properties of, 213
x-ray scatter corrections/subtleties of radiographic imaging, 214–217
- Signal-to-noise ratio (SNR), 267
DQE and, 360–365
measurement, 361–365
Rose model, 361, 361f, 364
spatial frequency, 364
spatial resolution, omission of, 364
step wedges, 362–364, 362f, 363f, 363t
of Poisson random variable, 343
RMS and, 343
- Silicon-based detectors, 340
- Silicon carbide (SiC) crystals, characterization of, 392
- Simulation of radiography, 115
- Single-detector systems, 262–263; *see also* [Digital radiography \(DR\)](#)
- Single-energy gauging system, 238
- Single-gain corrections, 268
- Single-photon emission computed tomography (SPECT), 39, 149, 377–380, 378f, 379f, 380f, 381f, 382f
- Sinograms, 250, 253, 301–303
ring-removed, 458, 459
- Skyshine, 154
- Slice thickness, defined, 384
- Slit collimators, 217
- SmartCheck x-ray backscatter AIT, 486
- Snell's law, 104–105; *see also* [Refraction](#)
- SNMs (special nuclear materials), 420, 421, 421f, 470
- Sodium iodide, 262
- Solar Power Tower, 443, 444, 444f, 445
- Somatic effects, 136
- Source-detector geometry, 267
- Source emitter surface (SES), 225
- Source functions, family of, 331
- Source irradiance, 218, 270
- Source-side collimator, 254
- Source-spot blur, significance of, 336
- Source unsharpness, 332
- Space hardware, NASA, 442–445
advanced ablator materials, 442–445, 443f, 444f
fuel cell pump, diagnosis of failure, 445, 447f
rocket booster nozzle, 445, 446f
- Spatial invariance, measurement of MTF, 358–359
- Spatial resolution
area detectors, 337, 338–339, 419
beam hardening for, 341
components of, 335–339, 336f, 338f
data acquisition time and, 378
for DR and CT images, 336
KB reflection optics microscopes, 401, 402f
for linear-array detectors, 337–338, 339
object scatter on, 336
partial volume effects, 338
of pinhole (camera) microscope, 395–397, 396f
refractive lens microscope, 408
source-spot blur, significance of, 336
- Special nuclear materials (SNM), 132, 420, 421, 421f, 470
- Specificity, 21
- Spectra, 166–168; *see also* [X-ray tubes](#)
- Specular reflection, 99
- Speed, 247
- SpekCalc, 372, 373f
- Sponge porosity, 439
- Stand-alone EDSs, 475
- Stanford Linear Accelerator Center (SLAC), 179
- Stardust reentry capsule bond, 427, 428f, 429f
- Stardust shield, CT for, 443–445
- Stationary charge, 57
- Step-and-shoot data acquisition, 254
- Step functions, blur and, 356, 356f, 357, 357f
- Stepper motor, 227, 228
- Step wedge, 277–278, 278f
- Stereolithography (STL), 234
- Stopping power
of CsI(Tl), 333, 334f
detector, 335, 340
estimating, 332, 333
- Structured scintillators, 195–197, 201
- Submillimeter waves, 14
- Subtleties of radiographic imaging, 214–217; *see also* [Signal \(detected\) in x-ray imaging, sources of](#)
- Superscrew dislocations (SSDs), 392, 393
- SureScan nonrotating gantry CT system, 481, 481f, 482f
- Surface crack, 19f
- Swank noise, 188
- Synchrotron radiation, 241
- Synchrotrons, 175
- Synchrotron white-beam x-ray topography (SWBXT) imaging, 392–393, 393f
- Synchrotron x-ray source, 175–176, 211; *see also* [Electron accelerator-based sources](#)
- System scattered photons, 246

T

- Takeoff angle, 166, 167f
- Tamon Ten statue, 460, 462f
- Targets
DS laser ICF, 449, 450, 451f, 452, 452f
D-T solid-layer single-shell fusion, 422–424, 423f, 424f
LoTRT, 424–425, 425f, 426f
- Techniques, imaging, 369–413
active and passive (emission) CT, 377–380, 378f, 379f, 380f, 381f, 382f
automated defect recognition, 384–386, 385f
contrast agents, 369
dual energy for effective-atomic number, 369–377
high-energy, 374–377, 375f, 376f
low-energy, 370–374, 371t, 372f, 373f, 374f
physical basis for multiple-energy applications, 370–377
- overview, 369
- tomosynthesis, depth information without CT, 380, 382f, 383–384, 383f, 384f
- x-ray diffraction topography, 392–393, 393f
- x-ray forward and backscatter, 386–392, 387f, 389f, 390f, 391f
- x-ray microscopy and x-ray optics, 393–413
advantages, 394
diffraction optics microscopes, 409, 410–413, 411f, 412f, 413f
overview, 393–395, 394f
pinhole, 395–398, 396f
reflection optics microscopes, 399–407
refractive lens microscopes, 408–409, 409f, 410f
types, comparison of, 394, 394t

- Teflon, photoelectric absorption for, 370
Tek84, 486, 487f
Temporal control of x-ray source, 160
Tenth-value layer (TVL), 135, 155, 155f, 156t; *see also Shielding*
Terahertz (THz), 14
Teratogenic effects, 136
Terrestrial x and γ radiation, 148; *see also Natural background radiation*
Terrorist attacks, against US, 469, 469f
Test phantoms and test objects for system evaluation, 324–325
Thales amSi flat panel, detector, 453–454, 466
Thales flat panels, 269
Thermal area detector, 13f
Thermal diffusivity, 13f
Thermal imaging, 12–13; *see also Electromagnetic radiation methods*
Thermal neutrons, imaging with, 495–504
 boron, addition, 499, 499f
 Buna N, composition, 502, 503t
 corn rootworms, study of, 501, 502f
 CT radiographs, 499, 501f
 detection of corrosion in aircraft, 499
 detectors, 497–499, 498t
 flange configuration, 501, 502, 503f
 Inconel 625, composition, 502, 503t
 kinked O-ring, 499, 501f
 mass attenuation coefficients, 495, 496f
 photodiode arrays, 498
 PSP for, 497–498
 sources for, 495, 496
 accelerators, 496
 ^{252}Cf source, 496, 497f
 collimation, 496, 497f
 nuclear reactors, 495
 XRF, 499, 500f
Thermal protection system (TPS), components in, 443
Thermography, 12
Thermoluminescent dosimeters (TLD), 145, 146f
Thermopolis specimen, 457, 458f
Thomson scattering, 179–182; *see also Laser-driven x-ray sources*
Three-dimensional applications, high-energy photon, 424–469
 automotive, 432–441
 fuel pump, 441, 441f, 442f
 metal castings, 434, 435–440, 435f, 436f, 437f, 438f, 439f
 planetary transmission gear assembly, 440, 441f
 windshield wiper motor, 440, 440f
 aviation safety, DR and CT of pitot tubes, 427, 428, 430f, 431f
 CT and tomosynthesis of DoD ordnance, 452–457
 MFF, 455–457, 456f, 457f
 of WDU-17/B conventional warhead, 453–455, 453f, 454f, 455f
 CT of structures, by additive manufacturing, 466–469, 466f, 467f, 468f, 469f
 DR and CT of art and objects of cultural significance, 459, 460, 462–465
 Kongo Risiki, statue of, 460, 462f
 Michelangelo Buonarroti's statue of David, concerns with, 462–465, 463f, 464f, 465f
 pictures of period furniture, 460, 461f
 Tamon Ten statue, 462f, 466
DS laser ICF targets, 449, 450, 451f, 452, 452f
exploring limits of MeV imaging, 9 MV and 15 MV linacs, 445, 448f, 449, 449f, 450f
inspection of joinery, 425, 426–427
 metal weldment, 426, 427f
 Stardust reentry capsule bond, 427, 428f, 429f
LoTRT targets, 424–425, 425f, 426f
LX-17 HEs, characterization, 428, 429, 430, 432, 432f, 433f, 434f, 435f
NASA space hardware, 442–445
 advanced ablator materials, 442–445, 443f, 444f
 fuel cell pump, diagnosis of failure, 445, 447f
 rocket booster nozzle, 445, 446f
tomosynthesis of *Archaeopteryx* fossil, 457–459, 458f, 459f, 460f, 461f
turbomolecular vacuum pumps, 441, 442f
Three-dimensional (3D) printing, *see also Additive manufacturing (AM)*
Tilted-fan approach, 299
Time-delay integration (TDI), 192
Tissue equivalent, 143
Tissue weighting factor, 137, 138t
Titanium tube welds, inspection of, 384–386, 385f
Tomography
 CT, *see Computed tomography (CT)*
 IMPACT, 378, 379f
 IMT, 504
 PET, 377–380, 378f, 379f, 380f, 381f, 382f
 planar
 defined, 380
 image, estimating, 380, 382f, 383
 Rapiscan RTT system, 482, 483f
Tomosynthesis, CT and
 of *Archaeopteryx* fossil, 457–459, 458f, 459f, 460f, 461f
 depth information without, 380, 382f, 383–384, 383f, 384f
 of DoD ordnance, 452–457
 MFF, 455–457, 456f, 457f
 WDU-17/B conventional warhead, 453–455, 453f, 454f, 455f
Topography, x-ray diffraction, 392–393, 393f
Total attenuation/x-ray and γ -ray attenuation phenomena, 92–96; *see also Attenuation measurement units*
Total external reflection
 of x-rays, 104, 105; *see also Refraction*
Total internal reflection, 105, 105n
Tracer, NDE methods with; *see also Nondestructive evaluation (NDE)*
 dye penetrant testing, 18
 leak testing, 20
 magnetic particle testing, 18–19
Tracer gas, 20
Track-etch detectors, 498
Translucent material, 10
Transmission-anode geometry, 170
Transmission-anode tubes, 170
Transmission-anode x-ray tube, 170; *see also X-ray tubes*
Transmission imaging
 fundamental observed contrast for, 345
 noise, components of, 339–341, 341f
 properties of, 329
 x-ray, 358–359

Transmission x-ray digital radiograph, 8f
 Transmission x-ray radiograph, 44f
 Transportation Security Administration (TSA), 470–471, 472, 474, 484, 486
 Triaminotnitrobenzene (TATB), 428, 429, 430
 Tritium, 148
 True positive rate (TPR), calculation, 366–367
 Tungsten, 38
 photoelectric attenuation for, 370, 373–374
 Turbomolecular vacuum pumps, 441, 442f
 Turning mirror, 198
 Twin towers, 469f
 Two-dimensional applications, high-energy photon, 417–424
 automatic transmission, 418–419, 419f, 420f
 dual-MeV radiography for high-Z material discrimination, 419, 420–422, 421f, 422f, 422t
 40 mm grenades, DR of, 417–418, 418f
 phase contrast radiography of D-T solid-layer single-shell fusion target, 422–424, 423f, 424f

U

Ultrasonic testing, 16–17; *see also* Acoustic energy
 Ultrasonic waves, 43n
 Umbra, 159f
 Undulators, 176
 United States (US), protecting, 469–492
 all ports of entry, 470, 470f
 DHS, 469–470, 472, 474
 DoD, 469–470
 overview, 469–472, 469f, 470f, 471f
 terrorist attacks, 469, 469f
 threat vectors in civil aviation, 471, 471f
 TSA, 470–471, 472, 474, 484, 486
 x-ray imaging
 backscatter of passengers, 484, 485–487, 485f, 486f, 487f
 CT to inspect checked luggage, 474–478, 474f, 475f, 476f, 477f, 478f, 479f
 DR and backscatter to inspect carry-on luggage, 472–474, 472f, 473f, 474f
 DR and diffraction to inspect checked luggage, 478, 480, 480f
 nonrotating gantry security CT systems, 480–484
 radiography and backscatter for cargo NII, 487–492, 488f, 489f, 490f, 491f, 492f
 Rapiscan nonrotating gantry CT system, 482, 483f
 SureScan nonrotating gantry CT system, 481, 481f, 482f
 XinRay laboratory prototype nonrotating gantry CT system, 482, 484, 484f, 485f
 Unmodified (elastic or Rayleigh) scatter, 82
 US Air Force, 499
 U.S.S. Cole guided missile destroyer, 469f

V

Vacuum systems, 164; *see also* X-ray tubes
 Varian (BioImaging Research)
 linear detector array, 490
 mobile waste inspection trailer, 378, 381f
 Veiling glare, 129
 Vertical alignment cylinder (VAC), 304
 VG Studio MAX, 325

Vibrothermography, 13
 Virtual detector, 256, 268
 Visible-light microscopes, 394t, 395
 Visualization tools, 326
 Voxel values, 287

W

Wallis transform, 301
 Warhead, WDU-17/B conventional, 453–455, 453f, 454f, 455f
 Waste drum nondestructive assay system, 378, 379f, 380f
 Wave functions, 59, 60
 Wavelength, 70
 WDU-17/B conventional warhead, CT of, 453–455, 453f, 454f, 455f
 Weiner filter deconvolution, 271
 Weldment, metal, 426, 427f
 White radiation, 62
 Wiener filter, 215
 Wiggler, 176
 Windshield wiper motor, 440, 440f
 Wire image quality indicator, 276
 Wölter objective reflection optics microscopes, 401, 402–407, 403f, 404f, 405f, 406f, 407f
 World Federation of NDE Centers, 3

X

XCOM program, 92, 96
 XDi, 480
 XinRay laboratory prototype nonrotating gantry CT system, 482, 484, 484f, 485f
 Xradia Inc., 411, 412f, 413f, 425, 452
 X-ray and γ -ray imaging
 features of, 43–48, 47t
 practical/operational issues, 53
 shortcomings, 48–53
 X-ray and γ -ray sources, physics of, *see* High-energy photons, types of
 X-ray attenuation, 205, 209t
 X-ray detectors, 270
 X-ray fluorescence (XRF), 81, 499, 500f
 X-ray gauging, 415
 X-ray history
 computed tomography (CT), 39–40
 Coolidge tube, 38–39
 discovery of x-rays, 29–33
 foundation, 27–29
 industrial computed tomography, 40–41
 paper on x-rays, 34–36
 radiation accidents, 41–42
 radiation therapy, 38
 radioactivity, discovery of, 36–37
 X-ray imaging, 6–9; *see also* Nondestructive evaluation (NDE)
 backscatter imaging, *see* Backscatter imaging
 diffraction system, *see* Diffraction system
 forward imaging, *see* Forward imaging
 high-energy photon applications, *see* High-energy photon applications
 neutron and proton imaging, *see* Neutron and proton imaging
 protecting US, 469–492; *see also* United States (US)
 quality, *see* Image quality

- radiography, *see* Radiography
techniques, *see* Techniques
transmission imaging artifacts, 341–342
- X-ray phase-contrast radiography, 1108–112
- X-ray phase effects; *see also* High-energy photon (x-ray/
 γ -ray) interactions with matter
about, 99–101
diffraction, 106–108
refraction
about, 102–104
Snell's law, 104–105
total external reflection of x-rays, 105
- x-ray phase-contrast radiography, 108–112
- X-ray radiation generation, electrons and, *see* Electrons
and x-ray radiation generation
- X-ray scatter corrections, 214–217; *see also* Signal
(detected) in x-ray imaging, sources of
- X-ray simulation (XRSIM), 117–119; *see also* Ray tracing
- X-ray sources, 266
- X-ray tubes; *see also* Electrically powered x-ray sources
common design elements/subsystems of x-ray tubes
anode, 161–163
heel effect, 168–169
high-voltage power supply, 164
high-voltage power supply waveforms, 164–165
kV versus kV_p, 165–166
spectra, 166–168
vacuum, 164
x-ray window, 163–164
- x-ray tube configurations/tube-like sources
contemporary cold cathode x-ray tube, 174
liquid-anode x-ray tube, 174
metal–ceramic x-ray tube, 169–170
microfocus x-ray tube, 173
reverse-geometry x-ray source, 173–174
rotating-anode x-ray tubes, 171–173
transmission-anode x-ray tube, 170
- X-ray window, 163–164